Mehmet Ertuğrul
İ.Yücel Özbek
Abdullah Başçi *Editors*

International Symposium on Applied Sciences and Engineering

Proceedings of ISASE 2021

ERTUAL AKADEMİ

ISBN: 978-605-68837-2-9

ISASE2021

INTERNATIONAL SYMPOSIUM ON APPLIED SCIENCES AND ENGINEERING

BOOK OF FULL TEXT

07-09 April 2021 / Erzurum, Turkey

Organized by

Sponsored by

15 May 2021

Book of Full Text of the International Syposium on Applied Sciences and Engineering (ISASE2021)

Prof. Dr. Mehmet ERTUGRUL

Assoc. Prof. Dr. İ. Yücel ÖZBEK

Assoc. Prof. Dr. Abdullah BAŞÇİ

Editors

Copyright

Original material in this book may be reproduced with the permission of the publisher, provided that (1) the material is not reproduced for sale or profitable gain, (2) the author is informed, and (3) the material is prominently identified as coming from the International Symposium of Appliend Sciences and Engineering: The authors are responsible for the contents of their abstracts and full pappers. The views expressed in the abstracts and fulltex in this publication are those of the individual authors and are not necessarily shared by the editor or the reviewers.

All rights reserved
2021
ISBN: 978-625-7960-32-8

Published by the Office of International Affairs, Atatürk University, Erzurum, TURKEY

Committee

Chairman
Assoc. Prof. Dr. İ. Yücel ÖZBEK

Co-Chairman
Prof. Dr. Mohd Nizar Hamidon
Assoc. Prof. Dr. Burak Erkayman
Assoc. Prof. Dr.Güven Turgut
Assoc. Prof. Dr. Abdullah Başçi

Honorary Committee
Prof. Dr. Ömer ÇOMAKLI (Rector of Atatürk University)
Prof. Dr. Bülent Çakmak (Rector of Erzurum Technical University)
Prof. Dr. Mehmet Ertuğrul

Secretary
Assoc. Prof. Dr. Abdullah Başçi

Organizing Committee
Assoc. Prof. Dr. Rıza Polat, **Turkey**
Assoc. Prof. Mehmet Emin Arzutuğ, **Turkey**
Assoc. Prof. Dr. Ahmet Dumlu, **Turkey**
Assoc. Prof. Dr. Kağan Koray Ayten, **Turkey**
Prof. Dr. Burak Özpineci, **USA**
Assoc. Prof. Dr. Badiea A. Mohammed, **Yemen**
Assoc. Prof. Dr.Serkan BAYAR, **Turkey**
Assoc. Prof. Dr. Gökay Akkaya, **Turkey**
Assoc. Prof. Dr. Oğuz Akın DÜZGÜN, **Turkey**
Assist. Prof. Dr. Mustafa Tolga Yurtcan, **Turkey**
Assist. Prof. Dr. Emin A. Oral, **Turkey**
Assist. Prof. Dr. Yousef Sardahi,**USA**
Assist. Prof. Dr. Engin Kocadağıstan, **Turkey**
Assist. Prof. Dr. Çağlar YÜKSEL, **Turkey**
Assist. Prof. Dr. Bilal USANMAZ,**Turkey**
Prof. Dr. Xerman De la Fuente Leis, **Spain**
Prof. Dr. Javier Campo, **Spain**
Prof. Dr. Anis Nurashikin Nordin,**Malaysia**
Assoc. Prof. Dr. Nur Hüseyin Kaplan,**Turkey**
Assist. Prof. Dr. Çağlar Duman,**Turkey**
Assoc. Prof. Dr. Demet İSKENDEROĞLU,**Turkey**
Assoc. Prof. Dr.Harun GÜNEY,**Turkey**
Assist. Prof. Dr.Hacı Mehmet Güzey,**Turkey**
Assist Prof. Muhammed Fatih Çorapsız, **Turkey**
Assist. Prof. Dr. Barış Özyer, **Turkey**
Assoc. Prof. Dr. Semet ÇELİK, **Turkey**
Assoc. Prof. Dr. Bekir GÜRBULAK, **Turkey**

Heads of Local Committee
Hussein M.A. MOHAMMED, Ataturk University, **Turkey**
Onur Erdem Korkmaz, Ataturk University, **Turkey**
Aslı Nur Ömeroğlu, Ataturk University, **Turkey**

Local Committee
Atakan Abuşoğlu, Ataturk University, **Turkey**
Merve Acar, Ataturk University, **Turkey**
Ayşe Bağıran, Ataturk University, **Turkey**
Kaan Can, Ataturk University, **Turkey**
Mehmet Yılmaz, Ataturk University, **Turkey**
Bahadır Özkılbaç, Ataturk University, **Turkey**
Serdar Tezgel, Ataturk University, **Turkey**
Nurgüneş Önal, Ataturk University, **Turkey**
Oğuzhan Çelebi, Ataturk University, **Turkey**
Elif Akarsu, Ataturk University, **Turkey**
Rukiye Aksakal, Ataturk University, **Turkey**
Emir Çepni, Ataturk University, **Turkey**
Burcu Tiryaki, Ataturk University, **Turkey**
Mustafa Bulut, Ataturk University, **Turkey**
Hayriye Tuğba Sekban, Bayburt University, **Turkey**
Nida Kumbasar, Ataturk University, **Turkey**
Rabiye Kılıç, Ataturk University, **Turkey**
Fatih Tutar, Ataturk University, **Turkey**
Hilal Kübra Sağlam, Ataturk University, **Turkey**
Merve Polat, Ataturk University, **Turkey**
Faruk Baturalp Günay, Ataturk University, **Turkey**
Ibrahim A. Alameri, Sana'a University, **Yemen**
Elif ERÇARIKÇI, Ataturk University, **Turkey**
Sedanur Keleş, Ataturk University, **Turkey**

Scientific Committee
Prof. Dr. Recep Sadeler, Ataturk University, **Turkey**
Prof. Dr. Abdulkadir Cüneyt Aydın, Ataturk University, **Turkey**
Prof. Dr. Mehmet Ertuğrul, Ataturk University, **Turkey**
Prof. Dr. Davut Hanbay, İnönü University, **Turkey**
Prof. Dr. Uğur Cem Hasar, Gaziantep University, **Turkey**
Prof. Dr. Ahmet Cansız, İstanbul Technical University, **Turkey**
Prof. Dr. Hayrunnisa Nadaroğlu, Ataturk University, **Turkey**
Prof. Dr. Emre Gür, Ataturk University, **Turkey**
Prof. Dr. Mutlu Kundakçi, Ataturk University, **Turkey**
Prof. Dr. Amer Ali Sallam, Taiz University, **Yemen**
Prof. Dr. Hasan Efeoğlu, Ataturk University, **Turkey**
Prof. Dr. Bülent Çavuşoğlu, Ataturk University, **Turkey**
Prof. Dr. Mehmet Akif Ceviz, Erzurum Technical University, **Turkey**
Prof. Dr. Ferhat Bülbül, Erzurum Technical University, **Turkey**
Prof. Dr. Songül Duman, Erzurum Technical University, **Turkey**
Prof. Dr. Çağrı Çırak, Erzincan Binali Yıldırım University, **Turkey**
Prof. Dr. Tevhit Karacalı, Ataturk University, **Turkey**
Prof. Dr. Mohammed Al-Bukhaiti, Sana'a University, **Yemen**
Prof. Dr. Temel Kayıkçıoğlu, Karadeniz Technical University, **Turkey**
Prof. Dr. Ali Gangal, Karadeniz Technical University, **Turkey**
Prof. Dr. İlker Kazaz, Erzurum Technical University, **Turkey**
Prof. Dr. Ebru Şenadım Tüzemen, Cumhuriyet University, **Turkey**
Prof. Dr. İdris Akyüz, Eskişehir Osmangazi University, **Turkey**
Prof. Dr. İsmail Hakkı Altaş, Karadeniz Technical University, **Turkey**
Prof. Dr. Naci Genç, Van Yüzüncü Yıl University, **Turkey**
Prof. Dr. Mustafa Ulutaş, Karadeniz Technical University, **Turkey**
Prof. Dr. Aytunç Ateş, Ankara Yıldırım Beyazıt University, **Turkey**
Prof. Dr. Anis Nurashikin Nordin, International Islamic University, **Malaysia**
Prof. Dr. Xerman De la Fuente Leis, University of Zaragoza, **Spain**

Prof. Dr. Nor Ashidi Mat Isa, University of Science, **Malaysia**
Prof. Dr. Sulaiman Wadi Harun, University of Malaya, **Malaysia**
Prof. Dr. İrfan Kaymaz, Erzurum Technical University, **Turkey**
Prof. Dr. Ali Fatih Yetim, Erzurum Technical University, **Turkey**
Prof. Dr. Ömer Gündoğdu, Ataturk University, **Turkey**
Prof. Dr. Norhayati Soin, University of Malaya, **Malaysia**
Prof. Dr. Resul Daş, Fırat University, **Turkey**
Assoc. Prof. Dr. Abdullah Başçi, Ataturk University, **Turkey**
Assoc. Prof. Dr. İbrahim Yücel Özbek, Ataturk University, **Turkey**
Assoc. Prof. Dr. Ahmet Dumlu, Erzurum Technical University, **Turkey**
Assoc. Prof. Dr. Kağan Koray Ayten, Erzurum Technical University, **Turkey**
Assoc. Prof. Dr. Rıza Polat, Ataturk University, **Turkey**
Assoc. Prof. Dr. Burak Erkayman, Ataturk University, **Turkey**
Assoc. Prof. Dr. Oğuz Akın Düzgün, Ataturk University, **Turkey**
Assoc. Prof. Dr. Güven Turgut, Erzurum Technical University, **Turkey**
Assoc. Prof. Dr. Mohamed Bajash Al-Sharabi, Taiz University, **Yemen**
Assoc. Prof. Dr. Mehmet Emin Arzutuğ, Ataturk University, **Turkey**
Assoc. Prof. Dr. Badiea A. Mohammed, Taiz University, **Turkey**
Assoc. Prof. Dr. Kader Dağcı Kıranşan, Ataturk University, **Turkey**
Assoc. Prof. Dr. Onur Şenol, Ataturk University, **Turkey**
Assoc. Prof. Dr. Hülya Öztürk Doğan, Ataturk University, **Turkey**
Assoc. Prof. Dr. Mustafa Erdem Sağsöz, Ataturk University, **Turkey**
Assoc. Prof. Dr. Nur Hüseyin Kaplan, Erzurum Technical University, **Turkey**
Assoc. Prof. Dr. Halim Kovacı, Ataturk University, **Turkey**
Assoc. Prof. Dr. Erdal Sönmez, Ataturk University, **Turkey**
Assoc. Prof. Dr. Abdulkerim Karabulut, Erzurum Technical University, **Turkey**
Assoc. Prof. Dr. Fatma Bayrakçeken Nişancı, Ataturk University, **Turkey**
Assoc. Prof. Dr. Bilal Nişancı, Ataturk University, **Turkey**
Assoc. Prof. Dr. Engin Yener, Iğdır University, **Turkey**
Assoc. Prof. Dr. Muhammed Yasin Çodur, Erzurum Technical University, **Turkey**
Assoc. Prof. Dr. Özkan Bayram, Bayburt University, **Turkey**
Assoc. Prof. Dr. Önder Aydemir, Karadeniz Technical University, **Turkey**
Assoc. Prof. Dr. Fatih Tosunoğlu, Erzurum Technical University, **Turkey**
Assoc. Prof. Dr. Esra Kavaz, Ataturk University, **Turkey**
Assoc. Prof. Dr. Güzin Ulutaş, Karadeniz Technical University, **Turkey**
Assoc. Prof. Dr. Ezgi Topçu, Ataturk University, **Turkey**
Assoc. Prof. Dr. Gökçe Hacıoğlu, Karadeniz Technical University, **Turkey**
Assoc. Prof. Dr. Ebru Akkemik, Siirt University, **Turkey**
Assoc. Prof. Dr. Emre Özkop, Karadeniz Technical University, **Turkey**
Assoc. Prof. Dr. Gökay Akkaya, Ataturk University, **Turkey**
Assoc. Prof. Dr. Abdullah Mohsen Zeyad, Jazan University, **KSA**
Assoc. Prof. Dr. Akın Özçift, Manisa Celal Bayar University, **Turkey**
Assoc. Prof. Dr. Murad A. Rassam, Taiz University, **Yemen**
Assoc. Prof. Dr. Asrulnizam Abd Manaf, University of Science, **Malaysia**
Assoc. Prof. Dr. Abdul-Malik Momin, Sana'a University, **Yemen**
Assoc. Prof. Dr. Bassam A. Tayeh, Islamic University of Gaza, **Palestine**
Assoc. Prof. Dr. Eyüphan Manay, Erzurum Technical University, **Turkey**
Assist. Prof. Dr. Emin Argun Oral, Ataturk University, **Turkey**
Assist. Prof. Dr. Bilal Usanmaz, Ataturk University, **Turkey**
Assist. Prof. Dr. Bilal Tütüncü, Van Yüzüncü Yıl University, **Turkey**
Assist. Prof. Dr. Muhammet Raci Aydın, Iğdır University, **Turkey**
Assist. Prof. Dr. Mustafa Tolga Yurtcan, Ataturk University, **Turkey**
Assist. Prof. Dr. Fatma Karagöl, Ataturk University, **Turkey**
Assist Prof. Dr. Gökhan Öztürk, Ataturk University, **Turkey**
Assist. Prof. Dr. Yousef Sardahi, Marshall University, **USA**
Assist.Prof Dr. Ferhat Bozkurt, Ataturk University, **Turkey**

Assist. Prof. Dr. Mete Yağanoğlu, Ataturk University, **Turkey**
Assist. Prof. Dr. Amin Saif Ahmed, Taiz University, **Yemen**
Assist. Prof. Dr. Ahmet Coşkunçay, Ataturk University, **Turkey**
Assist. Prof. Dr. Deniz Dal, Ataturk University, **Turkey**
Assist. Prof. Dr. Aysel Kekillioğlu, Nevşehir Hacı Bektaş Veli University, **Turkey**
Assist. Prof. Dr. Ghazi Hassan Ali Alnowaini, Taiz University, **Yemen**
Assist. Prof. Dr. Yaşar Özkan Yeşilbağ, Erzincan Binali Yildirim University, **Turkey**
Assist. Prof. Dr. Fatma Nur Tuzluca Yeşilbağ, Erzincan Binali Yildirim University, **Turkey**
Assist. Prof. Dr. Hatice Bayrakçeken, Ataturk University, **Turkey**
Assist. Prof. Dr. İbrahim Hakkı Karakaş, Bayburt University, **Turkey**
Assist. Prof. Dr. Hayrunnisa Mazlumoğlu, Ataturk University, **Turkey**
Assist. Prof. Dr. Ömer Çoban, Ataturk University, **Turkey**
Assist. Prof. Dr. Miraç Dilruba Geyikoğlu, Ataturk University, **Turkey**
Assist. Prof. Dr. Muhammed Fatih Çorapsız, Ataturk University, **Turkey**
Assist. Prof. Dr. Çağlar Duman, Erzurum Technical University, **Turkey**
Assist. Prof. Dr. Onur Çomaklı, Erzurum Technical University, **Turkey**
Assist. Prof. Dr. İrfan Yıldırım, Erzurum Technical University, **Turkey**
Assist. Prof. Dr. Sibel Morkoç Karadeniz, Erzincan Binali Yildirim University, **Turkey**
Assist. Prof. Dr. Burcu Bozkurt Çırak, Erzincan Binali Yildirim University, **Turkey**
Assist. Prof. Dr. Meltem Gör Bölen, Erzurum Technical University, **Turkey**
Assist. Prof. Dr. Hilal Koç Polat, Erzurum Technical University, **Turkey**
Assist. Prof. Dr. Hacı Mehmet Güzey, Erzurum Technical University, **Turkey**
Assist. Prof. Dr. Muhammed Yiğider, Erzurum Technical University, **Turkey**
Assist. Prof. Dr. Turgay Duman, Erzurum Technical University, **Turkey**
Assist. Prof. Dr. Aytaç Levet, Ataturk University, **Turkey**
Assist. Prof. Dr. Sevda Sarıtaş, Ataturk University, **Turkey**
Assist. Prof. Dr. Mehmet Öztürk, Karadeniz Technical University, **Turkey**
Assist. Prof. Dr. Esra Odabaş Yıldırım, Ataturk University, **Turkey**
Assist. Prof. Dr. Ali Ünlütürk, Erzurum Technical University, **Turkey**
Assist. Prof. Dr. Sait Taş, Ataturk University, **Turkey**
Assist. Prof. Dr. Türkay Kotan, Erzurum Technical University, **Turkey**
Assist. Prof. Dr. Fatih Mehmet Nuroğlu, Karadeniz Technical University, **Turkey**
Assist. Prof. Dr. Mehmet Saadeddin Öztürk, Karadeniz Technical University, **Turkey**
Assist. Prof. Dr. Bilge Han Tozlu, Hitit University, **Turkey**
Assist. Prof. Dr. Dilek Okuyucu, Erzurum Technical University, **Turkey**
Assist. Prof. Dr. Sulaiman Al-Safi, Sana'a University, **Yemen**
Assist. Prof. Dr. Eyüp Gedikli, Karadeniz Technical University, **Turkey**
Assist. Prof. Dr. Mustafa Şinasi Ayas, Karadeniz Technical University, **Turkey**
Assist. Prof. Dr. Tuba Çakıcı, Ataturk University, **Turkey**
Assist. Prof. Dr. Fares Saeed Saeed Al-Zaghir Al-Areqi, Sana'a University, **Yemen**
Assist. Prof. Dr. Faruk Yeşildal, Ataturk University, **Turkey**
Assist. Prof. Dr. Barış Özyer, Ataturk University, **Turkey**
Assist. Prof. Dr. Fatih Akyol, Yıldız Technical University, **Turkey**
Assist. Prof. Dr. Gülşah Tümüklü Özyer, Ataturk University, **Turkey**
Assist. Prof. Dr. Murat Kıranşan, Gümüşhane University, **Turkey**
Assist. Prof. Dr. Kenan Çiçek, Iğdır University, **Turkey**
Assist. Prof. Dr. Asuman Günay Yılmaz, Karadeniz Technical University, **Turkey**
Assist. Prof. Dr. Kamil Orman, Erzincan Binali Yıldırım University, **Turkey**
Assist. Prof. Dr. Hatem Al-Dois, Emirates International University, **Yemen**
Assist. Prof. Dr. Alpaslan Bayraktar, Iğdır University, **Turkey**
Assist. Prof. Dr. Engin Kocadağıstan, Ataturk University, **Turkey**
Assist. Prof. Dr. Levent Bayındır, Ataturk University, **Turkey**
Assist. Prof. Dr. Kutsi Tuncer, Ataturk University, **Turkey**
Assist. Prof. Dr. Bahri Gür, Iğdır University, **Turkey**
T.A.Dr. Ercüment Yılmaz, Karadeniz Technical University, **Turkey**
T.A. Hilal Kübra Sağlam, Ataturk University, **Turkey**

Assist. Dr. Merve ACAR, Ataturk University, **Turkey**
Assist. Dr. Esra Cinan, Ataturk University, **Turkey**
Assist. Dr. Mine AKSOY, **Turkey**
Dr. Mehmet Bozuyla, **Turkey**
Dr. Hamet Shamasi, **Iran**
Dr. Mesut Atasoy, **Turkey**
Dr. Mojtaba Farhangmehr, **Turkey**

CONTENTS

Committee ..... **iii**
Welcome to ISASE2021 ..... **xv**
Message from Chair, ISASE2021 ..... **xvi**
Message from Dean of the Faculty of Engineering – Ataturk University, Turkey ..... **xvii**
Message from Director of the Institute of Advanced Technology (ITMA), UPM, Malaysia ..... **xviii**
Message from Vice Rector of Erzurum Technical University, Turkey ..... **xix**
Message from Deputy Vice-Chancellor ..... **xx**
of Universiti Putra Malaysia, Malaysia ..... **xx**
Message from Vice Rector of Atatürk University, Turkey ..... **xxi**

INVITED SPEAKERS

Non-linearity assessment of Class E Switching GaN HEMT RF Amplifier for broadband transponder
Basuki Rachmatul Alam, ... 24
Ensuring Quality of Data in the Internet of Things for Healthcare Monitoring Applications Via Anomaly Detection Methods
Assoc. Prof. Dr. Murad A. Rassam 25
Characterization of Polybutylene Succinate/EFB fibre/Modified Tapioca Starch and Glycerol for Food Packaging Application
Khalina A., Rafiqah S.A. 26
Nanoparticle Network as an Effective In-MaterioReservoir Computing Device
Yuki Usami, Hirofumi Tanaka 27
Effect of Nitrogen Doping of Carbon Supports on PEM Fuel Cell Performance
Prof. Dr. Ayşe Bayrakçeken Yurtcan 28
Passive Surface Acoustic Wave Resonator Platform for Wireless Sensor Applications
Prof. Dr. Mohd Nizar Bin Hamidon 29
Glass Ionomer Cement Using Alumino-Silicate-Fluoride Based Glass Ceramics
Mohd Hafiz Mohd Zaid, Khamirul Amin Matori, Esra Kul 30
Dye Sensitized Solar Cell Efficiency Enhancement
Assoc. Prof. Ts. Dr. Suhaidi Shafie 31
Decision Making Mechanisms in Hybrid Energy Storage Technologies
Prof. Dr. Ahmet Cansız 32
Wired and Wireless Extreme Fast Chargers **33**
Prof. Dr. Burak Özpineci 33
Plastic Brick as an Alternative Conventional Brick: Fabrication, Mechanical and Thermal Properties
Badiea A. M., Ibtisam M. K., Amer H. A., Adel A.A 34
Investigation of different steel simple connections under column-loss scenario: considering the effects of a transverse beam
Mohammed A. Alrubaidi, Sulaiman I. Al-Safi 35
Recent trends about gas sensing through semiconductor
Prof. Dr. Vincenzo Guidi 36
Coupled Maxwell and density functional description of the interaction of light and nanostructures
Prof. Dr. Varga KALMAN 37
Stabilization by thermal fluctuations of a new skyrmionic phase at low temperature in cubic helimagnets: Are new phases still waiting to be discovered?
Victor Laliena, Javier Campo 38
Blockchain in Healthcare: Applications, Potentials, and Challenges
Dr.Fathey M.A.Mohammed 39
Antenna With Electromganetic Band Gap (EBG) Structure For Wireless Application
Prof. Dr. Mohamad Kamal A. Rahim 40
3D tomographical imaging of localized surface plasmon resonances of cylindrical and dimeric spherical nanocrescents
Prof. Dr. Karim Abbasian 41
Thin Film Solar Photovoltaic Cells – Status and Way Forward
Prof. Dr. Nowshad Amin 42
Screen-printed group IV semiconductors on Silicon
Marwan Dhamrin, Shota Suzuki, Masahiro Nakahara, Moeko Matsubara 43
Electromagnetic Micropump Incorporating the Polymer Composite based Magnetic Membrane for Biomedical Application
Assoc. Prof. Dr. Jumril Yunas 45
Grid of The Future (GoTF) Advancing Grid Transformation in Malaysia
Prof. Dr. M. Zainal Abidin Ab Kadir 46

Application of Natural Mode Series on Material Characterization at Microwave Frequencies
Prof. Dr. Uğur Cem HASAR 47
Laser Line Scan surface processing: nanostructure and microstructure control
A. Cubero, E. Martínez, H. Santos, H. Amaveda, J. A. Bea, L. Porta, A. Frechilla, E. Lacruz, F. Toldra-Reig, D. Muñoz-Rojas, L.A. Angurel, G. F. de la Fuente 48
Laser remelting of Al2O3 coatings on Cu: A way to increase thermal conductance in heat sinks
A. Cubero, E. Martínez, G. F. de la Fuente, I. G. Cano, S. Dosta, L.A. Angurel 49
Enhancing the Performance of Coiled Carbon Nanofibers/Mill Scale Nanocomposites at X- and Ku-band Frequency
Ismayadi Ismail, Mehmet Ertugrul, Mohd Nizar Hamidon, Rabaah syahidah Azis, Intan Helina Hasan, Yasar Ozkan Yesilbag, Fatma Nur Tuzluca, Gokhan Ozturk, Ugur Cem Hasar 50
Phenomenological Aspects of Thin-Walled Cylindrical Reservoirs, Experimental Work-Overview
Prof. Dr. Abdulkadir Cüneyt AYDIN 51
Impacts of Carbon Quantum Dots on Chili (Capsicum annuum L.) Plant Growth
Suraya Abdul Rashid, Tan Tong Ling 52
Hyperspectral Imaging: Basics and its Application for Ground Based Surveillance System for Explosive Detection
Assoc. Prof. Dr. Alper Koz 53
Neuroimaging in everyday life with a novel brain imaging modality
Assist. Prof. Dr. Sinem Burcu Erdoğan 54
Neurorobotics and Brain computer interface for robotic rehabilitation
Dr. Noman Naseer 55
Enhanced Performance of Flexible Microstrip Patch Antenna with Ferrite Thick Film Inclusion
Intan Helina Hasan, Mohd Nizar Hamidon, Alyani Ismail, Ismayadi Ismail, Nur Alin Mohd Azhari, Saman Azhari, Muhammad Asnawi Mohd Kusaimi, Farah Nabilah Shafiee 56
EEG based Brain Computer Interface System Design Techniques
Onder Aydemir 57
Functional Nanomaterials for Electronic Applications
Dr. Zainab Yunusa 58
Engineering of Carbon-Based Nanofiller ReinforcedPolyurethane Nanocomposites
Levent TRABZON 59
Multi-Objective Optimal Controls
Assist. Prof. Dr. Yousef Sardahi 60
Applications of the Renewable Energy in Yemen
Abdul-Malik Momin 61
MM-RAM composites as a wide band radar absorber
Prof. Dr. Mehmet Ertugrul 62

ORAL PRESENTATIONS

ROS Based SLAM and Navigation for Automated Guided Vehicle Simulated with Gazebo
İbrahim Öztürk, Abdullah Başçi, References 69
Switching Sequence and Modulation Techniques of Modular Multilevel Converter
Nasiru B. Kadandani, References 73
Design and Optimization of CPW-Fed Patch Printed Antenna for Underwater Communication
Nor Hidayah Daud, Alyani Ismail, Aduwati Sali 74
High Gain Receiving Antenna Developed for ISAR Applications Using 2.4 GHz WLAN Signals
Göker Şener 78
Design and Simulation of Crossed Walls Security Detection System
Muhammad Baballe Ahmad, Mukhtar Ibrahim Bello, Abubakar SAdiq Muhammad 82
The Need for Artificial Egg Incubation
Muhammad Baballe Ahmad, Abubakar Sadiq Muhammad, Ishaq Auwal Balarabe 86
COVID-19 Detection from Chest X-Ray Images Using Dense Convolutional Network
Ferhat Bozkurt, Mete Yağanoğlu 89
Theoretical Investigation of Biomofs For Anesthetic Xe Recovery
Zekiye Erarslan, Yeliz Gürdal 93
Comprehensive Study on the Interfacial charge transfer dynamics of Inorganic Nanowires Incorporated Bulk Heterojunction Photoactive Layer
Kai Jeat Hong, Sin Tee Tan, Kok-Keong Chong, Chi Chin Yap 94
Calibration-Free Broadband Determination of Soil Permittivity by Coaxial Line Measurements
Hafize Hasar, Taskin Oztas, Mustafa Yildırim Canbolat, Nevzat Aslan 97
Electrochemical Synthesis and Characterization OF MoO3 Nanostructured Photoelectrodes
Emir Çepni, Ahmet Korkmaz, Hülya Öztürk Doğan 101
Green Synthesis of Nanoflowers and Investigation of Their Usability in Wastewater Treatment
Hayrunnisa NADAROGLU 104



Effect of Nitrogen Doping of Carbon Supports on PEM Fuel Cell Performance
Ayşe Bayrakçeken Yurtcan 106
Application of Copperas as Chemical Coagulant for Industrial Water Treatment
Hamzah, Sofiah, Che Harun, Mohd Hakim, Mohamad, Nurul Aqilah, Awang, Mohamad, Wan Abdul Rahman, Wan Rafizah 109
Modification of bentonite: Effect of different treatments on the adsorption ability - A mini review
Aiizat Ikhwan bin Abdul Jalil, Suzylawati binti Ismail 112
Review on the potential of superhydrophilic polymeric mixed matrix membrane in loop heat pipe application for miniaturized cooling system
Nor Aini Ahmad, Syamsul Rizal Abd Shukor 115
A New Heat Sink Design for Cooling Microprocessors and Investigation of Cooling Performance
Mehmet Emin Arzutuğ, Abdullah Başçi 120
Boiler Efficiency and CO2 Emission with Different Types of Bituminous Coal at Thermal Coal Fired Power Plant
Salmi b Samsudin, Nuraini bt Abd Aziz, Abdul Aziz b Hairuddin 124
3D Printing: Functionality Graded Materials (FGM) via Fused Deposition Modelling (FDM)
Zairul Amri Zakaria, B.T.H.T Baharudin, MKA Ariffin 129
Crease Lines Effect to the Energy Absorption of Thin-walled Structures 133
Siti Marhainis, A. M., Nuraini, A. A., Azmah Hanim, M. A 133
Three dimensional simulation and analysis on Ti6Al4V turning using FEM
Yavuz KAPLAN 137
Effect of Different Penetrator Shapes on the Quasi-Static Perforation Response of Bilayer Plates
Nahit Öztoprak 139
Anthocyanin of Natural Dyes as Photosensitizer for Solar Cell Application
Nurul Alfatihah Mohd Arifin, Hasiah Salleh, Ahmad Nazri Dagang 143
Titanium Oxide Plasma Treated to Enhance the Performance of Hybrid Solar Cells
Nur Salihah Alias, Ahmad Nazri Dagang, Hasiah Salleh 144
Minor Criteria of Erbium Oxide Determining the Zinc Tellurite Glass Performance
Nazirul Nazrin Bin Shahrol Nidzam, Halimah Mohamed Kamari, Masera Marian Mukhtar 145
Effect of Sb Doping on the Surface Morphology, Structural, Properties of Zinc Oxide Thin Films
Elif AKARSU, Mehmet ERTUĞRUL 147
Decision Making Mechanisms in Hybrid Energy Storage Technologies
Ahmet Cansız 150
Integral Terminal Sliding Mode Controller for Trajectory Tracking Control of Unmanned Ground Vehicle
Hayriye Tuğba SEKBAN, Kaan CAN, Abdullah BAŞÇİ 155
Performance Evaluation of Microstrip Antenna Based on Different Shapes of Defected Ground Structure (DGS) at 28 GHz
Alyani Binti Ismail, Mohd Fadlee Bin A Rasid, Mohd Nizar B Hamidon, Raja Syamsul. A. Raja Abdullah, Nafaa Mohamad Shebani 161
Facile Design of a Metamaterial Absorber for X-band Radar Applications
Aykut Coskun, Ahmet Teber, Mehmet Ertugrul 167
Inverter based OTA Design for Second-Order G_m-C filters
Mesut Atasoyu 171
A study of cure kinetics of polyurethane/epoxy compositions filled with modified boron nitride
Nikita Bratasyuk, Vjacheslav Zuev 174
Preparation of Manganese-Containing Magnetic Nanocomposites for Biomedical Applications
Okan Icten 178
Positron annihilation lifetime spectroscopy: a sensitive probe to determine free volume holes in polymers
Meshude Akbulut Söylemez 179
Effective Desulfurization of Coal with Oak Ash
Gizem Hazan Çağlayan, Ubeyde İpek 181
Short-term Variations of Pore-water Pressure Due to Diurnal Temperature Changes in Soil Slopes
Nuraddeen Muhammad Babangida, Khamaruzaman Wan Yusof, Muhammad Raza Ul Mustafa 184
The effect of waste mineral additives and long-term moisture insulation in volcanic ash-based geopolymer concretes
Yavuz YEGİN, Rıza POLAT, Fatma KARAGÖL, Ramazan DEMİRBOĞA 188
Effects of the damping coefficient on interconnected adjacent buildings for different soil conditions
Yavuz Selim HATİPOĞLU, Oğuz Akın DÜZGÜN 194
Shear Wall Effectiveness of Reinforced Concrete Structures
Barış ERDİL, Yusuf GÜNDÜZ,
Numerical simulation of Organic-Inorganic Lead Halide Perovskite (CH3NH3PbI3) solar cells using 1D-SCAPS simulator
Hajar Benali, Bouchaib Hartiti, Fatima Lmai, Hicham Labrim, Philippe Thevenin 203

Effect of thiourea concentration on characteristics of CZTS thin layer prepared by low cost sol gel method for solar energy applications
Ahmed ZITI, Bouchaib HARTITI, Hicham LABRIM DERS, Abdelkrim BATAN, Salah FADILI, Abderraouf RIDAH, Mounia TAHRI, Amine BELAFHAILI, Philippe THEVENIN 206
The effect of window film on building energy consumption in hot climate zone
Kübra Sümer Haydaraslan, Yalçın Yaşar 212
Examination of the Effect of Heat Treatment Process on High Temperature-High Activity Nickel Aluminide Coating on CM247LC
Ahmet Arda Inceyer, Gökhan Güven, Kaan Demiralay 216
The use of low-cost technique to prepare pure TiO_2 thin films
Youssef DOUBI, Bouchaib HARTITI, Maryam SIADAT, Hicham LABRIM, Salah FADILI, Mounia TAHRI, Amine BELFHAILI, Philippe THEVENIN 218
A DFT study of Electronic and optical properties of Si-doped ZnS for solar device
Abdessamad Najim, Labrim Hicham, Salah Fadili, Philippe Thevenin 222
Copper oxide thin films on silicon substrate by Pulsed Laser Deposition
Mustafa Tolga Yurtcan, Gökhan Uygur 225
A New Technique For Fire Detection In Airplanes
Mehmet MASAT, Mehmet ERTUĞRUL 228
WiFi-Femtocell Offloading Algorithms in Heterogenous LTE Network
Suhailah Mahzan, Mohd Amiruddin Abd Rahman, Caceja Elyca Anak Bundak, Mahamod Ismail 231
Bird Sound Detection with Convolutional Neural Networks using Raw Waveforms and Spectrograms
Tee Yun Hong, Muhammad Mun'im Ahmad Zabidi 236
An Iterative Method Based on Hazy Image Model for Remote Sensing Image Enhancement
Y. Demir, N. H. Kaplan 238
WEIGHTING OF QUESTIONS WITH FASTTEXT ALGORITHM IN MULTIPLE CHOICE EXAMS
Adem CANPOLAT, Barış ÖZYER 242
Distance Measurement with Optical Sensor 245
Atıl Emre COSGUN, Hasan DEMİR 245
Performance Comparison of Common Routing Protocols in VANETs Using NS3 and SUMO
Nurgüneş Önal, Bülent Çavuşoğlu 246
A Case Study on 132 kV Overhead Line Performance against Lightning via Installation of Transmission Line Arresters in Malaysia
Rasyidah Mohamad Idris, Wan Zulhilmi Wan Mokhtar, Iryani Mohamed Rawi 250
Magnetoacoustic Tomography with Magnetic Induction: Multiphysics Imaging Approach_A Short Review
Sani Saminu, Abd El Kader Isselmou, Guizhi Xu, Adamu Halilu Jabire, Shuai Zhang, Adamu Ya'u Iliyasu 254
Electrical Energy Systems and Electric Transportation
Dominic April, MTE Kahn 259
Heteroatom-Doped Graphene Aerogels as an Anode for Sodium-ion Batteries
Sarah Umeera Muhamad, Nor Fazila Mahamad Yusoff, Nurul Hayati Idris 263
Graphenated Carbon Nanotubes Cotton as Potential Counter Electrode in Dye-Sensitized Solar Cells Application
Microwave absorbing properties of Fe_3O_4 from waste mill scales
Madiha Fathi Elmahaishi, Raba'ah Syahidah Azis, Ismayadi Ismail 267
Fe-Modified Silica/Polyurethane Composite for the Adsorption of Dyes from Aqueous Solution
Siti Nurul Ain Binti Md. Jamil, Nur Afiqah Binti Ahmad, Abdul Halim Bin Abdullah, Thomas Shean Yaw Choong .. 272
Nur Hana Binti Faujan 272
Effect of Acrylo-POSS Nanoparticles on the Passenger Carcass Tire Compound Properties
Çağıl Şenol Erdem, Nazlı Yazıcı, Öznur Kavacık, Sezgin Gökçesular, Güralp Özkoç, Mehmet Kodal 273
LBM simulation of fluid division by baffle in L shape cavity
Shayan Naseri Nia, Faranak Rabiei, M.M Rashidi 274
Effect of surface treatment on Ti substrates for Dye Sensitized Solar Cell Under Back Illumination Method
Izad Syahrul Ariffin Mohd Ismail, Suhaidi Shafie, Nor Hapishah Abdullah, Adam Tan Mohd Amin, Mohd Nizar Hamidon, Izzatul Hidayah Azizan 276
Pt/Graphene Catalysts Prepared by Supercritical Deposition with Different Pt Precursors
Meryem Samancı, Ayşe Bayrakçeken Yurtcan 279
Hydrogen Purification and Compression Methods for Future Energy
Yasemin Aykut, Ayşe Bayrakçeken Yurtcan 282
Comparison of Classifiers According to Number of Trials
Onur Erdem Korkmaz, Onder Aydemir 285
Oceans Energy for the South Africa Coastline Michee Ntonto Lunkamba
Michee Ntonto Lunkamba 290
Brain Oscillatory Responses during Listening to Quranic Acoustics
Samhani Ismail, Mohd Hanifah Jusoh, Mohammed Faruque Reza 293

A Novel Beam Steering Method Using Dispersive Superstrates with Low Dielectric Constant
Muhammed S. Boybay.....297
Transition from Ionic to Electronic Conductivity in Mixed Ionic-Electronic Tellurite Glass: Its Effects on Optical Properties
M.S. Sutrisno, R. Hisam.....301
Catalytic effect of $CoTiO_3$ synthesized via solid-state method on the dehydrogenation performance of $LiAlH_4$
N.A. Ali, M.Ismail.....302
Mechanical properties of arrowroot starch-based biopolymers plasticized with glycerol
Tarique Jamal, S.M. Sapuan.....303
Effect of $BaMnO_3$ catalyst synthesized by solid state method on MgH_2 as a potential hydrogen storage material
N A Sazelee, M Ismail.....306
Effect of Fuel Type onto Photocatalytic Activities of Copper Aluminate Nanoparticles Synthesized by Microwave-Assisted Combustion method using different fuels
İbrahim Hakkı Karakaş, Zeynep Karcıoğlu Karakaş.....307
Slow pyrolysis of disinfected COVID-19 non-woven polypropylene (PP) waste
M.M. Harussani, U. Rashid.....310
Advance in Fabric Face Mask Combatting COVID-19: A Mini Review
Syahida Farhan Azha, Suzylawati binti Ismail.....313
Cubic-Like Mn_2O_3 as an Anode for Sodium-Ion Batteries Applicatio
Nor Fazila Mahamad Yusoff, Nurul Hayati Idris.....317
Investigation of Floor Vibrations of Steel Structure Under Earthquake
Oğuzhan Çelebi, Bayrak Barış, Abdulkadir Cüneyt Aydın.....318
Operational Modal Analysis of A Historic Turkish Cupola
Dilek Okuyucu, Memduh Şenol Çavdar, Zabiullah Fakuori, Dursun Burak Özdoğan, Yusuf Gedik.....325
Operational Modal Analysis of An Adobe Cottage
Dilek OKUYUCU, Memduh Şenol ÇAVDAR, Zabiullah FAKUORI, Burak GEDİK, Muhammet ÖZDEMİR.....330
A Product Improvement Story for Lightweight Pumice Blocks
Zabiullah FAKUORI, Memduh Şenol ÇAVDAR.....335
The Process of Developing A New Lintel Product Using Pumice: First Stage
Kübra YILMAZ, Zabiullah FAKUORI, Memduh Şenol ÇAVDAR.....340
Combination Effect of Ruthenium Complexes, Ru-PIP with Olaparib in MDA-MB-231 breast cancer cells
Nur Aininie Yusoh, Haslina Ahmad, Suet Lin Chia.....345
PRODUCTION OF FLEXIBLE NiCo2S4/rGO NANOCOMPOSITE PAPER MATERIALS
Elif ERÇARIKCI, Zeriş AKSU, Ezgi TOPÇU.....346
Graphene Nanoplatelets as Adsorbent for Removal of Pharmaceutical from Water
Fatin Ahza Rosli, Haslina Ahmad, Khairulazhar Jumbri.....349
PV Monitoring System: Data Logger Based on PcDuino a Single Board Computer
ELWATI Jaafar, ELMAJDOUB Khalid, HARTITI Bouchaib.....350
Voice Pathology Classification Using Machine Learning
Hussein Mahmood Abdo Mohammed, Asli Nur Omeroglu, Merve Polat, Emin Argun Oral, Ibrahim Yucel Ozbek.....354
An Ultrathin Transparent Metamaterial Absorber Using an ITO Resistive-film
Gökhan ÖZTÜRK, Yunus KAYA, Uğur Cem HASAR.....358
Classification of Snoring Sounds
Rabiye KILIÇ, Nida KUMBASAR, Hilal Kübra SAĞLAM, Emin Argun ORAL.....362
Comparative analysis of Microstrip Patch Antenna on different substrate material using slit technique for x-band application
Auwalu Aminu Abubakar, Zainab Yunusa.....366
IRRADIANCE IMPACT ON THE PV POWER OUTPUT
Thomas Lionel Makosso, Ali M Almaktoof, Khaled Aboalez.....370
Analytical Solution of Brillouin Amplifier Equations for the Lossless Medium Working in Saturation Region
Fikri Serdar GÖKHAN.....373
Adaptive-Network-based Fuzzy Inference System based MPPT Control for Stand-Alone PV Systems
Mehmet YILMAZ, Muhammed Fatih ÇORAPSIZ.....376
Application of a Microwave Metamaterial Sensor for Detection of Water Adulteration Level within Fatty Milk
Kadir Yüzgüleç, Oğuzhan Akgöl, Vedat Özkaner.....378
Preliminary Investigation on the Soil Water Content Based on the Soil Series of Terengganu State, Malaysia
Eng Giap Goh, Rudiyanto.....381
Treatment of Aqueous Solutions With Ammonia Content By Direct Contact Membrane Distillation
Ayşegül ÇEVİK, Ahmet Bora YAVUZ, Osman Nuri ATA.....384
Demolition Techniques And Rize Urban Renewal Project 1. Stage Example
Ali Gurbuz, Volkan Tavşan.....388
Elastoplastic Analysis of Unreinforced Masonry Walls with Openings

Edin Nurkovic, Metin Karslioglu, Zeynep Unsal Aslan, Bilge Doran 392
The Effect of Beam Stiffness on Performance-Based Seismic Design of Reinforced Concrete Frames
Ibrahim A. Alameri and Sulaiman Al-Safi 396
Vector Signal Strength Different for Magnetic Field Indoor Positioning System
Caceja Elyca Anak Bundak, Mohd Amiruddin Abd Rahman, Che Nursyamimi Binti Che Saidi 397
Classification of Covid-19 Chest X-Rays Based on HOG Feature Descriptor Using SVM
Ferhat Bozkurt 401
Classification of Butterfly Camouflage Images Based on Feature Extraction with Local Binary Patterns
Erkan Bayram, Vasif Nabiyev 405
Effect Of Software Development Methodology On Software Quality
Süleyman Emir TURNA, Kökten Ulaş BİRANT, Muhammad Baballe Ahmad, Fatima Alkasim Nababa,Abubakar Sadiq Muhammad 416
Stability and Repeatability Properties of TiO_2/B_2O_3 Thick Film Gas Sensor for Detecting Hydrogen at Optimum Operating Temperature
Siti Amaniah Mohd Chachuli, Mohd Nizar Hamidon, Mehmet Ertugrul, Md. Shuhazlly Mamat, Omer Coban 420
A Facile Synthesis of Rutile-Anatase TiO_2 Nanocuboid: The Effect of Chloride Ion
Kam Sheng Lau, Masliana Muslimin, Norhashimah Ramli, Chin Hua Chia, Mohammad Hafizuddin bin Hj Jumali, Sin Tee Tan 424
Effects of Nanostructured Graphitic Concentration on the Performance of Transition-Metal-Oxide-Based Supercapacitors
Jun Yan Lim, Kam Sheng Lau, Chin Hua Chia, Sin Tee Tan 425
Effect of cobalt titanate on the hydrogen storage properties of magnesium hydride
M.Ismail, N.A. Ali 427
The Turbidity Removal Performance by Purified Natural Coagulant in Water Treatment
Amina Adedoja Owodunni, Suzylawati Ismail 428
The Development of a Smart Moisture Monitoring System for Precision Agriculture
Labib Sharrar, Salinda Buyamin, Mohamad Shukri Zainal Abidin 431
Fabrication and Characterization of ZnO/Polyaniline Based Fet Structure H_2 Gas Sensor
Mücella ÖZBAY KARAKUŞ 435
Lithium-ion-based Static UPS versus Lead-acid-based Rotary UPS: Total Cost of Ownership
P.K. Ngongo, MTE Kahn 436
Hardware Simulator for Microgrid Systems
E.P. Muluh, M.T.E Kahn 440
Performance study of a new smart parabolic trough collector system integrated with hybrid tubular thermoelectric generator
Abderrahim Habchi, Bouchaib Hartiti, Hicham Labrim, Salah Fadili, Abdelilah Benyoussef, Naoual Belouaggadia 444
Numerical Simulation of Photovoltaic Characteristics of Cadmium Telluride Thin Film Based Solar Cells
Salaheddine Moujoud, Salah Fadili, Bouchaib Hartiti, Philippe Thévenin, Ali Faddouli, Chaymaa Rachidy 450
Improved Approach of Dark Object Subtraction (DOS) for Classification of Oil Palm Cover in Different Space and Time with Landsat-8 Images
Zhi Hong Kok, Abdul Rashid Mohamed Shariff, Siti Khairunniza Bejo 455
Mathematical Modeling of COVID-19 Using Fractal-Fractional Derivatives
Zeeshan Ali, Faranak Rabiei, Kamal Shah, Zanariah Abdul Majid 458
Mathematical Model for COVID-19 Outbreak in Pakistan
Zeeshan Ali, Faranak Rabiei, Zanariah Abdul Majid, Kamal Shah 460
A Numerical Method for The Solution to A Class of Fractional Delay Differential Equations of Nonlinear Type
Ömür Kıvanç Kürkçü 461
Augmented Reality Application with Marker Technology Improves Automobile Engine Assembly
Lai Lai Win, Faieza Abdul Aziz, Norhisham Seyajah, Huda hatam Dalef, Rohidatun M.W., Nadia Abdul Rani, Nalienaa Muthu 465
Analysis on Materials of Bus Superstructure in Compliance to R66
Nur Isnida Razali, Nuraini Abdul Aziz, Ameen Topa 469
Mass Fraction Effect on Mechanical Properties of E-Glass Fiber Reinforced Polyethylene Composites
Samet Sanbur, Cemal Koçhan, Çiçek Özes 474
High-Efficiency Smart Pump Controller
Yavuz Sümer, Arash Ravanbakhshazar, Ahmet Kain 478
Leader-Follower Formation Control of Quadrotors: A Simple Virtual Leader Approach 479
Kaan Can, Abdullah Başçi 479
Modelling and Simulation the Position Control of Flexible Manipulator Using Gyroscopic Actuator
Abbas Moloody, Mohd Sapuan Salit, Azizan Bin As'arry, Raja Kamil, Tang Sai Hong ..... **Error! Bookmark not defined.**
Kinematic Analysis of a Novel 5-DOF FDM Printer Based on Parallel Mechanism
Mehran Mahboubkhah, Ahmet DUMLU, Kagan Koray AYTEN 490

Adaptive Sliding Mode Control of Mobile Robot and Comparison with PID Controller
Mustafa Ayyıldız, Umut Tilki 494
MM-RAM Composites as a Wide Band Radar Absorber
Mehmet Ertugrul 499
IMPLEMENTING THE P&O ALGORITHM FOR STAND-ALONE SMALL WIND TURBINE SYSTEM
Ahmed Zentani, AMA Almaktoof, MTE Kahn 503
Analysis and Evaluation of Electricity Consumption in Low Voltage Distribution Grids in Ankara Metropolitan Area
Ali KARAÇOBAN, Ahmet KARAARSLAN 507
Inversion Coefficient Design Methodology for the Design of Inverter based OTA
Mesut Atasoyu 511
The Need for Solar Power Energy
Muhammad Baballe Ahmad, Isa Ibrahim, Umar Shehu 515
The Challenges Faced using the Radio Frequency Identification (RFID) System
Muhammad Baballe Ahmad, Mukhtar Ibrahim Bello, Isa Ibrahim 519
Handover Management in SDN-based 5G Small Cell Network
Nurul Hayati Idris 5251
Design and Analysis of Parameterized Signed Booth's Multiplier in FPGA
Bahadır Özkılbaç, Tevhit Karacalı 526
Comparison of Classical ML with DL Methods for Network Intrusion Detection in IoT
Siham Amarouche, Kerem Küçük 530

POSTER PRESENTATIONS

Electrospun CA/MSNs nanofibrous mats for controlled release of methylene blue
Haslina Ahmad, Yianchee Gan 538
Detecting the main topics of citizens' comments in e-government
Gunay Iskandarli 539
ANN-based statistical downscaling for daily rainfall estimation
Khaled Alramalwi, Okan Fıstıkoğlu 543
Fault Tolerant Control of Five-phase IPMSMs under Opened Phase Fault Based on MTPA Operation
Y. Zafari, A. Hosseyni, S.Shoja- Majidabad 547
Photovoltaic Properties of Graphene Quantum Dots- based Dye-sensitized Solar Cell
Ramisha Rabeya, Savisha Mahalingam, Lau Kam Sheng, Abreeza Manap, Meenaloshini Satgunam, Chia Chin Hua, Md. Akhtaruzzaman 552
Formulating and Characterizing Lyotropic Liquid Crystalline Nanoparticles Loaded Anti-Atherosclerosis Drugs for Better Encapsulation Efficiency
Mardhiah Maslizan, Mohd Mokrish Md Ajat, Intan Diana Mat Azmi 554

Welcome to ISASE2021

It is a pleasure for us to offer you Full Text Book for the International Symposium on Applied Sciences and Engineering (ISASE2021). Our goal was to create a scientific platform between our universities that introduces the newest results on internationally recognized experts to local students and colleagues and simultaneously displays relevant Turkish achievements to the world. The positive feedback of the community encouraged us to proceed and transform a single event into a conference series. Now, ISASE2021 is honored by the presence of over 187 colleagues from 20 different countries. We accepted contributions from all fields of science and applied engineering to promote multidisciplinary discussions. The focal points of the conference emerged spontaneously from the submitted full- texts: Electrical Electronics Engineering, Physics and Nanotechnology, Computer Engineering, Civil Engineering, Biomedical Engineering, Applied Mathematics and Modeling, Chemical Science and Engineering, Material Science and Engineering, Mechanical Engineering, Mechatronics and Robotics Engineering and others. In this conference, 39 invited, 137 oral and 11 poster presentations presented in 36 session in 3 parallel rooms. Our warmest thanks go to all invited speakers, authors, and contributors of ISASE2021 for attending to the conference. We look forward to meeting you again in one of the forthcoming ISASE2021 events in Malaysia.

Prof. Dr. Mehmet ERTUGRUL
Assoc. Prof. Dr. İ. Yucel ÖZBEK
Assoc. Prof. Dr. Abdullah BAŞÇİ

Editors

Message from Chair, ISASE2021



Honorable Vice Rectors of the co-organizing universities, honorable distinguished invited speakers and participants.

Ladies and Gentlemen,

On behalf of the Organizing Committees, I am pleased to welcome you to the 2nd International Symposium on Application Sciences and Engineering. The Conference is a platform that brings together researchers, scientists and professionals to discuss innovative ideas and various topics related to next-generation technologies and applications. The aim of the three-day conference is to create a platform to share knowledge and develop new partnerships among everyone with experience and expertise in the fields of applied sciences and engineering.

I would like to share with you how happy and proud as we are scientists, because we have the opportunity to do better for humanity and the universe. I would like to also share a few more sentences from a paper published in Nature in 1943. “Studying science is free to all, it speaks in one language, it has but one object, but it is the handmaid of all art, all industry and all human progress. It is neither limited by time or space. It belongs to the world and is of no country and no age.” On the other hand, science and technology are moving so rapidly that even those who work on the same topics sometimes feel that they are behind the others. In 1926, Nikola Tesla said: "We shall be able to communicate with one another instantly, irrespective of distance”. He also said “When wireless is perfectly applied, the whole earth will be converted into a huge brain". Isn't that an amazing prediction? We have to think about this prediction and learn from it. What did people think in that time and what do we think today on Tesla’s words? I hope that this conference will have more or less an impact on the path of science for humanity.

NOW, I would like to give you a brief information about the conference. This is the second of the ISASE conference, which is jointly organized Ataturk Univ, UPM and ETU. The first was in 2018 and we plan to do it annually from now on. In this conference, we have total 187 papers, which are accepted as a result of the 3 referee evaluations for each paper. 39 of the presentations are invited talks, 11 of them are poster and rest of them are oral presentations. The papers submitted from 20 different countries including (Azerbaijan, Canada, China, Indonesia, Iran, Iraq, Italy, Japan, Libya, Malaysia, Morocco, Nigeria, Pakistan, Palestine, Russia, South Africa, Spain, Turkey, USA, Yemen). Main topics are from the fields of Materials Science and Engineering, Electrical-Electronics Engineering, Physics, Chemistry, Chemical Engineering, Mechanical Engineering, Computer Engineering, Civil Engineering, Robotics. All accepted papers will be published in a conference book.

I would like to thank all the participants for their contribution to the conference. I am also grateful to UPM, ETU and AU administrations for their support. I would also like to thank Mohd Nizar Hamidon from UPM for helping us whenever we need it. I also want to point out that we should thank these people. Mehmet Ertuğrul, E. Argun Oral, Abdullah Basci, Aslınur Ömeroglu, Hussein Alameri, Onur E. Korkmaz, and other volunteers whose name I cannot count. We could not come to this point today without their enormous effort.

I wish the conference to be successful and beneficial,

and I present my respects to all of you.

Thank you

Assoc. Prof. Dr. İ. Yücel ÖZBEK

Chair, ISASE2021

Message from Dean of the Faculty of Engineering – Ataturk University, Turkey



Dear Deputy Rectors, Dear Chair,

Ladies and Gentlemen, my colleagues, dear students;

I am very pleased to be here today for the opening of the ISASE2021 conference. This conference is a joint activity of Universiti Putra Malaysia (UPM), Erzurum Technical University and Atatürk University, where we have been developing our bilateral relations increasingly every year. As the Dean of the Engineering Faculty, I must express that I am very excited that our relations have reached this level. However, that is not enough, and I believe we have the potential to take this much further.

Concepts such as new generation universities and industry 4.0 have begun to surround our lives and the revolution is taking place rapidly. With the Industry 4.0 revolution, the most needed occupational group will undoubtedly be the fields of Applied Sciences and Engineering. With this revolution that is taking place, production processes are very different from classical industry. Today; Information and communication technologies such as artificial intelligence, machine learning, internet of things, cloud technologies, quantum processors, 3D printers deeply affect the flow of life. On the other hand, knowledge-based production produces much more economic value. All these developments both highlight the university and demand changes from it. It is no longer sufficient for universities to transfer existing knowledge through education. Now, in the new university approach, being able to achieve or actively contribute to the cycle of research, patents, commercialization and branding of the product comes to the fore. Students are expected to have skills such as innovative thinking, research, creativity, design, solving complex problems, and critical thinking. In addition to these, they are expected to have teamwork, respect for themselves and others, empathy, communication skills using verbal, written and digital media.

I believe that this conference will be an environment that contributes to the development of our bilateral relations as well as the development of new engineering insights. I hope this conference will bring benefits to everyone working in the fields of applied sciences and engineering, as well as to you, our universities, our countries and all humanity. I would like to end my speech by encouraging you to participate in all events and discussions on digital platforms for the next three days. I would like to express that I would be pleased to host you here at the first face-to-face conference to be held after the pandemic. I wish everyone a successful, safe and efficient conference.

Best regards.

Prof. Dr. Recep SADELER

Dean of the Faculty of Engineering

Ataturk University

Message from Director of the Institute of Advanced Technology (ITMA), UPM, Malaysia



In the Name of Allah, the most Beneficent, the most Merciful.

Assalamualaikum Warahmatullahi Wabarakatuh
First of all, I would like to thanks Ataturk University and Erzurum Technical University for allowing us Universiti Putra Malaysia to jointly organized the International Symposium on Applied Sciences and Engineering for the second time. This had shown a strong collaboration between us which had started few years back.

The symposium is a good platform for fellow colleagues and researches to share and discuss knowledge and findings while expanding networks. This year the symposium is held using online platform (webinar) due to the current Covid-19 pandemic and my doa (pray) this pandemic can be over soon so that all of us can visit each other after this.

It is an honor for me to see many reputable speakers for varies country in this symposium. I believe that each of the speakers will share their research findings that will benefit every participant in the related areas of the symposium. This is rare opportunity to interact in this new norm and establish networking with all speakers and presenters.

I would like to thanks The honorable Prof. Dr. Omer Comakli, Reactor of Ataturk University, Prof. Dr. Bulent Cakmak, Reactor of Erzurum Technical University and Prof. Dr. Mohd Roslan Sulaiman, Vice Chancellor of Universiti Putra Malaysia for sporting this symposium. I would also like to express my gratitude to the editorial staff, member of the organizing committee, secretarial staff and everyone who have worked hard to make sure this symposium successful one.

Finally, it is my personal dream and hope that much strong bonding between three universities and can be expended to university in both countries.

Prof. Dr. Mohd Nizar Bin Hamidon

Director of the Institute of Advanced Technology (ITMA), UPM

Message from Vice Rector of Erzurum Technical University, Turkey



I would like to thank organizing committee of the International Symposium on Applied Science and Engineering (ISASE 2021) for their invaluable effort to bring this prominent symposium to life despite all the hardship experienced during the covid-19 pandemic.

As a young university established in 2010, I would like to give some brief information about our university. Erzurum Technical University was founded as the second state university. Currently, there are 15 active departments in 5 faculties at the university, and the total number of students is nearly 4500, along with more than 250 academics serving in the university.

I would like to mention that digital tools, which have entered our lives thoroughly with the pandemic, can provide the opportunities for both our research and development studies and organizing such symposiums. During the pandemic period, almost all of us either gained experience of teaching or took courses on a subject we were interested in using online education tools. I believe that digitalization of learning and teaching processes creates new opportunities, despite the fact that our entire education life has been almost face to face before the pandemic. We have the opportunity to easily obtain any information or application we need in our active research through online educational tools.

Although attending congresses and symposiums online is not considered as efficient as face-to-face participation at the moment, I believe that we will begin to benefit as we get used to this situation. One of the most important advantages is the decrease in the costs of attending such symposiums. However, more importantly, I think that prominent scientists and academics have the opportunity to participate in online congresses and symposiums more comfortably than face-to-face participation due to effects such as time and travel restrictions. I believe this will give young researchers the chance to interact online with important names in their fields. I think that even after the pandemic, organizing conferences and symposiums as a hybrid will be more beneficial than face-to-face participation in terms of the effectiveness of congresses and symposiums.
Finally, I would again like to thank the committee that organized the ISASE 2021 symposium, the participants and everyone who contributed to the event.

Prof. Dr. İrfan KAYMAZ

Vice Rector

Erzurum Technical University

Message from Deputy Vice-Chancellor of Universiti Putra Malaysia, Malaysia



In the Name of Allah, the most Beneficent, the most Merciful. Assalamualaikum Warahmatullahi Wabarakatuh I am truly happy to see that Malaysian and Turkish Scientific Committees have come together through the International Symposium on Applied Sciences and Engineering 2021 (ISASE 2021) organized by both countries. As two strong members of Islamic community, we need to take the pioneering role to increase the scientific collaborations among Islamic nations especially. Universiti Putra Malaysia (UPM), as a premier institution of higher learning and research will always support efforts towards achieving excellence through various programs which are in line with our mission to make meaningful contributions towards wealth creation, nation building and universal human advancement through the exploration and dissemination of knowledge. Known as one of the top Research Universities in Malaysia, UPM strives to continue to provide new meaning to the progress, growth and development of the nation and the world every year. The entire university community should maintain momentum to sustain international excellence as higher education is a very competitive industry. I would like to thank all presenters for their valuable contributions. UPM, Ataturk University and Erzurum Technical University had put forth great efforts to make this conference possible. Our delegates had an opportunity to see the facilities in Turkey, and scientists from both countries had a chance to discuss further collaborations. I sincerely hope that these conference series open the path for successful and fruitful international collaborations. We are honored and would like to welcome all of you for the next series of this conference in Malaysia. Thank you.

“With Knowledge We Serve”

Prof. Dr. Ir. B.T. Hang Tuah Baharudin

Universiti Putra Malaysia Deputy Vice-Chancellor

Message from Vice Rector of Atatürk University, Turkey



Honorable Vice Rectors, Conference Chair/co-chairs and distinguished participants,
Good Morning/Afternoon/Evening wherever you are on the planet!

I would like to start with passing Atatürk University Rector Prof. Dr. Ömer ÇOMAKLI's warm welcome to the participants and sincere thanks to the conference organizers.

It is a great pleasure to be a part of 2nd International Symposium on Applied Sciences and Engineering (ISASE2021). This conference is jointly organized by Atatürk University, Erzurum Technical University and University Putra Malaysia as an outcome of a fruitful collaboration between two brotherly countries, Turkey and Malaysia. We are passing through difficult times. Coronavirus pandemic has once again showed us the importance of international collaborations in overcoming the global challenges in every area of science and technology. Therefore, we value this initiative to further develop.

Atatürk University, established in 1957 in Erzurum, a historic city located in the north east part of Turkey. As a city placed on the historical silk road Erzurum has always been a center for education throughout the history. Well-known madrasas such as over thousand-years-old Yakutiye and Double Minaret Madrasas, where medicine, science, mathematics, astronomy and engineering were taught together with Islamic sciences, are located in the city center of Erzurum. Atatürk University is a place of knowledge and wisdom that enlightens us today with the heritage it has inherited from the history. It is an institution with a strong background in social sciences and humanities, health sciences, science and technology with well-educated human resources and infrastructure, strives with all its power to raise qualified and skillful people. Atatürk University adapts itself to the needs of the next generation within the scope of the project called "Next Generation University Design and Transformation", a participatory action research process initiated three years ago by our Rector Prof. Dr. Ömer Çomaklı. *Internationalization* was determined as one of the three main priority of the university together with *Entrepreneurship* and *Digitalization* with the motto "*Mowing forward in service of life*".

Distinguished participants,

Atatürk University is among the 20 prioritized pilot universities in internationalization announced by the Higher Education Council of Turkey. In this context, Atatürk University aims to be a world-renowned university with an international profile going through internationalization. I would like to share few facts about status of internationalization in our university.

Atatürk University;

- ✓ have bilateral agreements with more than 300 universities or higher education institutions in more than 60 countries around the World,
- ✓ is among the top 15% of all universities on a national scale in terms of the number of student mobility (500 students joined the mobility programs in 2019 before the pandemic),
- ✓ has a total of 4769 (2062 in Formal Education and 2707 in Open Education) international students in the 2020-2021 Academic Year. This is around 6%, of all our students and we are aiming to increase this to 10% in 5 years.
- ✓ was ranked 17th in the overall standings and 14th among the public universities in Turkey in terms of the number of international students,
- ✓ fully defined the target strategies for internationalization by focusing on contributing to the internationalization of students, faculty members and administrative staff through mobility programs,

bilateral agreements and various activities, and creating a platform for attracting distinguished foreign academics and researchers,

- ✓ activated the Joint Diploma in 5 programs (Electrical-Electronics Engineering, Industrial Engineering, Chemical Engineering, Food Engineering, and Biology) with the Universiti Putra Malaysia (UPM). We are now working with 3 other universities currently to increase joint degrees to at least 10 programs.
- ✓ a model University in international student mobility with our internship opportunities and English Programs (Faculty of Medicine and Faculty of Nursing) as well as university-scale undergraduate / graduate English course pools.

Although we have several international relations, increasing our cooperation with sister universities in Malaysia is one of our main goals. In this context, we see UPM as a strategic partner. We started dual degree programs in different fields with the UPM. We strongly support academic staff and student exchange activities among our universities. We consider the conference series held at Atatürk University or UPM respectively as a platform where relations between our universities will be further developed. I would like to express that the conference is not only a scientific conference, but also a bridge that will help to further develop the very strong relations that exist between our countries.

Distinguished participants,

I would like to finish with thanking to the organizing committee chair, co-chairs and the members. I know how challenging to organize such an international event particularly people are worrying about their health and safety at the time of Coronavirus Pandemic. I also would like to thank for your interest and participation. I greet you all, with the hope to meet again in person in Turkey or Malaysia in the future.

I wish you all a very fruitful conference.

Prof. Dr. Mustafa SÖZBİLİR

Vice Rector of Atatürk University

INVITED SPEAKERS

Non-linearity assessment of Class E Switching GaN HEMT RF Amplifier for broadband transponder



Basuki Rachmatul Alam,
MSc, PhD School of Electrical Engineering
and Informatics Institute of Technology
Bandung, Indonesia
basuki.rachmatul@stei.itb.ac.id

***Abstract*-The Class-E switching RF amplifier has shown microwave power performance with high theoretical efficiency approaching 100%. This theoretical efficiency can be reached as outcome of switching of RF transistor releasing current and voltage signal at the output load in half period right subsequently. The present and incoming broadband and high power RF and microwave transmission of 4G, 5G, IoT, V2x (vehicle-to-vehicle), M2M (machine-to-machine), Lo-Ra (long range) and other new generation wireless technology transponders may need high efficiency front-end to save battery energy at even higher rate of transmission as well as in autonomous-remote nature of operation. Therefore, verification of class E switched RF amplifier performance requires even more than standard RF power measurement, non-linear broadband assessment is needed. Class E switching RF amplifier with single transistor and dual transistors topology separating switching and amplifying functions have been simulated and analyzed. Single and dual transistor switched GaN HEMT RF Amplifiers have shown microwave power performance up to near 80% PAE and over 40dBm power performance under single tone signal. Non-linearity two-tone characterization with 20MHz and 100MHz tone signal spacing have been conducted resulting deterioration of PAE down to less than 60% and intermodulation distortion IMD3 with OIP3 49.7dBm.**

Ensuring Quality of Data in the Internet of Things for Healthcare Monitoring Applications Via Anomaly Detection Methods



Assoc. Prof. Dr. Murad A. Rassam
Taiz University YEMEN
muradrassam@ieee.org

***Abstract*-Internet of things (IoT) refers to the system of connected devices that are used for controlling, monitoring, or collecting data from objects to facilitate the life of humans and increase the level of well-being in providing services. The use of the IoT in healthcare (specifically personal healthcare) has risen sharply among different specific IoT applications. Remote monitoring of patients is considered one of the most important applications that helps healthcare givers taking the right decisions at a suitable time. In these applications, sensors are planted on the body of the patient to read the critical vital signs such as heart rate, pulse, blood pressure, oxygen saturation among others. However, the collected sensor readings in some circumstances are susceptible to malicious attacks, hardware faults, misplacement of sensors, in addition to various environmental factors. To ensure the quality of data for making the right decisions by healthcare givers, anomaly detection methods are necessary to detect abnormal readings and helps in analyzing them to decide the source of abnormality. In this talk, the state of art researches in the field of anomaly detection for healthcare monitoring applications is explored. Some future research directions will be highlighted to help in advancing ensuring the quality of healthcare data collection for human wellbeing.**

Characterization of Polybutylene Succinate/EFB fibre/Modified Tapioca Starch and Glycerol for Food Packaging Application



Khalina A.
Faculty of Engineering
Institute of Tropical Forestry and
Forest Products (INTROP)
Universiti Putra Malaysia, 43400
Serdang, Selangor, Malaysia
email: khalina@upm.edu.my

Rafiqah S.A
Institute of Tropical Forestry and
Forest Products (INTROP)
Universiti Putra Malaysia, 43400
Serdang, Selangor, Malaysia

***Abstract*- Increasing attention has been attracted on biodegradable and eco-friendly bio-composites products. In addition, many of the bio-sourced monomers are inherently less toxic than those used in conventional polymers. In this work, was focusing on biodegradable polybutylene succinate filled with modified tapioca starch, empty fruit bunches (EFB) fibre and glycerol as plasticizer by using hot press technique. Analysis of the characteristic of materials in terms of chemical, thermal, physical, mechanical, and morphological characteristics of the composite were studied. From mechanical analysis showed increased values of mechanical strength for both tensile and flexural testing with increase of 10% of EFB fiber content. The tensile strength of composite increases respectively by 0.30 MPa with the increase of EFB fibre content up to 30 wt%. Meanwhile, the flexural strength of composite containing 20% to 30% EFB fiber are increase by 4.3MPa respectively. Increasing trends in the performance of tensile strength and flexural properties were shown for the glycerol loadings up to 10 wt%. Besides, thermal stability for composite with 10.wt% glycerol loading showed the highest thermal stability. This is due to better interfacial bonding and better interaction between polymer, starch and fibre compounding. The percentage of water absorption increased as the EFB fibre loading increased and reached the equilibrium of absorption on day 8. In addition, SEM testing shows good interfacial bonding between PBS, starch and EFB fibre for all percentage especially for 30% fibers content. Good interfacial bonding will enhance good properties of the compound material for future application.**

Nanoparticle Network as an Effective In-Materio Reservoir Computing Device



Yuki Usami
Research Center for Neuromorphic AI Hardware, Kyushu Institute of Technology,
Kitakyushu 8080196, Japan
usami@brain.kyutech.ac.jp

Hirofumi Tanaka
Director of Research Center for Neuromorphic AI Hardware,
Kyushu Institute of Technology,
Kitakyushu 8080196,
Japan tanaka@brain.kyutech.ac.jp

***Abstract*— In recent years, the superior computational power of deep learning based on software has been widely recognized, and the practical applications of artificial intelligence are rapidly expanding. On the other hand, the hardware for replacing to such artificial intelligence (AI) algorithms is facing the physical limitsof scaling in silicon CMOS technology, and performance improvement is expected to hit the ceiling. For this reason, there is a growing interest in hardware technologies that physically implement artificial neural networks (ANNs), neuromorphic or brainmorphic information processing systems, and the applications (hereafter referred as AI systems in this paper), as well as new materials and devices. A critical difference between the presently required device functionality and that in conventional computational systems is the use of dynamics. By cleverly using nanomaterials' nonlinearity and networkstructure, devices that spontaneously generate pulses, noise, and other physical phenomena are expected to be realized to utilize for the AI hardware. These devices will enable drastically lower power consumption and higher integration of AI systems. In the learning process of ANNs, it is necessary to constantly change and store the weights of the weighted sum (sum-of-products) part. In our research center, we have been working on materials that can complement CMOS for AI systems by using molecules and nanocarbon materials, and further, we are trying to apply them to autonomous AI robots. This paper introduces these nanomaterials and networks' formation as devices, the key points of the devices' functionalization, application to robots, and other recent research results.**

We formed a random network consisting of SWNTs and POMs as following previous reported method[1].We found that the device generates neuron-like pulses when a high voltage is applied[2]. This enabled us to control noise and pulses generation. Such dynamic signal generation is attributed to the multiple discharges of POM molecules. Reservoir computing simulations also showed that this system could be used for time series memory[2]. In this study, we applied a sinusoidal signal to an SWNT/Por- POM random network using porphyrin-gradient sandwich POM (Por-POM), which is more redox-sensitive, and the Lissajous plot of the output signal from one of the multiple electrodes plotted against the input signal showed nonlinear switching behavior. A memory state was generated due to the reversible redox of Por-POM, and the input signal was highly interacted with the reservoir system. The dynamics are also confirmed by the higher harmonic generation (HHG) from the FFT analysis, and NARMA-2 task which considers states up to a two-step delay. The NARMA-2 task successfully generated signals that predictably follow the target waveform using a linear regression model. These results indicate that the nonlinearity of SWNT/Por-POM and memory integrity are important factors for reservoir operation. We also used Ag/Ag2S core-shell nanoparticles (NP) as a reservoir device to obtain similar results with SWNT/Por-POM. Voice recognition and robot-hand grabbing stuff recognition[3] was conducted by the reservoir devices[4]. Details will be presented at the presentation.

References. [1] H. Tanaka et al., Adv. Mat. 18, 1411 (2006). [2] H. Tanaka *et al.*, Nat. Commun. 9, 2693 (2018). The article was selected as the most read 50 articles published in Nat. Commun. in 2018 (Physics). [3] Kyutech won the RoboCup world series of Domestic Standard Platform League by TOYOTA HSR in 2017 and 2018. The same robot was used for the demonstration. [4] T. Kotooka, H. Tanaka et al., Nature Portfolio (2021), DOI: 10.21203/rs.3.rs- 322405/v1.

Keywords*— *Neuromorphic AI Hardware, Physical Reservoir Computing, Material Intelligence

Effect of Nitrogen Doping of Carbon Supports on PEM Fuel Cell Performance



Prof. Dr. Ayşe Bayrakçeken Yurtcan
Engrineering Faculty Deparment of Chemical Engineering
Atatürk University Erzurum,Turkey
abayrakceken@atauni.edu.tr

***Abstract*— PEM fuel cells seem to be promising alternative energy conversion devices for portable and mobile applications. The most important component of a PEM fuel cell is its anode and cathode electrodes where the half cell reactions are occuring. In this respect, it is crucial to increase the active sites of the catalysts used in the electrodes in order to get better performances. Active sites of the carbon supported electrodes can be increased by doping carbon material with heteroatom such as nitrogen. In this study, two different nitrogen doping routes will be discussed including a) nitrogen doping carried out during the synthesis of carbon-based material b) carbon-based material treatment with nitrogen-containing chemicals.**

Keywords— PEM fuel cell, nitrogen doping, carbon

Passive Surface Acoustic Wave Resonator Platform for Wireless Sensor Applications



Prof. Dr. Mohd Nizar Bin Hamidon
Universiti Putra Malaysia
mnh@upm.edu.my

***Abstract*-Due to the Internet of Thing (IoT), the demand on passive, high sensitivity, and wireless system for sensors has increased tremendously. Surface Acoustic Wave (SAW) is one of the technologies that a suitable to imply in the system because it acquired advantages such as high sensitivity, low power consumption, and wireless capability. The operating principle of SAW have enabled the construction of passive sensor where the signal can be transmitted and interrogated wireless. In this paper a double surface acoustic resonator (DSAWR) system operated around 433 MHz center frequency is adopted consists of capacitor, inductors, two commercialized SAW resonators and sensing element will be presented in details.**

Glass Ionomer Cement Using Alumino-Silicate-Fluoride Based Glass Ceramics



Mohd Hafiz Mohd Zaid
Department of Physics, Faculty of Science, Universiti Putra Malaysia, 43400, Serdang, Selangor, Malaysia

Khamirul Amin Matori
Department of Physics, Faculty of Science, Universiti Putra Malaysia, 43400, Serdang, Selangor, Malaysia
Material Synthesis and Characterization Laboratory, Institute of Advanced Technology, Universiti Putra Malaysia, 43400, Serdang, Selangor, Malaysia
khamirul@upm.edu.my
Corresponding author's phone: +6016-267 3321

Esra Kul
Department of Prosthodontics, Faculty of Dentistry, Ataturk University, 25030 Erzurum, Turkey

***Abstract*-The success of Glass Ionomer Cement (GIC) innovations in dentistry over the last 40 years has attracted interest among researchers. However only few of them used Alumino-Silicate-Fluoride (ASF) based glass ceramics from waste material to fabricate the GIC. In this research, soda lime silica (SLS) glass and clam shell (CS) vitreous waste were utilized as a source of silicon dioxide (SiO_2) and calcium oxide (CaO), respectively with the empirical formula of $[(x)CS\cdot(45\text{-}x)SLS\cdot15CaF_2\cdot20P_2O_5\cdot20Al_2O_3]$ where x = 5 and 20 (wt.%) were synthesized by using conventional melt quenching techniques to produce ASF based glass ceramics. Then, GIC was fabricated using three main components of ASF based glass ceramics, polyacrylic acid (PAA) and water. The thermal, physical, structural, chemical and mechanical properties of ASF glass ceramics and GIC had been determined by using X-ray fluorescence (XRF), differential scanning calorimetry (DSC), density measurement, X-ray diffraction (XRD), fourier transform infrared spectroscopy (FTIR), field emission scanning electron microscopy (FESEM), energy dispersive X-ray (EDX) and compressive strength test (CST). The different physical behaviors of ASF bioglass were closely related to the CaF_2 content in each composition. The structural analysis shows the presence of various chemical bonds showing the formation of ASF bioglass. The ASF bioglass has many applications in dental field and efforts to improve its formulation can promise a better future in medical procedures**

Keywords- bioglass, ASF based glass ceramics, Glass Ionomer Cement

Dye Sensitized Solar Cell Efficiency Enhancement



Assoc. Prof. Ts. Dr. Suhaidi Shafie
Universiti Putra Malaysia
suhaidi@upm.edu.my

***Abstract*-Solar energy is one of the most efficient renewable energy sources that can be harvested at minimum cost. The growth of solar photovoltaic system implemented on rooftop or solar farm to generate power is significant and dominated by China, United States, Japan and India. Therefore, the availability of cost effective solar cell is essential to support the solar PV demand. Meanwhile, in recent years, commercially available silicon and thin film solar cell dominate solar cell market due to its high efficiency and stability. However new type of solar cell such as organic solar cell, perovskite solar cell and dye-sensitized solar cells (DSSCs) have been intensively studied and developed. DSSCs have attracted considerable attention due to its advantages such as of low production cost, non-toxic material and simple fabrication process. However, more effort is needed to enhance the DSSC overall efficiency toward commercialization. DSSC highest efficiency reported by EPFL in 2020 was 13%. In this session, DSSC efficiency enhancement utilizing $TiCl_4$ surface treatment, $AgNP/TiO_2$ plasmonic nanocomposite and doping of graphene quantum dots (GQD) into the TiO_2 will be presented. The $TiCl_4$ improve the surface contacts between FTO and TiO_2 film while incorporation of AgNP onto the TiO_2 has considerably improved the absorption in the visible region of solar spectrum due to the surface plasmon effect by silver nanoparticles. Then a method of doping the GQD into TiO_2 has also been studied in which the GQD can enhance the visible light absorption in DSSC and improve the charge collection efficiency. All these techniques show significant improvement in light absorption and charge collection efficiency which reflects to the DSSCs energy conversion efficiency.**

Decision Making Mechanisms in Hybrid Energy Storage Technologies



Prof. Dr. Ahmet Cansız
Electrical Engineering Dept. Istanbul Technical University Istanbul, Turkey.
acansiz@itu.edu.tr

***Abstract*-The generation of electricity increases continuously to meet the demand of industry. The limited energy resources and the necessity of renewable energy require energy storage. Since the electricity is generated from various energy sources, effective energy storage also requires effective electromechanical energy conversion. Increasing energy demand and associated factors has led to the development of hybrid energy storage systems. Decision-making mechanisms are main control procedures in the energy storage systems to maintain efficiency. In this article, methods and procedures are examined for the hybrid energy storage systems based on battery energy storage systems supported by high power density devices consisting of supercapacitor, superconducting magnetic energy storage and superconducting flywheel energy storage.**

Keywords—Energy Storage, supercapacitor, Battery, Flywheel.

Wired and Wireless Extreme Fast Chargers



Prof. Dr. Burak Özpineci
Oak Ridge National LaboratoryUSA
burak@ornl.gov

***Abstract*-With the recent demand for faster charging electric vehicles to rival the refill time of conventional vehicles, the interest in high power wired and wireless charging is increasing. While recent industry demonstrations have shown 450kW wired charging, Oak Ridge National Laboratory (ORNL) has recently demonstrated a 120kW static wireless charging system using a single power conversion system and a single transmitter/receiver coil pair. Now the focus switches to more than 300kW wireless charging and dynamic wireless charging. Dr. Ozpineci will talk about current status in wired and wireless charging, and the associated challenges.**

Plastic Brick as an Alternative Conventional Brick: Fabrication, Mechanical and Thermal Properties



Badiea A. M
Industrial and Manufacturing Systems Engineering, Engineering & IT College,
Taiz University, Yemen

Ibtisam M. K
Chemical Engineering Department, Faculty of Engineering, Soran University, Kurdistan Region

Amer H. A
Industrial and Manufacturing Systems Engineering, Engineering & IT College,
Taiz University, Yemen

Adel A.A
Industrial and Manufacturing Systems Engineering, Engineering & IT College,
Taiz University, Yemen
School of Manufacturing Systems Engineering, University Malaysia Parlis, Parlis, Malaysia

***Abstract*- Plastic waste is a non-biodegradable waste that does not decompose as an organic hydrocarbon materials. Plastic has a good properties that cab be molten and used as a binder for many reinforcement. It is a major challenge to re-use the plastics as a matrix with many fillers to be a composite material possesses a mixed characterization of those composed of. This study is an attempt to fabricate a new material since it is given a name of plastic brick to reveal that it is new product. Many researches in our lab have been achieved regarding on the plastic waste and others waste materials with small size diameters or unsymmetrical shape to enable us to meet and beyond the standard product. The plastic brick manufactured possesses a good properties of compressive strength, water absorption comparing with the standard requirement and can be used as an alternative conventional bricks of fly ash brick and burnt brick. Statistical method was used to design the experiments and to make a correlation between the independent variables and dependent variable.**

Keywords: ***Plastic waste, Glass waste, Non-biodegradable waste, Building materials, Brick industry, Compressive strength, Water absorption.***

Investigation of different steel simple connections under column-loss scenario: considering the effects of a transverse beam



Mohammed A. Alrubaidi
Department of Civil Engineering,
Sana'a University, Sana'a, Yemen
En_moh88@hotmail.com

Sulaiman I. Al-Safi
Department of Civil Engineering,
Sana'a University, Sana'a, Yemen
alsafi11@hotmail.com

***Abstract*-This study investigated experimentally the progressive collapse risk of two one-third scale single story, sub-assemblage, consisting of a double-span beam and two end columns within the frame plane connected to a transverse beam at the middle joint (three-dimensional (3D)). Progressive collapse was simulated by applying a vertical dynamic loading on the middle column. In these tests, two steel beam-to-column connections were studied experimentally. The two tested specimens were shear-connection that signified the prevalent type of steel beam-column joints. The two tested specimens along with another 2D steel frame with simple connection, tested in the literature, were used to calibrate 3D finite element (FE) models prepared using ABAQUS software. The validated FE models were then employed to investigate the risk of progressive collapse for eight different types of steel simple beam-column joints under middle column-loss scenario. Out of the eight specimens, two connections were designed as welded single shear plate 2D and 3D; two joints were bolted double angle 2D and 3D; two joints were welded double angle 2D and 3D and the last two connections were hybrid welded and bolted double angle 2D and 3D. Performance of different simple connections was compared based on their modes of failure and load-displacement response in both flexural and catenary action stages.**

Keywords—Progressive collapse; Steel beam-column connection; Column removal scenario; Catenary action; simple connections; FE.

Recent trends about gas sensing through semiconductor



Prof. Dr. Vincenzo Guidi
Ferrara University Italy
guidi@fe.infn.it

***Abstract*-Nowadays, in order to satisfy the market demands, materials and devices for sensor production must be increasingly miniaturized, eco-friendly, energetically efficient, reliably multitasking, and low-cost. Moving towards these requirements and simultaneously satisfying the strong demand for novel applications, chemoresistive gas sensors have been widely investigated for electronic and olfactometric systems. So far, the research in sensing materials, ranging from the mostly used metal-oxides or most recent non-oxides semiconductors, to conductive polymers or organic-inorganic hybrids, has allowed producing highly performing devices. Besides, the film deposition techniques, the synthesis processes used to obtain nanostructured powders, i.e. sol-gel technique, precipitation reaction and hydrothermal synthesis, play a significant role on the sensing properties of the materials. For the most part of chemoresistive gas sensors, the variation of film electrical resistance induced by bulk/surface charge transfer is promoted by using high temperatures that entails high-power consumption, lower durability and safety risk in presence of flammable gases. Then, room temperature operation is an extremely valuable goal in gas sensing research, due to intrinsic safety of sensors working in harsh or industrial environment. Moreover, the reduction of power consumption and, consequently, of the associated electronics size is highly demanded. In recent years, photo-activation mechanism has represented a precious alternative to achieve room temperature gas sensing using energy activations, which depend on the band gap of the materials, to create a suitable concentration of electron-hole pairs. In a chemoresistive gas sensor the film provides both the receptor and transducer functions, while the substrate is for mechanical support but it could also perform an active role in the gas-sensing process. Alumina substrates feature good properties of stability, mechanical strength and electrical insulation, while being chemical inert. Their developed technology can be easily adapted for Si-based micromachined hotplates, which has already demonstrated to reduce the power consumption and to be integrable in IC platforms.**

Coupled Maxwell and density functional description of the interaction of light and nanostructures



Prof. Dr. Varga KALMAN
Vanderbilt University
USA
varga1kalman@gmail.com

***Abstract*-We have developed a time-dependent orbital free (TD-OF) approach coupled with the Maxwell equations to describe the interaction of electromagnetic waves and matter. The coupled Maxwell TD-OF equations describe the electron and photon dynamics in a microscopic framework on equal footing. In the coupled frame, the densities and current are calculated in a quantum mechanical approach in the presence of a time-dependent vector potential and then the Maxwell equations are solved with the calculated time-dependent microscopic currents and densities – yielding the new vector potential that couples the EM fields to the quantum equations. A new approach, the Riemann-Silberstein formalism is used to solve the Maxwell-equation by the propagation of "the wave function of the photon". The approach allows for electrodynamic simulations to be performed for systems of experimentally relevant size with a quantum description of the electrons. Computational challenges of gap plasmonics (charge transfer plasmons, plasmonic tunnel junctions, high harmonic generation) and 2D plasmonics (real space mapping, edge plasmons, terahertz plasmonics) will be discussed.**

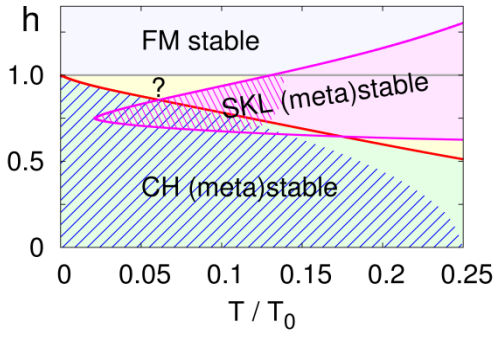
Stabilization by thermal fluctuations of a new skyrmionic phase at low temperature in cubic helimagnets: Are new phases still waiting to be discovered?



Victor Laliena
Aragon Material Science Institute,
CSIC-University of Zaragoza, Zaragoza,
E-50009, Spain
laliena@unizar.es

Javier Campo
Aragon Material Science Institute,
CSIC-University of Zaragoza,
Zaragoza, E-50009, Spain
JAVIER.CAMPO@csic.es

***Abstract*-The role of thermal fluctuations in the stabilization of the magnetic states that appear in cubic helimagnets is theoretically analyzed, using a saddle point expansion to obtain the free energy. It is shown that in the low temperature region thermal fluctuations destabilize the conical state and stabilize the skyrmion lattice (SKL) near the transition to the forced ferromagnetic state. Also, a new phase, whose features cannot be determined with our method, appears in this region of the phase diagram (Fig.1 Left) [1]. This new state, and the SKL at low temperature, have been recently found in Cu_2OSeO_3 [2, 3]. It is also shown that at high temperature and low field, near the phase boundary, thermal fluctuations stabilize the SKL, which becomes the equilibrium state (Fig. 1 Right) [4]. Comparisons with recent experimental results [2, 3] and with the computations of Mühlbauer et al. [5] are given.**



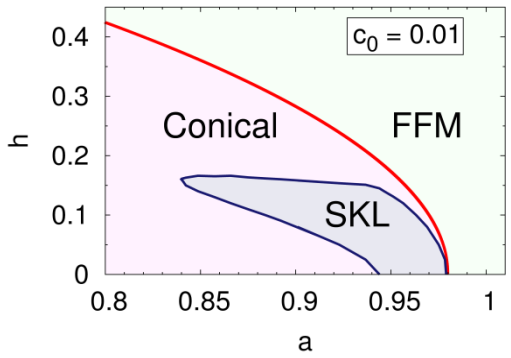


Fig. 1: *Left, theoretical phase diagram of the cubic helimagnet, including the effect of Gaussian fluctuations, in the low T region. Right, same in the high T region (the parameter a controls the variation of temperature).*

References

1. V. Laliena and J. Campo, Phys. Rev. B96, 134420 (2017)
2. F. Qian et al. Sci. Adv. 2018 ;4 : eaat7323 21 (2018)
3. A. Chacon et al., https://doi.org/10.1038/s41567-018-0184-y Nature Physics, (2018).
4. V. Laliena, G. Albalate, and J. Campo, Phys. Rev. B98, 224407 (2018).
5. S. Mühlbauer et al., Science 323, 915 (2009).

Blockchain in Healthcare: Applications, Potentials, and Challenges



Dr.Fathey M.A.Mohammed
School of Computing , UUM Malaysia
fathey.m.ye@gmail.com

***Abstract*-Healthcare is the major concern of any nation for its overall growth. Currently, due to COVID19 pandemic, many countries are suffering from a dramatic increase in the number of patients, and it may be more difficult for patients to access primary care services. Moreover, COVID-19 pandemic is reshaping healthcare with technology. New technologies are fundamentally changing the way heath care services are provided. Never before has health informatics played a greater role in public health than during the COVID-19 pandemic. Accordingly, there is a need for reorienting the model of heath care; optimize current and develop alternative delivery platforms for essential health services. Due to its decentralized nature, blockchain technology is a suitable driver for the much-needed shift towards integrated healthcare, providing new insights and addressing some of the main challenges of many healthcare areas. This research explores the applications, potentials, and challenges of Blockchain technology in health care industry. Research gaps and suggestions for future researches will also be highlighted.**

Antenna With Electromganetic Band Gap (EBG) Structure For Wireless Application



Prof. Dr. Mohamad Kamal A. Rahim
Advanced RF & Microwave Rsearch Group
School of Electrical Engineering Faculty of Engineering
Universiti Teknologi Malaysia 81310 UTMJB
Johor, Malaysia
email: mdkamal@utm.my

***Abstract*-With the recent development of emerging technologies such as the fifth-generation networks (5G) and the internet of things (IoT), the development of antenna with electromagnetic band gap structure (EBG) has attracted much attention as a solution on some challenging factors such as bandwidth consumptions, efficiency, beam shifting, cost reduction and the components' sizes. The EBG structure can be used as a reconfigurable antenna for frequency and pattern and capable to operate with different parameter needs. The pattern reconfigurable antenna offers diversity pattern configurations and beam steering to cater to the congested signal environment problem while maintaining the performances, and operating frequency and increasing the signal and data security. The pattern reconfigurable antenna using electromagnetic bandgap (EBG) structure is presented in this talk for beam-steering configurations. Three types of antenna which are linear and circular polarization with pattern reconfigurable incorporated with EBG structure, the tunable frequency and polarization with pattern reconfigurable using EBG structure and dual-band pattern reconfigurable using EBG structure were designed and analysed. The EBG patches structure are located at both right and left on the same plane of radiating antenna. The EBG is designed so that its surface wave of bandgap covers the radiation of the antenna. As a result, the surface waves excited by the patch antenna are inhibited from propagation by the EBG and caused the radiation pattern of the antenna will be tilted on another side. PIN diode switching mechanism is introduced to reconfigure the EBG structure. The operating frequency of the proposed antenna is 2.45 GHz for linear and circular polarization single band antenna while 2.45 GHz and 5.8 GHz for linear polarization dual-band antenna. With average gain of 3 dB for all designs, the proposed antennas capable to have beam shifting at three different angles (0°, +26° and - 26°). Simulated and measured results are presented, thus verifying the proposed antennas concept. Pattern reconfigurability enables wireless communication systems to avoid congested environments and save energy by redirecting signals toward intended users only**

3D tomographical imaging of localized surface plasmon resonances of cylindrical and dimeric spherical nanocrescents



Prof. Dr. Karim Abbasian
University of Tabriz Iran
k_abbasian@tabrizu.ac.ir

***Abstract*-Showing a real graph through a cross section of human body with ultrahigh resolution and extreme contrast is the main challenge for medical imaging systems. Also, plasmonic tomography approaches promise noise floors below the photon shot noise level with unobtainable increased signal to noise ratio (SNR). Then, plasmonic tomography can result in faster and accurate biomedical detections below to sub cell voxel sizes.**

Here, a dimeric arrangement including two spherical nanocrescents with tips pointing at each other in nanometer proximities has been proposed. Hybridization of the plasmonic modes in close proximities leads to a 48% enhancement in Purcell factor inside the gap compared to the single spherical nanocrescent. The 3D bright surface plasmon modes of the nanocrescent are investigated by a nanometer resolved tomographic cathodoluminescence (CL) spectroscopy combined with radiative local density of optical states (LDOS) calculation.

In this work, the boundary element method (BEM) with the electron beam and point dipole sources are used to numerically solve the retarded full Maxwell equations. Then, by simultaneous iterative reconstruction technique (SIRT) tomographic reconstructions are produced from a set of 2D CL maps in different orientations. The CL achieving procedure and associated radiative LDOS are, first, validated for well-established cylindrical nanocrescent and then applied to the spherical nanocrescent dimer. The 3D obtained plasmonic dimer with promising radiative optical properties shows enormous potential to play the main role in applications such as *in vivo* biosensing, tumor and cancerous cell diagnosing based on plasmonic-enhanced fluorescence and also surface-enhanced Raman spectroscopy (SERS).

Thin Film Solar Photovoltaic Cells – Status and Way Forward



Prof. Dr. Nowshad Amin
Institute of Sustainable Energy, Universiti Tenaga Nasional (*@The National Energy University*),
Jalan IKRAM-UNITEN, 43000 Kajang,
Selangor, Malaysia
E-mail: nowshad@uniten.edu.my

***Abstract*- Ever since the demonstration of practically usable solar cell at Bell Labs (1954, 6% efficiency), tremendous advent has happened attributing to the rigorous efforts of researchers around the world that led to multi mega watt-peak solar farms of today for electrical power generation. Researchers try to find energy harvesting in the form of electricity from various potential opto-electronic materials starting from inorganic silicon based to organic based ones of today. Even though, the so-called first generation solar cells, mainly crystalline or multi-crystalline silicon, are still dominating, the quest for other options presented many other potential candidates such as amorphous silicon, cadmium telluride, copper-indium-sulphide etc. since early 70s. Ever since the second generation solar cells came into the scenario, most of these are thin films based that require many supporting layers to form the complete cells in homo or hetero junction configurations but within a total thickness of 2-10 micron. Cutting edge technologies in layer deposition or device fabrication have led to successful commercialization of these 2nd generation solar cells like CIS or CdTe, with a total over few GWps of yearly production in recent years. This talk will include 2nd generation solar cells that are thin films of CdTe, CIS etc as absorbers and their way forward. Some futuristic research works will be discussed from our ongoing works. Related issues on the possible optoelectronic materials for various solar PV generation as well as R&D prospects will also be discussed to demonstrate the potentialities of future solar photovoltaic technology.**

Screen-printed group IV semiconductors on Silicon



Marwan Dhamrin
Graduate School of Engineering, Osaka University, Japan
Core Technology Center, Toyo Aluminium K.K. Japan

Shota Suzuki
Graduate School of Engineering, Osaka University, Japan

Masahiro Nakahara
Graduate School of Engineering, Osaka University, Japan

Moeko Matsubara
Graduate School of Engineering, Osaka University, Japan

***Abstract*-Multi-junction solar cells which combine multiple p–n junctions of different bandgap energies to absorb the spectrum of the sun, are the state-of-the-art approach for achieving high efficiency. This structure allows us to reduce the carrier thermalization losses arising from the absorption of photons with excess energy compared to the semiconductor bandgap, as well as transmission losses of photons with insufficient energy. This type of solar cell can theoretically obtain an extremely high efficiency of 49% in three junctions under non concentrated sunlight [1]. However, the main reasons for their limited use so far are the high cost and other technical drawbacks associated with the Ge substrate on which these cells are fabricated. Thus, it is desired to transfer the Ge to a low-cost Si wafer platform, and several approaches such as wafer bonding [2-4], lift-off [5], sample recycling and growing sacrificial thick buffer layers of SiGe/Ge have been introduced [6-10]. Nevertheless, these processes are still costly to introduce into the current photovoltaic market.**

In this paper, we will demonstrate single-crystalline Si_xGe_{1-x} thick layer epitaxial growth on large area Si substrates by sintering a screen-printed Al-Ge paste at high temperatures. The SixGe1-x formed layers show good uniformity with thicknesses up to 20 □m. Ge content of more than 30% are achieved. From the XRD patterns, the crystalline Si_xGe_{1-x} peak has been detected in the vicinity of 2θ = 66.2 ~ 68.8deg. The formed Si_xGe_{1-x} /Si wafer can be used with Ge buffer layer to fabricate high efficiency III-V multi-junction solar cells on cheap silicon substrates allowing the terrestrial solar cell module application of the expensive III-V compound solar cells.

In addition, the developed Si_xGe_{1-x} /Si can be used as virtual substrate will decrease the fabrication cost of devices such as hetero-junction bipolar transistors (HBTs), strained-channel metal-oxide-semiconductor field effect transistors (MOSFETs), mid-and far infrared photo-detectors, and resonant tunnelling diodes allowing a new horizon for cost reduction of next generation of communication electronics and devices.

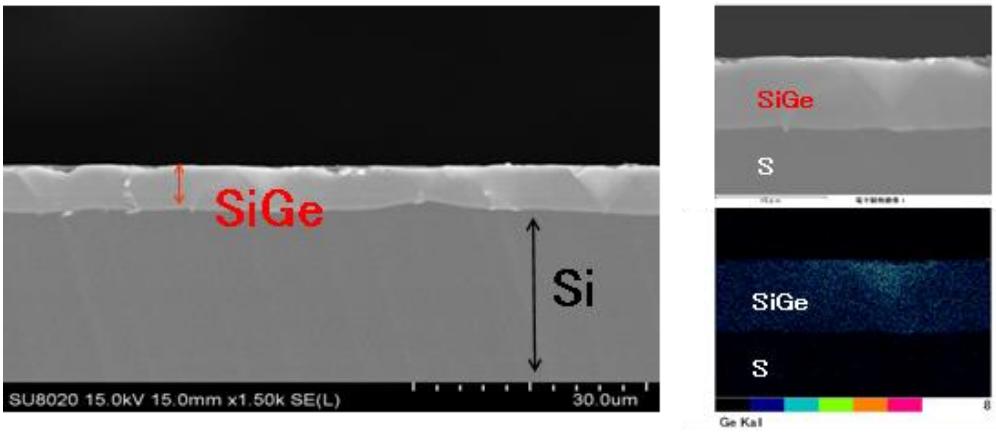


Figure 1 : SEM cross section images of the Si_xGe_{1-x} layer on Si. EDX analysis of the Ge content in the Si_xGe_{1-x} layer.

References

1. A. De Vos, J. Phys. D: Appl. Phys. 13, 839 (1980).
2. H. Kanbe, M. Miyaji, M. Hirose, N. Nitta, and M. Taniwaki, Appl. Phys. Lett. 91, 142119 (2007).
3. H. Kanbe, M. Miyaji, and T. Ito, Appl. Phys. Express 1, 072301 (2008).
4. H. Kanbe, M. Hirose, T. Ito, and M. Taniwaki, J. Electron. Mater. 39, 1248 (2019).
5. M. Konagai, M. Sugimoto, and K. Takahashi, J. Cryst. Growth 45, 277 (1978).
6. Y. B. Bolkhovityanov and O. P. Pchelyaknov, Physics-Uspekhi. 515, 437 (2008).
7. D. J. Paul, Semicond. Sci. Technol. 19, R75 (2004).
8. W. Leitz, M. T. Currie, A. Y. Kim, J. Lai, E. Robbins, E. A. Fitzgerald, and M. T. Bulsara, J. Appl. Phys. 90, 2730 (2001).
9. M. De Seta, G. Capellini, Y. Busgy, F. Evangelisti, M. Ortolani, M. Virgilio, G. Grosso, G. Pizzi, A. Nucara, and S. Lupi, Appl. Phys. Lett. 95, 051918 (2009).
10. V. A. Shah, A. Dobbie, M. Myronov, D. J. F. Fulgoni, L. J. Nash, and D. R. Leadley, Appl. Phys. Lett. 93, 192103 (2008).

Electromagnetic Micropump Incorporating the Polymer Composite based Magnetic Membrane for Biomedical Application



Assoc. Prof. Dr. Jumril Yunas
Institute of Microengineering and
Nanoelectronics, The Universiti Kebangsaan
Malaysia, Bangi, 43600, Malaysia
Phone: +60389118541
jumrilyunas@ukm.edu.my

***Abstract*-In this presentation we report the current development of electromagnetic (EM) microfluidic pumps incorporating the magnetic polymer composite for the transport of microfluidic based biomedical-sample. The EM micropump consists of three main components, namely the electromagnetic part, the micro-actuator and the microfluidic part including the inlet and outlet tubings, valveless fluid channel and chamber (Fig 1). The electromagnetic part includes the electromagnetic coils and permanent magnet while the micro-actuator includes a deformable actuator magnetic membrane made of polydimethylsiloxane (PDMS) with embedded NdFeB magnetic particles. The magnetization curves of the synthesized magnetic composite using VSM proved that the cured polymer composites do not block the magnetic performance of the magnetic particles embedded in it. The micropump system is fabricated using a MEMS process with additional bonding process. Various types of the magnetic membrane as well as electromagnetic coil designs were characterized to find optimum pump performance. As the results, it is found that the fabricated micropumps were able to deliver fluidic sample within a large flow-rate range from 6 µl/min down to several nl/min which can be adjusted by setting the input electrical current parameters, such as intensity, frequency and type of the AC current signal. The developed system will benefit for the precisely bio-sample transport in biomedical application.**

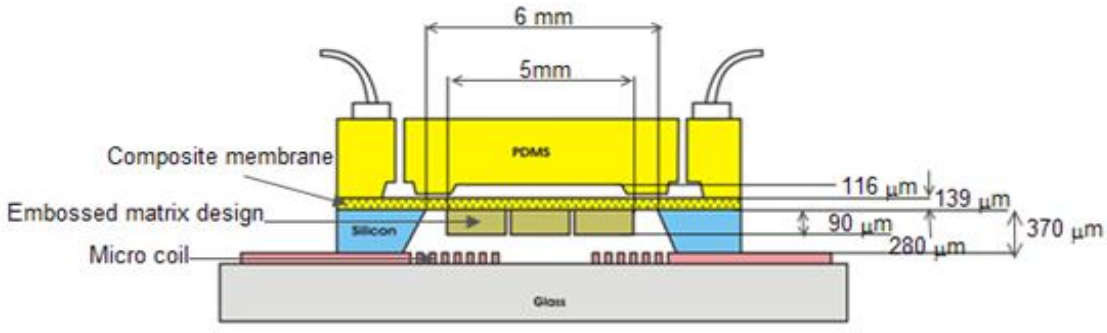


Fig1. The schematic cross section view of EM micropump system

Grid of The Future (GoTF) Advancing Grid Transformation in Malaysia



Prof. Dr. M. Zainal Abidin Ab Kadir
University Putra Malaysia
mzk@upm.edu.my

***Abstract*-Efficient and reliable transmission and distribution of electricity is a fundamental requirement for providing societies and economics with essential energy resources. The utilities in the industrialized countries are today in a period of change and agitation. Large parts of the power grid infrastructure are reaching their designed end of life time, since a large portion of the equipment was installed in the 1960s. On the other hand there is a strong political and regulatory push for more competition and lower energy prices, more energy efficiency and an increased use of renewable energy like solar, wind, biomasses and hydro. In industrialized countries the load demand has decreased or remained constant in the previous decade, whereas developing countries have shown a rapidly increasing load demand. Aging equipment, dispersed generation as well as load increase might lead to highly utilized equipment during peak load conditions. If the upgrade of the power grid should be reduced to a minimum, new ways of operating power systems have be found and established. For this reason, Tenaga Nasional Berhad of Malaysia (TNB) has allocated USD 0.67bil from the total of USD 4.4bil capital investment in transmission and distribution grid secured under the second Regulatory Period (2018-2020) for the Grid of the Future. They are continuing to invest in digitisation and automation as well as improve its performance and reliability. This talk will share Malaysia's aspiration to be amongst the most technologically advanced and reliable power transmission in the world in order to meet future challenges and growing demand in an increasingly liberalized generation market for securing a sustainable, secure and competitive energy supply**

Application of Natural Mode Series on Material Characterization at Microwave Frequencies



Prof. Dr. Uğur Cem HASAR
Gaziantep University Turkey
uchasar@gantep.edu.tr

***Abstract*- Material characterization has been an important and active research field especially in recent years due to rapid development of synthetic materials such as graphene, metamaterials, and carbon nanotube. Such a characterization could be realized by correlating the measured electromagnetic properties to the measured/known mechanical, physical and chemical properties of the material under test. Electromagnetic characterization of materials could be implemented by application of natural mode series through the application of singularity expansion method. In this invited work, we will firstly briefly discuss the techniques for precise evaluation of natural mode series such as Prony's method, Matrix pencil method, and E-pulse method, and next present a new technique for such evaluation (a graphical method). Then, the close relation between thickness resonance frequencies and late-time natural resonance frequencies is examined. Finally, we will demonstrate how these natural mode series could be applied for electromagnetic characterization of simple materials.**

Laser Line Scan surface processing: nanostructure and microstructure control



A. Cubero
Instituto de Nanociencia y Materiales de Aragón (INMA), CSIC-Universidad de Zaragoza, Zaragoza 50009, Spain

H. Amaveda
Instituto de Nanociencia y Materiales de Aragón (INMA), CSIC-Universidad de Zaragoza, Zaragoza 50009, Spain

A. Frechilla
Instituto de Nanociencia y Materiales de Aragón (INMA), CSIC-Universidad de Zaragoza, Zaragoza 50009, Spain

D. Muñoz-Rojas
Laboratoire des Matériaux et du Génie Physique (LMGP) UMR 5628 CNRS 38016 GRENOBLE, France

E. Martínez
Instituto de Nanociencia y Materiales de Aragón (INMA), CSIC-Universidad de Zaragoza, Zaragoza 50009, Spain

J. A. Bea
Instituto de Investigación en Ingeniería de Aragón, Universidad de Zaragoza, Zaragoza 50018, Spain

E. Lacruz
Instituto de Nanociencia y Materiales de Aragón (INMA), CSIC-Universidad de Zaragoza, Zaragoza 50009, Spain

L.A. Angurel
Instituto de Nanociencia y Materiales de Aragón (INMA), CSIC-Universidad de Zaragoza, Zaragoza 50009, Spain

H. Santos
Instituto de Nanociencia y Materiales de Aragón (INMA), CSIC-Universidad de Zaragoza, Zaragoza 50009, Spain

L. Porta
Instituto de Nanociencia y Materiales de Aragón (INMA), CSIC-Universidad de Zaragoza, Zaragoza 50009, Spain

F. Toldra-Reig
Laboratoire des Matériaux et du Génie Physique (LMGP) UMR 5628 CNRS 38016 GRENOBLE, France

G. F. de la Fuente
Instituto de Nanociencia y Materiales de Aragón (INMA), CSIC-Universidad de Zaragoza, Zaragoza 50009, Spain

***Abstract*-Laser surface processing entails nowadays the use of many different types of laser sources, as well as various ways of irradiating the surface of materials. In principle, it is a rather simple task to focus a laser beam onto a surface and perform a desired scan, either via rastering or by selectively moving the beam with commercially available galvanometer scanners. The latter are driven by software programs that are often similar, and offer numerous possibilities with regard to beam scanning algorithms. These are applied to Laser Additive Manufacturing (LAM) for example, to produce complex geometry polymer and metal 3D objects.**

Nevertheless, beam scanning suffers from particular limitations, as the beam needs to move at a fast rate in order to fill a desired area within a reasonable timelength. In addition, although beam scanning offers great flexibility for many applications, it does not provide conditions for optimum microstructure control.

For the latter reason, we have developed the so-called "Laser Line Scan" surface processing methods, in order to improve large-area productivity and control of microstructure on many different types of materials.

After a brief introduction to the different aspects involved in the beam and line scanning methods, a number of examples will be reviewed where Laser Line Scanning has been applied in order to achieve surfaces with desired superconducting, magnetic, luminescent and mechanical properties.

Acknowledgements: This research is supported by project SPRINT (EU H2020-FETOPEN 801464) and by Gobierno de Aragón "Construyendo Europa desde Aragón" (research group T54_20R).

Laser remelting of Al2O3 coatings on Cu: A way to increase thermal conductance in heat sinks



A. Cubero
Instituto de Nanociencia y Materiales de Aragón (INMA), CSIC-Universidad de Zaragoza, Zaragoza 50009, Spain

G. F. de la Fuente
Instituto de Nanociencia y Materiales de Aragón (INMA), CSIC-Universidad de Zaragoza, Zaragoza 50009, Spain

S. Dosta
Centre de Projecció Tèrmica (CPT), Dept. Ciència de Materials i Química Física, Universitat de Barcelona, Barcelona, Spain

E. Martínez
Instituto de Nanociencia y Materiales de Aragón (INMA), CSIC-Universidad de Zaragoza, Zaragoza 50009, Spain

I. G. Cano
Centre de Projecció Tèrmica (CPT), Dept. Ciència de Materials i Química Física, Universitat de Barcelona, Barcelona, Spain

L.A. Angurel
Instituto de Nanociencia y Materiales de Aragón (INMA), CSIC-Universidad de Zaragoza, Zaragoza 50009, Spain

***Abstract*-There are several applications where heat generated during work has to be evacuated in order to avoid an excessive temperature rise that could damage the system. Thermal sprayed coatings on metals is an alternative that has been used as a barrier to protect metallic components and to provide electrical insulation and good thermal conductance. One of its advantages is that there is no limitation in shapes and sizes. Moreover, the high porosity values and the presence of metastable phases can deteriorate the dielectric properties of alumina. Laser remelting is an alternative to achieve denser and more homogeneous coatings. We present some results obtained using a near-infrared laser (λ = 1060-1070 nm). Adjusting the laser processing parameters, it is possible to transform the metastable □-Al_2O_3 phase of the as-sprayed coatings to stable □-Al_2O_3, to obtain a denser coating and to control crack generation in the ceramic material. After laser treatments, thermal resistance values 3 to 4 times lower in, comparison with the plasma-sprayed samples, were achieved.**

These ideas have been applied to allow the application of currents above 400 A in a superconducting coil, cooled in high vacuum by thermal conduction using a cryocooler.

Enhancing the Performance of Coiled Carbon Nanofibers/Mill Scale Nanocomposites at X- and Ku-band Frequency



Ismayadi Ismail
Institute of Advanced Technology, Universiti Putra Malaysia, 43400 Serdang, Selangor, Malaysia

Rabaah syahidah Azis
Institute of Advanced Technology, Universiti Putra Malaysia, 43400 Serdang, Selangor, Malaysia

Fatma Nur Tuzluca
Department of Physics, Erzincan Binali Yıldırım University, 24100 Erzincan, Turkey

Mehmet Ertugrul
Department of Electrical and Electronics Engineering, Atatürk University, 25240 Erzurum, Turkey

Intan Helina Hasan
Institute of Advanced Technology, Universiti Putra Malaysia, 43400 Serdang, Selangor, Malaysia

Gokhan Ozturk
Department of Electrical and Electronics Engineering, Atatürk University, 25240 Erzurum, Turkey

Mohd Nizar Hamidon
Institute of Advanced Technology, Universiti Putra Malaysia, 43400 Serdang, Selangor, Malaysia

Yasar Ozkan Yesilbag
Department of Physics, Erzincan Binali Yıldırım University, 24100 Erzincan, Turkey

Ugur Cem Hasar
Department of Electrical and Electronics Engineering, Gaziantep University, Gaziantep 27310, Turkey

***Abstract*-Our research work focused on enhancing the performance of microwave absorbing materials (MAMs) in term of high absorption level and operating in a broad frequency range. The resulted performance was achieved using a hybrid material of carbon nanofibers and nanosized mill scale from waste. Generally, in MAMs, the problem of applying a passive coating would result in high absorption of electromagnetic (EM) wave but narrow frequency range. Our hypothesis was to combine carbon and magnetic materials to broaden the bandwidth. Hence our research work aimed to hybridize carbon nanofiber with nanoparticles mill scale waste and investigate the effect of mill scale catalyst size on the performance of EM-wave absorption at 8-18 GHz. Mill scale was washed and milled at 4 different milling time and then applied as catalyst in chemical vapour deposition (CVD) process. Ethanol was used as carbon source to synthesis CNF at 750 ºC. The resulted materials from CVD process was then mixed with epoxy resin as polymer composite and was then put into a sample holder for EM-wave measurement with 3 different thickness. We have successfully synthesized CNF with coiled, spiral, twisted nanostructures which was advantageous in enhancing the absorption of the EM-wave. Maximum absorption was obtained by majority of the samples with reflection loss of ≤-20 dB (99% signal absorbed). The as-synthesized CNF catalyst by mill scale waste using CVD method can be a promising candidate as potential EM absorbing material especially for RADAR wave absorbers**

.

Phenomenological Aspects of Thin-Walled Cylindrical Reservoirs, Experimental Work-Overview



Prof. Dr. Abdulkadir Cüneyt AYDIN
Ataturk University, Engineering Faculty,
Department of Civil Engineering, 25030,
Erzurum, TURKEY
acaydin@atauni.edu.tr

***Abstract*- Thin-walled cylindrical members are widely used for not only liquid storage tanks, but also for marine structures. The lightness and high strength of these members revealed their wide handling from nuclear reactors to spacecrafts, including dams, and missiles, etc. Thus, cylinders and/or cone shells are in consideration for their behavior, while evacuation. The present work is unified for buckling and post buckling behavior, including retrofitting by carbon reinforced polymers, and the effect of the dent. The artificially created dents are observed for their thickness ratio for the cylinder and dent depth. The height and radius of the test models are evaluated for within the range of theoretical and for out-of-range considerations. Some transformation coefficients for theorical concepts are considered for carbon fiber reinforcements. Furthermore, the retrofitting concept for cylindrical shells is observed.**

Impacts of Carbon Quantum Dots on Chili (Capsicum annuum L.) Plant Growth



Suraya Abdul Rashid
Institute of Advanced Technology,
Universiti Putra Malaysia, 43400 UPM
Serdang, Selangor, Malaysia
suraya_ar@upm.edu.my

Tan Tong Ling
Institute of Advanced Technology, Universiti
Putra Malaysia, 43400 UPM Serdang,
Selangor, Malaysia
tongling@upm.edu.my

***Abstract*- Chili (Capsicum annuum L.) is one of the major economic value vegetable crops grown in Malaysia and has a very high demand mainly for its pungency and flavouring. However, local production of chili is insufficient enough for local demand due to high population growth and growing variety of foods made using chili pepper. Thus, a lot of farmers prefer to grow chili to meet market needs and to attain higher profit. In this study, a facile, efficient, and green microwave-assisted method was used to prepare fluorescence carbon quantum dots (CQD) with empty fruit bunches (EFB) biochar to determine the application of carbon quantum dots as photosynthesis enhancer for the chili plant cultivation. The effects of CQD on the photosynthetic efficiency of chili plants were determined by measuring the maximum net assimilation rate, rubisco catalytic activity, electron transfer rate, stomatal conductance, and water use efficiency of the leaf. CQD was first introduced into plant via foliar spraying at the fixed concentration of 150 mg/L. As a result, foliar application of CQD significantly promoted photosynthetic capacity than control, advocating enhanced photons capture and sustainable agriculture practices.**

Keywords—carbon quantum dots, photosynthesis, chili, foliar spraying, growth

Hyperspectral Imaging: Basics and its Application for Ground Based Surveillance System for Explosive Detection



Assoc. Prof. Dr. Alper Koz
Middle East Technical University TURKEY
koz@metu.edu.tr

***Abstract*-Hyperspectral images (HSI) are formed of many spectral bands which are captured in a wide and continuous manner at hundreds of differentwavelengths across the electromagnetic spectrum. It has been one of thecore research areas in remote sensing and geoscience in the last 15 yearswith enormous number of applications ranging from video surveillance andenvironment monitoring to land-cover mapping and agriculture analysis. Inthis talk, we will begin with the basics of hyperspectral imaging withinthe scope of target detection. Its application for ground basedsurveillance systems for explosive detection will be explored by revealingthe challenges for such a system from the point of detection performance,acquisition speed, spectral registration, and radiance-to-reflectanceconversion. We will then present the initial results for the prototypesurveillance system and discuss the future perspectives.**

Neuroimaging in everyday life with a novel brain imaging modality



Assist. Prof. Dr. Sinem Burcu Erdoğan
Acıbadem University Turkey
berdogan83@gmail.com

***Abstract*-Functional Near Infrared spectroscopy (fNIRS) is a relatively novel, field deployable, noninvasive brain imaging modality which uses low levels of near infrared light for measuring local hemodynamic changes induced by cortical brain activation. Over the past 2 decades, fNIRS systems have been designed to monitor hemodynamic changes caused by task-induced brain activation during various cognitive and mental tasks such as motor imagination, music imagination, mental object rotation and mental arithmetic tasks. fNIRS based systems fulfill the desired characteristics of an ideal brain computer interface system such as ease of use in terms of short set-up time and calibration, safety, portability, wearability, modest equipment size, low operating costs and affordability. The ability of fNIRS to detect brain activation during such BCI compatible tasks have suggested its suitability for BCI designs. In this talk, after giving a brief background of the physical and physiological principles underlying fNIRS measurements and their neural correlates, I will present examples of how this technique can operate effectively in naturalistic settings and clinical environment with miniaturized wireless designs.**

Neurorobotics and Brain computer interface for robotic rehabilitation



Dr. Noman Naseer
Head of Neurorobotics Research Group,
Department of Mechatronics, Air University,
Islamabad
noman.naseer@mail.au.edu.pk

***Abstract*- Neurorobotics is the combined study of neuroscience, robotics and artificially intelligent systems. It can be used to provide a means of communication for people suffering from severe motor disabilities or with limb amputation. This talk with focus on development of electromyography (EMG)-based control of prosthetic arm and electroencephalography (EEG)-based control of external devices including a wheelchair for rehabilitation of mobility in paralyzed individuals. Details of a recently developed functional near-infrared spectroscopy (fNIRS) system for brain-imaging and its application for brain-computer interface will be presented. All necessary steps involved in developing EMG-, EEG- and fNIRS-based neurorobotics interfaces including bioinstrumentation, filtering, pattern recognition and control command generation will be discussed. Some recent works done at Neurorobotics Research Group at Air University, Islamabad will be presented as well.**

Enhanced Performance of Flexible Microstrip Patch Antenna with Ferrite Thick Film Inclusion



Intan Helina Hasan
Institute of Advanced Technology, Universiti Putra Malaysia, Selangor, Malaysia
i_helina@upm.edu.my

Mohd Nizar Hamidon
Institute of Advanced Technology, Universiti Putra Malaysia, Selangor, Malaysia
Faculty of Engineering, Universiti Putra Malaysia, Selangor, Malaysia

Alyani Ismail
Faculty of Engineering, Universiti Putra Malaysia, Selangor, Malaysia

Ismayadi Ismail
Institute of Advanced Technology, Universiti Putra Malaysia, Selangor, Malaysia

Nur Alin Mohd Azhari
Institute of Advanced Technology, Universiti Putra Malaysia, Selangor, Malaysia

Saman Azhari
Institute of Advanced Technology, Universiti Putra Malaysia, Selangor, Malaysia

Muhammad Asnawi Mohd Kusaimi
Institute of Advanced Technology, Universiti Putra Malaysia, Selangor, Malaysia

Farah Nabilah Shafiee
Institute of Advanced Technology, Universiti Putra Malaysia, Selangor, Malaysia

***Abstract*-Research on microstrip patch antenna (MPA) has been growing in the past few decades due to its planar profile and easy fabrication. Its simplicity of structure which includes a conductive patch, a dielectric substrate, a ground plane and a microstrip feeder is making it more popular for integration in electronic and telecommunication devices focusing on flexibility. There is however few disadvantages of MPA, such as narrow bandwidth, low power and limited material selection if current printed circuit board (PCB) etching fabrication technique is used. Ferrite substrates are known to be able to help overcome this issue, but the dielectric and magnetic properties of bulk ferrites are difficult to control and manipulate.**

This work aims to solve mentioned problems by using thick film technology which utilizes screen printing method to include ferrite thick film in the MPA structure as substrate overlay to help enhance the bandwidth performance of MPA. Preparation of the paste by mixing nanopowders with linseed oil as organic vehicle and characterization of the ferrite thick film paste were carried out to investigate properties of the thick film. Results showed that the thick film exhibited moderate permittivity and permeability, which is suitable for MPA fabrication. The actual fabricated MPA with ferrite thick film inclusion on polyimide substrate (Kapton film) showed that the thick film improved the performance of MPA with firing temperature of 300°C. MPA with YIG thick film exhibited improved return loss of -23.67 dB but reduced -10dB bandwidth to 0.70 GHz, while Q factor was increased to 8.4. As for MPA with NZF thick film, the return loss and bandwidth improved to -28.73 dB and 1.16 GHz respectively, while the Q factor reduced to 5.10.

As conclusion, a novel ferrite thick film paste with linseed oil as organic vehicle has been successfully developed and characterized. Furthermore, ferrite thick film inclusion in MPA fabrication has proven to enhance the bandwidth of the antenna, leading to a success in fabrication of MPA on flexible substrate with enhanced performance. The flexibility of the antenna may have vast possibilities in various applications in the future, such as wearable antenna, and flexible telecommunication devices.

EEG based Brain Computer Interface System Design Techniques



Onder Aydemir
Karadeniz Technical University Turkey
onderaydemir@ktu.edu.tr

***Abstract*-Brain Computer Interfaces (BCIs) are systems that make it possible for people to use a computer cursor, robot arm, mobile phone or various electronic devices with only their thought. BCIs can use signals received from devices that measure various brain activity such as electroencephalography (EEG), near infrared spectroscopy (NIRS), electrocorticography (ECoG), magnetoencephalography, functional magnetic imaging and positron emission tomography. These methods for recording neural activity have their own advantages and disadvantages. For example, ECoG has a very good signal-to-noise ratio and while it is suitable for long-term use, this method is painful and involves some serious risks due to the insertion of the microelectrodes. On the other hand, EEG is painless, has high spatial resolution and low installation cost. Since EEG has more advantages over other methods, BCI studies are commonly EEG-based. Furthermore, the detectability of the brain's responses to different stimuli also varies. All these motivate researchers to increase the speed and efficiency of feature extraction and classification components, especially the method of obtaining the BCI input signal and the experimental paradigm, in order to increase the performance of the communication system between the brain and the output device of the BCI.**

Although, in general, BCIs take EEG signal as input, they might use various kind of paradigm design techniques include motor imagery, event-related P300 potentials or steady-state visually evoked potentials. In motor imagery based BCI designs during users imagine a motor activity, their EEG signals are evaluated and when the related pattern is recognized the command is sent to electronic device. Although it provides control signals without receiving external stimuli, avoiding visually induced eye irritation, the classification accuracy of motor imagery based BCIs is relatively low. On the other hand, the P300-based BCIs generally utilize the Farwell and Donchin paradigm design technique, in which a subject could choose among 36 alphanumeric characters, presented in a 6x6 matrix in which a row or column was randomly intensified on a computer screen. In such a system, a user focuses his/her attention on the specific target character, which he/she would like to spell and mentally counts how many times the character flashed in the matrix. It should be noted that he/she ignores any flashes which do not match the target character. While the one of common advantage of P300 based BCI is, it can be generalized for subjects, its main disadvantages is that its paradigm might be memorized by the participants and the performance of the system might be decreased. In a steady state visual evoked potentials (SSVEP) based BCI paradigm, the frequency spectrum of the EEG signals to the flickering stimulus frequency on which the subject focuses his/her attention on the specific cell. SSVEP is evoked response EEG that has two main advantages. One of them is it can be generalized and the second one is it requires no training process.

As a conclusion in order to compensate the disadvantages of the EEG based BCI paradigm techniques, hybrid paradigms might be utilized. Therefore, not only the performance of such systems can be increased, but also they can be generalized for the participants.

Functional Nanomaterials for Electronic Applications



Dr. Zainab Yunusa
Bayero University Kano Nigeria
zee2yunusa@gmail.com

***Abstract*-The miniaturization of electronic devices and advances in nanomaterial research and production has made the application of functional nanomaterials at the forefront of scientific and industrial attention. Recent advances in carbon nanomaterials such as carbon nanotubes, graphene, graphene nanoribbons(GNRs) and other green carbon nanomaterials from organic sources such as rice husk and carbon charcoal have shown excellent results when deployed in electronics, bioelectronics, optoelectronics and photonic applications. The advantages of nanomaterials in terms of good electrical and thermal conductivity and its light weight has made them suitable candidates when used in electronic applications. In this paper, different carbon nanomaterials will be deployed in some electronic applications such as conducting patch material in microstrip patch antennas and also as a sensing material for gas sensors. Results obtained have shown remarkable improvement in antenna performance characteristics. Similarly, the results obtained when deployed as a gas sensing material has shown enhanced selectivity, good response and recovery times and stability at room temperature.**

Engineering of Carbon-Based Nanofiller Reinforced Polyurethane Nanocomposites



Levent TRABZON
Istanbul Technical University, Mechanical Engineering DepartmentMEMS Research Center – www.mems.itu.edu.tr

***Abstract*-Polyurethane (PU) foams are used in a widespread range of applications such as insulators materials, but their applicability is limited due to their poor mechanical and materials properties. Thus, it is critical to improve its properties in order to utilize PU foams in many different areas with enhanced performance. It seems appealing to modify PUs using nanoparticles. One- dimensional carbon nanotubes (CNTs) and two dimensional graphene nanoplatelets (GNPs) owingto their unique properties can be used as hybrid nanofillers to form well dispersed three-dimensional networks, which can overcome the dispersion problem of single nanofillers. Three types of GNPs with various flake sizes and specific surface areas (SSA) were used to study influence of GNP types on the synergistic effect of MWCNT/GNP hybrid nanofillers. We have extensively studied mechanical, materials, thermal and acoustical properties of nano-enhanced PU foams. As an example of mechanical properties, there is an outstanding synergetic effect between MWCNTs and GNPs with a flake size of 1.5 µm and a higher SSA, which tensile strength of PU was enhanced by 43% as compared to 19% for MWCNTs and 17% for GNPs at 0.25 wt%. In thistalk, research findings on the nano-modified PU foams will be presented in detailed ways with modelling to some extent.**

Multi-Objective Optimal Controls



Assist. Prof. Dr. Yousef Sardahi
Marshall University USA
sardahi@marshall.edu

***Abstract*-In this talk, the state-of-art of multi-objective optimal control will be discussed. Feedback controls are usually designed to achieve multiple and often conflicting performance goals. These incommensurable objectives can be found in both time and frequency domains. For instance, one may want to design a control system such that the closed-loop system response to a step input has a minimum percentage overshoot, peak time, rise time, settling time, tracking error, and control effort. Another designer may want the controlled system to have a maximum crossover frequency, maximum phase margin and minimum steady-state error. However, most of these objectives cannot be achieved concurrently. Therefore, trade-offs must be made when the design objective space includes two or more conflicting objectives. These compromise solutions can be found by techniques called multi-objective optimization algorithms. Unlike the single optimization methods which return only a single solution, the multi-objective optimization algorithms return a set of solutions called the Pareto set and a set of the corresponding objective function values called the Pareto front. An extensive discussion of this topic will be introduced during the conference.**

Applications of the Renewable Energy in Yemen



Assoc. Prof. Dr. Abdul-Malik Momin
Sana'a University YEMEN
dramalikmomin@yahoo.com

Short Summary:

Yemen enjoys a very diverse natural environment. The application of Renewable Energy is limited to: Solar Energy, Wind Energy, Biomass Energy and Geothermal Energy.

Solar Energy: The average sunshine hours exceed 3000 hours/year and average solar insolation is more than 16-28 MJ / m ^{2} /day.

Wind Energy: Yemen has a long coastal strip of over more than 2500 kilometers and a width of 30 to 60 kilometers along the Red Sea, Gulf of Aden and Arabian Sea. Average Annual wind speed exceeds 5 m/sec.

Biomass: Yemen is an agricultural country with a large amount of waste.

Geothermal Energy: Yemen is characterized by the volcanic nature.

Note: The geographical situations of many countries particularly within 40 degrees latitudes (N and S) give an extensive application of solar energy.

- **From the literature review it was mentioned that all the Arab countries including Yemen, the duration of the sun shine hours is about 10 hours a day.**
- **For the importance of the solar energy and its application, it is requested that the global education and training program should be launched out with the help of Solar Energy Society.**
- **There should be a proper link between the academic work and the labor market requirements.**
- **For the application of the solar energy, it is important to study climatological data. The data should be collected in a proper and systematic way to avoid any uncertainty in the experimental results.**

The applications of the Solar Energy in Yemen is limited to:

- **Solar water heating.**
- **Solar distillation for producing clean drinking water.**
- **Solar dryer for agricultural uses as crop drying.**
- **Photovoltaic systems for producing electricity.**

Strategy of Ministry of Electricity and Energy in Republic of Yemen

- **Optimize the utilization of domestic energy resources.**
- **Increasing the share of the Renewable Energy in the electricity generation.**
- **Access to Renewable Energy Technology to be incorporated in governmental development plans.**

Strategies to Renewable barriers and promote Renewable Energy and Energy Efficiency:

- **A strong policy.**
- **Resources utilization and market access.**
- **Financing (capital cost).**
- **Institutional Arrangement.**
- **Information and capacity building.**
- **Legal frame work.**

MM-RAM composites as a wide band radar absorber



Prof. Dr. Mehmet Ertugrul
Ataturk University, Engineering Faculty,
Department of Electrical and Electronics
Engineering, 25240 Erzurum-TURKEY
ertugrul@atauni.edu.tr

Abstract-The reduction of the radar cross section (RCS) is achieved by absorbing at least 90% of the microwave in the specified frequency range. Thus, the target can be made almost invisible to the radar for given radar frequency range. Generally, microwave absorption is achieved by controlling resonance and scattering mechanisms of the microwaves. Shaping the target and coating/painting it with radar absorbent material is the most common method to reduce RCS. In recent years, many new materials have been developed for this purpose, from metamaterials (MM) to radar absorber materials (RAM). In this study, a wide range of the radar frequencies divided into 3 frequency regions as low, mid and high frequency regions for the 1-18 GHz range. A new layered hybrid device has been created by combining RAM and MM structures that provide maximum absorption in these 3 frequency regions. While MM was created in different geometries for each frequency region, RAM were obtained with different material, particle size and mixing ratios. It is possible to adjust the electrical and magnetic permeability of these materials with the mixing ratio and particle size of the conductive, insulating, magnetic portion of the materials. In this study, a new hybrid structure is proposed by using RAM and MM. An insulating layer is placed between RAM and MM. RAM contains nanomaterials insulator, conductor and magnetic materials such as BN, BaFe2O3, MXene and CNT. This structure was able to provide over 90% absorption for an ultrawide range bandwidth (15GHz) between 1-18GHz. Thus, a sandwich structure that gives absorption in different frequency ranges has been obtained. In addition, the coupling effects of the MMs in each of these layers were also examined. This structure was able to provide over 90% absorption for an ultrawide range bandwidth (15GHz) between 1-18GHz.

***Keywords*—Microwave absorption, Mxene, CNT, CST**

ORAL PRESENTATIONS

ROS Based SLAM and Navigation for Automated Guided Vehicle Simulated with Gazebo

İbrahim Öztürk
Dept. of Electrical & Electronics Engineering Ataturk University Erzurum, Turkey
ibrahim.ozturk@atauni.edu.tr

Abdullah Başçi
Dept. of Electrical & Electronics Engineering Ataturk University Erzurum, Turkey
abasci@atauni.edu.tr

***Abstract*— Today's technology shows that unmanned ground vehicles, which do not need any human intervention and can direct themselves and make decisions will replace existing vehicles in the future. These vehicles have critical technology that can operate autonomously, remotely controllable, perform predetermined tasks and perform mutual tasks. Examples of these are seen in the military industry, service sector, traffic, agriculture and many other fields. These developments increase the importance of unmanned ground vehicles (UGVs) in the future. However, UGVs need to solve the problems such as path following, obstacle avoidance, mapping, navigation, environmental perception and analysis, machine learning and swarm tasks. In this paper, we designed a two-wheeled mobile robot for SLAM and navigation in indoor environments. The designed robot uses light detection and ranging sensor (LIDAR), inertial measurement unit (IMU), HQ camera and encoders to calculate the approximate pose of the mobile robot. For navigation and localization, we used filters to deal with the uncertainty of robot pose and used some algorithm to avoidance obstacles and path following. The simulation results showed that the designed vehicle can smoothly and correctly locate itself, build the environment map, and navigate in indoor environments.**

Keywords*— *Unmanned Ground Vehicle (UGV), Mobile Robots, SLAM, Navigation, Localization, Gazebo/ROS, Solidworks, Obstacle Avoidance, Path following.

[1] INTRODUCTION

Unmanned ground vehicles (UGVs) are often referred to as mobile robots in academic literature. This paper consists of creating a mobile robot platform based on ROS (Robot Operating System) and Gazebo simulation environment. The first major work in the development of mobile robots was Shackey. Shackey was a test environment for use in artificial intelligence research funded by the Defence Advanced Research Projects Administration (DARPA) at the Stanford Research Institute in the late 1960s. [1] The Shakey project was considered a failure, as it could not fully implement autonomous operations. However, it formed the functional and performance foundations for mobile robots. By identifying the technological deficiencies; made significant contributions to the development of planning, image processing and artificial intelligence research. [2]

Various algorithms have been developed for solving path planning and obstacle avoidance problems, which are the biggest problems faced by mobile robots. Some algorithms and techniques used to solve these problems are presented in Kunchev's study. A dynamic control model has been proposed in which an autonomous vehicle will move from the starting point to the target point without collision. [3] UGVs use many sensors for perception and modeling of the environment, navigation, object tracking and, localization. The most common of these sensors are Light Detection and Ranging (LIDAR), Global Positioning System (GPS), ultrasonic range sensor, inertial measurement unit sensor (IMU) and cameras. By using these sensors, the vehicle is positioned precisely and detects the surrounding objects accurately in real-time. [4-7]

The paper is organized as follows. In Section 2, we describe designing and simulating of mobile robot platform. In addition, hardware and software parts and mathematical models of the robot are shown with a mobile robot. In Section 3, SLAM and navigation methods are described. Then simulation results of the work are presented.

[2] MATERIALS AND METHODS

This section consists of two parts, hardware and software. In the hardware section, it is explained how the mobile robot is designed and how this design is used in the simulation environment. In addition, it is mentioned which electronic component is used in mobile robot. In the second part, Robot operating system (ROS) and Gazebo simulation environment are mentioned.

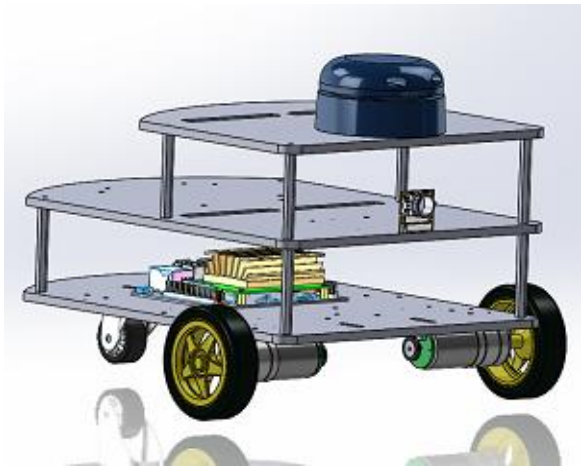


Fig. 1. 3D design of the mobile robot

A. Designing Mobil Robot Platform and Exporting

The system modeled in this paper is a mobile robot called the Otobot. Otobot is a two-wheeled vehicle and has a caster wheel. The castor wheel in the rear keeps the mobile robot stable and allows the chassis to remain horizontal. However, it can be converted to a four-wheeled vehicle if desired. The chassis of the vehicle has three floors and has an open structure shown in Figure 1. Our mobile robot was developed

by taking into account some specifications such as the driving system, mechanical structure, control systems, software requirements, and power systems. The mobile robot was designed with Solidworks. We use bottom-up design methodology which is where you build subsystems and then piece them together to create a more functional system.

After the design of the mobile robot is completed, the following steps have been applied to be used in the simulation environment.

- The coordinate frame of all parts has been determined shown in Figure.2 and coordinate frames are a key concept for standard system control problems and are just reference points that you can use to follow a body's position and orientation.
- Global origin, parent origin, and child origin of the parts have been determined. These are important origins because of what relates to the initial position of the robot in space.
- The axes of all rotating parts were determined. Axis is a crucial reference for motion and is line-oriented in space.

B. Hardware Components

The structure of the mobile robot consists of three parts: the robot chassis, actuators and electronic components. When designing the chassis, multiple screw holes were drilled for modularity, and then all components were assembled into the chassis. The brain of our robot is a development kit called Jetson Nano Developer Kit. Jetson Nano runs full desktop Ubuntu and is supported by the Jetpack 4.2. NVIDIA Jetson Nano was used in many projects in UGVs and UAVs. The robot has a light detection and ranging (LIDAR) sensor which name is Rplidar. LIDAR takes samples from the environment. It measures 360-degrees with a 0.9-degree angular resolution. Thus we can generate a map for the environment.

The two front wheels are controlled by the two actuators. Actuators are DC motors with an encoder that has a speed of 210 rpm and is a high-power gear motor. The motors also have 48 CPR encoders. Encoders have magnetic hall sensors. Encoder outputs are a 90-degree phase different square wave output. The amplitude of this square wave gives the speed of the motor, while the order of the waves indicates in which direction the motor is rotating. As a result of one revolution of the motor shaft, 48 pulses are received from the encoder output. The sensors, actuators, and controllers work with a 12-volt battery. Besides, the microcontroller, motor driver, voltage regulator, and inertial measurement unit (IMU) have been used on the mobile robot.

C. Software Environment

The software part of the mobile robot consists of two parts; control and automation and, design and simulation. First, the mobile robot designed with Solidworks, and then the model exported to The Unified Robotic Description Format (URDF). Then designed model was configured to simulate in Gazebo.

Second, robot actuator software was written with python and C++ languages for driving the motors and reading encoders. The motor encoders can be used for computing odometry massages and can transmit to the control computer. Other input signals are LIDAR and sensor data. The control computer takes this data from sensors and actuators. For autonomous driving, the control computer process data, control motors and, mapping the environment.

1) ROS Architecture

ROS (Robot Operating System) is an open-source and BDS licensed software system that enables to control of robots and robot components. It provides the services expected of an operating system, including hardware abstraction, low-level device control, message-passing between processes, and packet management. ROS does not have a real-time structure, but it is possible to integrate ROS with real-time code. The main goal of ROS is to support the reuse of code in robotics research and development. [8]

We can list the reasons why ROS is preferred in robotic applications as follows:

- Open source code,
- Inter-platform operability,
- Modular structure,
- Having an active community,
- Concurrent resource handling,
- High-end capabilities,
- ROS is packed with tons of tools for debugging, visualizing, and performing a simulation.

There are mainly three levels in ROS: the file-system level, computation graph level, and community level. ROS file-system includes meta-packages, packages, package manifest, messages, services, and repositories. There are a lot of ROS resources that enable a new community for ROS to exchange software and knowledge. The computation graph level describes how the ROS concept running. It's a back-end process that includes nodes, master, servers, messages, topics, services, and bags. [9]

ROS Master: That acts as a name server (DNS) for inter-node connectivity and communication. Connection and communication between nodes are not possible without the master. ROS Master records and provides the link between nodes and messages.

Nodes: We can think of it as an executable program. It shares information such as name, message type, URI address, and port that registered to the master at the beginning. One node can communicate with other nodes using ROS Topics, Services, and Parameters.

Topics: The topic is a name that is used to identify the content of the message. It is like the topics opened in a conversation. The communication using topics is unidirectional. If we want to implement a request/response, such as communication, we have to switch to ROS services.

Subscriber: The subscriber who wants to receive a publisher message notifies this request to the master. Master connects publisher and subscriber who wants to listen to the message. An asynchronous communication starts between the subscriber and the publisher.

Publisher: The publisher node sends contact information and subjects that want to publish to the master.

Services: When we need a request/response kind of communication in ROS, we have to use the ROS services. The services support one-time communication between the subscriber and the broadcaster. There is two-way synchronous communication.

Messages: Nodes communicate with each other by passing messages. The ROS message supports standard primitive datatypes and arrays of primitive types.

Bags: In ROS, messages are saved to a file in a bag format. These messages can be used again later. For example, if the vehicle takes LIDAR data and saves it in a bag format then this data can be used to driving the vehicle again without starting the LIDAR.

2) GAZEBO Simulation Platform

After designing the 3D model of a robot, the next phase is its simulation. The gazebo is a part of the Player Project. [10] Gazebo allows us to simulate three-dimensional projects. It enables us to produce realistic results with its physics engine. [11] Gazebo's development began in the fall of 2002 at the University of Southern California. The original creators were Dr. Andrew Howard and his student Nate Koenig. The need for simulator environments to provide high-accuracy, near-real results have resulted from the difficulty of working under various conditions. [12] Gazebo simulation has two main components are gzserver and gzclient. gzserver simulates the complete scene using a physics and sensor engine. gzclient provides the very essential Graphical Client that connects to the gzserver and renders the simulation scene along with useful interactive tools.

D. Kinematic Model of Mobile Robot

The two wheeled mobile robots use differential drive mechanism. It consists of two wheels mounted on common axis. Wheels are controlled independently. [13] The coordinate system of the mobile robot is shown in Figure 2. There are two different coordinate frames which are Inertial Coordinate Frame $[X^R\ Y^R]$ and Robot Coordinate Frame $[X\ Y]$. An inertial coordinate frame is a global frame that is fixed in the environment. A robot coordinate frame is a local frame attached to the mobile robot. [14] In Figure 2; ϑ is linear velocity, ϑ_r and ϑ_l linear velocity of right and left wheel, r is wheel radius, L is the distance of right and left wheel, ω is the angular velocity, θ is heading angle, C point is mid-point of the axis center of driving wheels, M is the center of mass and, d is the distance between the center of mass.

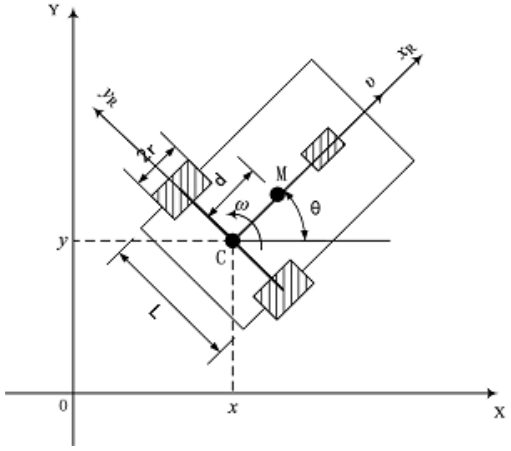


Fig. 2. Coordinate systems of the mobile robot

Robot position and orientation in the inertial coordinate frame and robot coordinate frame can be defined as below. [15]

$$q^r = \begin{bmatrix} X^R \\ Y^R \\ \theta^r \end{bmatrix}, \quad q^i = \begin{bmatrix} x \\ y \\ \theta \end{bmatrix} \tag{1}$$

We relate to the two coordinates frame by the following transformation: [14]

$$q^i = R(\theta) q^r \tag{2}$$

R(θ) is the orthogonal rotation matrix, that:

$$R(\theta) = \begin{bmatrix} \cos\theta & -\sin\theta & 0 \\ \sin\theta & \cos\theta & 0 \\ 0 & 0 & 1 \end{bmatrix} \tag{3}$$

For the differential drive of a mobile robot, the main purpose of kinematic modeling is to represent the robot velocities as a function of the driving wheels' velocities along with the geometric parameters of the robot. Component of linear velocities $\dot{x}$ and $\dot{y}$ derived from the coordinate system consisting of x and y position:

$$\dot{x} = \frac{r}{2}(\vartheta_r + \vartheta_l)\cos\theta \tag{4}$$

$$\dot{y} = \frac{r}{2}(\vartheta_r + \vartheta_l)\sin\theta \tag{5}$$

$$\dot{\theta} = \frac{r}{L}(\vartheta_r - \vartheta_l) \tag{6}$$

And we can define;

$$\dot{x} = \vartheta.\cos\theta \tag{7}$$

$$\dot{y} = \vartheta.\sin\theta \tag{8}$$

$$\dot{\theta} = \omega \tag{9}$$

If we combine equation (4), (5), (6) and (7), (8), (9), the linear velocity of wheels and vehicle and angular velocity of the vehicle can be defined as below;

$$\vartheta_r = \frac{2\vartheta + \omega L}{2r} \tag{10}$$

$$\vartheta_l = \frac{2\vartheta - \omega L}{2r} \tag{11}$$

$$\omega = \frac{r}{L}(\vartheta_r - \vartheta_l) \tag{12}$$

$$\vartheta = \frac{r}{2}(\vartheta_r + \vartheta_l) \tag{13}$$

Alternatively, the kinematic model can be obtained from linear and angular velocities of the mobile robot. [14]

$$q^i = \begin{bmatrix} \dot{x} \\ \dot{y} \\ \dot{\theta} \end{bmatrix} = \begin{bmatrix} \cos\theta & 0 \\ \sin\theta & 0 \\ 0 & 1 \end{bmatrix} \begin{bmatrix} \vartheta \\ \omega \end{bmatrix} \tag{14}$$

[3] SLAM AND NAVIGATION

A. Simultaneous Localization and Mapping (SLAM)

We use the SLAM for localization from estimating the pose of the robot and map the environment using the mounted sensors. Encoders and IMU sensors, cameras, and 2D laser sensors are used to calculate the approximate pose of the mobile robot. Sensor data always have an error. If we don't want to be affected by this error, we should use some filters like the Kalman filter and particle filter. SLAM is available at the platform ROS in Ubuntu. We chose the gmapping algorithm for this research. Gmapping algorithm use the Rao-Blackwellized Particle Filter (RBPF). It helps to map by taken data from sensors and robot pose. [16]

1) Kalman Filter

The Kalman Filter developed by Dr. R.E. Kalman and it used in NASA Apollo project. The Kalman Filter use to obtain a linear dynamic system. For this, it estimates the internal dynamics of the system from measurements taken in a noisy environment. [17] Model estimation is compared with observation. The difference is scaled by a multiplier known as

the Kalman gain. Then feedback is applied as an input to the model to improve the next predictions. [18]

$$\hat{X}_k = K_k.Z_k + (1 - K_k).\hat{X}_{k-1} \quad (15)$$

Here, $\hat{X}_k$ is prediction of x signal, k index is states, Z_k measured value and K_k is Kalman gain. This equation gives us to Kalman gain. In systems modeled with the linear state space, the state space model and the measurement value for the filter structure that predicts the next state according to the previous state and the measurement value is as follows.

$$X_{k+1} = AX_k + Bu_k + v_k \quad (16)$$

$$Z_k = HX_k + \omega_k \quad (17)$$

In the state space model and the measurement value, according to the vehicle model A state, B input and H observation matrices; X_k state space; u_k input and Z_k observation data; v_k process noise with covariance Q; ω_k indicates the measurement noise with R covariance.

There is a two equation set for calculation of the basic linear model:

1.Prediction /Time Update	2.Correction / Measurement Update
$x_k^- = Ax_{k-1} + Bu_k$ $P_k^- = AP_{k-1}A^T + Q$	$K_k = P_k^- H^T (HP_k^- H^T + R)^{-1}$ $x_k = x_k^- + K_k(Z_k - Hx_k^-)$ $P_k = (1 - K_k H)P_k^-$

First, we predict the next statement of the robot in equation set 1 and then these values send to the 2nd equation set. Sending values update in 2nd set and calculate again in 1st set. This circulation keeps going k times. It's feedback in the system.

2) Particle Filter – Monte Carlo Localization

Particle filter methods are recursive Bayesian Filters. The main feature of a particle filter is that it tries to show any probability density function with impulses in discrete values and the weight of these impulses. [19] It means that, if we know the changes in the system and compare them with the input signal, we can use the particle filter. With MCL, particles are initially spread uniformly and randomly throughout the entire map. Just like the robot, each particle has a x, y coordinate and an orientation vector. So each of these particles represent the hypothesis of where the robot might be. The MCL algorithm is composed of two main sections represented by two for-loops.

The first section is the motion and sensor update and the second one is the re-sampling process. Given a map, MCL is to determine the robot's pose represented by the belief X_t. At each iteration, the algorithm takes the previous belief X_{t+1}, the actuation command u_t and the sensor measurement z_t as input. Initially, the belief is obtained by randomly generating N particles. Then in the first loop, the hypothetical state is computed whenever the robot moves. Following, the particles' weight is computed using the latest sensor measurement. Now motion and measurements are both added to the previous state.

Algorithm 1 Monte Carlo Localization Algorithm

1: **procedure** MCL(x_{t-1}, u_t, z_t)
2: $X_t \leftarrow \phi$
3: *for i=1 to N loop*:
4: $x_t^i \leftarrow MotionUpdate(u_t, x_{t-1}^i)$
5: $w_t^i \leftarrow SensorUpdate(z_t, x_t^i)$
6: $X_t \leftarrow X_t + < x_t^i + w_t^i >)$
7: *end for*
8: *for i=1 to N loop*:
9: *draw* x_t^i *with probability* $\propto w_t^i$
10: $X_t \leftarrow X_t + x_t^i)$
11: *end for*
12: *return* X_t

In the second section of the MCL, a simple sampling process happens. Here, the particles with high probability survive and are re-drawn in the next iteration, while the others die. Finally, the algorithm outputs the new belief and another cycle of iteration starts implementing the next motion by reading the new sensor measurements. [20]

B. Navigation

The mobile robot for reach a defined destination point should know its position on the map. And of course, have a map which is using by the robot. [21] Also, the robot should use the algorithms of obstacle avoidance and path following to find an optimized route. Navigation has four main topics that sensing, localization, motion planning, and obstacle avoidance. Sensing means that the mobile robot take the encoders and inertial measurements unit data and estimate obstacles distance. Localization is given us to where the robot is. We provide this information from particle filter localization and adaptive Monte Carlo localization. Motion planning, which is called path planning. We use global path planning and local path planning algorithms. For avoiding static and dynamic obstacles we use the dynamic windows approach algorithm.

1) Costmap

We can separate costmap into two which are global costmap and local costmap. Global costmap provides a path plan for navigating and Local costmap provides path planning and obstacle avoidance in the given environment. In the given map, the mobile robot calculates the obstacle area, possible collision area, and movable area. Then determined area scored as a value between '0' and '255'. [21]

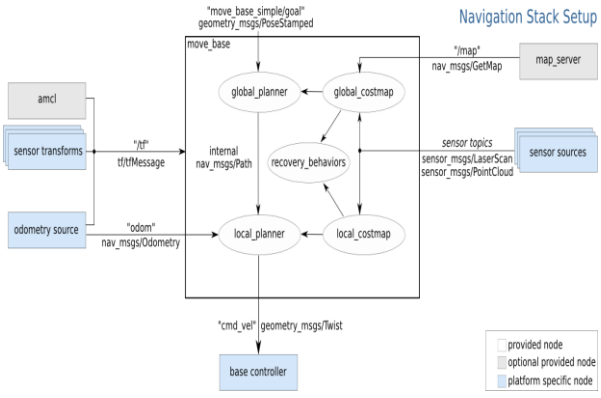


Fig. 3. Navigation stack of the robot. (Taken from ROSWiki)

2) Dynamic Windows Approach (DWA)

Dynamic Window Approach is a popular algorithm to obstacle avoidance and path planning. This method finds the

best path to the target by choosing the best pair of angular and linear velocities. [22-23]

$$G_{(\vartheta,\omega)} = \sigma\big(\alpha\,.heading(\vartheta,\omega) + \beta.dist(\vartheta,\omega) + \gamma.velocity(\vartheta,\omega)\big) \quad (18)$$

In this equation, $G_{(\vartheta,\omega)}$ is the objective function that used to calculate the translation velocity ϑ and rotational velocity ω . These velocities maximize the objective function. $heading(\vartheta,\omega)$ is difference between the direction of the robot and the direction of the target point, $dist(\vartheta,\omega)$ is distances to the obstacles, $velocity(\vartheta,\omega)$ are selected velocity, (α,β,γ) are weighting constants and $\sigma(x)$ is a smooth function of the equation.

[4] SIMULATION RESULTS

In this section, the simulation results are presented. The mobile robot ROS packages are created in the home directory. Project workspace includes; robot description files which include urdf and xacro files, configuration files and launch files of the mobile robot, gazebo files that world files, and gmapping and navigation files. The robot setup is shown in Figure 4.

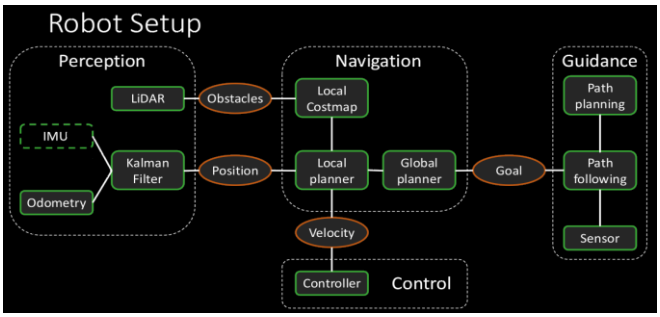


Fig. 4. Robot setup

First, we launch the gmapping algorithm in ROS and mapping the simulation environment. The map was created with map_server on ROS and saved in the project folder. The created map is shown in Figure 5. In Figure 6, the mobile robot is in the Gazebo simulation environment. We can see the lidar data that are blue ones. The Lidar sensor configure like real specifications. Range of lidar is 0.2 – 12 meter. Lidar sensor take 4000 sample per second.

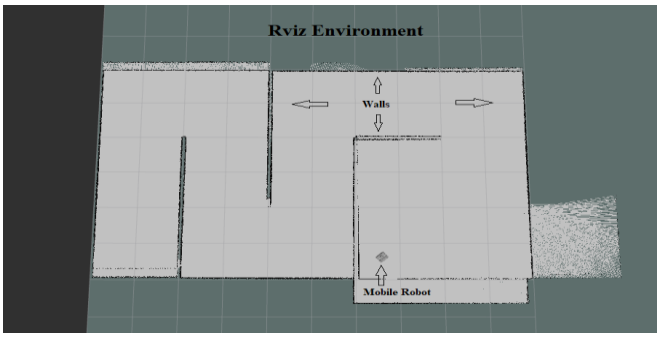


Fig. 5. Creating map at Rviz environment

After creating a map, the mobile robot ready for navigation. ROS navigation and AMCL (Adaptive Monte Carlo Localization) nodes are launched and in the Rviz (ROS Visualization Tool) we can choose a target point on the map. Then the mobile robot goes to the target. We can see the path planning of the robot in Figure 8. Red dots are lidar sensor data, red arrows are particles of Monte Carlo localization and the blue line is the path planning of the mobile robot. In Figure 9, running mobile robot nodes and topics visualizing the ROS computational graph. The tools name is "rqt_graph".

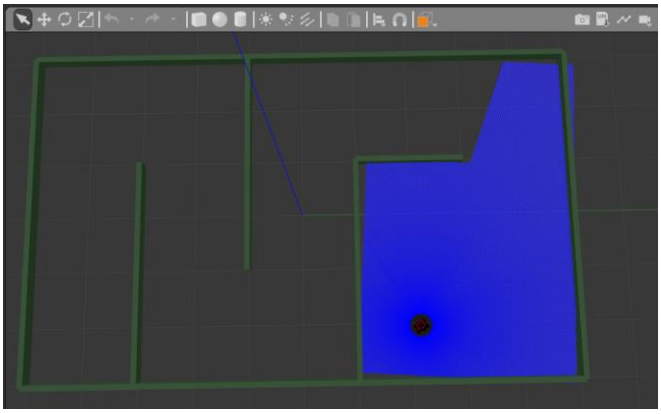


Fig. 6. Gazebo simulation environment.

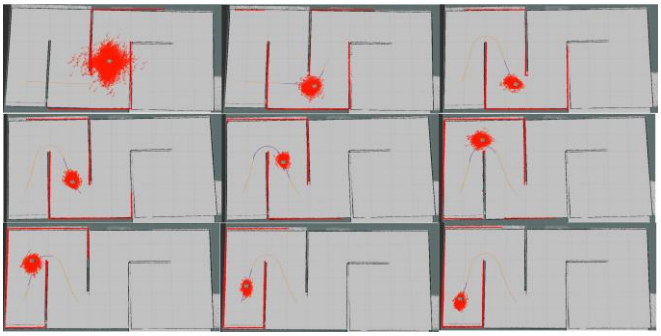


Fig. 7. Navigation of the mobile robot

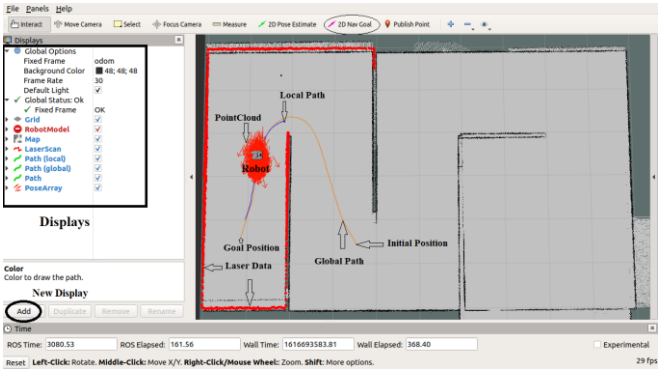


Fig. 8. Explanation of navigation screen.

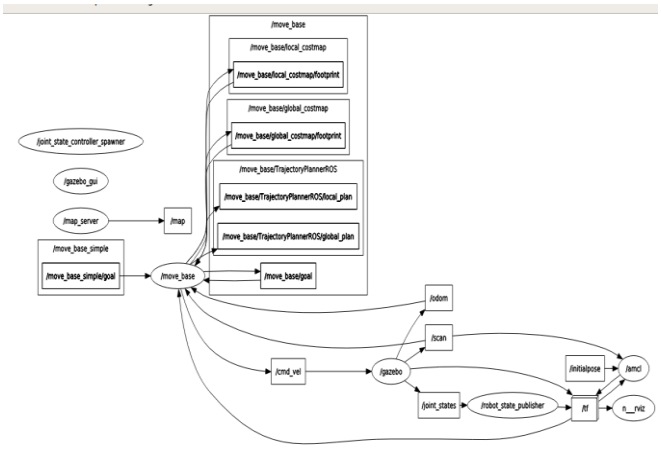


Fig. 9. Rviz rqt_graph flow chart

[5] CONCLUSION

In this paper, the mobile robot designed in real life has been tested in a simulation environment. The robot and all electronic equipment specifications are defined in a software environment. It has been observed that the robot successfully performs the localization, mapping, and navigation task in the defined environments. The mobile robot archive to avoid all obstacles on the road. After that, the methods applied in the simulation environment will be tested in a real environment on the designed robot. Errors originating from electronic devices will be eliminated.

References

[1] "Oral History: Bertram Raphael". IEEE Global History Network. Institute of Electrical and Electronics Engineers. Retrieved 2012-10-08.

[2] Richard D. Klafter “Mobile Robots, Research and Devolepment,” in International Encyclopedia of Robotics: Applications and Automation, Volume 2, pp.920-942, March 1988, doi:10.1002/9780470172308

[3] Kunchev, Voemir & Jain, Lakhmi & Ivancevic, Vladimir & Finn, R.. (2006). Path Planning and Obstacle Avoidance for Autonomous Mobile Robots: A Review. 537-544. 10.1007/11893004_70.

[4] Meiser, V., Hesselbarth, H., Henke, R., Rotach, T., & Seatovic, D. (2014). Autonomous unmanned ground vehicle as sensor carrier for agricultural survey tasks.

[5] Hamner, B., Singh, S., M. B. (2010). Improving Orchard Efficiency with Autonomous Utility Vehicles. 2010 ASABE Annual International Meeting, Carnegie Mellon University.

[6] Kurashiki, K., Fukao, T., Ishiyama, K., Kamiya, T., & Murakami, N. (2010). Orchard traveling UGV using particle filter based localization and inverse optimal control. In System Integration (SII), 2010 IEEE/SICE International Symposium on (pp. 31–36). doi:10.1109/SII.2010.5708297

[7] Stentz, A., Kelly, A., Rander, P., Herman, H., Amidi, O., Mandelbaum, R., Salgian, G., & Pedersen, J. (2003). Real-Time, Multi-Perspective Perception for Unmanned Ground Vehicles, Paper 16, Robotics Institute, Carnegie Mellon University.

[8] ROS Project (2007), ROS Wiki Project [Online], Available: http://wiki.ros.org/ROS/Introduction

[9] ROS Project (2007), ROS Wiki Project [Online], Available: http://wiki.ros.org/ROS/Concepts.

[10] Player/Stage project. (2016) The Player Project. [Online]. Available: http://playerstage.sourceforge.net/

[11] Takaya, Kenta & Asai, Toshinori & Kroumov, Valeri & Smarandache, Florentin. (2016). Simulation environment for mobile robots testing using ROS and Gazebo. 96-101. 10.1109/ICSTCC.2016.7790647.

[12] Gazebo Project. [Online]. Available: http://gazebosim.org/

[13] Başçi, Abdullah. (2016). Sensorless velocity and direction angle control of an unmanned vehicle. Turkish Journal of Electrical Engineering and Computer Sciences. 24. 580-589. 10.3906/elk-1310-245.

[14] Hatab, Rached. (2013). Dynamic Modelling of Differential-Drive Mobile Robots using Lagrange and Newton-Euler Methodologies: A Unified Framework. Advances in Robotics & Automation. 02. 10.4172/2168-9695.1000107.

[15] Kalyoncu, Mete & Demirbaş, Faik. (2017). Differential Drive Mobile Robot Trajectory Tracking With Using Pid And Kinematic Based Backstepping Controller. Selcuk University Journal of Engineering ,Science and Technology. 5. 1-15. 10.15317/Scitech.2017.65.

[16] Norzam, W.A.S & Hawari, H.F. & Kamarudin, Kamarulzaman. (2019). Analysis of Mobile Robot Indoor Mapping using GMapping Based SLAM with Different Parameter. IOP Conference Series: Materials Science and Engineering. 705. 012037. 10.1088/1757-899X/705/1/012037.

[17] Kalman, Rudolph & others,. (1960). A new approach to linear filtering and prediction problems. Journal of basic Engineering. 82. 35-45.

[18] Çayıroğlu, İbrahim (2012). Kalman Filtresi ve Programlama. Karabük University, Science and Technology Information Sharing. 2012-1.

[19] Gustafsson, Fredrik. (2010). Particle filter theory and practice with positioning applications. Aerospace and Electronic Systems Magazine, IEEE. 25. 53 - 82. 10.1109/MAES.2010.5546308.

[20] Sagarnil Das, October-2018. Robot localization in a mapped environment using Adaptive Monte Carlo algorithm. International Journal of Scientific & Engineering Research Volume 9, Issue 10, ISSN 2229-5518

[21] Pyo, Yoon Seok, et al. ROS Robot Programming. ROBOTIS Co.,Ltd., 2017.

[22] D. Fox, W. Burgard and S. Thrun, "The dynamic window approach to collision avoidance," in IEEE Robotics & Automation Magazine, vol. 4, no. 1, pp. 23-33, March 1997, doi: 10.1109/100.580977.

[23] Wikipedia Dynamic Window Approach. [Online]. Available: https://en.wikipedia.org/wiki/Dynamic_window_approach

Switching Sequence and Modulation Techniques of Modular Multilevel Converter

Nasiru B. Kadandani
Department of Electrical Engineering
Bayero University
Kano, Nigeria
nbkadandani.ele@buk.edu.ng

***Abstract*—Modular multilevel converter (MMC) has been considered as the most promising converter candidate for high voltage direct current (HVDC) transmission system and medium voltage drives applications. This paper presents an overview of the switching sequence and a review of the modulation techniques of MMC. Different modulation techniques were reviewed under two basic categories; space vector based algorithms and voltage level based algorithms.**

Keywords—Modular multilevel converter (MMC), submodule (SM), modulation, switching pattern.

[1] INTRODUCTION

Modular multilevel converter (MMC) is one of the recent versions of voltage source converters (VSCs) and a subject of hot research in power electronics. MMC has peculiar advantages over conventional two-level and three-level VSCs such as, modular design and scalability to different power and voltage levels, output voltage waveform with improved quality, current waveform with reduced harmonic distortion, very low electromagnetic interference and simple realization of redundancy making it a suitable choice for high voltage direct current (HVDC) transmission system and medium voltage drives [1].

This paper focuses on two aspects of MMC; the mode of switching of the power cells of the converter and its modulation techniques. Several parameters are required to be controlled for proper operation of the converter. The control loops are finally linked to the modulation voltage synthesis for providing appropriate gate signals for the converter switches. The modulation techniques proposed for MMC are categorised into space vector and voltage level based methods.

The remaining part of this paper is organized as follows: Section II presents switching sequence of MMC. In section III, a review of the modulation techniques in MMC is presented. Lastly section IV concluded the paper.

[2] SWITCHING SEQUENCE OF MMC

A three phase MMC is shown in Fig. 1. The basic building blocks of the configuration are *N*-identical series connected chopper cells known as *submodules* (SMs). During operation, SMs are continuously activated and deactivated and their values are added to yield the desired multilevel arm voltage. If $S(k)$ is the switching state of kth SM, then the total voltage across the upper and lower arm, v_{up} and v_{low} can be expressed as:

$$v_{up} = \sum_{x=1}^{N} S_{up}(k) \,.\, v_{C_up}(k) \qquad (1)$$

$$v_{low} = \sum_{x=N+1}^{2N} S_{low}(k) \,.\, v_{C_low}(k) \qquad (2)$$

where $S_{up}(k)$ and $v_{C_up}(k)$ are the switching state and capacitor voltage of kth SM in upper respectively while $S_{low}(k)$and $v_{C_low}(k)$ are the corresponding values in lower arm.

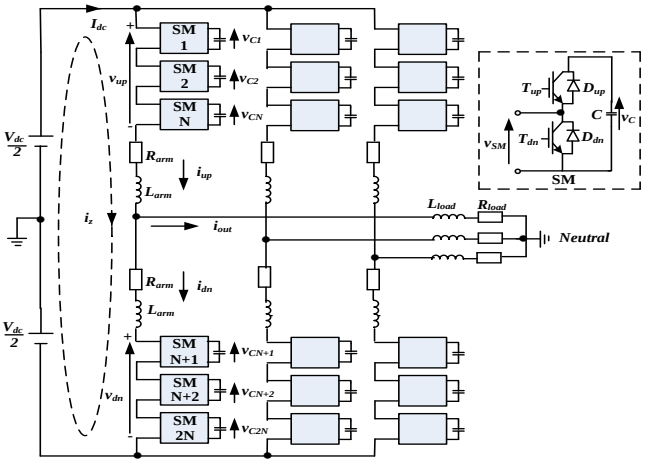


Fig. 1. Three-Phase MMC

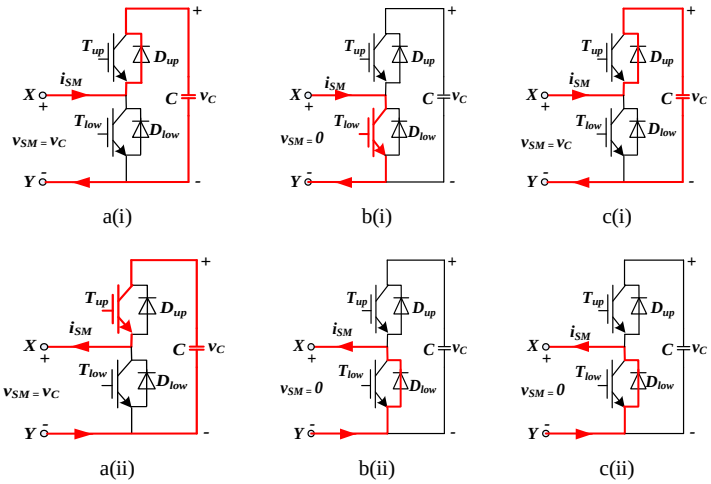


Fig. 2. Operational modes of HBSM: (a) - Insertion mode, (b) - Bypassing mode, and (c) - Blocking mode

As detailed in Fig. 2, an SM can operate in three modes; insertion, bypassing and blocking modes.

Insertion Mode: In this mode, the SM capacitor *C* will always be inserted into the arm of the converter and also being

charged or discharged depending on the direction of the SM current, i_{SM}. This can be seen in Fig. 2(a) where the upper IGBT, $T_{up}$and upper diode, D_{up} are switched on (Fig. 2a(i)) and when lower IGBT T_{low} and lower diode, D_{low} are switched off (Fig.2a(ii)). It can be seen that C charges when i_{SM} flow through the SM via D_{up} (with T_{up} being off) and discharges (through T_{up} and D_{low}) when i_{SM} flows out of the SM.

Bypassing Mode: In this mode, C will always be bypassed from the converter arm regardless of the direction of i_{SM}. This can be seen in Fig. 2(b) where T_{up} and D_{up} are switched off (Fig. 2b(i)) and when T_{low} and D_{low} are switched on (Fig.2b(ii)). In Fig. 2b(i) for instance, i_{SM} flows into the SM and turn on T_{low} with the current flowing through T_{low} instead of D_{low} that was blocked by the forward charged capacitor. In Fig. 2b(ii) however, i_{SM} flows out of the SM through D_{low} resulting in 0V across the SM.

Blocking Mode: This represents a situation when both upper and lower switches turn off as a result of fault or dead-bands between the two switches. Under that condition, v_{SM} assumes the value of v_C or zero depending on the direction of i_{SM}. In Fig. 2c(i) for example, T_{low} is blocked, hence i_{SM} can only flow through D_{up} and charge C, in this case v_{SM} will assume the value of v_C. In Fig. 2c(ii) however, i_{SM} flows out of the SM through D_{low}, hence v_{SM} will be zero.

During operation, the output AC voltage waveform, v_{ac} is synthesised by either subtracting the sum of SM voltages in the upper arm, v_{up} from the positive terminal of the DC link or by adding the sum of SM voltages in the lower arm, v_{low} from the negative terminal of the DC link. In this passion, v_{ac} will assume its maximum value when all the upper arm SMs are deactivated and minimum value when all the lower arm SMs are activated. As such, the control strategy of the two arms has to be complementary and their voltages has to match. In other words, deactivated SMs in the upper arm has to have corresponding number of activated SMs in the lower arm. A pictorial illustration of the mode of operations of SM in relation to output AC voltage synthesis is depicted in Fig. 3. For simplicity, an MMC with four SMs per arm is considered.

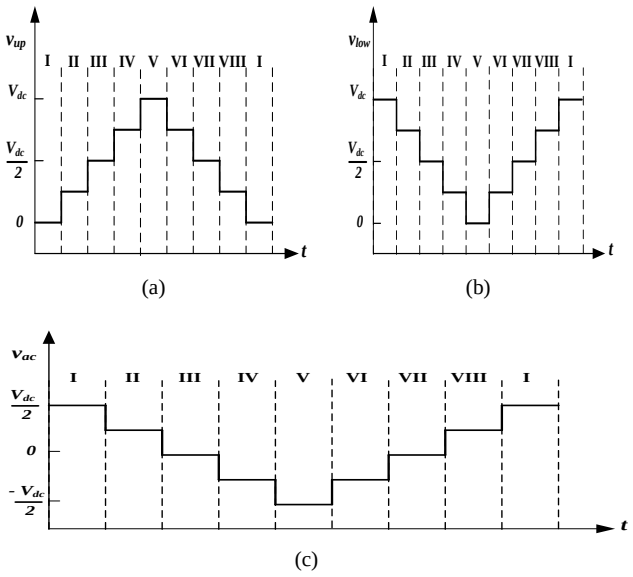


Fig. 3. Illustration of voltage waveform synthesis for a 4SM MMC: (a) - Upper arm voltage, (b) - Lower arm voltage, and (c) - Output voltage

For the illustrative converter, the operational mode is divided into eight sections capturing all the possible combinations of the number of SMs with ON-state in the upper arm, N_{up} and the number of SMs with ON-state in the lower arm, N_{low}. As can be seen in table 1, section I is the case when none of the SMs in the upper arm is in ON-state and all of the SMs in the lower arm are in ON-state. Section VIII is the opposite case; that is all of the SMs in the upper arm are in ON-state and none of the SMs in the lower arm is in ON-state. Section II through VII represents other possible combinations.

Table 1. Illustration of Switching Pattern of 4SM MMC

Section	N_{up}	N_{low}	N	v_{ac}	V_{dc}
I	0	4	4	$\frac{V_{dc}}{2}$	V_{dc}
II	1	3	4	$\frac{V_{dc}}{4}$	V_{dc}
III	2	2	4	0	V_{dc}
IV	3	1	4	$\frac{-V_{dc}}{4}$	V_{dc}
V	4	0	4	$\frac{-V_{dc}}{2}$	V_{dc}
VI	3	1	4	$\frac{-V_{dc}}{4}$	V_{dc}
VII	2	2	4	0	V_{dc}
VIII	1	3	4	$\frac{V_{dc}}{4}$	V_{dc}

The number of voltage level at the MMC output depends on the number of SMs. In general, for an MMC with N SMs per arm, an output AC voltage, v_{ac} with $N+1$ level will be generated. The higher the value of N, the better v_{ac} waveform approaches sinusoidal shape. The SM capacitor voltage, v_C will be regulated to its nominal capacitor voltage value based on the following relationship:

$$v_C = \frac{V_{dc}}{N} \tag{3}$$

However, the DC voltage, V_{dc} needs to be maintained at constant value during operation. To achieve this, the sum of total number of SMs with ON-state in the upper arm, N_{up} and the total number of SMs with ON-state in the lower arm, N_{low} in each phase of the converter has to be equal to the number of SMs per arm, N. Accordingly:

$$N = N_{up} + N_{low} \tag{4}$$

[3] MODULATION TECHNIQUES IN MMC

A. *Space Vector Modulation*

Space vector modulation (SVM) is based on representing the reference voltage in the alpha-beta plane as a vector to be generated by the converter. The output voltage level is synthesised from the switching states of the converter (otherwise known as space vectors). Typically, the voltage reference vector is generated as linear combination of multiple vectors at every sampling period. SVM algorithm is of two types; two-dimensional SVM (2D-SVM) and three-dimensional SVM (3D-SVM). The former as demonstrated in [2, 3] is calculated in alpha-beta plane and is typically applied in a balanced system that is free of triple harmonics. The latter as demonstrated in [4, 5] was a modification of the first

approach in which a third axis, gamma is added for the control of zero sequence or triple harmonics and is typically applied in both balanced and unbalanced system as well as in system with or without neutral. A hybrid 2D-3D SVM was also proposed in [6].

The main advantage of SVM is the degree of freedom of space vector placement in a switching cycle which results in good harmonic performance. However, the number of space vectors increases proportionally to the cubic of the number of voltage levels [7], as such the method is not a good choice for converters with large number of levels such as MMC used in HVDC system.

B. Multicarrier PWM

As the name indicates, the multicarrier PWM technique employs multiple carriers to control the semiconductor switches of the converter. As such, the technique is good for converters with high number of levels as in the case of MMC in HVDC system. Two types of multicarrier PWM are reported in literature; carrier phase shifted PWM (CPS-PWM) and level shifted PWM (LS-PWM).

i. Carrier Phase Shifted PWM (CPS-PWM)

The CPS-PWM technique involved assigning one carrier for each cell to be modulated. The *N* carriers have the same frequency but are phase shifted by 360°/*N* in order to generate a multilevel output voltage with minimum harmonic content [8]. The equivalent switching frequency of the converter, f_{eq} is given by:

$$f_{eq} = Nf_{cr} \tag{5}$$

where f_{cr} is the carrier frequency.

Fig. 4 shows the diagrammatic representation of CPS-PWM. In MMC, the number of carrier signals that are below the reference modulation voltage, v_m determines the number of SM to be inserted for any arm. The CPS-PWM technique provides equal conduction times for all the SMs [9].

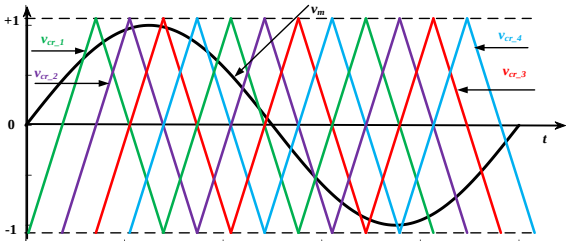


Fig. 4. CPS-PWM

ii. Level Shifted PWM (LS-PWM)

In LS-PWM, the multicarrier signals are arranged with defined shifts in amplitude such that each carrier is related with an output voltage level being generated by the converter. In other words, the *N* carrier signals are distributed vertically along the modulating signal that ranges from -1 to 1. In this process, the modulating signal is compared with each carrier for the activation of SMs alongside a dedicated capacitor voltage balancing controller.

Three types of LS-PWM are reported in the literature [9], namely; phase disposition PWM (PD-PWM), phase-opposition disposition PWM (POD-PWM) and alternate phase-opposition disposition PWM (APOD-PWM). In PD-PWM, the carrier signals are equally displaced from each other (Fig. 5(a)). In POD-PWM, the set of carriers in the negative range of the modulating signal are phase shifted by 180° from those in the positive range (Fig. 5(b)). In APOD-PWM, the carriers are shifted by 180° from each other (Fig. 5(c)). It is worth noting that very huge processing resources are required in implementing high number of carrier signals for each type of LS-PWM. Incidentally, PD-PWM allows scalable strategy such that a single carrier signal can be used by shifting it vertically as and when needed. This makes it the preferred choice in converter with large number of SMs.

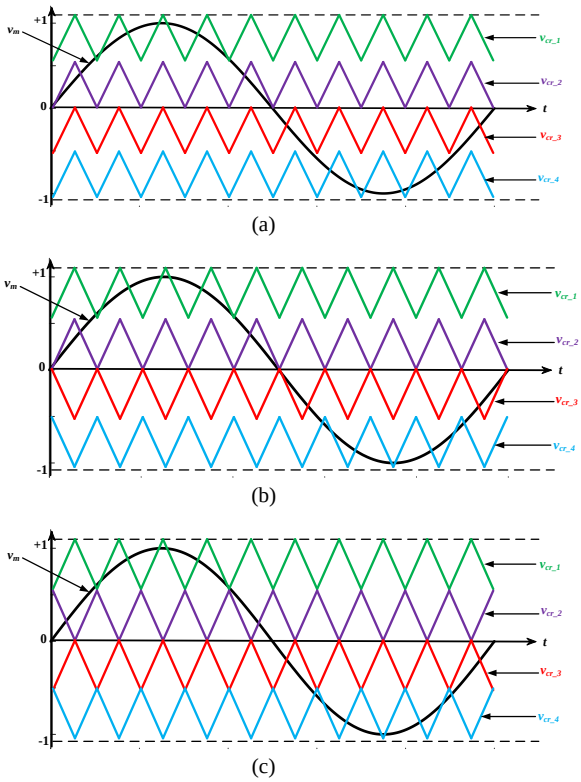


Fig. 5. LS-PWM: (a) - PD-PWM, (b) - POD-PWM, and (c) - APOD-PWM

C. Selective Harmonic Elimination

The As the name implies, SHE technique involves calculation of the switching angles for the cancellation of some selected harmonics. The output voltage waveform is decomposed using Fourier transform while the firing angles [10] or the switching patterns [11, 12] of the semiconductor switches are calculated for different modulation indices. The calculation of the switching angle is done offline and the results stored in a look-up table for interpolation to meet the operational requirement of the converter. Typically, switching angles for one quarter of a period are calculated and the concept of symmetry is applied to obtain the switching state for the rest of the period. The information can then be used to cancel out low frequency harmonics and improve the THD of the output voltage [13] as can be seen in Fig. 6.

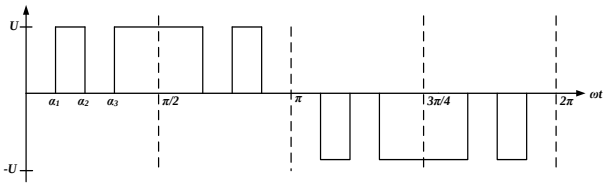


Fig. 6. Three-level SHE-PWM

It is worth to mention that SHE technique allows the cancellation of any unwanted harmonics and also allows the control of the amplitude of the fundamental frequency component. However, since the switching angles are calculated offline, the technique is limited to open loop system. Furthermore, SHE technique is not applicable to converters with high number of levels due to many switching angles that need to be calculated.

D. Nearest Level Modulation

In commercial converters where the number of SMs is in the range of hundreds, SHE and multicarrier PWM techniques would be impractical. For the case of SHE, calculation and handling of large look-up table of the switching angles will be an issue. For the multicarrier PWM, the switching frequency has to be high in order to suppress the capacitor voltage variation and reduce the THD level of the output voltage. The NLM technique overcome these limitations. The technique is not based on carrier waveform, but rather on an approximation such that the voltage levels which are nearest to the reference values are chosen for modulation. In other words, it generates the voltage level that is closest to voltage reference for full switching period. Some advantages of NLM include; easy implementation, high efficiency, low switching frequency, reduced switching losses, and less computational time. Based on the foregoing, NLM become the preferred choice for converters with high number of voltage levels such as MMC used in HVDC system [14, 15]. Fig. 7 shows an example of NLM. The round function determines the number of SMs to be switched on. For instance, if the input number is 4.7, the round function will return 5, being the nearest integer which upon multiplication by the SM capacitor voltage gives the voltage level that is close to the reference voltage being generated by the converter.

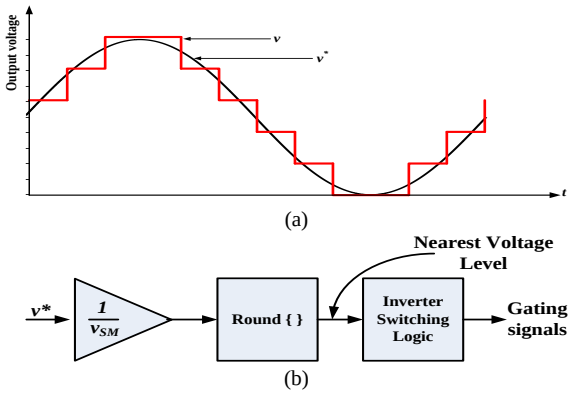


Fig. 7. NLM: (a) - Waveform synthesis, and (b) - Control diagram

[4] CONCLUSION

Different modulation techniques were reviewed under two basic categories; space vector based algorithms and voltage level based algorithms. The techniques based on SVM are further divided into 2D-SVM and 3D-SVM. The former is based on alpha-beta plane while the latter incorporates gamma axis to allow the control of zero sequence component. It was established that the number of space vectors in SVM technique increases proportionally to the cubic of the number of voltage levels. As such, the use of both 2D-SVM and 3D-SVM is limited to converter with low number of SMs. For a converter with large number of SMs, voltage level based modulation techniques will be the preferred choice. In particular, phase-shifted and level-shifted techniques are good choices for high frequency modulation while selective harmonic elimination and nearest level modulation are the corresponding choices for low frequency modulation. In the case of converter with hundreds/thousands of SMs, nearest level modulation will be considered against selective harmonic elimination which requires calculation of many switching angles.

References

[1] N. B. Kadandani, M. Dahidah, and S. Ethni, "Design and develeopment of modular multilevel converter for solid state transformer application," *Bayero Journal of Engineering and Technology (BJET)*, vol. 16, No. 1, pp. 31-41, 2021.

[2] M. M. Prats, J. I. León, R. Portillo, J. M. Carrasco, and L. G. Franquelo, "A novel space-vector algorithm for multilevel converters based on geometrical considerations using a new sequence control technique," *Journal of Circuits, Systems and Computers*, vol. 13. no. 4, pp. . 845–861, 2004.

[3] E. Levi, I. N. W. Satiawan, N. Bodo, and M. Jones, "A Space-Vector Modulation Scheme for Multilevel Open-End Winding Five-Phase Drives," *IEEE Trans on Energy Conv.*, vol. 27, no. 1, pp. 1-10, 2012.

[4] M. M. Prats, L. G. Franquelo, R. Portillo, J. I. Leon, E. Galvan, and J. M. Carrasco, "A 3-D space vector modulation generalized algorithm for multilevel converters," *IEEE Power Electronics Letters*, vol. 1, no. 4, pp. 110-114, 2003.

[5] L. G. Franquelo *et al.*, "Three dimensional space vector modulation algorithm for four-leg multilevel converters using abc coordinates," *IEEE Trans. on Ind. Electrons.*, vol. 53, no. 2, pp. 458–466, 2006.

[6] S. Albatran, Y. Fu, A. Albanna, R. Schrader, and M. Mazzola, "Hybrid 2D-3D space vector modulation voltage control algorithm for three phase inverters," *IEEE Trans. on Sustainable Energy*, vol. 4, no. 3, pp. 734-744, 2013.

[7] K. Li and C. Zhao, "New technologies of modular multilevel converter for VSC-HVDC application," *Asia-Pacific Power and Energy Engineering Conf., Chengdu*, pp. 1-4, 2010.

[8] B. Wu, "High power converters and AC drives," *New York: IEEE Press/Wiley*, 2005.

[9] G. S. Konstantinou and V. G. Agelidis, "Performance evaluation of half-bridge cascaded multilevel converters operated with multicarrier sinusoidal PWM techniques," *IEEE Conf. on Ind. Electrons. and Applcs., Xi'an*, pp. 3399-3404, 2009.

[10] A. Pérez-Basante, S. Ceballos, G. Konstantinou, J. Pou, J. Andreu, & I.M. Alegría, "(2N+1) Selective harmonic elimination PWM for modular multilevel converters: a generalized formulation and circulating current control method," *IEEE Trans. on Power Electrons.*, vol. 33, no. 1, pp. 802-818, 2018.

[11] Z. Salam, A. Majed, and A. M. Amjad, "Design and implementation of 15-level cascaded multi-level voltage source inverter with harmonics elimination pulse-width modulation using differential evolution method," *IET Power Electronics*, vol. 8(9), pp. 1740-1748, 2015.

[12] G. Konstantinou, M. Ciobotaru, and V. Agelidis, "Selective harmonic elimination pulse-width modulation of modular multilevel converters," *IET Power Electronics*, vol. 6(1), pp. 96-107, 2013.

[13] L. Li, D. Czarkowski, Y. Liu, and P. Pillay, "Multilevel selective harmonic elimination PWM technique in series-connected voltage inverters," *IEEE Transactions on Industry Applications*, vol. 36, no. 1, pp. 160-170, 2000.

[14] J. Peralta, H. Saad, S. Dennetiere, J. Mahseredjian, and S. Nguefeu, "Detailed and Averaged Models for a 401-Level MMC–HVDC System," *IEEE Transactions on Power Delivery*, vol. 27, no. 3, pp. 1501-1508, 2012.

[15] M. Guan, Z. Xu, and H. Chen, "Control and modulation strategies for modular multilevel converter based HVDC system," *IECON 2011 - 37th Annual Conference of the IEEE Industrial Electronics Society, Melbourne, VIC*, pp. 849-854, 2011.

Design and Optimization of CPW-Fed Patch Printed Antenna for Underwater Communication

Nor Hidayah Daud
Wireless and Photonics Networks Research Centre, Department of Computer and Communication Systems Engineering
Faculty of Engineering, Universiti Putra Malaysia
hidayahdaud0904@gmail.com

Alyani Ismail
Wireless and Photonics Networks Research Centre, Department of Computer and Communication Systems Engineering
Faculty of Engineering, Universiti Putra Malaysia
alyani@upm.edu.my

Aduwati Sali
Wireless and Photonics Networks Research Centre, Department of Computer and Communication Systems Engineering
Faculty of Engineering, Universiti Putra Malaysia
aduwati@upm.edu.my

Mohd Hafizal Ismail
Department of Nature Parks and Recreation Faculty of Forestry and Environment, Universiti Putra Malaysia
m_hafizal@upm.edu.my

Elfarizanis Baharudin
Department of Communication Engineering
Faculty of Electrical and Electronic Engineering,
Universiti Tun Hussein Onn Malaysia
elfa@uthm.edu.my

***Abstract*— This research presents the design of miniaturized CPW-fed rectangular patch antenna which applicable for various underwater activities by using radio wave communication. The design of the proposed CPW-fed rectangular patch antenna are simulated on thin FR4 dielectric substrate with the thickness of 0.80 mm. The proposed antenna is designed so that it covers 919 MHz ISM frequency band. In this work, the simulation results showed that the antenna structure have small in size with improved gain, simple structure, easy to fabricate, good return loss characteristics and less weight. A parametric study was conducted to study the effects of some geometrical parameters on the antenna performance. The proposed antenna has a bandwidth of 69.45 MHz, gain of 1.66 dBi, and an omni-directional radiation pattern. The total size of the proposed antenna is 76 mm × 38 mm × 0.8 mm.**

Keywords—CPW-fed patch antenna, complementary split – ring resonator (CSRR), rounded corner structure, underwater communication, electromagnetic (EM) waves

[1] INTRODUCTION

Underwater electromagnetic (EM) communications were intensively investigated with only a few practical applications in 1960s [1]. The study of underwater wireless media has attracted much attention for underwater communications in recent past years [2]. Several research on underwater wireless communication were reported in literature. Besides having the high cost of deployment, underwater wireless communication is known as a challenging communication medium when it is compared to terrestrial wired or wireless connections. This is because, underwater communication faces several challenges such as depth related impact on temperature, conductivity, water-air interface, winds, salinity, pressure, and waves motions [3]. However, all these drawbacks can be overcome by electromagnetic transmission. In comparison with the other waves, the properties of the EM wave proved that it is well-suited for underwater communication over a short distance [4].

The ISM frequency bands can be as high as 244 GHz or even as low as 6.7 MHz. The underwater communication has proven feasible in the MHz frequency such as 6.7 MHz and 433 MHz. This is because, the attenuation is less in low frequencies [5]. An antenna serves as one of the critical component in any wireless communication system [6]. Underwater radio frequency (RF) communication has high transmission power, lower gain and required large size antenna, thus resulted the designed antenna become complicated and difficult to fabricate besides being heavy and bulky. Conventional antennas performs poorly underwater since they are originally designed to radiate electromagnetic waves through the atmosphere [7]. Therefore, underwater communication needs an efficient antenna for wireless sensor network communication. This type of antenna must has a high gain, omni-directional radiation pattern, low frequency, and should be small size so that it can easily installed on the sensor surfaces [8].

In this paper, the configuration of the antenna consists of a rectangular patch antenna incorporated with two square type of complementary split-ring resonator (CSRR), rounded corner and loading bars structure, operating at 919 MHz frequency. The objectives of this research are to identify the suitable antenna design and investigate the potential of integrating several miniaturization techniques as a method to reduce the dimension of antenna. Besides, this research aims to fabricate and analyze the performance of antenna such as size of antenna, gain, matching impedance and radiation pattern that useful in EM underwater propagation. In order to achieve the research objectives, it is vital to know the overall process of this study. The findings results were discussed thoroughly followed by the discussions on the feasibility of using electromagnetic (EM) waves in an underwater communication system.

[2] ANTENNA DESIGN

A. Antenna Design in Air Condition

The geometry of the proposed underwater rectangular patch antenna with coplanar waveguide (CPW) was designed on a single-layer using a conventional FR4 substrate with a thickness, h of 0.80 mm and the loss tangent, tan δ of 0.025. A coplanar waveguide (CPW) is a one type of strip transmission line which consists of a conductor strip at the middle and two ground planes are located on either sides of centre conductor. All these lie in the same plane. The advantages of using a CPW are it has lower loss than the

microstrip line. More importantly, it needs a single conducting layer for fabrication, thus simplifying the fabrication process. In this study, the two square-shaped complementary split-ring resonator (CSRR) loading is found to be a novel technique to further reduce the size of a patch antenna as well as to enhance the gain. Besides, a novel rounded corners technique was introduced since it has found in the literature not only to enhance the impedance bandwidth but also the gain of the antenna [9]. The loading bar is used in this design to have a better control over the antenna impedance [10]. To connect the main radiating patch to the 50 Ω Sub Miniature Version A (SMA) connector, a quarter-wavelength transmission line feeding method is introduced in this study. The FR4 substrate from the lossy type was loaded from the material library to perform this design. The dielectric constant, ε_r of this substrate is 4.3. This antenna was designed for the working frequency at 919 MHz.

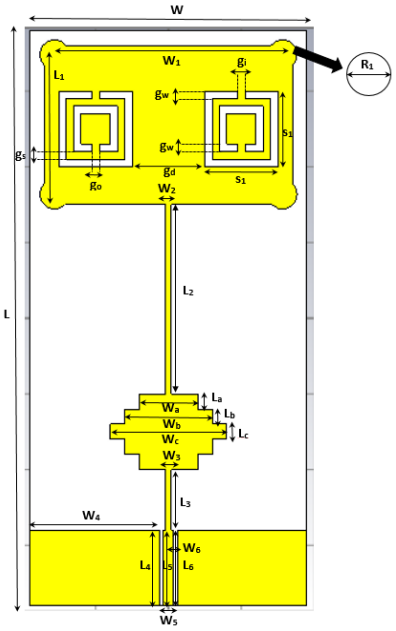


Fig. 1. The structure of the proposed CPW-fed patch antenna

Fig.l shows the dimensions of the antenna. The length of the CSRR, s_1 is 11.0 mm, the length of loading bars, W_a is 8.0 mm and the radius of small rounded corners, R_1 is 2.0 mm.

Table 1. Dimensions of Proposed Antenna

No	Dimensions			
	Parameter	*Value (mm)*	*Parameter*	*Value (mm)*
1	W	38.0	W_b	12.0
2	L	76.0	W_c	16.0
3	W_1	34.0	L_1	21.0
4	W_2	0.8	L_2	25.0
5	W_3	0.8	L_3	8.0
6	W_4	17.8	L_4	10.0
7	W_5	1.4	L_5	10.0
8	W_6	0.5	L_6	10.0
9	W_a	8.0	L_a	2.0
10	L_b	2.0	g_d	8.0
11	L_c	2.0	g_w	1.0
12	g_o	1.0	s_1	11.0
13	g_i	1.0	R_1	2.0
14	g_s	1.0		

B. *Antenna Design in Underwater Condition*

In this study, the proposed design was simulated in a normal water condition with a permittivity of 78 and the electrical conductivity of 1.59 S/m. The selection of the correct mesh is very important and key challenges in this design. This is because, the software unable to solve the simulation if the mesh is too dense. Furthermore, the increasing number of relative permittivity in underwater condition, will resulted the increasing of simulations time [11]. The propagation of electromagnetic waves in underwater condition is not the same as in the air condition due to the high dielectric constant and electrical conductivity. Therefore, in order to obtain good results, the weighty mesh is needed.

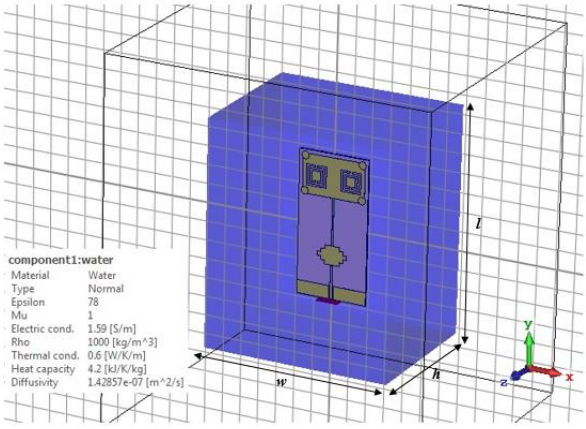


Fig. 2. The structure of the proposed CPW-fed patch antenna in simulated underwater condition

Table 2. Dimensions of Underwater Condition

No	Dimension of Normal Water Condition		
	Parameter	*Symbol*	*Value (mm)*
1	Width	*w*	100
2	Length	*l*	120
3	Thickness	*h*	80

Several setting need to be considered in designing the underwater antenna. There are *lines per wavelength* and *refine at PEC / lossy metal edges by factor* setting. *Lines per wavelength* defines the minimum number of mesh lines in each coordinate direction that are used for a distance equal to this wavelength. This setting has influenced the quality of the results and on the calculation time. Increasing this number leads to increases the total calculation of simulation time and resulted higher accuracy. The *refine at PEC / lossy metal edges by factor* setting is very useful, because the fields vary nearest to such edges and have to be sampled higher than elsewhere [11].

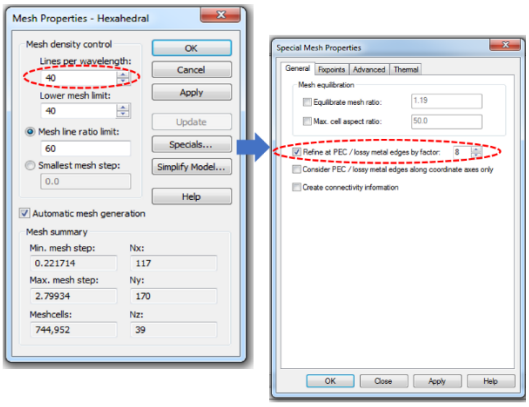


Fig. 3. The setting on the mesh properties in simulated underwater condition.

In this research, the frequency range of 0 GHz to 1.2 GHz was selected for the air condition. Since in underwater condition, the frequencies are 9 times lower than in air (free space) [11], therefore, the studied range in underwater is from 0 GHz to 0.133 GHz. Notice that, the relationship between the wavelength, λ with the propagation speed, c and the operating frequency, f is

$$\lambda = \frac{c}{f} \tag{1}$$

where $c = 3 \times 10^8$ m/s and the operating frequency in air, f_{air} is 919 MHz, hence, the calculated wavelength, λ is 326.44 mm.

$$f_{water} \approx \frac{f_{air}}{9} \tag{2}$$

However, if the operating frequency in air, f_{air} is 919 MHz, therefore, by using (2) the calculated frequency in underwater, f_{water} condition is 102.11 MHz.

Table 3. Theoretical Operating Frequencies in Air and Underwater Conditions

No	Theoretical Operating Frequencies	
	Case	Operating Frequencies (GHz)
1	Air Condition ($\varepsilon_r = 1$)	0.919 GHz
2	Underwater Condition ($\varepsilon_r = 78$)	0.102 GHz

[3] SIMULATION RESULTS

In this study, the design and simulation of the proposed antenna are performed by using CST microwave studio software with the criterion of lower return loss, S_{11} is -10 dB. The simulation on the proposed antenna had been performed until the design requirements are met. The total size of the proposed antenna structure have 76 mm × 38 mm which corresponds to 0.24λ × 0.11λ.

A. Parametric Studies in Air Condition

A parametric study were carried out on the most effective elements of the antenna structure. A step-by-step design process were carried out to obtain an optimized design for good impedance matching. In this works, several parameters such as the length of the CSRR, s_1, the length of loading bars, W_a and the radius of rounded corner, R_1 structure being the parameters controlling. From the simulation results, the resonant frequency, f_r is affected by adjusting the parameters of s_1, W_a and R_1. Therefore, in order to achieve back near to the operating frequency of 919 MHz, all the parameters need to be adjusted to a suitably value.

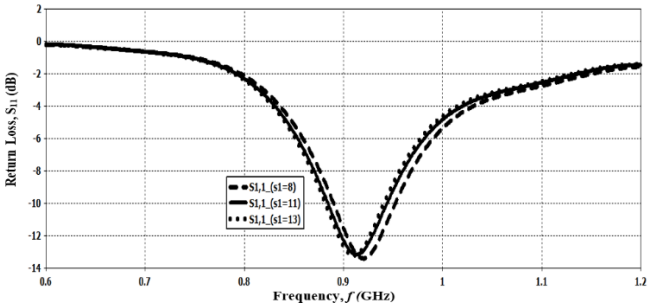


Fig. 4. The effect of variations on the length of the CSRR, s_1 structure.

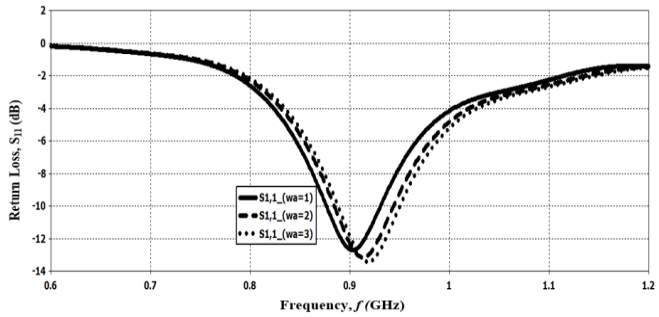


Fig. 5. The effect of variations on the length of loading bars, W_a structure.

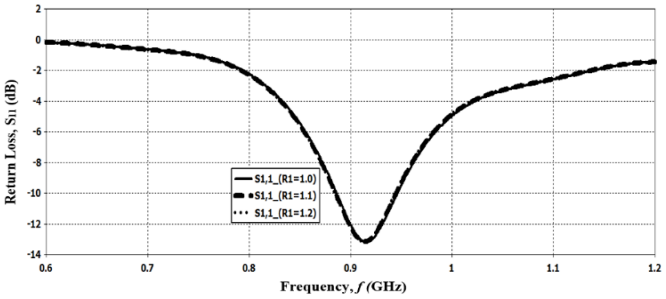


Fig. 6. The effect of variations on the radius of rounded corner, R_1 structure.

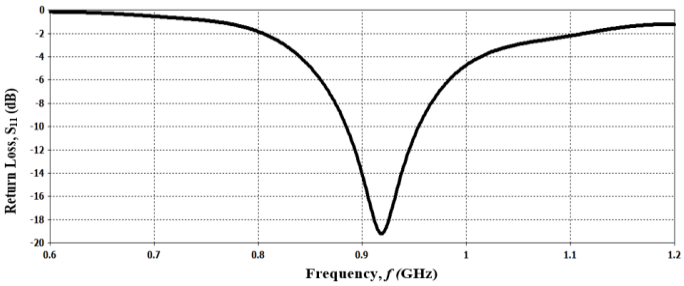


Fig. 7. Simulated result of return loss, S_{11} (dB) in air condition.

The simulated design produced good impedance matching with reflection coefficient being below -10 dB. The return loss, S_{11} (dB) of CPW-fed rectangular patch antenna with two square-shaped CSRR, rounded corners and loading bars structure resonates at -19.20 dB. The simulated < -10 dB value of bandwidth for the proposed antenna structure have been determined at the frequency range of 884.62 MHz to 954.07 MHz which corresponds to (69.45 MHz) 7.56 %. The radiation pattern of the antenna was observed when the antenna is operating in air condition. The simulated gain of the proposed antenna operating in air condition exhibits the

maximum gain of 1.66 dBi. The proposed antenna has omnidirectional radiation pattern.

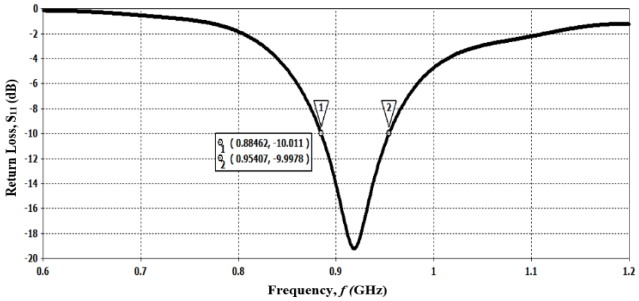


Fig. 8. Simulated bandwidth of the proposed antenna at 919 MHz.

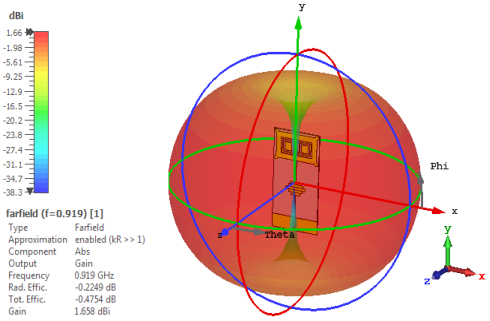


Fig. 9. Simulated 3D radiation pattern for the proposed antenna.

B. Parametric Studies in Underwater Condition

The simulated return loss, S_{11} in underwater condition resonates at -19.66 dB at 151 MHz. From the parametric simulations shown in Fig. 10, it is confirmed that the simulated results in underwater condition resulted the frequencies in underwater are 9 times lower than in air (free space) condition [11].

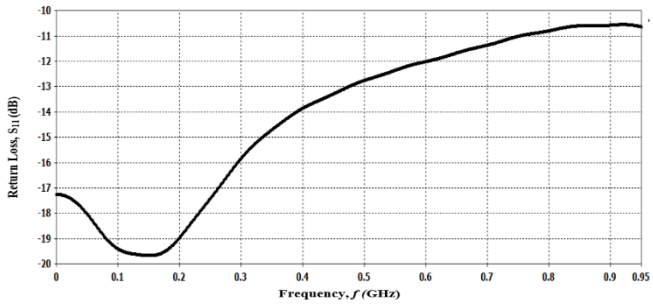


Fig. 10. Simulated result of return loss, S_{11} (dB) in underwater condition.

Therefore, in order to get the simulated return loss, S_{11} in underwater condition which resonates at 919 MHz, the setting on the *lines per wavelength* and *refine at PEC / lossy metal edges by factor* should be increased and adjusted near to the operating frequency of 919 MHz.

Table 4. Results on the Simulated Frequencies in Air and Underwater Conditions

No	Simulation Results on the Frequencies using CST Software	
	Case	Operating Frequencies
1	Air Condition (ε_r = 1)	0.918 GHz
2	Underwater Condition (ε_r = 78)	0.151 GHz

[4] CONCLUSION

This study investigated in details the parameters that contribute to miniaturization of antenna and the suitable method to enhance the gain. The performance of the proposed underwater antenna was assessed through the ability of designed antenna in obtaining a high gain, smaller size and matching impedance in air and underwater condition. This was done through the parametric simulations of several parameters effects which influenced the proposed underwater antenna. The effects being studied were return loss (S_{11}), the degree of impedance matching, radiation pattern and gain of the proposed underwater antenna. Future works includes to study how to get the simulated return loss, S_{11} in underwater condition resonates at operating frequency of 919 MHz, fabrication of the proposed antenna, propagation measurements, and further studies on antenna shape and method to increase the simulated gain.

REFERENCES

[1] S. I. In´acio, M. R. Pereira, H. M. Santos, L. M. Pessoa, F. B. Teixeira, M. J. Lopes, O. Aboderin, H. M. Salgado, “Antenna Design for Underwater Radio Communications,” *OCEANS 2016 - Shanghai*, Shanghai, China, 2016, pp. 1-6, doi: 10.1109/OCEANSAP.2016.7485705.

[2] S. Nasir, C. Abdulkadir, T. Y. Al-Naffouri, and A. Mohamed-Slim, “Underwater Optical Wireless Communications, Networking, and Localization: A Survey,” vol. 94, pp. 1–40, November 2019.

[3] M. Jouhari, K. Ibrahimi, H. Tembine and J. Ben-Othman, "Underwater Wireless Sensor Networks: A Survey on Enabling Technologies, Localization Protocols, and Internet of Underwater Things," in *IEEE Access*, vol. 7, pp. 96879-96899, 2019, doi: 10.1109/ACCESS.2019.2928876..

[4] S. K. Jha, P. Suraj, and R. K. Badhai. Bow-Tie Shaped Meander Line UWB Antenna for Underwater Communication. In: Gupta D., Khanna A., Bhattacharyya S., Hassanien A.E., Anand S., Jaiswal A. (eds) International Conference on Innovative Computing and Communications. Advances in Intelligent Systems and Computing, vol 1165. Springer, Singapore. 2021, https://doi.org/10.1007/978-981-15-5113-0_91.

[5] A. A. Abdou, A. Shaw, A. Mason, A. Al-Shamma'a, J. Cullen and S. Wylie, "Electromagnetic (EM) wave propagation for the development of an underwater Wireless Sensor Network (WSN)," SENSORS, 2011 IEEE, Limerick, Ireland, 2011, pp. 1571-1574, doi: 10.1109/ICSENS.2011.6127319.

[6] S. Chaimool, and P. Akkaraekthalin. CPW-Fed Antennas for WiFi and WiMAX. in Advenced Transmission Techniques in WiMAX/Book 1, 2012, " ISBN 978-953-307-965-33.

[7] H. M. Zali, I. Pasya, M. T. Ali and T. Kobayashi, "Measurement of wideband microstrip underwater antenna performance with buffer layer structure," *2017 IEEE 13th Malaysia International Conference on Communications (MICC)*, Johor Bahru, Malaysia, 2017, pp. 48-52, doi: 10.1109/MICC.2017.8311730.

[8] N. George, G. R. and D. C. N, "Design of wide band antenna for ocean communication: Review", International Journal of Advanced Computer Research, vol. 4, pp. 8, 2014.

[9] Q. Awais, H. T. Chattha, M. Jamil, Y. Jin, F. A. Tahir, and M. U. Rehman. A Novel Dual Ultrawideband CPW-Fed Printed Antenna for Internet of Things (IoT) Applications, Hindawi Wireless Communications and Mobile Computing, Volume 2018. Article ID 2179571, 9 pages, https://doi.org/10.1155/2018/2179571.

[10] A. Kumar, D. Parkash, and M. V. Kartikeyan. Planar Antennas For Passive UHF RFID Tag. Progress In Electromagnetics Research B, Vol. 19, 305-327, 2010.

[11] G. M. Aleix. UWB Antenna Design for Underwater Communications. Thesis, University of Barcelona, Barcelona, Spain. 2009

High Gain Receiving Antenna Developed for ISAR Applications Using 2.4 GHz WLAN Signals

Göker Şener
Electrical-Electronics Engineering Dept.
Cankaya University
Ankara, Turkey.
sener@cankaya.edu.tr

***Abstract*— This article presents a high gain parabolic reflector antenna developed for Inverse Synthetic-Aperture Radar (ISAR) applications. The purpose of this antenna is to receive the reflections from WLAN transmitters such as Wi-Fi and Wi-Max modems at 2.4GHz so that the received signals can be used to obtain ISAR images. ISAR technology is based on having images of moving objects with radar signals. Therefore, high gain and narrow beamwidth antennas are required to get high resolution images. For this purpose, a parabolic reflector antenna is designed with 5^0 beamwidth and 27.5dB antenna gain. With this antenna, a resolution of 87cm x 87cm area at distance of 10m is obtained. A wideband conical horn antenna with radius of 4.19 cm and height of 6cm is used as the feed element of this parabolic reflector. The reflector has a diameter of 1.5m and a depth of 28cm. Theoretical and computer simulation results of the proposed antenna are presented. In addition, image outputs at various distances are compared in a simulation of an ISAR application.**

Keywords—Dish antenna, high gain, ISAR, parabolic reflector antenna.

[1] INTRODUCTION

Synthetic aperture radar or SAR is a type of radar that provides high resolution by combining the radar images collected by multiple small radar beams electronically. By steering a narrow beam in space at different positions and angles, the data collected at the receiver makes it possible to obtain images of objects even with complex surfaces. SAR technology has found wide usage area especially in remote sensing and military applications [1].

Inverse synthetic aperture radar or ISAR is a type of radar based on the same technological infrastructure as SAR. The only difference is that instead of the radar transmitter scanning at different positions and angles, an image is obtained by combining the radar signals caused by the movement of the target. In ISAR technology, the waves emitted from a transmitter hit upon a moving target and the reflected waves are collected by the receiving antenna. If the receiver antenna has a narrowbeam radiation characteristics, then the reflections convey information from a smaller area of the target, hence the resolution increases. The overall image is obtained by mapping all the received signals onto a color scale according to their intensity.

There have been many studies on ISAR applications in literature. For example, in [2], the quality criterion of the ISAR image and the categorization of the what is called good image reception have been evaluated. In [3], image blurring due to target separation difficulties are corrected by signal processing techniques such as Fourier transform and segmentation. Similarly, ISAR image applications at close distances are examined in [4] and new algorithms are proposed for near field image reconstruction.

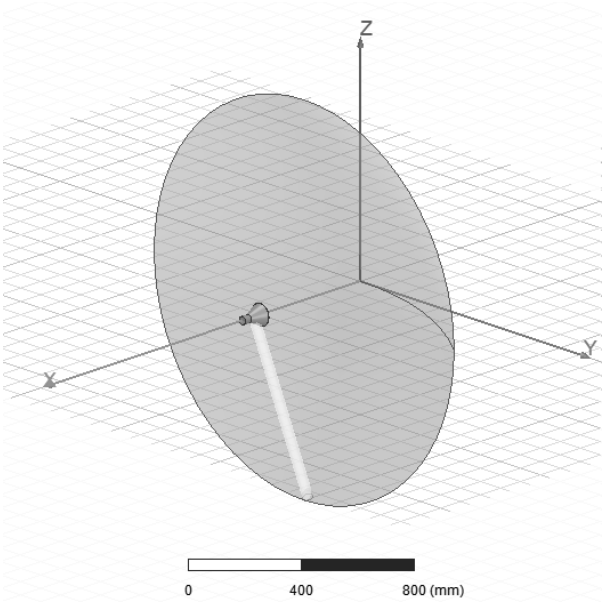


Fig. 1. 3D view of the proposed reflector antenna.

To improve ISAR image resolution and quality, a high gain and narrow beamwidth antennas are required. For this reason, horn antennas, array antennas or parabolic reflectors or satellite dishes are frequently used. For example, ISAR image quality has been analyzed using linear array and 2D array antennas in [5,6]. Again, in [7,8], parabolic reflector antennas are used in image processing applications. Generally, horn antennas can be considered as small size, medium gain and broadband antennas, array antennas are medium size, high gain and narrow band and parabolic reflector antennas can be considered as large size, high gain and broadband radiators [9].

The major advantages of parabolic reflector antennas are their low cost and ease of fabrication. The gain and beamwidth depends on the feed antenna characteristics as well as the reflector dimensions. Usually, pyramidal horn or conical horn antennas are used as feeding elements.

In this article, a parabolic reflector antenna is designed with a conical horn being used as the feeding element. A 3D view of the antenna is shown in Fig.1. This antenna is used as

the receiver at 2.4GHz, while a Wi-Fi modem with isotropic radiation is assumed to exist as the transmitter. The conical horn antenna has a wide operation band between 0.1-6GHz (VSWR<2) and radiates in linear polarization. The gain of the antenna is 29.44dB in the broadside direction and the beamwidth is 5^0 on both the elevation and azimuth planes. With these features, the proposed radar gives a resolution that is enough to scan a 87cm x 87cm square area at 10m distance (1.32dots/m^2) away from the antenna.

Antenna gain also increases with increased frequency. For example, the proposed antenna gives a much smaller beamwidth of 1^0 and a gain of 40dB at a frequency of 10GHz. However, it is impossible to use WLAN signals at these frequencies due to the fact that skin depth is very small, and the losses would be very high when penetrating walls.

The ISAR application with the proposed antenna is carried out at 10cm scan intervals on a target at 1m away from the system. The results are obtained for 1m, 2.5m and 5m target distances at the same resolution. As expected, it is observed that the resolution drops as the distance increases.

[2] ANTENNA DESIGN

A. *Conical Horn Antenna (The Feed)*

The dimensions of the conical horn antenna are shown in Fig.2. where "D" and "d" are the diameters of the apertures of the horn and the waveguide respectively. The radiated electric field analysis of the horn antenna can be evaluated by the Fourier transform of the electric field at the aperture of the antenna. The far field formulations of the conical horn antenna are in the form of Bessel functions and Legendre polynomials. For more detailed information, the reader can refer to [9,10].

The directivity of the conical horn is maximum for when the aperture diameter is given by [9]

$$D = \sqrt{3L\lambda}, \tag{1}$$

where L is the horn length and λ=12.5cm is the free space wavelength. From this formula, the aperture diameter of the horn is calculated to be 19cm. However, 8.4cm is used in the design, because large apertures block the reflected waves and reduce the overall gain. Also at 8.4cm, the beamwidth is wider which makes the radiation cover the entire reflector surface.

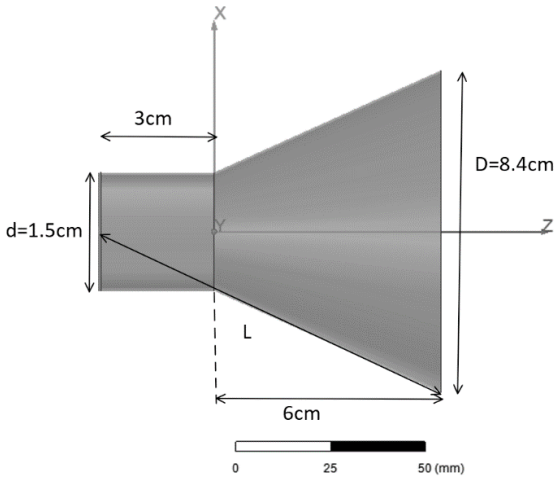


Fig. 2. Dimensions of the conical horn antenna used as the feed element of the parabolic reflector antenna.

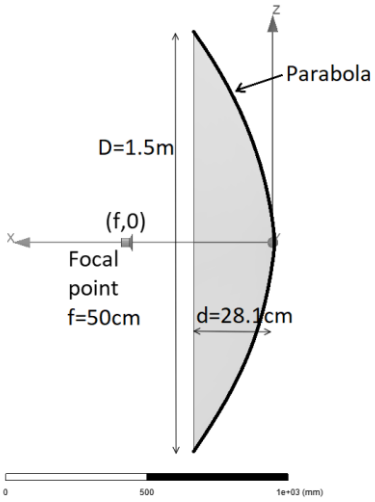


Fig. 3. Side view of the parabolic reflector with its dimensions.

B. *Parabolic Reflector*

Before designing the parabolic reflector, a mathematical analysis of a parabola is required. For this purpose, let us consider a parabola whose vertex is at the origin and is defined for $x \geq 0$ plane as shown in Fig.3. Here, "D" is the diameter of the aperture of the parabola and "d" is the distance of depth.

The equation of the parabola with respect to xz-plane can be written as

$$x = \frac{1}{4f} z^2 \tag{2}$$

where "f" is the focal length coordinate value on the x axis.

Also, the points (D/2, d) and (-D/2, d) are on the parabola, hence

$$\mathrm{d} = \frac{\left(\frac{\mathrm{D}}{2}\right)^2}{4f} \tag{2}$$

can be obtained.

The antenna gain is proportional to the aperture diameter "D". From (2), let us assume D=1.5m is used, which is a standard reflector diameter, and let f=50cm, then the depth of the parabola d=28.1cm is obtained.

The waves radiated from the feed at the focal point reflect from the parabolic surface and move in parallel to the axis of the parabola (x-axis). This direction is also known as the broadside of the antenna.

The effect of the supporting structure of the feed is neglected in the analysis because it is made of a dielectric material, and thus has minimal effects on the radiation of the antenna. Also, both the feed and the parabolic reflector are made of conducting materials.

[3] ANTENNA CHARACTERISTIC

The proposed antenna is simulated for various antenna properties. First, the impedance bandwidth is obtained to see in which frequency range the antenna is functional. For this purpose, Ansys HFSS computer software is used to plot the reflection coefficient (S11) at the entrance of the feed waveguide with respect to the frequency. The results are shown in Fig.4.

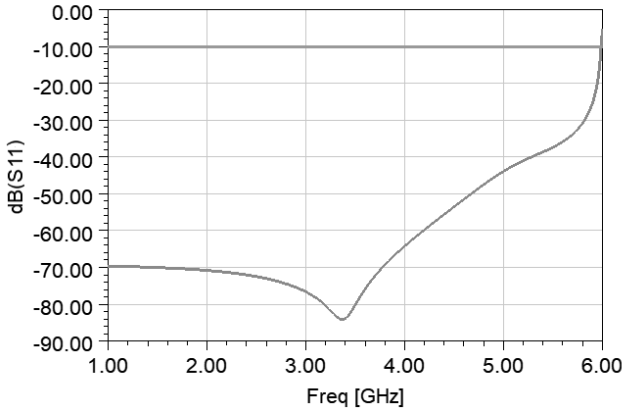
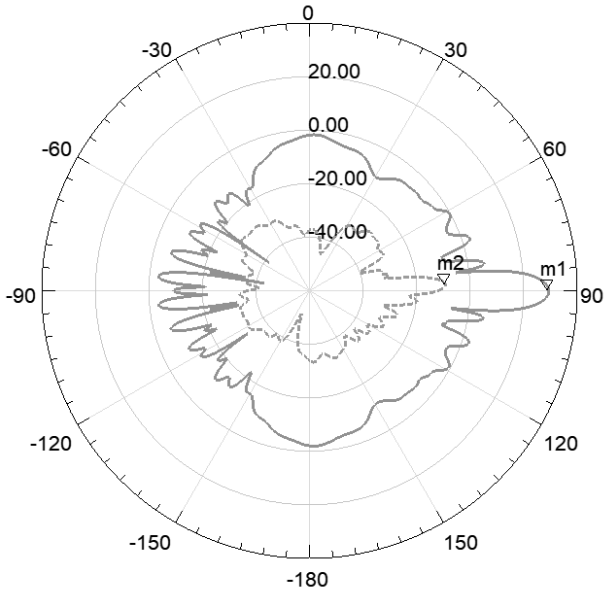


Fig. 4. S11 versus frequecy graph for the proposed antenna.

The results show that the antenna is usable from 1- 6GHz where S11(dB)≤10.

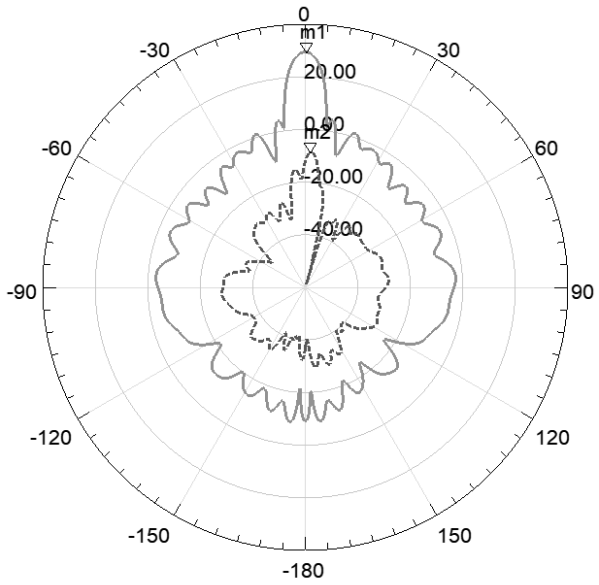
The radiation characteristics are plotted on the elevation and azimuthal planes separately for the antenna power gain in θ and φ spherical directions as shown in Fig.5 and Fig.6 respectively.



Curve Info	xdb10Beamwidth(3)
dB(GainPhi) Setup1 : LastAdaptive Freq='2.4GHz' Phi='0deg'	5.2326
dB(GainTheta) Setup1 : LastAdaptive Freq='2.4GHz' Phi='0deg'	5.5432

Name	Theta	Ang	Mag
m1	89.6000	89.6000	29.3980
m2	87.0000	87.0000	-9.2415

Fig. 5. Polar plot for the power gain on the elevation plane (φ=0 or xz-plane) for θ and φ components of the radiated power.



Curve Info	xdb10Beamwidth(3)
dB(GainPhi) Setup1 : LastAdaptive Freq='2.4GHz' Theta='90deg'	4.8827
dB(GainTheta) Setup1 : LastAdaptive Freq='2.4GHz' Theta='90deg'	5.7979

Name	Phi	Ang	Mag
m1	0.6000	0.6000	29.3421
m2	2.6000	2.6000	-8.5241

Fig. 6. Polar plot for the power gain on the azimuth plane (θ=900 or xy-plane) for θ and φ components of the radiated power.

The results show that in both vertical and horizontal polarizations, the antenna has a gain of 29.4dB and a beamwidth of about 5^0 at the broadside direction.

[4] ISAR APPLICATION

An ISAR application using the proposed antenna is presented with the HFSS computer simulation. The layout of the application is shown in Fig.1. Considering a monopulse radar system, an isotropic transmitter at a frequency of 2.4 GHz and the parabolic reflector antenna are placed at the origin of the coordinate system. The broadside of the antenna is aligned with the x-axis where there is an "F"-shaped metal target placed at distances of 5m, 2.5m and 1m away from the antenna. Fig.1 shows all the objects in their actual sizes.

With a 5^0 beamwidth, the arclength of the radar beam at distances of 5m, 2.5m and 1m are 43.6cm, 21.8cm and 8.7cm respectively. With a 1^0 beamwidth (reflector diameter at 7m) at the same distances, corresponding span lengths would be 8.7cm, 4.3cm and 1.7cm respectively.

The target is moved at steps of 10cm in both vertical and horizontal directions (z and y directions). The received signals are collected and converted into an image at the end of the entire scan process.

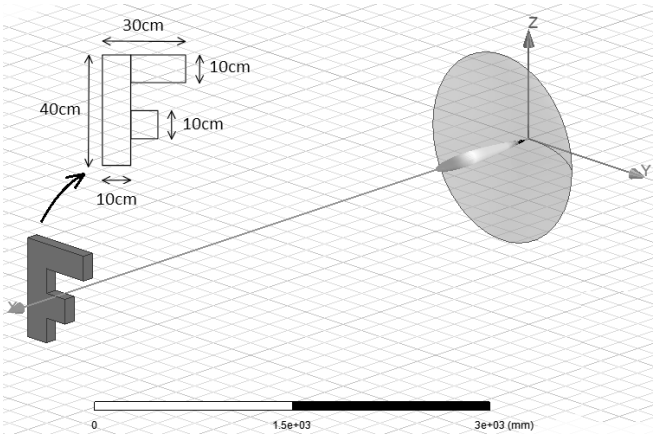


Fig. 7. An ISAR application using the proposed antenna conducted by HFHH computer software.

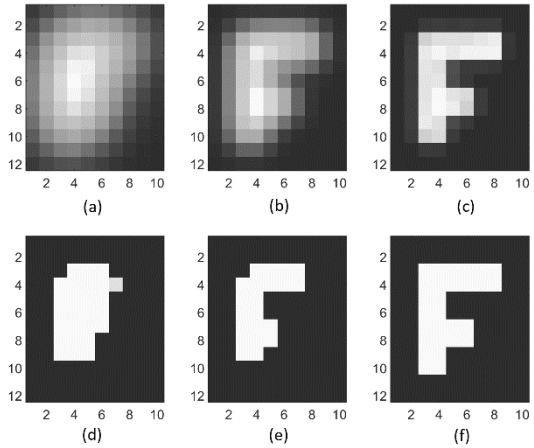


Fig. 8. ISAR images obtained at (a) 5m (b) 2.5m and (c) 1m. The corresponding processed images are shown in part (d), (e) and (f).

Matlab computer program is used to convert the received wave strengths into images. The results are shown in Fig.8.

[5] CONCLUSION

A parabolic reflector antenna has been designed to be used as a receiving antenna for an ISAR application at 2.4GHz WLAN applications. The following results are observed:

- Very narrow beamwidths are required to acquire useful images at far distances. As a rule of thumb, 1^0 beamwidth resolves 17cm length at 10m away from the antenna at 2.4GHz.
- Increasing frequency decreases the wavelength, and thus the gain increases. At 10GHz, the same parabolic reflector antenna has roughly a 1^0 beamwidth.
- Using array antennas with microstrip structures requires a total of 45 x 45 rectangular patches separated by 6cm to get a 1^0 beamwidth with 40dB gain. Thus, the total surface area of the array structure becomes 2.7m x 2.7m, which is not practical either.
- A single horn antenna of WR-430 waveguide feed can yield 5^0 beamwidth and 24.5dB broadside gain at 190cm horn length and 45cm x 35cm aperture dimensions. This is also not a practical size antenna, moreover it is only at 5^0 beamwidth.
- For ISAR applications, it seems more appropriate to use X-band antennas (8-12GHz) with very high directivities. The downside is the lack of penetration ability of the waves at such frequencies. This makes it difficult to obtain images behind walls.

REFERENCES

[1] V. C. Chen and M. Martorella, Inverse Synthetic Aperture Radar Imaging: Principles, Algorithms and Applications, SciTech Publishing, 2014.

[2] J.M. Steyn and W.A.J. Nel, "Using image quality measures and features to choose good images for classification of ISAR imagery", *IEEE International Radar Conference*, Lille, France, 2014.

[3] D. Xiao, F. Su, and J. Wu, "Multi-target ISAR Imaging Based on Image Segmentation and Short-time Fourier Transform", *IEEE 5th International Congress on Image and Signal Processing (CISP 2012)*, Chongqing, China, 2012.

[4] J. W. Smith, M. E. Yanik, and M. Torlak, "Near-Field MIMO-ISAR Millimeter-Wave Imaging", *IEEE Radar Conference (RadarConf20)*, Florence, Italy, 2020.

[5] L. Y. Tao, C. Y. Guang, and Y. C. Bin, "ISAR Imaging with Linear Array-Antenna", *2nd Asian-Pacific Conference on Synthetic Aperture Radar*, Xi'an, China, 2009.

[6] C. Ma, T. S. Yeo, H. S. Tan, J. Wang, and B. Chen, "Three-Dimensional ISAR Imaging Using a Two-Dimensional Sparse Antenna Array", *IEEE Geoscience and Remote Sensing Letters*, Volume: 5, Issue: 3, July 2008, pp. 378 – 382.

[7] C. Tienda, N. Bertl, M. Younis, and G. Krieger, "Characterization of the Cross-Talk SAR Image Produced by the Cross-Polarization in a Single Offset Parabolic Reflector", *IEEE 9th European Conference on Antennas and Propagation (EuCAP)*, Lisbon, Portugal, 2015.

[8] A. Naeemi and M. Neshat, "Antenna Design for mm-Wave Polarimetric Imaging System", *Sixth Iranian Conference on Radar and Surveillance Systems*, Isfahan, Iran, 2019.

[9] C. A. Balanis, Antenna Theory Analysis and Design, 2nd edition, John Wiley and Sons, New York, 1997.

[10] A.P. King, "Radiation Characteristics of Conical Horn Antennas", *Proc. IRE*, vol. 38, pp.249-251. March 1950.

Design and Simulation of Crossed Walls Security Detection System

Muhammad Baballe Ahmad
Department of computer engineering technology School of technology, kano state polytechnic Kano state, Nigeria
mbaballe@kanopoly.edu.ng

Mukhtar Ibrahim Bello
Department of computer science School of technology, kano state polytechnic Kano state, Nigeria
mibello2@gmail.com

Abubakar SAdiq Muhammad
Department of computer engineering technology School of technology, kano state polytechnic Kano state, Nigeria
asmuhammad@kanopoly.edu.ng

***Abstract*— The security detection system is exactly a method by which something is secure through a system of interworking components and devices. The rate of abduction and theft in the world is growing by the day; this imbibes fears that become a menace to the economy, peace, and development of any country nowadays. It is vital to develop viable technologies that will secure the properties and lives of humans as countermeasures to tackle this kind of problem. With the aid of the latest development in technology nowadays, it is possible to secure the properties and people's lives using a security detection system that will monitor, guide, and protect the environments that need to be secure against burglars and abductors. A security detection system was developed to watch over the four (4) square walls north wall, south wall, east wall, and west wall. Each of these walls is equipped with a sensor designed using a light-dependent resistor (LDR) and light-emitting diode (LED) whenever anything crossed the walls he or she blocked the light-dependent resistor (LDR) from receiving light from a light-emitting diode (LED) that makes the light-dependent resistor (LDR) to output 0 volts to peripheral interface controller (PIC), whenever the peripheral interface controller (PIC) detects 0 volts it sends a signal to liquid crystal display (LCD) to display that, that particular wall has been crossed, and the system will immediately rotate the dc motor that carries the closed-circuit television (CCTV) camera to stop at the crossed wall to capture a real-time video and send to the buzzer, the function of the buzzer is to sound an alarm informing an intrusion has occurred in that specific wall. If the peripheral interface controller (PIC) detects 5 volts from the entire walls light-dependent resistor (LDR) it means that none of the walls are being crossed, if all wall light-dependent resistor (LDR) output 5 volts the peripheral interface controller (PIC) will display on the liquid crystal display (LCD) "All walls OK".**

Keywords*— *Microcontroller, light crystal display, closed-circuit television, security detection system, break-in, abduction.

[1] INTRODUCTION

A security detection system can be used to identify trespassers, illegal entry, or break-ins into a secure zone or buildings. These days Security detection systems are mainly used in commercial, residential, industrial, schools, universities, and hospitals. The security detection system can also be used in prisons to monitor the prisoners and their movements. Today, the security detection system and closed-circuit television (CCTV) system is an essential part of any modern programmed security detection system. The simple design of any security detection system starts with considering the needs of the residents, measuring existing hardware and technology, reviewing the costs of the system, taking into account the watching choices, and lastly scheduling the installation. Now if we are going to look at the world's one of the richest countries which are the united states of America (USA) we can see that they are placed 6th in auto theft and 9th in the break-in. Their investigation also indicates that most of the break-in happened in banks, residential areas, as well as and offices. Non-Automated security detection systems were found non-reliable [1]. Doors were fitted with a lock and key system, which can be open easily. Even with the help of human presence as a security guard may not be reliable. Every system from the past is very much vulnerable. Our home is a place where security is a must need, to keep all the appliances and vulnerable safe. You as the homeowner should have the full assurance to step out from your house with the feeling that nothing is going to happened to your home or organization. This feeling will only arise when the house or organization needs to be secure is fully equipped with a reliable security detection system [2].

[2] RELATED WORKS

The development of the security detection system begins with the creation of man. To alert frightening information, man implements a form of a signal, through shouting and sound. He then later replaced it with the help of the clapping of hands and with the introduction of signals to inform society or to blowout a certain message if they are any kind of abduction or burglary, during the early periods of some African society especially in my country Nigeria. All such methods of notifications or warnings are necessary, undependable, and unmethodical. With the aid of innovation in technology nowadays, all those undeveloped methods of producing security were later changed by programmed security alarm systems in the late eighteenth period. These types of electronic security detection systems usually work without the support of any human being energy. The earliest electronic fire, a security detection system was established by a man named William .F. Channing. Late on an electrical electronics engineer, Mr. Moses G. Farmer invented the construction. This alarm system uses automatic indicator boxes to label the position of the fire outbreak and was first lunch in Boston, United States of America. The development of this alarm system by Dr. William was then followed by the improvement of various stylish and difficult fire and intruder security alarm system technology that is so many to measure. The most noteworthy among this security detection system technology is the use of remote signaling thief security alarm. This kind of security alarm system was the first design in the early 1970s [3]. This administers a fast inventive reaction to alarm calls. However, organizations and industries are based on the supply of security service apparatus that usually come in dissimilar designs to keep burgles and thugs away from the environment that are not built for them. Today, we have an innovative group of electronic security alarm systems with complexity at various levels. With the latest flow in crime rates in the world, it has become very essential to safeguard our buildings and our property with the aid of sophisticated stages of various advanced security alarm devices. The prices of such kinds of security alarm devices depend on the apparatus technology

and solicitation desires. These alarm security system devices are characterized by present electronic security alarm systems. Some of nowadays-modern security alarm systems are housebreaker alarms, threat alarms, industrial alarms, speed limit alarms, and anti-theft vehicle alarms. The intruder alarm security is initiate by a cycle, from a comprehensive automated circuit loop that is close with an alarm at its output, or an indication to inform the owner of danger. They are a central control box that normally observer different gesture indicators and the perimeter protections that give an alarm or notify the owner when any of this sensor is a trigger. Some of the intruder's security alarms system normally functions delicately on the conception of a magnetic contact and others. For those types of security systems working with the sensors, these devices are usually positioned at any entering of the industries, organizations, and building. In this case, the sensor will activate an alarm if the device gets a signal above its set inception. In the case of motion detection, the ultrasonic sensor is normally used; the point indicator can be used in the concession of a criminal alarm, theft, or illegal individuals at certain points such as doors or windows. For instance, when a precise environment needs to be look over the awareness of the burglar in the protected environment is used, which is executed with the help of ultrasonic sensors and is normally fixed at an appropriate location. Designing and Implementation of Security alarm detection system for organizations, industries, and houses based on Global System for Mobile Communications (GSM) technology was a review by Govinda et al. In 2014 that administer double ways to implementing security alarm detection system-using internet of things (IOT) [4]. Firstly is by the use of web cameras, in a case when there is any motion sensed by the camera, it will sound an alarm and sends a message to the industries, organizations, or homeowners that they are an intrusion. This technique of identifying intrusion against burglary or abduction is reasonably good, although costly because of the price of the cameras used in the development of the security system. The camera that is going to be used in the security system needs to be of great value which means it has to have a very wide range and the image quality should be good enough to identify. Likewise, if you going to work with a moving camera such as dome cameras, they are normally expensive more than the ones that are fixed in one place. Short message service (SMS) based system using Global System for Mobile Communications (GSM) was suggested by Daniel and Karri in the year 2005, they suggest using internet facilities to deliver an alert or messages to the place an intrusion took place rather than the ordinary short message service (SMS). Arvind and Jayashri 2013 have carried out a fingertip or fingerprint-based verification system to unlock a certain closed place or door. This type of security system aids users to unlock a certain place because they are the ones whose fingerprint is register to the system so if you put the unregistered fingertip it will not unlock the place or anything the finger is register to. This type of security detection system is connected with some more alarm security protection features this includes fire accidents and gas leakage sensors or detection devices. However, a great system, fingertip devices are complex and expensive, as they want amplified sensor resolution to join into the internet of things system. Some professionals likewise argue that merely depending on a fingertip sensor is not wise because it is quite simple to put someone fingertip on something and reproduce it, that is to duplicate the fingertip, that is why it is consistently considered to make use of fingertip scanners in a two ways authentication systems whereby an added layer of security system is made in the form of the passcode, PIN, or voice recognition. Some researchers suggested an idea of a powerful internet of things security system whenever a defect in one of the components used in the security system will not fail the whole security system. The knowledge of making use of numerous gadgets, which may not be directly or may be suitable with one another, however, it can be made to work in such a way that they can interchange a present item of the security detection system in case they are a failure. In a lineup with this, the prototypical can use connection among several appliances, which may result in conserving energy, therefore, making the prototypical more effective. An illustration administers of this said prototype will use a temperature sensor, Wi-Fi component, and an entrance sensor to change an unreliable system. Light-dependent resistor (LDR) and Laser rays sensor are also used to identify an invasion using the intruder's movement were suggested in the year 2016 [5]. The method the system will work is that a light ray is a face towards the light-dependent resistor (LDR) sensor and if they are an interruption between the light ray and the light-dependent resistor (LDR), the alarm linked to the sensor start alarming and sends a short message service (SMS) to the house owner or place where the intrusion takes place. This type of system will assist in solving the problems of securing the spaces, which may be out of range from your immovable cameras, but may face the same problems, which is faced with systems involving of Global System for Mobile Communications (GSM) components to send a short message service, which is that the transmission of the message is reliant on network coverage. Likewise, due to the condition of the light rays, which is a straight light beam, the intruders who knew about the security detection system and will be capable of dodging the light beams since it is only made up of one light-emitting diode and one light-dependent resistor facing each other's, rendering the whole security system useless, since an intruder can avoid it. An innovative method of implementing and design an electronic lock security system using the internet of things technology and Morse code. The authors said that this is a unique awareness, which has never been done previously and is going to the first of its kind "optical Morse code-based electronic locking system". This type of system makes uses Light-emitting diodes (LED) as an encipher intermediate to send signals. To make it more available to the overall community, the light-emitting diode (LED) in our mobile phones has been made use of. On the side of the receiver a photosensitive resistor as well as a microcontroller such as an Arduino processor, which normally can crack the photosensitive signal after collecting it from the light-emitting diode (LED). Upon untangling this signal, it can then transfer the present situation of this lock to a cloud system this will be going to be from where these owners of the house, organizations, or industries can be monitoring the whole security system. This author has made an experiment on the system in real-life time and it has shown to perform underneath various brightness surroundings with all the features functioning, as they are designed to operate [6]. For this purpose, this research has focused on the upkeep of home security. In this research, the liquid crystal display (LCD) is used as a user interface. Each one of the four walls has a light beam (transmitter) and a light-dependent resistor (receiver) the light beam is pointing at the light-dependent resistor (receiver) the system also has a real-time clock that use to save the time of when last a particular wall crossed and can be view by the user when pressing the view mode button. When the system is powered on, it displays on the liquid

crystal display (LCD) 'ALL 4 WALLS OK' and the motor that rotating the CCTV camera is by default located at the north wall. Whenever a wall (say east wall) is crossed by an intruder the system will alert the user (through buzzer) and display on the liquid crystal display (LCD) 'EAST WALL CROSSED' the system will also save the time at which the east-wall was crossed and will automatically control the motor to rotate and stay at east-wall to capture the real-time video of the area using closed-circuit television (CCTV) camera that is mounted on the motor. The system will remain at the east wall and keeps alarming the user with the help of a buzzer until another wall is crossed at the same time if all the walls are crossed it will still notify the house owner by displaying on the LCD the amount of the walls crossed and displaying a real-time video of the intrusion which is an advancement of the previous research mentioned in which none closed-circuit television is used and is only one light-emitting diode and one light-dependent resistor that is used. In this research, an intruder can hardly dodge the four light-emitting diodes and the four light-dependent resistors use in this research.

[3] RESULTS

This section is to deal with the description of the test performed on the various sections of the overall system and their corresponding result as well as the result of the overall system. The system is purposely made to improve the effectiveness and reliability of a wall-crossed detecting security system. Being something on which human life will depend on. The test was carried out on the system as a whole and during the simulation process, the results were obtained. The program for the wall-crossed detecting security system was written using MPLAB IDE. After the program was written, it was simulated using the MPLAB SIM that is part of the MPLAB software. This was done to ensure that the program performed as expected and to detect any bugs that exist in the program. The circuit diagram was drawn using Proteus ISIS, which is an electronics design software, and the respective programs for the peripheral interface controller (PIC) were loaded into the designed diagram. The circuit was then simulated to see if it performed the desired function. All necessary corrections were made to the software at this stage until the desired results are obtained.

S/No	***Test Conducted***	***Result obtained***
1	Press the play button	Ports, LCD, sensors initializing & LCD "time and date &"ALL WALLS OK"
2	If the north light-dependent resistor blocked from the light beam or moved away from it by pressing the negative sign of the LDR torch	LCD "north wall crossed" system rotate the motor until when it makes contact with the north point (north button pressed) it then stops to capture a real-time video by CCTV
3	If the south light-dependent resistor blocked from the light beam or moved away from it by pressing the negative sign of the LDR torch	LCD "south wall crossed" system rotate the motor until when it makes contact with the south point (south button pressed) it then stops to capture a real-time video by CCTV
4	If the west light-dependent resistor blocked from the light beam or moved away from it by pressing the negative sign of the LDR torch	LCD "west wall crossed" system rotate the motor until when it makes contact with the west point (west button pressed) it then stops to capture a real-time video by CCTV
5	If the east light-dependent resistor blocked from the light beam or moved away from it by pressing the negative sign of the LDR torch	LCD "east wall crossed" system rotate the motor until when it makes contact with the east point (east button pressed) it then stops to capture a real-time video by CCTV

[4] CONCLUSION

The purpose of this research was to generate awareness concerning the security actions people can perform in day-to-day life in response to the rise in burglary and abduction in the world today. This study reviewed some studies relating to the security detection system using the internet of things. This paper also filled the gap regarding the need for a home alarm system for security against intrusion, for a burglar to be appropriately identified without a security guard, which is easier, more peaceful, and stress-free. This research also reviewed some studies on the security alarm system from how it is originated which has not been done in most of the research papers and its advancement in technology and the problems encountered by many authors. Also in this work, we have seen the impact of deploying the four light-dependent resistors and four light-emitting diodes in the simulation and the design of the security detection system, and how reliable the system is.

REFERENCES

[1] M. B. Ahmad, M. Cavas, "Design and Simulation of Four Walls Crossed Security System against Intrusion Using PIC Microcontroller," American Journal of Engineering Research, vol. 7, no. 12, pp. 233-244, December 2018.

[2] M. B. Ahmad, M. Cavas, "Design and Simulation of personal computer

base Walls Crossed Security System against Intrusion Using PIC Microcontroller", International Journal of Engineering Science Invention, vol. 8, no. 03, pp. 59-74, March 2019.

[3] M. B. Ahmad, A. B Abdullahi, A. S. Muhammad, Y. B. Saleh, U. B. Usman, "The Various Types of sensors used in the Security Alarm system," International Journal of New Computer Architectures and their Applications, vol. 9, no. 2, pp. 50-59, September 2019.

[4] M. B. Ahmad, M. Cavas, "A Review Advancement Of Security Alarm System Using Internet Of Things (IoT)", International Journal of New Computer Architectures and their Applications, vol. 9, no. 2, pp. 38-49, September 2019.

[5] M. B. Ahmad, A. S. Muhammad, A. A. Abdullahi, A. Tijjani, A. S. Iliyasu, I. M. Muhammad, I. Ibrahim, S. Tijjani, Y. Idris, I. K. Dahiru, A. A. Umar, J. Sulaiman, A. L. Musa, S. A. Mohammed, S. I. Abdullahi, A. H. K. Naisa, M. Surajo, S. A. Muhammad, B. A. Imam, S. H. Ayagi, K. M. Sani, "Need For Security Alarm System Installation And Their Challenges Faced " International Journal of New Computer Architectures and their Applications, vol. 9, no. 3, pp. 68-76, 2019.

[6] M. B. Ahmad, A. S. Muhammad, A. S. Iliyasu, A. A. Umar, B. A. Imam, S. H. Ayagi, "Gabor Based Band Selection For Multispectral Palmprint Recognition System Using Feature Fusion", i-manager's Journal o Image Processing, vol. 6, no. 2, pp. 14-19, April - June 2019.

The Need for Artificial Egg Incubation

Muhammad Baballe Ahmad
Department of computer engineering technology School of technology, kano state polytechnic Kano state, Nigeria
mbaballe@kanopoly.edu.ng

Abubakar Sadiq Muhammad
Department of computer engineering technology School of technology, kano state polytechnic Kano state, Nigeria
asmuhammad@kanopoly.edu.ng

Ishaq Auwal Balarabe
Department of electrical engineering electronics School of technology, kano state polytechnic Kano state, Nigeria
hajwfy@yahoo.com

***Abstract*— An egg incubator is a device simulating avian incubation by keeping the eggs warm at a particular temperature range and in the correct humidity with the help of a turning mechanism that assists to hatch the eggs. A well develops an improved egg incubator system that is capable of hatching an enormous number of chickens at a time and attaining high hatchability. The main heating elements may consist of sets of bulbs, which are used in providing the warmth needed in the incubator for hatching the eggs. Data from the sensors was processed by the microcontroller and the various control element were activated to help in moderating the condition in the incubator using machine language programming. An egg incubator with consistent, active, and proficient operation normally has the capabilities of providing sufficient poultry chicken which can oblige every household in the world nowadays with enough quantity of protein on daily basis.**

Keywords—an egg, microcontroller, sensor, turning mechanism, and incubator.

[1] INTRODUCTION

An Egg incubator is one of the most recent developments that provide jobs opportunity especially for those who want to be excellent farmers. The egg incubator system is designed to automatically control the humidity and temperature of the incubator for different types of eggs. The main purpose of this egg incubator is to take over the animal job to incubate an egg to hatching. Both bird and chicken eggs have been incubated with the help of an artificial method for thousands of years ago. Both, the Egyptians and Chinese are credited with originating artificial incubation procedures. Our world population is now growing at an alarming rate and so is the demand for protein. Poultry is a good source of protein and it is affordable at a cheaper rate. A broody chicken (a chicken that wants to set and hatch eggs and raise the chickens) can normally hatch just about 10–12 eggs at once in three weeks, which decreases its production as it normally takes time to incubate and hatch the chickens [1]. Benjamin and Oye [2] noted that some large birds, such as albatross and condors, usually lay only on a single egg every two years. Due to the world growing population, depending on this type of natural incubation is not good enough, henceforward they are a need for artificial incubation [3]. The most animated factor of incubation is the constant temperature required for an egg embryo to develop over a specific period. The humidity is also critical; when the air surrounding the egg in incubation is too dry, the egg will likely lose too much water to the atmosphere, which can make the hatching process difficult or impossible.

[2] RELATED WORKS

Oluyemi and Roberts [4] recommended that the minimum and maximum temperature for the first eighteen days should be between 37.7℃ and 39.3℃ respectively. After the eighteen days of the incubation, the temperature should be reduced from 37.8℃ to 36.0℃ until the chickens were hatched. Henceforth, for the whole period of incubation, the temperature should be maintained within the range of 36℃ and 39℃ which is following the report by other researchers [4,5,6,7,8,9,10,11,12,13,14]. However, Lourens et al. [15]; King'ori [16]; Geneve [17] acknowledged that overheating of the egg is much more critical than under heating, it will assist in speeding up the rate of growth causing abnormal embryos growth in the initial stages, and lower the percentage of the hatchability. Running the incubator at 41℃ for 15 minutes will seriously affect the embryos [18] while running it at 35℃ for 3 to 4 hours will only slow the chicken‘s metabolic rate [17,19]. A rise in temperature above 40.5 ℃ is fatal [20]. A drop in temperature will delay the hatching but is less harmful than increasing the temperature [20, 21]. The production of the chickens from an emergent embryo is a very sensitive task, which usually needs appropriate monitoring. Komolafe et al. [22]. Oluyemi and Roberts [4] suggested that the minimum and maximum humidity values within eighteen days should be 52% and 62% respectively. After the first eighteen days, the relative humidity should be improved from 55% to 71% until the end of the period of the incubation process. Henceforth, for the whole period of the incubation, the relative humidity should vary between 52% and 71%. Wilson [23] stated that it is best to turn the eggs more than three times a day for manual turning; they should be turned at an odd number of times so that the eggs will not be in the same position every night because that is the longest period between turns. More so, candling is very helpful during the incubation process, as it aids to determine whether the embryo is developing. The usual time for testing is the 7th and 14th days of incubation, sometimes the testing is done merely once on the 10th day. The eggs must not be candled after the 18th day to avoid disquieting the unhatched chickens because they need to rest and should not be handled during the last few days [24].

[3] ADVANTAGES OF ARTIFICIAL EGG INCUBATION

Below are some of the impacts of using artificial incubation.

1. Some of the chickens can be hatched at a time in a short while.
2. Another advantage is that it is possible to plan when to hatch the chickens unlike with the hen one may not know when it can sit for the eggs.
3. Artificial incubation cannot spread diseases and parasites to the chickens and lastly, there is no cost for feeding a broody chicken since an incubator is used.
4. The Chances of the egg's spoilage are reduced since all the eggs are subjected to the optimum hatching temperatures.
5. There are no chances of the chicken damaging eggs through pecking, a common occurrence with natural incubation.

[4] DISADVANTAGES OF ARTIFICIAL EGG INCUBATION

1. One of the disadvantages of artificial incubation is that it is expensive to buy an incubator. Most of the incubators are highly-priced and cannot be affordable to small-scale farmers.
2. Artificial incubation requires a lot of labor since there will be a lot of egg turning.
3. Artificial incubation requires many skills to maintain and manage the incubator.
4. The egg incubator needs a power source to work. In most of the rural and remote areas, a consistent source of power is the major challenge.
5. Artificial incubation has a high risk of damaging the embryo and it can encourage eggs breaking especially during egg turning.

[5] COMPONENTS USED IN THE ARTIFICIAL EGG INCUBATION

1. Container: Depending on how many eggs you want to hatch at a time, you may want something small that will hold just 20-30 eggs or a larger, cabinet style unit that will hold several hundred. Determine how many eggs you want to incubate and then decide on the container. The more insulation it has, the less energy it will require to keep it at the correct temperature. You don't want something that will be drafty, but you do need some way for fresh air to come into the container. The developing embryos need oxygen just like you and I do. The shell is poreous and allows carbon dioxide to leave and oxygen to enter. A viewing window is handy for observing the eggs, especially while they hatch.

2. Heater: The size of the container, the amount of insulation it has, and the room temperature will all have an impact on how much energy, measured in Watts, you need for your incubator. Some of the popular table-top incubators (such as Little Giant and Hova-Bator) use a low wattage heating element. The Little Giant uses a 40 watt heater and the Hova-Bator uses a 25 watt heater. The larger Sportsman 1502 cabinet incubator uses a 225 watt heater.

3. Thermostat: Keeping a good temperature is so important for a good hatch. Developing embryos are quite particular about the temperature they need. A good thermostat will help you keep the temperature in the appropriate temperature range. The generally accepted ideal temperature is 99.5 degrees F (37.5 degrees C) for almost all birds. However, there are some exceptions. Emu eggs, for example, require a temperature between 96.5 - 97.5 degrees F.

4. Humidity control: Managing humidity in your incubator is a matter of keeping the appropriate amount of water surface area. As a general rule, the more water surface area, the higher the humidity will be in your incubator. You can use a container to hold water and refill it as needed. Many people find that putting a sponge in the water with part of the sponge above the water level will increase the humidity level. This is particularly helpful during the lock-down period the last 2-3 days of your hatch.

5. Thermometer and hygrometer: A thermometer will measure the temperature and allow you to adjust the thermostat accordingly. A hygrometer will measure the relative humidity. There are analog devices and digital types as well. All measurement devices will have some variability, so testing and calibrating your device is always a good idea.
6. Egg Turner: The egg turner will rotate the eggs gently back and forth to keep the yolk sack from sticking to the shell and providing needed exercise for the developing embryo. This can also be done by hand if you prefer not to spend money on an automatic egg turner.
7. Candler: An egg Candler is a modified light that allows you to make the egg glow enough to see if the egg is developing. With a good Candler, you can see the baby bird moving and how the air sack is developing. If the egg is not developing, you can remove it to make room for good eggs.

[6] CONCLUSION

In this paper, we have seen the various advancement in technology of the artificial egg incubator, its challenges, it components use and the impact of deploying it over the natural hatching.

REFERENCES

[1] K.., M., French, “Practical Poultry Revising”, United States Peace Corps Information Collection Exchange Manual MOOH, Washington D.C., United States, pp 12-21, 1981.

[2] N., N., Benjamin, D., Oye, “Modification of the Design of Poultry Incubator”, International Journal of Application or Innovation in Engineering 1: pp. 90-102, 2012.

[3] F., Swainston, Get Slim Stay Naturally: The Herbal Guide to Permanent Weight Loss. Book tango Publisher, Liberty Drive, Bloomington, Illinois, United State pp. 140, 2014

[4] J., A., Oluyemi, A., F., Roberts, “Poultry Production in Warm Wet Climates”’ Macmillan Publishers Limited, London and Basingstoke, United Kingdom, pp. 102, 1988.

[5] W., I., Okonkwo, O., C., Chukwuezie, “Characterization of a Photovoltaic Powered Poultry Egg Incubator”, 4th International Conference on Agriculture and Animal Science IACSIT Press, Singapore 47: pp. 1-6. 2012.

[6] N., Benjamin, D., N., Oye, “Modification of the Design of Poultry Incubator”, International Journal of Application or Innovation in Engineering 1: pp. 90-102, 2012.

[7] K., L., Osanyinpeju, A., A., Aderinlewo, O., R., Adetunji, S., A., Ajisegiri, “Performance Evaluation of a Solar Powered Poultry Egg Incubator”. International Research Journal of Advanced Engineering and Science Volume 3 (2): pp. 255-264, 2018.

[8] K., Kyimpong, K., P., Forson, “Design, and Construction of an Arduino Microcontroller-Based Egg Incubator”, International Journal of Computer Applications 168 (1): pp. 15- 23, 2017.

[9] N., T., Abraham, S., L., C., Mathew, A., P., Kumar, “Design, and Implementation of Solar PV Poultry Incubator”, International Journal of Engineering and Advanced Technology vol. 3 (3): pp. 289-291, 2014.

[10] T., Suriwong, S.,Banthuek, E., S., Singhadet, A., Jiajitsawat, “New Prototype of Thermoelectric Egg Incubator Integrated with Thermal Energy Storage and Photovoltaic Panels”, Maejo International Journal of Science and Technology vol. 11 (2): pp. 148-157, 2017.

[11] B., O., Bolaji, “Design, and Performance Evaluation of a Solar Poultry Egg Incubator”. Thammasat International Journal Science Technology vol. 13 (1): pp. 47-55, 2008.

[12] G., A., Ogunwande, E., O., Akinola, A., R., Lana, “Development of a Biogas-Powered Poultry Egg Incubator”, Ife Journal of Science vol. 17 (1): pp. 219-228, 2015.

[13] T., A., Adegbulugbe, A., O., Atere, O., G., Fasanmi, "Development of an Automatic Electric Egg Incubator", International Journal of Scientific and Engineering Research vol. 4 (9): pp. 914-918. 2013.

[14] M., F., Omar, H., Haris, C., M., Hidayat, M., N., Ismail, I., M., Seroji, M., N., "Smart Eggs Incubator System", International Journal of Simulation, Science and Technology vol. 17 (41): pp. 1-7, 2016.

[15] A., Lourens, H., Van den Brand, R., Meijerhof, B., Kemp, "Effect of Eggshell Temperature during Incubation on Embryo Development, Hatchability and Post Hatch Development", Journal of Poultry Science vol. 84: pp. 914-920. 2005.

[16] A., M., King'ori, "Review of the Factors That Influence Egg Fertility and Hatchability in Poultry", International Journal of Poultry Science vol. 10 (6): pp. 483-492, 2011.

[17] N., Geneve, "Classroom Chick Hatch Program Guidebook", Nova Scotia Department of Agriculture, Bible Hill, Nova Scotia, Canada, North America, pp. 23. 2013.

[18] E., S., Joseph, J., D., Michael, "Helpful Hints for Teacher on Incubation and Embryology of the Chick. Cooperative Extension System", University of Connecticut Publisher, Mansfield, Connecticut, Storrs, USA pp. 20 pp, 2011

[19] L., T., Egbeyale, O., M., Sogunle, "Hatchery Technology, and Management", Lecture Handout. Federal University of Agriculture, Abeokuta, Ogun State, Nigeria pp. 24, 2009.

[20] N., V., Wageningen, J., P., Meinderts, H., Kasper, "Hatching Eggs by Hens or in an Incubator", Digigrafi Publisher, Veenendaal, Netherlands pp. 80 pp, 2004.

[21] F., Wafadar, I., Puls, "Improving Hatching, and Brooding in Small-Scale Poultry", Agronomist Foundation and CTA, Wageningen, Netherlands pp. 80 pp, 2011.

[22] M., F., Komolafe, A., A., Adegbola, L., A., Are, T., I., Ashaye, Agricultural Science for West African Schools and Colleges. 2nd Edition. University Press Limited, Ibadan, Nigeria pp. 289, 1981.

[23] H., R., Wilson, "Physiological Requirement of the Developing Embryo: Temperature and Turning". In: Avian Incubation S.G. Tullet, Butterworth-Heinemann, London, U.K. Chapter 9, and pp 145-156, 1991.

[24] O., J., Adeosun, "Design and Construction of a Low-Cost Incubator". An Unpublished B.Sc. Project. Department of Agricultural Engineering, Faculty of Technology, Obafemi Awolowo University, Ile-Ife, Nigeria pp. 66, 1997.

COVID-19 Detection from Chest X-Ray Images Using Dense Convolutional Network

Ferhat Bozkurt
Department of Computer Engineering Ataturk University
Erzurum, Turkey
fbozkurt@atauni.edu.tr

Mete Yağanoğlu
Department of Computer Engineering Ataturk University
Erzurum, Turkey
yaganoglu@atauni.edu.tr

***Abstract*— One of the most important phase in preventing the spread of the COVID-19 epidemic is to effectively scanning people suspected of being infected. Radiology images of COVID-19 and other lung diseases like bacterial pneumonia, viral pneumonia have common features. X-Ray chest radiography is an effective tool to triage patients with pneumonia without COVID-19 to efficiently allocate hospital resources. However, this similarity makes it difficult for expert radiologists to detect COVID-19 cases. A reliable method for classifying non-COVID-19 and COVID-19 chest X-Ray images could be useful to reduce triage process and diagnose. In this study, COVID-19 is detected from chest X-Ray images using dense convolutional neural network (DenseNet121). In this study, a DenseNet121 model is proposed and experimental studies are performed on an open-access dataset by allocating on different size of test and training. DenseNet121 model can classify chest X-Ray images as COVID-19, normal, and viral pneumonia. Performance evaluations are performed on the accuracy of the techniques, and the results are compared with state-of-the-art deep learning-based approaches such as AlexNet, VGG19, Xception, InceptionV3, and ResNet50. In experimental studies, the highest accuracy (97%) is obtained with the proposed DenseNet121 model.**

***Keywords*— deep learning, DenseNet, X-Ray, COVID-19**

[1] INTRODUCTION

In late 2019, COVID-19 which is emerging as an upper respiratory and lung infection, first appeared in Wuhan-China. It is mostly transmitted by airway and contact, and it has been observed to affect the lungs of those infected to a great extent. The virus has spread rapidly since then and has become a global epidemic. The number of cases and related deaths continues to increase everyday [1]. Chest X-Ray images are used in the examination and monitoring and of distinct diseases like tuberculosis, atelectasis, infiltration, hernia, and pneumonia. Any technological tool that provides rapid and highly accurate monitoring of COVID-19 infection is beneficial for healthcare professionals. In this context, chest X-ray imaging is an easily accessible alternative tool in the diagnosis of COVID-19 [2]. X-Ray chest radiography is an effective tool to triage patients (medical classification of patients) with pneumonia without COVID-19 to efficiently allocate hospital resources. On the other hand, radiology images of COVID-19 and other lung diseases like bacterial pneumonia, viral pneumonia have common features. This similarity makes it difficult for expert radiologists to diagnose COVID-19 cases. A reliable method for classifying non-COVID-19 and COVID- 19 chest X-Ray images could be useful to reduce triage process and diagnose [3].

In literature, there are approaches based on various machine and deep learning methods that use chest X-Ray images for disease detection. The studies with deep learning techniques are gaining increasing popularity for radiology images. Pathak et al. [4] studied on pre-trained ResNet32 technique to diagnose COVID-19 disease. This technique based on transfer learning approach. In their study, they conducted experimental studies on a total of 852 CT scans that include 139 normal and 413 COVID-19. They achieved respectively testing and training accuracy of up to 93.01% and 96.22% with the proposed model. Zhao et al. [5] developed a method for the detection of COVID-19 based on a pre-trained DenseNet model. In experimental studies using the COVID-CT data set, they achieved an accuracy of 84.7%. Oğuz and Yağanoğlu [6] evaluated the performance of various classification methods for detecting COVID 19 cases from lung CT images using deep learning techniques. They achieved the best result with ResNet-50 and SVM classification methods with a 95.18% accuracy. Li et al. [7] used COVNet model to detect COVID- 19 disease. This model based the architecture of pre-trained ResNet50. Their dataset contains 4356 chest CT images taken from 3322 patients. They achieved 90% sensitivity by using this model. Asnaoui et al. [8] used deep learning techniques to classify pneumonia disease using CT and X- Ray images. In their studies, the performances of various deep learning techniques (VGG19, DenseNet201, VGG16, Xception, InceptionV3, ResNetV2, Inception, MobileNetV2, and ResNet50) based on the pre-trained transfer learning approaches were examined. They obtained the superior accuracy 96.61% from the ResNet50 model from experimental results. Xu et al. [9] proposed 3D convolutional network to remove potentially infected areas from CT scan images. They achieved an accuracy of 86.7% in predicting using viral pneumonia (Influenza-A), healthy, and COVID-19 patients. Wang et al. [10] used pre-trained ResNet50 architecture to classify COVID-19 from chest X-Ray images. COVIDx dataset in their study includes data from pneumonia, normal (healthy) and COVID-19 patients. According to their experimental results, they obtained 93.4% average accuracy. Turkoglu [11] proposed extreme learning based deep learning with multiple kernels for CT images to classify COVID-19 disease [11].

In this study, a DenseNet model is applied that could classify chest X-Ray images as normal (healthy), viral pneumonia, and COVID-19. The rest of the work is organized as follows. In section II, material and method are explained. In this section, the data set used in the experimental study and the DenseNet model applied are explained in detail. Experimental results are given in section III, and the discussion and conclusions part of the study is given in section IV.

[2] MATERIAL AND METHOD

A. Material

Chest X-Ray images in this study are obtained from the COVID-19 radiography database of the popular Kaggle database [12]. This data set consists of images referring to

three different classes as COVID-19, normal (healthy), and viral pneumonia. A total of 3886 chest X-Ray images are available as 1200 COVID-19, 1341 normal, and 1345 viral pneumonia images. Fig. 1 shows the categorical distribution of the X-Ray data used in the study over (70% training, 10% validation, and 20% testing).

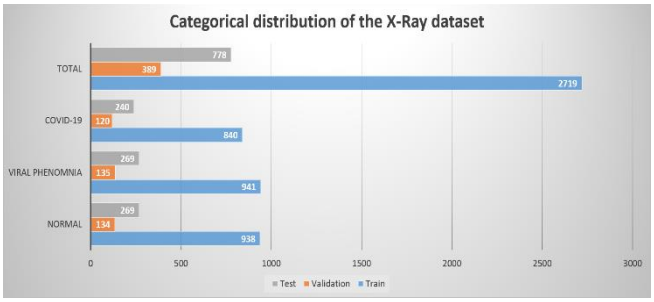


Fig. 1. Categorical distribution of the X-Ray dataset.

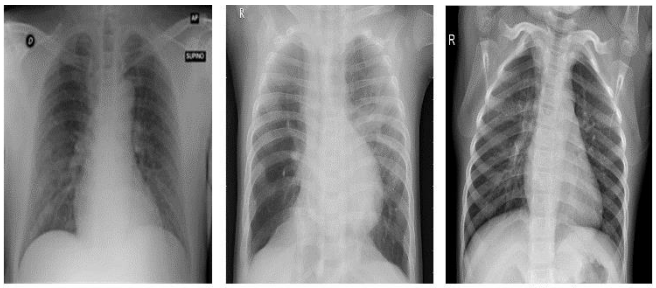


Fig. 2. COVID-19, Viral pneumonia and, normal (healthy) chest X-Ray images in dataset.

Fig. 2 shows image samples of COVID-19, viral pneumonia, and normal (healthy) cases from this dataset. The following findings are seen in the X-Ray images of COVID-19 and pneumonia patients. These common observations are ground-glass opacities, air space consolidation, bronchovascular thickening, vascular thickening, and bronchial wall thickening [13]. In this context, chest X-Ray images of COVID-19 and Pneumonia are similar and contain similar features. Therefore, there is a possibility of misdiagnosis in diagnosing by only examining these images.

B. Method

Deep learning techniques can reveal useful image features from the original images. CNN (Convolutional Neural Network) is a class of deep neural networks commonly applied to computer vision and natural language processing in deep learning. Recently, CNN is preferred in most studies and has proven to be extremely useful in feature extraction and machine learning. Deep CNN is a heuristic and robust network architecture in deep learning. It is widely used in pattern recognition and image classification. Machines developed with deep learning are known to perform better than humans in image classification [14].



Fig. 3. Fundamental architecture of one dense block in DenseNet [15].

CNN is essentially a regular version of multilayer perceptrons. CNN consists of an input, output and multiple hidden layers between them. CNN includes two basic operations as convolution and pooling. Hidden layers contain convolutional layers, ReLU (activation function) layers, pool layers, fully- connected layers, and normalization layers. The convolution process using multiple filters can extract features that protect relevant spatial information (feature map) from the dataset. Pooling (also called subsampling) is utilized to reduce the dimensionality of the feature maps from the convolution process. Maximum and average pooling are the most common pooling processes used in CNN. Compared to other classification algorithms, CNN requires much less preprocessing and can yield better results as the number of training data increases [14].

In standard CNN (ConvNet), input image goes along multiple convolutions and acquire high-level features. In Dense Convolutional Network (DenseNet), each layer acquires additional inputs from all previous layers and transfers on its own feature-maps to all next layers as shown in Fig. 3 [15]. DenseNet reduces the gradient descent problem, increases feature reuse, and reduces parameter usage. DenseNet has given good performance for various computer vision problems. The main structure block of DenseNet121 is the Dense Block. These Dense Blocks consist of convolution layers. DenseNet121 consists of 121 connected convolutional layers with a fully-connected layer of 1000 units as the final output layer [16]. In general, CNN architectures are hierarchical, so feature maps of l-1 layer is given as an input to the l.layer. However in DenseNet, the feature maps of all previous layers are combined and used as input for any particular layer. In addition, its own feature maps are used as input for all subsequent layers. Therefore, the feature maps of all previous X_0, X_1, ..., X_{l-1} layers are combined and used as input for layer X_l [16], [17].

DenseNet121 has four Dense blocks and a transition layer between both Dense blocks as shown in Fig. 4 [17], [18]. Each Dense block consists of several convolution layers, and each transition layer consists of a batch normalization, a convolution and a pooling layer. ReLU activation function is used in DenseNet to increase nonlinearity. In this model, the last layer of DenseNet121 is a global average pooling layer that generates features from the input image. These features are used by the classifier to make the final prediction. Thus, a fully-connected layer is followed by a softmax classifier that uses softmax activation function. A fully connected three-unit layer is used for classification (three classes: COVID-19, Viral Pneumonia, and Normal). Softmax activation normalizes the output of the fully connected layer and creates a probability distribution over the predicted output classes. This particular model improves the pass of information over the network and decreases the vanishing gradient problem. In addition,

DenseNet improves feature reuse and parameter efficiency and provides combined information of the network to each layer [18]. The most important reason for choosing DenseNet is that dense connectivity has a regularized effect and reduces overfitting in training on data that is not very big.

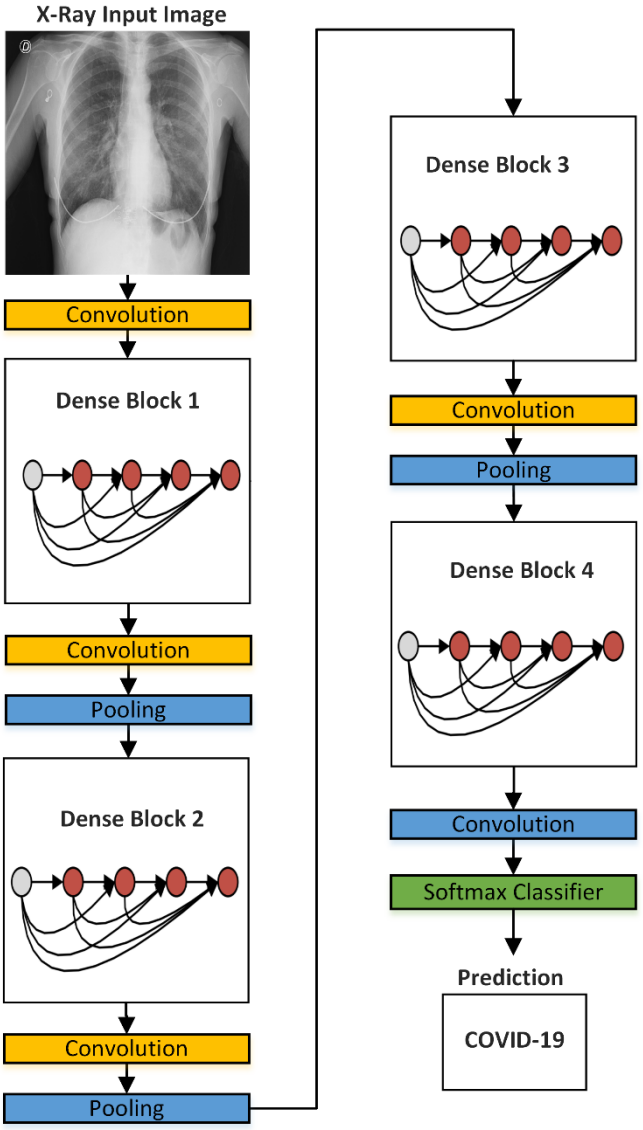


Fig. 4. The DenseNet121 architecture used in this study [17], [18].

[3] EXPERIMENTAL RESULTS

The experimental studies in this study were conducted on a desktop computer with Intel Core (i7) 8700U CPU @ 3.20 GHz, NVIDIA 4 GB GeForce-GTX 1050 Ti graphics and 16GB primary memory. The software was implemented using Python 3.7 and its related libraries. All images were resized uniformly to 256 × 256 before being transferred to the model in preprocessing stage. In this section, two types of experiments were conducted by dividing the data in different sizes. The data in the first experimental study (experiment1); 70% is reserved for training, 10% for validation and 20% for testing. The data in the second experimental study (experiment2); 85% is reserved for training, 5% for validation and 10% for testing. Performance evaluations for both experiments are given in Table I.

Table 1. Performance Evaluation of Densenet121 Model for Two Experiments

	Precision (%)	Recall (%)	F1-Score (%)	Accuracy (%)
Experiment1	97.31	97.23	97.26	97.17
Experiment2	96.71	96.59	96.63	96.53

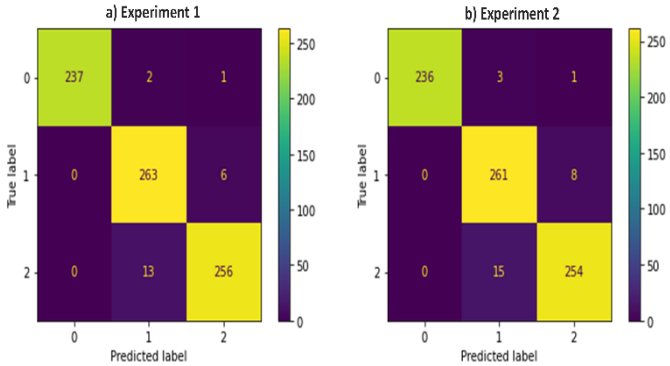


Fig. 5. Confusion matrices of DenseNet121 model for two experiments.

At this stage, the performance evaluation of the method was performed over four performance criteria such as recall, precision, F1-score, and accuracy. These values are calculated over confusion matrices for each class [19], [20]. Confusion matrices are obtained for each experiment as shown in Fig. 5. In this study, performance evaluations are performed for both experimental data as shown in Table I. According to these experimental studies, the accuracy value obtained with the proposed DenseNet121 technique is approximately 97%. In Fig. 6, training/test accuracy and training/test loss graphs for 50 iterations of the proposed technique are presented. Both training and test accuracy curves show a rising curve as the number of iterations increases. The loss curve shows the decrease in error rate. It shows that the training process and learning of the network are at a good learning rate. As shown in Fig. 6, while the loss value decreases in each iteration, the accuracy rate increases with the given training set and learning occurs. As shown in Table 2, CNN-based different popular techniques such as AlexNet, VGG19, Xception, InceptionV3, and ResNet50 have been compared with the proposed DenseNet121 technique. It was observed that the proposed model in this study gives superior results than other models.

Table 2. Comparison of Other Cnn-Based Deep Learning Techniques with Densenet121

	Precision (%)	Recall (%)	F1-Score (%)	Accuracy (%)
DenseNet121	97.31	97.23	97.26	**97.17**
AlexNet	95.78	95.88	95.81	95.76
VGG19	95.67	95.62	95.59	95.50
Xception	95.88	95.57	95.58	95.50
InceptionV3	93.70	93.88	93.75	93.70
ResNet50	93.50	93.50	93.41	93.32

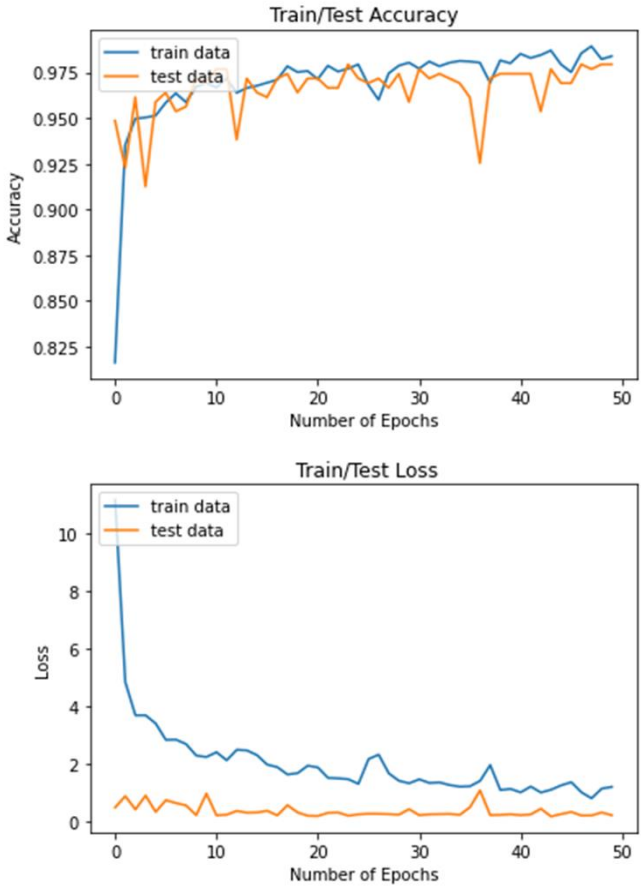


Fig. 6. Training/test accuracy and training /test loss graphs of the method.

[4] DISCUSSION AND CONCLUSIONS

In this paper, a dense CNN model is studied. Parameters and layers of this architecture were specially adjusted to get high performance from this model. Experimental studies are conducted on an open-access chest X-Ray images by allocating on different size of test and training. In this dataset, there are a total of 3886 images belonging to three classes: COVID-19, normal (healthy) and viral pneumonia. For this purpose, a DenseNet121 model is applied, which can classify chest X-Ray images. Performance evaluations are performed on the accuracy of the techniques, and the results are compared with state-of-the-art deep learning-based approaches such as AlexNet, VGG19, Xception, InceptionV3, and ResNet50. In experimental studies, the highest accuracy (97%) is obtained with the proposed DenseNet121 model. According to experimental results, both training and test accuracy curves show a rising curve as the number of iterations increases. The loss curve shows the decrease in error rate. It shows that the training process and learning of the network are at a good learning rate. In further studies, other deep learning-based techniques and data will be studied and comparisons will be made.

REFERENCES

[1] World Health Organization, "Coronavirus disease (COVID-19) Pandemic," https://www.who.int/emergencies/diseases/novel-coronavirus-2019 (accessed Feb. 1, 2020).

[2] A. M. Ismael and A. Şengür, "Deep learning approaches for COVID-19 detection based on chest X-ray images," Expert Systems with Applications, 164, 114054, 2021.

[3] Dai, Wei-cai, et al. "CT imaging and differential diagnosis of COVID-19," Canadian Association of Radiologists Journal 71.2, 195-200, 2020.

[4] Y. Pathak, P. K. Shukla, A.Tiwari, S. Stalin, and S. Singh, "Deep transfer learning based classification model for COVID-19 disease," Irbm, 2020.

[5] J. Zhao, Y. Zhang, X. He, and P. Xie, "Covid-ct-dataset: a ct scan dataset about covid-19," arXiv preprint arXiv:2003.13865, 2020.

[6] Ç. Oğuz and M. Yağanoğlu, "Determination of Covid-19 Possible Cases by Using Deep Learning Techniques," Sakarya Üniversitesi Fen Bilimleri Enstitüsü Dergisi, 25(1), 7-17, 2021.

[7] Li, Lin, et al. "Artificial intelligence distinguishes COVID-19 from community acquired pneumonia on chest CT," Radiology, 2020.

[8] K. E. Asnaoui, Y. Chawki, and A. Idri, "Automated methods for detection and classification pneumonia based on x-ray images using deep learning," arXiv preprint arXiv:2003.14363, 2020.

[9] X. Xu, et al. "A deep learning system to screen novel coronavirus disease 2019 pneumonia," Engineering 6.10, 1122-1129, 2020.

[10] L. Wang, Z. Q. Lin, and A. Wong, "Covid-net: A tailored deep convolutional neural network design for detection of covid-19 cases from chest x-ray images," Scientific Reports, 10(1), 1-12, 2020.

[11] M. Turkoglu, "COVID-19 Detection System Using Chest CT Images and Multiple Kernels-Extreme Learning Machine Based on Deep Neural Network," IRBM, 2021.

[12] M. E Chowdhury, et al. "Can AI help in screening viral and COVID-19 pneumonia?," IEEE Access 8, 132665-132676, 2020.

[13] C. Ouchicha, O. Ammor, and M. Meknassi, "CVDNet: A novel deep learning architecture for detection of coronavirus (Covid-19) from chest x-ray images," Chaos, Solitons & Fractals, 140, 110245, 2020.

[14] P. Kim, "Convolutional neural network. In MATLAB deep learning," pp. 121-147, Apress, Berkeley, CA, 2017.

[15] G. Huang, Z. Liu, L. Van Der Maaten, and K. Q. Weinberger, "Densely connected convolutional networks," In Proceedings of the IEEE conference on computer vision and pattern recognition, pp. 4700-4708, 2017.

[16] L. Sarker, M. Islam, T. Hannan, and A. Zakaria, "COVID-DenseNet: A Deep Learning Architecture to Detect COVID-19 from Chest Radiology Images," Preprints, 2020.

[17] S. Kumar, S. Mishra, and S. K. Singh, "Deep Transfer Learning-based COVID-19 prediction using Chest X-rays," medRxiv, 2020.

[18] F. Bozkurt, "Derin Öğrenme Tekniklerini Kullanarak Akciğer X-Ray Görüntülerinden COVID-19 Tespiti," Avrupa Bilim ve Teknoloji Dergisi, (24), 149-156, 2021.

[19] E. Erdem and F. Bozkurt, "A comparison of various supervised machine learning techniques for prostate cancer prediction," Avrupa Bilim ve Teknoloji Dergisi, (21), 610-620, 2021.

[20] M. Yağanoğlu, "Real time wearable speech recognition system for deaf persons," Computers & Electrical Engineering, 91, 107026, 2021.

Theoretical Investigation of Biomofs For Anesthetic Xe Recovery

Zekiye Erarslan
Bioengineering Alparslan Türkeş
Science and Technology University
Adana, Turkey
160102004@ogr.atu.edu.tr

Yeliz Gürdal
Bioengineering Alparslan Türkeş
Science and Technology University
Adana, Turkey
ygurdal@atu.edu.tr

Aim: The subject of this study is to investigate the adsorption based separation of anesthetic Xenon (Xe) gas from exhaled gas mixture using metal organic frameworks (MOFs) applying Grand Canonic Monte

Carlo simulations. We theoretically investigate the adsorption-based separation of anesthetic Xe from exhaled gas mixture of CO2, O2, and N2 using variety of BioMOFs, which are subclass of metal organic frameworks having organic biological linkers. This study is aimed at the design of close systems in which Xe cycle can be performed by separating Xe from the exhaled gas mixture using BioMOFs and then feeding it back to the anesthetic inhalation gas.

Method: We perform Grand Canonic Monte Carlo (GCMC) simulations in order to calculate adsorption isotherms of Xe/CO2, Xe/O2, and Xe/N2 gas mixtures as well as Xe adsorption selectivities. Xe feed gas molar composition is set to 0.8 for each binary gas mixtures. Dispersion type of interactions are modeled using Lennard-Jones potential and electrostatic interactions are evaulated via Ewald summation method. Density Derived Electrostatic Charges (DDEC) method is applied for determining partial charges of atoms in the BioMOF lattice. Gas adsorptions are calculated by running GCMC simulations from 0.1 to 10 bar and at 298 K. In our project, we use 8 representative BioMOFs with organic ligands of adenine and with different metal ions.

Results: We obtain high Xe adsorption and Xe adsorption selectivities for a set of BioMOFs under consideration. The highest Xe selectivity is obtained using IZUMUM for the Xe/N2 mixture at 0.1 bar which shows Xe selectivities as 95244, 710.63, and 484.61 for Xe/N2, Xe/CO2, and Xe/O2 mixtures, respectively. The second highest Xe selectivity is obtained using BEYSEF for the Xe/N2 mixture at 0.1 bar which shows Xe selectivities as 68085.3, 642.94, and 375.6 for Xe/N2, Xe/CO2, and Xe/O2 mixtures, respectively. The lowest Xe selectivity is obtained using XACZEH for the Xe/O2 mixture at 0.1 bar which shows adsorption selectivities as 3.2, 105.3, and 6437.5 for Xe/O2, Xe/CO2, and Xe/N2 mixtures, respectively. The reason why XACZEH results the lowest selectivity may be due to the size of pores or metal ions on the XACZEH, or the structure of the XACZEH. The metal ion of both IZUMUM and XACZEH is Cu. BEYSEF contains Co atoms in its structure, as a metal ion. The largest cavity diameter (LCD) of XACZEH BioMOF is almost as twice as bigger than that of IZUMUM. The largest cavity diameters (LCD) of XACZEH, IZUMUM, and BEYSEF are 10.61Å, 5.58Å, 5.62 Å, respectively. The pore limited diameter (PLD) of XACZEH, IZUMUM, and BEYSEF are 7.24Å, 4.65Å, 4.75 Å, respectively. Pore dimensions of both BEYSEF and IZUMUM are quite close to each other. The lowest Xe selectivity of XACZEH can be attributed to its relatively large pore size distribution with respect to the other BioMOFs in consideration.

Conclusion: We obtain relatively large Xe adsorptions and selectivities for all binary gas mixtures of Xe with respect to the limited study available in the literature. Thus, we conclude that BioMOFs are promising adsorbent materials for Xe separation from anesthetic gas mixtures which motivates using Xe in the clinical industry.

Keywords: Grand Canonical Monte Carlo simulations, metal organic frameworks, gas separation

Acknowledgement:

We acknowledge Tubitak 1002 Grant (Project ID: 120Z160) for financial support. Numerical calculations in this research are partially performed using TÜBİTAK ULAKBİM, High Performance and Grid Computing Center (TRUBA) sources. We acknowledge Behra Cantürk for fruitful discussions.

Comprehensive Study on the Interfacial charge transfer dynamics of Inorganic Nanowires Incorporated Bulk Heterojunction Photoactive Layer

Kai Jeat Hong
Advanced Material Device Laboratory, Department of Physics, Faculty of Science, University Putra Malaysia, Selangor, Malaysia.
Lee Kong Chian Faculty of Engineering and Science, Universiti Tunku Abdul Rahman, Selangor, Malaysia.
kaijeataaron94@gmail.com, aaron.hong92@1utar.my

Sin Tee Tan
Advanced Material Device Laboratory, Department of Physics, Faculty of Science, University Putra Malaysia, Selangor, Malaysia.
tansintee@upm.edu.my

Kok-Keong Chong
Lee Kong Chian Faculty of Engineering and Science, Universiti Tunku Abdul Rahman, Selangor, Malaysia.
chongkk@utar.edu.my

Chi Chin Yap
School of Applied Physics, Faculty Science and Technology, University Kebangsaan Malaysia, Selangor, Malaysia.
ccyap@ukm.edu.my

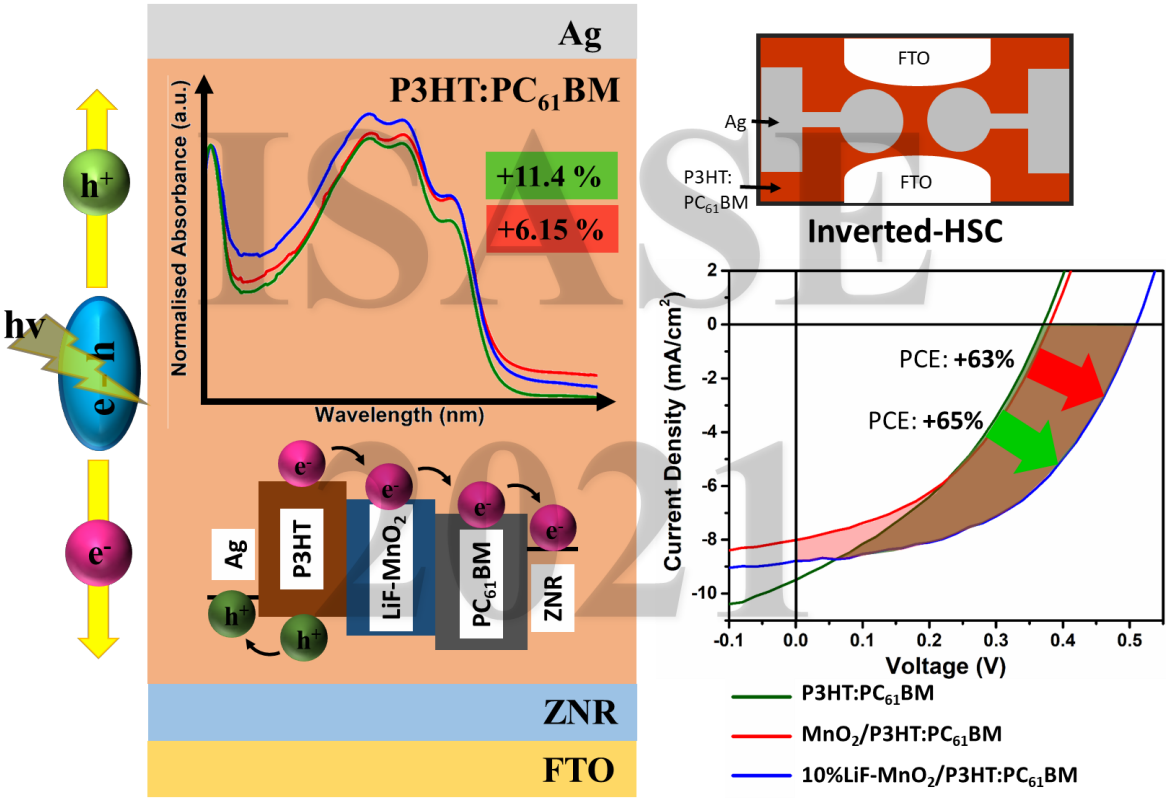


Figure 1: Schematic diagram of charge transfer dynamics in 10 wt% LiF-MnO_2 nanowires incorporated P3HT:$PC_{61}BM$, with the corresponding absorbance spectra and J-V characteristics.

Abstract

Low efficacy of interfacial charge transfer in organic-based bulk heterojunction (BHJ) photoactive layer is one of the major issues that influence device performance, which is mainly originated from geminate or/and non-geminate recombination [1,2]. To improve the charge transfer efficiency, an alpha-phase manganese dioxide (α-MnO_2) nanowires (NW) was incorporated into P3HT:$PC_{61}BM$ photoactive layer. This MnO_2 NW is an abundant material with a high active surface area [3]. However, its intrinsically low electrical conductivity has limited the charge transfer capability. In this project, the electrical conductivity properties of MnO_2 NW were modified via incorporating different *x* wt% of lithium fluoride (LiF) by using a solution blending method. A comprehensive correlation of (i) surface conductivity of MnO_2 NW incorporated with *x* wt% of LiF and (ii) charge transfer efficiency of *x* wt% LiF-MnO_2 NW based BHJ photoactive layer is elucidated. Four-point-probe analysis has confirmed an electrical conductivity enhancement of 26.5% for the 10 wt% LiF-MnO_2 NW than the controlled MnO_2 NW sample. The UV-Vis absorbance analysis has indicated an increment of 11.4% for the 10 wt% LiF-MnO_2 NW/ P3HT:$PC_{61}BM$ at the visible region, signifying an active electronic transition P3HT and higher molecular interaction between P3HT, $PC_{61}BM$ and MnO_2. For device testing, the 10 wt% LiF-MnO_2 NW exhibits an improvement of power conversion efficiency at 1.63-fold and 1.65-fold higher than that of pristine MnO_2 NW and without MnO_2 NW based devices, respectively. This performance enhancement can be attributed to (i) higher density of excitons dissociation at donor-acceptor (D-A) interfaces and (ii) presence of mid-bandgap in LiF-MnO_2 NW structure that promotes an efficient charge transfer. This study provides an alternative insight into the interfacial charge transfer mechanism via the incorporation of inorganic NW into the BHJ organic photoactive layer.

Methodology

Zinc oxide (ZnO) nanorods array (ZNR) was synthesised on the pre-cleaned fluorine-doped tin oxide (FTO) via two-step solution method, which are the (1) sol-gel seeding and (2) hydrothermal growth [4]. The ZnO nanorod layer served as electron transporting layer (ETL). A 0.4 M sol-gel precursor was prepared via dissolving zinc acetate dehydrate in ethanol based solvent. The precursor was aged for 20 hours, and then spin-coated on the FTO for three times at 3000 rpm for 30 seconds. The ZnO seeded substrates were then annealed at 300˚C for 60 minutes. After that, a 0.35 M of precursor solution was prepared by dissolving an equimolar of zinc nitrate hexahydrate and hexamethylenetetramine (HMT) in deionised water. The seeded substrates were submerged in the growth solution and heated at 90˚C for 15 minutes. Lastly, the as-synthesised ZNR were dried at 100˚C for 10 minutes.

For device fabrication, a photoactive layer was prepared from poly(3-hexylthiophene) (P3HT) and phenyl-C61-butyric acid methyl ester ($PC_{61}BM$) at 1:1 ratio. Meanwhile, the MnO_2 NW was synthesized from 0.04 M of aqueous solution mixture that consisted of potassium permanganate and ammonium fluoride. The mixture was heated at 180˚C for 3 hours. Then, the LiF was incorporated into the propanol-dispersed MnO_2 NW, at *x* wt% with respect to the NW. The *x* wt% LiF-MnO_2 NW was added accordingly to the photoactive solution, and constantly stirred for overnight. Subsequently, the photoactive solution was spin-coated on the ZNR samples for 60 seconds, and post-baked at 120˚C for 10 minutes. Finally, the photoactive layer coated samples were thermal deposited with silver (Ag) under vacuum condition (5.0×10^{-5} mbar).

Conclusion

The incorporation of LiF-MnO_2 NW into the BHJ photoactive layer is reported. The 10 wt% LiF-MnO_2 NW/P3HT:$PC_{61}BM$ based IOSC has recorded the highest 2.16%. This performance improvement can be

attributed to higher density of exciton dissociations at D-A interfaces and presence of mid-bandgap LiF-MnO_2 NW that promotes efficient interfacial charge transfer.

References

[1] P.E. Keivanidis, J.I. Khan, L. Katzenmeier, Z. Kan, S. Limbu, M. Constantinou, E. Lariou, G. Constantinides, S.C. Hayes, J.S. Kim, F. Laquai, Impact of Structural Polymorphs on Charge Collection and Nongeminate Recombination in Organic Photovoltaic Devices, J. Phys. Chem. C. 122 (2018) 29141–29149. doi:10.1021/acs.jpcc.8b09825.

[2] H. Cha, S. Wheeler, S. Holliday, S.D. Dimitrov, A. Wadsworth, H.H. Lee, D. Baran, I. McCulloch, J.R. Durrant, Influence of Blend Morphology and Energetics on Charge Separation and Recombination Dynamics in Organic Solar Cells Incorporating a Nonfullerene Acceptor, Adv. Funct. Mater. 28 (2018) 1–11. doi:10.1002/adfm.201704389.

[3] P. Gong, J. Xie, D. Fang, D. Han, F. He, F. Li, K. Qi, Effects of surface physicochemical properties on NH 3 - SCR activity of MnO 2 catalysts with different crystal structures, Chinese J. Catal. 38 (2017) 1925–1934. doi:10.1016/S1872-2067(17)62922-X.

[4] K.J. Hong, S.T. Tan, K.K. Chong, H.B. Lee, R.T. Ginting, F.S. Lim, C.C. Yap, C.H. Tan, W.S. Chang, M.H.H. Jumali, Synergy study on charge transport dynamics in hybrid organic solar cell: Photocurrent mapping and performance analysis under local spectrum, Curr. Appl. Phys. 18 (2018) 1564–1570. doi:10.1016/j.cap.2018.10.004.

Keywords: inorganic nanowire, organic photoactive layer, MnO_2, incorporation, charge transfer

Acknowledgement(s)

1. GP-IPM/2019/9673800
2. IPSR/RMC/UTARSRF/ PROGRAMME 2018-C1/001

Calibration-Free Broadband Determination of Soil Permittivity by Coaxial Line Measurements

Hafize Hasar
Department of Soil Science and Plant Nutrition Ataturk University Erzurum, TURKEY
hafize.hasar@tarimorman.gov.tr

Taskin Oztas
Department of Soil Science and Plant Nutrition Ataturk University Erzurum, TURKEY
toztas@atauni.edu.tr

Mustafa Yildırim Canbolat
Department of Soil Science and Plant Nutrition Ataturk University Erzurum, TURKEY
canbolat@atauni.edu.tr

Ugur Cem Hasar
Department of Electrical and Electronics Engineering Gaziantep University Gaziantep, TURKEY
uchasar@gantep.edu.tr

Yunus Kaya
Department of Electricity and Energy Bayburt University Bayburt, TURKEY
ykaya@bayburt.edu.tr

Nevzat Aslan
Pistachio Research Institute of Republic of Turkey Gaziantep, TURKEY
nevzat.aslan@tarim.gov.tr

Mehmet Ertugrul
Department of Electrical and Electronics Engineering
Ataturk University Erzurum, TURKEY
ertugrul@atauni.edu.tr

***Abstract*—A novel calibration-free de-embedding microwave method has been proposed for accurate relative complex permittivity measurement of soil samples loaded over a Bead into a EIA 1-5/8'' coaxial transmission line. It relies on raw (calibration-free) scattering parameter measurements and does not require any information about physical or electrical properties of the Bead used in measurements to support soil samples. Expressions for relative complex permittivity were derived using ACBD matrix representation of networks of the whole measurement configurations and application of trace and inverse matrix operations which allow us to eliminate the effect of unknown vector network analyzer imperfections (source/load match and tracking (frequency) errors) and effects of adapters and transitions. Relative complex permittivity of a soil dielectric material (polyethylene sample) was extracted over 1-2 GHz by the proposed method before starting to complex relative permittivity evaluation of two soil samples (with more than 90% sand texture and different electrical conductivities) obtained from different areas of the city Gaziantep in Turkey. From soil measurements, it is noted that an increase in electrical conductivity accompanies with an increase in loss behavior of soil samples with the same sand texture.**

Keywords—Microwave measurements, calibration-free, de-embedding, complex permittivity, soil.

[1] INTRODUCTION

Analysis of soil moisture content plays a key role in many basic biophysical processes such as plant growth and nutrition, germination of seeds, and nutrient transformations in the root zone [1]. Direct moisture measuring thermogravimetric method relies on water content evaluation of a fraction of soil from a bulk soil sample due to loss in mass in reference to its dry state, can be used [2]. However, it is time-consuming, destructive (removal of the soil sample from the field), and is applied in laboratory [3]. These drawbacks call for the development of indirect soil measurement methods. As indirect electromagnetic-based moisture measurement methods, the ground-penetrating radar (GPR) [4], the time-domain reflectometry (TDR) [5], capacitance methods [6], the open-ended coaxial probe [7] or the open-ended waveguide [3], and coaxial transmission-lines [8]–[11] can be enumerated.

The GPR method is effective for non-invasive electromagnetic properties of subsurface soils. However, it necessitates invasive reference soils [10]. Besides, the TDR method uses a short duration of pulse and determines dielectric constant of soils using propagation of time of electromagnetic signals. Nonetheless, it requires a proper design (depended on the probe). Open-ended coaxial probe or waveguide measurements can be applied to evaluate electromagnetic properties of soils [3], [7]. But, they require close contact with the sample and fringing fields at the coaxial probe or waveguide corners can decrease the measurement accuracy if not taken into consideration in the theoretical analysis.

Coaxial transmission lines could be used [8]–[11] for wideband complex permittivity measurement of soil samples. Their diameters can be arranged in such a manner that dielectric properties of larger soil samples could be efficiently measured. In a recent study, a EIA 1-5/8" coaxial transmission line was applied for broadband dielectric constant measurements of soil samples [10]. However, this method requires an accurate calibration [8], [9], and [11]. However, these one-port or two-port calibration techniques [8], [9], [11] necessitate either additional transmission lines with different lengths or precise variable load.

De-embedding techniques can be utilized for complex permittivity measurement without any formal calibration procedure [12]–[15]. The de-embedding techniques [14], [15] are applicable for coaxial-line measurements (feasible for measurements of genderless networks). Besides, the other de-embedding techniques [12]–[15] are suitable only for solid samples, but not soil samples. In this study, we propose a novel de-embedding line-line method for calibration-free complex permittivity measurement of soil samples within a EIA 1-5/8" coaxial transmission line measurement system composed of only two identical coaxial lines with different lengths.

[2] THEORETICAL ANALYSIS

The measurement configurations of our proposed method

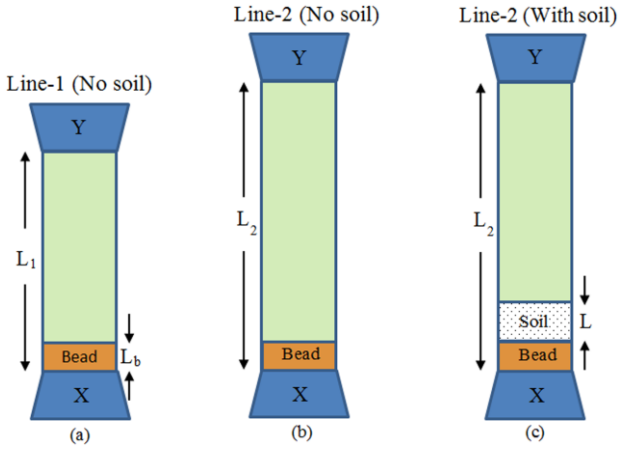


Fig. 1. Measurement configurations of our method with two identical lines with different lengths L_1 and L_2 for relative complex permittivity measurement of soil sample with length L poured on a solid dielectric bead with length L_b.

for relative complex permittivity ε_r evaluation of soil samples within a EIA 1-5/8" coaxial transmission line are presented in Fig. 1. As shown in Fig. 1(a), the shorter EIA 1-5/8" line of length L_1 with a dielectric bead (with length L_b) is assumed to be connected between two 3.5 mm Type-N/EIA 1-5/8" adapters via two Type-N lines to a vector network analyzer (VNA) (not shown for simplicity). The VNA imperfections (source/load match and tracking (frequency) errors) and effects of adapters and transitions are accounted into the two error networks X and Y. The configuration in Fig. 1(b) is similar to the configuration in Fig. 1(a), but a length change from L_1 to L_2. Soil sample with length L, as shown in Fig. 1(c), is assumed to be poured onto the bead inside the longer line with L_2.

In our analysis, we assume that the error networks X and Y do not change for each configuration in Fig. 1. It is also assumed that the measurement system is operated at its TEM (dominant mode). Using the ABCD network presentation, one can write for each measurement configuration in Figs. 1(a)-1(c)

$$M_a = T_X T_B T_{S0} T'_{L1} T_Y, \quad (1)$$

$$M_b = T_X T_B T_{S0} T'_{L2} T_Y, \quad (2)$$

$$M_c = T_X T_B T_S T'_{L2} T_Y, \quad (3)$$

where T_X and T_B represent the ABCD matrices of X and Y; T_B shows the ABCD matrix of the Bead section; T_S and T_{S0} indicate the ABCD matrices of soil-field and air-filled sections; and T'_{L1} and T'_{L2} correspond, respectively, to the ABCD matrices of the lines with L_1 and L_2 (without Bead and air-filled sections with length L).

The expressions of T_S, T'_{L1}, T'_{L2}, and T_{S0} can be written as

$$T_S = \frac{1}{2}\begin{bmatrix} \left(\frac{1}{T}+T\right) & z\left(\frac{1}{T}-T\right) \\ \frac{1}{z}\left(\frac{1}{T}-T\right) & \left(\frac{1}{T}+T\right) \end{bmatrix}, \quad (4)$$

$$T'_{L1} = \frac{1}{2}\begin{bmatrix} \left(\frac{1}{T_1}+T_1\right) & \left(\frac{1}{T_1}-T_1\right) \\ \left(\frac{1}{T_1}-T_1\right) & \left(\frac{1}{T_1}+T_1\right) \end{bmatrix}, \quad T_1 = e^{-jk_0(L_1-L_b-L)}, \quad (5)$$

$$T'_{L2} = \frac{1}{2}\begin{bmatrix} \left(\frac{1}{T_2}+T_2\right) & \left(\frac{1}{T_2}-T_2\right) \\ \left(\frac{1}{T_2}-T_2\right) & \left(\frac{1}{T_2}+T_2\right) \end{bmatrix}, \quad T_2 = e^{-jk_0(L_2-L_b-L)}, \quad (6)$$

$$T_{S0} = \frac{1}{2}\begin{bmatrix} \left(\frac{1}{T_0}+T_0\right) & \left(\frac{1}{T_0}-T_0\right) \\ \left(\frac{1}{T_0}-T_0\right) & \left(\frac{1}{T_0}+T_0\right) \end{bmatrix}, \quad T_0 = e^{-jk_0 L}, \quad (7)$$

$$T = e^{-jk_0\sqrt{\varepsilon_r}L}, \quad z = \sqrt{\frac{1}{\varepsilon_r}}. \quad (8)$$

Here, T_1 and T_2 the propagation factors of the air-filled region with lengths L_1 and L_2; and T and z are the propagation factor and the relative impedance of soil-filled region in reference to air.

Multiplying the inverse matrices of M_a and M_b with M_c and applying the trace operation (denoted by Tr), we obtained

$$\Omega_1 = T_r\left(M_c M_b^{-1}\right) = Tr\left(T_S T_{S0}^{-1}\right) = \frac{1}{4}\left[2\left(\frac{1}{T_0}+T_0\right)\left(\frac{1}{T}+T\right)-\left(\frac{1}{z}+z\right)\left(\frac{1}{T_0}-T_0\right)\left(\frac{1}{T}-T\right)\right] \quad (9)$$

$$\Omega_2 = T_r\left(M_c M_a^{-1}\right) = Tr\left(T_S T'_{L2}\left(T'_{L1}\right)^{-1} T_{S0}^{-1}\right) = \frac{1}{4}\left[2\left(\frac{\Delta}{T_0}+\frac{T_0}{\Delta}\right)\left(\frac{1}{T}+T\right)-\left(\frac{1}{z}+z\right)\left(\frac{\Delta}{T_0}-\frac{T_0}{\Delta}\right)\left(\frac{1}{T}-T\right)\right] \quad (10)$$

$$\Delta = e^{-jk_0\Delta L}, \quad \Delta L = L_2 - L_1. \quad (11)$$

From (9)-(11), one can derive

$$T = \frac{N \mp \sqrt{N^2-4}}{2}, \quad (12)$$

$$N = \frac{\frac{1}{T_0}\left(\Omega_1\Delta-\Omega_2\right)+T_0\left(\Omega_2-\frac{\Omega_1}{\Delta}\right)}{\Delta-1/\Delta}. \quad (13)$$

The correct value of T can be evaluated from (12) by enforcing the passivity principle; that is, $|T| \le 1$. Here, $|*|$ shows the magnitude of '*'.

Finally, ε_r can be determined as

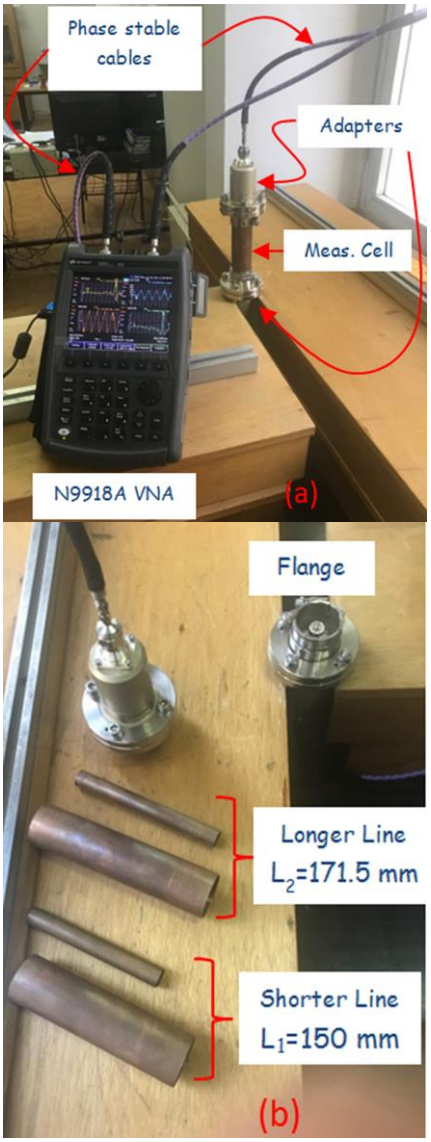


Fig. 2. (a) A picture of the measurement setup and (b) a picture of the shorter and longer coaxial lines with $L_1 = 150$ mm and $L_2 = 171.5$ mm.

$$\varepsilon_r = \left[\frac{j\ln(T) \mp 2\pi m}{k_0 L} \right], \quad m = 0,1,2,... \qquad (14)$$

It is seen from (9)-(14) that our proposed method does not require information about the Bead (its thickness and electromagnetic properties).

[3] Measurements and Dıcsussıon

A. Validation

Solid low-loss polyethylene dielectric material with length $L = 3.85$ mm was used to validate our proposed method from calibration-free scattering (S-) parameters of the configurations in Figs. 1(a)-1(c). Fig. 2(a) shows the setup used for our measurements. The measurement setup includes a VNA (N9918A from Keysight instruments) with a higher directivity greater than 32 dB, a dynamic range approximately 90 dB, and a frequency range between 30 kHz and 26.5 GHz. Two one-meter Type-N coaxial lines were applied to transmit electromagnetic energy to Type-N-to-EIA 1-5/8" adapters.

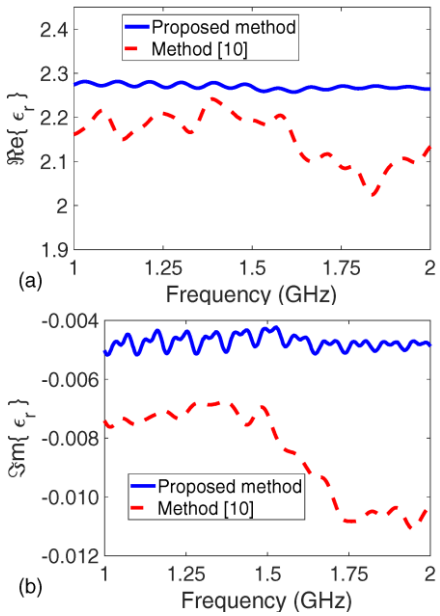


Fig. 3. (a) Real and (b) imaginary parts (over 1-2 GHz) of extracted complex permittivity ε_r a polyethylene sample with 3.85 mm by our method (denoted by the 'Proposed method') and the method [10] (denoted by the 'Method [10].').

Coaxial lines with lengths $L_1 = 150$ mm and $L_2 = 171.5$ mm (outer conductor with diameter 38.8 ∓ 0.075 mm and inner conductor with diameter 16.9 ∓ 0.050 mm) were connected as shown in Fig. 2(b) [8]-[11]. A polyethylene dielectric sample with length $L_b = 3.85$ mm was utilized as a Bead material in our measurements.

Fig. 3(a) and 3(b) illustrate the frequency dependencies (over 1-2 GHz) of the real and imaginary parts of permittivity of the polyethylene sample extracted by our method after applying moving average (averaging) over 30 MHz data [12], using calibration-free S-parameters. To validate our proposed method, the real and imaginary parts of permittivity of the polyethylene sample were also extracted by another method [10] using calibrated S-parameters. For measurements by this method [10], the short-open-load-thru calibration procedure was first implemented to calibrate the measurement system to the ends of 3.5 mm Type-N coaxial lines and then port extensions were applied to eliminate the effects of Type-N/EIA 1-5/8" adapters. It is seen from Figs. 3(a) and 3(b) that extracted relative complex permittivity of the polyethylene sample by our method is very close to the reference datum $2.26 - j0.0002$ [16], that by the method [10] has oscillatory behavior over the whole band and is far away from the reference datum.

B. Soil Measurements

Complex relative permittivities of two different soil samples with more than 90% sand texture with different electrical conductivities (ECs) were measured by our method. These soil samples, labeled as S1 and S2 (obtained from different areas of the city Gaziantep, Turkey) had EC values (pH values) of 95.70 mS/m (7.62) and 341 mS/m (8.14), respectively (measured by the conductivity bridge method). All samples have approximately 3% humidity values in

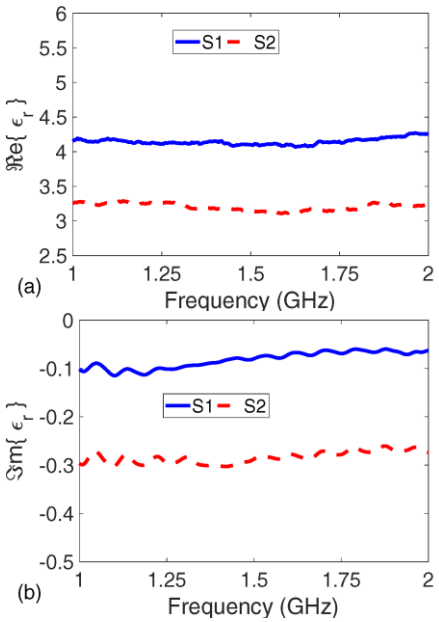


Fig. 4. (a) Real and (b) imaginary parts (over 1-2 GHz) of extracted relative complex permittivity of two soil samples with more than 90% sand texture having different electrical conductivities (S1 and S2 have conductivities of 95.70 mS/m and 341 mS/m respectively) by the proposed de-embedding line-line method.

reference to air-dry basis. Figs. 4(a) and 4(b) demonstrate the real and imaginary parts of the extracted complex permittivity of S1 and S2 ($L \cong 125$ mm) by our method. It is seen from Figs. 4(a) and 4(b) that an increase in electrical conductivity accompanies with an increase in loss behavior of soil samples. Furthermore, the results given in Figs. 4(a) and 4(b) agree with the results non-saline soil measurements in the study [8].

[4] Conclusıon

A calibration-free de-embedding line-line method has been proposed for complex permittivity determination of soil samples loaded into a EIA 1-5/8" coaxial transmission line measurement system. Complex permittivity value of a dielectric polyethylene sample was measured for validation of our method whose accuracy was compared with another method which requires a suitable calibration. Finally, complex permittivities of two different soil samples gathered from different areas of the city Gaziantep in Turkey with different electrical conductivities were measured. From these measurements, it is noted that an increase in electrical conductivity accompanies with an increase in loss behavior of soil samples with the same sand texture.

REFERENCES

[1] M. Bittelli, "Measuring soil water content: A review," Horttechnology ,vol. 21, no. 3, pp. 293–300, 2011.

[2] N. Romano, "Soil moisture at local scale: Measurements and simulations," J. Hydrol., vol. 516, pp. 6–40, Aug. 2014.

[3] G. Luciani, A. Berardinelli, M. Crescentini, A. Romani, M. Tartagni, and L. Ragni, "Non-invasive soil moisture sensing based on open-ended waveguide and multivariate analysis," Sens. Actuator A.: Phys., vol. 265, pp. 236–245, Oct. 2017

[4] A. Klotzsche, F. Jonard, M. Looms, J. van der Kruk, and J. Huisman, "Measuring soil water content with ground penetrating radar: A decade of progress," Vadose Zone J., vol. 17, no. 1, pp. 1-9, Jul. 2018

[5] T. J. Heimovaara, J. A. Huisman, J. A. Vrugt, and W. Bouten, "Obtaining the spatial distribution of water content along a TDR probe using the SCEM-UA Bayesian inverse modeling scheme," Vadose Zone J., vol. 3, no. 4, pp. 1128–1145, Nov. 2004

[6] C. Salat and A. Junge, "Dielectric permittivity of fine-grained fractions of soil samples from eastern Spain at 200 MHz," Geophysics, vol. 75, no. 1, pp. J1–J9, Jan. 2010

[7] N. Wagner, M. Schwing, and A. Scheuermann, "Numerical 3-D FEM and experimental analysis of the open-ended coaxial line technique for microwave dielectric spectroscopy on soil," IEEE Trans. Geosci. Remote Sens., vol. 52, no. 2, pp. 880–893, Feb. 2014.

[8] A. Lewandowski, A. Szyplowska, M. Kafarski, A. Wilczek, P. Barmuta, and W. Skierucha, "0.05-3 GHz VNA characterization of soil dielectric properties based on the multiline TRL calibration," Meas. Sci. Technol., vol. 28, no. 2, Art. No. 024007, Jan. 2017.

[9] A. Szyplowska, A. Lewandowski, S. B. Jones, P. Sabouroux, J. Szerement, M. Kafarski, A. Wilczek, and W. Skierucha, "Impact of soil salinity, texture and measurement frequency on the relations between soil moisture and 20 MHz-3 GHz dielectric permittivity spectrum for soils of medium texture," J. Hydrol., vol. 579, Art. No. 124155, Dec. 2019.

[10] K. Lauer, N. Wagner, and P. Felix-Henningsen, "A new technique for measuring broadband dielectric spectra of undisturbed soil samples," Eur. J. Soil Sci., vol. 63, pp. 224–238, Apr. 2012.

[11] A. Lewandowski, A. Szyplowska, A. Wilczek, M. Kafarski, J. Szerement, and W. Skierucha, "One-port vector network analyzer characterization of soil dielectric spectrum," IEEE Trans. Geosci. Remote Sens., vol. 57, no. 6, pp. 3661–3676, 2019.

[12] N. Jebbor, S. Bri, A. M. S`anchez, and M. Chaibi, "A fast calibration independent method for complex permittivity determination at microwave frequencies," Meas., vol. 46, no. 7, pp. 2206–2209, 2013.

[13] Z. Caijun, J. Quanxing, and J. Shenhui, "Calibration-independent and position-insensitive transmission/reflection method for permittivity measurement with one sample in coaxial line," IEEE Trans. Electromagn. Compat., vol. 53, no. 3, pp. 684–689, Aug. 2011.

[14] U. C. Hasar, "Self-calibrating transmission-reflection technique for constitutive parameters retrieval of materials," IEEE Trans. Microw. Theory Techn., vol. 66, no. 2, pp. 1081–1089, Feb. 2018.

[15] U. C. Hasar and Y. Kaya, "Self-calibrating noniterative complex permittivity extraction of thin dielectric samples," IEEE Trans. Electromagn. Compat., vol. 60, no. 2, pp. 354–361, Apr. 2018.

[16] G. Y. Chin and E. A. Mechtly, Properties of materials. Indianapolis, IN: Howard W. Sams Co., 1986, pp. 420, 423.

Electrochemical Synthesis and Characterization OF MoO3 Nanostructured Photoelectrodes

Emir Çepni
Department of Electrical and Electronic Engineering, Department of Nanoscience and Nanoengineering
Atatürk University Erzurum, Turkey
emircepni@atauni.edu.tr

Ahmet Korkmaz
*Department of Nanoscience and Nanoengineering Atatürk University*Erzurum, Turkey
ahmetkorkmaz381@gmail.com

Hülya Öztürk Doğan
Department of Nanoscience and Nanoengineering, Department of Chemistry and Chemical Processing Technologies
Atatürk University Erzurum, Turkey
hdogan@atauni.edu.tr

Tuba Öznülüer Özer
Department of Nanoscience and Nanoengineering, Department of Chemistry Atatürk University
Erzurum, Turkey
tozkim@atauni.edu.tr

***Abstract*— In recent years, the exploration for alternative energy sources has gained importance in order to meet the increasing energy need with the technological developments in the world. Molybdenum trioxide (MoO_3), a wide-band gap n-type semiconductor, contains a variety of attractive chemical and opto-electrical properties. In this study, MoO_3 nanostructures were synthesized on the fluorine doped tin oxide (FTO) coated glass by using electrochemical deposition technique. XRD, SEM and UV-VIS analysis were performed for the structural and morphological characterization of the as-synthesized nanostructures. The photovoltaic properties of the characterized electrodes were investigated by electrochemical method under 100 mW.cm^{-2} visible light illumination to be used as photoelectrodes in photovoltaic cells.**

Keywords—Molybdenum trioxide, electrochemical synthesis, nanostructure, photoelectrode

[1] INTRODUCTION

Various problems such as increasing energy need, global warming and depletion of fossil energy resources necessitate the search for renewable, cheap and clean energy resources. Converting solar energy into electrical energy with photovoltaic systems seems to be the most promising solution. For this purpose, although many methods related to the synthesis of materials with high conversion efficiency have been studied intensively, electrochemical methods that can allow the synthesis of environmentally friendly, cheap and size-controlled materials have not been reported much. Semiconductor material technology has an enormous potential to solve the world energy crisis and the environmental problems caused by the heavy consumption of non-renewable fossil fuels. Among these semiconductor materials, transition metal oxides such as NiO, WO_3, TiO_2 and ZnO have prominent usage potential in new generation batteries [1], electrochromic applications [2], solar cells [3] and sensor applications [4]. MoO_3 has many kinds of interesting structural, chemical, electrical and optical properties among various metal oxides. MoO_3 applications are widely used, especially due to its special crystal structure and excellent properties. Its astounding properties have been reported in various application fields such as supercapacitor, gas sensor and electrochromic materials [5-7]. Additionally, MoO_3 also has a wide range of uses as a catalyst in chemical reactions. MoO_3 can be a strong opponent to TiO_2 and ZnO as electron-trapping layer in metal oxide based photovoltaic cells.

[2] EXPERIMENTAL SECTION

A. *Fabrication of FTO-MoO_3 Electrodes*

A three electrode cell system was used for the electrochemical synthesis of MoO_3 nanostructures. For three electrode cell system, the working electrode FTO, the counter electrode Pt wire (approximately 99.95% purity, 0.5 mm diameter) and reference electrode Ag/AgCl were used. The FTO electrodes were cleaned before all electrochemical depositions. For this purpose, the FTO electrodes were kept in an ultrasonic bath for 15 minutes in ethanol and distilled water, respectively and dried under an Ar atmosphere.

The electrolyte solution is an aqueous solution containing 10 mM MoO_3 and 50 mM HCl. For electrochemical synthesis, the cycling voltamogram (CV) of the FTO electrode was analyzed in this electrolyte medium. Within the scope of the analyzed CV, the electrochemical deposition has been carried out at a potential of −1.1 V, about 5 min. During the electrodeposition process, oxygen gas was introduced in the cell at a constant flow rate of 3 mL.min^{-1} and the electrolyte was stirred at a speed of 1000 rpm. Synthesis procedure completed via thermal annealing of the as-synthesized electrodes in air atmosphere at 400 °C for 1 h to fabricate the FTO-MoO_3 photoelectrodes.

B. *Characterization of FTO-MoO_3 Electrodes*

Rigaku Miniflex X-ray diffractometer (XRD) (Cu-Kα (λ=15.405 Å) was used to investigate the structural characterization of MoO_3 nanostructures deposited electrochemically on the FTO electrode surface. The observed peaks at 12.7°, 23.3°, 25.7°, 27.3° and 38.9° corresponds to (020), (110), (040), (021) and (060) planes of MoO_3 (JCPDS No.05-0508), respectively (Fig. 1.). The XRD spectrum indicates the crystal formation of the MoO_3 nanostructures.

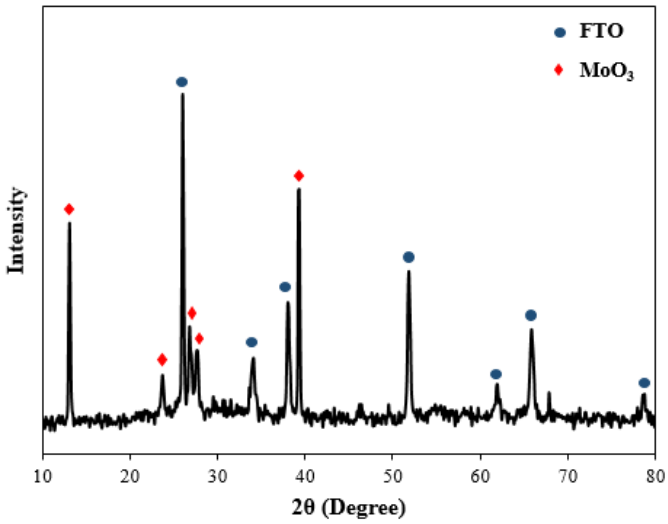


Fig. 1. XRD Spectra of FTO-MoO_3 electrode

The morphological structures of the fabricated FTO-MoO_3 electrodes were examined by using FEI quanta scanning electron microscope (SEM) images (Fig. 2.(a-c). The analyzed SEM images support that the nanostructures cover the FTO electrode surface homogeneously. At higher magnifications, Its seen that MoO_3 structures grew as nanoplates and formed to larger sheets by the integration of this nanoplates. This morphological structure of the FTO-MoO_3 electrodes is one of the main elements in the good photovoltaic properties.

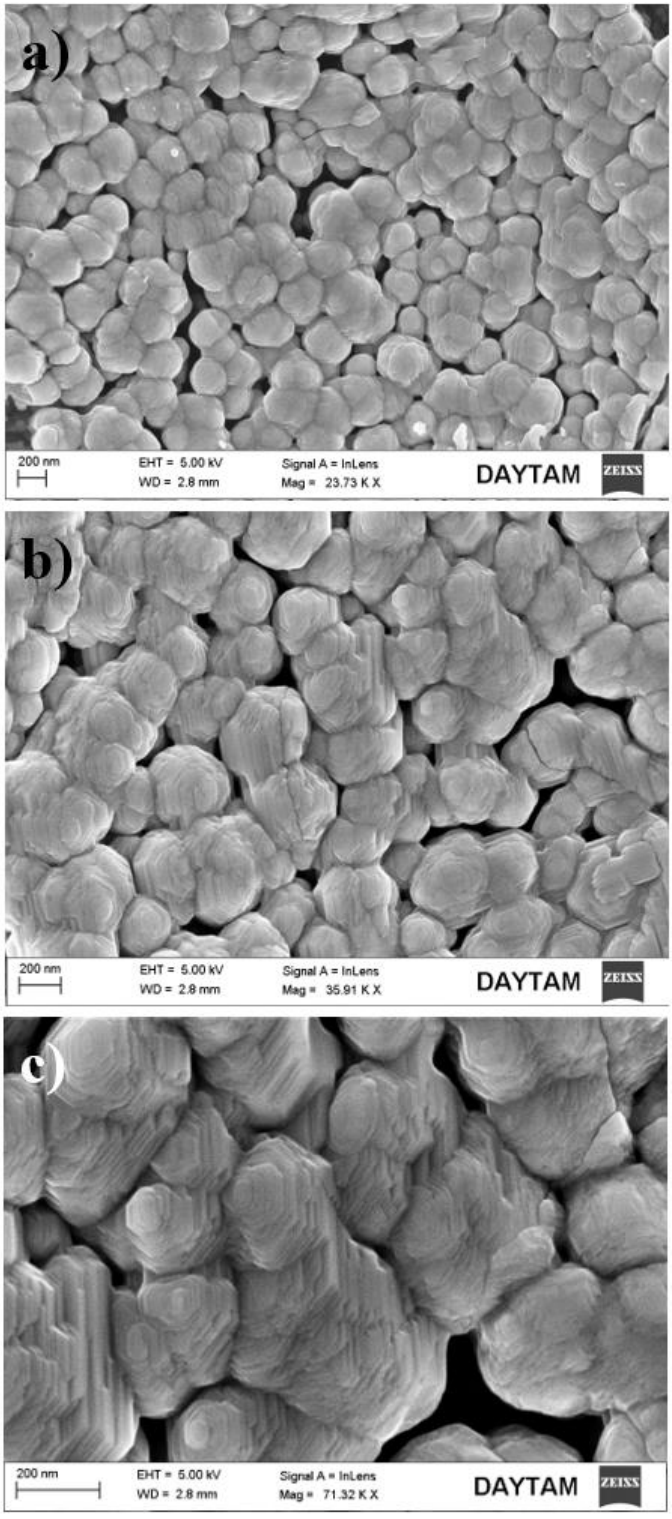


Fig. 2. SEM images of FTO-MoO_3 electrode

The optical absorbance spectra obtained by using UV-VIS spectroscopy was used to determine the optical band-gap value of MoO_3 nanostructures (Fig. 3.).

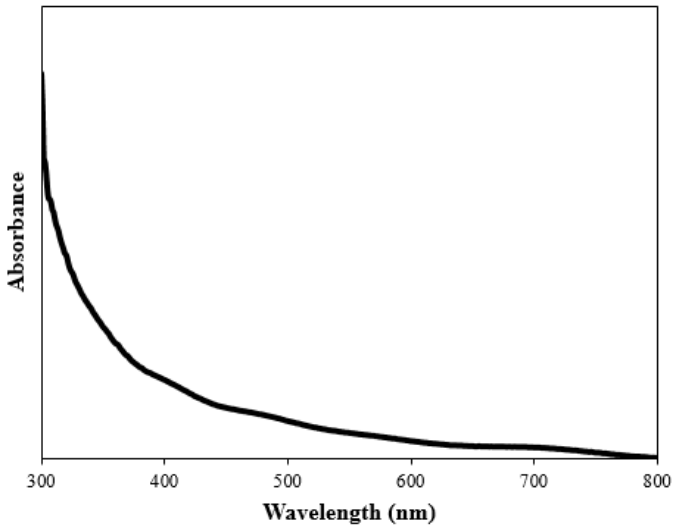


Fig. 3. UV–VIS absorbance spectra of FTO-MoO_3 electrode

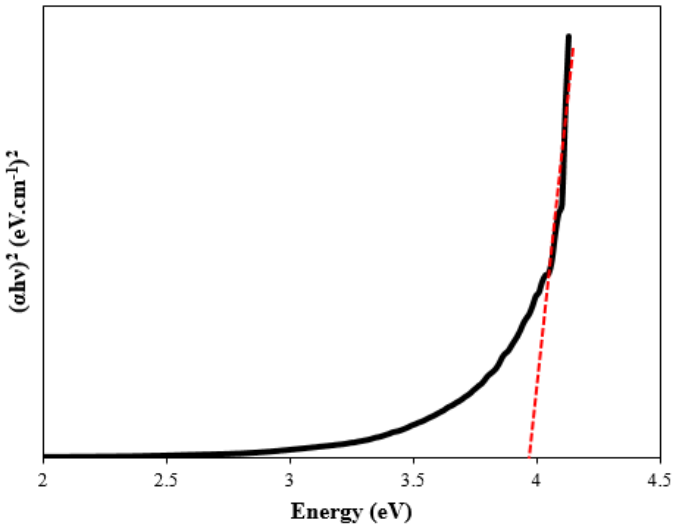


Fig. 4. Tauc plot for the FTO-MoO_3 electrode

The band-gap energy of the MoO_3 nanostructures calculated by Tauc plot as 3.95 eV which is attributed a wide energy range (Fig. 4.).

[3] RESULTS AND DISCUSSION

A. *Photovoltaic Properties of FTO-MoO_3 Electrodes*

The photoelectrochemical current densities of the electrochemically fabricated FTO-MoO_3 photoelectrodes were measured by using chronoamperometry at 0 V for 90 s in 0,1 M Na_2SO_4 electrolyte. Fig. 5. shows the FTO-MoO_3 photoelectrodes photocurrent–time diagram obtained by intermittent artificial sunlight illumination. As seen in Fig. 5., the photocurrent intensity increases swiftly to ~17.4 µA.cm^{-2} when the sunlight illumination is switched on. When the sunlight illumination is switched off, no photocurrent response was observed. Additionally, the photocurrent densities rise and fall immediately with the switching on and off of light illumination which is attributed to highly reproducible for numerous switching actions.

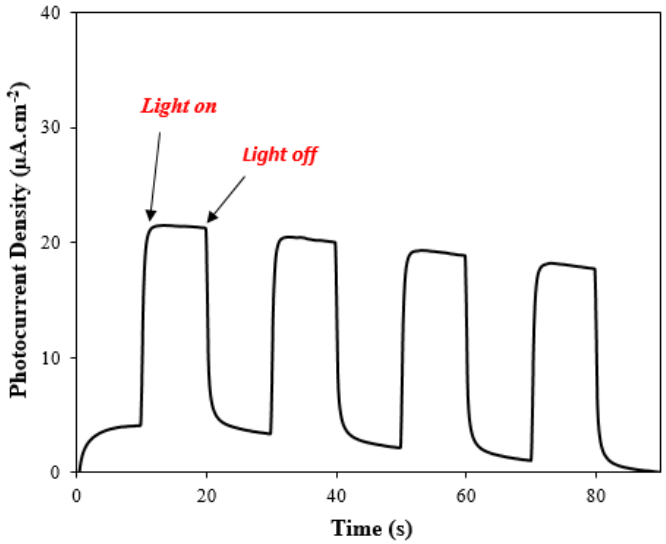


Fig. 5. The photocurrent–time diagram of the electrochemically fabricated FTO-MoO_3 photoelectrode in 0,1 M Na_2SO_4 electrolyte

B. *Conclusion*

In this study, FTO-MoO_3 photoelectrodes were synthesized successfully by using electrochemical deposition technique. The photovoltaic properties of the characterized photoelectrodes were investigated via photocurrent–time diagram. A photocurrent density of ~17.4 µA.cm^{-2} was measured for FTO-MoO_3 photoelectrode. The results indicate that FTO-MoO_3 photoelectrodes can be used in energy applications, such as solar cells, photoconversion, etc.

REFERENCES

[1] B. Varghese, M.V. Reddy, Z. Yanwu, C.S. Lit, T.C. Hoong, G.V. Subba Rao, B.V.R. Chowdari, A.T.S. Wee, C.T. Lim, and C. Sow, "Fabrication of NiO Nanowall Electrodes for High Performance Lithium Ion Battery," Chem. Mater., vol. 20, pp. 3360–3367, May 2008.

[2] M. Zhi, W. Huang, Q. Shi, M. Wang, and Q. Wang, "Sol–gel fabrication of WO3/RGO nanocomposite film with enhanced electrochromic performance," RSC Adv., vol. 6, pp. 67488–67494, July 2006.

[3] W. Zhu, X. Liu, H. Liu, D. Tong, J. Yang, and J. Peng, "Coaxial Heterogeneous Structure of TiO2 Nanotube Arrays with CdS as a Superthin Coating Synthesized via Modified Electrochemical Atomic Layer Deposition," J. Am. Chem. Soc., vol. 132, pp. 12619–12626, June 2010.

[4] Q. Li, D. Chen, J. Miao, S. Lin, Z. Yu, D. Cui, Z. Yang, and X. Chen, "Highly sensitive sensor based on ordered porous ZnO nanosheets for ethanol detecting application," Sensors and Actuators B: Chemical, vol. 326, pp. 128952–, January 2021.

[5] F. Wang, Z. Liu, X. Wang, X. Yuan, X. Wu, Y. Zhu, L. Fu, and Y. Wu, "A conductive polymer coated MoO3 anode enables an Al-ion capacitor with high performance," J. Mater. Chem. A, vol. 4, pp. 5115-5123, Mar 2006.

[6] H. Ji, W. Zeng, and Y. Li, "Facile synthesis of novel MoO3 nanoflowers for high-performance gas sensor," J Mater Sci: Mater Electron, vol. 30, pp. 6601–6607, February 2019.

[7] Y. Liu, Y. Lv, Z. Tang, L. He, and X. Liu, "Highly stable and flexible ITO-free electrochromic films with bi-functional stacked MoO3/Ag/MoO3 structures," Electrochimica Acta, vol. 189, pp. 184-189, January 2016

Green Synthesis of Nanoflowers and Investigation of Their Usability in Wastewater Treatment

Hayrunnisa NADAROGLU
Department of Food Technology, Erzurum Vocational College, Ataturk University, 25240 Erzurum, Turkey
Department of Nano-Science and Nano-Engineering, Institute of Science and Technology, Ataturk University, 25240 Erzurum, Turkey
*Corresponding author's phone: +90-442 231 1818
E-mail: hnisa25@atauni.edu.tr

***Abstract*-The consumption need and the amount of industrial wastes are increasing day by day in proportion to the increase in the world population. This situation causes serious environmental pollution and damage and poses a threat to the health of living beings. In this study, it is aimed to use nanoflowers obtained by green synthesis method in the removal of some azo dyes in wastewater. For this purpose, nanoflower synthesis was carried out using apple cider vinegar and the use of nanoflowers in the removal of some azo dyes from waste water was investigated. From the findings obtained, it was determined that nanoflowers synthesized at pH: 11.0 at room temperature can be used effectively in the removal of azo dyes at a rate of approximately 90-98%.**

Keywords- Green synthesis; Nanoflower; Remediation, Azo dye, Wastewater

[1] INTRODUCTION

Nano flowers are synthesized from organic, inorganic materials by the simple method of synthesis and sometimes a combination of both organic and inorganic materials to increase the stability and efficiency of the surface reaction.

The most important advantage of the green synthesis method is that it does not require toxic elements or extremely difficult conditions as in synthetic methods. It is possible to synthesize the hybrid nanomaterial to produce it by simply adding protein to the metal ion solution. For this reason, it has been determined that nanoflowers synthesized with the biological material involved in the synthesis can be obtained in less steps than with other methods.

Flower-like hybrid nanomaterials produced by this process are called "organic-inorganic hybrid nanoflowers" or "hybrid nanoflowers". When their synthesis mechanisms, physical properties, protein activities, stability and reproducibility are examined, it has been determined that they are quite stable, stable and suitable for use in different industrial areas.

Advantages of hybrid nanoflowers;

- Nanoflowers show high surface / volume ratio to increase surface adsorption by accelerating the kinetics of reactions.
- Nanoflowers show better charge transfer and immobilization to the carrier due to its large surface area.
- The efficiency of the surface reaction increases in the 3D structure of nano flowers.
- Synthetic methods such as ionotropic gelation, precipitation method and green synthesis for the preparation of nano flowers are simple, non-toxic and cost-effective.
- Due to the instability of proteins and enzymes, immobilization on the surface of metals increases stability.

[2] EXPERIMENTAL

2.1. Preparation of Apple Vinegar by Green Synthesis Method

Nanoflower synthesis was achieved by reduction of apple cider vinegar. Briefly; 1.2 ml of a solution of 125 mg / ml TPP (sodium tri polyphosphate) in the environment of 1% Chitosan acetic acid solution is added. Next, apple cider vinegar is added to the medium and the reaction mixture is stirred for 10 min at 300 rpm and the pH is adjusted to pH:11. Then 4.2 mL of 100 mM $CaCl_2$ is added to the medium. It is incubated for 12 hours at room temperature and the resulting precipitate is washed first with pure water, then with ethyl alcohol, then dried under vacuum in an oven at 40 ^oC .

2.3 Determination of Optimum Biosorption Conditions For Adsorption

The usability of synthesized Ca-Nanoflowers in the removal of some azo dyes from wastewater has been investigated. For this purpose; The optimum conditions of the reaction medium have been determined to determine the most suitable conditions for the removal of azo dyes [1].

2.4 Determination of Adsorption Kinetics

The decolorization reactions were performed spectrophotometrically at the wavelengths at which each dye exhibited maximum absorption. Decolorization was calculated by the following equation:

$$\text{Decoloration (\%)} = \frac{A_o - A_o}{A_o}\ x\ 100$$

Ao, A_1 are initial absorbance and absorbance after reaction, respectively.The adsorption kinetics of biosorbent materials and polluting components in dye solutions of different concentrations are investigated. In order to determine the adsorption constants, compatibility with first-order reaction kinetics and second-order reaction kinetics is examined [2,3].

2.5. Calculation of thermodynamic parameters

The adsorption on the surface was evaluated by calculating the Langmiur isotherm and Freundlich isotherm for the nanoflower adsorbent materials used in the biosorption of contaminating factors. Among the thermodynamic parameters, ΔG ° Gibbs free energy, ΔH^o enthalpy change and ΔSo entropy thermodynamic parameters were calculated [4].

[3] RESULTS AND DISCUSSION

3.1. Synthesis and characterization of nanoflower

Nanoflowers were synthesized using apple cider vinegar in one step and under mild conditions. The nanoflower structure obtained is given in Fig. 1 [5,6].

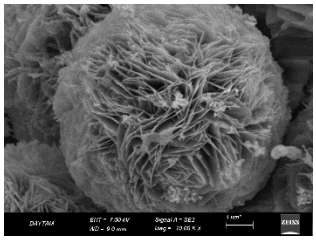


Fig. 1. SEM images of Ca-Nanoflower structure

As a result, it has been proven with the SEM image that nanoflowers are successfully synthesized using apple vinegar. It has been used in the removal of some azo dyes by using the Ca-Nanoflowers obtained and it has been determined that it is effective. Relevant information is presented in the Table 1 [7,8].

Azo dyes	Remidiation (%)
Acid red 37	93
Reactive black 5	98
Evans blue	95
Direct blue 5	90

[4] CONCLUSION

The synthesis of nanoparticles with various biological extracts in an effective, inexpensive and environmentally friendly method and the use of the nanoparticles as catalysts in environmental treatment applications are important in terms of economy, environment and human health.

REFERENCES

[1] A. Babagil, Purification and Characterization of Pectin Lyase Enzymes From Microorganism, Preparation of Enzymic Ca2+-Hybrid Nanoflower Structure and The Investigation of Use In Fruit Juice Clarification, Grad. Sch. Nat. Appl. Sci. (2018) 1–173.

[2] D.D. Gultekin, A. Alayli, H. Nadaroglu, Eco-friendly synthesis of nano copper and its use in fenton-like reactions for methylene blue degradation, Int. J. Chem. Technol. 4 (2020) 71–78. https://doi.org/10.32571/ijct.724056.

[3] H. Nadaroglu, E. Kalkan, H. Celik, Equilibrium studies of copper ion adsorption onto modified kernel of date (Fructus dactylus), Int. J. Environ. Sci. Technol. 12 (2015). https://doi.org/10.1007/s13762-014-0607-y.

[4] H. Nadaroglu, G. Mosber, A.A. Gungor, G. Adıguzel, A. Adiguzel, Biodegradation of some azo dyes from wastewater with laccase from Weissella viridescens LB37 immobilized on magnetic chitosan nanoparticles, J. Water Process Eng. 31 (2019). https://doi.org/10.1016/j.jwpe.2019.100866.

[5] A. Baldemir, Ü. Karaman, S. Yusufbeyoclu, A. Eken, N. Ildiz, S. Ilgün, C. Çolak, G. Kaçmaz, I. Öçsoy, S. Çankaya, Laurocerausus officinalis Roemer (Taflan) Meyve Ekstrelerinden Nanoçiçek Sentezi ile Akantamoebisidal Aktivitenin Arttirilmasinda Yeni Bir Strateji, Mikrobiyol. Bul. 52 (2018) 56–71. https://doi.org/10.5578/mb.66400.

[6] B.S. Batule, K.S. Park, S. Gautam, H.J. Cheon, M. Il Kim, H.G. Park, Intrinsic peroxidase-like activity of sonochemically synthesized protein copper nanoflowers and its application for the sensitive detection of glucose, Sensors Actuators B Chem. 283 (2019) 749–754. https://doi.org/10.1016/j.snb.2018.12.028.

[7] S. Mohan, V. Kumar, D.K. Singh, S.H. Hasan, Effective removal of lead ions using graphene oxide-MgO nanohybrid from aqueous solution: Isotherm, kinetic and thermodynamic modeling of adsorption, J. Environ. Chem. Eng. 5 (2017) 2259–2273. https://doi.org/10.1016/j.jece.2017.03.031.

[8] H. Nadaroglu, S. Cicek, A.A. Gungor, Removing Trypan blue dye using nano-Zn modified Luffa sponge, Spectrochim. Acta Part A Mol. Biomol. Spectrosc. 172 (2017) 2–8. https://doi.org/10.1016/j.saa.2016.08.052.

Effect of Nitrogen Doping of Carbon Supports on PEM Fuel Cell Performance

Ayşe Bayrakçeken Yurtcan
Engrineering Faculty Deparment of Chemical Engineering
Atatürk University Erzurum,Turkey
abayrakceken@atauni.edu.tr

***Abstract*—PEM fuel cells seem to be promising alternative energy conversion devices for portable and mobile applications. The most important component of a PEM fuel cell is its anode and cathode electrodes where the half cell reactions are occuring. In this respect, it is crucial to increase the active sites of the catalysts used in the electrodes in order to get better performances. Active sites of the carbon supported electrodes can be increased by doping carbon material with heteroatom such as nitrogen. In this study, two different nitrogen doping routes will be discussed including a) nitrogen doping carried out during the synthesis of carbon-based material b) carbon-based material treatment with nitrogen-containing chemicals.**

Keywords— PEM fuel cell, nitrogen doping, carbon

[1] INTRODUCTION

Nowadays, especially due to environmental sensitivities and the negative effects of fossil fuels on the environment, instead of the internal combustion engines, electric vehicles are on the agenda. In Europe by 2040 internal combustion engines will be completely dismantled and replaced by electric vehicles. Also in electric vehicles, there are two reliable ways to provide the electricity. One of them is lithium-based batteries and another is fuel cells. Thermodynamically fuel cells are open systems where the reactant gases are fed, and electricity can be obtained as long as the gases are fed. In the batteries the chemical energy is stored in the system and has to be recharged after its depletion. These two systems have their advantages and disadvantages.

In electric vehicles, proton exchange membrane (PEM) fuel cells are the most convenient type among the other fuel cells due to its lower operating temperature and higher power density. PEM fuel cell is an electrochemical system which also includes the anode and cathode electrodes and the electrolyte. At the anode side the fuel of hydrogen is oxidized with a reaction (HOR) to proton and electron on the mostly used electrocatalysts such as Pt nanoparticles over carbon support. The electrons are collected via an external circuit and sent to the cathode side where the oxygen reduction reaction (ORR) is occurred [1]. The schematic representation of the half cell reactions occurring in the PEM fuel cell is given in Figure 1. A better performing PEM fuel cell can be reached by using the best performing materials having lower resistances either for electron transfer and proton conduction. In this respect, electrocatalysts and the membrane are very crucial materials for a better performing PEM fuel cell.

[2] PEM FUEL CELLS

Mostly carbon supported Pt electrocatalysts are preferred in PEM fuel cells due to their high HOR and ORR activities. In recent years in order to decrease the cost of the fuel cells different non Pt group (non-PGM) electrocatalysts were searched as the catalysts but they did not reach the activities of Pt based electrocatalysts in the real time PEM fuel cell tests.

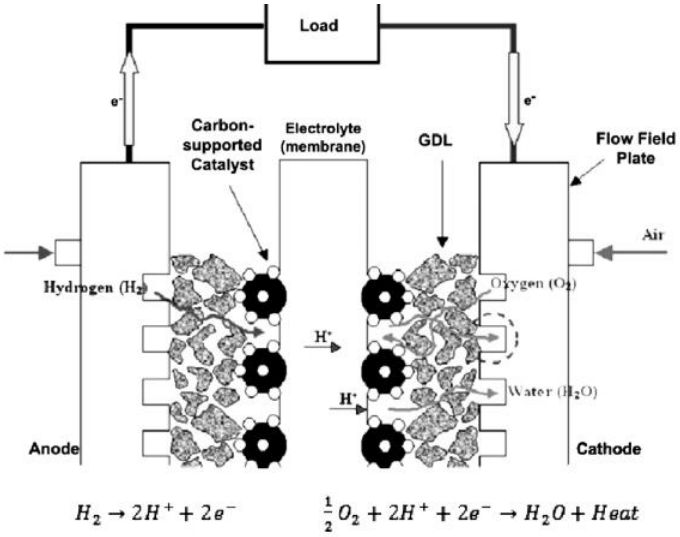


Fig. 1. Schematic representation of PEM fuel cell reactions [1].

The carbon material used in the electrocatalysts of PEM fuel cells have to provide high surface area and high electrical conductivity. High surface area will serve as the host for the Pt based nanoparticles and provide a better dispersion with small nanoparticle sizes. High electrical conductivity will decrease the resistance for electron transfer which is formed during the HOR at the anode side.

[3] NITROGEN DOPING OF CARBON MATERIALS

Chemical doping is an important technique that allows the properties of carbon materials to be changed. An important alternative was found for carbon based electrode materials by doping conventional carbon materials (e.g. carbon blacks, nanotubes, and fibers) with heteroatoms in order to increase their limited electrochemical activities. Carbon materials electronic properties can be changed by heteroatom doping. The number of active sites can be increased and the interaction between active sites and carbon structures can be improved via heteroatom doping. Heteroatoms used in the doping are B, P, S and N. Compared to others, carbon structures doped with nitrogen plays a more critical role. This is because carbon and nitrogen atoms have similar atomic sizes and nitrogen atoms has strong covalent bonding with carbon atoms [2].

There are studies in the literature in which different carbon structures are doped with nitrogen. The most studied of these carbon structures are graphene and carbon nanotubes. Nitrogen doping is done in two ways in the studies. In the first case, carbon-based material is treated with nitrogen gas at high temperatures and in the second case, carbon-based material is treated with a nitrogen-containing chemical. The nitrogen types that can be formed by the nitrogen doping of

graphene are given in Figure 2. Analyses showed that different nitrogen types can be formed such as pyrazole-N, pyrrolic-N, pyridinic-N and graphitic-N could be formed. Pyridinic-N is formed by the replacement of nitrogen with one of the carbons in the 6-carbon ring at the edge of the cavity. Pyridinic-N supplies the p-electron to the aromatic system and has only an electron pair. Pyrolic-N, sharing 2 p-electrons with the aromatic π-system denotes nitrogen and hydrogen from a 5-carbon ring with a carbon or 6-carbon ring on the edge of the cavity in the structure and can be replaced by bound carbon. Graphitic-N is from the four-component nitrogen group (Q-N). Graphitic-N is formed as a result of its replacement by carbon in the graphitic frame stack of nitrogen [3].

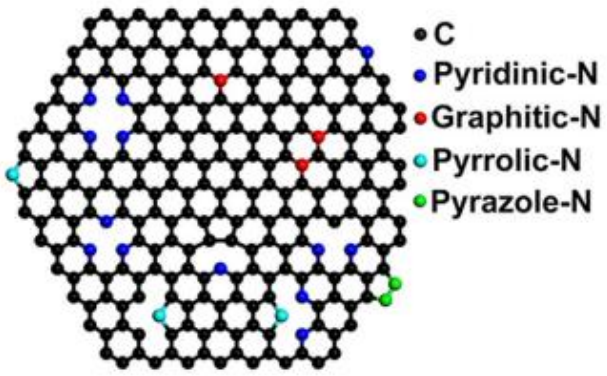


Fig. 2. Schematic representation of nitrogen structures formed in graphene [4].

According to the different types of nitrogen structures formed, N-graphene shows very different electronic properties. Hence in order to increase its performance in different applications, the amount of different required nitrogen additives should be higher for N-graphene [5,6]. In some studies it was observed that pyridinic-N and graphitic-N structures were the most common during nitrogen doping. It was observed that Pyridinic-N is formed in nano-spaces or on the edge of graphene [6,7]. Excessive amount of pyridinic-N shows that the nano-spaces are excessive, which decreases the conductivity of graphene. Graphitic-N on the other hand, is thermally more stable for applications such as ORR, molecular sensors, water oxidation and electromagnetic devices. In some studies, the ORR activity was increased with high graphitic-N/Pyridinic-N ratio. Therefore, it is important to increase the amount of graphitic-N. According to the literature it was observed that approximately 80% of the nitrogen additives obtained in the thermal treatment of graphene with ammonia were graphitic-N and the nitrogen additives are formed in defect regions in graphene and these defects are suitable for nitrogen doping as energy.

ORR is a sluggish reaction in the PEM fuel cell that has to be improved for a better fuel cell performance. In the literature it was stated that ORR proceeds with a 4 electron mechanism with nitrogen doped carbon-based materials. It was also said that nitrogen atom included in the structure in nitrogen-doped graphene layers increase the electron mobility and thus catalytically create new active sites. The reason for that is doped nitrogen makes the adjacent carbon atom positively charged and this positive charge density improves the catalytic activity. The bonding type of nitrogen atom to carbon atom also creates different effects [8]. Strong electronegativity of nitrogen atom changes the electronic structure of neighboring carbon atoms which is useful for the oxygen adsorption and eventually ORR process is accelerated [9].

[4] NITROGEN DOPING METHODS

Nitrogen doping of the carbon materials can be categorized as a) nitrogen doping carried out during the synthesis of carbon-based material which can be called as "Direct synthesis" b) carbon-based material treatment with nitrogen-containing chemicals which can be called as "Post treatment" [10]. Direct synthesis method involves the following;

- chemical vapor deposition (CVD)
- segregation method
- solvothermal and
- arc discharge method
- pyrolysis of N-containing precursors

Post-treatment method involves;

- thermal treatment
- plasma treatment
- and nitrogen-containing chemical treatment (such as ammonia or hydrazine hydrate) [10].

PEM fuel cell performances of the nitrogen doped carbon based materials were changed significantly depending on the type of the nitrogen formed. An example for the direct synthesis method which includes the pyrolysis of N-containing precursors is given in Figure 3. As can be seen from figure, zeolitic imidazole framework (ZIF-67) based nitrogen doped carbon material can be synthesized. In this case direct nitrogen doping is achieved by in-situ synthesis. In this process, nitrogen is provided from the precursor. There are different types of nitrogen precursors used for this type of nitrogen doping.

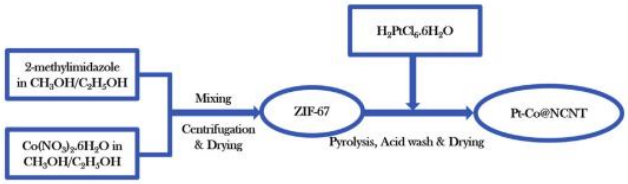


Fig. 3. Direct synthesis of nitrogen doped carbon via pyrolysis of N-containing precursors.

In another study, nitrogen doped carbon blacks were obtained by physically mixing the carbon black with melamine which is nitrogen source and then thermal treatment was carried out at different temperatures [11]. In this method, nitrogen doping level can be controlled by changing the melamine amount and also the pyrolysis temperature.

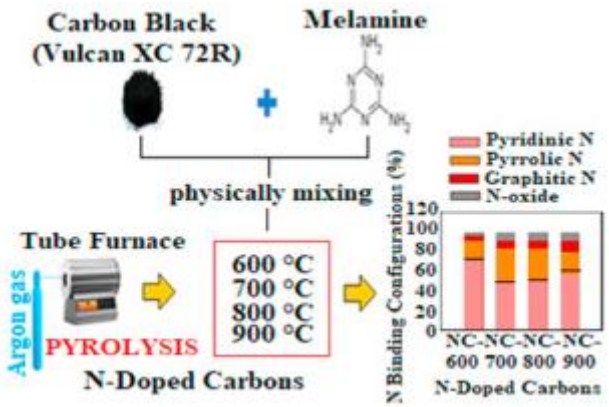


Fig. 4. Schematic representation of post-treatment nitrogen doping on carbon black [11].

Nitrogen doping levels significantly affect the structural and electrical properties of the carbon-based materials for possible different applications. It is essential to control the type and nitrogen doping level of the carbon based materials in order to improve the catalytic activities.

[5] CONCLUSIONS

Carbon supported Pt based electrocatalysts are the most important component in a PEM fuel cell since it is directly related with the reactions occurring in the fuel cell. In this respect it is very important to create new active sites which are catalytically active for the reactions. Nitrogen doping of the corresponding carbon-based material seems to be a promising approach for this phenomena. In the literature, wide range of different nitrogen doping methods were studied which affect the structural and electronic properties of the materials. The control of the nitrogen doping level and type will result in better catalytic activities.

REFERENCES

[1] S. G. Kandlikar, Z. Lu, "Thermal management issues in a PEMFC stack – A brief review of current status" Applied Thermal Engineering, vol.29, pp 1276-1280,2009.

[2] J. Li, Y. Zhang, X. Zhang, J. Han, Y. Wang, L. Gu, Z. Zhang, X. Wang, J. Jian, P. Xu, B. Song, "Direct transformation from graphitic C3N4 to nitrogen-doped graphene: An efficient metal-free electrocatalyst for oxygen reduction reaction", ACS Appl. Mater. Interfaces, vol. 7, pp 19626–19634,2015.

[3] T. Sharifi, F. Nitze, H.R. Barzegar, C.W. Tai, M. Mazurkiewicz, A. Malolepszy, L. Stobinski, T. Wågberg, "Nitrogen doped multi walled carbon nanotubes produced by CVD-correlating xps and raman spectroscopy for the study of nitrogen inclusion", Carbon, vol.50, pp 3535–3541,2012.

[4] X.F. Li, K.Y. Lian, L. Liu, Y. Wu, Q. Qiu, J. Jiang, M. Deng, Y. Luo, "Unraveling the formation mechanism of graphitic nitrogendoping in thermally treated graphene with ammonia", Scientific Reports, vol. 6, pp 23495,2016.

[5] Z. Luo, S. Lim, Z. Tian, J. Shang, L. Lai, B. MacDonald, C. Fu, Z. Shen, T. Yu, J. Lin, "Pyridinic n doped graphene: synthesis, electronic structure, and electrocatalytic property", J. Mater. Chem., vol. 21, pp 8038–8044, 2011.

[6] Y. Zhang, J. Ge, L. Wang, D. Wang, F. Ding, X. Tao, W. Chen, "Manageable N-doped graphene for high performance oxygen reduction reaction", Nature, Sci. Rep., vol. 3, pp 2771, 2013.

[7] F. Banhart, J. Kotakoski, A.V. Krasheninnikov, "Structural defects in graphene", ACS Nano, vol. 5, pp 26–41, 2011.

[8] J. Bai, Q. Zhu, Z. Lυ, H. Dong, J. Yu, L. Dong, "Nitrogen-doped graphene as catalysts and catalyst supports for oxygen reduction in both acidic and alkaline solutions", International Journal of Hydrogen Energy, vol. 38, pp 1413-1418,2013.

[9] A. S. Reyimjan, B. A. Alfred, P. S. Nalini, P. K. Swaminatha, N. P. Branko, "O2 Reduction on Graphite and Nitrogen-Doped Graphite: Experiment and Theory", J. Phys. Chem. B, vol. 110, pp 1787-1793,2006.

[10] R. Yadav, C.K. Dixit, "Synthesis, characterization and prospective applications of nitrogen-doped graphene: A short review", Journal of Science: Advanced Materials and Devices, vol. 2, pp 141-149,2017.

[11] A. Öztürk, A. Bayrakçeken Yurtcan, "Preparation and characterization of melamine-led nitrogen-doped carbonblacks at different pyrolysis temperatures", Journal of Solid State Chemistry, vol. 296, pp 121972,2021.

Application of Copperas as Chemical Coagulant for Industrial Water Treatment

Hamzah, Sofiah
Faculty of Ocean Engineering, Technology and Informatics Universiti Malaysia Terenganu Terengganu, Malaysia
sofiah@umt.edu.my

Che Harun, Mohd Hakim
Faculty of Ocean Engineering, Technology and Informatics Universiti Malaysia Terenganu Terengganu, Malaysia
m.hakim@umt.edu.my

Mohamad, Nurul Aqilah
Faculty of Ocean Engineering, Technology and Informatics Universiti Malaysia Terenganu Terengganu, Malaysia
nurulaqilahmohamad@gmail.com

Ali, Asmadi
Faculty of Ocean Engineering, Technology and Informatics) Universiti Malaysia Terenganu Terengganu, Malaysia
asmadi@umt.edu.my

Rasit, Nazaitulshila
Faculty of Ocean Engineering, Technology and Informatics Universiti Malaysia Terenganu Terengganu, Malaysia
nazaitulshila@umt.edu.my

Awang, Mohamad
Faculty of Ocean Engineering, Technology and Informatics Universiti Malaysia Terenganu Terengganu, Malaysia
mohamada@umt.edu.my

Wan Abdul Rahman, Wan Rafizah
Faculty of Ocean Engineering, Technology and Informatics Universiti Malaysia Terenganu Ternggangu, Malaysia
wanrafizah@umt.edu.my

A. Rahman Azmi, Alyza Azzura
Faculty of Science and Marine Environment Universiti Malaysia Terengganu Terengganu, Malaysia
alyza.azzura@umt.edu.my

***Abstract*—A conventional water treatment plant involves a coagulation-flocculation process to remove suspended colloidal and heavy metal to produce safe and clean drinking water to the public. Alum and PAC are the two chemicals that commonly used as coagulant but produced a larger volume of alum sludge at the end of water processing. This schedule waste sludge give obstacle to be disposed and utilization of aluminium based coagulant itself cause harmful effect to the public. This research proposed on the utilization of copperas which is co-product from the titanium dioxide industry as less expensive and less toxicity coagulant for industrial water treatment. For the first stage, the physical and chemical properties of raw water (intake for water processing in palm oil mill) was determined according to required parameters for domestic water. In the second stage of the study, the coagulation process was conducted using a jar test experiment with different formulations of copperas: lime (100: 0, 80:20, 60:40, 40:60 and 20:80 of copperas with lime respectively), different dosage (10-60 mg/L) and initial pH to determine the capability of copperas for water treatment. According to the the treated water, at the lowest dosage used (10 mg/L), native copperas and hybrid copperas: lime (80:20) were able to reduce turbidity around 80-83% with no significant changes of pH. It is hoped that the findings of this first phase of research can be a baseline data/parameter for a larger scale of treatment system and field test for water treatment.**

Keywords—coagulation, copperas, industrial water, water treatment

[1] INTRODUCTION (*Heading 1*)

Global demand for drinking water has been increasing exponentially with the world's population [1]. The growth of population, economic development, rapid urbanization, and climate change causes the countries in the world is facing a condition of water scarcity. In Malaysia, a major contribution of water resources is rainfall as raw surface water but due to the inefficient management of water usage tends to get a water crisis that is not properly treated water as clean drinking water.

Raw water from surface water sources is undergone a primary treatment namely coagulation and flocculation to remove colloidal impurities. This process coagulates colloidal particles into the larger particles of flocs and easy to settle down. Many coagulants and flocculants are widely used in conventional water treatment such as aluminium sulphate, poly-aluminium chloride and etc. The coagulation process could be considered as one of the most typical physicochemical processes used in water treatment due to its easy operation, relatively simple design and low energy consumption [2]. This is attributed to the combined costs of coagulant and pH adjustment chemicals, as well as that of disposal of the resulting sludge or water treatment residual [3].

Copperas or ferrous sulphate heptahydrate, a co-product from the manufacturing of titanium dioxide, was found to be a good alternative to replace alum as a coagulant in water treatment. It was abundantly available, high coagulation efficiency and less expensive. This coagulant had widely used on various types of wastewater treatment such as dye/textile, agricultural wastewater, dairy industry effluent and etc. Teh et al., (2016) reported on the use of ferrous sulphate can reduce about 50% of COD removal [4]. A study conducted on the use of iron (II) sulphate in municipal waste treatment, was found to be very effective coagulants in municipal water to minimize BOD and COD levels [5]. Other than that, copperas can be used in reducing the hexavalent chromium content for the cement industry. It also can be a medicine for allergic and used as a micro-nutrient in the agricultural through the application of using fertilizers.

In this study, jar test experiment was conducted using a different formulation of copperas/lime to industrial water in palm oil mill processing. Optimum parameter such as copperas dosage, pH, and stirring speed were studied. The findings of this research hopefully can unlock the potential of copperas from the titanium dioxide industry for water treatment.

[2] MATERIALS AND METHODS

In this study, raw water was collected from the intake point of water treatment in palm oil mill in Setiu, Terengganu.

Physico-chemical characteristic of water before and after treatment was determined according to the parameter referred by this industry.

Evaluation of copperas as coagulant was carried out by jar-test experiment. Coagulant formulation and dosage are the most critical parameters that should be determined before coagulant is dosed in the plant. Therefore, it was pivotal to determine the ideal formulation (copperas and lime) and dosage of copperas. In this study, coagulant used was copperas, and copperas:lime (80:20, 60:40, 40:60, and 20:80). Alum was used as control. Coagulation-flocculation experiment was carried out in a conventional jar-test apparatus consists of six paddle rotors to coagulate raw water. 1000 mL beaker was filled with 500 mL of raw water for each test run. All tests were performed at ambient temperature in the range of 24-28 ℃. Jar test was conducted at different coagulant dosage (10 to 60 mg/l). The raw sample was introduced to a rapid mixing of 120 rpm for 2 min followed by slow mixing at 80 rpm for 20 min and 30 minutes sedimentation time. The experiment was conducted to determine the effective reduction of turbidity, final pH and total dissolve solid (TDS) for every batch of a trial. After coagulation process, the samples were collected at 2 cm beneath the surface of the treated water for analysis. The parameters that influenced the performance of coagulation process such as copperas dosage, pH and stirring speed will be investigated. The treated and untreated water were analysed to determine the turbidity, pH and iron and manganese residue.

[3] RESULTS AND DISCUSSION.

The selected palm oil mill has processed their own water to be used in crude palm oil processing. In this mill, around 2000 m^3 water has been process daily which utilized 30 kg of alum and 20 kg of soda ash in coagulation treatment. This study was conducted to find out a new approach in coagulation process in which the utilization of copperas from titanium dioxide industry as coagulant and calcium hydroxide as coagulant aid.

A. Effect of coagulant formulation and dosage

Fig. 1 shows the data for turbidity removal of the treated water. It is observed that the removal efficiency of copperas: lime (80:20) was comparable with the capacity of alum to remove the turbidity. Even at the lowest dosage used in this study (10 mg/L), this hybrid coagulant was successfully removed the turbidity around 81.7% and achieved reading up to 6.1 NTU. Compared to alum, at the same dosage used it can only reduce the turbidity up to 9.75 NTU and higher dosage is needed to achieve the turbidity reading around 6 NTU.

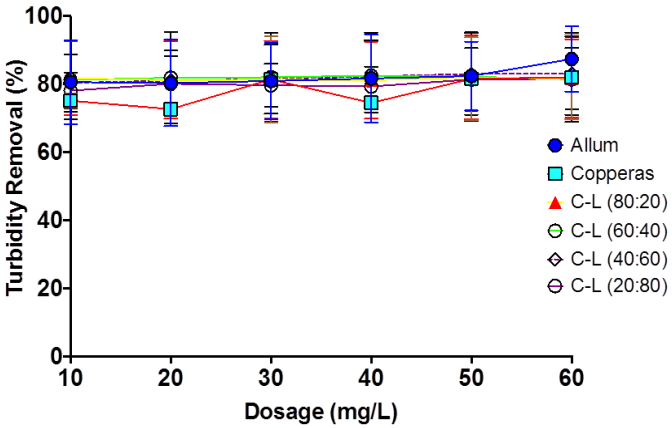


Fig. 1. Effect of coagulant formulation on turbidity removal (%)

Table 1. Effect Of Coagulant Dosage (80:20 Copperas:Lime) On Final Ph, Turbidity, And Total Dissolved Solid (Tds)Table Type Styles

Dosage (mg/L)	Final Turbidity (NTU)	Final TDS (mg/L)	Final pH
10	6.1	0.0303	8.5
20	6.3	0.0321	8.5
30	6.2	0.0301	8.7
40	6.3	0.0310	8.7
50	6.1	0.0312	8.8
60	6.2	0.4350	8.7

B. Effect of initial pH of raw water

Table 2 and Fig. 2 show the variation of turbidity removal efficiencies under the influence of pH for alum and copperas:lime (80:20). It was found that, for both coagulants, the turbidity removal of the effluents decreased with increasing of pH. When the pH of raw water was adjusted to pH 3, coagulation occurred rapidly and achieved the highest turbidity removal of 93.4% for alum and 91.5% for C:L (80:20). Then, the turbidity removal decreased with the increased of initial pH until pH 7. It was observed that the turbidity removal increased again for both coagulants from pH9 to pH11. Comparing both coagulants, alum had slightly higher turbidity removal than C:L (80:20) under the same coagulation pH except at pH 11. Both trends are comparable and had better performance under acidic and alkaline conditions.

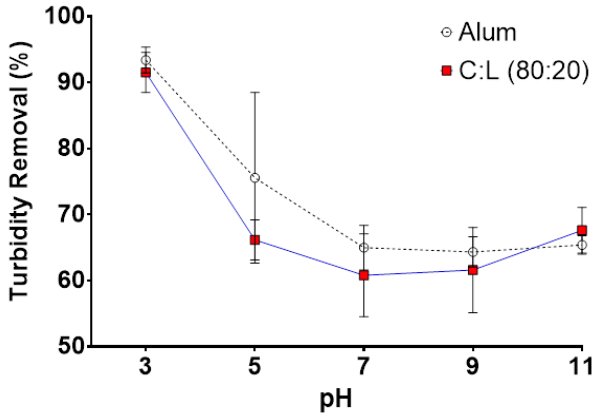


Fig. 2. Effect initial pH on turbidity removal using copperas:lime (80:20)

Table 2. Effect Of Initial Ph Value Of Copperas Dosage (80-20) On Turbidity, Final pH, and Total Dissolved Solid (TDS)

Dosage (mg/L)	Final Turbidity (NTU)	Final TDS (mg/L)	Final pH
10	1.5	0.235	9.5
20	6.2	0.062	9.5
30	7.1	0.088	9.6
40	7.0	0.064	9.6
50	6.1	0.297	9.7
60	1.5	0.235	9.5

C. Effect of stirring speed

Another important factors in achieving higher flocculation efficiency during the coagulation flocculation process is mixing speed. The highest turbidity 19.61 NTU was discovered at the stirring speed of 20 rpm. Turbidity decreased with increasing of stirring speed, and reached to slightly constant turbidity at stirring speed of 40 until 80 rpm. In contradict, TDS recorded the lowest value of 14.95 mg/L at lower stirring speed of 20 rpm and increased with the increased of stirring speed.

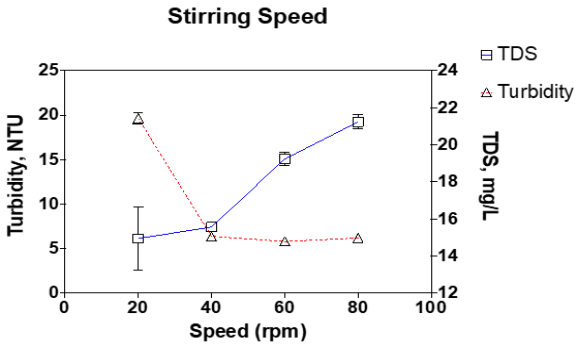


Fig. 3. Effect of stirring speed (rpm) on final turbidity value

[4] CONCLUSION

Overall findings show that copperas has promising performance as coagulant in water treatment. Turbidity removal of treated sample using copperas shows a better or comparable trend to Alum. Formulation of 80:20 of copperas: lime shows the best performance and could be used to run the semi-continuous water treatment skid for the next stage of study.

Generally, the study fulfils the research objectives. Copperas dosing, however, are found to be sensitive towards overdosing and can increase the iron residue in the treated water. It is then recommended a proper jar test and dosing formulation to be studied prior water treatment application in the plant. Different characteristics of raw water react differently and requires different dosing od coagulant. Since, copperas is iron based coagulants; hence overdosing would leave a stain mark on piping, fitting, and preparation site. Proper preparation of coagulant and training should be given to the operator to handle the coagulation process in order to get a clean and safe treated water.

Acknowledgment

The authors wish to Faculty of Ocean Engineering, Technology And Informatics, Universiti Malaysia Terengganu and Venator Asia Sdn. Bhd for the grant award, contribution and supports for this project.

REFERENCES

[1] Shahin, S. A., Mossad, M. & Fouad, M. (2019). Evaluation of Copper Removal Efficiency Using Water Treatment Sludge. *Water Science and Engineering*, 12(1), 37–44. Retrieved from https://doi.org/10.1016/j.wse.2019.04.001

[2] Ahmad, T., Ahmad, K., Ahad, A. & Alam, M. (2016). Characterization of Water Treatment Sludge and Its Reuse as Coagulant. *Journal of Environmental Management*, 182, 606–611. Retrieved from http://dx.doi.org/10.1016/j.jenvman.2016.08.010

[3] Keeley, J., Jarvis, P., Smith, A. D. & Judd, S. J. (2016). Coagulant Recovery and Reuse for Drinking Water Treatment. *Water Research*, 88, 502–509. Retrieved from http://dx.doi.org/10.1016/j.watres.2015.10.038

[4] Teh, C. Y., Budiman, P. M., Shak, K. P. Y. & Wu, T. Y. (2016). Recent Advancement of Coagulation-Flocculation and Its Application in Wastewater Treatment. *Industrial and Engineering Chemistry Research*, 55(16), 4363–4389.

[5] Ngteni, R., Hossain, M. S., Kadir, M. O. A., Asis, A. J. & Tajudin, Z. (2020). Kinetics and Isotherm Modeling for the Treatment of Rubber Processing Euent Using Iron (II) Sulphate Waste as a Coagulant. *Water (Switzerland)*, 12(6).

Modification of bentonite: Effect of different treatments on the adsorption ability - A mini review

Aiizat Ikhwan bin Abdul Jalil
School of Chemical Engineering Kampus Kejuruteraan, Universiti Sains Malaysia, 14300, Nibong Tebal Pulau Pinang. Malaysia
aiizatzack@gmail.com

Suzylawati binti Ismail
School of Chemical Engineering Kampus Kejuruteraan, Universiti Sains Malaysia, 14300, Nibong Tebal Pulau Pinang. Malaysia
chsuzy@usm.my

***Abstract*—The development of low cost and efficient adsorbent materials is high sought after. Bentonite and its modified form had been used for the removal of various type of water contaminants. This paper provides a review on the existing treatment for the modification of bentonite surface and its interlayer and its application in the removal of certain type of wastewater. The selected treatment that is discussed are treatment with epichloropolyhydrin-dimethylamine polyamine (EPI-DMA), metal oxide pillaring and acid activation treatment. The adsorption capacity and efficiency are presented, and the adsorption mechanism is briefly discussed.**

Keywords— Acid activated bentonite, Adsorption, EPI-DMA, Metal oxide pillaring

[1] INTRODUCTION

Adsorption is a method for removing organic and inorganic contaminants from wastewater. Development of various adsorbents for the removal of contaminants from dye and heavy metal wastewater. Clay mineral such bentonite had been used for the adsorption of these wastewater because of its microstructure and adsorptive characteristics. Bentonite is a layered aluminosilicate clay, consisting of sheets of octahedral alumina and tetrahedral silica in 2:1 ratio (Meng et al., 2020). Bentonite's ability to remove cationic ions had been proven by extensively by researchers [1]–[5]. This is due to the negative surface charge caused by the isomorphic substitution of the Al^{3+} cations with Mg^{2+} charge, which are balanced by exchangeable hydrated cations, commonly Na+ and Ca^{2+} in the interlayer space [6]. Modifications were made on bentonite to improve its adsorption ability. For example, methylene blue (MB) dye and copper (II) ions was adsorbed by EDTA-modified bentonite which shown improved adsorption ability. The modified bentonite had an improved adsorption up to 40% for MB dye and 100% for Cu (II) ions [2]. Other than that, bentonite can also be modified to have an improved adsorption ability towards anionic dye. Several treatments such as EPI-DMA treatment, metal oxide pillaring and acid activation were done to modify the surface charge of the adsorbent. These treatments help in improving the ionic attraction between the anionic ions with the changed surface charge of the adsorbent. This mini review discusses on the application of said treatments with its adsorption ability, adsorption efficiency and adsorption mechanism..

[2] BENTONITE TREATMENT METHODS

A. Epichloropolyhydrin-dimethylamine polyamine (EPI-DMA)

EPI-DMA is a non-toxic polycation that had been used to modify bentonite for the adsorption of anionic and cationic compounds [7]. It contains positively charged quaternary amine groups, which had been proved to be and effective decolourizing flocculant but unusable directly in a dynamic adsorption process. However, immobilizing EPI-DMA onto the surface of the bentonite substantially improve the adsorption affinity [8]. EPI-DMA had been utilized for ultrafiltration membrane [9], two-batch adsorption process [10] and adsorptive coating [11]. Each of the process had excellent removal of several type of dyes, such as disperse red (DR) reactive jade blue (RJB), acid scarlet GR(AS-GR) and acid dark blue 2G(ADB-2G) and brilliant green dye (BG) and acid red 1 (AR1). EPI-DMA managed to remove 97.1% of DR, 98.7% of RJB, 99% of AS-GR and ADB-2G, 95% of AR1 and 75% of BG. Meanwhile the adsorption capacity achieved by these processes was found at 93.4 mg/g for DR and RJB, 52.1 mg/g for AS-GR and 52.1 mg/g for ADB-2G, 29.6 mg/g for BG and 33.4 mg/g for AR1. The summary of adsorption capacity by EPI-DMA is shown in Table 1.

B. Metal oxide pillaring (MOP)

Pillaring is a treatment procedure that affect polynuclear cations between the clay layers by influencing the formation, intercalations, and its subsequent fixation. Due to the increase in the lamellar spacing and specific area increase, the resultant product became attractive for various reactions**.**

Pillaring had been used with many type of metals ions such as iron [12], aluminium [13], and chromium [14]. Each metal pillaring had been used diverse types of adsorbates such as rhodamine (RhB), chromium ions and lead (II) ions. Iron pillared bentonite managed to remove 95.7% of 100 mg/L RhB with adsorption capacity of 99.6 mg/g and increase to 246.1 mg/g when the concentration was set to 600 mg/L. Meanwhile, aluminium pillared bentonite adsorbed 10 mg/g of chromium ions with 100% removal. Chromium pillared bentonite managed to record 99% removal of lead (II) ions with 49.99 mg/g adsorption capacity. The pillaring procedure improves the structure of bentonite by increasing the interlayer spacing and increasing its surface area. It was proven by [15] where the specific surface area and pore size had significant increase. The resultant pillared bentonite had an adsorption rate that are 3-4 times higher than normal bentonite. The summary of adsorption capacity by MOP is shown in Table 1.

C. *Acid activated bentonite (AAB)*

Acid activation is the modification of clays, such as bentonite, with a hot solution of mineral acid (HCl or H_2SO_4). The treatment increases the specific surface area, porosity, and the surface acidity [16]. Researchers had implemented several types of acids for bentonite activation such as dicarboxylic acid [17], hydrochloric acid and sulphuric acid [18], [19]. Dicarboxylic acid activated bentonite was crosslinked with cerium metal and was used to the adsorption of fluoride. The adsorption capacity reached was 9.87 mg/g with 98% removal of fluoride. Other than that, hydrochloric and sulphuric acid activated bentonite was used for the removal of methyl orange (MO) dye and ciprofloxacin (CiP). Hydrochloric acid activated bentonite had an adsorption capacity of 274.7 mg/g for MO dye and 305.20 mg/g for CiP. Meanwhile, sulphuric acid activated bentonite had an adsorption capacity of 266.3 mg/g of MO dye. The summary of adsorption capacity by AAB is shown in Table 1.

[3] EFFECT OF PH AND ADSORPTION MECHANISMS

pH played a role in the adsorption ability of EPI-DMA bentonite. Low pH affects the imino groups of the dyes, protonating them, and allowing adsorption in the clay and EPI-DMA [10]. As pH level increase, the molecules are negatively charged, forcing EPI-DMA to be the only adsorption site. At higher pH, hydroxyl ions compete with anionic dye, decreasing adsorption rate. Electrostatic interaction and hydrogen bonding occur in the adsorption process [7]–[9], [11].

Similar findings is also found by [12] for pillared bentonite. They found that in acidic conditions, RhB ions were ionized, changing to a negative charge where it is able to interact with the iron ion in the interlayer of the iron pillared bentonite In neutral and alkaline conditions, the RhB ions are positively charged, allowing electrostatic interactions. In addition, hydrogen bonding could also occur between the hydroxyl group of the iron pillared bentonite and the oxygen of the xanthene ring and aromatic ring of the RhB molecule. The adsorbed water in the interlayer of the iron pillared bentonite also allow interaction with the N and O atoms in the RhB molecule.

The overall treatment of modified bentonite and its results are tabulate in Table 1.

Table 1. Adsorption capacity for removal of various adsorbates by different treatment processes

Bentonite treatment process	***Adsorbate***	***Adsorption capacity (mg/g)***	***Reference***
EPI-DMA	Disperse red	83.4	[9]
EPI-DMA	Acid scarlet GR and acid dark blue 2G dye	AS-GR: 52.1 DRB-2G: 47.0	[10]
EPI-DMA	Green dye and acid red dye	BG: 18.61 – 29.6 AR1: 13.25-33.4	[11]
EPI-DMA	Reactive blue K-GL dye	47.92 – 52.33	[7]
MoP	Rhodamine B dye	246.06	[12]
MoP	Chromium ions	10	[13]
MoP	Deoxynivalenol	-	[15]
MoP	Ethylene	4.75x10^-3	[20]
MoP	Lead (II) ions	49.99	[14]
AAB	Fluoride	9.78	[17]
AAB	Methyl orange dye	RF1: 274.7 RF2: 266.3	[18]
AAB	Copper and lead ions	Copper ion: 17.3 Lead ion: 107.2	[21]

[4] CONCLUSION

The modification of bentonite improves the adsorption ability and increasing the adsorbing range to anionic dyes. Each treatment methods are unique with different affects on the bentonite surface. The immobilization of EPI-DMA on bentonite allows the adsorption of anionic ions. The pillaring of bentonite with metal oxide increase the surface area, spacing and pore size in addition to new active sites due to metal ions. Acid activation increases the specific surface area, porosity, and surface acidity. The mostly found adsorption mechanism is found to be electrostatic interactions and hydrogen bonding. In addition, pH affects both the adsorbent and adsorbates, improving or impeding the adsorption process. Finally, the adsorption of previously difficult pollutants can be overcome with the modification of existing adsorbents.

REFERENCES

[1] M. A. Adebayo, J. I. Adebomi, T. O. Abe, and F. I. Areo, “Removal of aqueous Congo red and malachite green using ackee apple seed – bentonite composite,” *Colloid Interface Sci. Commun.*, vol. 38, no. June, p. 100311, 2020.

[2] M. L. F. A. De Castro, M. L. B. Abad, D. A. G. Sumalinog, R. R. M. Abarca, P. Paoprasert, and M. D. G. de Luna, “Adsorption of Methylene Blue dye and Cu(II) ions on EDTA-modified bentonite: Isotherm, kinetic and thermodynamic studies,” *Sustain. Environ. Res.*, vol. 28, no. 5, pp. 197–205, 2018.

[3] M. Fatiha and B. Belkacem, “Adsorption of methylene blue from aqueous solutions using natural clay,” *J. Mater. Environ. Sci.*, vol. 7, no. 1, pp. 285–292, 2016.

[4] B. A. Fil, C. Özmetin, and M. Korkmaz, “Cationic dye (methylene blue) removal from aqueous solution by montmorillonite,” *Bull. Korean Chem. Soc.*, vol. 33, no. 10, pp. 3184–3190, 2012.

[5] L. Laysandra *et al.*, “Adsorption and photocatalytic performance of bentonite-titanium dioxide composites for methylene blue and rhodamine B decoloration,” *Heliyon*, vol. 3, no. 12, p. e00488, Dec. 2017.

[6] C. S. Jefferson *et al.*, “What happens when chitosan meets bentonite under microwave-assisted conditions ? Clay-based hybrid nanocomposites for dye adsorption,” *Colloids Surfaces A*, vol. 609, no. June 2020, p. 125584, 2021.

[7] Q. Li, Q. Y. Yue, Y. Su, B. Y. Gao, and L. Fu, “Cationic polyelectrolyte/bentonite prepared by ultrasonic technique and its use as adsorbent for Reactive Blue K-GL dye,” *J. Hazard. Mater.*, vol. 147, no. 1–2, pp. 370–380, 2007.

[8] Y. Zhang, K. Xia, X. Liu, Z. Chen, H. Du, and X. Zhang, “Synthesis of cationic-modified silica gel and its adsorption properties for anionic dyes,” *J. Taiwan Inst. Chem. Eng.*, vol. 102, pp. 1–8, 2019.

[9] Q. Y. Yue, Q. Li, B. Y. Gao, A. J. Yuan, and Y. Wang, “Formation and characteristics of cationic-polymer/bentonite complexes as

adsorbents for dyes," *Appl. Clay Sci.*, vol. 35, no. 3–4, pp. 268–275, 2007.

[10] Q. Li, Y. Su, Q. Y. Yue, and B. Y. Gao, "Adsorption of acid dyes onto bentonite modified with polycations: Kinetics study and process design to minimize the contact time," *Appl. Clay Sci.*, vol. 53, no. 4, pp. 760–765, 2011.

[11] S. F. Azha and S. Ismail, "Immobilization of dye pollutants on composite adsorbent coating: Screening, efficiency and adsorption mechanism," *AIP Conf. Proc.*, vol. 2124, no. July, 2019.

[12] H. Xi, Q. Li, Y. Yang, J. Zhang, and F. Guo, "Synergistic modification of bentonite by acid activation and hydroxyl iron pillaring for enhanced dye adsorption capacity," *Water Sci. Technol.*, vol. 81.7, pp. 1518–1529, 2020.

[13] N. Ayub and M. N. Chaudhry, "Efficiency of aluminium pillared montmorillonite clays of Pakistani origin (Peshawar and Samwal) on the adsorption of chromium ions in aqueous solutions," *Polish J. Environ. Stud.*, vol. 30, no. 2, pp. 1039–1050, 2021.

[14] A. Georgescu, F. Nardou, V. Zichil, and I. D. Nistor, "Applied Clay Science Adsorption of lead (II) ions from aqueous solutions onto Cr-pillared clays," *Appl. Clay Sci.*, vol. 152, no. November 2017, pp. 44–50, 2018.

[15] Q. Zhang, Y. Zhang, S. Liu, Y. Wu, Q. Zhou, and Y. Zhang, "Adsorption of deoxynivalenol by pillared montmorillonite," *Food Chem.*, vol. 343, no. July 2019, p. 128391, 2021.

[16] P. Komadel and J. Madejová, "Chapter 10.1 - Acid Activation of Clay Minerals," in *Handbook of Clay Science*, vol. 5, F. Bergaya and G. Lagaly, Eds. Elsevier, 2013, pp. 385–409.

[17] A. Nagaraj, K. Pillay, S. Kishor Kumar, and M. Rajan, "Dicarboxylic acid cross-linked metal ion decorated bentonite clay and chitosan for fluoride removal studies," *RSC Adv.*, vol. 10, no. 28, pp. 16791–16803, 2020.

[18] J. V. Fernandes, A. M. Rodrigues, R. R. Menezes, and G. de A. Neves, "Adsorption of Anionic Dye on the Acid-Functionalized Bentonite," *Materials (Basel).*, vol. 13, no. 3600, pp. 1–19, 2020.

[19] A. Maged, S. Kharbish, I. S. Ismael, and A. Bhatnagar, "Characterization of activated bentonite clay mineral and the mechanisms underlying its sorption for ciprofloxacin from aqueous solution," *Environ. Sci. Pollut. Res.*, vol. 27, no. 26, pp. 32980–32997, 2020.

[20] P. Satwikanitya, I. Prasetyo, M. Fahrurrozi, and T. Ariyanto, "Adsorption of ethylene using cobalt oxide-loaded pillared clay," *J. Eng. Technol. Sci.*, vol. 52, no. 3, pp. 424–435, 2020.

[21] R. R. Pawar, Lalhmunsiama, P. G. Ingole, and S. M. Lee, "Use of activated bentonite-alginate composite beads for efficient removal of toxic Cu2+ and Pb2+ ions from aquatic environment," *Int. J. Biol. Macromol.*, vol. 164, pp. 3145–3154, 2020.

Review on the potential of superhydrophilic polymeric mixed matrix membrane in loop heat pipe application for miniaturized cooling system

Nor Aini Ahmad
School of Chemical Engineering, Engineering Campus, Nibong Tebal Universiti Sains Malaysia Penang, Malaysia
nor_aini@usm.my

Syamsul Rizal Abd Shukor
School of Chemical Engineering, Engineering Campus, Nibong Tebal Universiti Sains Malaysia Penang, Malaysia
chsyamrizal@usm.my

***Abstract*— Miniaturize cooling system is required to solve the heat generation in microprocessor and chip sets that cause damage in electronic components. Wick is an import part in the loop heat pipe for the miniaturized cooling system. Wick acts a capillary pump to complete the circulation of refrigerant liquid and vapour in cooling system. Common wick shows the weaknesses in term of corrosion due to metal oxidation, serious heat leak through the wicks, contact thermal resistance between wicks and vapor. To enhance the HLP performance, superydrophilic mixed matrix membrane shows the great potential as a wick. Superydrophilic mixed matrix membrane with the great wetting properties is developed via the combination of inorganic particles and hydrophilic polymer. The embedded of inorganic particle provides additional surface roughness, increase the overall porosity, hydrophilicity and additional strength to the wick structure. Polymer inorganic blending with sonication process is used for well inorganic particle dispersion. Meanwhile, the desired structure in the mixed matrix membrane can be tuned via phase inversion method. On top of that, superhydrophilic mixed matrix membrane offers flexibility in size and shape, lower production cost and porous structure with higher thermal performance.**

Keywords—*membrane, wick, loop heat pipe, miniaturized, cooling system* (key words**)**

[1] MINIATURIZED COOLING SYSTEM

Semiconductor and other mini and micro-scale technologies resulted increment in power density especially for high performance chips. Hot spots occurs around the microprocessors and chip sets however, the heat is not distributed evenly across a circuit board [1]. Thermal management of electronic devices or microprocessor becomes the technical challenge that need to be solved. The heat generation in the limited space available in the miniaturized electronic devices would cause to overheating, affect the functionality and consequently damage the electronic components [2]. To solve this problem, micro cooling technology is applied by the development of miniaturized loop heat pipe consisted of evaporator, condenser, vapor and liquid lines.

[2] LOOP HEAT PIPE (lhp)

Loop heat pipe (LHP) uses as a miniaturized cooling system with more than two times magnitude of the heat transfer and solve the problem of the electronics thermal control systems compared to conventional heat pipe [3, 4]. Loop heat pipe (LHP) is an effective heat-transfer device that applies the phase-changed latent heat of the refrigerant to transport heat to a heat sink. The application of miniature loop heat pipe effectively dissipate a heat load of 12W at all test orientations under natural convection with zero power consumption when the chip-junction temperatures were below 85 °C and cooling energy savings of up to 80% [5].

Various structures of LHP was proposed by researches a miniature LHP consisting of a flat disk-shaped evaporator [6], LHP with a flat rectangular evaporator and boiling pool [7], LHP with two part separators of boiling and suction chambers [3], flat and cylindrical shapes of evaporator [8]. The cylindrical evaporator efficiently works for linear heat dimension or large heating power compared to flat evaporators when the vapor pressure of working fluid is large. The advantages of flat evaporator is able to reduce heat resistance and weight of the evaporators since that cylinder-flat conversion is unnecessary when the LHPs apply to flat heat sources [9]. Flat evaporators are widely used than cylindrical evaporator since the driving force of the fluid circulation in an LHP is capillary force generated by wick [10]. Meanwhile, porous wick in LHP works as a capillary pump to drive the cycle of refrigerant and block the vapor to back flow into the liquid line at the same time to complete the circulation of the working fluid in the loop [3, 11]. Fig. 1(a) shows a typical LHP is composed of an evaporator, a condenser, a compensator, wicks and fluid lines. The wicks are placed in the evaporator to allow heat transfer over in long distance with small size capillary and less pressure loss. As heat source is applied to the evaporator, the refrigerant liquid evaporates in the evaporator chamber and generate capillary pressure to force the vapour move along the vapour line to the condenser as shown in Fig. 1(b). The presence of wick in the evaporator to prevent the refrigerant vapor back flow to evaporator once the capillary pressure increase.

There are two types of wick used in a HLP. The function of the secondary wick is to ensure that the primary wick maintains wetted with refrigerant liquid all the times especially in microgravity conditions and vent vapor bubbles to the compensation chamber [4, 12]. The wet condition of primary wick provides good thermal link between the compensation chamber and the core which are physically separated in the evaporator [13].

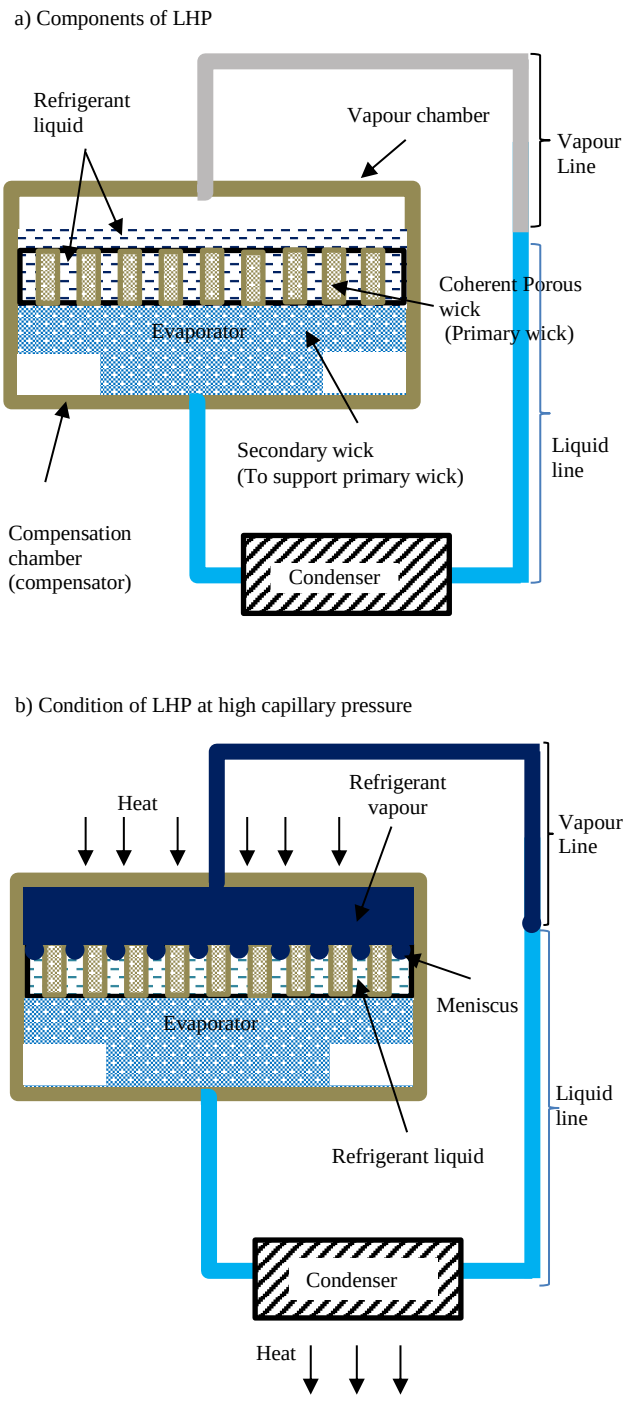


Fig. 1. Component and circulation of an LHP

Wick is significantly affecting the performance of LHP, researches are conducted on the manufacturing method, material, thermal conductivity, porosity, permeability, capillary radius and others. Table 1 shows different types of wicks are used in LHP as reported in literatures. Various metal based wick such as sintered copper [3], copper form [14] and composite stainless steel-nickel 16] are applied in LHP. Metal wicks with high thermal conductivity (TC) can improve the heat transfer by increasing the temperature of the refrigerant liquid in short time and enhance the overall performance of a LHP. High TC wick reduced the startup time and lower thermal resistance [14, 15]. Unfortunately, high TC wicks lead to the increase of heat leakage, especially in the section close to the compensation chamber [16]. Metal based wicks also cause the contact thermal resistance between wicks and vapor. Besides that, common wicking material such as copper, stainless steel, copper-nickel are easily oxidized by the refrigerant liquid and cause corrosion. Although sintered porous wick structures attract considerable attention over the last few decades however the material and the processing methods are expensive, difficult and time-consuming. Thus, many researchers use low thermal conductivity material such as ceramic [17], polytetrafluoroethylene (PTFE) [18], cement [19] and zeolite [20]. In addition, researchers also introduce low thermal conductive coating such as grapheme oxide [21] on the metal wick to improve the heat performance. The present of nanoparticle on the coating layer enhance the surface roughness and surface hydrophilicity for better contact between wick surface and refrigerant liquid [22, 23]. However, thick multilayers or excessive coat on microporous metal wick may cause high mass transfer resistance for the refrigerant liquid to move along the layers/coating and reduce the permeability. Thick multilayers coating on porous copper cause more nucleate-boiling bubbles trapped in nanostructured wicks hence lead to heat pipe failure and burnout of electronic device being cooled [21, 24]. Also there is high possibility for the nanoparticle in the coating leach out when in contact with refrigerant liquid and high refrigerant vapor pressure.

Besides that other factors are considered in the wick selection including porosity, wettability and pore size. The wick with too small pore size and low porosity, is not suggested in LHP due to high thermal resistance. As reported by Zhu, Chen [15] refrigerant liquid tends to adhere to the wick with too small pore size and low porosity. Adhesion of refrigerant to the wick surface is due to high surface tension on the wick. Smaller pore size results high capillary effect, where high pressure is required to force the refrigerant liquid move out from the smaller pore wick [22]. Thus, small amount of refrigerant liquid drips onto the heating surface. Consequently, less the refrigerant liquid evaporate and the degree of superheating become higher resulting to the thermal resistance increment. Meanwhile, wick wettability influences the bubble contact diameter, nucleation frequency of pool-boiling heat transfer and critical heat flux. Wick with great hydrophilicity due to high surface roughness and lower contact angle will increase the wettability and the capillary force. High capillary force will drive the transportation of refrigerant liquid from condenser to the evaporator [20]. Good capillary results to good heat transfer and consequently shows high heat transfer efficiency. Due to poor performance in capillary process and heat transfer, biporous wicks is used to improve the weakness of monoporous wick. The addition of larger pore in the wicks improved the capillary performance of the wick however it reduced the material strength at large heat flux [25].

Based on all the literatures present, wick with least thermal resistant, highly wetted, biporous structure, simple fabrication method, strong yet flexible and affordable are required in HLP for miniaturized cooling system. Thus, superhydrophilic mixed matrix membrane could be used as a wick to improve the performance of LHP.

Table 1. Shows different types of wick used in LHP as reported in literatures

Material/ Fabrication	Features	Ref.
Commerial Ceramic	Porosity: 50% Pore distribution= 1-3 µm T_{conduc}: 4 W/m K Working satisfactory Water = 5 -15 W Acetone = 15 -25 W	[17]
Sintered pure zeolite wick Sintered composite Zeolite/Copper wick	Capillary pump (gr/s) Zeolite 100 µm : 0.45 75% Zeo-25% Cu; 100 µm: 0.74 50% Zeo-50% Cu; 100 µm: 1.15 25% Zeo-75% Cu; 100 µm: 1.46 Capillary pressure (kPa) Zeolite: 6.6 x 10^5 kPa 75% Zeo-25% Cu: 8.4x 10^5 kPa 50% Zeo-50% Cu: 6.7 x 10^5 kPa 25% Zeo-75% Cu: 14.6 x 10^5 kPa Water contact angle (ºC) Zeolite 100 µm: 36.3 75% Zeo-25% Cu: 50.1 50% Zeo-50% Cu: 42.1 25% Zeo-75% Cu; 83.8	[20]
Al_2O_3-coated MoS_2 thin film wick	Pore size (µm) MoS_2 thin: 0.103 ± 0.0027 Al_2O_3-coated MoS_2: 0.128 ± 0.0090 Water contact angle (º) MoS_2 thin: 70.8 ± 1.3 Al_2O_3-coated MoS_2: 55.2 ±1.2	[23]
Sintered polytetrafluoroethylene (PTFE) wick at 363-383 ºC	Pore size: 1.7 µm Porosity: 50% Particle size: 300-500 µm T resistance at using ethanol At 200 W = 0.145 ºC/W	[18]
Sintered nickel wick at 600-650 ºC	Pore size: 3.6 µm Porosity: 70% Type-255 nickel powder T_{resist} at using ethanol At 200 W = 0.156 ºC/W	[18]
Cement-adhesive wick	Pore size: 3 – 10 µm Porosity: 35-45% T_{resist} using water At 5 ºC = 0.729-2.959W/K At 20 ºC = 0.430 W/K At 45 ºC = 0.350 W/K	[19]
Copper screen mesh wick 4 layers mesh with 100 mesh/ inch and wire diameter of 90 µm	Pore size: 90 µm Capillary pressure: 1600 Pa Porosity: 63% Total resistance using water 50W= ~0.70 °C/W 150 W= ~0.25 °C/W 250W= ~ 0.17 °C/W	[26]
Charcoal wick Carbonization at 300 ºC	Combined pore size : 100 µm (long pore) and 6 µm (spherical pore) Porosity: 20% Capillary pressure: 1140 Pa (long pore) 20571 Pa (spherical pore) Total resistance using water 50W= ~0.87 °C/W 150 W= ~0.25 °C/W 250W= ~ 0.17 °C/W	[26]
Sintered Copper felt wick Cutting method using multi-tooth tool	Porosity: 70% T_{resist} using water At 50 W = 0.1480 ºC/W At 75 W = 0.0960 ºC/W At 100 W = 0.0680 ºC/W At 150 W = 0.0315 ºC/W T_{resist} using ethanol At 50 W = 0.1200 ºC/W At 75 W = 0.0990 ºC/W At 100 W = 0.0700 ºC/W At 150 W = 0.0455 ºC/W	[3]
Three layers copper foam wick	Porosity of Cu= 92.57% Porosity of Ni= 96.99% Pore size: 100 pores per inch (both wicks) T_{conduc} Cu = ~337 W/(mK T_{conduc} Ni= 57 W/(mK T_{resist} with Ethanol of Cu and Ni 30 W= ~0.32 ºC/W 100 W= ~0.17 ºC/W T_{resist} with Ethanol of Ni 30 W= ~0.74 ºC/W 100 W= ~0.35 ºC/W	[14]
Stainless steel 3D layers wick	Maximum and minimum thermal resistance at different water temperatures 25 ºC; 12 W: ~0.77 ºC/W 25 ºC; 84 W: 0.260 ºC/W 30 ºC; 12 W: ~0.78 ºC/W 30 ºC;96 W: 0.221 ºC/W 35 ºC; 12 W: ~0.72 ºC/W 35 ºC;108 W: 0.193 40 ºC; 12 W: ~0.59 ºC/W 40 ºC; 96 W: 0.215	[27]
Copper/ Graphene oxide (GO) coating Spray coating	Thickness of Copper: 42.0 ± 0.1 mm Thickness of GO: 3.0 ± 0.1 mm GO coating concentration: 2 mg/l GO volume: 5, 6 & 19 ml Capillary pressure (P_{cap}) Before: ~3.6 to ~3.7 kPa After: ~3.8 to ~4.5 kPa Permeability: Before : ~2.25 to ~5.25 x 10^{-4} m^2 After : ~1.6 to ~1.85 x 10^{-4} m^2 Copper/ 5 ml of GO (best sample): Boiling point (lowest): 12.25 ΔT_{sat},ºC Cooling efficiency, h_{eff}: 15 kWm^{-2} $ºC^{-1}$	[21]
Commercial sintered mixed stainless steel-nickel wick	Pore size: 120, 60, 15 and 5 µm Porosity: 40, 30, 15 and 5 % T_{conduc}: 32 W/m K (both wicks) Refrigerant liquid: Water $T_{resist.}$ at 35 W 120 µm: 1.34 W/ºC 60 µm: 1.41 W/ºC $T_{resist.}$at 45 W 120 µm: 1.1 W/ºC 60 µm: 1.4 W/ºC T_{resist} at 55 W 120 µm: 0.9 W/ºC 60 µm: 0.93 W/ºC No thermal resistance recorded at 15 and 5 µm for 35 to 55 W	[15]

*Thermal resistance ($T_{resist.}$); *Thermal conductivity (T_{conduc})

[3] superhydrophiLic POLYMERIC mixed matrix membrane

Superhydrophilic polymeric mixed matrix membrane with great wetting properties is inheriting the both of inorganic and polymeric properties. Inorganic membrane is hydrophilic, greater chemical resistance, thermal and mechanical stability. However it is brittle, high cost, heavy and complicated process. Meanwhile, polymeric membrane is hydrophilic, low cost, simple process but low mechanical stability. Polymer inorganic blending with sonication [28] and phase inversion method [22, 29] can be used to fabricate mixed matrix membrane with different membrane structure according to the applications. Polymeric systems with the specific functional group being attached at the end of the polymer chain can form chemical bonds with inorganic particles for the fabrication of mixed matrix membrane. The presence of groups can either be ionic or donate lone-pair electrons for chelating effect [30]. Hydrophilic polyethersulfone (PES) with water contact angle about 60-70^{o} is commonly used as the polymer source for porous membrane matrix. PES shows excellent mechanical strength, outstanding chemical resistance and thermal stability. To enhance the PES hydrophilicity by lowering the water contact angle, PES formulation can added with hydrophilic additive such as poly(ethylene glycol) derivatives [31], poly(vinylpyrrolidone) [32] and zwitterionic polymers [33].

Meanwhile, zeolite, metal organic frameworks, graphene oxide, titanium oxide are some examples of inorganic particles. The presence of hydroxyl groups (-OH) in organic particles increase the membrane hydrophilicity [34]. The addition of inorganic particles in the membrane matrix enhances the surface roughness, porosity and strength. The addition of surface roughness on the hydrophilic surface enhance the membrane wetting into superhydrophilic membrane. On the other hand, hydrophilic membrane in aqueous solution commonly faces swelling problem, which significantly affect the membrane structure and performance. However, the addition of inorganic particles provide extra strength by reducing the swelling in the membrane structure [35, 36]. Thus, polymeric mixed matrix membrane with superhydrophilic properties has high potential to be used as wick in LHP for miniaturized cooling system.

Acknowledgment

This work was supported by Ministry of Higher Education Malaysia for providing financial support via FRGS Grant (203. PJKIMIA 6071387) and MyBrain15. Also USM Post-Doctoral Research Fellow Scheme 2020-2021

REFERENCES

1. Congatec. *Full speed ahead while keeping a cool head*. 2020 [cited 2020 April, 6, 2020]; Available from: https://www.congatec.com/en/technologies/cooling-solutions/heat-pipe-cooling.html.
2. Ping, H.C., et al., *High Power Electronic Component: Review.* Rec. Patents Eng., 2008. **2**(3): p. 174-188.
3. Tang, Y., et al., *A novel miniaturized loop heat pipe.* Appl. Therm. Eng., 2010. **30**(10): p. 1152-1158.
4. Ambirajan, A., et al., *Loop Heat Pipes: A Review of Fundamentals, Operation,and Design.* Heat Tran. Eng., 2012. **33**(4-5): p. 387-405.
5. Zhou, G., J. Li, and Z. Jia, *Power-saving exploration for high-end ultra-slim laptop computers with miniature loop heat pipe cooling module.* Appl. Energy, 2019. **239**: p. 859-875.
6. Wang, D., et al., *Experimental study of the loop heat pipe with a flat disk-shaped evaporator.* Exp. Therm. Fluid Sci., 2014. **57**: p. 157-164.
7. Lu, X. and J.-J. Wei, *Experimental study on a novel loop heat pipe with both flat evaporator and boiling pool.* Int. J. Heat Mass Tran., 2014. **79**: p. 54-63.
8. Maydanik, Y.F., M.A. Chernysheva, and V.G. Pastukhov, *Review: Loop heat pipes with flat evaporators.* Appl. Therm. Eng., 2014. **67**(1): p. 294-307.
9. Song, H., et al., *Experimental study of an ammonia loop heat pipe with a flat plate evaporator.* Int. J. Heat Mass Tran., 2016. **102**: p. 1050-1055.
10. Yang, Y., et al., *Experimental investigation and visual observation of a vapor–liquid separated flat loop heat pipe evaporator.* Appl. Therm. Eng., 2016. **101**: p. 71-78.
11. Maydanik, Y.F., *Loop heat pipes.* Appl. Therm. Eng., 2005. **25**(5): p. 635-657.
12. J., K. *Operating Characteristics of Loop Heat Pipes* in *29th International Conference on Environmental System*. 1999. Denver, Colorado. : Society of Automotive Engineers, Inc.
13. Adoni, A.A., Ambirajan, A., Jasvanth, V. S., Kumar, D., Dutta, P., *Effects of Mass of Charge on Loop Heat Pipe Operational Characteristics.* J. Thermoplastic. Heat Tran. Eng., 2009. **23**(2): p. 346-355.
14. Zhou, W., et al., *Development and tests of loop heat pipe with multi-layer metal foams as wick structure.* Appl. Therm. Eng., 2016. **94**: p. 324-330.
15. Zhu, K., et al., *Operation characteristics of a new-type loop heat pipe (LHP) with wick separated from heating surface in the evaporator.* Appl. Therm. Eng., 2017. **123**: p. 1034-1041.
16. Xin, G., et al., *Development of composite wicks having different thermal conductivities for loop heat pipes.* Appl. Therm. Eng., 2018. **136**: p. 229-236.
17. Santos, P.H.D., et al., *Development of LHPs with ceramic wick.* Appl. Therm. Eng., 2010. **30**(13): p. 1784-1789.
18. Wu, S.-C., et al., *Study of PTFE wick structure applied to loop heat pipe.* Appl. Therm. Eng., 2015. **81**: p. 51-57.
19. He, S., et al., *Experimental study on transient performance of the loop heat pipe with a pouring porous wick.* Appl. Therm. Eng., 2020. **164**: p. 114450.
20. Midiani, L.P.I., et al., *Characterization of capillary pumping amount in novel sintered zeolites and hybrid zeolite-Cu for heat pipe applications.* Int. J. Heat Mass Tran., 2019. **145**: p. 118759.
21. Jo, H.S., et al., *Modifying capillary pressure and boiling regime of micro-porous wicks textured with graphene oxide.* Appl. Therm. Eng., 2018. **128**: p. 1605-1610.
22. Ahmad, N.A., et al., *Membranes with Great Hydrophobicity: A Review on Preparation and Characterization.* Sep. Purif. Rev., 2015. **44**(2): p. 109-134.
23. Liu, P., Y. Zhu, and S. Zhang, *Hydrophilicity characterization of Al2O3-coated MoS2 particles by using thin layer wicking and sessile drop method.* Powder Technol., 2015. **281**: p. 83-90.
24. Choi, J., et al. *Experimental Investigation on Boiling Phenomena of Bi-Layer Composite Porous Wicks Textured With Nano-Porous Layer*. in *ASME 2014 International Mechanical Engineering Congress and Exposition*. 2014.
25. Ling, W., et al., *Thermal performance of loop heat pipe with porous copper fiber sintered sheet as wick structure.* Appl. Therm. Eng., 2016. **108**: p. 251-260.
26. Solomon, A.B., et al., *Application of bio-wick in compact loop heat pipe.* Appl. Therm. Eng., 2020. **169**: p. 114927.
27. Li, J. and L. Lv, *Experimental studies on a novel thin flat heat pipe heat spreader.* Appl. Therm. Eng., 2016. **93**: p. 139-146.
28. Ahmad, N.A., et al., *CO_2 removal using membrane gas absorption with PVDF membrane incorporated with POSS and SAPO-34 zeolite.* Chem. Eng. Res. Design, 2017. **118**: p. 238-247.
29. De Guzman, M.R., et al., *Increased performance and antifouling of mixed-matrix membranes of cellulose acetate with hydrophilic nanoparticles of polydopamine-sulfobetaine methacrylate for oil-water separation.* J. Membr. Sci., 2021. **620**: p. 118881.
30. Bashambu, L., R. Singh, and J. Verma, *Metal/metal oxide nanocomposite membranes for water purification.* Mat. Today: Proceedings, 2020.
31. Zhang, S., et al., *Fast and facile fabrication of antifouling and hemocompatible PVDF membrane tethered with amino-acid modified PEG film.* Appl. Surf. Sci., 2018. **428**: p. 41-53.
32. Song, H., et al., *Hemocompatibility and ultrafiltration performance of surface-functionalized polyethersulfone membrane by blending comb-like amphiphilic block copolymer.* J. Membr. Sci., 2014. **471**: p. 319-327.
33. Wang, J., M. Qiu, and C. He, *A zwitterionic polymer/PES membrane for enhanced antifouling performance and promoting hemocompatibility.* J.

Membr. Sci., 2020. **606**: p. 118119.
34. Lu, J., et al., *FAS grafted superhydrophobic ceramic membrane.* Appl. Surf. Sci., 2009. **255**(22): p. 9092-9099.
35. Xie, Z., et al., *Separation of aqueous salt solution by pervaporation through hybrid organic–inorganic membrane: Effect of operating conditions.* Desalination, 2011. **273**(1): p. 220-225.
36. Ahmad, N.A., C.P. Leo, and A.L. Ahmad, *Amine wetting evaluation on hydrophobic silane modified polyvinylidene fluoride/silicoaluminophosphate zeolite membrane for membrane gas absorption.* J. Nat. Gas Sci. Eng., 2018. **58**: p. 115-125.

A New Heat Sink Design for Cooling Microprocessors and Investigation of Cooling Performance

Mehmet Emin Arzutuğ
Dept. of Chemical Engineering Ataturk University Erzurum, Turkey
arzutug@atauni.edu.tr

Abdullah Başçi
Dept. of Electrical & Electronics Engineering Ataturk University Erzurum, Turkey
abasci@atauni.edu.tr

***Abstract*— In this study, a new generation heat sink developed to meet the heat absorption needs of new generation central processing unit (CPU) and its experimental performance has been investigated. In the development of the heat sink, it combines three effects such as swirl flow, mini-channel and nanofluid, which are effective on heat transfer. However, in the presented study, a water-ethylene glycol mixture only without nanoparticle has been used in the mini-channels which used as heat fins of the cooler. In addition, the cooling surface is 20 times larger than the heater surface in the design. So, absorbed heat from CPU is easily removed in the heat sink to the air by using liquid flow. Also, a pump providing liquid flow, a fan providing air flow and a control card controlling the pump and fan depending on the surface temperature are used in the designed cooler. According to experimental data, the heat flux reached in 10 minutes is 820 W/cm^2. The energy absorbed is 103 times more than that produced in the first minute and 309 times more in the 10th minute. As a result, in the proposed design, the heat removed from the CPU is increased compared to the heat absorbed by the conventional air cooler.**

Keywords*— *Heat sink, Swirl flow, Heat Fin, Nano-fluid, Mini-channel, Central processing unit, Heat flux.

[1] INTRODUCTION

Thermal energy removal with high heat flux by using swirl flows and single-phase nanofluids flowing in mini-channels is one of the new technologies for cooling of new generation CPUs. CPUs, one of the most important inventions offered by advanced technology, are used in many fields such as industry, robotics, communication, automotive, space technology as well as computers located at the centre of human life. Today, the heat thrown into the air by the CPU of a current desktop computer is between 50 and 150W and the normal operating temperatures range is between 55 and 85^{o}C. Depending on the processing speed of the CPUs, the amount of current flowing over them changes and they get warm with the increase in the amount of current. Because the materials from which CPUs are manufactured are only suitable for operation in certain temperature ranges, if the critical temperature of 120^{o}C is exceeded, the CPUs can be physically damaged. The main challenge in cooling CPUs is to dissipate more heat than is produced while keeping the CPU temperature below the target temperature of 85^{o}C [1].

Nowadays, it is known that the average heat flux of new generation CPUs and MEMSs under normal operating conditions is 150 W/cm^2 and this value also reaches a peak value of 250 W/cm^2 in some cases. In order for the new generation CPUs to operate in a safe temperature range, this heat must be removed with a higher heat flux (such as 1000 W/cm^2). The cooling of the new generation CPUs will not be solved by conventional heat sinks, but by the production of compact and highly effective new generation heat sinks that can electronically control the heat absorption rate. Kazuhisa Yuki [2] has made experimental study about minichannel heat sinks. He has used single phase fluid in minichannels with different thickness, channel width, number of fins. At the end of experiment, he has reported that heat flux of heat sink has been reached 300W/cm^2. In the research which used single phase fluid and minichannels or microchannels for cooling CPUs has been reported that absorbed heat per cm^2 from CPU has been measured respectively 109, 428, 790 and 1250W by Bruno et al. [3], Lee and Hoo [4], Pijenburg et al. [5], Tuckerman-Pease [6] and Prasher et al. [7].

Heat transfer, in heat exchangers generally occurs between two fluids and a metal wall separating them. Creating strong turbulent flows on both sides of this wall, using nanofluids in both fluids and using mini-channels to increase the surface area of this wall has a positive effect for heat transfer. It is known that turbulent flows, one of the flow types, have a great positive effect on heat/mass transfer. Swirl flow, which is one of the strong turbulent flows, also increases the convective heat transfer on the heat transfer surface and provides high heat fluxes between the fluid and the solid surface. Turbulent flows reduces the thermal resistance by affecting boundary layer thickness. The role of nanofluid's flows in reducing the thermal resistance is provided by the nanoparticles forming micro-sized vortexes in the boundary layer because of Brownian Motion [8,9]. Since the use of mini or micro channels in flow systems increases the heat/mass transfer area that comes into contact with the single phase fluid, as in finned surfaces, the heat/mass transfer between the solid surface and the fluid increases [10].

Many researchers such as Kakaç et al. [9], Lee et al. [11] and Masuda et al. [12] found the effective thermal conductivity of heat transfer solutions of nanoparticles with low concentration (1-5%) such as Al_2O_3, CuO, Cu, SiO, TiO and stated that it could increase the convective heat transfer coefficient by more than 20%. The improvement of mass transfer using nanofluids is explained by three different mechanisms: hydrodynamics, diffusion, and blocking of the active surface by solid particles. It has been noted by the researchers that the first two mechanisms increase the mass transfer rate, but the third mechanism decreases the mass transfer rate [13,14]. In the case of using nanofluids, generating swirl flow in the swirl flow channel, collapse and clumping in the developed cooler will be prevented. Thus, the accumulation of solid nanoparticles on the heat transfer surface, i.e. the formation of thermal resistance, would be prevented.

In the literature, researchers have informed that the liquid-cooled heat sink can provide almost an order of magnitude reduction in thermal resistance due to the higher thermal conductivity of water. Based on studies about cooling of CPU in recent years [15], it is seen that conventional air cooling systems are insufficient for new generation CPUs. Besides, the heat absorbers using dual-phase fluids require a lot of power, a pump, a condenser surge valve and a radiator. For these reasons, the development of new generation heat coolers is one of the primary issues in heat transfer studies [15].

In the heat sink developing in this research, the water with 5% (v/v) ethylene glycol solution without nanoparticles was used as a heat transfer fluid. The main factors that affect the heat sink thermal performance are air velocity, choice of material, and fin design [15]. The used fins in this research have the mini-channel geometry and there is fluid flow in fins. However, the conventional type heat sink which is rod, but there is no fluid flow in the fins. So, in used the conventional type heat sinks, heat is transferred by conduction in the fins and exhausted by convection to air. However, in the heat sinks developed in this research, heat is transferred by convection mainly in the fins and exhausted by convection to air, also.

In this study, a new generation heat sink, consisting only of water-ethyleneglycol without any phase change and not containing nanofluid, is developed and its heat absorption performance compared to conventional systems has been investigated. Experimental results shown that the heat sink developed absorbs much higher heat than conventional systems and can be used reliably in desktop computers, workstation systems and MEMS.

[2] METHOD

The heat sink designed in this research consists of three parts as shown in Figure 1. In the heat sink, water and ethylene glycol (5.0%) mixture is used as a heat carrier fluid. The lowest part called as the swirl flow chamber, is made of aluminium, and contacts with the CPU. In this part, the liquid swirl stream is generated and transferred upward in a vertical pipe. In the middle section where there are mini-channels positioned laterally, liquid flow in the vertical pipe is poured into an annular flow channel by passing through the mini channels. Mini-channels made of copper are used as heat fins in the heat sink. The heat transfer fluid, which is taken into an annular geometry chamber, is then collected in a storage tank, from here it is suctioned by a centrifugal pump and pumped back to the swirl flow chamber. The air turbine (24,000 rpm) that is placed at the top of the heat sink provides air flow over the mini-channels used as heat fins. thus, the heat transferred by liquid flow is thrown into the air by convection from the outer surface of 264 mini-channels with a length of 2.60cm and an inner diameter of 0.8mm. Both the liquid pump and the air turbine are controlled by the control card.

In the current study, an aluminium heater block with a size of 40x40x10mm^3 with two resistors inside was used instead of the CPU. This aluminium block gives a constant flux of heat from the surface of the heater that touches the heat sink. However, the other surfaces of the heater are insulated against heat transfer with an insulating material. Electrical energy is transformed into heat energy with 100% efficiency. So, the produced heat in heater have been transferred to heat sink. The aluminium heater is designed by passing electrical current through two 40W resistors placed in an aluminium block.

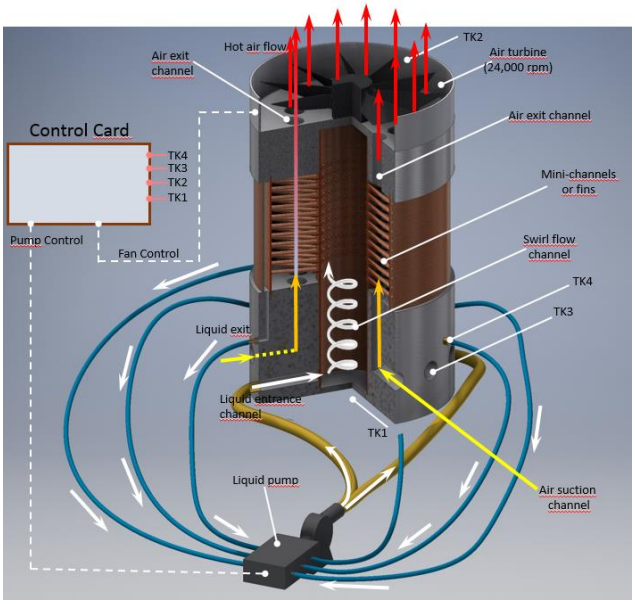


Fig. 1. Schematic representation of the heat sink system.

According to the design in the research, the heat drawn from a small surface of 40mmx40mm size is discharged from a large surface. In addition, the heat carried by the convection mechanism in the fin is thrown into the air by convection. The photograph of the prototype of heat sink and structure of mini-channels are shown Figure 2.

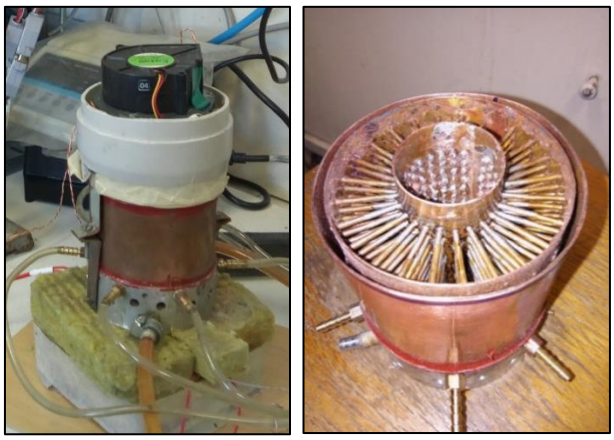


Fig. 2. The prototype of heat sink and structure of mini-channels.

With a control card mounted on the system, the speed of the pumps and fans can be controlled, thus it is aimed to provide energy efficiency and reduce the noise level. One simple CPU cooling solution is accomplished via the use of a basic heat sink. Conventional a heat sink used to cool a CPU dissipate heat generated within a solid material to air. A heat sink is used to increase the contact surface of a solid material that comes into contact with a fluid or fluid flow on the solid surface. Heat sink performance have been tested by using the system in Figure 3. In this system, an aluminium block of 2 cm in height and 4cmx4cm in size was placed between the heat absorber and the heater, and silver paste was applied to the contact surfaces to reduce the thermal contact resistance. Aluminium block and heater are insulated with rock wool heat insulation material on all sides. Thus, the generated heat is only transferred to the upstream, that is, to the heat absorber.

[3] EXPERIMANTAL RESULTS

By applying 1.5A electric current at a constant current to

the heater, the heat with a constant heat flux is transferred to the heat sink through the aluminium block. After steady state conditions are met, temperature measurement is made using 2 thermocouples placed at T_1 and T_2 points shown in Figure 3. Aluminum material heat conduction coefficient (k) is 240W/mK as obtained from the literature [16]. The product of the heater's current output value gives the value of heat produced. In the expression of Fourier's Law (Equation-1), the value of k, the difference between T_1 and T_2 temperatures and the distance between the two temperature measurement points (1.5cm) was replaced by the thermal flow rate (J/s).

$$\boldsymbol{Q = -kA\frac{\Delta T}{\Delta z}} \quad (1)$$

where, A is the cross-sectional area in the direction where heat transfer occurs. (m^2).

ΔT is the temperature difference between T_1 and T_2, (^oC).

z is direction where heat transfer occurs, (m).

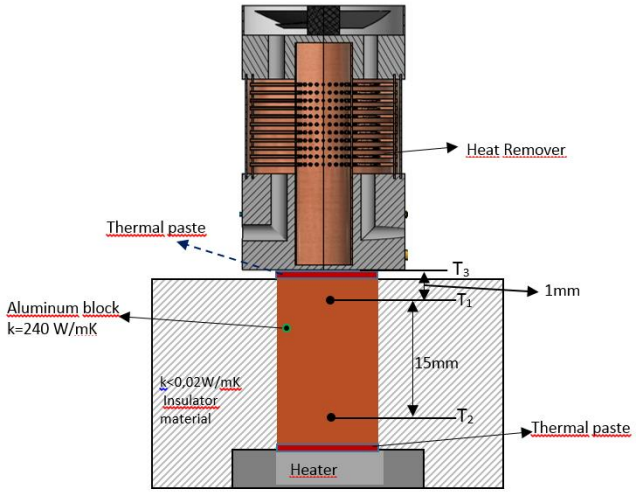


Fig. 3. Heat sink performance test system.

The heat flux values were measured when the swirl intensity was 0.5 in case of constant air flow and the water-ethylene glycol flow rate was 2.84 L/min. A powerful pump has been used to overcome pressure drop, and to attain fluid flow in the system.

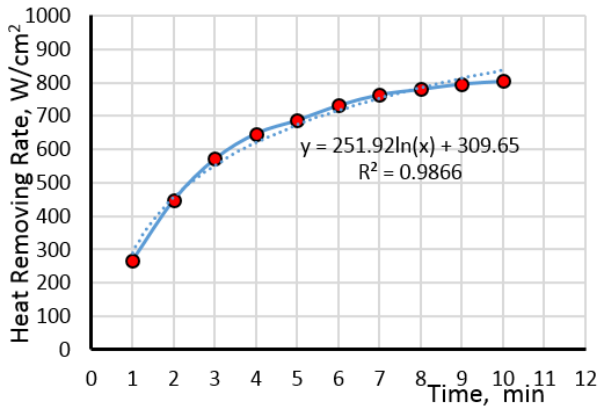


Fig. 4. The cooling performance of the heat sink.

According to the temperature data obtained at different times, the heat flux values (W/cm^2) of the heat sink are measured and graphed in Figure 4. It was observed that the heat absorbed according to the increasing time increased exponentially. According to the graph, it was seen that the heat absorbed with increasing time increased exponentially. It is seen that temperature change with time on the contact surface of the heat sink and the aluminium heater in Figure 5. According to this graph, it was observed that the temperature dropped sharply and remained constant at $60W/cm^2$ after 10 minutes.

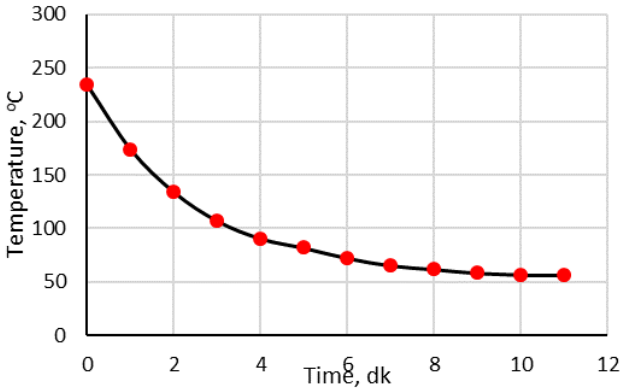


Fig. 5. Temperature change with time on the contact surface of the heat sink and the aluminum heater.

When the heat energy produced by the CPU and the heat energy absorbed by the heat sink is compared, it is seen from Figure 6. that the heat absorbed in the first minute is 103 times greater than the heat produced by CPU. At the end of 10 minutes, it is seen that the absorbed heat is 310 times greater than the heat produced by the CPU.

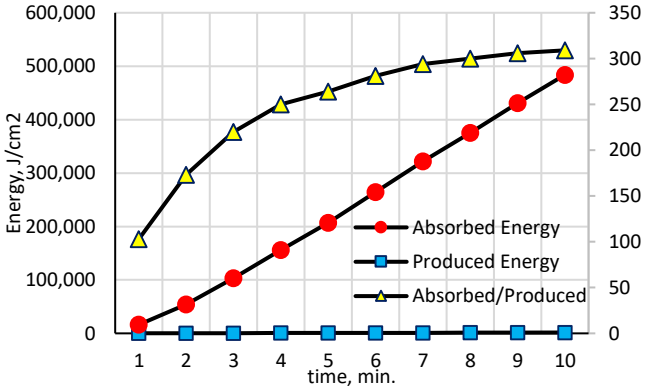


Fig. 6. Absorbed heat energy by heat sink versus produced energy by CPU.

According to the experimental results, it was determined that in case of constant air flow, the swirl intensity, and the constant flow rate of water- ethylene glycol mixture (without nanofluid), the absorbed heat reached 820 W/cm^2 in ten minutes. Testing of other parameters continues within the scope of the research. The purpose of designing a heat sink with this performance is to lower the CPU temperature very quickly when needed.

[4] CONCLUSION

With the use of proposed heat sink, the absorbed heat per cm^2 is increased compared to the heat flux value of a conventional air cooler of 200 or $250W/cm^2$. Thus, the heat was absorbed more quickly from the CPU surface and sent to the mini channels faster than the conventional heat sink. The heat in the cooler is transferred to the mini channels (fins) and from the outer surface of the mini channels to the air by

convection. In the study, it was tested whether the heat can be absorbed at high fluxes with only the designed heat exchanger without considering the energy consumption (pumping and air turbine energy costs). As a result, it has been found that almost twice more heat has been absorbed than that of a conventional air cooler with the same surface area as the proposed heatsink.

REFERENCES

[1] A.Kays, T. Al, H.A. Eqbal and N.J. Namal, "Experimental investigation of water cooled minichannel heat sink for computer processing unit cooling", Int. Journal of Engineering Research and Application, vol 7(3), pp. 38-49, 2017.

[2] K. Yuki and K. Suzuki, "Applicability of minichannel cooling fins to the next generation power devices as a single-phase-flow heat transfer device,"Transactions of The Japan Institute of Electronics Packaging, vol.4(1), pp.52-60, 2011.

[3] B. Agostini, M. Fabbri, J.E. Park, L. Wojtan, J.R. Thome and B. Michel, "State of the Art of High Heat Flux Cooling Technologies," Heat Transfer Enginnering, vol. 28(4), pp. 258-281, 2007.

[4] P.S. Lee and J.C. Ho, "Experimental study on laminer heat transfer in microchannel heat sink" Proc. Inter. Society Conference on Thermal Phenomena, (2002), pp.379-386.

[5] R.H.V. Pijenburg, R. Dekker, C.C.S. Nicole, A. Aubry and E.H.E.C. Eummelen, "Integrated-microchannel coling in silicone" Proc. Solid-State Device Research Conf., (2004), pp.129-132.

[6] D.B. Tuckerman and R.F.W. Pease, "High-Performance Heat Sink for VLSI", IEEE Electron Device Letters, vol.2, p.p. 126-129, 1981.

[7] R.S. Prasher, J.Y. Chang, L. Sauciuc, S. Narasimhan, D. Chau, G. Chrysler, A. Myers, S. Prstic, C. Hu, Nano and Micro Technology – Based Next generation Package-Level cooling solutions, Intel Technology Journal, Electronic Package Technology Development, vol. 9(4), p.p.285-296, 2005.

[8] H.A. Mohamed, G. Bhaskaran, N.H. Shuaib, R. Saidur, "Heat transfer and fluid flow characteristics in microchannels heat exchanger using nanofluids: A review", Renewable and Sustainable Energy Reviews, vol.15, p.p.1502-1512, 2011.

[9] S. Kakaç and A. Pramuanjaroenkij, "Review of convective heat transfer enhancement with nanofluids, International Journal of Heat and Mass Transfer, vol.52, p.p. 3187-3196, 2009.

[10] T. Dixit and I. Ghosh, "Review of micro-and mini-channel heat sinks and heat exchangers for single phase fluids", Renewable and Sustainable Energy Reviews, vol. 41, p.p. 1298-1311, 2015.

[11] S. Lee, S.U.S. Choi, S. Li, J.A. Eastman, "Measuring thermal conductivity of fluids containing oxide nanoparticles, Trans. ASME J. Heat Transfer", vol.121, p.p.280-289, 1999.

[12] H. Masuda, A. Ebata, K.Teramae, N. Hishinuma, "Alteration of thermal conductivity and viscosity of liquid by dispersing ultra fine particles (Dispersion of g-Al_2O_3, SiO_2, and TiO_2 ultra-fine particles)", Netsu Bussei, vol.7, p.p. 227-233, 1993.

[13] O.N. Sara, F. Içer, S. Yapıcı, B. Sahin, "Effect of suspended CuO nanoparticles on mass transfer to a rotating disc electrode", Experimental Thermal and Fluid Science, vol.35, p.p. 558-564, 2011.

[14] A. Caprani, M. Marie de Fricquelmont-Loizos, L. Tamisier, P. Peronneau, "Mass transfer in laminer flow at a rotating disc electrode in suspensions of inert particles, Journal of the Electrochemical Society, vol.135(3), p.p. 635-642, 1988.

[15] J.D. Carr, "An Examination of CPU cooling technologies", (Thermal Management Options for Engineers). PDF online: https://dsiventures.com/wp-content/uploads/2019/04/CPU-Cooling-Technologies.pdf

[16] The heat transfer coefficient of Al material (The Engineering Toolbox web page). Existed Online: https://www.engineeringtoolbox.com/heat-exchanger-material-thermal-conductivities-d_1488.html

Boiler Efficiency and CO2 Emission with Different Types of Bituminous Coal at Thermal Coal Fired Power Plant

Salmi b Samsudin
Department of Mechanical & Manufacturing Engineering Faculty of Engineering University Putra Malaysia
Selangor, Malaysia
salmis@tnb.com.my

Nuraini bt Abd Aziz
Department of Mechanical & Manufacturing Engineering Faculty of Engineering University Putra Malaysia
Selangor, Malaysia
nuraini@upm.edu.my

Abdul Aziz b Hairuddin
Department of Mechanical & Manufacturing Engineering Faculty of Engineering University Putra Malaysia
Selangor, Malaysia
ahziz@upm.edu.my

Siti Ujila bt Masuri
Department of Mechanical & Manufacturing Engineering Faculty of Engineering University Putra Malaysia Selangor, Malaysia
ujila@upm.edu.my

Abstract **− In 2021, coal-fired power generation is expected to increase by 2.8 percent which mostly contributes to Asian country demand. The market for renewable energy is increasing but with slow expansion due to cost and reliability in supplying power. Forecast by International Energy Agency (IEA) in 2018, the thermal coal plant was the main contributor in generating electricity until the year 2040. Faced with the stringent environment policy gazette by the government, thermal coal plants must manage and control the emission emit to the environment. Besides supporting the national growth, is essential to reduce hazardous emission such CO2 in maintaining a sustainable environment. Therefore, power plants must study the mechanism to reduce CO2 by looking at the power plant process, fuel types, upgrading machines, and other alternatives. An experimental study was conducted at a thermal coal plant generating 700 megawatts in evaluating the fuel types factor to the CO2 emission produced. This study focus to find out the relation between the boiler plant efficiency which outcome of the power plant process to the fuel types, coal. Coal has been used as fuel at thermal plants generating 700 megawatts. This study found the different coal types resulted in different boiler efficiency and produce less CO2 to the environment. Coal with a high calorific value (CV) produces less CO2 and coal with high CV produces a high rate of CO2 emitted to the environment. Moreover, the study found an increase of 1 percent boiler efficiency resulted in decreasing from 11 percent to 8 percent of CO2 release to the atmosphere.**

Keywords— Thermal Plant, Coal, Efficiency, CO2 Emission

[1] INTRODUCTION

Global consumption for the electricity sector is forecast to rebound about 2.9 percent in 2021 which is exceeding compared to the year 2019 [10]. Applicable methods to improve efficiency and heat rate at thermal coal plants will help to reduce emissions to the environment. Indirectly, it could have a trembling effect on fuel saving and reduced greenhouse gas emissions. Therefore, every step should be taken to enhance the efficiency and heat rate of the steam power cycle. As suggested by most researchers, integrating and upgrading the CO2 capture unit to remove CO2 from flue gas on the combustion process before emit to the atmosphere can improve the CO2 emission [2] [4] [10]. It's can be archived by improving the net efficiency of the power generation cycle including combustion process, heat rate, and upgrading the operational mechanism installed. Moreover, the power plant operating condition and procedure may strategize and adjust according to the designed power plant process and configuration. Such a process; pre-heating, sealing mechanism, and protection system would be establishing for utilizing the proper resources within the power plant system [3], [2]. For the thermal coal plant, several methodologies can be applied to gain maximum plant efficiency with minimum coal consumption. Reduction in coal consumption at specific net power output as electrical energy resulting from a less rate of CO2 emitted to the environment [13], [15]. Power plant performance can be described by measuring the heat rate and efficiency. The efficiency for the power plant is referring to the conversion from the energy of fuel as input to the electrical energy as output. The means of heat rate can be defined as:

$$HR = F / E \quad (1)$$

where,

HR = ratio of heat rate, Btu/kWh

F = input of energy from the heat energy of fuel

E = output of energy (generating)

The heat rate for the thermal coal plant describes the efficiency of the unit in generating electricity. Less heat in producing electricity makes the heat rate better. Consequently, a generating unit can thus improve its efficiency by reducing the fuel it uses relative to a specific amount of electricity generated, thus reducing the amount of CO2 emitted. A percentage improvement in heat rate is nearly equivalent to an equal percentage improvement in the emissions rate in terms of the change in CO2 emissions. The difference stems from the small variation in carbon per Btu across coal varieties [11]. The heterogeneity in heat rates across coal-fired generation units can partly be explained by technical characteristics determined at the time of plant construction that cannot be changed without a major overhaul. This category includes size, age, firing type, and the technology employed. Higher efficiency is generally associated with plants that are used more efficient manner [3], [14].

Besides, the boiler must operation insufficient manners. The relationship between the heat rate and utilization is responding accordingly, as efficiency tends to be lower at very low and very high levels of utilization [5]. Such methodology, boiler with lower utilization may be ramped up and down more frequently, which requires additional fuel input as the temperature in the boiler fluctuates. Moreover, fuel types and behaviour of the plant parameters contribute to that as well. Besides, the result of plant efficiency measures the losses from the power plant process. It helps the operator on monitoring and control the plant and partially make a proper action plan [4], [15]. Several factors shall consider by the plant managers on controlling the power plant process. The techniques, management, technology, and process may improvise the existing efficiency of the plant. Major components and mechanisms involved in the combustion process such as oxygen, types of fuel, temperature, and pressure must improve as well [2], [8].

As discussed before, the effectiveness of combustion in converting the internal energy into heat energy with the sufficient process describers thermal plant efficiency [1], [8]. Factor cause the heat process lower can affect the efficiency of the plant. Heat transfer mechanism, conduction, convection, and radiation is taking part in the power plant process including the combustion. As such, the boiler efficiency is calculated with the ratio of heat output and input. Efficiency is presented in percentage according to the (British Standard, BS 845:1987, the year 1987. Thus, boiler efficiency is the ratio of heat output to heat input. In addition, the boiler efficiency is an indicator to measure the optimum process of heat transfer by the equipment involved [11], [13].

The chemical reaction between fuel and oxygen involves in the combustion process. Reaction rapidly takes part in performing combustion. When combustible elements of fuel combine with O2, heat energy comes out. During combustion combustible elements like Carbon, Sulphur, Hydrogen, combine with oxygen and produce respective oxides. The source of oxygen in fuel combustion is air. By volume, there is 21% of Oxygen presents in the air and by weight, it is 23.2% [4], [12]. In fact, about 79% of volume nitrogen in the air not involves in combustion proses and the reaction characteristically gives off hear and light as well. The complete combustion performs as equation below:

$$\text{Fuel} + O2 \rightarrow CO2 + H2O \qquad (2)$$

The heat transfer is directly related to the CO emission emitted to the atmosphere. In calculating the fuel content with Carbon Dioxide, the specific carbon content in the fuel must be multiplied by the weight of CO2 molecular to the carbon weight of molecular. Therefore, the emission of Carbon Dioxide can be measured as below:

$$qCO2 = cf / hf\ MCO2 / Mm \qquad (3)$$

The qCO2 is the specific CO2 emission [kgCO2/kWh], cf is defines as specific carbon content in the fuel [kgC/kgfuel], hf is representing the specific energy content in the fuel [kWh/kgfuel], MC is for Molecular Weight Carbon [kg/kmol Carbon] and MCO2 measures the Molecular Weight Carbon Dioxide [kg/kmol CO2]. CO2 emission is directly related to the specific heat energy content, carbon content, and molecular weight. The less heat from fuel consumption, the less CO2 emitted to the atmosphere. Agreed by most researchers, heat rate is affecting the power plant performance [3], [15], [16]. In contrast, heat rate measures the efficiency of the thermal plant. In meantime, heat rate is influencing by considering power plant Greenhouse Gas (GHG) emissions for carbon dioxide output for every unit of energy production for each capacity [1], [15]. Supporting that, the figure below demonstrates the relationship between efficiency for the supercritical thermal plants the CO2 emission.

Bituminous coal was used as the main fuel type for this supercritical thermal plant. The figure, its shows decreasing in the percent CO2 emitted to the atmosphere with the increase of net plant efficiency.

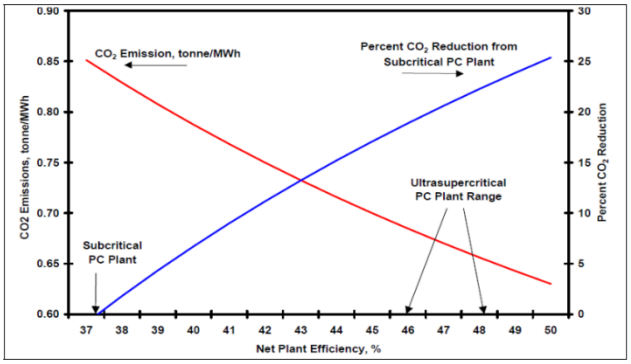


Fig. 1. Carbon Dioxide Emissions vs. Net Plant Efficiency (IEA, 2018)

According to the previous research, the power plants are aggressively looking for the opportunity to improve efficiency and in the meantime reducing gas emission. Power plants exploring the methodology and exploring the new mechanism to achieve that. It's proven when the subcritical plant can achieve at best 40% efficiency for subcritical plant and reduce 4% of CO2 emission. Due to that, is good to carry out the experimental research and exploring the method to get the same results and relationship, or better [10], [16].

[2] PROCESS AND METHODOLOGy

This experimental study was conducted at conventional thermal coal plant placed in Asia region. In year 2003, this thermal plant was built up and installed with a subcritical boiler with tangential firing concepts.

Table 1. Boiler Design and Characteristic

Thermal System	Pressure (bar)	Temperature °C	Steam Flow (tonne/hrs)
Main Steam	175	540	2213
Hot Reheat	38	540	1927
Condenser	70	-	-

Refer to Table 1, the arrangement and function for superheated main steam piping, cold reheat steam piping and hot reheat steam piping was installed at this power plant which is according to the ASTM and ASTME standards. The basic operational concepts as per the Table presented below. Connected to the main grid system, this plant was designed in

responding to the frequency. This conventional plant design for the steady-state operation which as baseload for the country and in the meantime can operate at cycle loading. For security and protection to the grid system, this plant functions with load rejection and overload in operation in line. Table 1 shows the designed one unit of the boiler and the characteristic of this thermal plant. This boiler type at 700 megawatts maximum generation will be used for this study.

For the power plant process, the boiler drum with boiler circulation pump was installed together with the following two-type concept According to the power plant design, this thermal plant efficiency is 35 percent. This plant was designed with coal types combustion, condensate and feeding water system, thermodynamic conceptual, chemical reaction, standard demineralized water processing, heating the process with high-pressure heaters and low-pressure heaters, pulverizes, and flue gas circulation system [3], [9].

The flue gas process and circulation are designed to perform at nominal flow gas, required by the combustion process. Figure 2 shows the schematic process for the flue gas system at this thermal coal plant. Oxygen in the combustive air mixes with the coal as fuel and produces heat and combustion gases from the furnace chamber. This plant was installed with two Induced Drought (ID) which function to remove flue gas from the furnace to the atmosphere throughout the chimney. The hot flue gas was inducing with energy which followed the sequences of the process before getting to the ID fans.

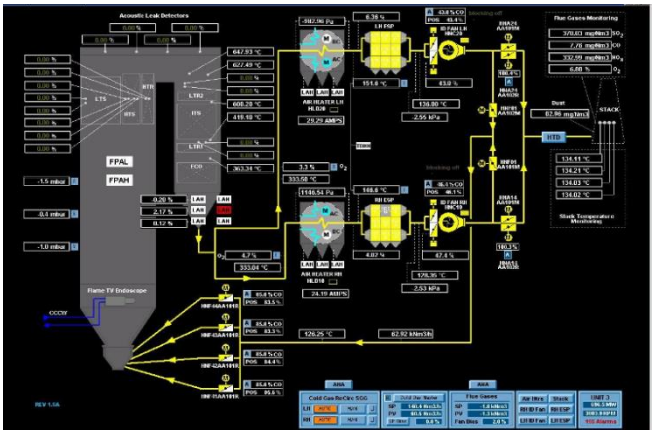


Fig. 2. Boiler Operation and Gas Flow Circulation

Regenerative air heaters (RAH) function to heat up the combustion air and distribute the air to each corner of the burner at the single compartment level. The downstream air ducts for RAH are connected with the ducting of combustion air for Force Drought (FD) fans. FD fan also functions to balance the air combustion in total air for combustion. Installed also is a Primary Air (PA) fan to transport pulveriser fuel to the furnace. There are 7 pulverisers connected at this power plant which perform to reduce raw coal to become as power at sizes between 30-70um. This process is critically important to ensure continued fuel supply to the boiler in performing combustion. Before coal was fired in the furnace, coal analysis was carried out which included ultimate analysis and proximate analysis to perform coal characteristics and specifications. Table II represents the coal specification with different coal types. Coal analysis measures calorific value, content for carbon, hydrogen, nitrogen, oxygen, ash, moisture, sulfur and HG1 for each type of coal.

Table 2. Coal Specification

Coal types	Unit	A	B	C	D	E
Calorific value	kcal/kg	4852	5013	5262	5320	5410
Carbon	%	73.3	69.85	74.19	74.70	75.2
Hydrogen	%	5.18	4.99	5.51	5.59	5.40
Nitrogen	%	0.93	1.02	1.61	1.27	1.50
Oxygen	%	20.43	20.33	17.99	17.07	17.21
Ash	%	1.7	2.8	4.4	4.6	5.1
Moisture	%	27.8	25.0	23.5	22.3	21.1
Sulphur	%	0.11	0.21	0.45	0.72	0.74
HGI	-	47	54	45	50	44

[3] RESULTS AND FINDING

Boiler efficiency was measured according to the formula. CO2 was captured during selected coal-fired at based loading, 700 megawatts. Selected coal was fired for 5 days and the average reading was recorded through the storage web data system. During the testing, there is no limitation or duration for the boiler to ensure the data capture is not interrupted. Coal types with different CV, fuel firing rate, steam generation rate, boiler efficiency and measurement of heat loss due to Carbon and CO content in coal presented in Table III below. The average reading for all types of coal is presented including the firing rate for fuel, generation of steam, temperature for the feed water system and amount of CO emitted to the atmosphere.

Table 3. Boiler Parameters

Coal types	Unit	A	B	C	D	E
Calorific value	kcal/kg	4852	5013	5262	5320	5410
Fuel firing rate	tones/hrs	366	348	330	318	312
Steam generation rate	tones/hrs	2250	2250	2250	2250	2250
Feed water temperature	°C	270	270	270	270	270
Boiler efficiency	%	66.61	67.82	68.12	69.51	70.08
Heat loss due to CO	%	3.80	3.51	3.64	3.61	3.50
CO	mg/Nm3	80.1	70.4	62.1	59.4	55.1

The statistical analysis was carried out on predicting the boiler efficiency to the sub-bituminous coal CV. Figure 3 shows the relationship between boiler efficiency to the coal calorific value. Coal type A with CV at 4852 kcal/kg come out with 66.61% efficiency meanwhile coal type E with CV at 5410 kcal/kg come out with 70.08% efficiency meanwhile coal type E.

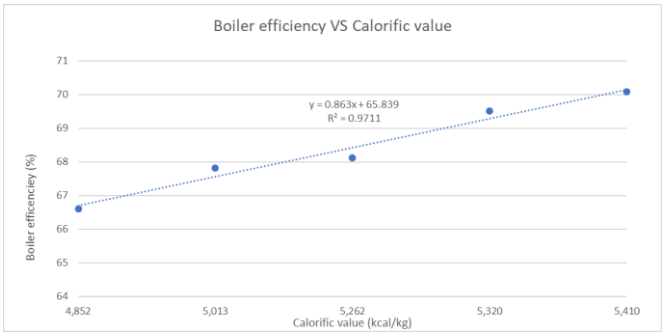


Fig. 3. Boiler efficiency with different coal calarofic value

It shows, for the increment of 0.3% of efficiency resulted in the difference of about 600 kcal/kg and reduce the consumption of coal by about 50 tones/hrs. Therefore, coal with high CV resulted in less consumption for the fuel used and less producing the CO emitted to the atmosphere. In addition, the boiler efficiency is linearly related to the CO emitted to the atmosphere. High boiler efficiency is producing less CO in the atmosphere. As shown in Figure 4, coal types A with CV at 4852 kcal/kg produced 80.1 mg/Nm3 of CO meanwhile coal types E with CV at 5410 kcal/kg produced 55.1 mg/Nm3 of CO. As found, the CO emit into the environment is increasing with the fuel firing rate increase. Fuel firing rate increase due to coal consumption for the tonnage of coal to produce same megawatt increase. The coal calorific value is representing the amount of energy in coal for the heat transfer and combustion process in the furnace [12], [14].

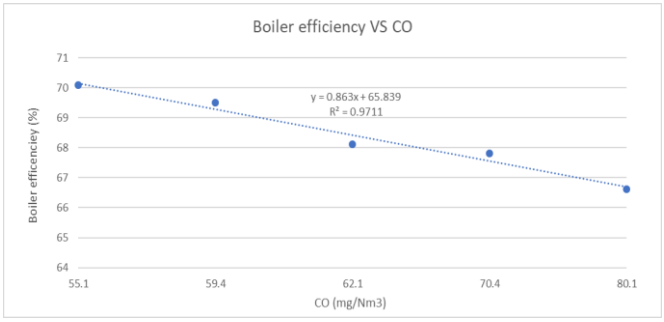


Fig. 4. Boiler efficiency with CO

[4] RECOMENDATION

There is many factor cause for decreasing of efficiency in thermal plant. Mechanical wear and tear, mechanical availability, insufficient thermal process, defective equipment and machine installed at the power plant, preventive maintenance, and corrective maintenance activities are the factors influencing the power plant performance, efficiency [16]. By considering the effect of lower efficiency, the CO2 being emitted per unit of electricity shall be measure as well. It affects the consumption of fuel used for generating electricity at the maximum capacity. Therefore, there are several techniques available in improving efficiency at the existing thermal plant. Plant upgrading, equipment refurbishment, improvise the proper procedure and standard process helps the operator to enhance the optimum performance for the plant. Operation and maintenance (O&M) process and activity shall be looking up to enhance the best practices and for the latest technology available around the world. However, the cost still the main factor in considering the program in increasing efficiency to balance the need and financial performance [13], [15].

The power plant should consider to installed Flue Gas Desulphurization (FGD) to improve flue gas outlets emit to the environment such as SOx, NOx and CO. FGD purposely removes sulfur dioxide in the flue gas in compliance with environmental requirements. In addition, Dry De-SOx and NOx technology are firmly to reduce and eliminate gas emission from the combustion process and flue gas [14]. For the combustion process, such a mechanism and procedure are developing to minimize the CO and other gas emission release to the environment. Excess oxygen, burner tilt position, de-superheating spray water and operation of pulverizes is the methodology to improve the power plant process. Besides, complete combustion can be performing by optimizing the flue gas process. Sufficient combustion air including drought system, induced drought system, and primary air system as the factors that contribute to the total air for the combustion process. As discussed before there are many ways to improve and minimize emissions emitted to the environment. Advance technologies, process, procedure, and the system is the methodology to improvise the current practices, reducing CO to the atmosphere.

[5] CONCLUSION

The study shows boiler with high efficiency produced less CO2 due to less consumption of fuel. Consumption of fuel is directly related to the coal CV which represent the amount of heat released by the complete combustion. High coal CV produces high boiler efficiency and resulted from less CO in the atmosphere. Therefore, to minimize the CO emission, the selective coal with high CV may use for firing.

REFERENCES

[1] Beer, J. M. (2007). High efficiency electric power generation: The environmental role. Progress in Energy and Combustion Science, 33(2), 107-134.
[2] Campbell, R. J. (2013). Increasing the efficiency of existing coal-fired power plants.
[3] Carrington, G., & Stephenson, J. (2018). The politics of energy scenarios: Are International Energy Agency and other conservative projections hampering the renewable energy transition?. Energy research & social science, 46, 103-113.
[4] De Souza, G. F. M. (2012). Thermal power plant performance analysis. London: Springer.
[5] Gupta, R. D., Ghai, S., & Jain, A. (2011). Energy efficiency improvement strategies for industrial boilers: a case study. Journal of engineering and technology, 1(1), 52.
[6] Harris, M. L., Alexander, D., Harteis, S. P., & Sapko, M. J. (2015). Collecting representative dust samples: A comparison of various sampling methods in underground coal mines. Journal of Loss Prevention in the Process Industries, 36, 195-202.
[7] Howell, J. R., & Buckius, R. O. (1987). Fundamentals of engineering thermodynamics. McGraw-Hill.
[8] Howell, J. R., & Buckius, R. O. (1987). Heat Transfer Engineering.
[9] Ikeda, M., Makino, H., Morinaga, H., Higashiyama, K., & Kozai, Y. (2003). Emission characteristics of NOx and unburned carbon in fly ash during combustion of blends of bituminous/sub-bituminous coals☆. Fuel, 82(15-17), 1851-1857.
[10] International Energy Agency. (2018). World energy outlook. Paris: OECD.
[11] Judt, W. (2020). Numerical and Experimental Analysis of Heat Transfer for Solid Fuels Combustion in Fixed Bed Conditions. Energies, 13(22), 6141.
[12] Murehwa, G., Zimwara, D., Tumbudzuku, W., & Mhlanga, S. (2012). Energy efficiency improvement in thermal power plants. International Journal of Innovative Technology and Exploring Engineering (IJITEE), 2(1), 20-25.
[13] Nagy, T., & Mizsey, P. (2015). Model verification and analysis of the CO2-MEA absorber–desorber system. International Journal of Greenhouse Gas Control, 39, 236-244.
[14] Nuraini, A. A., Salmi, S., & Aziz, H. A. Efficiency and Boiler

Parameters Effects in Sub-critical Boiler with Different Types of Sub-bituminous Coal. Iranian Journal of Science and Technology, Transactions of Mechanical Engineering, 1-10.

[15] Salmi, S., & Nuraini, A. A. (2020). Effect of Coal with High Moisture Content on Boiler Operation Parameters at Thermal Coal Fired Power Plant. PalArch's Journal of Archaeology of Egypt/Egyptology, 17(9).

[16] Sanpasertparnich, T., & Aroonwilas, A. (2009). Simulation and optimization of coal-fired power plants. Energy Procedia, 1(1), 3851-3858.

3D Printing: Functionality Graded Materials (FGM) via Fused Deposition Modelling (FDM)

Zairul Amri Zakaria
Department of Mechanical Engineering
Nilai University Negeri Sembilan, Malaysia
zairul@nilai.edu.my

B.T.H.T Baharudin
Departmet of Mechanical and Manufacturing Engineering Universiti Putra Malaysia Selangor, Malaysia
hangtuah@upm.edu.my

MKA Ariffin
Departmet of Mechanical and Manufacturing Engineering Universiti Putra Malaysia Selangor, Malaysia
khairol@upm.edu.my

MIS Ismail
Departmet of Mechanical and Manufacturing Engineering Universiti Putra Malaysia Selangor, Malaysia
ms_idris@upm.edu.my

N. Ismail
Departmet of Mechanical and Manufacturing Engineering Universiti Putra Malaysia Selangor, Malaysia
napsiah@upm.edu.my

***Abstract* - Additive Manufacturing (AM) or 3-Dimensional (3D) Printing is a means of production by building up material, layer upon layer. AM offers a high level of customisation and avoids expensive tooling costs or lengthy programming time as well as offering a significantly faster method of production. Within AM, Fused Deposition Modelling (FDM) is perhaps the most widely used system owing to its simplicity. The main purpose of this study is to develop a Functionality Graded Material (FGM) that is biocompatible and can be used to produce a shaped component using FDM technology. The chosen material is poly (lactic acid) (PLA) to be mixed with polypropylene to improve the mechanical properties of PLA. In order to deliver the composite, a proposed new mixing system has been developed comprising a hopper based feed utilising granules of different materials which will be melted and mixed at point of use immediately prior to being fed to the gear system to control the ratio of these materials to achieve the FGM component to suit specific application. The mixed materials with the specific ratio will then be delivered to the print head of the FDM system to print the desired components**

Keywords—Additive Manufacturing (AM), 3-Dimensional (3D) Printing, Fused Deposition Modelling (FDM), Functionality Graded Material (FGM)

[1] INTRODUCTION

Additive Manufacturing (AM) or 3-Dimensional (3D) Printing is a process that enables parts to be manufactured directly from Computer Aided Design (CAD) data via the additive deposition of individual cross-sectional layers of the part [1]. As opposed to traditional subtracting manufacturing methods, this process reduces waste during manufacturing and can be separated into several categories by their input materials and the forming process [2].Under the ISO/ASTM 52900:2015 partnership, AM is defined as the *"process of joining to make parts; (clause of 2.6.1 of this standard defines parts as joined material forming a functional element that could constitute all of a section of intended product), from 3D model data, usually layer upon layer (under clause 2.3.10 of this standard, a layer is defined as material laid out, or spread, to create surface), as opposed to subtractive manufacturing and formative manufacturing methodologies"* [3-4]. The most popular process under the 3D Printing is Fused Deposition Modelling (FDM) at 66% market share owing to its simplicity that mimics a standard 2D inkjet printer and also being the cheapest type of 3D Printing Technology [5].

[2] FUSED DEPOSITION MODELLING (FDM)

The FDM process is the most extensively capitalised Rapid Prototyping (RP) technique that builds parts layer-by-layer by heating thermoplastic material to a semi-fluid state and extruding it through a nozzle determined by computer-controlled paths, subsequently solidifying to form a rigid structure [6]. Compared to other AM processes, FDM offers major advantages as it does not require any solvent and only uses filaments that are fed from the 3D printer's bays to the print head [7]. The execution of the print job by FDM is achieved using two separate types of material, modelling material and support material; the modelling material is the substance forming the finished piece whilst the support material forms supporting scaffolding structures that facilitate the manufacturing process but which are discarded post manufacture [6]. The two filaments (the two substances) are extruded through two separate nozzles contained in a single liquefier or extrusion head, rather like separate colours printed through different ink jets contained in the one print head of a typical ink-jet printer [8]. The programming or set up of the FDM process is minimal compared to the time typically taken to program a Computer Numerical Control (CNC) Machine and the ability of the FDM process to create almost any shape or geometric feature gives it a distinct advantage over other AM processes, particularly in terms of cost savings [9].

A. Working Principles of FDM

The working mechanism FDM machine is firstly, the 3D model information stored in a STL file is converted into geometry consisting multiple layers by using specific software. These layers provide the information regarding the actuation of FDM machine's print head and base throughout the process. If overhangs exist in the 3D model, support structures will be generated in the STL file and sliced into multiple layers [10]. In the next step, a filament coil is feed to the printer head. The controller of the machine will determine when the printhead extrudes the melted filament according to the shape of the model current layer. A drive gear that attached to the stepper motor will pull the filament into the printhead and ensures that the process occurs smoothly and at an optimal feed rate. Thirdly, the heating devices, usually a heating element placed outside the printer head, will heat the thermoplastics to the filament melting temperature. The liquid thermoplastics are ready to be extruded in the next step. Finally, the physical model will be built layer upon layer, starting from the bottom to the top. The printhead is actuated by stepper or servo motors which can move in x and y directions. The printhead moves according to the profile of the model's current layer and extrudes the melted thermoplastics.

When the current layer is complete, the base will move down in horizontal direction and start the next layer with the same process, until the model is fulfilled [10].

B. *Materials of FDM*

The A range of differing thermoplastic polymers are employed in FDM printing, such as poly-lactic acid (PLA), acrylonitrile butadiene styrene (ABS), polyamide 6.6 (PA 6.6) and polycarbonate [11]. These can even be blended with materials such as wood or metal to form thin filaments used principally in the construction of small models; they do not yet have the mechanical properties to resist mechanical stress and are often weaker than non-composite polymers [12]. One aspect of note relates to metal-filled printing polymer, which may actually exhibit reduced mechanical strength but, used in combination with another material of higher tensile strength, may successfully be made stronger [13]. PLA has been successfully combined with silver nanowires thereby increasing conductivity and increasing the mechanical properties of the resulting nanocomposite [14].

For a number of reasons, PLA is often selected as the core substance. PLA, along with ABS, is already a widely used polymer in FDM printing [15]. It is noteworthy that its properties include biocompatibility; it does not cause inflammation, does not adversely affect the immune system and is non-toxic [13]. In consequence it is particularly useful in medical applications. It is also biodegradable and has excellent bonding and adhesive qualities lending it useful for composites [13]. Degradation over time can even prove useful in biomedical applications where it mimics the slow degradation of bone and other tissue. Although FDM printed objects using polymer-metal composite material are not typically as strong as those constructed of pure polymers or metal, studies have demonstrated that small metal concentrations can still effectively be embedded into a polymer filament without unduly affecting the tensile and flexural properties of the object whilst, at the same time, resulting in a range of other desired benefits such as magnetic, conductive or optic properties [16]

C. *Issues with FDM*

FDM systems have several limitations, perhaps the most significant constraint being the lack of availability of commercial FDM printers with the ability to print large scale products [17]. Additionally, the current FDM process has limited capability to handle a wide range of filament sizes and, consequently, the mass flow rate of the deposition resulting in a slow build-up of fine layers thereby limiting manufacturing and prototyping capabilities [18]. Furthermore, the fine diameter of the filament that is fed to the print head results in a tendency to buckle due to high stress around the drive wheels [7]. A variation of FDM, the Adaptable Filament Deposition System (ADPS), is a recent innovation that partially resolves some of these issues by providing a system of effectively varying the filament diameter at the head, but the system is still based on filament that is mechanically fed and which is prone to buckling at high stress [18].

[3] FUNCTIONALITY GRADED MATERIALS (FGM)

FGM are composite materials which are created to achieve spatial variation of their properties. This can be accomplished by forming compound of two materials whose volume fraction is changed across certain direction [19]. The smooth transition of two type of materials provide thermal protection and structural integrity. The toughness of metal can be mated with the refractoriness of a ceramic without any compromise in the toughness of the metal or the refractoriness of the ceramic [20]. There are many advantages brought about by the FGM such as reducing the magnitude of thermal stress especially at the critical locations as well as provide capabilities of part integration. Since the ratio of the materials can be controlled within the FGM as well as the gradual transition from one material to another this can possibly reduce the stress concentration [21].

A. *Applications of FGM*

One of the crucial betterments in industrial production is through the advancement of materials. FGM provide the ability of producing advanced performance materials that have been used in many fields such as manufacturing, aerospace, biology, nuclear energy and electromagnetism through the inventive integration of organic and inorganic materials such as metals, polymers and ceramics. In aerospace industry, FGM with the capability of high thermal shock resistance, thermal fatigue resistance, temperature resistance together with its high hardness, wear and corrosion resistance the attributes that cannot be achieved by the traditional materials make it suitable for use as turbine blades. In manufacturing, FGM layers between the Cr0MO shank and ceramic tip of a cutting tool improve the thermal strength [22-23]

[4] PROPOSED FDM DESIGN

The aim of this paper is to propose a method to develop and fabricate FGM using FDM technique. The following section as shown in Fig. 001 will describe the working principle of the propose design of a 3D printer (FDM) that is able to print a FGM using two different materials, being Poly (Lactic Acid) (PLA) and Polypropylene grafted-maleic anhydride (PP-g-MA).

A. *Hopper based feeding system*

The proposed design will have two (2) hoppers to allow for the mixing of two materials with different melting points but will incorporate an interface to allow for the future addition of more material feeds if required. The hopper will act as a material reservoir (container) into which is placed the initial material, either in granule or powder form or broken filament. A simple control valve will be placed in the bottom of this container to control the amount of the initial material that will be dropped into the heating tube. The valve opening and closing will be automatically controlled. Two types of materials, A and B, both in broken filament form or granules, will be deposited into the hopper system. Material A through Hopper A and Material B through Hopper B. Once both materials enter their respective hoppers, they will start to melt.

B. *Heating Block*

The heating block is the major component of the system. The heating block will be surrounded by heating elements to heat the block above the melting point of the chosen material. A total of three (3) heating elements will be incorporated, one placed in each of the Ratio Gear Systems and another element

This work is financially supported by Ministry of Education, through the Fundamental Research Grant Scheme FRGS//1/2018/TK03/UPM/02/6).

at the bottom of the heating block. Type K Thermocouple will be placed on the body of the heating block to measure and control the temperature of the heating block. The heater will be Proportional-Integral-Derivative (PID) tuning to ensure that the desired temperature is maintained throughout the printing process and to improve the accuracy of the process. There are three (3) mechanisms within the heating block, Ratio Gear System, Mixer and Gear Nozzle

C. Ratio Gear System

Once the chosen material passes the hopper system, the melted material will go through a pair of spur gear systems. All of the parameters of these gear systems, being the pitch circle diameter (PFD), module, number of teeth and the thickness of the gear are identical. The module of these gear system will be kept to a minimum to control the amount of material that will be mixed. Materials A and B will each go through a gear system, the function of which is to control the mixing ratio between these two (2) materials. This particular printer can print a single type of FGM component as per the details below in Fig. 002, within that single part, the mixing ratio of the Material A and B can be varied according to the desired function. The system programming of this printer must be capable of allowing the printer to print a product with different material ratios for different sections. A ratio of Material A and B within this component varied at 3 positions, the conditions of which are as follows:

a. **Condition 1 -** The ratio of Material A and B on the first section along its length (the first 40 mm) is an equal ratio (1:1), therefore the gear system for each material will turn at the same speed. The amount of material that will be deposited to the mixer will be the same.

b. **Condition 2 -** The ratio of Material A and B on the second section along its length is 1:2, it means that the amount of Material B is double that of a Material A. Therefore, the gear system of the Material B will turn twice the speed of that Material A.

c. **Condition 3 -** The ratio of Material A and B on the last section of this FGM component is 1:4. The amount of material B is four times that of Materials A, therefore the gear system of the Material B will turn four times faster than the gear system of Material A

D. Mixer and Gear Nozzle

Once the gear systems have produced the desired ratio, the mixed materials will be deposited into a mixer to mix both materials properly. The mixer consists of two leadscrews that will be controlled by another set of spur gears. Once the materials are mixed, the combined material will be deposited into another gear system, the function of which is to control the quantity of material to be deposited into the Print Nozzle. The material will be deposited into the Heated Bed through the Print Nozzle to print the desired component. It should also provide sufficient pressure so the mixed materials can be pushed through the print nozzle.

E. Printing Bed

With most conventional FDM machine, the print nozzle moves in X, Y and Z Axis to print the desired component whilst the printing platform itself remains in a fix position. However, since the proposed FDM has to carry the Heating Block as well as the Hopper system, the print nozzle will be attached to the fixed structure whilst the printing bed will move. The system has a total of four (4) Stepper Motors to control the movement in the X, Y and Z direction. Two (2) motors control the movement in Z direction (up and down movement) and the other 2 motors control the movement in X and Y direction, respectively. There are six (6) limit switches on the system, two (2) limit switches on each axis to ensure that the printing bed will not over travel.

The chosen materials to be fabricated to produce the FGM component via FDM is Poly (Lactic Acid) (PLA); this material was chosen due to its characteristics of biodegradability, biocompatibility; it does not cause inflammation and is non-toxic. Material that is chosen to be mixed with PLA is Polypropylene grafted-maleic anhydride (PP-g-MA), the combination of these two materials can improve the performance of PLA in terms of modulus, tensile strength, toughness and elongation at break.

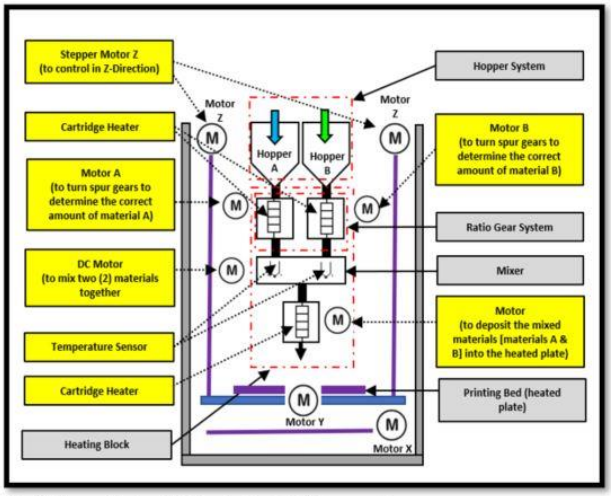


Fig. 001: Proposed design of FDM system to print FGM component

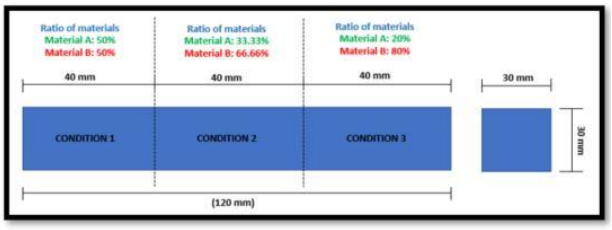


Fig. 002: Example of FGM component to be printed using proposed FGM machine

CONCLUSION

The development of FGM components through FDM is crucial not only in engineering but other areas but the cost and method of producing the FGM make it prohibitive in certain applications. A lightweight, quick and time and cost saving FDM manufacturing process is perceived by many as the next generation of manufacturing, an inaugural process that will revolutionise how design and manufacture taking place. To produce a material based on PLA suitable for biomedical use, one of the most important goals is to avoid a second surgical procedure to remove unnecessary inserts and implants. Traditionally, titanium has been used in this type of application, but, in this case, a second surgical procedure is needed to remove the titanium device. PLA polymer has also

been used to produce biodegradable screws and fixation pins, plates, and suture anchors and, although such types of absorbable screws and pins have been gaining widespread clinical use, they are mainly used only in cases where high mechanical stiffness or strength is not required. PLA alone does not provide sufficient strength, or contain sufficient qualities, to be useful in more demanding or load bearing biomedical applications. Using PLA as a base for a new composite can provide us with a biodegradable composite suitable for such orthopaedic areas as the knee, shoulder, foot and ankle, hand, wrist, elbow, pelvis, and zygomatic fractures. The primary materials to form the basis of developing new composites will likely include poly lactic acid (PLA), acrylonitrile butadiene styrene (ABS), polyamide 6.6 (PA 6.6) and polycarbonate.

Additionally, the properties of each may be significantly altered by the addition of metal fibres or micro particles having the potential to improve tensile strength or conductivity. As a base polymer, PLA may prove particularly useful in medical applications due to its properties of biocompatibility; it does not cause inflammation, does not adversely affect the immune system and is non-toxic. Furthermore, it is biodegradable. PLA has excellent adhesive properties and bonds well with other composites. The properties of individual polymers are well-known and documented but how they react in different composite forms and combination remains relatively unchartered territory.

This research endeavours to develop a fundamental understanding of the various polymers and how their mixing could potentially increase the mechanical strength whilst retaining properties of biodegradability, biocompatibility, and non-toxicity necessary for medical applications. Fundamentally, through this research, various materials properties will be studied and investigated in terms of their mechanical strength and other desired properties that are needed for specific applications and new composite materials will be formed using a “hopper system” to mix them immediately prior to feeding the FDM print head whereby objects with greater mechanical properties will be instantly created.

Acknowledgment

This work is financially supported by Ministry of Education, through the Fundamental Research Grant Scheme (FRGS//1/2018/TK03/UPM/02/6).

REFERENCES

[1] Qattawi, A., Alrawi, B. and Guzman, A, “Experimental optimization of fused deposition modelling processing parameters: a design-for-manufacturing approach,” Procedia Manufacturing, 10, pp.791-803, 2017.

[2] Yagnik, D., “Fused Deposition Modeling–A Rapid Prototyping technique for Product Cycle Time Reduction cost effectively in Aerospace Applications,” In International Conference on Advances in Engineering and Technology (ICAET) (pp. 62-68),2014.

[3] ASTM Committee F42 on Additive Manufacturing Technologies and ASTM Committee F42 on Additive Manufacturing Technologies. Subcommittee F42. 91 on Terminology, 2012. *Standard terminology for additive manufacturing technologies*. ASTM International.

[4] Standard, A.S.T.M., F2792-12a: Standard Terminology for Additive Manufacturing Technologies (ASTM International, West Conshohocken, PA, 2012). *P. Jain, AM Kuthe, Feasibility study of manufacturing using rapid prototyping: FDM approach, Procedia Eng*, *63*, pp.4-11, 2013.

[5] Dey, A. and Yodo, N., “A systematic survey of FDM process parameter optimization and their influence on part characteristics,” Journal of Manufacturing and Materials Processing, *3*(3), p.64, 2019.

[6] Yagnik, D., “Fused Deposition Modeling–A Rapid Prototyping technique for Product Cycle Time Reduction cost effectively in Aerospace Applications,” In International Conference on Advances in Engineering and Technology (ICAET) (pp. 62-68), 2014.

[7] Pollard, D., Ward, C., Herrmann, G. and Etches, J., “Filament Temperature Dynamics in Fused Deposition Modelling and Outlook for Control,” Procedia Manufacturing, 11, pp.536-544, 2017.

[8] Novakova-Marcincinova, L. and Kuric, I., “Basic and advanced materials for fused deposition modeling rapid prototyping technology,” Manuf. and Ind. Eng, 11(1), pp.24-27, 2012.

[9] Han, S., Xiao, Y., Qi, T., Li, Z. and Zeng, Q., “Design and Analysis of Fused Deposition Modeling 3D Printer Nozzle for Color Mixing,” Advances in Materials Science and Engineering, 2017.

[10] Shi, Z., Peng, Y. and Wei, W., “Recent advance on fused deposition modeling,” Recent Patents on Mechanical Engineering, *7*(2), pp.122-130, 2014.

[11] Noorani, R., “Rapid Prototyping: Principles and Applications,” John Wiley & Sons: Hoboken, NJ, USA, ISBN 978-0-471- 73001-9, 2005.

[12] Wu, W.Z.; Ye, W.L.; Wu, Z.C.; Geng, P.; Wang, Y.L.; Zhao, J., “ Influence of layer thickness, raster angle, deformation temperature and recovery temperature on the shape-memory effect of 3D-printed polylactic acid samples,” Materials, 10, 970, 2017.

[13] Senatov, F.S.; Zadorozhnyy, M.; Niaza, K.V.; Medvedev, V.V.; Kaloshkin, S.D.; Anisimova, N.Y.; Kiselevskiy, M.V.; Yang, K.C., “ Shape memory effect in 3D-printed scaffolds for self-fitting implants,” Eur. Polym. J., 93, 222–231, 2017.

[14] Ahn, S.H., Montero, M., Odell, D., Roundy, S. and Wright, P.K., “Anisotropic material properties of fused deposition modeling ABS,” Rapid prototyping journal, 8(4), pp.248-257, 2002.

[15] Palacio, J., Orozco, V.H. and López, B.L., “Effect of the molecular weight on the physicochemical properties of poly (lactic acid) nanoparticles and on the amount of ovalbumin adsorption,” Journal of the Brazilian Chemical Society, 22(12), pp.2304-2311, 2011

[16] Grimmelsmann.N, Kreuziger.M, Korger.M, Meissner.H, Ehrmann. A, “Adhesion of 3D printed material on textile substrates,” Rapid Prototyping J. 2015.

[17] la’aldin Alafaghani, A.Q. and Ablat, M.A., “Design Consideration for Additive Manufacturing,” Fused Deposition Modelling, 2017.

[18] Chennakesava, P. and Narayan, Y.S., “Fused deposition modeling-insights,” In Proceedings of the International Conference on Advances in Design and Manufacturing ICAD&M (Vol. 14, pp. 1345-1350), 2014.

[19] Udupa, G., Rao, S.S. and Gangadharan, K.V., “Functionally graded composite materials: an overview,” Procedia Materials Science, 5, pp.1291-1299, 2014.

[20] Vasiraja, N. and Nagaraj, P., “The effect of material gradient on the static and dynamic response of layered functionally graded material plate using finite element method,” Bulletin of the Polish Academy of Sciences: Technical Sciences, pp.827-838, 2019

[21] Mahamood, R.M., Akinlabi, E.T., Shukla, M. and Pityana, S.L., “Functionally graded material: an overview, 2012.

[22] Birman, V. and Byrd, L.W., “Modeling and analysis of functionally graded materials and structures,” 2007.

[23] Bohidar, S.K., Sharma, R. and Mishra, P.R., “Functionally graded materials: A critical review,” International Journal of Research, *1*(4), pp.289-301, 2014.

Crease Lines Effect to the Energy Absorption of Thin-walled Structures

Siti Marhainis, A. M
Malaysia Italy Design Institute Universiti Kuala Lumpur Kuala Lumpur, Malaysia
smarhainis@unikl.edu.my

Nuraini, A. A
Department of Mechanical and Manufacturing Engineering, Faculty of Engineering Universiti Putra Malaysia
Selangor, Malaysia
nuraini@upm.edu.my

Azmah Hanim, M. A
Department of Mechanical and Manufacturing Engineering, Faculty of Engineering Universiti Putra Malaysia
Selangor, Malaysia
azmah@upm.edu.my

***Abstract*—In recent years, large interest has been given to thin-walled structures as energy absorbing device because of its ability in reducing the negative effects of impacts. These energy absorbing devices should have low initial peak force to avoid the occurrence of premature bending that would not be beneficial to the energy absorbing devices. Addressing the issue, this paper focuses on the role of crease lines that are applied to the surface of thin-walled structure to the produced initial peak force, energy absorption and collapse pattern when the thin-walled structure undergoes axial crushing. Two types of thin-walled structures which are pre-folded with horizontal and inclined crease lines are investigated with finite element analysis simulation. Consequently, the results show that thin-walled structures having both incline and horizontal crease lines exhibit lower initial peak force when compared to the thin-walled structures having only horizontal crease lines. The thin-walled structure with both incline and horizontal crease lines results in a reduction of 11.92% of the initial peak force value when compared to the straight thin-walled structure without any crease lines while the thin-walled structure having only horizontal crease lines only exhibit 0.03% reduction. However, the thin-walled structure having both the incline and horizontal crease lines also has the lowest energy absorption that is 4387.24J, when compared to the other analyzed thin-walled structures.**

Keywords— thin-walled structures, axial crushing, crease line, finite element analysis

[1] INTRODUCTION

Numerous works were done in the field of automotive especially to the thin-walled structures, specifically in improving its performance of energy absorbing feature during vehicle collisions [1]. Studies have shown that the thin-walled structure design parameters which comprise of and not limited to; cross section, thickness, materials, fillers, wall design and joints affect the total energy absorption of the thin-walled structure [2] under impact.

Abramowicz [3] have presented in his study that energy dissipation which is transmitted along the thin-walled structure surfaces are sourced from three main factors. These three conditions are necessary to keep the thin-wall structure having a kinematic continuity and they are also proven to be responsible for the energy absorption of the thin-walled structures [4].

Apart from high energy absorption capability, evidence also suggests that ideal energy absorption devices should have low initial peak force and progressive and smooth collapse pattern [5] [6]. This is mainly to reduce injuries of vehicle passengers during initial impact and to diminish the possibility of premature bending of the thin-walled structures [7]. Consequently, several studies have suggested methods to reduce the initial peak force while providing the progressive and smooth collapse pattern through applying triggers and dents to the thin-wall structures, [8] [9] [10] [11]. Even with the many suggested methods, the automotive industry is inclined with the application of dents and pattern to the crash-box that is stamped out on the surface of the crash box [12] [13].

Zhang et. al [14] presented the use of pyramid shaped pattern on the surface of the thin-wall square tube with recorded numerical analysis success. However, the experimental results of structures with patterns revealed that the expected octagonal collapse mode is difficult to trigger and sensitive to manufacturing imperfections, apart from the complexity on developing the pyramid pattern [7] [15] [16].

Furthermore, Ma et.al [17] proposed a pre-folded pattern that is applicable in reducing the initial peak force while allowing the thin-walled structure to collapse progressively smooth and at the same time giving high energy absorption. This is also confirmed by by Yang et. al [18], [19], [20] while Song et. al [21], Qureshi and Bertocchi [1] and Wu et.al [22] also presented several other patterns that were applied to the wall of the thin-wall structure which give positive results in the view of crashworthiness and energy absorption.

In this paper, the effectiveness of crease lines applied to the wall of the thin-wall structures is studied using numerical analysis as an initial attempt of the patterns comparative study. The initial idea is that the stationary plastic hinge line is presented by a horizontal crease line while the traveling plastic hinge line is presented by an inclined crease line.

[2] MATERIAL AND METHODOLOGY

A. Geometric Modelling

Two thin-walled structures with different crease line orientation are created to investigate the collapse mode and the initial peak force developed when they are axially crushed while a straight square thin-walled structure was used as a benchmark. The width, height and wall thickness of the straight square thin-walled structure B-00, were b=93mm, H=300mm, and t=2.0mm. All of the Computer Aided Design (CAD) models of the thin-walled structures are constructed using a Computer Aided Engineering (CAE) software, namely Altair Hyperworks. The CAD models are built first using nodes and lines, and surfaces is then generated from those lines.

Structure B-H1 has five sections are created on the thin-walled structure which encompasses nine crease lines. The horizontal crease lines represent the stationary plastic hinge lines which appeared in the thin-walled structure deformation mode. The dihedral angle, θ of the crease lines is decided to

be 178°to give the thin-walled structure the least pre-folded crease lines [23].

To represent the traveling hinge lines, inclined crease lines are added to the existing straight square thin-walled structure. However, the inclined crease lines could not be visualized without the existence of the horizontal crease lines, thus, the horizontal crease lines are maintained, with the addition of inclined crease lines at the corners of the thin-wall structure [23]. The thin-walled structure is labelled B-V1. The dihedral angle, θ is kept 178° and according to the equation developed by Ma and You [5], written as equation 1, the corner width, is calculated to be 2mm, while l is the module length. Figure 1 shows the geometry models.

$$\theta = 2\cos^{-1}\left[\left(\sqrt{2}-1\right)\frac{c}{l}\right] \tag{1}$$

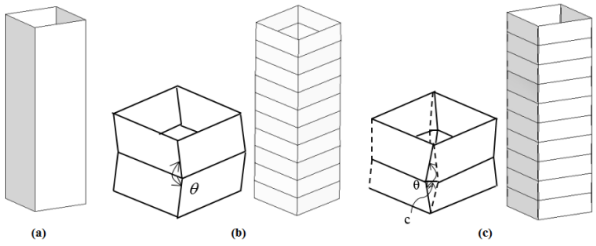


Fig 1. The geometry model. (a) B-00, (b) B-H1 and (c) B-V1.

B. Numerical Model

The developed thin-walled structures analyzed to investigate the initial peak force, P_{peak} , the crush force efficiency, (CFE), the energy absorbtion, (E), the specific energy absorption (SEA) and the collapse mode. Figure 2 shows the force - displacement characteristics of an axially crushed thin-walled structure. The curve shows the required force to deform the thin-walled structure and its displacement as it deforms. The area under the curve is the total energy absorbed and is given by the expression;

$$E = \int_0^{S_f} P.ds \tag{2}$$

where the energy absorbed, E (kJ) maximum crush distance, ds (mm), is the length of the crush specimen and P is the crushing force.

Furthermore, equation 2 can be written with better characteristics describing the progressive crushing mode by;

$$E = \int_0^{S_f} P.ds = P_{mean}\left(S_f - S_i\right) \tag{3}$$

where P_{mean} is the mean crush force and and S_f is the initial length and final length of the crushed portion of the energy absorber structure.

The CFE on the other hand can be defined as a mean crushing force, P_{mean}, divided by the initial peak force, P_{peak} and it is expressed by;

$$CFE = \frac{P_{mean}}{P_{peak}} \tag{4}$$

CFE is an important parameter that is used to evaluate the performance of energy absorbing structures. Low values of CFE gives an indication of high peak forces experienced by the thin-walled structures that would lead to potential damage and pre-mature collapses.

Other than CFE, the performance of an energy absorber structure can also be decided by its specific energy absorption (SEA). This can be expressed by specific energy absorption;

$$SEA = \frac{E}{m} \tag{5}$$

where E is the total energy absorbed and m is the mass of the material.

Equation 5 can also be written as;

$$SEA = \frac{E}{V\rho} \tag{6}$$

where V is the volume of the energy absorber structure material and ρ is the density of the material.

The above expression can also be expressed as follows:

$$SEA = \frac{E}{m} = \frac{P_m\left(S_f - S_i\right)}{V\rho} = \frac{P_m\left(S_f - S_i\right)}{AL\rho} \tag{7}$$

where A is the cross-sectional area and L is the length of the energy absorber structure.

From the general equations of energy absorption presented, it is concluded that the important criteria affecting the performance of an energy absorber are material density, the cross-section and the length of the thin-walled structure.

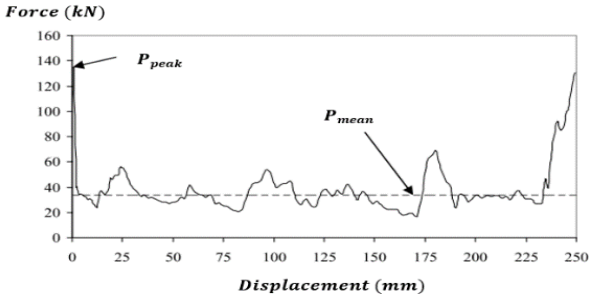


Fig 2. Force-displacement curve for axial crushing of a thin-walled rectangular tube [24].

The initial peak force of each structure was generated from the results of numerical model analysis. LS-DYNA, a commercial finite element software package was used for the simulation of the axial crushing process and Altair Hyperworks, is used as the pre-processing software. The finite element model uses mesh of mixed element type, while the size of the elements are chosen to be 5 mm.

The crushing scenario was modelled with a thin-walled structure placed on a flat surface and being crushed by a moving rigid wall of 275 kg in mass and having initial impact velocity that is set to be 56 km/h [25]. This crushing scenario is shown in figure 3. The boundary conditions on the other hand, were assigned to the tube lower edges in all 6 degrees of freedom. Mild steel is chosen as the material and the mechanical properties of the materials are: density, ρ=7830kg/m^3; Young's Modulus, E=200GPa; Poisson's Ratio, ν=0.3; σ_y=207 MPa ; σ_u=400 MPa and ultimate strain, ε_u= 15% [26].

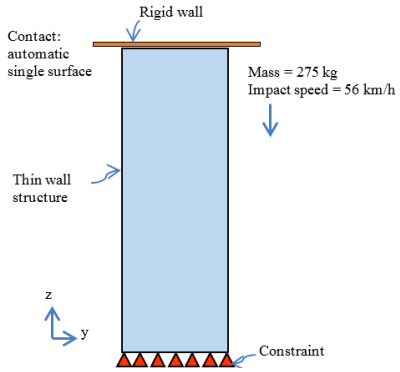


Fig 3. The analysis set-up for axial crushing.

[3] Results And Discussion

The axial crushing of B-00 as the benchmark is shown in figure 4 where B-00 collapses from the upper end and gradually folds three times when subjected to an axial load. This is due to the propagation of the horizontal stationary plastic hinge lines and inclined travelling plastic hinge. The force versus displacement curve of B-00 is also plotted in figure 5. The recorded initial peak force, P_{peak} of B-00 is 209.21 kN and this peak force is then followed by a number of crests and troughs, where the mean crush force, P_{mean} is 61.6 kN.

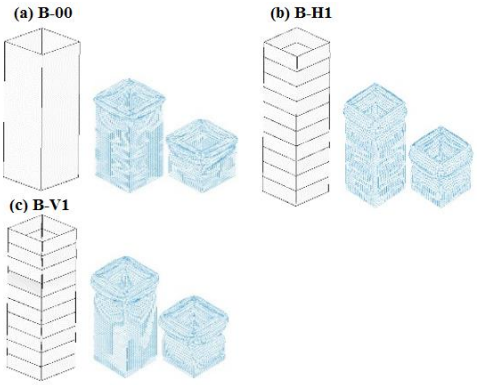


Fig 4. Profiles of (a) B-00, (b) B-H1 and (c) B-V1 at different stages of axial crushing process.

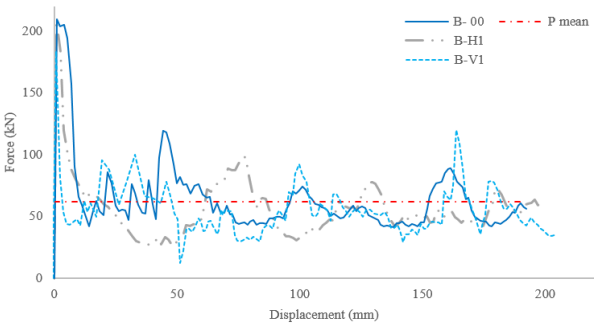


Figure 5. Force-displacement plots of B-00, B-H1 and B-V1.

Consequently, B-H1 collapse from the upper end similar to the benchmark model and progressively folded three times axially. The pre-folded horizontal crease lines on B-H1 guides the collapse progression where the initial peak force recorded was slightly lower than B-00, that is 209.15 kN. B-V1 on the other hand, had much lower initial peak force compared to B-00 and B-H1 that is 184.27 kN. The collapse of B-V1 also begins at the upper end and it is gradually folded three times. The curves of the force-displacement for all structures are plotted in figure 4 and the collapse profile for all structures are shown in figure 5.

From the numerical analysis, it is shown that when pre-folded horizontal crease lines were added, there is only slight reduction of initial peak force, which is 0.03%. This may be due to the angle of the horizontal crease lines are not large enough that the structure is behaving almost as the straight thin-walled structure. However, when the inclined lines are added, the reduction of the initial peak force value reduces dramatically, that is 11.92 % lower than the benchmark value. The resistance of the thin-walled structure to the crush load is minimize due to the inclined crease lines added at the corners, hence resulting the low initial peak force.

In addition to that, the crush force efficiency (CFE) of B-V1 also proves to be better than B-H1 when it recorded 28.74 % CFE which is 0.02% less than B-00, while B-H1 recorded a value of 26.47% CFE.

From the recorded initial peak force and CFE by all structures, B-V1 promises as the better thin-walled structure than B-H1. However, this contradicts with the recorded energy absorption (EA) and specific energy absorption (SEA) where B-H1 is better when compared to B-V1 and similar outcome is also observed with the SEA. These numerical results are summarized into table 1.

Table 1. Obtained Numerical Results of the Axially Crushed Thin-Walled Structure

Thin-walled Type	c (mm)	θ (deg)	Final Length (mm)	Peak Force (kN)	Peak Force Reduction (%)	Crush Force Efficiency, CFE (%)	Energy Absorption, E (J)	Specific Energy Absorption, SEA (J/kg)
B-00	-	-	192.41	209.21	-	29.44	6627.15	3875.36
B-H1	-	178	196.62	209.15	0.03	26.47	5722.63	3346.43
B-V1	2	178	217.16	184.27	11.92	28.74	4387.24	2565.53

It can be seen that less energy absorbed by B-V1 is due to the stiffening of the thin-walled structure which is the result from the inclined lines where they aid to the resistance of axial crushing process. This has lead to B-V1 having less crushed length, thus, less energy absorption.

[4] CONCLUSION

The numerical results presented that both horizontal and inclined crease lines are an important factor to the initial peak force value. It is shown that even though the horizontal crease lines directs and initiates the collapse mode, the initial peak force value does not differs much from the benchmark structure. Consequently, with the addition of the inclined crease lines to the thin-walled structure, the initial peak force is reduced effectively, though the SEA shows having no improvement.

More attention should be given to the inclined crease lines and parametric studies should be done, especially to investigate the effects of geometric parameter, which consists of dihedral angle θ and corner width c, to the initial peak force.

Acknowledgment

The author acknowledged the support of Universiti Putra Malaysia under Putra Grants (GP-IPS), GP-IPS/2013/9392800 for this research.

REFERENCES

[1] O. M. Qureshi and E. Bertocchi, "Crash performance of notch triggers and variable frequency progressive-triggers on patterned box beams during axial impacts," Thin-Walled Struct., vol. 63, pp. 98–105, 2013.

[2] C. Zhou, Y. Zhou, and B. Wang, "Crashworthiness design for trapezoid origami crash boxes," Thin-Walled Struct., vol. 117, no. February, pp. 257–267, 2017.

[3] W. Abramowicz, "Thin-walled structures as impact energy absorbers," Thin-Walled Struct., vol. 41, no. 2–3, pp. 91–107, 2003.

[4] T. Wierzbicki and W. Abramowicz, "On the Crushing Mechanics of Thin-Walled Structures," J. Appl. Mech., vol. 50, pp. 727–734, 1983.

[5] J. Ma and Z. You, "Energy absorption of thin-walled beams with a pre-folded origami pattern," Thin-Walled Struct., vol. 73, pp. 198–206, 2013.

[6] K. Yang, S. Xu, S. Zhou, J. Shen, and Y. M. Xie, "Design of dimpled tubular structures for energy absorption," Thin-Walled Struct., vol. 112, no. November 2016, pp. 31–40, 2017.

[7] J. Ma, Y. Le, and Z. You, "Axial Crushing Tests of Thin-walled Steel Square Tubes with Pyramid Patterns," 51st AIAA/ASME/ASCE/AHS/ASC Struct. Dyn. Mater. Conf., no. AIAA 2010-2615, pp. 1–10, 2010.

[8] X. M. Qiu and T. X. Yu, "Some Topics in Recent Advances and Applications of Structural Impact Dynamics," Appl. Mech. Rev., vol. 64, no. 3, p. 034001, 2011.

[9] S. Lee, C. Hahn, M. Rhee, and J.-E. Oh, "Effect of triggering on the energy absorption capacity of axially compressed aluminum tubes," Mater. Des., vol. 20, no. 1, pp. 31–40, 1999.

[10] A. Asanjarani, S. H. Dibajian, and A. Mahdian, "Multi-objective crashworthiness optimization of tapered thin-walled square tubes with indentations," Thin-Walled Struct., vol. 116, pp. 26–36, 2017.

[11] Q. Wang, S. Li, Z. Liu, G. Wu, J. Lei, and Z. Wang, "Geometric design and energy absorption of a new deployable cylinder tube," Mech. Adv. Mater. Struct., p. 15376494, 2020.

[12] J. Ma and Z. You, "Energy Absorption of Thin-Walled Square Tubes With a Prefolded Origami Pattern — Part I : Geometry and Numerical Simulation," J. Appl. Mech., vol. 81, no. January 2014, pp. 1–11, 2013.

[13] H. Nikkhah, F. Guo, Y. Chew, J. Bai, J. Song, and P. Wang, "The effect of different shapes of holes on the crushing characteristics of aluminum square windowed tubes under dynamic axial loading," Thin-Walled Struct., vol. 119, no. June, pp. 412–420, 2017.

[14] X. Zhang, G. Cheng, Z. You, and H. Zhang, "Energy absorption of axially compressed thin-walled square tubes with patterns," Thin-Walled Struct., vol. 45, no. 9, pp. 737–746, 2007.

[15] M. Shi, Y. Chen, J. Ma, and Z. You, "Energy absorption of origami crash box: Numerical simulation and theoretical analysis," Proc. ASME Des. Eng. Tech. Conf., vol. 5B–2018, p. 86261, 2018.

[16] J. Ma, H. Dai, M. Shi, L. Yuan, Y. Chen, and Z. You, "Quasi-static axial crushing of hexagonal origami crash boxes as energy absorption devices," Mech. Sci., vol. 10, no. 1, pp. 133–143, 2019.

[17] J. Ma, D. Hou, Y. Chen, and Z. You, "Quasi-static axial crushing of thin-walled tubes with a kite-shape rigid origami pattern: Numerical simulation," Thin-Walled Struct., vol. 100, pp. 38–47, 2016.

[18] K. Yang, S. Xu, J. Shen, S. Zhou, and Y. M. Xie, "Energy absorption of thin-walled tubes with pre-folded origami patterns: Numerical simulation and experimental verification," Thin-Walled Struct., vol. 103, pp. 33–44, 2016.

[19] K. Yang, S. Xu, S. Zhou, and Y. Min, "Multi-objective optimization of multi-cell tubes with origami patterns for energy absorption," Thin-Walled Struct., vol. 123, no. November 2017, pp. 100–113, 2018.

[20] S. Yao, H. Zhu, M. Liu, Z. Li, and P. Xu, "Energy absorption of origami tubes with polygonal cross-sections," Thin-Walled Struct., vol. 157, p. 107013, 2020.

[21] J. Song, Y. Chen, and G. Lu, "Axial crushing of thin-walled structures with origami patterns," Thin-Walled Struct., vol. 54, pp. 65–71, 2012.

[22] S. Wu, G. Li, G. Sun, X. Wu, and Q. Li, "Crashworthiness analysis and optimization of sinusoidal corrugation tube," Thin-Walled Struct., vol. 105, pp. 121–134, 2016.

[23] A. M. Siti Marhainis, A. A. Nuraini, M. A. Azmah Hanim, and B. B. Sahari, "Axial Crushing of Thin-walled Structure with Crease Lines.," Aust. J. Basic Appl. Sci., vol. 9, no. 19, pp. 20–26, 2015.

[24] G. Nagel, "Impact and Energy Absorption of Straight and Tapered Rectangular Tubes," Queensland University of Technology, 2005.

[25] F. Tarlochan, F. Samer, A. M. S. Hamouda, S. Ramesh, and K. Khalid, "Design of thin wall structures for energy absorption applications: Enhancement of crashworthiness due to axial and oblique impact forces," Thin-Walled Struct., vol. 71, pp. 7–17, 2013.

[26] "MatWeb, LLC." [Online]. Available: http://www.matweb.com/search. [Accessed: 12-Dec-2019].

Three dimensional simulation and analysis on Ti6Al4V turning using FEM

Yavuz KAPLAN
Pamukkale University Faculty of Technology Department of Mechanical Engineering Denizli, Turkey
ykaplan@pau.edu.tr

Aim: **The direct approach to study cutting forces in machining is very expensive and time consuming. The modeling and simulation software of machining process provide to researchers simulate of real work conditions without the costs and risks. In this work, finite element method (FEM) is carried out to study the effect of cutting parameters (cutting speed, feed rate, and depth of cut) on cutting forces during dry turning of titanium alloy.**

Method: **Numerical simulations with FEM were performed using Deform-3D software. The FEM code was based on an implicit Lagrangian computational routine. The finite element mesh was linked to the workpiece and followed its deformation. The turning processes were carried out with TNMA carbide inserts at three different cutting speeds (100m/min, 150m/min, 200m/min) three different feed rates (0.2mm/rev, 0.4mm/rev, 0.6mm/rev) and two different depth of cut (1mm, 2mm).**

Results: **The view of turning tests carried out with FEM is given in Figure 1. The role of cutting parameters on average cutting force obtained in the FEM simulation is shown in Figure 2. The results show that feed rate and depth of cut are the most effective parameters on the cutting force. Cutting forces increase significantly with increasing feed rate and depth of cut. With the increase of feed rate and depth of cut the contact between the workpiece and tool increased, and at the same time, the chip volume cut per unit of time increased and the resistance shown by the metal against rupturing caused a higher cutting force [1-3]. Cutting speed do not affect the cutting force significantly at 1mm and 2mm depth of cut. The obtained results are consistent with the literature [4-6].**

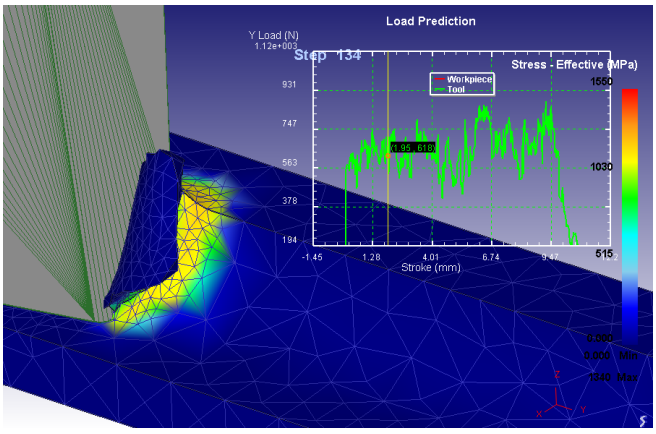


Fig. 1. Three-dimensional FEM process during turning of Ti6Al4V

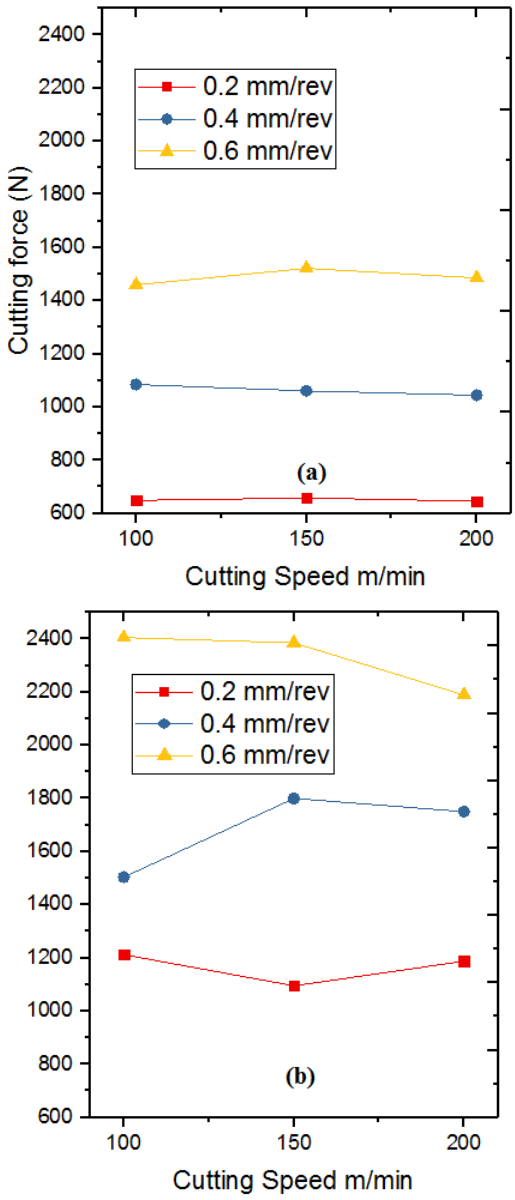


Fig. 2. Average cutting force values during turning of Ti6Al4V with different depth of cut (a) 1mm (b) 2mm

Conclusion: **Consequently, FEM is shown to be preferable to experiments for obtaining cutting forces values for the turning process. In turning Ti6Al4V titanium alloy, use of lower feed rate, higher cutting speed and lower depth of cut are recommended to obtain minimum cutting forces for the specified test range.**

Keywords— Turning, Finite element method, Ti6Al4V, Cutting force

REFERENCES

[1] B. Fnides, M. A. Yallese, H. Aouici, "Hard turning of hot work steel AISI H11: Evaluation of cutting pressures, resulting force and temperature," Mechanics, 72, 59-63, 2008.

[2] S. Thamizhmanii, S. Hasan, "Measurement of surface roughness and flank wear on hard martensitic stainless steel by CBN and PCBN cutting tools," J. Achiev. Mater. Manuf. Eng., 31, 415-421, 2008.

[3] R.V.S. Singh, B. Latha, V. S. Senthilkumar, "Modeling and analysis of thrust force and torque in drilling GFRP composites by multi-facet drill using Fuzzy Logic," Int. J. Recent Trends Eng. 1, 2009.

[4] L. Liang, X. Liu, X. Q. Li, Y. Y. Li, "Wear mechanisms of WC–10Ni3Al carbide tool in dry turning of Ti6Al4V," Int. J. Refract. Met. H. 48, 272-285, 2015.

[5] D. W. Tan, W. M. Guo, H. J. Wang, et al, "Cutting performance and wear mechanism of TiB2-B4C ceramic cutting tools in high speed turning of Ti6Al4V alloy," Ceram. Int., 44, 15495-15502, 2018.

[6] E. Chiappini, S. Tirelli, P. Albertelli, M. Strano, M. Monno, "On the mechanics of chip formation in Ti–6Al–4V turning with spindle speed variation" Int. J. Mach. Tool. Manu. 77, 16-26, 2014.

Effect of Different Penetrator Shapes on the Quasi-Static Perforation Response of Bilayer Plates

Nahit Öztoprak
Department of Mechanical Engineering Dokuz Eylul University Izmir, Turkey
nahit.oztoprak@deu.edu.tr

***Abstract*—In this study, a metal-polymer bilayer plate configuration is developed using a hot pressing technique, where mechanically and chemically treated 6061-O aluminum (Al) alloy is stacked with glass fiber-reinforced polypropylene (GFRP) composite. The quasi-static perforation experiments are carried out using a universal testing machine to evaluate the perforation response of metal-polymer laminate and the monolithic PP composite. The influence of penetrator shapes on the response is also investigated under an edge-clamped condition by cylindrical indenters of 12.7 mm diameter with the hemispherical and flat tips. The results reveal that the perforation resistance increases with the presence of the AA6061-O layer. The typical failure modes of the bilayer plates are plugging of the Al layer and delamination of the thermoplastic composite.**

Keywords—fiber-metal laminate, thermoplastic composite, quasi-static perforation test

[1] INTRODUCTION

Fiber-reinforced composites have attracted massive interest in academia as well as automotive, aerospace and marine industries owing to their high strength to weight ratio, outstanding corrosion resistance and good fatigue characteristics [1]. It is well known that thermoset and thermoplastic polymers are used as matrix materials in the composites. Compared to thermoset composites, inherent recyclability, ease of fabrication and high toughness provide significant advantages to thermoplastic composites in engineering applications [2]. Furthermore, thermoplastic composites are weldable and repairable materials unlike thermosetting composites [3]. They are widely replacing structural materials in many industries due to their cost effectiveness [4,5].

Polypropylene (PP) composites have come into focus because of the specific combination of unique properties achieved with light weight and lower cost [6,7]. They also show a great potential with high chemical and water resistance [8]. Nevertheless, enhancing the impact resistance of the composites still remains a scientific challenge [9]. Creating an aluminum (Al) alloy-composite bilayer material may be an effective alternative to improve impact perforation resistance [10]. Therefore, the motivation of this research is the smart combination of Al alloy and thermoplastic composite as the key for developing impact resistant structures for possible applications in various industries.

[2] EXPERIMENTAL

A. Fabrication of Polypropylene Composites

In this work, thermoplastic composites are manufactured using a hydraulic press (Fontijne Presses - LabEcon60 Laboratory Platen Press, The Netherlands) with the maximum capacity and temperature of 600 kN and 300°C, respectively. The long E-glass reinforced (30 wt.%) PP granules of 411.6 g are homogeneously distributed into the metallic mold ($350 \times 350 \times 3$ mm^3) for the fabrication of the PP composite considering the granule density and the mold dimensions. Table 1 shows the typical properties of the homopolypropylene composite granules [11]. Afterwards, the mold is placed in the hot press machine, which is kept at a constant force of 100 kN and constant temperature of 200 ℃ for an hour, followed by a cold press for 16 hours at a constant force to avoid warpage failure. In order to compare with metal-polymer bilayer plates, a PP composite sheet of 6 mm is also produced using the same procedure.

B. Manufacture Process of Bilayer Plates

AA6061 sheets (300 mm x 100 mm x 3.2 mm^3) in the O-temper condition are used in this experiment to place a metallic layer in front of the thermoplastic composite. Mechanical and chemical modifications are performed on the AA6061-O to provide strong bonding between the Al layer and the composite before the manufacturing of the bilayer plates. First, Al sheets are cleaned with acetone and then abraded with #400 grits sandpaper. The sheets cleaned through tap water and dried with the help of compressed air are exposed to hydrochloric acid (HCl) aqueous solution with 11% volumetric concentration at room temperature for 30 min in the next step. After the metals are again washed with running water and left to dry at ambient temperature, they are treated with alkaline etching of 10 wt.% sodium hydroxide (NaOH) aqueous solution for 2 min at 70 °C. Lastly, the sheets are washed through distilled water and dried with compressed air. After the mechanical and chemical treatments, bilayer plates are prepared by placing AA6061-O sheets on the thermoplastic composite of 3 mm thickness. The metal-polymer configuration is pressed for 60 min at 200 °C under a load of 100 kN in order to produce a hybrid laminate with an approximate thickness of 6 mm. Finally, the bilayer plates are cooled down to room temperature and then prepared for mechanical characterization by abrasive waterjet cutting in dimensions of 100×100 mm^2. Front and rear surfaces of the bilayer plates are demonstrated in Fig. 1.

Table 1. Physical and Mechanical Properties

Properties	**Duramax LFT30-PP**
Glass fiber percent (%)	30
Density (g/cm^3)	1.12
Tensile strength (MPa)	105
Flexural strength (MPa)	148
Izod impact, unnotched (kJ/m^2)	34

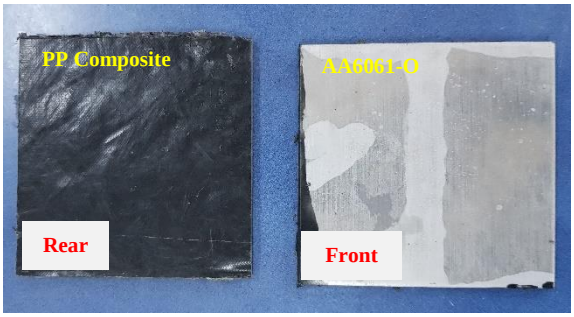


Fig. 1. AA6061-O based bilayer plates

C. *Quasi-static Perforation Tests*

The penetration experiments are applied to the bilayer plates to determine quasi-static perforation resistance and failure mechanism of the hybrid structures. Moreover, perforation resistance behavior of the monolithic PP composite with the same thickness is examined for comparison. The effect of punch shape on the response is also evaluated under an edge-clamped condition by the cylindrical indenters of 12.7 mm diameter with the hemispherical and flat tips. The perforation fixture adapted to the testing machine and the penetrators of different shapes used in this research are shown in Fig. 2. Three samples are tested for each penetrator. The constant displacement rate is chosen as 1.25 mm/min in all tests. The force–displacement curves are recorded during each test.

[3] RESULTS AND DISCUSSION

The perforation response of the monolithic thermoplastic composite is presented for hemispherical and flat indenters in Fig. 3 and Fig. 4, respectively. From the figures, it can be inferred that the PP composite provides a better perforation resistance against the flat tip compared to that of hemispherical punch. The calculated average load is found to be 2039.52 N and 1657.92 N in the perforation tests with the flat and hemispherical tips, respectively. In other respects, there is no significant difference between the mean stroke elongation values at maximum resistance load. In a way, it can be said that a large amount of energy is absorbed through the flat penetrator. In both cases, penetration, perforation and friction regions are observed. Generally, the penetration force increases linearly up to a certain point, followed by a slower load increment that culminates in the maximum resistance load where the elastic deformation ends. After the penetration, matrix damage and fiber pressing are observed with the movement of the tip through the thickness of the composite in the plateau-like region [12]. Last region is ascribed to the frictional force between the penetrator and the composite. Load drop draws the attention for all samples by the end of perforation. Front and rear face views of the samples after the perforation tests are also demonstrated in Fig. 5 and Fig. 6, respectively. The matrix shear cracking is observed as the main damage mechanism in the tests with both penetrators. At the rear surfaces, delamination and fiber pull-out are seen unlike front faces.

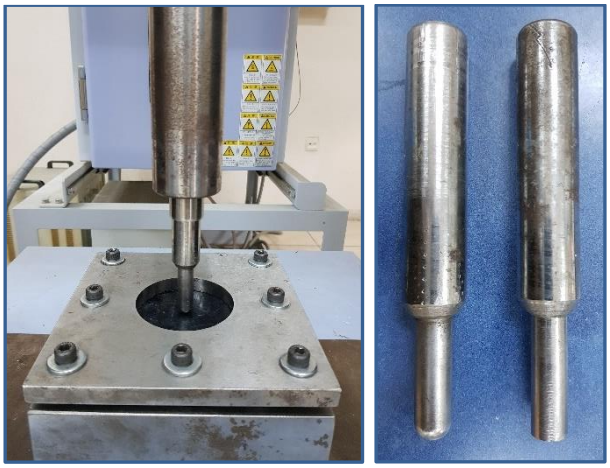


Fig. 2. Photos of the test fixture and penetrators

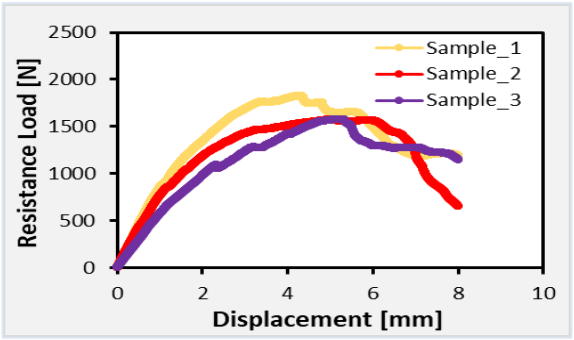


Fig. 3. Resistance force versus displacement curves of the monolithic PP composite with hemispherical punch

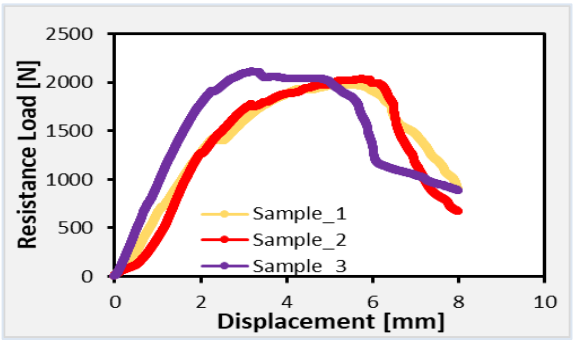


Fig. 4. Resistance force versus displacement curves of the monolithic PP composite with flat punch

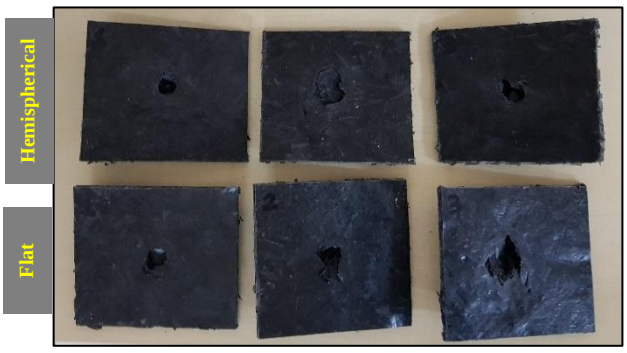


Fig. 5. Perforation damage of the front faces for the composite samples



Fig. 6. Perforation damage of the rear faces for the composite samples

The use of the metallic layer (AA6061-O) to enhance the perforation resistance of the thermoplastic composite is investigated in this study. Fig. 7 and Fig. 8 show the quasi-static perforation test results of the bilayer plates through the hemispherical and flat penetrators, respectively. It is evident from the figures that a higher resistance load is noted for both penetrators compared to the PP composite of the same thickness. Unlike the samples of the monolithic composite, higher resistance force is seen in the use of the hemispherical punch. The average load is calculated as 8110.37 N and 10859.04 N in the perforation tests with the flat and hemispherical tips, respectively. Moreover, it has been realized that there is a significant difference in penetrator displacement at maximum load. The average stroke displacement is calculated as 9.77 mm and 16.37 mm in the perforation tests with the flat and hemispherical tips, respectively. A noticeable stiffening at the initial loading is further observed in both cases with the application of the Al layer. The response exhibits a non-linear increase up to a maximum load with the displacement increment. Deformation is observed in whole bilayer plate as the Al layer in contact with the penetrator experiences tensile stretching. Both layers are damaged at maximum load. Therefore, the sudden load drop is at the ground of the explanation, as can be seen in the figures. After plugging and perforation, friction region caused by the friction of the penetrator in the bilayer plate is followed. Considering the failure modes of the bilayer plates observed during and after the quasi-static perforation tests, Fig. 9 and Fig. 10 demonstrate the front and rear faces of the samples by different penetrators. The surfaces for the hemispherical penetrator can be characterized by plugging shear out and bulging at the front and rear faces, respectively. At the composite side, it is further observed that the damage is mainly delamination and interfacial debonding for the composite layer. Dome-like shape formation of the 6061-O Al protective layer is seen. The pictures of the samples tested by flat penetrator also indicate the plugging at the front face. There are petal-like formations on the rear faces. As it is noticeable from the figure that the main failure modes at these faces are delamination and pulled out fibers of the composite. The metal sheet takes a button-shaped form unlike the hemispherical tip.

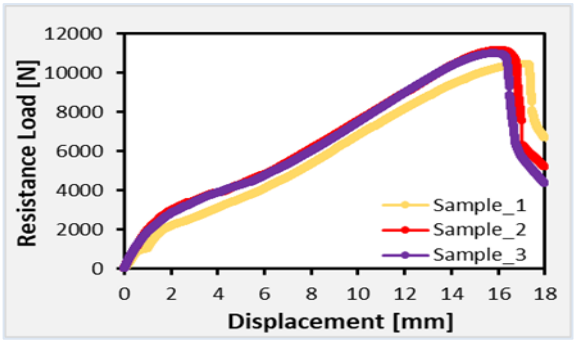


Fig. 7. Quasi-static perforation response of the metal-composite bilayer plate with hemispherical punch

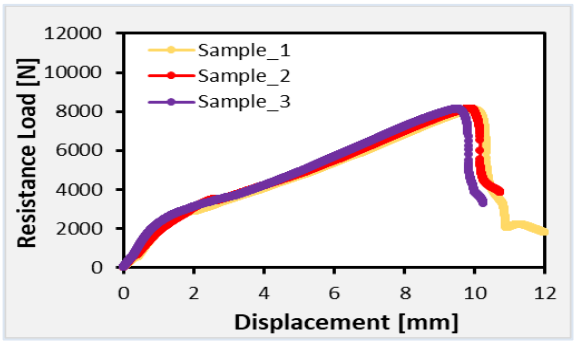


Fig. 8. Quasi-static perforation response of the metal-composite bilayer plate with flat punch



Fig. 9. Perforation damage of the bilayer plate with hemispherical punch

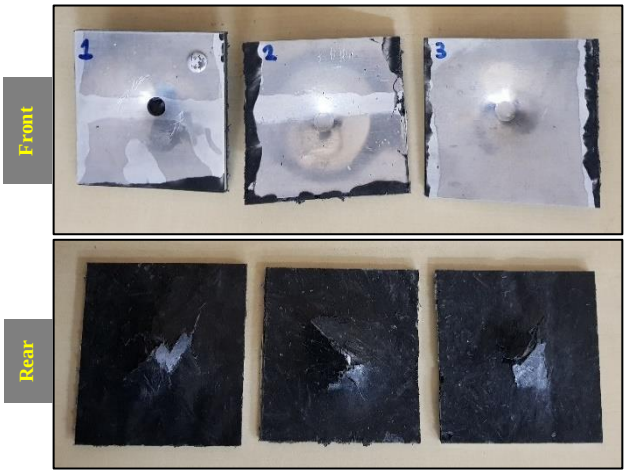


Fig. 10. Perforation damage of the bilayer plate with flat punch

[4] CONCLUSIONS

The Al alloy-GFRP bilayer plates are successfully fabricated through the hot-pressing technique without using any adhesive. In the research, the quasi-static perforation behavior of the bilayer plates and the monolithic thermoplastic composite is evaluated. The effect of different penetrator shapes on the responses is also studied. The experimental results indicate that the presence of the AA6061-O layer significantly increases the absorbed penetration energy compared to the PP composite of the same thickness. In opposition to the flat indenter in the monolithic composite, higher resistance load is obtained with the hemispherical tip for the bilayer plates. Plugging at the metal face and delamination at the composite are considered as the main damage mechanisms for both penetrators.

REFERENCES

[1] I. Derbali, S. Terekhina, L. Guillaumat, and P. Ouagne, "Rapid manufacturing of woven comingled flax/polypropylene composite structures," International Journal of Material Forming. vol. 12, pp. 927-942, 2019.

[2] B. Jongbloed, J. Teuwen, R. Benedictus, and I. F. Villegas, "On differences and similarities between static and continuous ultrasonic welding of thermoplastic composites," Composites Part B: Engineering. vol. 203, 108466, 2020. https://doi.org/10.1016/j.compositesb.2020.108466.

[3] S. K. Bhudolia, G. Gohel, K. F. Leong, and S. C. Joshi, "Damping, impact and flexural performance of novel carbon/Elium® thermoplastic tubular composites," Composites Part B: Engineering. vol. 203, 108480, 2020. https://doi.org/10.1016/j.compositesb.2020.108480.

[4] O. Demircan, A. Al-darkazali, İ. İnanç, and V. Eskizeybek, "Investigation of the effect of CNTs on the mechanical properties of LPET/glass fiber thermoplastic composites," Journal of Thermoplastic Composite Materials. vol. 33(12), pp. 1652-1673, 2020.

[5] A. Di Ilio, L. G. Di Genova, and A. G. Stamopoulos, "Implementation of the modified V-Notched Rail Shear method for characterizing glass fibre thermoplastic composites at sub-zero and elevated temperatures," Polymer Testing. vol. 93, 106874, 2021. https://doi.org/10.1016/j.polymertesting.2020.106874.

[6] M. Sano, H. Oguma, M. Sekine, Y. Sekiguchi, and C. Sato, "High-frequency welding of glass–fibre-reinforced polypropylene with a thermoplastic adhesive layer: Effects of ceramic type and long-term exposure on lap shear strength," International Journal of Adhesion and Adhesives. vol. 59, pp. 7-13, 2015.

[7] C. Ralph, P. Lemoine, E. Archer, and A. McIlhagger, "Mechanical properties of short basalt fibre reinforced polypropylene and the effect of fibre sizing on adhesion," Composites Part B: Engineering. vol. 176, 107260, 2019. https://doi.org/10.1016/j.compositesb.2019.107260.

[8] T. Yamamoto, and Y. Ota, "Creating a laminated carbon fiber-reinforced thermoplastic using polypropylene and nylon with a polypropylene colloid," Composite Structures. vol. 255, 113038, 2021. https://doi.org/10.1016/j.compstruct.2020.113038.

[9] N. Miqoi et al., "Detection and evaluation of barely visible impact damage in woven glass fabric reinforced polyamide 6.6/6 composite using ultrasonic imaging, X-ray tomography and optical profilometry," International Journal of Damage Mechanics. 2020. In press. https://doi.org/10.1177/1056789520957703.

[10] B. Yu, V. S. Deshpande, and N. A. Fleck, "Perforation of aluminium alloy-CFRP bilayer plates under quasi-static and impact loading," International Journal of Impact Engineering. vol. 121, pp. 106-118, 2018.

[11] http://nuhkompozit.com.tr/duramax-lft-pp-en/duramax-lft-pp-30/ (accessed February 22, 2021).

[12] R. Yahaya, S. M. Sapuan, M. Jawaid, Z. Leman, and E. S. Zainudin, "Quasi-static penetration and ballistic properties of kenaf–aramid hybrid composites," Materials & Design. vol. 63, pp. 775-782, 2014.

Anthocyanin of Natural Dyes as Photosensitizer for Solar Cell Application

Nurul Alfatihah Mohd Arifin
Faculty of Ocean Engineering Technology and Informatics Universiti Malaysia Terengganu Terengganu, Malaysia p3760@pps.umt.edu.my

Hasiah Salleh
Faculty of Ocean Engineering Technology and Informatics Universiti Malasysia Terengganu Terengganu, Malaysia hasiah@umt.my

Ahmad Nazri Dagang
*Faculty of Ocean Engineering Technology and Informatics Universiti Malaysia Terengganu*Terengganu, Malaysia
nazri.dagang@umt.my

Aim: Alternative energy sources such as wind, solar, biomass, hydro, and geothermal have become imperative for green energy solution. A growing demand of solar cell is yet another promising option toward green energy providing opportunity to explore natural dye extracts from plant.

Method: The natural dyes were extracted from fruit peel of Punica Granatum (PG), Garcinia Mangostana (GM), Hylocereus Costaricensis (HC) and Melastoma Malabathricum (MM). This fruit peels were washed thoroughly with deionized wated to remove dust and organics impurities before extraction and oven-dried at 60 ^{0}C for 12 hours. The dried plants were crushed into fine powder and were soak into ethanol for 3 days.

Results: UV-vis spectroscopy was used to characterize the optical absorption of the natural dyes. The result show that the presence of anthocyanin from PG, GM, HC and MM at wavelength of 534 nm, 536 nm, 536 nm and 542 nm, respectively. The energy gap of PG, GM, HC and MM were 3.018 eV, 2.667 eV, 2.796 eV and 2.794 eV, respectively. The dyes were then evaluated their highest occupied molecular orbital (HOMO) and lowest unoccupied molecular orbital (LUMO).

Conclusion: Therefore, this study provides significant contributes towards explaining the potential of natural dyes as the promising photosensitizer in the development of the solar cell application.

Keywords—anthocyanin, photosensitizer, solar cell

Titanium Oxide Plasma Treated to Enhance the Performance of Hybrid Solar Cells

Nur Salihah Alias
Faculty of Ocean Engineering Technology and Informatics Universiti Malaysia Terengganu 21030 Kuala Nerus, Terengganu
p4151@pps.umt.edu.my

Ahmad Nazri Dagang
Faculty of Ocean Engineering Technology and Informatics Universiti Malaysia Terengganu 21030 Kuala Nerus, Terengganu
nazri.dagang@umt.edu.my

Hasiah Salleh
Faculty of Ocean Engineering Technology and Informatics Universiti Malaysia Terengganu 21030 Kuala Nerus, Terengganu
hasiah@umt.edu.my

Aim: **A hybrid solar cell (HSC) is a third-generation solar cell that combines the advantages of organic and inorganic materials as active materials. The application of titanium oxide (TiO_2) in a hybrid solar cell (HSC) is well known as a promising photocatalyst and has received a lot of attention from solar cell researchers. However, the power conversion efficiency, PCE of HSC is still low because of insufficient surface area for light-harvesting and recombination on transparent conducting oxide (TCO). A surface modification of TiO_2 nanoparticle is considered an alternative method to enhance the performance of the HSCs.**

Method: **Plasma treatment of TiO_2 nanoparticles was carried out to enhance the efficiency of hybrid solar cells. The TiO_2 nanoparticles layer was treated using an atmospheric pressure plasma jet (APPJ) with helium gas.**

Results: **The effect of TiO_2 nanoparticles before and after plasma treatment were investigated by using X-ray diffraction (XRD), scanning electron microscopy (SEM) and ultraviolet-visible (UV-Vis) spectrophotometry. The study results revealed that the modification to TiO_2 increase the surface area and dye absorption amount on TiO_2.**

Conclusion: **It was observed that the performance power conversion efficiency (PCE) of hybrid solar cell with plasma-treated TiO_2 increased compared to untreated TiO_2.**

Keywords—Hybrid solar cell, titanium oxide, plasma treatment, atmospheric pressure plasma jet, surface area

Minor Criteria of Erbium Oxide Determining the Zinc Tellurite Glass Performance

Nazirul Nazrin Bin Shahrol Nidzam
Glass and Dielectric Lab Department of Physics Faculty of Science Universiti Putra Malaysia Serdang, Malaysia
nazirulnazrin@ymail.com

Halimah Mohamed Kamari
Glass and Dielectric Lab Department of Physics Faculty of Science University Putra Malaysia Serdang, Malaysia
halimahmk@upm.edu.my

Masera Marian Mukhtar
Glass and Dielectric Lab Department of Physics Faculty of Science Universiti Putra Malaysia Serdang, Malaysia
mariann.masera@gmail.com

***Abstract*— Ternary tellurite based glasses $[(TeO_2)_{0.7}(ZnO)_{0.3}]_{1-x}(Er_2O_3)_x$ was prepared by melt quenching method and the concentration has been selected from 0.01 to 0.05 on the interval of 0.01. Generally, the oxygen packing density, polaron radius and interionic distance of erbium have been closely linked to the polarization of the ions $Er3^+$ and the appearance of non-bridging oxygen (NBO). Till, the reflection loss and the optical coefficient transmission are highly dependent on the transparency phase of the glass that has been in the UV-Vis region.**

Keywords—Erbium oxide, tellurite, glass, melt-quenching method

[1] INTRODUCTION

Glass system does not consist of any crystalline phase, but it has high rigidity while retaining its liquid structure. The atoms in a liquid form are connected to one another, and they form in a random structure. There are two mechanisms that occur when a liquid is heated which are; the vibration of atoms and the movement of atoms or molecules in a random motion [1].

Present-day, the investigations on the new fiber optics materials with superior properties than silica based fiber optics were carried out. Nonetheless, the high vibrations of atoms in the silica fiber at high power lead to the conversion of light energy into sound energy. This effect will reduce the capabilities of fiber optics to transmit more power. This situation indirectly will lessen the ability of fiber optics to transmit light and restrict the number of information that can be transmitted in a telecommunications system [2].

Broadband optical amplifiers, in a few studies, have been reported to improve the bandwidth in a future communications system. More effective and excellent optical glass materials, however, are still ongoing. The promising materials of rare-earth doped tellurite glass have driven the improvement in the communication system which will require the investigations of new materials. Bang up to date, there are still limited numbers in the study of rare-earth and doped tellurite-based glass system. Therefore, the investigations on erbium doped tellurite-based glass system are still needed since it is still limited data to support its future optical applications [2].

[2] MATERIALS AND METHODOLOGY

The glass sample of $[(TeO_2)_{0.7}(ZnO)_{0.3}]_{1-x}(Er_2O_3)_x$ where x is equivalent to 0.01, 0.02, 0.03, 0.04 and 0.05 were prepared by using a melt quenching method. The raw materials of the elements were mixed by using a mortar and pestle for 30 minutes. The mixture was placed into an alumina crucible and put into the first furnace set at 400°C for a period of one hour. The alumina crucible was used due to its durability in handling high temperatures and will not react with the raw materials during the melting process as opposed to porcelain crucibles [1]. The sample was placed inside the second furnace at 900°C for two hours for the melting process. When the melting process was completed, the molten liquid was cast into a stainless steel cylindrical shape mould which was preheated at 400°C in the same period of time as the melting process previously. Then, the sample was annealed at 400°C for one hour, and the furnace was turned off after the specified time. The glass sample temperature was cooled down to room temperature and will eventually be polished until it has become flat, smooth and parallel for both surfaces [2].

[3] RESULTS AND DISCUSSION

The amount of rigidity of oxide in a synthesized glass network can be achieved using the packing density of oxygen (OPD) [3]. Oxygen packing density (OPD) can be defined as the tightness of packing of the oxide network [4]. Figure 1 presents the values of the OPD for different Er^{3+} concentration based on zinc tellurite glass system [5]. The OPD value decreased in the beginning from 66.6 to 63.1 and then increase from 63.1 to 65.3 with increasing Er^{3+} ions in the network. The changes in each concentration are due to the structural changes in the glass network with the formation of TeO_3 and TeO_4, yield non-bridging and bridging oxygen [6].

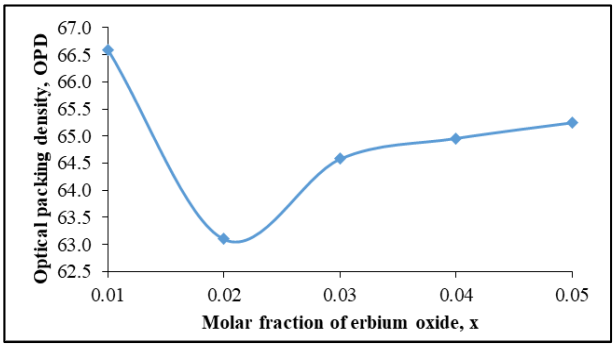


Fig. 1. Oxygen packing density against erbium oxide concentration.

Figure 2 shows the variations optical transmission coefficient (T) and the reflectivity/reflection loss (RL) respectively, with the addition of Er^{3+} ions in the glass series. The reflection loss from the glass surface was obtained using Fresnel's formula from the refractive index (n) as reported by Nazrin et al., (2019) [7]. The relationship between T and RL depicts that at a constant absorption, the value of T increased when RL decreased and vice versa. The escalation in the T value with inflation in the Er^{3+}ions, therefore, has encouraged a decline in the RL value, make the glasses more transparent in the UV–V is region [6].

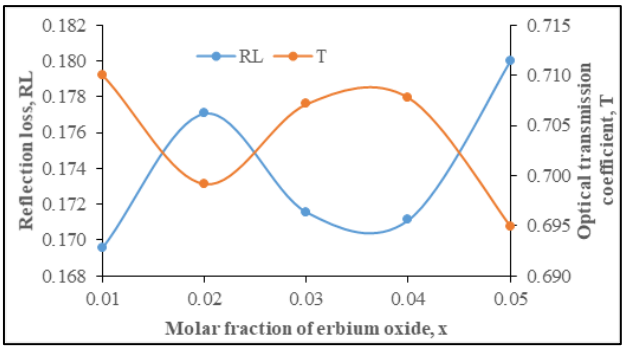


Fig. 2. Reflection loss and optical transmission coefficient against erbium oxide concentration.

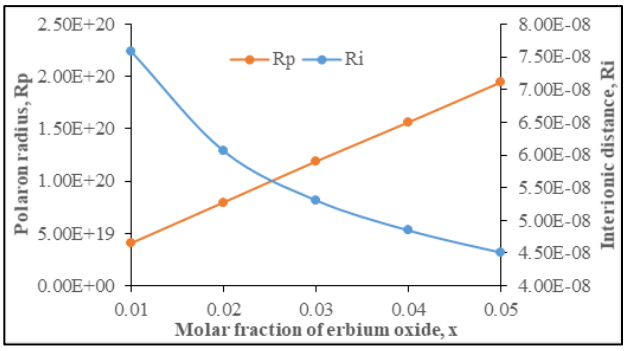


Fig. 3. Polaron radius and erbium inter-ionic distance against erbium oxide concentration.

Polaron is a quasi-particle formed by a conduction electron or hole in a polar semiconductor, ionic crystals, or alkali oxides/halides with its self-induced polarization. Polarons are studied to describe the polaron interaction between an electron and the longitudinal optical phonons. The polaron radius is the linear atomic/ionic displacement field of a polaron. When the polaron radius is of the order of the lattice constant, the polaron is called a small polaron. When the radius is much larger than the lattice constant of the material, the polaron is termed as a large polaron [8]. Currently, the value of the polaron radius increased with increasing concentration of Er^{3+} ions in the glass system as plotted in Figure 3. The incline in the polaron radius will cause an increase in the polarizability of a material. The trend has got the agreement that the polaron is a large polaron as the values have exceeded the lattice constants of the individual oxides in the glass. Concurrently, this circumstance will ultimately increase the glass electrical conductivity [8]. The interionic distance has been inclining as the Er^{3+} ions increased. The progress of this parameter can be associated with the inclination in the number of non-bridging oxygen (NBOs). The dopant ions in the glass network will break bonds by producing NBOs as a result of erbium ion acts as network modifier. A large value at the initial concentration of dopant in interionic distances improves the glass density ions. In addition, this condition can also be supported by a stronger field strength inside the glass network especially at the early concentration of dopant [4].

[4] CONCLUSION

Components of [(TeO2)0.7(ZnO)0.3]1-x(Er2O3)x glass system have been successfully studied. It can be concluded that the behavior of oxygen packing density, polaron radius and interionic distance have been influenced by the existence of erbium ions. The reflection loss and optical coefficient transmission have been inversely proportional, representing the effectiveness of the transparency of the studied glass system.

REFERENCES

[1] Nazrin, S. N., Halimah, M. K., Muhammad, F. D., Latif, A. A., & Asyikin, A. S. (2021). Impact of erbium-doped zinc tellurite glasses on Raman spectroscopy, elastic and optical properties. Chalcogenide Letters, 18(1).

[2] Halimah, M. K., Asyikin, A. S., Nazrin, S. N., & Faznny, M. F. (2021). Influence of erbium oxide on structural, physical, elastic and luminescence properties of rice husk biosilicate zinc borotellurite glasses for laser application. Journal of Non-Crystalline Solids, 553, 120467.

[3] Tafida, R. A., Halimah, M. K., Muhammad, F. D., Chan, K. T., Onimisi, M. Y., Usman, A. & Umar, S. A. (2020). Structural, optical and elastic properties of silver oxide incorporated zinc tellurite glass system doped with Sm3+ ions. Materials Chemistry and Physics, 246, 122801.

[4] Halimah, M. K., Hamza, A. M., Muhammad, F. D., Chan, K. T., Umar, S. A., Umaru, I., & Geidam, I. G. (2019). Effect of erbium nanoparticles on structural and spectroscopic properties of bio-silica borotellurite glasses containing silver oxide. Materials Chemistry and Physics, 236, 121795.

[5] Usman, A., Halimah, M. K., Latif, A. A., Muhammad, F. D., & Abubakar, A. I. (2018). Influence of Ho^{3+} ions on structural and optical properties of zinc borotellurite glass system. Journal of Non-Crystalline Solids, 483, 18-25.

[6] Umar, S. A., Halimah, M. K., Chan, K. T., & Latif, A. A. (2017). Polarizability, optical basicity and electric susceptibility of Er^{3+} doped silicate borotellurite glasses. Journal of Non-Crystalline Solids, 471, 101-109.

[7] Nazrin, S. N., Halimah, M. K., & Muhammad, F. D. (2019). Comparison study of optical properties on erbium-doped and silver-doped zinc tellurite glass system for non-linear application. Journal of Materials Science: Materials in Electronics, 30(7), 6378-6389.

[8] Umar, S. A., Halimah, M. K., Chan, K. T., & Latif, A. A. (2017). Physical, structural and optical properties of erbium doped rice husk silicate borotellurite (Er-doped RHSBT) glasses. Journal of Non-Crystalline Solids, 472, 31-38.

Effect of Sb Doping on the Surface Morphology, Structural, Properties of Zinc Oxide Thin Films

Elif AKARSU
Department of Electrical and Electronics engineering Ataturk University
Erzurum,Turkey
elif.akarsu@atauni.edu.tr

Mehmet ERTUĞRUL
Department of Electrical and Electronics engineering Ataturk University
Erzurum,Turkey
ertugrul@atauni.edu.tr

***Abstract*— Doping is a simple and useful concept to introduce deficiency levels to the bandgap that can foster therapeutic recombination of electron-hole pairs. Many articles have been devoted to the investigation of the photocatalytic activity of Sb doped ZnO. [2] Zinc oxide (ZnO) belongs to the semiconductor II-VI, which has a 3.37 eV wide bandgap, 60 meV high exciton energy, high bond strength, and high optical gain at room temperature. Because of these properties, ZnO has many applications in optoelectronic devices such as flat panel displays and light-emitting diodes. ZnO can be used as a transparent conductive oxide (TCO). Pure zinc oxide has been added with various arrangements. [4] In this study we would like to see the effects of Sb doping on ZnO thin films.**

Keywords—surface morphology, zinc oxide, doped, doping, thin films

I. INTRODUCTION

ZnO thin films without additives and Sb additives It is collected on the glass surface using the spray pyrolysis technique. Zinc chloride was utilized as the zinc source material. The initial solution of zinc chloride [$ZnCl_2$] at 0.05 M concentrations in distilled water was utilized to spray. 10 g of [$ZnCl_2$] were dissolved in 50 ml of distilled water under a magnetic stirrer.[1] Antimony trichloride [$SbCl_3$] is used as a source of antimony doped. The molar fraction of the $SbCl_3$ additive was added to the upper solution with different contents (molar ratio of sb to Zn 0.1,1,5,2,3,5%). Introduction II-VI Certain diversified properties of the Vurtzite phase give ZnO a special ranking among many oxides. Its wide bandwidth of 3.37 eV, its wide and high binding energy of 60 meV, and its low production cost make it more attractive than other transparent conductive oxides such as TiO_2. Furthermore, ZnO-based nanomaterials have found many applications, particularly in systems such as light-emitting diodes (LEDs) and photocatalysts. So far, among the various semiconductors used in the photodegradation of organic pollutants, ZnO nanostructures have been extensively studied for their better environmentally friendly properties, non-toxicity, low cost, and good stability. It also absorbs large fractions of the solar spectrum compared to other photocatalysts such as ZnO, TiO_2, and ZnS. The most effective way to improve the visible light absorption of ZnO nanomaterials is to reduce bandgap energy by introducing intermediate states. By doping ZnO nanocrystals (NCs) with antimony, particle size, morphology, and induced surface deficiencies will have a significant effect on photocatalytic activity. Besides, doping is a simple and useful concept to introduce deficiency levels to the bandgap that can foster therapeutic recombination of electron-hole pairs. Many articles have been devoted to the investigation of the photocatalytic activity of Sb doped ZnO. [2]. Zinc oxide (ZnO) belongs to the semiconductor II-VI, which has a 3.37 eV wide bandgap, 60 meV high exciton energy, high bond strength, and high optical gain at room temperature. Because of these properties, ZnO has many applications in optoelectronic devices such as flat panel displays and light-emitting diodes. ZnO can be used as a transparent conductive oxide (TCO). [4] Pure zinc oxide has been added with various arrangements.

II. EXPERIMENTAL DETAILS

Undoped and Sb-doped ZnO thin films were placed on the glass substrate using the spray pyrolysis technique. Zinc chloride is used as a zinc source. The starting solution containing Zinc chloride [$ZnCl_2$] at 0.05 M concentrations in distilled water was used to spray. 10 g of [$ZnCl_2$] were dissolved in 50 ml of distilled water under magnetic stirring.[1] Antimony trichloride [$SbCl_3$] is used as a source of antimony doped. The molar fraction of the $SbCl_3$ additive was added to the above solution with different contents (molar ratio of sb to Zn 0.1,1,5,2,3,5%). %). The solution was magnetically stirred for 2 hours to obtain a homogeneous mixture. Glass substrates were kept in concentrated sulfuric acid for 48 hours to remove any surface impurities present on them.

The glass substrate is then washed with Hydrogen peroxide, as well as with acetone, isopropyl alcohol, ethanol, and finally with deionized water using an ultrasonic bath and dried. During precipitation, the temperature is maintained at 590 ° C when the spray nozzle is fixed at a distance of 25 cm from the substrate, the solution is sprayed at a rate of 2.5 mL/min.

III. XRD ANALYSIS

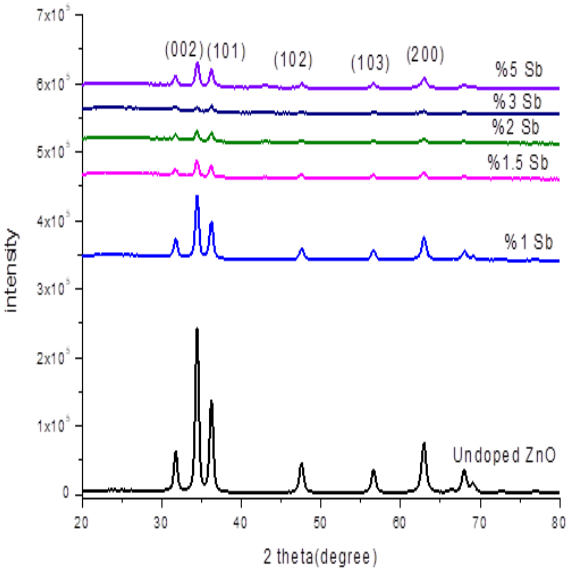


Fig. 1. XRD pattern of undoped and Sb doped ZnO thin films.

XRD studies were conducted to examine the structure of undoped and Sb-doped ZnO thin films. Figure 1 shows the XRD pattern of doped and Sb-doped ZnO thin films. Undoped and Sb-doped films display hexagonal wurtzite polycrystalline structures.[3]

The peaks of (002), (101), (102), (103), and (200) are observed for pure ZnO, 1 wt% Sb, 1.5 wt% Sb, 2 wt% Sb, 3 wt% Sb and 5. Sb. examples by weight.[6]

The values of the distance between planes (d) are determined by Bragg's law.

$$n\lambda=2d\sin\theta \quad (1)$$

In equation (1) n equals 1, λ, and θ is the wavelength and diffraction angle of the X-ray beam. The defined values are given in Table 1.

The lattice constants for ZnO are calculated by equation.

$$1 / d^2 = 4/3 ((h^2 + k^2 + hk) / a^2) + (l^2 / c^2) \quad (2)$$

where d is the interplanar separation h, k, l is the crystal plane index, a, and c are the lattice parameters respectively. The calculated values of "a" and "c" matched well with the declared values (a = 2.7108 Å, c = 3.2273 Å). [1] This clearly shows that the inclusion of Sb in the ZnO cage does not spoil the cage. Offset at the peak positions is used to calculate the changes in the lattice parameter of the films. It was observed that the contribution did not cause any change in the cage parameter and did not show any cage deterioration.

The crystal quality of ZnO thin films is determined according to the crystallite size calculated from the peak measurements in the diffraction pattern. The crystallite size (D) in the film was determined using Scherrer's formula.

$$D =0.9\lambda/\beta\cos\theta \quad (3)$$

where β is full width at half maximum (FWHM) and it is determined by using the equation [5]

$$\beta^2 =\beta^2obs - \beta^2 \quad (4)$$

inst. B obs and β inst are the value in XRD peak and instrumental broadening. [1]

mean crystallite size (D) values are presented in Table 1

Table 1. Mean crystallite size (D) values.

Sb , wt %	Orientation	FWHM	D, nm	a, Å	c, Å	d, Å
0	(002)	0,37364	17,899	2,7108	3,2273	2,6039
0	(103)	0,4272	17,899	2,7108	3,2273	1,4768
1	(002)	0,36212	18,46	2,7098	3,2273	2,6039
1	(103)	0,41239	18,46	2,7098	3,2273	1,4768
1,5	(002)	0,38977	17,158	2,7108	3,225	2,6002
1.5	(103)	0,4534	17,158	2,7108	3,225	2,6002
2	(002)	0,37545	17,81	2,7108	3,2273	2,6039
2	(103)	0,42792	17,81	2,7108	3,2273	1,4768
3	(002)	0,37021	18,063	2,7108	3,2273	2,6039
3	(103)	0,41595	18,063	2,7108	3,2273	1,4768
5	(002)	0,36564	18,288	2,7108	3,2273	2,6039
5	(103)	0,4098	18,288	2,7108	3,2273	1,4768

Table 2. The Dislocation Density and microstrain values

Sb, wt %	Dislocation Density	Micro Strain
0	3,12	-0,91
1	2,93	-0,86
1,5	3,39	-0,95
2	3,15	-0,91
3	3,06	-0,9
5	2,98	-0,89

Dislocation density (∑) and micros strain (£) values for the samples are determined by equations.[5]

$$\sum=1/D^2 \quad (5)$$

$$£=(1/\sin\theta).* [(\lambda/D)- \beta*\cos\theta] \quad (6)$$

The calculated values are presented in Table 2 and they vary between (2,93-3,15) lines/m^2 and (-0,86-0,95). Their variation with Sb doping is the same.

IV. SEM ANALYSIS

SEM images of different resolutions were examined (Figs. 2-7).

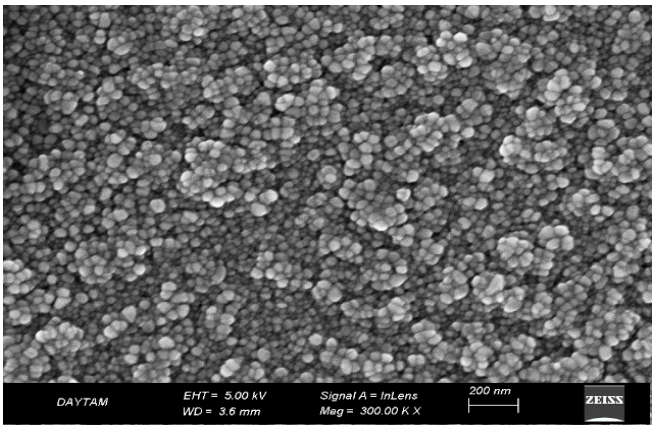


Fig. 2. SEM image of undoped ZnO thin film 300.00 K

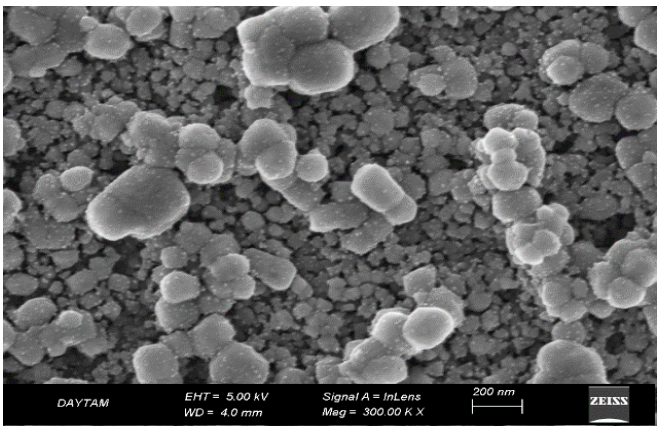


Fig. 3. SEM image of %1 Sb doped ZnO thin film 300.00 K

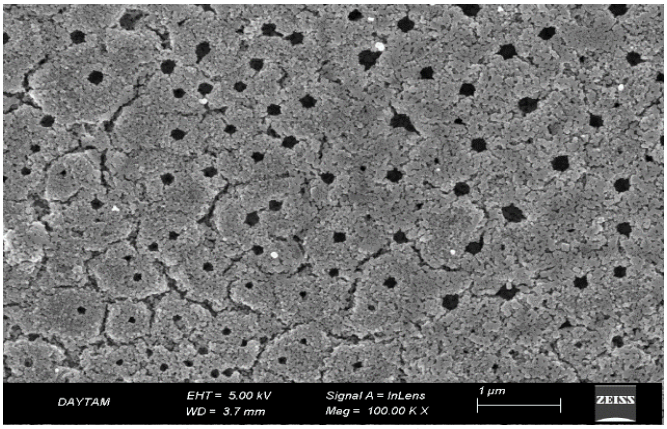


Fig. 4. SEM image of %1.5 Sb doped ZnO thin film 100.00 K

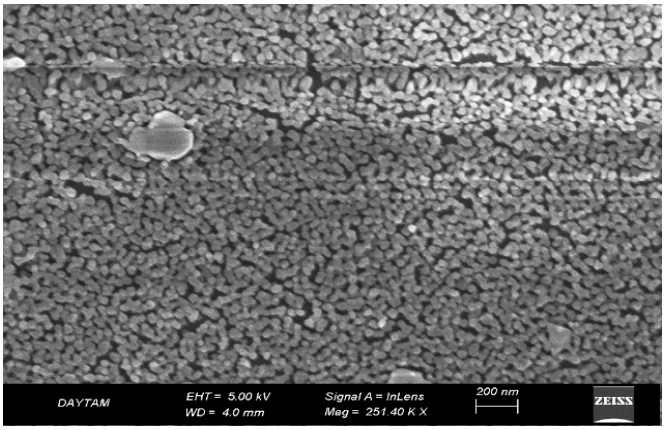


Fig. 5. SEM images of %2 Sb doped ZnO thin 250.00 K

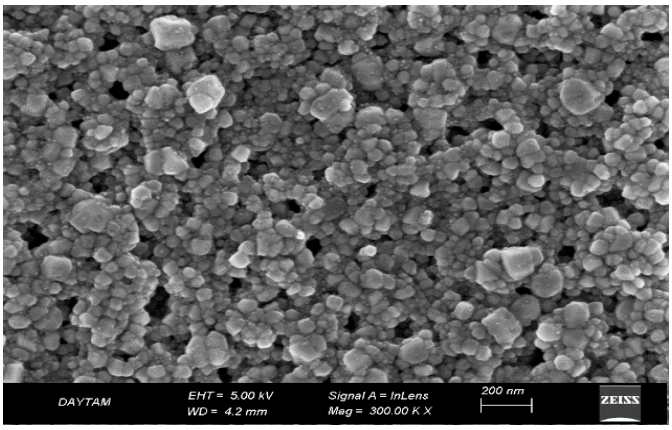


Fig. 6. SEM image of %3 Sb doped ZnO thin 300.00 K

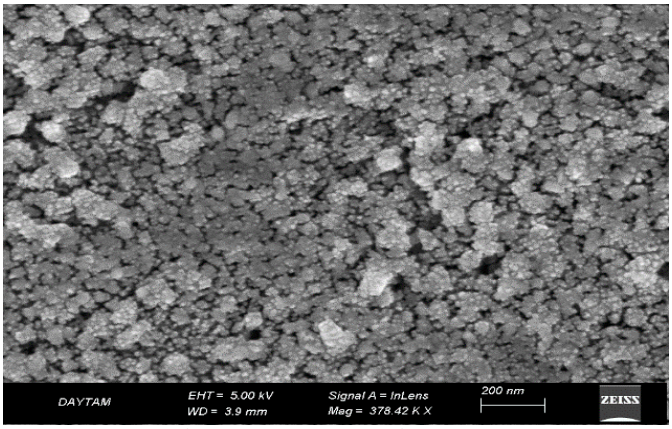


Fig. 7. SEM image of %5 Sb doped ZnO thin film 300.00 K

V. CONCLUSION

When 1% doped, larger structures were obtained compared to the non-doped image. When the contribution level reaches 1.5%, we see that a porous structure is obtained. A uniform structure is obtained when the additive level increases to 2%.

Hexagonal structures were obtained when the additive level was 3%. This is highly desirable as the gas holding capacity increases. It was also observed that the particle size decreased with 1.5% and 2% doping. It was observed that the particle size increased again as it increased above 2%.

REFERENCES

[1] Demet İskenderoğlu, Harun Güney. "Synthesis and characterization of ZnO: Ni thin films were grown by spray-deposition", Ceramics International, 2017

[2] Ramzi Nasser, Walid Ben Haj Othmen, Habib Elhouichet, Mokhtar Férid. "Preparation, characterization of Sb-doped ZnO nanocrystals and their excellent solar light has driven photocatalytic activity", Applied Surface Science, 2017

[3] N. Sadananda Kumar, Kasturi V. Bangera, G. K. Shivakumar. "Properties of antimony doped ZnO thin films deposited by spray pyrolysis technique", Semiconductors, 2015

[4] N. Sadananda kumar, Kasturi V. Bangera, C. Anandan, G.K. Shivakumar. "Properties of ZnO: Bi thin films prepared by spray pyrolysis technique", Journal of Alloys and Compounds,2013

[5] G. Turgut, S. Duman, F. S. Ozcelik, B. Gurbulak, S. Doğan. "Lutetium incorporation influence on ZnO thin films coated via a sol-gel route: spin coating technique", Journal of Materials Science: Materials in Electronics, 2016

[6] Güven Turgut, Demet Tatar, Bahattin Düzgün. "Relationship Between the Doping Levels and Some Physical Properties of SnO2:Sb Thin Films Spray-Deposited on Optical Glass", Asian Journal of Chemistry, 2013

Decision Making Mechanisms in Hybrid Energy Storage Technologies

Ahmet Cansız
Electrical Engineering Dept. Istanbul Technical University Istanbul, Turkey.
acansiz@itu.edu.tr

***Abstract*—The generation of electricity increases continuously to meet the demand of industry. The limited energy resources and the necessity of renewable energy require energy storage. Since the electricity is generated from various energy sources, effective energy storage also requires effective electromechanical energy conversion. Increasing energy demand and associated factors has led to the development of hybrid energy storage systems. Decision-making mechanisms are main control procedures in the energy storage systems to maintain efficiency. In this article, methods and procedures are examined for the hybrid energy storage systems based on battery energy storage systems supported by high power density devices consisting of supercapacitor, superconducting magnetic energy storage and superconducting flywheel energy storage.**

Keywords—Energy Storage, supercapacitor, Battery, Flywheel.

[1] INTRODUCTION

Energy has been a great role in the history of human kind. Up until now the humanity have benefited from the energy offered by the nature as needed. One of the most important supply offered by the nature is fire. There is no certain information about when fire was discovered. However, it is certain that human being have been able to use fire consciously since the Neolithic times. Lightning may have been the first inspiration for the use of fire. Apart from these, the most important energy source of our world is the sun. The energy we receive from the sun affects our lives directly or indirectly.

Energy can be defined as the capacity to do work. Since energy makes the plants to operate, its storage is strongly correlated for sustainable development in the industry. In addition, energy storage (ES) is necessary for energy conversion since energy can be found in different forms, such as chemical, electrical, thermal, light, mechanical and nuclear. Major ES devices are batteries, supercapacitors (SC), superconducting magnetic energy storage (SMES), superconducting flywheel energy storage (SFES), electromagnetic flywheel energy storage (EMFES), mechanical flywheel energy storage (MFES), pumped hydro energy storage (PHES) and compressed air energy storage (CAES) [1-3]. A large variety of battery types and technologies are being used for ES applications. Li-Ion technology is the most understood and developed battery energy storage (BES) method [4]. Batteries are high energy but low power density devices. For grid applications generally high power and low energy density devices are recommended so that the efficiency in the grid is sustained. Some of the high power density storage (HPDS) devices to work with the Li-Ion batteries are SC, SMES and SFES. The specifications and the comparison of these devices in terms of energy efficiency (η), energy density (e), power density (p), response time (τ), cycle life or life time (CL), cost (C), power rating (P) and discharge time (T) are given in Table 1 [1-3].

Table 1. Energy storage devices and their specifications.

	Li-Ion	SMES	SFES	SC
η	70-85	95-98	95	95
e	100-200	30-100	5-50	<50
p	25-1000	10^4-10^5	10^3-5×10^3	4000
τ	30	5	5	5
CL	500-2000	10^6	>20,000	>50,000
C	150-1300	High	380-2500	250-350
P	0.05-100	0.1-1	0.0001-20	0.01-1
T	min-8 h	ms-s	s-min	ms-min

η(%), e(Wh/kg), p(W/kg), τ(ms), CL(s), C($/kWh), P(MW), T(min).

From Table 1, it can be seen that SC, SMES and SFES have high specific power but low specific energy. SC and SMES are more suitable for power quality applications in electric power delivery because of their fast response time. Li-ion batteries have not only high specific energy but also specific power. In addition, Table 1 provides the nominal discharge time at rated power for given energy storage systems. For instance, the discharge time is less than an hour for the devices of SC, SMES and SFES while on the other hand, it is up to 10 hours for Li-Ion batteries. There are of course higher nominal discharge times longer than 10 hours such as Pumped Hydroelectric Storage (PHS), CAES and Thermal Energy Storage (TES), which are outside the scope of the ES systems under consideration. Discharge efficiency and self-discharge are also important parameters for the ES which shows the transmission ability and dissipation of energy in the grid, respectively. From Table 1, Li-Ion batteries have daily self-discharge ratios to be used for medium-term storage applications. SCs, SMES, SFES have very high daily self-charge ratios, which can be used short-term storage, up to hours or even shorter. The PHS, CAES and TES may be suitable for long-term storage durations.

Considering all kinds of ES methods, as some of them given in Table 1, any particular ES device or method can only meet specific needs of technical requirements of industrial demand. There are various reasons that affect the use of ES method in particular applications: Specific power and energy demand are the main reasons. Applicability and environmental conditions are also effective. These conditions forces various ES devices to unite into hybrid energy storage system (HESS). Supporting BES in the grid applications is one of the situation conditioned by a hybrid storage. HESS provides an increase in the BES life, improving system efficiency and reducing the installation costs where the use of renewable energy is mostly applied [5, 6]. Proper functioning

of a grid depends on particular components; power management or control and ES system or devices. Consequently, an appropriate combination of energy source with the storage method can lead higher energy supply efficiency with lower cost. There are number of literature regarding the HESSs such as SMES/battery in electrical bus [7] and micro-grid power [8].

The existed studies so far focused on the coupling of BES and alternative high power density storage (HPDS) devices. In this study we examined the hybrid designs of BES with the combination of at least two alternative HPDS devices simultaneously. In this context, working mechanisms of BES and HPDS systems are introduced first and then the decision making mechanism are examined with the case study scenarios. The parameters are determined to optimize the efficiency of ES system. Li-Ion BES system is selected to work with SC, SMES and SFES systems are introduced.

[2] ENERGY STORAGE

The power grid and BES system consist of a battery and alternative HPDS elements such as SC, SMES or SFES. The BES system is coupled with a bidirectional AC/DC converter capable of transferring power in both directions, which provide inputs to the control scheme. Similar schemes are applicable for SC, SMES and SFES. Due to low energy density HPDS is rarely used alone in ES systems. Schematic view of grid connected renewable energy system (RES) with HES of SMES/SFES/SC unit with BES system is shown in Fig.1 [3].

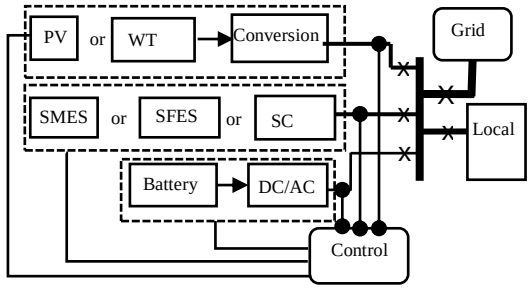


Fig.1. Schematic view of grid connected RES with HES of SMES/SFES/SC units with BES.

II.1. Battery Energy Storage (BES)

Batteries store the energy in the chemical form. To maintain stable supply-demand conditions in power systems, storing energy at off-peak periods and feed it back into the network during the periods of high demand is proposed. The regulation of supply–demand conditions can be realized through the BES system. This is achieved with a bidirectional converter via obtaining energy from the grid working as a rectifier. The energy from the grid is fed into to the grid where the converter is working as an inverter at this time. The energy flow is controlled in terms of measured current and voltage comparing with the reference values by switching structure. The BES system consists of a battery, a bidirectional AC/DC converter capable of transferring power in both directions. The operating BES system is provided by its state of charge (SOC) which depends on the maximum battery capacity.

The BES system has a limitation according to the conditions of bi-directional energy flow. For this reason, sizing the ES system has a crucial importance to meet the power conditioning. The best solution to this task is to construct HES systems and decision mechanisms to minimize the voltage fluctuations occurring in the grid during charging and discharging processes. As a high power density support to the grid, one of the best scheme is to hybrid the BES with a SC. SMES and SFES are also considered to be secondary support mechanisms.

II.2. Supercapacitor Energy Storage (SCES)

The SCs store the energy in the form of electric field. The SCs have ability to discharge the energy stored in the order of few seconds. The SCES unit generally comprises of multi SC cells connected in series. Each cell has an operating a specific voltage of per cell, so the total terminal voltage is the cumulative [9]. The basic configuration of SCES is given in Fig.2. The SCES connected to the grid consists of SCs, AC/DC rectifier, DC/AC inverter and a controller. During the normal operation, SC stores energy in the form of electric field provided by the rectifier through the grid. When needed (the power outage of load fluctuations occur) the energy stored in the SCs feed the load through the inverter. Realization of reactive and active power balance is provided through the controller.

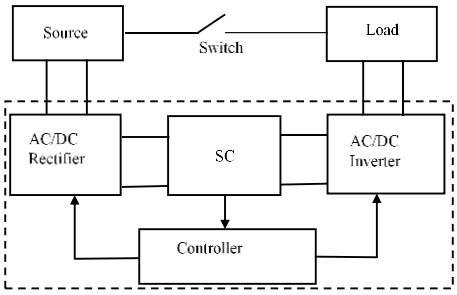


Fig. 2. Simplified equivalent configuration for SC.

II. 3. Superconducting Magnetic Energy Storage (SMES)

SMES is a device that stores energy in the form of magnetic field created by electric currents. It is the only device that stores electricity without the need of energy conversion. The stored energy physically carried by electric currents circulating in the SMES coil, which exhibit practically zero resistivity. Basic configuration of a current source inverter (CSI) based SMES unit, given in Fig.3, consists of a transformer, additional power electronics elements and a SMES coil. The power electronics part consists of a pulse width modulation (PWM) converter using IGBT by a DC-Link capacitor and a SMES [3]. The DC-DC chopper provides a power electronics interface between the AC power system and the SMES coil. The energy can be stored or withdrawn from the SMES.

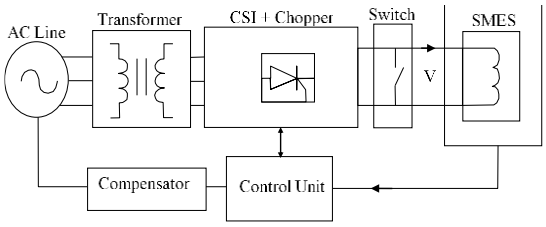


Fig. 3. A typical SMES and its system components.

II.4. Superconducting Flywheel Energy Storage (SFES)

Flywheels store the energy in the kinetic form. The energy stored in the flywheel is used to assist in power grid regulation and will quickly compensate for the mismatch between

electricity supply and demand. The energy stored in the flywheel acts as a buffer, making it possible to provide uninterrupted energy to the load in case of problems in the electrical energy supply given by the grid to the load. The fact that energy can be stored in the flywheel very quickly and have a very high charge/discharge cycle shows the importance of these systems. The use of superconducting levitation provides passive control mechanism during the operation of the flywheel [10].

The main parts of the SFES system include flywheel, motor-generator and power electronics components. As shown in Fig. 4, the system consists of the flywheel where the energy is stored in the rotating mass, an electric machine operating both as a motor and a generator, and power electronics converters. Power electronics converters operate the electric machine as a motor via a motor driver in order to accelerate the flywheel to a certain speed during the energy storage phase. When it is desired to use the energy stored in the flywheel, the motor driver operates the electrical machine as a generator and the rectifier on the input side operates in the inverter mode and transfers the energy stored in the flywheel to the load. Both the motor driver and the network side rectifier allow bi-directional power flow.

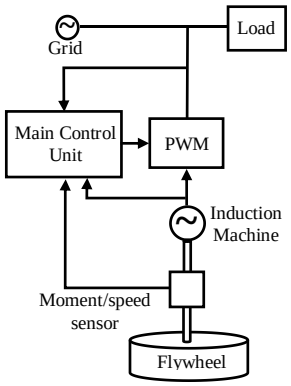


Fig. 4. A typical SFES system and its components.

Power electronics provides a control interface between electric machine and power transmission. In this sense, power electronics is the most vital part of the FES system. Power electronics converters consist of a rectifier operating on the network side according to the PWM principle that can allow bidirectional power flow and a variable speed motor driver on the motor side. A three phase voltage source inverter/rectifier is used to charge/discharge the flywheel. Power from the flywheel or supplied to the flywheel is kept at a certain voltage in a DC bus.

[3] Battery and Hybrıd Energy Storage

In a hybrid energy storage (HES) system, such as one coupled with a battery, when the output power from the power generation is higher than a reference value (grid), the battery and alternative HPDS unit stores the excess power. Otherwise, the HPDS element delivers power to the network. In the following procedure, determination of which HPDS element to support the battery system in terms of the modes of operation is decided. This procedure is maintained by decision making mechanism described in the following.

The generated power and ES system are connected to the grid through the switching controllers. If the voltage is maintained within the limits, no switching occurs. If the voltage goes beyond the limits, the switching occurs and decision mechanism take part in supporting the first peak of the fault or disturbance. While the system is operating with the utility network, the voltage levelling is provided by the HPDS as soon as a disturbance is detected. Once the HPDS degrades the battery starts to operate. The BES continues to operate until its state of charge (SOC) is less than critical value. If the SOC falls below the critical value, the BES is disconnected and the system is connected to the main grid.

In order to control the energy flow in the grid, the potential coupling mechanisms with the BES system can be provided with alternative HPDS devices such as SC, SMES and SFES. For the case of the battery-SC hybrid energy storage, the system is connected to inverter terminal through individual DC/DC converter. This topology is fault tolerant in case failures occur in the battery or the SC in the expense of additional converters. The additional control system is constructed to perform the decision mechanism among the HPDS devices.

The HESS sizing problem includes determining the number of BES cells and HPDS modules to maintain continuous bi-directional power flow. For instance, in the case of BES and SMES design, the sizing should meet both the power and energy requirements to sustain both long-term and short-term power fluctuations. In this sense, sizing HESS can be considered in terms of the energy dispatching requirement sets battery size to guarantee load demand and the SMES to guaranteed power fluctuation prevention. The battery is sized without consideration of the energy stored by the SC, SMES or SFES.

Performance of high and low power density ES devices are actually differing from each other. For instance, BES as a low power density device charges and discharges at fixed potential while on the other hand, HPDS devices such as SC, SMES and SFES discharges with decrease in the potential and charges with the increase in the potential. High power-low energy density property of SCs, SMES and SFES can complement the low power-high energy BES. In fact, suitable combinations of these systems can lead battery–SC hybrid storage systems for high-power – high-energy applications.

The SMES is one of the best alternative to work with BES as a HPDS device. Other HPDS devices such as SC and SFES also work with BES in similar fashion. A typical performance of BES system with the support of SMES can be seen in Fig. 5. Fig. 5(a) shows that sudden outage of power where there is no ES device for backup, while (b) shows voltage decrease with time on the HES system where BES and SMES are functioning together, and (c) indicate the smooth operation of the HES system where the voltage is maintained during the switching.

Another alternative HPDS device as SFES is given in Fig. 4, which can also work with BES system. Studies showed that the addition of an SFES or FES system in the grid can improve the power quality. The fluctuations in RES such as in the wind power can be reduced by charging or discharging the FES system [12]. As shown in Fig. 6, the data of the rotational frequency of a flywheel as a function of time is a self-energy discharge indicator for the SFES system. The SFES self-discharges under no load condition is much higher compared to the other ES systems. However, since the stored energy is proportional with the mass and the square of the rotational frequency of the flywheel, there is no upper limit on the flywheel except the constraints set by physical strength of flywheel material. To use SFES system for HPDS purpose is

more effective for large systems.

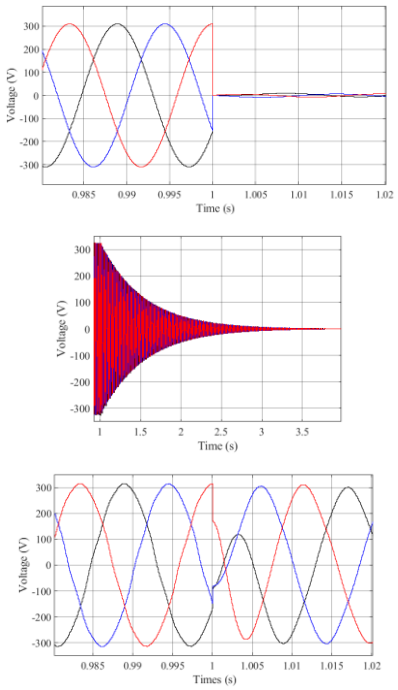


Fig. 5. a) The system voltage without the support of ES, b) With the support of SMES. c) System voltage with SMES and Battery are functioning together.

A similar working mechanism HES consisting of BES with a SCES given in Fig. 2 have the components are inverter, controller, and load [11]. The SC is directly connected in parallel with the BES. In power outage, the BES provide the primary energy for long duration, and SCs only serve for peak power smoothing.

As indicated above, the energy stored in SFES is proportional with the square of the rotational frequency of the flywheel, which makes it a valuable candidate as HPDS device. On the other hand, the discharge of energy from the flywheel is similar to the BES. Fig. 7 shows the remaining energy percentages as a function of time for BES, SFES and other kinds of flywheels such as electromagnetic flywheel energy storage (EMFES) and mechanical flywheel energy storage (MFES). Similar discussion in Fig. 6 also applicable in Fig. 7 to compare the best complementary ES systems for BES.

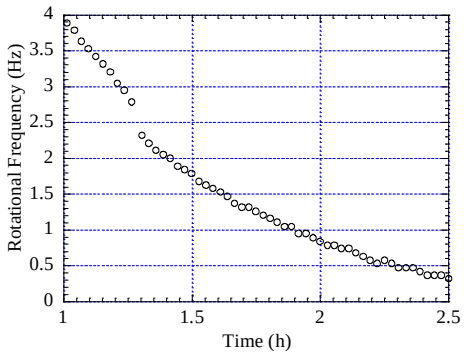


Fig. 6. Low speed free spin down of flywheel energy storage rotor: Rotational frequency versus time.

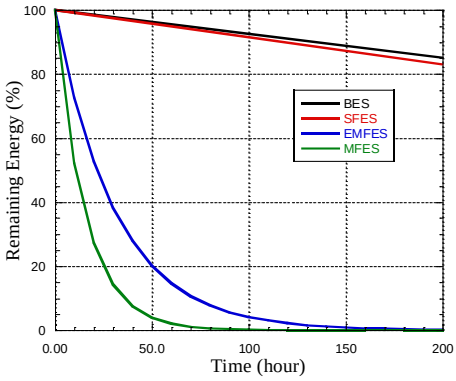


Fig. 7. Energy storage performances of BES, SC, MFES, electromagnetic, superconducting flywheel energy storage systems.

The working mechanisms of BES with particular HPDS devices such as SC, SMES and SFES are explained so far can be reconfigured to work in a more sophisticated level. In this procedure the BES system can be design to work with two HPDS devise simultaneously. There are three possible combinations to support BES system, which are SC-SMES, SC-SFES and SMES-SFES. Setting the primary support storage unit for the BES also creates additional 3 more alternatives. It is an optimization problem to assess the best configuration among the others. In addition, to sustain the best BES coupling with HPDS device require an optimal energy management scheme. In this scheme, the intention is to minimize the magnitude/fluctuation of current flowing in/out of battery so that the energy loss in the HESS is minimized. In other words, the optimization provides the solution to solve the current flow fluctuation. The formulation of BES with SC, MES and SFES are provided so far brings the question of which combination is the best for particular application. The energy management scheme for a BES/HPDS is mathematically formulated as an optimization problem. A future study is planned to use optimization techniques to determine successful hybrid combinations for particular grid requirements.

[4] CONCLUSIONS

In this article the alternative solutions of HPDS devices coupling with BES were examined. The existing literature so far suggest that the hybrid energy storage is possible for BES as Li-Ion battery with SCs, SMES and SFES. The BES systems not only work with a single HPDS device but also multi-use of these devices simultaneously. It is suggested that the working mechanisms of BES and HPDS systems relied on the decision making mechanism, which require case study scenarios. A future study is planned for the optimization procedures regarding the BES-HPDS coupling.

REFERENCES

[1] H. Ibrahim, A. Ilinca and J. Perron, “Energy storage systems--Characteristics and comparisons”, Renew Sustain Energy Rev., 12, 1221-1250, 2008.

[2] X. Luo, J. Wang, M. Dooner, J. Clarke, “Overview of current development in electrical energy storage technologies and the application potential in power system operation”, Applied Energy, 137, 2015, 511-536.

[3] A. Cansiz, C. Faydaci, M.T. Qureshi, O. Usta and D.T. McGuiness, “Integration of a SMES–Battery-Based Hybrid Energy Storage System into Microgrids”, J. Supercond. Novel Magn., 31, 1449-1457, 2018.

[4] V.A. Boicea, “Energy Storage Technologies: The Past and the Present”, Proceedings of the IEEE, 102, 11, 1777, 2014.

[5] A. Khaligh, Z. Li, “Battery, Ultracapacitor, Fuel Cell, and Hybrid Energy Storage Systems for Electric, Hybrid Electric, Fuel Cell, and Plug-In Hybrid Electric Vehicles: State of the Art”, IEEE Trans. Veh. Technol., 59, 6, 2806, 2010.

[6] W. Li, G. Joos, J. Belanger, “Real-time simulation of a wind turbine generator coupled with a battery supercapacitor energy storage system”, IEEE Trans. Ind. Electron., 57, 4, 1137, 2010.

[7] J. Li, M. Zhang, Q. Yang, Z. Zhang, W. Yuan, “SMES/Battery Hybrid Energy Storage System for Electric Buses”, IEEE Trans. Applied Supercond., 26, 4, 5700305, 2016.

[8] J. Li, R. Xiong, Q. Yang, F. Liang, M. Zhang, W. Yuan, “Design/test of a hybrid energy storage system for primary frequency control using a dynamic droop method in an isolated microgrid power system”, Applied Energy, 201, 257, 2017.

[9] H. Wei, W. Xin, G. Jiahuan, Z. Jianhua and Y. Jingyan, "Discussion on application of super capacitor energy storage system in microgrid", Int. Conf. on Sust. Power Gen. and Supply, Nanjing, China, 2009, 1-4.

[10] A. Cansiz, A.M. Campbell and T.A. Coombs, “An Evershed type superconducting flywheel bearing”, Physica C, 390, 305-310, 2003.

[11] T. Ma, H. Yang and L. Lu, “Development of hybrid battery–supercapacitor energy storage for remote area renewable energy systems”, Applied Energy, 153, 56-62, 2015.

[12] T-T. Nguyen, H-J. Yoo and H-M. Kim, “A Flywheel Energy Storage System Based on a Doubly Fed Induction Machine and Battery for Microgrid Control”, Energies, 8, 5074-5089, 2015.

Integral Terminal Sliding Mode Controller for Trajectory Tracking Control of Unmanned Ground Vehicle

Hayriye Tuğba SEKBAN
Department of Electronics & Automation, Bayburt University
Bayburt, Turkey
tugbasekban@bayburt.edu.tr

Kaan CAN
Department of Electrical & Electronics Engineering Ataturk University,
Erzurum, Turkey
kaan.can@atauni.edu.tr

Abdullah BAŞÇİ
Department of Electrical and Electronics Engineering Ataturk University Erzurum, Turkey
abasci@atauni.edu.tr

***Abstract*— In this paper, trajectory tracking control of an unmanned ground vehicle (UGV) is performed by using the integral terminal sliding mode control (ITSMC) method. Firstly, a kinematic controller is designed to predict linear and angular velocities that will bring UGV to asymptotic stability. Then, ITSMC is designed, which could bring the UGV to its real velocity by providing finite time convergence. Finally, a trapezoidal and sinusoidal reference signals are applied as linear and angular velocity reference to UGV, respectively. Simulation results show the effectiveness of the ITSMC.**

Keywords*— *unmanned ground vehicle, kinematic control, sliding mode control, terminal sliding mode control

[1] INTRODUCTION

Unmanned ground vehicles (UGV) is a general name given to vehicles that can move autonomously and used on land. Today, UGVs designed are able to navigate on their own in dispersed environments, avoid obstacles, recognize objects, plan their paths and generally decide on their own [1]. Technological developments have led to the frequent preference of UGVs in different industrial processes such as service, medical, construction and demolishing, military, remote inspection, safety and socialization. In addition, the fact that they can be used in uninhabitable environments such as nuclear events and the discovery of planets has increased the interest in UGVs day by day.

When the studies conducted in the field of unmanned ground vehicles in recent years are examined, it is seen that certain subjects such as trajectory tracking, obstacle avoidance, path planning, navigation, localization and mapping [1]. Trajectory tracking control problem is one of the most popular problems of UGV. In recent years, many studies have been carried out on the kinematics, dynamics and controller designs of UGVs for solving the trajectory tracking control problem [2]. Firstly, linear control methods such as LQR, gain scheduling and PID were used to solve the trajectory tracking control problem [3-5]. However, the fact that UGVs are nonlinear systems with high complexity has caused these control methods to not give the desired results. On the other hand, it has been observed that most of the designed controllers are based on the kinematics of the vehicle [6-7]. UGV has various difficulties such as having non-holonomic constraints, including parameter uncertainties, and being affected by external disturbances, which led to the inability to achieve satisfactory tracking performance by using controllers based on only kinematic model in real applications. For this reason, in order to overcome all these situations, controllers that take into account both the dynamics and kinematics of the vehicle have been designed. Backstepping method, input-output linearization, finite-time control technique, intelligent control and sliding mode control (SMC) etc. nonlinear control method has been used [8-12]. Among these controller methods, SMC has attracted great attention [13-15].

SMC is a control technique that can be easily applied to nonlinear systems, is not affected by external disturbances and parametric uncertainties, responds quickly, is easy to design and robust [16-17]. However, the disadvantages of this controller are that it produces chattering in systems and provides asymptotic stability in infinite time. The chattering effect can be reduced by using various ways such as filtering, discontinuous approximation, saturation function, fuzzy control, high-order sliding mode controller [18]. The problem of asymptotic convergence of system states in infinite time has been tried to be overcome with the terminal sliding mode controller (TSMC).

TSMC has been successfully applied to many systems such as motors, spacecraft, and multi-robot systems [19-21]. In the TSMC technique, a nonlinear term is added to the sliding surface to ensure that the system states converge to the origin in finite time. Dynamical systems that are stable in finite time converge to the desired position faster and are more stable by eliminating disturbances [22]. On the other hand, the first TSMC can cause the problem of singularity around equilibrium point that will result in an unlimited control signal. [23]. For the solution of this situation, control methods such as nonsingular TSMC, continuous nonsingular TSMC for MIMO systems and integral TSMC (ITSMC) have been developed [24-25]. The surface of integral terminal based SMC is composed of a linear function of the tracking errors that consist of their sign or fractional integrals, and then the finite-time convergence could be obtained [26]. In addition, ITSMC provides finite time convergence and solves the singularity problem.

In this paper, SMC and ITSMC are used for trajectory tracking control of UGV. The performance of ITSMC and SMC is compared in the simulation environment and it is observed that ITSMC showed better tracking performance.

[2] MATERIAL AND METHOD

A. Unmanned Ground Vehicle (UGV)

The non-holonomic UGV used in this study is as shown in figure 1. There is one caster wheel in the front and two independent fixed wheels at the rear.

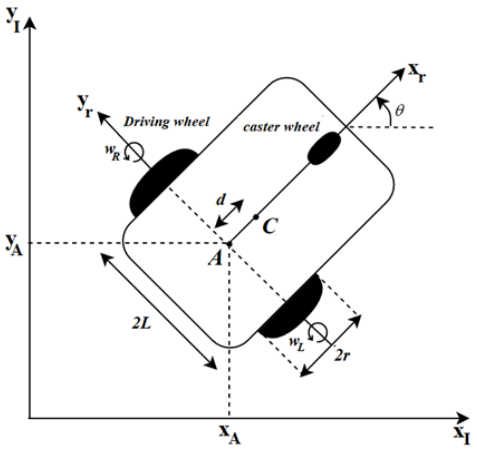


Fig. 1. The structure of UGV

The terminologies of Fig. (1) are as follows.

x_I, y_I	Global axis
x_r, y_r	Local axis
x_A, y_A	Coordinate components with respect to point A
A	The midpoint of the two wheels
C	Center of gravity of the vehicle
d	Distance between point A and C
r	Radius of the wheel
L	Distance of each wheel to point A
v	Linear speed of vehicle (body speed)
ω	Angular velocity of the vehicle
ω_R	Angular velocity of the right wheel
ω_L	Angular velocity of the left wheel
θ	Angle between the local axis and global axis

Rotation matrix $R(\theta)$ is used to determine the vehicle position between the global axis (q^I) and the local axis (q^r) and these expressions are as specified in (1).

$$q^I = \begin{bmatrix} x^I \\ y^I \\ \theta^I \end{bmatrix}, q^r = \begin{bmatrix} x^r \\ y^r \\ \theta^r \end{bmatrix}, R(\theta) = \begin{bmatrix} \cos\theta & -\sin\theta & 0 \\ \sin\theta & \cos\theta & 0 \\ 0 & 0 & 1 \end{bmatrix} \quad (1)$$

B. Kinematic Model of UGV

The main purpose of kinematic modeling used for UGV is to express the linear and angular velocities of the vehicle by using the geometry of the vehicle and the speeds of the drive wheels. The linear velocity of the vehicle is equal to the average of the linear velocities of both wheels and is calculated as follows.

$$v = \frac{v_R + v_L}{2} = \frac{r}{2}(\omega_R + \omega_L) = \frac{r}{2}(\dot{\varphi}_R + \dot{\varphi}_L) \quad (2)$$

The change of vehicle body angle is calculated as follows.

$$\omega = \dot{\theta} = \frac{v_R - v_L}{2L} = \frac{r(\omega_R - \omega_L)}{2L} = \frac{r}{2L}(\dot{\varphi}_R - \dot{\varphi}_L) \quad (3)$$

The velocities of the point *A*, which is the center of the vehicle, according to the global coordinate axis are calculated as in (4) using the orthogonal rotation matrix.

$$\dot{q}^I = \begin{bmatrix} \dot{x}_A^I \\ \dot{y}_A^I \\ \dot{\theta}_A^I \end{bmatrix} = \begin{bmatrix} \frac{r}{2}\cos\theta & \frac{r}{2}\cos\theta \\ \frac{r}{2}\sin\theta & \frac{r}{2}\sin\theta \\ \frac{r}{2L} & -\frac{r}{2L} \end{bmatrix} \begin{bmatrix} \dot{\varphi}_R \\ \dot{\varphi}_L \end{bmatrix} \quad (4)$$

The velocities of the vehicle can be rewritten in terms of linear and angular velocities in the body axis of the vehicle as in (5).

$$\dot{q}_A = \begin{bmatrix} \dot{x}_A^I \\ \dot{y}_A^I \\ \dot{\theta}_A^I \end{bmatrix} = \begin{bmatrix} \cos\theta & 0 \\ \sin\theta & 0 \\ 0 & 1 \end{bmatrix} \begin{bmatrix} v \\ \omega \end{bmatrix} \quad (5)$$

C. Dynamic Modeling of the UGV

The dynamic equation is used to express the relationship between the position, velocity and acceleration of a mechanical system in the presence of external forces. Most non-holonomic mechanical systems are expressed by the following dynamic equation [27].

$$M(q)\,\ddot{q} + V(q,\dot{q})\,\dot{q} + F(\dot{q}) + G(q) + \tau_d = B(q)\,\tau - A^T(q)\,\lambda \quad (6)$$

Terminologies for Equation (6) are as follows [28-29].

$M(q)$	Symmetric positive definite inertia matrix
$V(q,\dot{q})$	Centripetal and Coriolis matrix
$F(\dot{q})$	Surface friction matrix
$G(q)$	Gravity vector
τ_d	Vector containing unmodified dynamics and disturbances
$B(q)$	Input matrix
τ	Output vector
$A(q)$	Matrix on kinematic constraints
λ	Lagrange multiplier vector
$q, \dot{q}, \ddot{q}$	Position, velocity and acceleration vectors, respectively.

Many methods such as Lagrange method, Newton-Euler method and Kane method are used to obtain the dynamic equation of UGV. The Lagrange dynamical approach is a simple and powerful method used to derive equations of motion systematically by taking into account the potential and kinetic energies of a given system [27]. $M(q)$, $V(q,\dot{q})$, $B(q)$ and $A^T(q)$ matrices are obtained by using the Lagrange dynamic approach with the assumption that the vehicle moves in a horizontal plane and there is no disturbance, surface friction and gravity. In order to eliminate the problems that may arise from not knowing the Lagrange multiplier in (6), the expression $A^T(q)\lambda$ should be eliminated in the equation. For this, first of all, generalized coordinate velocities should be defined as given below.

$$\begin{bmatrix}\dot{x}_A\\ \dot{y}_A\\ \dot{\theta}_A\\ \dot{\varphi}_R\\ \dot{\varphi}_L\end{bmatrix}=\begin{bmatrix}\frac{r}{2}\cos\theta & \frac{r}{2}\cos\theta\\ \frac{r}{2}\sin\theta & \frac{r}{2}\sin\theta\\ \frac{r}{2L} & -\frac{r}{2L}\\ 1 & 0\\ 0 & 1\end{bmatrix}\begin{bmatrix}\dot{\varphi}_R\\ \dot{\varphi}_L\end{bmatrix} \quad (7)$$

Then, if we rearrange (7) by defining the reduced vector as $\eta=\begin{bmatrix}\varphi_R\\ \varphi_L\end{bmatrix}$, (8) is obtained.

$$\dot{q}=S(q)\eta \quad (8)$$

The $S(q)$ in (8) is the transformation matrix and the derivative of (8) is written as follows.

$$\ddot{q}=\dot{S}(q)\eta+S(q)\dot{\eta} \quad (9)$$

The $S(q)$ matrix is the null space of the $A(q)$ matrix. This expression is given in (10).

$$A(q)^T S(q)^T=0 \quad (10)$$

If (8) and (9) are replaced in (6) and arranged by multiplying both sides of the equation by $S(q)^T$, the dynamic equation of UGV is obtained as in (11).

$$\tilde{M}(q)\dot{\eta}+\tilde{V}(q,\dot{q})\eta=\tilde{B}(q)\tau \quad (11)$$

In the equation, $\tau\in R^{(n-m)\times m}$ and the matrices $\tilde{M}(q)$, $\tilde{V}(q,\dot{q})$ and $\tilde{B}(q)$ are obtained by using the following equations.

$$\left.\begin{array}{c}\tilde{M}(q)=S(q)^T M(q)S(q)\\ \tilde{V}(q,\dot{q})=S(q)^T M(q)\dot{S}(q)+S(q)^T V(q,\dot{q})S(q)\\ \tilde{B}(q)=S(q)^T B(q)\end{array}\right\} \quad (12)$$

Using (2), (3) and (11), an alternative form can be obtained by rearranging the linear and angular velocities of the UGV as follows [2].

$$\begin{bmatrix}\left(m+\frac{2I_w}{R^2}\right) & 0\\ 0 & \left(I+\frac{2L^2}{2R^2}I_w\right)\end{bmatrix}\begin{bmatrix}\dot{v}\\ \dot{w}\end{bmatrix}+\begin{bmatrix}0 & -m_c dw\\ m_c dw & 0\end{bmatrix}\begin{bmatrix}v\\ w\end{bmatrix}=\begin{bmatrix}\frac{1}{R} & 0\\ 0 & \frac{L}{R}\end{bmatrix}\begin{bmatrix}u_1\\ u_2\end{bmatrix} \quad (13)$$

where m is the total mass of UGV, m_c is the mass of UGV without motors and wheels, I is the total equivalent inertia, I_w is the moment of inertia of each drive wheel [27]. Equation (13) is shown in simplified form as in (14) [2].

$$\tilde{M}\dot{X}+\tilde{V}X=\tilde{B}u \quad (14)$$

$$u=\begin{cases}u_1=\tau_R+\tau_L\\ u_2=\tau_R-\tau_L\end{cases}\quad\text{and}\quad X=\begin{bmatrix}v\\ w\end{bmatrix} \quad (15)$$

The expressions τ_R and τ_L in (15) express the torque of the right and left wheel, respectively. Equation (13) is the equation of the nonlinear model of UGV. Equation (14) is the linearized dynamic model equation of UGV and when it is rearranged, (16) is obtained [2].

$$\begin{bmatrix}\left(m+\frac{2I_w}{R^2}\right) & 0\\ 0 & \left(I+\frac{2L^2}{2R^2}I_w\right)\end{bmatrix}\begin{bmatrix}\dot{v}\\ \dot{w}\end{bmatrix}=\begin{bmatrix}\frac{1}{R} & 0\\ 0 & \frac{L}{R}\end{bmatrix}\begin{bmatrix}u_1\\ u_2\end{bmatrix} \quad (16)$$

[3] Controller Design

A. *Kinematic Controller*

The kinematic controller is used to estimate linear and angular velocities and thus, it provides the system asymptotically stable. For the controller design, the error between the reference position (q_r) and the current position (q_A) is expressed as in (17) [30].

$$e_P=\begin{bmatrix}x_e\\ y_e\\ \theta_e\end{bmatrix}=\begin{bmatrix}\cos\theta & -\sin\theta & 0\\ -\sin\theta & \cos\theta & 0\\ 0 & 0 & 1\end{bmatrix}\left[q_r-q_A\right] \quad (17)$$

The kinematic based control rule proposed by Kanayama is expressed as follows [30].

$$\begin{bmatrix}v_c\\ \omega_c\end{bmatrix}=\begin{bmatrix}v\cos\theta_e+k_x x_e\\ \omega+v(k_y y_e+k_\theta\sin\theta_e)\end{bmatrix} \quad (18)$$

k_x, k_y, k_θ are the positive gain values of the backstepping based kinematic controller.

B. *Dynamic Controller Design*

a) *Terminal Sliding Mode Controller*

SMC is a nonlinear control technique that is very robust and can be easily applied to nonlinear systems. However, reaching stability in infinite time limits its use. To overcome this situation, a terminal sliding mode controller (TSMC) was developed in the early 1990s by Venkataraman and Gulati. Besides having all the advantages of SMC, TSMC guarantees that the system states converge to the origin in finite time. For TSMC design, firstly nonlinear sliding surface is determined and then control signal is generated. The control signal consists of two stages. In the first part, the equivalent control is designed for dealing with the system dynamics and sliding surface. In the second part, the switching control is responsible for keeping the system dynamics on the sliding surface [31]. Integral terminal sliding surface is proposed as given below [32].

$$s(t)=e_c(t)+\beta\int |e_c|^{\sigma_c}\,\mathrm{sgn}(e_c)dt \quad (19)$$

Here, β is the positive shear constant and $\beta\rangle 0$. $0\langle\sigma_c\langle 1$, e_c is the trajectory error and $\dot{e}_c$ is the derivative of the trajectory error and these expressions are written as follows [2].

$$e_c(t) = q - q_r = [e_v\ , e_\omega]^T$$
$$\dot{e}_c(t) = \dot{q} - \dot{q}_r = [\dot{e}_v\ , \dot{e}_\omega]^T \quad (20)$$

Here q_r is the reference trajectory and q is the current trajectory. The TSMC signal is written as follows [2].

$$u = u_{eq} + u_d \quad (21)$$

Here, u_{eq} is the equivalent control signal and u_d is the switching signal. After that, if the system is on the sliding surface, then $s(t) = 0$. The condition required for the system states to remain on the sliding surface is $\dot{s}(t) = 0$ and $s\dot{s}\langle 0$ satisfies the convergence condition [2]. The derivative of the sliding surface is written as follows.

$$\dot{s}(t) = \dot{e}_c(t) + \beta |e_c|^{\sigma_c}\ \mathrm{sgn}(e_c) \quad (22)$$

Moreover, the finite time ts that is obtained from $e(t) \neq 0$ to $e(t_s) = 0$ is given by;

$$t_s = \frac{1}{\beta(1-\sigma_c)} |e(0)|^{1-\sigma_c} \quad (23)$$

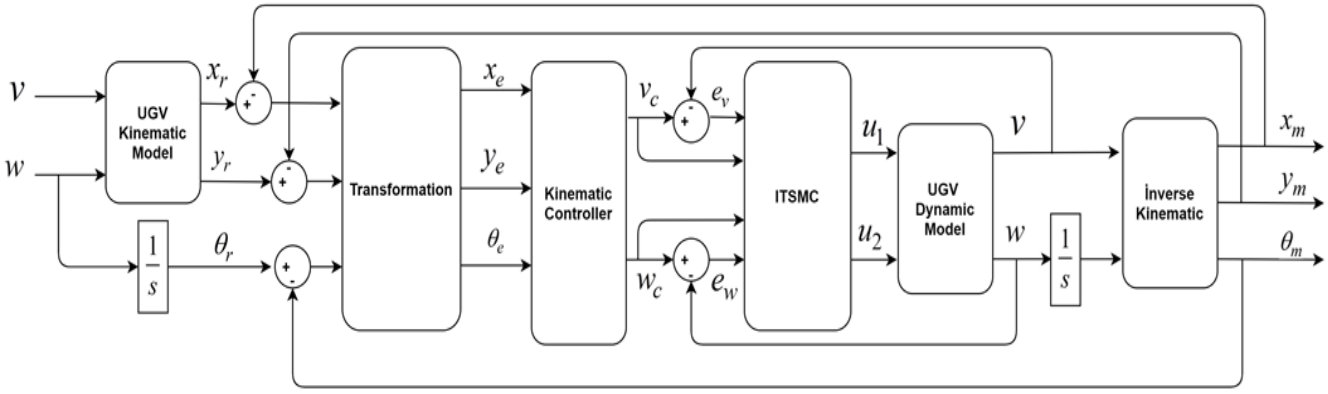


Fig.2. The control block diagram of UGV

By using (22), derivative expressions of sliding surfaces belonging to linear and angular velocities are obtained as follows.

$$\dot{s}_1(t) = \dot{e}_v(t) + \beta |e_v|^{\sigma_1}\ \mathrm{sgn}(e_v)$$
$$\dot{s}_2(t) = \dot{e}_w(t) + \beta |e_w|^{\sigma_2}\ \mathrm{sgn}(e_w) \quad (24)$$

If (20) is written in (24), equivalent control signals are obtained as follows. Angle between the local axis and global axis.

$$u_{eq1} = R\left(m + \frac{2I_w}{R^2}\right)\left[\dot{v}_c(t) + \beta |e_v(t)|^{\sigma_1}\ \mathrm{sgn}\, e_v(t)\right]$$
$$u_{eq2} = \frac{R}{L}\left(I + \frac{2L^2}{2R^2} I_w\right)\left[\dot{w}_c(t) + \beta |e_w(t)|^{\sigma_2}\ \mathrm{sgn}\, e_w(t)\right] \quad (25)$$

[4] SIMULATION RESULTS

In this section, the simulation results are presented. In Fig. (3), the linear velocity tracking performances of the controllers are given for trapezoidal reference signal. From the figure, the ITSMC has better tracking performance and less deviations. Also, the proposed controller has responded faster to the changes than the SMC when the changing part of the reference signal is applied. In Fig. (4), the angular velocity tracking performances of the controllers are given for sinusoidal reference signal. It is clear that the ITSMC has kept the system on the reference trajectory at points where the sinus sign changes its directions. On the other hand, the SMC is not adequate to eliminate errors that occurred while the UGV was following the reference trajectory and thus, the UGV has made significant deviations.

The switching control signal is selected as follows.

$$u_{sw1}(t) = k_1\, \mathrm{sgn}(s_1)$$
$$u_{sw2}(t) = k_2\, \mathrm{sgn}(s_2) \quad (26)$$

k_1 and k_2 are positive constants and sgn(s) function is defined as follows.

$$\mathrm{sgn}(s) = \begin{cases} -1 & if \quad s\langle 0 \\ 0 & if \quad s = 0 \\ 1 & if \quad s\rangle 0 \end{cases} \quad (27)$$

Total TSMC signal is obtained as in (28).

$$\left.\begin{aligned} u_1(t) &= R\left(m + \frac{2I_w}{R^2}\right)\left[\dot{v}_c(t) + \beta |e_v(t)|^{\sigma_1}\ \mathrm{sgn}\, e_v(t)\right] + k_1\, \mathrm{sgn}(s_1) \\ u_2(t) &= \frac{R}{L}\left(I + \frac{2L^2}{2R^2} I_w\right)\left[\dot{w}_c(t) + \beta |e_w(t)|^{\sigma_2}\ \mathrm{sgn}\, e_w(t)\right] + k_2\, \mathrm{sgn}(s_2) \end{aligned}\right\} \quad (28)$$

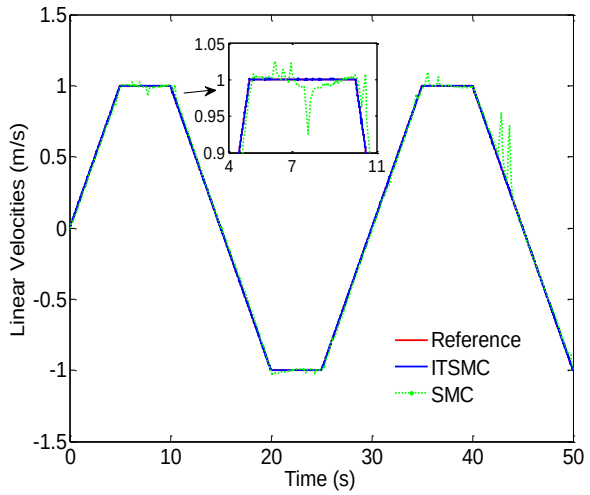


Fig. 3. The linear velocity tracking performances of both controllers for trapezoidal reference

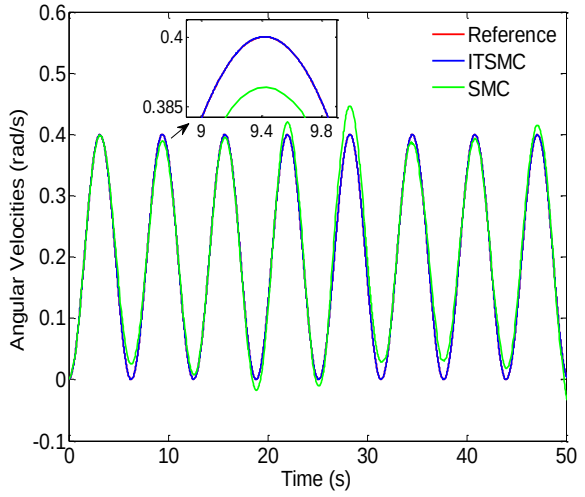


Fig. 4. The angular velocity tracking performances of both controllers for sinusoidal reference

In Fig. (5), the control signals generated by each controller for linear velocity control are given. One can see that the proposed controller has produced the control signal with less chattering than the SMC. Moreover, the SMC could not provide the required velocity reference for the system. In Fig. (6), the control signals produced for angular velocity tracking are presented. Form the figure, although both controllers have produced the same amplitude control signal, the SMC has produced the control signal with more chattering and also, the proposed controller has provided better orientation for the UGV.

[5] CONCLUSION

In this paper, the ITSMC is proposed to realize trajectory tracking control of an UGV for trapezoidal linear velocity and sinusoidal angular velocity references. To compare the ITSMC, a well-known SMC is also applied for the same linear and angular velocity references. The simulation results show that the proposed controller has better reference tracking performances in both linear and angular velocities as well as has smaller steady state error and less overshoot. Also, it can be observed that the ITSMC has responded faster to changing part of the references when it is compared to the SMC.

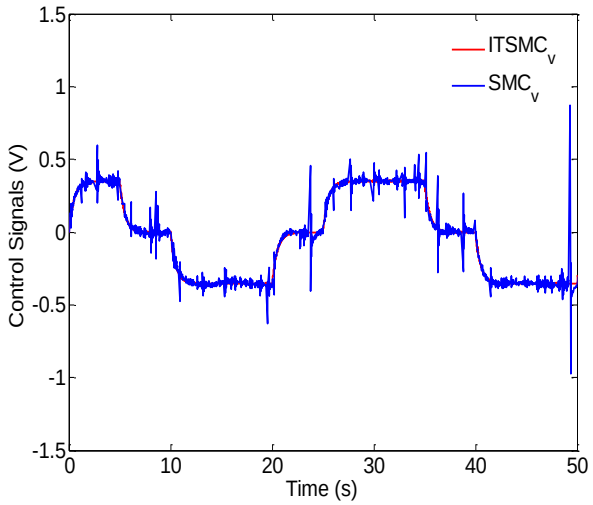


Fig. 5. The control signals genertaed by controllers for linear velocity tracking

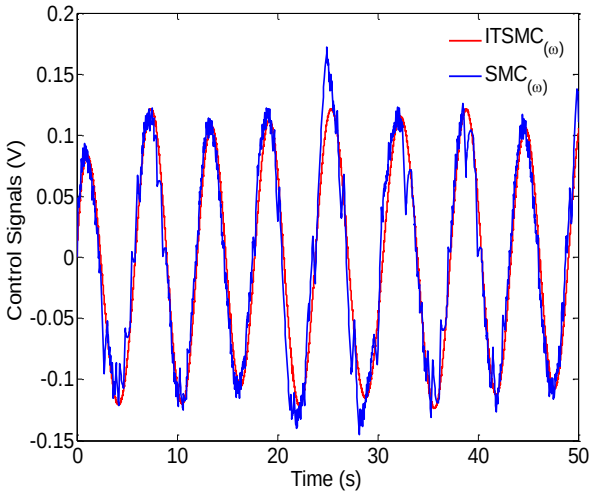


Fig. 6. The control signals genertaed by controllers for angular velocity tracking

REFERENCES

[1] G. S. Tzafestas, "Mobile Robot Control and Navigation: A Global Overview," J Intell Robot Syst (2018) 91:35–58.

[2] B. B. Mevo, M. R. Saad, and R. Fareh, "Adaptive Sliding Mode Control of Wheeled Mobile Robot with Nonlinear Model and Uncertainties," 2018 IEEE Canadian Conference on Electrical & Computer Engineering (CCECE).

[3] W. Sun, J. VandenBerg, and R. Alterovitz, "Stochastic extended LQR for optimization-based motion planning under uncertainty," IEEE Transactions on Automation Science and Engineering, vol. 13, no. 2, pp. 437-447, January 2016.

[4] E. Alcala, V. Puig, J. Quevedo, and T. Escobet, "Gainscheduling LPV control for autonomous vehicles including friction force estimation and compensation mechanism," IET Control Theory and Applications, vol. 12, no. 12, pp. 1683-1693, August 2018.

[5] A. Haytham, Y. Z. Elhalwag, A. Wassal, and N. M. Darwish "Modeling and Simulation of Four-Wheel Steering Unmanned Ground Vehicles using A PID controller," 2014 International Conference on Engineering and Technology (ICET) 19-20 April 2014 Cairo, Egypt.

[6] A. Zou, Z. Hou, M. Tan, and Z. Zhao, "Tracking control of a nonholonomic mobile robot using a fuzzy-based approach," in Fuzzy Systems and Knowledge Discovery, vol. 4223 of Lecture Notes in Computer Science, pp. 826–835, Springer, Berlin, Germany, 2006.

[7] R. Carelli, J. Santos-Victor, F. Roberti, and S. Tosetti, "Direct visual tracking control of remote cellular robots," Robotics and Autonomous Systems, 54, 2006, 805–814.

[8] D. Chwa, "Tracking control of differential-drive wheeled mobile

robots using a backstepping-like feedback linearization," IEEE Transactions on Systems, Man, and Cybernetics-Part A: Systems and Humans, vol. 40, no. 6, pp. 1285-1295, Novermber 2010.

[9] D. Kim, and T. Oh, "Tracking control of a two-wheeled mobile robot using input-output linearization," Control Engineering Practice, vol. 7, no. 3, pp. 369-373, July, 1999.

[10] M. Ou, H. Du, and S. Li, "Finite-time formation control of multiple nonholonomic mobile robots," International Journal of Robust and Nonlinear Control, vol. 24, no. 1, pp. 140-165, August 2014.

[11] L. Ding, S. Li, H. Gao, C. Chen, and Z. Deng, "Adaptive partial reinforcement learning neural network-based tracking control for wheeled mobile robotic systems," IEEE Transactions on Systems, Man, and Cybernetics: Systems, May 2018.

[12] A. Basci, K. Can, K. Orman, and A. Derdiyok, "Trajectory Tracking Control of a Four Rotor Unmanned Aerial Vehicle Based on Continuous Sliding Mode Controller," Elektronika Ir Elektrotechnika, vol. 23, no. 3, 2017.

[13] D. K. Chwa, J.H. Seo, P.K. Kim, and J. Y. Choi, "Sliding Mode Tracking Control of Nonholonomic Wheeled Mobile Robots," Proceedings of the American Control Conference Anchorage, AK May 8-1 0,2002.

[14] D. Chwa, "Sliding-mode control of nonholonomic wheeled mobile robots in polar coordinates," IEEE Trans. on Control Systems Technology, vol. 12, no. 4, pp. 637-644, July, 2004.

[15] Y. Li, L. Zhu, Z. Wang, and T. Liu, "Trajectory Tracking for Nonholonomic Wheeled Mobile Robots Based on an Improved Sliding Mode Control Method" 2009 ISECS International Colloquium on Computing, Communication, Control, and Management.

[16] K. Can, and A. Başçi, "Position Control of a Ball & Beam Experimental Setup Based on Sliding Mode Controller," International Journal of Applied Mathematics, Electronics and Computers. IJAMEC, Special Issue, pp.29–35, 2017.

[17] H. T. Sekban, K. Can, and A. Başçi, "Real-Time Application of Sliding ode Controller for Coupled Tank Liquid Level System," International Journal of Applied Mathematics, Electronics and Computers. IJAMEC, vol. 4, pp. 301–306, 2016.

[18] A. Basci, and A. Derdiyok, "The application of chattering-free sliding mode controller in coupled tank liquid-level control system," Korean J. Chem. Eng., vol. 30, no. 3, pp. 540-545, 2013.

[19] O. Özdal, "Model dayanaklı kayan kipli denetim," M. Tur. thesis, Hacettepe University, Ankara, Turkey, 2008.

[20] G. Bartolini, A. Pisano, E. Punta, and E. Usai, "A Survey of Applications of Second-order Sliding Mode Control to Mechanical Systems," Int. J. Contr., vol. 76, pp. 875-892, 2003.

[21] A. Levant, "Higher-order Sliding Modes, Differentiation and Output-feedback Control," Int. J. Contr., vol. 76, pp. 924-941, 2003.

[22] A. Pisano, and E. Usai, "Output-feedback Control of an Underwater Vehicle Prototype by Higher-order Sliding Modes,"Automatica, vol. 40, pp. 1525-1531, 2004.

[23] V. Behnamgol, and A. R. Vali, "Terminal Sliding Mode Control for Nonlinear Systems with Both Matched and Unmatched Uncertainties," Iranian Journal of Electrical & Electronic Engineering, vol. 11, no. 2, June 2015.

[24] K.-B. Park, and J.-J. Lee, "Comments on "A robust MIMO terminal sliding mode control scheme for rigid robotic manipulators"," IEEE Transactions on Automatic Control, vol. 41, no. 5, pp. 761–762, 1996.

[25] X. Guo, Z. Liang, and C. Li, "Finite time tracking control of mobile robot based on non-singular fast terminal sliding mode," Systems Science & Control Engineering: An Open Access Journal 2018, vol. 6, no. 1, pp.492–500, 2018.

[26] T. Binazadeh, and M. H. Shafiei, "Nonsingular terminal sliding-mode control of a tractor–trailer system," Systems Science & Control Engineering: An Open Access Journal, vol. 2, pp. 168–174, 2014.

[27] R. Dhaouadi, and A. Abu Hatab, "Dynamic Modelling of Differential-Drive Mobile Robots using Lagrange and Newton-Euler Methodologies: A Unified Framework," Adv Robot Autom 2013, vol. 2, no.2, 2013.

[28] G. Yuan, G., "Tracking Control of A Mobile Robot Using Neural Dynamics Based Approaches," Degree of Master of Science in School of Engineering, University of Guelph, Canada, 2001.

[29] Z. Feng, and J. Fei, "Design and Analysis of Adaptive Super Twisting Sliding Mode Control for a Microgyroscope," January 3, 2018 Plos one.

[30] Y. Kanayama, Y. Kimura, F. Miyazaki, and T. Noguchi, "A stable tracking control method for an autonomous mobile robot," in Robotics and Automation, 1990. Proceedings., 1990 IEEE International Conference on, 1990, pp. 384-389.

[31] Z. Feng, and J. Fei, "Design and Analysis of Adaptive Super Twisting Sliding Mode Control for a Microgyroscope," January 3, 2018 Plos one.

[32] X. Feng, and C. Wang, "Robust Adaptive Terminal Sliding Mode Control of an Omnidirectional Mobile Robot for Aircraft Skin Inspection" International Journal of Control Automation and Systems, vol. 19, no.10, pp. 1-11, 2021.

Performance Evaluation of Microstrip Antenna Based on Different Shapes of Defected Ground Structure (DGS) at 28 GHz

Alyani Binti Ismail
Wireless and Photonics Networks Research Centre, Department of Computer and Communication Systems Engineering
Faculty of Engineering, Universiti Putra Malaysia Serdang, Malaysia
alyani@upm.edu.my

Mohd Fadlee Bin A Rasid
Wireless and Photonics Networks Research Centre, Department of Computer and Communication Systems Engineering
Faculty of Engineering, Universiti Putra Malaysia Serdang, Malaysia
fadlee@upm.edu.my

Mohd Nizar B Hamidon
Institute of Advanced Technology
Department of Electrical and Electronic Engineering Faculty of Engineering
Universiti Putra Malaysia
Serdang, Malaysia
mnh@upm.edu.my

Raja Syamsul. A. Raja Abdullah
Wireless and Photonics Networks Research Centre, Department of Computer and Communication Systems Engineering
Faculty of Engineering, Universiti Putra Malaysia Serdang, Malaysia
r_syamsul@upm.edu.my

Nafaa Mohamad Shebani
Wireless and Photonics Networks Research Centre, Department of Computer and Communication Systems Engineering
Faculty of Engineering,
Universiti Putra Malaysia
Serdang, Malaysia
nafah@yahoo.com

***Abstract*—In this paper a 5G microstrip antenna operating at 28 GHz is designed and evaluated. The antenna is designed on PTFE/Teflon substrate with dielectric constant of 2.1, loss tangent of 0.0002, and thickness of 1.58 mm, and it simulated by Computer Simulation Technology (CST) software. In addition, the evaluation of the designed antenna performance is done depending on two different shapes of defected ground structure (DGS) which are rectangular slot, and concentric annular ring slot. Further, a combination of rectangular and concentric annular ring slots is proposed in order to improve the performance of conventional microstrip antenna at 28 GHz. In all cases, realized gain, bandwidth, return loss, VSWR, and efficiency are studied to evaluate the antenna performance. Moreover, the comparison between all cases in this work is done, and the best obtained case is compared with proposed antennas in previous works.**

Keywords—Microstrip antenna, 5G, DGS, slots, 28 GHz, rectangular slot, concentric annular ring slot.

[1] INTRODUCTION

5G technology is introduced to achieve many requirements, such as faster rate of data transmission, greater capacity, cost effectiveness, less latency, high energy efficiency, better security, and anti-interference [1]. Recently, mmWave band has received attention for many applications to meet the requirements of 5G technology. However, mmWave band suffers from many issues such as high path loss. To overcome these issues, qualified peak realized gains of the mm-Wave antennas or antenna arrays are required [2].

Microstrip antenna is widely used in various wireless communication systems due to its advantages, which are low profile, low cost, small size, easy fabrication, easy integration. However, conventional microstrip antenna suffers from drawbacks such as narrow bandwidth, small gain, high dielectric losses, higher cross polarization, low impedance bandwidth, and high mutual coupling when used as array elements [3]. There are number of techniques that used to enhance the parameters of conventional microstrip antenna, such as slots in patch [4, 5], different feeding techniques, frequency selective surface (FSS), Electromagnetic Band Gap (EBG), and Defected Ground Structure (DGS) [3,6]. DGS is one of popular techniques that is used to improve the microstrip antenna performance without reducing its benefits.

In this paper, a conventional microstrip antenna operating at 28 GHz is designed and evaluated. Furthermore, many shapes of DGS are etched in the ground plane in order to enhance the gain, bandwidth, and efficiency of the designed antenna. In this work, 28 GHz band (26.5-29.5 GHz) is chosen because it has a lower attenuation in mmWave bands.

[2] DGS STRUCTURE

DGS structure is obtained by etching off a simple shape defect from the ground plane of microstrip antenna [7]. DGS has two types, single defect, and group of small defects in periodic or non-periodic manner. Different shapes of DGS are presented in literature such as circular, square, rectangular, concentric ring, dumbbell, U and V-shaped, hairpin DGS, cross-shaped DGS, hexagonal DGS, and combined structures. Figure 1. Shows different shapes of DGS [8].

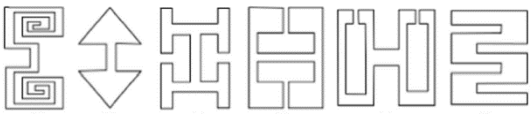


Fig. 2. Different shapes of DGS

[3] SIMULATION RESULTS AND DISCUSSION

A. Design of single element microstrip antenna at 28 GHz

The general configuration of antenna is illustrated in Figure 2. In this section, a single element microstrip antenna operating at 28 GHz is designed based on design procedure in [9], and the feed line is designed based on procedure in [10]. The proposed antenna is design on PTFE/Teflon

substrate with dielectric constant of 2.1, thickness of 1.58 mm, and loss tangent of 0.0002. The optimization is done in order to get the best performance of the designed antenna. The dimensions of this antenna after optimization are illustrated in Table 1.

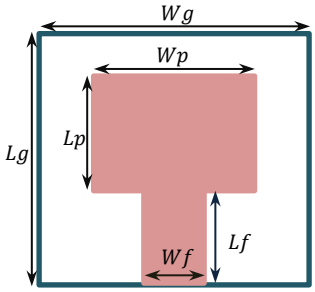


Fig. 1. Configuration of coventional microstrip antenna

Table 1. Dimensions of Designed Antenna

Parameter		Value (mm)
Patch	Wp	4.73
	Lp	2.769
Ground	Wg	13.7830
	Lg	11.9867
Feed Line	Wf	2.00
	Lf	1.990

Figure 3 shows the variation of return loss versus frequency of antenna after optimization. From the Figure, it can be noted that the simulated antenna is resonant at 28.04 GHz with return loss of -34.585 dB. Moreover, based on -10 return loss, the simulated antenna has 4.716 GHz bandwidth with 16.617 % impedance bandwidth, moreover, VSWR at resonant frequency is 1.038. At 28 GHz, realized gain, and efficiency of this antenna is 8.562 dBi, and -1.229 dB respectively.

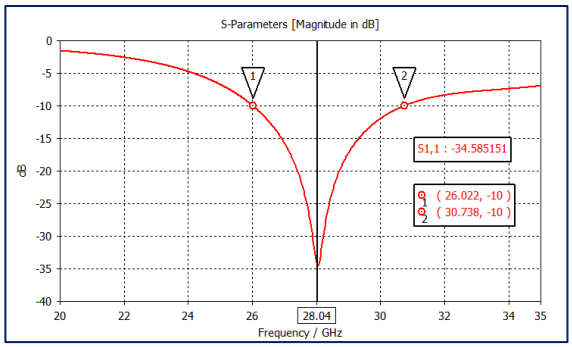


Fig. 2. Return loss versus the frequency of designed antenna

B. *Effects of DGS shape on the antenna performance*

Case 1: Changing the dimensions of rectangular slot

In this case, a rectangular slot with length of (Ls) and width of (Ws) is etched off in ground plane as illustrated in Figure 4.

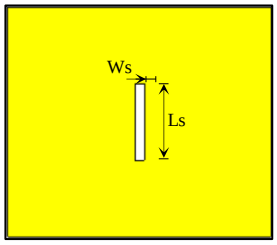


Fig. 3. Microstrip antenna with rectangular slot

In this case, there are two procedures to study the performance of the microstrip antenna.

a) Changing the width of rectangular slot with fixed slot length

In this case, the rectangular slot has a fixed length of 1.687 mm, and several values of the slot width are chosen, which are 0.5, 1, 1.5, 2, 2.5, and 3 mm. Figure 5 shows the variation of return loss versus frequency of antenna with changing the width of rectangular slot. From the Figure, it can be noted that, the resonant frequency of the antenna with rectangular slot is almost constant at the width of slot less than or equal 2 mm, and the resonant frequency is shifted to right side when the width of slot is greater than 2.5 mm.

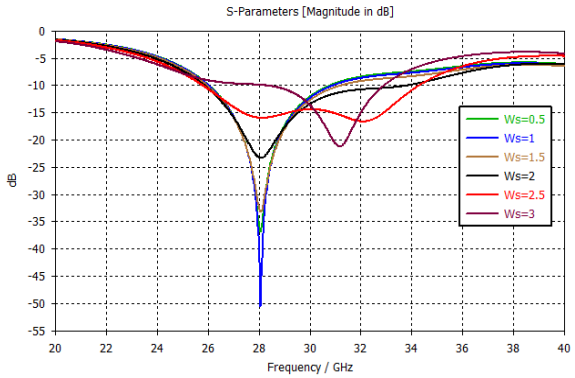


Fig. 4. Return loss versus the frequency of designed antenna with changing the width of rectangular slot

Table 2 shows the radiation parameters of the microstrip antenna with different values of the rectangular slot width. From the Table, it can be observed that, the values of bandwidth and gain of the antenna with rectangular slot are enhanced over conventional antenna values at 28 GHz. Moreover, the values of gain and bandwidth are increased with increasing the width of the rectangular slot. The best values of bandwidth, impedance bandwidth, realized gain, and efficiency are 8.502 GHz, 28.31%, 9.16 dBi, 84.53% respectively, that are obtained at 1.687 mm slot length and 2.5 mm slot width.

Table 2. The Radiation Characteristics of Proposed Antenna with Changing the Width of Rectangular Slot

Length s of rectangular slot (Ls) (mm)				1.687		
Ws (mm)	0.5	1	1.5	2	2.5	3
Resonant Frequency (GHz)	28.06	28.06	28.08	28.08	28.019	31.18
Return loss (dB)	-36.88	-50.47	-33.23	-23.28	-15.97	--
VSWR	1.03	1.01	1.05	1.15	1.38	--

Bandwidth (GHz)	4.759	4.90	5.278	7.998	8.502	--
Impedance Bandwidth (%)	16.76	17.22	18.46	26.79	28.31	--
Realized gain (dBi)	8.576	8.628	8.628	8.914	9.16	--
Efficiency (%)	75.51%	76.21	76.21	79.98	84.53	--

b) Changing the length of rectangular slot with fixed width

In this case, the width of rectangular slot is fixed at 2 mm, and the slot length has many values 1, 1.5, 2, 2.5, and 3 mm. Variation of return loss versus frequency of antenna with changing the length of rectangular slot is shown in Figure 6. From the Figure, it can be noted that, the resonant frequency of the antenna with rectangular slot is almost constant with slightly changing around 28 GHz at all lengths of rectangular slot.

Table 3 shows the radiation parameters of the microstrip antenna with different values of the rectangular slot length. From the Table, it can be shown that, the values of bandwidth and gain of the antenna with rectangular slot are enhanced over conventional antenna values at 28 GHz. Moreover, the values of gain and bandwidth are increased with increasing the length of the rectangular slot, but they are slightly decrease when the slot width is 3 mm. The best values of bandwidth, impedance bandwidth, realized gain, and efficiency are 8.269 GHz, 27.648%, 9.139 dBi, 84.64 % respectively, that are obtained at 2 mm slot width and 2.5 mm slot length. From the point of view of matching and reflected power, the lower values of return loss and VSWR are -28.07 dB, and 1.08 respectively at 2 mm slot width and 1 mm slot length.

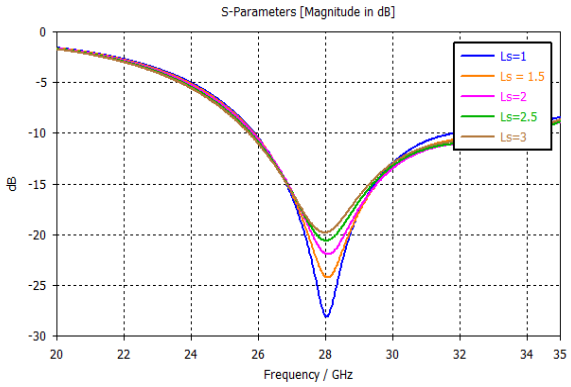


Fig. 5. Return loss versus the frequency of designed antenna with changing the length of rectangular slot

Table 3. The Radiation Characteristics of Proposed Antenna with Changing the Length of Rectangular Slot

Width of rectangular slot (Ws) (mm)			2		
Length (Ls) (mm)	1	1.5	2	2.5	3
Resonant Frequency (GHz)	28.04	28.08	28.08	28.02	27.98
Return loss (dB)	-28.07	-24.22	-21.94	-20.58	-19.80
VSWR	1.082	1.131	1.174	1.206	1.228
Bandwidth (GHz)	5.987	7.754	8.219	8.269	8.051
Impedance Bandwidth (%)	20.73	26.07	27.445	27.648	27.059
Realized gain (dBi)	8.824	8.888	8.934	9.139	8.989
Efficiency (%)	78.40	79.54	80.57	84.64	82.04

Case 2: Changing the dimensions of concentric annular ring slot

In this case, a concentric annular ring slot, with inner radius (r_i) and outer radius (r_o), is etched off in ground plane as illustrated in Figure 7. The simulation of this antenna is repeated many times to determine the optimum point of the center of annular ring slot; the obtained optimum center is located at (0,-Wg/4) point. Figures 8 and 9 illustrate the variation of return loss versus frequency of antenna with concentric annular ring slot for different values of inner radius of concentric annular ring slot. In Figure 7, the outer radius is 1.5 mm, and the values of inner radius are 0.5, 1, and 1.25 mm, while in Figure 8, the outer radius is 2 mm, and the values of inner radius are 0.5, 1, 1.25 and 1.5 mm.

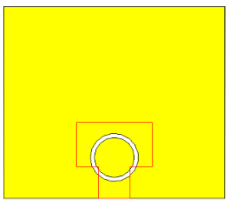


Fig. 6. Microstrip antenna with concentric annular ring slot

From Figures 8 and 9, it can be noted that, the resonant frequencies of the microstrip antenna with concentric annular ring slot are within 28 GHz band, except the case when the outer radius is 2 mm, and the inner radius is 1.5 mm, the resonant frequency is out of 28 GHz frequency band. Also, in Figure 8, it can observed that, the resonant frequency shifted to the right with increase the inner radius value, in contrast, in Figure 9, it can observed that, the resonant frequency shifted to the left with increase the inner radius value.

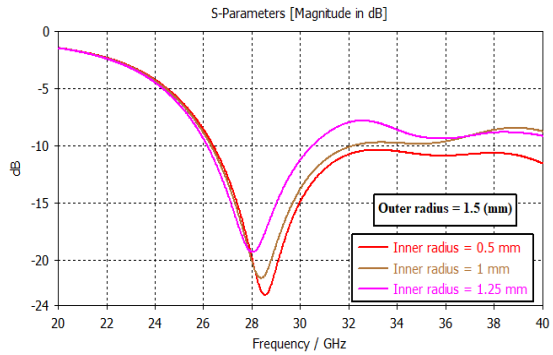


Fig. 7. Return loss versus the frequency of designed antenna with changing the inner radius of annular ring slot at the outer radius is 1.5 mm

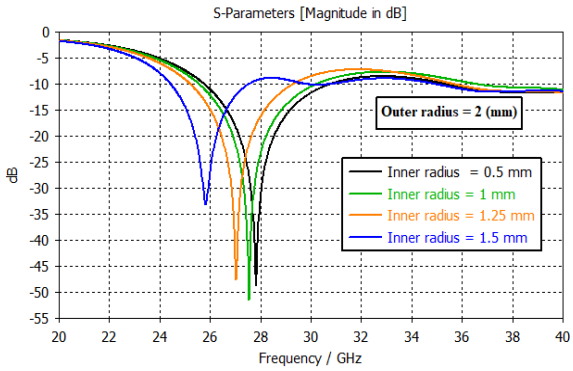


Fig. 8. Return loss versus the frequency of designed antenna with changing the inner radius of annular ring slot at the outer radius is 2 mm

Table 4 shows the radiation parameters of the microstrip antenna with different values of radii of the concentric annular ring slot. From the Table, it can be noted that, the best values of bandwidth, impedance bandwidth and realized gain are 6.75 GHz, 22.66%, and 8.34 dBi respectively, which obtained at outer radius of 1.5 mm, and inner radius of 0.5 mm. From the point of view of matching and reflected power, the lower values of return loss and VSWR are obtained at outer radius of 2 mm, and inner radius of 0.5 mm,, which are -48.71 dB, and 1.007 respectively.

Table 4. The Radiation Characteristics of Proposed Antenna with Changing the Dimensions of Concentric Annular ring Slot

Outer radius (mm)	1.5			2		
Inner radius (mm)	0.5	1	1.25	0.5	1	1.25
Resonant Frequency (GHz)	28.54	28.38	28.02	27.82	27.54	27.04
Return loss (dB)	-23.05	-21.59	-19.33	-48.71	-51.42	-47.46
VSWR	1.151	1.182	1.242	1.007	1.015	1.01
Bandwidth (GHz)	6.75	5.8	4.34	5.01	4.66	4.09
Impedance Bandwidth (%)	22.66	20.12	15.31	17.72	16.72	15.01
Realized gain (dBi)	8.34	8.28	8.14	7.94	7.70	7.08
Efficiency (%)	71.94	71.94	72.28	71.29	71.94	73.79

Case 3: Combined of rectangular slot and concentric annular ring slot

As presented in Figure 10, a combination of two different shapes of DGS structures is proposed in order to make more improvements of gain, efficiency, and bandwidth of the conventional antenna. The proposed combination consists of rectangular slot and concentric annular ring slot.

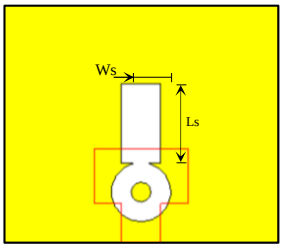


Fig. 9. Microstrip antenna with different shapes of DGS, concentric annular ring and a rectangular slots

Figures 11 and 12 illustrate the variation of return loss versus frequency of antenna with concentric annular ring and rectangular slots for different values of length of rectangular slot, from 2 to 6 mm, when the width of rectangular slot is 2, and 2.5 mm respectively. In all cases, the inner radius of the concentric annular ring is 0.5 mm, and the outer radius is 1.5 mm, in addition, it centered at (0,-Wg/4).

The radiation parameters of microstrip antenna with different shapes of DGS, concentric annular ring and rectangular slots for different values of length of rectangular slot, from 4 to 6 mm, are tabulated in Table V. From the Table, it can be observed that, the best value of bandwidth, and impedance bandwidth are 11.75 GHz, and 36.63% respectively, which achieved at the width of rectangular slot is 2 mm, and the length of rectangular slot is 4 mm. Moreover, the best value of realized gain is 9.367 dBi and efficiency is 84.10% at width and length of rectangular slot are 2.5 mm, and 4 mm, respectively. From the point of view of matching and reflected power, the lower values of return loss is -47.75 dB, and VSWR is 1.008, these values are obtained at the width of rectangular slot is 2 mm, and the length of rectangular slot is 6 mm.

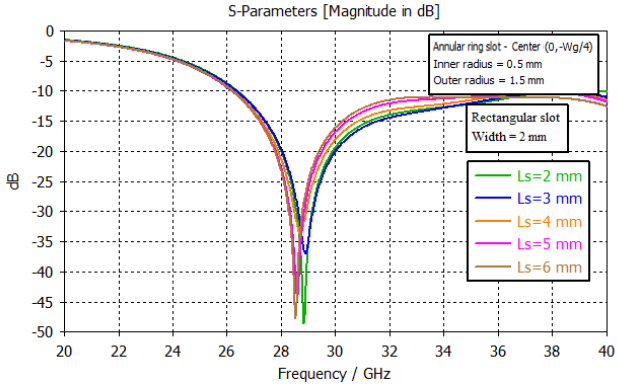


Fig. 10. Return loss versus the frequency of designed antenna with changing the length of rectangular slot at rectangular slot width is 2 mm

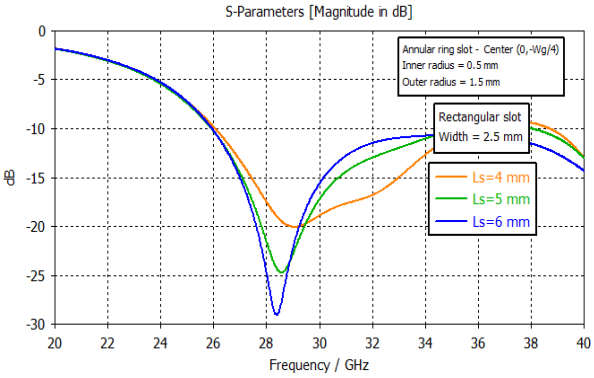


Fig. 11. Return loss versus the frequency of designed antenna with changing the length of rectangular slot at rectangular slot width is 2.5 mm

TABLE I. The Radiation Characteristics of Proposed Antenna with Different shapes of DGS, Concentric Annular Ring and Rectangular Slots for Different Values of Length of Rectangular Slot

annular ring slot		Inner radius (mm)		0.5		
		Outer radius (mm)		1.5		
Ws	2			2.5		
Ls (mm)	4	5	6	4	5	6
Resonant Frequency (GHz)	28.7	28.58	28.52	29.04	28.56	28.38
Return loss (dB)	-33.75	-44.40	-47.75	-20.06	-24.71	-29.03
VSWR	1.042	1.012	1.008	1.221	1.131	1.074
Bandwidth (GHz)	11.75	11.59	6.82	9.67	9.38	9.23
Impedance Bandwidth (%)	36.63	36.24	23.05	31.30	30.64	30.14
Realized gain (dBi)	9.032	9.048	9.009	9.367	9.299	9.325
Efficiency (%)	79.09	78.63	77.46	84.10	81.87	80.54

C. Comparison between conventional antenna and antennas with DGS structure at 28 GHz

The best values at 28 GHz, which are obtained in all previous cases is listed in Table VI in order to specify the best configuration among the DGS shapes.

TABLE II. Comparison between Conventional Antenna and Three Cases of Designed Antenna with Different Shapes of DGS at 28 GHz

Case	Realized gain (dBi)	Bandwidth (GHZ)	Efficiency (%)
Conventional Antenna	8.562	4.716 (16.62 %)	75.35
Case1	9.16	8.502 (28.31 %)	84.64
Case 2	8.34	6.75 (22.66 %)	73.79
Case 3	9.367	11.75 (36.63 %)	84.10

From Table VI, it can be noted that, the realized gain is enhanced in case 1 and case 3 over the values of conventional antenna, while the bandwidth is improved in all antennas with DGS over conventional antenna. As a comparison, case 3, antenna with rectangular and concentric annular ring slots achieved the best values of gain, bandwidth, and impedance bandwidth, which are 9.367 dBi, 11.75 GHz, and 36.63 % respectively.

The designed antenna with rectangular and concentric annular ring slots is compared with other 28 GHz antennas that are published in previous works. This comparison is listed in Table VII. From the Table, it can be noted that, the proposed antenna gives a good results compared to antenna that are published in previous works. But, these improvements are achieved with larger antenna size.

TABLE III. Comparison between Proposed Antenna and Other Antennas in Previous Works at 28 GHz

Reference	DGS Shape	Realized gain (dBi)	Bandwidth (GHz)	Area (mm2)
[2]	Two F-shaped	6	4.59	25.00
[11]	Ring shaped	6.87	0.87	52.27
[12]	No	6.76	1.91	224.0
[13]	No	8.92	3.10	324.0
[14]	No	7.55	1.062	72.25
[15]	X-shaped	5.23	2.1	26.30
[16]	Concentric two rectangular	9.51	--	36.00
Proposed design	concentric annular ring and a rectangular slots	9.367	11.75 (36.63%)	165.22

[4] CONCLUSION

In this paper a conventional microstrip antenna was designed at 28 GHz and simulated by CST software. To improve the gain, bandwidth, and efficiency of the designed conventional antenna, different shapes of DGS were etched in ground plane; these shapes are rectangular slot, concentric annular ring slot, and proposed combination of rectangular and concentric annular ring slots. Based on the obtained results, it can be concluded that, the microstrip antenna with rectangular and concentric annular ring slots achieved a best values of realized gain and bandwidth, where the realized gain was increased by 0.8050 dBi, and bandwidth was increased by 7.0340 GHz (20.01 %). In addition, the efficiency of antenna is improved by (8.75%)

Therefore, the proposed antenna with proposed combination DGS shape, rectangular and concentric annular ring slots, can be used properly for 5G applications at the desired band (27.5–29.5 GHz).

REFERENCES

[1] E. Hajlaoui, A. Zaier, A. Khlifi, J. Ghodhbane, M. Ben Hamed, and L. Sbita, “4G and 5G technologies: A Comparative Study,” 2020 Int. Conf. Adv. Technol. Signal Image Process. ATSIP 2020, 2020, doi: 10.1109/ATSIP49331.2020.9231605.

[2] P. MoukalaMpele, F. MoukandaMbango, and D. B. O. Konditi, “A small dual band (28/38ghz) elliptical antenna for 5g applications with dgs,” Int. J. Sci. Technol. Res., vol. 8, no. 10, pp. 353–357, 2019.

[3] A. K. Arya, M. V. Kartikeyan, and A. Patnaik, “Defected ground structure in the perspective of microstrip antennas: A review,” Frequenz, vol. 64, no. 5–6, pp. 79–84, 2010, doi: 10.1515/FREQ.2010.64.5-6.79.

[4] N. Shebani, A. Kaeib, and A. Zerek. "Design and Performance Evaluation of Rectangular Microstrip Antenna for 5G Communication systems at 48.6 GHz." 6th International Conference on Engineering & MIS 2020, 2020, doi.org/10.1145/3410352.3410801

[5] E. Karakaya, F. Bagci, A. E. Yilmaz, and B. Akaoglu, "Metamaterial-Based Four-Band Electromagnetic Energy Harvesting at Commonly Used GSM and Wi-Fi Frequencies," Journal of electronic materials, Vol. 48, No. 4, 2019, doi.org/10.1007/s11664-019-06962-9

[6] A. Qayyum, A. H. Khan, S. Uddin, O. Ahmad, J. S. Khan, and S. Bashir, "A Novel mmWave Defected Ground Structure Based Microstrip Antenna for 5G Cellular Applications," Proc. - 2020 1st Int. Conf. Smart Syst. Emerg. Technol. SMART-TECH 2020, pp. 28–31, 2020, doi: 10.1109/SMART-TECH49988.2020.00023.

[7] T. A. and Md Mushfiqur Rahman, , Md Shabiul Islam , Hin Yong Wong and M. T. Islam, "Performance Analysis of a Defected Ground-Structured Antenna Loaded with Stub-Slot for 5G Communication," vol. 19, no. 2634, pp. 1–16, 2019.

[8] A. B. Mustafa and T. Rajendran, "An Effective Design of Wearable Antenna with Double Flexible Substrates and Defected Ground Structure for Healthcare Monitoring System," *J. Med. Syst.*, vol. 43, no. 7, 2019, doi: 10.1007/s10916-019-1306-5.

[9] Constantine A. Balanis, "Antenna Theoryanalysis And Design", fourth edition, John Wiley & Sons, Inc., 2016.

[10] Pozar, "Microwave Engineering", fourth edition, John Wiley & Sons, Inc., 2012.

[11] A. Qayyum, A. H. Khan, S. Uddin, O. Ahmad, J. S. Khan, and S. Bashir, "A Novel mmWave Defected Ground Structure Based Microstrip Antenna for 5G Cellular Applications," *Proc. - 2020 1st Int. Conf. Smart Syst. Emerg. Technol. SMART-TECH 2020*, pp. 28–31, 2020, doi: 10.1109/SMART-TECH49988.2020.00023.

[12] Y. Rahayu, L. Afif, M. R. Radhelan, I. Yasri, and F. Candra, "Design of 28 Ghz Microstrip Mimo Antennas for Future 5G Applications," *Sinergi*, vol. 22, no. 3, p. 149, 2018, doi: 10.22441/sinergi.2018.3.002.

[13] S. Kamal *et al.*, "A 28 GHz mmWave Circular Microstrip Antenna with Rectangular Slots on Air-Substrate," vol. 1, pp. 1–4, 2021, doi: 10.1109/rfm50841.2020.9344772.

[14] K. A. Fante and M. T. Gemeda, "Broadband microstrip patch antenna at 28 GHz for 5G wireless applications," *Int. J. Electr. Comput. Eng.*, vol. 11, no. 3, p. 2238, 2021, doi: 10.11591/ijece.v11i3.pp2238-2244.

[15] V. Gupta and S. Vijay, "A Novel Design of Compact 28 GHz Printed Wideband Antenna for 5G Applications," *Int. J. Innov. Technol. Explor. Eng.*, vol. 9, no. 3, pp. 3696–3700, 2020, doi: 10.35940/ijitee.c9011.019320.

[16] A. Chaudhari and P. Mukherji, "Improved performance of antenna using DGS for 5G applications," International Research Journal of Engineering and Technology (IRJET), Vol. 07, Issue: 09, pp. 378–382, 2020.

Facile Design of a Metamaterial Absorber for X-band Radar Applications

Aykut Coskun
Department of Electronics and Automation Bayburt University
Bayburt, Turkey
aykutcoskun@bayburt.edu.tr

Ahmet Teber
Department of Electricity and Energy Bayburt University Bayburt, Turkey
ahmetteber@bayburt.edu.tr

Mehmet Ertugrul
Department of Electrical and Electronics Engineering Ataturk University Erzurum, Turkey
ertugrul@atauni.edu.tr

***Abstract*—A simple design of X-band metamaterial absorber (MA) for radar applications is reported using a single unit cell of three layers of a copper-dielectric substrate (FR-4)-copper. Therefore, an efficient meta-surface (PCM) is also investigated depending on the incident angle from 0 degree to 50 degree and the polarization angle from 0 degree and 90 degree with the increment of 10 degree. The extracted electromagnetic consititutive parameters are used to reinforced insights into the proposed structure's absorption mechanism, which are influenced by magnetic resonance. For this study, -10dB (absorption range 90%) is assumed the reference absorption level. The results indicated that the suggested MA is applicable for X-band radar applications.**

Keywords—metamaterial absorber, X-band, frequency selective surface, radar applications

[1] INTRODUCTION

Metamaterial absorbers (MAs) have potential applications of sensors, reduction of radar cross section (RCS), energy harvesting obtaining from microwaves, solar cells, etc [1]–[3]. The first application of nearly perfect MAs was attempted by Landy et al. in 2008. Their results indicated that an absorption (or no reflection) of the incident wave occurs by forced electric and magnetic resonances [4].

Metamaterial absorbers has become a long-standing research interest in the field of microwaves. During the a few decades, single layer unit cells, multi-layer structures, multi-resonance unit cells, etc. have taken place in the literature with the increment of absorber band-width [5]–[7]. The weakness of multi-layer structures are increasing design cost and complexity because of their high profile structure. The recent applications are also provided that the usage of the lumped elements, resistive screen for increasing the absorber band-width are under focus by researchers. The lumped resistances with larger unit cell size of 12 mm, and substrate thickness with relative absorption band-width (RAB) of 73.69% are achieved [8]. To achieve ultra wideband meta-absorber using low profile split ring resonator (SRR) with RAB, Ghosh et al. [9] proposed a candidate material. Low-cost FR-4 epoxy substrates have become relevant approach to deal with the larger unit cell size, which gives limitations with smaller effective area. For example, Shi et al. [10] have designed wideband meta-absorber with RAB of 60.48% using smaller unit cell dimension and substrate height of 2.7mm on FR-4 substrate. A thin dual broadband cross polarization conversion meta-surface is proposed to convert an x-polarized wave into a y-polarized wave (and vice versa) in the frequency bands of both 5-9.7 GHz and 11.2-15GHz) [11].

We report a metamaterial absorber for the absorption in the frequency range of 8 GHz and 12 GHz with substrate height of 0,11λ. The wavelength (λ) is computed considering the points under -10 dB along the X-band. The single layer unit cell size is 9.8 mm as a square shape in this study. Design of unit cell structure and material are proposed in the Section 2. In the Section 3, the absorption mechanism or the theory of absorption for analysis using CST Studio Suite EM simulation and analysis software. This paper will be concluded including results and conclusions.

[2] STRUCTURE DESIGN

The CST-Microwave Studio software (CST 2020) is used to examine the absorption performance and other analysis parameters of the proposed structure in free space. We performed a simulation on the unit cell MA structure with the periodic boundary condition along the x-y plane. EM radiation is polarized with the wave vector perpendicular to the structure (Fig. 1). Namely, the proposed MA is along with directions of field vectors including the electric field, the magnetic field, and the propagation direction (E(x), H(y), and k(z), respectively).

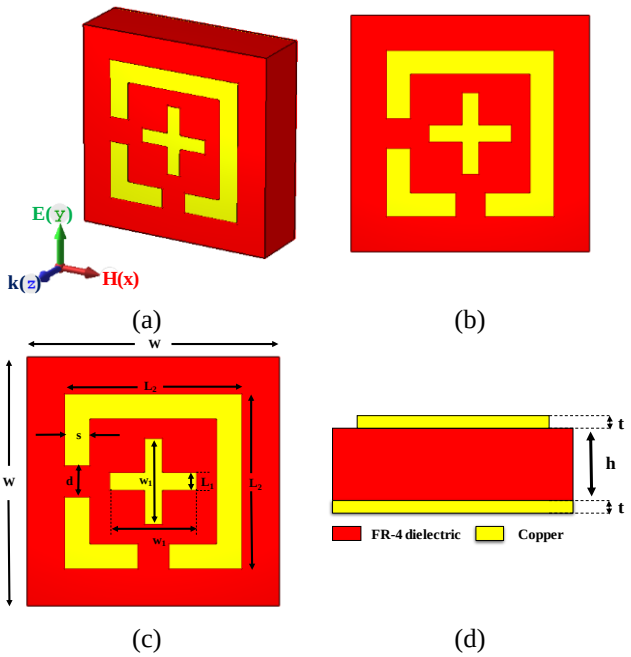


Fig. 1. Illustration of the suggested MA unit cell (a) 3-D view, (b) top view, (c) top view with dimensions, and (d) side view

The proposed metamaterial structure consists of three layers, where copper is completely covered along bottom-layer as grounded. The top layer is created a periodic structure of copper, which behaves as a frequency selective surface (FSS). The susbtrate on the middle layer is a dielectric FR-4 material inserted between top and bottom layers.

Copper (annealed) is used to cover the top and bottom layers with the same thickness (t=0,035mm) including the conductivity value (σ) of $5.8x10^7$ S/m. The dielectric constant, the loss tangent (tanδ), and the height (h) of FR-4 (lossy) substrate is 4.3, 0.025, and 2.9 mm, respectively. As known, geometric parameters and configuration of a unit cell structure determine MA's resonant frequency. In order to design a MA absorber, matching impedance between free space and a MA is a crucial to make sure that the incident power is coupled to an MA with a minimum reflection [4]. Therefore, they must be carefully optimized. After optimization we have done, here, the geometric parameters are provided for the proposed metamaterial in the Table 1.

Table 1. Geometric Parameters Of Unit Cell

Parameters (mm)					
W	***w1***	***L1***	***L2***	***d***	***s***
9.8	3.4	0.7	6.9	1.2	2

[3] Theory

Absorption mechanism can be explained impedance matching of the MA structure and free-space at the interface. The metamaterial absorption is obtained by:

$$A(\omega) = 1 - R(\omega) - T(\omega) \tag{1}$$

where the absorption, reflection, and transmission of the MA structure are the frequency-dependent *A(ω), R(ω)* and *T(ω)*, respectively. The *T(ω)* and *R(ω)* are calculated by using S-parameter $S_{11}(\omega)$ and $S_{21}(\omega)$, where

$$T(\omega) = |S_{21}(\omega)|^2 \tag{2}$$

$$R(\omega) = |S_{11}(\omega)|^2 \tag{3}$$

As known, once a material is completely backed with a metallic surface and its thickness is thick enough (because of skin depth effect) to block the transmission of the incident wave so that *T(ω)* equals to zero. It means that the absorption can be simplified as *A(ω)* = 1 – *R(ω)*. Then, the absorption is obtained by using input impedance and free space impedance as flow:

$$A(\omega) = 1 - \left| \frac{Z_{in}(\omega) - Z_0}{Z_{in}(\omega) + Z_0} \right|^2 \tag{4}$$

where input impedance (Z_{in}) can be obtained by the parallel configuration of meta-surface and conductor-backed impedance. Z_0 is the characteristic free space impedance.

In order to prove the impedance matching at the resonant frequency range, the real and imaginary part of the normalized input impedance (Z) should be approximately one and zero, respectively so that Z can be calculated following by:

$$Z = \sqrt{\frac{(1+S_{11})^2 - S_{21}^2}{(1-S_{11})^2 - S_{21}^2}} = \frac{1+S_{11}}{1-S_{11}} \tag{5}$$

The electromagnetic constitutive parameters are available to clarify the physics mechanism of the projected structure, whether the absorption occurs because of either a magnetic resonance or an electric resonance (or both). The effective constitutive parameters (permittivity and permeability) are calculated using S_{11} parameter by the following equations, where k_0 is the wave number and d is the travelled distance by the incident wave.

$$\varepsilon_{eff} = 1 + \frac{2j}{k_0 d} \frac{S_{11} - 1}{S_{11} + 1} \tag{6}$$

$$\mu_{eff} = 1 + \frac{2j}{k_0 d} \frac{S_{11} + 1}{S_{11} - 1} \tag{7}$$

[4] RESULTS

After all design optimization is done, the absorption (%), the effective input impedance to show impedance matching, extracted electromagnetic consititutive parameters to understand insights into the proposed structure's Physics mechanism, absorption of the projected MA using different polarization angles in the range 0-90 degree, and the calculated effective input impedance (Z) for both TE and TM polarization at the incidence angles in the range of 0-50 degree are provided here, respectively.

A. Absorption of the Suggested MA Structure

The absorption of the suggested MA at normal incidence (0 degree at z-direction) for both TE and TM polarizations are illustrated in Fig. 2.

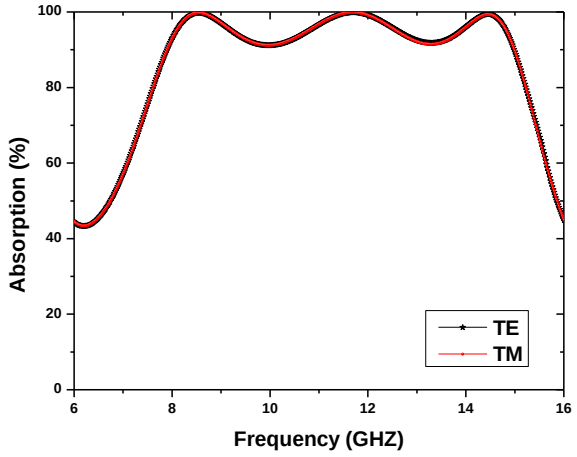


Fig. 2. Absorption spectra of the suggested MA under normal incidence for TE and TM polarizations

The designed MA displays three separate absorption peaks under -10dB at 8.55 GHz, 11.70 GHz, and 14.46 GHz between 7.9 GHz to 15 GHz frequency band. The corresponding maximum absorptivities (%) based on the peak values are 99,68, 99,62, and 99,59, respectively. The absorptivity larger than 80 percent is obtained in the frequency range of 7.9 to 15 GHz. Therefore, the suggested MA is available for the X-band radar applications. When considering the relative absorption band-width (RAB), it approximately reaches 62% above 90% absorptivity, which means how a good property is.

$$RAB = 2 \times \frac{(f_H - f_L)}{f_H + f_L} \tag{8}$$

where f_H and f_L are the higher and lower frequencies. Based on the absorption of the suggested MA structure, the spectra are steady for both polarizations as shown in the Fig. 2.

B. *Effective Imput Impedance*

The impedance matching is occured at the resonant frequency range so that the suggested MA is achieved as good absorption range under -10dB, which is proofed by the elements of the normalized input impedance.

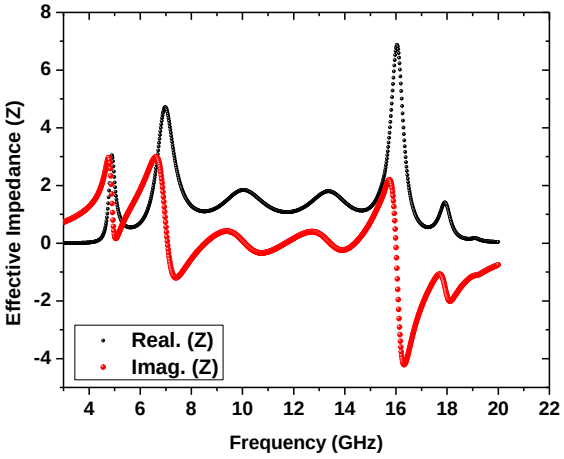


Fig. 3. Effective impedance of the proposed MA for normal incidence

C. *Exctracted Electromagnetic Constitutive Parameters*

The calculated real and the imaginary parts of ε_{eff} and μ_{eff} are shown in the Fig. 4a-b, respectively. Real part permeability is obtained as negative values. Thus, it can be said that the suggested structure responds to an external applied field and generates a magnetic dipole in the opposite direction of the external field. As a result, magnetic resonance is the primary driving force behind the MA structure [12].

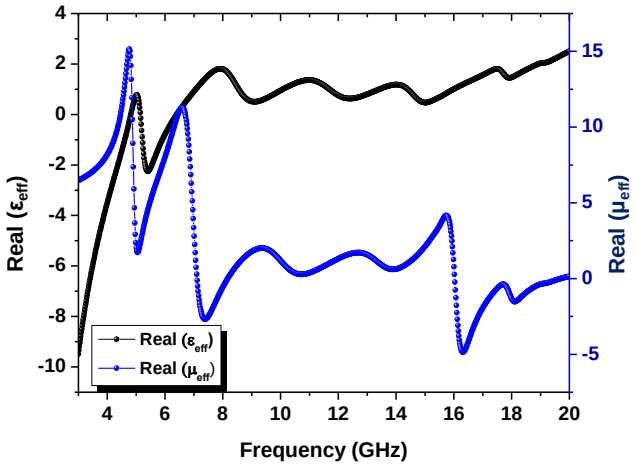


Fig. 4. Extracted electromagnetic constitutive parameters (real part of ε_{eff} and μ_{eff})

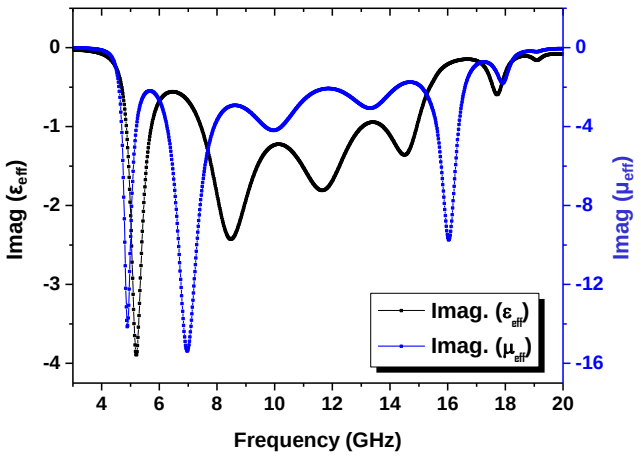


Fig. 5. Extracted electromagnetic constitutive parameters (imaginary part of ε_{eff} and μ_{eff})

D. *Absorption based on polarization angles*

In this study, we also studied regarding the absorption performance for different polarization angles for TE polarization angles to investigate the polarization behaviors (Fig. 6).

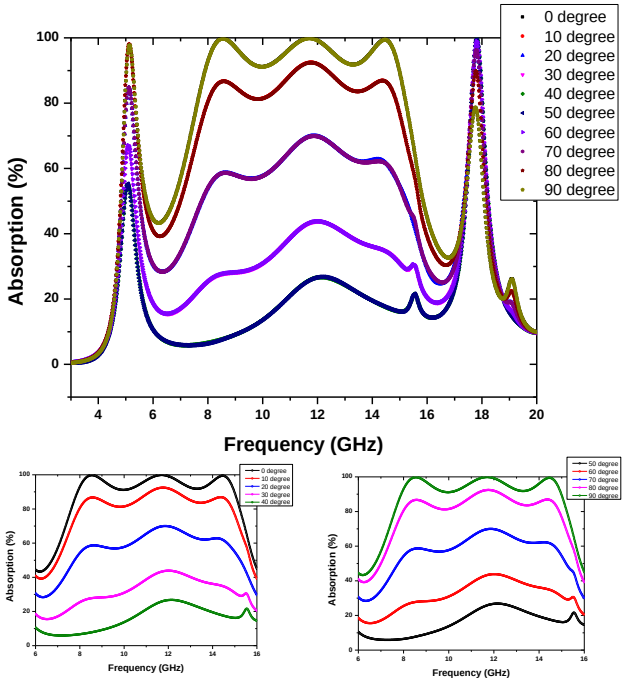


Fig. 6. Absorption of the suggested MA including polarization angles in the range of 0^0-90^0 for TE polarizasyon

The absorbency of the MA structure decreases with the increasing the polarization angle until 40 degree. When keep going the increment of polarization angle, the absorbency of the suggested MA increases asymmetrically until the absorbency rate for zero degree. Another result is that the absorbency is almost identical in the circumstances of the polarization of 0^0 and 90^0, 10^0 and 80^0, 20^0 and 70^0, 30^0 and 60^0, 40^0 and 50^0, respectively. Moreover, the band-width of the suggested MA keeps relatively constant with changing the polarization angle.

E. *Absroption based on incident angle*

The proposed MA absorber behavior with an obliquely incident wave is investigated under both TE and TM polarizations (Fig. 6 and Fig. 7). For that purpose, different incident angles from 0^0 to 50^0 are applied to observe the absorption. For both polarizations in X-band, the absorbency spectra is maintanined higher that 80% until the incident angle up to 40^0. When increasing the incident angle from the 40 degree, it is obtained that there exist some strong oscillations from 12 GHz to 16 GHz. That results is compatible with the literature [9], [13].

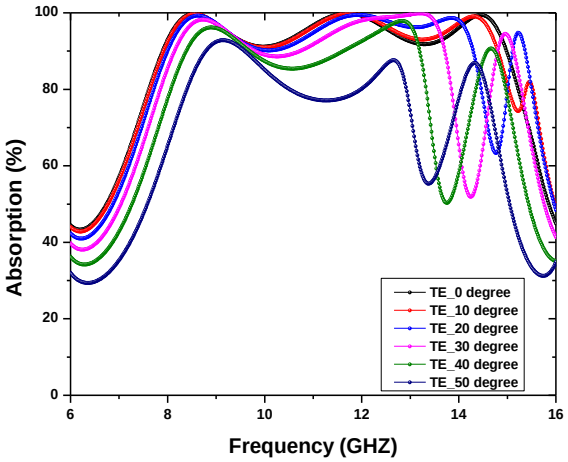


Fig. 7. Absorption efficiencies based on incident angle (from 0^0 to 50^0) for TE Polarization

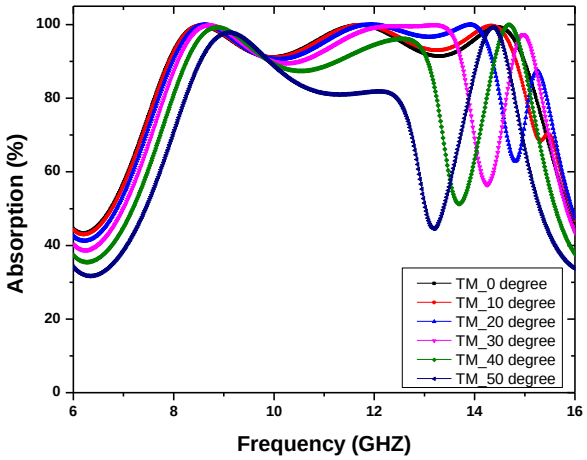


Fig. 8. Absorption efficieincies based on incident angle (from 0^0 to 50^0) for TM polarizarion

[5] CONCLUSIONS

We have proposed a facile design of a metamaterial absorber for radar applications, which covers the X-band with the same absorptivity range above 90%. A good property of impedance matching is also achieved. Based on the polarization angles, the proposed MA has good absorption results until 40^0 in X-band. Moreover, the absorptivity decreases with the increment of polarization angles. For the X-band, we obtained 90 percent absorptivity including three resonant peaks. The suggested absorber is encouraging X-band radar applications such as RCS and reduction of electromagnetic interference (EM).

REFERENCES

[1] C. M. Watts, X. Liu, and W. J. Padilla, "Metamaterial electromagnetic wave absorbers," *Adv. Mater.*, vol. 24, no. 23, 2012, doi: 10.1002/adma.201200674.

[2] E. Unal, F. Dincer, E. Tetik, M. Karaaslan, M. Bakir, and C. Sabah, "Tunable perfect metamaterial absorber design using the golden ratio and energy harvesting and sensor applications," *J. Mater. Sci. Mater. Electron.*, vol. 26, no. 12, pp. 9735–9740, 2015, doi: 10.1007/s10854-015-3642-7.

[3] M. Bagmanci, M. Karaaslan, E. Unal, O. Akgol, M. Baklr, and C. Sabah, "Solar energy harvesting with ultra-broadband metamaterial absorber," *Int. J. Mod. Phys. B*, vol. 33, no. 8, 2019, doi: 10.1142/S0217979219500565.

[4] N. I. Landy, S. Sajuyigbe, J. J. Mock, D. R. Smith, and W. J. Padilla, "Perfect metamaterial absorber," *Phys. Rev. Lett.*, vol. 100, no. 20, 2008, doi: 10.1103/PhysRevLett.100.207402.

[5] C. Zhang, Q. Cheng, J. Yang, J. Zhao, and T. J. Cui, "Broadband metamaterial for optical transparency and microwave absorption," *Appl. Phys. Lett.*, vol. 110, no. 14, 2017, doi: 10.1063/1.4979543.

[6] G. Sen, M. Kumar, S. N. Islam, and S. Das, "Broadband metamaterial absorber on a single-layer ultrathin substrate," *Waves in Random and Complex Media*, vol. 29, no. 1, pp. 153–161, 2019, doi: 10.1080/17455030.2017.1418099.

[7] F. Ding, Y. Cui, X. Ge, Y. Jin, and S. He, "Ultra-broadband microwave metamaterial absorber," *Appl. Phys. Lett.*, vol. 100, no. 10, 2012, doi: 10.1063/1.3692178.

[8] S. Li, J. Gao, X. Cao, W. Li, Z. Zhang, and D. Zhang, "Wideband, thin, and polarization-insensitive perfect absorber based the double octagonal rings metamaterials and lumped resistances," *J. Appl. Phys.*, vol. 116, no. 4, 2014, doi: 10.1063/1.4891716.

[9] S. Ghosh, "An Ultrawideband Ultrathin Metamaterial Absorber Based on Circular Split Rings," *IEEE Antennas Wirel. Propag. Lett.*, vol. 19, no. 3, pp. 512–514, 2020, doi: 10.1109/LAWP.2020.2968144.

[10] Y. Shi, Y. C. Li, T. Hao, L. Li, and C. H. Liang, "A design of ultra-broadband metamaterial absorber," *Waves in Random and Complex Media*, vol. 27, no. 2, pp. 381–391, 2017, doi: 10.1080/17455030.2016.1250974.

[11] M. I. Khan and F. A. Tahir, "An angularly stable dual-broadband anisotropic cross polarization conversion metasurface," *J. Appl. Phys.*, vol. 122, no. 5, p. 053103, 2017, doi: 10.1063/1.4997456.

[12] P. V. Tuong *et al.*, "Symmetric metamaterials based on flower-shaped structure," *Mater. Chem. Phys.*, vol. 141, no. 1, pp. 535–539, 2013, doi: 10.1016/j.matchemphys.2013.05.057.

[13] S. Bhattacharyya, "A Broadband Microwave Metamaterial Absorber with Octave Bandwidth," *Mapan - J. Metrol. Soc. India*, vol. 31, no. 4, pp. 299–307, 2016, doi: 10.1007/s12647-016-0180-6.

Inverter based OTA Design for Second-Order G_m-C filters

Mesut Atasoyu
Deparment of Electrical and Electronics
Engineering, Artvin Coruh University
matasoyu@itu.edu.tr

***Abstract*—In this paper, a second-order transconductance (G_m)- capacitor (C) low pass filter is proposed based on inverter-based operational transconductance amplifiers(OTAs) to perform optimal power-efficient filter design. Furthermore, the inversion coefficient (IC) transistor sizing method is used to optimize the power and speed performance of the inverter-based OTA. The proposed filter achieves 1.5% total harmonic distortion (THD), and 44° phase margin, consuming almost 852-μW supply voltage power. As a result, the calculated and simulated values of the unity gain bandwidth are in a good agreement.**

***Index Terms*—Inversion coefficient (IC), g_m/I_D, Inverter based OTA, G_m-C Filter.**

I. Introduction

Today, there is an increased demand for low-power circuits for biomedical and Internet of Things (IoT) applications. Biosignals have amplitude range from 1-μV to 10-mV and frequency range from 10-Mhz to 10-kHz [1], [2]. For the application of bio-signal processing, transconductance (G_m)-capacitor (C) filter is widely exploited to achieve the signal processing at this amplitude and frequency range. The cut-off frequency of the G_m-C filter is a function of G_m and load capacitor(C_L). From the noise standpoint, the determination of G_m values is trading off between noise and frequency operation of the circuit, such high G_m values healing the input-referred output noise [3].

The main building block of the G_m-C filter is well-known circuitry. An operational transconductance amplifier (OTA) is the main block of this filter and is a power-hungry unit. Among the literature OTA designs, the Nauta's design has high-performance power efficiency [4], [5]. A fully differential inverter-based OTA is considered to be a viable option to address this low power requirement by replacing it with a conventional current mirror OTA design.

The design of the transistors in this power-hungry circuit is demanding transistor sizing techniques. The g_m/I_D is the prominent transistor sizing tool [6]. The g_m/I_D is taken as a design parameter instead of transistor overdrive voltage which has squared root relation with the drain current causing difficulty to an accurate setting of transistor bias current. Furthermore, the inversion coefficient (IC) technique was purposed to scale the drain current to define g_m/I_D parameter such a way to bias transistors more accurately [7], [8].

In this work, the second-order G_m-C low pass filter is structured with inverter-based OTAs. The performance optimization of the inverter-based OTA is realized employing the IC transistor sizing technique to operate the circuit at optimal speed and power efficiency. Furthermore, the integrity of the inverter-based OTA studied in single-ended and fully differential second-order G_m-C low pass filter topologies. These filter performances are compared in terms of their gain and phase responses.

This paper is organized as follows. Section II briefly explains the design and circuit operation of OTA. Section III discusses the design procedure of fully differential OTA based second order-G_m-C filter and its performance simulation results. Section IV concludes this paper.

II. Inverter based OTA Design

Inverter-based OTA was aimed firstly by Nauta [4] for power-efficient design. The current-reuse mechanism of the inverter stage, the G_m of the inverter-based OTA has two times higher value than the current mirror-loaded OTA. Further, this bigger G_m value helps to reduce the input-referred noise of this topology four times less than such current loaded differential OTA, as well as this noise source value highly rely on the G_m value [3]. The g_m of inverter-based OTA design has g_m linearization due to class-AB operation [3]. To emphasize, inverter-based OTA has full output swing helping do higher slew-rate(SR) performance.

The schematic of a fully differential inverter-based OTA is shown in Fig. 1. The core of the design is two inverters composed of PMOS transistors (M_{3-4}) and NMOS transistors (M_{5-6}). The output common-mode feedback resistors are R_{CM}=1MΩ. The current mirror circuitry is composed of PMOS transistors (M_{1-2}) and NMOS transistors (M_{7-8}) and these transistors biased via the current sources (I_{B1} and I_{B2}). The power supply voltage is V_{DD}=1.2V and the common-mode voltage (V_{CM}) is 0.6V

A. IC based Transistor Sizing

Channel length (L) parameter value of included all transistors is chosen equal and determined for gain and phase margin constraints as a value of L=140nm, from g_m/I_D charts that are not provided in this work. Further, to mitigate the input-referred noise sources, we assume the output G_m value as 1mS. The unity gain frequency (f_u) is calculated comprising G_m value and the load capacitor C_L= 50pF as follows:

$$G_m = 2 * \pi * f_u * C_L \tag{1}$$

The calculated f_u is 3.1MHz. The biasing current value flows into the branches of M_{5-6} transistors as equal value of 75μA

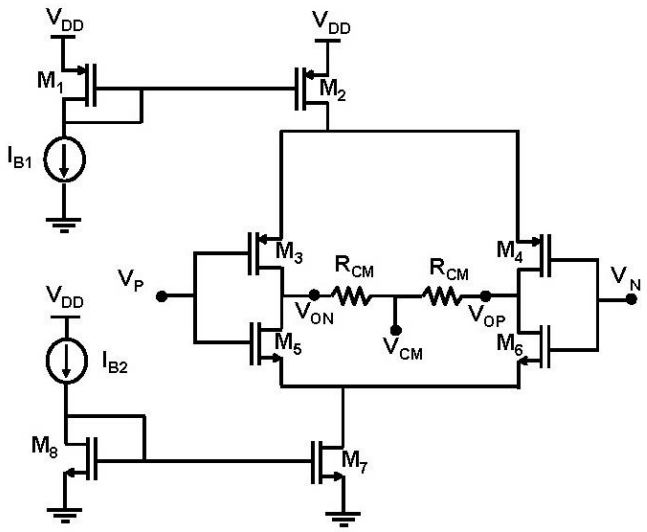


Fig. 1: The schematic of an inverter based OTA.

that is obtained via g_m/I_D and IC methodologies. The biasing current value of I_{B1} and I_{B2} current sources is 150μA. Using these calculated values, all-transistor sizes of the inverter-based OTAs are calculated and the calculated value is optimized to 1.65X higher values as a reason of not included parasitic effects such as output resistors of transistors. The calculated transistor sizing values are given in Table-I.

Table-I	
Transistor	Size
$M_{1,2}$	W=14.89μm
$M_{3,4}$	W=7.67μm
$M_{5,6}$	W=1.81μm
$M_{7,8}$	W=3.45μm

III. Second-Order G_m-C Filters

In this work, single-ended and fully differential second-order low pass filters were designed in 65nm CMOS technology parameters. All simulations results were performed via SPICE tools. The transistor sizes and bias currents of the used inverter based OTAs in single-ended and fully differential second-order filters have same values.

A. The Single Ended Inverter based OTA G_m-C Low Pass Filter

The single ended output OTA configuration is utilized for single-ended second-order G_m-C filter as viewed in Fig. 2.

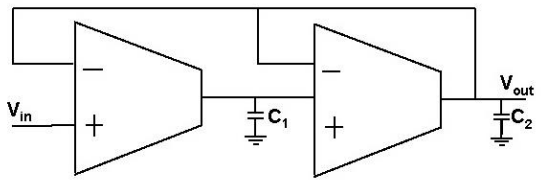


Fig. 2: The block representation of single ended G_m-C low pass filter.

The cut-off frequency and quality factor of this structure can be written:

$$\omega_o = \frac{g_m}{\sqrt{C_1 C_2}} \qquad Q = \sqrt{\left(\frac{C_2}{C_1}\right)} \tag{2}$$

The gain and phase results of this second-order filter where is employed inverter-based OTAs implies that this amplifier is not applicable in this filter topology due to deteriorated gain performance in the closed-loop configuration of these amplifiers as shown in Fig. 3.

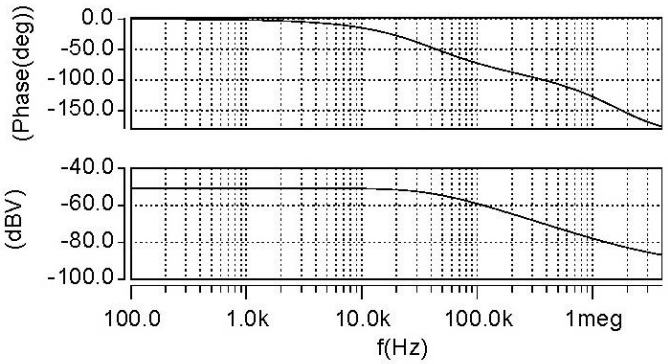


Fig. 3: The gain and phase results of single ended G_m-C low pass filter.

B. Fully Differential Inverter based OTA G_m-C Low Pass Filter

The fully differential input and output inverter-based OTAs are employed in the second-order fully differential G_m-C filter structured in cascaded form as shown in Fig. 4. The cut-off frequency and quality factor of this fully-differential structure are the same given above in the single-ended topology when its transfer function is derived for differential input voltage and output voltage.

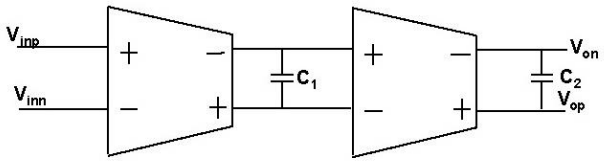


Fig. 4: The block representation of second order fully differential G_m-C low pass filter.

The gain and phase response of the fully-differential filter are given in Fig. 5. The filter gain is high and 29.5 dB and the phase margin is 49° at unity gain. The gain values of the filter are derived for the value of L=140nm and L=240nm in Fig. 6.

It is important to say when setting the L values to low gain configurations of the filter such as 0dB gain value, it is difficult to bias transistors of the inverters in strong inversion. For this reason, we biased the inverter-based OTAs to the high gain value that reduces the input swing of the inverter-based OTA due to high open-loop gain value.

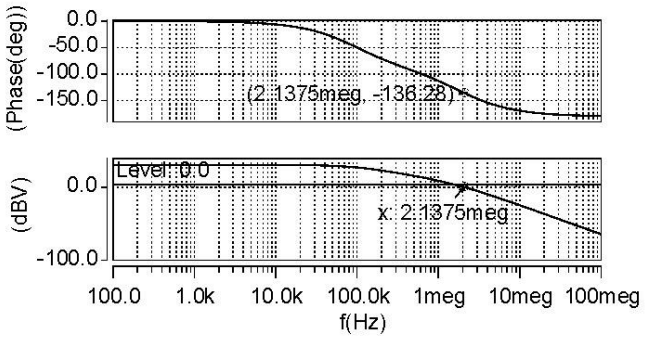


Fig. 5: The gain and phase results of the fully differential G_m-C low pass filter.

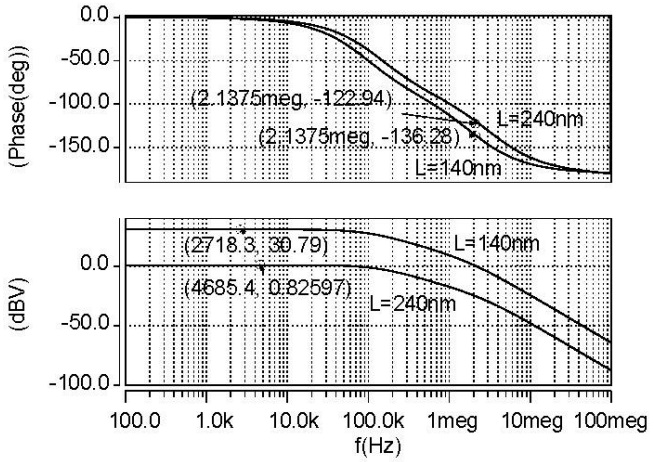


Fig. 6: The gain and phase results of the second-order G_m-C low pass filter varies with L values.

Transient analysis of the proposed filter is performed where the simulation setup is configured by applying the sinusoidal signal which has a voltage range -2mV to 2mV with DC voltage ($VDD/2$) with 1μs period. Fig. 7 shows the output signal of the filter follows in good agreement with the phase of the applied input signal and the input signal is amplified from a single input voltage value of 4mV to differential output voltage of 14mV. Total harmonic distortion (THD) was calculated from the FFT simulation result as a value of 1.5%.

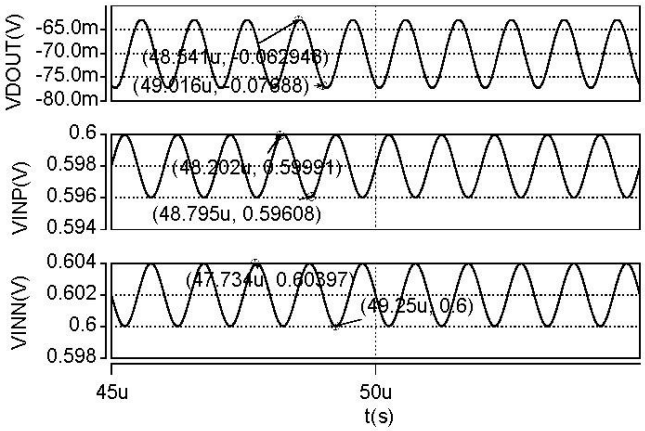


Fig. 7: The transient response of he second-order fully-differential G_m-C low pass filter.

IV. Conclusion

In this paper, a second-order G_m-C low pass filter proposed based on an inverter based OTA to perform optimal power efficient filter design. Furthermore, the IC transistor sizing method is used to optimize power and speed performance of the inverter based OTA. The proposed filter achieves 1.5% THD, and 44° phase margin, consuming almost 852-μW supply voltage power.

References

[1] R. R. Harrison, "A versatile integrated circuit for the acquisition of biopotentials," in *2007 IEEE Custom Integrated Circuits Conference*. IEEE, 2007, pp. 115–122.

[2] J. R. M. Krishna and T. Laxminidhi, "Widely tunable low-pass gm- c filter for biomedical applications," *IET Circuits, Devices & Systems*, vol. 13, no. 2, pp. 239–244, 2018.

[3] M. Gambhir, V. Dhanasekaran, J. Silva-Martinez, and E. Sanchez-Sinencio, "A low power 1.3 ghz dual-path current mode gm-c filter," in *2008 IEEE Custom Integrated Circuits Conference*. IEEE, 2008, pp. 703–706.

[4] B. Nauta, "A cmos transconductance-c filter technique for very high frequencies," *IEEE Journal of Solid-State Circuits*, vol. 27, no. 2, pp. 142–153, 1992.

[5] H. Luo, Y. Han, R. C. Cheung, X. Liu, and T. Cao, "A 0.8-v 230-μ w 98-db dr inverter-based σ δ modulator for audio applications," *IEEE Journal of Solid-State Circuits*, vol. 48, no. 10, pp. 2430–2441, 2013.

[6] C. Enz and A. Pezzotta, "Nanoscale mosfet modeling for the design of low-power analog and rf circuits," in *2016 MIXDES-23rd International Conference Mixed Design of Integrated Circuits and Systems*. IEEE, 2016, pp. 21–26.

[7] D. Foty, D. Binkley, M. Bucher *et al.*, "Starting over: gm/id-based mosfet modeling as a basis for modernized analog design methodologies," in *Technical Proc. 2002 Intl. Conf. on Modeling and Simulation of Microsystems*, vol. 1, 2002, pp. 682–685.

[8] M. Manghisoni, L. Gaioni, L. Ratti, V. Re, and G. Traversi, "Assessment of a low-power 65 nm cmos technology for analog front-end design," *IEEE Transactions on Nuclear Science*, vol. 61, no. 1, pp. 553–560, 2014.

A study of cure kinetics of polyurethane/epoxy compositions filled with modified boron nitride

Nikita Bratasyuk
Faculty of Applied Optics ITMO University
Saint-Petersburg, Russia
bratasyukna@gmail.com

Vjacheslav Zuev
Faculty of Applied Optics ITMO University
Saint-Petersburg, Russia
zuev@hq.macro.ru

***Abstract*—Fillers with enhanced thermal conductivity (hexagonal boron nitride and its modified analogue) were introduced into polyurethane/epoxy compositions. The curing kinetics of these compositions were studied using dynamic and isothermal DSC and kinetics parameters (rate constants and activation energies) were calculated. It was shown that the curing process has complex character and includes several of concurrent reactions, i.e. polyaddition reactions and the cationic polymerization of oxirane rings. The increase of loading level leads to the formation of less ordered PU/epoxy networks. The thermal conductivity of compositions increased proportionally to the filler loading levels and maximal values found for composition with surface modified hexagonal boron nitride (1.5-fold increase).**

Keywords— polyurethane/epoxy composites, curing kinetics, thermal conductivity, boron nitride, activation energy

[1] INTRODUCTION

For advanced opto-electronic applications need a development a coatings with high level of thermal conductivity. The well-developed approach to these coatings based on epoxy resins filled with boron nitride (h-BN) [1,2]. However, the available data in the literature are insufficient and need more study to understand a relationship between the kinetics of composite formation, the filler dimensions, the surface properties of fillers and the ultimate properties of resulting composite. Previously was found that such parameters as the size and shape of the BN particles, their surface properties including treatments of the particles by coupling agents what increase particle-polymer matrix interconnection influence on thermal conductivity of epoxy based composites [3].

One of the most common way to increase the thermal conductivity of polymer composites connected with using of exfoliated two-dimensional (2D) materials, for example, graphene, molybdenum disulfide or hexagonal boron nitride [4,5]. The exfoliation process as a rule has been connected with the surface modification of particles too [6]. Hence, we can to compare the effect of the surface modification of particles and changing its dimensionality on thermal conductivity and formation kinetics of polymer composites at same time to exclude the effect of particle size.

The inherent disadvantage of epoxy coatings is its brittleness. To overcome this downside epoxy resins have been used many approaches. From many possibilities we modified epoxy composition by such elastic polymers as polyurethanes (PUs).

The main aim of this research is to investigate the cure kinetics PU/epoxy filled with h-BN and its surface modified analogue and to determine influence of fillers on thermal conductivity of resulting polymer composites.

The reported study was funded by RFBR, project number 20-31-70001.

[2] EXPERIMENTAL PART

A. Materials

Hexagonal boron nitride with purity at least 98% was supplied by Umeks Industrial company (Ufa, Russia). Modified h-BN (mBN) particles were prepared using the method described by Yu et al [7]. All fillers have similar particles size (less than 40 μm).

PU/epoxy composition was prepared as described in our previous paper [8]. The ratio of a diglycidyl bisphenol-A and PEG-400 was 9:1. As hardener was used Etal-45M (mixture of aromatic amines with sebacic acid, AO ANPC Epital, Russia). The calculated amount of fillers was added at sonification to mixture diglycidyl bisphenol-A and PEG-400 before cure.

B. Characterization of filled composites

Dynamic DSC measurements were performed by simultaneous TGA/DSC instrument SDT Q600 (TA Instruments) at a heating rate of 10 °C/min over the temperature range of 25-200 °C. Exactly same amount of the reaction precursors (20−25 mg) was used in hermetically sealed corundum pan in each case.

Isothermal DSC measurements were performed using SDT Q600 (TA Instruments) instrument. The isothermal cure temperatures were 110, 120 and 130 °C. Weight of sample was 15-20 mg, material of pan – alumina, nitrogen flow rate – 40 ml/min. Indium and zinc standards were used to calibrate DSC apparatus. Samples were heated to the isothermal curing temperature at a heating rate 120 °C /min. The cure reaction was assumed to be complete when the heat flow of the samples leveled off to the baseline and became stable.

Thermal conductivity was measurement using method described by Moradi et. al. [9]. The differential scanning calorimetry has been used to measure the thermal conductivity of filled composites. Measurements were made on a SDT Q600 (TA Instruments) instrument with a nitrogen flow of 40.0 ± 0.1 ml/min. The tests were run from 80 to 180 °C at a heating rate of 10 °C/min. The diameters of samples were 6.0 ± 0.05 mm, heights – 1.8 ± 0.05 mm. To determine the thermal conductivity of solid materials a disk of pure indium was placed on the upper circular end surface of the sample. The indium disk had a 4 ± 0.2 mm diameter and weighed 45.2 mg.

[3] RESULTS AND DISCUSSION

A. Morphology of BN and mBN

According to received SEM pictures (Fig.1) the fillers contain various particle agglomerates. The size distribution functions for samples were calculated (Fig. 2). For calculation we used our original approach based on applying the Schulz-Flory distribution [10]. Mean grain sizes are 10-12 μm for

boron nitride and 18 μm for modified boron nitride. Increase of mean grain size for mBN can be attributed to particles aggregation during synthesis.

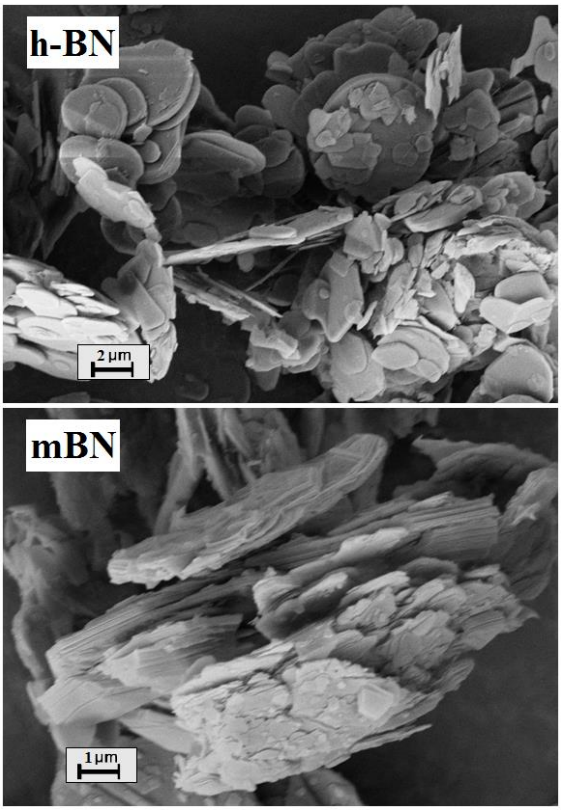


Fig. 1. Size distribution functions of h-BN and mBN

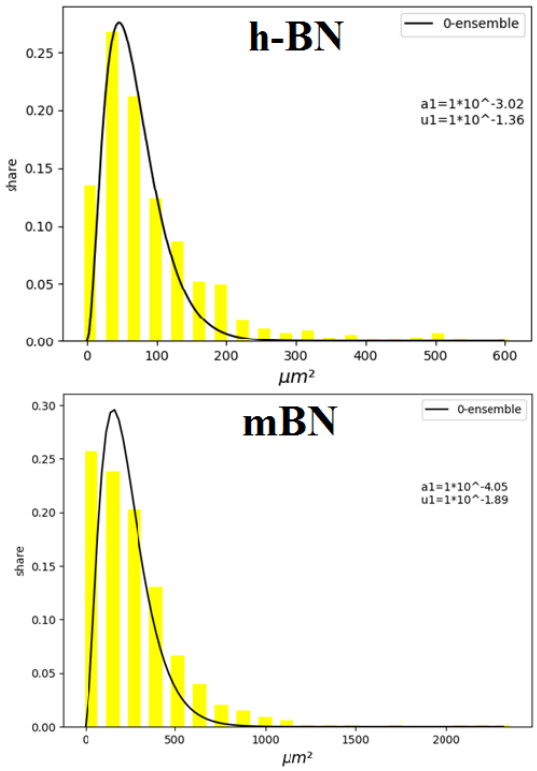


Fig. 2. Size distribution functions of h-BN and mBN

As one can see from SEM images, mBN particles have patchy surface with thick blade-like edges. Also its surface is enriched by hydroxyl groups, which is confirmed by the data of IR spectroscopy.

B. *Cure kinetics*

The number of papers described the curing of epoxy with boron nitride is extremely large [2]. However, the majority of these papers have limited themselves to comparison of the positions of maxima of isothermal DSC curves without calculation of rate constants, thus not gaining to the detailed analysis of filler effects [9]. We used Ozawa-Wall-Flynn method for estimation of activation energies (Fig. 3) at different cure degrees using data of dynamic DSC. In addition, constant rate were calculated both at dynamic and at isothermal heating. The method for calculating the activation energy was described in detail earlier [8]. Kamal model [11,12] was used for calculation kinetic parameters at autocatalytic curing of PU/epoxy compositions. The rate of cure is given by (1):

$$da/dt = (k_1 + k_2 a^m)(1-a)^n \quad (1)$$

where a – conversion, k_1 – non-autocatalytic reaction rate constant, k_2 – autocatalytic reaction rate constant, t – time, m and n – orders of the no-autocatalytic and autocatalytic reactions, respectively.

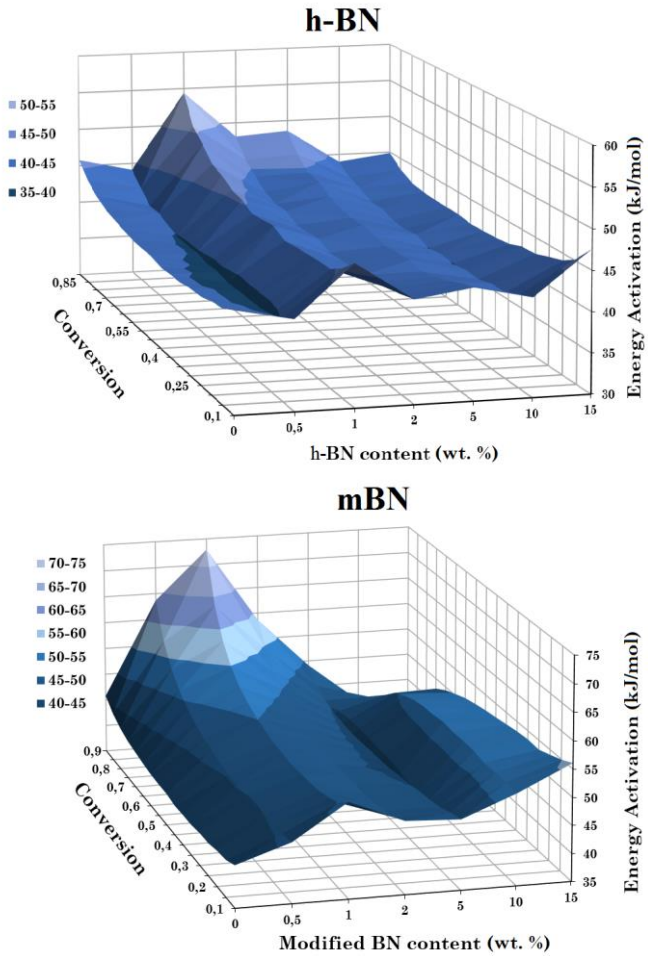


Fig. 3. Dependence of curing activation energy (Flynn-Wall-Ozawa model) on filler concentrations and conversion for compositions filled with h-BN and mBN

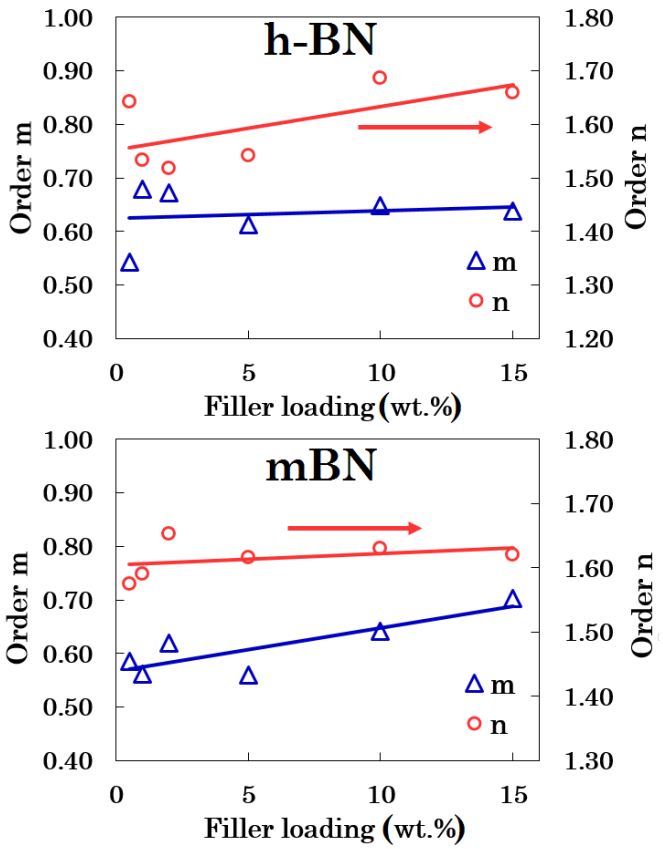


Fig. 4. Influence of filler on reaction order n for the nth order reaction and reaction order m for the autocatalytic reaction

Graphical-analytical method, proposed by Kenny [13], was used to calculate the main kinetic parameters (k_1, k_2, m, n) in Kamal equation. The final values of k_1, k_2, m, n are given in Fig. 4 and Fig. 5.

An increase of value m with rising curing temperature is observed for all types of used fillers, simultaneously, the n values are decreased. It means that high temperature promote the autocatalytic curing. The increase of value m shows rising impact of the autocatalytic process in common curing.

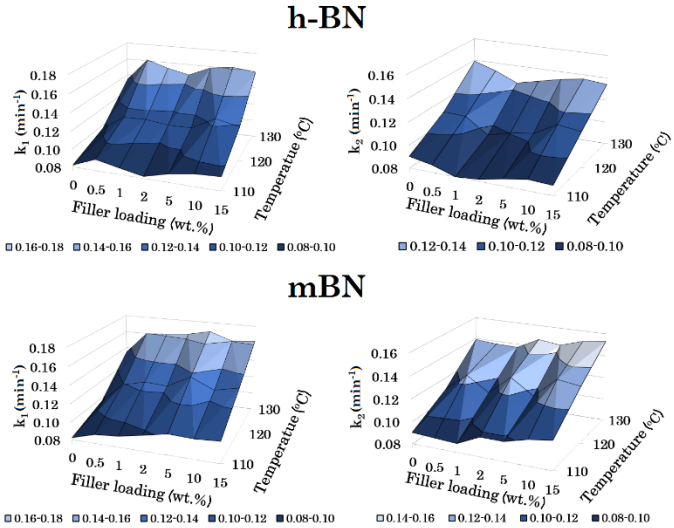


Fig. 5. Dependence of curing rate constants k_1 and k_2 on filler concentrations

The neutral fillers such as h-BN did not show the concentration dependence of the rate constants. The modified boron nitride particles with hydroxylated surface increased a rate of polymer formation at high concentrations (10-15 wt.%), when the diffusion and spatial limitations for access of the functional groups to their surfaces have been lost.

A particularly interesting effect was observed at low filler concentrations (1-2 wt.%). It is well known, that oxirane rings can polymerize also by cationic polymerization with such initiator as free proton, which is commonly used for preparation coatings [14]. In the system under study, this pathway is inferior and can be supressed by absorption of protons by fillers particles. The superior proton absorption ability is maximal for boron nitride with surface hydroxyl groups explains the maximal decrease of rate constants for compositions with small and intermediate concentrations of these particles. The commercial BN and its modification consists of large bubble-like structures with a diameter of tens of micrometers (Fig.1). However, after introduction into prepolymer mixture by our method it was observed completely exfoliated. The formation of nanosheets can significantly increase the specific surface area of such particles compared to commercial fillers BN. This can lead to the increase of adsorbing properties as well. The possibility of such pathway as cationic polymerization indirectly supports the results on activation energy (Fig. 3). As one can see, the maximal values of activation energy were observed for low filler concentration.

The increase of the values of activation energy with conversion is related to diffusion limitation [14]. These limitations are maximal for long bulky molecules and, as is known for anionic polymerization [15], the growth centers are located inside macromolecular skein. Polyaddition reactions do not have such limitations, therefore, their activation energies weakly depend on conversion [16]. This is observed for compositions with high concentrations of fillers. Such reactions lead to macromolecules with lower molecular weights and less organized network with a number of defects. This should be manifested in mechanical properties.

C. Thermal conductivity

The results of thermal conductivity testing are given in Fig. 6. These results shown in accordance with SEM data about good dispersion of fillers uniform growth thermal conductivity with filler concentration. The value of thermal conductivity of composites are fully defined by own filler thermal conductivity. However, the interaction of fillers with polymer matrix is also important. The composites filled with modified boron nitride particles, which are incorporate in polymer matrix in results of chemical reactions, shown the best thermal conductivity. Hence, the increase of connection between fillers and polymer matrix leads to increase thermal conductivity too.

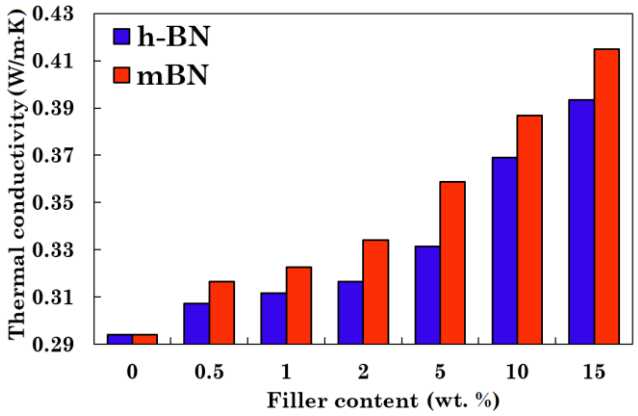


Fig. 6. Dependence of thermal conductivity on filler concentration for composites filled with h-BN and mBN

[4] CONCLUSIONS

In present research was described the study of curing kinetics of PU/epoxy compositions filled with boron nitride and boron nitride with surface modified hydroxyl groups. It was shown that the presence of fillers change the curing pathway in dependence on its concentrations. The cationic polymerization of oxirane groups leads to formation the more ordered PU/epoxy network and the reinforcement of composition. The excess of filler concentration in 2 wt.% leads to suppression of this pathway and formation less ordered structure. The thermal conductivity of PU/epoxy compositions with good dispersed fillers determines the specific thermal conductivity of fillers. However, the incorporation of fillers into PU/epoxy network through the chemical reactions with filler surface hydroxyl groups increases the thermal conductivity resulting polymer composite.

REFERENCES

[1] H. Chen, V.V. Ginzburg, J. Yang, Y. Yang, W. Liu, Y. Huang, L. Du and B. Chen, "Thermal conductivity of polymer-based composites: Fundamentals and applications," Prog. Polym. Sci., vol. 59, pp. 5941-5985, 2016.

[2] N. Burger, A. Lachachi, M. Ferriol, M. Lutz, V. Toniazzo and D. Ruch, "Review of thermal conductivity in composites: Mechanisms, parameters and theory," Prog. Polym. Sci., vol. 61, pp. 1-28, 2016.

[3] K. Gaska, A. Rybak, C. Kapusta, R. Sekula and A. Siwek, "Enhanced thermal conductivity of epoxy-matrix composites with hybrid fillers," Polym. Adv. Technol., vol. 26, pp. 26-31, 2015.

[4] D. Akinwande, C. Huyghebaert, C.-H. Wang, et al., "Graphene and two-dimensional materials for silicon technology," Nature, vol. 573, pp.507-518, 2019.

[5] Z. Cheng, Z. Ma, H. Ding and Z. Liu, "Environmentally friendly, scalable exfoliation for few-layered hexagonal boron nitride nanosheets (BNNSs) by multi-time thermal expansion based on released gases," J. Mater. Chem. C, vol. 7, pp. 14701-14708, 2009.

[6] X. Wang, S. Ji, X.-Q. Wang, H.-Y. Bian, L.-R. Lin, H.-Q. Dai and H. Xiao, "Thermally conductive, super flexible and flame-retardant BN-OH/PVA composite film reinforced by lignin nanoparticles," J. Mater. Chem. C, vol. 7, pp. 14159-14169, 2019.

[7] B. Yu, W. Xing, W. Guo, S. Qiu, X. Wang, S. Lo and Y. Hu, "Thermal exfoliation of hexagonal boron nitride for effective enhancements on thermal stability, flame retardancy and smoke suppression of epoxy resin nanocomposites via sol–gel process," J. Mater. Chem. A, vol. 4, pp. 7330-7340, 2016.

[8] N. A. Bratasyuk and V. V. Zuev, "The study of the curing mechanism, kinetic and mechanical performance of polyurethane/epoxy composites using aliphatic and aromatic amines as curing agents," Thermochim. Acta, vol. 687, 178598, pp. 1-11, 2020.

[9] S. Moradi, Y. Calventus , F. Romбn, P.Ruiz and J. M Hutchinson, "Epoxy composites filled with boron nitride: cure kinetics and the effect of particle shape on the thermal conductivity," J. Therm. Anal. Calor., vol. 142, pp. 595-603, 2020.

[10] D. V. Pikhurov and V. V. Zuev, "Kinetics of formation of microstructure in polyurethane foams infused with micro and nanosized carbonaceous fillers," Polym. Eng. Sci., vol. 59, pp. 941-948, 2019

[11] Y.Zhao and D. Drummer, "Influence of Filler Content and Filler Size on the Curing Kinetics of an Epoxy Resin," Polymers, vol. 11, 1797, 2019.

[12] J. Wan, C. Li, Z.-Y. Bu, C.-J. Xu, B.-G. Li and H. Fan, "A comparative study of epoxy resin cured with a linear diamine and a branched polyamine," Chem. Eng. J., vol. 188, pp. 160-172, 2012.

[13] J.M. Kenny, "Determination of autocatalytic kinetic model parameters describing thermoset cure," J. Appl. Poly. Sci., vol. 51, pp. 761–764, 1994.

[14] J. Herzberger, K. Niederer, H. Pohlit, J. Seiwert, M. Worm, F. R. Wurm and H. Frey, "Polymerization of ethylene oxide, propylene oxide, and other alkylene oxide: Synthesis, Novel Polymer Architectures, and Bioconjugation," Chem. Rev., vol. 116, pp. 2170-2243, 2016.

[15] J. Schawe, "Kinetic studies of complex reactions—part 1: model free kinetics," Mettler-Toledo UserCom, vol. 18, pp. 13–16, 2003.

[16] G.Odian, Principles of polymerization, 4th ed., Wiley-Interscience, Hoboken, NJ, 2004.

Preparation of Manganese-Containing Magnetic Nanocomposites for Biomedical Applications

Okan Icten
Faculty of Science Department of Chemistry
Hacettepe University
Ankara, Turkey
okanicten@hacettepe.edu.tr

Aim: **Cancer is the second leading cause of death after cardiovascular disease in the world. Despite significant efforts to treat cancer, there has been minimal advancement in the past 30 years. Conventional cancer methods include some side effects such as permanent hair loss, fetal damage, skin problems, specific drug delivery, and multidrug resistance. Early cancer detection and treatment are challenging with conventional methods. Therefore, it is necessary to develop new materials that can be used in cancer detection and treatment methods. Nanotechnology allows researchers to develop advanced materials for the early detection and effective treatment of cancer. In particular, magnetic nanocomposites represent one of the most exciting prospects in the nanotechnology field [1]. The most popular magnetic particles in nanocomposites are Fe_3O_4, γ-Fe_2O_3, $MnFe_2O_4$, $MgFe_2O_4$, $CoFe_2O_4$ because they are biocompatible biodegradable and have high transition temperatures and excellent chemical stability [2]. Magnetic nanocomposites can be used for cell separation, immunoassay, magnetic resonance imaging (MRI), drug and gene delivery, minimally invasive surgery, radionuclide therapy, hyperthermia, photothermal therapy (PTT), and artificial muscle applications [3]. In addition to magnetic particles, nanosystems, including manganese, have been extensive of great interest as candidates for MRI T1-weighted contrast agents owing to their efficient positive contrast enhancement effects. Additionally, nanostructures containing manganese can be combined with various photothermal agents (Au and CuS nanoparticles, carbon nanotube, graphene, and polydopamine) for PTT applications. Recent studies are therefore directed towards the development of new materials which can be potentially used in multiple applications. Therefore, this study aims the synthesis and characterization of manganese-containing magnetic nanocomposites for biomedical applications.**

Method: **In this study, citrate-coated Fe_3O_4 and $MnFe_2O_4$ nanoparticles were synthesized via the co-precipitation method and solvothermal synthesis, respectively. Then, in order to have the potential to be used in MRI and PTT applications, citrate-coated Fe_3O_4 nanoparticles were modified with manganese metal-organic frameworks (Fe_3O_4@CA-Mn-MOF) while $MnFe_2O_4$ nanoparticles were coated with polydopamine ($MnFe_2O4$@PDA).**

Results: **The obtained different nanocomposites were characterized by powder X-ray diffraction (XRD), vibrational spectroscopy (FT-IR), thermal analysis (TGA), scanning and transmission electron microscopy (SEM and TEM), and room temperature magnetization. Besides, the photothermal effects of the obtained materials were generally examined in this study. Analysis results indicated that Fe_3O_4 nanoparticles consisted of spherical structures with a size of approximately less than 20 nm were coated with citrate (6%), and manganese metal-organic frameworks, which were nanorod-shaped particles of an average length of about 250 nm and 35 nm in width, were successfully prepared in the presence of these citrate-coated Fe_3O_4 nanoparticles. Similarly, $MnFe_2O_4$ nanoparticles prepared by solvothermal consisted of uniform spherical particles of nearly 100 nm in size, and these particles were approximately 35% coated with PDA. All other analyzes performed to characterize the synthesized nanocomposite structures in detail supported each other. The photothermal effects of the obtained materials were generally examined, and it was seen that after 900 s irritation with 808 nm NIR laser, the temperature of the dispersion of nanocomposites reached up to 36 °C and 42 °C (from 28.5 °C) for Fe_3O_4@CA-Mn-MOF and $MnFe_2O4$@PDA, respectively.**

Conclusion: **In conclusion, due to their appropriate size, morphology, magnetic properties, and chemical composition, $MnFe_2O4$@PDA nanocomposites have the potential to be used in MRI and PTT, while Fe_3O_4@CA-Mn-MOF nanocomposites can be a potential candidate for MRI.**

Keywords—cancer, magnetic particles, manganese, nanocomposites, MRI and photothermal therapy.

REFERENCES

[1] Corr SA, Rakovich YP, Gun'ko YK. Multifunctional magnetic-fluorescent nanocomposites for biomedical applications. Nanoscale Research Letters. 2008;3:87-104.

[2] Islam K, Haque M, Kumar A, Hoq A, Hyder F, Hoque SM. Manganese Ferrite Nanoparticles (MnFe2O4): Size Dependence for Hyperthermia and Negative/Positive Contrast Enhancement in MRI. Nanomaterials. 2020;10:2297.

[3] Ramanujan RV. Magnetic particles for biomedical applications. Biomedical materials: Springer; 2009. p. 477-91.

Positron annihilation lifetime spectroscopy: a sensitive probe to determine free volume holes in polymers

Meshude Akbulut Söylemez
Hacettepe University,
Department of Chemistry, Beytepe,06800
Ankara, Turkey
meshude@gmail.com

Aim: **Positron annihilation lifetime spectroscopy (PALS) is a useful and sensitive tool to get detailed information about the size and size distribution of the defects in metals and also free volume holes in polymers. The effect of the electron beam irradiation on the size and size distribution of the free volume holes in the blends of low-density polyethylene with ethylene vinyl alcohol (EVOH) and ethylene vinyl acetate (EVA) copolymers was investigated. The effects of the ionizing radiation on the polymers are mainly crosslinking and chain scission. The change of the free volume holes provides the information about the change in the micro structure of blends due to the crosslinking or chain scission. Besides, the effect of the blend component was also investigated.**

Method: **The flexible films of the blends of the low-density polyethylene (LDPE) were prepared by melting extrusion process using a twin-screw extrusion. The blends were irradiated by e-beam. The total absorbed doses were 25, 50, 75 and 100 kGy. The chemical characterization of the blends before and after e-beam irradiation was carried out by employing attenuated total reflectance Fourier transform infrared spectroscopy (ATR-FTIR). The size of the free volume holes was investigated by PALS. The thermal characterization of the blends was performed by employing differential scanning calorimetry (DSC), and the dynamic mechanic properties of the samples was investigated by Dynamic mechanical analysis (DMA). The change in the mechanical properties due to the irradiation of the blends were also investigated by static mechanical test. In the case of LDPE/EVA blends the size of the free volume holes was also investigated as a function of blend composition.**

Results: **Preparation of polymer blends is an effective, economic and easy method to obtain materials with desired properties for end use [1]. In order to predict and improve physical properties of blends it is necessary to know the mechanism of interaction between two phases and atomic scale microstructure in terms of size and size distribution of free volume holes. However, conventional methods cannot give any detail information about free volume holes due to their small size. Positron annihilation lifetime spectroscopy (PALS) is a powerful probe to measure the size of free volume holes in atomic scale [2, 3]. Positrons have been successfully used for materials research, as they are extremely sensitive to defects, phase transitions, and heterogeneities [4].**

The structures of the LDPE/EVA blends were characterized by ATR-FTIR. The common peaks result from the PE and EVA can be seen in different composition of blends. PALS is a powerful tool for determining the size of cavities in polymeric networks. The positron annihilation lifetime spectra of the blends were resolved into four components τ_1, p-Ps lifetime; τ_2, lifetime of free positrons; τ_3 and τ_4 o-Ps lifetime components. The annihilation lifetime of the third and fourth components is directly proportional to the size of the free volume holes in amorphous and crystalline parts of the polymers. The radius of the free volume holes was determined by using the following equation developed by Tao and Eldrup [5].

$$\tau_{o-Ps} = 0.5\left[1-\frac{R}{R+\Delta R}+\frac{1}{2\pi}\sin\left(\frac{2\pi R}{R+\Delta R}\right)\right]^{-1}$$

In this equation τ o-Ps is the lifetime of the o-Ps in ns, R is the radius of free volume holes in nm, and ΔR is a constant whose value is 0.1656 nm. The intensity of the free positrons in PE/EVA blends decreases with a decrease in the amount of polar component of the blend, EVA as can be seen in Fig. 1. The free positron intensity shows an increase due the increasing in polar groups in the network [6]. In the case of the PE/EVOH blends, the size of the free volume holes shows a significant decrease with increasing in dose. The E-Modulus and tensile strength of blends increase as the nonpolar component and irradiation dose increase. With increasing nonpolar component and irradiation dose, the elongation at break values for blends decrease, which is an expected result given the relationship between modulus and elongation.

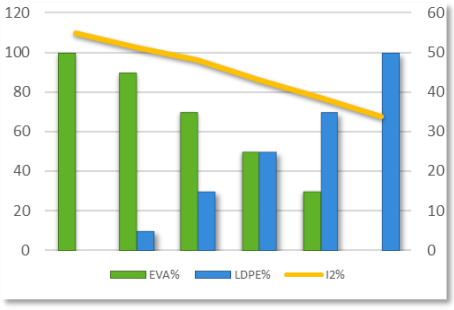


Fig. 1. The change in intensity of free positrons with increasing in PE content of blend.

Conclusion: **The detailed investigation of the effect of the blend composition and e-beam irradiation on the size of free volume holes was carried out. Radiation effects in polymers have shown that radiation-induced crosslinking occurs only in the amorphous phase of a semi-crystalline polymer, so the crystallinity of irradiated EVOH and poly vinyl acetate films is nearly unchanged.**

Keywords—free volume holes, polymer, polymer blends, positron annihilation spectroscopy

REFERENCES

[1] W. Brandt, S. Berko, W. W. Walker, "Positronium Decay in Molecular Substances,", Phys. Rev., vol. 120, pp. 1289-1295, November 1961.
[2] C. L. Wang, T. Hirade, F. H. J. Maurer, M. Eldrup, N. J. Pedersen, "Free-

volume distribution and positronium formation in amorphous polymers: Temperature and positron-irradiation-time dependence,", J. Chem. Phys., vol. 108, no 11, pp. 4654-4661, October 1998.

[3] J. H. Lind, P. L. Jones, G. W. Pearsall, "A positron annihilation lifetime study of isotactic polypropylene,", J. Polym. Sci. A, vol. 24, no 11, pp. 3033-3047, November 1986.

[4] C. L. Wang, Y. Kobayashi, W. Zheng, C. Zhang, "Positronium formation in PE/EVA polymer blends at low temperatures,", Polymer, vol. 42, no 6, pp. 2359-2364, March 2001.

[5] M. A. Söylemez, O. Guven, "Detailed positron annihilation lifetime spectroscopic investigation of atrazine imprinted polymers grafted onto PE/PP non-woven fabrics,", J. Mol. Recognit., vol. 31, no 1, pp. e2676, January 2018.

[6] G. Çelik, M. Barsbay, O. Güven, "Towards new proton exchange membrane materials with enhanced performance via RAFT polymerization,", Polym. Chem., vol. 7, pp. 701-714, November 2015.

Effective Desulfurization of Coal with Oak Ash

Gizem Hazan Çağlayan
Mus Alparslan University *Department of Environmental Engineering*, Muş, Turkey
corresponding author:
g.hazan.caglayan@gmail.com

Ubeyde İpek
Fırat University Department of Environmental Engineering, Elazığ, Turkey
ubeydeipek@gmail.com

Abstract*— Desulfurization from coal will prevent many environmental damages, especially air pollution. Therefore, this process is essential in order to eliminate the harmful environmental effects of coal. Research on the desulfurization process is very important to environmental, economic and social development worldwide. In the literature, various chemical, physical and biological desulfurization method are available. In this study; Ermenek and Tunçbilek (in Turkey) coal samples were used for the desulfurization process by liquid basic extraction of oak ash. When the results obtained are examined; it has been observed that oak ash can be used instead of chemicals, physical process or microorganisms for desulfurization process.

***Keywords*— desulfurization, oak ash, coal, reuse**

[1] INTRODUCTION

Coal is a non-renewable fossil resource that has been used as an energy source for centuries. [1]. Sulfur in coal is found in inorganic and organic forms. [2]. The inorganic sulfur forms of coal are in the form of pyrite, sulfide and sulfate. Pyrite is found as the main inorganic sulfur part of most coal. Generally, pyritic sulfur is present in the same amount as organic sulfur content. [3].

Sulfur components of coal reason many environmental problems such as air pollution, acid rain, etc. [4], [5], [6]. Therefore, the effective desulfurization process of coal is a great importance to environmental protection, control acid rain and reduce the pollution of PM2.5 to the environment [7].

Desulfurization of coal application processes: (1) desulfurizing coal using pre-use preparation or cleaning techniques, (2) fixing sulfur using additives during coal combustion, (3) desulfurizing flue gas after combustion [8].

In this study, the desulfurization process of Ermenek and Tunçbilek coals was observed using basic extraction liquids of oak ash. Before and after this process; total sulfur contents of each coal were measured. Finally, the obtained analysis results were compared with previous physical, chemical and biological studies and their applicability was investigated.

[2] MATERIAL AND METHOD

The coals were crushed to a particle size of 250 mesh using the ASTM D2013. Total sulfur contents were measured using the IR ASTM D4239. Afterwards, 10 g and 20 g oak ash samples were extracted in 100 ml and 200 ml of distilled water at 100°C for 30 min, respectively and then, the mixtures were filtered to obtain basic liquids. The 2 g Ermenek and Tunçbilek coals were re-extracted in the basic liquid of oak ash at 100°C for 1 hour and then filtered again. This investigation setup showed Fig 1.

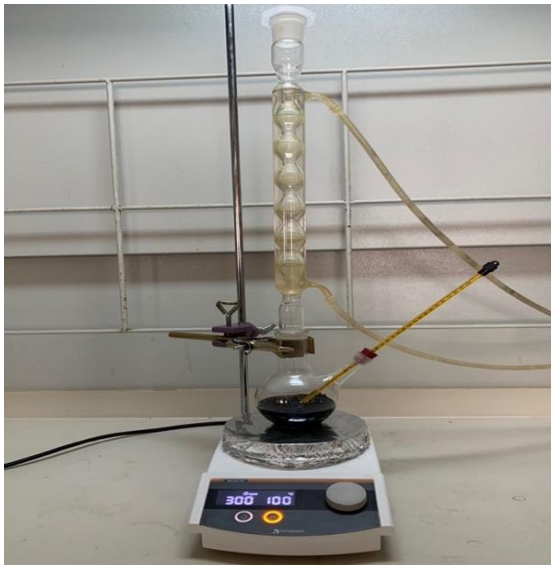


Fig. 1. Experimental setup.

They were dried in oven at 103°C for 1 hour and then measured again total sulfur contents using the IR ASTM D4239.

This study analyzed the total desulfurization rate after treating two different types of coal (Ermenek and Tunçbilek) in a basic extraction liquid of oak ash. Before the desulfurization process, the properties of Ermenek and Tunçbilek coals analyzed and given Table 1-2.

Table 1. Ermenek Coal Analysis Results.

Parameter	Original Coal	Dry Coal	Test Method
Moisture %	22.98	--	ASTM D3173 ASTM D3302
Volatile Matter %	30.34	39.40	ASTM D3174
Ash %	9.45	12.27	ASTM D3175
Total Sulfur %	1.77	2.21	ASTM D 4239
Lower calorific value kcal/kg	4270	5709	ISO 1928
Upper calorific value kcal/kg	4562	5924	ASTM D5865

Table 2. Tunçbilek Coal Analysis Results.

Parameter	Original Coal	Dry Coal	Test Method
Moisture %	15.36	--	ASTM D3173 ASTM D3302
Volatile Matter %	31.66	37.40	ASTM D3174
Ash %	11.45	13.52	ASTM D3175
Total Sulfur %	2.14	2.43	ASTM D 4239
Lower calorific value kcal/kg	5502	6518	ISO 1928
Upper calorific value kcal/kg	5791	6842	ASTM D5865

[3] RESULTS

In the current study; desulfurization by oak ash-based extraction liquid of Ermenek and Tunçbilek coals have been examined. Figure 2 shows that the total sulfur removals of 2 g Ermenek coal.

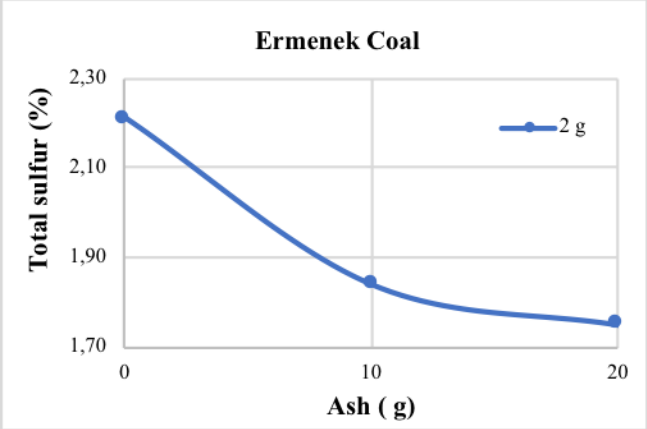


Fig. 2. The removal of total sulfur for Ermenek coal.

Figure 2 shows the amount of total sulfur removed from 2 g of coal reacting with 10 g and 20 g of oak ash extraction liquid. Before desulfurization; the total sulfur content of Ermenek coal was measured as 2.21%. After desulfurization; total sulfur content of Ermenek coal decreased to 1.84% (for 10 g) and 1.75% (for 20 g). Afterward, the same processes were repeated for Tunçbilek coal. Figure 3 shows that the total sulfur removals of 2 g Tunçbilek coal.

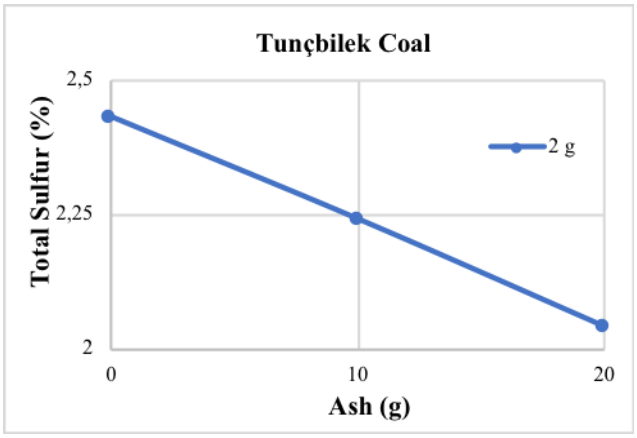


Fig. 3. The removal of total sulfur for Tunçbilek coal.

Figure 3 shows the amount of total sulfur removed from 2 g of coal reacting with 10 g and 20 g of oak ash extraction liquid. Before desulfurization; the total sulfur content of Tunçbilek coal was measured as 2.43%. After desulfurization; total sulfur content of Tunçbilek coal decreased to 2.24% (for 10 g) and 2.04% (for 20 g).

During the years, researchers investigated various desulfurization methods of different types of coal. Wang et al. (2020) observed desulfurization by flotation, acid washing, HCl-HF-HNO_3 treatment and ultrasonication. Total sulfur from Yanzhou coal (Shandong, China) was measured 4.32%. After desulfurization by flotation, acid washing, HCl-HF-HNO_3 treatment and ultrasonication; total sulfur content decreased to 2.83%, 3.27%, 3.09% and 1.86%, respectively [9]. Singh et al. (2018) investigated high-sulfur coal samples collected from Giral lignite mine was desulfurized using bacteria Burkholderia sp. GR 8–02 isolated from native lignite. After desulfurization, the total sulfur content of coal sample decreased from 4.23% to 2.99% [10]. Liu et al. (2017) investigated desulfurization of Yihai coalfield (in China) contains 4.97% total sulfur content. Final total sulfur content of the desulfurized coal with DP06 was reduced to 2.63% [11].

[4] DISCUSSION

In this study, it was aimed to remove the total sulfur content of the coal by using the basic extraction liquid obtained from oak ash.

The results obtained from this study are expressed:

- The total sulfur removal efficiencies of Ermenek coal obtained as 17% (10 g) and 21% (20 g) respectively.
- The total sulfur removal efficiencies of Tunçbilek coal obtained as 8% (10 g) and 17% (20 g), respectively.

As a result of these experiments, it can be said that the basic liquid from oak ash is an effective method as desulfurization from coal.

ACKNOWLEDGMENT

This study was supported by Fırat University with the BAP Project No. MF.15.15, 2016. In addition, we would like to thank the employees of Elazığ Governorship Environmental Measurement and Analysis Laboratory for their support.

REFERENCES

[1] P. A. Çelik, D. Ö. Aksoy, S. Koca, H. Koca and A. Çabuk, "The approach of biodesulfurization for clean coal technologies: A review," International Journal of Environmental Science and Technology, vol. 16(4), pp. 2115-2132, 2019.

[2] F. Liu, Y. Lei, J. Shi, L Zhou, Z. Wu, Y. Dong and W. Bi, "Effect of microbial nutrients supply on coal biodesulfurization," Journal of Hazardous Materials, vol. 384, pp. 121324, 2020.

[3] W. Li and Y. Tang, "Sulfur isotopic composition of superhigh-organic-sulfur coals from the Chenxi coalfield, Southern China," International Journal of Coal Geology, vol. 127, pp. 3-13, 2014.

[4] Y. Zhang, P. Liang, T. Jiao, J. Wu, and H. Zhang, "Effect of foreign minerals on sulfur transformation in the step conversion of coal pyrolysis and combustion," Journal of Analytical and Applied Pyrolysis, vol. 127, pp. 240-245.

[5] J. Hou, Y. Ma, S. Li, J. Shi, L. He and J. Li, "Transformation of sulfur and nitrogen during Shenmu coal pyrolysis," Fuel, vol. 231, pp. 134-144, 2018.

[6] E. Şahinoglu, "Cleaning of high pyritic sulfur fine coal via flotation," Advanced Powder Technology, vol. 29(7), pp. 1703-1712, 2018.

[7] J. Xu, X. Liu, C. Song, Z. Du, F. Wang, J. Luo, X. Chen and A. Zhou, "Biodesulfurization of high sulfur coal from Shanxi: Optimization of the desulfurization parameters of three kinds of bacteria," Energy Sources, Part A: Recovery, Utilization, and Environmental Effects, vol. 42(18), pp. 2297-2315, 2021.

[8] W. Xia, Y. Li, W. He, and Y. Peng, "Desulfurization of low rank coal co-pyrolysis with reduced iron powder followed by dry magnetic separation," Journal of Cleaner Production, vol. 204, pp. 525-531, 2018.

[9] M. Wang, Y. Shen, Y. Hu, J. Kong, J. Wang, and L. Chang, "Effect of pre-desulfurization process on the sulfur forms and their transformations during pyrolysis of Yanzhou high sulfur coal," Fuel, vol. 276, pp. 118124, 2020.

[10] A. K. Singh, A. Kumar, P. K. Singh, A. L. Singh, and A. Kumar, "Bacterial desulphurization of low-rank coal: A case study of Eocene Lignite of Western Rajasthan, India," Energy Sources, Part A: Recovery, Utilization, and Environmental Effects, vol. 40(10), pp. 1199-1208, 2018.

[11] T. Liu, J. H. Hou and Y. L. Peng, "Biodesulfurization from the high sulfur coal with a newly isolated native bacterium, Aspergillus sp. DP06," Environmental Progress & Sustainable Energy, vol. 36(2), pp. 595-599, 2017.

Short-term Variations of Pore-water Pressure Due to Diurnal Temperature Changes in Soil Slopes

Nuraddeen Muhammad Babangida
Department of Civil Engineering,
*Bayero University, Kano*Kano, Nigeria.
nmbabangida.civ@buk.edu.ng

Khamaruzaman Wan Yusof
Dept. of Civil & Env. Engineering,
Universiti Teknologi PETRONAS,
Perak Darul Ridzuan, Malaysia.
khamaruzaman.Yusof@utp.edu.my

Muhammad Raza Ul Mustafa
Dept. of Civil & Env. Engineering,
Universiti Teknologi PETRONAS,
Perak Darul Ridzuan, Malaysia.
raza.mustafa@utp.edu.my

***Abstract*—The effect of temperature can easily be interpreted as that which, improves matric suction or reduce pore-water pressure (PWP). However, this may not always be the case, as temperature may well have the reverse effect especially during short-periods. This study investigates how diurnal temperature changes affect PWP and the type of relationship that exist between the two quantities. Time series of PWP and diurnal temperature was collected from field measurements on an instrumented slope. Analysis of the records showed that, during the course of the day, PWP rises when temperature rises, and vice versa. It was found that for the short term, PWP can rise when high temperatures are experienced, and a typical rise of up to 4 kPa can be experience for a diurnal temperature change between day and night. The results also, suggest that exposure to high temperature conditions after rainfall may lead to unanticipated, elevated levels of PWP. This increase can affect stability of unsaturated soil slopes, by lowering the slope's factor of safety. Up to 2% loss in factor of safety could result due to such temperature induced PWP rise.**

Keywords*—*Pore-water pressure, rainfall, slope, slope stability, diurnal temperature

[1] INTRODUCTION

Rainfall infiltration has been labelled as the major factor that affects the rise in pore-water pressure (PWP) or decrease in matric suction [1], [2]. In contrast, temperature aids the recovery of matric suction or loss of PWP.

Studies and analysis of PWP fluctuations have been central to slope related works, from PWP modeling [3]–[7], slope stability analysis and management [8]–[12] to slope monitoring and failure warning systems [13], [14]. Positive PWP are known to develop in shallow regions of unsaturated slopes and ultimately cause failure [15].

The effect of temperature on PWP has been investigated by a number of studies [16], [17]. Thota et al., [18] has shown an increase of 24% and 39% as a result of temperature rise between 25ºC–40ºC and 25ºC–60ºC respectively. Fuentes et al., [19] insisted that temperature rise causes development of excess PWP. They further asserted that in low permeability soils; a temperature increase of 30ºC may cause up to 1 Mpa increase in PWP. Although not all studies of PWP versus temperature are slope related, however, the study of [20] developed a model of undrained shear strength that incorporated temperature changes, while [21] proposed a model of soil water retention curve that incorporates temperature changes. Salager et al., [22] showed that for the same soil, with the same moisture content, the matric suction is different at different temperatures.

Other than results from [23] (which showed PWP to increase during the day and fall during the night, with a fluctuation of approximately 4.5kPa), literature search reveals no decent study on the behavior of PWP due to diurnal changes of temperatures. To this end, this study extensively looks to analyze the time series of PWP and temperature, and the largely unexplained short term (period of a day or less) diurnal effect of temperature on PWP. Focus will be on post-rainfall, high temperatures (which could lead to increase in PWP to undesirable thresholds) and how this could affect unsaturated soil slopes.

[2] METHODOLOGY

One way to tackle changes of PWP is by field observation using tensiometers. Temperature effects are more pronounced, near the surface of the soil thus, higher PWP fluctuations could be recorded near the soil surface. Therefore, a methodology was designed, that entailed field observation of PWP at depth of 1.5 m and the surrounding air temperature changes. A slope for instrumentation and relevant data collection was selected within Universiti Teknologi PETRONAS (UTP), Malaysia. The slope is well exposed to sunlight, with no drainage structure on or around it. The study slope was instrumented with four jet fill tensiometers with attached transducers and data loggers. A rain gauge fitted with air temperature sensor was installed at the Toe. Each set of tensiometers were installed at 0.6 m and 1.5 m depth respectively and were separated by 0.5 m distance between them. Resolution of data collected was at 30 minutes interval, this will give a better understanding of how the PWP behaves during and immediately after rainfall events.

[3] RESULTS AND DISCUSSIONS

Three months data, amounting to 4464 data points was considered in the analysis. From this dataset, a daily time series of PWP and temperature was developed. Records of PWP at 1.5 m depth at the toe and ambient temperatures at 0200 hours (representing low/nigh temperature conditions) and 1400 hours (representing high/day temperature conditions) were considered. Thus, a single observation of peak temperature during the day and minimum temperature during the night was extracted. This was used to form a 12-hour time series of temperature and PWP. In the analysis, two different time series are considered integral to the study, these are:

This study is financed by Malaysian Ministry of Higher Education's fundamental research grant scheme no 0153AB-I61.

Post-rainfall low temperatures; these are time spans after rainfall, over relatively long periods of low temperature, such that, only influence of rainfall can be observed from the PWP records.

Pre-rainfall high temperature; Relatively long periods of high temperatures, with no preceding *significant rainfall*, such that only influence of temperature can be observed from the PWP records.

Significant rainfall in this context is, rainfall that is enough to cause a noticeable change in PWP at the selected depth of 1.5 m. This is needed to know the threshold of rainfall events that are expected to cause a noticeable rise in PWP. To establish the *significant rainfall*, five different rainfall events (shown in Table 1) were isolated. These events have no post-rainfall high temperatures (this is important, to eliminate the effect of temperature induced PWP rise) and no second storm followed these events for more than 30 hours. Additionally, the slope's *response time* (the time taken for significant rainfall event to infiltrate up to 1.5 m depth) to worst PWP levels, was observed and established from Fig. 1.

A. *Pore-water Pressure Data*

Fig. 1 shows, *post-rainfall low temperature* conditions. It was established that the *response time* for PWP to reach worst conditions at 1.5 m depth is up to 12 hours, this is depicted by the events of 5th, 16th and 26th November 2014 on Fig. 1. Plot of 5th, 16th and 26th November 2014 showed a brief gain in matric suction after about 13 hours, and a subsequent rise in PWP is noticed afterwards. This gain in matric suction is typically induced by new high temperatures during that period. Further fluctuations are seen onwards along the plots, which are caused by temperature fluctuations over the course of the day.

Table 1. Isolated Rainfall events that preceded low temperature conditions

Date & Time	Rainfall (mm)	Duration (hrs)
05/11/14 18.30	40.5	6.0
16/11/14 19.00	31.5	2.0
22/11/14 19.30	4.5	2.5
26/11/14 15.00	30.5	4.5
28/11/14 17.30	8.0	1.5

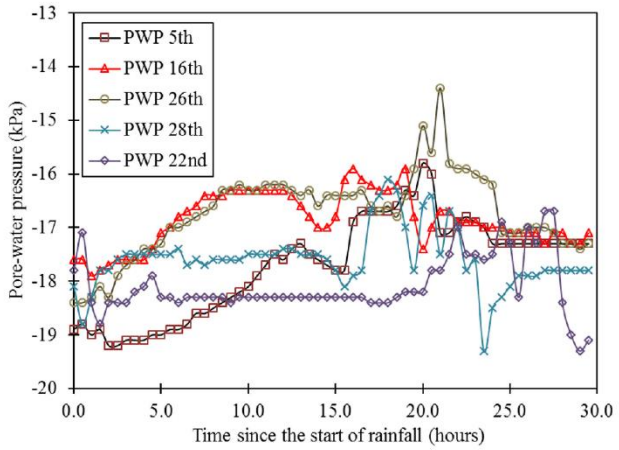


Fig. 1. Post rainfall PWP record, with three PWP records (5, 16 & 26 November) rising after rainfall, indicating the rainfall is of significance, and two PWP records (28th & 22nd November) largely not affected by the preceding rainfall, indicating that the rainfall is insignificant.

Some records stand peculiar from the other days. These include some 3 days in November (8th, 14th and 22nd), 5 days in December (1st, 8th, 15th, 23rd, and 25th) and 6th January 2015. Within these days the PWP during the night happens to be equal or more than the PWP during the day. Field observations showed that these days recorded some of the lowest (day time) temperatures of 23 oC-24 oC and thus PWP did not rise because of these low temperature conditions.

The influence of rainfall infiltration on the rise of PWP has already been established, and can be seen in Fig. 2. In many instances PWP had increased after a certain rainfall event. However, few other PWP peaks exist, which are not characterized by any antecedent rainfall. As evident from Fig. 2; peaks of 9th and 21st November, those of 11th and 19th December and that of 18th January are typical examples. The PWP rise in these days are primarily induced by high temperatures of 35ºC average.

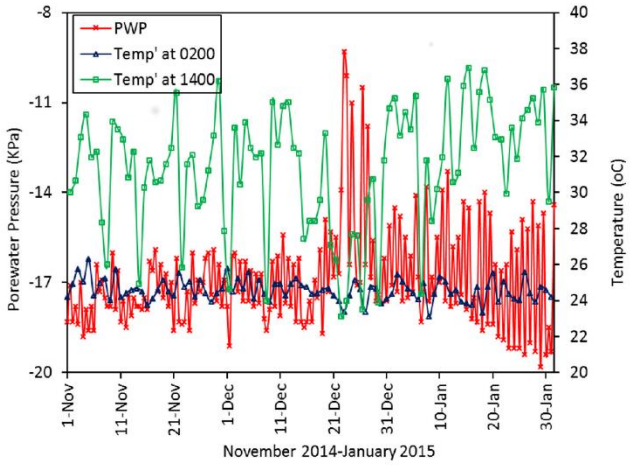


Fig. 2. Shows PWP during the day and night, and in most instances the PWP during the day is higher than that during the night.

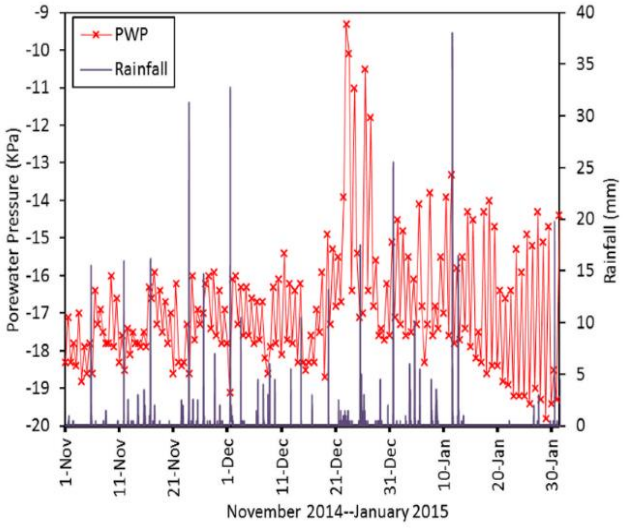


Fig. 3. Rainfall and PWP fluctuations over the three months period, with PWP rising after rainfall events, and occasionally rising even without any rainfall event.

The above observations or PWP rising during high temperatures can be attributed to vapor transport within the soil. Parlange *et al.* [24] established that vapor movement is due to convective movement caused by the influence of diurnal changes of temperature and the corresponding thermal expansion and contraction of soil air. Typically, everything

starts when the sun heats up the soil surface; a temperature gradient is formed and vapor moves from the warmer surface to deeper, cooler region of the soil and condenses. This results in increased local moisture content. However, loss of moisture does occur due to evaporation at the warmer surface, thus causing moisture to be sucked from the deeper region (since the warmer surface is at higher suction). At the end of the day there is a moisture transport in both directions. Ultimately there is a net increase of moisture at the cooler region and thus the rise in PWP.

This net moisture transport changes are significantly influence by soil physical properties. For example, in fine grained soils, vapor movement could be quite significant since they retain substantial amount of water within them. Such moisture movement may not be experience in coarse grained soils. It is worth noting that such changes of PWP can only occur in moist soils. A saturated soil has little or no void space to allow vapor transport. Likewise, a very dry soil has little or no moisture to allow such process to occur.

B. Effect of Temperature on Slope Stability

To evaluate the impact of temperature on a slope, one of the events where temperature increase of 8.5ºC had induced PWP rise was considered. The high (32ºC) and low (23.5ºC) temperatures of 24th of November, resulted in PWP records of -16.2 kPa and -18.6 kPa respectively. These were used to evaluate the change in factor of safety (FoS). A number of assumptions were made, which include: that the PWP is uniform at all 1.5 m depth (at toe and crest). For simplicity, the slope was assumed to be homogenous and isotropic. The first analysis was evaluated with PWP of -16.2 kPa (at 1.5 m depth) and the second with PWP of -18.6 kPa (at 1.5 m depth). The FoS was evaluated using SLOPE/W. Additional strength is added to the slope due to negative PWP, through incorporation of the angle for suction related strength (ϕ^b). Typically ϕ^b is taken as half of effective angle of internal friction ($0.5\,\phi'$) in unsaturated soil zone [25]. Stability analysis was then conducted, with FoS sought at 1.5 m depth. Fig. 4 shows one of the stability models. While Table 2 shows the difference in the FoS for varying PWP records (high & low).

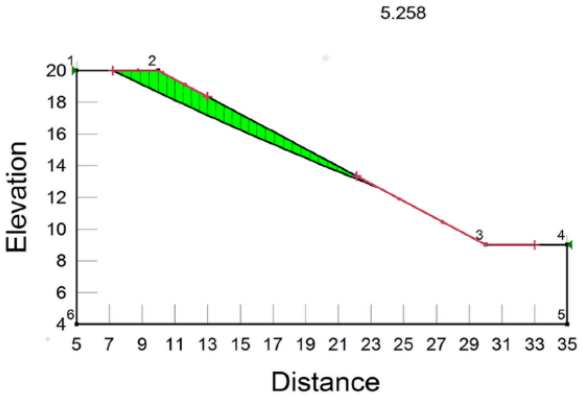


Fig. 4. Slope stability model (suction incorporated) with stability evaluated at the depth of around 1.5 m.

Table 2. Factor of safety evaluated at two different PWP levels that are typical of records during diurnal temperatures changes.

Method	PWP (kPa)	FoS	% Difference in FoS
Morgenstein	-18.6	5.468	2.10
	-16.2	5.258	
Bishop	-18.6	5.369	1.96
	-16.2	5.173	

The FoS was evaluated using Morgenstein and simplified Bishop methods. Table 2 shows the difference in the FoS during the day and during the night, i.e. at two different PWP records. The FoS is high, because it is not evaluated at the critical plane. There is a difference of about 2% between FoS evaluated during the day (32 ºC), and that at night (23.5 ºC). The influence of PWP on the FoS, thus can be translated, as the influence of temperature, since the PWP changes are temperature induced. These changes are very much in agreement with studies of Thota *et al.* [18], whom reported a decrease of 5% in FoS and 24% increase in PWP due to variation of temperature (25ºC- 40ºC).

[4] CONCLUSIONS

It has been established herein that in unsaturated soils, diurnal temperature changes have significant effect on PWP when considered on short-term basis. PWP rises during high temperatures and decreases during night or low temperature conditions, and the cycle repeats itself over again. However, over the long-term period, temperature improves suction recovery in soils due to prolonged effect of evaporation at the surface, causing a daily moisture loss without replenishment.

Post-rainfall high temperature periods have been established as periods when FoS may slightly reduce. Two slope models (suction incorporated), evaluated with PWP taken between 12-hour periods, at depth of 1.5 m (PWP at -18.6 kPa, obtained during low temperatures and -16.2 kPa, during high temperatures) showed a reduction of 2% in the FoS. This reduction, happened without any additional influx of rainfall.

Diurnal rise of temperature influences changes in PWP. The cyclic nature of PWP is most noticeable in relatively shallow depth. Nevertheless, this effect is worth monitoring, most especially in moist unsaturated slopes with shallow slip plane, and its addition will certainly bring about some improvement in models of PWP in unsaturated soils. This is especially important where a certain rainfall threshold is used as the trigger for a hill slope failure.

REFERENCES

[1] H. Rahardjo, E. C. Leong, and R. B. Rezaur, "Effect of antecedent rainfall on pore-water pressure distribution characteristics in residual soil slopes under tropical rainfall," *Hydrol. Process.*, vol. 22, no. 4, pp. 506–523, Feb. 2008, doi: 10.1002/hyp.6880.

[2] M. L. Lee, K. Y. Ng, Y. F. Huang, and W. C. Li, "Rainfall-induced landslides in Hulu Kelang area, Malaysia," *Nat. Hazards*, vol. 70, pp. 353–375, 2014, doi: 10.1007/s11069-013-0814-8.

[3] M. R. Mustafa, R. B. Rezaur, H. Rahardjo, and M. H. Isa, "Prediction of pore-water pressure using radial basis function neural network," *Eng. Geol.*, vol. 135–136, pp. 40–47, May 2012.

[4] M. R. Mustafa, R. B. Rezaur, S. Saiedi, H. Rahardjo, and M. H. Isa, "Evaluation of MLP-ANN training algorithms for modeling soil pore-water pressure responses to rainfall," *J. Hydrol. Eng.*, vol. 18, no. 1, pp. 50–57, 2013.

[5] M. R. Mustafa, R. B. Rezaur, H. Rahardjo, M. H. Isa, and A. Arif, "Artificial neural network modeling for spatial and temporal variations of pore-water pressure responses to rainfall," *Adv. Meteorol.*, vol. 2015, pp. 1–39, 2015, doi: 10.1155/2015/273730.

[6] N. M. Babangida, M. R. U. Mustafa, K. W. Yusuf, and M. H. Isa, "Prediction of pore-water pressure response to rainfall using support vector regression," *Hydrogeol. J.*, vol. 24, no. 7, pp. 1821–1833, 2016, doi: 10.1007/s10040-016-1429-4.

[7] K. W. Yusof, N. M. Babangida, M. R. U. Mustafa, and M. H. Isa, "Linear kernel support vector machines for modeling pore-water pressure responses," *J. Eng. Sci. Technol.*, vol. 12, no. 8, pp. 2202–2212, 2017.

[8] T. L. T. Zhan and C. W. W. Ng, "Analytical analysis of rainfall infiltration mechanism in unsaturated soils," *Int. J. Geomech.*, vol. 4,

no. 4, pp. 273–284, 2004, doi: 10.1061/(ASCE)1532-3641(2004)4:4(273).

[9] A. Rahimi, H. Rahardjo, and E.-C. Leong, "Effect of antecedent rainfall patterns on rainfall-induced slope failure," *J. Geotech. Geoenvironmental Eng.*, vol. 137, no. 5, pp. 483–491, May 2011, doi: 10.1061/(ASCE)GT.1943-5606.0000451.

[10] H. Rahardjo, T. T. Lee, E. C. Leong, and R. B. Rezaur, "Response of a residual soil slope to rainfall," *Can. Geotech. J.*, vol. 42, pp. 340–351, 2005, doi: 10.1139/T04-101.

[11] H. Rahardjo, X. W. Li, D. G. Toll, and E. C. Leong, "The effect of antecedent rainfall on slope stability," *Geotech. Geol. Eng.*, vol. 19, pp. 371–399, 2001, doi: 10.1023/A:1013129725263.

[12] A. B. Huang, J. T. Lee, Y. T. Ho, Y. F. Chiu, and S. Y. Cheng, "Stability monitoring of rainfall-induced deep landslides through pore pressure profile measurements," *Soils Found.*, vol. 52, no. 4, pp. 737–747, 2012, doi: 10.1016/j.sandf.2012.07.013.

[13] H. Rahardjo, A. S. Nio, F. R. Harnas, and E. C. Leong, "Comprehensive Instrumentation for Real Time Monitoring of Flux Boundary Conditions in Slope," *Procedia Earth Planet. Sci.*, vol. 9, pp. 23–43, 2014, doi: 10.1016/j.proeps.2014.06.015.

[14] K. Sako, R. Fukagawa, and T. Satomi, "Slope monitoring system at a slope behind an important cultural asset," *J. Disaster Res.*, vol. 6, no. 1, pp. 70–79, 2011.

[15] I. Tsaparas, H. Rahardjo, D. G. Toll, and E.-C. Leong, "Infiltration characteristics of two instrumented residual soil slopes," *Can. Geotech. J.*, vol. 40, no. 5, pp. 1012–1032, Oct. 2003, doi: 10.1139/t03-049.

[16] M. W. Bo, M. Fabius, and K. Fabius, "IMPACT OF GLOBAL WARMING ON STABILITY OF NATURAL SLOPES," 2008.

[17] A. Uchaipichat, "Temperature and Suction Effects on Slope Stability under Undrained Condition," *Appl. Mech. Mater.*, vol. 858, pp. 98–103, 2017, doi: 10.4028/www.scientific.net/AMM.858.98.

[18] S. K. Thota, T. D. Cao, F. Vahedifard, and E. Ghazanfari, "Geo-Congress 2019 GSP 310 214," in *8th International Conference on Case Histories in Geotechnical Engineering*, 2019, pp. 214–226.

[19] R. Fuentes, N. Pinyol, and E. Alonso, "Geomechanics for Energy and the Environment Effect of temperature induced excess porewater pressures on the shaft bearing capacity of geothermal piles," *Geomech. Energy Environ.*, vol. 8, pp. 30–37, 2016, doi: 10.1016/j.gete.2016.10.003.

[20] A. Uchaipichat, "Simulation of Thermal Effect on Undrained Shear Strength of Saturated Porous Media.," *Eur. J. Sci. Res.*, vol. 113, no. 1, pp. 106–111, 2013.

[21] F. Vahedifard, T. D. Cao, S. K. Thota, and E. Ghazanfari, "Nonisothermal Models for Soil Water Retention Curve," *J. Geotech. Geoenviron. Eng.*, vol. 144, no. 9, 2018.

[22] S. Salager, M. El Youssoufi, and C. Saix, "Influence of temperature on the water retention curve of soils. Modelling and experiments," in *Experimental Unsaturated Soil Mechanics*, Springer Berlin Heidelberg, 2007, pp. 251–258.

[23] X. B. Tu, a. K. L. Kwong, F. C. Dai, L. G. Tham, and H. Min, "Field monitoring of rainfall infiltration in a loess slope and analysis of failure mechanism of rainfall-induced landslides," *Eng. Geol.*, vol. 105, no. 1–2, pp. 134–150, Apr. 2009, doi: 10.1016/j.enggeo.2008.11.011.

[24] M. B. Parlange, a T. Cahill, D. R. Nielsen, J. W. Hopmans, and O. Wendroth, "Review of heat and water movement in field soils," *Soil Tillage Res.*, vol. 47, pp. 5–10, 1998, doi: 10.1016/S0167-1987(98)00066-X.

[25] I. GEO-SLOPE, *Stability Modeling with SLOPE / W*, 2012th ed., no. July. Calgary, Alberta, Canada: GEO-SLOPE International, Ltd., 2012.

The effect of waste mineral additives and long-term moisture insulation in volcanic ash-based geopolymer concretes

Yavuz YEGİN
General Directorate of Infrastructure Investments, Ministry of Transport And Infrastructure Ankara, Turkey
yeginyavuz@gmail.com

Rıza POLAT
Department of Civil Engineering
Engineering Faculty, Atatürk University Erzurum, Turkey
rizapolat@gmail.com
rizapolat@atauni.edu.tr

Fatma KARAGÖL
Department of Civil Engineering
Engineering Faculty, Atatürk University Erzurum, Turkey
fatma.karagol@atauni.edu.tr

Ramazan DEMİRBOĞA
College of Engineering, Department of Architectural Engineering, Alfaisal University, Riyadh, Saudi Arabia
rdemirboga@yahoo.com

***Abstract*— In this study, the effect of using blast furnace slag and red mud as substitutes for binder in volcanic ash-based geopolymer concretes, activator type and ratio on compressive strength were investigated. For this purpose, volcanic ash based geopolymer concrete mixtures were produced by adding 30% blast furnace slag and red mud separately. While for three groups mixture, only NaOH was used, in other groups, NaOH + NS was used in the ratio of 1/1 and 1/2. In addition, the effect of long-term application of the insulation applied in heat curing in geopolymer concretes after heat curing has been investigated. As a result; the highest compressive strength result was obtained by adding 30% blast furnace slag to volcanic ash. A mixture of 1/1 of NaOH and Na_2SiO_3 activators was determined as the optimum activator mixture. It has been determined that the insulation applied to the samples after the heat curing has no positive effect.**

Keywords*— *geopolymer, volcanic ash, alkaline activator, blast furnace slag, red mud, insulated

[1] INTRODUCTION

The term geopolymer was first introduced and developed in 1979 by Davidovits [1]. Geopolymers are a new class of three-dimensional inorganic polymers obtained by reacting an aluminosilicate material (e.g. metakaolin, volcanic ash, etc.) with an alkaline solution. The basic monomer unit consists of the "sialate" (O-Si-O-Al-O) structure, which is composed of SiO_4 and AlO_4 compounds in tetrahedral structure and alternatively bonded by sharing all oxygen. [2, 3]. Under high alkaline conditions, reactive aluminosilicates dissolve rapidly. SiO_2 and Al_2O_3 are released in alkali hydroxide and alkali silicate solutions and the polymerization takes place. These ~~liberated~~ released Si and Al are connected with oxygen atoms. In addition, K^+ or Na^+ positive ions are settled in the frame gaps and balanced by negative charges. Si and Al ions in the solution combine in different proportions to form polymer structures like "polysylate" according to the Si/Al ratios [4]. The most commonly used natural origin aluminosilicates are metakaolin, volcanic ash and their mixtures with some waste materials such as slag, red mud, rice husk ash, etc. There are many studies for these aluminosilicate materials, ranging from the establishment of basic synthesis conditions to their analysis [5, 6].

Geopolymers attract attention in the field of building materials because of the low CO_2 emulsion in their production and for this reason, they are more environmentally friendly compared to normal Portland cement [7]. Geopolymer is a new binder material that shows the same properties as regular Portland cement. However, the geopolymer binder is a waste material or an unprocessed natural material, it has a different significance than normal Portland cement in terms of its environmental impacts [8].

A lot of research has been done on the materials used in the production of geopolymer binders. Belgian scientist Purdon first discovered the production of geopolymer binders with blast furnace slag in 1940 [9]. Geopolymers with blast furnace slag produced with NaOH and Na_2SiO_3 were used in large-scale structures in the early 1950s. In the design of water channels in the USA in 1953, 97% blast furnace slag, 1.5% NaCl and 1.5% NaOH mixture were used [9]. In 1957, in Ukraine, Victor Glukhovsky developed binders with blast furnace slag as geopolymer concrete [9]. Wang et al [10] obtained the highest compressive strength from geopolymer concretes with blast furnace slag. The durability properties and compressive of geopolymer concrete with 100% blast furnace slag and a silica modulus of 1.1 are much better than other mixtures [11]. Geopolymer concretes (with 50% red mud and 50% blast furnace slag) showed better results in protecting steel bars from corrosion than normal cement mortar [12].

The use of Si and Al-containing raw materials in geopolymer production has an important place. One of the most important of these is red sludge, which is aluminum production residue. Researchers have worked to produce geopolymer concrete by mixing red mud alone or with other materials in specific proportions. Geopolymer binder was produced from red mud using activators such as NaOH and Na_2SiO_3 [13, 14]. In both studies, optimum ratios of red sludge, blast furnace slag and activators were investigated. As a result, it was found that blast furnace slag has a positive effect as a substitute material.

The types of activators used in the production of geopolymer and their rate greatly affect the geopolymer formation [15-20]. Researchers have done many studies to find the optimum molarity and examined the effects of the activators they determined according to the raw material

they are used. The ratio of Na_2SiO_3 to NaOH and optimum molarity varies according to the oxide composition of the binding solids [20].

Another important stage of geopolymer production is the heat curing stage in the oven. At this stage, when the geopolymer samples, inside sealed plastic bags that are not affected by the temperature and are used to prevent the evaporation of the water inside, are placed in the heat curing oven [15]. After the geopolymer samples are placed in the molds, their surfaces are covered with a vacuum bag film and placed in the oven [21]. In Aygörmez ([22]); It was aimed to see the effect of sealed plastic bags curing by making the temperature curing of the produced geopolymer samples both with and without sealed plastic bags. He found that the sealed plastic bag curing had a positive effect on the compressive strength compared to the no-bag cure. Although there are many studies on the insulation of the heat curing, no studies have been found on the insulated waiting of the samples kept in the laboratory after heat curing.

[2] EXPERIMENTAL

In the study, volcanic ash used as the main aluminosilicate source in geopolymer production was obtained from Isparta Gölcük region. As a substitute material, blast furnace slag obtained from Karçimsa Cement Industry and Trade Corporation and red mud obtained from Konya Seydişehir Eti Aluminum Corporation were used materials. Volcanic ash, supplied from nature in raw form, was ground in a ball mill for 3 hours to reduce its grain size. Particle size and distribution are given in Figure 1.

Table 1. The binders' chemical properties

Chemical analysis (%)	SiO_2	Al_2O_3	K_2O	Na_2O	CaO	Fe_2O_3	MgO	TiO_2
Volcanic Ash	59.00	16.50	5.30	4.80	4.10	3.80	2.10	-
Blast Furnace Slag	37.40	10.38	0.67	0.39	30.93	1.30	7.21	-
Red Mud	13.57	21.80	-	6.47	13.55	27.39	-	3.12

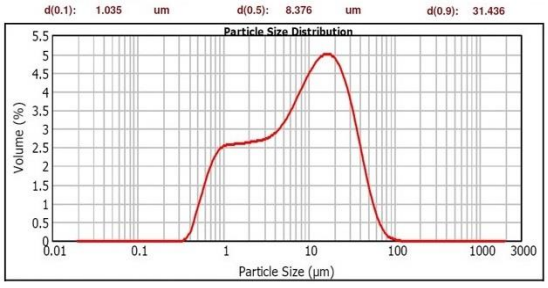


Fig. 1. The volcanic ash's size distribution

As aggregate; washed stream aggregates in two different grain classes as 0-4 mm and 4-8 mm were used. The sieve analysis results of the aggregates used in the mixture were determined to remain within the boundary granulometry values given in TS 802 (Table 2).

Table 2. The sieve analysis of aggregate

Grain Size (mm)	0.063	0.125	0.25	0.5	1	2	4	8	11.2
Passing (%)	4	7	12	25	47	68	81	97	100

NaOH, in the form of solid beads of 99% purity used as the activator, was obtained from Merck. Na_2SiO_3 has been supplied in liquid form as 2 modules. The chemical compositions of the activators are given in Table 3.

Table 3. Sodium hydroxide's and sodium silicate's chemical properties (%)

Physical and chemical properties	Sodium hydroxide	Sodium silicate (2 Modules)
Molecular formula	NaOH	Na_2SiO_3
Molecular mass (g/mol)	40.00	122.06
Color	White	Colorless Liquid
pH	13–14	11-12.5
Density (gr/cm^3)	2.13	1.37-1.41
Na_2 O content (%)	-	11.0-12.5
SiO_2 content (%)	-	21.5 -24.5
H_2O content (%)	-	67.5- 63.0

As a result of preliminary experiments [23], the molarity of NaOH was chosen as 14 M and the module of Na_2SiO_3 as 2 modules in the produced mixtures. Samples were produced by preparing 3 different alkali solutions to determine the ratio of $NaOH/Na_2SiO_3$. Prepared solution types are given in Table 4. Alkali activators were prepared 24 hours before the production of geopolymer concrete and the NaOH (14M) solution was allowed to cool for a while. Furthermore, in cases where Na2SiO3 was required, the activators were mixed in the specified proportions and were kept in airtight containers until the sample production time.

Table 4. Alkaline Solution Types

Solution Type	Activator	$NaOH/Na_2SiO_3$
Type 1	NaOH	-
Type 2	$NaOH/Na_2SiO_3$	1/1
Type 3	$NaOH/Na_2SiO_3$	1/2

In order to adjust the flowability in the concrete, polycarboxylic ether-based, second generation superplasticizer additive (SP), supplied from BASF was used. When the researchers [20, 22, 24-30] examined optimum geopolymer mixture calculations and chemical content of the binders used volcanic ash, they found that it would be appropriate to add blast furnace slag and red mud up to 30% of the total binder. In the study, the geopolymer concrete mixture with 500 dosage binder and 0.50 solution/binder ratio was produced (Table 5). Additional water and SP were used in all mixtures of 10% and 1.5% of the total binder, respectively.

In cases where additives such as blast furnace slag will be added into the binder, the binders in solid form are mixed together and mixed for 5 minutes to form a homogeneous mixture. Aggregates were added to the prepared binder and mixed for 3 minutes to form aggregate and binder dry mixture. In the mixture, SP was mixed with the solution by adding 2/3 of the SP into the solution. 2/3 of the solution with SP was slowly poured into the dry mixture and mixed for 1 minute at the lowest speed, the remaining solution was added and mixed for 2 more minutes. By adding 1/3 of the SP into the additional water, the speed of the mixer was brought to a medium level, and the additional water with SP was added to it and mixed at medium speed for 2 minutes. After all components of the mixture were added, the mixture was mixed for 2 minutes at the highest speed.

Table 5. The mixture proportions in (kg) for 1 m^3

Code	Volcanic Ash	Blast Furnace Slag	Red Mud	Na_2SiO_3 (2 modules liquid)	NaOH Solution (14 M)	Aggregate (mm)		Additional Water 10%	Super Plasticizer 1.5%	TOTAL
						0-4	4-8			
VA	500	-	-	-	250.00	927.95	457.05	50	7.5	2192.50
VA1				125.00	125.00	938.00	462.00			2207.50
VA2				166.67	83.33	941.35	463.65			2212.50
BFS	350	150	-	-	250.00	944.70	465.30			2217.50
BFS1				125.00	125.00	956.76	471.24			2235.50
BFS2				166.67	83.33	959.44	472.56			2239.50
RM	350	-	150	-	250.00	944.70	465.30			2217.50
RM1				125.00	125.00	956.76	471.24			2235.50
RM2				166.67	83.33	959.44	472.56			2239.50

In order to prevent geopolymer concretes from sticking to the steel molds, high-temperature resistant grease, will resist the oven curing temperature and not be separated from the mold at high temperatures, was used.

While the geopolymer samples are placed in the oven, sealed plastic bags that will not be affected by the temperature are used in order to prevent the evaporation of the water inside [15].

All geopolymer concretes produced were insulated for 48 hours at 90ºC temperature cure. The samples that completed their curing were left to cool down slowly until they reached the laboratory temperature after 48 hours in order not to experience thermal shocks, and when they reached the laboratory temperature, they were kept with insulation and uninsulated until the experiment day.

To identify the effect of the activator ratio and mineral additives, the samples were kept to the sealed bag curing for 3, 28 and 56 days and their compressive strengths were determined. Besides, to examine the effect of long-term sealed bag curing on compressive strength, a group sample was taken out of the sealed bag after 28 days and kept in the laboratory conditions until the experiment day.

[3] RESULTS AND DISCUSSION

A. *Only volcanic ash based geopolymer concretes*

The compressive strength results of the geopolymer concrete mixtures using only volcanic ash as the aluminosilicate source are given in Table 6 and Figure 2.

When the results given in Figure 2 are examined, it is seen that the compressive strength of geopolymer concretes produced with activator with a $NaOH/Na_2SiO_3$ ratio of 1/2 is approximately 50% less. Compressive strengths of samples with activator ratio of 1/1 are almost the same with geopolymer samples contain only NaOH [31],.

To be able to activate volcanic ash, the SiO_2/Al_2O_3 molar ratio of the amorphous phase must be not less than 4 [32]. When the compressive strength results are examined, it is seen that the SiO_2 ratio of the mixture approaches the optimum ratio with an activator ratio of 1/1. Depending on the initial silica module of the NaOH powder, the mechanical properties of the geopolymer mortar increase or decrease [33]. When the $NaOH/Na_2SiO_3$ ratio was 1/2, the compressive strength decreased by approximately 50%. Compressive strengths of samples produced without adding Na_2SiO_3 and at the rate of 1/1 were almost the same.

Table 6. Compressive strength results of only volcanic ash based samples

Code	3 Days (insulated)	28 Days (insulated)	56 Days (insulated)
VA	22.36	19.65	28.31
VA1	22.99	20.61	28.62
VA2	10.71	10.67	17.60

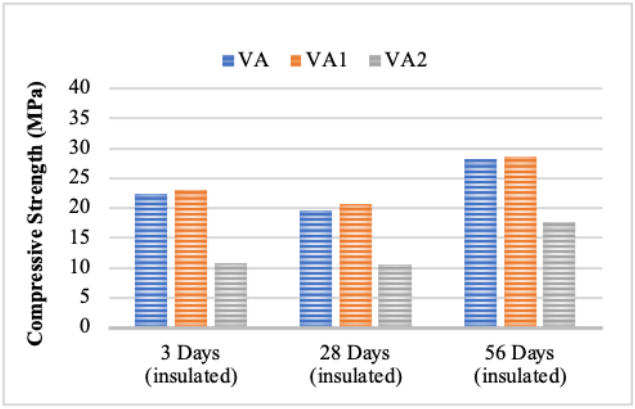


Fig. 2. Compressive strength results of only volcanic ash based samples

B. *Geopolymer concretes with blast furnace slag additives*

The compressive strength results of the geopolymer concrete with the volcanic ash-based binder containing 30% blast furnace slag, produced by using the solution obtained by mixing 14 M NaOH solution and 2 modules Na_2SiO_3 (NaOH / Na_2SiO3 ratio 1/1 and 1/2), are given in Table 7 and Figure3.

Compressive strength results of the samples with 1/1 activator ratio remained almost unchanged depending on the time and the highest compressive strength result was obtained on the 56th day. It has been determined that geopolymer samples produced with blast furnace slag additive are more stable compared to other mixtures.

Table 7. Compressive strength results of samples with blast furnace slag additives

Code	3 Days (insulated)	28 Days (insulated)	56 Days (insulated)
BFS	17.18	26.07	21.64
BFS1	26.89	27.66	28.44
BFS2	23.44	26.60	28.52

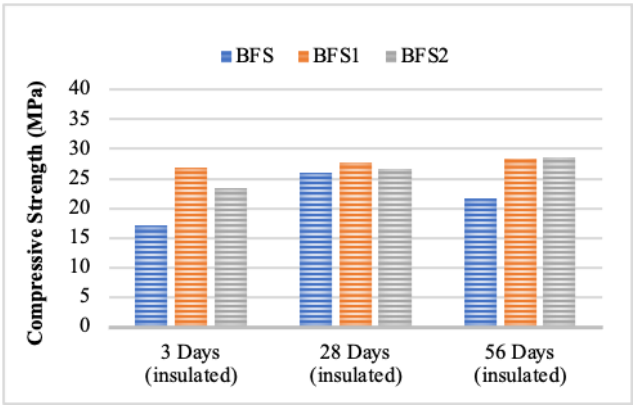


Fig. 3. Compressive strength results of samples with blast furnace slag additives

The use of 1/1 of Na_2SiO_3 is more stable in compressive strength than the one used at 1/2. Samples with blast furnace slag have higher compressive strength than samples without additives.

As the slag percentage increases in geopolymer mortars, their compressive strength also increases [34, 35]. In the studies conducted by researchers such as Lemougna et. al. [31] and Robayo-Salazar et. al. [35], the positive effect of the addition of blast furnace slag was observed, as in this study. The compressive strengths of samples produced with the activator ratio of 1/1 are approximately 10% more than other samples.

C. Geopolymer concretes with red mud additives

The compressive strengths of the geopolymer concrete mixtures with volcanic ash-based binder containing 30% red mud, produced by using the solution obtained by mixing 14 M NaOH solution and 2 modules Na_2SiO_3 (NaOH / Na_2SiO_3 ratio 1/1 and 1/2), are given in Table 7 and Figure 4.

Table 8. Compressive strength results of samples with red mud slag additives

Code	3 Days (insulated)	28 Days (insulated)	56 Days (insulated)
RM	26.00	23.81	31.86
RM1	19.95	18.01	21.54
RM2	17.25	16.04	18.32

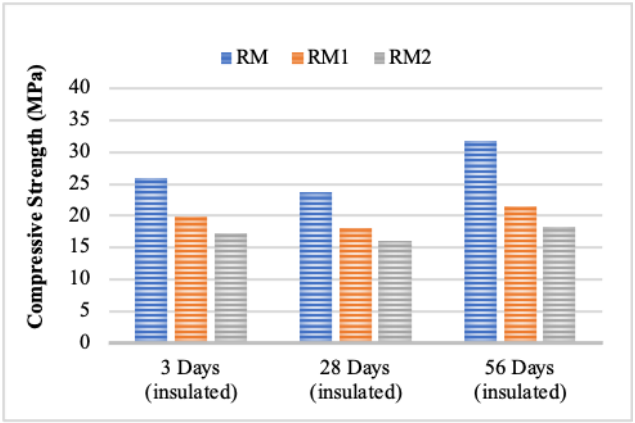


Fig. 4. Compressive strength results of samples with red mud slag additives

It has been determined that the compressive strength results of geopolymer mixtures that contain only NaOH are higher than the other two mixtures. Furthermore, in the samples containing NaOH/Na_2SiO_3, a higher compressive strength result was obtained at the ratio of 1/1 than the ratio of 1/2. When the 56-day compressive strength results are examined, the highest compressive strength result was obtained from the sample produced without additives, with a compressive strength of 31 MPa.

It is established that an increase in the SiO_2/Na_2O ratio was beneficial for the strength development of geopolymers with red mud. However, this rate of increase was limited to 1.3 at most.[14]. The mixing ratio in the study is also at a rate close to this rate. The optimum red sludge ratio was determined as 30% in red mud geopolymer concretes [36]. This also showed parallelism with the literature on the activator and red mud ratio used in the study.

The water content in the geopolymer mixtures is very important for obtaining the desired compressive strength[37]. The decrease in compressive strength may be due to the excessive use of alkaline activators. Because using excessive alkali activator causes to high alkali concentration in the pore solution. Moreover, the high alkali content may cause efflorescence in the internal structure of the geopolymer and released Na+ ions have a poor binding ability with the network structure [38-41]

D. Comparison of insulated and uninsulated samples

The compressive strengths of insulated samples for 56 days and the compressive strengths of samples cured for 28 days with sealed bags and 28 days without bags are given in Table 9 and Figure 5. In all samples except VA and VA1 samples, the compressive strength values of the samples kept uninsulated were higher than the other samples. This shows that the mineral additive makes the geopolymer samples more stable. In addition, it has been determined that the optimum ratio in the mixture calculation is very important in the production of geopolymer.

In the BFS sample, the compressive strength value of the sample kept in the laboratory without insulation was found to be approximately 78% higher. In the VA1 sample, the compressive strength value of the insulated sample was found to be 24% lower than the uninsulated sample.

In the samples with mineral additives, the sealed plastic bag curing had a positive effect in the oven. However, later in the laboratory environment, it has been observed that the sealed plastic bag curing has not a positive effect on the compressive strengths of samples with mineral additives. [15, 22, 42] In their study, they state that the sealed plastic bag during oven curing is very important in geopolymer production.

Since 2% to 9% lower compressive strength was obtained in the insulated mixtures containing red mud during the 56-day compared to the uninsulated, it has been observed that long-term sealed plastic bags will have a negative effect.

Arslan et. al. [43]performed a cure method in the oven with a fireproof bag to prevent evaporation. However, they did not investigate its long-term effect.

Table 9. Compressive strength results of insulated and uninsulated samples

Code	56 Days (insulated)	56 Days (uninsulated)
VA	28.31	26.47
VA1	28.62	21.81
VA2	17.60	21.32
BFS	21.64	38.57
BFS1	28.44	28.49
BFS2	28.52	29.32
RM	31.86	33.02
RM1	21.54	22.01
RM2	18.32	19.73

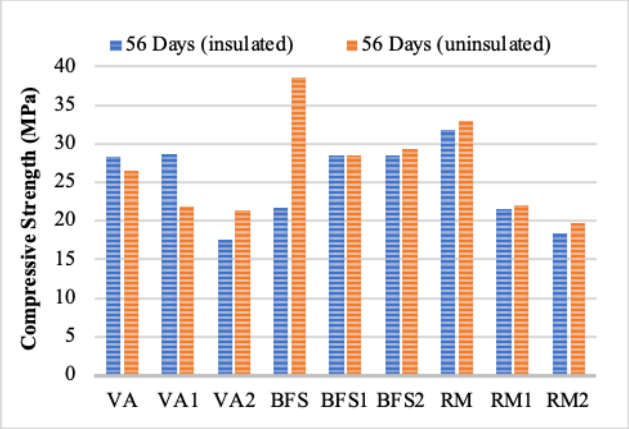


Fig. 5. Compressive strength results of insulated and uninsulated samples

[4] CONCLUSIONS

- Adding mineral additives to volcanic ash provides a positive effect.
- The positive effect of using red sludge as a substitute material was obtained only for RM mixture.
- Adding 30% of blast furnace slag to the volcanic ash used as an aluminosilicate source gave the highest result in terms of compressive strength.
- The use of NaOH and Na_2SiO_3 in the ratio of 1/1 as activator has been determined as the optimum ratio in all mixture types.
- Generally, long-term insulation did not have a positive effect on the compressive strength of the samples.

ACKNOWLEDGMENT

This work was supported by Atatürk University BAP Coordination Unit within the scope of the project numbered FBA-2019-7448.

REFERENCES

[1] J. Davidovits, "Synthesis of new high temperature geo-polymers for reinforced plastics/composites," SPE PACTEC 79 Society of Plastic Engineers, vol. 151-4, 1979.

[2] J. Davidovits, "Geopolymers - Inorganic Polymeric New Materials," (in English), J Therm Anal, vol. 37, no. 8, pp. 1633-1656, Aug 1991, doi: Doi 10.1007/Bf01912193.

[3] J. Davidovits, "Properties of Geopolymer Cements, Published in Proceedings. ," presented at the First İnternational Conference on Alkaline Cements and Concretes, Scientific Research Institute on Binders and Materials, Kiev State Technical University, Kiev, Ukranie, 131-149., 1994.

[4] K. A. Komnitsas, "Potential of geopolymer technology towards green buildings and sustainable cities," (in English), Procedia Engineer, vol. 21, pp. 1023-1032, 2011, doi: 10.1016/j.proeng.2011.11.2108.

[5] J. Baenla, J. B. B. Mbah, I. B. D. Li Ndjock, and A. Elimbi, "Partial replacement of low reactive volcanic ash by cassava peel ash in the synthesis of volcanic ash based geopolymer," (in English), Constr Build Mater, vol. 227, Dec 10 2019, doi: ARTN 116689

[6] M. F. Zawrah, S. E. A. Sawan, R. M. Khattab, and A. A. Abdel-Shafi, "Effect of nano sand on the properties of metakaolin-based geopolymer: Study on its low rate sintering," (in English), Constr Build Mater, vol. 246, Jun 20 2020, doi: ARTN 118486

[7] E. Mcnulty, "Geopolymers: An Environmental Alternative to Carbon Dioxide Producing Ordinary Portland Cement," Department of Chemistry, The Catholic University of America, 2009.

[8] M. Kaur, J. Singh, and M. Kaur, "Microstructure and strength development of fly ash-based geopolymer mortar: Role of nano-metakaolin," (in English), Constr Build Mater, vol. 190, pp. 672-679, Nov 30 2018, doi: 10.1016/j.conbuildmat.2018.09.157.

[9] J. Davidovits, Geopolymer Chemistry and applications, 5th edition ed. Saint Quantin, France, 2020.

[10] J. J. Wang, J. H. Xie, C. H. Wang, J. B. Zhao, F. Liu, and C. Fang, "Study on the optimum initial curing condition for fly ash and GGBS based geopolymer recycled aggregate concrete," (in English), Constr Build Mater, vol. 247, Jun 30 2020, doi: ARTN 118540

[11] M. G. Khalil, F. Elgabbas, M. S. El-Feky, and H. El-Shafie, "Performance of geopolymer mortar cured under ambient temperature," (in English), Constr Build Mater, vol. 242, May 10 2020, doi: ARTN 118090

[12] X. Z. Liang and Y. S. Ji, "Experimental study on durability of red mud-blast furnace slag geopolymer mortar," (in English), Constr Build Mater, vol. 267, Jan 18 2021, doi: ARTN 120942

[13] W. Hu, Y. T. Ma, M. Koehler, H. R. Gong, and B. S. Huang, "Mix design optimization and early strength prediction of unary and binary geopolymer from multiple waste streams," (in English), J Hazard Mater, vol. 403, Feb 5 2021, doi: ARTN 123632

[14] J. P. Liu, X. Y. Li, Y. S. Lu, and X. H. Bai, "Effects of Na/Al ratio on mechanical properties and microstructure of red mud-coal metakaolin geopolymer," (in English), Constr Build Mater, vol. 263, Dec 10 2020, doi: ARTN 120653

[15] D. Hardjito, Rangan. B.V., "Development and Properties of Low-Calcium Fly Ash-Based Geopolymer Concrete ", 2005.

[16] J. L. Provis, Deventer, J. S. J., Geopolymers; structure, processing, properties and industrial applications. Wood head publishing limited, Oxford Cambridge, New Delhi., 2009.

[17] O. Zeybek, "Uçucu Kül Esaslı Geopolimer Tuğla Üretimi," Yüksek Lisans Tezi, Mühendislik Fakültesi, Anadolu Üniversitesi, Eskişehir, 2009.

[18] P. W. Ken, M. Ramli, and C. C. Ban, "An overview on the influence of various factors on the properties of geopolymer concrete derived from industrial by-products," (in English), Constr Build Mater, vol. 77, pp. 370-395, Feb 15 2015, doi: 10.1016/j.conbuildmat.2014.12.065.

[19] Saloma, Hanafiah, D. O. Elysandi, and D. G. Meykan, "Effect of Na2SiO3/NaOH on Mechanical Properties and Microstructure of Geopolymer Mortar Using Fly Ash and Rice Husk Ash as Precursor," (in English), Aip Conf Proc, vol. 1903, 2017, doi: Artn 050013

[20] M. S. Reddy, P. Dinakar, and B. H. Rao, "Mix design development of fly ash and ground granulated blast furnace slag based geopolymer concrete," (in English), J Build Eng, vol. 20, pp. 712-722, Nov 2018, doi: 10.1016/j.jobe.2018.09.010.

[21] S. E. a. R. Wallah, B.V. , "Low Calcium Fly Ash Based Geopolymer Concrete: Long Term Properties," Faculty of Engineering, Curtin University of Technology., Research Report GC2, 2006.

[22] Y. Aygörmez, "Kolemanit atığı ve silis dumanı katkılı metakaolin tabanlı geopolimer harcın mekanik ve durabilite

özelliklerinin incelenmesi," Doktora Tezi, Yıldız Teknik Üniversitesi Fen Bilimleri Enstitüsü, İstanbul, 2018.
[23] Y. YEGİN, "Isparta Gölcük Yöresi Volkanik Külünden Üretilen Geopolimer Betonun Özelliklerinin Fabrika Atıkları ve Nano Malzemeler ile İyileştirilmesi," Civil Engineering Doctoral Thesis, Fen Bilimleri Enstitüsü, Atatürk University, Erzurum, 2020.
[24] İ. Türkmen, Karakoç, M. B., Kantarcı, F., Maraş, M. M., Demirboğa, R., "Fire resistance of geopolymer concrete produced from Elazığ ferrochrome slag," FIRE AND MATERIALS, vol. 40, 836–847., 2016.
[25] J. Y. Ye, W. S. Zhang, and D. Shi, "Properties of of an aged geopolymer synthesized from calcined ore-dressing tailing of bauxite and slag," (in English), Cement Concrete Res, vol. 100, pp. 23-31, Oct 2017, doi: 10.1016/j.cemconres.2017.05.017.
[26] C. Çolak, "Mechanical and Durability Propertıes of Alkali Activated Slag Concrete," MS Thesis, Fen Bilimleri Enstitüsü, İstanbul Teknik Üniversitesi İstanbul, 2018.
[27] A. Özcan, "Ferrokrom Cürufu ve Yüksek Fırın Cürufu Kullanılarak Üretilen Geopolimer Betonların Asit, Tuz ve Sülfat Etkilerine Karşı Dayanıklılığının Araştırılması," Yüksek Lisans Tezi Fen Bilimleri Enstitüsü. , İnönü Ünivesitesi, Malatya, 2018.
[28] Z. Q. Sun, X. C. Lin, and A. Vollpracht, "Pervious concrete made of alkali activated slag and geopolymers," (in English), Constr Build Mater, vol. 189, pp. 797-803, Nov 20 2018, doi: 10.1016/j.conbuildmat.2018.09.067.
[29] M. Kurtuluş, "Yüksek fırın cürufunun aktifleştirilmesinde aktivatör tipinin ve aktivatör ekleme zamanının macun dolgu özelliklerine etkisi," Yüksek Lisans Tezi, Fen Bilimleri Enstitüsü, Karadeniz Teknik Üniversitesi Trabzon, 2019.
[30] E. A. Llano-Guerrero, L. Y. Gomez-Zamorano, and E. Jimenez-Relinque, "Effect of the addition of TiO2 nanoparticles in alkali-activated materials," (in English), Constr Build Mater, vol. 245, Jun 10 2020, doi: ARTN 118370
[31] P. N. Lemougna *et al.*, "Thermal stability of one-part metakaolin geopolymer composites containing high volume of spodumene tailings and glass wool," (in English), Cement Concrete Comp, vol. 114, Nov 2020, doi: ARTN 103792
[32] P. N. Lemougna *et al.*, "Review on the use of volcanic ashes for engineering applications," (in English), Resour Conserv Recy, vol. 137, pp. 177-190, Oct 2018, doi: 10.1016/j.resconrec.2018.05.031.
[33] T. Luukkonen *et al.*, "Influence of sodium silicate powder silica modulus for mechanical and chemical properties of dry-mix alkali-activated slag mortar," (in English), Constr Build Mater, vol. 233, Feb 10 2020, doi: ARTN 117354
[34] T. A. Aiken, J. Kwasny, W. Sha, and M. N. Soutsos, "Effect of slag content and activator dosage on the resistance of fly ash geopolymer binders to sulfuric acid attack," (in English), Cement Concrete Res, vol. 111, pp. 23-40, Sep 2018, doi: 10.1016/j.cemconres.2018.06.011.
[35] R. A. Robayo-Salazar, M. de Gutierrez, and F. Puertas, "Study of synergy between a natural volcanic pozzolan and a granulated blast furnace slag in the production of geopolymeric pastes and mortars," (in English), Constr Build Mater, vol. 157, pp. 151-160, Dec 30 2017, doi: 10.1016/j.conbuildmat.2017.09.092.
[36] S. Singh, M. U. Aswath, and R. V. Ranganath, "Performance assessment of bricks and prisms: Red mud based geopolymer composite," (in English), J Build Eng, vol. 32, Nov 2020, doi: ARTN 101462
[37] P. R. Vora and U. V. Dave, "Parametric Studies on Compressive Strength of Geopolymer Concrete," (in English), Chemical, Civil and Mechanical Engineering Tracks of 3rd Nirma University International Conference on Engineering (Nuicone2012), vol. 51, pp. 210-219, 2013, doi: 10.1016/j.proeng.2013.01.030.
[38] F. Skvara, L. Kopecky, V. Smilauer, and Z. Bittnar, "Material and structural characterization of alkali activated low-calcium brown coal fly ash," (in English), J Hazard Mater, vol. 168, no. 2-3, pp. 711-720, Sep 15 2009, doi: 10.1016/j.jhazmat.2009.02.089.
[39] R. M. Hamidi, Z. Man, and K. A. Azizli, "Concentration of NaOH and the Effect on the Properties of Fly Ash Based Geopolymer," (in English), Proceeding of 4th International Conference on Process Engineering and Advanced Materials (Icpeam 2016), vol. 148, pp. 189-193, 2016, doi: 10.1016/j.proeng.2016.06.568.
[40] Z. H. Zhang, J. L. Provis, X. Ma, A. Reid, and H. Wang, "Efflorescence and subflorescence induced microstructural and mechanical evolution in fly ash-based geopolymers," (in English), Cement Concrete Comp, vol. 92, pp. 165-177, Sep 2018, doi: 10.1016/j.cemconcomp.2018.06.010.
[41] A. G. Wang *et al.*, "The Durability of Alkali-Activated Materials in Comparison with Ordinary Portland Cements and Concretes: A Review," (in English), Engineering-Prc, vol. 6, no. 6, pp. 695-706, Jun 2020, doi: 10.1016/j.eng.2019.08.019.
[42] M. M. Yadollahi, A. Benli, and R. Demirboga, "The effects of silica modulus and aging on compressive strength of pumice-based geopolymer composites," (in English), Constr Build Mater, vol. 94, pp. 767-774, Sep 30 2015, doi: 10.1016/j.conbuildmat.2015.07.052.
[43] A. A. Arslan *et al.*, "Influence of wetting-drying curing system on the performance of fiber reinforced metakaolin-based geopolymer composites," (in English), Constr Build Mater, vol. 225, pp. 909-926, Nov 20 2019, doi: 10.1016/j.conbuildmat.2019.07.235.

Effects of the damping coefficient on interconnected adjacent buildings for different soil conditions

Yavuz Selim HATİPOĞLU
Department of Civil Engineering Bayburt University Bayburt, Turkey
yhatipoglu@bayburt.edu.tr

Oğuz Akın DÜZGÜN
Department of Civil Engineering Atatürk University Erzurum, Turkey
oaduzgun@atauni.edu.tr

***Abstract*— Earthquake, which is a dangerous and inevitable natural disaster, leaves behind many unusable and damaged buildings as well as much loss of life and property. One of the most important and effective ways to get rid of these negative situations is to equip the buildings with structural control systems. Viscous dampers are one of the important and effective parts of the structural control system that increases safety and comfort in buildings. However, the effect of the damping coefficient of viscous damping devices on the structural control system is very important. Also, the effect of different soil properties on the structural behavior is crucial. In this study, the dynamic behavior of the coupled structures by viscous dampers on three different soil types under the earthquake excitation at different damping coefficients is investigated. The damping coefficients are selected as 10^3 N.s/m, 10^4 N.s/m, 10^5 N.s/m, 10^6 N.s/m and 107 N.s/m. The Viscous boundary condition is applied to the ground boundaries so that the earthquake waves do not reflect. Dynamic responses of adjacent buildings in the cases of coupled and uncoupled are compared and examined in terms of displacement and acceleration. When the results are examined, it can be seen that the effective damping coefficient for viscous damping devices should be close to 10^5 N.s/m. Besides, in general, it can be seen that viscous damping devices cause a reduction of up to 40% in displacement and acceleration values.**

Keywords--Structural Control Systems, Adjacent Structures, Viscous Dampers, Soil Structure Interaction

[1] INTRODUCTION

Due to the rapidly increasing population and land constraints in our country and in the world, close and multi-story housing is common, especially in megacities. Due to the lack of land, multi-story and close-up buildings are built on ground types with poor bearing capacity. Since we cannot change the formation and intensity of the earthquake, which is natural forgiveness, the buildings to be built must be earthquake resistant. Researchers are developed various structural control systems so that the earthquake energy affects the structural elements of the buildings less and the buildings are much safer. In the early 1970s, the idea of connecting two adjacent buildings is first proposed [1]. Instead of reinforcing a single building in itself, there is the economic advantage of reinforcing two buildings together and the possibility of preventing two adjacent buildings from colliding with each other during seismic effects. This advantage and possibility have led to the detailed investigation of this idea. Viscous damping devices are one of the devices used in the structural control systems of multi-story buildings and proven by researchers [2-14]. Connecting adjacent buildings with viscous dampers led to a reduction of the dynamic response of adjacent buildings by up to 40% [2, 4].

"Fig.1" shows the structural control system realized by the method of connecting two adjacent buildings.



a) Triton Square Office Complex b) KI (Kajima Intelligent)

Fig. 1. Example of Structural Control System applied by connecting buildings .

In the structural control system, the dynamic properties of the buildings, the soil properties underneath of the buildings, the damping coefficient of the damping devices, the number of these devices, and their distribution in the buildings are important. However, if the damping coefficient of viscous damping devices is not chosen appropriately, it may cause disturbances in the behavior of buildings [2]. For this reason, it is very important to select the appropriate device damping coefficient according to the dynamic properties of the buildings and soils to be connected.

It is clear that soil types affect structural behavior. Unfortunately, very few studies of the structural control systems of adjacent buildings take into account the effect of the soil. Studies that take into account the impact of the soil are carried out by [2-4, 15-17].

In this study, the effect of the damping coefficient of viscous damping devices on the structural control system is investigated in terms of the displacement and acceleration of the top floor, taking into account the soil-structure interaction. The damping coefficient of viscous damping devices is considered as 10^3 N.s/m, 10^4 N.s/m, 10^5 N.s/m, 10^6 N.s/m, and 10^7 N.s/m and the effect of connected buildings on the structural control system is investigated.

[2] MODELLING OF THE SYSTEM

All models and analyzes of this study are carried out in two dimensions (2D) using the ANSYS program, which works with the finite elements.

A. Modeling of Adjacent Buildings

Column, beam, floor heights, and material properties of

the buildings that will be connected by a viscous damper are the same. The only difference is that the two buildings that will be connected to each other have different floors. Since the effect of the damping coefficient of viscous dampers on structural control is investigated, other effective factors are kept constant. The floor number of one building is kept constant as 12 floors, while the other is modeled as 15, 18, and 21 floors. For ease of expression, the building, whose number of floors is kept constant as 12, is called Building A, and the other one is called Building B. The buildings are modeled as a two-span frame system. The distance between the two buildings and the floor heights of both buildings is 3 meters. Detailed information about the buildings to be connected is given in Table 1 in detail.

Table 1. Dimensions And Material Properties Of Structural Elements

	Values and Units
Column	500 x 500 mm
Beam	300 x 600 mm
Modulus of Elasticity	30000 MPa
Unit Volume Weight	25 kN/m^3
Poisson's Ratio	0,2

B. Modeling of The Soil System

Three different soil types are identified. While determining the characteristics of the soil types selected in the study, care is taken to ensure that they can represent the characteristics of soft, medium-stiff, and stiff soil types. The soil medium is modeled on the assumption that the soil is a linear elastic and semi-infinite medium. To prevent the reflection of earthquake waves from the soil boundaries and to increase the accuracy of the analysis results, a permeable viscous boundary model is applied to the soil boundaries "Fig.2". While modeling the soil, the element called Plane182 in the element library of the ANSYS program is used. Similarly, Combin14 spring element is used for the permeable viscous boundary condition. The characteristics of the soil types are given in "Table 2" in detail.

Table 2. Properties of Soil Types

	Type I	**Type II**	**Type III**
E (MPa)	35	400	6000
υ	0,25	0,3	0,35
ρ (kN/m3)	17	19	21
Vs (m/s)	90.75	284.56	1028.69
Vp (m/s)	157.18	532.35	2141.39

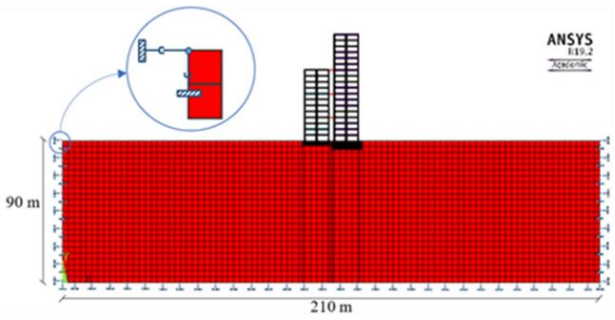


Fig. 2. Soil model in present study.

C. Modeling of Viscous Dampers

The damping coefficient of viscous dampers, the distribution and number of dampers along the height of the building affect the performance of structural control systems. Since the damping coefficient of viscous dampers will be examined in this study, other parameters are kept constant and the stiffness value of viscous dampers is assumed to be zero. When studies on the structural control of viscous dampers are examined, it is not necessary to attach viscous dampers to all floors [2, 4, 18, 19]. It is stated by the researchers that similar performance can be achieved with half the number of dampers connected to all floors. For this reason, in this study, examinations are carried out by placing viscous dampers in two layers. Also, viscous dampers are modeled linearly.

When modeling viscous dampers, Combin14 spring element in the ANSYS program element library is used.

The damping coefficient of viscous damping devices is determined as 10^3 N.s/m, 10^4 N.s/m, 10^5 N.s/m, 10^6 N.s/m and 10^7 N.s/m.

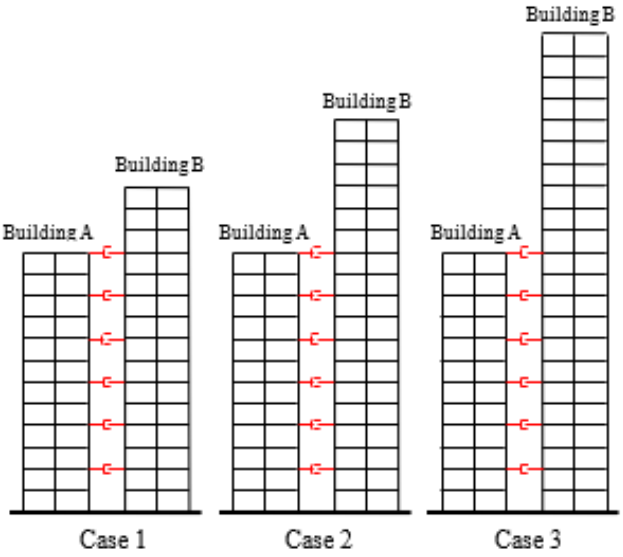


Fig. 3. Distribution of viscous dampers to floors.

D. Earthquake Acceleration Data

In this study, YARIMCA (KOERI330) acceleration data in the north-south direction of the 1999 Kocaeli earthquake was taken from the PEER Strong Motion Database data center, which was arranged to be suitable for use in time-defined structural analysis, is used "Fig. 4". Kocaeli earthquake is a large earthquake with a magnitude of 7.8 Mw and a magnitude of 10 on the Richter scale [20].

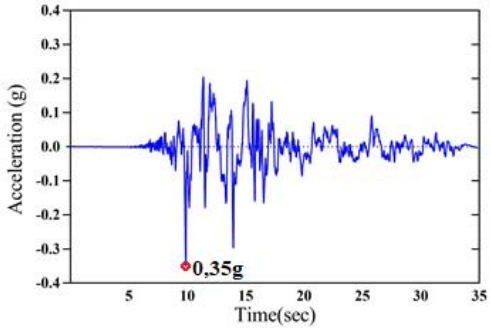


Fig. 4. The north-south direction of the 1999 Kocaeli Earthquake.

[3] RESULTS

Two adjacent buildings on different soil types are interconnected by viscous dampers and the resulting top floor

displacement and acceleration values are examined. The top floor displacement and acceleration values obtained from the analysis results after the buildings are connected to each other are compared with the top floor displacement and acceleration values obtained from the analysis results before the buildings are connected to each other in percentage (%). Negative values indicate decrease; positive values indicate increase compared to the value formed before the buildings are connected to each other.

Below, the graph of the displacement and acceleration values occurring on the top floor of 12-storey A and 15-18-21-storey B buildings coupled by viscous dampers is given according to different soil types and fixed support. In the first part of the graph, the change in the displacement and acceleration values at the top floor of Building A after the 12-storey Building A is connected with the 15-18-21-storey Building B is given. In the second part of the graph, the change in the displacement and acceleration values occurring on the top floor of Building B is given.

Fig. 5 shows the change of the top floor displacement values of Buildings A and B on the fixed support. When the performance of the two buildings is evaluated together, it can be said that the maximum effect in the connection of Building A and 15-21-storey B Buildings is achieved at a damping coefficient of 10^5 N.s/m. In the 18-storey Building B, the maximum performance can be achieved with viscous dampers with a damping coefficient of 10^5 N.s/m and 10^6 N.s/m. In general, it is seen that the top floor displacement values decrease by 30% in Building A and by over 40% in Building B. It seems clear that an increase in the damping coefficient above the optimum value causes a decrease in the effect of viscous dampers on structural control and even in some cases an increase in structural responses.

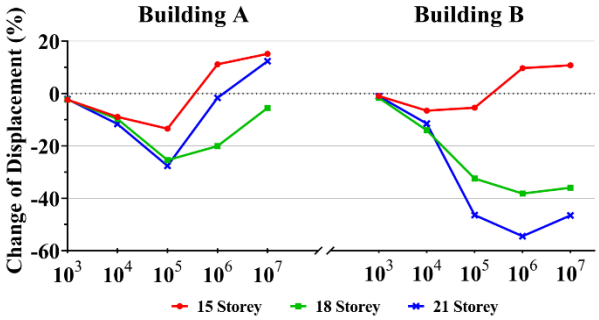


Fig. 5. The change of the displacement of the top floor (Fixed Support).

In Fig. 6, the change of the top floor acceleration values of the A and B Buildings on the fixed support is given. When Fig. 7 is examined, it can be said that there is no need to connect the 12-storey Building A and the 15-storey Building B with viscous dampers. In the connection of Building A with other Building B, it can be said that the maximum performance is obtained by viscous dampers with a damping coefficient of 10^5 N.s/m and 10^6 N.s/m. It is observed that the acceleration values of the top floor decreased by 30% in Building A and 40% in building B.

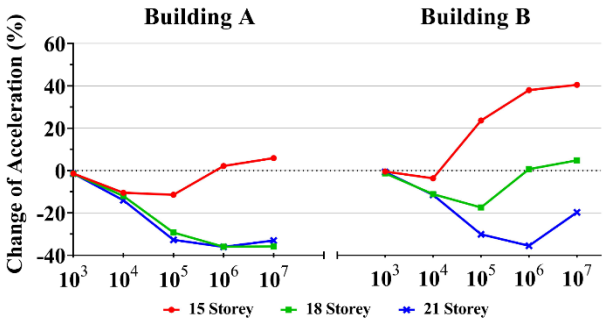


Fig. 6. The change of the acceleration of the top floor (Fixed Support).

Figs. 7-8 show the change in displacement and acceleration values of the top floor of Buildings A and B on Soil Type I. When the figures are examined it can be said that the effective damping coefficient for maximum performance is between 10^5 N.s/m and 10^6 N.s/m values. Especially when the acceleration values of Building B are examined, it is seen that it will be more beneficial to have a damping coefficient of 10^5 N.s/m. When the related graphs are examined, it can be stated that the displacement and acceleration values decreased by 40% or more.

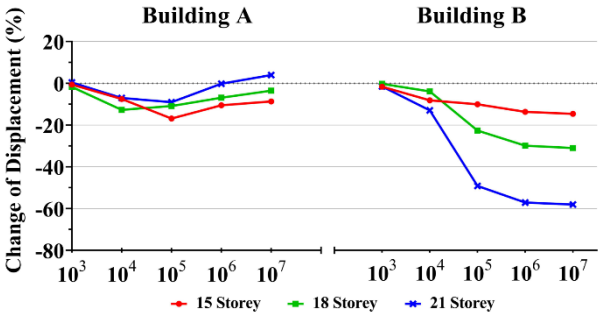


Fig. 7. The change of the displacement of the top floor (Soil Type I).

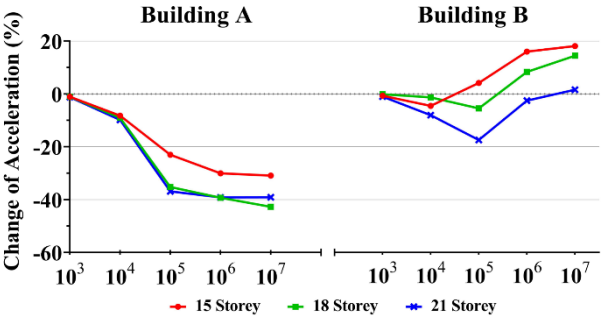


Fig. 8. The change of the acceleration of the top floor (Soil Type I).

Figs. 9-10 show the change in displacement and acceleration values of the top floor of Buildings A and B on Soil Type II. When the figures are examined, it can be said that the viscous damper damping coefficient, which is effective for maximum performance, is 10^5 N.s/m when the change in the displacement and acceleration values occurring at the top floor are evaluated together. When the related graphs are examined, it is seen that the displacement and acceleration values decreased by 40% or more.

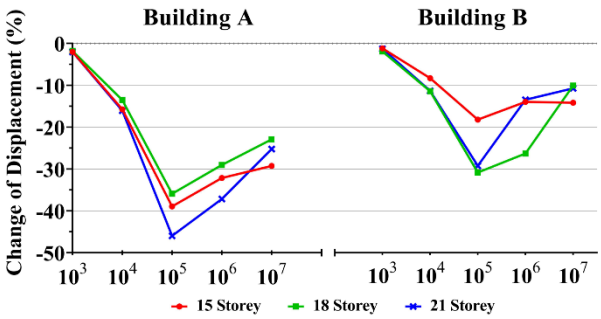


Fig. 9. The change of the displacement of the top floor (Soil Type II).

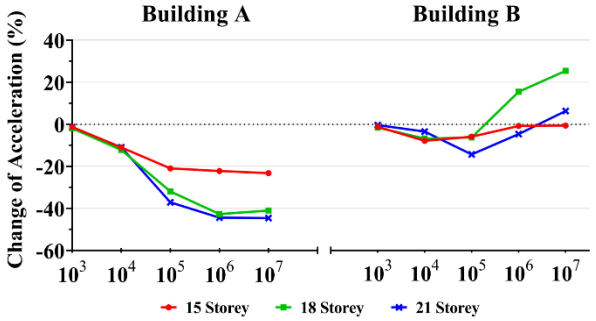


Fig. 10. The change of the acceleration of the top floor (Soil Type II).

Figs. 11-12 show the change in displacement and acceleration values of the top floor of Buildings A and B on Soil Type III. When the figures are examined, it can be said that the effective viscous damper damping coefficient for maximum performance is between 10^5 N.s/m and 10^6 N.s/m values. Especially when the acceleration values of the B Buildings are examined, it is obvious that it will be more beneficial to have the damping coefficient of the damping devices 10^5 N.s/m. When the related graphs are examined, it can be said that the displacement and acceleration values decreased by 40% or more.

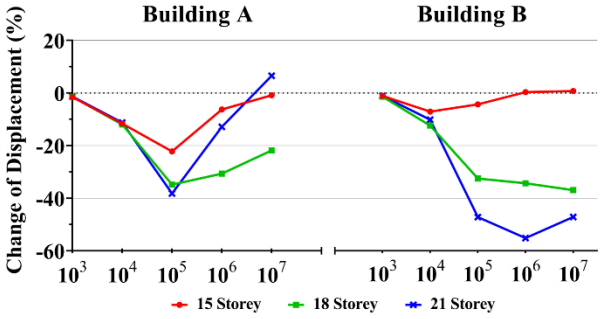


Fig. 11. The change of the displacement of the top floor (Soil Type III).

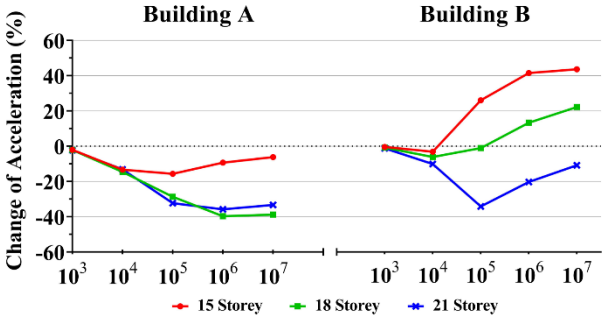


Fig. 12. The change of the acceleration of the top floor (Soil Type III).

It is clear that soils significantly affect the structural response of buildings. To demonstrate this situation more clearly, the change in the displacement values of the 12-storey Building A and the 15-storey Building B on different soils is given on the same graph "Fig. 13". When Figure 13 is examined, it becomes evident that soil-structure interaction must be taken into account in the analysis of structural control systems.

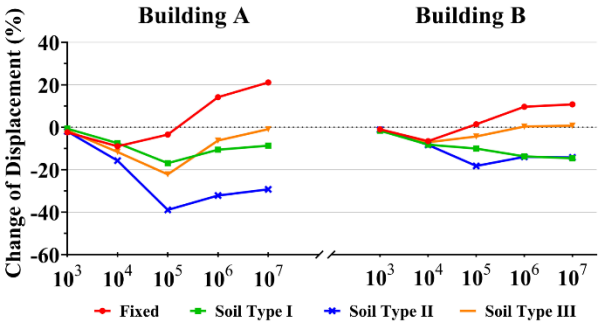


Fig. 13. The change of the acceleration of the top floor (Soil Type II).

[4] CONCLUSIONS

In this study, the effect of the damping coefficient of viscous damping devices on the structural control system is investigated by considering the soil-structure interaction. While examining this effect, the change in the displacement and acceleration values on the top floor of the buildings has been taken into account. Three different soil types are determined, with properties quite different from each other. At the boundaries of the soil system, the viscous boundary condition is applied to prevent the reflection of earthquake waves. 15-18 and 21-storey B Buildings are connected to the 12-storey Building A with viscous dampers. Viscous dampers are connected to the buildings at every two floors and from the same floor level. The damping coefficients of viscous damping devices are determined as 10^3 N.s/m, 10^4 N.s/m, 10^5 N.s/m, 10^6 N.s/m and 10^7 N.s/m. All models and analyzes are made in 2D in the ANSYS program. Acceleration records by the time domain of the Kocaeli Earthquake are used in all analyzes. The results of the study can be summarized as follows.

- In cases where the damping coefficient is 10^3 N.s/m and 10^4 N.s/m, the two buildings act as if they are not connected to each other at all.
- In cases where the damping coefficient is 10^7 N.s/m, the two buildings act as if they are connected by a rigid rod.
- Viscous dampers with a damping coefficient of 10^5 N.s/m or 10^6 N.s/m are highly effective in significantly reducing displacement.
- Viscous dampers with 10^5 N.s/m damping coefficient are very effective in significantly reducing the acceleration.
- Considering the change in displacement and acceleration values together, it can be said that the most effective damping coefficient is 10^5 N.s/m.
- Viscous dampers are very effective in reducing the displacement and acceleration values of two multi-story buildings. Structural responses are likely to be reduced by 40% with a suitable damping coefficient

for the buildings to be connected.

- Considering the soil-structure interaction, the analysis results vary significantly. Therefore, soil-structure interaction should be considered in the analysis of structural control systems.

REFERENCES

[1] R. Klein, K. RE, and S. JJ, "Investigation of a method to stabilize wind induced oscillations in large structures," 1972.

[2] Y. S. Hatipoğlu, "Investigation of the dynamic behavior of adjacent building-soil system interconnected by viscous dampers," PhD Thesis, Institute of Science, Atatürk University, Erzurum, Turkey, 2021.

[3] Y. S. Hatipoğlu and O. A. Düzgün, "Investigation of the effectiveness of viscous dampers connected to adjacent buildings on dynamic behavior under soil-structure interaction effects," Sigma, vol. 11, no. 1, pp. 51-72, 2020.

[4] Y. S. Hatipoğlu and O. A. Düzgün, "Investigation of Dynamic Behavior of Adjacent Tall Buildings Interconnected with Fluid Viscous Dampers Considering Soil-Structure Interaction," Erzincan Üniversitesi Fen Bilimleri Enstitüsü Dergisi, vol. 13, no. 3, pp. 1116-1131, 2020.

[5] C. C. Patel, "Dynamic response of viscous damper connected similar multi-degree of freedom structures," International Journal of Earth Sciences and Engineering, vol. 4, no. 6, pp. 1068-1071, 2011.

[6] R. E. Christenson, B. F. Spencer, and E. A. Johnson, "Experimental verification of semiactive damping of stay cables," (in English), Proceedings of the 2001 American Control Conference, Vols 1-6, pp. 5058-5063, 2001.

[7] M. C. Constantinou and M. Symans, Experimental and analytical investigation of seismic response of structures with supplemental fluid viscous dampers. National Center for earthquake engineering research Buffalo, NY, 1992.

[8] C.-Y. Hou, "Fluid Dynamics and Behavior of Nonlinear Viscous Fluid Dampers," Journal of Structural Engineering, vol. 134, no. 1, pp. 56-63, 2008.

[9] D. Lee and D. P. Taylor, "Viscous damper development and future trends," (in English), Struct Des Tall Buil, vol. 10, no. 5, pp. 311-320, Mar 2001.

[10] L. A. Pérez, S. Avila, and G. Doz, "Seismic response control of adjacent buildings connected by viscous and hybrid dampers," in Dynamics of Civil Structures, Volume 4: Springer, 2014, pp. 433-440.

[11] M. Symans and M. Constantinou, "Passive fluid viscous damping systems for seismic energy dissipation," ISET Journal of Earthquake Technology, vol. 35, no. 4, pp. 185-206, 1998.

[12] M. E. Uz and M. N. S. Hadi, "Dynamic analyses of adjacent buildings connected by fluid viscous dampers," vol. 1, pp. 139-150, 2009.

[13] Y. L. Xu, S. Zhan, J. M. Ko, and W. S. Zhang, "Experimental investigation of adjacent buildings connected by fluid damper," (in English), Earthquake Engineering & Structural Dynamics, vol. 28, no. 6, pp. 609-631, Jun 1999.

[14] X. L. Zhao, L. J. Bao, and B. Xue, "An energy-dissipating approach for adjacent retrofitted structures," (in English), Struct Des Tall Spec, vol. 27, no. 15, p. e1508, Oct 25 2018.

[15] A. A. Farghaly, "Optimization of Viscous Dampers with the Influence of Soil Structure Interaction on Response of Two Adjacent 3-D Buildings under seismic load," Optimization, vol. 4, no. 01, 2014.

[16] C. C. Patel and R. Jangid, "Influence of soil-structure interaction on response of adjacent SDOF structures connected by viscous damper," 2008.

[17] X. Zhao, S. Wang, D. Du, and W. Liu, "Simplified analysis of frame structures with viscoelastic dampers considering the effect of soil-structure interaction," Earthquake Engineering and Engineering Vibration, vol. 16, no. 1, pp. 199-217, 2017.

[18] A. Bhaskararao and R. Jangid, "Seismic response of adjacent buildings connected with dampers," in 13th World Conference on Earthquake Engineering, vol. 3143, 2004.

[19] C. C. Patel and R. S. Jangid, "Seismic response of dynamically similar adjacent structures connected with viscous dampers," The IES Journal Part A: Civil & Structural Engineering, vol. 3, no. 1, pp. 1-13, 2010.

[20] Anonim. "August 17, 1999 Kocaelı Earthquake - Turkey."http://www.koeri.boun.edu.tr/depremmuh/eqspecials/kocaeli/earthquake1.htm" (accessed 2017).

Shear Wall Effectiveness of Reinforced Concrete Structures

Barış ERDİL
Department of Civil Engineering, Van Yuzuncu Yil University Van, Turkey
bariserdil@yyu.edu.tr

Yusuf GÜNDÜZ
Department of Civil Engineering, Van Yuzuncu Yil University Van, Turkey
yusufgunduz.3116@gmail.com

***Abstract*—A trial-and-error procedure are generally followed to determine the shear wall amount required to strengthen reinforced concrete buildings. In order to determine the location and size of the shear walls, their efficiency related to those parameters should be known clearly. For this reason, the aim of this study is to determine the shear wall amount required for strengthening before a structural analysis is made using simple equations. Accordingly, different amount of shear walls with several thicknesses were designed and placed at several locations of artificial plans and their effect on those artificial buildings were examined. After the structural analysis, it is found that if the amount of shear wall is increased keeping the shear wall ratio the same, shear and moment effectiveness of those shear walls reduce. Having reduction in shear wall effectiveness, the amount of lateral forces transferred to the other load carrying members increase which results in damage in those members.**

Keywords— Reinforced concrete, shear wall

[1] INTRODUCTION

Recent earthquakes in Turkey revealed that damages of the reinforced concrete structures could be attributed to the common deficiencies, such as quality and strength of concrete and steel, location and size of the structural system elements, irregularities etc. [1,2]. Those investigations lead to the development, update and/or change in the principles of earthquake resistant design. However, each earthquake reveals that development in the codes is not followed rapidly by the construction industry [3].

Although earthquake damages and their reasons are common, there exist also a beneficial common observation: buildings having shear walls behave well during seismic activities. Shear walls having great in-plane stiffness reduce the interstory drift ratios and carry the huge amount of shear forces and moments. It is necessary to increase the horizontal stiffness of the structure in order to limit the horizontal displacements caused by the horizontal loads acting on the structure as a result of the earthquake. In order to achieve this, load carrying vertical elements must be designed in certain dimensions. In a system that is completely composed of shear walls, the greatest displacement between floors under bending moment occurs in the upper floors, while in the frame system it occurs in the lower floors [4]. When shear wall and frame systems are used together, the bending is carried by frame elements, and shear is taken by shear walls [5].

The amount of shear walls directly affects the horizontal load carrying capacity of the building and the relative floor displacements [6,7,8]. As a result of dynamic analysis, large displacement demands may arise in buildings with low shear wall quantities, causing the distribution of loads between frame elements and shear walls to change and increase the slope of the moment curve. For this reason, it is recommended that the ratio of shear wall be 0.6% for each direction of the building in order to meet the life safety performance level [5]. In another study, it is stated that in low and medium-height buildings where the ratio of shear wall is 1%, the relative floor displacement ratio is below 2%, and the life safety performance level can be met in these buildings [9]. In some studies, the amount of shear wall for each direction of the earthquake is given depending on the total floor area (%0.13) [10] or the floor area of the building (%0.4) [11]. Investigating the damaged buildings after Van Earthquakes it was realized that if the amount of the load carrying vertical elements (per total floor area) is greater than %0.4, it may be possible to meet the life safety performance level [12].

Due to their great stiffness, shear walls significantly affect the center of rigidity of the building. In earthquake codes, it is stated that center of mass and rigidity should be as close to each other as possible in order to prevent torsion during an earthquake. It has been stated that shear walls provide great torsional stiffness provided that they are placed on the exterior grids of the building [13,14].

In the literature, although the minimum amount of shear walls required to ensure life safety performance level in buildings is given, the information related to their size and location is not clear. For example, when one recommends 0.6% shear walls at each direction of the building, the point including the number of shear walls and their minimum sizes to attain the most effective performance is unclear. In this study, a total of 154 models having number of stories varying from 2 to 8, having 2 different wall ratio (0.25% and 0.5%) and 3 different shear wall amounts (one, two or four shear walls) were analyzed and the effectiveness of shear walls was investigated.

[2] MATERIAL AND METHOD

Within the scope of this study, the effect of shear wall amount and position on shear force, moment, fundamental period and displacements was investigated on buildings with bidirectional symmetry with a floor area of 480 m^2. In the first model (M1) which is used as reference, one single shear wall is placed at the center of the building. In the second through fifth models (M2, M3, M4, M5) shear wall was divided into two and placed symmetrically to the other axes. Finally, in the last 6 models (M6, M7, M8, M9, M10, M11), shear wall in M1 is divided into four and again placed symmetrically to the other axes to prevent torsion (Figure 1).

This work has been supported by Van Yuzuncu Yil University Scientific Research Projects Coordination Unit under grant number FYL-2018-7232.

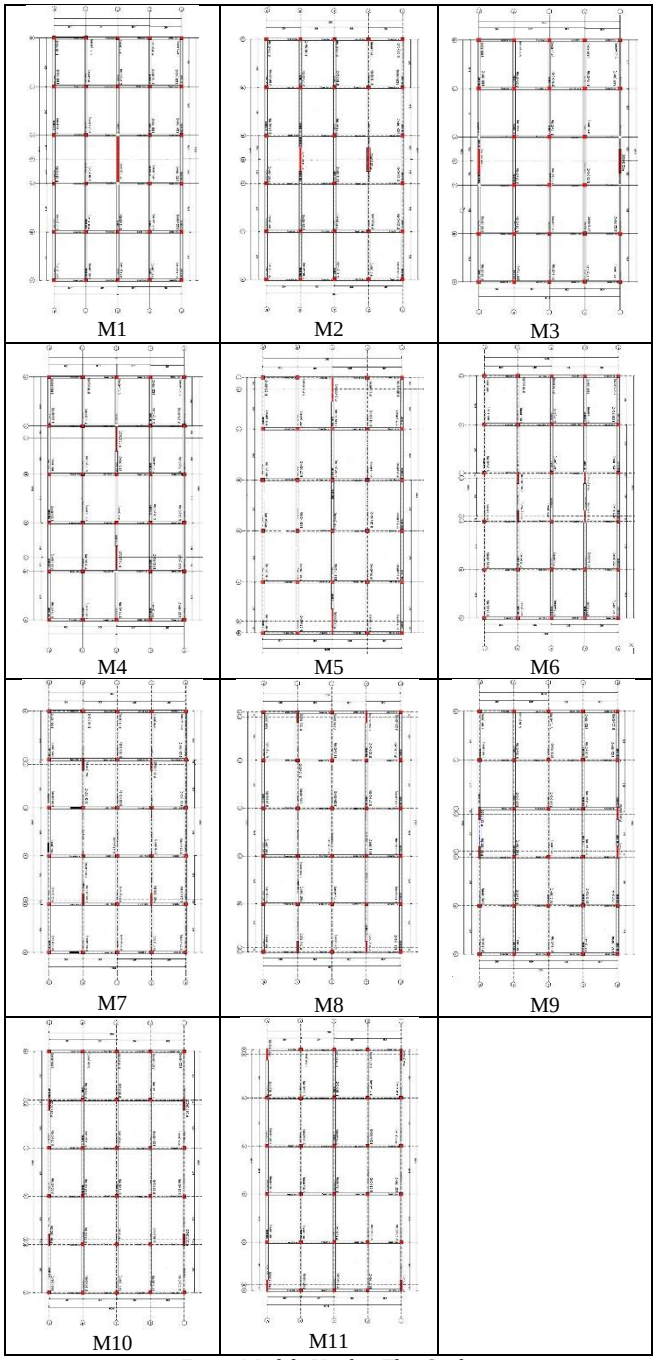


Fig. 1. Models Used in This Study

The story height of was kept constant as 3 m, and columns with 40x40 cm in dimension were placed on the axes other than the shear wall. All beams were 30x60 cm and all slab thicknesses were 15 cm. C25 concrete and S420 reinforcement were assumed. In addition, live load on the slab was taken as Q = 2 kN/m^2 and the infill wall load on the beams were taken as 8 kN/m. Mode superposition method was used for earthquake loading and the number of modes in which the mass could reach 95% was taken into consideration. In order to have fair comparison in the models, soil effect was neglected, and columns and shear walls were assumed to have fixed supports at the base.

In the linear elastic analysis carried by SAP2000v20 [15], it has been tried to understand to what extent the size and amount of the shear wall affects the behavior of the building keeping the shear wall ratio constant. In models where four shear walls were used, as the thickness of the shear wall increased, the ratio of length/thickness (l_w/t_w) became smaller than 6. However, in any case, since the length of these elements is longer than other columns, it contributes more stiffness to the rigidity of the system. Since the column and shear wall are generally separated from each other in terms of design rules rather than structural analysis, in this study, the shear wall expression is used theoretically for the elements with $l_w/t_w<6$. Shear walls were modeled as area elements and 1 m mesh size were applied.

[3] RESULTS AND DISCUSSION

A. *Effect on Overturning Moments*

Figure 2 gives the relationship between the ratio of the total moments at the base of the shear wall (M_{sw}) to the total overturning moment at the base of the building (M_{dev}) and the floor height (N). As can be seen from the figure, if the required shear wall is divided into 2 and 4 in a structure keeping the shear wall ratio the same, less moments will develop at the base of the shear walls. The decrease in the moment can be attributed to the decrease in the shear wall length and thus its stiffness. In a structure, if the shear wall is divided into two equal parts by keeping the shear wall ratio constant, the moment carried by the shear walls will decrease by 20% - 25%, and when it is divided into four equal parts, the decrease will be up to 50% (Figure 1). In addition, it can be seen from the figure that the moments carried by the shear walls decrease depending on the floor height. Shear wall efficiency decreases when overturning moments increase. As a result, it can be said that increasing the number of shear walls by shortening the length of the shear wall keeping the shear wall ratio the same causes a decrease in the overturning moments carried by the shear walls, and as the number of floors increases, shear wall efficiency decreases more. Shear walls were observed to be more effective when they were placed far from the center.

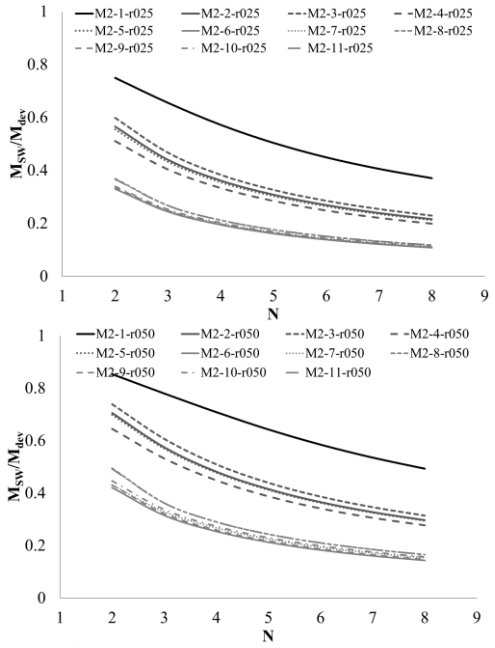


Fig. 2. Change in Moment Ratio by The Number of Stories

B. *Effect on Shear Forces*

Dividing the shear wall into pieces causes a decrease in shear wall efficiency in terms of shear force demand (Figure 3). Although the shear force carried by the the single shear wall (V_{sw}) was 87% of the total base shear force (V_t), keeping

the shear wall ratio constant and increasing the number of shear walls to two reduces the base shear force carried by the shear walls to approximately 80%. When the shear wall is divided into four equal parts in the same way, the base shear force carried by the shear walls changes between 68-78%. As can be seen from the four shear wall models, if the shear walls are placed closer to the center of the building, they are exposed to more base shear force. When shear walls are placed in the corners of the building, their efficiency decreases significantly. In addition to these, as can be seen from Figure 3, with the increase in the number of stories, 3-6% decrease is observed in the V_{sw}/V_t value. As a result, it can be said that when the shear wall ratio is kept constant and the number of shear walls is increased by shortening the length, the base shear force carried by shear walls decreases, and this reduction amount is only slightly affected by the number of floors.

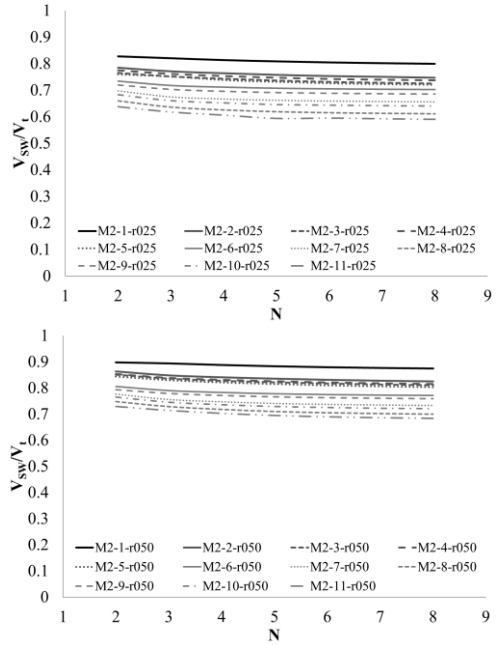


fig. 3. Change ın Shear Wall by The Number of Stories

It is seen from Table 1 that there is a difference in shear wall efficiency of approximately 10% between single-shear wall system and 2-shear wall system, and approximately 30% between single-shear wall system and 4 or more shear wall systems.

Table 1. Shear Force Efficiency

SW Ratio	Single Shear Wall		2 Shear Walls		4 Shear Walls	
(V_{sw}/A_{f_t} %)	V_{sw}/V_t	SW Eff.	V_{sw}/V_t	SW Eff.	V_{sw}/V_t	SW Eff.
0.25	0.82	1	0.74	1.108	0.62	1.32
0.50	0.89	1	0.82	1.085	0.71	1.25

C. *Effect on Fundamental Period*

Since the ratio of the long sides of the shear walls to the short sides is high, these elements are quite rigid compared to the columns. These properties of shear walls make them indispensable for earthquake loads. As it can be seen, using one piece of shear walls with the same ratio will provide a significant stiffness contribution to the structure, thus decreasing the relative story displacements, and this decrease brings along a decrease in the period in that direction of the structure (Figure 4). When the shear wall ratio is kept constant, but its number is increased, there will be a loss of stiffness, so there will be an increase in fundamental periods. As can be seen from Figure 4, the periods of the two and four shear wall models are separated from the single shear wall model and are accumulated at the top. It can also be seen from the figure that the period increases linearly with the increase in number of stories of the structure. Since nonlinear behavior is not taken into account in the structure, it is usual for the period to change with height.

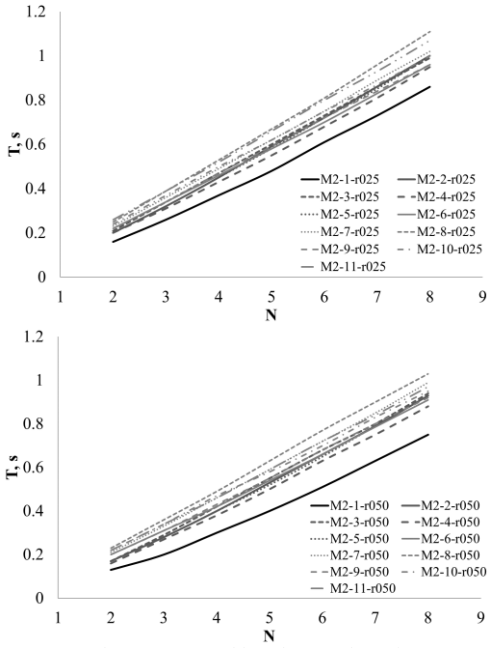
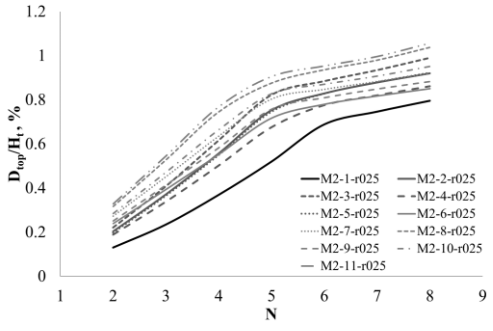


Fig. 4. Change ın Period by The Number of Stories

D. *Effect on Roof Displacement*

As can be seen from Figure 4, roof displacement ($D_{x,top}$) values of the single-shear wall model are lower than the two-shear wall models. When shear wall is divided into four the shear wall efficiency reduces further, and roof displacement increases compared to the other models. As the building height increases, shear wall efficiency decreases and the roof displacement increases, but the peak displacement ratios decrease. For example, while the peak displacement is 0.78 cm in the single shear wall system having two stories, it is 1.97 cm in the four-shear wall model (ratio 2.53). While the roof displacement value is approximately 19.1 cm in the single shear wall system with 8 eight stories, this value is 25.4 cm in the four-shear wall system (ratio 1.33) (Figure 5). It can be said that, when shear wall ratio is kept constant and the number of shear walls is increased, in other words, when a shorter but more shear wall is used, the roof displacements increase as the shear wall stiffness decreases.



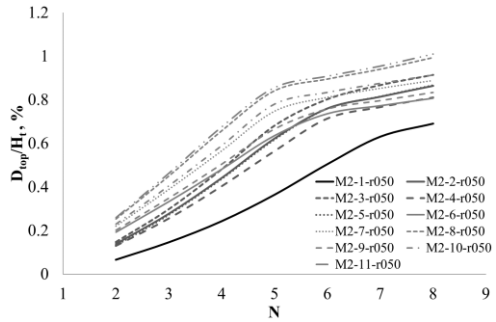


Fig. 5. Change ın Roof Dısplacment by The Number of Storıes

[4] CONCLUSIONS

In this study, shear force, moment, fundamental period, and roof displacements were obtained as a result of the analysis performed on 154 models with two different shear wall ratios and 2-7 stories.

The purpose of using shear walls as a strengthening element lies in their great stiffness. It has been observed that if the shear wall in a structure is placed by dividing it into two or four parts keeping the shear wall ratio constant, there will be a decrease in the total base moment carried by the shear walls. In addition, the moment carried by the shear walls decreased by 20% - 25% by dividing the single shear wall system into two equal parts, and 50% by dividing it into four equal parts.

The shear force carried by the shear walls is also affected by the number of shear walls. Dividing the shear walls into pieces with the same ratio caused a decrease in the shear force efficiency. In the analysis, it was observed that the shear force efficiency of the shear wall decreased by 6-8% by dividing it into two equal parts and by 10% to 22% by dividing it into four equal parts.

As a result of the analysis made on the models with four shear walls, it was found that shear force efficiency increases if the shear walls are placed close to the center of the building, and if they are placed outside the building, they will bear more moment.

Due to their high rigidity, shear walls significantly reduce the lateral displacements. The reduction in displacement leads to decrease in fundamental period. In the analysis, it was seen that the period of single shear wall system is less than that of two and four curtain wall systems. When the shear wall ratio is kept constant and the number of shear walls is increased, roof displacements increase. This increase is attributed to the decrease in stiffness. In addition, doubling the ratio of shear wall brought about a 15% decrease in roof displacement. However, it was observed that the displacement did not change much depending on the shear wall ratio in two and three story buildings.

ACKNOWLEDGMENT

This work has been supported by Van Yuzuncu Yil University Scientific Research Projects Coordination Unit under grant number FYL-2018-7232.

REFERENCES

[1] Sezen H., Whittaker A. S., Elwood K. J., Mosalam K. M. “Performance of reinforced concrete buildings during the August 17, 1999 Kocaeli, Turkey earthquake, and seismic design and construction practise in Turkey”, Engineering Structures, 2003, 25(1), 103-114.

[2] Akansel V., Ameri G., Askan A., Caner A., Erdil B., Kale Ö., Okuyucu D. “The 23 October 2011 Mw=7.0 Van (Eastern Turkey) Earthquake: Interpretations of Recorded Strong Ground Motions and Post-Earthquake Conditions of Nearby Structures”, Earthquake Spectra, 2014, 30(2), 657-682.

[3] Erdil B. “Why RC buildings failed in the 2011 Van, Turkey, Earthquakes: construction versus design practices”, Journal of Performance of Constructed Facilities, 2016, 31(3), 04016110.

[4] Aktan S., Kıraç N. “Betonarme binalarda perdelerin davranışa etkileri”, Eskişehir Osmangazi Üniversitesi Mühendislik Mimarlık Fakültesi Dergisi, 2010, 23(1):15-32.

[5] Kazaz I. “Seismic deformation demands on rectangular structural walls in frame-wall systems”, Earthq. Struct, 2016, 10(2), 329-350.

[6] Wallace J. W. “Seismic design of RC structural walls. Part I: new code format”, Journal of Structural Engineering, 1995, 121(1), 75-87.

[7] Yakut A., Soydaş O. “ Evaluation of shear wall indexes for RC buildings”, In 9th US National and 10th Canadian Conference on Earthquake Engineering, 2010, Paper (No. 371).

[8] Burak B., Comlekoglu H. G. “ Effect of shear wall area to floor area ratio on the seismic behavior of reinforced concrete buildings”, Journal of Structural Engineering, 2013, 139(11), 1928-1937.

[9] Yurdakul O., Tunaboyu O., Avşar O. “Effects of shear wall ratio on the seismic behavior of buildings having inadequate seismic resistance”, 10th US National Conference on Earthquake Engineering (10NCEE) at: Anchorage, Alaska, USA, 2014

[10] Sozen M. “As simple as it gets: The Anatolian formula for earthquake resistant design”, Türkiye İnşaat Mühendisliği 16. Teknik Kongresi, Turkish Chamber of Civil Engineers, Ankara, Turkey, 2001.

[11] Ersoy U. “A simple approach for preliminary design of reinforced concrete structures to be built in seismic regions”, Teknik Dergi Digest, 2013, 24(120), 1701–1715.

[12] Erdil, B. “2011 Van Earthquakes: Design vs Construction”, Disaster Science and Engineering, 2018, 4(1), 1-11.

[13] Öztürk D., Nuhoğlu A., Bozdoğan K. B. “Betonarme yapılarda beton sınıfının taşıyıcı sistem davranışına etkisi”, Deprem Sempozyumu, Kocaeli, Türkiye, 506-511, 23-25 Mart 2005

[14] Uçar T., Merter O. “Planda perde yerleşiminin betonarme perde-çerçeveli binaların deprem davranışına etkisi” Dokuz Eylül Üniversitesi Mühendislik Fakültesi Mühendislik Bilimleri Dergisi, 2009, 11(2): 11-18.

[15] Computers and Structures Inc. (CSI) SAP2000 “Linear and Nonlinear Static and Dynamic Analysis and Design of Three-Dimensional Structures”. Version 14, Berkeley, CA

[16]

Numerical simulation of Organic-Inorganic Lead Halide Perovskite ($CH_3NH_3PbI_3$) solar cells using 1D-SCAPS simulator

Hajar Benali
ERDyS Laboratory, GMEEM & DD Group, Hassan II University of Casablanca, FSTM Mohammedia Morocco
benalihajar6@gmail.com

Bouchaib Hartiti
ERDyS Laboratory, GMEEM & DD Group, Hassan II University of Casablanca, FSTM Mohammedia Morocco
b.hartiti@univh2m.ac.ma

Fatima Lmai
ERDyS Laboratory, Renewable Energies and Condensed Material Group, Hassan II University Faculty of Science AIN CHOCK
Casablanca Morocco
lmai.fatima@gmail.com

Hicham Labrim
National Center for Energy Sciences and Nuclear Technique (CNESTEN) Morocco
hichamlabrim@yahoo.fr

Philippe Thevenin
LMOPS Laboratory, University of Lorraine Metz France
philippe.thevenin@univ-lorraine.fr

***Abstract*—An organic-inorganic perovskite Methylammonium lead iodide ($CH_3NH_3PbI_3$) is a promising photo-absorber material for solar cells due to its direct band gap nature (1.55eV), high absorption coefficient, ambipolar carrier transport property, large diffusion length, enhanced carrier lifetime. Its has gained significant notice in photovoltaic application as a result of their low fabrication cost and high efficiency that stepped from 3.8 % in 2009 to up to 22 % in 2018.In the present paper, a device simulation of $CH_3NH_3PbI_3$ based solar cells is performed by using SCAPS simulator. Perovskite absorber layers $CH_3NH_3PbI_3$ is sandwiched in between the (PEDOT: PSS) as hole transport layer (HTL) and (PCBM) as electron transport layer (ETL) to design the heterojunctions for the simulation. $CH_3NH_3PbI_3$ solar cell was optimized by varying the thicknesses of the $CH_3NH_3PbI_3$ absorber ,the (PEDOT: PSS) as hole transport layer (HTL) and (PCBM) as electron transport layer (ETL) to design the heterojunctions for the simulation. The optimized structure was simulated at different operating temperatures to inspect their impact on device performance.. In each case, Voc, Jsc, FF, and the efficiency were calculated.**

Keywords— hybrid perovskite $CH_3NH_3PbI_3$, solar cells, electron transport layer (ETL), hole transport layer (HTL), scaps.

[1] INTRODUCTION (*Heading 1*)

Recently, methylammonium lead halide perovskite solar cells have received remarkable attention over worldwide [1], following a fast surge of advancement in very short period of time. The excellent absorption coefficient, low exciton-binding energy, tunable optical bandgap, large charge carrier mobility, and low temperature processing method making it hottest photovoltaic technology in all over the world [5] and high power conversion efficiency (PCE) of lead-based perovskite which exceeds 20% [3].]. Perovskite materials, can be Using to fabricate semi-transparent solar cells that can be mounted onto windows, especially for sky scrapers7. These lightweight cells can also be integrated into everyday electronic accessories such as smart watches, backpacks, self-charging cellphones etc. For large panels, the installation would be easier without requiring bulky and expensive mechanical structures[6].However, presence of toxic heavy metal like lead associated over whole lifecycle of perovskite solar cells (PSCs) which can also create environmental damage particularly due to its deterioration over time in humid atmosphere [2]. The simulations are performed by utilizing the solar cell capacitance simulator SCAPS (ver.3.3.02) under AM1.5G illumination. SCAPS is a one-dimensional opto-electrical simulator that is applied to structures of many semiconductor layers. Its working principle is based on solving continuity and Poisson equations. The number of layers can be increased up to seven layers and the simulation can be done under both light and dark conditions. It also allows defect levels in bulk and at interfaces. It can be applied to crystalline solar cells as well as amorphous cells[4]. In the present work, we have performed comparative simulation study for lead-based $CH_3NH_3PbI_3$ absorbing material in PSC to explore the impact of variation in thickness of absorbing layer and operating temperature of device.

[2] SIMULATION PARAMETERS

Table 1. Various parameters used for simulation study [7].

Layer / Propriety	PEDOT/Pss	$CH_3NH_3PbI_3$	PCBM	SnO_2:F
Thickness (µm)	0.080	0.8	0.5	0.5
Band gap (eV)	2.2	1.55	2.100	3.5
Electron affinity(eV)	2.9	3.75	3.9	4.0
Dielectric Permittivity	3.000	6.500	3.900	9.0
CB effective density of states(cm^{-3})	2.200×10^{15}	2.200×10^{15}	2.200×10^{19}	2.200×10^{17}
VB effective density of states(cm^{-3})	1.800×10^{18}	2.200×10^{17}	2.200×10^{19}	2.200×10^{16}
Thermal speed of electrons(cm/S)	1.00×10^{7}	1.00×10^{7}	1.00×10^{7}	1.00×10^{7}
Thermal speed of holes(cm/S)	1.00×10^{7}	1.00×10^{7}	1.00×10^{7}	1.00×10^{7}
Electron mobility(cm^2/ V.S)	0.01	2.0	0.001	2.000×10^{1}
Hole mobility(cm^2/ V.S)	0.0002	2.0	0.002	1.000×10^{1}
Shallow donor densityN_d(cm^{-3})	1.000×10^{13}	1.000×10^{13}	1.000×10^{16}	1.000×10^{16}
Shallow acceptor densityN_a(cm^{-3})	1.000×10^{16}	1.000×10^{16}	1.000×10^{13}	1.000×10^{13}
Defect densityN_t (cm^{-3})	1.000×10^{15}	1.000×10^{15}	1.000×10^{15}	1.000×10^{15}

The basic parameters of ETL, HTL and FTO which are based on some previously published literature of the solar cell under investigation are shown in table I.

[3] RESULTS AND DISCUSSION

Figures 1.a and 1.b show the results of the simulation of I-V characteristics on the cell PEDOT:Pss / $CH_3NH_3PbI_3$ / PCBM/ SnO_2:F under light and in darkness respectively, with:

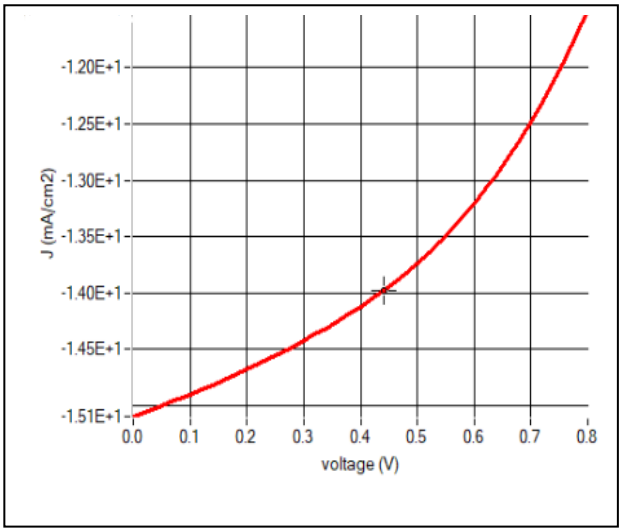


Fig. 1.a. I-V Feature under light

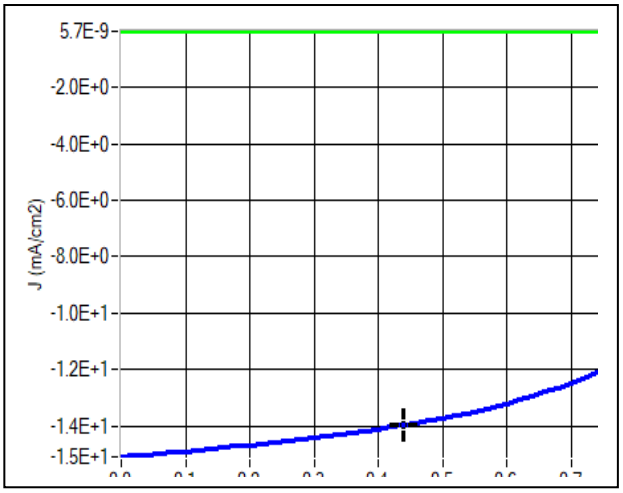


Fig. 1.b. I-V Feature in darkness

Open circuit voltage V_{oc}=1.8273 V, short circuit current J_{sc}= 15.1000 mA/cm^2, form factor FF=33.31 and conversion efficiency η=9.19%.

The quantum efficiency of the cell is given in figure 2 shows a small peak between the 0 -10% values and a decrease due to recombinant losses.

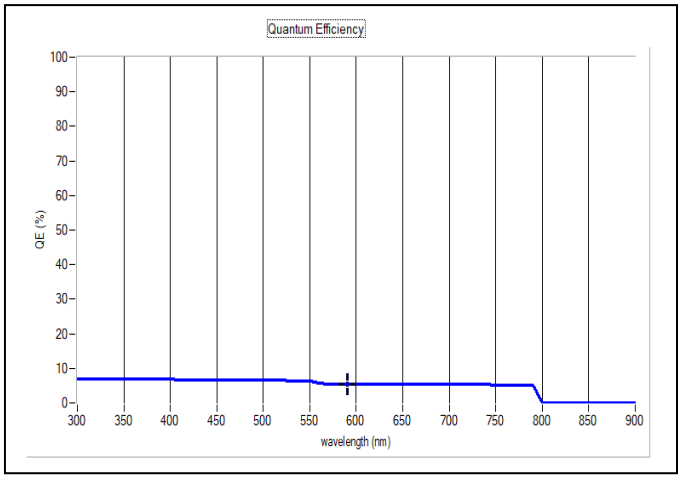


Fig. 2. PEDOT:Pss/ $CH_3NH_3PbI_3$/PCBM/ SnO_2:F Cell EQ Quantum Yield.

A. *Influence of the operating temperature on the cell parameters:*

Temperature plays a very important role in the performance of the solar cell. The value that corresponds to the optimal operation of the cell is T=360 K. the results of the simulation show that the parameter most affected by the temperature variation is the open circuit voltage V_{oc} , its influence on the latter is shown in Figure3.

Table 2. simulation I-V for different temperature values.

T(K)	V_{oc}(V)	J_{sc}(mA/cm^2)	FF	η(%)
300	1.8273	15.1000	33.31	9.19
310	1.8346	15.2042	33.32	9.29
320	1.8384	15.3021	33.37	9.39
330	1.8388	15.3907	33.46	9.47
340	1.8354	15.4733	33.60	9.54
350	1.8281	15.5513	33.79	9.61
360	1.8170	15.6247	34.03	9.66

The values obtained for open-circuit voltage and short-circuit current are shown in Table II.

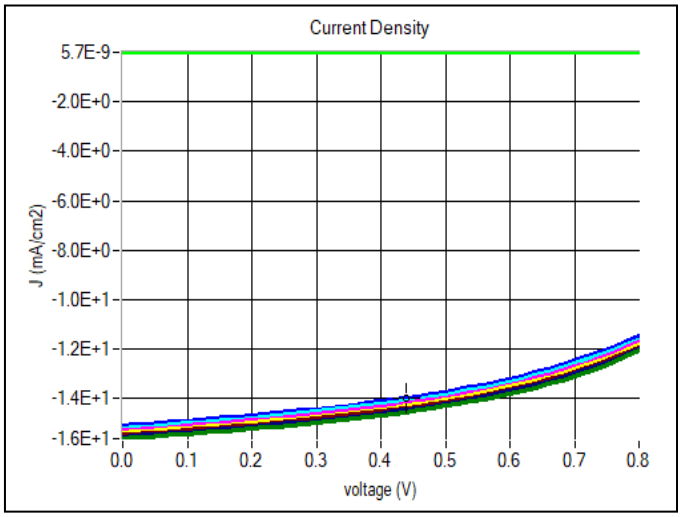


Fig. 3. I-V simulations for different temperature values. T varies from 300K (red), to 360K (blue) in steps of 10K.

Indeed, when the temperature increases the gap band becomes narrower and this accelerates the phenomenon of

recombination of electron-hole pairs between the conduction band and the valence band.The reduction of V_{oc} leads to an increase in the FF form factor as well as the conversion efficiency η of the solar cell.

B. Influence of layer thickness on the I-V quantities of the cell.

a) Influence of layer thickness of PEDOT:Pss.

The effect of the variation in the thickness of the PEDOT:Pss layer on the I-V quantities of the cell is given in Table III.

Table 3. V parameters for different layer thicknesses of PEDOT:Pss.

Thickness (μm)	V_{oc}(V)	J_{sc}(mA/cm^2)	FF	η(%)
0.07	1.7700	15.1508	34.06	9.13
0.08	1.8273	15.1000	33.31	9.19
0.09	1.7616	14.9654	33.91	8.94

V_{oc} and J_{sc} values decrease as the thickness of the PEDOT:Pss layer increases as it absorbs fewer and fewer long-wavelength photons, negatively influencing the rate of electron-hole generation.For thicker layers the generation of electron-hole peers occurs away from the interfaces which is why we observe an increase in efficiency. A thickness of 0.08 μm seems to be adequate to have an optimal yield (9.19%).

b) Influence of layer thickness of $CH_3NH_3PbI_3$:

The effect of the variation in the thickness of the $CH_3NH_3PbI_3$ layer on the I-V quantities of the cell is given in Table IV.

Table 4. V parameters for different layer thicknesses of $CH_3NH_3PbI_3$.

Thickness (μm)	V_{oc}(V)	J_{sc}(mA/cm^2)	FF	η(%)
0.7	1.6654	16.1716	34.85	9.39
0.8	1.7616	14.9654	33.91	8.94
0.9	1.8823	13.6935	32.65	8.41

The photovoltaic parameters decrease when the layer thickness ($CH_3NH_3PbI_3$:) increases due to the increase in material resistance, and this leads to the inhibition of electron movement. Then we select 0.7 μm as the ideal value.

c) Influence of layer thickness of PCBM:

The effect of the variation in the thickness of the $CH_3NH_3PbI_3$ layer on the I-V quantities of the cell is given in Table V.

Table 4. V parameters for different layer thicknesses of PCBM.

Thickness (μm)	V_{oc}(V)	J_{sc}(mA/cm^2)	FF	η(%)
0.4	2.1542	13.8406	29.91	8.92
0.5	1.8723	13.6835	32.64	8.40
0.6	1.6938	13.5386	34.32	7.87

Photovoltaic parameters decrease with increased thickness. The reason is that the higher the thickness of the layer is (PCBM), the distance between the two layers increases, making it difficult to move electrons between the two layers. Then we select 0.4 μm as the ideal value.

[4] CONCLUSION

In recent years, the world of photovoltaic conversion has undergone a profound change associated with the growing interest in photovoltaic energy. In order to improve the performance of photovoltaic devices, a simulation with the SCAPS software was carried out. Indeed, the intrinsic properties of the cell are very important and largely influence the performance of the cell such as the operating temperature, the thicknesses of the layers composing the cell. This is shown in the I-V characteristics. The optimum conversion efficiency of 9.39% for a 0.7μm absorbent layer thickness at temperature of 300 K.

REFERENCES

[1]. M. Kumar , A. Raj , A. Kumar , A. Anshul. An optimized lead-free formamidinium Sn-based perovskite solar cell design for high power conversion efficiency by SCAPS simulation. Optical materials 108 (2020) 110213.

[2]. M. Kumar, A. Kumar, A. Raj , P. C. Sati , M. Sahni ,A. Anshul. Organic-inorganic perovskite-based solar cell designs for high conversion efficiency: A comparative study by SCAPS simulation.materials today:proceeding (2020).

[3] R.N.Mohottige, S. P. K. Vithanage. Numerical Simulation of a New Device Architecture for CIGS-Based Thin-Film Solar Cells using 1D-SCAPS Simulator. Journal of Photochemistry & Photobiology, A: Chemistry(2020).

[4] D. Danilchuk, B. Nour, L. Dahal. Development of Low-cost Hybrid Perovskite Solar Cells. Department of Electrical Engineering Alternative Energy Innovation Center (AEIC), On Undergraduate Research (NCUR) (2016).

[5] A. Babayigit, A. Ethirajan, M. Muller, B. Conings, Toxicity of organometal halide perovskite solar cells, Nat. Mater. 15 (2016) 247–251, https://doi.org/10.1038/ nmat4572.

[6] S. Abdelaziz , A. Zekry , A. Shaker , M. Abouelatta. Investigating the performance of formamidinium tin-based perovskite solar cell by SCAPS device simulation. Optical materials 101(2020)109738.

[7] Mandadapu, U., Vedanayakam, S. V., Thyagarajan, K.Simulation and analysis of lead based perovskite solar cell using SCAPS-1D. Indian J. Sci. Technol, 10,1-8 .(2017).

Effect of thiourea concentration on characteristics of CZTS thin layer prepared by low cost sol gel method for solar energy applications

Ahmed ZITI
ERDyS laboratory GMEEM & DD Group, Hassan II University of Casablanca, FSTM BP 146 Mohammedia 20650, Morocco
ziti.ahmed91@gmail.com

Bouchaib HARTITI
ERDyS laboratory GMEEM & DD Group, Hassan II University of Casablanca, FSTM BP 146 Mohammedia 20650, Morocco
b.hartiti@univh2m.ac.ma

Hicham LABRIM DERS
CNESTEN, Rabat, Morocco
hichamlabrim@yahoo.fr

Abdelkrim BATAN
Materials Sciences Group University Moulay Ismail of Meknes, FST Errachidia, Department of Chemistry, BP 509 Boutalamine 52000 Errachidia, Morocco
kbatan@gmail.com

Salah FADILI
ERDyS laboratory GMEEM & DD Group, Hassan II University of Casablanca, FSTM BP 146 Mohammedia 20650, Morocco
safadili@yahoo.fr

Abderraouf RIDAH
LIMAT laboratory Department of Physics FSB, Hassan II University of Casablanca,Morocco
abderraoufridah@yahoo.fr

Mounia TAHRI
DERS, CNESTEN, Rabat, Morocco
mouniatahiri@gmail.com

Amine BELAFHAILI
Centre for Electron Microscopy Faculty of Sciences, Mohammed V University, Rabat, Morocco
aminebela@hotmail.com

Philippe THEVENIN
LMOPS University of Lorraine, METZ, France
aminebela@hotmail.com

***Abstract*—Quaternary semiconductor CZTS absorber material was synthesized by the sol gel method deposited by the dip-coating technique on ordinary glass substrates. In this work, we have investigated the influences of thiourea concentration: S/(Cu+Zn+Sn) equal 1.5, 1.7, 1.9, 2.1 and 2.3 on the structural, morphological, optical and electrical properties. The thin layers have been analyzed by various characterization techniques including: X-ray diffractometer (XRD), Raman scattering experiments, scanning electron microscopy (SEM), UV-visible spectrophotometer and four-point probe method. XRD patterns indicated kesterite CZTS with privileged orientation at (112) plane, SnS and SnS_2 supplementary phases were observed with CZTS phase in the XRD spectra of the films elaborated with very low and very high thiourea concentration. The pure kesterite CZTS phase was formed for the CZTS thin layers elaborated with the S/(Cu+Zn+Sn) ratio equal 1.7, 1.9 and 2.1. Raman measurements confirmed the existence of CZTS absorber layer in all prepared samples using single Raman characteristic peak at 332 cm-1. (SEM) images showed the homogeny and dense surfaces morphologies. Energy gap of CZTS absorber layer reduced ranging from 1.56 to 1.47 eV with S/(Cu+Zn+Sn) ratio increased. The values of sheet resistance are between 422.05 and 511.50 (Ω/square). These characteristics are adaptable for solar energy applications.**

Keywords—CZTS, sol gel, thiourea concentration, dip-coating

[1] INTRODUCTION

Chalcogenide thin film solar cells have the possibility to reduce the cost of photovoltaic technology. Chalcopyrite semiconductor materials are promising for high-efficiency and low cost based thin film PV technology. Copper indium gallium selenide (CIGS) absorber layer based solar cells currently hold the world record efficiency at 22.9% offering a promising materiel candidate for solar cells based thin films [1]. CIGS thin film has appropriate characteristics as absorber layer in the photovoltaic energy applications such as band gap of 1.5 eV, optical absorption coefficient higher than 104 cm-1 and p type semiconductor [2]. However, the problem found in CIGS is the costly and scarcity of Indium and gallium. This problem has limited the future of solar cells-based CIGS thin films [3]. Copper zinc tin sulphur Cu2ZnSnS4 (CZTS) thin film has non-toxic low cost and earth abundant elements, the properties of CZTS are similar to CIGS which make the interesting candidate for photovoltaic devices. 30 years ago Ito and Nakazawa achieved the first fabrication of solar cells based CZTS thin films prepared by atom beam sputtering method with a CZTS powder target. The CZTS solar cells indicated an open circuit voltage of 165 mV under light of AM 1.5 and optical band gap determined for CZTS absorber material is 1.45 eV [4]. The champion conversion efficiency of solar cells based kesterite Cu2ZnSn(S,Se)4 was reported by Wang et al with an efficiency of 12.6% in 2014 [5]. This photovoltaic device was produced by toxic and reactive hydrazine hydrate. The theoretical conversion efficiency about of (~32%) was achieved by Shockley-Quessier for CZTS solar cells [6].Several vacuum and non-vacuum methods were utilized to elaborate CZTS thin films including spray pyrolysis [7], electrodeposition [8], sputtering [9], thermal evaporation [10], pulsed laser deposition [11], co-evaporation [12], silar [13], electron beam evaporation [14], sol gel spin coating [15], sol gel dip-coating [16].

Sol gel method is simple and low-cost method for the preparation of thin films. Agawane et al elaborated a sol gel solution using copper chloride, zinc acetate, tin chloride and thiourea and deposited by spin coating technique to study the effect of annealing temperature on the physical properties of kesterite CZTS absorber layers, the best power conversion efficiency of 3.01% with optical band gap 1.48 eV is showed for the annealing temperature at 575°C [17]. Patel et al prepared CZTS thin films by dip-coating technique to investigate the effect of annealing temperature on some physical properties [18].

In our study, the prepared films were analyzed using X-ray diffraction (XRD), Raman spectroscopy, scanning electron microscopy (SEM), UV-Vis spectrophotometer and four-point probe method are used to determine some physical characteristics. We study the influence of thiourea concentration: $\frac{S}{mtal} = 1.5, 1.7, 1.9, 2.1\ and\ 2.3$ on the structural, morphological, optical and electrical properties.

[2] EXPERIMANTAL DETAIL

Numb Sol-gel solution is prepared by the four chemical precursors copper chloride, zinc chloride, tin chloride and thiourea by the following ratios: Zn/Sn = 1, Cu/(Zn + Sn) = 1.05 and S/(Cu+Zn+Sn) equal 1.5 (Su-1.5), 1.7 (Su-1.7), 1.9 (Su-1.9), 2.1 (Su-2.1) and 2.3 (Su-2.3), so we have five solutions at different concentrations of thiourea. The solutions produced are deposited by the dip-coating deposition technique at a speed of 40 mm / min on ordinary glass substrates, then the substrates are dried in an oven at a temperature of 120°C. for 15 min, the deposition and drying is repeated four times to obtain an adaptable thickness, finally the substrates are annealed in air at a temperature of 350 ° C for 10 min, the thicknesses of the thin layers of CZTS are estimated between 1.88 and 2 µm. The samples were analyzed by X-ray diffractometer (XRD) with CuKα radiation (λ=1.54056 Å) in angle 2**θ** in the range over 15 to 60 degrees at 0.02° scanning rate (D2 Phaser-Bruker) and Raman experiment using a laser excitation wavelength λ=532 nm in the wave number range between 100 and 1000 cm^{-1} to control structural properties, the morphological properties were characterized by using scanning electron microscopy (SEM) (Jeol scanning microscopy IT 100 (JSM-IT 100)). The optical properties were analyzed by using UV-Visible spectrophotometer in the wavelength range of 450-850 nm (Spectrovio junior kit-SV2100). The electrical sheet resistance was determined by using four-point probe method.

[3] RESULTS AND DISCUSSION

A structural properties

Figure 1 shows the X-ray diffraction of CZTS thin films at different concentrations of thiourea. All the films indicated the peaks corresponding to CZTS thin layers located at around 28 °, 32 ° and 56 °, respectively (112), (220) and (312) planes. The preferential direction of the (112) plane and of the peaks corresponding to CZTS thin layers confirmed the existence of kesterite CZTS phase of all films adapted by the file (JCPDS N °: 26-0575). Low and high concentration of thiourea present some additional phases, SnS additional phase is observed in the sample Su-1.5 [19]. SnS and SnS_2 additional phases of are observed in sample Su-2.3 [15, 20].the presence of additional phase SnS in the samples Su-1.5 is due to the difficulty of solubility of four elements in the aqueous solution, in the small quantity of sulfur we obtained nonhomogeneous solution. The existence of SnS and SnS_2 additional phase is due to saturation of the sulfur in the aqueous solution. The secondary phase SnS_2 does not have a very significant effect on the performance of solar cells [21], The S/(Cu+Zn+Sn) ratio between 1.7 and 2.1 presents a pure kesterite phase of CZTS. These results are comparable to the results obtained by various research works [22-24].

The inter-reticular distance dhkl is given according to Bragg's low by the formula (1), the lattice parameters of samples have been calculated using the equation (2) [25]. The expression of volume (V), in the case of a tetragonal structure, is expressed using relation (3). The preferential direction for crystal was approximated using a texture coefficient Tc(hkl), the texture coefficient was calculated following the equation (4) [26]. The c/2a ratio defines the deviation from the ideal tetragonal structure, this ratio is equal to 1 for ideal tetragonal structure. The crystallite size (D) of the thin layers was approximated using the Debye-Scherrer's from the XRD peaks with the equation (5) [27], where λ is the wavelength of X-ray radiation. The microstrain (ε) can be estimated from the relation (6) [28]. The source of the "ε" is linked to the elaboration conditions. The dislocation density (δ) is defined as the dislocation lines per unit volume of the crystal [29] and can be approximated from the crystallite size 'D' using equation (7) [30]. The number of crystallites (N) can be determined from crystallite size "D" and film thickness "d" using equation (8) [31].

$$d_{hkl} = \frac{n\lambda}{2\sin(\theta)} \quad (1)$$

$$\frac{1}{d_{hkl}^2} = \frac{(h^2+k^2)}{a^2} + \frac{l^2}{c^2} \quad (2)$$

$$V = a^2 c \quad (3)$$

$$T_c(hkl) = \frac{\frac{I(hkl)}{I_0(hkl)}}{N_r^{-1}\sum\frac{I(hkl)}{I_0(hkl)}} \quad (4)$$

$$D = \frac{0.94\,\lambda}{\beta\cos(\theta)} \quad (5)$$

$$\varepsilon = \frac{\beta\cos(\theta)}{4} \quad (6)$$

$$\delta = \frac{1}{D^2} \quad (7)$$

$$N = \frac{d}{D^3} \quad (8)$$

These values are comparable with those reported for the single crystal data (a=b=5.427 Å and c = 10.848 Å) [32]. This c/2a ratio is 1 for this ideal structure [33]. The volume values are comparable to the obtained by Shiyan et al. by electrochemical deposition method [34]. The texture coefficient is much higher than 1, the values of Tc and the high intensity of the peak corresponds to (112) plane confirms the preferential orientation to this plane. The c/2a ratio values are close to 1. The crystallite size increases with the increase in the concentration of thiourea from 5.5 to 9.09 until the ratio S/(Cu+Zn+Sn) to equal 1.9 and then it decreases from 9.09 to 8.12. The best size of the crystallites of 9.09 nm is obtained in the sample Su-1.9 indicates less

structural defects: a dislocation density equal to 1.21×10^{16} (Lines/m^2) and micro-deformation equal to 3.21×10^{-2} from the structural information of Su-1.9 we have indicated of this sample has appropriate structural properties compared to the other samples. Structural parameters of CZTS thin layers are shown in Table 1.

Raman experiments used to give information on the vibrational modes of CZTS thin films indicate the kesterite CZTS structure has been formed. Figure 2 demonstrates that Raman shift of CZTS elaborated at various thiourea concentrations, we can show from Figure 2 one vibrational mode positioned at 332 cm^{-1}. These results have confirmed the formation of pure kesterite CZTS structure. The additional phases observed in XRD plots like SnS_2 (vibrational modes located at: 215 and 312 cm^{-1}) and SnS (vibrational modes situated at: 163, 220 and 228 cm^{-1}) [35] are not observed in the Raman experiments which indicates low quantity of these phases with kesterite CZTS structure. No other binary and ternary phases such as Cu_2SnS_3 (vibrational modes positioned at: 298, 318 and 349 cm^{-1}) and ZnS (vibrational modes indexed at: 273, 286 and 352 cm^{-1}) found with CZTS phase [36, 37]. The vibrational characteristic mode of CZTS thin layers is observed in the range of 332-338 cm^{-1} by several others [38, 39]. This change is caused by the existence of internal stress in the material. The obtained results are comparable to the reported by other research papers [40, 41].

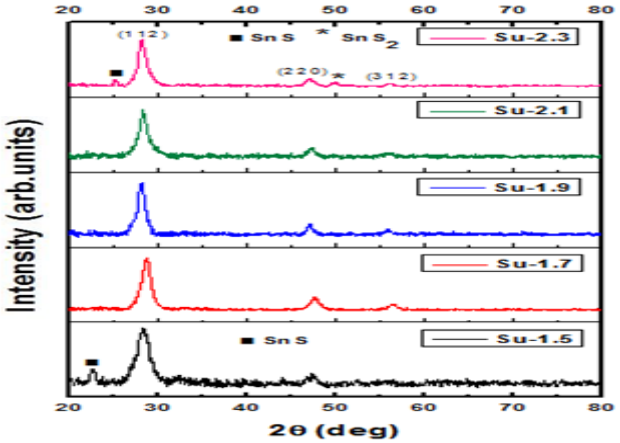


Fig. 1. XRD of samples prepared at different thiourea concentration

Table 1. Structural parameters of CZTS thin films for (112) plane

Sample	Su-1.5	Su-1.7	Su-1.9	Su-2.1	Su-2.3
2θ (112)	28.60	28.57	28.48	28.46	28.26
d (112)(Å)	3.11	3.12	3.13	3.13	3.15
a (Å)	5.395	5.374	5.407	5.420	5.431
c (Å)	10.83	11.04	10.92	10.87	10.07
$\frac{c}{2a}$	1.003	1.027	1.010	1.003	0.927
V (Å^3)	315.21	318.83	319.45	319.55	326.69
$T_c(112)$	1.99	1.77	1.78	1.91	2.17
D (nm)	5.50	7.54	9.09	9	8.12
$\varepsilon \times 10^{-2}$	5.29	3.87	3.21	3.25	3.63
$\delta \times 10^{16}$ (Lines/m2)	3.30	1.75	1.21	1.23	1.51
$N \times 10^{18} m^{-2}$	11.20	4.43	2.42	2.41	3.17

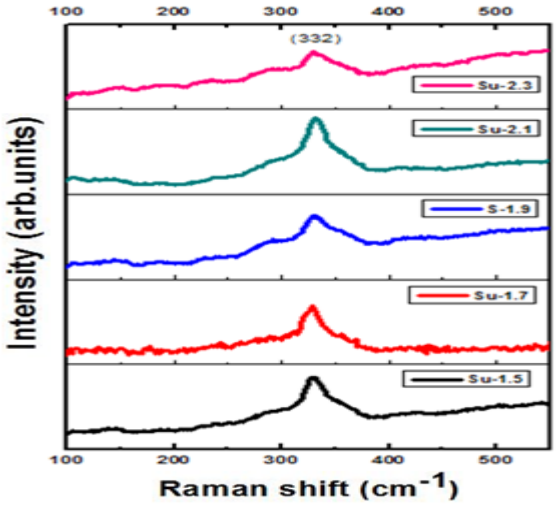


Fig. 2. Raman spectra of CZTS produced at different concentration of thiourea

B. Morpgical properties

Figure 3 shows the SEM images of CZTS thin layers prepared at different concentrations of thiourea. The SEM of the Su-1.5 sample is shows some grains distributed in the surface of CZTS, the holes and cracks are also observed throughout the surface morphology, the presence of these holes is attributed to the evaporation of small amount of sulfur during the annealing process the S/(Cu+Zn+Sn) ratio equal to 1.5 is insufficient to obtain a good morphology of the area. To improve the morphology of the CZTS surface, the concentration of thiourea is increased at the S/(Cu+Zn+Sn) ratio equal to 1.7, the SEM image of the Su-1.7 sample indicate a smooth and uniform surface without any holes and cracks, it can be shown that the increase of thiourea concentration at the S/(Cu+Zn+Sn) ratio equal to 1.7 is suitable for finding a homogeneous surface adaptable to photovoltaic applications. The homogeneity of the surface of CZTS is a very important factor to show the distribution of the four chemical elements (Cu, Zn, Sn, S) in surface morphology of CZTS thin layers. The SEM image of Su-1.9 sample shows a uniform surface with distributed grains throughout the CZTS surface morphology characterized by the absence of cracks and holes. The surface of this sample is adaptable to photovoltaic applications. The SEM image of the Su-2.1 sample demonstrated some grains in the surface morphology of this film, the excess of sulfur is clear in the surface of CZTS produced at the S/(Cu+Zn+Sn) ratio equal to 2.1. The sample which has a high concentration of thiourea (Su-2.3) presents a morphological surface without cracks and holes, the excess of sulfur is also very clear in the sample Su-2.3. We therefore conclude that the surface morphology of the Su-1.7 and Su-1.9 samples is adaptable to photovoltaic applications.

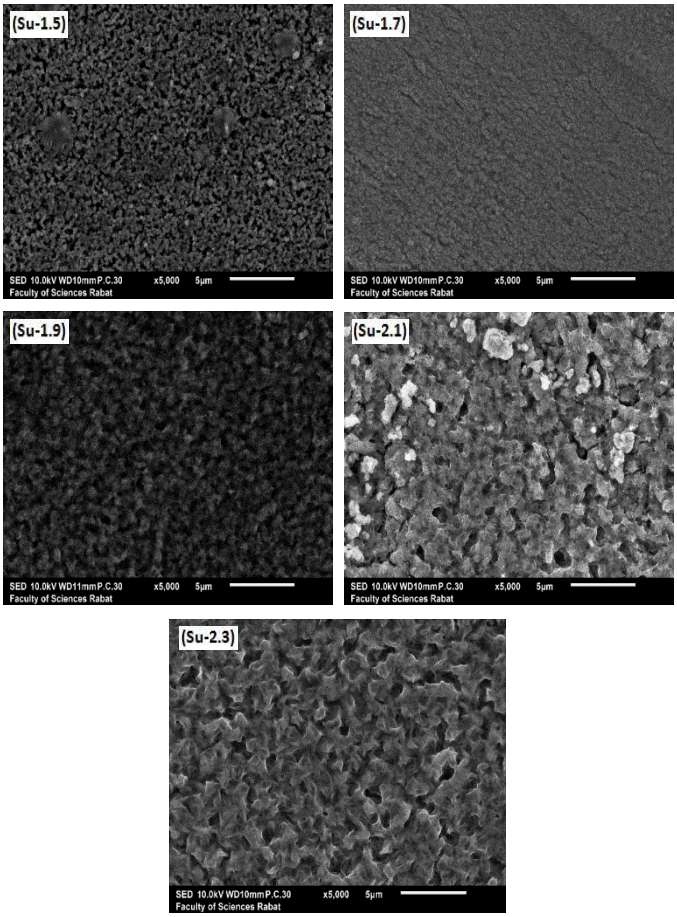


Fig. 3. SEM micrographs of CZTS thin films at different concentrations of thiourea

C. Optical properties

The transmittance and absorbance data of the CZTS thin layers were examined by UV-visible spectrophotometer. The wavelength of the incident light is between 450 and 850 nm. Figure 4 shows the transmittance as a function of the wavelength λ, the transmittance of the films decreases with the increase in the concentration of thiourea in the visible region. The radiation transmittance is less than 17% at a wavelength of 850 nm. The low transmittance of the thin layers of CZTS is due to high absorption of photonic energy by the samples, is also probably due to the high thickness of these films. Figure 5 shows the absorbance spectra of CZTS thin films with respect to the wavelength λ, the absorbance of incident photon energy increase with increasing of thiourea concentration, the maximum absorbance of films Su-1.5, Su-1.7, Su-1.9, Su-2.1 and Su-2.3 being respectively 1.58, 1.80, 1.71, 1.75 and 1.72. These results are close to the obtained ones by Mau et al. for CZTS absorber material deposited by dip-coating technique and Bakr et al. for CZTS absorber layers elaborated by spray pyrolysis [42, 43].

The absorption coefficient is calculated by the measured transmittance data and the thickness of the thin layers produced at different concentrations of thiourea using relation (9). The gap energies were determined by the application of Tauc formula (10) [20, 44].

$$\alpha = \frac{1}{d}\ln\left(\frac{1}{T}\right) \qquad (9$$

$$(\alpha h\nu) = K(h\nu - E_g)^n \qquad (10$$

where "d" is the thickness, K is a constant, hν is the incident photon energy, $n = \frac{1}{2}$ for direct allowed transition, 2 for indirect allowed transition. The optical absorption coefficient of all the thin layers of CZTS shown in Figure 6 has the values greater than 10^4 cm^{-1}; these results are in accordance with the literature for the CZTS absorbent material for solar energy applications [45, 46]. Figure 7 presents the graph of the energy of the optical band gap (Eg) for the thin layers of CZTS. The forbidden band was determined by extrapolating the linear part of the curve as a function of the energy of the photons hν to $(\alpha h\nu)^2 = 0$. The gap energies obtained are 1.56, 1.54, 1.51, 1.50 and 1.47 eV for the CZTS samples: Su-1.5, Su-1.7, Su-1.9, Su-2.1 and Su-2.3 respectively. The increasing of thiourea concentration in CZTS solution causes more absorbance, this behaviour decreases the energy gap of samples Su-1.7 and Su-1.9 are more favorable for photovoltaic applications [47-50].

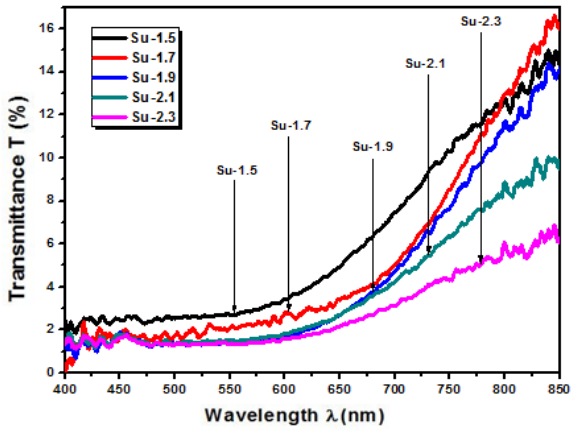


Fig. 4. Transmittance of CZTS thin layer with various thiourea concentrations

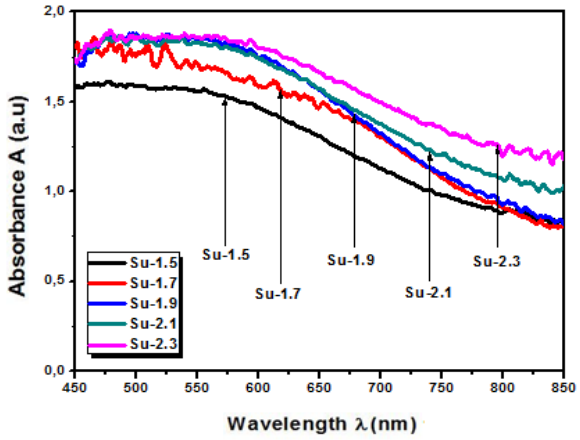


Fig. 5. Absorbance of CZTS thin layer with various thiourea concentration

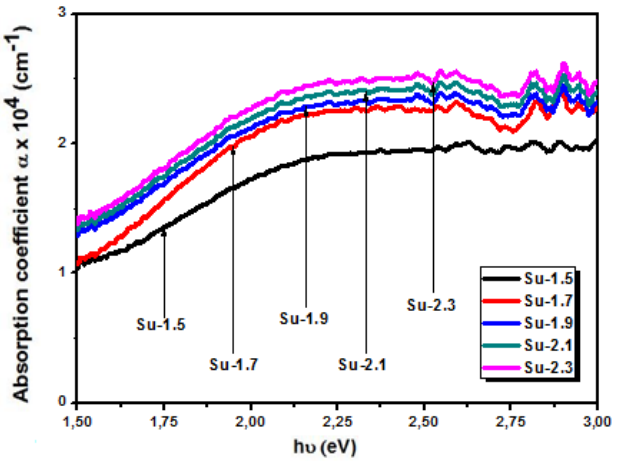


Fig. 6. Absorption coefficient of CZTS absorber material with different thiourea concentration

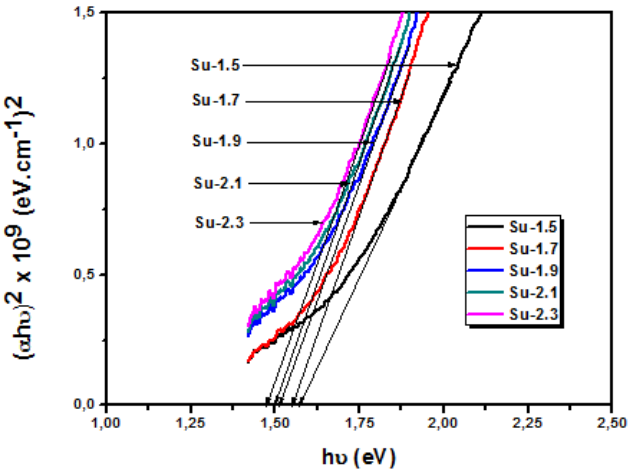


Fig. 7. Determination of the optical band gap of the thin layers of CZTS by the extrapolation plot from the variation of $(\alpha h\nu)^2$ as a function of hν

D. Electrical properties

Figure 8 shows the behavior of sheet resistance as a function of the concentration of thiourea of CZTS thin layers deposited by the dip-coating technique. The sheet resistance values are 460.24, 447.95, 428.26, 422.05 and 511.50 (Ω / square) for samples Su-1.5, Su-1.7, Su-1.9, Su-2.1 and Su-2.3, respectively. We note that the sheet resistance decreases with the increase in the concentration of thiourea until the S / (Cu+Zn+Sn) ratio equal to 2.1 and after increases, these results are favorable for photovoltaic solar cells applications [51, 52].

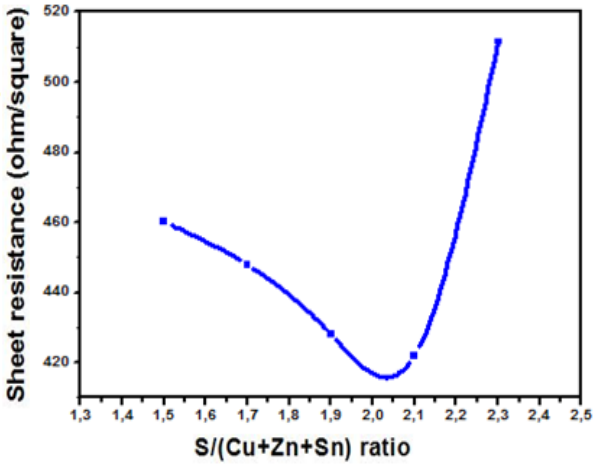


Fig. 8. Sheet resistance of CZTS thin films as a function of S/(Cu+Zn+Sn) ratio

[4] Conclision

CZTS thin layers were prepared by the sol-gel method and deposited on ordinary glass substrates by the dip-coating technique. All CZTS thin films exhibited a kesterite crystal structure with preferential orientation along the (112) plane. The secondary phase SnS is observed in the Su-1.5 sample, SnS and SnS2 are showed in the samples Su-2.3 the crystallite size size varies between 5.50 and 9.09 nm, the Raman scattering measurement confirms the formation of kesterite CZTS by the presence of the peak obtained at 332 cm-1. The surface morphology of CZTS of samples Su-1.7 and Su-1.9 is smooth and uniform. The gap energy decreases from 1.56 to 1.47 eV with thiourea concentration increased. The sheet resistance values of CZTS thin layer are in the range of 422.05-511.50 (Ω /square), the sheet resistance resistance values are favorable for photovoltaic applications.

ACKNOWLEDGMENT

Professor. Bouchaib HARTITI, Senior Associate at Abdus Salam International Centre for Theoretical Physics (ICTP), is very grateful to ICTP for financial support. Technical support from LMOPS loboratory in University of Lorraine, France is also acknowledged.

REFERENCE

[1] T. Kato, J-L. Wu, Y. Hirai, H. Sugimoto, and V. Bermudez, IEEE Journal of Photovoltaics, 1-6 (2018).
[2] A. Kotbi, B. Hartiti, S. Fadili, A. Ridah, P. Thevenin, Opt Quant Electron **48**:524 (13) (2016).
[3] H-W. Tsai, C-W. Chen, S. R.Thomas, C-H. Hsu, W-C. Tsai, Y-Z Chen, Y-C. Wang, Z.M.Wang, H-F. Hong & Y-L. Chueh, Scientific Reports 6:19102 (2016).
[4] K. Ito and T. Nakazawa, Japanese Journal of Applied Physics 27(11):2094-2097 (1988).
[5] W. Wang, M.T. Winkler, O. Gunawan, T. Gokmen, T.K. Todorov, Y. Zhu, D.B. Mitzi, Adv. Energy Mater. 4, 1–5 (2014).
[6] W. Shockley and H. J. Queisser, Journal of Applied Physics, Volume 32, pp. 510-519 (1961).
[7] C. Kim and S. Hong, Molecular Crystals and Liquid Crystals, vol 645, pages 217-224 (2017).
[8] A. Tang, Z. Li, F. Wang, M. Dou, Y. Pan, J. Guan J. Applied Surface Science, 402, 70–77 (2017).
[9] B-T. Jheng, P-T Liu, M-C. Wu, Solar EnergyMaterials & SolarCells 128, 275–282 (2014).
[10] K. Wang, O. Gunawan, T. Todorov, B. Shin, S. J. Chey, N. A. Bojarczuk, D. Mitzi, and S. Guhaa, Applied Physics Letters 97(14):143508-143508-3 (2010).

[11] A.V. Moholkar, S.S. Shinde, A.R. Babar, Kyu-Ung Sim, Ye-bin Kwon, K.Y. Rajpure, P.S. Patil, C.H. Bhosale, J.H. Kim, Solar Energy 85 1354–1363 (2011).
[12] B. Arvid Schubert, B. Marsen, S. Cinque, T. Unold, R. Klenk, S. Schorr and H-Werner Schock, Prog. Photovolt: Res. Appl.; 19:93–96 (2011).
[13] S. S. Mali, Pravin S. Shinde, C. A. Betty, P. N. Bhosale, Y. W. Oh, P. S. Patil, Journal of Physics and Chemistry of Solids 73 735–740 (2012).
[14] E. M. Mkawi, Y. Al-Hadeethi, E. Shalaan, E. Bekyarova, Journal of Materials Science: Materials in Electronics, Volume 29, pp 20476–20484 (2018).
[15] R. Hosseinpour, M. Izadifard, M. E. Ghazi, and B. Bahramian, Volume 47, pp 1080–1090 (2018).
[16] A. Ziti, B. Hartiti, H. Labrim, S. Fadili, H. T. Nkuissi, A. Ridah, M. Tahri, P. Thevenin, Applied Physics A, (3) 125:218 (2019).
[17] G.L. Agawane , A.S. Kamble, S.A. Vanalakar, S.W. Shin, M.G. Gang, Jae Ho Yun, Jihye Gwak, A.V. Moholkar, Jin Hyeok Kim, Materials Letters, 158, 58–61 (2015).
[18] K. Patel, V. Kheraj, D. V. Shah, C. J. Panchal and N. G. Dhere, Journal of Alloys and Compounds, 663, 842-847 (2015).
[19] M.A. Olgar, M. Tomakin, T. Kucukomeroglu, E. Bacaksız, MRX-111064.R2 page 1-23 (2019).
[20] A. Ziti, B. Hartiti, H. Labrim, S. Fadili, M. Tahri, A. Belafhaili, A. Ridah, P. Thevenin, Journal of Sol-Gel Science and Technology, 91:364–373, (2019).
[21] W. Wang, G. Chen, H. Cai, B. Chen, L. Yao, M. Yang, S. Chen and Z. Huang, Journal of Materials Chemistry A 6(6) (2017).
[22] N. A. Bakr, S. A. Salman, S. A. Hameed, International Journal of Applied Engineering Research, Volume 13, Number 6 pp. 3379-3388 (2018).
[23] C. Yan, K. Sun, F. Liu, J. Huang, F. Zhou, X. Hao, Solar Energy Materials & Solar Cells 160 (2017) 7–11.
[24] J. Chen, F. Wang, B. Yang, X. Peng, Q. Chen, J. Zou and X. Dou, Coatings, 9, 130 (2019).
[25] D. Lee, S. Park, J.H. Kim, Curr. Appl. Phys. 11(1), S88–S92 (2011)
[26] Shiyou Chen, X. G. Gong, Aron Walsh, and Su-Huai Wei, Appl. Phys. Lett. 94, 041903 (2009).
[27] C. P. Nikam and S. R. Gosavi, Advances in Applied Science Research, , 5:267-272 (2014).
[28] M. Balaji J. Chandrasekaran, M. Raja, S. Rajesh, J Mater Sci: Mater Electron (2016).
[29] K. Ravichandran, P. Philominathan, Solar Energy 82 1062–1066(2008).
[30] S. A-Jabbar Jassim , A. A. R. Ali Zumaila , G. A. A. Al Waly, Results in Physics 3 173–178 (2013).
[31] Bouhaf Kherkhachia, A. Attafa, H. Saidia, A. bouhdjara, H. Bendjdidia, Y. Benkhettaa, R. Azizia, M.S. Aida, Optik 127 2266–2270 (2016).
[32] Y.B. Kishore Kumar, P. Uday Bhaskar, G. Suresh Babu, and V. Sundara, Phys. Status Solidi A 207, No. 1, 149–156 (2010).
[33] H. W. Spiess, U. Haeberlen, G. Brandt, A. Räuber, J. Schneider, Phys. Stat. Sol. (b), vol.62, p. 183, 1974.
[34] T. Shiyani, M. Patel, I. Mukhopadhyay and A. Ray, journal IETE Technical Review, Volume 33, page 2-6, Issue 1, (2016).
[35] I.P. Parkin, L.S. Price, T.G. Hibbert, and K.C. Molloy, journal of Materials chemistry vol 11, 1486-1490 (2001).
[36] E. A. Lund, H. Du, W. M. Hlaing OO, G. Teeter, and M. A. Scarpulla, Journal of Applied Physics 115, 173503 (2014).
[37] T. Chandel, V. Thakur, S. Halaszova, M. Prochazka, D. Hasˇko, D. Velic and R. Poolla, Journal of Electronic Materials, 47(8), 5477-5487 (2018).
[38] M. Guc, S. Levcenko, I.V. Bodnar, V. Izquierdo-Roca, X. Fontane, L.V.Volkova, E.Arushanov & A. P-Rodríguez, 6:19414 (2016).
[39] J. H. Nkuissi Tchognia, B. Hartiti, A. Ridah, J-M Ndjaka, P. Thevenin, Optical Materials 57, 85-92 (2016).
[40] K. Diwate, K. Mohite, M. Shinde, S. Rondiya, A. Pawbake, A. Dated , H. Pathane , S. Jadkare, Energy Procedia 110) 180 – 187 (2017).
[41] M. Z. Ansari, S. Munjal, N. Khare, Thin Solid Films,
Volume 657, Pages 95-100 (2018).
[42] T. Truong Mau, H. Kim, J. Ceram. Process. Res. 13(3), 301–304 (2012).
[43] N. A. Bakr , Z.T. Khodair, H. I. Mahdi, International Journal of Materials Science and Applications, ISSN: 2327-2635 (Print); ISSN: 2327-2643, (2016).
[44] J. Tauc, R. Grigorovici, A. Vancu, Phys. Stat. Sol. 15, 627–637 (1966)
[45] A. Aldalbahi, EM. Mkawi, K. Ibrahim, Farrukh MA, Sci Rep 6:32431 53 (2016).
[46] A. Chavda, M. Patel, I. Mukhopadhyay, Ray A, ACS Sustain Chem Eng 4 (4):2302–2308 (2016).
[47] K. Woo, Y. Kim and J. Moon, Energy Environ. Sci, 5, 5340-5345 (2012).
[48] M. P. Suryawanshi,P. S. Patil, S. W. Shin, K. V. Gurav, G. L. Agawane, M. G. Gang, Jin Hyeok Kim and A. V. Moholkar, RSC Adv, 4 (36), 18537 (2014).
[49] [29] G. Chen, W. Wang, S. Chen, Z. Whang, Z. Huang, B. Zhang, X. Kong, Journal of Alloys and Compounds 718, 236e245 (2017)
[50] S. Lee, J. M. Kim, H. S. Woo, Y. Chul Jo, A. I. Inamdar, S. M. Pawar, H. Sang Kim, Woong Jung, H. Sik Im, Current Applied Physics 14(3):254–258 (2013).
[51] X. Yu, A. Ren, F. Wang, C. Wang, J. Zhang, W. Wang, L. Wu, W. Li, G. Zeng, and L. Feng, International Journal of Photoenergy Volume 2014, Article ID 861249, 6 pages (1-6) (2014).
[52] B. Dahal, L.P. Joshi, S.N. Pandey, S.P. Shrestha, Asian J. Chem. Sci. 2(4), 1–8 (2017).

The effect of window film on building energy consumption in hot climate zone

Kübra Sümer Haydaraslan
Faculty of Architecture, Department of Architecture Süleyman Demirel University, Isparta, Turkey
kubrahaydaraslan@sdu.edu.tr

Yalçın Yaşar
Faculty of Architecture, Department of Architecture Karadeniz Technical University Trabzon, Turkey
yyasar@ktu.edu.tr

***Abstract*—Building envelope elements (roof, flooring, exterior wall, window, door, etc.) affect the energy consumption of buildings. These elements provide heat interaction between the indoor and outdoor environments in buildings. Windows are one of the most important elements in the heat transfer occurring in the building envelope. Therefore, it is possible to reduce the energy consumption of the building with the measures taken in the windows. In the selection of the elements that make up the building envelope, parameters such as the climate, location, and function of the building are taken into consideration. In this study, it is aimed to reduce the energy consumption of existing buildings in the hot climate zone due to windows. The users do not prefer considering the cost issue, replacing window systems in existing buildings. In this study, window film was applied to the windows in the window systems of the buildings built by the Housing Development Administration in Antalya. The effects of window films applied to buildings were examined through the building energy simulation program and, if applied, the primary energy consumption, CO_2 emission, and global cost of the building were calculated. With the study, it was found that it is possible to reduce the energy consumption of the existing buildings in the hot climate zone due to the window systems with simple precautions. (*Abstract*)**

Keywords— building energy consumption, window film, hot climate zone, energy efficiency measures (*key words****)***

[1] INTRODUCTION (*Heading 1*)

Buildings are one of the areas where energy is consumed the most. Buildings consume 40% of the total energy [1]. This energy consumed is mostly for the heating and cooling of buildings. This consumption rate continues to increase due to the increase in comfort conditions of building users and climate change [2]. It is estimated that the temperature increase due to climate change will increase in the range of 1.1 ° C - 6.4 ° C by the end of this century [3]. It is stated that this increase in temperature will raise the need for cooling in buildings located in hot climatic regions [4]. Countries are conducting studies by taking precautions to reduce energy use in buildings [5].

Building envelope elements (roof, flooring, exterior wall, window, door, etc.) affect the energy consumption of buildings. These elements provide heat interaction between the indoor and outdoor environments in buildings. In the selection of building envelope elements, parameters such as climate, location, the function of the building are taken into consideration. Windows are one of the most important elements in heat transfer from the building envelope. It is possible to reduce the energy consumption of the building with the measures taken on the windows. The IEA has recommended the application of low-cost window film to developing countries in hot climates [6]. Studies have shown that the heat transfer coefficient of window can be reduced by up to 50% with the application of film to windows. One of these studies was conducted by Kou [7], in the study, the heat transfer coefficient of the glass decreased from 5-7 W/m^{2}K to 2.8 W/m^{2}K. Other work on this subject belongs to Solovyev. In the study, the heat loss caused by the glass was reduced by covering the existing glasses with low-e film [8].

With the development of technology, the life span of the buildings has increased. It is estimated that 75-90% of the existing buildings will continue to be used in 2050 in the coming years [9, 10]. Accordingly, the EU stated that existing buildings should be renewed to reduce their energy consumption. It aims to renew 3% of the existing buildings every year [11,12]. Low-cost suggestions in renovation work to reduce building energy consumption in buildings attract more attention of building users. On the other hand, it is expected that the temperature increase due to climate change will increase the demand for cooling. Therefore, the need for electrical energy increases more than other energy needs [4]. Suggestions to reduce the cooling needs of buildings in hot climate regions are important because fossil fuels are mostly used as an energy sources [13]. In this study, the existing buildings built by the Housing Development Administration (TOKI) in Antalya, which is located in a hot climate zone, are studied. In the study, suggestions have been made to reduce the cooling load of the buildings. This study made recommendations to reduce the cooling load of buildings. These recommendations are for windows that are most effective in indoor comfort conditions. For this study, the primary energy consumption, CO_2 emission, and global cost of the building were calculated by applying window film to the window surface of the building.

[2] METHOD

In hot climate regions, the amount of energy consumed for cooling buildings is more than the energy consumed for heating. In addition, it is estimated that temperatures due to climate change will increase (IPCC). This situation indicates that there will be an increase in the amount of energy consumed for cooling in hot climate regions. For this reason, the primary energy consumption and reduction of CO_2 emission of existing buildings in a hot climate zone were studied. The study was carried out for existing buildings built by TOKI in the province of Antalya (30.42 ° E, 36.53 ° W) in the Mediterranean Region. The energy model of the buildings was created with the building energy simulation program DesignBuilder. Case primary energy consumption, CO_2 emission, and Global cost values of the buildings were calculated. From these values;

Primary energy consumption (kWh/annual);

$$Primary\ energy\ consumption = \sum (Energy\ consumption\ x\ P.E.Conversion\ Coefficient) \quad (1)$$

is calculated according to the Formula 1. Turkey's the primary energy conversion factor is 1 for natural gas and other fuels

and also is 2.36 for electricity [14].

CO_2 emissions;

$$CO_2 = \sum(Energy\ consumption\ x\ CO_2\ Conversion\ Coefficient) \quad (2)$$

is calculated according to the Formula 2. Turkey's the CO_2 conversion coefficient is 0.467 for solid fuel, 0.234 for natural gas, and 0.626 for electricity [14].

The global cost calculation was made to determine which measures are more appropriate for primary energy consumption and CO_2 emissions. Global cost is the total cost of today's value, including initial investment costs and operating costs, over the life cycle.

Global cost;

$$Cg(\tau) = CIn + \sum_j \left[\sum_i^{\tau}(Cy(\tau) + Cr(\tau)) - Vf,\tau(j)\right] \quad (3)$$

It is calculated according to the formula. $Cg(\tau)$ global cost, CIn initial investment cost, $Cy(\tau)$ operating cost (maintenance, operation, and energy costs), Cr(τ): Renovation cost and Vf, τ (j) last corresponding to τ of component j means value. When operating cost $Cy(\tau)$ calculated for a certain period, the time value of money, including market interest rate, and the inflation rate is considered. The market interest rate and the inflation rate for Turkey are 0,122 and 0,133 [15,16].

Primary energy consumption, CO_2 emission amount and global cost of the current situation of the buildings were calculated in accordance with the above formulas. It has been observed that these values differ in the buildings with the same architectural type in the settlement. This is due to the differences in the positioning, orientation and shading of the buildings on the land. For this reason, the building with average energy consumption was determined to calculate the window film application situation in the study. In the current situation, primary energy consumption and CO_2 emissions per square meter of the buildings have been calculated (Figure 1). The closest building to average primary energy consumption and CO_2 emission is the building with the B8 code. The effect of the measures has been studied on this building. Applying window film to the inner surface of existing glasses is an easier application in terms of cost than replacing the window system. Three different window films were applied to the B8 building, which was determined as a reference in the study. Properties of window films are given in Table 1.

Table 1. Window film properties [17]

		S2	S3	S4
Solar Transmittance (%)	:	43	38	36
Outside Solar Reflectance (%)	:	28	23	27
Inside Solar Reflectance (%)	:	28	23	27
Visible Transmittance (%)	:	68	53	51
Outside Visible Reflectance (%)	:	13	23	23
Inside Visible Reflectance (%)	:	4	22	27
Emissivity	:	0.09	0.77	0.37

A. Definition of Reference Building

According to the TS 825 Building Heat Insulation Rules, Antalya province is in the I. Zone degree day zone [18]. Reference buildings in Antalya province were built in 2018. It was designed in 2 types of architectural plans as B and C types. While buildings are heated with solid fuel boilers, they are cooled by individual air conditioning. The domestic hot water of the buildings is provided by an electric water heater. The site and architectural plans of the reference buildings and the heat transfer coefficient information of the buildings are given in the Table 2.

[3] RESULTS

A. Investigation of the effect of window film

In this study, it has been studied to reduce the energy consumption caused by the transparent surfaces of the buildings. In this study, the effect of window film in developing countries was examined. The existing buildings in the hot climate zone are taken as reference in the study. Three different window films were applied to these buildings. At the end of this application, primary energy consumption, CO_2 emission and global cost calculations of the buildings were made. According to the results of the calculations, the S2 (%2.25) coded window film reduced the primary energy consumption the most, and the S3 (%1.51) coded window film was the lowest. No window film is cost optimum in terms of global cost. If the cost is ignored, it is the S2 coded window film that reduces both heating and cooling loads the most (Figure 2, Figure 3).

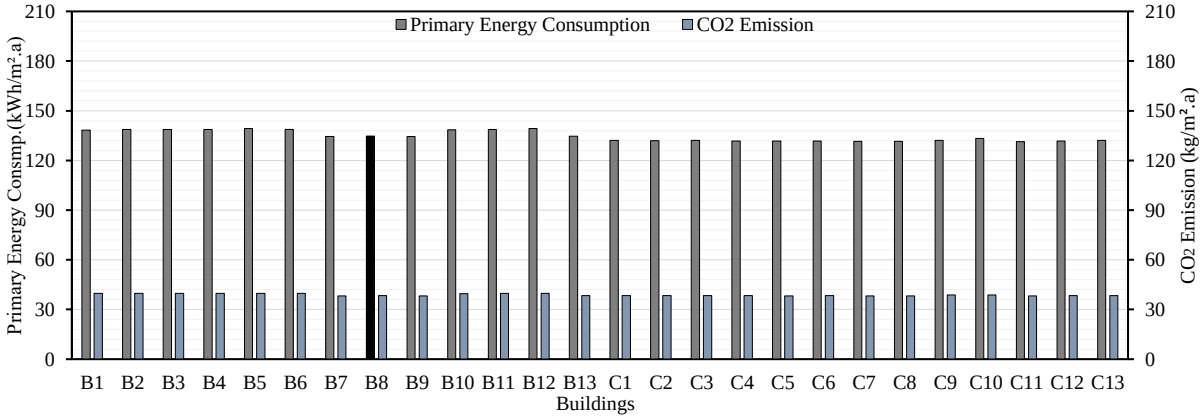
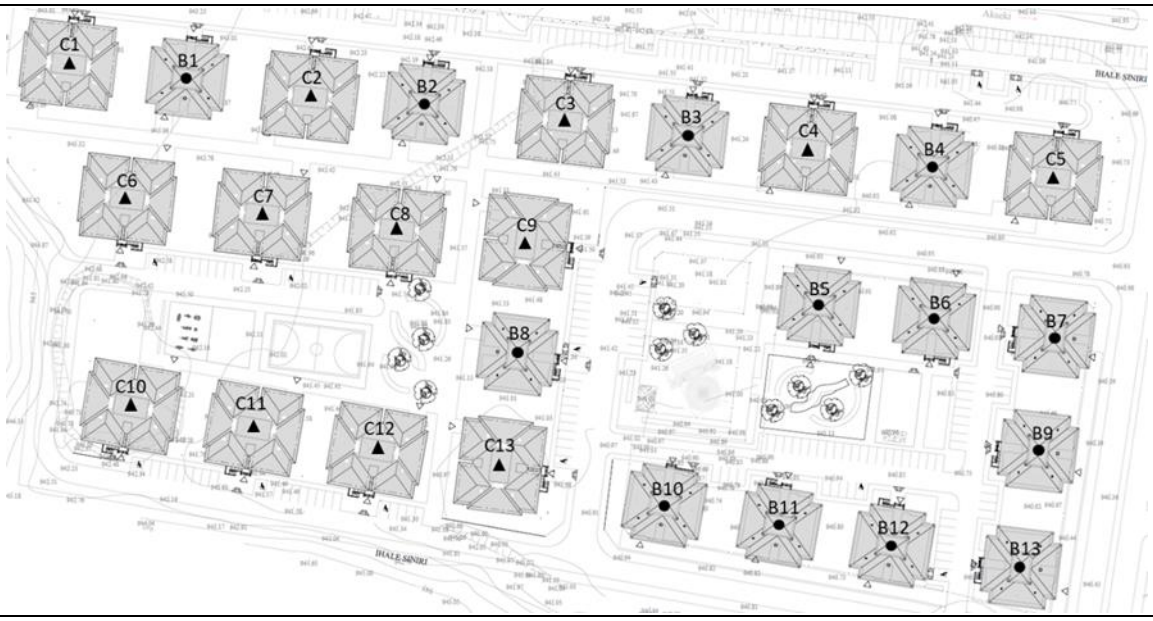


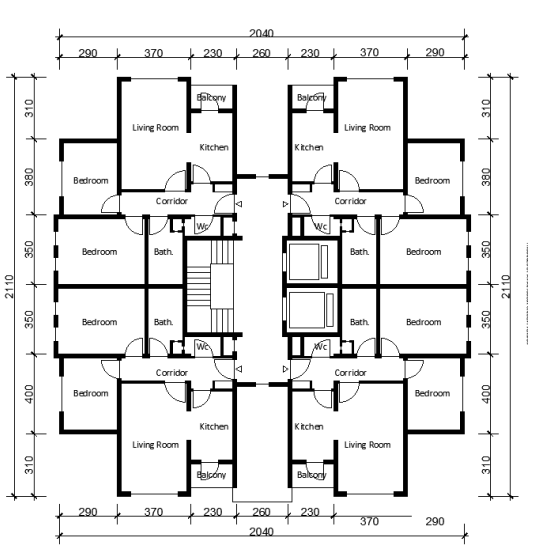
Figure 1. Primary energy consumption and CO_2 emission results of buildings in Antalya settlement

Table 2. Site plan of the buildings, architectural plan, information about the buildings

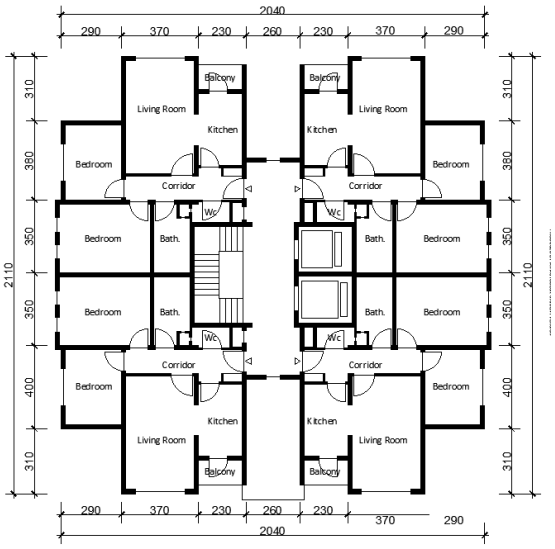
Site Plan



Architectural plan, (a) B type (b) C type



(a)



(b)

U_{wall}	: 0.356 W/m^{2}K	$U_{floor\ (semi\text{-}exposed)}$	: 0.453 W/m^{2}K
$U_{ceiling\ (semi\text{-}exposed)}$	: 0.263 W/m^{2}K	U_{window}	: 1.9 W/m^{2}K
$U_{partition}$	: 1.099 W/m^{2}K	Infiltrasyon	: 0.8 (n/h)

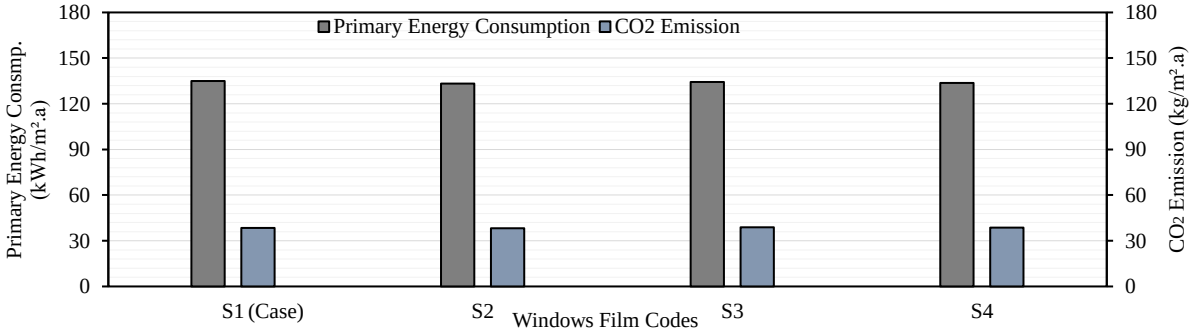


Figure 2. Primary energy consumption and CO_2 emission change compared to window films

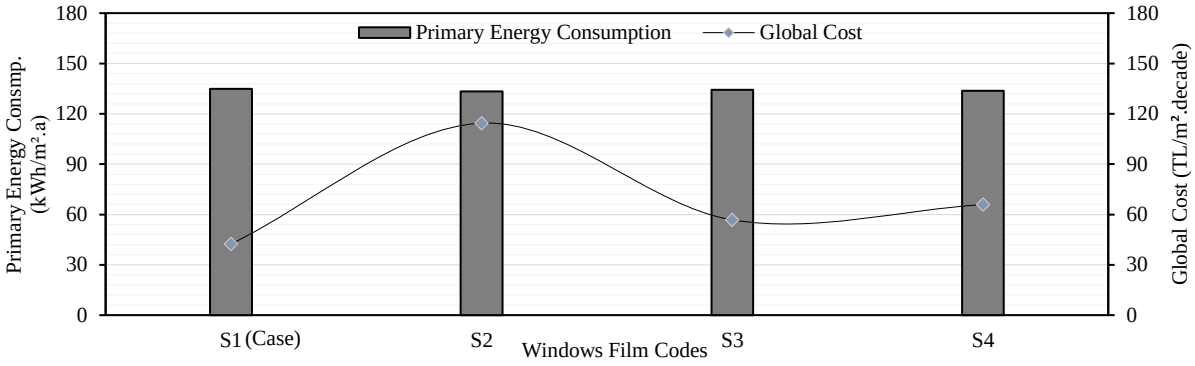


Figure 3. Primary energy consumption and global cost change compared to window films

On the other hand, S3 and S4 coded window films, which are among the solutions that are cost-optimal and minimize primary energy consumption, give an average result. Accordingly, S3 reduced primary energy consumption by 1.51%, while S4 reduced primary energy consumption by 1.96%.

[4] CONCLUSION

The increase in energy consumption in recent years has accelerated the studies of countries on energy efficiency. Buildings are among the areas with the highest energy consumption in developed and developing countries. Turkey is among the developing countries. In recent years, the increase in energy demand from buildings in Turkey is an annual average of 4.4%. With the measures, it is possible to reduce the energy consumption of the buildings by 25% - 45%.

In this direction, the study has been aimed at reducing the energy consumption of existing buildings located in a hot climate zone. It has been observed that the recommendations of the IEA are in place with the addition of window film to the transparent surfaces of the buildings. With the use of window film, the energy consumption of buildings can be reduced. Window film application offers a simple solution in terms of cost. Recommended window films reduce energy consumption at different rates. However, the study has shown that it is possible to reduce energy consumption and CO_2 emission by applying window film to existing buildings located in hot climate regions.

ACKNOWLEDGMENT

This study was supported by Karadeniz Technical University through Scientific Research Projects Coordination Unit (BAP).

REFERENCES

[1] J. Kurnitski, K. Kuusk, A. Uutar, T., Kalamees, E., Pikas, “Energy and Investment Intensity of Integrated Renovation and 2030 Cost Optimal Savings,” Energy and Buildings, vol. 75, pp. 51-59, 2014.

[2] International Energy Agency, www.iea.org, Accessed 10 Jan 2019.

[3] Report of the Intergovernmental Panel on Climate Change (IPCC), Contribution of Working Groups I, II and III to the Fifth Assessment Report of the Intergovernmental Panel on Climate Change, Geneva, Switzerland, 2014.

[4] Global Energy CO2 Status Report, www.webstore.iea.org, Accessed 02 March 2019.

[5] K. Sümer Haydaraslan, Y Yalçın, “Investigation of The Energy Plans in Terms of The Building Sector,” The International Civil Engineering & Architecture Conference, Trabzon, Turkey, pp. 443-457, 17-20 April 2019.

[6] International Energy Agency, Technology Roadmap, www.iea.org, Accessed 10 April 2019.

[7] R. Kou, Y. Zhong, J. Kim, Q. Wang, M. Wang, R. Chen, Y. Qiao, “Elevating low-emissivity film for lower thermal transmittance,” Energy and Buildings, vol. 193, pp. 69-77, 2019.

[8] A.A. Solovyev, S.V. Rabotkin, N.F. Kovsharov, “Polymer Films with Multilayer Low-e Coatings,” Materials Science in Semiconductor Processing, vol. 38, pp. 373-380, 2015.

[9] K. Huang, R. Hwang, “Future Trends of Residential Building Cooling Energy and Passive Adaptation Measures to Counteract Climate Change: The Case of Taiwan,” Applied Energy, vol. 184, pp. 1230-1240, 2016.

[10] Transition to Sustainable Buildings: Strategies and Opportunities to 2050, www.iea.org, Accessed 8 April 2019.

[11] European Comission, Energy Efficiency, www.ec.europa.eu, Accessed 15 November 2019.

[12] Energy Efficiency Directive 2012/27/EU of the European Parliament and of the Council, Accessed 25 October.

[13] Energy Technology Perspectives, www.iea.org, Accessed 20 July 2019.

[14] Housing Certificate Guide, Turkish Green Building Council, 2016.

[15] The Central Bank of the Republic of Turkey, www.tcmb.gov.tr, Accessed 5 July 2019.

[16] Energy performance of buildings - Economic evaluation procedure for energy systems in buildings. Standard EN 15459:2007, Brussels, 2007.

[17] Products, Architectural Window Film, www.solargard.com, Accessed 15 March 2019.

[18] Turkish Standards Institution. Binalarda Isı Yalıtım Kuralları, Turkey, 2013.

Examination of the Effect of Heat Treatment Process on High Temperature-High Activity Nickel Aluminide Coating on CM247LC

Ahmet Arda Inceyer
Materials Science and Engineering Gebze Technical University Kocaeli, Turkey *Materials Institute* Tübitak Marmara Research Center Kocaeli, Turkey
ainceyer@gtu.edu.tr

Gökhan Güven
Materials Institute Tübitak Marmara Research Center Kocaeli, Turkey
gokhan.guven@tubitak.gov.tr

Kaan Demiralay
Materials Institute Tübitak Marmara Research Center Kocaeli, Turkey
kaan.demiralay@tubitak.gov.tr

Havva Kazdal Zeytin
Materials Institute Tübitak Marmara Research Center Kocaeli, Turkey
havva.zeytin@tubitak.gov.tr

Metin Usta
Materials Science and Engineering Gebze Technical University Kocaeli, Turkey *Materials Institute* Tübitak Marmara Research Center Kocaeli, Turkey
ustam@gtu.edu.tr

Aim: **Nickel base superalloy (NBS) CM247LC was modified from the chemical composition of Mar-M247 superalloy. This alloy is especially used in hot sections of aero-engine and advanced gas turbine because of its superior high temperature strength. As the nickel base superalloys operate in high temperature environment, the application of thermal barrier coating (TBC) is inevitable for thermal protection. TBCs generally consist of Y_2O_3 stabilized ZrO_2 top-coat, nickel aluminide (NiAl) bond coat and thermally grown oxide layer (α-Al_2O_3) between the bond coat and top-coat. NiAl bond coat is the most critical component of TBCs due to the protection the substrate from oxidation and corrosion. In this context, microstructural features and phase type of NiAl bond coat are essential for TBCs lifetime.**

Aluminizing process with chemical vapor deposition techniques is called chemical vapor aluminizing (CVA). CVA process is used for NiAl bond coat production at high temperatures which are between 850-1100°C. During the CVA process, aluminum diffuses into the substrate and forms NiAl bond coat. NiAl bond coat is produced under three different conditions with CVA technique which are high temperature (at temperatures higher than 1000°C)-high activity (HTHA), low temperature (at temperatures below than 1000°C)-high activity (LTHA), high temperature-low activity (HTLA). NiAl bond coat can include different phases such as γ'-Ni_3Al, δ-Ni_2Al_3, β-NiAl due to the CVA process temperature and activity. However, β-NiAl is desired phase among these phases due to its high melting point (1638°C) and more ductile feature. Generally, Al-rich brittle δ-Ni_2Al_3 phase formed with high activity process is transformed into desired β-NiAl phase by HT process. This study aims to examine the effect of HT process on the microstructure, type of formed phases and hardness of the HTHA nickel aluminide coating on CM247LC in this study.

Method: **NBS CM247LC was used for base metal. Before coating process, surface preparation techniques (grinding and polishing) were applied to disk-shaped CM247LC specimen. The specimen was coated with HTHA CVA method to produce NiAl coating on CM247LC. CVA process was carried out for 4 hours at 1070°C. During the coating process, Ar and HCl gases were send to CVA reaction chamber. After CVA process was completed, HT process of 4 hours CVA coating was performed in CVD reactor at 1050°C for 2 hours under the conditions of argon atmosphere and atmospheric pressure. Al-Cr (50 wt% Al – 50 wt% Cr) granules were used for Al source. After the coating and HT processes were completed, NiAl coatings were systematically characterized by SEM (scanning electron microscope, Philips XL30S FEG), XRD (X-ray diffraction, Rigaku Smartlab), EDS (Energy Dispersive X-ray spectroscopy), Vickers hardness analyze techniques. The hardness measurements of the aluminide coatings were performed by the under 10g load.**

Results: **SEM cross-sectional microstructures of the NiAl coatings before and after HT are given in Fig. 1. NiAl coatings are composed of two different layers which are the additive layer and inter-diffusion zone (IDZ). IDZ occurs due to the phase transformation from γ + γ' to NiAl structure. The overall and IDZ thickness of 4 hours CVA coating are 46,51 µm and 20,56 µm, respectively. HT process at 1050°C for 2 hours increases the thickness of the 4 hours CVA coating due to the formation of IDZ. The overall and IDZ thicknesses of 4 hours CVA coating after HT process are 53,41 µm and 27,46 µm, respectively. IDZ layers of the coating before and after HT process are rich with precipitate forming elements such as W, Co, Ta and include intermetallic precipitates. The main phase of the additive layer of 4 hours CVA coating is Al-rich δ-Ni_2Al_3. However, the phase of the additive layer of 4 hours CVA coating after HT is β-NiAl. The matrix of IDZ layers of all coatings compose of Ni-rich NiAl phase due to the outward diffusion of Ni element during the coating and HT processes. The hardnesses of the additive layers of 4 hours CVA coatings before and after HT process are 721 HV and 505 HV, respectively. The hardnesses of the IDZ layers of 4 hours CVA coating before and after HT are higher than 1000 HV.**

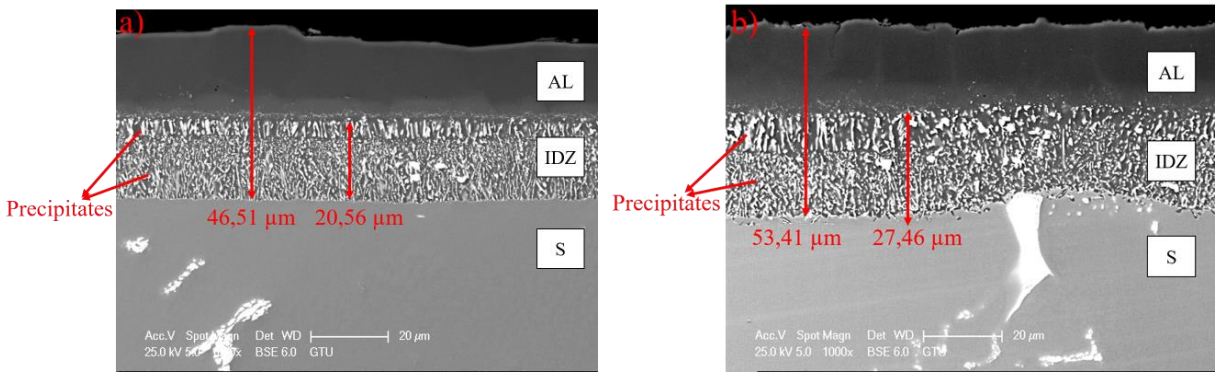


Fig. 10. SEM cross-sectional microstructures of HTHA NiAl coatings; a) 4 hours CVA coating, b) 4 hours CVA coating after HT (AL: additive layer, IDZ: Inter-diffusion zone, S: substrate).

Conclusion: **In this study, the effect of HT process on nickel aluminide coating was investigated. The following conclusions can be drawn from this study:**

(1) The IDZ layer forms not only during CVA coating process but also during the HT process.

(2) HT process induces to increase the IDZ thickness of 4 hours CVA coating due to the more Ni outward diffusion.

(3) HT process causes the phase transformation from δ-Ni_2Al_3 to desired β-NiAl owing to the more Ni outward and Al inward diffusion.

(4) The hardness of the additive layer of 4 hours CVA coating reduces after HT process because of the phase transformation phenomena.

Keywords— chemical vapor aluminizing (CVA), nickel aluminide bond coat, nickel-based superalloys, heat treatment.

The use of low-cost technique to prepare pure TiO_2 thin films

Youssef DOUBI
ERDyS laboratory, MEEM & DD Group Hassan II University of Casablanca Mohammedia, Morocco
LCOMS University of Lorraine Metz, France
youssef.doubi@univ-lorraine.fr

Bouchaib HARTITI
ERDyS laboratory, MEEM & DD Group Hassan II University of Casablanca Mohammedia, Morocco
bhartiti@yahoo.fr

Maryam SIADAT
LCOMS University of Lorraine Metz, France
maryam.siadat@univ-lorraine.fr

Hicham LABRIM
Science of Materials Unit / DESCNESTEN Rabat, Morocco
hichamlabrim@yahoo.fr

Salah FADILI
ERDyS laboratory, MEEM & DD Group Hassan II University of Casablanca Mohammedia, Morocco
safadili@yahoo.fr

Mounia TAHRI
UGPC/DSTE/DERS CNESTEN Rabat, Morocco
mounia.tahri@gmail.com

Amine BELFHAILI
Centre for Electron Microscopy Faculty of Sciences, Mohammed V University Rabat, Morocco
amine.belfhaili@gmail.com

Philippe THEVENIN
LMOPS University of Lorraine Metz, France
philippe.thevenin@univ-lorraine.fr

Abstract*— The realization of the sensitive layer of a gas sensor is a very significant stage in technology of the sensing one. In this work we made an elaboration of the sensitive layer of gas sensors device produced by spray pyrolysis. We investigated the structural and optical proprieties of pure TiO_2 with the techniques of characterization such as diffraction of X-ray (XRD), Spectroscopy Raman and UV-Visible spectrophotometer. The preferential orientation of TiO_2 at (101) plane shows the good crystallization of TiO_2 anatase with crystallite size equal 20.34 nm and low dislocation density. The vibration modes in Raman spectra confirm the formation of TiO_2 with a single phase. All TiO_2 thin films has a good optical propriety with a high value of transmittance in the visible wavelength. The TiO_2 band gap decrease from 3.42 to 3.28 eV with the TiO_2 solution flow increase from 1 to2 ml /min. These TiO_2 results suitable for sensor applications.

Keywords*—Sensitive layer, Anatase, band gap, crystallite size, sensor

[1] INTRODUCTION

Titanium oxide TiO_2 is a semiconductor with interesting physico-chemical properties, particularly due to its high chemical stability in a basic medium and its photo-catalytic activity. Titanium dioxide is characterized in three crystal structures: rutile, anatase and brookite and more rarely the bronze variety (TiO_2-B). TiO_2 is used in a wide variety of finished products such as paints, cosmetics (sun creams, toothpastes, etc.), medicines, foodstuffs and construction products (building and public works). In micrometric form, titanium dioxide dust is a source of ocular irritation and mechanical irritation of the respiratory tract. In nanometric form, TiO2 does not appear to be allergenic on the upper layer of the skin, but it may potentiate another allergen [1].

TiO_2 can be using in gas sensor application, the gas sensor it is a device that detects the presence of one or more types of gas in an environment, typically as part of a safety system. TiO2 plays the most important role in gas sensors, it is the sensitive layer to detect the polluting elements in the environment. In literature the TiO_2 was applicated to monitoring ammonia [2], application to SO_2 [3] and for hydrogen detection [4]

The TiO2 thin films can be prepared by a lot techniques such as: Sputtering magnetron [5], atomic layer deposition (ALD) [6], Sol gel associated to spin coating [7] and dip coting [8], epitaxy by molecular beam (MBE) [9], micro-emulsion technique [10], spray pyrolysis [11], etc.

In this paper we elaborated the TiO2 thin films by spray pyrolysis with various solutions flow. The spray pyrolysis is a chemical technique, manufacturing the samples at low cost and simple to using. The TiO_2 thin films were prepared and characterized by X-ray diffraction, Raman spectroscopy and UV-visible spectrophotometer. The structural properties show the phase of TiO_2 thin films with a good crystallization. The Raman spectroscopy confirms this anatase phase of TiO_2 with a vibration's modes at 144, 396, 518 and 637 cm^{-1}. The optical properties were carrier out and the films have a high transparency and logical variation with various solutions flow.

[2] MATERIALS AND METHODS

TiO_2 thin films were prepared by Spray Pyrolysis (SP) technique, as illustrated in the schematic Fig.1. TiO2 solution was prepared by dissolving Titanium (IV) propoxide in a mixing of Ethanol (EtOH). The solution was of yellow color and and was pulverized by compressed air. The TiO2 solution deposited at three flow such as: 1, 1.5 and 2 ml/min. The distance between the spray nozzle heads and the substrate was maintained at 40 cm. The thin films were prepared with a spray duration of 15 minutes onto ordinary glass. The substrates are ordinary glass (borosilicate) with a square surface 2 x 2 cm^2 and a thickness equal to 1 mm. The choice of glass is due to the economic criterion and it makes it possible to carry out a good optical characterization of the thin layers which adapts well for their transparency. The substrates are washed with a mixture of methanol and acetone boiling for 10 min and rinsed with distilled water.

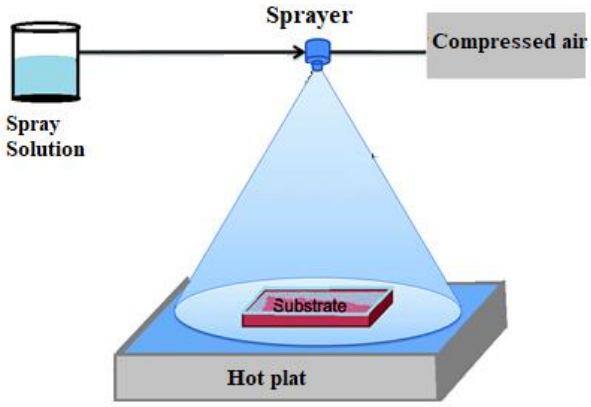


Fig. 1. Schematic illustration of the spray pyrolysis technique with various components

The TiO_2 thin films were characterized by X-ray diffraction technique (XRD) equipped by wavelength of Cu Ka (λ= 0,15406 nm), Raman measurement with frequency ranged between 100 to 1000 cm^{-1} and UV–visible Spectrophotometer with the wavelength ranged between 290 and 1000 nm.

[3] Results and discussions

A. *Structural propreties*

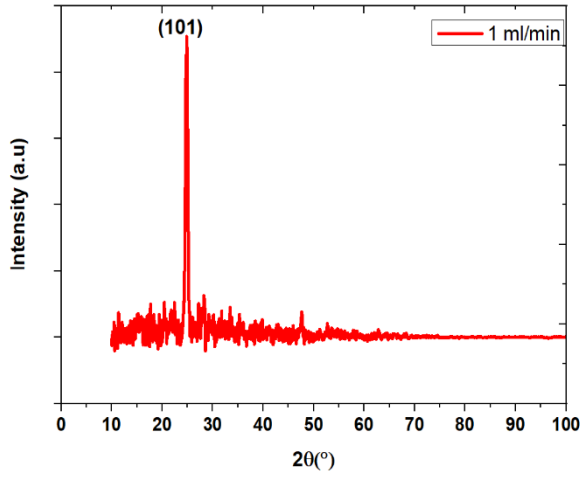


Fig.2. Typical X-ray diffraction of pure TiO2 thin film prepared at flux equal 1ml/min

Fig.2 presented the X-ray diffraction patterns TiO_2 thin films elaborated by spray pyrolysis. Broad peak was located at 2**θ** around matching to (101) plane, the high intensity of peak located at 25.12° showed a privileged direction along (101) plane. According to (JCPDS:00-004-0477) all peaks existed in Fig.2. were proved the formation of pure TiO_2 with tetragonal structure (anatase phase of TiO_2). Our TiO_2 results are similar to the reported using RF magnetron sputtering with oxygen flow rate [12] and better than M Ben Karoui et al,[13]. Crystallite size (D) of TiO_2 thin films was approximated from Debye Scherrer's relation and dislocation density were used in previous works [14]. In this study the crystallite size of the sample prepared by solution flow 1ml/min equal 20.34 nm and the density of dislocation equal 0.155 x 10^{-4} nm^{-2}, the good crystallite size of thin films materials indicate smaller dislocation quantity [15].

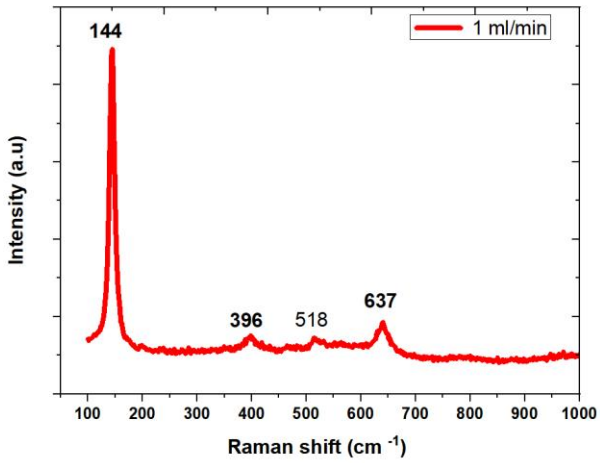


Fig.3. Raman spectra of anatase TiO_2 prepared by spray pyrolysis at 1 mL/min

Fig.3 presented the Raman spectra of the TiO_2 thin films prepared by spray pyrolysis. The vibrations modes confirm the phase formation of TiO_2 anatase, this result is similar to other one of TiO_2 prepared for photocatalytic application [16].

B. *Optical properties*

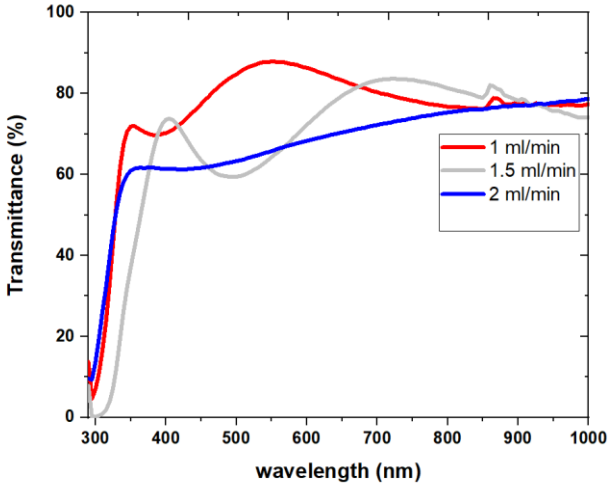
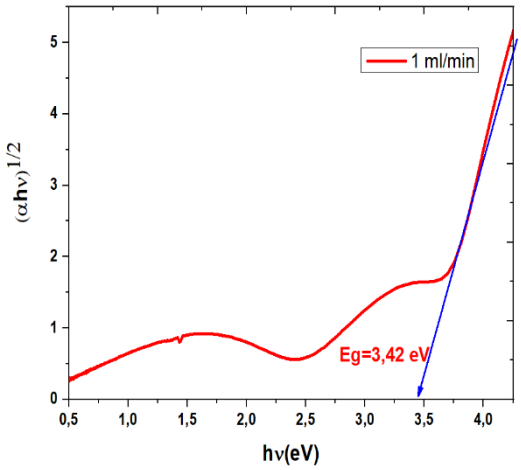
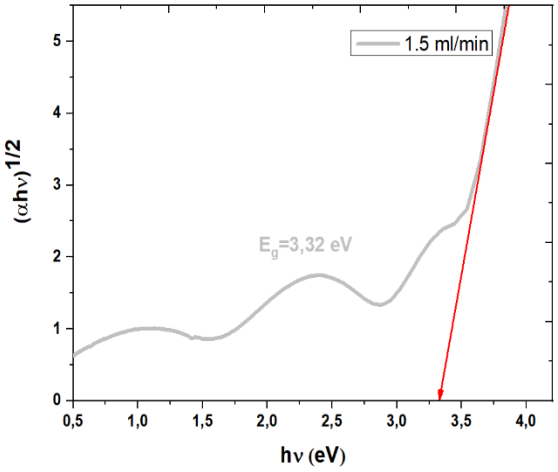


Fig.4. Transmittance spectra of pure TiO_2 elaborated by spray pyrolysis at various solution flow 1, 1.5 and 2 mL/min

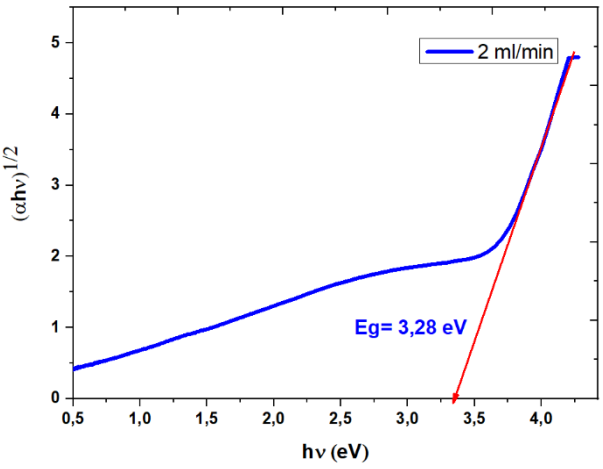
Fig.4 shows the transmittance spectra of TiO_2 thin film. The pure TiO_2 have a high transmittance value nearly to 90% in the visible wavelength for the sample prepared at 1 ml/min. The transmittances of TiO_2 thin films decreases with increasing of TiO_2 solution flow from 1, 1.5 and 2 ml/min are 90%, 80%, and 70% respectively, this behaviour is due to the more absorption of incident photon energy from TiO_2 thin films when the solution flow was increased. Additionally, the decreasing of transmittance with increasing of solution flow proves the increasing of TiO_2 densities, these results are comparable to obtained one in literature [17]



(a)



(b)



(c)

Fig.5. Band gap of TiO_2 prepared by spray pyrolysis by various solutions flows : (a) 1 ,(b) 1.5 and (c) 2mL/min

The optical band gap was determined by extrapolation of the linear region from the $(\alpha h\upsilon)^{1/2}$ versus $h\upsilon$ shown in Fig.5. The optical band gaps are 3.42, 3.32 and 3.28 eV for TiO_2 samples deposited at various solution flow 1, 1.5 and 2 mL/min respectively, the band gap decreases with increasing of solution flow, these results are probably due to the increasing of TiO_2 density when solution flow increased. These results are similar to literature [18, 19].

[4] CONCLUSION

This paper proves the synthesis possibility of pure TiO_2 thin films using spray pyrolysis on ordinary glass substrates. The as-deposited films exhibited a tetragonal structure with (101) preferential orientation. The good crystallization of TiO_2 was proved by crystallite size equal a 20.34 nm and low dislocation density about 0.155 x 10^{-4} nm^{-2}. The apparition of TiO_2 vibration modes confirm the TiO_2 formation with a single phase of anatase. The average transmittances of the samples is near to 90% in the visible wavelength and decrease with decreasing of TiO_2 solution flow. The optical band gap decreases from 3.42 to 3.32 eV for the TiO_2 samples prepared at 1 to 1.5 ml/min and from 3.32 to 3.28 eV for 1.5 to 2ml/min, these results may be due to densification of TiO_2 thin films and increasing of films thickness. The TiO_2 thin films prepared in this work have a good optical and structural properties for potential applications in sensor devices.

ACKNOWLEDGMENT

This research paper is performed with the support of the Franco-Moroccan PHC Toubkal program.

REFERENCES

[1] Online site-web : Dioxyde de titane (TiO_2) et risque de cancer | Cancer et environnement (cancer-environnement.fr)

[2] Karunagaran, B., Uthirakumar, P., Chung, S. J., Velumani, S., & Suh, E.-K. (2007). TiO2 thin film gas sensor for monitoring ammonia. Materials Characterization, 58(8-9), 680–684.

[3] Nisar, J., Topalian, Z., De Sarkar, A., Österlund, L., & Ahuja, R. (2013). TiO2-Based Gas Sensor: A Possible Application to SO2. ACS Applied Materials & Interfaces, 5(17), 8516–8522.

[4] Li, Z., Yao, Z., Haidry, A. A., Plecenik, T., Xie, L., Sun, L., & Fatima, Q. (2018). Resistive-type hydrogen gas sensor based on TiO2: A review. International Journal of Hydrogen Energy.

[5] Zhao, Y.-X., Han, S., Yi, H. L., Hu, C.-H., Hua, L.-Y., Chin, T. L., … Weng, K. W. (2017). Photocatalytic properties of TiO 2 films prepared by bipolar pulsed magnetron sputtering. Surface and Coatings Technology, 320, 630–634.

[6] Hackler, R. A., Kang, G., Schatz, G. C., Stair, P. C., & Van Duyne, R. P. (2018). Analysis of TiO2 Atomic Layer Deposition Surface Chemistry and Evidence of Propene Oligomerization using Surface-Enhanced Raman Spectroscopy. Journal of the American Chemical Society.

[7] Patil, K. ., Sathaye, S. ., Khollam, Y. ., Deshpande, S. ., Pawaskar, N. ., & Mandale, A. . Preparation of TiO2 thin films by modified spin-coating method using an aqueous precursor. Materials Letters, (2003). 57(12), 1775–1780.

[8] Malnieks, K., Mezinskis, G., & Pavlovska, I. (2016). Effect of Different Dip-Coating Techniques on TiO2 Thin Film Properties. Key Engineering Materials, 721, 128–132.

[9] Malnieks, K., Mezinskis, G., & Pavlovska, I. Effect of Different Dip-Coating Techniques on TiO2 Thin Film Properties. Key Engineering Materials, (2016), 721, 128–132.

[10] Anukunprasert, T., Saiwan, C., & Traversa, E. (2006). Microstructure effect of nanocrystalline titanium dioxide prepared by microemulsion technique on photocatalytic decomposition of phenol. Journal of Materials Research, 21(12), 3001–3008.

[11] Aji, B. B., Shih, S. J., & Pradita, T. Controlled crystal phase of TiO2by spray pyrolysis method. Journal of Physics: Conference Series (2017), 817, 012021

[12] Shakoury, R., & Zarei, A.. Optical and Structural Properties of TiO2 Thin Films Deposited by RF Magnetron Sputtering. Silicon (2018)

[13] M Ben Karoui, Z Kaddachi and R Gharbi. Optical properties of nanostructured TiO2 thin films, Journal of Physics: Conference Series 596 (2015) 012012

[14] Y. Doubi, B. Hartiti, L. Hicham et al., Effect of annealing time on

structural and optical proprieties of TiO2 thin films elaborated by spray pyrolysis technique for future gas sensor application, Materials Today: Proceedings (2020).

[15] D. Naveena, L. Thirumalaisamy, R. Dhanabal K. Sethuraman, and A. C. Bose, ACS Applied Energy Materials (2020), 3, 11, 10550-10559

[16] Dundar, I., Krichevskaya, M., Katerski, A., & Acik, I. O.TiO2 thin films by ultrasonic spray pyrolysis as photocatalytic material for air purification. Royal Society Open Science (2019). , 6(2), 181578

[17] Li, Q., Qi, J., Song, J., Zhu, L., & Zhao, Y. The optical and electrical properties regulation of TiO2 mesoporous thin film in perovskite solar cells. Journal of Materials Science: Materials in Electronics, (2020).

[18] [A. Elfanaoui, A. Ihlal, A. Taleb, L. Boulkaddat, E. Elhamri, M. Meddah, K. Bouabid and X. Portier, The synthesis of TiO2 thin film by Chemical Bath Deposition (CBD) method, J. CONDENSED MATTER VOLUME 13, NUMBER 3 DECEMBER 2011 MJCM, VOLUME 13, NUMBER 3, 2010.

[19] I. Sta, M. Jlassi, M. Hajji, M.F. Boujmil, R. Jerbi, M. Kandyla, M. Kompitsas, and H. Ezzaouia, Structural and optical properties of TiO2 thin films prepared by spin coating, Journal of Sol-Gel Science and Technology 72, 421 (2014)

A DFT study of Electronic and optical properties of Si-doped ZnS for solar device

Abdessamad Najim
ERDyS Laboratory, MEEM & DD Group *Hassan II University of Casablanca* Casablanca, Morocco
najimabdessamad95@gmail.com

Bouchaib Hartiti
ERDyS Laboratory, MEEM & DD Group *Hassan II University of Casablanca* Casablanca, Morocco
b.hartiti@univh2m.ac.ma

Mehmet Ertugrul
Faculty of Engineering, Department of Electrical and Electronics Engineering
Atatürk University Erzurum, Turkey
ertugrul@atauni.edu.tr

Labrim Hicham
Centre National de l'Energie, des Sciences et des Techniques Nucléaires
Rabat, Morocco
hichamlabrim@yahoo.fr

Salah Fadili
ERDyS Laboratory, MEEM & DD Group *Hassan II University of Casablanca* Casablanca, Morocco
safadili@yahoo.fr

Philippe Thevenin
University of Lorraine, LMOPS Metz, France
philippe.thevenin@univ-lorraine.fr

***Abstract*— Based on density functional theory (DFT), an electronic structure calculation implemented for pure and doped ZnS by Si, using the PBEsol-GGA approximation. This study shows that Si-doped ZnS changes from semiconductor to metal. However by increasing the concentration of doping Si to ZnS the absorption coefficient and the cut-off decrease.**

Keywords—ZnS, PBEsol-GGA, Band Structure, doped, DFT

[1] INTRODUCTION

The ZnS is among the semiconductors used in different application such us, solar cells [1] [2] and nano-optoelectronic [3] [4]. The zinc blende ZnS structure with a direct band gap of 3,6 [1]. Several work have been interested to improve the properties of ZnS by doping element such us Pb [1], Cu [3], Al [5], Mn [6], and Co [7]. Absike et al. [1] studied theoretically Si-Pb doped and co-doped of ZnS with different concentrations x=3.125%, 6.25% and 12.5% using GGA and mBJ. The bandgap has been found that is decreased from 3.6 to 1.41, 1.38, for 6.25% of Si and Pb doping. Wu et al. [5] fond that doping by Al changes ZnS from semiconductor into metal. In recent year, the reported study on Si doped ZnS are investigated using GGA and mBJ with different concentration x=3.125%, 6.25% and 12.5% [1]. In this paper, electronic structure and optical characteristics of Si doped ZnS by Perdew−Burke−Ernzerhof GGA modified for solids (PBEsol-GGA), has not reported to the best of our available knowledge. In this study, based on the density functional theory (DFT), we studied ZnS with and without Si-doping.

[2] COMPUTATIONAL METHODS

The ground state properties were obtained using the FP-LAPW approach within the framework of DFT, as implemented in the WIEN2k code [8]. We have used the PBEsol-GGA [9] [10] for the electronic and optical properties in this calculation. The atomic spheres of muffin tin radius named usually by (RMT) which are optimized at 2.42 and 1.98 units (a.u.) for Zn and S atoms respectively. The energy cutoff has been chosen to be Kmax×RMT = 8 where Kmax is the heightest value of the reciprocal lattice vectors employed in the plane wave expansion. This parameter controls the size of the basis sets in the calculations. The coordinates of atoms and the lattice parameters of Zn(1-x)SixS (x=0%, x=8% and 12.5%) have been completely relaxed before calculating electronic structure. We have been fixed at −6.0 Ry the separation between the core and a valence state wich usully designed by the cut-off energy. The energy cutoff parameter R×Kmax egual to 7, where R is the average radius of the muffin-tin (MT) spheres, and Kmax is the cutoff for the wave function basis. For several Si doping concentration, three different ZnS supercells (1×1×3 and 1×1×2) have been discussed. Here, one Zn atom was replace with one Si atom for a doping concentration of 8% and 12.5% respectively. The Monkhorst-Pack grids of 12×12×12, 11×11×3 and 10×10×5 have been used for Brillouin zone sampling whiting the doping concentration of 8.3% and 12.5% respectively. The total energy has been used to 10-5 Ryd/unit cell in the current study.

[3] RESULTS AND DISCUSSIONS

A. *Structural Properties*

Our calculation scheme are implemented to a zinc blend ZnS, the positions atoms are Zn (0,0,0) and S (1/4,1/4,1/4), which are obtained by a series of calculation for cell relaxation under Win2k [11] [8], this method is based on the equation of Birch Murnaghan to determine the optimal value of the volume for pure and Si doped ZnS and to get the optimum lattice parameters. Fig.1 shows the calculated total energy fitted with Murnaghan equation [11], versus volume according to Zn(1-x)SixS (x=0, 0.08, 0.12). The values of the lattice parameters, the bulk modulus B(Gpa) and its derivatives B' are provided in table.1

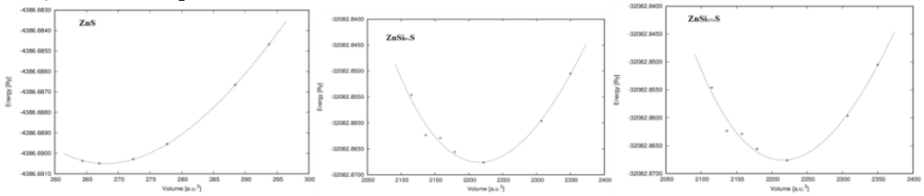


Fig.1. The variation of total energy as a function of volume for $Zn_{(1-x)}Si_xS$ (x=0,8%,12%).

Table 1. the lattice constants a, Bulk modulus B(GPa), and its Pressure Derivative B' of ZnS, $ZnSi_{8\%}S$ and $ZnSi_{12\%}S$

	a(A)	*B(Gpa)*	*B'*
ZnS	5.4153	86.1063	6.4894
$ZnSi_{8\%}S$	5,2917	134.0152	25.7080
$ZnSi_{12\%}S$	5,2917	69.8220	5.9406

B. Density of states and bands structure

Based on the relaxed structural parameters, the electronic structure, including the band structure, density of states (DOS) and partial density of state (PDOS), of pure and Si doped ZnS are determined by using the PBEsol-GGA [9] [10] realized in WIEN2k code [11] [8]. From Figure 2, we fund from the band structure of pure ZnS has direct band gap 1.93 eV, is mainly caused by the charge transfer between the p orbital of S and d orbital of Zn. From Figure 3 and Figure 4, the doped ZnS with Si at 8% and 12% shows a transfert of pure ZnS from semiconductor into metal, because of a charge transfer between the p orbital of Si and p orbital of S, also on the valence band is dominated by Zn-d and S-p and Si-p states.

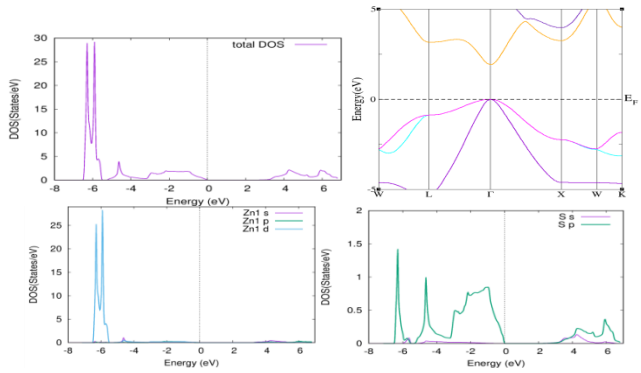


Fig.2. Energy Band structure, DOS and PDOS of ZnS.

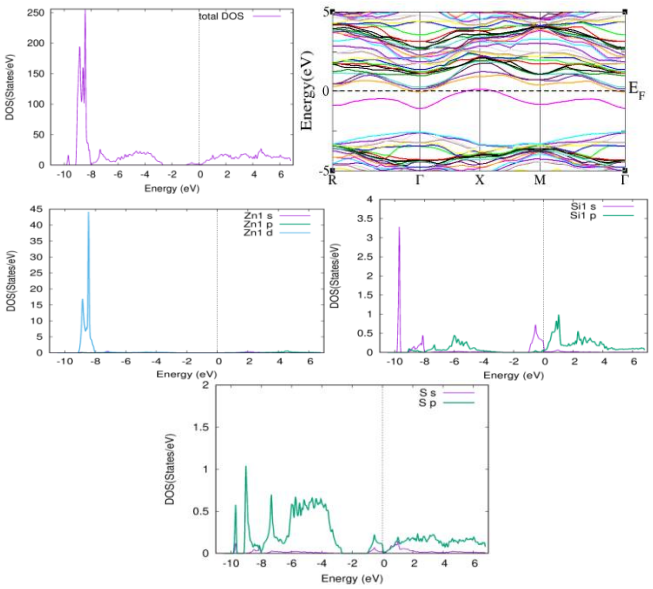
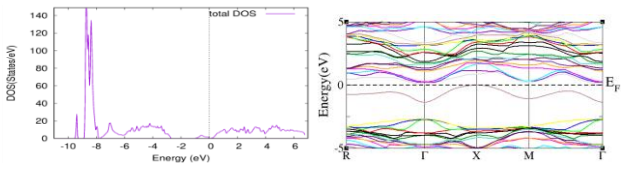


Fig. 3. Energy Band structure, DOS and PDOS of ZnSi(8%)S.



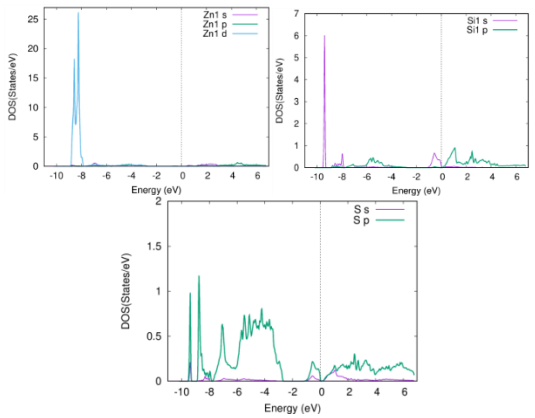


Fig. 4. Energy Band structure, DOS and PDOS of ZnSi(12%)S.

C. Optical properties:

Using the dielectric function given by [12] $\varepsilon(\omega)=\varepsilon1(\omega)+i\varepsilon2(\omega)$, the dielectric function enables us to draw the absorption coefficient. From figure 5, we have traced the absorption coefficient for Zn(1-x)SixS (x=0,8%,12%). The highest value is located at ~8 eV for ZnS, ZnSi8%S and ZnSi12%S.

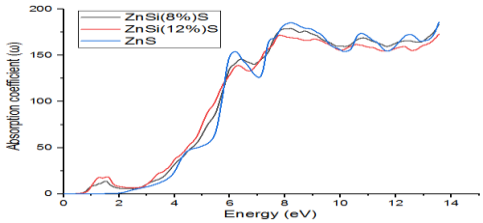


Figure 5. Absorption coefficient of ZnS, $ZnSi_{8\%}S$ and $ZnSi_{12\%}S$

[4] C

ONCLUSION

The electronic structures and optical characteristics of silicon-doped ZnS systems were studied using the pseudo plane wave potential method. A series of ZnS supercell models were constructed and the band structure, DOS and PDOS of doped and pure ZnS systems were calculated and analyzed. The results show that an obvious variation and narrow energy gap. The DOS of the doped Si atoms affect the bandgaps. In addition, the optical characteristics of ZnS systems have been analyzed. The diminution of the absorption coefficient and the cut-off of the absorption are obtained with the augmentation of the Si doping concentration in the ZnS system.

REFERENCES

[1] H. Absike, H. Labrim, B. Hartiti, K. Douhou, and H. Ez-Zahraouy, "Ab initio calculations on electronic, optical, and thermoelectric properties of (Si, Pb) (co)-doped ZnS for solar cell device applications," *J. Phys. Chem. Solids*, vol. 132, pp. 10–17, Sep. 2019, doi: 10.1016/j.jpcs.2019.03.030.

[2] S. S. Yesilkaya, U. Ulutas, and H. M. A. Alqader, "Effect of Na doping on the properties of ZnS thin films and ZnS/Si heterojunction cells," *Mater. Lett.*, vol. 288, p. 129347, Apr. 2021, doi: 10.1016/j.matlet.2021.129347.

[3] C. Liu *et al.*, "Cu-doping ZnO/ZnS nanorods serve as the photoanode to enhance photocurrent and conversion efficiency," *Microelectron. Eng.*, vol. 103, pp. 12–16, 2013, doi: 10.1016/j.mee.2012.09.006.

[4] S. Kim *et al.*, "Highly luminescent InP/GaP/ZnS nanocrystals and their application to white light-emitting diodes," *J. Am. Chem. Soc.*, vol. 134, no. 8, pp. 3804–3809, 2012, doi: 10.1021/ja210211z.

[5] A. L. Wu, L. Guan, T. K. Gu, and P. Y. Feng, "Study on electronic and optical properties of Al-doped ZnS from density function theory," *Adv.*

Mater. Res., vol. 734–737, pp. 2405–2410, 2013, doi: 10.4028/www.scientific.net/AMR.734-737.2405.

[6] M. Hassan, N. A. Noor, Q. Mahmood, and B. Amin, "Investigation of ferromagnetic semiconducting and opto-electronic properties of Zn1−xMnxS ($0 \leq x \leq 1$) alloys: A DFT-mBJ approach," *Curr. Appl. Phys.*, vol. 16, no. 11, pp. 1473–1483, 2016, doi: 10.1016/j.cap.2016.08.014.

[7] Q. Mahmood, S. M. Alay-e-Abbas, M. Hassan, and N. A. Noor, "First-principles evaluation of Co-doped ZnS and ZnSe ferromagnetic semiconductors," *J. Alloys Compd.*, vol. 688, pp. 899–907, 2016, doi: 10.1016/j.jallcom.2016.07.302.

[8] K. Schwarz, P. Blaha, and G. K. H. Madsen, "Electronic structure calculations of solids using the WIEN2k package for material sciences," *Comput. Phys. Commun.*, vol. 147, no. 1–2, pp. 71–76, 2002, doi: 10.1016/S0010-4655(02)00206-0.

[9] J. P. Perdew *et al.*, "Restoring the density-gradient expansion for exchange in solids and surfaces," *Phys. Rev. Lett.*, vol. 100, no. 13, 2008, doi: 10.1103/PhysRevLett.100.136406.

[10] J. P. Perdew, K. Burke, and M. Ernzerhof, "Generalized gradient approximation made simple," *Phys. Rev. Lett.*, vol. 77, no. 18, pp. 3865–3868, 1996, doi: 10.1103/PhysRevLett.77.3865.

[11] V. Tyuterev and N. Vast, "Murnaghan's equation of state for the electronic ground state energy," *Comput. Mater. Sci.*, vol. 38, pp. 350–353, Dec. 2006, doi: 10.1016/j.commatsci.2005.08.012.

[12] "Ambrosch-Draxl, C.; Sofo, J. O. Linear Optical Properties of Solids within the Full-Potential Linearized Augmented Planewave Method. Comput. Phys. Commun. 2006,175,1−14

Copper oxide thin films on silicon substrate by Pulsed Laser Deposition

Mustafa Tolga Yurtcan
Department of Nanoscience and Nanoengineering, Atatürk University
Erzurum, Turkey
yurtcan@atauni.edu.tr

Gökhan Uygur
Department of Nanoscience and Nanoengineering, Atatürk University
Erzurum, Turkey
gokhanuygur87@gmail.com

***Abstract*— Pulsed Laser Deposition technique was used in order to deposit copper oxide thin films onto silicon substrates. Without RCA cleaning depositions were not successful. Copper oxide has three different phases and single-phase CuO thin film depositions was not possible. Best result achieved at 300 °C and 100 mTorr without any Cu_4O_3 phase, confirmed by XRD. Film thickness was about 400-460 nm and average arithmetic mean roughness was calculated as 2.19 nm.**

Keywords—copper oxide, PLD, thin film

[1] INTRODUCTION

Copper oxide is a non-toxic, low cost semiconductor with a common component, Cu [1]. Copper oxides are used in gas sensors [2], biosensors, thin film transistors, capacitors [3], CO oxidation [4], solar cells, magnetic storage devices, lithium batteries [5], dye molecule breakdown, photochemical applications [6], optoelectronic devices [1], antibacterial surface production [7], dry and liquid batteries, and superconductor applications [3], [8].

Thin film copper oxide production methods are collected under two main headings: Chemical Vapor Deposition (CVD) and Physical Vapor Deposition (PVD). With the CVD method, it is ensured that the material that turns into gas phase because of chemical reaction in vacuum environment is deposited on the substrate. In CVD method, heat is not given from outside, heat is released because of chemical reaction. In the PVD method, the material to be coated is evaporated by ion bombardment or heating in a vacuum environment and transported onto the substrate.

Within the scope of this study, pulsed laser deposition (PLD) method used to deposit copper oxide thin films on p-Si(100) substrates and it has been tried to be determined, how CuO/Si thin films are affected by temperature and pressure parameters with XRD, SEM and AFM analysis.

[2] MATERIALS AND METHODOLOGY

A. Copper oxides

Copper oxides have two main phases as CuO-copper(II)oxide and Cu_2O-copper(I)oxide known as Cupric oxide and Cuprous oxide, respectively. In addition, there is an interphase as Cu_4O_3 [9]. CuO is monoclinic, Cu_2O is cubic and Cu_4O_3 is tetragonal [10]. Usually copper oxides are p–type semiconductors [11], but there are cases where it exhibits n-type semiconductor properties [12], [13]. Band gap of CuO varies between 1.2-1.9 eV, where Cu_2O's vary 1.8-2.5 eV [11].

To prepare the CuO target tablet, Alfa Aesar brand 99% purity copper(I)oxide powder (Fig 1.a) weighed approximately 12.5 grams (Fig 1.b) and filled into a one inch diameter die set (Fig 2.a) and pressed by a hydraulic press. Pressed pellet sintered at 900 °C [14] for 10 hours and copper(II)oxide PLD target has been prepared (Fig 2.b).



Fig. 1. a. Alfa Aesar Cu_2O powder, b. used powder



Fig. 2. a. Die set, b. CuO PLD target

B. Substrate preparation

B-doped silicon wafer (p-type) in (100) orientation was purchased commercially from MTI company with 4 inch diameter, 0.5 mm thickness, 7~13 ohm.cm resistance range and one side polished. The silicon wafer was sliced by using DAD322 brand precision slicer and turned into substrates. RCA-1, RCA-2 and RCA-3 processes applied in order to remove the organic and metallic contamination on the surface of the silicon substrate. Substrate than pasted in a glovebox in order to avoid oxidation of silicon.

C. Pulsed Laser Deposition (PLD)

Complete P180 PLD system by Neocera used for experiments [15] and all parameters except deposition temperature and pressure was fixed. Deposition temperature values were 300, 400 and 500 °C, where deposition pressure varied from 50 to 200 mTorr with 50 mTorr steps. After each experiment system cooled down to room temperature with 10

°/min to avoid cracks.

[3] RESULTS AND DISCUSSIONS

Depositions were unsuccessful before RCA cleaning process. After through RCA cleaning, copper oxide thin film deposition was successful confirmed by XRD. None of the samples was single-phase copper oxide in the given range. Best crystallinity for CuO with very low Cu_2O phase achieved with 300 °C and 100-mTorr sample without any Cu_4O_3 phase (Fig 3).

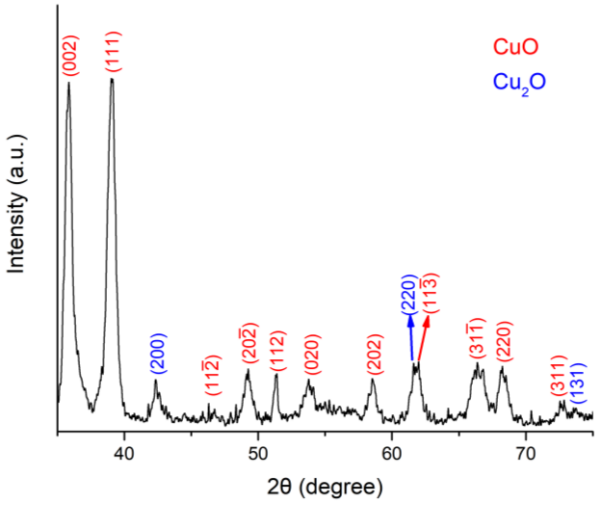


Fig. 3. XRD image of 300 °C 100 mTorr sample

Film thickness measured with a Zeiss Sigma 300 Scanning Electron Microscope, and found between 400-460 nm (Fig 5). All the sample surfaces were homogeneous and similar with different sized particles depending on the deposition pressure and temperature. None of the samples had cracks through the surfaces caused by thermal expansion coefficient difference between substrate and coating.

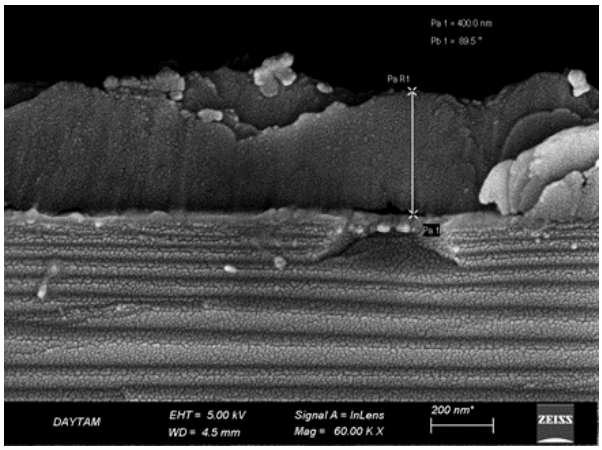
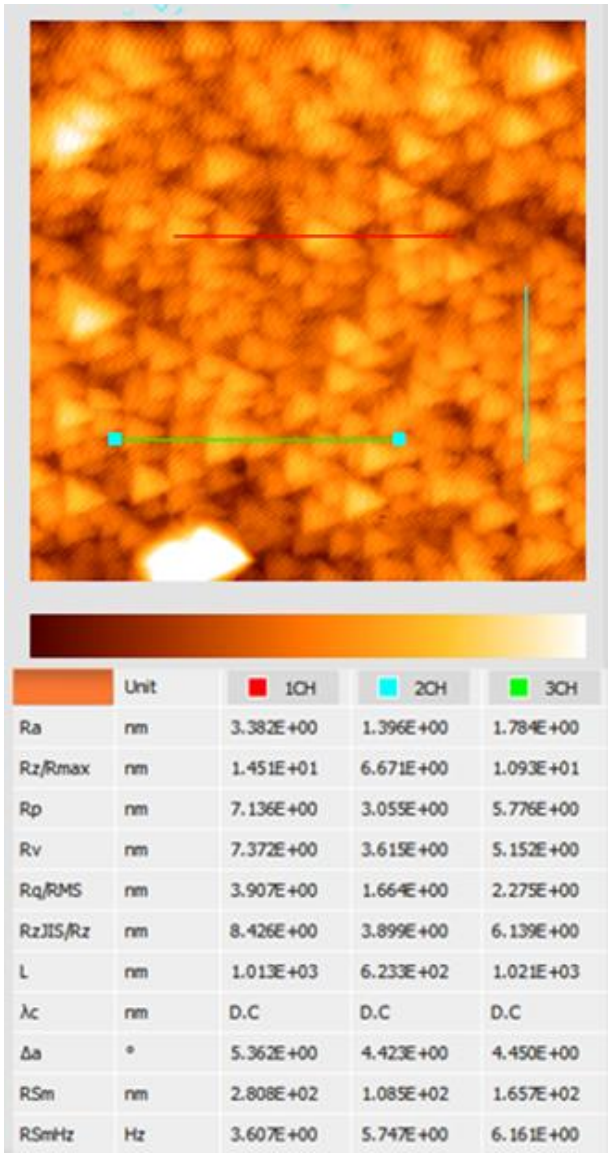


Fig. 4. Cross-section SEM image of 300 °C 100 mTorr sample

Hitachi 5100N brand AFM device used for determination of the surface roughness of the best thin film (at 300 °C, 100 mTorr). The arithmetic mean roughness (Ra) was taken along the specified red, green and blue lines and their average was calculated and found to be 2.19 nm. The maximum value between peaks and troughs were 14.5 nm (Fig 4).



	Unit	1CH	2CH	3CH
Ra	nm	3.382E+00	1.396E+00	1.784E+00
Rz/Rmax	nm	1.451E+01	6.671E+00	1.093E+01
Rp	nm	7.136E+00	3.059E+00	5.776E+00
Rv	nm	7.372E+00	3.615E+00	5.152E+00
Rq/RMS	nm	3.907E+00	1.664E+00	2.275E+00
RzJIS/Rz	nm	8.426E+00	3.899E+00	6.139E+00
L	nm	1.013E+03	6.233E+02	1.021E+03
λc	nm	D.C	D.C	D.C
Δa	°	5.362E+00	4.423E+00	4.450E+00
RSm	nm	2.808E+02	1.085E+02	1.657E+02
RSmHz	Hz	3.607E+00	5.747E+00	6.161E+00

Fig. 5. AFM image of 300 °C 100 mTorr sample

[4] CONCLUSION

Deposition on silicon was not successful before RCA cleaning process of the substrate. In the given deposition temperature and pressure range, single-phase growth was not possible for copper oxides. Best result achieved at 300 °C and 100 mTorr without any Cu_4O_3 phase. All the thin films were polycrystalline and temperature and pressure rise resulted increase of Cu_4O_3 phase in thin films.

REFERENCES

[1] B. Balamurugan and B. R. Mehta, "Optical and structural properties of nanocrystalline copper oxide thin films prepared by activated reactive evaporation," *Thin Solid Films*, vol. 396, no. 1–2, pp. 90–96, 2001, doi: http://dx.doi.org/10.1016/S0040-6090(01)01216-0.

[2] J. Pike, S.-W. Chan, F. Zhang, X. Wang, and J. Hanson, "Formation of stable Cu2O from reduction of CuO nanoparticles," *Appl. Catal. A Gen.*, vol. 303, no. 2, pp. 273–277, 2006, doi: https://doi.org/10.1016/j.apcata.2006.02.008.

[3] U. C. Bind *et al.*, "Ion implantation induced phase transformation and enhanced crystallinity of as deposited copper oxide thin films by pulsed laser deposition," *Superlattices Microstruct.*, vol. 84, pp. 24–35, 2015, doi: 10.1016/j.spmi.2015.03.064.

[4] B. White *et al.*, "Complete CO Oxidation over Cu 2 O Nanoparticles Supported on Silica Gel," *Nano Lett.*, vol. 6, no. 9, pp. 2095–2098, Sep. 2006, doi: 10.1021/nl061457v.

[5] A. Chowdhury, P. K. Bijalwan, and R. K. Sahu, "Investigations on the role of alkali to obtain modulated defect concentrations for Cu2O thin films," *Appl. Surf. Sci.*, vol. 289, pp. 430–436, Jan. 2014, doi: 10.1016/j.apsusc.2013.10.183.

[6] H. Xu, W. Wang, and W. Zhu, "Shape Evolution and Size-Controllable Synthesis of Cu2O Octahedra and Their Morphology-Dependent Photocatalytic Properties," *J. Phys. Chem. B*, vol. 110, no. 28, pp. 13829–13834, Jul. 2006, doi: 10.1021/jp061934y.

[7] R. G. B. Madera, M. M. Martinez, and M. R. Vasquez, "Effects of RF plasma treatment on spray-pyrolyzed copper oxide films on silicon substrates," *Jpn. J. Appl. Phys.*, vol. 57, no. 1S, p. 01AB05, Jan. 2018, doi: 10.7567/JJAP.57.01AB05.

[8] K. A. Aadim, A. A. K. Hussain, and M. R. Abdulameer, "Effect of Laser Pulse Energy on the Optical Properties of Cu2O Films by Pulsed Laser Deposition," *Acta Phys. Pol. A*, vol. 128, no. 2015, pp. 419–422, 2015, doi: 10.12693/APhysPolA.128.419.

[9] X. Wang, J. C. Hanson, A. I. Frenkel, J.-Y. Kim, and J. A. Rodriguez, "Time-resolved Studies for the Mechanism of Reduction of Copper Oxides with Carbon Monoxide: Complex Behavior of Lattice Oxygen and the Formation of Suboxides," *J. Phys. Chem. B*, vol. 108, no. 36, pp. 13667–13673, 2004, doi: 10.1021/jp040366o.

[10] C. R. Iordanescu *et al.*, "Structure and morphology of Cu-oxides films derived from PLD processes," *Dig. J. Nanomater. Biostructures*, vol. 6, no. 2, pp. 863–868, 2011.

[11] F. Gao, X.-J. Liu, J.-S. Zhang, M.-Z. Song, and N. Li, "Photovoltaic properties of the p-CuO/n-Si heterojunction prepared through reactive magnetron sputtering," *J. Appl. Phys.*, vol. 111, no. 8, p. 84507, 2012, doi: Artn 08450710.1063/1.4704382.

[12] L. Yu, L. Xiong, and Y. Yu, "Cu2O homojunction solar cells: F-doped N-type thin film and highly improved efficiency," *J. Phys. Chem. C*, vol. 119, no. 40, pp. 22803–22811, 2015, doi: 10.1021/acs.jpcc.5b06736.

[13] P. Samarasekara, *Characterization of Low Cost p-Cu2O/n-CuO Junction*, vol. 2. 2010.

[14] R. K. Gupta, K. Ghosh, and P. K. Kahol, "Effect of temperature on current–voltage characteristics of Cu2O/p-Si Schottky diode," *Phys. E Low-dimensional Syst. Nanostructures*, vol. 41, no. 5, pp. 876–878, 2009, doi: http://dx.doi.org/10.1016/j.physe.2008.12.025.

[15] M. T. YURTCAN, "Deposition of grid-like single-crystal Ce2O3 thin films on LaAlO3(100) substrate by pulsed laser deposition," *J. Mater. Sci. Mater. Electron.*, vol. 32, no. 3, pp. 3854–3862, Feb. 2021, doi: 10.1007/s10854-020-05129-1.

A New Technique For Fire Detection In Airplanes

Mehmet MASAT
Department of Aviation Management
Erzurum Vocational School Atatürk
University Erzurum, Turkey
mehmet.masat@atauni.edu.tr

Mehmet ERTUĞRUL
Department of Electrical and
Electronics Engineering Atatürk
University Erzurum, Turkey
ertugrul@atauni.edu.tr

***Abstract*— The aim of this study is to provide a reference document on current risks and proposed reductions for smoke and fire incidents in commercial transport aircraft. The screen printing technique was used as the gas sensor production technique for the produced sensor with tin oxide was used as metal oxide in the produced samples. The samples produced were examined under the gases with specified gas detecting properties, and it was concluded that they can be used simultaneously with smoke detectors in order to increase the detection reliability and reduce the alarm time with the smoke detectors currently used in today's passenger aircraft.**

Keywords*— Screen Printing Technique , Carbon Dioxide, Carbon Monoxide, Gas Sensor

I. INTRODUCTION

For many years, commercial aircraft operated on the principle of not leaving enough oxygen in the environment to control the risk of cargo compartment fires under the main passenger cabin. A cargo fire that caused body loss in a commercial passenger plane caused the thought that the risk of fire that may occur in the cargo section should be perceived [1].

Federal Aviation Rules (FAR) required fire detectors in B, C and E cargo compartments. According to FAR 25.857, 25.858 certification standards, the fire must be detected within 1 minute after it starts. This determination is made with smoke sensors in cargo compartments of type B, C and E [2].

Fire detectors must be able to operate reliably in environmental conditions to prevent false alarms. The cargo compartments on aircraft have only a single source fire sensor which is smoke sensors. It is known that most of the warnings given by the smoke detectors are false alerts and there are financial losses due to flight delay, flight cancellation and emergency landing situations, therefore, it is necessary to use multi-source sensors on new generation aircraft [3].

The aim of this study is to provide a reference document on current risks and proposed reductions for smoke and fire incidents in commercial transport aircraft. For this purpose, metal oxide carbon dioxide detector was produced with the screen printing technique in order to detect carbon dioxide and carbon monoxide gases from the sensors required to observe the occurrence of a fire that may occur in the aircraft and to make the necessary controls.

The purpose of choosing the screen printing technique as the sensor construction technique is to synthesize the smallest size films for gas sensor applications and to convert them into gas detectors. It is also closely related to the mechanical and electrical properties of sensitive layers which vary depending on ambient conditions.

II. EXPERIMENTAL STUDIES

A. Fabrication of Thick Film Gas Sensor

In the SnO_2 thick film gas sensor fabrication made within the scope of this thesis, the screen printing method was used and the planar structure of the thick film to be produced is given in Figure 1 .1.

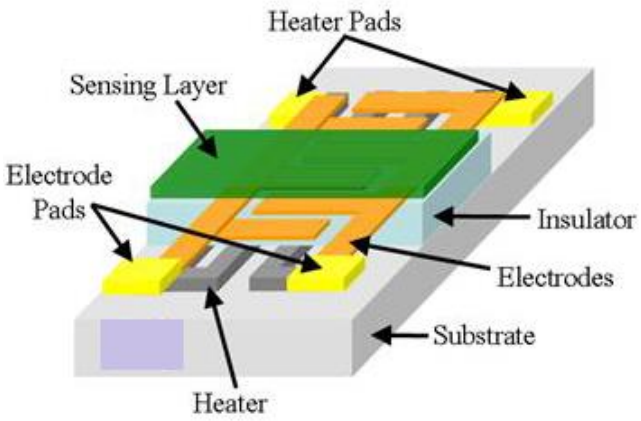


Fig. 1. Thick film gas sensor structure[5]

B. Preparation of Binder and Paste

Both of the bonding preparation techniques described in the screen printing method were used for comparison. The rates encountered in the literature study [4-7] to determine the proportions of chemicals to be used in the compounding were tested one by one, and the rates decided to be used in this thesis study are as given in Table 1.1.

Table 1. Chemicals and Ratios Used In Binder Preparation

Binder made with linseed oil		Binder made with ethyl cellulose	
	wt(%)		wt(%)
linseed oil	85	ethyl cellulose	10
m–xylene	12,5	α–terpineol	90
α–terpineol	2,5		

For the preparation of the binder, first, linseed oil and m–xylene were mixed and they subjected to magnetic stirring at 40 °C on hot plate. The stirring process was continued for about 4 hours.

After that α–terpineol was added then the temperature of was decreased to 30°C. The stirring was continued for about 2 hours to obtain a sticky liquid form binder.

Thick film gas sensor pastes usually comprise a semiconducting metal oxide powder, inorganic additives and organic binders.

In this research, tin oxide (SnO_2) was used as the base sensitive metal oxide powders.
Sensitive powder (SnO_2) was mixed with 40 wt% and binder was mixed with 60 wt% and they subjected to magnetic stirring at 40 °C on hot plate for 24 hour.

C. *Film Preparations*

The SnO_2 thick films were prepared by screen print technic using Al_2O_3 substrate. Silver electrodes were printed on an Al_2O_3 substrate. After printing the electrodes, it was kept at room temperature for 10 minutes. After this electrodes were kept at 125 °C for 10 minutes for drying. Finally electrodes were kept at 350 °C for 20 minutes for firing.

Sensitive layer was printed with sensitive paste on electrodes. After printing the sensitive layer, films were left at room temperature for 20 min to insure the paste is leveled off and settled and then the films are subjected to a drying and firing process.

The sensitive layer was dried in three steps: first it was subjected to 50°C for 5 minutes and then temperature was increased to 100 °C for another 5 minutes, and finally it was dried at peak temperature of 125 °C for last five minutes. Finally film was kept at 450 °C for 30 minutes for firing.

III. RESULTS AND DISCUSSION

A. *Measurements of SnO_2 Based Gas Sensor*

The values used during the measurement of the SnO_2 sample measured at 300 ℃ temperature are given in Table 2.1.

Table 2. Values Used During the Measurement Of The SNO_2 Sample

Temprature	300 °C
Time to measure	600 sn
External gas sweeping time	600 sn
Gas measured	CO_2
External gas	Azot (N_2)
Period (Per Ppm)	1
PPM list	1000 - 500
Voltage source level	5 V

In order to clean the environment from various gases, nitrogen gas was sent to the environment for 50 seconds during the measurement process number 1 of the SnO_2 sample. Then, measurements were taken by giving the carbon dioxide gas to be measured together with nitrogen gas at the rate of 5000, 2500 and 1000 ppm in the 50th second and shown in Figure 2.1.

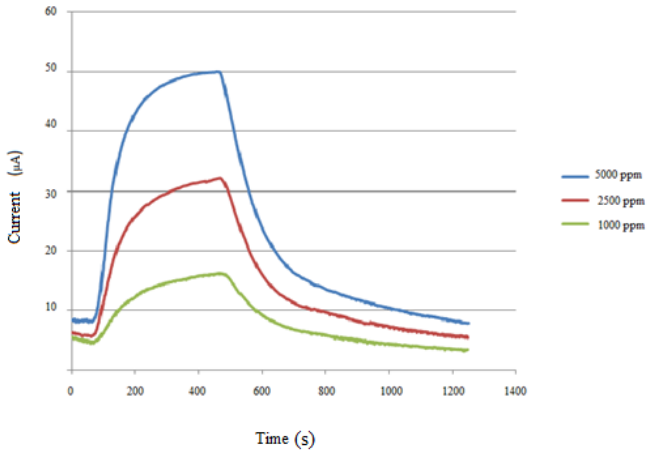


Fig. 2.1. Gas sensor measurement chart of SnO_2 sample under 5000, 2500 and 1000 ppm CO_2

In the literature search, Wang et al. Subjected the sensors they produced in their pure SnO_2 thick film gas detector study to approximately three heat treatments at different periods between 400 and 950 ° C. They made the gas sensor measurements of their samples in the temperature range of 240 ℃ - 600 ℃ and 500 ppm - 30000 ppm, and they made measurements for different ppm levels at different temperatures, and measured the resistance change depending on time [8].

The measurements of the SnO_2 sample used in this thesis were made at various CO_2 concentrations and measurement temperatures, and similar and better results were obtained with the data in this range. When the response times of the measurements were examined, it was observed that it was between 50 and 65 seconds. This observed value has been observed to meet the requirement for a fire detector that can be used in commercial aircraft, to react within 60 seconds from the start of the fire.

B. *XRD Analysis of Samples Produced With SnO_2*

The structure of the made with SnO_2 based sample produced by the screen printing method was examined by the XRD technique and is shown in the figure below.

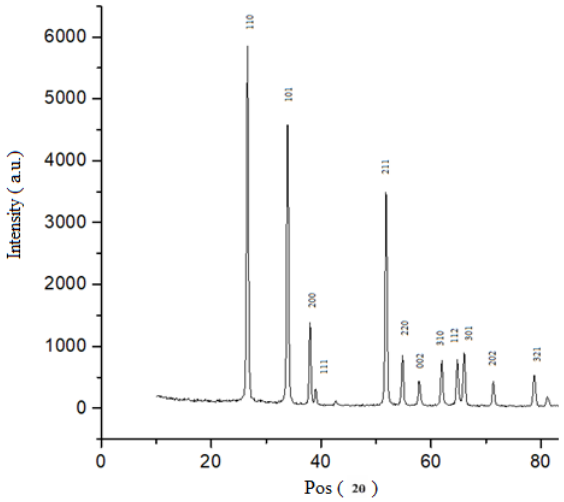


Fig. 2.2. XRD graph of the SnO_2 sample

In the graphic shown in Figure 2.2. It has been observed that it gives reflection. When these planes are compared with

other studies [9-13] and with the JCPDS 71-0652 card number XRD database phases, it was observed that they are reflective peaks of pure SnO2.

IV. CONCLUSION

At the end of the study, the SnO_2-added samples produced were examined under the gases with specified gas detection properties. When the response times of the measurements were examined, it was observed that it was between 50 and 65 seconds. This observed value has been observed to meet the requirement for a fire detector that can be used in commercial aircraft, to react within 60 seconds from the start of the fire. It was concluded that they can be used simultaneously with smoke detectors to increase detection reliability and reduce alarm time with smoke detectors currently used in today's passenger aircraft.

REFERENCES

[1] Society, R.A. Smoke, Fire and Fumes in Transport Aircraft. 2013 [cited 2019 08.12.2019]; Available from: https://flightsafety.org/files/RAESSFF.pdf.

[2] Department of Transportation, F.A.A., FAA Database of Reported Fire Related Events for all Civil Flights between 2002-2014. 2014.

[3] Smoke or Fumes Occurrences on Transport Airplanes 2017 [cited 2018 15.03.2018]; Available from: https://www.fire.tc.faa.gov/pdf/TC-16-49.pdf.

[4] Hadı Nezhad Shahrokh Abadı,M.(2010), "Development Of Nanocrystallıne Thıck Fılm Gas Sensors", Universiti Putra Malaysia.

[5] Liu, Z. and D. Chung, Low-temperature air-fireable glass-free metallic thick-film electrical conductor materials. Journal of electronic materials, 2001. 30(11): p. 1458-1465.

[6] Zhu, M. and D. Chung, Active brazing alloy paste as a totally metal thick film conductor material. Journal of electronic materials, 1994. 23(6): p. 541-549.

[7] Rane, S., et al., Firing and processing effects on microstructure of fritted silver thick film electrode materials for solar cells. Materials Chemistry and Physics, 2003. 82(1): p. 237-245.

[8] Wang, D., et al., CO2-sensing properties and mechanism of nano-SnO2 thick-film sensor. Sensors and Actuators B: Chemical, 2016. 227: p. 73-84.

[9] Bhagwat, A.D., et al., Synthesis of nanostructured tin oxide (SnO2) powders and thin films prepared by sol-gel method. 2015.

[10] Lv, P., et al., Study on a micro-gas sensor with SnO2–NiO sensitive film for indoor formaldehyde detection. Sensors and Actuators B: Chemical, 2008. 132(1): p. 74-80.

[11] Chaparadza, A. and S.B. Rananavare, Room temperature Cl2 sensing using thick nanoporous films of Sb-doped SnO2. Nanotechnology, 2008. 19(24): p. 245501.

[12] Kim, I.J., et al., Sensitivity enhancement for CO gas detection using a SnO2–CeO2–PdOx system. Sensors and Actuators B: Chemical, 2005. 107(2): p. 825-830.

[13] Lee, J.-S., et al., Structural and optoelectronic properties of SnO2 nanowires synthesized from ball-milled SnO2 powders. Journal of Crystal Growth, 2004. 267(1-2): p. 145-149.

WiFi-Femtocell Offloading Algorithms in Heterogenous LTE Network

Suhailah Mahzan
Dept. of Electrical, Electronic and Systems Engineering Universiti Kebangsaan Malaysia UKM Bangi, Malaysia
a144242@siswa.ukm.edu.my

Mohd Amiruddin Abd Rahman
Dept. of Physics Universiti Putra Malaysia UPM Serdang, Malaysia
mohdamir@upm.edu.my

Caceja Elyca Anak Bundak
Dept. of Physics Universiti Putra Malaysia UPM Serdang, Malaysia
mohdamir@upm.edu.my

Mahamod Ismail
Dept. of Electrical, Electronic and Systems Engineering Universiti Kebangsaan Malaysia UKM Bangi, Malaysia
a144242@siswa.ukm.edu.my

***Abstract*— One of the main challenges for mobile operators is to manage the exponential growth of data traffic that overloads and congests the network. Currently, Heterogeneous Network (HetNet) that encompasses different cell types and multiple radio access technologies (RATs) been deployed to boost the capacity and extend the coverage. Mobile data offloading has been introduced to resolve overloaded traffic in Cellular Node-B (NB) to other RATs such as Wi-Fi Access Points (APs) and Small Cells Femtocell (FC). However, inappropriate selection Point of Attachment (PoA) contributes to traffics unbalance among them during offloading, thus leading to inefficient utilization of network resource and lower capacity. In this paper, we analyses the offloading algorithms performance in HetNet. Three types of offloading algorithms been proposed which are the Wi-Fi AP, FC, and AP-FC offloading. A heterogeneous network model was simulated which consists of a NB, 6 APs, and 50 FCs were uniformly distributed away from the NB. The system performance was evaluated in terms of blocking probability, PoA utilization and network throughput. Simulation results has shown that offloading either to APs or FCs tend to reduce up to 30\% of the NB traffic, thus reducing the user blocking probability. However, there are no significant performance differences between the proposed algorithms in term of PoA utilization and network throughput. Wi-Fi AP offloads algorithm outperformed FC and AP-FC algorithms in particular for cell-edge users.**

Keywords*— *WiFi, Femtocell, LTE Network, Offloading

[1] INTRODUCTION

Mobile communication is growing rapidly and become the most cutting-edge telecommunications industries. The First Generation (1G) such as Enhanced/Total Access Communication System (ETACS) mobile communication used analog technology and support voice communication. Later, the system evolved to the Second Generation (2G) which applied digital technology and led into various standards such as Global System for Mobile (GSM) communication, TDMA based Personal Digital Cellular (PDC) and Code Division Multiple Access (CDMAOne)[1]. The Third Generation (3G) was introduced to support more services such as data, video and multimedia as well as voice. The present Fourth Generation (4G) such as Long Term Evolution/LTE-Advanced (LTE/ LTE-A) technology provides further enhancement compared to 3G technology such as improved multimedia, video-streaming, global-access and worldwide-portability through devices. Plus, 4G LTE offers improved data transfer rates, wide range of facilities, and better performance and security [2].

Alongside 4G developments, other Radio Access Technology has been introduced such as Worldwide Interoperability for Microwave Access (WiMAX) and Wireless Fidelity (Wi-Fi). WiMAX uses private, licensed spectrum IEEE 802.16 and provides Wi-Fi-like service with guaranteed performance to larger public areas [3]. Wi-Fi uses shared Industry Scientific and Medical (ISM) spectrum and operates at short distances, making it ideal for low-cost, private networks or free public systems [3].

One of the features in 4G LTE is Heterogeneous Networks (HetNet), a modern mobile communications network comprising a combination of different cell sizes and Radio Access Technology (RAT) [4]. HetNet environment comprises macrocells and small cells (femto, pico), and work simultaneous with other RATs to encounter capacity issue and the subscriber's experience, by applying data offloading approach.

Data offloading becomes a popular choice to alleviate congestion in cellular networks through bandwidth sharing, while maintaining Quality of service (QoS) at reduced cost. Offloading are defined as offloading the targets or specifically the User Equipments (UEs) [5]. Offloading transfers the data that was originally targeted to cellular network to other technologies that already existed within the area [6] . By offloading, congestion in the cellular network of radio data could be reduced and some key performance indicators could be improved.

However, there are some issues to be addressed when implementing offloading. First, the algorithm should be reliable as improper selection of targeted network could cause degredation of QoS and contributes to high blocking ratio. Second, the algorithm needs to ensure that the traffic load has been uniformly distributed among RATs. A balanced network could be achieved by distributing users from overloaded network to less preferred Point of Attachment (PoA).

The focus of this paper is to address the overloading issues in macrocell which is the NB network by developing offloading algorithm mainly for HetNet environment. Moreover, we need at same time to ensure fair network resource allocation between PoAs after offloading. This would be achieved by femtocell reallocation after offloading process.

[2] SYSTEM MODEL

The system simulation models include HetNet topology, path loss models and offloading algorithms:

A. HetNet Topology

The simulation scenario which represents the HetNet encompasses LTE NB, Wi-Fi APs and LTE FC networks. The network operator normally has full control over Wi-Fi and FC traffic to guarantee reduction of the congestion on NB network and provide better experience to the customers. Hence, in this simulation, we assume data-offloading was fully controlled by network operators, where the subscribers are automatically connected to either an NB or a Wi-Fi AP or FC to access the Internet.

The simulated system is composed of a single cell NB, 6 Wi-Fi APs operating on IEEE 802.11n standard and 50 FCs, where APs and FCs all are located within the NB cell coverage as shown in Fig. 1. The location of the 6 Wi-Fi APs is fixed relative to NB, while the locations of FC is unplanned and located randomly near the edge of NB cell. The cell radius of NB, AP, and FC is 1000 m, 100 m, and 50 m, respectively. Users are randomly distributed inside the macro NB, Wi-Fi and FC cells. The architecture considers a congested area with high demand of requested data. The main objective of the simulation is to improve the capacity of the traffic data in terms of throughput network, blocking probability and number of utilization PoA. An offloading technique is used to solve the congestion issue in the cellular network, by offloading the users to Wi-Fi or FC from NB network. In the proposed offloading algorithm, users are connected NB, AP or FC.

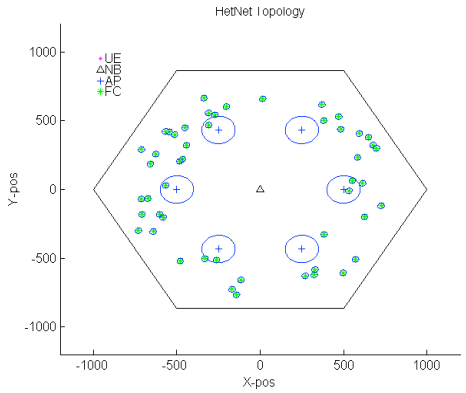


Fig. 1. Simulated HetNet Topology

B. Propagation Models

The selection of PoA depends on the mobile signal reception that is subject to the radio channel model and impairment such as fading and shadowing. However, it is mainly depend on the UE distance from PoA and the operating frequency.

The propagation models differ according to type of the network (LTE NB, Wi-Fi AP and LTE FC). NB network serve the largest coverage and the propagation loss could be estimated based on empirical path loss model such as the 3GPP LTE and COST231 models[7]. The model is applicable in urban and suburban areas with tall buildings. The propagation model is given as follows:

$$L(dB) = 40\left(1 - (40 \times 10^{-3}h)\right)\log_{10}(R) - 18\log(h) + 21\log(f) + 80 \quad (1)$$

where h is the height of the antenna above roof level that is assumed to be 15 m, R is the transmitter-receiver distance (in km) and f is the frequency of the transmitter (in MHz).

In this simulation, the propagation model for NB operates in 2 GHz. This is because, most of LTE models are assumed using these frequencies. For NB propagation model:

$$L(dB) = 15.3 + 37.6\log(d) \quad (2)$$

where d is the distance between transmitter-receiver (in meters).

Wi-Fi network in this simulation practices TG*n* path loss model based on the empirical model developed by the IEEE standards organization. This model consists of an open and closed environment model that has different values. For this simulation, the path loss in AP is as follows [8]:

$$L(dB) = 23.3 + 36.7\log(d) \quad (3)$$

For the FC network, the propagation model applied was a 2-slope model which is the outdoor propagation model. The propagation model for FC is written as follows:

$$L(dB) = L1 + 10L2\log(d) \quad (4)$$

The common values of L1 and L2 are 28 dB and 3.5 dB respectively, while d is the Euclidean distance between FC and the user in meters [9].

C. Offloading Algorithm

Data offloading is an alternative way where data traffic firstly targeted to NB is transferred to other radio access technologies (RAT). In this simulation, there are three data offloading algorithms proposed which are the data offloading to AP, FC, and either AP or FC which is randomly chosen based on the set criteria.

The first algorithm is to offload traffics to six APs using unlicensed Wi-Fi spectrum. The RSS value of each access point is collected and the maximum RSS value among APs is selected as target networks. However, the resource availability for the network will be checked before the data is offloaded to the network. If the AP is available, users at NB will offload to the AP.

The second offloading algorithm chose FC network as the target. Apart from the NB station site, the simulated environment consists of 50 FCs that are randomly developed. Before data is offloaded to the FC, the RSS measurement for each site station will be identified, and compared. The maximum RSS value within the 50 FC will be the targeted network as alternative source.

The third algorithm is the integration of AP and FC offloading strategy. The targeted network is chosen based on the maximum RSS value between AP or FC and the selection

is asymmetrical. The simulated environment fully utilizes PoA for three network layers of NB, AP and FC.

After offloading, the fairness in terms of the utilization of PoA and the number of active users is checked. If target FC networks are under or overloaded, users on FC will be redistributed to another FC network. Fig. 2 shows the process flow of the simulation.

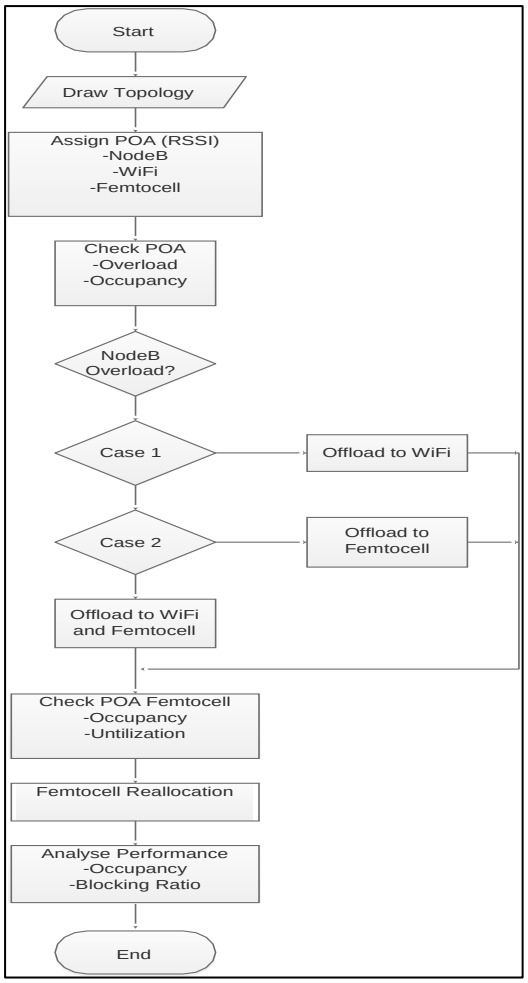


Fig. 2. Simulation Flowchart

[3] PERFORMANCE EVALUATIONS

The system performance was evaluated according to the following network metrics: throughput, blocking and utilization.

A. *Network Throughput*

Network throughput is defined the amount of data successfully sent to the recipient within a given time frame. Network throughput is measured in bits per second (bps) units. The assessment of network throughput is as in Equation (5).

$$T(x) = \text{Network Throughput}(x) \tag{5}$$

x is the PoA.

B. *Blocking Probability*

Blocking probability is defined as the number of blocked users over the total users. The value of the blocking probability is between 0 and 1. If the value approaches 0, it indicates that the data-offloading algorithm is efficient, thus more users could be served. The blocking probability, B is determined as in Equation (6).

$$B = \frac{\text{number of blocked user connections}}{\text{total users}} \tag{6}$$

C. *Utilization PoA*

The number of utilized PoA is obtained by calculating the number of active base station in the simulation as in Equation (7).

$$U = \sum_{k=1}^{N} Active\ Point\ of\ Attactment(PoA) \tag{7}$$

where *N* is the maximum number of active PoA. The purpose of this parameter is to ensure that network traffic is well distributed in all PoA. The factor of network traffic being unbalanced when there is PoA that get excessive or inactive data requests. With maximum utilization of PoA, the blocking ratio between connections PoA-user can be reduced.

[4] SIMULATION SETUP

Simulations of the three offloading algorithms were done using MATLAB. Table \ref{tab2} lists the main simulation parameter settings.

Tablo 1. Parameters Used In Simulation

	LTE NB	***LTE FC***	***Wi-Fi AP***
cc	we	re	rr
Cell radius	100 0m	50 m	100 m
Operation frequency	2.0 GHz	2.6 GHz	2.4 GHz
Resource block	100	4	10
Power Transmit	21 dBm	10 dBm	24 dBm
Gain Transmit	1 dB	12 dB	5 dB
Noise	-121 dBm	-110 dBm	-104 dBm

A. *Simulation assumption*

Below are some assumptions and considerations:

- The user's location is placed randomly inside NB, AP and FC coverage area.
- User movement is limited due to density.
- The number of users tested is 100, 200,300 and 400.
- Users data demand varies between 1-5 Mbps.
- The user statistic is collected based on the PoA.

[5] RESULTS AND ANALYSIS

The performance is evaluated based on three criteria as follows:

1) PoA utilization, 2) blocking probability, 3) network throughput.

The simulation was performed for different numbers of users generated randomly inside the NB cell. The number of users tested was ranged from 100 to 400 with a step value of 100. Fig. 3 shows the number of users that requested to connect to the PoA. Without offloading, the PoA option is only based on the maximum RSS level. If the number of user exceeds available resources, there is tendency that the user will be blocked.

Fig. 4 shows network throughput for without offloads condition and applying offloading algorithms. In terms of network throughput, Fig. 3(a) shows the network throughput without offload condition that receive high demand for a requesting data, where greater than 300 Mbps. Fig. 3(b), (c) and (d) shows the performance of the network after three type offloading algorithms were applied. Based on the result, it is shown that the network throughput after offload increases from 20 to 30 percent.

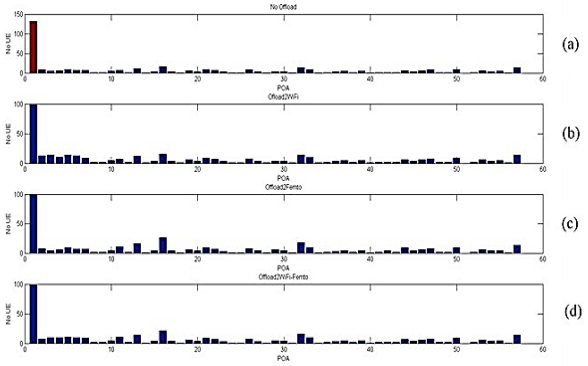


Fig. 3. Number of User Requested to Connect with PoA

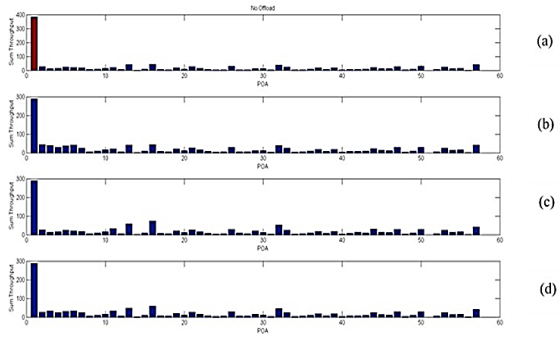


Fig. 4. Network Throughput

The number of PoA being utilized is successfully enhanced with three offloading algorithm when increasing number of users as shown in Fig. 5. There is no significant difference in terms of the amount of PoA utilization for three offloading algorithms.

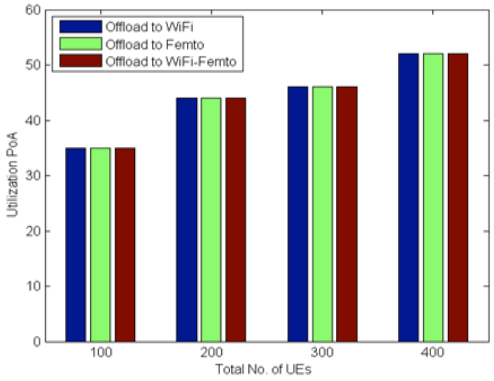


Fig. 5. Utilization PoA vs. No. of UE

Fig. 6 shows the blocking ratio with the increasing number of users. Based on the result, the performance of the blocking probability for offloading algorithm over Wi-Fi is lower than the other algorithm despite increasing number of users.

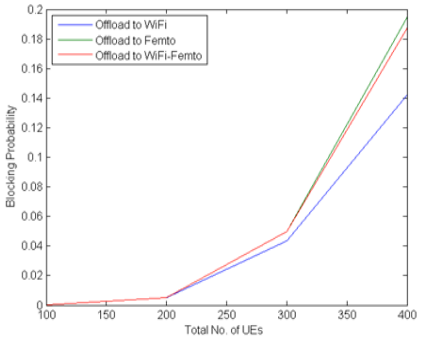


Fig. 6. Blocking Probability

[6] CONCLUSIONS

This paper proposed and analysed the performance of three offloading algorithms: Wi-Fi AP offloading, offloading using FC and AP-FC offloading. By deploying AP and FC to offload the traffic loads, better performance is achieved in term of blocking probability, PoA utilization and network throughput compared to without offloading condition. Wi-Fi AP offloading algorithm performs the best among them as it guarantees and maximizes the user capacity.

REFERENCES

[1] S. Khan, M. Zeeshan, and Y. Ayaz, "Implementation and analysis of MultiCode MultiCarrier Code Division Multiple Access (MC–MC CDMA) in IEEE 802.11ah for UAV Swarm communication," *Phys. Commun.*, vol. 42, p. 101159, 2020, doi: 10.1016/j.phycom.2020.101159.

[2] E. T. Tchao, J. D. Gadze, and J. O. Agyapong, "Performance evaluation of a deployed 4G LTE network," *Int. J. Adv. Comput. Sci. Appl.*, vol. 9, no. 3, pp. 165–178, 2018, doi: 10.14569/IJACSA.2018.090325.

[3] H. Luo, Z. Huang, and T. Zhu, "A survey on spectrum utilization in wireless sensor networks," *J. Sensors*, vol. 2015, 2015, doi: 10.1155/2015/624610.

[4] B. Feng *et al.*, "HetNet: A Flexible Architecture for Heterogeneous Satellite-Terrestrial Networks," *IEEE Netw.*, vol. 31, no. 6, pp. 86–92, 2017, doi: 10.1109/MNET.2017.1600330.

[5] F. Rebecchi, M. Dias De Amorim, V. Conan, A. Passarella, R. Bruno, and M. Conti, "Data offloading techniques in cellular networks: A survey," *IEEE Commun. Surv. Tutorials*, vol. 17, no. 2, pp. 580–603, 2015, doi: 10.1109/COMST.2014.2369742.

[6] L. Hu *et al.*, "Realistic indoor Wi-Fi and femto deployment study as the offloading solution to LTE macro networks," *IEEE Veh. Technol. Conf.*,

2012, doi: 10.1109/VTCFall.2012.6399042.

[7] P. K. S. Archana, J.P.Sharma, Dinesh.Sharma, "Outdoor Propagation Path Loss Models: A Review," vol. 2014, no. June, pp. 1–2, 2014, [Online]. Available: https://repositories.lib.utexas.edu/handle/2152/39127%0Ahttps://cris.brighton.ac.uk/ws/portalfiles/portal/4755978/Julius+Ojebode%27s+Thesis.pdf%0Ausir.salford.ac.uk/29369/1/Angela_Darvill_thesis_esubmission.pdf%0Ahttps://dspace.lboro.ac.uk/dspace-jspui/ha.

[8] L. Gonsioroski, A. B. Dos Santos, R. M. L. Silva, L. R. A. Da Silva Mello, C. H. R. Oliveira, and P. G. Castellanos, "Channel Measurement and Modeling for Path Loss Prediction in Vegetated Environment for IEEE 802.11ah Network," *Proc. - 2020 IEEE Latin-American Conf. Commun. LATINCOM 2020*, 2020, doi: 10.1109/LATINCOM50620.2020.9282327.

[9] H. Claussen, L. T. W. Ho, and L. G. Samuel, "Self-optimization of coverage for femtocell deployments," *7th Annu. Wirel. Telecommun. Symp. WTS 2008*, pp. 278–285, 2008, doi: 10.1109/WTS.2008.4547576.

Bird Sound Detection with Convolutional Neural Networks using Raw Waveforms and Spectrograms

Tee Yun Hong
Devices Development GroupIntel Penang
Penang, Malaysia
yun.hong.tee@intel.com

Muhammad Mun'im Ahmad Zabidi
School of Electrical Engineering
Universiti Teknologi Malaysia
Skudai, Johor,
Malaysiamunim@utm.my

***Abstract*— Animal monitoring is important for the preservation and conservation of the environment. This research aimed to determine the most suitable image type to the 2D Convolution Neural Network (CNN) model,to train a bird activity detector that is low in memory usage with decent accuracy. To enable this investigation, two architecturallyidentical 2D CNNs based on bulbul architecture was developed. These two 2D CNNs used time-domain image and spectrogram image as input respectively. Accuracy, model size and training time were used to determine the best model among these two CNNs. Bird audio and Urban8k audio were used as positive dataset and negative dataset respectively. For both CNN models, performance comparison was made among four-layer CNN, five-layer CNN and six-layer CNN. There was one winner for 2DCNN using wav image and 2D CNN using spectrogram image. These two winners were then being compared to determine the overall best model for bird activity detector. For this research,the overall best model was five-layer CNN using spectrogram image. The accuracy achieved was 97.12%, the model size was 6MB and the training time was fourteen minutes. The additional arithmetic operations required in converting wav to spectrogramwas deemed acceptable due to the much better accuracy achieved.Spectrogram image was the most suitable image type to 2D CNN to train a bird activity detector that is low in memory usage with decent accuracy.**

Keywords—bird sound detection, urban sound detection, con- volutional neural networks

I. INTRODUCTION

Animal monitoring is important for the preservation and conservation of the environment. It allows researchers andenvironmental activists to assess the impacts of human ac- tivities on Earth. Among all the animals, birds are one of the most commonly monitored as the change of bird population could indicate any subtle change of the ecosystem of thatparticular region. Monitoring the bird's population is importantfor the conservation of nature. One of the most effective methods is automatic bird sound recognition. Scientists needto evaluate the impact of human activities on the animal population, while the bird population is a good indicator of changes in biodiversity. The large volumes of audio recorded make manual inspection not feasible. Hence, an automatic bird monitoring system is crucial and beneficial for the nature conservation movement. The main advantages of an automaticbird sound recognition system are the long-term recordingwithout requiring an observer, deployment in hard to access areas and recognition of nocturnal birds and obscured birds.

Remote acoustic monitoring is typically done using Au- tonomous Recording Units (ARUs). They are embedded sys- tems running on battery and have limited storage [1]. To save storage, it is crucial to have a bird activity detector that decideswhether the received sound belongs to a bird or not before recording the sound. Convolutional neural networks (CNNs) have been shown to perform well as bird sound detectors but they require a lot of energy. We believe that a low complexity solution to bird sound detection has sufficient accuracy for thetask.

II. RELATED WORK

A. Bird Sound Detection

Bardeli et al. [2] studied the feasibility of using bird sound for the identification of birds in a noisy environment. The spectrogram generated from wavelet and noise estimation for effective noise reduction. The proposed method was able to identify the breeding territories of two targeted bird species and produced mapping similar to those produced by experi- enced bird observers. The research results demonstrated that the usage of bird sound for species identification is feasible.

P. Rai et al. [3] proposed an automatic identification model of four different bird species using support vector machine (SVM) and Mel Frequency Cepstral Coefficients (MFCCs). SVMs is a type of kernel-based machine learning method for linear classification. MFCCs are compact yet informative, making them the most used features to describe the spectrum of an audio recording. MFCCs were generated by extracting cepstral features extracted from the Mel scale of each audio waveform. They are represented in Mel units rather than in Hertz (Hz). Hamming window was used to make the audio signal stationary while still being able to avoid discontinuities and reduces mismatch. The overall accuracy was 64%, while the maximum accuracy was 89.74%.

B. 2D CNN

Incze et al. [4] employed the transfer learning techniqueand fine-tune the MobileNet [5] architecture for bird sound recognition. The impact of the number of classes used andthe type of colour maps used (grayscale and RGB) on the model accuracy was investigated. With three classes and two types of spectrograms, a total of six different configurations were used. During data preprocessing, the data was normalizedand split into three-

second long chunks, and discarded the last shorter one. Every segment was evaluated to make sure it was not too quiet, and the chunk is discarded if the gain is toolow. The remaining segments were converted into spectrogram using Short-time Fourier Transform (STFT). This paper ran each configuration five times, before averaging the results. It was found that as the number of classes increased, the model accuracy decreased. It was also found that the model that used Red, Green, Blue (RGB) spectrogram performed better, showing higher accuracy by an average of 7.4%. This paper successfully showed that fine-tuning a pre-trained MobileNet can improve model accuracy.

The traditional method for bird species prediction using birdbioacoustics address the segmentation and classification pro- cess separately, which leads to propagated error. Narasimhan et al. [6] presented a new approach that performs these two processes simultaneously using CNN with encoder-decoderarchitecture. The main challenge of detecting and recognizing bird syllables is the overlapping of syllables in time and frequency, as there are often multiple birds singing simul- taneously. Complex background noises might also overlapwith bird syllables and occlude the pattern. Decoupling of segmentation and classification limits the classification per- formance as it depends heavily on the segmentation results. This paper proposed a CNN network with encoder-decoder architecture, which was designed for semantic segmentationof images (linking of a pixel on an image to a class label).This allows the classification at the pixel level. The proposed algorithm improved the performance of syllable segmentation and species classification, with a hamming loss of 9.24, compared to the hamming loss of 11.1 of the base model(decoupled segmentation and classification).

Bird species identification based on spectrogram can achievehigh performance but requires a large amount of data to prevent overfitting. Transfer learning enables a model to be trained with limited samples. Xie et al. [7] proposed a trainingmodel made up of two parts, the first part is a pre-trained model used for feature extraction, while the second part is a classifier consists of two fully connected hidden layers with a softmax layer attached. As the type and duration ofthe spectrogram may affect the performance of identification, by using a single set of audio signals as the source data and fixing the duration, three kinds of time-frequency trans- form methods were used to generate the spectrogram. Three types of spectrograms were used: STFT spectrogram, Mel spectrogram and Chirplet spectrogram. It was found that the Chirplet spectrogram gave the highest performance. As the transfer learning model achieve lower mean average precision (MAP) compared to the base model, to improve the MAP, multi-channel identification models made up of two fusion modes (result fusion mode and feature fusion mode) werebeing investigated. It was found that the result fusion mode outperforms the feature fusion mode, and the best MAP was 0.9998.

An Iterative Method Based on Hazy Image Model for Remote Sensing Image Enhancement

Y. Demir
Faculty of Engineering and Architecture, Electrical and Electronics Engineering Department, Erzurum
Technical University, Erzurum, TURKEY
yasin.demir@erzurum.edu.tr
huseyin.kaplan@erzurum.edu.tr

N. H. Kaplan
Faculty of Engineering and Architecture, Electrical and Electronics Engineering Department, Erzurum
Technical University, Erzurum, TURKEY

***Abstract*— Image enhancement methods developed for remotely sensed images have to improve the quality of the image without distorting the outline of the image. In this study, an iterative enhancement method based on the hazy image model is proposed. In previous work, unknown parameters of the model, namely; transmission map and airlight are estimated by standard deviation and average of the image. In this work, the use of different statistics, such as median is included. Moreover, an iterative correlation based method is proposed. The visual and quantitative results show that the use of the median and correlation of the image is also possible.**

***Keywords*—remote sensing images, hazy image model, image enhancement**

[1] INTRODUCTION

Remote sensing is monitoring, analysing and object tracking at a certain distance from the earth without a physical connection. Remote sensing images, which have many applications such as agriculture, meteorology and defense must be of high quality. Advanced image processing algorithms are required to obtain high quality images. Image enhancement methods should be applied to improve the quality of the remote sensing images [1,2].

Histogram Equalization (HE) is the basic method in these applications [3]. Although useful for object detection, the enhanced images are of low quality. For this reason, improved HE methods are proposed [4-7]. These are bi-Histogram Equalization (BHE) [7], Recursive Mean-Seperate Histogram Equalization (RMSHE) [5]. Although they give better results than basic HE methods, they could not find a solution to the problems of oversaturation and undersaturation. Therefore, 2D based histogram methods are used [4,6]. However, these methods are not useful for automated applications, due to the time consumption. Recently, an Adaptive Gamma Correction with Weighting Distribution (AGCWD) method is proposed [8]. Another method combines the Discrete Wavelet Transform with Singular Value Decomposition (DWT-SVD)[9]. In addition to these methods, Fue et al. proposed a Regularized Histogram Equalization combined with Discrete Cosine Transform(RHE-DCT)[10]. Moreover, image enhancement methods with learning algorithms have been proposed recently [11,12].

A more recent method uses the hazy image model [13]. In this study, the unknown parameter is airlight of hazy image model have been estimated by the mean value, and the another unknown parameter which transmission is estimated by standard deviation of the image.

Motivated by the results of [13], in this study, different statistical properties of the image have been used to obtain the enhanced image. For this purpose, we first used median of the image instead of the mean value to estimate the airlight. Secondly, we used the median value instead of the standard deviation to estimate the transmission. Finally, we proposed an iterative method based on the correlation coefficient. For this, we first evaluated the prior enhancement by using the method given in [13]. Then, the correlation of the input image and prior enhanced image is calculated as the new airlight value to obtain the second enhanced image.

Rest of this paper organized as follows: In Section II, the hazy image model is explained. In Section III, the statistical models is explained. In Section IV, statistical elements are applied to hazy image model and the experimental results are given. In Section V, the results of the study has been concluded.

[2] RELATED WORK

The generally used hazy image model can be given as follows:

$$I(m,n)=J(m,n)t(m,n)+A\left(1-t(m,n)\right) \tag{1}$$

In equation (1), (m,n), is the pixel location $I(m,n)$ is the hazy image, $t(m,n)$ the transmission map, A is spherical atmospheric airlight and $J(m,n)$ the original image brightness. According to this equation, $J(m,n)$ can be defined as follows.

$$J(m,n)=\frac{I(m,n)-A\left(1-t(m,n)\right)}{t(m,n)} \tag{2}$$

The image enhancement method uses the following values. For airlight, the average value of the original picture can be used [13].

$$A=\frac{1}{MN}\sum_{m=1}^{M}\sum_{n=1}^{N}I(m,n) \tag{3}$$

In equation (3), $I(m,n)$ is the value of the pixel at location (m,n), and M, N represent the dimensions of the original image. The transmission map is estimated by the use the mean value and standard deviation of original image, as.

$$t(m,n)=1-\sigma_l\frac{I(m,n)}{A} \tag{4}$$

σ_l is standard deviation of original image, $I(m,n)$ is the

intensity value of the input image at location (m,n) and A is spherical atmospheric air light calculated by the mean value of the original image. This method will be called as Mean-Std.Dev.[13].

[3] PROPOSED METHOD

First, we propose the use of the median of the input image to estimate the airlight as:

$$A = Med(x) = \begin{cases} x\left[\frac{n}{2}\right] & \text{if } n \text{ is even} \\ x\left[\frac{n-1}{2}\right] + x\left[\frac{n+1}{2}\right] & \text{if } n \text{ is odd} \end{cases} \quad (5)$$

Here A is atmospheric airlight calculated by the median value of the original image, n is the number of elements of array and $x[n]$is the value of nth element. The transmission map estimation is carried put as given in (4). This combination will be called as Median-Std.Dev..

Secondly, we propose to use the airlight value as given in (3). Instead of the transmission estimation given in (4), the following estimation is used:

$$t(m,n) = 1 - M_I \frac{I(m,n)}{A} \quad (6)$$

where M_I is the median of the original image I , $I(m,n)$ is the intensity value of the input image at location (m,n) and A is atmospheric airlight calculated by the mean value of the original image. This combination will be called as Mean-Median.

In addition to all above, we propose an iterative enhancement method. First, we calculate the pre enhanced image by Mean-Sta. Dev. method. In the first iteration, the unknown parameter transmission map is estimated by using the correlation coefficient of the input image and pre enhanced image.

$$t_1 = 1 - r_1 \frac{I}{A} \quad (7)$$

where

$$r_1 = corr(I, I_1) \quad (8)$$

Here, I is the input image, I_1 is the pre enhanced image, A is atmospheric airlight calculated by the mean value of the original image, and $corr()$ is the correlation coefficient operator. The transmission map is estimated as in (4). For the further iterations, the transmission map is estimated by the correlation coefficient calculated between two adjacent iteration results. In this method the most suitable results are obtain in fourth iteration.

$$t_i = 1 - r_i \frac{I}{A} \quad (9)$$

This combination will be called as Mean-Correlation.

[4] Experimental Results

The proposed method has been applied to two remotely sensed images. First remote sensing image used for experimental purposes consists of agricultural fields [14].

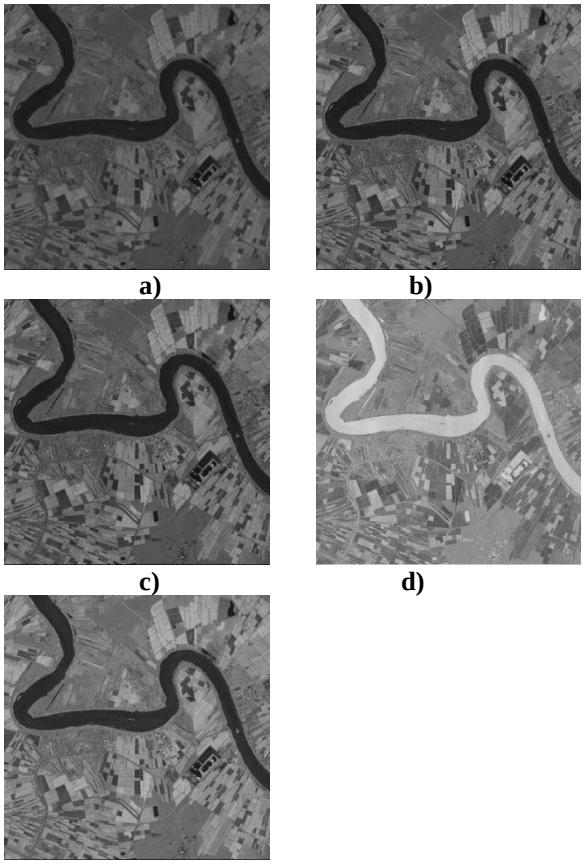
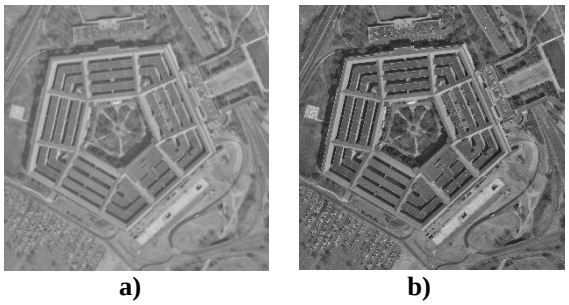
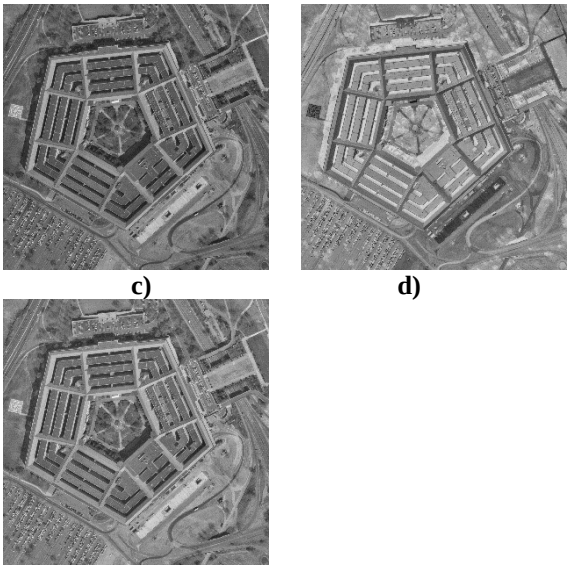


Fig.1. (a) Original image Enhancement results for (b) Mean-standard deviation[13] (c) Median-standard deviation (d) Mean-median (e) Mean-correlation

Fig.1.a demonstrates the input image, while Fig.1.b-e shows the enhancement results obtained by Mean-Std.Dev.[13], Median-Std.Dev., Mean-Median, and Mean-Correlation, respectively.

As seen in Fig.1, color information has been preserved and edge information has been improved in the Median-Std.Dev. method and the Mean-Std.Dev.[13] method. Color information distortions are seen in the Mean-Median method. In Mean-Correlation method color information has been preserved and edge information has been improved better than Mean-Median method.





c) **d)**

Fig. 2. (a)Original image Enhancement results for (b) Mean-standard deviation[13] (c) Median-standard deviation (d) Mean-median (e) Mean-correlation

Second remote sensing image used for experimental purposes consists of *The Pentagon* image[14]. Fig.2.a demonstrates the input image, while Fig.2.b-e shows the enhancement results obtained by Mean-Std.Dev.[13], Median-Std.Dev., Mean-Median, and Mean-Correlation, respectively.

As seen in Fig.2, color information has been preserved and edge information has been improved in the Median-Std.Dev. method and the Mean-Std.Dev.[13] method. Color information distortions are seen in the Mean-Median method. In Mean-Correlation method color information has been preserved and edge information has been improved better than Mean-Median method.

Some quality metrics are used to make a more objective comparison. Contrast gain of image (CG) is the first quality metric used for comparison. Higher brightness range of the image the higher CG value. The second quality criteria is enhancement measure of image (EME). The higher EME value means that better enhancement. Another criteria is discrete entropy (DE). The higher DE value indicates that the image has rich details.

The quantitative comparison for Fig.1 are given in Table 1. The highest CG value is observed in the Median-Mean method which means the highest contrast improvement is achieved by Median-Mean method. The highest EME value is observed in Mean-Correlation method which means the highest enhancement performance is achieved by Mean-Correlation method and the highest DE value in the Median-Std.Dev. and Mean-Std.Dev.[13] method.

Table 1. The Quantitative Results of Fig. 1

Index	CG	EME(10^5)	DE
Mean-Std. Dev.[13]	0.1205	10.96	**6.36**
Median-Std. Dev.	0.1202	11.00	**6.36**
Mean-Median	**0.1602**	5.56	6.08
Mean-Correlation	0.1043	**13.37**	6.25

The quantitative comparison for Fig.2 are given in Table 2. The highest CG value is observed in the Median-Mean method which means the highest contrast improvement is achieved by Median-Mean method. The highest EME value is observed in Mean-Correlation method which means the highest enhancement performance is achieved by Mean-Correlation method and the highest DE value in the Median-Std.Dev. and Mean-Std.Dev.[13] method.

Table 2. The quantitative results of fig. 2

Index	CG	EME(10^3)	DE
Mean-Std. Dev.[13]	0.1116	9.66	**6.73**
Median-Std. Dev.	0.1118	9.66	**6.73**
Mean-Median	**0.2454**	7.96	2.85
Mean-Correlation	0.0915	**10.75**	6.57

It is observed that the Median-Std.Dev. method and the Mean-Std.Dev[13]. method perform the similar results in both visual and quantitative results. The mean-Median method performs the best CG value. The Mean-Correlation method performs the best EME value. The Median-Std.Dev. method and the Mean-Std.Dev.[13] methods perform the best DE value.

[5] CONCLUSION

In this study, hazy image model based enhancement method have been studied with different statistics of the image. Moreover, an iterative correlation based method is proposed. The method uses the median value for the estimation of the airlight. The method uses the median and correlation coefficient values for another unknown parameter, the transmission map. This process carried on iteratively, by calculating a new correlation coefficient between two adjacent results. In remote sensing image enhancement methods are expected that the color and edge information to preserve as much as possible. The color and edge informations are preserved in Median-Std.Dev. and Mean-Correlation methods. Comparing the proposed methods with the former method, it is observed that it preserves the color information and edge information slightly better than the former method. For future studies, an adaptive iteration method may be developed for better results.

REFERENCES

[1] N. H. Kaplan, I. Erer, and N. Gulmus, "Remote sensing image enhancement via bilateral filtering" *in 2017 8th International Conference on Recent Advances in Space Technologies (RAST)*, pp. 139-142, June 2017.

[2] N. Hüseyin Kaplan and I. Erer, "Remote Sensing Image Enhancement via Robust Guided Filtering," *2019 9th International Conference on Recent Advances in Space Technologies (RAST)*, pp. 447-450, 2019.

[3] R.C. Gonzalez, R.C. Woods, Digital Image Processing, 3rd ed. Englewood Cliffs, NJ: Prentice-Hall, 2007.

[4] T. Celik and T. Tjahjadi, "Contextual and variational contrast enhancement", *IEEE Transactions on Image Processing*, vol. 20, no. 12, pp. 3431–3441, Dec. 2011.

[5] S. Chen and A. Ramli, "Contrast enhancement using recursive mean-separate histogram equalization for scalable brightness preservation," *IEEE Transactions on Consumer Electronics*, vol. 49, no. 4, pp. 1301–1309, Nov. 2003.

[6] T. Celik, "Two-dimensional histogram equalization and contrast enhancement," *Pattern Recognition*, vol. 45, no. 10, pp. 3810–3824, Oct. 2012.

[7] Y. Kim, “Contrast enhancement using brightness preserving bi-histogram equalization,” *IEEE Transactions on Consumer Electronics*, vol. 43, no.1, pp. 1–8, Feb. 1997.

[8] S. C. Huang, F. C. Cheng, and Y. S. Chiu, “Efficient contrast enhancement using adaptive gamma correction with weighting distribution,” *IEEE Transactions on Image Processing*, vol. 22, no. 3, pp. 1032–1041, Mar. 2013.

[9] H. Demirel, C. Ozcinar, G. Anbarjafari, “Satellite image contrast enhancement using discrete wavelet transform and singular value decomposition”,*IEEE Geoscience and Remote Sensing Letters* vol. 7, no. 2, pp. 333–337, Apr. 2010.

[10] X. Fu; J. Wang; D. Zeng; Y. Huang; X. Ding, "Remote Sensing Image Enhancement Using Regularized-Histogram Equalization and DCT", *IEEE Geoscience and Remote Sensing Letters*, vol. 12, no.11, pp.2301-2305, Nov. 2015.

[11] D. Hong, X. Wu, L. Gao, B. Zhang and J. Chanussot, "Learning Locality-Constrained Sparse Coding for Spectral Enhancement of Multispectral Imagery," *in IEEE Geoscience and Remote Sensing Letters*, Dec. 2020.

[12] Z. Yang, B. Zhao, X. Ma, M. Luo, J. Han and W. Si, "Super Resolution Enhancement of Satellite Remote Sensing Images of Transmission Tower Based on Multi-map Residual Network and Wavelet Transform," *2020 International Conference on Computer Vision, Image and Deep Learning* (CVIDL), pp. 16-20, 2020.

[13] N. Kaplan, “Remote sensing image enhancement using hazy image model”, *Optik*, vol.155, pp. 139-148, 2018.

[14] *http://sipi.usc.edu/database/*

Weighting of Questions With Fasttext Algorithm in Multiple Choice Exams

Adem CANPOLAT
Department of *Open Education Atatürk University* Erzurum, Turkey
ademcanpolat@atauni.edu.tr

Barış ÖZYER
Department of Computer Engineering Atatürk University Erzurum, Turkey
baris.ozyer@atauni.edu.tr

***Abstract*—The fact that the questions to be asked in the exams are either extremely difficult or easy, that can negatively affect the students while studying for any exam. The difficulty distribution is necessary to be homogeneously distributed in the exams for evaluating accurately the success of students. For this reason, the difficulty level of each problem should be determined in advance by experts. In this study, we analyzed the difficulty levels of the exam questions of Ataturk University Open Education Faculty by using the FastText algorithm. We initially combine the words in the question and their correct answer and then eliminate unnecessary words, punctuation marks and numerical expressions. We used Zemberek Library to obtain the stems of each word. N-gram is used to extract features. We created a separate model for each course and tested it with the FastText algorithm over the last text. The experimental results show that the FastText Algorithm Trigram achieved a 50% and above success rate in one hundred twenty-nine out of three hundred and twenty-six lessons. In the analysis made without separating the questions from all courses as a whole, the highest success is measured as 42% with bigram.**

Keywords—FastText, Text Classification, Question Difficulty

[1] INTRODUCTION

There are a total of 47 programs available in different fields in the Open Education Faculty at Atatürk University. In these programs, there are 420 courses in total, including common courses and selected courses for each program as well. 200,000 students enrolled in these programs. For each course, students take a total of 7 exams, which are two final exams, two make-up exams, and one three course exam, throughout one semester. The difficulty level of the questions is determined by considering the answers given by the students manually each exam. In this study, our goal is to determine the difficulty level by using the algorithms developed in the field of text classification through the questions asked in exams.

Classification of difficulty levels of question texts and determination of difficulty levels is an interesting topic that researchers have studied in recent years. The difficulty levels of the question texts can basically be evaluated by considering relationships between their answers. In this context, "Stackoverflow"[1] and "Yahoo! Answers "[2] examined the questions in the community question answering services [3]. In order to determine the difficulty level of each question, the expertise level of the user who gave the best answer to the question was looked at. The questions are labeled as easy, normal or difficult, according to the expertise score of the user who responded on the site. The tag words were then determined for each question and these tag words were used to determine the difficulty of the problem. In another study, artificial neural network based on Bloom's taxonomy was used to classify difficulty of questions [4]. In [5], 12.038 questions belonging to the medical exam held in USA were used to investigate the difficulty of multiple choice questions. In this study, the difficulty level of the questions was labeled based on the correct answers given by the students. After a set of pretreatment steps, the questions were classified using Random Forests, Linear Regression, SVM, Gaussian Processes, Dense NN (3 layers) algorithms.

In recent years, deep learning-based methods [6] are widely used in the text classification problem. However, it is well known that huge amount of data is needed to get high accuracy for these methods. In this study, we used FastText algorithm, which performs similar results with much fewer data compared to deep learning algorithms. FastText is not as complex as deep learning algorithms and does not contain hidden layers. However, it offers similar results to deep learning algorithms in a much shorter time [7]. Besides, the number and complexity of preprocessing are very low in the FastText algorithm. It does not require long dimensional vectors and preprocesses such as Bag of Word (BoW) [8]. Although deep learning methods can reduce the pre-processes in BoW algorithms, but large data set is needed for the learning process. In this context, FastText provides more accurate results with less data with a short learning time[9]. Because of these advantages, FastText algorithm is used for text classification in this study.

The FastText algorithm has been studied on different problems in the last years. In [10], the authors investigated whether the person had flu or not through the tweets posted using Twitter data. FastText algorithm was used in this study and a high accuracy rate was achieved. The highest classification accuracy is achieved by using the 5-gram features, together, with all the proposed additional features (F-measure = 89.9%). In another study, word value vectors of sentences were extracted and averaged using pre-trained FastText vectors [11]. The emerging new vectors are classified on SVM. FastText, Glove [12] and Word2Vec [13] algorithms were used on detecting harmful comments for Roman Urdu, a language widely used in social media in South Asia[14]. After the model was created, an accuracy rate of 86.35% was achieved.

[2] Methot

A. Preparing Dataset

Figure-1 depicts the block diagram of preprocessing steps for dataset preparation. The questions in the data set are classified with unigram and trigram through the FastText Library.

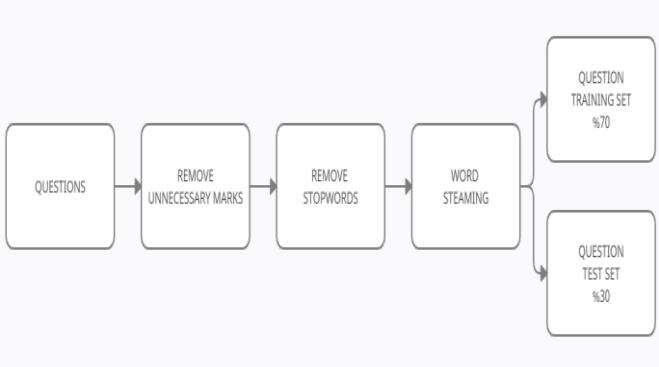


Figure 1. Preprocessing Steps

Item difficulty indexes were calculated by considering the answers given by the students to the questions asked in the previous exams. In this study, the item difficulty index (P) was calculated by the ratio of the total number of correct answers to the number of students answering the test. It is calculated by the formula P = R / T, where R is the number of correct answers and T is the total number of students who answered the question (i.e. correct + false + blank answers)[15]. Based on the calculated item difficulties, the questions were labeled as "Easy", "Medium" and "Difficult" as indicated in Table 1.

Table 1. QuestIon DIffIculty Ranges

Item Difficulty Index (P)	Label
P<=0.4	Hard
P>0.4 & P<=0.7	Medium
P>0.7	Easy

The labeled questions were transferred to the data set. Since the option of the correct answer to a question contains important information in defining the question, question texts and correct answer options were considered as a whole. The wrong answer options were not included in the classification. Later, punctuation marks and stop words were removed from the text. Then, with the help of Zemberek Library[16] the roots of the words were found and the texts were restated so that they only consist of word roots. Table 2 shows the rewriting of a problem after pre-processing.

Table 2. PreprocessIng on sample questIon

Example Question	Omuzların aşağı düşüp içe doğru bükülmesi ne tür bir beden dili anlamı içerir?
Correct Answer	Kendinden emin olmayan
After Preprocessing	omuz düş iç bük tür beden dil anlam içer kendi emin

The questions in our data set were divided into training and test groups with an equal number of difficulty levels for each course. As shown in Table 2, 70% of the questions in each lesson were used for training.

Table 3. Number of lessons and questIons In the data set

Total Number of Courses	Number of Training Questions	Number of Test Questions
326	6184	2342

B. *N-Gram*

N-grams can be defined as an array of n items from a given text or speech sample [17]. Items can be syllables, letters or words, depending on the application. N-grams are typically collected from a text or speech corpus. When Latin numerical prefixes are used, number 1 n-gram is termed "unigram"; N-gram number 2 is called "bigram" and number 3 n-gram is called "trigram." In computational biology, a polymer or oligomer of a known size is called k-mer instead of n-gram, and "monomer" is called "dimer", "Trimer "is named with proper names using Greek numerical prefixes such as" tetramer."It is a method frequently used to make sense of the text in text classification [18].

As an example to show on the sample text; "omuz düş iç bük tür beden dil anlam içer kendi emin" text for trigram [omuz düş iç], [düş iç bük], [iç bük tür], [bük tür beden], [tür beden dil], [beden dil anlam], [dil anlam içer], [anlam içer kendi], [içer kendi emin].

C. *FastText*

FastText is a library created by the Facebook Research Team to learn sentence classification efficiently[19]. The FastText Model allows an unsupervised or supervised learning algorithm to obtain vector representations of words. FastText uses neural networks for word embedding. The number and complexity of preprocessing are very low in the FastText algorithm. It does not need long dimensional vectors and preprocesses like the BoW. As shown in Fig. 2, it is a multi-layer perceptron composed of a trainable embedding layer, a hidden mean layer and a softmax dense layer. The hidden vector is generated by averaging the embedded word, which makes the fastText a BoW model. The fastText offers a very fast solution to text classification. It typically takes less than a minute in training a large data corpus with millions of samples. It gives the state of-the-art performance.

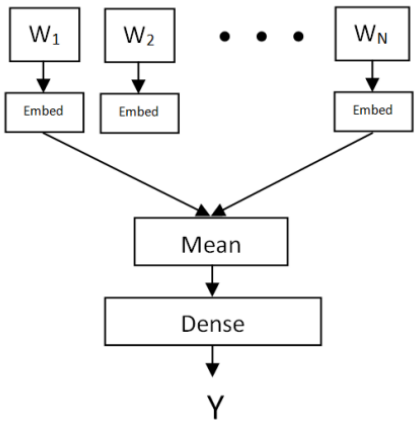


Figure 2. Illustration of the fastText model [20]

[3] EXPERIMENTAL RESULTS AND DISCUSSION

The lessons that show the best performance among the results obtained as a result of the studies are shown in Table 4. We use F-measure as a performance metric for evaluation. When all the results were examined, 325 out of 326 lessons had a performance above 0.33 for the unigram, while 324 had a performance above 0.33 for the trigram. It was observed that FastText algorithm results for Trigram gave better results in

general compared to unigram. The distribution of the questions to the units can be shown as the reason for the change in the rates according to the lessons. There are 14 units in each lesson and it is easier to determine the difficulty level of a question prepared from the same unit in another exam than a question prepared from a different unit. Due to the low number of questions pertaining to the courses, precision and recall values were the same in this study.

Table 4. Some cources wIth the best accuracy wIth Fastext

	Accuracy-Precision-Recall (25 Epoch)	
Course Name	**Unigram**	**Trigram**
İstatistik Analiz	1.00	1.00
Veteriner Biyokimya	0.92	0.95
İstatistiğe Giriş	0.89	0.77
İlk Dönem İslam Tarihi	0.87	0.89
Kamu Yönetimi	0.87	0.90
Temel Fotoğrafçılık	0.84	0.78
Laboratuar Teknikleri ve Prensipleri	0.81	0.81
Yoksulluk ve Sosyal Hizmet	0.78	0.70
İslam Hukukuna Giriş	0.78	0.76
İslam Sanatları Tarihi	0.78	0.87

[4] CONCLUSION

As a result of our study using the fastText library over the questions asked in the Atatürk University Open Education Faculty exams, we achieved a performance of 33% and above in 324 lessons for the trigram. Thanks to the high rate of success achieved, the difficulty levels of the questions will be determined with the fastText model made while preparing the exam questions and the questions labeled as difficult will be sent to the field experts. The difficulty of the question to be asked by the field experts and the content of the unit will be compared, and its adequacy in measuring knowledge will be determined. After the field expert report, the relevant question can be used in the exam. Thanks to this process, the difficulty level distribution of the questions will be homogeneous. In this way, students' success in exams will be increased by providing features such as measuring the main information that should be in a question, being included in the unit, being understandable and conforming to the format of the test question. As a result, the quality of education will increase. In our future study, the comparison of the question texts with the texts in the unit file and the difficulty level of the question will be investigated over the frequency of passing a question in the unit.

REFERENCES

[1] Stackoverflow, Accessed on: March, 2021. [Online]. Available: https:// stackoverflow.com/.

[2] Yahoo Answers!, Accessed on: March, 2021. [Online]. Available: https://answers.yahoo.com/.

[3] J. Liu, Q. Wang, C. Y. Lin, and H. W. Hon, "Question difficulty estimation in community question answering services," EMNLP 2013 - 2013 Conf. Empir. Methods Nat. Lang. Process. Proc. Conf., no. October, pp. 85–90, 2013.

[4] N. Yusof and C. Hui, "Determination of Bloom's cognitive level of question items using artificial neural network," 2010, pp. 866–870, doi: 10.1109/ISDA.2010.5687152.

[5] L. A. Ha, V. Yaneva, P. Baldwin, and J. Mee, "Predicting the Difficulty of Multiple Choice Questions in a High-stakes Medical Exam," pp. 11–20, 2019, doi: 10.18653/v1/w19-4402.

[6] Z. H. Kilimci and S. Akyokus, "Deep learning- and word embedding-based heterogeneous classifier ensembles for text classification," Complexity, vol. 2018, 2018, doi: 10.1155/2018/7130146.

[7] V. Zolotov and D. Kung, "Analysis and optimization of fasttext linear text classifier," arXiv, pp. 1–9, 2017.

[8] Y. Zhang, R. Jin, and Z. H. Zhou, "Understanding bag-of-words model: A statistical framework," Int. J. Mach. Learn. Cybern., vol. 1, no. 1–4, pp. 43–52, 2010, doi: 10.1007/s13042-010-0001-0.

[9] A. Amalia, "An Efficient Text Classification Using fastText for Bahasa Indonesia Documents Classification," pp. 69–75, 2020.

[10] A. Alessa, "Text Classification of Flu-related Tweets Using FastText with Sentiment and Keyword Features," pp. 366–367, 2018, doi: 10.1109/ICHI.2018.00058.

[11] W. Ma, H. Yu, and J. Ma, "Study of Tibetan Text Classification based on fastText," vol. 90, no. Iccia, pp. 374–380, 2019.

[12] HANSON ER, "Musicassette Interchangeability. the Facts Behind the Facts," AES J. Audio Eng. Soc., vol. 19, no. 5, pp. 417–425, 1971.

[13] K. W. Church, "Emerging Trends: Word2Vec," Nat. Lang. Eng., vol. 23, no. 1, pp. 155–162, 2017, doi: 10.1017/S1351324916000334.

[14] H. H. Saeed, M. H. Ashraf, F. Kamiran, A. Karim, and T. Calders, "Roman Urdu toxic comment classification," Lang. Resour. Eval., 2021, doi: 10.1007/s10579-021-09530-y.

[15] S. M. Sim and R. I. Rasiah, "Relationship between item difficulty and discrimination indices in true/false-type multiple choice questions of a para-clinical multidisciplinary paper," Ann. Acad. Med. Singapore, vol. 35, no. 2, pp. 67–71, 2006.

[16] A. A. Akın and M. D. Akın, "Zemberek, An Open Source Nlp Framework for Turkic Languages.," Structure, vol. 10, pp. 1–5, 2007.

[17] C. Five, "Applications of n-grams in textual information systems," vol. 4, no. 1, pp. 295–321, 1982.

[18] "N-Gram." Accessed on: March, 2021. [Online]. Available: https://en.wikipedia.org/wiki/N-gram.

[19] A. Joulin, E. Grave, P. Bojanowski, M. Douze, H. Jégou, and T. Mikolov, "FastText.zip: Compressing text classification models," pp. 1–13, 2016, [Online]. Available: http://arxiv.org/abs/1612.03651.

[20] Y. Su, R. Lin, and C.-C. J. Kuo, "On Tree-structured Multi-stage Principal Component Analysis (TMPCA) for Text Classification," no. July, 2018, [Online]. Available: http://arxiv.org/abs/1807.08228.

[21]

Distance Measurement with Optical Sensor

Atıl Emre COSGUN
Aksaray University Ortaköy Vocational High School Aksaray, Turkey
atilcosgun@gmail.com

Hasan DEMİR
Aksaray University Ortaköy Vocational High School Aksaray, Turkey
hasanfe_88@hotmail.com

Aim: **The aim of this study is to design a system with high sensitivity and low cost that can measure distance without contact. The aim of this study is to design a system with high sensitivity and low cost that can measure distance non-contact.**

Method: **For this purpose, about 28 cm lenght and 3cm radius cylindrical container, opt101 sensor and arduino microprocessor were used. Optical sensors are used in many areas such as part surface inspection, distance measurements, baccode systems, medical fields, part detection, and etc. The Opt101 sensor is a kind of optical sensor. It can measure in the spectrum from 300nm to 1100nm. The measurements of the distance were obtained depending on the light source's distance from the OPT101 sensor. Because the sensor affected by the light intensity and gives output voltages depend on the source. The measurements were realized at a distance between 2cm and 18 cm. For each cm was got a 50-sampling measurement and got mean values of the data. The distance started to begin at 2cm and continued to 18 cm. Totally 17 steps were realized. Out of this range, the taken data was unclear.**

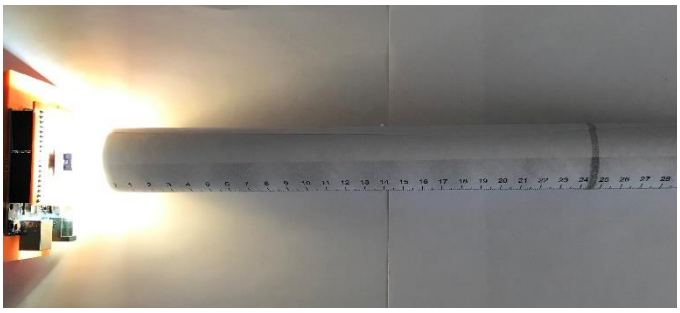


Fig.1 Distance Measurment System

Results: **Successful results were obtained by moving the light source towards the sensor which placed in the cylinder. The equation of the graph is obtained with the 3rd order polynomial function as R ^ 2 = 0.9970.**

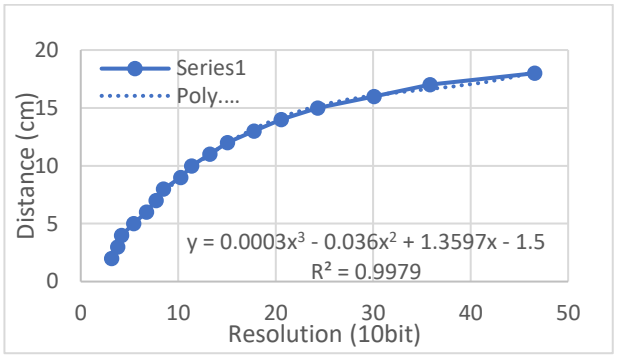


Fig.2 Graph of the distance and ADC

Conclusion: **Our sensor gives a good result at a specific range (2-18cm) depending on the intensity of the light. Although the measurements are carried out in a 10 mm range, the overall system dynamics which depend on light intensity distance were obtained as a 3rd-degree polynomial function. In this way, it could be obtained more sensitive results.**

Keywords— optical semsors, distance, opt101, non-contact

Performance Comparison of Common Routing Protocols in VANETs Using NS3 and SUMO

Nurgüneş Önal
Department of Electrical & Electronic Engineering Ataturk University
Erzurum, Turkey
nurgunes.onal@atauni.edu.tr

Bülent Çavuşoğlu
Department of Electrical & Electronic Engineering Ataturk University Erzurum, Turkey
bcavusoglu@atauni.edu.tr

***Abstract*— Vehicular Ad-hoc Networks (VANETs) are intelligent transportation systems (ITS) that help avoid congestion and provide safer roads. VANETs provide wireless communication among vehicles and between vehicles and road side units. The vehicles act like nodes and every node has high mobility and fast changing topology. To make a connection between nodes routing is done with the help of routing protocol. The performance of communication depends on how better the routing takes place in the network. This paper aims to evaluate the performance of commonly used routing protocols (OLSR, AODV, DSDV, DSR) in a vehicular scenario using network simulator NS3 and road traffic simulator SUMO. The performance evaluation parameters are Average Goodput, MAC/PHY Overhead and End-to-End Delay. The results of simulation show that the performance of the DSR protocol in terms of MAC/PHY overhead and Goodput metrics is higher than the other protocols evaluated in this paper. As for End-to-End Delay metric, DSDV protocol has the lowest delay for the packet to be delivered from the source node to the destination node.**

Keywords—VANETs, NS3, SUMO, Routing Protocols

I. INTRODUCTION

The rapid increase in the number of vehicles on the roads has led to the need for advanced technologies to increase road safety. VANETs (Vehicular Ad-hoc Networks) is an intelligent transport system that allows vehicles to collect and relay information from other moving vehicles quickly and dynamically. In VANETs, vehicles act like nodes. As shown in Fig. 1., VANETs allow communicate among moving vehicles or between vehicles and road-side units without any infrastructure. VANETs provide two types of vehicular communication: vehicle to vehicle (V2V) and vehicle to infrastructure (V2I). First, V2V communication is the communication between two or more vehicles which share information with each other through a wireless hardware equipment known as on-board unit (OBU). Second, V2I communication is the communication between vehicles and wireless access points known as road-side unit (RSU). The performance of communication depends on how better the routing of data used in the network. The main goal of this paper is to compare four commonly used routing protocols in an urban scenario in order to get a better understanding of which one has better performance. The remaining paper is organized as follows: Section-II briefly describes the studied routing protocols of VANETs, Section-III explains performance evaluation metrics. Section-IV and Section-V respectively give simulation environment and analysis of results. Finally, Section -VI concludes the paper.

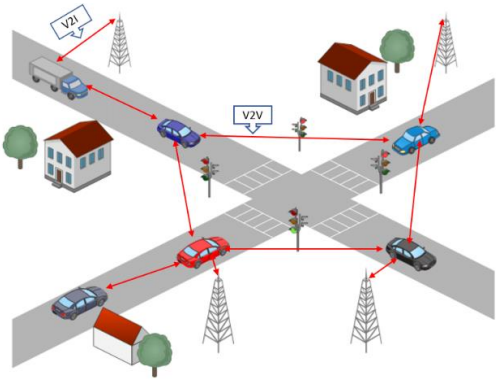


Fig. 1. Vehicular ad-hoc networks

II. STUDIED VANET ROUTING PROTOCOLS

Routing is the process that helps the nodes of a vehicular network to exchange information about the topology and connection state with one another in order to decide the best path [1]. Routing protocols are needed to provide routes to packets that contain information. In VANETs, packets on the network are sent between moving vehicles and the vehicle density on a road increases and decreases. So, the use of correct routing protocol is important. In our VANETs scenario, we studied topology-based routing protocols. Topology based routing protocols use link information that exists in the network to send the packets from source to destination. Topology-based routing protocols are of two types as reactive (on demand) and proactive (table driven) as shown in Fig. 2.

A. Reactive Routing Protocols (On Demand)

Reactive routing protocol is called on demand routing because it discovers routes only if there is any request. When a node wants to forward any data packet to another node, only the path to the target node is discovered. It keeps record of the used routes [2].

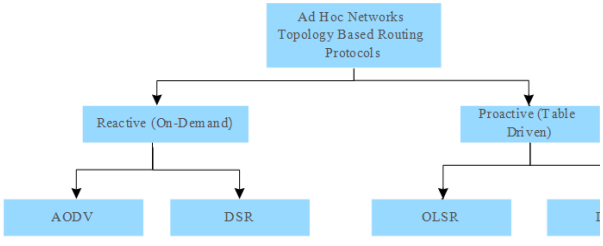


Fig. 2. Routing protocols

1) AODV (Ad hoc On-Demand Distance Vector Routing): Routes are only established on demand in AODV, and only those that are in use are kept. To decide the routes to the destination in AODV, the source node sends a route request packet (RREQ) to all of its neighbors, who then broadcast the RREQ to their neighbors, and so on, until it reaches the destination or any intermediate node that has new knowledge about the route to the requested destination [3]. Each node that receives a packet keeps the address of the neighbor node to which the packet was sent and ensures that the return path is established.

2) DSR (Dynamic Source Routing): The complete route information to a destination is kept at the source node in the route cache. Every data packet has a source route stored in its packet header. In DSR, the source routing system is used, while in AODV, the routing tables of in-between nodes are renewed. Similar to AODV, the path exploration method is used. To begin communication between two nodes, the source first looks destination in the stored route cache. RREQ starts the route discovery process if the destination isn't in the route cache. All the intermediate nodes of the system rebroadcast RREQ packet after add up of its address to the record catalog until it reaches to the destination. The source receives a route reply packet (RREP) from the destination. RREP is recorded in the route cache when it is received at the source [4].

B. *Proactive Routing Protocols*

Proactive routing protocol is also called as table-driven protocol. Table-driven means that the routing table contains information on all connected nodes. Every node has a routing table, which it exchanges with neighboring nodes when needed and keeps updated in response to changes in the network's topology [2]. The shortest possible route is searched for each candidate region.

1) OLSR (Optimized Link State Routing Protocol): OLSR is an ad hoc routing protocol that uses a proactive routing protocol to update its routing table whenever a connection change. The OLSR discovery route system works by sending RREQ messages to all nodes that become neighbor nodes in order to establish a relationship with each node on the network, and each node calculates the shortest path to each node [5].

2) DSDV (Destination Sequenced Distance Vector): DSDV is a protocol based on the Bellman-Ford algorithm [6]. Each node in the network holds the routing table ready to communicate with other nodes as a common feature of proactive routing protocols. These tables contain a list of all target nodes as well as the number of hops required to get to them. The goal node, next node, distance, and sequence number are kept in each row of the tables [7].

III. PERFORMANCE EVALUATION PARAMETERS

The performance of reactive and proactive routing protocols used has been evaluated on the basis of Average Routing Goodput, MAC/PHY overhead and End to End Delay.

A. *Average Goodput*

Average Goodput is the ratio of the cumulative received bytes for the routing protocol over the total simulation time as shown equation (1). The higher the value of the goodput in a routing protocol, the more data is successfully routed over the network.

$$Average\ Goodput = Cumulative\ Received\ Bytes\ /\ Total\ Simulation\ Time \quad (1)$$

B. *MAC/PHY Overhead*

Overhead stems from the packets related to only route update in the network. These packets do not contain any information related to the actual message [8]. Total physical bytes represent the total amount of data actually transmitted at physical layer for each vehicle. Application bytes represents the sum of Basic Safety Message (BSM) transmitted bytes and cumulative transmitted bytes from routing protocol [9]. MAC/PHY overhead is the ratio given by equation (2). Since the network bandwidth is shared by both types of packets (routing and actual message), the smaller the rate, the better the performance for the routing protocol.

$$MAC/PHY\ overhead = (total\ phy\ bytes - total\ app\ bytes)\ /\ total\ phy\ bytes \quad (2)$$

C. *End to End Delay*

End-to-End Delay determines the total time it takes for the packet to be delivered from the source node to the destination node.

IV. SIMULATION SCENARIO

For the experimental setup, the simulation was run on Ubuntu 20.04 operating system with Network Simulator [10] version 3.28 and SUMO [11] version 1.8.0 as a road traffic simulator. As shown in Fig. 3. and Fig. 4., we use a real-world urban map downloaded from Open Street Map [12] for a part of Erzurum city Turkey. The urban area of Erzurum with the highest traffic density is selected for the simulation area with coordinates 39.908345-41.273903. Fig. 5. shows the movement of mobile nodes (vehicles).

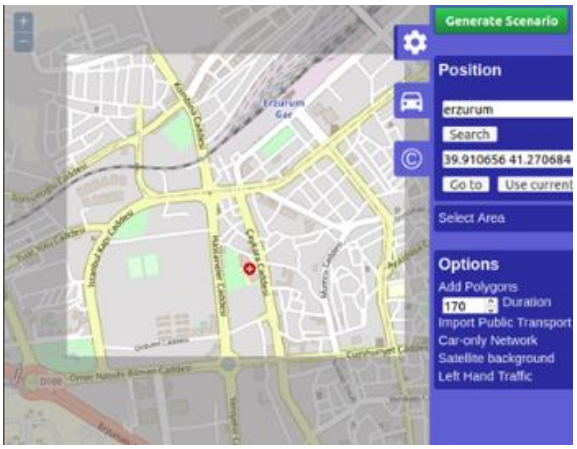


Fig. 3. Generate scenario using sumo.

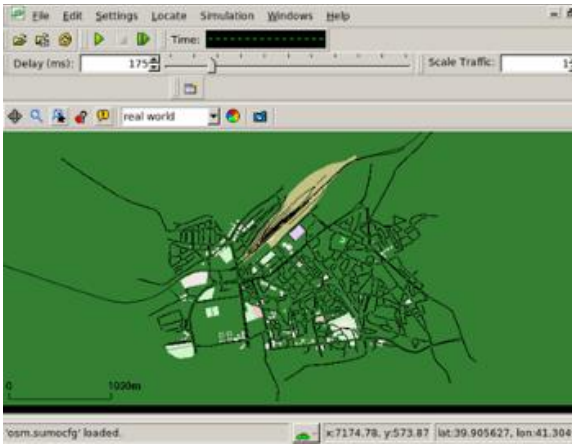


Fig. 4. Simulation using sumo.

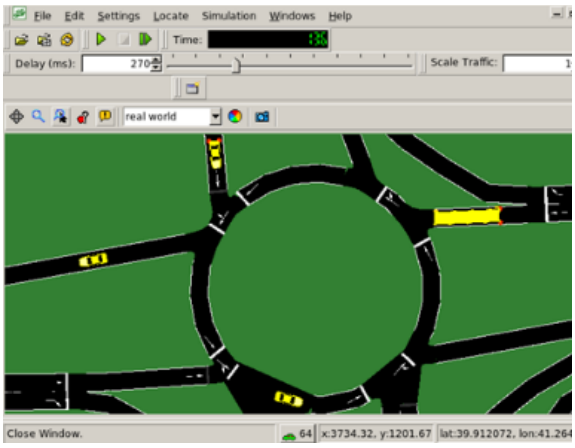


Fig. 5. Movement of mobile nodes.

The simulation was set up to evaluate the performance of four routing protocols (OLSR, AODV, DSDV and DSR) under varying node densities (30, 50, 70, 90 and 110). Table I. shows the details of the simulation setup.

V.SIMULATION ANALYSIS

A. *Average Goodput*

The result in Fig. 6. shows that AODV protocol performs better in scenarios with small number of nodes. But as the number of nodes increases, Goodput of AODV protocol gradually decreases. DSR protocol shows better performance in terms of Goodput with increasing number of nodes. When it comes to OLSR protocol, the Goodput gives poor performance with high number of nodes.

Table 1. Simulation Setup

Parameters	**Specifications**
Operating System	Ubuntu 20.04 LTS
Simulator	NS-3.29
Routing Protocol	OLSR, AODV, DSDV, DSR
Simulation Time	170s
Package Size	200 bytes
Node Speed	20 m/s
Number of Nodes	30, 50, 70, 90, 100
IEEE Scenario	VANET (802.11p)
MAC protocol	IEEE 802.11p
Transmission Power	20 dBm
Transmission Range	145m
Mobility Model	Random Waypoint
Propagation Model	Two Ray Ground

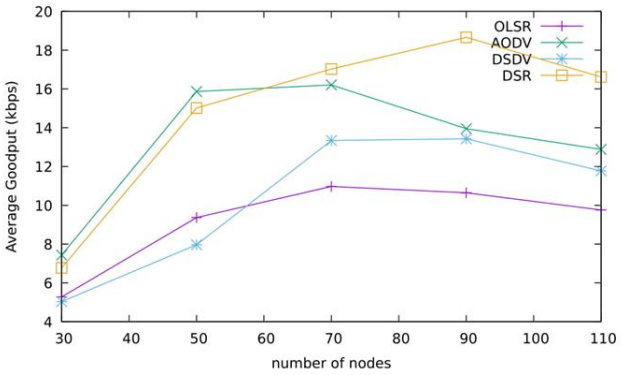


Fig. 6. Average goodput vs number of nodes.

B. *MAC/PHY Overhead*

Fig. 7. shows the comparison of MAC/PHY Overhead among routing protocols. We can observe that DSR protocol provides a better result than the other protocols. The AODV has highest MAC/PHY Overhead, because it broadcasts a large number of control message packets to maintain the route.

C. *End to End Delay*

Fig. 8. shows OLSR protocol gives poor performance in all scenarios of nodes. The result shows that AODV protocol performs better in scenarios with small number of nodes, but as the number of nodes increases, delay of AODV protocol also increases. Reason is that AODV protocol makes a path request only when a node has a packet to send, which causes extra delay that is noticeable as the number of nodes increases. When it comes to DSR protocol, its delay is higher than AODV protocol. The reason behind this is that DSR protocol uses all possible route to send packet from source node to destination node which causes more delay. DSDV routing protocol has the lowest delay with the high-density nodes.

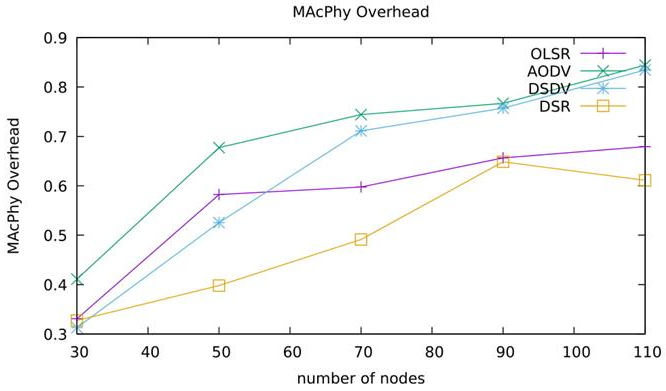


Fig. 7. MAC/PHY overhead vs number of nodes.

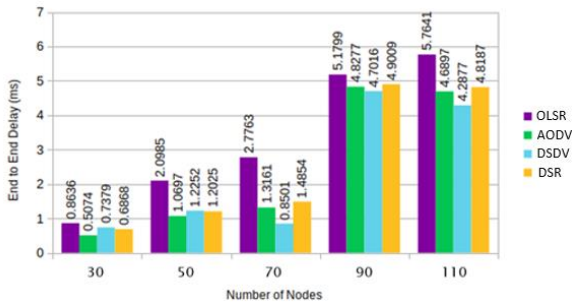


Fig. 8. End-to-end delay vs number of nodes.

VI. Conclusıon

In this paper, VANET simulation is performed in an urban area of Erzurum city Turkey with the most well-known routing protocols (OLSR, AODV, DSDV, DSR) using SUMO and NS-3 simulator. These protocols are applied with varying number of network sizes with a constant node speed. The Average Goodput, MAC/PHY Overhead and End to End Delay are the parameters used for the evaluation of the performance. According to the Average Goodput, the best result has been obtained DSR protocol. The second-best result belongs to the AODV protocol but in this protocol the goodput decreases as the node density increases. The poorest Average Goodput belongs to OLSR. Compared to other protocols, the DSR protocol also gives the best results according to the MAC/PHY Overhead performance metric. OLSR protocol gives the highest End-to-End Delay both in the low and high density of the nodes. End-to-End Delay performance of the DSDV protocol is better, but there is no big difference with the DSR protocol in terms of End-to-End Delay metric.

REFERENCES

[1] M. Erritali, B. El. "Performance evaluation of ad hoc routing protocols in VANETs." International Journal of Advanced Computer Scienceand Applications 3.2, 2013

[2] S. Sharma, P. Sharma. "Comprehensive study of various routing protocols in VANET." 2019 International Conference on Intelligent Computing and Control Systems (ICCS). IEEE, 2019, pp. 1272-1275

[3] B. Amina, E. Mohamed. "Performance evaluation of VANETs routing protocols using SUMO and NS3." 2018 IEEE 5th International Congress on Information Science and Technology (CiSt). IEEE, 2018, pp. 525-530

[4] P. Kumar, A. Verma, P. Singhal. "VANET Protocols with Challenges-A Review." 2019 6th International Conference on Computing for Sustainable Global Development (INDIACom). IEEE, 2019, pp. 598-602

[5] R. Aji Pratama, L. Rosselina, D. Sulistyowati, R. Fitri Sari and R. Harwahyu. "Performance Evaluation on VANET Routing Protocols in The Way Road of Central Jakarta using NS-3 and SUMO." 2020 International Seminar on Application for Technology of Information and Communication (iSemantic). IEEE, 2020, pp. 280-285

[6] Ford Jr, Lester R., "Network flow theory. " Rand Corp Santa Monica Ca, 1956.

[7] M. Dener, S. Toklu. "DSDV ve DSR Manet Yönlendirme Protokollerinin Başarım Değerlendirmesi." Politeknik Dergisi 12.3 2009: 157-166.

[8] Deepak, R. Kumar. "Performance Comparison of Routing Protocols in VANETs using Network Simulator-NS3" International Journal of Research in Electronics and Computer Engineering (IJRECE), 2018, 2097- 2104

[9] T. Wang, A. Hussain, M.N.M. Bhutta, Y. Cao. "Enabling bidirectional traffic mobility for ITS simulation in smart city environments." Future Generation Computer Systems 92 2019: 342-356.

[10] R. Manual, G. N. U. Texinfo, B. Pdf, G. N. U. General, P. License, F. S. Foundation, W. a. N. Y. W. Ranty, F. For, and P. P. See, “ns-3 Tutorial,” System, no. January, pp. 1–46, 2011. [Online]. Available: www.nsnam.org

[11] M. Behrisch, L. Bieker, J. Erdmann, D. Krajzewicz. "SUMO–simulation of urban mobility: an overview." Proceedings of SIMUL 2011, The Third International Conference on Advances in System Simulation. Think Mind, 2011.

[12] OpenStreetMap Foundation, “OpenStreetMap,” 2013. [Online]. Available: http://www.openstreetmap.org/

A Case Study on 132 kV Overhead Line Performance against Lightning via Installation of Transmission Line Arresters in Malaysia

Rasyidah Mohamad Idris
Faculty of Engineering School of Electrical Engineering University Teknology Malaysia Johor, Malaysia
rasyidah@fke.utm.my

Wan Zulhilmi Wan Mokhtar
Faculty of Engineering School of Electrical Engineering University Teknology Malaysia Johor, Malaysia
wan_kakaroct@yahoo.com.my

Iryani Mohamed Rawi
TNB Labs Head (Product Certification) Tenaga Nasional Berhad Selangor, Malaysia
iryani@tnb.com.my

***Abstract*— Lightning has been recognized as one of the most significant causes contributing to the transmission line outages in Malaysia. In this paper, a case study on the 132 kV Sungai Siput – Silibin GIS transmission line was selected in improving line performance by installing Transmission Line Arresters (TLA) to minimize outages to the transmission line. The TLA is used as protection against lightning to reduce the back flashover rate at the transmission line. Considering the cost involved, the TLA is not practically installed at each conductor on the transmission tower. Thus, a thorough study of lightning is conducted to identify the appropriate economic location and quantity needed to install the TLA at the corresponding transmission line. The benefit of installing the TLA at optimum locations will decrease the rate of back flashover that occurs when lightning strikes the transmission tower, thus reducing the number of lines tripping. The identification of exact TLA location on the overhead transmission lines and line performance is simulate using TFlash software. All the data gathered in this paper are obtained from Tenaga Nasional Berhad (TNB). The results will be analyzed to get the economical and optimum location of TLAs in the 132kV Sungai Siput – Silibin Gas Insulated Switchgear (SSPT-SBGS) overhead transmission line.**

Keywords*— *Transmission Line Arrester (TLA), lightning, overhead transmission line, line performance.

[1] INTRODUCTION (*Heading 1*)

Malaysia is a tropical country where the location is a lengthways equatorial line with high moisture and heat. Warm air from tropical latitudes that have lower density will rise upwards. As the humidity cools, it releases energy that allows the rising air packs to cool less than the surrounding cold air that raises clouds. When an unstable air mass is present in the atmosphere, it will lead to cumulonimbus cloud development that produces lightning and thunder. Despite the fascinating phenomenon, lightning can also cause damages and fatalities to humans and equipment.

According to the study, which involves different universities across the globe, Malaysia has the highest flash rate density (FRD) in Asia, which is about 93.96 fl km^{-2} yr^{-1}. In Asia, Kuala Lumpur stood out as one of the spots with the highest rate of lightning occurrences [1]. Lightning can cause damages to electrical equipment and to the power system. Malaysia Meteorology Services indicated that lightning statistics occurred 200 days a year in Malaysia and suspected to cause between 50 to 60 percent of trippings in transmission and distribution networks in Tenaga Nasional Berhad (TNB) [2]. To ensure the consistency and sustainability of the electrical power supply, the domestic utility company TNB had an initiative by conducting numerous research to reduce the number of outages due to lightning. In the TNB system, auto recloses breakers shall act upon lightning faults. The disadvantage of this breaker is that it will permanently lock out if multiple lightning strikes occurred simultaneously within 25 seconds. From the year 2001 to 2015, high voltage overhead transmission lines (OHL) recorded 1576 cases of breaker auto recloses. The transmission load loss of 2,514 MW was recorded by the Malaysian power grid due to nuisance outages from lightning activities [3].

The auto recloses system was acceptable, but it cannot sustain the electricity supply. Installation of the transmission line arresters (TLA) to improve lightning performance is more efficient than conventional methods [4]. TLA can improve transmission line lightning performance where a pilot project in 132kV Salak South – Pantai overhead lines in 2001 is a successful project reducing the number of tripping in the Klang Valley area.

Although TLA is an effective method to improve line performances and reducing outages, it is not practical to install TLA on each phase of the transmission tower due to economic reasons for better line performance. TLA installed at proper locations enhances the reduction of outage relating to back flashovers and shielding failure. Certain essential parameters that have to be taken into account include conductor, insulator, tower location, ground flash density, tower footing resistance, and tower dimension when calculating the line performance related to lightning.

This study aims to present the transmission line performance of lightning-related with the installation of TLA at 132kV overhead transmission line. The purpose of this paper is to improve line performances against lightning.

[2] LIGHTNING

Lightning is a phenomenon that occurs when the upper atmosphere is unstable. When an unstable air mass is present in the atmosphere, it will lead to cumulonimbus cloud development that produces lightning and thunder. Generally, strikes can be divided into 2 categories: downward-moving lightning and upward-moving lightning [5].

A. Back Flashover Occurrences

Back flashover event occurs when the lightning strikes and hits the earthing systems consisting of overhead ground wire, the top of the tower, and the pole. It is the major lightning problem that can cause surges on transmission line systems. The current will move through the overhead ground wire and the body of the tower. The tower surge impedance effectively performs if the traveling wave is mirrored to the phase

conductors and the top of the tower; therefore, the induced voltage will increase.

B. Shielding Failure Occurrences

Shielding of overhead transmission is a tool to protect the lines from damages to the phase conductors due to direct lightning strikes [7]. A shielding failure event occurs when the lightning strikes directly on the phase conductor [8]. Shielding wire is also known as earth wire, is the best position vertically on top of the tower. The failure events happen when the lightning current is below 20 kA. The back flashover is differing where it arises when the current of lightning is higher above 20 kA.

C. Nearby Strike Occurrences

When the lightning strikes on the ground at the nearby transmission lines, it will create electromagnetic field disturbance; hence induce voltages on overhead lines and other conductors. These induced voltages can cause a flashover to a lower voltage transmission line but not significant for higher voltage transmission lines with large insulation levels.

[3] LINE PARAMETER FOR LIGHTNING

A. Tower Surge Impedance

The tower surge impedance is a significant parameter for calculating the transmission line performance when the lightning strike occurs. Measuring the surge impedance may seem easy and straightforward since it is a natural process. However, the tower dimensions must be considered since it will reflect the tower impedance measurement that makes it complicated, complex, and expensive. There are several methods for determining the surge impedance, whether theoretical or experimental. The analytical method is the lowest cost in determining the tower surge impedance; this method is related to equations based on geometric shapes similar to real towers. Many experimental and theoretical studies have been done in understanding the tower surge impedance.

B. Tower Footing Resistance (TFR)

The back flashover that moves from the phase conductor to the tower occurs when the lightning strikes the shielding wire or the top of the tower. The insulator string allowed the lightning surge voltage to reflect the tower impedance surge depending on the footing resistance. As the surging travel down the grounding system, it will develop a voltage surge along with the tower. If the footing resistance higher, it will allow the large voltage through the insulator string. Apart from that, the voltage surge magnitude is contingent on the magnitude of the tower ground resistance. The main problem is not easy to decrease the tower footing resistance, especially in a mountain area. Therefore, the tower footing design significantly impacts the lightning performance on a transmission line [6]. In the TNB system, the structure or tower insulation design is essential with the grounding of transmission line structure. Therefore, a good TFR is vital since the tripping number due to lightning is high. The footing resistance of each tower is practically kept low.

C. Shielding Wire

The shielding wire or overhead ground wire (OHGW) covers the phase conductor from lightning placed high on the towers' peak. A more comprehensive top tower cross arm provides a wider angle for better protection. The purpose of positioning the shielding wire high above is to protect the phase conductors from direct lightning strikes. It may be grounded directly or indirectly through short gaps. Besides that, it will reduce the voltage caused by the external electromagnetic fields, reduce the impedance of the leakage from OHGW or increase the surge impedance of the OHGW. The shield wire place at every pole for effective results. Its effectiveness in distribution lines highly depends on the ground lead and phase conductor's insulation.

[4] RESEARCH METHODOLOGY

In this study, the line outages data collected from TNB Centralized Transmission Information System (CTIS). The line outage data was compared to the lightning stroke information obtained from TNB Lightning Detection Network (LDN). The line outages data are from 2003 to 2010, where date of event, time, and affected phase are shown.

A. Line Details

The overhead transmission lines of 132kV SSPT-SBGS, was selected based on its high number of recorded outages. The tower geographical along the line observed located in hilly terrain and passes through residential areas. The commission date of these lines is on 24 March 1997. The transmission line is a double circuit with a route length of approximately 32.1 km consist of 99 towers. The phase conductor used in these lines is 2 x 300mm^2 ACSR Batang, while the insulator suspension is glass type.

B. Grid Connection

The grid connection of the 132kV SSPT-SBGS overhead transmission lines connected as Tee-Off where the Associated Pan Malaysian Cement (APMC) substation located between the Sungai Siput (SSPT) substation to Silibin GIS (SBGS) substation.

C. Terrain Characteristic



Fig. 1. Tower Elevation Graph

The terrain characteristic reflects the line performance against lightning. Figure 1 shows the elevation graph of the tower. From the graph, we can analyze that the Sungai Siput substation route transmission lines are hilly terrain and slowly to the lowest elevation, which is the Silibin GIS located at ground level. The Google Earth Pro plot the towers at that transmission line. The actual tower coordinate was obtained from TNB data. Therefore, the topography of the tower can be analyzing.

Figure 2 shows the plotted tower altitude. It is observed at the site condition that the line located in hilly terrains are mostly in the woods and flat terrains are mostly urban-

residential and plantation areas.



Fig. 2. Geographical Tower Location

D. Ground Flash Density

The Ground Flash Density (GFD) measurement in Peninsular Malaysia was detect using smart sensors technology and place at strategic locations. In TNB, this sensor technology is called Lightning Detection Network (LDN). The main target is to monitor and analyze lightning activities. Figure 3 shows the GFD map at Peninsular Malaysia. The stroke is shown on the map based on its detected latitude and longitude. The LDN collected lightning stroke data regarding the number of stroke counts, percentage of stroke occurrence, the maximum and minimum peak values (kA), standard deviation, and mean value. In the 132kV SSPT-SBGS transmission line simulation, the regional stroke density is in the range of 20 – 30 flashes per km^2 per year based on the GFD map.

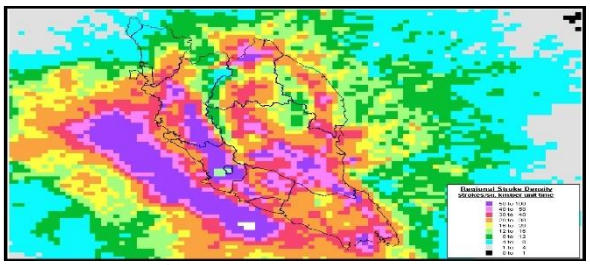


Fig. 3. GFD Map for Peninsular Malaysia [9]

[5] Case Study

Results were obtained from the 132kV SSPT-SBGS transmission line simulation using TFlash Software. The analysis is based on the rate of back flashover, total flashover per year, and shielding failure flashover to discover the location of tower that required TLA to be installed where it is important to take into consideration the quantity of TLA being used and economical location to installed TLA at the selected tower to improve the line performances.

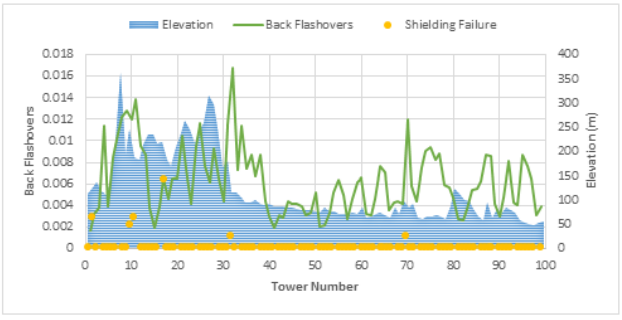


Fig. 4. Back Flashovers versus Elevation

Figure 4 shows the result of back flashovers occurs versus the elevation of the tower. From the analysis, it can be concluded that the tower at high elevation affecting the shielding failures. The higher elevation will give a high potential of shielding failure occurred.

The TFR which has been identified to have higher back flashovers, shall be improved since it is the first action and most economical solution to improve lines performances against lightning.

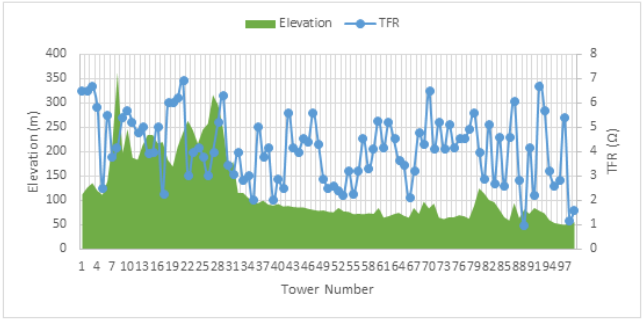


Fig. 5. Elevation versus TFR

Table I. Transmission Line Performance

Descriptions	Without TLA	With TLA
No of TLA Installed	0	129
Direct Strike Per Year	160.824	160.824
Back Flashovers	0.614	0.192
Shielding Failure Flashovers	0.016	0.000
Flashovers from Nearby Strikes	0.000	0.000
Total Flashovers	0.631	0.192
Direct Strike Per 100km/Year	514.807	514.807
TL Performance (Flashovers/100km-Year)	2.019	0.616
Expected Range (Flashover/100km-year)	N/A	0.318 to 1.164
Percent of Line Performance Improvement	N/A	68.73%
Descriptions	Without TLA	With TLA
No of TLA Installed	0	129
Direct Strike Per Year	160.824	160.824
Back Flashovers	0.614	0.192
Shielding Failure Flashovers	0.016	0.000

Figure 5 shows the relationship between elevation and TFR value. The elevation level does not affect the TFR value, whether the tower is located in hilly terrain or sloping areas. The values of TFR must be less than 10 ohms for 132kV transmission line towers. If the TFR cannot be improved, then TLA is essential in improving lines performances. The factors that influence the installation of TLA depends on the towers, which are:

1. Higher ground elevation
2. High soil resistivity
3. Exposed to open space.

In these transmission lines, reducing the tower footing resistance is not an option because the value of TFR is not influencing the tower elevation. Since tower no 1 to tower no 31 is in hilly terrain, the soil resistivity is high because of the rocky ground. Tower no 32 to tower no 99 located at sloping areas and near residential areas make it exposed to open space. In this 132kV SSPT-SBGS transmission lines, the higher TFR values is 7 ohms, which the TFR does not require an improvement.

[6] RESULT

Figure 6 shows that the potential of back flashover occurred reduced after TLA installs at the selected tower.

Most of the arrester installed at the middle of phase conductor. The nearest tower might have a higher back flashover value.

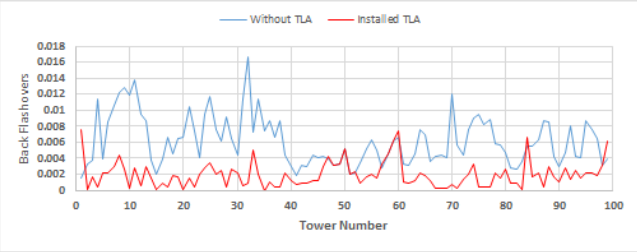


Fig. 6. Comparison of Back Flashover Rate

Table 1 summarizes transmission line performances after the installation of TLA in the simulation process. From the data obtained, the TL performance reduced to 0.616, and the TL improvement increased to 68.73%. In Malaysia, the ideal range of TL Performance is less than 1.82 flashover/100km-year.

TLA is installed mostly at middle line 1 and line 2. The selected phase conductor being chosen to install an arrester to give protection to the transmission line.

[7] CONCLUSION

Lightning study and analysis performed from the data obtained based on simulation of 132kV SSPT-SBGS transmission line. In this simulation, the towers that are potentially exposed to induced strike can be determined by simulated stroke. Besides that, the data gathered from previous lightning strikes along the transmission line being study. Thus, the towers that are possible to flashovers due to lightning can be identified.

The TFlash Software is a useful program to study the line performance, calculate potential total flashover, and improve TL performance study to other overhead transmission lines. Utility service providers can use this study to improve line performance over lightning that can cause outages to the line. This study can be a reference to further extended to determine the best method to reduce the transmission line's back flashover rate. Installing an arrester at a selected tower is the best solution after improvement of the tower footing resistance cannot be completed because it has limitation at the hilly terrain area due to high resistivity of ground.

REFERENCES

[1] R. I. Albrecht, S. J. Goodman, D. E. Buechler, R. J. Blakeslee, and H. J. Christian, “Where are the lightning hotspots on earth?,” *Bull. Am. Meteorol. Soc.*, vol. 97, no. 11, pp. 2051–2068, 2016, doi: 10.1175/BAMS-D-14-00193.1.

[2] N. Abdullah, M. P. Yahaya, and N. S. Hudi, “Implementation and use of lightning detection network in Malaysia,” *PECon 2008 - 2008 IEEE 2nd Int. Power Energy Conf.*, no. PECon 08, pp. 383–386, 2008, doi: 10.1109/PECON.2008.4762504.

[3] CIGRE WG01 SC33, “Guide to procedures for estimating the lightning performance of transmission lines,” *CIGRE Rep. 63*, vol. 01, no. October, p. 64, 1991.

[4] D. Caulker, H. Ahmad, and Z. Abdul-Malek, “Lightning interaction with 132 kV transmission line protected by surge arresters,” *Proc. Univ. Power Eng. Conf.*, vol. 2011-Janua, no. January, 2011.

[5] S. Shivalli, “Lightning Phenomenon , Effects and Protection of Structures from Lightning Sanketa Shivalli,” *IOSR J. Electr. Electron. Eng.*, vol. 11, no. 3, pp. 44–50, 2016, doi: 10.9790/1676-1103014450.

[6] M. You, B. H. Zhang, L. Y. Cheng, Z. Q. Bo, and A. Klimek, “Lightning model for HVDC transmission lines,” *IET Conf. Publ.*, vol. 2010, no. 558 CP, pp. 0–4, 2010, doi: 10.1049/cp.2010.0337.

[7] F. Alonso, “A simplified method for optimizing line shielding angle to maximize lightning performance,” *Proc. IEEE Power Eng. Soc. Transm. Distrib. Conf.*, pp. 1–5, 2012, doi: 10.1109/TDC.2012.6281491.

[8] A. H. A. Bakar, D. N. A. Talib, H. Mokhlis, and H. A. Illias, “Lightning back flashover double circuit tripping pattern of 132 kV lines in Malaysia,” *Int. J. Electr. Power Energy Syst.*, vol. 45, no. 1, pp. 235–241, 2013, doi: 10.1016/j.ijepes.2012.08.048.

[9] N. Abdullah and Norhasliza Mohd Hatta, "Cloud-to-ground lightning occurrences in Peninsular Malaysia and its use in improvement of distribution line lightning performances," *2012 IEEE International Conference on Power and Energy (PECon)*, Kota Kinabalu, Malaysia, 2012, pp. 819-822, doi: 10.1109/PECon.2012.6450330.

[10] W. R. Gamerota, J. O. Elismé, M. A. Uman, and V. A. Rakov, “Current waveforms for lightning simulation,” *IEEE Trans. Electromagn. Compat.*, vol. 54, no. 4, pp. 880–888, 2012, doi: 10.1109/TEMC.2011.2176131.

Magnetoacoustic Tomography with Magnetic Induction: Multiphysics Imaging Approach_A Short Review

Sani Saminu
State Key Laboratory of Reliability and Intelligence of Electrical Equipment Hebei University of Technology Tianjin 300130, China
sansam4k@gmail.com

Guizhi Xu
State Key Laboratory of Reliability and Intelligence of Electrical Equipment Hebei University of Technology Tianjin 300130, China
gzxu@hebut.edu.cn

Shuai Zhang
State Key Laboratory of Reliability and Intelligence of Electrical Equipment Hebei University of Technology
Tianjin 300130, China
zs@hebut.edu.cn

Abd El Kader Isselmou
State Key Laboratory of Reliability and Intelligence of Electrical Equipment Hebei University of Technology
Tianjin 300130, China
isselmou_kader@yahoo.com

Adamu Halilu Jabire
Department of Electrical and Electronics Engineering Taraba Statee University Jalingo, Nigeria
adamu.jabire@tsuniversity.edu.ng

Adamu Ya'u Iliyasu
Advanced RF and Microwave Research Group, School of Electrical Engineering, Faculty of Engineering, Universiti Teknologi Malaysia (UTM), 81310 UTM, Johor Bahru, Malaysia
alhaji080@gmail.com

***Abstract*—Magnetoacoustic tomography with magnetic induction (MAT-MI) is one of the multiphysics imaging techniques that combines the principle of magnetic field excitation and acoustic vibration. It is a noninvasive imaging technique developed in order to achieve high electrical impedance contrast of biological tissue as well as high spatial resolution close to ultrasound imaging. The feasibility to reconstruct high spatial resolution conductivity images using MAT-MI method has been demonstrated by both computer simulation and experimental studies. This work reviews the summary of fundamental ideas of MAT-MI and major techniques developed in recent years. First, the physical mechanisms underlying MAT-MI imaging are described including the magnetic induction and Lorentz force induced acoustic wave propagation. Second, experimental setups and various imaging strategies for MAT-MI are reviewed. Finally, we give our opinions on existing challenges and future directions for MAT-MI research. With all the reported and future technical advancement, MAT-MI has the potential to become an important noninvasive modality for electrical conductivity imaging of biological tissue.**

Keywords—MAT-MI, Multiphysics, Noninvasive Imaging, Biological Tissues, MRI.

[1] INTRODUCTION

Multiphysics problems, which include hybrid imaging techniques have been given great attention and enormous research interest over the years [1,2]. They are called hybrid because they utilize couplings of physical modalities in which the measurement quantities and excitation are belong to different physical modalities [3,4]. Medical imaging techniques are playing increasingly important roles in biomedical research and clinical diagnosis. A number of efforts have been made to improve our ability to characterize tissue properties such as to image the electrical impedance of biological tissues using noninvasive measurements. Also, Electrical properties of biological tissue including electrical conductivity σ and permittivity γ are very important in understanding the interactions and the effects of electromagnetic fields on our body. Also, biophysical parameters in the studies and analysis of electromagnetic therapies like transcranial stimulation methods and electrophysiology reflects the structural, functional and pathological conditions of tissues [5-7]. In addition, tissue electrical properties may serve as an imaging contrast for possible diagnosis and research applications due to their changes under physiological and pathological conditions [8]. They are determined by the molecular composition, cellular structure, amount of intra- and extra-cellular fluids, mobility and concentration of ions, temperature and many other factors. Therefore, measurements of tissue electrical properties could provide valuable information for guidance of neuronal stimulation in neuroscience, radio frequency patient safety in magnetic resonance imaging (MRI), and could be used as a new endogenous biomarker for example in oncology [9-11].

A number of efforts have been made over the decades to developed different hybrid imaging methods in order to characterize tissue properties and to measure electrical properties of biological tissue, which include Electrical Impedance Tomography (EIT) [12,13], magnetic resonance electrical impedance tomography (MREIT) [14,15]. magnetic induction tomography (MIT) [16], and magnetoacoustics tomography (MAT) [17-19]. To addressed the limitations of these proposed methods such as low spatial resolution, degraded sensitivity, and shielding effect as in EIT [20]. Use of MRI machine which makes MREIT more expensive and high level current injection requirement for good SNR value. For MIT, due to ill-posed inverse problem, the spatial resolution of this technique is also limited. Also, for the methods that coupled electromagnetic field and acoustic field such as in MAT and HEI or MAET or LFEIT, the problem of the "shielding effect" associated with the use of surface electrodes for current injection or voltage measurement, i.e. regions surrounded by low-conductive tissue become invisible, still exists in these methods [21-23]. Therefore, MAT-MI has been proposed as an alternative and suitable method to image electrical tissues.

MAT-MI utilizes magnetic induction to induce eddy current in the conductive sample and generates acoustic vibrations through the same Lorentz force coupling mechanism as in MAT or HEI. Ultrasound waves are then

sensed to reconstruct the electrical conductivity related images. Ever since the MAT-MI method was proposed, there have been many numerical studies [24-26] and experimental studies using physical phantoms [27,28] or biological tissues [29-31] demonstrating the feasibility and performance of MAT-MI. Advancement on experimental system design [32,33] and image reconstruction algorithms [34,35] has also been achieved in recent years. In addition, similar to the reverse mode of HEI or MAET, i.e. applying ultrasound transmission and measuring the Lorentz force induced current or voltage for imaging electrical conductivity, the reverse mode of MAT-MI named magneto-acousto-electrical tomography with magnetic induction (MAET-MI) has also been developed recently [36,37], which uses ultrasound stimulation and coil measurement of the dynamic magnetic field generated by Lorentz force induced current in conductive imaging objects.

This report is aim at providing an overview over the basic background concepts of theories and physical principles behind MAT-MI imaging methodology. Also review of numerical, experimental studies during these recent years have been presented. Finally, the report would be concluded with challenges and future direction for technical improvement.

[2] BACKGROUND

As shown in fig 1. the basic principle of MAT-MI is that the conductive object with electrical conductivity σ(r) (where r is the position vector is placed in a static magnetic field B_0 and a time-varying magnetic stimulation with magnetic flux density B_1 is applied to induce eddy current J inside the object volume Ω. the conductivity distribution σ(r) and field B_1 determined the induced current while the system frequency considered is in MHz and the displacement current is much smaller than the conduction current [38], so permittivity which is related to tissue capacitance is neglected. the Lorentz force F described in (1) formed the eddy current by moving charged iron and therefore generates ultra sound pressure signal to be detected by ultra sound probes so that electrical conductivity map of the object's can be estimated.

$$F = J \times B_0 \quad (1)$$

MAT-MI two essentials mechanisms are described as follows [39]:

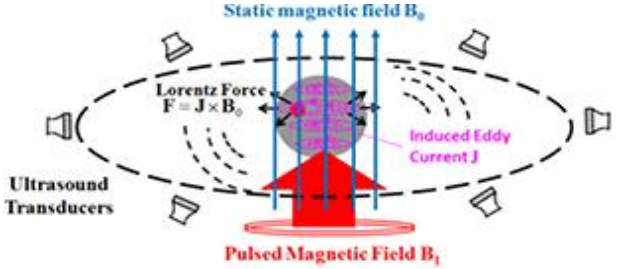


Fig. 1. Basic Principle of MAT-MI

2.1 Magnetic induction in conductive tissue sample

In MAT-MI, the magnetic induction problem can be regarded as quasi-static and by that the spatial and temporal functions of the time-varying magnetic field can be separated, i.e.

$$\mathbf{B_1}(\mathbf{r},t) = \mathbf{B_1}(\mathbf{r})f(t) \quad (2)$$

From (2), it shows that magnetic field in the tissue can be well approximated by the field produced by the coil in the absence of the tissue and can be estimated with the known coil geometry [40].

Using the magnetic vector potential $\mathbf{A}(\mathbf{r},t)$ as $\mathbf{B_1} = \nabla \times \mathbf{A}$. According to Faraday's law, we have

$$\nabla \times \left(E + \frac{\partial A}{\partial t}\right) = 0 \quad (3)$$

where $\mathbf{E}(\mathbf{r}, t)$ is the electrical field intensity. Therefore the electrical field intensity $\mathbf{E}(\mathbf{r},t)$ can be written as:

$$E = -\nabla \emptyset - \frac{\delta A}{\delta t} \quad (4)$$

where $\phi(\mathbf{r}, t)$ is the electrical scalar potential. According to Ampere's law and because we ignore the displacement current, the current density $\mathbf{J}(\mathbf{r},t)$ is solenoidal as:

$$\nabla . \mathbf{J} = 0 \quad (5)$$

In addition, according to Ohm's law, the current density is related to the electrical field through conductivity as:

$$\mathbf{J} = \boldsymbol{\sigma}\mathbf{E} \quad (6)$$

Combining Equations (4)-(6), we can have:

$$\nabla . (\sigma \nabla \emptyset) = -\nabla . \left(\sigma \frac{\delta A}{\delta t}\right) \quad (7)$$

According to the quasi-static condition, Faraday's Law and Ohm's Law, the similar spatial and temporal separation holds for the magnetic vector potential, induced electrical field and eddy current density, i.e. $\mathbf{A}(\mathbf{r},t) = \mathbf{A}(\mathbf{r})f(t)$, $\phi(\mathbf{r},t) = \phi(\mathbf{r})f'(t)$, $\mathbf{E}(\mathbf{r},t) = \mathbf{E}(\mathbf{r})f'(t)$ and $\mathbf{J}(\mathbf{r},t) = \mathbf{J}(\mathbf{r})f'(t)$ where the prime denotes the first order time derivative.

2.2 Lorentz force induced acoustic wave propagation

With magnetically induced eddy current $\mathbf{J}$ and the static magnetic field $\mathbf{B}_0$, the Lorentz force acting on the eddy current over unit volume can be written as

$$\mathbf{F} = \mathbf{J} \times \mathbf{B}_0 \quad (8)$$

Note here that we assumed $B_1 << B_0$ as the strength of the dynamic field for magnetic induction is much smaller than that of the static field in most of the MAT-MI experiment systems. According to Newton's second law of motion and assuming the particle velocity $\mathbf{v}$ caused by the Lorentz force is small as described in Equation (9) [41,42]:

$$\frac{\partial(\rho 0 \boldsymbol{v})}{\partial t} = -\nabla p + \boldsymbol{J} \times \boldsymbol{B_0} \quad (9)$$

where ρ_0 is the density of the material at rest and p is acoustic pressure. Taking the divergence of both sides of (9), we have Equation (10):

$$\frac{\partial(\nabla.(\rho 0 \boldsymbol{v}))}{\partial t} = -\nabla^2 p + \nabla . (\boldsymbol{J} \times \boldsymbol{B_0}) \quad (10)$$

In addition, we have the conservation of mass as in (11) and the definition of the adiabatic compressibility of the medium βs is shown in in Equation (12):

$$\nabla . (\rho 0 \boldsymbol{v}) = -\frac{\partial \rho}{\partial t} \quad (11)$$

$$\beta_s \boldsymbol{p} = \frac{\boldsymbol{\rho}}{\boldsymbol{\rho 0}} \quad (12)$$

where ρ is the density variation. Combining Equations (10)-(12) and using the relationship $C_s = \frac{1}{\sqrt{\rho 0 \beta s}}$where c_s is the acoustic speed in the medium, we can derive the wave

equation with the Lorentz force induced acoustic source [36]:

$$\nabla^2 p - \frac{1}{c_s^2}\frac{\partial^2 p}{\partial t^2} = \nabla.(\boldsymbol{J} \times \boldsymbol{B_0}) \quad (13)$$

Note here that in MAT-MI, the static magnetic field is generally generated from some external sources such as permanent magnets placed outside the imaging object volume, thus $\nabla \times \mathbf{B}0 = 0$ inside the imaging object volume [40,41].

[3] EXPERIMENTAL SETUP

The experimental setup for MAT-MI has three essential components, static magnetic field, dynamic magnetic field, and ultrasound transducer to capture ultrasound signals as shown in fig. 2.

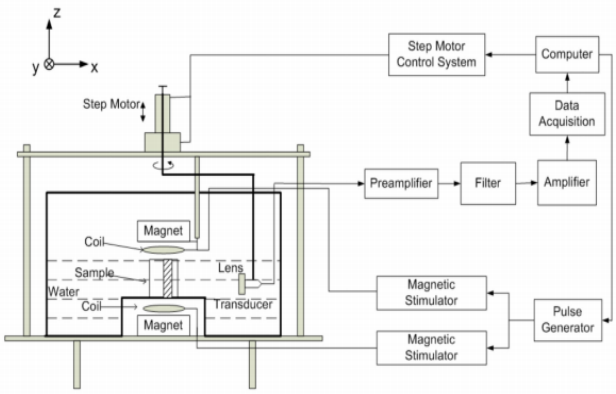


Fig. 2. MAT-MI Experimental Setup

Permanent magnets usually generate the static magnetic field to give a field strength of 0.1-0.3 Tesla in *z* direction around the sample [43], superconducting magnet is used with a 9.4 T MRI scanner, the imaging sample is rotating while the coil and transducer were fixed due to limited space in the MRI bore. For dynamic magnetic field generation, Computer controlled magnetic stimulators are used to drive the coil load around the sample. MAT-MI system which used pulse magnetic stimulations, high voltage and high current switches to control capacitor discharge through connected coil load have been used by magnetic stimulators. High voltage capacitors that charged up to 600v is proposed in [25], While [34] use as high as 24kv. The corresponding maximum dynamic magnetic field, which can be measured by small sensing coils around the imaging object, ranged from 0.00125 T to 0.07 T [45]. Magnetic stimulations sent through different coils have also been explored in the past but most MAT-MI system used a single magnetic stimulation generated through one coil set, such as a Helmholtz coil pair, which produces a region with a nearly uniform magnetic field [35]. In addition, MAT-MI systems using different coil sets to generate different magnetic stimulations and consequently different eddy current pattern in the conductive tissue sample have also been developed in the so-called multi-excitation MAT-MI system [46].

Ultrasound transducer mounted in certain scanning system that can either rotate the transducer or the imaging sample can be used to acquire MAT-MI signals around the imaging sample. Signal detected by the transducer are then filtered, amplified and fed to the data acquisition system. In MAT-MI, the magnetic induced eddy current in conductive tissues and the Lorentz force induced acoustic source are intrinsically distributed in the three-dimensional (3D) tissue volume. Induced force acoustic source is needed to map the 3D electrical conductivity distribution. Three-dimensional MAT-MI systems have been previously developed based on ultrasound focusing and cylindrical scanning [47]. As shown in Fig. 2, through ultrasound focusing in the *Z* direction, we can localize the MAT-MI acoustic sources in a specific *XY* plane. A 2-dimensional (2D) MAT-MI image can be obtained at each cross section of the 3D object and vertical scans in the *Z* direction can provide a stack of 2D images, thus forming a 3D volume image of the object. With such a circular scan, the spatial resolution of the MAT-MI image in each slice is mainly determined by the central frequency and bandwidth of the transducer, while the resolution in *Z* direction is determined by the focusing beam width. For imaging objects that are uniform in the *Z* direction and with homogeneous static and dynamic magnetic field, the whole MAT-MI system can be simplified as a 2D system, in which only 2D ultrasound scan is needed [48,49]. For 2D ultrasound scans, besides the circular scan mode with large scanning radius around the objects using unfocused transducer, scanning in *B*-mode scan using focused transducer may also be used [50].

[4] CHALLENGES AND FUTURE DIRECTIONS

In spite of many technical advances achieved in these years on MAT-MI, limitations still exist in currently available MAT-MI methods in the aspects of dynamic magnetic stimulation, instrumentation and reconstruction algorithms and further improvement is necessary to make it useful and applicable in clinical setup.

4.1 Dynamic Magnetic Stimulation

With the use of solid-state high voltage and high current switch, the dynamic magnetic stimulation used in MAT-MI system has been substantially improved to about 0.07T in its maximum dynamic range. There may be some space of improvement in terms of the magnetic stimulations. Note here that with the increased magnetic stimulation strength, the assumption $B_1 << B_0$ may need to be modified to include the contribution of $J \times B_1$ in the induced Lorentz Force. MAT-MI imaging speed may be further improved by using electrically controlled ultrasound phased array instead of single element transducer and mechanical scanning.

4.2 Instrumentation

Another technical challenge in MAT-MI instrumentation is the electromagnetic interference (EMI) caused by the time varying magnetic field on the ultrasound transducer. Related to the turn off transients in the stimulator and the impulse response of the transducer, such EMI usually contaminates the MAT-MI signal for substantial long period (tens of μs) and have been observed to have some low frequency variations. Therefore, further band-pass filtering is usually needed before MAT-MI image reconstruction. Better ways to avoid the EM contamination to the ultrasound transducer, such as better EM shielding or the use of optical fiber based transducers may be further explored to allow acquiring ultrasound signals in a closer distance (e.g. when using transducer with shorter focus) and further improve the MAT-MI signal quality.

4.3 Reconstruction Algorithm

For electrical conductivity reconstruction through mapping MAT-MI acoustic sources such as the multi-excitation MAT-MI method, more sophisticated coil pattern designs may help better improve the inverse conditions and

the final image quality. On the other hand, the recently developed beam-forming current density vector source method has shown great potential for electrical conductivity reconstruction with the use of only single magnetic excitation. Ultrasound bandwidth limitations have been successfully tackled using inverse filtering in that method. Further improvement may be achieved by considering the conductivity gradient term using iterative process when calculating the electrical conductivity from the estimated current density vector.

4.4 MAT-MI in Clinical Application

In vitro or in vivo, animal experiments need to be further conducted to assess the MAT-MI method for high-resolution conductivity imaging. Different types of soft tissues, organs or the whole body may be explored in the future imaging studies. The most possible clinical application of MAT-MI is believed to be tumor detection especially in cancer screening and detection.

A recent work on magneto acoustic tomography with the aid of magnetic nanoparticles suggested such possibility; employing the magnetomotive force, magneto acoustic tomography in a MAT-MI compatible setup was demonstrated as a high-spatial-resolution approach to reconstruct the in vivo distributions of nanoparticles, and to further highlight tumor by a high contrast [51].

[5] CONCLUSION

This report reviews fundamental ideas of MAT-MI and major techniques developed in recent years. First, the physical mechanisms underlying MAT-MI imaging are described including the magnetic induction and Lorentz force induced acoustic wave propagation. Also, experimental setups and various imaging strategies for MAT-MI are reviewed and compared together with the corresponding experimental results. Finally, some of the existing challenges and future directions for MAT-MI research have been highlighted. With all the reported and future technical advancement, MAT-MI has the potential to become an important noninvasive modality for electrical conductivity imaging of biological tissue.

REFERENCES

[1] S.C. Qun Zhang, Multiphysics Modeling: Numerical Methods and Engineering Applications. United States of America: Tsinghua University Press Limited. Published by Elsevier Inc. 2016.

[2] A. Isselmou, G. Xu, S. Zhang, S. Saminu, I. Javaid, I. S. Ahmad, "Differential Deep Convolutional Neural Network Model for Brain Tumor Classification," Brain Sci. 11(3), 2021, 352.

[3] T. Widlak, O. S. "Hybrid tomography for conductivity imaging," physics.med-ph, 2011, 32.

[4] A. Isselmou, G. Xu, S. Zhang, S. Saminu, "Modified Self-Organizing Map Algorithm for Brain Tumor Detection and Analysis Using Magnetic Resonance Brain Images," Journal of Biomedical Engineering and Medical Imaging (6)2, 2019.

[5] X. Li, S. Hu, L. Li, S. Zhu, "Numerical study of magnetoacoustic signal generation with magnetic induction based on inhomogeneous conductivity anisotropy," Comput Math Methods Med. 2013; 2013:161357.

[6] A. Isselmou, G. Xu, S. Zhang, S. Saminu, I. Javaid, I. S. Ahmad "Brain Tumor identification by Convolution Neural Network with Fuzzy C-mean Model Using MR Brain Images." International Journal of Circuits, Systems and Signal Processing, 14, 2020, pp. 1096-1102.

[7] R.J. Sadleir, V. T. "Transcranial direct current stimulation (tDCS) in a realistic head model," Neuroimage, 51, 2010, pp. 1310–8.

[8] X. Li, K. Yu, B. He, "Magnetoacoustic tomography with magnetic induction (MAT-MI) for imaging electrical conductivity of biological tissue: a tutorial review," Physics in Medicine & Biology, 61, 2016, pp. 249–270.

[9] A. Isselmou, G. Xu, S. Zhang, S. Saminu, I. Javaid, "Deep Learning Algorithm for Brain Tumor Detection and Analysis Using MR Brain Images," ICIMH 2019, Ningbo, China,2019, pp. 28-32.

[10] S. Mandija, Non-Invasive Characterization of Brain Tissue Electrical Properties with MRI, PhD thesis, Utrecht University, the Netherlands, 2018

[11] A. Isselmou, G. Xu, S. Zhang, S. Saminu, "Brain Tumor Detection and Classification by Hybrid CNN-DWA Model Using MR Images. Current Medical Imaging," 17(1), 2021, pp. 1096-1102.

[12] P. Grasland-Mongrain, J.M. Mari, J.Y. Chapelon, C. Lafon, "Lorentz force electrical impedance tomography," Irbm. 34 ,2013, pp. 357–60.

[13] P. Grasland-Mongrain, F. Destrempes, J.M. Mari, R. Souchon, S. Catheline, J.Y. Chapelon, et al. "Acousto-electrical speckle pattern in Lorentz force electrical impedance tomography," Phys Med Biol., 60, 2015, pp. 3747–57.

[14] J.K. Seo, E.J. Woo, "Electrical tissue property imaging at low frequency using MREIT," IEEE Trans. Biomed Eng. 61, 2014, pp. 1390–9.

[15] L. Guo, G. Liu, H. Xia, "Magneto-Acousto-Electrical Tomography With Magnetic Induction for Conductivity Reconstruction," IEEE Trans Biomed Eng. 62, 2015, pp. 2114–24.

[16] L. Ke, W. Zu, Q. Du, J. Chen, X. Ding, "A bio-impedance quantitative method based on magnetic induction tomography for intracranial hematoma," Med. Biol. Eng. Comput. 58, 2020, pp. 857–869.

[17] L. Wang, H. Xia, G. Li, "Influence of transducer aperture on magnetoacoustic tomography resolution," In Proceedings of the 2020 12th International Conference on Bioinformatics and Biomedical Technology, Xi'an, China, 2020, pp. 22–24.

[18] L. Wang, G. Liu, "Novel reconstruction algorithm of magnetoacoustic tomography based on ring transducer array for acoustic speed inhomogeneous tissues," Med. Phys. 47, 2020, pp. 3533–3544.

[19] S.G. Wang, S.Q. Zhang, R. Ma, T. Yin, Z.P. Liu, "A study of acoustic source generation mechanism of Magnetoacoustic Tomograph,". Comput Med Imag Grap. 38, 2014, pp. 42–8.

[20] P. Grasland-Mongrain, R. Souchon, F. Cartellier, A. Zorgani, J.Y. Chapelon, C. Lafon, S. Catheline, "Imaging of Shear Waves Induced by Lorentz Force in Soft Tissues," Phys Rev Lett. 2014; 113

[21] L. Kunyansky, "A mathematical model and inversion procedure for magneto-acousto-electric tomography," Inverse Probl. 2012; 28.

[22] H. Xia, G. Liu, X. Huang, L. Guo, Y. Yang, and M. Lu, "The Forward and Inverse Problem Based on Magneto-Acoustic Tomography with Current Injection," Journal of Biomedical Science and Engineering, 10, 2017, pp. 97-105.

[23] L. Kunyansky, C.P. Ingram, R.S. Witte, "Rotational magneto-acoustic-electric tomography (MAET): Theory and experimental validation," Phys. Med. Biol. 62, 2017, pp. 3025–3050.

[24] X. Sun, D. Fang, D. Zhang, Q. Ma, "Acoustic dipole radiation based electrical impedance contrast imaging approach of magnetoacoustic tomography with magnetic induction," Med Phys., 40, 2013, 052902.

[25] L. Zhou, X. Li, S. Zhu, B. He, "Magnetoacoustic tomography with magnetic induction (MAT-MI] for breast tumor imaging: numerical modeling and simulation," Phys Med Biol. 56, 2011, pp. 1967–83.

[26] H. Ammari, S. Boulmier, and P. Millien, "A Mathematical and Numerical Framework for Magnetoacoustic Tomography with Magnetic Induction," Journal of Differential Equations, 259, 2015, pp. 5379-5405.

[27] R. Xia, X. Li, B. He, "Comparison study of three different image reconstruction algorithms for MAT-MI," IEEE Trans Biomed Eng. 57, 2010, pp. 708–13.

[28] X.D. Sun, F. Zhang, Q.Y. Ma, J. Tu, D. Zhang, "Acoustic dipole radiation based conductivity image reconstruction for magnetoacoustic tomography with magnetic induction," Applied Physics Letters. 2012, 100

[29] L. Zhou, S. Zhu, B. He, "A reconstruction algorithm of magnetoacoustic tomography with magnetic induction for an acoustically inhomogeneous tissue," IEEE Trans Biomed Eng. 61, 2014, pp. 1739–46.

[30] A.R. Zywica, "Magnetoacoustic tomography with magnetic induction for biological tissue imaging: numerical modelling and simulations,"

Archives of Electrical Engineering, 65(1), 2015, pp. 141–150.

[31] A.R. Żywica, "Magnetoacoustic Tomography with Magnetic Induction for Biological Tissue Imaging: Numerical Modelling and Simulations," Archives of Electrical Engineering, 65(1), 2016, pp. 141-150.

[32] X. Shi, G. Liu, X. Yan, Y. Li, "Simulation research on magneto-acoustic concentration tomography of magnetic nanoparticles with magnetic induction," Comput Biol Med. 2020, 119:103653.

[33] A. R. Zywica, M. Ziolkowski and S. Gratkowski, "Detailed Analytical Approach to Solve the Magnetoacoustic Tomography with Magnetic Induction (MAT-MI) Problem for Three-Layer Objects," Energies, 13, 2020, 6515.

[34] R. Ma, M. Yang, S. Zhang, X. Zhou, T. Yin, "Analysis of the singular values for conductivity reconstruction in magnetoacoustic tomography with magnetic induction," IEEE Access, 8, 2020, pp. 51753–51760.

[35] L. Mariappan, B. He, "Magnetoacoustic tomography with magnetic induction: bioimepedance reconstruction through vector source imaging," IEEE Trans Med Imaging. 32, 2013, pp. 619–27.

[36] M. Dai, X. Chen, T. Sun, L. Yu, M. Chen, H. Lin, S. Chen, "A 2D magneto-acousto-electrical tomography method to detect conductivity variation using multifocus image method. Sensors, 18, 2018, 2373.

[37] I. Hidayat, I.; I.D. Darpita, I. D.; S.K. Wijaya, S. K.; P. Prajitno, P. (2019). "The development of magnetoacoustic tomography system with current injection," Proceedings of the 4th International Symposium on Current Progress in Mathematics and Sciences (iscpms2018) - Depok, Indonesia, 2018, 2168, 020016.

[38] M. Ziolkowski, S. Gratkowski, A.R. Zywica, "Analytical and numerical models of the magnetoacoustic tomography with magnetic induction," COMPEL Int. J. Comput. Math. Electr. Electron. Eng. 37, 2018, pp. 538–548

[39] A.R. Zywica, M. Ziolkowski, S. Gratkowski, "Transient Lorentz force density distribution in a single and double layer conducting spheres," In Proceedings of the International Interdisciplinary PhD Workshop (IIPhDW), Swinouj´scie, Poland, 2018.

[40] X.H. Yan, Y. Zhang, G.Q. Liu, "Simulation research on effect of magnetic nanoparticles on physical process of magneto–acoustic tomography with magnetic induction," Chin. Phys. B, 27, 2018, 104302

[41] Z. Yu, S. Dai, Q. Ma, G. Guo, J. Tu and D. Zhang, "Conductivity Anisotropy Influence on Acoustic Sources for Magnetoacoustic Tomography with Magnetic Induction," IEEE Transactions on Biomedical Engineering, doi:10.1109/TBME.2018.2805697

[42] S. Zhen, M. Zhen, "Numerical simulation of endoscopic magnetoacoustic tomography with magnetic induction." Comput. Biol. Med., 90, 2017, pp. 1–14.

[43] L. Mariappan, Q. Shao, C. Jiang, K. Yu, S. Ashkenazi, J.C. Bischof, B. He, "Magneto acoustic tomography with short pulsed magnetic field for in-vivo imaging of magnetic iron oxide nanoparticles," Nanomedicine. 12, 2016, pp. 689–99.

[44] L. Mariappan, G. Hu, B. He, "Magnetoacoustic tomography with magnetic induction for high-resolution bioimepedance imaging through vector source reconstruction under the static field of MRI magnet," Med Phys. 41, 2014, 022902.

[45] X.D. Sun, X. Wang, Y.Q. Zhou, Q.Y. Ma, and D. Zhang, "Reception pattern influence on magnetoacoustic tomography with magnetic induction," Chinese Physics B, 24(1), 2015, pp. 1-9.

[46] X. Li, B. He, "Multi-excitation magnetoacoustic tomography with magnetic induction for bioimpedance imaging," IEEE Trans Med Imaging. 29, 2010, pp. 1759–67.

[47] Z. Wei et al. "Image Reconstruction in Magnetoacoustic Tomography with Magnetic Induction With Variable Sound Speeds," IEEE Trans. Biomed. Eng., 63(12), 2016, pp. 2585-2594.

[48] G. Guo,Y. Gao,Y. Li et al., "Second harmonic magnetoacoustic responses of magnetic nanoparticles in magnetoacoustic tomography with magnetic induction," [J]. Chin. Phys. B, 29(3), 2020, 034302.

[49] X. Yan, Y. Pan, Y. Zhang, S. Guang, "Simulation study on forward problem of magnetoacoustic tomography with magnetic induction based on nanoparticles," Prog. Electromangetics Res. Lett.87, 2019, pp. 75–80.

[50] Z. Yuqi, W. Jiawei, S. Xiaodong, M. Qingyu, Z. Dong, "Transducer selection and application in magnetoacoustic tomography with magnetic induction," Journal of Applied Physics, 119(9), 2016, 094903.

[51] X.H. Yan, Y. Zhang, G.Q. Liu, "Simulation research on effect of magnetic nanoparticles on physical process of magneto–acoustic tomography with magnetic induction," Chin. Phys. B, 27, 2018, 104302.

Electrical Energy Systems and Electric Transportation

Dominic April
Department of Electrical, Electronic and Computer Engineering Cape Peninsula University of Technology Cape Town, South Africa
dominicgapril@gmail.com

MTE Kahn
Department of Electrical, Electronic and Computer Engineering Cape Peninsula University of Technology Cape Town, South Africa
kahnt@cput.ac.za

***Abstract*—This paper provides an overview of the connection between electrified transport and energy systems. The increasing electrification of vehicles to hybrid electric vehicle reduces the dependence of transportation on fossil fuels and reduces carbon emissions. Hybrid electric vehicles come with economic and environmental benefits that are significantly reshaping the modern transportation sector. Electric transportation (ET) also brings challenges to Smart Grid (SG) and Microgrid (MG) deployment. These include power quality, power reliability and control. There thus is a need to explore enabling technologies for electric transportation that are compatible with MGs and the evolving SG. The unreliable and inconsistent nature of Renewable Energy Resources (RER) based generation is due to its dependence on weather conditions and requires efficient, reliable, flexible and distributed energy storage technologies that will enable energy to be available for consumption when needed. The Electric Vehicle (EV) storage battery may play an important role in accommodating RER based generation and be a viable contributor towards deployment of MG systems. Electric transportation technology comes with the feature of Vehicle to Grid (V2G) and other application concepts that enable energy to be stored and fed back to the main grid during periods of high demand. The objective of this paper is to explore the electric transportation industry and its impact on the electric system. The V2G technology and its implementation is reviewed. Further, the paper investigated some issues and challenges of energy storage technologies in electric vehicles and also reviews the role of EVs in reducing carbon emission to the atmosphere.**

Keywords—storage, smartgrid, microgrid, Electric transportation, renewable energy, distributed generation

[1] INTRODUCTION

Globally, the power sector is predominantly reliant on fossil fuels for energy generation [1]. Conventional transportation systems, utilize internal combustion engines, which are major contributors to air pollution [2]. There is a call for cleaner, sustainable energy production as conventional fossil fuels are not only damaging to the environment, but are also depleting at an advanced rate [3]. The current electric grid is predominantly centralized and unidirectional, which warrants a revolutionary change as global energy demand is estimated to increase by 50%, by 2030 [4].

The transport sector is the second highest industry responsible for air pollution across the globe, as it produces nearly a quarter of greenhouse gas (GHG) emissions. The electric power generation sector contributes 40% towards GHG emission, with the transportation sector contributing 30%, as illustrated in Fig. 1. GHG emission from renewable energy resources is in the region of 5% [5].

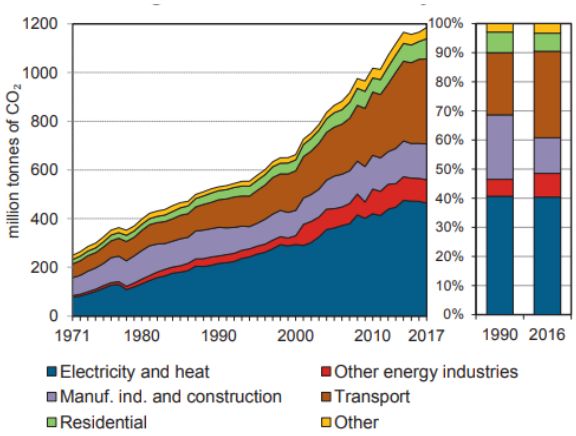


Fig. 1. Co_2 emissions by sector (Africa), 2019 [6]

[2] METHOD

This report presents a review of interplay between the electrical energy system and electric transportation. The following is discussed:

- Electric Transportation
- Energy storage technologies deployed for EVs
- Impact of EV integration on the grid
- EV charging infrastructure
- Vehicle-to-other applications
- Policy Landscape

A conclusion is presented in the final section.

[3] ELECTRIC TRANSPORTATION

The transportation industry is predominantly dependent on oil, utilizing roughly 60% of its total consumption [4]. It is predicted that oil consumption will increase by 54%, by 2035 [3]. Furthermore, the International Energy Agency (IEA) warns that a reduction in global oil demand, especially from the transport sector, is crucial to reaching net-zero emission ambitions [4]. There thus exists an urgent need to convert the transportation sector from running off crude oil, to utilizing electricity.

Electric transportation is increasing in popularity, gaining interest annually due to its promising environmental and economic benefits. According to [5], electric car sales soared in recent years, with around 17 thousand on the roads in 2010, escalating to 7.2 million by 2019. Electric transportation is classified in the following categories [4]:

(a) Battery Electric Vehicles (BEV) - fully operated through electricity.

(b) Hybrid Electric Vehicles (HEV) - function through a combination of the combustion engine and BEV, where

the battery is utilized for power delivery at low speeds and the combustion engine at higher speeds.

(c) Plug-In-Hybrid Electric Vehicle (PHEV) - Similar to HEV, with the added feature of charging through an electric outlet.

(d) Extended Range Electric Vehicle (EREV) – a combination of BEV and PHEV, with reduced emissions and improved efficiency.

Fig. 2 illustrates the power flow of a PHEV and BEV setup.

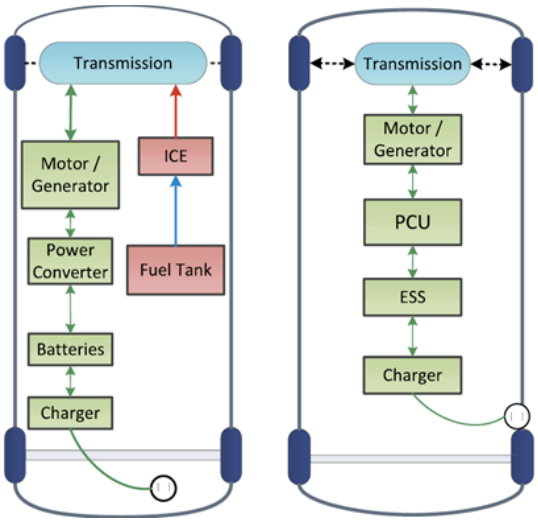


Fig. 2. Power flow of PHEV and BEV EV [2].

Research on transportation electrification indicates that the technology shows promising advantages on various challenges such as fuel economy, energy security and climate change. The use of EVs also unlocks innovative technologies in the energy sector. These include concepts such as vehicle to grid (V2G), whereby electric transportation vehicles can deliver stored energy back to the grid [2].

[4] Energy Storage Technologies Deployed for EVs

The emergence of electric transportation will not only see transport energy demand satisfied by electricity, but also a large source of distributed energy storage into the industry. The potential exists to utilize this stored energy in a way that will shift net BEV demand, in response to the electric industry's needs [7].

With the exclusion of hydropower, RE currently contributes less than 5% to electricity production. However, the contribution of RE resources towards power production is estimated to reach up to 25% by 2030 [2]. The integration of renewable energy resources to a smart grid comes with challenges and considerations with regards to control, monitoring, management, and design [8]. Using EVs in power systems together with renewable energy resources is reported to be ideally suited for the provision of ancillary services. The nature of RE resources depends on weather conditions which are highly uncertain. The penetration of electric vehicles needs energy storage systems (ESS) that will provide flexible generation, as ESS are key for reliable and efficient operation. Classification of ESS in electric transportation is illustrated in Fig. 3.

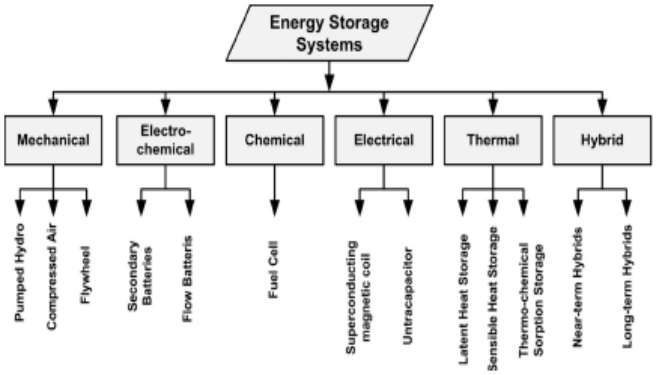


Fig. 3. Classification of ESS in electric transportation. [4].

The ability to store electrical energy is also a major challenge in the development of EV interaction with the SG. To encourage the participation of EVs in the SG, there is a need to introduce high performance energy storage technologies. Key technologies of efficient energy storage systems are a) power electronics, b) power source, and c) power flow control strategy [4].

[5] Impact of Electric Vehicle Integration on the Grid

The impact that electric vehicle grid integration (EVGI) may have, can be classified into negative and positive categories.

On the negative side, the excessive integration of EVs into the grid can impact the load profile. It may also result in voltage and frequency imbalances, excessive harmonic injection, instability, and power degradation [2].

The positive impact of EVGI is summarized in Table 1.

Table 1. Positive impact of EVGI

Advantages	Description/Method
Power Management	Scheduled charging/discharging may lead to improved power management Peak load demand can be met by scheduling discharging during peak hours
Power quality improvement [2]	Voltage surges by uncontrolled DER penetration can be addressed through controlled EVGI Voltage flickers can be smoothed out Power Factor can be corrected as required Harmonics is controllable Voltage imbalance can be addressed by the distribution of power flow through phases
Regulation [9]	Frequency regulation by correcting grid frequency deviation Voltage regulation by supplying/absorbing reactive power Improvement in stability of isolated electric networks Ramping power absorption
RE support [10]	Utilising EVs for energy storage can mitigate the uncertainty of RE

[6] ELECTRIC VEHICLE CHARGING INFRASTRUCTURE

The overall EV charging infrastructure is generally made up of a power infrastructure and control, and communication infrastructure, as is illustrated in Fig. 4.

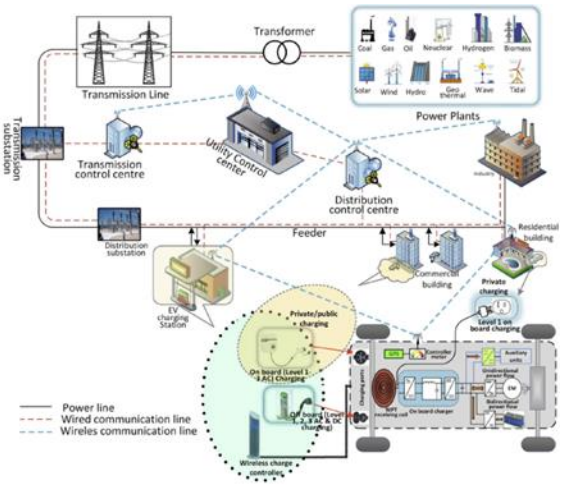


Fig. 4. Schematic diagram of EV charging infrastructure [2].

The power infrastructure provides an electric platform for bi-directional power flow between EVs and the grid, which can be classified according to the types of power used, contact requirement, accommodation of the charging circuit and direction of power flow [2]. Control and communication represents the element of the control of EV charging, through real-time monitoring and feedback. Despite the fact that EV charging loads the power system with additional demand, it can be scheduled to reduce peak demand [9] and reduce charging cost. This is possible through proper management- and coordination of grid-connected EV charging stations based on the control architecture and communication infrastructure [2].

A classification of ESS in electric transportation is illustrated in Fig. 5.

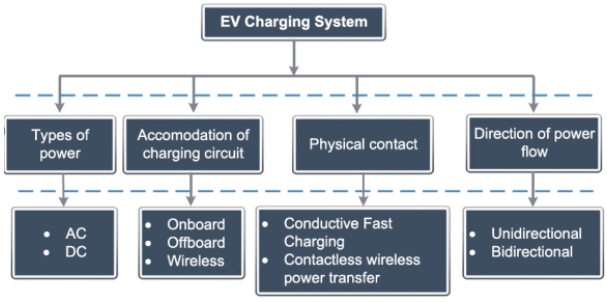


Fig. 5. Classification of EV charging infrastructure [2].

[7] VEHICLE-TO-OTHER APPLICATIONS

Electric transportation application has potential to provide power to homes, buildings and also feed energy back into the grid. The concept of vehicle to other application technology works by using stationary electric transportation as an electric power sink that can be used to withdraw power as required. The application provides bi-directional charge and discharge between electric vehicle and other power applications. The use of batteries in electric vehicles can also provide a solution for grid operators to balance demand, supply irregularities and help reduce demand of homes and buildings that have tariffs based on maximum consumption. Fig. 6 provides an illustration of a smart charging concept of a vehicle to grid application.

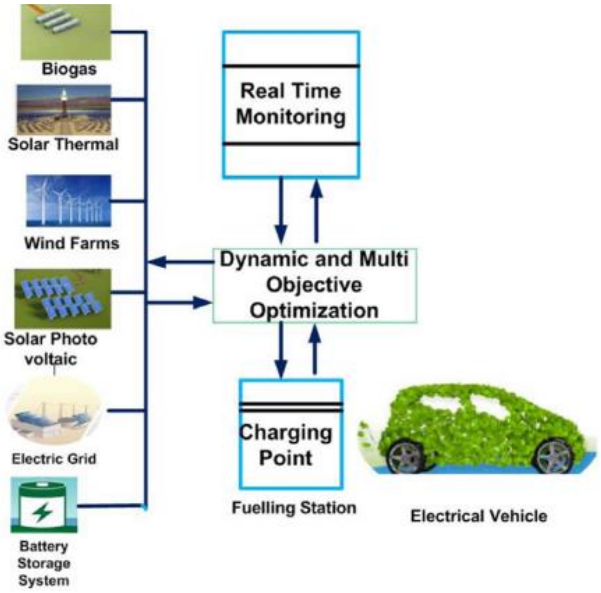


Fig. 6. Smart and optimum charging infrastructure for EVs in the SG under the V2G concept [4].

[8] POLICY LANDSCAPE

The electric transportation regulations and standards are based on its interface with the smart grid. The transition from a traditional power grid to a SG that requires sustainable operation and control needs to be regulated. These regulations and standards are implemented to cover communication system technologies and power systems according to IEEE, NIST, and IEC standards.

The policy landscape is based on the energy trilemma of energy security, carbon reduction and costs. Government's commitment is towards developing the nation's energy system and transportation industry policies by accentuating the requirement for generational mix, to deliver a secure source of electricity at an affordable price to its people.

[9] CONCLUSION

Electrical transportation can have several positive impacts on the economy, environment and electrical system operation. Advantages of the increased penetration of electric vehicles include reduced fossil fuel dependence, a substantial decrease of GHG emissions, as well as the ability to contribute to a smart grid integration of renewable energy into existing centralized electric grids. Increased innovative technology development in electric transportation will progressively integrate intelligent systems to regulate various electric grid parameters, such as voltage measurement and energy management. Some negative and positive impacts of Electric Vehicle to grid integration were reviewed. The successful implementation of the coupling EV-RES technology includes and requires the full contribution of government, power utilities, electrical vehicle manufactures, policymakers and owners.

REFERENCES

[1] K. B. Hamad and M. TE Kahn, "Modelling and Control of a grid-tied Power Conditioning Unit for a Megawatt Fuel Cell System," *Int. J. Eng. Technol.*, vol. 9, no. 1, pp. 149–163, 2020.

[2] H. S. Das, M. M. Rahman, S. Li, and C. W. Tan, "Electric vehicles standards, charging infrastructure, and impact on grid integration: A technological review," *Renew. Sustain. Energy Rev.*, vol. 120, no. November 2019, 2020, doi: 10.1016/j.rser.2019.109618.

[3] M. Uddin, M. F. Romlie, M. F. Abdullah, S. Abd Halim, A. H. Abu

Bakar, and T. Chia Kwang, "A review on peak load shaving strategies," *Renew. Sustain. Energy Rev.*, vol. 82, no. August 2017, pp. 3323–3332, 2018, doi: 10.1016/j.rser.2017.10.056.

[4] N. Shaukat *et al.*, "A survey on electric vehicle transportation within smart grid system," *Renew. Sustain. Energy Rev.*, vol. 81, no. June 2017, pp. 1329–1349, 2018, doi: 10.1016/j.rser.2017.05.092.

[5] L. Abdallah and T. El-Shennawy, "Reducing carbon dioxide emissions from electricity sector using smart electric grid applications," *J. Eng. (United Kingdom)*, vol. 2013, 2013, doi: 10.1155/2013/845051.

[6] International Energy Agency (IEA), "CO2 emisions from fuel combustion," *IEA Publ.*, pp. 1–165, 2019.

[7] G. Mills and I. MacGill, "Assessing Electric Vehicle storage, flexibility, and Distributed Energy Resource potential," *J. Energy Storage*, vol. 17, pp. 357–366, 2018, doi: 10.1016/j.est.2018.01.016.

[8] U. Tun, H. Onn, M. Taha, A. Almaktoof, and M. Kahn, "Modelling and analysis of a grid-connected multi-phase power conditioning system for high megawatt fuel cell stacks Khlid Ben Hamad , Mohamad H Taha , Ali Almaktoof , and Mohamed TE Kahn," no. March 2020, 2019.

[9] J. García-Villalobos, I. Zamora, J. I. San Martín, F. J. Asensio, and V. Aperribay, "Plug-in electric vehicles in electric distribution networks: A review of smart charging approaches," *Renew. Sustain. Energy Rev.*, vol. 38, pp. 717–731, 2014, doi: 10.1016/j.rser.2014.07.040.

[10] J. A. Domínguez-Navarro, R. Dufo-López, J. M. Yusta-Loyo, J. S. Artal-Sevil, and J. L. Bernal-Agustín, "Design of an electric vehicle fast-charging station with integration of renewable energy and storage systems," *Int. J. Electr. Power Energy Syst.*, vol. 105, no. July 2018, pp. 46–58, 2019, doi: 10.1016/j.ijepes.2018.08.001.

Heteroatom-Doped Graphene Aerogels as an Anode for Sodium-ion Batteries

Sarah Umeera Muhamad
Energy Storage Research Group,
Faculty of Ocean Engineering Technology and Informatics)
Universiti Malaysia Terengganu
Terengganu, Malaysia
umeeramuhamad@gmail.com

Nor Fazila Mahamad Yusoff
Energy Storage Research Group,
Faculty of Ocean Engineering Technology and Informatics
Universiti Malaysia Terengganu
Terengganu, Malaysia
nfazilamyusoff@gmail.com

Nurul Hayati Idris
Energy Storage Research Group,
Faculty of Ocean Engineering Technology and Informatics
Universiti Malaysia Terengganu
Terengganu, Malaysia
nurulhayati@umt.edu.my

Aim: **Sodium ion batteries (SIBs) have attracted extensive attention in large-scale energy storage mainly due to the natural abundance and low cost of sodium resources to replace lithium-ion batteries, but the slow diffusion kinetics of sodium ions hinders their energy density and electrochemistry performance. However, it is essential to produce a promising electrode material with a large surface area, which provides more active reaction sites and contact areas for electrode materials and electrolytes, and has high conductivity to ensure rapid electron transport and high porosity to access freely sodiation/de-sodiation and shorten the diffusion distance for sodium ions. Carbon materials, such as graphene, are especially promising for materials development in the energy storage and conversion fields. Graphene, a two-dimensional (2D) carbon material only a single atomic thick, including extremely low electrical and thermal resistivity, high surface area and exceptional mechanical elasticity. 2D free-standing graphene films and powders have paved the way for promising energy applications. Recently, much effort has been spent trying to improve the number of active sites in electrode materials within 3D network/aerogel structures derived from graphene.**

Method: **Herein, a porous interconnected three-dimensional (3D) heteroatom (such as nitrogen, or sulfur)-doped graphene aerogel (GA) were prepared via a one-pot hydrothermal treatment.**

Results: **X-ray diffraction and Raman spectroscopy confirm the formation of heteroatom doping in GA composites. From 3D morphology and pore size, in conjunction with heteroatom-doping, this composite could lead to a promising anode for SIBs with high electrochemical performances.**

Conclusion: **Thus, GA has been considered as one of the fascinating carbonaceous anodes for SIBs in recent years.**

Keywords— Graphene aerogel; Heteroatom; Freeze-drying; Anode; Sodium-ion batteries

Graphenated Carbon Nanotubes Cotton as Potential Counter Electrode in Dye-Sensitized Solar Cells Application

Yusnita Yusuf
Institute of Advanced Technology
University Putra Malaysia Selangor, Malaysia
yusnita5890@gmail.com

Suhaidi Shafie
Department of Electrical and Electronic Engineering University Putra Malaysia
Selangor, Malaysia
suhaidi@upm.edu.my

Ismayadi Ismail
Institute of Advanced Technology
University Putra Malaysia Selangor, Malaysia
ismayadi@upm.edu.my

Fauzan Ahmad
Malaysia-Japan International Institute of Technology University Teknologi Malaysia (of Affiliation)
Kuala Lumpur, Malaysia
fauzan.kl@utm.my

Mohd Nizar Hamidon
Department of Electrical and Electronic Engineering University Putra Malaysia
Selangor, Malaysia
mnh@upm.edu.my

Pandey Shyam Sudhir
Biological Functions Engineering
Kyushu Institute of Technology
Kitakyushu, Japan
shyam@life.kyutech.ac.jp

***Abstract*—In this study, we provide a comparative study of graphenated-carbon nanotubes cotton (g-CNTC) and conventional platinum (Pt) as an electrocatalyst for triiodide reduction in dye-sensitized solar cells (DSSCs). The results obtained from FESEM, Raman, and J-V measurements respectively, which expose the microstructure, graphitization and J-V characteristics were analyzed. Interesting features of these measurements were obtained and will be presented in detail. Briefly, the photovoltaic conversion energy of g-CNTC and Pt with efficiency of 2.83% and 3.12% respectively.**

Keywords—DSSCs, platinum-free, carbon counter electrode, carbon nanotubes cotton, g-CNTs

[1] INTRODUCTION

Dye-sensitized solar cells (DSSCs) are considered as next generation in photovoltaic technologies. It was introduced in 1991 by O'Regan and Gratzel. It has attracted attention because of their benefits lie on easy fabrication, light, economic ways, and outstanding performance in low light condition [1][2][3][4]. DSSC structure consists of semiconductor metal oxide usually deposited on the Fluorine-tin oxide (FTO) transparent photoelectrode, sensitized dye, electrolyte and counter electrode [5][6]. Semiconductor metal oxide typically used in DSSCs are Titanium dioxide, Tin(II) oxide and Zinc oxide. Photoelectrode compose of semiconductor layer and sensitized dye. It channels the electrons from the dye to external loads. The sensitized dye such as N719 dye responsible for light absorption and electron transfer through electron injection from the dye into the conduction band of the semiconductor photoanode. The electrolyte contains redox couple usually iodide/triiodide. The counter electrode serves as catalyst and generates photocurrent when the electrons transfer from the external circuit to the electrolyte to reduce triiodide reduction in regenerating the dye after injecting the electrons. The working cycle of the DSSC begins when the dye molecules absorb photons of sufficient energy under the sunlight irradiation to induce the transfer of electrons from the ground states to excited states and the excited electrons are introduced into the semiconductor layer conduction band. After they are transferred to the conductive substrate, the current flows to the counter electrode via the external circuit. At the same time, the reaction of oxidation/reduction occurring in the electrolyte. The dye molecules in the reduced oxidation state are receiving electrons through the external circuit which turns the dye molecules to their original state.

Platinum (Pt) has been widely used for the catalyst which proven a good catalytic activity and low resistance. The best efficiency of 12.3% was obtained using Cobalt(ll/lll)-based redox electrolytes and Pt-based counter electrodes [7]. However, Pt-based counter electrode easily to corrode when interact with liquid-based electrolyte and high cost. It also was found to degrade over time when in contact with the liquid electrolyte, consequently, decrease the performance of DSSC. In order to solve the problems, looking for the affordable materials, simple fabrication and good stability with help the economical way in large-scale production of DSSCs.

Presently, carbon-based materials such as graphene [8], graphite [9] and carbon black [10] are remarkable materials and being studied to Pt alternatives. This material has provided a significant characteristic such as high electrical conductivity, high surface area, resistance to iodine corrosion.

Hence, we approach graphenated-carbon nanotubes cotton (g-CNTC) for counter electrode. There is limited of report on the synthesis of g-CNTC via single route process to obtain g-CNTC in cotton bulk form and in application of DSSCs. Therefore, this work provides a comparative study of g-CNTC which later to use it as potential counter electrode.

[2] EXPERIMENTAL DETAILS

A. Materials

The materials used to synthesis CNT cotton were purchased from the following providers: ferrocene (98%) Sigma Aldrich, thiophene (99%) Alfa Aesar and ethanol Hmbg. Meanwhile, materials for DSSC fabrication were ethyl cellulose (48% ethoxyl), hexachloroplatinic acid hexahydrated obtained from Sigma Aldrich. Alpha-terpineol (97%) was supplied from Acros organics. Fluorine doped tin oxide (FTO) coated glass from Zhuhai Kaivo Optoelectronic Technology Co. Ltd (<15 Ω/sq). Ti-Nanoxide D/SP paste, N719 dye and polymer spacer were purchased from Solaronix Switzerland.

B. Synthesis of G-CNTC using FCCVD method

G-CNTC was synthesized using floating catalyst chemical vapor deposition (FCCVD) at 1100 °C using a mixed gas of argon (200 sccm) and hydrogen (100 sccm) as carrier gas,

thiophene as growth rate enhancer (0.86 wt%), ferrocene as catalyst (1.9 wt%) and ethanol as carbon source. This synthesis was carried out by injecting carbon sources with flow rate of 6 ml/hr, while the parameters such as temperature, catalyst precursor, and gas flow rate were fixed. The detailed synthesis of CNT reported in the literature [11][12][13][14]. The optical micrograph of synthesize g-CNTC presented in Fig. 1. The sample produced during the synthesis was in cotton bulk and eventually crushed by ball milling energy in 30 minutes to make a grinded powder.

C. *Preparation of counter electrode*

The preparation of g-CNTC paste through a simple mixing process. The weight ratio of carbon to binder (20:70). Binder consists of alpha terpineol and ethyl cellulose. The binder then stirred on the hotplate until the ethyl cellulose dissolved in the alpha terpineol. Subsequently, the amount of g-CNTC was added little by little into the binder to prevent the agglomerates. Then, the mixture was left to stir for 24 hours to obtain homogenous conductive paste. Eventually, the paste was deposited using doctor blade method onto FTO glass by single layer coating. The coated electrode was sintered at 500 °C for 30 mins. For comparison, the reference electrode composed of platinum electrode was annealed at the same condition.

D. *Preparation of photoanode*

The cleaned photoanode glass was pre-treated in 40mM $TiCl_4$ solution under 80 °C for 1 hour. This treatment is to ensure the adhesion of TiO_2 on the FTO glass. Then, the glass was rinsed with deionized water followed by sintering at 500 °C for 30 minutes. The single layer of TiO_2 paste was deposited onto the treated FTO glass using screen-printing method with active area of 0.25 cm^2. The coated electrode was then dried on hotplate for 20 minutes to prevent the active layer from thermal shock during heat treatment. Then, coated TiO_2 was sintered at 450 °C for 30 mins. The sintered electrode was treated in 40mM TiCl4 solution again using the same procedure. The post-treatment photoanode was immersed in 4 mM of N719 dye for 48 hours and kept at room temperature.

E. *DSSC assembly and I-V measurement*

The photoanode loaded with dyes has been rinsed and dried. Then, the photoanode along with counter electrode were assembled which attached with 60 µm spacer. Finally, the electrolyte was injected into the solar cells device and immediately sealed with UV-cured resin. This is to prevent the electrolyte from evaporate during testing. The solar cell device was measured using solar simulator accordingly.



Fig. 1 Optical micrograph as-synthesized g-CNTC

[3] Research Findings

A. *Microstructural analysis*

The FESEM image of g-CNTC grown by single step floating catalyst CVD present in Fig. 2. The structure provide graphene foliates on a CNT. This structure is called hybrid structure of graphenated CNTs. A leaf-like growing from the CNT stem is called graphene foliates. It has a long visible nanotube with the diameter of 0.04 µm which indicated that the CNT produces multiwall CNT and consists of g-CNTC foliates growing out from the sidewalls of multiwall CNTs.

B. *Raman analysis*

The Raman spectra demonstrated in Fig. 3, display a dominant peak at 2698 cm^{-1} (2D), D and G band at 1356 cm^{-1} and 1589 cm^{-1} respectively. An increase in G band peak at 1589 cm^{-1} when the foliate structures are present on the CNTs. On the other hand, the increase of 2D band cause the existing of single layer of graphene [15]. The intensity ratio of D and G (I_D/I_G) band can be used to estimate the number of structural defects that exist in carbon materials. In this analysis, the ratio is 0.85 indicated a good graphitic of synthesized g-CNTC.

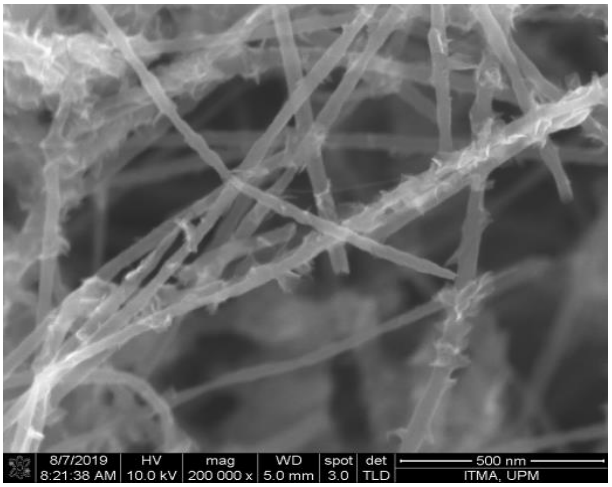


Fig. 2 Microstructure of g-CNTC

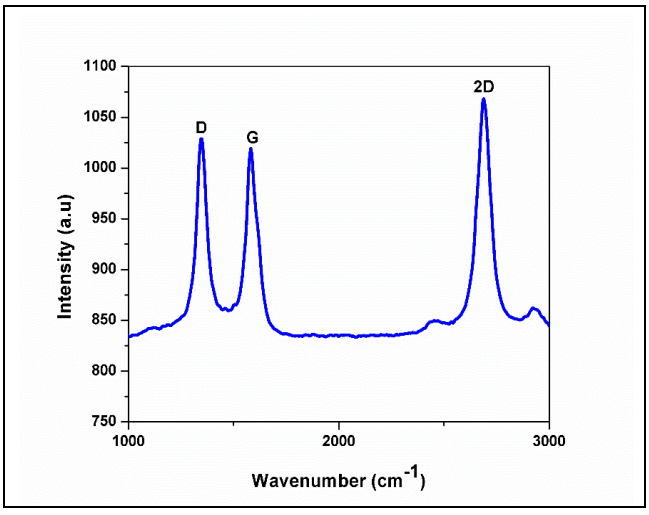


Fig. 3 Raman spectra of g-CNTC

C. *Current density-voltage measurement characteristics*

The J-V measurement of fabricated DSSCs was presented in Fig. 4 and tabulated in Table I. The measurement tested using simulated solar under 100mW/cm^2 (1.5AM) with an active area of 0.25 cm^2. The Jsc, Voc, and FF of the cell device with a conventional Pt counter electrode are 11.51 mA/cm^2, 0.67 mV and 0.40 respectively. An overall efficiency of 3.12%. For comparison, the corresponding parameters of applied g-CNTC counter electrode are 9.11 mA/cm^2, 0.66 mV, 0.47, and obtained efficiency of 2.83%. The efficiency was lower than the reference due to the decreased of Jsc. It suggests that the reduction of iodide/triiodide in the electrolyte is lower than that conventional Pt. The performance is lower may cause during the fabrication process, and any residue vehicles during firing process of the g-CNTC electrode.

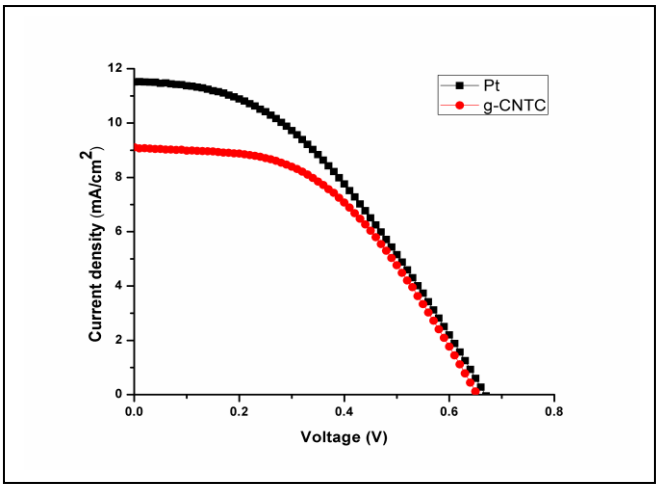


Fig. 4 J-V curve measurement

Table I. J-V Characteristics

Samples	Voc (V)	Jsc (mA/cm^2)	FF	Efficiency (%)
Pt	0.67	11.51	0.40	3.12
g-CNTC	0.66	9.11	0.47	2.83

[4] CONCLUSION

In conclusion, we have provided that g-CNTC can be used as electrocatalyst for triiodide reduction in DSSCs. The efficiency of 2.83% is obtained from g-CNTC counter electrode. The overall performance can be enhanced with varying the thickness of deposited g-CNTC.

ACKNOWLEDGMENT

This research work was supported by Universiti Putra Malaysia under UPM-Kyutech grant No. 9300465.

REFERENCES

[1] S. Buda, S. Shafie, S. Abdul Rashid, H. Jaafar, and A. Khalifa, 'Response surface modeling of photogenerated charge collection of silver-based plasmonic dye-sensitized solar cell using central composite design experiments', in *Results Phys.*, vol. 7, 2017, pp. 493–497.

[2] N. F. M. Sharif, M. Z. A. A. Kadir, S. Shafie, S. A. Rashid, W. Z. Wan Hasan, and S. Shaban, 'Charge transport and electron recombination suppression in dye-sensitized solar cells using graphene quantum dots', in *Results Phys.*, 2019, vol. 13.

[3] M. Q. Lokman *et al.*, 'Enhancing photocurrent performance based on photoanode thickness and surface plasmon resonance using Ag-TiO_2 nanocomposites in dye-sensitized solar cells', in *Materials (Basel).*, vol. 12, no. 2111, 2019.

[4] A. Khalifa *et al.*, 'Comprehensive performance analysis of dye-sensitized solar cells using single layer TiO_2 photoanode deposited using screen printing technique', in *Optik (Stuttg).*, vol. 223, no. September, 2020 p. 165595.

[5] R. Eisenberg and D. G. Nocera, 'Preface: Overview of the forum on solar and renewable energy', in *Inorg. Chem.*, vol. 44, no. 20, 2005, pp. 6799–6801.

[6] A. Hagfeldt, G. Boschloo, L. Sun, L. Kloo, and H. Pettersson, 'Dye-sensitized solar cells', in *Chem. Rev.*, vol. 110, no. 11, 2010, pp. 6595–6663.

[7] M. G. Aswani Yella, Hsuan-Wei Lee, Hoi Nok Tsao, Chenyi Yi, Aravind Kumar Chandiran, Md.Khaja Nazeeruddin, Eric Wei-Guang Diau, Chen-Yu Yeh, Shaik M Zakeeruddin, 'Porphyrin-sensitized solar cells with yield shorter electron lifetimes when used in the DSC', in *Science*, vol. 334, no. December, 2011, pp. 629–633.

[8] E. Igman, O. Bayram, A. Mavi, U. C. Hasar, and O. Simsek, 'Photovoltaic performance of non-covalent functionalized single-layer graphene in dye-sensitized solar cells (DSSCs)', in *J. Mater. Sci.*, vol. 56, no. 6, 2021, pp. 4184–4196.

[9] F. Karim *et al.*, 'Nanostructured dye sensitized solar cells with different counter electrodes', in *Am. J. Phys. Chem.*, vol. 9, no. 1, 2020, p. 1.

[10] H. Jaafar, M. F. Ain, and Z. A. Ahmad, 'Performance of dye-sensitized solar cell (DSSC) using carbon black-TiO_2 composite as counter electrode subjected to different annealing temperatures', in *Opt. Quantum Electron.*, vol. 52, 2020, no. 4.

[11] I. Nur Izzaiti, I. Ismayadi, M. M. Shuhazly, and A. N. Lyana, 'Effect of carbon source injection rate on CNT film via loating catalyst CVD method', in *Solid State Phenom.*, vol. 290, 2019, pp. 113–121.

[12] N. L. Adnan, I. Ismail, and M. Hashim, 'Effect of ferrocene concentration on the carbon nanotube cotton synthesized via floating catalyst CVD method', in *Aust. J. Basic Appl. Sci.*, vol. 9, no. 12, 2015, pp. 109–113.

[13] I. Ismail, J. Md Yusof, M. A. Mat Nong, and N. L. Adnan, *Synthesis of carbon nanotube-cotton superfiber materials*. in Elsevier Inc., 2018.

[14] I. Ismail, S. Mamat, N. L. Adnan, Z. Yunusa, and I. H. Hasan, 'Novel 3-Dimensional cotton-like graphenated-carbon nanotubes synthesized via floating catalyst chemical vapour deposition method for potential gas-sensing applications', in *Journals Nanomater.*, vol. 2019, 2019, pp. 1–10.

[15] O. Fesenko, G. Dovbeshko, A. Dementjev, R. Karpicz, T. Kaplas, and Y. Svirko, 'Graphene-enhanced raman spectroscopy of thymine adsorbed on single-layer graphene', in *Nanoscale Res. Lett.*, vol. 10, no. 1, 2015, pp. 1–7.

Microwave absorbing properties of Fe_3O_4 from waste mill scales

Madiha Fathi Elmahaishi

Department of Physics Faculty of Science, University Putra

Malaysia43400 UPM, Serdang, Selangor, Malaysia
gs57071@student.upm.edu.my

Department of Physics, Material Synthesis and Characterization Laboratory (MSCL), Institute of Advanced Materials, Faculty of Science, University Putra Malaysia43400 UPM, Serdang, Selangor, Malaysia
rabaah@upm.edu.my

Ismayadi Ismail
Material Synthesis and Characterization Laboratory (MSCL), Institute of Advanced Materials, Universiti Putra Malaysia, 43400 UPM
Serdang, Selangor, Malaysia
ismayadi@upm.edu.my

Raba'ah Syahidah Azis

***Abstract*—In this work, the powder samples have been extracted from mill scale waste materials with the magnetite (Fe_3O_4) as the raw utilized, and synthesized using a magnetic separation process. The waste mill scales in the form of flakes were grinding for 1, 4, 8 days to form a homogeneous powder to gain the micron size of powder using steel pot ball milling. While Fe_3O_4 nanoparticles were prepared using the high energy ball milling (HEBM) method with three milling time variations of 3, 6, and 12 hours. The effect of milling time has been investigated. Effect of particle size on the microwave absorption properties in high-frequency bands (8 - 18 GHz) (X and Ku band) frequency range was studied by vector network analyzer (VNA). The results of this work, the optimum minimum reflection loss (RL) of the particles obtained after 8 days of conventional-milling reaches – 30.83 dB at 9.72 GHz with a thickness of 2 mm. While the best maximum refection loss of –20.59 dB at the frequency and bandwidth of 16.35 GHz was achieved in the Nano-particles Fe_3O_4 milled for 3 hours with a thickness of 1 mm. The effective frequency bandwidth (RL ≤ −10 dB) is 2.43 GHz. The purpose of this research was to focus on the influence of particle size on the electromagnetic properties of magnetite reutilized from waste steel product.**

Keywords— magnetite, particle size, high-energy ball milling, a conventional miller, microwave absorption.

I. INTRODACTION

Recently, the research on microwave absorbing materials (MAMs) has devoted many efforts due to the rapid advancement of science and technology, which in turn lead to the rapid proliferation of wireless gadgets, electrical equipment, and information systems that operate at super high frequency range has led to the continuous rise in electromagnetic (EM) interference with electronic equipment [1, 2]. The high emission of EM waves into the atmosphere is a severe health danger, which is harmful to people's health and affects the normal operation of electronic equipment [3]. Fabrication of EM wave absorptive materials capable of dissipating unwanted EM energy has been widely explored as a viable solution to tackle this issue, reducing EM radiation, and improving the human living environment [4, 5]. Strong absorption, light-weight, wide absorption bandwidth, reduced-thickness MAMs, and low cost, strong attenuation property, and good impedance match are all desirable characteristics of an effective microwave absorbing materials (MAM) [6 - 8].

Ferrite materials such as Fe_3O_4, have been widely applied in the magnetic resonance, magnetic sensor, and microwave absorption field due to their low cost, excellent magnetic properties, and distinct absorption properties among the options for EM wave absorbers. Magnetic absorbers have been singled out as potential microwave absorption materials because their high saturation magnetization gives them a high value in the gigahertz range, allowing them to exhibit electromagnetic properties with higher working frequencies and a wider frequency band [9-11]. Since lower coercivity favored for the increase of permeability, which improves microwave absorption, a small sized nanomaterial is preferred [12]. However, the metallic nature, i.e., eddy current, limits their application at high frequency band, so, among magnetic materials, metallic powders are unable to maintain stability and are easily oxidized when they come into the Nano world [13, 14]. These issues hampered the widespread use of metallic materials for microwave absorption. Magnetite materials, which include various types of ferrites [15- 16] , carbonyl iron [17], and inorganic magnetic microspheres [18], have been extensively studied and used in practice due to their high saturation magnetization and high coercivity, both of which lead to magnetic energy loss [19].

Compared to metallic absorbers, magnetite (Fe_3O_4) has an inverse spinel cubic structure, and is an important magnetic absorber [20, 21]. It is endowed with high dielectric properties, excellent complex permeability and permittivity, which are significant governing parameters in EM wave absorption. This is due to its unique magnetic properties, such as high magnetization saturation, high Curie temperature, high resistivity, good chemical stability, and a high scientific resonance frequency [22]. Thus, have greater potential as high-performance microwave absorbers, permanent magnets, and recording medium [23]. Therefore, a great deal of studies has been done to design novel absorbers with advanced performances [24-26]. Though magnetite is very attractive as an MAM, it has some limitations because of rapid decrease in permeability value at microwave frequency, large density, an impedance mismatch and poor antioxidation which impedes its performance as an ideal MAM [27]. To enhance the properties of magnetite, and to give advantages properties for using as-prepared Fe_3O_4 to design MAM, this by improving the size of the particle using ball-milling techniques. The ball-milling can not only reduce particle size but also introduce numerous defects, which strengthens the dielectric relaxation. At the same time, the multi-interfacial polarization induced between silicates and magnetite during the ball milling process, resulting in the improvement of the Fe_3O_4 properties as microwave absorption performance. Additionally, the synergy effect of dielectric loss and magnetic loss can be optimized to form good impedance matching [28].

Magnetite particles (Fe_3O_4) obtained from millscale possess strong magnetic properties and hetero-interfaces formed by impurities, which are expected to be helpful in improving EM wave absorption. So far, however, there has been little discussion on the microscopic absorption properties of Fe_3O_4 gained from a waste mill scales product.

Furthermore, considering microwave absorption strongly correlates with particle size, we conduct ball milling to enhance the EM wave properties of Fe_3O_4 since ball milling can conveniently control the size of the magnetite. The size and morphology of the particles are two important characteristics influencing their electrical, optical, and magnetic properties [29]. Syntheses of (Micron and Nano) particles with variable size or homogeneous morphology have been intensively tried particularly for magnetic iron oxides with spinel structure, of magnetite (Fe_3O_4) [30, 31].

In this study, magnetite was extracted from waste millscale by using high intensity of magnetic field and reduced size by using conventional milling method (CM) to reduce the size of the particles to the Micron particles. Then, the Micron particle size reduced from micro-particles to nanoparticles size after high energy ball mill (HEBM), which is one of the simplest methods to reduce the size of the particles to the nanoparticles. The effect of the milling time was reported to affect the particles size, specific surface area, and the electromagnetic properties as well. The microwave absorption properties of magnetic particles milled at different milling time were tested in the range of 8.0–18.0 GHz, and the mechanism of EM wave loss was elaborated upon.

II. RESEARCH METHODS

A- *Preparation of Fe_3O_4*

The raw mill scales were obtained from steel factories in Malaysia. The mill scales were crushed using the conventional steel ball milling for 1, 4, 8 days to obtain the micron-sized powder. The milled powder was purified by using magnetic separation technique to extract magnetic compound Fe_3O_4. The magnetic separation routes were carried out similar to the previous reports by Azis et al. [32]. The powder mixtures was further milled using a high energy ball milling (HEBM) a SPEX8000D mill in a hardened steel vial together with grinding balls having a diameter of 12 mm each. The milling time of 3, 6, 12 hours and the ball to powder weight ratio (BPR) ratio of 10:1 with fixed rotating speed at 1450 rpm, were used to obtain nanoparticles powder.

B- Composite preparation and microwave properties measurement

The composite samples were prepared for electromagnetic microwave absorption measurement. The Fe_3O_4 powder was mixed with epoxy resin as a matrix. The composite samples were prepared by mixing the Fe_3O_4 powder samples in epoxy polymer matrix with weight ratio of 70:30 and then, the mixture was mixed homogeneously by using a mini vortex mixer for 30 minutes at speed of 3000 rpm (rotation per minutes). The mixtures were poured in the standard waveguide rectangular mould with inner dimension 23 × 10 mm (X-band) and 15 × 7 mm (Ku-band) respectively, with fixed thickness 1, 2 and 3 mm. The samples were dried for 24 h at room temperature. The variation of complex permeability, complex permittivity, as well as Reflection Loss (RL) with frequency of the composite samples were analyzed using a PNA network analyzer N5227A via transmission reflection line method (TRL). The composites specimens were measured in the 8-12 GHz (X-band) and 12-18 GHz (Ku-band) frequency range.

III. RESULTS AND DISCUSIONS

Fig. 1 shows the reflection loss (RL) response of Micro Fe_3O_4-CM composites at different thickness of 1 mm, 2 mm and 3 mm conventional milling method. The electromagnetic microwave absorbing properties of Fe_3O_4 was measured using a VNA. Ideal absorbing properties represent $Z_0 = Z_{in} = 1$ in which a material allows an EM wave to penetrate easily and completely absorbs the EM energy within itself. Here Z_0 is the impedance of free space and Z_{in} is the input impedance at the free space-absorbing materials interface. RL refer to the absorption ability of a material is defined as (1):

$$RL\ (dB) = 20 \log \frac{(z_{in}-1)}{z_{in}+1} \quad (1)$$

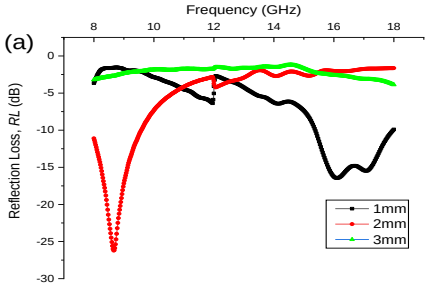
Where Z_{in} is the normalized input impedance obtained from the following (2):

$$z_{in} = z_0 \sqrt{\frac{\mu_r}{\varepsilon_r}} \tan h\,[j(\frac{2\pi f t}{c})\sqrt{\mu_r \varepsilon_r}] \quad (2)$$

Where f is the frequency of the incident wave, t is the thickness of the absorber, c is the velocity of EM waves in free space, μ_r is the relative permeability, ε_r is the relative permittivity. Generally, by having RL values less than −10 dB and −20 dB indicating more than 90% and 99% of the introduced EM wave being absorbed [33, 34]. Based on the model of the metal-backed matching as a microwave-absorption layer, the reflection loss (RL) values were calculated according to the transmission-line theory [35].

A- *Evaluation of the microwave absorption performance for Micron size Fe_3O_4 gained by Conventional Milling (CM)*

Fig. 1(a-c) shows the plots of the RL versus frequency for the Micron Fe_3O_4-CM at various thicknesses in the frequency range of 8–18 GHz. It can be seen that all three samples exhibit well microwave absorption properties in the test frequency range. The best minimum RL are observed of –26.21 dB, –25.96 dB, and –30.83 dB for the samples of 1 day, 4 days, and 8 days are achieved at bandwidth of 8.66 GHz, 15.39 GHz, and 9.72 GHz with the matching thickness of 2.0 mm, 1.0 mm, and 2.0 mm, respectively. From the graph, the value of maximum reflection loss with respect to the frequency for each conventional milling time was tabulated in Table 1.



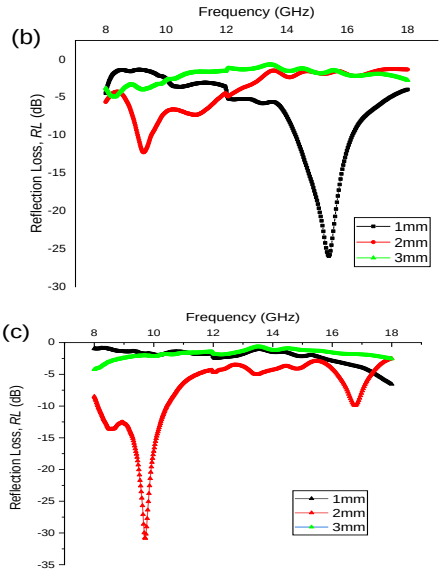


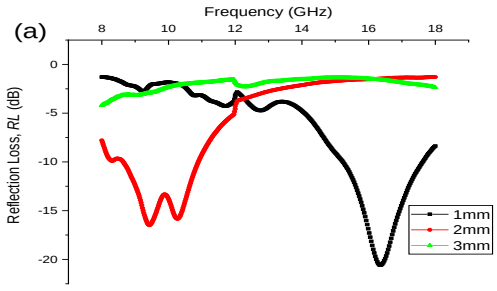
Fig. 1. Reflection loss curve (RL) for Fe_3O_4 via a CM method at various milling time (a) 1 day, (b) 4 days, and (c) 8 days at thicknesses of 1,2 and 3 mm.

Table 1. Microwave Absorption Properties Of Magnetite Prepared By Conventional Milling Method At Thickness Of 1, 2, 3 (MM)

Milling time (days)	*Peak value, f_m (GHz)*	*Thickness (mm)*	*Minimum RL value (dB)*	*Frequency bandwidth (GHz) (RL<−10 dB)*
1	16.11	1	-16.44	2.52
	8.66	2	-26.21	1.76
	10.52	3	-1.90	0.56
4	15.39	1	-25.96	1.86
	9.26	2	-12.26	0.50
	8.28	3	-4.94	0.60
8	12.06	1	-2.48	1.17
	9.72	2	-30.83	2.30
	10.00	3	-2.18	0.76

B- Evaluation of the microwave absorption performance for Nano size Fe_3O_4 gained by high energy ball mill HEBM

The performance of the micro-size CM samples of microwave absorption was also compared with that of the nanoscale HEBM samples. The variation in reflection loss with frequency for all samples of Fe_3O_4-HEBM composites after 3, 6 and 12 days HEBM milling time is shown in Fig. (2), (a), (b) and (c) are the reflectivity curves of 3-, 6-, and 12-hours milling time, respectively. The maximum reflection loss with respect to the frequency are shown in Table 2.



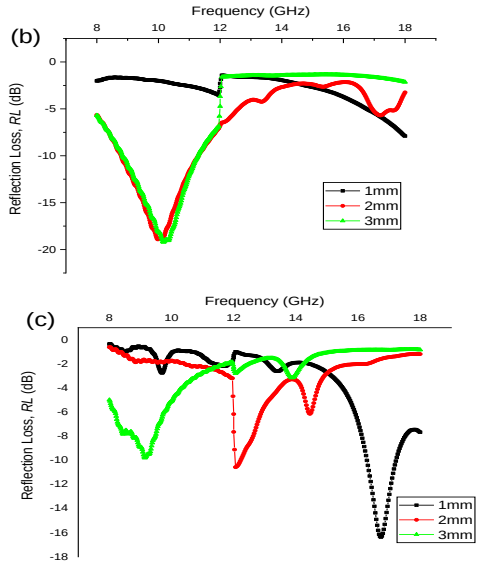


Fig. 2. Reflection loss curve (RL) for Fe_3O_4 prepared via a HEBM method at various milling hours, (a) 3 hours, (b) 6 hours, and (c) 12 hours at thicknesses of 1, 2 and 3 mm.

Table 2. Microwave Absorption Properties Of Magnetite Prepared By Conventional Milling Method At Thickness Of 1, 2, 3 (MM)

Milling time (hours)	*Peak value, f_m (GHz)*	*Thickness (mm)*	*Minimum RL value (dB)*	*Frequency bandwidth (GHz) (RL<−10 dB)*
3	16.35	1	-20.59	2.43
	9.42	2	-16.48	2.26
	12.27	3	-2.28	1.11
6	11.96	1	-3.53	1.99
	9.98	2	-18.91	2.48
	10.16	3	-19.20	2.44
12	16.74	1	-16.36	0.93
	12.06	2	-10.56	0.21
	9,14	3	-9.80	0.00

It was observed that as milling time increases, the peak of the reflection loss shifts to lower frequencies. After milling for 3 h, the Nanoparticles had the largest reflection loss peak near 16.35 GHz with a reflectance of –20.59 dB. At the same time, with the ball milling time increased to 6 h, due to the imaginary part of the dielectric constant decreases, the impedance matching performance still similar, and absorbing performance has improved with wider frequency bandwidth (GHz) (RL<−10 dB). It seems that most of these particles exhibit semi-irregular results and the ball milling effectively reduces particle size. Even though ball milling is beneficial in improving some properties, overextended milling has an alternative effect. At appears that the longer milling time, the maximum Absorption value was decreased. For 3-hour milling time, the RL value is about –20.59 dB at 16.35 GHz frequency, while for a 6-hour milling time, the absorption is around –19.20 dB at a frequency of about 10.16 GHz. As for 12-hour milling time, the minimum reflection loss decreases to about –16.36 dB with the increase of frequency band to 16.74 GHz.

Conclusions

In summary, we investigated the electromagnetic properties of the magnetite extracted from mill scale waste with different particle sizes in the frequency range of 8–18 GHz. The results indicate that the particle size has great

effects on the EM properties of the Fe_3O_4 that resulted after different milling times. The Fe_3O_4 with micro-particle size of 8 days conventional milling time shows the optimum microwave absorption properties, which has the minimum RL of –30.83 dB at 9.72 GHz with a matching thickness of 2.0 mm. The corresponding bandwidth of RL less than −10 dB is 2.30 GHz. While, the Fe_3O_4 with smaller particle size (after 3 hours milling time) exhibit optimum microwave absorption properties, –20.59 dB at high frequency band (16.35 GHz) and thin thickness (1 mm) than the corresponding larger ones in Microscale due to the improved impedance matching. Due to small thickness required of the absorbing material, this sample can be employed economically of microwave radiations in reducing EMI, radar absorbing materials and other applications.

ACKNOWLEDGMENT

The authors acknowledge the financial support from Fundamental Research Grant Scheme (FRGS/1/2016/STG02/UPM/01/2), Ministry of Higher Education Malaysia

REFRENCES

[1] Yadav, P., Rattan, S., Tripathi, A., & Kumar, S., "Swift heavy-ions irradiated nano-magnetite/exfoliated nanographite/polymethylmethacrylate nanocomposites with excellent microwave-absorption performance,". Materials Letters, vol. 253, pp. 222-225, 2019.

[2] Yu, S., Ng, V. M. H., Wang, F., Xiao, Z., Li, C., Kong, L. B., & Zhou, K, "Synthesis and application of iron-based nanomaterials as anodes of lithium-ion batteries and supercapacitors" Journal of Materials Chemistry A, 6(20), 9332-9367.I. S. Jacobs and C. P. Bean, "Fine particles, thin films and exchange anisotropy," in Magnetism, vol. III, G. T. Rado and H. Suhl, Eds. New York: Academic, 1963, pp. 271–350, 2018.

[3] Adebayo, L. L., Soleimani, H., Yahya, N., Abbas, Z., Ridwan, A. T., & Wahaab, F. A, "Investigation of the broadband microwave absorption of citric acid coated Fe3O4/PVDF composite using finite element method," Applied sciences, 9(18), p. 3877, 2019.

[4] Zou, T., Wu, Y., & Li, H, "Electromagnetic and microwave absorbing properties of carbon-encapsulated cobalt nanoparticles," Materials Letters, vol. 214, pp. 280-282, 2018.

[5] Suo, Q., Xu, B., Wang, J., & Huang, B, "Effect of high energy ball milling on electromagnetic properties of FeNi absorbing materials," In AIP Conference Proceedings (Vol. 1955, No. 1, p. 020006). AIP Publishing LLC, April 2018.

[6] Cui, G., Lu, Y., Zhou, W., Lv, X., Hu, J., Zhang, G., & Gu, "Excellent microwave absorption properties derived from the synthesis of hollow Fe3o4@ reduced graphite oxide (RGO) nanocomposites," Nanomaterials, 9(2), p. 141, 2019.

[7] Kong, L., Yin, X., Yuan, X., Zhang, Y., Liu, X., Cheng, L., & Zhang, L, "Electromagnetic wave absorption properties of graphene modified with carbon nanotube/poly (dimethyl siloxane) composites," Carbon, vol. 73, pp. 185-193, 2014.

[8] Chen, S., Chi, M., Zhu, Y., Gao, M., Wang, C., & Lu, X, "A Facile synthesis of superparamagnetic Fe3O4 nanofibers with superior peroxidase-like catalytic activity for sensitive colorimetric detection of L-cysteine," Applied Surface Science, vol. 440, pp. 237-244, 2018.

[9] Liu, J. R., Itoh, M., Jiang, J., & Machida, K. I, "Electromagnetic wave absorption properties of ε-Fe3N/Y2O3 nanocomposites derived from Y2Fe17 intermetallic compound," Journal of magnetism and magnetic materials, vol. 277(3), pp. 251-256, 2018.

[10] Yan, L., Wang, J., Han, X., Ren, Y., Liu, Q., & Li, F, "Enhanced microwave absorption of Fe nanoflakes after coating with SiO2 nanoshell," Nanotechnology, vol. 21(9), p. 095708, 2010.

[11] Lv, R., Kang, F., Gu, J., Gui, X., Wei, J., Wang, K., & Wu, D, "Carbon nanotubes filled with ferromagnetic alloy nanowires: Lightweight and wide-band microwave absorber," Applied Physics Letters, vol. 93(22), pp. 223105, 2008.

[12] Wang, Z., Wu, L., Zhou, J., Shen, B., & Jiang, Z, "Enhanced microwave absorption of Fe 3 O 4 nanocrystals after heterogeneously growing with ZnO nanoshell," RSC advances, vol. 3(10), pp. 3309-3315, 2013.

[13] Yan, S. J., Zhen, L., Xu, C. Y., Jiang, J. T., Shao, W. Z., & Tang, J. K, "Synthesis, characterization and electromagnetic properties of Fe1−xCox alloy flower-like microparticles," Journal of magnetism and magnetic materials, vol. 323(5), pp. 515-520, 2011.

[14] Liang, Y. J., Zhang, L., Chen, M., Fan, L., Liao, W., Xun, Y., & Yang, A, "Anisotropic shaped Fe3O4 nanoparticles: Microwave-assisted thermal decomposition synthesis and their electromagnetic properties," AIP Advances, vol. 10(8), p. 08520, 2020.

[15] Huang, L., Liu, X., & Yu, R, "Enhanced microwave absorption properties of rod-shaped Fe2O3/Fe3O4/MWCNTs composites," Progress in Natural Science: Materials International, vol. 28(3), pp. 288-295, 2018.

[16] Silva, L. M., Nascimento, M., Mota, I. O., Oliveira, E. M., & Castro, J. A, "Analysis of the microwave heating effect in the efficiency of comminution of iron ore particles," 2015.

[17] Zhang, J., Ma, J., Fan, X., Peng, W., Zhang, G., Zhang, F., & Li, Y, "Graphene supported Au-Pd-Fe3O4 alloy trimetallic nanoparticles with peroxidase-like activities as mimic enzyme," Catalysis Communications, vol. 89, pp. 148-151, 2017.

[18] Dong, N., He, F., Xin, J., Wang, Q., Lei, Z., & Su, B, "Preparation of CoFe2O4 magnetic fiber nanomaterial via a template-assisted solvothermal method," Materials Letters, vol. 141, pp. 238-241, 2015.

[19] Wang, S., Zhao, Y., Xue, H., Xie, J., Feng, C., Li, H., & Jiao, Q, "Preparation of flower-like CoFe2O4@ graphene composites and their microwave absorbing properties," Materials Letters, vol. 223, pp. 186-189, 2018.

[20] Wu, N., Liu, C., Xu, D., Liu, J., Liu, W., Shao, Q., & Guo, Z, "Enhanced electromagnetic wave absorption of three-dimensional porous Fe3O4/C composite flowers," ACS Sustainable Chemistry & Engineering, vol. 6(9), pp. 12471-12480, 2018.

[21] Adebayo, L. L., Soleimani, H., Yahya, N., Abbas, Z., Ridwan, A. T., & Wahaab, F. A, "Investigation of the broadband microwave absorption of citric acid coated Fe3O4/PVDF composite using finite element method," Applied sciences, vol. 9(18), p. 3877, 2019.

[22] Shanenkov, I., Sivkov, A., Ivashutenko, A., Zhuravlev, V., Guo, Q., Li, L., & Han, W, "Magnetite hollow microspheres with a broad absorption bandwidth of 11.9 GHz: toward promising lightweight electromagnetic microwave absorption," Physical Chemistry Chemical Physics, vol. 19(30), pp. 19975-19983, 2017.

[23] Qu, B., Zhu, C., Li, C., Zhang, X., & Chen, Y, "Coupling hollow Fe3O4–Fe nanoparticles with graphene sheets for high-performance electromagnetic wave absorbing material," ACS applied materials & interfaces, vol. 8(6), pp. 3730-3735, 2016.

[24] Sarkar, D., Ghosh, A., Rakshit, R., & Mandal, K, "Magnetic properties of Fe3O4 nano-hollow spheres," Journal of Magnetism and Magnetic Materials, vol. 393, pp. 192-198, 2015.

[25] Adebayo, L. L., Soleimani, H., Yahya, N., Abbas, Z., Ridwan, A. T., & Wahaab, F. A, "Investigation of the broadband microwave absorption of citric acid coated Fe3O4/PVDF composite using finite element method," Applied sciences, vol. 9(18), p. 3877, 2019.

[26] Sui, M., Sun, X., Lou, H., Li, X., Lv, X., Li, L., & Gu, G, "Synthesis of hollow Fe 3 O 4 particles via one-step solvothermal approach for microwave absorption materials: Effect of reactant concentration, reaction temperature and reaction time," Journal of Materials Science: Materials in Electronics, vol. 29(9), pp. 7539-7550, 2018.

[27] Cui, G., Lu, Y., Zhou, W., Lv, X., Hu, J., Zhang, G., & Gu, G, "Excellent microwave absorption properties derived from the synthesis of hollow Fe3o4@ reduced graphite oxide (RGO) nanocomposites," Nanomaterials, vol. 9(2), p. 141, 2019.

[28] Yan, P., Shen, Y., Du, X., & Chong, J, "Microwave Absorption Properties of Magnetite Particles Extracted from Nickel Slag," Materials, vol. 13(9), p. 2162, 2020.

[29] Zulaikah, S., Mufti, N., Fuad, A., & Dwi, L. D, "Effect of mechanical milling on particle size, magnetic susceptibility and dielectric of synthetic toner colorant magnetite extracted from Indonesian iron sand," In AIP Conference Proceedings (Vol. 1617, No. 1, pp. 156-160). American Institute of Physics, September 2014.

[30] Liang, Y. J., Zhang, L., Chen, M., Fan, L., Liao, W., Xun, Y., & Yang, A, "Anisotropic shaped Fe3O4 nanoparticles: Microwave-assisted thermal decomposition synthesis and their electromagnetic properties," AIP Advances, vol. 10(8), p. 085208, 2020.

[31] Adebayo, L. L., Soleimani, H., Yahya, N., Abbas, Z., Wahaab, F. A., Ayinla, R. T., & Ali, H, "Recent advances in the development OF Fe3O4-BASED microwave absorbing materials," Ceramics International, vol. 46(2), pp. 1249-1268, 2020.

[32] Raba'ah Syahidah Azis, M. H., Yahya, N., & Saiden, N. M, "A study of sintering temperatures variation on microstructure development of strontium hexaferrite millscale-derived," Pakistan Journal of Applied Sciences, vol. 2(12), pp. 1092-1095, 2002.
[33] Sun, G., Dong, B., Cao, M., Wei, B., & Hu, C, "Hierarchical dendrite-like magnetic materials of Fe3O4, γ-Fe2O3, and Fe with high performance of microwave absorption," Chemistry of Materials, vol. 23(6), pp. 1587-1593, 2011.
[34] S.M. Lee, "International Encyclopedial of Composites," VHC Publishers, NewYork, p. 404, 2015.
[35] Cai, X. D., Jiang, X. J., Xie, W., Mu, J. Y., & Yin, D. F, "Effect of particle size on the preparation and microwave absorption properties of FeSiAl magnetically soft alloy hollow microspheres," Defence technology, vol. 14(5), pp. 477-483, 2018.

Fe-Modified Silica/Polyurethane Composite for the Adsorption of Dyes from Aqueous Solution

*Note: Sub-titles are not captured in Xplore and should not be used

Siti Nurul Ain Binti Md. Jamil
Chemistry Department *Faculty of Science* Universiti Putra Malaysia *43400 UPM Serdang* Selangor, Malaysia
ctnurulain@upm.edu.my

Nur Afiqah Binti Ahmad
Chemistry Department *Faculty of Sciemce* Universiti Putra Malaysia *43400 UPM Serdang* Selangor, Malaysia
afiqahh@gmail.com

Abdul Halim Bin Abdullah
Chemistry Department *Faculty of Science* Universiti Putra Malaysia *43400 UPM Serdang* Selangor, Malaysia
halim@upm.edu.my

Thomas Shean Yaw Choong
Department of Chemical and Environmental Engineering *Faculty of Engineering* Universiti Putra Malaysia *43400 UPM Serdang* Selangor, Malaysia
csthomas@upm.edu.my

Nur Hana Binti Faujan
Chemistry Department *Faculty of Sciemce* Universiti Putra Malaysia *43400 UPM Serdang* Selangor, Malaysia
nurhana@upm.edu.my

Aim: Dyes from textile industry has contributed to 22% of the total volume of industrial wastewater in Malaysia. Therefore, removal of dyes from the contaminated water is important because the quality of the water is highly affected by the presence of dyes. Adsorption technique is one of the commonly used techniques for water treatment due to the cost effectiveness and high adsorption rate. In the present work, Fe-modified silica (FMS) particles act as both adsorbent and catalyst. FMS particles has high surface area, low toxicity, and chemically stable over a wide range of pH. However, application of the adsorbent alone might lead to emergence of secondary pollutant, where the adsorbent could leach into the water and hardly be retrieved. In addition, the application of adsorbent particles in aqueous media resulted to particles' agglomeration, thus, reduce the adsorption efficiency.

Method: In this study, an 'in-house' palm-oil based-flexible polyurethane (PU) foam was polymerized, and FMS particles were impregnated onto the PU foam by using an immersion-drying method. The composite was characterized by using FT-IR spectroscopy analysis, the surface morphology was observed by using Scanning Electron Microscope. The thermal behavior of the composite was investigated by using Thermogravimetric (TG) analysis.

Results: Morphological analysis of FMS/PU proved that FMS was successfully impregnated onto the surface of PU. Compression test and TG analysis showed that the FMS/PU composite has good flexibility and thermal stability, respectively. Optimum condition for adsorption of dyes was evaluated by varying several parameters: mass of loaded adsorbent, pH of dyes, initial concentration of dyes and contact time. The maximum dyes removal by FMS/PU was 94.5% and 89.9% for methylene blue and malachite green (in 180 minutes), respectively. Adsorption isotherm and kinetic study were conducted to study the adsorption mechanism.

Conclusion: This study shows the potential of FMS/PU composite adsorbent to capture methylene blue and malachite green dyes from aqueous solution without formation of secondary pollution in water system.

Keywords—malachite green, methylene blue, silica adsorbent, organic pollutants, polyurethane foam

Effect of Acrylo-POSS Nanoparticles on the Passenger Carcass Tire Compound Properties

Çağıl Şenol Erdem
Dept. of Polymer Science and Tech. Kocaeli University Kocaeli, Turkey
cagilsenol@gmail.com

Nazlı Yazıcı
Dept. of Chemical Engineering
Kocaeli University Kocaeli, Turkey
nazliyazici93@gmail.com

Öznur Kavacık
Dept. of Compound Development
Brisa Bridgestone Sabancı Tire Inc.
Kocaeli, Turkey
o.kavacik@brisa.com.tr

Sezgin Gökçesular
Dept. of Compound Development
Brisa Bridgestone Sabancı Tire Inc.
Kocaeli, Turkey
s.gokcesular@brisa.com.tr

Güralp Özkoç
Dept. of Chemical Engineering
Kocaeli University Kocaeli, Turkey
guralp.ozkoc@kocaeli.edu.tr

Mehmet Kodal
Dept. of Chemical Engineering
Kocaeli University Kocaeli, Turkey
mehmet.kodal@kocaeli.edu.tr

Aim: **Tire is a composite material composed of rubber, various chemicals and reinforcing textile fibers such as Aramid and Nylon 6.6. In this study, it has been studied within the scope of the needs of the tire industry, which needs continuous improvement due to increasing customer demands and country regulations. One of the most important components of a tire is the carcass compound that provide stability and strength to the tire. In this study, for the first time in the literature, it was aimed to investigate the effects of polyhedral oligomeric silsesquioxane nanoparticles having acrylo functional groups (A-POSS) on the mechanical, rheological and thermal properties of a carcass compound based on NR/SBR carcass compound.**

Method: **A standard carcass compound recipe consisting of natural rubber (NR) and styrene butadiene rubber (SBR) reinforced with carbon black was prepared as reference compound. The A-POSS content in carcass compound was selected as 3 phr and 6 phr. All compounds were mixed in banbury mixer and then milled two-roll open mill. By using a moving die rheometer (MDR), important rheological parameters and optimum cure time of compounds were obtained at 160 °C temperature. Vulcanization was carried out in a hydraulic hot press at 160°C for their respective optimum cure times. In order to analyze the rheological, mechanical, dynamical, thermal and structure properties, Mooney viscometer, tensile test, DisperGrader, rubber process analyzer (RPA), thermal gravimetric analyzer (TGA), differential scanning calorimeter (DSC) and Fourier transform infrared spectrometer (FTIR) were used respectively.**

Results: **Differential scanning calorimeter (DSC) and Fourier transform infrared spectroscopy (FTIR) analyses showed that A-POSS both reacted with sulphur and participated in vulcanization reaction of NR/SBR compound. The addition of A-POSS to the NR/SBR compound significantly increased the thermal stability and mechanical properties of the carcass compound. Moreover, it was observed that A-POSS improved the processability and process scorch safety of NR/SBR compound. In addition, hysteresis has improved, which is an indication of lower rolling resistance in the tire.**

Conclusion: **In the presence of A-POSS nanoparticles in NR/SBR carcass compounds, processability, mechanical, dynamical and thermal properties improved because A-POSS could accompany with vulcanization reaction thanks to its multiple vinyl groups.**

Keywords—natural rubber, styrene butadiene rubber, POSS, mechanical properties

LBM simulation of fluid division by baffle in L shape cavity

Shayan Naseri Nia
School of Engineering Monash University Malaysia 47500 Serang, Malaysia
shayan.naserinia@monash.edu

Faranak Rabiei
School of Engineering Monash University Malaysia 47500 Serang, Malaysia
faranak.rabiei@monash.edu
faranak.rabiei@gmail.com

M.M Rashidi
Shanghai Key Lab of Vehicle Aerodynamics and Vehicle Thermal Management Systems, Tongji University, Shanghai, China
mm_rashidi@yahoo.com

Aim: In this research, the fluid flow and heat transfer of a Cu-water nanofluid in a L-shaped enclosure with a baffle is numerically simulated using the Lattice Boltzmann Method (LBM).

Method: A schematic representation of the baffled L shape model used in this study is shown in Fig. 1. It is a two-dimensional cavity with *H* as height, *W* as width, and *h* as its thickness. The height and width are both equal to 1 m (*H* = *W*), and the aspect ratio of thickness to height (*h/H*) is 0.4. The length and position of the baffle are *L* and *S*, respectively, which vary according to the baffle configuration. A short and a long length, as well as a near and far position, are inspected in all combinations. The position of the baffle is based on its distance from the left wall (AB). The value of baffle length and position can be defined as their ratio to the height of the enclosure (*L/H*, *S/H*).

The boundary conditions are also shown in Fig. 2. The west (AB) and south (BC) boundaries are hot walls that are maintained at a temperature of $T_h = 1$, while the north boundaries (DE, EF) and the baffle are cold walls kept at $T_c = 0$. The rest of the walls (CD, FA) are considered adiabatic. The cavity is filled with the Cu-water nanofluid.

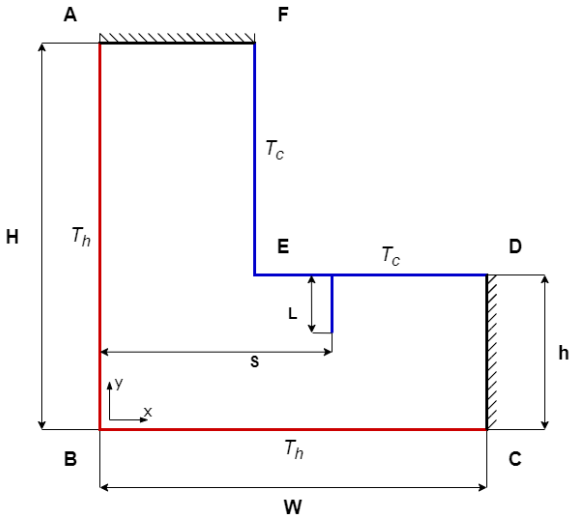


Fig. 1: Geometry of the L shape enclosure.

In LBM, the collection of particles is considered a unit and particle distribution functions are used to describe the property of collective particles. The distribution functions are evaluated by the kinetic Boltzmann equations. In this project, a multi distribution function LBM model is considered which has the following lattice Boltzmann equations [1]:

For flow field:
$$f_i\left(x+c_i\Delta t,t+\Delta t\right)=f_i\left(x,t\right)-\frac{\Delta t}{\tau_v}\left[f_i\left(x,t\right)-f_i^{eq}\left(x,t\right)\right]+\Delta tF_i \quad (8)$$

For energy field:
$$g_i\left(x+c_i\Delta t,t+\Delta t\right)=g_i\left(x,t\right)-\frac{\Delta t}{\tau_c}\left[g_i\left(x,t\right)-g_i^{eq}\left(x,t\right)\right] \quad (9)$$

Then, the hydrodynamic variables are calculated as the moments of particle distribution functions:

$$\rho=\sum_{i=0}^{8}f_i\ ,\quad \rho u=\sum_{i=0}^{8}f_ic_i\ ,\quad T=\Sigma_{i=0}^{8}g_i$$

For full details of used parameters in this research can be found in published article [1].

Results: From Fig. 2, it is clear that increasing nanoparticle concentration (ϕ) increases the average Nusselt ($\overline{Nu}$) unconditionally. Therefore, increasing nanoparticle concentration always contributes to the natural convection. This increment in the $\overline{Nu}$ values has a linear variation with ϕ. Moreover, comparing the results for different *Ra* numbers, shows that $\overline{Nu}$ values for *Ra* = 10^3 and 10^4 are almost similar, while for *Ra* = 10^5 they are significantly higher. On the other hand, the $\overline{Nu}$ for baffled L shape are notably increased in all *Ra* numbers. The complete results of this study is available in [1].

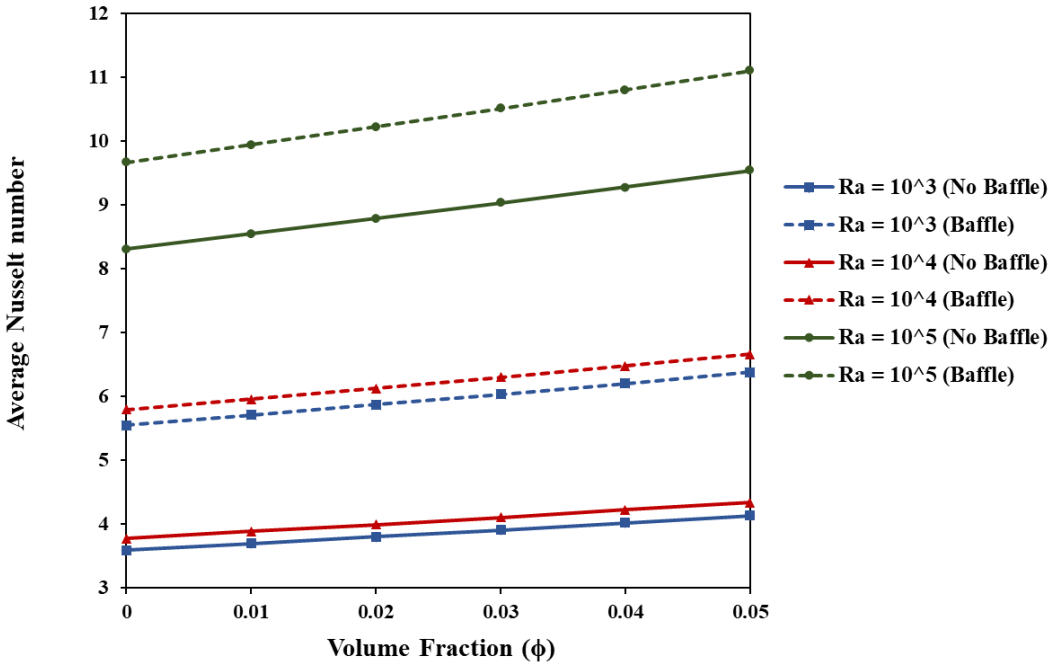


Fig. 2: Variation of the total average Nusselt number of the hot walls with volume fraction, for the no baffle L shape and baffled L shape model.

Conclusion: The simulation results were analysed in the form of isotherms, streamlines, local and average Nusselt numbers. Hence, the following results were achieved for this study:

- In all *Ra* numbers, the addition of baffle significantly increases the Nusselt number values.
- In low *Ra* numbers, the addition of the baffle is much more effective in increasing Nusselt number than increasing the *Ra* number.
- The Nusselt number results are greater at High *Ra* number of 10^5.

Keywords— Lattice Boltzmann, natural convection, L-shape enclosure, baffle.

Reference:

[1] Shayan Naseri Nia., Faranak Rabiei., M.M.Rashidi., T.M.Kwang. (2020). Lattice Boltzmann simulation of natural convection heat transfer of a nanofluid in a L-shape enclosure with a baffle. Results in Physics, https://doi.org/10.1016/j.rinp.2020.103413

Effect of surface treatment on Ti substrates for Dye Sensitized Solar Cell Under Back Illumination Method

Izad Syahrul Ariffin Mohd Ismail
Insititute of Advanced Technology
Universiti Putra Malaysia
Selangor, Malaysia
izadsyahrulariffin@gmail.com

Nor Hapishah Abdullah
Insititute of Advanced Technology
Universiti Putra Malaysia
Selangor, Malaysia
hapishah@upm.edu.my

Mohd Nizar Hamidon
Electrical and Electronic Engineering
Universiti Putra Malaysia
Selangor, Malaysia
mnh@upm.edu.my

Suhaidi Shafie
Electrical and Electronic Engineering
Universiti Putra Malaysia
Selangor, Malaysia
suhaidi@upm.edu.my

Adam Tan Mohd Amin
Faculty of Engineering & Built Environment, Universiti Kebangsaan Malaysia
Selangor, Malaysia
adamtan86@gmail.com

Izzatul Hidayah Azizan
Cogdev Malaysia Sdn. Bhd Cyberjaya
Selangor, Malaysia
i33atulhidayah@gmail.com

Abstract—**Previously, researchers have attempted to enhance titanium by modifying its surface properties, including via hydrogen peroxide (H_2O_2) pre-treatment, varying from minutes, hours and even to weeks. Titanium (Ti) foil has been used as substrate in this study ~~and~~ with chemical pre-treatment process by using hydrogen peroxide (H_2O_2). The performances between Ti foil with pre-treatment and without pre-treatment process are compared respectively. It is shown that pre-treated Ti foil has an increment in the optical and electrical contact area between Ti foil substrate and TiO2 semiconductor layer, resulting in the improvement of its performance due to the reduction of charge transfer resistance and better electron transport properties. The efficiency of 0.27% is obtained from pre-treated Ti foil with J_{sc} of 0.63 mA/cm^2, V_{oc} 0.59 and FF 0.74 under AM1.5 condition and back illumination method.**

Keywords— DSSC, titanium foil, titanium dioxide, back illumination

I. Introduction

Recently, Dye sensitized Solar Cell (DSSC) has been receiving global attention due to its high conversion efficiency with low processing cost and simple fabrication process [1]. Typically, DSSC component consists of three main components: iodide/triiodide (I^-/I_3^-) electrolyte solution, counter electrode to catalyze (I^-/I_3^-) and dye sensitized TiO_2 nanoparticles semiconductor on transparent conductive oxide (TCO). Most commonly TCO type that have been widely used in DSSC is fluorine doped tin oxide (FTO) due to its high light transmittance. However, FTO is heavy and rigid which is unsuitable for flexible DSSC application [2].

Best replacement for rigid FTO substrate is plastic and metal substrate. However, thermal instability of plastic substrate limits the TiO_2 semiconductor layer sintering temperature to 150°C which leads to poor necking between TiO_2 nanoparticles and decrease the performance devices [3]. Therefore, several researches have proposed metal as photoanode substrate to obtain flexible properties of DSSC including Titanium (Ti), W and stainless steel (StSt). Among the metal substrates, Ti is an excellent alternative due to its superior corrosion resistance against I^-/I_3^- electrolyte solution, good flexibility, low sheet resistance and high temperature tolerance which can improve the electrical contact between TiO_2 nanoparticles and TCO substrate [4-5].

In this study, the performance of DSSC then further improved by introducing high density networked TiO_2 nanosheet onto the Ti surface. This has been achieved by chemical pre-treatment process involving H_2O_2. The networked TiO_2 nanosheet provides high surface area enhancing the electrical contact between Ti and TiO_2 semiconductor layer leading to the improvement of electron transfer and injection. The photoanode with chemical pre-treatment show a remarkable enhancement in the energy conversion efficiency for back-illuminated method.

II. Materials

All of the following chemical reagents were purchased from commercial suppliers: Ti foil (99.6%; Luoyang Combat Tungsten & Molybdenum Material Co, Ltd), Isopropyl Alcohol, Ethanol, Acetone (Merck), Ethyl Cellulose, Alpha Terpineol, Titanium (IV) Oxide anatase-nanopowder, Hydrogen Peroxide (Sigma Aldrich), Tri-iodide electrolyte (Solaronix), Surlyn 1702 film (25μm thick, Dupont), Di-tetrabutylammoniumcis-bis (isothiocyanato) bis (2,2-bipyridyl-4,4-dicarboxylato) Ruthenium (II) (Solaronix).

III. Experiment

A. Photoanode Preparation

Three quantities of Ti foil were cut with 3 cm x 2.5 cm dimension (labelled as Photoanode A, B and C respectively). Photoanode B and Photoanode C were polished using sandpaper before rinsed with Deionized (DI) water to remove unwanted oxidized layer and surface contamination. All of the photoanodes were then cleaned using detergent, acetone and IPA for 20 minutes respectively. Photoanode C was subjected to chemical pre-treatment process which was performed by soaking Ti foil into H_2O_2 solution (30wt%, 20ml) at 70°C for 30 minutes. After that, it was rinsed again with DI water and dried under airflow before annealing at 450°C for 30 minutes to enhance crystallization of TiO_2 nanosheet. While the other two photoanodes were left without chemical pre-treatment process.

B. Titanium Dioxide Preparation

The TiO_2 anatase powder was pre-heated at 450°C for 30 minutes to eradicate any absorbed organic impurities and moisture [6]. After that, the pre-heated TiO_2 anatase powder was grounded in porcelain mortar with 0.2 mL glacial acetic acid and it was diluted by addition of 0.2 mL DI water gradually, followed by addition of alpha terpineol into the solution acting as a binder. This solution was then subjected to magnetic stirring for 1 hour until it became creamy white paste followed by sonication and stirring process. The homogenous solution was then evaporated on the hotplate at 80°C until up to 1/10 of its original volume.

The evaporated TiO_2 sol-gel paste was coated on the Ti foil using doctor blade method to form working area of 1 cm x 1 cm. Coated TiO_2 film was then annealed at 450°C for 30 minutes and slowly cooled down to 80°C. After cooling process, the TiO_2 coated onto Ti foil was immersed in $4x10^{-4}$ M N719 dye solution (contain of mixture of Di-tetrabutylammoniumcis-bis (isothiocyanato) bis (2,2-bipyridyl-4,4 dicarboxylato) Ruthenium (II) and ethanol) for 24 hours under room temperature to complete the sensitizer uptake process.

C. Counter Electrode Preparation

ITO-PET was cut to form dimension of 3 cm x 2.5 cm. Then, it was cleaned using detergent and Isopropyl Alcohol for 10 minutes sequentially before it was rinsed with DI water. However, due to the opaqueness of Ti foil, the DSSC must be operated under back-illumination method (shine form counter electrode side). ITO-PET which acts as a counter electrode substrate must be high transparency enough thus it was coated using sputter coater (Emitech, K575X) with ultrathin Pt film (7nm) [7].

D. DSSC Asembly and Characteristics Measurement

The N719 dye loaded Ti foil photoanode substrate was rinsed using ethanol and dried under an air flow. Surlyn polymer spacer with 25 µm thickness was cut into 0.5 cm x 1.5 cm and applied around the N719 dye loaded TiO_2 film and heated using hotplate at 120°C. The counter electrode part was sandwiched together with photoanode part as illustrated in Fig.1. Proper amount of electrolyte solution containing iodide/triiodide redox couple (I^-/I^-_3) was injected into the gap between photoanode and counter electrode using capillary action. The result was evaluated using solar simulator (1000W Xe lamp, Abet Technology, USA) under testing condition of AM 1.5 back illumination at 100 mW cm^{-2} incident light intensity. Photocurrent-voltage (I-V) characteristics curve was plotted and recorded using computer-controlled source meter (Keithley 4200, USA). Meanwhile, surface morphological and elemental analysis was done using Field Emission Scanning Electron Microscope – Energy Dispersive X-Ray (FESEM-EDX) (FEI Nova NanoSEM 230) at scale of 20 µm.

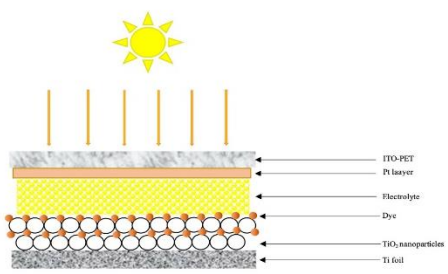


Fig. 1 DSSC schematic diagram

IV. Result and Discussion

All of the photoanodes were subjected to FESEM-EDX analysis and I-V characteristics to identify the elemental combination and surface morphological as well as optical characteristics performance. The result of elemental surface analysis and I-V characteristics performance of Photoanode A, B and C are shown in Fig. 2 and Fig. 3 respectively.

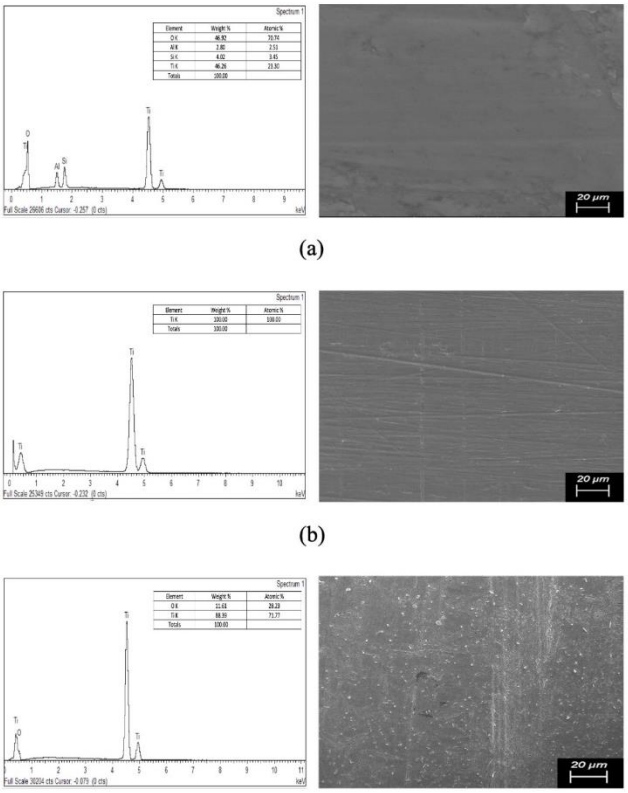


Fig. 2 FESEM-EDX Analysis of (a) Photoanode A, (b) Photoanode B and (c) Photoanode C

Fig. 2 shows the FESEM-EDX analysis for untreated surface (Photoanode A), without chemical pre-treatment process (Photoanode B) and after chemical pre-treatment process (Photoanode C) respectively. The EDX analysis in Fig. 2(a) determined the presence of various element on the surface of Photoanode A that contained percentage of atomic element (%) for aluminium (Al) and silicon (Si) and percentage of atomic element (%) for Ti and O. While, in Fig. 2(b) show the various element were completely eliminated after rubbed with sandpaper (Fig. 2b).

Fig 2(c) shows roughened surface on the surface of Photoanode C as well as high density of networked TiO_2 nanosheets after undergone H_2O_2 pre-treatment process as described in [1]. I-V characteristics have been performed in order To study the effect of roughened surface morphology to the optical performance.

Fig. 3 shows the I-V curve performance complete solar cell for Photoanode A, B, and C meanwhile Table 1 summarizes the characteristics of all content. DSSC which contains Photoanode C, shows a remarkable increase (0.63

mA/cm^2) in the short-circuit current density (J_{SC}) as compared with Photoanode A and B (0.36 and 0.44 respectively). Moreover, it has shown better efficiency (η) of 0.27% as compared to the rest of the untreated photoanodes. This also indicates that by removing the passive tarnish oxide layer on the Ti foil substrate will reduce the electrical contact resistance between the Ti foil and nanocrystalline interface, thereby increasing the Jsc value.

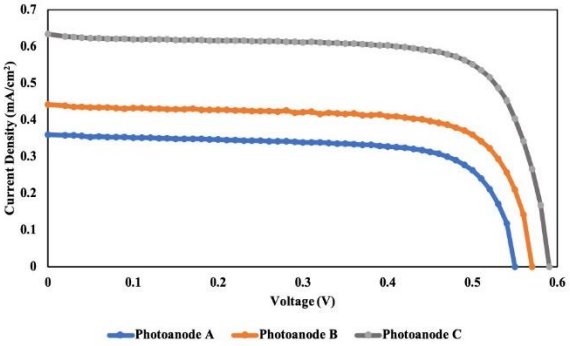


Fig. 3 I-V curve characteristics performance

TABLE I. COMPARISON DETAIL OF DSSC PERFORMANCE

Sample	DSSC Performance			
	J_{sc} (mA/cm^2)	V_{oc} (V)	FF	η (%)
Photoanode A	0.36	0.55	0.72	0.14
Photoanode B	0.44	0.57	0.72	0.18
Photoanode C	0.63	0.59	0.74	0.27

The I-V characteristics also have shown that the roughened surface and networked TiO_2 nanosheet formed on the Photoanode C has increased the surface area for electrical contact between TiO_2 nanoparticles and Ti substrates as well as providing a rapid pathway for electron transport.

Tsai *et al.* [8] had also prepared a roughened surface on Ti foil substrate by performing H_2O_2 pre-treatment process of Ti foil. Due to the roughened surface of the pre-treated Ti foil in this research work, the electrical contact between TiO_2 nanoparticles and Ti foil substrate was significantly increase which enhanced electrical interaction between TiO_2 nanoparticles to the treated Ti foil substrate. Hence, the resistance of charge transfer at the TiO_2 and conducting layer interface was observed to be reduced as well as the sheet resistance, which would increase the efficiency of charge transfer from TiO_2 nanoparticles to the H_2O_2 treated Ti foil. Therefore, the J_{sc} was significantly enhanced.

Besides that, Tsai *et al.* also showed that networked TiO_2 nanosheet and roughened surface provided shorter pathway for electron travels which allowed rapid electron transport as well as extra dye adsorption and contribute to the photocurrent enhancement even though it was not the primary cause of remarkable enhancement of J_{sc}.

V. CONCLUSION

In summary, by performing H_2O_2 pre-treatment process on the Ti foil substrate, the energy conversion efficiency was significantly improved as discussed in previous section. The formation of high density networked TiO_2 on the Ti foil substrates provides a larger surface area for electrical contact between Ti foil substrate and TiO_2 nanoparticles. Hence, it provides direct path to the Ti substrate for rapid electron transportation. Due to this characteristic, H_2O_2 treated Ti foil substrate shows great improvement as compared to untreated H_2O_2 pre-treatment process.

REFERENCES

[1] C. H. Lee, W. H. Chiu, K. M. Lee, W. F. Hsieh, and J. M. Wu, "Improved performance of flexible dye-sensitized solar cells by introducing an interfacial layer on Ti substrates," *J. Mater. Chem.*, vol. 21, no. 13, pp. 5114–5119, 2011.

[2] J. Qi, H. Xiong, J. Zhang, Q. Zhang, Y. Li, and H. Wang, "Effects of release agents on the film morphology of TiO2photoanodes for FDSSCs by the roll-to-roll method," *J. Alloys Compd.*, vol. 702, pp. 366–371, 2017.

[3] H. Iftikhar, G. G. Sonai, S. G. Hashmi, A. F. Nogueira, and P. D. Lund, *Progress on electrolytes development in dye-sensitized solar cells*, vol. 12, no. 12. 2019.

[4] J. H. Park *et al.*, "Fabrication of a Efficient Dye Sensitized Solar Cell with Stainless Steel Substrate," vol. 155, no. 7, 2008.

[5] K. Onoda, S. Ngamsinlapasathian, T. Fujieda, and S. Yoshikawa, "The superiority of Ti plate as the substrate of dye-sensitized solar cells," *Sol. Energy Mater. Sol. Cells*, vol. 91, no. 13, pp. 1176–1181, 2007.

[6] S. Shaban, S. Shafie, Y. Sulaiman, F. Ahmad, M. Q. Lokman, and N. F. M. Sharif, "Flexible photoanode on titanium foil for back-illuminated dye sensitized solar cells," *IEEE Int. Conf. Semicond. Electron. Proceedings, ICSE*, vol. 2018-Augus, pp. 197–200, 2018.

[7] Y. L. Lee, C. L. Chen, L. W. Chong, C. H. Chen, Y. F. Liu, and C. F. Chi, "A platinum counter electrode with high electrochemical activity and high transparency for dye-sensitized solar cells," *Electrochem. commun.*, vol. 12, no. 11, pp. 1662–1665, 2010.

[8] T.-Y. Tsai, C.-M. Chen, S.-J. Cherng, and S.-Y. Suen, "An efficient titanium-based photoanode for dye-sensitized solar cell under back-side illumination," *Prog. Photovoltaics Res. Appl.*, vol. 21, no. 2, pp. 226–231, 2011.

Pt/Graphene Catalysts Prepared by Supercritical Deposition with Different Pt Precursors

Meryem Samancı
Engrineering Faculty Deparment of Chemical Engineering
Atatürk University Erzurum, Turkey
meryemsamanci@gmail.com
https://orcid.org/0000-0002-0904-3651

Ayşe Bayrakçeken Yurtcan
Engrineering Faculty Deparment of Chemical Engineering
Atatürk University Erzurum, Turkey
ayse.bayrakceken@gmail.com
https://orcid.org/0000-0002-8964-0869

***Abstract*—In this study, two different Pt catalysts were synthesized by using 1,5-dimethyl platinum cyclooctadiene and platinum(II)acetylacetonate precursors on graphene nanoplates (GNPs). Supercritical carbon dioxide deposition technique was used in the catalyst synthesis. Electrochemical and physicochemical analyzes were performed on the synthesized materials. As a result of the PEM fuel cell tests, the catalyst prepared by using Pt(COD)Me_2 provided better current (332.7 mA/cm^2) and power density (199.4 mW/cm^2).**

Keywords—PEM fuel cell, graphene nanoplateles, supercritical carbon dioxide deposition

[1] INTRODUCTION

As an alternative clean energy technology, the proton exchange membrane fuel cell (PEMFC) is widely used in residential, transportation and military applications. However, there are several factors that currently limit the commercialization of the fuel cell system such as low stack performance, short life and high cost. Catalyst layer composition is a key component in determining both batch performance and service life. Therefore, catalyst layer composition optimization is essential to improve membrane electrode assembly (MEA) stability and continuity, increase stack life and reduce overall system cost.

Graphene has unique mechanical properties such as high mechanical flexibility, high surface area, chemical stability, superior electrical and thermal conductivity. Therefore, it is a promising alternative as alternative electrode support material in most fuel cells, especially PEM fuel cells. In this study, two different Pt catalysts were synthesized by using Pt(COD)Me_2 and Pt(acac)$_2$ precursors over graphene nanoplatelets (GNPs). Supercritical carbon dioxide ($ScCO_2$) deposition technique was used in the catalyst synthesis [1]. It is aimed to use Pt in the most efficient way with this technique. Electrochemical and physicochemical analyzes were performed on the synthesized materials. In this way, it will be tried to reach the catalyst that gives the best results in the PEM fuel cell.

[2] METHODS

A. Synthesis of Pt catalysts

Commercial graphene (graphene nanoplatelets, GNPs-XG Sciences) was used as the support material in the synthesis. In the synthesis of Pt electrocatalyst, 1,5-dimethyl platinum cyclooctadiene Pt(COD)Me_2 and platinum (II) acetylacetonate Pt(acac)$_2$ precursors were used as Pt source. $ScCO_2$ technique was used for the adsorption process under supercritical conditions. N_2 gas was used in the thermal reduction process.

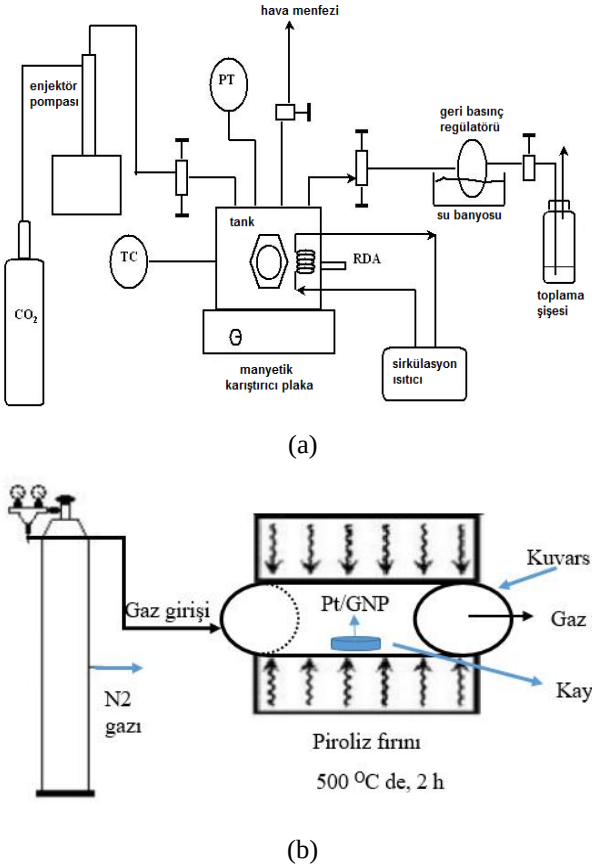


Fig.1. (a) Schematic representation of the reactor system in which the supercritical adsorption process, (b) Representation illustration of the thermal reduction process.

Catalyst synthesis consists of two stages. The first stage is adsorption of Pt precursor over graphene (Fig.1a) and the second stage is the thermal reduction of these precursors to Pt (Fig.1b). First of all, the support material and Pt precursor were mixed in certain proportions (Pt(COD)Me_2/GNP 2:3, Pt(acac)$_2$/GNP 1:1) and placed in the reactor. The reactor temperature is set to 80 °C for Pt(COD)Me_2/GNP catalyst and 50 °C for Pt(acac)$_2$/GNP catalyst. By adjusting the reactor pressure to 3500 psi, supercritical CO_2 was introduced into the system. Under these conditions, it was kept for 6 hours in order for the Pt precursor to dissolve well and adsorb to the support surface. After the adsorption process, the sample is removed from the reactor and thermally reduced in N_2 environment at 500 °C for 2 hours in a tubular oven. Thus, it was transformed into metallic form.

B. *Characterization of Support Material*

The following characterization methods were used for the characterization of the support material. Morphological structure (such as surface area, pore diameters, pore size distribution) was determined by nitrogen adsorption/ desorption isotherm analysis using the Brunauer, Emmett and Teller (BET) method. Micromeritics 3Flex 3-port BET surface area device was used for surface area analysis. Determination of surface groups is made with FTIR device. IR spectra were taken using a Fourier Transform Infrared Spectrometer (Perkin Elmer Spectrum One). Spectra were obtained in the range of 4000-400 cm^{-1} at room temperature. The crystal structure was made using X-ray diffractometer (PANalytcal Empyrean X-Ray Diffractometer) in the range of $10°\leq 2\theta \leq 90°$. Raman spectroscopy (WITech alpha 300R) was used to obtain information about the bonds made by atoms or molecules.

C. *Characterization of Pt catalysts*

Inductively Matched Plasma-Mass Spectrometry (ICP-MS) (Agilent 7800) was used to determine the amount of Pt in the synthesized catalysts.

D. *PEM Fuel Cell Tests*

The fuel cell performances of MEAs prepared using Pt/GNP electrocatalysts were tested using a single fuel cell in a test station with a capacity of 600 W (Henatech). Before starting PEM fuel cell applications, MEA was prepared. The preparation of MEA was carried out in 3 stages; preparation of the catalyst solution (electrocatalyst, ionomer solution (Nafion), 2-propanol and water), application of the catalyst solution to the gas diffusion layer (GDL) (spraying) and hot pressing of the catalyst containing gas diffusion layers into the Nafion membrane (135 °C, 400 psi 4 minutes). In this study, prepared Pt/GNP catalysts were used as cathode electrodes and commercial Tanaka (67%) as anode electrodes.

[3] RESULT AND FINDINGS

Multipoint BET surface area, BJH pore volume data of graphene support material are given in Table 1 and BJH pore size distribution values and nitrogen adsorption-desorption isotherm curves are given in Figure 2. According to the BET analysis results, the specific surface area of commercial graphene nanoplatelets was found to be 710.3 m^2/g. It was observed that commercial graphene conforms to Type IV isotherm and H2 type hysteresis curve according to the classification made by IUPAC. With the Type IV isotherm, it was seen that the structure consists of mesopores with a large density. H_2-type hysteresis is also a characteristic of spherical agglomerated systems, but solids giving such hysteresis do not have a well-defined pore size distribution and pore shape.

Table 1. BET analysis data of graphene support material

Material	BET surface area (m^2/g)	Average pore diameter (nm)	BJH pore volume (cm^3/g)	Average particle size (nm)
GNP	710.34	5.63	1.189	8.45

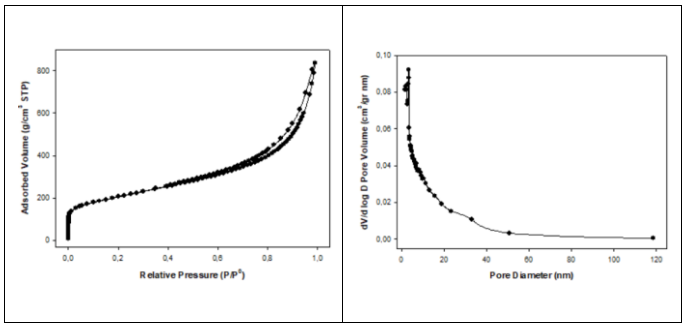


Fig.2. BET isotherms and pore size distributions of GNP.

When we look at the FTIR spectrum belonging to graphene in Figure 3 a few peaks between 3100 and 3400 cm^{-1} wave numbers represent the –OH asymmetric stress due to the presence of water between graphene layers. Several peaks between 1400, 1550 and 1650 cm^{-1} describe C=C bonds [2].

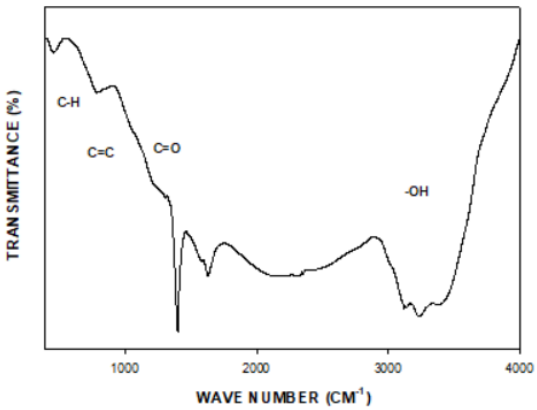


Fig.3.FTIR spectrum of GNP

G band gives information about sp^2 hybridization by showing the degree of graphitization (Fig. 4a). The D band represents the irregular carbon structure in the lattice of sp^3 hybridized carbon atoms. The value ratio between the D band and the G band (ID/IG) is used to determine the degree of irregularity in the graphene's lattice structure [3]. Table 2 shows Raman shear values in D and G band and D and G peak intensity values of GNP. In the light of these data, the defects in the structure were examined by calculating the ID/IG value.

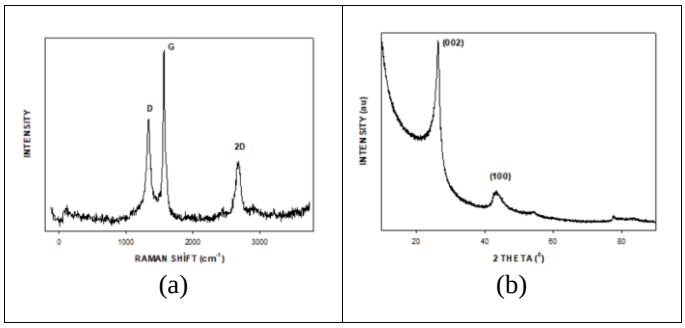


Fig.4. (a) Raman and (b) XRD spectrums of GNP.

Table 2. Results of raman spectrum of GNP

Material	Raman shift (cm^{-1})		D peak intensity (au)	G peak intensity (au)	ID/ IG
	D band	*G band*			
GNP	1335.18	1563.47	572	923	0.62

In the Fig. 4b the XRD spectrum of GNPs is given. While the large sharp diffraction peak at 26.3˚ corresponds to the (002) plane of graphite, the diffraction peak at 43.3˚ is shown to have the (100) plane of the graphitic crystal structure [4]. The XRD analysis of the (002) peak is given in Table 3.

Table 3. XRD peak (002) analysis of GNP

Material	Peak (2θ)	d (Å)	Crystal size D (Å)	Number of layers N
GNP	26.3˚	3.4	11.9	3.5

Inductively coupled plasma mass spectrometry (ICP-MS) is a type of mass spectrometer that uses an inductively coupled plasma to ionize the sample. Inductively Coupled Plasma-Mass Spectrometry (ICP-MS) (Agilent 7800) was used to determine the amount of Pt in the catalysts. According to the results of ICP analysis, the amount of Pt by mass in Pt(COD)Me_2/GNP and Pt(acac)$_2$/GNP catalysts was found to be 25.882% and 30.1%, respectively.

To evaluate the PEM fuel cell performance of graphene / Pt catalysts, a MEA cell with 0.4 mgPt/cm^2 loading was prepared. Measurements were taken with a 600-W Henatech^{TM} brand fuel cell test station.

PEM fuel cell polarization curves for Pt/GNP catalysts are given in the Figure 5. According to the PEM fuel cell analysis results, the current density and power density values at 0.6 V for Pt catalysts are given in Table 4. The catalyst prepared by using Pt(cod)Me_2 precursor gave better results than the one prepared by using Pt(acac)$_2$ precursor although it has less Pt loading.

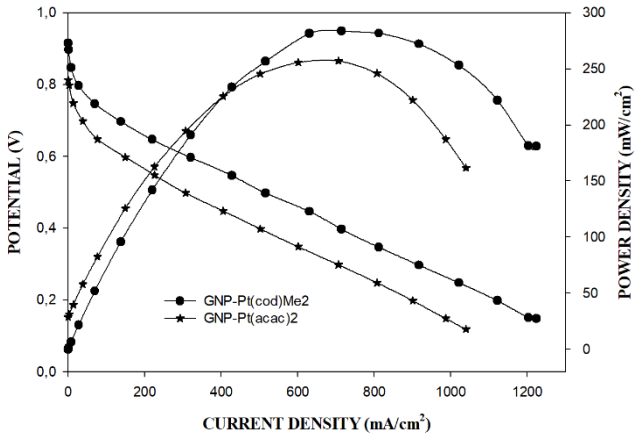


Fig.5. PEM fuel cell results for Pt/GNP catalysts.

[4] CONCLUSIONS

In this study, two different Pt catalysts were synthesized using two different Pt precursors on the same graphene support material. PEM fuel cell tests of these two catalysts was carried out. As a result of the tests, the current density values for Pt(cod)Me_2/GNP and Pt(acac)$_2$/GNP at 0.6 V were found to be 332.7 and 157.1 mA/cm^2, respectively. Power density values of Pt(cod)Me_2/GNP and Pt(acac)$_2$/GNP were found to be 199.4 and 95.6 mW/cm^2, respectively. The current and power density values of Pt(cod)Me_2/GNP catalyst were 2 times higher than Pt(acac)$_2$/GNP.

Table 4. Current and power density values of catalysts at 0.6 V

Pt Catalysts	0.6 V	
	Current density (mA/cm^2)	Power density (mW/cm^2)
Pt(cod)Me_2/GNP	332.7	199.4
Pt(acac)$_2$/GNP	157.1	95.6

ACKNOWLEDGMENT

This work is supported by the Scientific Research Projects (BAP) Coordination Unit of Atatürk University with FDK-2020-8560 project number. Thank you to BAP for their support.

REFERENCES

[1] E. Daş, Selmiye A.G., Lale I.Ş., Ayşe B.Y., "Thermodynamically controlled Pt deposition over graphene nanoplatelets: Effect of Pt loading on PEM fuel cell performance. " International Journal of Hydrogen Energy, vol.42, pp. 19246–19256, 2017

[2] A.E.F. Oliveira, G.B. Braga, C.R.T. Tarley, A.C. Pereira, "Thermally reduced graphene oxide: synthesis, studies and characterization. " Journal of Materials Science, vol.53, pp. 12005–12015, 2018

[3] M. Dresselhaus, A. Jorio, R. Saito, "Characterizing graphene, graphite, and carbon nanotubes by Raman spectroscopy. " Annu. Rev. Condens. Matter Phys., vol.1, pp. 89-108, 2010

[4] N.M.S. Hidayah, W.-W. Liu, C.-W. Lai, N. Z. Noriman, C.-S. Khe, U. Hashim, H.C. Lee, "Comparison on graphite, graphene oxide and reduced graphene oxide: Synthesis and characterization.", AIP Conference Proceedings, vol.1892, pp. 150002, 2017

Hydrogen Purification and Compression Methods for Future Energy

Yasemin Aykut
Engrineering Faculty Deparment of Chemical Engineering Atatürk University Erzurum,Turkey
yaseminn.aykut@gmail.com

Ayşe Bayrakçeken Yurtcan
Engrineering Faculty Deparment of Chemical Engineering Atatürk University Erzurum,Turkey
abayrakceken@atauni.edu.tr

***Abstract*—It is undeniable that hydrogen will play a major role in meeting our energy needs in the future, thanks to its superior properties and clean by-products. When it comes to the development of hydrogen technologies, it is of great importance to work on the purification and compression of hydrogen as well as production methods. This study reviews that the available methods of hydrogen compression and purification technologies.**

Keywords—compression, hydrogen, purification, storage

[1] INTRODUCTION

With the increase in world population and technological level, the need for total energy is increasing. Fossil fuels are used as the primary energy source to meet this energy demand. As a result of the uncontrolled use of these fuels, the accumulation of greenhouse gases in the atmosphere are caused many environmental problems such as global warming and climate changes [1]. Due to these problems that cannot be neglected, the search for alternative energy sources is among the most important research topics of the 21st century. The energy source that can be an alternative to fossil fuels must be both environmentally friendly and sustainable. For this reason, among the proposed alternative energy sources, hydrogen technologies attract more attention [2].

Hydrogen is not a primary energy source, but an energy carrier that can be produced from any energy source. Apart from the physical and chemical properties of hydrogen, its high energy content on the basis of mass and the fact that the end product is only water in its use as fuel increases its importance in being an ideal energy carrier. Today, hydrogen energy is used in the space and aviation sector, communication sector, automotive industry, and researches continue for its applicability in different fields with the developing technology [3].

Since hydrogen has feature which is able to carry and store of energy more efficiently than electricity it is seen as the ideal energy source of the future. Especially developments in fuel cells increase the interest in hydrogen technologies [4]. This situation is made it important to develop technologies used in the production, purification and storage processes in the hydrogen value chain. In addition to purifying the hydrogen mixture obtained by different methods for its usability, it is also required to be compressed for easy and reliable storage [3].

[2] PURIFICATION AND COMPRESSION METHODS OF HYDROGEN

A. *Hydrogen Purification Methods*

There are various methods for removing impurities from hydrogen obtained by different production methods. Hydrogen purification methods can be listed as shown in Figure 1[4].

a) Cryogenic: Purification of hydrogen by this method is carried out at very low temperatures. Although the purity value of the hydrogen obtained is limited, it can be used industrially [4]. As hydrogen is liquid as a result of purification, it can be stored for long-distance transportation. The disadvantage of this method cost and energy used is the high due to the large capacity [5].

b) Membran: It is aimed to purify the impurities with proper membrane selection. The process is completed by applying high pressure to the membrane with only hydrogen permeability and passing hydrogen at lower pressure and purity to the opposite side [6]. In this method, higher purity hydrogen is obtained compared to the cryogenic method. The disadvantage of the method is that the pressure or vacuum used to provide the required partial pressure difference requires energy. Although this method is ideal for small applications, the cost is too important for large membrane sizes [3,7].

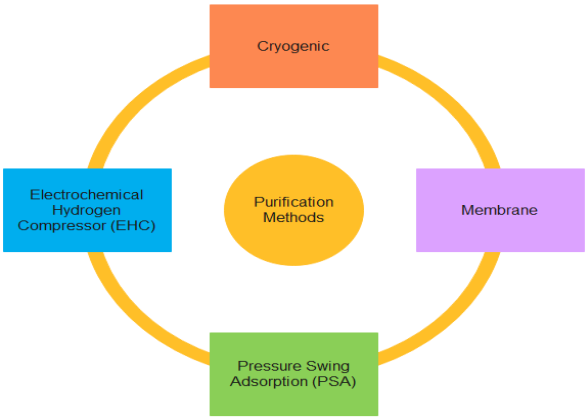


Fig. 2. Summary of the hydrogen purification methods.

c) Pressure swing adsorption (PSA): The process of hydrogen purification with PSA method is carried out by adsorbing impurities by solid surfaces under high pressure [8]. The appropriate surface selection and pressure value should be selected according to the impurity type. In the method it is possible to recover the adsorbent and be used again [3,4].

d) Electrochemical hydrogen compressor (EHC): Although it is called a compressor, it can also be used to purify hydrogen [8]. This device consists of anode, cathode and a solid electrolyte. It has a working principle of

oxidizing pure hydrogen at the anode and reducing and compressing hydrogen at the cathode [9].

B. Hydrogen Compression Methods

The compressors are used in the compression process to store the purified hydrogen at low pressure. These compressors are divided into two as mechanical and non-mechanical compressors [3].

1) Mechanical Compressors:

It is the most widely preferred type of compressor today. In these systems, with reducing the volume using a mechanical force, hydrogen is compressed and obtained at higher pressure. Generally used mechanical compressor types are shown in Figure 2 and in following brief information is given about these compressor types [5].

a) Reciprocating piston compressors: It consists of a cylindrical piston system equipped with two separate valves for inlet and outlet. Compression of hydrogen is accomplished by the reciprocating motion of a piston attached to a crankshaft [3,10] This method is used in large-scale industries and high pressure hydrogen is obtained.The disadvantages of the system are that the moving parts cause vibration, noise, and the lubrication process creates the danger of explosion [8].

b) Diaphragm compressors: Unlike piston compressor, there is a diaphragm that contracts and expands instead of a piston moving inside the cylinder [3]. The back and forth movements of the diaphragm reduce the volume of the gas chamber and is provided hydrogen compression. The diaphragm is simultaneously in contact with hydrogen on one side and oil on the other. For this reason, stainless steel, stainless chrome nickel steel and duplex steel materials are used in the production of diaphragm plates [9].

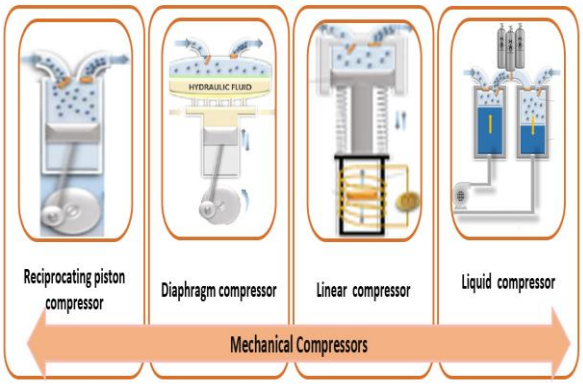


Fig. 3. Mechanical compressor types.

The advantages of this method include low power consumption and low cooling needs and high efficiency. One of the disadvantages of this compressor is that its durability is reduced due to mechanical stresses during operation [4]. Moreover, due to the limited volume of compression, the diaphragm damages earlier at high flow rate [8].

c) Linear compressors: In this system, the piston is directly connected to a linear motor combined with springs. Since the number of moving parts is low, its cost is low. Liner motors used for piston movement are magnetic This type of compressor is preferred in small sized businesses and cryonic systems [3,11]. Important advantages are the ability to obtain high purity hydrogen and the silent operation of the system. The inability to control the displacement of the piston in the system and the need for oscillating pressure are stated as disadvantages [9].

d) Liquid compressors: These systems are positive displacement devices that use fluids for compression. It performs the compression process as a semi-isothermal process [8]. Although there is a combination of compression of liquid and gas in the system, the heat generated as a result of the compression process is absorbed by the walls of the compression volume and the liquid. Because liquid has high density and high heat capacity [3,11]. In this case, the use of additional heat exchangers is not required and the cost is reduced. The advantages of this system is high compression efficiency, no pollutant, low cost and low noise. Liquid leaks and corrosion are the disadvantages of this system [5,6].

2) Non-mechanical Compressors:

The actual compression work performed in commonly used mechanical compressor systems is about one-third of the amount of energy stored in the compressed gas obtained and compressor efficiency is low in power applications [3,9]. Considered these parameters and other problems encountered in mechanical compressors, a non-mechanical compressor has been developed as an alternative for the compression of hydrogen [8]. Non-mechanical compressors used in hydrogen compression are shown in Figure 3 and information about these compressor systems is given below [11].

a) Cryogenic compressor: The principle of operation of the system has based on feed liquid hydrogen to a cryogenic pump through a vacuum insulated tube and stabilizing it to a desired pressure by means of a cryogenic compressor [12].

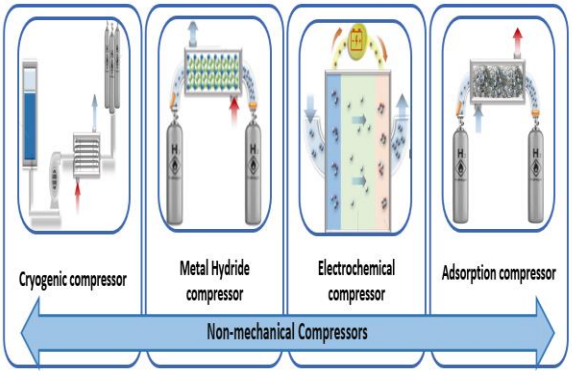


Fig. 4. Non- mechanical compressor types.

It is preferred to pressurize the liquid hydrogen instead of compressing in case hydrogen which is gas, since high pressure values are reached at very low temperatures in the system. In this system, higher volumetric efficiency is achieved than mechanical compressors. The biggest disadvantage in the use of the system is the failure to provide the desired vacuum stability and the cost [8, 11].

b) Metal hydride compressor: These systems also are defined thermally powered compressors and the hydrogen is compressed in the system without moving parts [3]. Hydrogen is absorbed and desorbed using the hydride forming properties of metals, alloys and intermetallic compounds. The biggest advantage of this system is that it can be operated using waste industrial heat instead of electricity. it is other advantages of the system can be listed as safe, noiseless and no moving parts [5,8]. Low efficiency and it is high cost of the parts in the system are listed as the disadvantages of the system [9].

c) Electrochemical compressor: This type of compressor is also known as an electrochemical hydrogen pump [8]. Its working principle is based on the same basic principles as the proton exchange membrane fuel cell. Low pressure hydrogen is fed to the cell in the system and is separated into protons and electrons at the anode. As protons flow through the polymer electrolyte, electrons follow an external path. When the protons and electrons reach the cathode part of the cell, they recombine to form hydrogen molecules, resulting in hydrogen at higher pressure [3,13]. These compressors has operate quietly, without vibration, with high efficiency and safely. Disadvantages are cell resistance and back diffusion of hydrogen [9].

d) Adsorption compressor: It takes advantage of the change in temperature without any mechanical moving units in the system [8]. Adsorption of hydrogen occurs on the surface of a porous solid with high surface area and high adsorption potential under specific temperature and pressure conditions. After adsorption, desorption of hydrogen occurs with the effect of the heat given to the system and hydrogen density increases in the bulk phase [11, 13]. At the end of this process, high pressure hydrogen is obtained. The advantages of the system are the absence of moving parts, vibration and noise and absorbent cost are low. Difficulties in thermal management and low temperature operation are listed as disadvantages of the system [8, 9].

[3] CONCLUSIONS

This review summarizes the current technology related to purification and compression methods that are critical for the continuity of hydrogen technologies. During the selection of these methods, the importance of making a decision by considering the area where hydrogen will be used is emphasized.

For the continuity of hydrogen technologies, is made purification and compression processes with higher efficiency and without much cost will allow further development of hydrogen technology available today. In this sense, it is extremely important to consider basic and applied researches as covering all processes from hydrogen production, purification, compression and storage all stages.

[4] REFERENCES

[5] P. Preuster, A. Alekseev, P. Wasserscheid, “Hydrogen storage technologies for future energy systems” Annual Review of Chemical and Biomolecular Engineering, vol.8, pp 445-471,2017

[6] T. N. Veziroglu, S. Sahin, “ 21st Century’s energy: Hydrogen energy system”, Energy Conversion and Management, vol. 49, pp. 1820–1831, 2008.

[7] N. Armaroli, V. Balzani, “The hydrogen ıssue” Chemistry Sustainability Energy Materials, 4, pp. 21-36, 2011

[8] A. Peschel, “Industrial perspective on hydrogen purification, compression, storage, and distribution”, Fuel Cells, 20(4), pp. 385-393, 2020

[9] R. Agrawa ,lS.R .Auvil, S.P. DiMartino, J.S. Choe, J.A. Hopkins, “Membrane/cryogenic hybrid processes for hydrogen purification” Gas Separation & Purification, vol. 2, pp. 9-15 1988,

[10] L.Schorer, S.Schmitz, A.Weber, “Membrane based purification of hydrogen system (MEMPHYS)” International Journal of Hydrogen Energy, vol. 44, pp. 12708-12714, 2019

[11] H. T. Lu, W. Li, E. S. Miandoab, S. Kanehashi, G. Hu, “The opportunity of membrane technology for hydrogen purification in the power to hydrogen (P2H) roadmap: a review” Frontiers of Chemical Science and Engineering, pp.1-19, 2020

[12] M. Rhandi, M. Tregaro,F. Druart, J. Deseure, M.Chatenet, “Electrochemical hydrogen compression and purification versus competing technologies: Part I. pros and cons”, Chinese Journal of Catalysis, vol.41, 756-759, 2020

[13] G. J. Grashoff, C. E. Pilkington, C. W. Corti, “The Purification of hydrogen: A review of the technology emphasising the current status of palladium membrane diffusion” Platinum Metals Review, 27, (4) 157-169, 1983

[14] H.P. Bloch, J.J. Hoefner, “Reciprocating compressors: operation and maintenance”. Gulf Professional Publishing, pp.44-56, 1996.

[15] G. Sdanghi, G. Maranzana, A. Celzard, V. Fierro, “Review of the current technologies and performances of hydrogen compression for stationary and automotive applications” Renewable and Sustainable Energy Reviews, vol. 102(C), pp. 150-170, 2019.

[16] G. Petitpas, P.Bénard, L.E. Klebanoff, J.Xiao, S.Aceves, “A comparative analysis of the cryo-compression and cryo-adsorption hydrogen storage methods” International Journal of Hydrogen Energy vol. 39, pp. 10564-10584, 2014,

[17] G. Sdanghi, G. Maranzana, A. Celzard, V. Fierro, “Towards non-mechanical hybrid hydrogen compression for decentralized hydrogen facilities” Energies, vol. 13, pp.3145, 2020

Comparison of Classifiers According to Number of Trials

Onur Erdem Korkmaz
Ispir Hamza Polat Vocational College, Ataturk University, Erzurum, Turkey

Onder Aydemir
Department of Electrical and Electronics Engineering, Faculty of Engineering, Karadeniz Technical University, Trabzon, Turkey
onurerdem.korkmaz@atauni.edu.tr

Abstract—Pattern recognition and machine learning based studies have attracted considerable interest in recent years. Because of the fact that there is no a fixed feature and classification method that can solve all kinds of pattern recognition and machine learning problem, in studies determining the most appropriate feature and classifier together with its parameters requires research and is a time-consuming process. Comparison of classifiers from different perspectives gives the researchers an idea about the solution of their problems. In the literature, while classifiers were compared in different feature distributions, sizes or classification performance criteria, there were limited studies about classifiers which compared in terms of number of trials which was an important parameter especially for researchers. In this study, Support Vector Machines, k Nearest Neighbor, and Linear Discrimination Analysis classifiers for four different feature spaces were compared in terms of different trial counts. The results revealed that the classification accuracy for different distribution types and classifiers changed depending on the number of trials. Furthermore, as the number of trials increased, the standard deviation decreased. It means that the stability increased as expected with the increase in the number of trials. It can be said that the k Nearest Neighbor algorithm generally provides superior classification accuracy for all types of distributions.

Keywords — Classifier Comparision, Support Vector Machines, k Nearest Neighbor, Linear Discrimination Analysis

1. INTRODUCTION

The machine learning model is created with the features of the signals in the training set. According to this model, the process of assigning the signals that are not included in the learning set to the best class is called classification. The algorithms that perform this process are called classifiers.

When the studies on classifier comparison are examined in the literature, the advantages and disadvantages of a newly developed method over existing methods were examined. Some studies were aimed at determining which classifier is suitable for different data distributions (Coskun & Baykal, 2011). In addition, there were studies that make classifier comparison using different numbers of features (Coskun & Baykal, 2011).

The performance of classifier algorithms is mostly tested using data obtained from experimental studies. However, there were criticisms in the literature that such studies would not produce objective and definitive results (Hand, 2006). These criticisms arise from the fact that data could be preprocessed for purposive. In addition, criticisms were made due to the fact that the model parameters were at the initiative of the person making the application. Similarly, there were also evaluations that the production of artificial data for the purpose and therefore the evaluations made cannot produce correct results (Salzberg, 1997). However, despite all these criticisms, comparing the classification algorithms from different angles was important for researchers to select an appropriate classifier for their problems.

Classifier performances have been compared from different aspects in the literature. In the of Lorena et al., the distribution model of 35 different plant species was investigated using seven machine learning algorithms (support vector machine (SVM), k nearest neighbor (k-NN), naive bayes (NB), multi-layer perceptron, decision tree, random forest, genetic algorithm) (Lorena et al., 2011). In Murtagh's work, the classifiers were compared by calculating the area under the Recipient Operator Characteristic (ROC) curve according to the sensitivity and specificity criteria (Murtagh, 1997). In the study conducted by Tran et al., SVM, k-NN and multilayer perceptron (MLP) algorithms were compared using hyperbolic, ramp and step functions (Tran, Toh, Srinivasan, Wong, & Low, 2005). When the results are examined, it is seen that the best classification algorithm is SVM with 83.69% classification accuracy. They also concluded that the data set distribution should be considered in order to determine a suitable classifier. In another study, Dixon and Brereton compared four different classifiers (linear discrimination analysis (LDA), radial basis function (RBF), SVM, quadratic discriminant analysis (QDA)) using six artificial data sets (Dixon & Brereton, 2009). According to the results, it is said that data distribution should be considered first in order to determine the appropriate classifier. Aydemir and Kayıkçıoğlu compared the performances of classifiers on low dimensional feature vectors in their study (Aydemir & Kayikcioglu, March 2013). A comparison was made with classification accuracy, sensitivity, specificity, Kappa and calculation time. They found that NB and SVM algorithms are more suitable for low dimension features.

Classifier performances have been compared in many respects in the literature. However, no comparison was made depending on the number of trials as was done in this study. The number of trials is a parameter that researchers cannot make clear decisions in pattern recognition and machine learning-based studies. In this study, the performances of SVM, k-NN and LDA classifiers were compared in two-

dimensional feature spaces in four different distributions and different trial numbers. The results showed that the k-NN method was more successful for different trial numbers.

In the next part of the study, the used data sets are introduced. The method used is given in the third section and in the fourth section, the findings are presented with figures. In the last part of the study, results and discussion part are given.

2. DATA SET DESCRIPTION

Four different artificial data sets were produced in order to conduct the proposed method. These data sets are detailed below.

2.1. Data Set 1

In the graph, the horizontal axis shows the first feature set and the vertical axis shows the second feature set. The horizontal axis values (s1x) and vertical axis values (s1y) of Class 1 were produced with the seed 6 and seed 7 command in MATLAB respectively. Similarly, Class 2 values were generated using the seed 8 and seed 9 commands. With the seed command, the same value data is generated each time. This allows other researchers to make comparisons. The distribution of data set 1 is shown in Figure 1. In this figure, the + symbols represent Class 1, the o symbols represent Class 2 data. The MATLAB code used to create data set 1 is given in the Appendices.

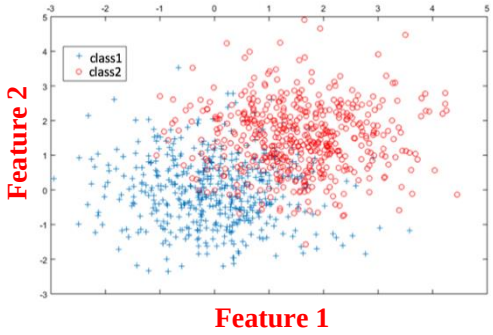


Figure 1. Distribution of data set 1.

2.2. Data Set 2

Data set 2 was produced in different distributions using the seed 6, 7, 8 and 9 command. The distribution of data set 2 is shown in Figure 2. The MATLAB code used to create data set 2 is given in the Appendices.

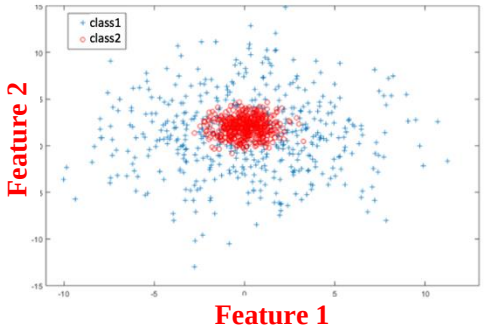


Figure 2. Distribution of data set 2.

2.3. Data Set 3

Data set 3 was produced in different distributions using the seed 10, 11, 12 and 13 command. The distribution of data set 3 is shown in Figure 2. The MATLAB code used to create data set 3 is given in the Appendices.

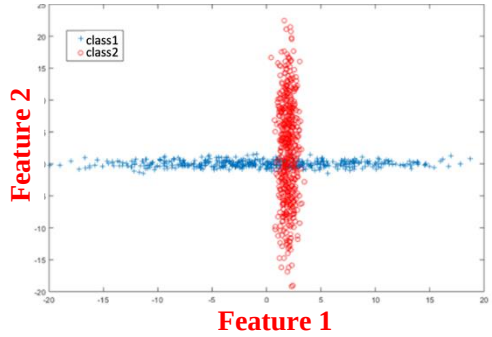


Figure 3. Distribution of data set 3.

2.4. Data Set 4

Data set 4 was produced in different distributions using the seed 14, 15, 16 and 17 command. The distribution of data set 4 is shown in Figure 4. The MATLAB code used to create data set 4 is given in the Appendices.

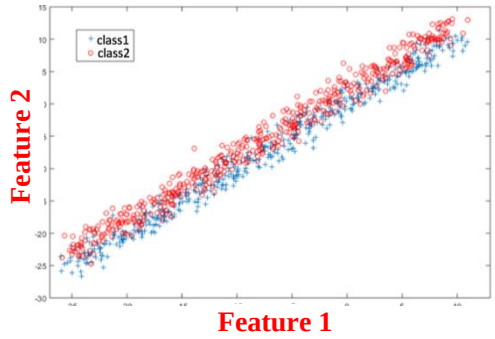


Figure 4. Distribution of data set 4.

3. METHOD

In this study, the performances of k-Nearest Neighbor, Support Vector Machines and Linear Discriminat Analysis algorithms were compared in terms of sample numbers. In this study, k-NN algorithm based on Euclidean distance is used. Euclidean distance for $P = (p_x, p_y) - Q = (q_x, q_y)$ points located on a two dimensional plane is calculated as follows (Çalışkan & Soğukpınar, 2008);

$$d = \sqrt{(p_x - p_y)^2 + (q_x - q_y)^2} \qquad (1)$$

In the DVM algorithm, there are linear and nonlinear classification types according to kernel type. In this study, radial based function is used. The main purpose is to make the in class distribution the smallest and the between classes distribution the highest (Mika, Ratsch, Weston, Scholkopf, & Mullers, 1999).

Half of the N trials were randomly allocated as training and the other half as a test set. Classifier training was conducted

with N / 2 number of trials, and random subsampling cross-validation method was used. During the classifier training phase, the most suitable k parameter for k-NN was determined by searching between 1 and 25 with 1 step. The most suitable sigma parameter for SVM was determined by searching 0.1 to 4.5 in 0.1 steps. Since there is no parameter setting for LDA, no parameter was searched for this classifier.

The accuracy criterion was obtained by dividing the number of correctly classified trials by the total number of trials as given in equation 2.

$$A = \frac{NCCT}{TNT} x100 \qquad (2)$$

In this equation, NCCT represents the number of correctly classified trials and TNT represents the total number of trials.

4. RESULTS

In order to eliminate the instability of the training and test sets randomness, the training and test sets were randomly divided into 100 times and the classification accuracies were calculated 100 times according to this distribution. Thus, the average classification accuracy and their standard deviation values were calculated for both validation and test accuracies.

The results of the three classifiers are given in Figure 5, Figure 6, Figure 7 and Figure 8, respectively. When Figure 5 is examined, it is seen that the standard deviation decreases and the stability increases as the number of trials increases in all three classifiers. It is seen that SVM classifier has superiority in low number of trials and k-NN classifier gives better results as the number of trials increases. When Figure 6 is examined, it is seen that the k-NN algorithm gives better results than the others. The performance of the LDA classifier is positively affected by the increasing number of trials. When examined in Figure 7, it is seen that the k-NN classifier has a clear superiority and is not affected by the number of trials. The performance of the SVM classifier improves as the number of trials increases. As the number of trials increases, the success of the LDA classifier decreases. When examined in Figure 8, While the LDA algorithm less than other algorithms in other distribution types, it gave the best result in this distribution. This distribution is more suitable for the LDA and gives a better result.

5. DISCUSSION AND CONCLUSION

When the results are examined for all distributions and classifiers, the stability increases as the number of trials increases. In addition, the accuracy for different distribution types and classifiers depending on the number of trials. In addition, the k-NN classifier gives the best results for all distribution types, followed by SVM and LDA classifiers, respectively. In the next time, the study will be expanded by adding classifiers such as Artificial Neural Network and Naïve Bayes. In addition, experiments will be carried out with artificial and real data types in different distributions.

APPENDIX

The MATLAB code used to create dataset 1 is given below.

```
randn('seed',6)
s1x=randn(1,numberoftrials1);
randn('seed',7)
s1y=randn(1,numberoftrials1);
randn('seed',8)
s2x=1.5+randn(1,numberoftrials2);
randn('seed',9)
s2y=1.5+randn(1,numberoftrials2);
```

The MATLAB code used to create dataset 2 is given below.

```
randn('seed',6)
s1x=4*randn(1, numberoftrials1);
randn('seed',7)
s1y=1+4*randn(1, numberoftrials1);
randn('seed',8)
s2x=randn(1, numberoftrials2);
randn('seed',9)
s2y=2+randn(1, numberoftrials2);
```

The MATLAB code used to create dataset 3 is given below.

```
randn('seed',10)
s1x=8*randn(1, numberoftrials1);
randn('seed',11)
s1y=0.5*randn(1, numberoftrials1);
randn('seed',12)
s2x=2+0.5*randn(1, numberoftrials2);
s2y=2+8*randn(1, denemesayısı2);
```

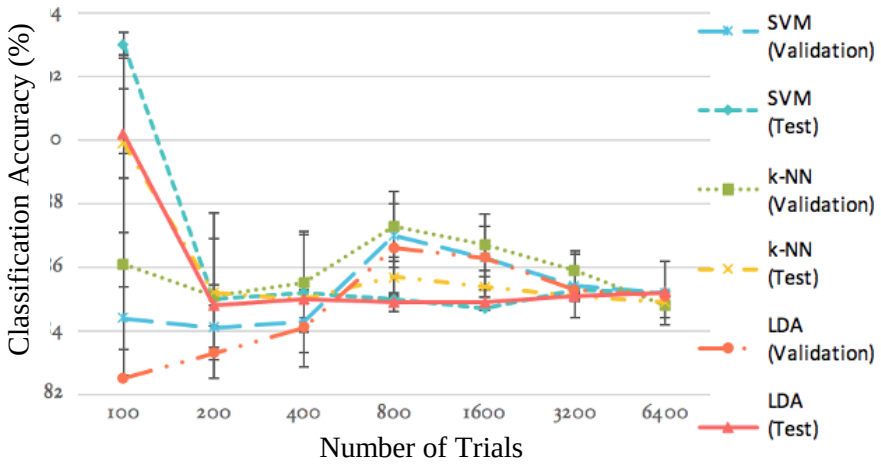


Figure 5. Results of Data set 1

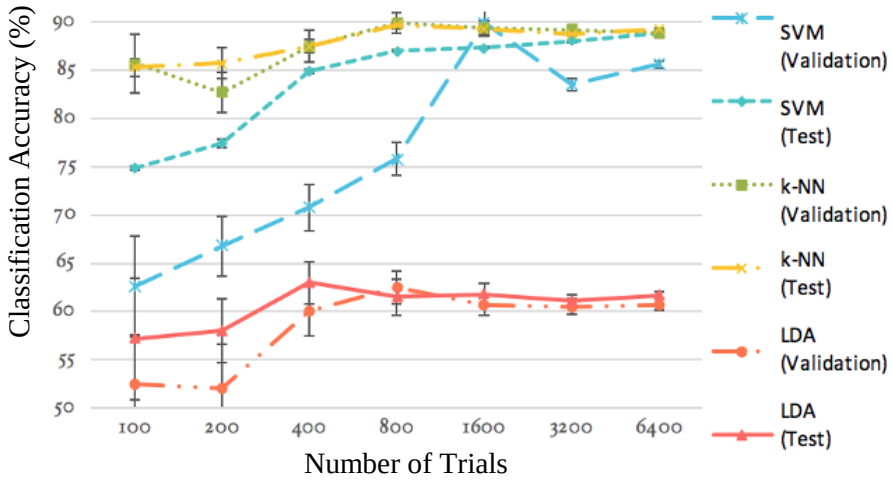


Figure 6. Results of Data set 2

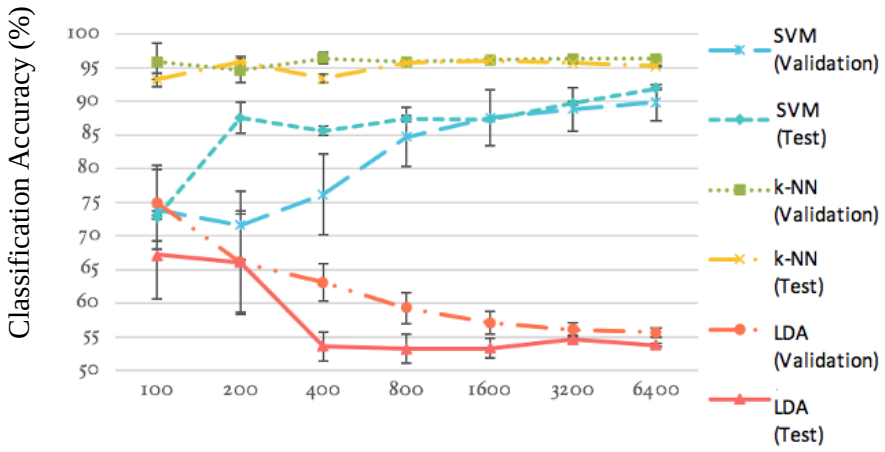


Figure 7. Results of Data set 3

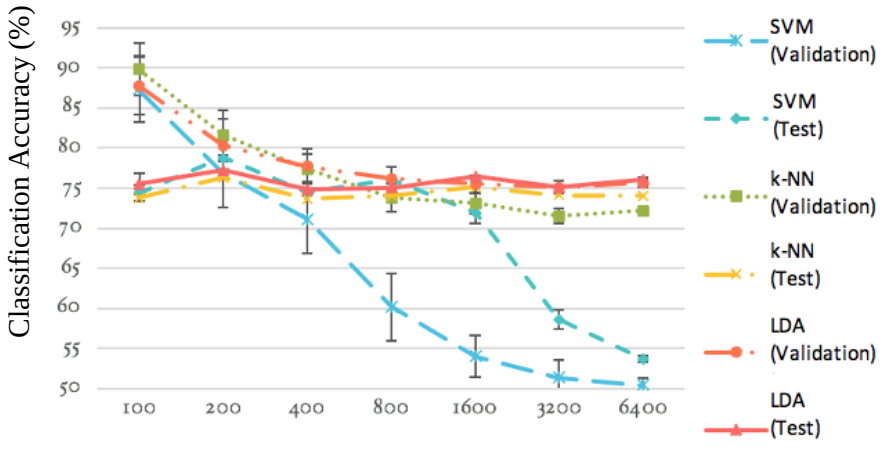


Figure 8. Results of Data set 4

The MATLAB code used to create dataset 4 is given below.

```
A=30;
theta=2*pi*A/360;
R=[cos(theta) -sin(theta); sin(theta) cos(theta)];
s1x=8*randn(1, numberoftrials1);
s1y=0.5*randn(1, numberoftrials1);
S1=[s1x;s1y]'*R;
s2x=2+8*randn(1, numberoftrials2);
s2y=2+1*randn(1, numberoftrials2);
S2=[s2x;s2y]'*R;
```

REFERENCE

Aydemir, O., & Kayikcioglu, T. (March 2013). Comparing Common Machine Learning Classifiers In Low-Dimensional Feature Vectors For Brain Computer Interface Applications. *International Journal of Innovative Computing, 9*, 1145-1157.

Çalışkan, S. K., & Soğukpınar, İ. (2008). KxKNN: K-Means ve K En Yakin Komşu Yöntemleri İle Ağlarda Nüfuz Tespiti. *EMO Yayınları*, 120-124.

Coskun, C., & Baykal, A. (2011). Veri Madenciliğinde Sınıflandırma Algoritmalarının Bir Örnek Üzerinde Karşılaştırılması. *Akademik Bilişim Konferansı Bildirileri 2011 İnönü Üniversitesi, Malatya Türkiye*, 51-58.

Dixon, S. J., & Brereton, R. G. (2009). Comparison of performance of five common classifiers represented as boundary methods: Euclidean distance to centroids, linear discriminant analysis, quadratic discriminant analysis, learning vector quantization and support vector machines, as dependent on data structure. *Chemometrics and Intelligent Laboratory Systems, 95*(1), 1-17.

Hand, D. J. (2006). Classifier technology and the illusion of progress. *Statistical Science*, 1-14.

Lorena, A. C., Jacintho, L. F., Siqueira, M. F., De Giovanni, R., Lohmann, L. G., De Carvalho, A. C., & Yamamoto, M. (2011). Comparing machine learning classifiers in potential distribution modelling. *Expert Systems with Applications, 38*(5), 5268-5275.

Mika, S., Ratsch, G., Weston, J., Scholkopf, B., & Mullers, K.-R. (1999). *Fisher discriminant analysis with kernels.* Paper presented at the Neural networks for signal processing IX: Proceedings of the 1999 IEEE signal processing society workshop (cat. no. 98th8468).

Murtagh, F. (1997). Machine learning, neural and statistical classification - Michie,D, Spiegelhalter,DJ, Taylor,CC. *Journal of Classification, 14*(1), 185-188. Retrieved from <Go to ISI>://WOS:A1997WV89900015

Salzberg, L. (1997). Methodological Note On Comparing Classifiers, Pitfalls to Avoid and a Recommended Approch Data Mining and Knowledge Discovery. *Kluwer Academic Publisher*, 317-328.

Tran, Q.-L., Toh, K.-A., Srinivasan, D., Wong, K.-L., & Low, S. Q.-C. (2005). An empirical comparison of nine pattern classifiers. *IEEE Transactions on Systems, Man, and Cybernetics, Part B (Cybernetics), 35*(5), 1079-1091.

Oceans Energy for the South Africa Coastline Michee Ntonto Lunkamba

Michee Ntonto Lunkamba
Micheelunkamba15@gmail.com / +27780626227

Abstract— At this time, several research projects were carried out on the use of alternative renewable resources following numerous problems related to the use of fossil fuel as an energy supplier. There is a range of different procedures which can be used, and the ocean has been established as a possible source for such renewable energy. Several techniques were therefore established and used to extract energy from the sea in a realistic, functional manner, while other techniques are still in various stages of growth. The report describes these potential sources of ocean energy, dealing explicitly with only those inside and above the water column. Oceans are the world's largest solar power collectors. With oceans spanning over 70% of the surface of the earth, the amount of energy stored by the oceans is huge. The energy can be harvested from the ocean through waves, mare current, and thermal gradients within the water body. The lunar gravity pulls drives mainly the tides and the wind drives the waves on the oceans. In theory, such ocean-based renewable resources can often meet the global energy needs but are extremely difficult to harvest for large-scale production economically. Different methods, including three main techniques in this chapter. This paper discusses various methods, including three principal techniques for the collection of energy from the oceans: wave power, tide power, and ocean thermal energy conversion.

Keywords: wave energy, ocean thermal, tide energy, wind energy, current energy.

1 INTRODUCTION

The paper focuses on the study of 'Oceans Energy for the South Africa Coastline', which and concerns methods for improving energy on the coastline of South Africa. The demand for renewable energies is increasing globally in response to climate change and energy security concerns. Several countries have pledged to reduce greenhouse gas emissions and invest in a prosperous low carbon future under the Paris Agreement in the fight against climate change in 2015. Global renewables investments now outstrip the projected demand for fossil fuels. It must be understood at the beginning that ocean conditions differ greatly across the globe, and an energy extraction suitable in one region is not feasible in another. Consequently, it is important to have a clear understanding of the ocean environment in the region in order to assess a specific oceanic process and its power generation potential. This means that for each source of energy, each oceanographic area should be considered separately. This introductory chapter starts with the study of ocean energy as a source of renewables, before introducing the concept of a wave absorbing, thermal, wind, and current energy conversion device, the main theme of this thesis. A brief history of wave-energy is provided to provide a context for the creation of these energy sources and is important for understanding them. A summary of the aims and purposes of this study and the development of this thesis follows.

Specific work has been conducted into alternative, renewable resources following the various problems related to the use of fossil fuels for energy production. The ocean has been established as a possible source, and a variety of different processes can be exploited. Therefore, a range of techniques has been developed and used to extract ocean energy in a realistic, useful way, although others are still in different stages of growth. This report describes these potential sources of sea energy those in and over the water column; no further sources on the seabed or on the solid ground are available [1].

The method used to isolate variables from the expansion of Havelock's was used to measure the speed potential over the fluid domain and provided the wave excitement forces for different draft-to-radius frequencies in relation to incident wave frequencies. In addition, seawater is highly corrosive, with materials that are used in the ocean to prevent failure carefully selected and kept. Another major problem is biofouling, and any open surface will soon produce algae and crustaceans that hinder movement and reduce efficiency. The work in-depth in the ocean is also a significant problem.

This research has to do with the investigation of ocean energy for South Africa's coastline of water waves in water of infinite depth by a vertical hollow cylinder. Practically speaking, the proper placement of the instrument should be stressed so that waves can be detected as broadly as possible. The geologically recent surface is distinguished by several surface characteristics associated with a separate structure that suggests past and current geophysical activity with implications of habitability [2]. In this research, I propose a theory of material transport from the ocean to the surface.

South Africa's ocean operates most with wave energy harvesters [3] whereas by the low frequencies and its irregular amplitudes and high frequencies. This is the main problem because the harvester's energy is not a peaceful ideal for ocean energy for the South Africa coastline. However, they think that wave energy harvesting could be a better solution since it comes also from the wind and indirectly from the sun [4]. It could have a lesser impact on the environment and requires-I an esteem-a lower investment. It could also be a protection for aggressed shores by wave impact reduction. The evolution of PM could help to increase power density, reducing weight and cost [5]. Technology is taking a larger path that even some investors are able or wish to support. Require huge financial outlays for the construction of a modern power plant [6].

As per the literature review, energy generated by the ocean stream power plants is a relatively new technology, a new concept, and growth in a market in terms of capacity and future investments. Indeed, wave, tidal, salinity gradients are untapped resources that offer a lot of hours of public and academic debate, in terms of their potential.[11]. Technology is taking a larger path that even some investors are able or wish to support. Require huge financial outlays for the construction of a modern power plant [8]. As the product of ocean energy, is to have high potential energy

and a lot of natural phenomena will describe the approximate gravity of the surface of the ocean, depending on the circumstances with risk in the sea, and water level from the ocean current scale [6]. South Africa operates most with wave energy harvesters whereas by the low frequencies and irregulars of the amplitude energy generated by the coastline and most companies operate on tidal and wave energy technology [12].

Options for renewable energy on the South Africa coastline are being considered. Wave energy is adequate in the south-western sector of the country, while the Agulhas Current on the southeast coast has strong, consistent currents that offer enormous potential. Tidal energy is not enough to be considered viable at this stage, while offshore wind energy is unlikely because of limited shallow water areas. Off the north-east province of KwaZulu-Natal warm sub-tropical waters brought southward by the Agulhas Current also offer possibilities for ocean temperature energy conversion (OTEC) [13]. The near-zonal southern coastline is marked by several large half-heart or crenulated bays opening to the southeast, suggesting that these sections of the coastline are in dynamic equilibrium with the prevailing south-westerly swell regime. Sediments have built out beyond the headlands, forming sediment sinks for the eastward-moving longshore sand-drift [14]. This description of the southeastern shelf of Africa has covered extensive shelf and slope areas. They fall within the western boundary of the current region, although the presence of Madagascar serves to isolate the Mozambique Channel region. It is these intense currents flowing off. The shore of the shelf break that fornicates the corresponding coastal oceans. Particularly because of the no law shelves. Nonetheless, it must be appreciated that the subdivision of South Africa's coastal ocean into this segment has been done as a convener and that there are substantial differences between the various sub-regions discussed here [17]. There are several crenulated East facing bays along the southern coast and the largest continental shelf – the Agulhas Bank – is about 270 km inland offshore. The key features on the shoreline are False Bay and St. Helena Bay in the west, which figure 1 shows.

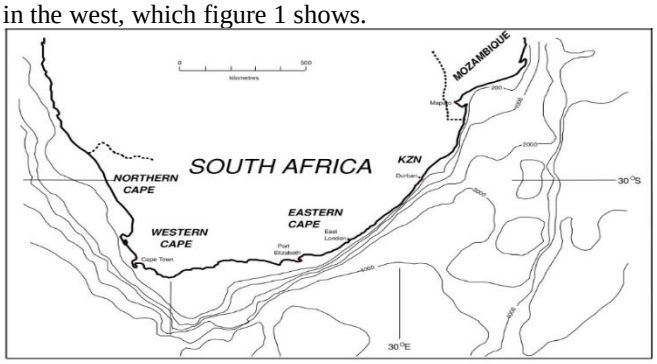


Figure 11: Bathymetry around South Africa

Initially, it should be recognized that ocean conditions vary widely around the world, and an energy extraction that can be adequate in an area will not be feasible in others. Consequently, to evaluating an oceanic process and it is potential to generate energy, it is necessary to have a good knowledge of the ocean environment in the area. It means that each oceanographic region must be considered separately for each power source. There are several potential ocean energy sources available for South Africa's coastline:

- Currents
- Tides
- Waves
- Wind
- Thermal

Note that potential sources such as osmosis and ocean biofuels are not included. In the case of wind power, only the situation on the ocean itself will be considered since there are several wind farms in operation and under construction on adjacent land.

Ocean Current Energy: In the last 8 years, Eskom started a measurement program that identified both the most suitable locations as well as broader current structures. This applies to the Agulhas current. However, vertical and southern fine-scale scissors need to be well-defined to offer underwater turbine systems design criteria, while commercial systems need to be optimized for the high-speed flow core and downstream wakes of the individual generating units. Currently, the 1.5m/s flow is probably too low to use the already developed technology for applications with tidal streams where the speeds are usually much faster than 2 m/s. Nevertheless, several innovative turbine designs are being developed that can be used in the future. It was also showcased that the cut-in speed would almost double the power available by reducing the minimum operating speed from 1.5 m/s to 1.0 m/s.

Ocean Wave Energy: The west and south coast of South Africa produces considerable wave energy, which provides this potential source in the future with a wide range of devices being developed worldwide. It is however important that wave power maps of the entire South African coast and digital bathymetric data are produced to implement such equipment.

Offshore Wind Energy: The use of wind energy in South Africa is becoming increasingly common, and significant wind resources are highly likely to be available offshore. Although few offshore areas which are suitably shallow may be built, a more detailed evaluation must be done for the offshore wind potential to be clarified.

Ocean Thermal Energy: Oceanic conditions appear appropriate on the northern coast of the KZN for the use of the surface-waters differential at depths of about 1000 m. The shelf is also very narrow, so there is no need to take unnecessary cable lines to the shore. At this point, however, the temperature and current structures in the area must be confirmed by a measurement program. Although the OTE concept has been in operation for some time, prototype plants still need to be solved before commercial plants become viable. There are technical problems. Nevertheless, various countries are now spending substantial funds on resolving these problems.

2 DESIGN RATIONALE

A simple approach needs to be discussed to achieve the aim of this study:

Firstly, in comparison to the information collected on ocean energy to help in identifying the gaps and obstacles to the commercial development of wave and tidal technologies, strategic technologies agendas for more mature renewable energy technologies will be compared. In the interview process, the wave and tidal-energy developers have been meeting to collect information with key technical and management on a range of topics including technology development, installation, maintenance and reliability, supply chain, and barriers to

the economy, regulation, and legislation. To this end, a standard questionnaire was developed for interviews with a variety of developers, to gather common information and determine where problems are that have greatly affected other developers.

There was a wide variety of inputs that will be taken into consideration for the design of our project, since early as well as older developers were approached for interviews. There have been several countries representing technology developers and several levels of readiness for technology. This allowed a wide range of responses to barriers throughout the investigation of South Africa's coastline. It is important to bear in mind that research and innovation will still be required, even though mature technological options exist. It was thus necessary to recognize both research and innovation technologies at an earlier stage and those in full-scale implementation at a mature stage.

3 EXPECTED OUTCOMES

After modelling the network and running all the analysis, it is expected to see the results of:

- After sea testing, some experiences can be taken forward as lessons learned in future deployments. It is important to ensure that this learning is properly utilized by the industry, so that there are no repetitions of setbacks.
- Several modules, including cables, hydraulic pads and non-return valves, and build up batteries, were performing significantly less efficiently than expected.
- There will be a lot of creativity in this field. The need to adjust the current intervals.
- Offshore wind maintenance will account for 80 percent of single parts weighing less than 25 kg. [I.e., replacing one-man work]. Our design goal is to facilitate and convenient component access at low costs.
- The price of petrol and gas is too high for ocean energy [and quality standards]. For example, wet mate connectors [suitable for deployment] to 3000 m are not necessary in the ocean-energy sector.
- The rotor angle values.
- The critical clearing time at each step.

Based on the results, we will understand why the system we are doing the investigation on ocean energy and how we will be able to improve it.

4 CONCLUSSION

This paper introduces new energy and demonstrates how the coastal energy network in South Africa will function if it suffers from great disturbances. Faults and wide renewable energy penetration can impact the system enormously. It will also be understood how important the critical clearing time is.

Previous analysis has shown that renewable energy in the oceans can make up a component of the South African business energy mix. At the beginning, however, it should be recognized that most technologies remain in the phases of development and at this point, a system for direct implementation cannot be purchased off the shelf. Of the five possible renewable ocean energy sources which are tidal energy, only that has no chance of generating significant electricity in South Africa.

5 REFERENCES

[1] South African Department of Environmental Affairs, “National Climate Change Response Green Paper,” *Built Environ.*, no. 33, pp. 3–40, 2010, [Online]. Available: file:///C:/Users/01445593/Google Drive/DDPP/111012nccr-whitepaper.pdf.

[2] UNIDO, “Industrial Energy Efficiency Improvement in South Africa through Mainstreaming the Introduction of Energy Management Systems and Energy Systems Optimization,” no. i, pp. 1–84, 2015.

[3] W. Du Plessis, “Energy efficiency and the law: A multidisciplinary approach,” *S. Afr. J. Sci.*, vol. 111, no. 1–2, pp. 1–8, 2015, doi: 10.17159/sajs.2015/20130302.

[4] Dme, “National Energy Efficiency Strategy of the Republic of South Africa Department of Minerals and Energy First Review October 2008,” *October*, no. 32342, 2009.

[5] A. Khaligh and O. C. Onar, “Ocean Wave Energy Harvesting,” *Energy Harvest.*, pp. 223–304, 2018, doi: 10.1201/9781439815090-4.

[6] SEA, “Sustainable energy solutions for South African local government: a practical guide,” *Sustain. Energy Africa*, p. 24, 2017, doi: 10.1016/j.braindev.2010.03.002.

[7] T. Kawaguchi and T. Arikawa, “A Theory for Wave Energy Conversion by Bottom-Mounted Oscillating Bodies A Theory for Wave Energy Conversion by Bottom-Mounted Oscillating Bodies,” no. June, 2019.

[8] Treasury, “Economic transformation, inclusive growth, and competitiveness: Towards an Economic Strategy for South Africa Prepared by Economic Policy, National Treasury,” *World Econ. Forum*, pp. 1–62, 2018, [Online]. Available: http://www.treasury.gov.za/.

[9] J. R. Joubert, “An investigation of the wave energy resource on the south african coast, focusing on the spatıal distribution of the south west coast,” no. March, p. 183, 2008.

[10] O. Green and G. Studies, “OECD Green Growth Studies,” *Director*, p. 104, 2012, doi: 10.1787/9789264115118-en.

[11] O. Farrok, K. Ahmed, A. D. Tahlil, M. M. Farah, M. R. Kiran, and M. R. Islam, “Electrical power generation from the oceanic wave for sustainable advancement in renewable energy technologies,” *Sustain.*, vol. 12, no. 6, 2020, doi: 10.3390/su12062178.

[12] S. Zou, “Digital Commons @ Michigan Tech Optimal Control of Wave Energy Converters,” 2018.

[13] D. Lande-Sudall, T. Stallard, and P. Stansby, “Co-located offshore wind and tidal stream turbines: Assessment of energy yield and loading,” *Renew. Energy*, vol. 118, pp. 627–643, 2018, doi: 10.1016/j.renene.2017.10.063.

[14] E. Schumann, “Tidal and Inertial Currents Around South Africa,” no. January, 2015, doi: 10.1061/9780872623736.156.

[15] E. Schumann, “Wind-driven mixed layer and coastal upwelling processes off the south coast of South Africa Wind-driven mixed layer and coastal upwelling processes off the south coast of South Africa,” no. November, 2014, doi: 10.1357/002224099321549639.

[16] H. Winkler, “Renewable energy policy in South Africa : policy options for renewable electricity,” vol. 33, pp. 27–38, 2005, doi: 10.1016/S0301-4215(03)00195-2.

[17] D. Johnson and C. J. S. Fourie, “An overview of energy efficiency in South African hard rock mining AN OVERVIEW OF ENERGY EFFICIENCY IN SOUTH AFRICAN HARD,” no. July 2014, 2012, doi: 10.1109/SAEEC.2012.6408583.

Brain Oscillatory Responses during Listening to Quranic Acoustics

Samhani Ismail
*Faculty of Medicine, Universiti Sultan Zainal Abidin (UniSZA),*Terengganu, Malaysia.
samhanismail@gmail.com

Mohd Hanifah Jusoh
Department of Orthopaedics, School of Medical Sciences, Universiti Sains Malaysia (USM), Kelantan, Malaysia.
hanifahjusoh@gmail.com

Mohammed Faruque Reza
Department of Neurosciences, School of Medical Sciences, Universiti Sains Malaysia (USM), Kelantan, Malaysia.
faruquereza@gmail.com

***Abstract*— Quranic texts are rich in rhythmic contributing elements which produce sound full of aesthetic cadence. This is believed to be the reason of relaxation effect to its listeners, as well as cognition enhancement. However, the neural mechanism on how the auditory stimulus affects humans' brain is still a dearth. Hence this study was performed to examine the oscillatory waveforms and spectral power changes due to Quranic Fatihah Chapter listening which reflects its neural mechanism of action. Brain electrical data were measured by using the Electroencephalography followed by waveform analysis and Discriminant Analysis. Results showed that the waveforms amplitude were reduced, rhythmic and synchrony patterns were observed during listening to the Fatihah Chapter acoustics stimulus. Spectral power analysis showed that listening to Quranic sound stimulus activates greater neural population associated with behavioral and cognition enhancement.**

Keywords*— *Brain oscillation, Brain waveform, Cognitive neurosciences, quantitative Electroencephalography, Quranic therapy, Spectral power.

[1] INTRODUCTION

Oscillations are prevalent features of the brain recording and are critical for efficient communication within and across brain areas [1]. The oscillatory waveforms may inform underlying physiological process generating those oscillations [2]. Listening to Quranic acoustical stimulus has been described over long periods of time produces definite changes in physiology and mental state along with cognitive function. The neurophysiological correlates of Fatihah Chapter listening had been determined by current study by using electroencephalography which provides relatively noninvasive method of study to see specific changes in humans' beta brainwave rhythms.

[2] LITERATURE REVIEW

A. Quantitative Electroencephalography

The role of oscillations in the language domain is much less established. The only non-invasive neuroimaging methods able to reveal brain oscillations are electroencephalography (EEG) and magnetoencephalography (MEG), which make them the methods of choice to study Fatihah Chapter sound processing at different time scales [3-4].

B. Listening to Fatihah Chapter

Listening to Quranic acoustical stimulus has been described over long periods of time produces definite changes in physiology and mental state along with cognitive function. The neurophysiological correlates of the Fatihah Chapter listening had been determined by current study by using electroencephalography which provides relatively noninvasive method of study to see specific changes in humans' brainwave rhythms. We aimed to investigate the brainwaves changes during listening to rhythmic Fatihah Chapter recitation which alter cortical functioning and corticofugal controls that may significantly modify the processing of information at brainstem and the thalamic levels [5].

[3] METHOD

EEG, a noninvasive medical imaging technique was used to read the scalp electrical activity generated by brain structures. The principle is, when brain cells are activated, local current flows are produced. The electrical activity of pyramidal neurons is the principle source of EEG potentials because the apical dendritic of those cells are parallel to one another and always oriented perpendicular to brain surface. Furthermore, they often cross several layers and allow input from different cortical layers to be integrated along the dendritic tree.

A. Sound

The Fatihah Chapter acoustics stimulus was acquired from the Internet open source which was downloaded in the *.wav* file. Fatihah Chapter acoustics stimulus used in this experiment is a recitation by a renowned Egyptian Qari, Sheikh Abdul Basit bin Abdul Samad. While the Arabic News also derived from Internet open source.

B. Participant

- Participants were selected among Malay Muslim which were 40 healthy normal adults (14 males:14 females) which routinely pray, hence familiar to Fatihah Chapter sound. They were not Arabic speakers, hence they don't understand Arabic language or Arabic News, but might understand or not understand the Fatihah Chapter. We are not aiming to evaluate the semantic level of the Quranic listening, but just to the rhythms level of the acoustics itself. This is due to the knowledge that brainwaves rhythms can interact with the Quranic acoustics rhythms where the interaction will synchronize and modify the brain rhythms, known as brainwave entrainment process.
- This mean age was 31.12 years with range of 20.3 to 50 years.

C. EEG materials and methods

EEG data from fourteen healthy normal adults non-Arabic speakers (14 male : 14 female) were recorded by 128-channel Geodesic EEG System (GES) (Electrical Geodesics, Inc.) placed over the frontal, parietal, occipital and temporal lobes

in accordance with the extended version of the International 10-20 system [6].

- *GSN sensor arrays:* EEG recording was performed by using 128-electrode sensor net of Geodesic EEG System (GES) (Electrical Geodesics, Inc.) with impedance of ≤ 50kΩ. GES consists of GSN sensor arrays, EEG acquisition software (Net Station) and relevant GES hardware.
- *Net Support Kit:* A Net Support Kit containing accessories such as a measuring tape, pipettes, syringes, china markers and clean towels sized approximately 40 x 60 centimeters, provided by EGI were utilized well.
- *Electrode placement:* Scalp circumferences were measured and electrodes were placed according to the International 10-20 system. 19 electrodes representing 128-electrode channel used by this study.
- *Stimulation paradigm:* The auditory stimulations from Fatihah Chapter, Rest and Arabic News come in random sequence, within the same length of 5, 8, 6, 6, 10, 8 and 20 seconds with intensity was set at 65 dB.
- *EEG acquisition:* This study was conducted in Event Related Potential/Magnetoencephalography Laboratory in Hospital Universiti Sains Malaysia (HUSM). Subjects closed their eyes during the experiment and sit comfortably in a sound-treated chamber with dimmed light.
- *EEG signal pre-processing:* EEG signals were pre-processed by using EGI Net Station software 4.5.1. Data were filtered through highpass of 0.3 and low pass of 50Hz, artefact detection for bad channel, eye blink and eye movement, bad channel replacement and montage operation. The .ref files were transferred to EDF files.
- *BESA Operation:* The EDF files were opened by Brain Electrical Stimulation Analysis (BESA Research 6.0 Software, Germany) and the waveform were built.
- *Fast Fourier Transform:* The raw waveform length were selected and transferred into Fast Fourier Transform (FFT) - spectrum. Power spectrum of the brain oscillation from the verse 1 to verse 7 were acquired from each subjects.
- *Data normalization:* The data in the form of FFT were opened by Microsoft Excel. The data were checked for their outliers and then recoded and normalized by using SPSS 21.0.
- *Statistical analysis:* The normalized data were undergoing statistical analysis including Discriminant Analysis.

D. Waveform Analysis

- After pre-processing, the data then viewed by the Top Viewer waveforms that were exported into encapsulated postscript.
- The oscillatory waveforms from the listening to Fatihah Chapter, Arabic News and Rest were evaluated.

E. Spectral Power

In this study, the significantly different spectral power from the brain oscillations was determined by Discriminant Analysis (DA) coupled with Repeated Measures ANOVA which produce the same number of p value as reported below. DA was a multivariate statistical technique which commonly used to build a predictive model of group discrimination to classify the observed predictor variables into one of the groups. It constructs a discriminant function (DF) for each group by equation:

$$f(G_i) = k_i + \sum_{j=1}^{n} w_{ij} P_{ij}$$

Where *i* is the number of groups (G), Ki is the constant inherent to each group, n is the number of parameters used to classify a set of data into a given group, and w*j* is the weight coefficient assigned by DF analysis (DFA) to a given parameter (P*j*).

In this study, Discrmininant Analysis was applied by using XLSTAT statistical packages to determine whether the groups differ with regard to the mean of a variable and to use that variable to predict group membership.

[4] RESULTS AND DISCUSSION

Brainwave entrainment knowledge has been applied in psychological therapy especially by music therapy and brainwave entrainment meditation therapy which raised level of melatonin, enhanced cognitive performance, reduced the level of anxiety and raised quality of life. Yet, the neural oscillation evoked by Quranic acoustics stimulus is less uncovered. In order to learn the oscillatory behavior during listening to the rhythmical Quranic ss, we conducted EEG recording.

Result shows that there are oscillatory changes in the Beta brainwaves. Relative to Arabic News, more brain regions were activated during listening to the Fatihah Chapter.

A. Oscillatory waveform analysis

Oscillations of the EEG are less stereotyped and waveform analysis is a challenging and tends to be technique-oriented. The neural signals were filtered to get Beta (14-30Hz) frequency band. This narrowband filtering inherently assumes that the oscillation of interest is sinusoidal. These continuous waveforms exhibited the comparative brain oscillations as a result of acoustics stimulation under three conditions of Rest, Fatihah Chapter and Arabic News.

1) They exhibit the features of oscillatory that presented some characters which manifested the underlying physiology.

a) During Rest condition, generally, the waveforms exhibited relatively high voltage amplitude and the waveform went through with fluctuating pattern, visible at most areas.

b) While for the rhythmicity, they showed rhythmic pattern in the continuous EEG recording but looks like only few areas were synchronously engaged.

c) However, seeing the EEG recording during Fatihah Chapter listening, we found that the most obvious difference was the amplitude, which was decreased in all brain areas compared to Rest.

d) This may be due to entrainment or synchronous effects of brain oscillations to external stimuli of Fatihah Chapter acoustics that having rhythmic pattern of sound waveform, pitch and intonation that may interact and locked the brainwave signals.

2) Synchronization among brain region also obvious in Fatihah Chapter, as well as the synchrony pattern among the brain hemisphere. Synchrony refers to the simultaneous appearance of rhythmic or morphologically distinct patterns over different regions of the head, either on the same side (unilateral) or both sides (bilateral).

a) This is may be due to brain balance induced by this Quranic sound stimulus which believed to increase humans' cognitive ability such as memory and attention.

B. *Spectral power changes*

Through statistical analyses, the mean score of beta spectral power density of The Fatihah Chapter acoustics stimulation was significantly different at all the electrodes at the frontal region (Fp1, Fp2, F3, F7, F4, F8 and Fz) (P value = 0.015, 0.027, 0.0001, 0.0001, 0.015, 0.001 and 0.000, respectively), at the right superior and inferior parietal (P4, P8) (P value = 0.001, 0.025, respectively), the right middle temporal (T8) (P value = 0.000) and at the left occipital (O1) (P value = 0.019), with P value was set at 0.05. Thus we have sufficient evident to reject null hypothesis and accept the alternative hypothesis, meaning that there are significantly different changes in the beta spectral power of The Fatihah Chapter rhythmic acoustics stimulation.

By the way, less electrodes were statistically changed during listening to Arabic News; Fp1, F3, F7, Fp2, F4 and Fz electrodes channels in the frontal region (P value = 0.004, 0.0001, 0.001, 0.012, 0.002, 0.0001, respectively), both the right superior and inferior parietal (P4 and P8) (P value = 0.031, 0.017, respectively).

From this study, we found that Beta oscillations were in the pattern of power spectral reduction. More electrodes were significantly reduced during listening to Fatihah Chapter compared to Arabic News.

This indicates of high integration from different brain areas. Furthermore, greater neural ensemble was activated during listening to the Fatihah Chapter. Attention, inhibitory control of irrelevant impulses and perseverance in goal-directed action were postulated. In addition, familiarity with Fatihah Chapter perhaps contributes. Greater activation at the right temporal during Fatihah Chapter suggested for rhythmic auditory perception and melodious intonation contains high energy and rhythms. Motor area activation was also recorded which believed to be associated with movement planning and execution.

C. *Figures and Tables*

a) The oscillatory waveforms from the Fatihah Chapter and Arabic News listening and Rest were presented below. The mean of significantly changed spectral power from the Fatihah Chapter and Arabic News followed and tabulated in bar graph.

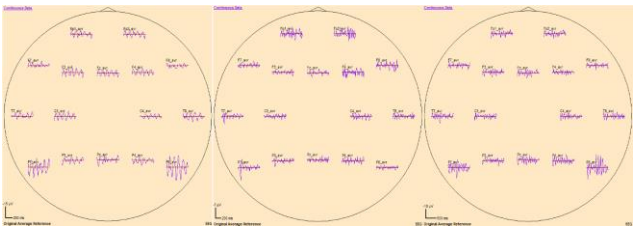
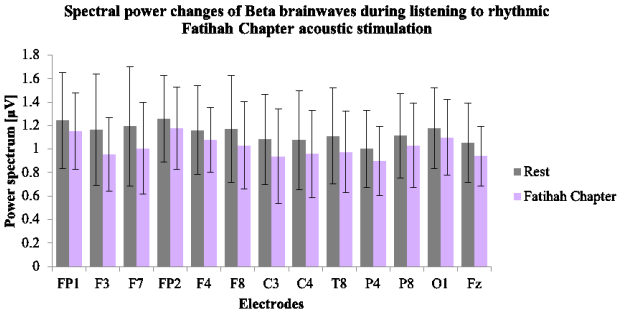


Fig. 1. Oscillatory waveforms from (from left) Rest, Arabic News and Fatihah Chapter. Noted here that there are differences in the amplitude, rhythms and pattern which shows that brainwave entrainment was occurred.



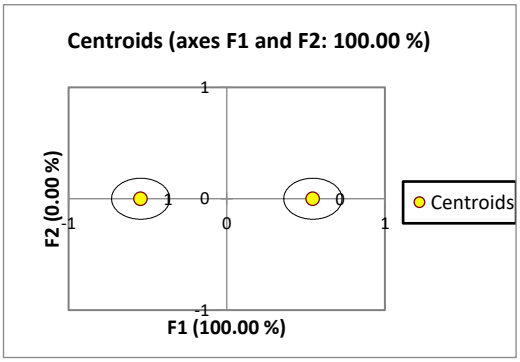


Table 1. Confusion Matrix For The Estimating Sample

from \ to	*Fatihah Chapter*	*Rest*	*Total*	*% correct*
Fatihah Chapter	138	58	196	70.41%
Rest	65	131	196	66.84%
Total	203	189	392	68.62%

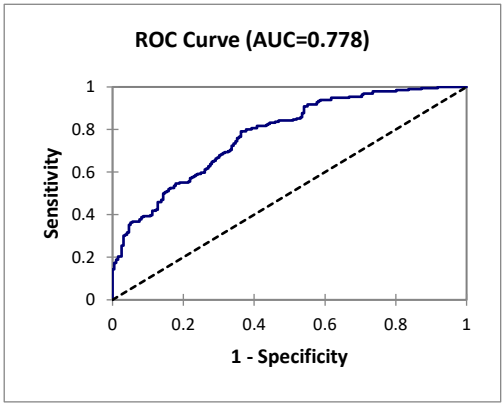
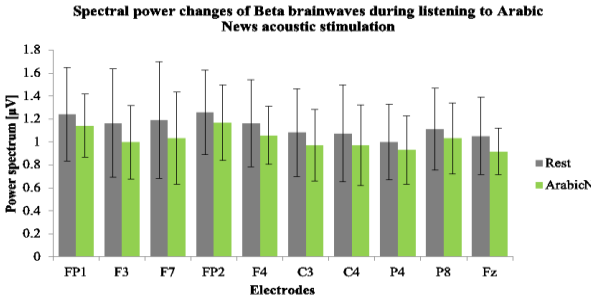


Fig.2. The mean score of spectral power that significantly reduced during listening to the Fatihah Chapter. 13 electrodes from the frontal, temporal, parietal and occipital brain areas were involved. Centroid model showed that the groups were discriminating well with confusion matrix estimated to 68.62%. Area under curve is 0.778



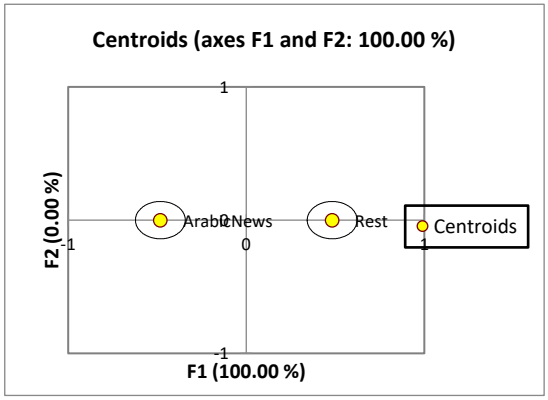


Table 2. Confusion Matrix For The Estimating Sample

from \ to	*Arabic News*	*Rest*	*Total*	*% correct*
Arabic News	125	71	196	63.478%
Rest	76	120	196	61.22%
Total	20	191	392	62.50%

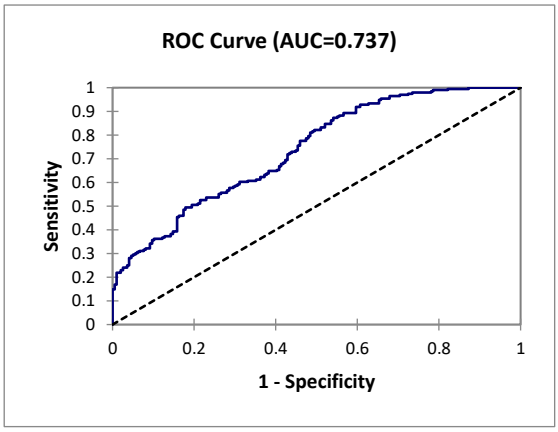


Fig. 3. The mean score of spectral power that significantly reduced during listening to Arabic News. 10 electrodes from the frontal and parietal were involved. Centroid model showed that the groups were discriminating well with confusion matrix estimated to 62.50%. Area under curve is 0.737

ACKNOWLEDGMENT

The author would like to acknowledge the support from the USM Short Term Research Grant (304/PPSP/61313160), the Incentive Grant and the Ministry of Higher Education, Malaysia.

REFERENCES

[1] S. R. Cole, and B. Voytek, “Brain oscillations and the importance of the waveform shape,” Trends in Cognitive Sciences, vol 21, 2017, pp137-149.

[2] E. J. Peterson, and B. Voytek, “Alpha oscillations control cortical gain by modulating excitatory-inhibitory background activity,” bioRxic, 2017.

[3] O. Hauk, A-L. Giraud, and A. Clarke, “Brain oscillations in language comprehension,” Language, Cognition and Neuroscience, 32:5, 2016: 533-535.

[4] F. L. da Silva, “EEG and MEG: relevance to neuroscience,” Neuron, 80,5, 2013: 1112-1118.

[5] N. Singh, and S. Telles, “Neurophysiological effects of the meditation based on evoked and event related potential recordings,” BioMed Research International, 2015.

[6] H. H. Jasper, “Electrode system of the International Federation,” Electroencephalography and Clinical Neurophysiology, 10, 1958: 371-375.

A Novel Beam Steering Method Using Dispersive Superstrates with Low Dielectric Constant

Muhammed S. Boybay
Department of Electrical and Electronics Engineering Igdir University Igdir, Turkey
msboybay@uwaterloo.ca, https://orcid.org/0000-0003-0503-2557

***Abstract*—Beam steering is an important concept in communication systems, radar and wireless power transfer applications. Although the concept of beam steering using phased array antennas is known for decades, cost of such systems limit its applicability. In this study, metamaterials are employed to steer a narrow beam. A metamaterial superstrate is designed and it is shown that the direction the main beam can be changed by changing the operation frequency. Numerical studies show that the direction of the main beam can be changed up to 25 degrees when the permittivity of the superstrate changes from 0.08 to 1. The maximum steering angle is limited by the angle between faces of the superstrate. Findings are verified by theoretical calculations.**

Keywords—Metamaterials, beam steering, antenna arrays, microstrip patch antennas

[1] INTRODUCTION

Metamaterials have been a very attractive research field SINCE early 2000s when first double negative materials are designed and experimentally verified [1]-[3]. In the last decade, extraordinary properties of metamaterials enabled their use in various applications such as planar antennas [4], energy harvesting [5], [6], near field sensors [7]-[9], rotation sensors [10], [11], cloaking [12], [13], etc. Recently commercial products emerged in communication, security, wireless charging and defense industries.

In planar antenna technologies, metamaterial based magnetodielectric materials are employed in the substrate of patch antennas to improve the operation bandwidth [14]. In [15], anisotropic metamaterials are employed in the superstrate of patch antennas to improve the gain. Finally in [16] the superstrate concept is used to develop a new beam steering method based on the dispersive nature of metamaterials that eliminates the need for phase shifters. Although the new beam steering method is introduced in \cite{b16}, the method is limited in steering range unless a very high an dynamic range in the dielectric constant of the superstrate is provided.

In this study, the new beam steering method is modified and a different regime in the permittivity function of metamaterials is used. In the new regime, the imaginary part of the permittivity is smaller and high dielectric constants are not required. In addition, the steering range is only limited by the geometry of the superstrate and the material properties do not change the range. The new technique is demonstrated using numerical tools and verified with the theory.

[2] METHODS

A. Beam steering method

In conventional superstrates, top and bottom surfaces are parallel to each other. In the new concept the top surface of the superstrate is tilted so that the incident wave is perpendicular to the bottom surface but oblique to the top surface. When combined with the frequency dependent permittivity of metamaterials, the superstrate geometry steers the beam to a different direction at different frequencies. The steering mechanism is governed by the Snell's Law and can be formulated as

$$\theta = \alpha - arcsin\sqrt{\epsilon'(f)}sin\alpha \qquad (1)$$

where α is the angle between top and bottom surface of the superstrate, $\epsilon'(f)$ is the real part of the permittivity and θ is the steering angle which is defined as the deviation in the direction with respect to the initial beam direction.

In this study a new permittivity range is employed which spans [0, 1] interval. Therefore the range of the steering angle is [0, α] and only limited by α.

B. Material selection

The dispersive nature of the metamaterials are often described by Lorentz Model [17]. The Lorentz Model is given by

$$\epsilon(\omega) = \epsilon_\infty + \frac{(\epsilon_s - \epsilon_\infty)\omega_0^2}{\omega_0^2 + i\omega\delta - \omega^2} \qquad (2)$$

where ω is the angular frequency, ω_0 is the resonance frequency and δ is related to the loss factor of the material, i.e. related to ϵ''. Other parameters and selected values are given in Fig. 1.

Vertical lines in Fig. 1 represent the operation interval. The interval is between 2.286 GHz and 2.425 GHz. Corresponding dielectric constant values are 0 and 1, respectively. The objective of this study is to demonstrate the operation principle of the new method and the same concept can be applied to other frequency bands with appropriate material parameters. The center frequency and bandwidth can be modified based on the application requirements.

[3] Microstrip patch antenna array

In order to generate a beam at the operation frequency a microstrip patch antenna is designed. The antenna is designed at the fundamental mode TM_{010} [18]. Fig. 2 shows the designed structure. The structure is excited with a 50 Ω coaxial line (RG-58/U) and the feeding location is optimized

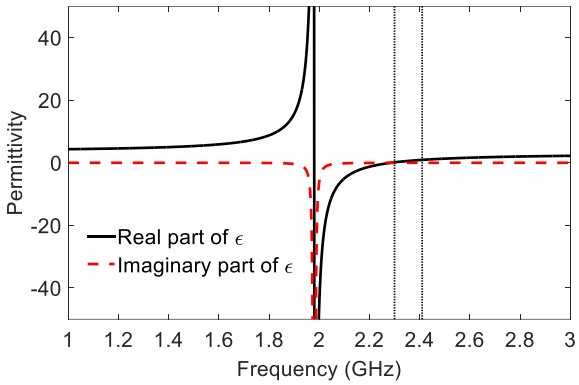


Fig. 6. Real and imaginary part of the permittivity. The Lorentz Model is used to design the material. The parameters are $\epsilon_\infty = 3$, $\epsilon_s = 4$, $f_0 = \frac{\omega_0}{2\pi} =$ 1.98 GHz and $f_{damping} = \frac{\delta}{2\pi} = 5$ MHz

using full wave simulations. The substrate is assumed to be Rogers RT/duroid 5880 with a thickness of 4.5 mm in order to improve the gain. Bottom surface of the substrate is covered with ground plane. Details of the design is provided in Fig. 2. Scattering parameters of the antenna is presented in Fig. 3.

In order to present the beam steering effectively, a high directivity antenna is needed. Therefore the designed microstrip patch antenna is used to design an array antenna and the directivity is improved. The designed structure is presented in Fig. 4. Due to the radiation characteristics of the patch antenna, the array is designed as a broadside array with three elements. All the elements are excited with the same phase and no active or passive phase shifters are used in the design. The dimensions and excitation of the array elements are identical to Fig. 2 and the separation between antennas, *s*, is 63.5 mm in y direction. The array elements are aligned in z and x directions.

The scattering parameters of the antenna array are presented in Fig. 5, without the superstrate. All array elements operate at the same band and cross couplings between elements are low. The ports are numbered starting from the left hand side. Please note that due to the symmetry of the structure, the behavior of the first and third elements are almost identical. Therefore S_{11} and S_{33}, S_{12} and S_{32}, are similar.

The radiation patterns of single microstrip patch and 3 element array are presented in Fig. 6. In the case of the array

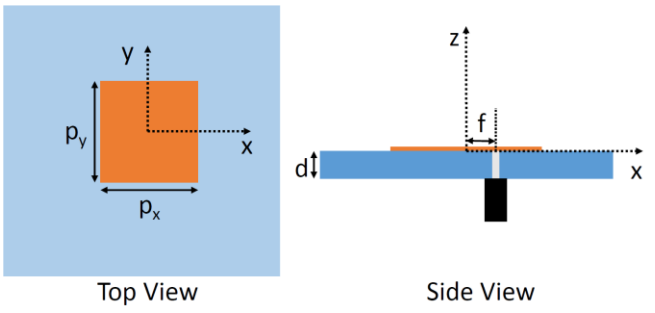


Fig. 7. The microstrip patch antenna designed for beam generation. $p_x =$ 39.5 mm, $p_y = 30.8$ mm, $f = 6.4$ mm, $d = 4.5$ mm and the copper thickness is 0.03 mm. The permittivity of the substrate is 2.2 with a loss tangent equal to 0.0009. The coaxial line has an inner radius equal to 0.405 mm and an outer radius equal to 1.45 mm. The dielectric material of the coaxial line is polyethylene with a permittivity of 2.25.

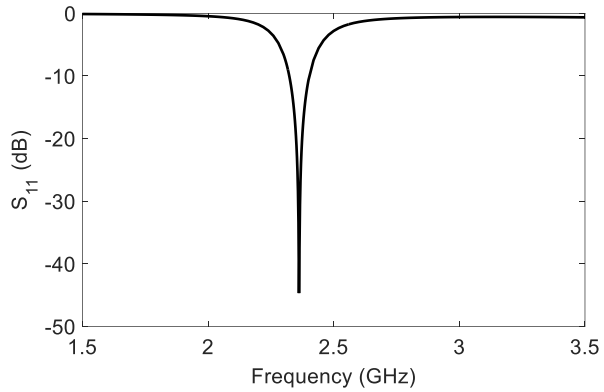


Fig. 8. Reflection coefficient for a single patch antenna. The operation band is centered at 2.362 GHz with a bandwidth of 905 MHz.

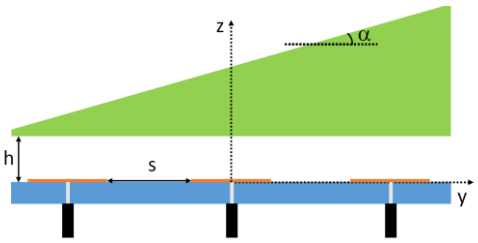


Fig. 9. The array antenna with metamaterial superstrate. Separation between antenna elements is $s = 63.5$ mm, the separation between array and the superstrate is $h = 200$ mm and the angle $\alpha = 30°$. The main radiation beam is directed in z direction. Bottom surface of the substrate is covered with ground plane except for the feed locations.

configuration, all elements are excited with the same magnitude and phase. The z direction corresponds to 0 degrees and the azimuth angle, φ is 90 degrees. Therefore the figure represents the radiation pattern in yz plane. The array provides a narrower beam with a directivity of 9.66 dB, while the single microstrip patch has a wider beam with a directivity of 6.44 dB.

[4] RESULTS AND DISCUSSIONS

In order to analyze array with superstrate, the top surface of the superstrate is terminated with a perfectly matched layer. For sake of simplicity and to reduce computation time, other boundaries of the structure are terminated with a conductive wall. This modification slightly tilts the main beam, around 1

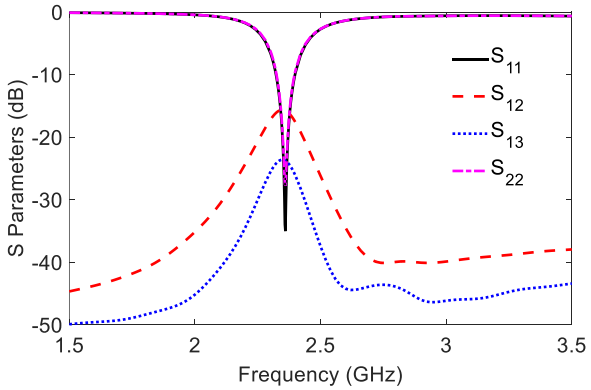


Fig. 10. Scattering parameters of the antenna array presented in Fig. 4 without the superstrate.

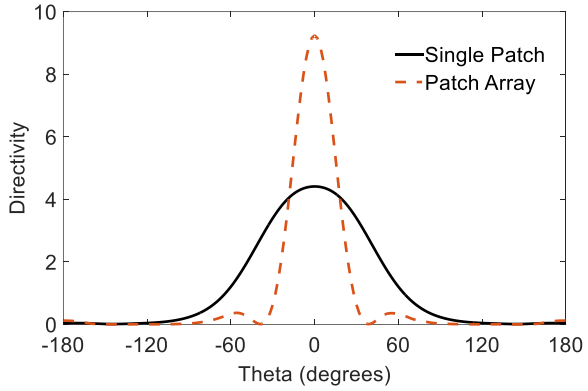


Fig. 11. Directivity of array and single microstrip patch antenna as a function of elevation in linear scale. The array provides a narrower beam and provides a better analysis for beam steering.

degrees and the symmetry of the beam is distorted. The behavior of the radiation pattern is presented in Fig. 7 for different permittivity values. In order to effectively compare different cases, the directivities are plotted in linear scale and normalized. The results clearly demonstrate the change in the beam direction as permittivity of the superstrate changes. Please note that each permittivity value corresponds to a different frequency as presented in Fig. 1. As a result when a wide band pulse is fed to the system, the pulse can be divided in narrower bands and each band will have a different direction.

Fig. 8 provides a comparison between numerical results and theoretical calculations. The numerical results represents the main lobe angles obtained from the simulation, i.e. the peak locations presented in Fig. 7. The theoretical results are calculated using (1). As expected the steering angle is limited with the angle between top and bottom surfaces of the superstrate. The numerical results provide slightly higher steering as a result of the conductive walls placed in x and y directions.

[5] CONCLUSIONS

A new beam steering method is presented. Metamaterial superstrate with permittivity values between 0 and 1 is employed for changing the direction of the main radiation

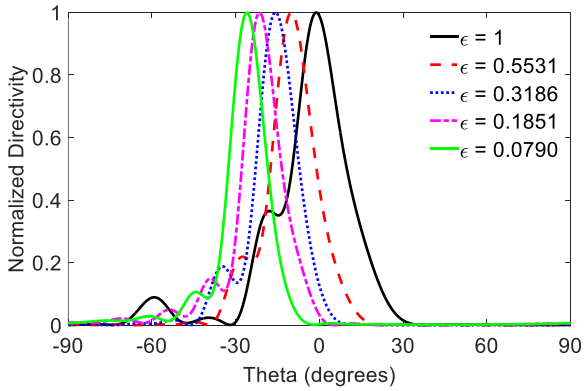


Fig. 12. Normalized directivity for the array with different superstrate permittivity values. As permittivity is reduced, the beam shifts to negative elevations. The boundary conditions on the surfaces perpendicular to x and y directions distort the symmetry of the radiation pattern.

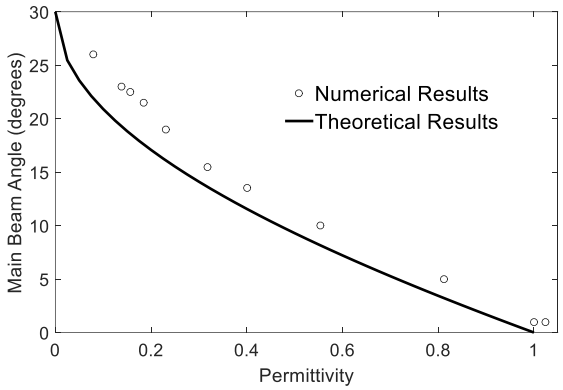


Fig. 13. Reflection coefficient for a single patch antenna.

lobe. The angle between top and bottom surfaces of the superstrate is the limit for steering angle. Theoretical and numerical results are in good agreement.

REFERENCES

[1] J. Pendry, A. J. Holden, D. J. Robbins, and W. J. Stewart, "Magnetism from conductors and enhanced nonlinear phenomena," IEEE Trans. Microwave Theory Tech., vol. 47, pp. 2075-2084, November 1999.

[2] J. Pendry, A. J. Holden, W. J. Stewart, and I. Youngs, "Extremely low frequency plasmons in metallic mesostructures," Phys. Rev. Lett., vol. 76, pp. 4773-4776, June 1996.

[3] R. A. Shelby,D. R. Smith, and S. Schultz, "Experimental verification of a negative index of refraction," Science, vol. 292, pp. 77-79, April 2001.

[4] A. D. Tadesse, O. P. Acharya, and S. Sahu, "Application of metamaterials for performance enhancement of planar antennas: A review," Int J RF Microw Comput Aided Eng, 30:e22154, January 2020.

[5] O. M. Ramahi, T. S. Almoneef, M. AlShareef, and M. S. Boybay, "Metamaterial particles for electromagnetic energy harvesting," Appl. Phys. Lett. 101, 173903, October 2012.

[6] T. S. Almoneef, and O. M. Ramahi, "Metamaterial electromagnetic energy harvester with near unity efficiency," Appl. Phys. Lett. 106, 153902, March 2015.

[7] M. S. Boybay, and O. M. Ramahi, "Near-field probes using double and single negative media," Phys. Rev. E 79, 016602, January 2009.

[8] M. S. Boybay, and O. M. Ramahi, "Material Characterization Using Complementary Split-Ring Resonators," IEEE Trans. Instrum. Meas. vol. 61, pp. 3039-3046, November 2012.

[9] M. A. H. Ansari, A. K. Jha, and M. J. Akhtar, "Design and Application of the CSRR-Based Planar Sensor for Noninvasive Measurement of Complex Permittivity," IEEE Sensors vol. 15, pp. 7181-7189, December 2015.

[10] A. Ebrahimi, W. Withayachumnankul, S. F. Al-Sarawi, and D. Abbott, "Metamaterial-Inspired Rotation Sensor With Wide Dynamic Range,"IEEE Sensors vol. 14, pp. 2609-2614, August 2014.

[11] O. Altintas, M. Aksoy, O. Akgol, E. Unal, M. Karaaslan, and C. Sabah, "Fluid, Strain and Rotation Sensing Applications by Using Metamaterial Based Sensor," J. Electrochem. Soc., vol. 164, pp. B567-B573, September 2017.

[12] D. Shin, Y. Urzhumov, Y. Jung, et al., "Broadband electromagnetic cloaking with smart metamaterials," Nat. Commun., vol. 3:1213, November 2012.

[13] W. Cai, U. K. Chettiar, A. V. Kildishev, and V. M. Shalaev, "Optical cloaking with metamaterials," Nature Photon., vol. 1. pp. 224-227, April 2007.

[14] L. Yousefi, B. Mohajer-Iravani, and O. M. Ramahi, "Enhanced Bandwidth Artificial Magnetic Ground Plane for Low-Profile

Antennas," in IEEE Antennas and Wireless Propagation Letters, vol. 6, pp. 289-292, July 2007

[15] H. Attia, L. Yousefi, M. M. Bait-Suwailam, M. S. Boybay and O. M. Ramahi, "Enhanced-Gain Microstrip Antenna Using Engineered Magnetic Superstrates," IEEE Antennas and Wireless Propagation Letters vol. 8, pp. 1198-1201, October 2009.

[16] A. Kurt, and M. S. Boybay, "A Novel Low-Cost Beam Steering Method Using Dispersive Superstrate," 2018 IEEE International Symposium on Antennas and Propagation & USNC/URSI National Radio Science Meeting, Boston, MA, USA, pp. 2547-2548, 2009.

[17] N. Engheta and R. W. Ziolkowski, "Metamaterials: Physics and Engineering Explorations" Wiley, 2006.

[18] C. A. Balanis, "Antenna Theory Analysis and Design - Third Edition" Wiley-Interscience, 2005.

Transition from Ionic to Electronic Conductivity in Mixed Ionic-Electronic Tellurite Glass: Its Effects on Optical Properties

M.S. Sutrisno
Faculty of Applied Sciences Universiti Teknologi MARA Selangor, Malaysia
noahahmad99@gmail.com

R. Hisam
Faculty of Applied Sciences Universiti Teknologi MARA Selangor, Malaysia
rosdiyana@uitm.edu.my

Aim: **Mixed ionic-electronic 98[20Li_2O-xBi_2O_3-(80-x)TeO_2]-2Ag (x = 3, 5, 7, 11, 13 and 15 mol%) glasses were prepared by melt-quenching technique to investigate their AC conductivity and optical properties. Furthermore, relationship between AC conductivity and optical properties is elucidated by exploring the bonding character of the glass samples.**

Method: **The mixed ionic electronic glasses were made using a melt-quenching technique with the chemical composition 98[20Li_2O-xBi_2O_3-(80-x)TeO_2]-2Ag (x = 3, 5, 7, 11, 13 and 15mol%). Using an agate mortar and pestle, the powders of Li_2CO_3, Bi_2O_3, TeO_2, AgCl were mixed and homogenised. The mixture was then put in an alumina crucible and melted for an hour in a box furnace at 1173K. For annealing, the molten glasses were quenched in a stainless-steel mould and held at 623K for 2 hours 30 minutes. Finally, the annealed bulk glasses were ground into fine powder for measurements of infrared (IR) absorption and UV-Visible spectra. Solartron Impedance Analyzer 1255/1287 connected to a sample holder with an applied potential of 500mV over a temperature range of 295 to 473K and frequency range of 10-2 to 106 Hz was used to obtain impedance properties of glass samples. A double-beam Shimadzu UV-VIS spectrophotometer with a wavelength range of 200-2500 nm was used to measure optical absorption in glass samples. Kubelka-Munk functions and Dimitrov-Komatsu relations were used to evaluate the absorption spectra.**

Results: **Structural analysis revealed the increase of NBO up to x=5 mol% before dropping at x=7 mol% followed by a further increase at x> 7 mol%. The nonlinear behaviour of AC conductivity with Bi_2O_3 showed an initial increase in σ_{AC} until reaching a minimum at x= 7 and 11 mol% before increasing again at x > 11 mol%. The minimum is suggested to be due to the blocking effects of Bi_2O_3 towards ionic conduction caused by mixed ionic-electronic (MIE) effect. To elucidate the nature of ionic-electronic conductivity transition occurred at x=7 mol%, bonding parameters optical basicity Λ and interionic interaction parameter A were examined. Optical basicity Λ initially increased at x < 7 mol% and dropped at x = 7 mol% whereas opposite trend was observed in interionic interaction parameter A. The anomalous decrease of Λ at x = 7 mol% indicated the decrease in oxygen donor character that reduce the ionic bonding and promote covalent bonding in glass samples that may attributed to blocking effects by MIE effect. Meanwhile, steep increase of interionic interaction parameter A at x = 7 mol% indicated the reduction in unshared electron density between cation-anion pair thereby promote covalent bonding that suggested to be due to blocking effects by MIE effect. Interestingly, the anomalous drop in optical properties coincided with a minimum in σ_{AC} at x= 7 mol% for the same glass composition. The anomalous behaviour of refractive indices n and optical susceptibility χ with Bi_2O_3 showed an initial increase in n and χ until reaching a minimum at x= 7 mol% before increasing again at x > 7 mol%. The minimum is suggested to be due to the blocking effects of Bi_2O_3 caused by mixed ionic-electronic (MIE) effect that eventually contribute to reduction of polarization.**

Conclusion: **In conclusion, due to MIE effect, blocking effect at x = 7 mol%, plays a major role in changing the glass samples nature of conductivity and bonding structure thereby may induce notable effect in optical properties.**

Keywords—mixed ionic-electronic, optical, AC conductivity

Catalytic effect of $CoTiO_3$ synthesized via solid-state method on the dehydrogenation performance of $LiAlH_4$

N.A. Ali
Energy Storage Research Group, Faculty of Ocean Engineering Technology and Informatics
Universiti Malaysia Terengganu
Kuala Nerus, Terengganu, Malaysia
nurulllamirah@gmail.com

M.Ismail
Energy Storage Research Group, Faculty of Ocean Engineering Technology and Informatics
Universiti Malaysia Terengganu
Kuala Nerus, Terengganu, Malaysia
mohammadismail@umt.edu.my

Aim: **Hydrogen as a clean energy carrier has been considered as the fuel for future. Lithium aluminum hydride ($LiAlH_4$) has received special attention as the most promising material for solid state hydrogen storage due to its high hydrogen storage capacity (10.5 wt.%). The application of $LiAlH_4$ is hindered by its high decomposition temperature, slow desorption kinetics and poor reversibility. In the present work, the catalytic effect of the $CoTiO_3$ catalyst that was synthesized via solid-state method was investigated.**

Method: **The hydrogen storage performance of the $LiAlH_4$-$CoTiO_3$ was characterized by using pressure composition temperature (PCT), differential scanning calorimetry (DSC), x-ray diffraction (XRD) and scanning electron microscopy (SEM).**

Results: **The $CoTiO_3$ catalyst present notable effect on the dehydrogenation performance of $LiAlH_4$. The onset decomposition temperature of $LiAlH_4$ with the addition of 5 wt.%, 10 wt.%, 15 wt.% and 20 wt.% of $CoTiO_3$ catalyst was reduced to around 113 °C and 140 °C for the first and second decomposition step. The isothermal desorption kinetics revealed that the $LiAlH_4$-$CoTiO_3$ sample desorbed hydrogen 35 times faster than undoped $LiAlH_4$. The $LiAlH_4$-$CoTiO_3$ sample could desorb 3.5 wt.% of hydrogen in 30 minutes while the undoped $LiAlH_4$ desorbed < 0.1 wt.% of hydrogen. From the Kissinger analysis, the apparent activation energy of the $LiAlH_4$-$CoTiO_3$ sample for the first and second decomposition step was reduced to 75.2 kJ/mol and 91.8 kJ/mol, 28.0 and 24.9 kJ/mol lower than undoped $LiAlH_4$. The $LiAlH_4$-$CoTiO_3$ sample presents uniforms and smaller particle size distribution compared than undoped $LiAlH_4$ that irregular in shape with some agglomerations.**

Conclusion: **The experimental results suggested that the $CoTiO_3$ catalyst promoted significant improvement on the dehydrogenation performance of $LiAlH_4$.**

Keywords—hydrogen storage, catalytic effect, $CoTiO_3$, lithium aluminum hydride

Mechanical properties of arrowroot starch-based biopolymers plasticized with glycerol

J. Tarique
Department of Mechanical and Manufacturing Universiti Putra Malaysia Selangor, Malaysia
tarique5496@gmail.com

S.M. Sapuan
Department of Mechanical and Manufacturing Universiti Putra Malaysia Selangor, Malaysia
sapuan@upm.edu.my

A. Khalina
Institute of Tropical Forest and Forest Products (INTROP) Universiti Putra Malaysia nSelangor, Malaysia
khalina@upm.edu.my

R.A. Ilyas
School of Chemical and Energy Engineering Universiti Teknology Malaysia line 4: Johar, Malaysia
ahmadilyasrushdan@yahoo.com

S.F.K. Sherwani
Department of Mechanical and Manufacturing Universiti Putra Malaysia Selangor, Malaysia
faisalsherwani786@gmail.com

M.M.Harussani
Department of Mechanical and Manufacturing Universiti Putra Malaysia Selangor, Malaysia
mmharussani17@gmail.com

***Abstract*— The aim of this research was to investigate the development of thermoplastic films of arrowroot starch using glycerol as a plasticizer at the ratio of (15, 30, and 45 percent w/w, starch basis) utilizing the solution casting method. The developed biopolymers were analyzed in terms of the tensile strength (TS), Young's modulus (YM), and elongation at break (EAB). The tensile strength, as well as modulus of plasticized arrowroot starch films, were substantially decreased from 9.34 to 1.95 MPa and 620.79 to 36.08 MPa, respectively, whereas elongation at break (EAB) was increased from 2.41 to 57.33 %. Glycerol was found to be critical in adapting the properties of these films to make them more desirable for food packaging applications.**

Keywords*— *Arrowroot starch biopolymer, Glycerol, Mechanical properties, Solution casting method

1. INTRODUCTION

Packaging is vital in ensuring food safety and controlling the interaction between food and environment [1]–[3] Petroleum-based plastics have a wide range of uses in the packaging industry due to their outstanding properties, they are still significant causes of environmental issues owing to their non-biodegradability. As a result, petroleum-based plastics are considered as the major factor, if not the only one, causing solid waste generation and build up in the environment. They are non-biodegradable and derived from non-renewable resources. Because of the accelerated decline of petroleum deposits, these non-biodegradable petroleum-based polymers have raised concern about the widespread use of packaging [4],[5]. As a result of these worries, the substitution of petroleum-based packaging with recycled and bio-degradable polymer materials has been encouraged, as mitigating associated environmental problems with natural polymers is important. In this way, the rhizomes of arrowroot (Maranta arundinacea) have arisen as potential sources of starch and fibre.

Natural biopolymers have been explored as possible alternatives to synthetic plastics to address the current environmental crisis created by non-biodegradable plastics. One of the most commonly available biopolymers for packaging applications is starch. Aside from its widespread availability, it is also inexpensive, reusable, and biodegradable. Biopolymers can be classified as synthetic or natural based on their origins, such as agro polymers (starch or cellulose), animal polymer-based (chitin), microbial (exopolysaccharides and polyhydroxyalkanoate) polymers, chemically synthesized from agro-based resource monomer (polylactic acid), and chemically synthesized from conventionally synthesized monomers [6],[7].

2. MATERIALS AND METHODS

2.1 Materials

Native arrowroot starch was extracted from tubers purchased from Norient Jaya Sdn Bhd in Kuala Lumpur, Malaysia. Whereas Evergreen Engineering & Resources Sdn. Bhd., Selangor, Malaysia, supplied the glycerol (with 99.5 % purity). Distilled water was used as the solvent for processing filmogenic solutions.

2.2 Preparation of biopolymers

The arrowroot-based films were fabricated via the traditional solution casting technique. For neat arrowroot starch (AS) film, an amount of 10 g AS was dissolved in 180 mL distilled water for 15 minutes with constant stirring until completely gelatinized at 80±2 ℃. Glycerol-plasticized film was obtained by dispersing 10 g AS in 180 mL distilled water, containing glycerol (0, 15, 30, and 45%, w/w, starch basis). The heating process continued foe an additional 5 minutes at 80 ±2 ℃. The film forming solutions were left to cool down, prior to their casting in glass petri dishes. The fresh casted films were put in an oven at 45 ℃ to allow evaporation. After 24 hours of drying, films were peeled from the casting surfaces and stored in desiccators.

2.3 Mechanical properties

Mechanical testing was performed using an Instron 3365 Universal testing machine (High Wycombe, UK) in accordance with ASTM D882-02 (2002) as shown in Figure.1. Films samples were cut into rectangular strips (70 mm × 10 mm) and placed between the grips. Initial grip

separation and test speed were set to 30 mm and 2 mm/min, respectively. Force and distance were recorded during extension of the films to break. TS, EAB, and (YM) were calculated using the average value of the measurements.

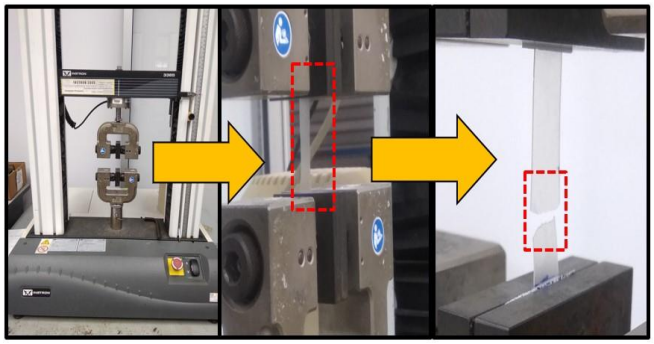


Figure.1 Mechanical testing setup for arrowroot starch-based biopolymers.

3. RESULTS AND DISCUSSION

Mechanical properties such as tensile strength and elongation at break are essential to prevent stress that develops during storage, processing, and handling, while Young's modulus of films shows the stiffness of the material [8]. The tensile strength as well as modulus of plasticized arrowroot starch films were substantially decreased from 9.34 to 1.95 MPa and 620.79 to 36.08 MPa, respectively, whereas elongation at break (EAB) was increased from 2.41 to 57.33 % as shown in Table.1. This occurred due to glycerol's high compatibility with starch, which allowed glycerol to interfere with amylose packing within the starch matrix through H-bonding [9]. The reduction in TS with plasticizer addition was also observed by Tang et al. [10], who reported reduction in TS from 20 to 6 MPa of corn starch/ montmorillionite film plasticized with 20% w/w glycerol. Several studies have found that as plasticizer concentrations increased, the TS of starch-based biopolymers decreased [11]–[13].

Plasticizers minimize the intermolecular bonds between amylose, amylopectin, and amylose-amylopectin in the starch matrix and thus replace them with hydrogen bonds formed between plasticizer and starch molecules, resulting in the observed increase in film elongation. By having more chain mobility, such destruction and rebuilding of starch molecular chains decreases rigidity and facilitates durability of films. Zavareze et al [14], reported that the elongation of polymeric materials depends on the mobility of their molecular chains.

Table.1 Effect of glycerol concentration on mechanical properties of arrowroot starch films.

Sample	Glycerol (%)	Tensile strength (MPa)	Young's Modulus (MPa)	Elongation at break (%)
Control	0	16.48±1.1	1258.9±92	2.49±0.6
G15	15	9.34±1.3	620.79±120	2.41±0.2
G30	30	2.42±0.5	52.26±4.7	46.62±6.1
G45	45	1.95±0.2	36.08±2.6	57.33±5.1

4. CONCLUSION

In current research, the results demonstrated that the addition of glycerol to AS films resulted in the decrease in tensile strength and Young's modulus but increase in elongation at break. Thus, it reduced the tensile strength of glycerol plasticised films by subsequently weakening the hydrogen bonds between starch chains. In brief, the tensile strength of 15% glycerol exhibited high than other plasticized films. In summary, this paper presents a potential biopolymer for the development of biodegradable films.

ACKNOWLEDGMENT

This work was funded by Universiti Putra Malaysia for the financial support through the Grant Putra Berimpak (vote-9679800).

REFERENCES

[1] R. A. Ilyas, S. M. Sapuan, M. R. Ishak, and E. S. Zainudin, "Development and characterization of sugar palm nanocrystalline cellulose reinforced sugar palm starch bionanocomposites," Carbohydr. Polym., vol. 202, pp. 186–202, Dec. 2018, doi: 10.1016/j.carbpol.2018.09.002.

[2] K. Z. Hazrati, S. M. Sapuan, M. Y. M. Zuhri, and R. Jumaidin, "Extraction and Characterization of Potential Biodegradable Materials Based on Dioscorea hispida Tubers," Polymers (Basel)., vol. 13, no. 4, p. 584, 2021, doi: 10.3390/polym13040584.

[3] A. Nazrin, S. M. Sapuan, M. Y. M. Zuhri, R. A. Ilyas, R. Syafiq, and S. F. K. Sherwani, "Nanocellulose Reinforced Thermoplastic Starch (TPS), Polylactic Acid (PLA), and Polybutylene Succinate (PBS) for Food Packaging Applications," Front. Chem., vol. 8, no. 213, pp. 1–12, Apr. 2020, doi: 10.3389/fchem.2020.00213.

[4] T. Jamal, S. M. Sapuan, A. Khalina, R. A. Ilyas, and M. D. Hazrol, "EFFECT OF GLYCEROL CONCENTRATION ON THE PHYSICAL PROPERTIES OF ARROWROOT STARCH (Maranta arundinacea) BIOPOLYMER FILM," in 7th Postgraduate Seminar on Natural Fibre Reinforced Polymer Composites 2020 EFFECT, 2020, no. November, pp. 26–29.

[5] H. Abral et al., "Highly transparent and antimicrobial PVA based bionanocomposites reinforced by ginger nanofiber," Polym. Test., no. October, p. 106186, Oct. 2019, doi: 10.1016/j.polymertesting.2019.106186.

[6] R. A. Ilyas and S. M. Sapuan, "The Preparation Methods and Processing of Natural Fibre Bio-polymer Composites," Curr. Org. Synth., vol. 16, no. 8, pp. 1068–1070, Jan. 2020, doi: 10.2174/1570179416082001201056 16.

[7] M. N. Norizan, K. Abdan, R. A. Ilyas, and S. P. Biofibers, "Effect of fiber orientation and fiber loading on the mechanical and thermal properties of sugar palm yarn fiber reinforced unsaturated polyester resin composites," Polimery, vol. 65, no. 2, pp. 34–43, 2020, doi: 10.14314/polimery.2020.2.5.

[8] R. A. Ilyas and S. M. Sapuan, "Biopolymers and Biocomposites: Chemistry and Technology," Curr. Anal. Chem., vol. 16, no. 5, pp. 500–503, Jul. 2020, doi: 10.2174/1573411016052006030953 11.

[9] M. G. A. Vieira, M. A. Da Silva, L. O. Dos Santos, and M. M. Beppu, "Natural-based plasticizers and biopolymer

films: A review," Eur. Polym. J., vol. 47, no. 3, pp. 254–263, 2011, doi: 10.1016/j.eurpolymj.2010.12.011.

[10] X. Tang, S. Alavi, and T. J. Herald, "Effects of plasticizers on the structure and properties of starch-clay nanocomposite films," Carbohydr. Polym., vol. 74, no. 3, pp. 552–558, 2008, doi: 10.1016/j.carbpol.2008.04.022.

[11] S. M. A. Razavi, A. Mohammad Amini, and Y. Zahedi, "Characterisation of a new biodegradable edible film based on sage seed gum: Influence of plasticiser type and concentration," Food Hydrocoll., vol. 43, pp. 290–298, 2015, doi: 10.1016/j.foodhyd.2014.05.028.

[12] M. Rodríguez, J. Osés, K. Ziani, and J. I. Maté, "Combined effect of plasticizers and surfactants on the physical properties of starch based edible films," Food Res. Int., vol. 39, no. 8, pp. 840–846, 2006, doi: 10.1016/j.foodres.2006.04.002.

[13] D. Muscat, B. Adhikari, R. Adhikari, and D. S. Chaudhary, "Comparative study of film forming behaviour of low and high amylose starches using glycerol and xylitol as plasticizers," J. Food Eng., vol. 109, no. 2, pp. 189–201, 2012, doi: 10.1016/j.jfoodeng.2011.10.019.

[14] E. D. R. Zavareze et al., "Development of oxidised and heat-moisture treated potato starch film," Food Chem., vol. 132, no. 1, pp. 344–350, 2012, doi: 10.1016/j.foodchem.2011.10.090.

Effect of $BaMnO_3$ catalyst synthesized by solid state method on MgH_2 as a potential hydrogen storage material

N A Sazelee
Energy Storage Research Group, Faculty of Ocean Engineering Technology and Informatics Universiti Malaysia Terengganu
Kuala Nerus, Terengganu, Malaysia
atiqahsazelee19@gmail.com

M Ismail
Energy Storage Research Group, Faculty of Ocean Engineering Technology and Informatics Universiti Malaysia Terengganu
Kuala Nerus, Terengganu, Malaysia
mohammadismail@umt.edu.my

Aim: **The addition of catalyst by a ball milling process was found to be one of the efficient methods to improve the absorption/desorption kinetics and high decomposition temperature of MgH_2. In this study, $BaMnO_3$ has been successfully synthesized via the solid-state method and it was milled with MgH_2.**

Method: **The hydrogen storage performance of MgH_2 was systematically investigated by using pressure composition temperature (PCT), differential scanning calorimetry (DSC), scanning electron microscopy (SEM) and X-ray diffraction (XRD).**

Results: **For onset decomposition temperature, the temperature was reduced from 420 °C for as-received MgH_2 and 343 °C for as-milled MgH_2 to 282 °C ($BaMnO_3$-doped MgH_2). The absorption kinetics showed that $BaMnO_3$-doped MgH_2 able to absorb 6.0 wt.% compared to as-milled MgH_2 (5.0 wt.%) at 250 °C in 5 minutes. Meanwhile, the desorption kinetics results revealed that the $BaMnO_3$-doped MgH_2 sample can release about 5.3 wt.% of hydrogen in 60 minutes at 300 °C, while as-milled MgH_2 only released about 0.3 wt.% of hydrogen. The activation energy value was calculated by the Kissinger equation, and the result exposed that the activation energy value was 99 kJ/mol for $BaMnO_3$-doped MgH_2 and 144 kJ/mol for the as-milled MgH_2. Additionally, the addition of the $BaMnO_3$ catalyst revealed that the morphology of the samples became smaller compared to as-milled MgH_2 and as-received MgH_2.**

Conclusion: **Hence, it can be speculated that the hydrogen storage performance of MgH_2 was improved after the addition of $BaMnO_3$ catalyst due to a reduction in particle size and less agglomeration.**

Keywords— Magnesium hydride; solid-state hydrogen storage; metal oxide catalyst; catalytic effect

Effect of Fuel Type onto Photocatalytic Activities of Copper Aluminate Nanoparticles Synthesized by Microwave-Assisted Combustion method using different fuels

İbrahim Hakkı Karakaş
Engineering Faculty Chemical Engineering Department Bayburt Unıversity
Bayburt, Turkey
ihkarakas@bayburt.edu.tr

Zeynep Karcıoğlu Karakaş
Engineering Faculty Environmental Engineering Department Ataturk Unıversity
Erzurum, Turkey
kzeynep@atauni.edu.tr

***Abstract*—It is known that the reactive chemicals and synthesis technique used for synthesis have a strong influence on the structural and morphological properties of the final products. Since the fuel material used for the combustion reaction directly affects the reaction taking place, it is inevitable that the product particles will affect the surface properties. In this study, copper aluminate spinel nanoparticles synthesized using different fuels via microwave assisted combustion method were used as photocatalysts in the process of photocatalytic oxidation of a food dye known as tartrazine and the effect of fuel type on their photocatalytic activity was discussed. In the combustion reaction, urea and glycine were used as fuel. Synthesized samples were characterized by methods such as XRD, FT-IR, BET, SEM and TEM. Later, in order to evaluate the effects onto their photocatalytic activities of fuel type, they were used as photocatalyst in the photocatalytic degradation of the tartrazine. In photocatalysis experiments with both catalysts, stirring speed was applied as 400 rpm, temperature 20℃, initial pollutant concentration 100 ppm and catalyst dosage 1 g/L. The results obtained show that $CuAl_2O_4$ nanoparticles prepared with both fuels exhibit very good photocatalytic activity. Moreover, it was seen that the sample prepared by using urea as fuel was exhibited more good photocatalytic activity than the sample prepared with glycine. In the experiment performed with the sample produced with urea was removed almost all of the dyestuff content in solution at approximately 100 min.**

Keywords: Copper Aluminate, Tartrazine, Glycine, Urea, Photocatalysis

[1] INTRODUCTION

Nanotechnology is a technological infrastructure that has the potential to affect our lives in many areas and is expected to make changes that can be considered revolutionary in many areas. Nanotechnology, described as the new industrial revolution of the twenty-first century, is a field of research that has the potential to radically change our vision and expectations on the development of new materials or the improvement of existing ones. This potential of nanotechnology is a great source of motivation for many researchers working in this field. While nanotechnology causes revolutionary changes in all areas, it is not possible that technologies related to drinking water and wastewater treatment will not be affected by this change. The role of nanotechnology in designing innovative infrastructure systems has also the potential to revolutionize the applications of treatment technologies.

On the other hand, the most important factor limiting the environmental use of nanomaterials is their high production costs. Using microwaves instead of traditional heating systems for heating processes in synthesis studies can significantly reduce these costs. When microwave-assisted synthesis methods were compared to other traditional synthesis methods, they have some important advantages such as rapid and homogeneous heating, selective heating of the surface, energy saving, higher efficiency, shorter preparation time, high purity, lower processing costs, smaller and homogeneous particle size distribution.

In this study, the effects onto the structural properties, morphological properties and photocatalytic activities of the synthesized samples of the fuel type used in the synthesis of copper-aluminate nanoparticles with microwave-assisted combustion method, which is a high-efficiency, low-cost and environmentally friendly method, were investigated.

[2] MATERIALS AND METHOD

A. Preparation of Materials

In this study, in which copper aluminate nanoparticles were synthesized using different fuels by microwave-assisted combustion method, aluminum and copper nitrate salts were used as starting reagents and glycine and urea as fuel. The aluminum nitrate nonahydrate, copper nitrate hexahydrate, Glycine and urea used were purchased from Sigma-Aldrich. Tartrazine used in photocatalysis experiments was purchased from Merck. In addition, the lamp (254 nm) with a light intensity of 44 W/cm^2 as a UV light source was purchased from Cole Parmer.

B. Synthesis Method

The mixture obtained by mixing copper nitrate, aluminum nitrate and fuel material in certain proportions is homogenized with the help of a magnetic stirrer.Then, the mixture is subjected to microwave irradiation during five minutes in a microwave oven. Here, the reaction takes place

and at the end of this process, a dark powder is obtained. The obtained powder was heat treated at 800℃. The cooled sample was firstly characterized and then it was used as photocatalyst in the process of photocatalytic degradation of a food dye known as tartrazine. The synthesis reactions occurred with Glycine and Urea are given by Equation 1 and Equation 2 below, respectively.

For Urea;

$$3Cu(NO_3)_2 + 6Al(NO_3)_3 + 20C_2H_5NO_2 \longrightarrow 3CuAl_2O_4 + 40H_2O + 32N_2 + 20CO_2 \quad (1)$$

For Glycine

$$9Cu(NO_3)_2 + 18Al(NO_3)_3 + 40CO(NH_2)_2 \longrightarrow 9CuAl_2O_4 + 100\ H_2O + 56N_2 + 80\ CO_2 \quad (2)$$

Heat treatment was applied at 800℃ for 2 hours to complete the conversion to the solid product taken from the microwave system. The product obtained at the end of the process was washed, dried and ground.

C. Characterization

The characterization of the structural and morphological properties of the samples produced by using different fuels were made with various advanced analysis techniques such as X-ray diffraction (XRD), Scanning Electron Microscope (SEM), Transmission Electron Microscope (TEM). Accordingly, Bruker D8 Discover (Germany) XRD system for XRD analysis, FEI (USA) Nova Nano SEM 450 system was used for SEM studies and FEI (USA) Talos F200S (200kV) system was used for TEM imaging. In addition, Micromeritics (USA) Gemini VI model Surface analyzer system was used for BET surface area measurements.

D. Photocatalysis Experiments

The studies made to investigate the effects of fuel type onto photocatalytic activities of spinel copper aluminate nanoparticles synthesized via microwave assisted combustion method were performed in glass reactor. The reactor is delicately insulated with a shiny aluminum folio in order to prevent the daylight effect. An UV-C type lamp (254 nm) was used as UV radiation source. The lamp is suitable for operation by dipping directly into solution and has a light intensity of 44 $\mu W/cm^2$. During the experimental periods, the contents of the reactor were mechanically mixed with 300 rpm constant mixing speed.

[3] RESULTS AND DISCUSSION

In the combustion reaction, metal nitrates directly act as oxidants, and glycine or urea acts as a reducing agent/fuel. In addition, the heat required for combustion is provided through microwave radiation, unlike traditional systems. For this purpose, the reactive mixture taken into a microwave oven, warms up and start to burn after a very short time and thus combustion reaction occurs. At the end of this process, a dark colored powder is obtained. this powder called as precursor sample. XRD analysis were performed on precursor samples, and the resulting diffractograms are given in Figure 1.

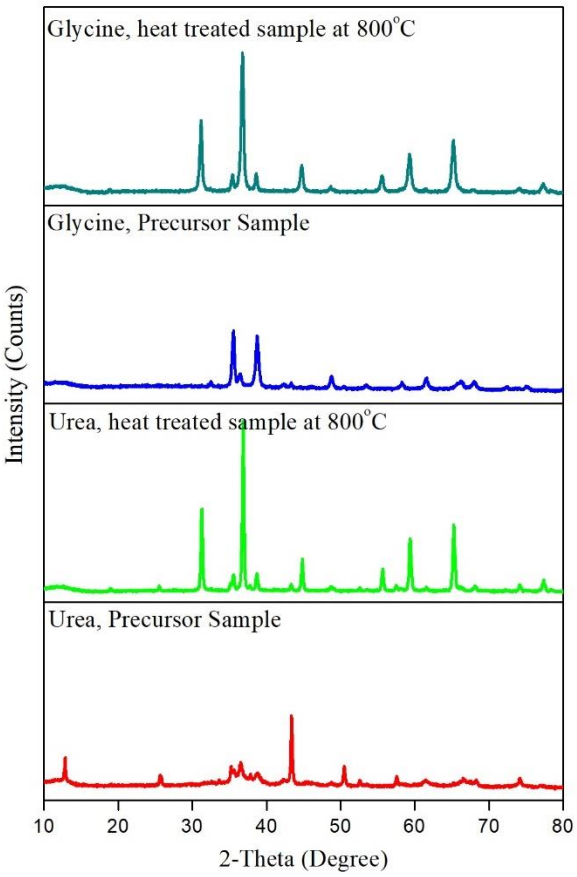


Fig. 1. X-Ray diffractograms taken before and after heat treatment of samples prepared with different fuels

According to the XRD Analyses given in Figure 1 for Precursor samples, it seems that only microwave radiation is not sufficient for conversion. In order to overcome this situation, the samples were heat treated at 800℃. it was seen that the samples prepared with both fuels were completely converted to copper aluminate after heat treatment. The X-ray diffractograms of these samples were compared with standard diffraction cards and determined that they were fully compatible with the standard diffraction cards identified for the spinel $CuAl_2O_4$ phase in databases.

The surface properties of porous materials are characterized by various surface parameters mostly derived from gas sorption data. The characterization of various surface properties of the synthesized nanoparticles was made using the technique based on the absorption of nitrogen gas at 77K. This method is the most common applied technique to determine the surface properties of porous materials by gas adsorption. In this study, the sample prepared with only microwave support was analyzed after the heat treatment applied at 800℃. Before the analysis, degas was made in an inert gas atmosphere for 2 hours at 110℃. The adsorption-desorption isotherms measured after heat treatment of the samples produced with both fuels are given in Figure 2.

Gas absorption isotherms reflect the relationship between porosity and sorption properties of porous materials. Adsorption isotherms are classified by IUPAC according to the various surface properties. When the obtained isotherms were compared with the isotherms determined by IUPAC

classification, it was seen that they were compatible with Type 3.

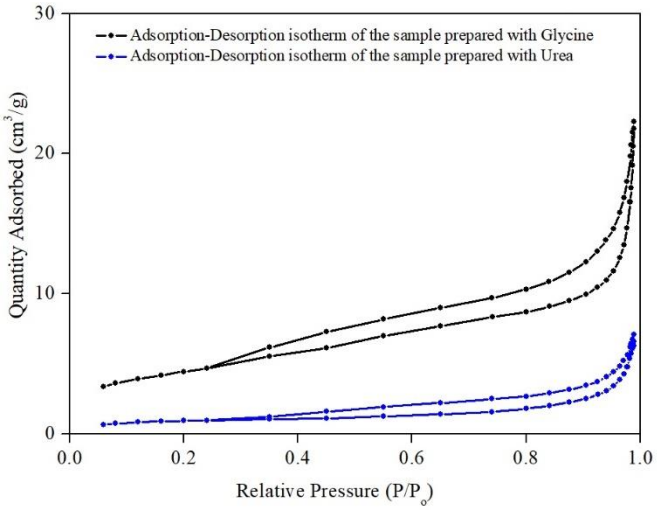


Fig. 2. Adsorption-desorption isotherms of samples prepared by applying heat treatment

However, type 3 isotherm defines low porosity or non-porous materials.[1] According to this result; the synthesized samples can be evaluated as a low porosity material. Another property used to characterize the surface properties of porous materials is the surface area. Surface areas can also be calculated with a method known as BET theory using gas sorption data measured at 77K. BET surface areas [2] and Langmuir surface areas of synthesized samples were calculated by using gas sorption data and this data are presented in Table 1.

TABLE 1. THE VARIOUS SURFACE PROPERTIES OF THE SAMPLES SYNTHESIZED BY USING DIFFERENT FUELS

Surface Properties	Glycine	Urea
Single Point Surface Area, (m^2/g)	15.5362	11.7122
BET Surface Area, (m^2/g)	16.1848	11.9134
Langmuir Surface Area, (m^2/g)	22.3791	16.1971
t-Plot Micropore Area, (m^2/g)	0.9535	3.2966
t-Plot External Surface Area, (m^2/g)	15.2313	8,6168

A.

Copper aluminate particles synthesized with different fuels were prepared synthetically and used as photocatalyst for dye removal from wastewater containing tartrazine at a concentration of 100 ppm. Catalyst dosage was applied as 1 g/L in the study. Samples were taken at specific time intervals and concentrations were determined based on color measurement with a UV-VIS spectrophotometer. The results obtained from photocatalysis trials with copper aluminates prepared with both types of fuels are given in Figure 3.

When the observed removal efficiencies are compared, it is seen that the sample prepared with urea exhibits a better photocatalytic activity. In the studies on nanoparticle synthesis, it is known that the synthesis method and the reagents used for synthesis are highly effective on the structural properties of the product nanoparticles.[3] Therefore, surface properties and surface porosity are also affected by these changes. Since photocatalysis is a process that takes place on the surface of the particles, photocatalytic activity of the synthesized nanoparticles is inevitably affected by changes in synthesis conditions.[4]

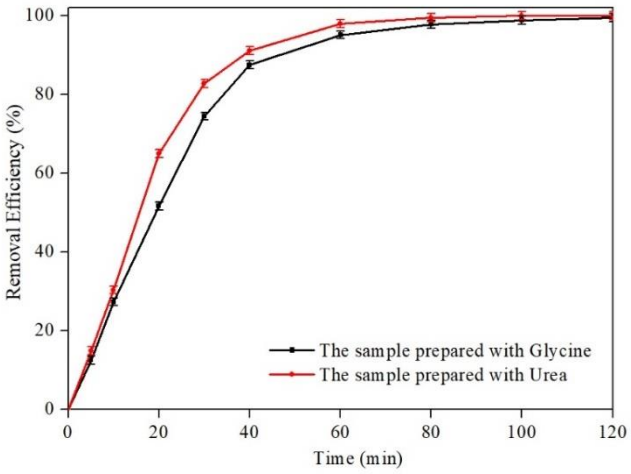


Fig. 3. The removal efficiencies obtained from photocatalysis trials performed with copper aluminates prepared with different fuel types

[4] CONCLUSIONS

In this study, the effect of the type of fuel used for the synthesis reaction on the photocatalytic properties of copper aluminate nanoparticles synthesized by microwave-assisted combustion was investigated. Accordingly, the substance used as a fuel in combustion reactions has the potential to significantly affect the structural and morphological properties of the synthesized samples. Although the surface area of the sample prepared with glycine was greater than the surface area of the sample prepared with urea, it was determined that the copper aluminate nanoparticles prepared with urea exhibited better photocatalytic activity. This difference shows the strong relationship between crystal structure and catalytic properties. It also shows the effects of starting reagents on the structural properties of product materials.

ACKNOWLEDGMENT

This study was supported by 2019/02-69001-06 Project number of Bayburt University Scientific Research Projects Coordination Unit. We are grateful to Bayburt University for their support.

REFERENCES

[1] Z. Alothman, A Review: Fundamental Aspects of Silicate Mesoporous Materials, Materials, 5 (2012) 2874-2902.
[2] S. Brunauer, P.H. Emmett, E. Teller, Adsorption of Gases in Multimolecular Layers, Journal of the American Chemical Society, 60 (1938) 309-319.
[3] Z. Karcıoğlu Karakaş, R. Boncukcuoğlu, İ.H. Karakaş, M. Ertuğrul, The effects of heat treatment on the synthesis of nickel ferrite (NiFe2O4) nanoparticles using the microwave assisted combustion method, Journal of Magnetism and Magnetic Materials, 374 (2015) 298-306.
[4] İ.H. Karakas, The effects of fuel type onto the structural, morphological, magnetic and photocatalytic properties of nanoparticles in the synthesis of cobalt ferrite nanoparticles with microwave assisted combustion method, Ceramics International, 47 (2021) 5597-5609.

Slow pyrolysis of disinfected COVID-19 non-woven polypropylene (PP) waste

M.M. Harussani
Advanced Engineering Materials and Composites Research Centre (AEMC), Department of Mechanical and Manufacturing Engineering Universiti Putra Malaysia 43400 UPM Serdang, Selangor, Malaysia
mmharussani17@gmail.com

S.M. Sapuan
Advanced Engineering Materials and Composites Research Centre (AEMC), Department of Mechanical and Manufacturing Engineering, Universiti Putra Malaysia 43400 UPM Serdang, Selangor, Malaysia

U. Rashid
Institute of Advanced Technology Universiti Putra Malaysia (UPM) Serdang 43400, Malaysia.
u.rashid@upm.edu.my

K. Abdan
Laboratory of Biocomposite Technology, Institute of Tropical Forestry and Forest Products (INTROP), Universiti Putra Malaysia 43400 UPM Serdang, Selangor, Malaysia
khalina@upm.edu.my

S.M. Sapuan
Laboratory of Biocomposite Technology, Institute of Tropical Forestry and Forest Products (INTROP), Universiti Putra Malaysia 43400 UPM Serdang, Selangor, Malaysia
sapuan@upm.edu.my

J. Tarique
Advanced Engineering Materials and Composites Research Centre (AEMC), Department of Mechanical and Manufacturing Engineering, Universiti Putra Malaysia 43400 UPM Serdang, Selangor, Malaysia
tarique5496@gmail.com

***Abstract*—According to Ministry of Health Malaysia (MOH), total utilization of personal protective equipment (PPE) of healthcare workers is 59 million units per month. Therefore, for duration of 2 months, 2.1 billion items had been used due to the increasing COVID-19 cases. Polypropylene (PP) is the most common plastic polymers profusely used as raw materials in medical PPE. PP wastes degrade in approximately 20 to 30 years in landfills. Currently, the practice used by MOH is burning the PPE after it had been disinfected with chlorine. Burning of plastic wastes can release important atmospheric pollutants. Thus, this study had proposed the pyrolysis approach in treating the wastes. Disinfected PP samples were collected from local healthcare center and converted into char products via low temperature (450 ºC to 600 ºC) slow pyrolysis in laboratory-scale batch reactor. Noticeably, plastic PP wastes pyrolysed at low temperature resulting in higher amount of char yields with distinct molecular structures via FTIR analysis. Whereas the yielded chars can be utilized in F&B sectors for barbeque applications and as heating source for boiler systems in factories.**

Keywords— Green technology, COVID-19 related waste, slow pyrolysis, thermochemical decomposition, polypropylene waste

[1] INTRODUCTION

At the fourth quarter of 2019, the globe was fiercely assaulted by a severe coronavirus syndrome (SARS-CoV-2 or COVID-19) pandemic. As a result, a public health emergency was proclaimed by the WHO on 30 January 2020 due to the COVID-19 outbreak [1]. As announced on 20 March 2021, the global outbreak of COVID-19 has been affected by 103 million active cases with 2.7 million deaths from 219 countries and regions [2]. In order to treat the piling up infected COVID-19 patients, increasing demand on personal protective equipments (PPE) supply happened. Thus, accumulates the number of petroleum-based PPE production. For instance, Singh et al. [3] had reported that the compound annual rate of growth in the PPE demand globally was 6.5 % from year 2016 to 2020, roughly from $40 billion to $58 billion. According to WHO [1], an approximate 89 million surgical masks, 76 million pairs of medical gloves, 1.6 million pairs of goggles and 30 million gowns are part of the essential PPE demanded monthly by the global. Therefore, increasing number of plastic waste had associated to negative impacts towards the health of the environment.

Table 1. Literature studies on pyrolysis of PP plastic waste

Plastic	Process	Char yields (wt.%)	References
PP	Spouted bed reactor (T= 450 ºC)	0	[4]
PP	Horizontal steel reactor (T = 300 ºC, β = 20 ºC/min, t = 30 min)	1.34	[5]
PP	Batch reactor (T = 740 ºC, β = 10 ºC/min)	1.6	[6]
PP	Batch reactor (T = 450 ºC, β = 25 ºC/min)	2.3	Our works
PP	Semi-batch reactor (T = 450 ºC, P = 1 atm, β = 25 ºC/min, catalyst FCC)	3.6	[7]

PPE was used as their primary barrier from viral and bacterial infections, including isolation gowns, respirators, gloves, head and shoe nets which mainly made of polypropylene (PP) plastic. Polypropylene wastes (PP) degrade in approximately 30 years in open landfills. These plastics contain additive materials as colorants, plasticizers and stabilizers [8]. In municipal solid wastes, waste plastics can account for around 28% of total cadmium. Open combustion of plastic waste can release major air pollutants. The current incinerator and the proposed pyrolysis process vary greatly. The end products of the burning process are primary carbon dioxide and water whereas low molecular weight compounds are the end products of the waste pyrolysis plant. The gaseous substance is hydrogen, methane and carbon

monoxide; methanol, acetone, acetic acid and other organic matter are liquid products; coke and carbon black are primarily the solid output, which they are yielded and collected properly [9]. Thus, many researchers had proposed this pyrolysis approach as a proper green technology for waste management, especially in treating infected plastic wastes. Some studies are summarized in Table 1 on PP plastic thermochemical decomposition.

[2] MATERIALS AND METHODS

A. *Materials*

The pyrolysis experiments were performed with 0.25 mm PP waste powder. The PP powder was prepared from used PPEs and facemasks Next, the collected materials were shredded using FRITSCH Universal Cutting Mill PULVERISETTE 19, Idar-Oberstein, Germany with 0.25 mm perforation sieve cassette into 0.25 mm-size PP powder. The samples then were directly used for sample characterizations and used for the laboratory-scale pyrolysis experiments with specified parameters.

B. *Experimental*

Slow pyrolysis study was executed for PP wastes using batch reactor at a fixed heating rate of 3 ºC/min with 1.5 atm pressure under nitrogen gas environment (99.9992 % purified N_2 gas). Prior to thermal degradation study, thermal-gravimetric analysis (TGA) analysis were done in order to determine the optimum temperature in which degradation of PP occurs. Fixed lower heating rate with residence time of 5 h had been used to produce maximum amount of char yields. Next, the amount of char (by weight) was collected and measured using electronic balance. The char yields (wt.%) had been calculated with Eq. (1) and recorded, which then analysed.

$$Solid\ product\ yield = m_{product}t/m_{waste} \times 100 \qquad (1)$$

where $m_{product}$ is amount of char and m_{waste} is the pyrolysed waste amount. Next, in order to characterize the char samples, Fourier-transform infrared (FTIR) -attenuated total reflective (ATR) analysis had been done.

[3] RESULTS AND DISCUSSION

A. *Effects of pyrolysis temperature for char yields*

The yields of char derived from PP waste powder obtained from the lab-scale pyrolysis experiments, summarized in Figure 1. In all the cases, the yield of char products was significant. Char yield was discovered maximum at lower pyrolytic temperature. The pyrolysis of PP powder at 450 ºC produced the highest amount of carbon char, 2.3 wt.%, compared to other different process temperature. This is associated to a slower and inefficient decomposition of propylene trimer at lower temperature than that of at higher temperature, where the decomposition, including the weakening of polymer PP chain branches and its backbone double bonds begun at temperature of 390 ºC [10]. Therefore, low process temperature results in greater amount of char, but the heating value of the char increases with temperature, this parameter need to be taken into care for fuel applications and soil amendment agent for agriculture. This result is twice the char yields by previous studies from Ahmad et al. [5] and Demirbas et al. [6] with 1.34 and 1.6 wt.%, respectively. Thus, it shows the application of low process temperature and heating rate of pyrolysis as well as longer residence time via batch reactor are significant in improving the yield of solid char.

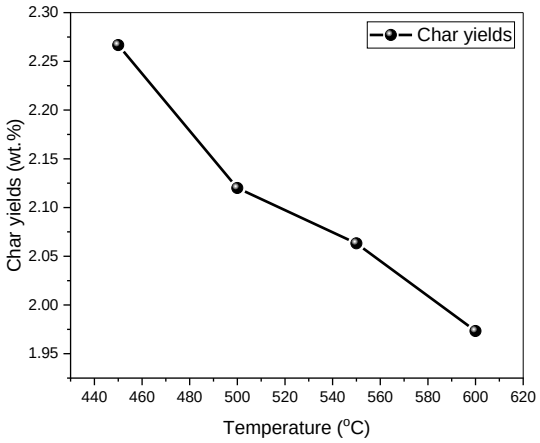


Fig. 14. Graph of char yields (wt.%) for different pyrolytic temperatures (ºC)

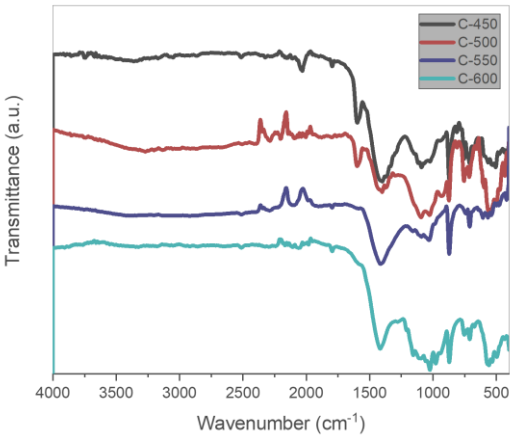


Fig. 15. FTIR-ATR spectra of raw PP and chars collected from pyrolysis with different temperatures.

B. *Functional group analysis*

ATR-FTIR spectrum of PP-derived char samples, C-450, C-500, C-550 and C-600, which were yielded at different pyrolysis temperatures, show consistency in their functionality and characteristics features as represented by Figure 2. Broad absorption bands with weak intensity at range 3400 to 3300 cm^{-1} corresponded to the hydroxyl –OH groups stretching and bending that attributed the physisorption of water molecule (moisture) on the surface of C-450, C-500, and C-550. The area of spectrum between 1400 to 1500 cm^{-1} or 1585 to 1600 cm^{-1} demonstrated the presence of C=C stretching vibrations due to aromatic ring and an intense absorption peak of stretching vibration from C=C bond from alkenes arise in the spectral range of 1600 to 1680 cm^{-1}. It is recorded in the char spectrum, the absorption peaks were discovered at 1420 cm^{-1} and 1600 cm^{-1}, respectively. In the outcome, aliphatic bands and alkene bands were considerably reduced in the C-550 and C-600 spectrums, while aromatic groups C=C and CH were achieved. This is due to the improvement of aromatic structures of chars as the pyrolytic temperature increased.

[4] CONCLUSION AND FUTURE OUTLOOKS

Medical plastic waste mainly derived from COVID-19 cases should be converted into gasoline-range hydrocarbons via slow valorisation processes. Environmental issues include air pollutants such as dioxin formation in plastic waste incineration endangering the sustainability of the environment. The results from this work showed that the solid chars produced at differentt pyrolytic temperatures had different physical characteristics which influenced its reactivity and solubility. It was found that when the pyrolysis temperature was increased from 400 ºC to 600 ºC, the amount of aliphatic bands and alkene bands reduced and the char yield decreased from 2.30 wt.% to 1.97 wt.%. Thus, optimum temperature in producing maximum amount of solid products are achieved. However, further studies on presence of catalysts and physical activation in order to produce higher quality char for fuel applications, barbeque applications in F&B sectors such as restaurants and hotels, nanofillers in composite additives and sensor applications as well as water adsorbents in water treatment application.

ACKNOWLEDGMENT

The author gratefully acknowledged Ministry of Higher Education (MoHE) for funding this project via Post COVID-19 Special Research Grant 2020 (Vote No. 5540346) and also Universiti Putra Malaysia for providing research facilities..

REFERENCES

[1] WHO, “COVID-19 Public Health Emergency of International Concern (PHEIC) Global research and innovation forum,” *World Health Organization (WHO)*, 2020. [Online]. Available: https://www.who.int/publications/m/item/covid-19-public-health-emergency-of-international-concern-(pheic)-global-research-and-innovation-forum. [Accessed: 07-Feb-2021].

[2] Worldometer, “COVID-19 Coronavirus Pandemic,” 2021. [Online]. Available: https://www.worldometers.info/coronavirus/. [Accessed: 07-Feb-2021].

[3] N. Singh, Y. Tang, and O. A. Ogunseitan, “Environmentally sustainable management of used personal protective equipment,” *Environ. Sci. Technol.*, vol. 54, no. 14, pp. 8500–8502, 2020.

[4] R. Aguado, M. Olazar, M. J. San José, B. Gaisán, and J. Bilbao, “Wax formation in the pyrolysis of polyolefins in a conical spouted bed reactor,” *Energy & fuels*, vol. 16, no. 6, pp. 1429–1437, 2002.

[5] I. Ahmad *et al.*, “Pyrolysis study of polypropylene and polyethylene into premium oil products,” *Int. J. green energy*, vol. 12, no. 7, pp. 663–671, 2015.

[6] A. Demirbas, “Pyrolysis of municipal plastic wastes for recovery of gasoline-range hydrocarbons,” *J. Anal. Appl. Pyrolysis*, vol. 72, no. 1, pp. 97–102, 2004.

[7] M. S. Abbas-Abadi, M. N. Haghighi, H. Yeganeh, and A. G. McDonald, “Evaluation of pyrolysis process parameters on polypropylene degradation products,” *J. Anal. Appl. Pyrolysis*, vol. 109, pp. 272–277, 2014.

[8] H. Yaşar, “World of plastics,” *Ankara, TMMOB Mech. Eng. Publ.*, pp. 59–63, 2004.

[9] M. M. Harussani, S. M. Sapuan, A. Khalina, R. A. Ilyas, and M. D. Hazrol, “Review on Green Technology Pyrolysis for Plastic Wastes,” in *7TH POSTGRADUATE SEMINAR ON NATURAL FIBRE REINFORCED POLYMER COMPOSITES 2020*, 2020, pp. 50–53.

[10] A. Witkowski, A. A. Stec, and T. R. Hull, “Thermal decomposition of polymeric materials,” in *SFPE handbook of fire protection engineering*, Springer, 2016, pp. 167–254.

Advance in Fabric Face Mask Combatting COVID-19: A Mini Review

Syahida Farhan Azha
School of Chemical Engineering Kampus Kejuruteraan, Universiti Sains Malaysia, 14300, Nibong Tebal, Penang.
Malaysia
syahidafarhan@usm.my

Suzylawati binti Ismail
School of Chemical Engineering Kampus Kejuruteraan, Universiti Sains Malaysia, 14300, Nibong Tebal, Penang.
Malaysia
chsuzy@usm.my

***Abstract*— With recent Covid-19 pandemic phenomena, the simplest shield/personal protective equipment (PPE) to limit the spread of this virus or other air-borne diseases is to wear a facemask as recommended by WHO for health protection. The supply of disposable face masks will keep on increasing since the mask should only worn once and thrown away right after used. This is because as masks are used, they collect exhaled airborne pathogens/viruses that remain living in the masks' fibers, rendering them infectious when handled besides creating secondary issue related to abundant used facemask disposal. In this situation, people need a way to use reusable facemask, yet still can maintained the filtration performance, and most importantly can shield users from infected and illness. This mini review discussed on the advance research such as membrane filter and super-hydrophobic coating on fabric-based face mask that possibly be applied as a preventive measure in combatting Covid-19 via effective method without neglecting the impact into environment.**

***Keywords*— Fabric face mask, super-hydrophobic coating, membrane filter, Covid-19**

[1] INTRODUCTION: COVID-19

The World Health Organization (WHO) has declared the coronavirus disease 2019 (COVID-19) as a pandemic since it has covering over a wide range of geographic area and affecting an exceptionally high proportion of the population. Within more and less 16 months since the emergence of Covid-19 in Wuhan, Hubei province in China in late December 2019, it has infected 123 million people in 221 countries and reported more than 2.7 million death [1], [2]. A novel coronavirus (nCoV) is a new strain from family of viruses and at first has been recognized transmitted from animals (civet cats) to humans. Upon analysis of negative-stain by electron microscopy, researchers have determined the diameter of this virus to range between 60 nm to a maximum diameter of 150 nm. The TEM captures of Covid-19 was shown in Fig. 1 [3]. Covid-19 presents with respiratory symptoms or gastrointestinal diseases and could infects people of all ages. The emergency warning signs present with more severe symptoms such as difficulty breathing, shortness of breath, persistent pain, pressure in chess, fever, cough, fatigue, sore throat etc [4].

[2] FACE MASK FOR COMBATTING COVID-19

The use of facemasks and respirators is strongly recommended by the World Health Organization (WHO) and the Centre for Disease Control and Prevention (CDC) as a standard for transmission-based precaution [5], [6]. Amidst the challenging Covid-19 phenomena and possible future airborne diseases, the use of face masks is the first and most crucial shield for every individual. Standard facemasks rely on physical filtration which collects and accumulates pathogens in the surface or within the mask materials, which they can remain viable and infectious for extended period of time. Therefore, proper use of facemasks is essential to provide the desired level of protection. In Malaysia, the government has enforced a new rule requiring all individuals to wear facemask once in crowded places and in public, starting 1st August 2020. This is due to the increasing numbers of infected patients with new infection cluster detected in few states in Malaysia. After more than half years of implementation, together with the increasing awareness among citizen in protecting themselves and others, the usage of facemask nowadays becoming a norm.

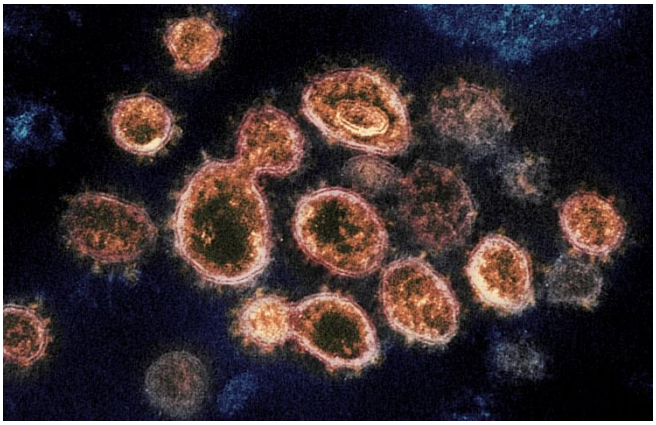


Fig. 1 TEM image of novel coronavirus

Using a disposable face mask during the peak pandemic period seems acceptable. However for a long run, the disposable face masks will lead to the unforeseen environmental problems, especially in the disposal of non-biodegradable facemask wastes. According to an analysis by scientist from University College London, if every person in the United Kingdom (UK) used one-single mask each day for a year, an extra 66,000 tons of contaminated waste would be created [7]. Cost of the disposable mask will be another limiting factor especially for low- and middle- income countries [5]. The problem is that low-resources countries might not have the ability or finances to adopt infection control enforcement and respiratory protection guidelines equivalent to those originating from high-resources countries.

With the current scenarios where economic and educational sectors are progressing open especially in Malaysia, standard operating procedures (SOP) established requires public to protect themselves and the least precaution to be taken is wearing facemask in congested/enclosed areas including schools. Besides, under the current global pandemic situation, the shortage of masks is still severe.

[3] FABRIC-BASED FACE mask

Fabric-based facemask is commercially made from various type of materials such as cotton, silk, chiffon, or hybrid fabric material such as cotton-silk, cotton-chiffon. The cotton fabric is massively used due to soft, warmth, washable, reusable, hygroscopicity, biodegradability, able to filter dust and breathability [8]. However, the current fabric facemask still have some limitations and disadvantages. It will cause the respiratory droplets which contains the virus to remain on the surface. Fabric mask has the highest penetration of particles at 95 % followed by disposable surgical face masks at 44 % and N95 respirators at 0.01 – 0.1 %. Thus, the transmission of bacteria and virus can rapidly spread onto the human respiratory system [9]. The risk of contamination is highest for fabric mask as it might originate from self – contamination because of repeated usage. Besides, from mask handling to mask removal and disposal procedure, live and active pathogens can easily cross-contaminated hands, fingers, skin, mucus membranes (nose, eyes, mouth), surfaces, fabrics, clothes, and patients.

In these situations, the WHO has issued that non-medical masks can be made of different combinations of fabric mainly made from woven and non-woven fabrics, and required at least three layers, depending on the material of fabric used. Factor such as filtration efficiency, breathability, number and combination of materials used, layering or shape, coating and maintenance should be taken into consideration, even there are no fix standards been enforced. People need a way to use reusable face masks, but still maintain the filtering performance, and most importantly protect patients/users from infection and disease.

Table 1 shows the non-medical disposable and fabric facemasks available in the market. The material used for the fabrication of fabric face mask were varied, ie. 100 % from cotton based and microfiber interlock, while non-medical disposable using polypropylene spun bond & melt blown non-woven fabric. The design also diverse with double-layered mask, added with reversible features, 3 ply washable and disposable designed, and come with adjustable nose bar and ear loop. The fact is, most of the fabric face mask not intended to be used in medical or clinical setting and their functional benefits were designed to be comfortable and easy to wear for longer periods of time. The breathability, washable, reasonable in price, anti-dust, stretchable are among the benefits of fabric face mask that people looking for. However, the choices of the face mask by certain people based on the fashion and the brand. Therefore, the awareness on the safety should be prioritized instead of the appearances.

[4] RECENT ADVANCE MODIFICATION IN FABRIC FACE MASK MATERIALS

The innovative and advance materials as effective antiviral fabrics been an urgent need during this Covid-19 pandemic. Even-though existing materials used for facemasks provide good level of protection, the enthusiastic research efforts is required in order to improve the filtering efficiency and anti-microbial functionalities especially in safety issues. The surface modifications should resistant to viral adhesion and can kill viruses. Therefore, few recent advances studied in facemask modification for efficient filtration and removal of viruses has been introduces.

A. Face mask modification by advance membrane filter

The filtration efficiency of surgical grade N95 mask provides the highest level of protection and given approximately 85 % due to its wider pore size (~300nm). However, since the Covid-19 virus shown a 65-150 nm diameter, an efficient mask has to be developed. A group of researchers has demonstrated a flexible and nanoporous membrane to achieve a reusable N95 mask with a replaceable membrane and indirectly enhanced the filtration efficiency. They introduced silica based nanoporous template using a combination of lithography and KOH-based isotropic etching steps. The pores has attained smaller than the virus particles which is 5 nm in size and lesser than 0.12 g in weight. The membrane also achieve self-cleaning properties as well as breathability (airflow rates above 85L/min) over a wide range of pore sizes, densities, membrane thickness and pressure drops. Thus, the innovation can be applied as an anti-Covid-19 membrane filter for face mask [10].

B. Face mask modification by super-hydrophobic coating

By nature, cotton fabric mask has hydroxyl (-OH) groups that makes it hydrophilic. The hydrophilicity characteristic of cotton fabric makes it easily wetted by water, oil, various liquid, bacteria and viruses. High affinity towards various liquids increase the chance of bacterial growth and stains on the face masks. Hence, modification of cotton fabric mask is necessary to attain super-hydrophobic coating properties (water contact angle between 150° and 180°). Super-hydrophobic phenomena tend to have a low water tilt angle on surfaces with low contact angle hysteresis (CAH), low adhesion, water repellence and antifouling properties [11]. The super-hydrophobic mask can repel and effectively prevents the respiratory droplets from environment (containing water droplet, bloods, viruses or bacteria) from attaching mask and directly protect the users.

Fig. 2 shown the example of surface wettability of pristine/unmodified cotton cloth by the measurement of water contact angle (WCA). Water was absorbed quickly on the uncoated surface due to its hydrophilic nature (WCA ± 0). There have an active hydroxyl group presence on the fabric surface. Therefore, it will create a chance of bacterial growth and stain on the face mask. The fabric mask can prevent respiratory droplets larger than 20-30μ in size, and the use of multiple layers efficiently blocks respiratory droplets less than 1-10μ in size. While, the average size of coronavirus is about 70-80 nm. Hence, approximately 97% of particles could penetrate the fabric masks.

Fig. 3 exhibits the surface wettability of modified cotton cloth with superhydrophobic coating by the measurement of water contact angle (WCA). Water was repelled on the modified surface due to its superhydrophobic nature (WCA > 150). The superhydrophobic coating will increase the WCA because the active hydroxyl group (presence on the fabric surface) are attached chemically with one of the low surface energy material used for modification. Therefore, it could prevent the bacteria, virus and infected water droplet from accumulate on the facemask surface. Besides, the additional measures of obstructing the entrance of viruses entities through the modified mask also can be avoided. Therefore, the facemask can provide the best protection at every condition especially in a high-risk environment.

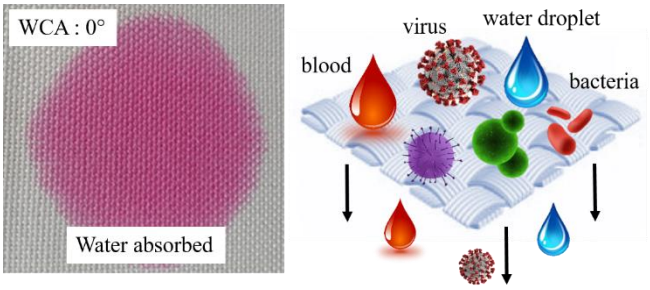


Fig. 1. Surface wettability of unmodified cotton cloth and measurement of water contact angle.

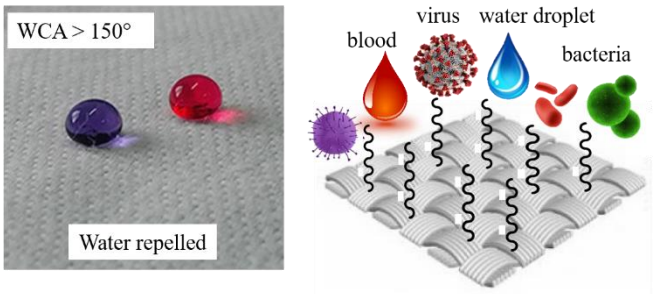


Fig. 2 Surface wettability of modified cotton cloth and measurement of water contact angle.

Illustration in Fig. 4 shows the super-hydrophobic coating on outer layer of fabric and the filter slotted in pocket mask. Through the application of super-hydrophobic coating on the outer layer of fabric face mask, the outside contaminants from environmental such as water droplet, blood, bacterial or virus having difficulty in penetrating or bound onto the filtration layer due to the hydrophobic coating developed on the surface.

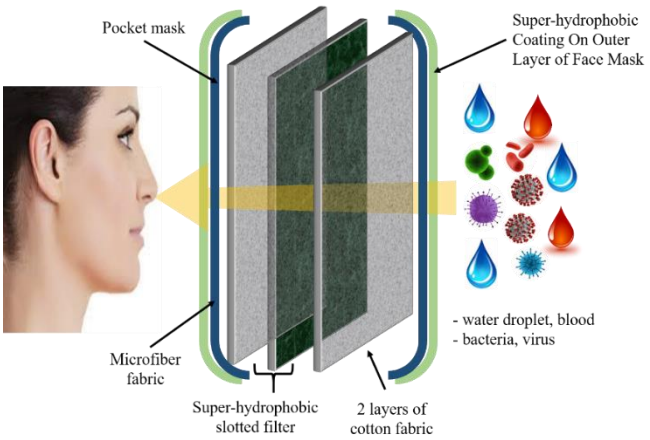


Fig 4. Illustration of super-hydrophobic coating on outer layer of fabric face mask.

[5] CONCLUSION

The recent advance modification of fabric mask was aimed to improve the filtering protection with anti-bacterial or anti-virus function, as well as reusable to serve the purpose of environmental friendly application, cost saving, and importantly minimum the chances of risk. A significant group of users targeted to people with respiratory symptoms; observational cases, i.e., people with a history of close contact with infected or suspected cases and are under medical observation; and the general population. These are the groups that possibly receive the benefit of the innovation, especially in countries or area having issues of limited facemask supply. The impact can be measured through the reduction number of infected cases within a short and medium-term. In a longer-term, it is expected to have zero reported issue related to abundant disposal of contaminated facemask waste besides, a well-controlled air-borne diseases cases.

ACKNOWLEDGEMENT

The authors acknowledge the Prototype Research Grant Scheme (PRGS) (203/PJKIMIA/6740049) provided by the Ministry of Higher Education, Malaysia.

REFERENCES

[1] WorldOmeter, “Covid-19 Coronavirus Pandemic.” [Online]. Available: https://www.worldometers.info/coronavirus/#countries. [Accessed: 21-Mar-2021].
[2] M. Martí *et al.*, “Protective face mask filter capable of inactivating SARS-CoV-2, and methicillin-resistant staphylococcus aureus and staphylococcus epidermidis,” *Polymers (Basel).*, vol. 13, no. 2, pp. 1–12, 2021.
[3] “New Images of Novel Coronavirus SARS-CoV-2,” *National Institute of Allergy and Infectious Diseases*. [Online]. Available: https://www.niaid.nih.gov/news-events/novel-coronavirus-sarscov2-images. [Accessed: 01-Apr-2021].
[4] S. J. Fong, N. Dey, and J. Chaki, “An Introduction to COVID-19,” *Artif. Intell. Coronavirus Outbreak*, pp. 1–22, Jun. 2020.
[5] A. A. Chughtai, H. Seale, T. C. Dung, L. Maher, P. T. Nga, and C. R. MacIntyre, “Current practices and barriers to the use of facemasks and respirators among hospital-based health care workers in Vietnam,” *Am. J. Infect. Control*, vol. 43, no. 1, pp. 72–77, 2015.
[6] J. Howard *et al.*, “An evidence review of face masks against COVID-19,” *Proc. Natl. Acad. Sci. U. S. A.*, vol. 118, no. 4, pp. 1–12, 2021.
[7] M. Karmacharya, S. Kumar, O. Gulenko, and Y.-K. Cho, “Advances in Facemasks during the COVID-19 Pandemic Era,” *ACS Appl. Bio*

Mater., 2021.
[8] S. Beesoon, N. Behary, and A. Perwuelz, "Universal masking during COVID-19 pandemic: Can textile engineering help public health? Narrative review of the evidence," *Prev. Med. (Baltim).*, vol. 139, no. August, p. 106236, 2020.
[9] D. Wang *et al.*, "Selection of homemade mask materials for preventing transmission of COVID-19: A laboratory study," *medRxiv*. 2020.
[10] N. El-atab, N. Qaiser, H. Badghaish, S. F. Shaikh, and M. M. Hussain, "Flexible Nanoporous Template for the Design and Development of Reusable Anti-COVID-19 Hydrophobic Face Masks," *ACS Nano*, no. 14, pp. 7659–7665, 2020.
[11] I. Das and G. De, "Zirconia based superhydrophobic coatings on cotton fabrics exhibiting excellent durability for versatile use," *Sci. Rep.*, vol. 5, no. December, pp. 1–11, 2015.

Table 1. The non-medical disposable and fabric facemasks available in the market

	Features	**Non-Medical Disposable Face Mask**	**Brand A (Eco-Mask)**	**Brand B**
1	**Appearance**			
2	**Material**	Polypropylene Spunbond & Meltblown Non-Woven Fabric	Microfiber interlock and two layers of cotton interlock	100 % Cotton fabric
3	**Design & features**	3 ply disposable face mask	3 ply washable face mask	double-layered reversible woven fabric
4	**Functional Benefits:**	-Anti gems & bacteria, -Anti dust & air particles -Glass fibre free -Breathable -High filtration capacity -Adjustable nose bar	-Breathable -Washable -Anti dust -Adjustable ear loop	-Breathable, washable, comfortable and easy to wear for longer periods of time. -Not intended for use in medical or clinical setting.
	Features	**Brand C (Anveerus)**	**Brand D (Levi's)**	**Brand E (Jovian)**
1	**Appearance**			
2	**Material**	100% Copper Ion Infused Face Mask,	100 % Cotton fabric	Lycra fabric
3	**Design & features**	High-quality stretchable, soft, light and cooling fabric with elastic ear loop straps.	double-layered reversible woven fabric	Neoprene printed fabric.
4	**Functional Benefits:**	-Copper Ion infused into the threads. -Copper is naturally self-sterilizing and anti-microbial, minimize the risk of contracting or spreading bacteria, germs and viruses.	-Breathable, -washable, -not intended for use in medical or clinical setting, -Designed to be comfortable and easy to wear for longer periods of time.	Stretchable anti-dust advanced breathable With attached non-woven filter pocket.

Cubic-Like Mn_2O_3 as an Anode for Sodium-Ion Batteries Applicatio

Nor Fazila Mahamad Yusoff
Energy Storage Research Group, Faculty of Ocean Engineering Technology and Informatics Universiti Malaysia Terengganu
Terengganu, Malaysia
nfazilamyusoff@gmail.com

Nurul Hayati Idris
Energy Storage Research Group, Faculty of Ocean Engineering Technology and Informatics Universiti Malaysia Terengganu
Terengganu, Malaysia
nurulhayati@umt.edu.my

Aim: **Sodium-ion (Na-ion) batteries are a promising candidate for next-generation batteries due to the abundance of sodium, low cost and comparatively high levels of safety.**

Method: **In this work, Mn_2O_3 powders are synthesized by thermal conversion of $MnCO_3$. The structural and electrochemical properties of Mn_2O_3 are identified and analysed.**

Results: **In combination with the formation of the Mn_2O_3 subunits on the surface, the cubic-like Mn_2O_3 (1.0–1.5 µm in sizes) could facilitate the electrolyte to penetrate into the inner core through their porous structure, and provides more active sites for Na^+ diffusion path. The cubic-like Mn_2O_3 have an initial reversible capacity of 544 mAh/g at 100 mA/g with a Coulombic efficiency of >90% over 200 cycles.**

Conclusion: **Outstanding electrochemical performance can be derived from the structure of Mn_2O_3, a relatively high surface area, and ample surface active sites which in turn improve the kinetics of continuous charge transfer, ion diffusion, and capacity. The results indicate that Mn_2O_3 as the potential to be explored as an anode in the development of Na-ion batteries. In the future, Na-ion batteries have the potential to have an important area in the field of energy storage.**

Keywords— Mn_2O_3, Cubic-like, $MnCO_3$, Anode, Sodium-ion batteries

Investigation of Floor Vibrations of Steel Structure Under Earthquake

Oğuzhan Çelebi
Department of Civil Engineering
Ataturk University
Erzurum, Turkey
celebioguzhan@atauni.edu.tr

Bayrak Barış
Department of Civil Engineering
Ataturk University
Erzurum, Turkey
baris.bayrak@atauni.edu.tr

Abdulkadir Cüneyt Aydın
Department of Civil Engineering
Ataturk University
Erzurum, Turkey
acaydin@atauni.edu.tr

***Abstract*— In this study, the performance, dynamic response and slab vibrations of the horizontal and vertical bearing elements and floors, which constitute the engineering structures under earthquake hazard today, were investigated. In addition, repair and reinforcement procedures are also discussed in order to minimize floor vibrations caused by earthquake effects on existing steel structure members. The results have been discussed for comfort and fitness level of people by Turkey Building Earthquake Regulation the proposed non-linear time history analysis done. The findings obtained for the vibration of the floors are discussed and some design methods have been proposed to minimize the problems of ground motion vibration. In this study was examined a two story of steel structure that serving as a restaurant. By analyzing the designed steel structure on the time domain, it was found that the floors vibrate more than the vibration limit values recommended by the regulations. These vibrations were tried to be minimized by increasing the stiffness of the floors of the steel structure. However, the columns of the steel structure were supported with diagonal elements and analyzed again. It was determined that the damping rate of the steel floors increased and their vibrations decreased through the reinforcement processes. It has also been observed that the steel structure has reached a controllable damage level. It has been suggested that the slabs should be connected to the main carrier beams in a fully rigid manner in order to minimize the vibrations of the steel floors. However, if the floors are not rigidly mounted on the main carrier beams, it has been suggested that the columns should be supported with plastic hinged diagonals at both ends.**

Keywords*— *earthquake, floor vibration, steel structures, time domain analysis

[1] INTRODUCTION

Buildings where people have been should be designed to be both comfortable and safe for people. The earthquake affects the buildings not only reduce the safety of the building, but also cause the comfort of people and the deterioration of the important items in the building. For example, in some public buildings such as bridges and hospitals, earthquake affects should be very limited [1]. Vibration of floors under earthquake is one of these problems. These vibrations in the floors cannot damage the structure to a great extent, but they cause the comfort of the people in the building to be reduced or important items to be damaged [2]. Therefore, floor vibrations must be taken into account when designing structures [3].

Passive, semi-active, active and hybrid control systems are used to reduce flooring vibrations that may occur in buildings [4]. Although passive systems are successful in reducing floor vibrations, they also have some disadvantages since they do not adapt to any earthquake [5]. Active, semi-active and hybrid control systems can adapt themselves against earthquakes, but they can create stability problems in the building if an appropriate control algorithm is not used and an external power supply is not made [6-8]. Due to the difficulty, cost and some negative features of structural control systems, the method of repair and reinforcement comes to the fore in controlling floor vibrations. Repair and reinforcement applications can be done with different properties of fly ash, polymer-based materials or carbon fiber [9-12]. Apart from this, repair and reinforcement applications can be performed by using support elements that increase the stiffness of the structural elements [13,14].

Two different strengthening procedures are discussed for the two-story steel structure used in this study. The first of these strengthening procedures is the bending profiles placed between the ground floor main bearing columns with cross pressure bars and diagonally to the ground floor slab. Another strengthening procedure is to increase the rigidity of the floor beams by supporting the skid-resistant bodies and bending heads. For the three different models obtained, the performance levels of the ground floor central column and a ground floor beam were examined. Apart from this, the vertical deflection controls of the slabs were made for three different models. Finally, the vibrations caused by the floors under the effect of earthquakes used in the study were discussed.

In this study, SAP2000 program was used for nonlinear analysis in time domain and MATLAB program was used to detect vibrations in the frequency domain. In order to determine the damages that may occur in the structure, the frequency domain is used in the method [15].

[2] STRUCTURE INFORMATION

The two-story steel structure to be used in the study is located in Erzurum Province Oltu District at 40.5 latitude and 41.8 longitude [17]. The steel grade used in the building is S235 N / NL [19]. The columns that make up the structure are HEA450 for the ground floor and HEA400 profile for the 1st floor. The main beam profiles that make up the load-bearing system are IPE300 and the secondary beams are IPE120. For strengthening procedures, the columns are laterally supported with the L150X12 profile and the slabs with the IPE300 profile in the bending direction. In the other strengthening procedure, the heads of the beams are supported with 15 mm thick stiffening plates and the beam webs laterally with 15 mm stiffening plates. The static and cross-section properties of the profiles used in the building are presented in Table 1 and the damaged structure (excessive floor vibrating structure) in Figure 1, and the reinforced structure in Figure 2 and Figure 3.

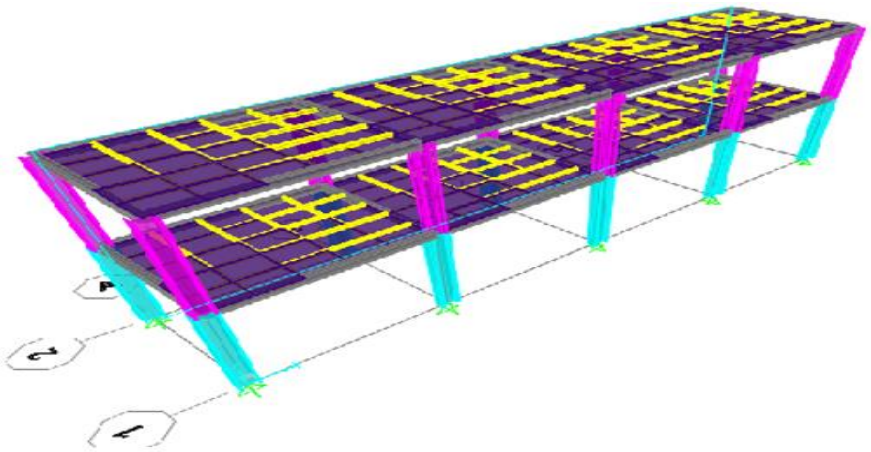


Fig. 1. Damaged structure

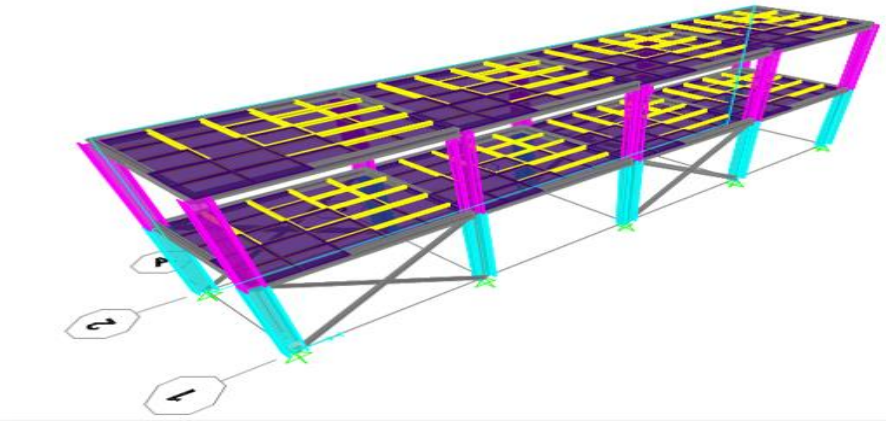


Fig. 2. Reinforced structure where floors are bending and columns are supported laterall

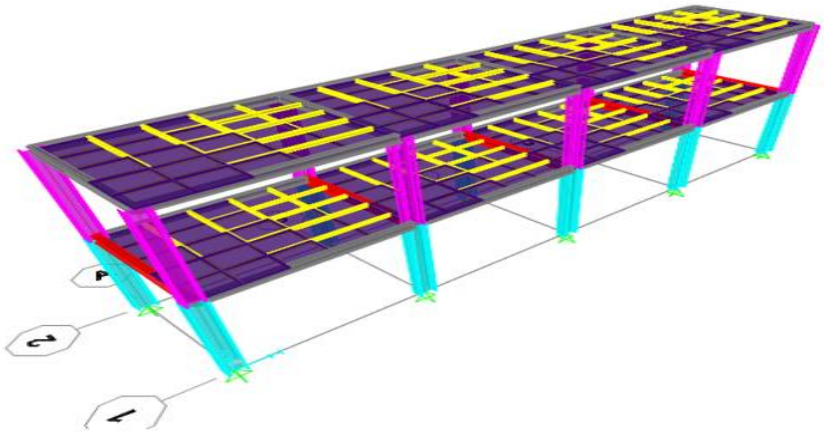


Fig. 3. The structure in which the beam flanges are supported against bending and the webs against sliding

Table 2. Statıc And Cross-Sectıon Informatıon Of Profiles

Profil	h (mm)	b (mm)	t_w (mm)	t_f (mm)	A (cm^2)	I_x (cm^4)	I_y (cm^4)	W_{px} (cm^3)	W_{py} (cm^3)	i_x (cm)	i_y (cm)
HEA450	440	300	11.5	21	178	63722	9465	5571	965.5	18.9	7.29
HEA400	390	300	11	19	159	45069	8564	2562	872.9	16.8	7.34
IPE300	300	150	7.1	10.7	53.8	8356	603.8	628.4	125.2	12.46	3.35
IPE120	120	64	4.4	6.3	13.2	318	27.7	60.73	13.58	4.9	1.45

Table 1 shows the cross-section heights of the profile (h), flange width (b), body thickness (t_w), flange thickness (t_f), cross-section area (A), x-axis moment of inertia (I_x), y-axis moment of inertia (I_y), x-axis plastic section strength moment (W_{px}), y-axis plastic section (W_{py}). the moment of resistance, ix the x-axis the radius of inertia, and the y-axis the radius of inertia. Figure 3 shows Turkey Earthquake Building Standard expressed strengthening procedure was performed according to Figure 4.

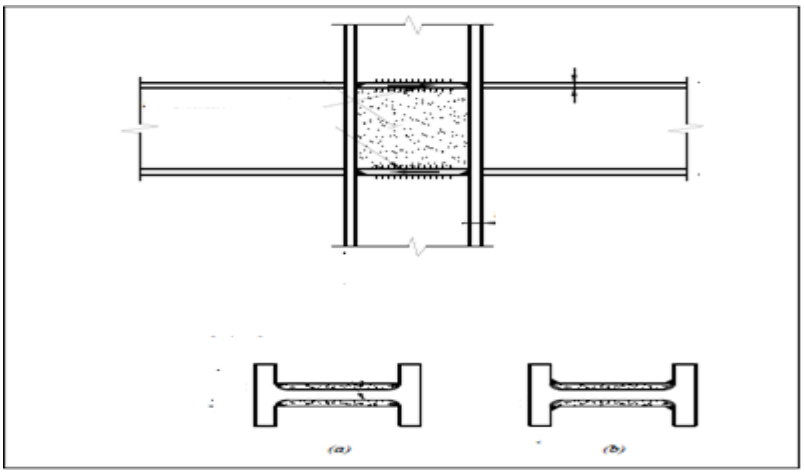


Fig. 4. Supporting beams with stiffness plates [16]

[3] EARTHQUAKE DATA USED IN STRUCTURE ANALYSIS

Earthquake information used for calculation in the time domain of the structure is presented in Table 2. The first has been obtained spectral acceleration-period diagram for structure according to structure of located by using the Turkey Dangerous Earthquake Maps [17]. According to Turkey Earthquake Building Standard $0.2T_p$ and $1.5T_p$ seismic interval in the spectrum values, the same values must ensure that at least 90% capacity within the range of the elastic acceleration spectrum. Earthquake spectra was scaled within the scope of this criterion and entered as data on the building [18]. The unscaled version of the earthquake spectra is presented in Figure 5 and the scaled version in Figure 6. By taking the average of this earthquake spectra, three different models defined as the structure under the average earthquake were analyzed, and the results were discussed.

Table 2. Earthquake Data

Earthquake's	Station	Date	PGA* (N-S)** (cm/sn^2)
Dinar Earthquake	Afyon Dinar Meteorology Station Directorate	01.10.1995	281.62
Van Earthquake	Van Muradiye Meteorology Directorate	10.23.2011	178.5
İzmit Earthquake	Yarimca Petkim Station	17.08.1999	264.81

*Peak Ground Acceleration (PGA)
** Nourth- South (N-S)

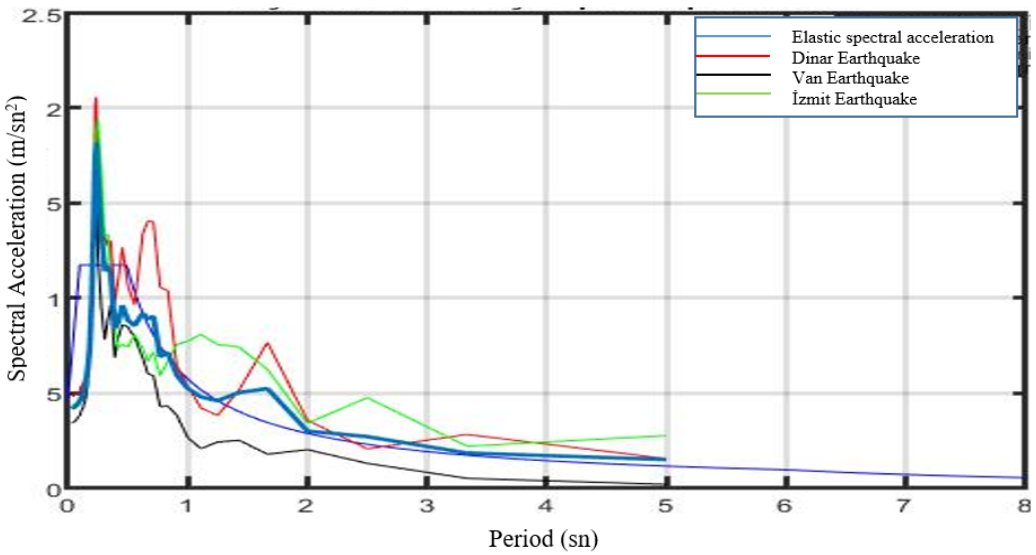


Fig.5. Unscaled earthquake spectra

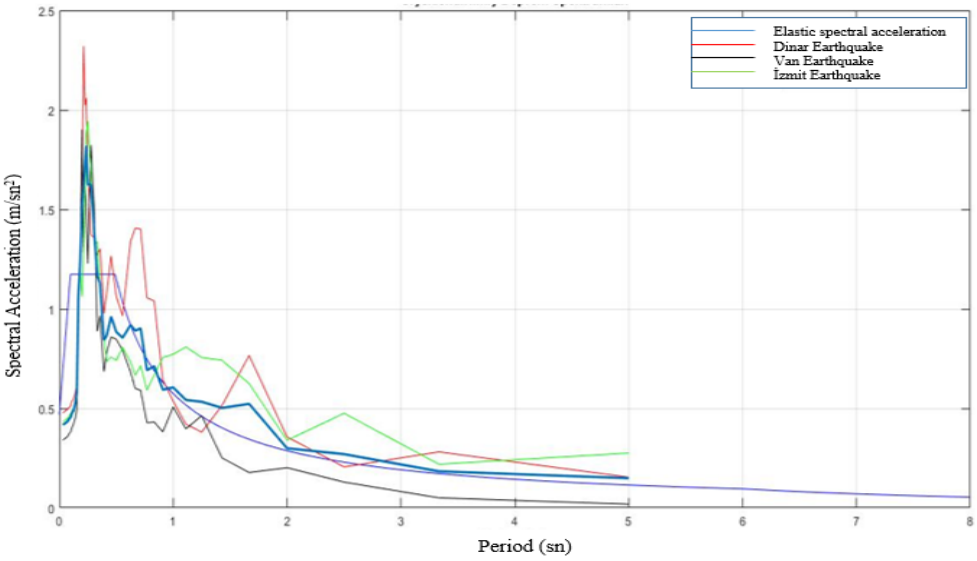


Fig. 6. Scaled earthquake spectra

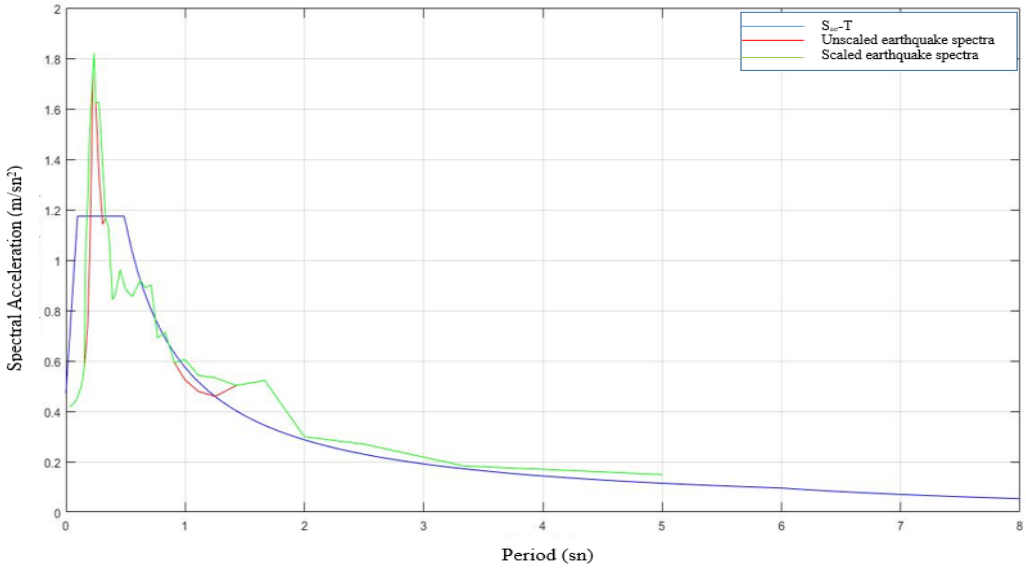


Fig. 7. Means of earthquake spectra's

IV. ANALYSİS RESULTS

The Structure was performed according to a nonlinear time history and equivalent lateral load analysis according to defined in Turkey Building Earthquake Standard. In the analysis results, the vertical deflections in the slab, the performance levels for the columns and beams taken as reference, and the vibrations caused by the earthquakes in the slab were taken into consideration.

A. Performance Levels

The columns and beams damage limits determined according to the rotation of yield that obtained using by profiles cross section and static information for the columns and beams Table 5c.1 obtained from Table 5c.2 respectively at Turkey Building Earthquake Standard [16]. However, the performance levels of the members that make up the structure are determined by reducing the bending stiffness according to the Steel Structures Standard. In this case, the axial, shear and bending stiffness of all the members in the structure have been reduced to as 0.80 EI [19].

Damage limit values for columns;

$$\Theta_y=[(W_pF_{ye}l_b)/(6EI_k)][1-(P/P_{ye})] \quad (1)$$

In Equation (1), Θy is the yield rotation, P is the axial compressive force in the column under earthquake loads, and P_{ye} is the column design axial force value. The damage limit values of the columns are defined for systems with limited ductility level, which is the most unfavorable case. In this case, as defined in the Turkey Building Earthquake Regulations Limited Damage Level (IO) can be controlled damage level (LS) and collapse prevention performance level taken as 0.25θy, 3θy, 4θy for respectively. Columns should be calculated to determine the performance of the design axial compressive strength P_{ye}, by the Turkey Steel Structures Regulation 2016 is calculated as follows [19].

$$P_{ye}=F_{cr}A_g \quad (2)$$

Where, F_{cr} is the critical buckling stress, and A_g is the cross-sectional area without loss. According to the steel structures regulation,

$$(\lambda/i) > 4.71\sqrt{E/Fy} \text{ and } F_{cr}=0.877F_{el} \quad (3)$$

In Equation (3), F_y shows the yield strength of the column (235 MPa for S235 steel grade) and the elasticity modulus of steel grade E. F_{el} represents the elastic buckling load and is calculated according to Equation (4).

$$F_{el} = (\pi^2E)(\lambda/i)^2 \quad (4)$$

In Equation (4), L_c is the buckling length of the column, and it is calculated as KL in the steel structures regulation. Here K is the buckling length coefficient and taken as 1.0 to stay on the safe side. It was taken as 4 m, L being the length of the column. Therefore, the buckling length of the column was calculated as 4 m. Where I, indicates the smallest radius of inertia and is obtained from Table 1.

$$F_{el}=(\pi^2E)/(\lambda/i)^2 = \pi^2(200000)/(400/7.29)^2$$

$$(\lambda/i)=54.87>4.71\sqrt{200000/235}=43.45$$

$$F_{cr}=0.877F_{el}=0.877*654=573.55 \text{ MPa}$$

$$P_{ye}=F_{cr}A_g=39800*573.55=1029 \text{ kN}$$

In Table 1, the yield rotation of the columns according to the cross-section and static information of the HEA450 column and the P values obtained from the analysis results are presented in Table 3. The performance levels of the column for 3 different models are presented in Table 4.

Table 3. Yield Rotation And Damage Limit Values In The Column Due To Different Earthquakes

Earthquakes	**P (kN)**	**P_{ye} (kN)**	**$W_{px}.F_y.L/6EI_x$**	**Θ_y**	**IO**	**LS**	**CP**
Dinar Earthquake	**339.299**	**10209**	**0.00395**	**0.0038**	**0.0010**	**0.0115**	**0.0153**
Van Earthquake	**176.81**	**10209**	**0.00395**	**0.0039**	**0.0010**	**0.0116**	**0.0155**
İzmit Earthquake	**195.33**	**10209**	**0.00395**	**0.0039**	**0.0010**	**0.0116**	**0.0155**
Impactıng Earthquake	**237.1463**	**10209**	**0.00395**	**0.0039**	**0.0010**	**0.0116**	**0.0154**

Table 4. Performance Levels For Three Different Model's Of The Columns

	Model 1		**Model 2**		**Model 3**	
Earthquakes	ϴT	D.L	ϴT	D.L	ϴT	H.S
Dinar Earthquake	0.02005	CP	-0.0013	IO	0.01685	IO
Van Earthquake	0.0117	LS	-0.000905	IO	0.01435	IO
İzmit Earthquake	0.01305	LS	-0.00102	IO	0.0134	IO
Impactıng Earthquake	0.014933	LS	-0.001075	IO	0.01486667	IO

In Table 4, ϴ presents the total displaced pivot rotation at the column, D.L the damage level of the column, the CP pre-collapse performance level, the LS Advanced damage level, and the IO apparent damage level. Yield rotation about the beam is calculated according to Equation (5) [19].

$$\Theta_y=(W_pF_{ye}l_b)/(6EI_k) \quad (5)$$

Table 5. Performance Levels Of The Beam

	Model 1		**Model 2**		**Model 3**	
Earthquakes	ϴT	D.L	ϴT	H.S	ϴT	H.S
Dinar Earthquake	0.0592	CP	0.0021	IO	0.0219	LS
Van Earthquake	0.0283	CP	0.00148	IO	0.0179	IO
İzmit Earthquake	0.0312	CP	0.00167	IO	0.0176	IO
Impactıng Earthquake	0.039567	CP	0.00175	IO	0.01913333	IO

B. Floor Vıbratıons

Vertical deflections caused by earthquakes on the floor of the building are presented in Table 6 and slab vibrations in Figure 8. It has been determined that it is the method that reduces the floor deflections in the structure the most and increases the stiffness of the floor beams. However, reinforcement with diagonal members keeps the floor vibrations caused by the earthquake to a minimum. Considering the comfort of people, the use of diagonal members is the most appropriate method.

Table 6. Deflections

Earthquake	**Model 1 (m)**	**Model 2 (m)**	**Model 3 (m)**
Dinar	0.00469	0.000189	0.00141
Van	0.00249	0.000137	0.00125
İzmit	0.00275	0.000182	0.0012
Impactıng Earthquake	0.00331	0.000129	0.001287
Equivalent Earthquake	0.0022	0.0035	0.0008

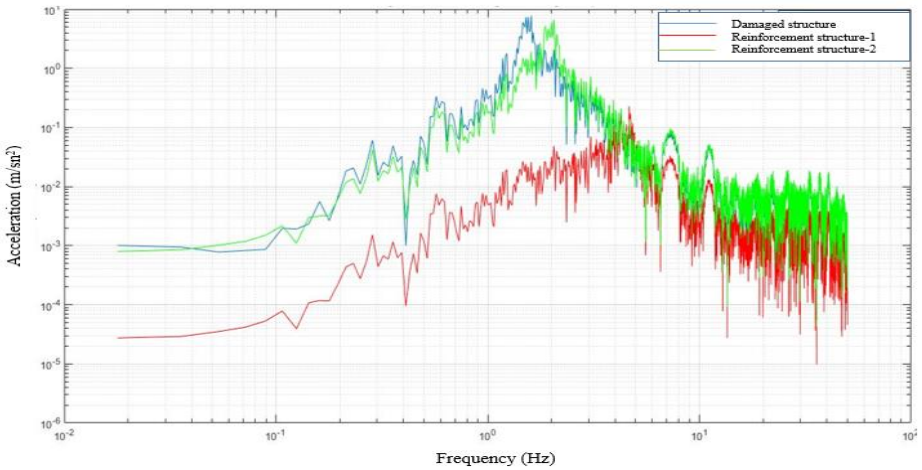


Fig. 8. Floor vibration of three models

V. RESULTS AND DISCUSSION

In the study, a series of reinforcement procedures was applied in order to reduce the floor vibrations in the damaged structure and to keep the structure at a controllable damage level by using nonlinear analysis method in the time domain. It has been determined that the damaged structure column and beam are at the performance prevention collapse level. After the columns were supported laterally and the floors were bending, the structural elements reached an obvious damage level. It was concluded that the load-bearing members reached an obvious damage level as a result of supporting the floor beams in shear and bending, which is the other reinforcement method, but the load-bearing columns were more difficult than the other reinforcement method. Apart from that, limited deflections occurred in the floor after the reinforcement procedures were applied. Finally, floor vibrations were reduced by 50% as a result of supporting the columns laterally and in the bending direction of the floor and floor vibrations were reduced by 2% as a result of the application of the other reinforcement method. In this case, considering both the safety of the building, the comfort of the people and the economy, it is foreseen that the floor beams will be supported with stiffness plates in the direction of bending and sliding in order for this structure to provide the specified performance.

REFERENCES

[1] F. Casciati, J. Rodellar, and U. Yildirim, ‘‘Active and semi-active control of structures -theory and applications: A review of recent advances’’, J. Intell. Mater. Syst. Structure, vol. 23, pp.1181-1195, 2012.

[2] W. Varela, and R. Battista, ‘‘Control of vibrations induced by people walking on large span composite floor decks,’’ Eng. Structure, vol. 33(9), pp. 2485-2494, 2011.

[3] A. Pavic, and M. Willford, “Vibration serviceability of post- tensioned concrete floors, Appendix g in post-tensioned concrete floors design handbook”, Technical report 43, 2005.

[4] E. J. Hudson, and P. Reynolds, ‘‘Implications of structural design on the effectiveness of active vibration control of floor structures,’’ Struct. Cont. Health Monitoring., vol. 21(5), pp.685-704, 2014.

[5] J. D. Marshall, and F.A. Charney, ‘‘A Hybrid passive control device for steel structures 2'physical testing,’’ Jour. of Const. Steel Research, vol. 66(10), pp.1287–1294, 2010.

[6] R. Fortun, J.M. Orus, J. Alfonso, F.B. Girmeno, and, J.A. Castellanos, "Flatness-based active vibration control for piezoelectric actuators." IEEE/ASME Transactions on Mechatronics, vol. 18(1), pp. 221-229, 2013.

[7] X. Shao, A. M. Reinhorn, and M.V. Sivaselvan, ‘‘Real-time hybrid simulation using shake tables and dynamic actuators,’’ ASCE Jour. of Struct. Engineering, vol. 137(7), pp.748–760, 2011.

[8] M.G. Soto, and H. Adeli, ‘‘Semi-active vibration control of smart isolated highway bridge structures using replicator dynamics,’’ Engineering Structures vol. 186, pp.536–552, 2019.

[9] A. Öz, B. Bayrak, and A.C. Aydın, "The effect of trio-fiber reinforcement on the properties of self-compacting fly ash concrete," Construction and Building Materials, vol. (274), 121825, 2021.

[10] L. Yan, ‘‘Effect of alkali treatment on vibration characteristics and mechanical properties of natural fabric reinforced composites,’’ Journal of Reinforced Plastics and Composites, vol. 31(13), pp. 887-896, 2012.

[11] K. U. Shafi, Y. L. Chi, A. S. Naveed, and J. K. Kim, ‘‘Vibration damping characteristics of carbon fiber-reinforced composites containing multi-walled carbon nanotubes,’’ Composites Science and Technology vol. (71), pp.1486–1494, 2011.

[12] M. Rajesh, P. Jeyaraj, and N. Rajini, ‘‘Free vibration characteristics of banana/sisal natural fibers reinforced hybrid polymer composite beam,’’ Procedia Engineering, vol. (144), pp. 1055-1059, 2016.

[13] S. Nakamura, T. Okumatsu, T. Nishikawa, and T. Okabayashi, “A fatigue damage of a diagonal member in a steel truss bridge due to wind-induced vibration,” Developments in International Bridge Engineering -Selected Papers from Istanbul Bridge Conference, pp. 211-220, 2014.

[14] O. Çelebi, and A. C. Aydın, "Earthquake performance of historical Şenkaya Yünören Bridge," University of Niğde Ömer Halis Demir Journal of Engineering Sciences, vol.10(1), pp.284-300, 2021.

[15] O. F. Sak, and K. Beyen, "Damage analysis of the structures in time-frequency domain with wavelet transform method," Technical Journal, vol.30, pp.8835-8860, 2019.

[16] TBDY (2018), “Turkey Building Earthquake Regulatıon, Regulation on Buildings to be Constructed in Disaster Areas, ”Ministry of Public Works and Settlement Disaster Affairs, Ankara.

[17] AFAD, Republic of Turkey Prime Ministry Disaster and Emergency Management, Ministry of Interior, Ankara, https://tadas.afad.gov.tr/.

[18] Chopra, A., “Dynamics of structures: Theory and Applications to Earthquake Engineering,” Prentice Hall, Englewood Cliffs, NJ., 1995.

[19] TÇYY, “Turkey Steel Structural’s Regulatıon, Regulation on Design, Calculation and Construction Principles of Steel Structures.,” Environment and Urban ministry Ankara.

[20] A. Aghayare, and W. Jason, “Structural steel desıgn,” 2nd Ed., Drexel University, New York, 2018.

Operational Modal Analysis of A Historic Turkish Cupola

Dilek Okuyucu
Department of Civil Engineering
Faculty of Engineering and Architecture Erzurum Technical University
Erzurum, Turkey
okuyucu@erzurum.edu.tr

Memduh Şenol Çavdar
Department of Civil Engineering
Faculty of Engineering and Architecture Erzurum Technical University
Erzurum, Turkey
msenolcavdar@gmail.com

Zabiullah Fakuori
Department of Civil Engineering
Faculty of Engineering and Architecture Erzurum Technical University
Erzurum, Turkey
zabih.safari@gmail.com

Erdem Erkmen
Department of Civil Engineering
Faculty of Engineering and Architecture Erzurum Technical University
Erzurum, Turkey
erdem.erkmen76@erzurum.edu.tr

Dursun Burak Özdoğan
Department of Civil Engineering
Faculty of Engineering and Architecture Erzurum Technical University
Erzurum, Turkey
bozdoganitu@gmail.com

Yusuf Gedik
Department of Civil Engineering
Faculty of Engineering and Architecture Erzurum Technical University
Erzurum, Turkey
bozdoganitu@gmail.com

Meliha Yilmaz
Department of Civil Engineering Faculty of Engineering and Architecture Erzurum Technical University
Erzurum, Turkey
melihay066@gmail.com

Burak Şahin
Department of Civil Engineering Faculty of Engineering and Architecture Erzurum Technical University
Erzurum, Turkey
burak.sahin74@erzurum.edu.tr

Abstract*— *Cupola type tomb structures are remarkable examples of Turkish-Islamic architecture. Cupolas are constructed for notable people of ancient Turkish-Islamic states. These masonry monumental structures generally have very simple plans close to circle consisting of a basement for a grave plus a ground floor for visitors and two layers of the ceiling with a dome inside and cone outside. There are several numbers of cupolas in Erzurum city which belong to Saltuklu and the Seljukian Turkish-Islamic States. This manuscript provides brief information about Turkish cupolas in Erzurum city and results of the operational modal analysis of one of the anonymous cupolas of the Three Cupolas area with a rectangular plan.

Keywords— ***Turkish Cupola, Historic Masonry, Saltuklu Government, Erzurum, Operational Modal Analysis***

Introduction

Erzurum is located on the east part of Anatolian Region of Turkey. History of the city dates back to 4th century A.C.; hosting civilisations like Byzantines, Persians and miscellaneous Turkish states [1]. Among all, one of the Turkish states takes special attention by Turkish-Islamic history point of view: Saltuklu Government. Soon after Malazgirt Victory of Sultan Alparslan against Byzantine Empire; Saltuklu State was founded in Erzurum and around and Erzurum was announced to be the capital city of the government. Hence, Erzurum was crowned as the capital city of the first Turkish-Islamic state founded on the Anatolian land. Until the Saltuklu State collapsed in 1202, the government built a number of remarkable structures onto the land like a kind of the seal [1]. The most important ones can be mentioned as cupola ("kümbet" in Turkish) type buildings. Cupola type construction in Erzurum starts with Saltuklu Government and then continues during Seljukian period.

The cupola is essentially a monumental tomb structure. It should be mentioned that cupola type grave structures were constructed for important people of that time. This type of constructions are unique examples of Turkish-Islamic architecture. These masonry monumental structures generally have very simple plans close to circle consisting of a basement for a grave plus a ground floor for visitors and two layers of the ceiling with a dome inside and cone outside. Reference [1] mentions total of nine cupolas at Erzurum city centre. An aerial view of Three Cupolas area is taken from reference [2] and presented in Fig. 1.



Fig.1. Three Cupolas area of Erzurum [2]

On the other hand, Turkey is located on one of the most active seismic zones of earth [3]. Fig. 2, taken from reference [4], provides a closer look to seismicity of Turkey. Earthquake hazard map of Turkey presented in Fig. 2 points out the high seismicity of Erzurum city and around. Reference [5] states information about the destructive earthquakes in Erzurum history and damage states of well-known historic buildings of today. From this point of view historic structure, especially cupola type masonry constructions provide valuable information about seismicity of the region. This situation attracts researchers of the mentioned area.



Fig. 2. Earthquake hazard map of Turkey [4]

Considering the historic importance of Erzurum city by Turkish-Islamic government background, Yakutiye Municipality of Erzurum city has announced 2021 as *Saltuklu Year*. The municipality plans a group of activity and organisations to point out Saltuklu government. Technical investigation of historic structures from Saltuklu time is one of the projects. Authors study on this part and herein manuscript was prepared.

Three Cupolas ("Üç Kümbetler" in Turkish) region shown in Fig.1 is settled in old city centre of Erzurum, within the borders of inner castle. There are total of four cupolas in this area one of which belongs to the Emir Saltuk Bayındır who is the founder of the Saltuklu government. Rest of the three are classified as *anonymous* cupolas due to the lack of reliable information about the owner. One of the anonymous cupolas, *the smallest one in volume*, of the region is dated back to 14th century and has a rectangular plan. This cupola was constructed after collapse of the Saltuklu state. Authors started the project of cupola evaluation from this anonymous structure.

Soon after the official permission procedures finalized, site studies started. Current situation of the cupola was investigated. Stone type was classified. Finite element model was created for theoretical modal analysis and operational modal analysis was carried out for structural model calibration.

[4] MATERIAL AND METHOD

The research was started by the site visits to Three Cupolas area. The object of this text, *anonymous cupola*, is presented in Fig. 3. The structure is dated back to 14th century by reference [1] and much more sources. The owner of the grave underneath is unknown. The structure has a rectangular shape in plan with the dimensions of 4.60x4.65 meters and 3.6 meters of wall height. The structure has two layers of ceiling. Inner one is a stone vault and the outer is a stone cone.



Fig.3. Anonymous cupola

Destructive testing of historic masonry material in Turkey is strictly forbidden. Hence, non-destructive methods are adopted for material characterisation and dynamic identification of the structural system details of which are presented in the following part.

A. *Material Studies*

Basalt and andesite type volcanic rocks were commonly used in historic masonry constructions in Erzurum and around. Reference [6] presents calibration equations for *concrete Schmidt hammer* to be used to estimate compression strength of andesite and basalt type stones. These equations were planned to be used for material characterization of the cupola. However, site studies provided some surprising information about the stone used in the cupola. Existence of basalt was very low. Another stone, *like concrete*, was primarily used for construction. A close view of the mentioned rock is presented in Fig. 4. It was understood that this stone is a local material called "Sivişli stone" or "Erzurum concrete" among the local people. Neither in the literature nor in the technical people's archive, could research team reach technical information about Sivişli stone.



Fig.4. A close view from Sivişli stone

Sivişli is the name of a village which is ~15 km away from Erzurum city centre. The stone has been recently used in restoration of Erzurum castle and some other historic masonry. The quarry of the stone was found in the village and information was taken from the elder people of the site. Stone samples were taken and prepared for material tests at the laboratory. Rough stones were precisely cut and used for material evaluation. Unit weight and compressive strength

properties were studied. Compression tests on cubic blocks were realized in a universal testing machine by applying displacement controlled loading as shown in Fig. 5.

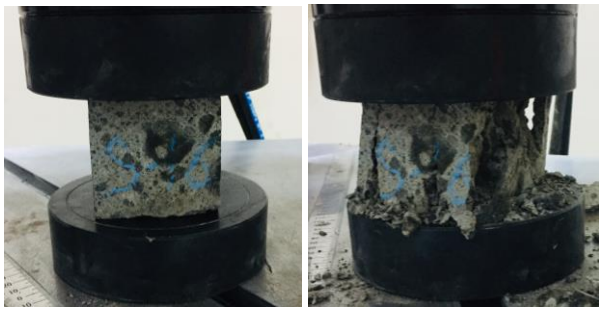


Fig. 5. Compressive strength test of Sivişli stone block

B. *Finite Elemnt Model and Theoretical Modal Analysis*

Finite element model of the anonymous cupola was created in SAP2000 software [7] as shown in Fig. 6. The cupola has 4.60x4.65 meters plan dimensions, wall height of 3.60 meters and ~0.65 meters of wall thickness.

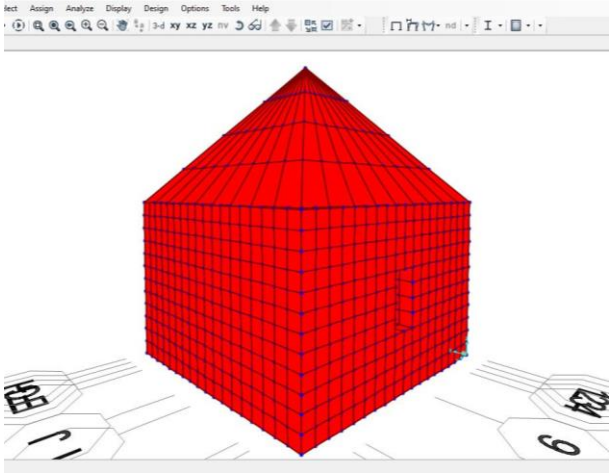


Fig. 6. Finite element model of the cupola

Walls of the cupola deserve a special attention due to their construction technique. The walls were constructed in three layers as depicted in Fig. 7. Inner and outer walls were constructed by Sivişli cut stone and the layer among is rubble. This structural state was taken into consideration during finite element modelling stage.

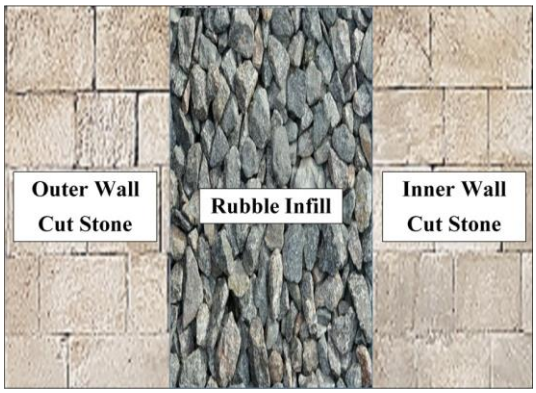


Fig.7. Schematic view of cupola wall section

Eight-node solid elements were used for modelling and macro modelling approach was adopted. Theoretical modal analysis was carried out on this model. The results of theoretical modal analysis were valued for sensor instrumentation of operational modal analysis and structural model calibration with respect to that of operational modal analysis results.

C. *Operational Modal Analysis*

Operational Modal Analysis (OMA) is also called output-only modal analysis, ambient response analysis, ambient modal analysis, in-operation modal analysis, and natural input modal analysis. A typical modal test of a structure is performed by measuring the input forces and output responses for a linear, time-invariant mechanical system. The excitation is either transient (impact hammer testing), random, burst-random or sinusoidal (shaker testing). The advanced signal processing tools used in operational modal analysis techniques allow the inherent properties of a mechanical structure (resonance frequencies, damping ratios, mode patterns) to be determined by only measuring the response of the structure without using an artificial excitation. This technique has been successfully used in civil engineering structures for in-situ estimation of modal behaviour parameters. References of [8, 9, 10, 11, 12, 13] are various examples of operational modal analysis applications.

Considering the theoretical modal analysis results; a sensor instrumentation scheme was studied. Ultra high sensitive accelerometers were mounted to the structure for measurements of structural response of the cupola to the ambient vibrations as depicted in Fig. 8.



Fig. 8. Instrumentation for acceleration response measurement of the historic cupola

Sampling and recording rate was 100 Hz. Acceleration data was processed in Artemis Modal Pro software [14]. Spectral density functions were calculated and experimental modal parameters were estimated. A general screen view from data processing with Artemis Modal Pro software is presented in Fig. 9. Furthermore, modal assurance criteria values were studied for validation of the experimental mod shapes.

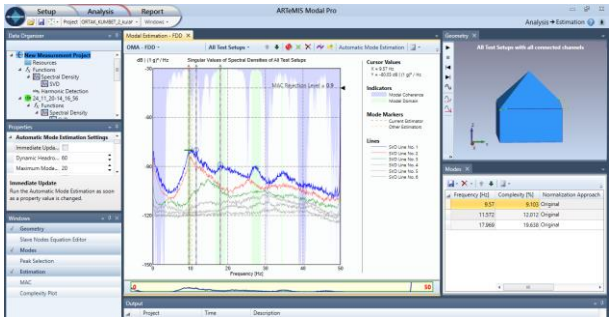


Fig. 9. Modal parameter estimation over spectral density functions

Theoretical and experimental modal behaviour parameters were compared at the final stage.

[5] RESULTS AND DISCUSSIONS

More than 150 block specimens of Sivişli stone was tested in the laboratory. Unit weight and compressive strength parameters were studied. Average test results of Sivişli stone blocks are presented in Table 1.

Table 1. Material properties of Sivişli stone

Compressive Strength (MPa)	Secant Modulus (MPa)	Tangent Modulus (MPa)	Initial Zone Slope (MPa)	Unit Weight (kN/m3)
19	1600	2100	1500	20

19 MPa of compressive strength is too low when some other natural stones like andesite and basalt are concerned [6]. Compression tests on Sivişli stone blocks were done by displacement controlled loading to estimate the behaviour after peak load. One of the stress-strain relationship behaviour of the Sivişli stone specimens is presented in Fig. 10. The behaviour is very similar with that of normal strength concrete stated in reference [15].

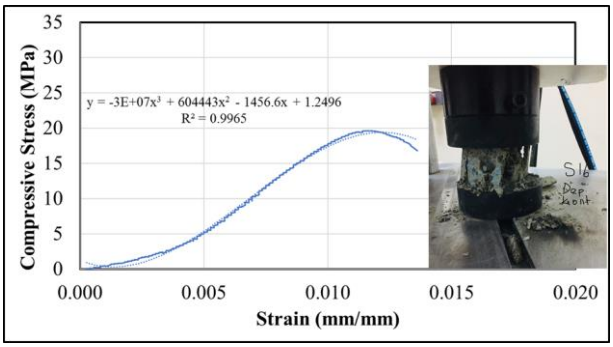


Fig. 10. Stress-strain behaviour of s Sivişli stone sample under compression

Average compressive strength of the stone was estimated to be ~19 MPa and unit weight is 20 kN/m^3. Compressive strength value was used to calculate modulus of elasticity of the inner and outer cut stone walls with respect to Turkish Seismic Code-2007 [16] and Turkish Seismic Code-2018 [17]. It should be underlined that any material tests could be done for infill rubble. Any reliable results from ultrasound velocity tests could be estimated. Hence, material properties of rubble infill were assumed as 5 MPa and 20 kN/m^3 for compressive strength and unit weight, respectively.

Experimental modal parameters were estimated over the data processing in Artemis Modal Pro software [14]. The important point in this stage is the validation of the mod shapes. A statistical indicator called modal assurance criteria was used to evaluate disparity of the mod shapes from each other. Fig. 11 shows experimental modal frequencies and related modal assurance criteria values. The values at the corners of the matrix are closer to zero while the values at the diagonal are equal to one. This means that mod shapes are independent from each other and can be valued for further steps.

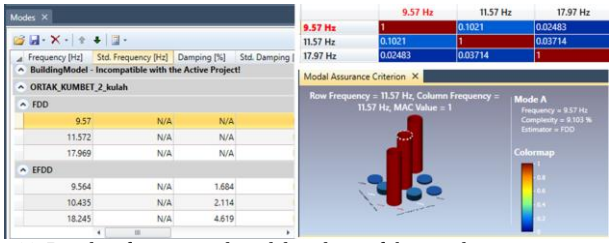


Fig.11. Results of operational modal analysis of the cupola

Before statements about comparisons of theoretical and experimental modal frequencies, it should be mentioned that theoretical and experimental mode shapes were defined to be identical in the same order. First and second mode shapes are associated with translational movements of the cupola in both perpendicular plan directions and the third one is the torsional movement around the vertical axis.

Theoretical and experimental modal frequencies are presented together in Table II. This table also shows the results of the theoretical modal analysis which adopted a trial and error process to precisely estimate experimental modal frequencies.

Table 2. Theoretical and experimental modal frequencies of the cupola

	Frequency (Hz)			
	Experimental	Theoretical		
Mode Number	OMA	Trial	TSC-2007	TSC-2018
1	9.56	9.70	30.66	59.38
2	10.44	9.84	31.11	60.25
3	18.25	15.82	50.03	96.89
4	9.56	9.70	30.66	59.38
	Modulus of Elasticity:	E=20*fk	E=200*fk	E=750* fk

Differences of theoretical modal analysis results from experimental results were calculated and presented in Table III. In both Table II and Table III, f_k is the compressive strength of Sivişli stone unit.

Table 3. Differences in between theoretical and experimental modal frequencies

	Difference in Frequency with Respect to OMA Values (%)			
	Experimental	Theoretical		
Mode Number	OMA	Trial	TSC-2007	TSC-2018
1	0.00	1.38	220.60	520.85
2	0.00	-5.71	198.17	477.40
3	0.00	-13.28	174.22	431.03
4	0.00	1.38	220.60	520.85
	Modulus of Elasticity:	E=20*fk	E=200*fk	E=750*fk

Results presented in Table II and Table III show that, theoretical modal analysis carried out on the finite element model with the material properties defined according to Turkish Seismic Code–2007 [16] and Turkish Seismic Code–2018 [17] calculated quiet high frequencies compared to operational modal analysis results. It should be pointed out that, above mentioned code requirements are not valid for historic masonry. Possible adoption of the code approaches to the historic masonry were studied by this way.

Error level in between theoretical and experimental frequencies was lowered by adopting modulus of elasticity of the Sivişli stone wall as 20 times of Sivişli stone unit compressive strength. This is a trial and error process which needs experimental results for verification.

III. CONCLUSIONS

This text provides information about the operational modal analysis of a historic Turkish cupola in Erzurum. In-situ dynamic identification of the cupola was studied, in other words. Turkey has a huge number of historic cupolas and other various historic masonry constructions. Hence, studies about historic masonry buildings by non-destructive applications are needed for condition evaluation and other structural applications. With this viewpoint, the following items can be stated as main concluding remarks of the study:

- Theoretical and experimental mod shapes of the cupola are defined to be the same
- Neither Turkish Seismic Code -2007 nor Neither Turkish Seismic Code – 2018 approaches well corresponds for historic masonry modelling for this application
- Material characterisation for Sivişli stone is ongoing for non-destructive testing.
- More operationa modal analysis studies are needed for better material characterisation / dynamic identification of historic masonry.

ACKNOWLEDGMENT

Authors present sincere thanks and gratefulness to Dr. Mahmut UÇAR, *mayor of Erzurum Yakutiye Municipality*, for his encouragement and logistical supports at the site. Cooperation and helps provided by Mr Cemal ALMAZ, *Culture and Tourism Provincial Manager of Erzurum*, made this study possible. His and his team's efforts are deeply acknowledged.

REFERENCES

[1] H. Yurttaş, H. Özkan, Z. Köşklü, Ş. Tali, D. Okuyucu, G. Geyik, M. Kındığılı, "The city where roads, waters and art meet: Erzurum", Kariyer Publications, Ankara, 2008.

[2] https://www.kulturportali.gov.tr/turkiye/erzurum/gezilecekyer/uc-kumbetler (Date of access: April 1, 2021)

[3] S. Bhattacharya, S. Nayak, S. C. Dutta, "A critical review of retrofitting methods for unreinforced masonry structures" International Journal of Disaster Risk Reduction, Vol. 7, pp. 51-67, 2014.

[4] https://deprem.afad.gov.tr/deprem-tehlike-haritasi (Date of access: April 1, 2021)

[5] S. Tozlu, "Earthquakes in Erzurum History", Proceedings of natural disasters and earthquake seminar in Anatolia throughout history", pp. 93-119, 2000.

[6] D. B. Özdoğan, "Investigation of the use of Schmidt hammer method for defintion of material properties of historical masonry structures: Application of Erzurum Kadana Mosque", MSc Thesis, Erzurum Technical University, Institute of Science, 2018.

[7] SAP2000, Structural Analysis Software, Erzurum Technical University, 2020.

[8] D. Okuyucu, "Operational Modal Analysis Application on a Single Storey Reinforced Concrete Building", Dicle University Journal of Engineering, Vol. 11-3, pp. 1407-1419, 2020.

[9] E. Şafak, M. Çelebi, "Recorded seismic response of Pacific Park Plaza. II: system ıdentification", Journal of Structural Engineering, Vol. 118, pp. 1566–1589, 1992.

[10] S. E. Aslay, D. Okuyucu, "Technical evaluation of abscissa damage of Erzincan Değirmenliköy church", Journal of the Faculty of Engineering and Architecture of Gazi University, Vol. 35-1, pp.387-402, 2020.

[11] G. Zonno, R. Aguilar, R. Boroschek, P.B. Lourenço, "Analysis of the long and short-term effects of temperature and humidity onthe structural properties of adobe buildings using continuous monitoring", Engineering Structures, Vol. 196, No.109299, 2019.

[12] R. Aguilar, M. F. Noel, L. F. Ramos, "Integration of reverse engineering and non-linear numerical analysis for the seismic assessment of historical adobe buildings", Automation in Construction, Vol. 98, pp. 1-15, 2019

[13] Y.C. Zhu, Y. L. Xie, S.K. Au, "Operational modal analysis of an eight-storey building with asynchronous data ıncorporating multiple setup", Engineering Structures, Vol. 165, pp. 50-62, 2018.

[14] Artemis Modal Pro, Operational Modal Analysis Software, Erzurum Technical University, 2020.

[15] U. Ersoy, G. Özcebe, T. Tankut, "Reinforced concrete", Middle East Technical University Press, Ankara, 1999.

[16] Turkish Seismic Code 2007, Published by Turkish Environment and Urban Ministry Disaster and Emergency Management Presidency, Official Gazette: 06/03/2007-26454.

[17] Turkish Seismic Code 2018, Published by Turkish Environment and Urban Ministry Disaster and Emergency Management Presidency, Official Gazette: 18/03/2018-30364.

Operational Modal Analysis of An Adobe Cottage

Dilek OKUYUCU
Department of Civil Engineering
Faculty of Engineering and Architecture Erzurum Technical University
Erzurum, Turkey
okuyucu@erzurum.edu.tr

Memduh Şenol ÇAVDAR
Department of Civil Engineering
Faculty of Engineering and Architecture Erzurum Technical University
Erzurum, Turkey
msenolcavdar@gmail.com

Zabiullah FAKUORI
Department of Civil Engineering
Faculty of Engineering and Architecture Erzurum Technical University
Erzurum, Turkey
zabih.safari@gmail.com

Dursun Burak ÖZDOĞAN
Department of Civil Engineering
Faculty of Engineering and Architecture Erzurum Technical University
Erzurum, Turkey
bozdoganitu@gmail.com

Burak GEDİK
Department of Civil Engineering
Faculty of Engineering and Architecture Erzurum Technical University
Erzurum, Turkey
burak.gedik@erzurum.edu.tr

Muhammet ÖZDEMİR
Department of Construction
Doğubeyazıt Ahmed-I Hani Vocational School Ağrı İbrahim Çeçen University
Ağrı, Turkey
muhammet_ozdemir25@hotmail.com

Muhammet ŞAHİN
Department of Civil Engineering Faculty of Engineering and Architecture Erzurum Technical University
Erzurum, Turkey
muhammetsahin48@gmail.com

***Abstract*— Adobe is one of the oldest construction materials of all times. It is possible to see adobe skyscrapers in Shibam-Yemen or traditional houses in Harran-Turkey. The use of adobe as a construction material is a remarkable sign of historic Karaz Culture in the Erzurum region. As a part of an archaeological reanimation project; a number of adobe cottages were constructed in Pulur (Ömertepe) Village of Erzurum by the Department of Archaeology of Atatürk University. A site study was realized on the newly constructed adobe buildings from a structural engineering point of view through the permission provided by the project team. Experimental modal behaviour parameters of one of the adobe cottages were studied in-situ. This manuscript provides information about the results of the operational modal analysis of the studied adobe cottage together with its material properties.**

Keywords*— *Adobe Structure, Karaz Culture, Erzurum, Operational Modal Analysis, Material Property

1. INTRODUCTION

Adobe is essentially a dried mud brick, combining the natural elements of earth, water, and sun. It is an ancient building material usually made with tightly compacted sand, clay, and straw or grass mixed with moisture, formed into bricks, and naturally dried or baked in the sun without an oven or kiln as shown in Fig. 1 [1].



Fig.1. Adobe making [1]

Adobe is a world-wide material. From skyscrapers in Shibam-Yemen to public houses in Şanlıurfa-Turkey, various types of adobe construction still stand and are functional as exampled in Fig. 2 from reference [2]. Adobe is a low strength material and lack of resistance against water is the most pronounced property. However, it is cheap and low level of workmanship is enough for construction. Not only for its affordable finance for all people but also for its natural and sustainable features; is adobe still a preferred construction material all over the world. Even during the Covid19 pandemic, people spend efforts to maintain their adobe constructions, *even in high seismicity areas*, as stated in reference [3]



Fig. 2. Adobe structures from Yemen and Turkey

If the topic is adobe construction, seismicity becomes the most challenging issue of its survival. Turkey is located on one of the most active seismic zones of the earth. Existing building stock in urban areas mostly consists of vulnerable reinforced concrete buildings. However, adobe structures still exist in rural areas of the country. Reference [4] provides Fig. 3 and Fig 4; which are the maps for distribution of high seismicity regions of the earth and distribution of adobe buildings across the globe.

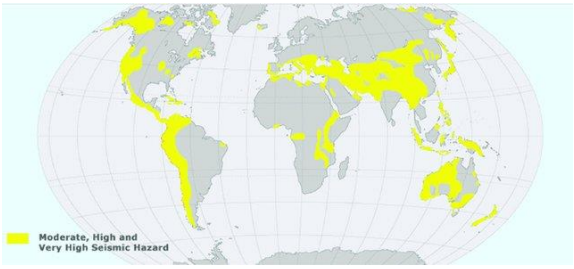


Fig. 3. Distribution of high seismicity regions of the earth [4]

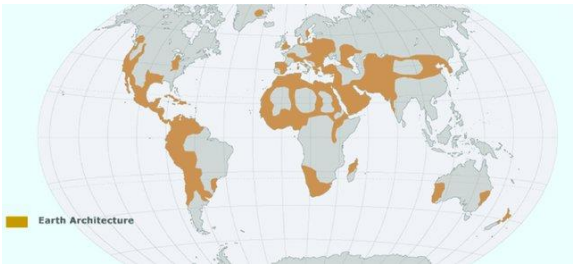


Fig. 4. Distribution of adobe buildings across the globe [4]

Fig. 3 and Fig. 4 indicate that, high seismicity regions like west coasts of South America and Anatolian part of Turkey occupy adobe building concentrations. A picture from Duygulu Village of Sivrice-Elazığ is depicted in Fig. 5. This visual material is providing a general view of the total collapse of a group of neighbouring adobe houses after January 24, 2020 Elazığ-Sivrice earthquake of Mw=6.8.



Fig. 5. Total Collapse of Adobe Structures in Sivrice Earthquake - Duygulu Village – *Courtesy of Dilek Okuyucu*

On the other hand, ruins of adobe constructions present valuable information about ancient cultures. Eastern Anatolia of Turkey is the region of important passages between east and west and north and south due to its high and rugged geography. Although settlements in this difficult geography have been seen since the Paleolithic Age, it is understood that the main organized settlements started with the Bronze Age. In this period, it is seen that a new culture including Eastern Anatolia has emerged. 4000 B.C. from the end of the 2000 B.C. This culture, which is seen in the geography extending from the Caucasus to the Euphrates, which has been active until the beginning of the thousand, is named with various names. The name of "Karaz culture" is one of the names given [5].

Karaz culture appears in Erzurum and its surroundings during the Late Chalcolithic and Bronze Age [6]. A very important feature of the Karaz culture that stands out is the *adobe architecture*. Although the architectural structures could not be fully unearthed during the excavations, it is known that there are single or double rooms with adobe walls and vertical corners [6]. Reference [7] also points out the adobe construction tradition of Karaz culture pointing out the small village occupations. Archaeological traces of the Karaz culture indicates small-scale villages (1 or 1.5 hectares) built on the slopes. Houses in these settlements are generally single-room, rectangular or round planned and they are made of adobe and the filling is made of mud; stated in reference [7].

Although Karaz culture goes back to 7000 years before, a reanimation project of Karaz culture occupations has been started by Prof. Dr. Mehmet Işıklı from Department of Archaeology of Atatürk University. The project is called "Experimental Archaeology Village". Adobe houses and related facilities of Karaz culture are planned to be constructed and exhibited in Pulur (Ömertepe) Village of Erzurum [8].

Some of the adobe houses of the project stated in reference [8] has been constructed as the first phase. A general view from site studies is presented in Fig. 8. Authors of herein manuscript joined the project for material and structural behaviour evaluation of the adobe houses.



Fig. 8. A general view from adobe houses of Experimental *Archaeology Village* project

Together with the fact that Turkey is a land of large amount of adobe structures and these structures are still being constructed in rural areas, Turkish Seismic Code 2018 banned to build adobe buildings [9]. The topic may be open to technical negotiation in almost non-seismic areas of Turkey. Since, Turkish Seismic Code 2007 allowed adobe construction and states the technical rules [10].

The research team of herein text has carried out a technical evaluation study on one of the selected adobe cottages of "Experimental Archaeology Village". Dynamic identification of the selected adobe cottage by operational modal analysis is the focus of the study.

Accessible literature provided two remarkable research examples on adobe constructions which can be linked to herein manuscript. Reference [11] focuses on the study of the short and long-term structural behaviour of existing adobe buildings through the long-term monitoring of ambient vibration and environmental conditions. With this purpose, reference [11] describes in detail the case study of the San

Pedro Apostol Church of Andahuaylillas located in Cusco, inside the Andean region of Peru, a 16th century church considered as a masterpiece of South American baroque architecture. Text finally correlates obtained results of natural frequencies of adobe church with ambient parameters, demonstrating different timescale influences in the modal properties due to daily and seasonal variations of the environmental conditions.

Additionally, reference [12] aims at presenting a methodology that integrates reverse engineering tools with a combination of advanced and simplified analytical methods to perform predictive analysis of the structural behaviour of historical adobe buildings under seismic loads. The methodology proposes the joint use of terrestrial laser scanner and photogrammetry to obtain accurate geometrical models. Validation study of the mentioned methodology was carried out on the church of San Juan Bautista de Huaro, located in Cusco, Peru from 16th century. Operational modal analysis of the historic adobe church was also done and results were compared with that of the proposed method.

Within the concept of the research, adobe material samples taken from the project site and used in cottage constructions were tested at the laboratory. Finite element model of the selected cottage was created and theoretical modal analysis was carried out. Considering the theoretical mod shapes an accelerometer instrumentation scheme was studied for operational modal analysis of the cottage. Operational modal analysis of the adobe cottage is the main topic of herein manuscript. This application was done to estimate in-situ dynamic behaviour parameters of the adobe cottage. The results of operational modal analysis were used to verify mechanical properties of adobe walls that were assigned for finite element model.

2. MATERIAL AND METHOD

The study was started by a site visit to Pulur (Ömertepe) Village to see "Experimental Archaeology Village" project [8]. The project consists of a number of single-room adobe cottages. One of them was selected for structural evaluation. Material samples were taken, finite element model of the cottage was created for theoretical modal analysis and operational modal analysis was carried out at the final stage.

A. Material Studies

A general view from project site is presented in Fig. 8, above. Adobe blocks, *mud brick* in other words, were cast in-site by the aid of villagers. Block samples were taken from the site and studied at the laboratory. Unit weight and compressive strength properties were studied. Compression tests on cubic adobe blocks were realized in a universal testing machine by applying displacement controlled loading as shown in Fig. 9.



Fig. 9. Compressive strength test of adobe block

B. Finite Elemnt Model and Theoretical Modal Analysis

Finite element model of the selected cottage was created in SAP2000 software [13] as shown in Fig. 10. The cottage has 4.60x5.45 meters plan dimensions, wall height of 2.10 meters and 0.45 meters of wall thickness. The cottage has a door opening with the dimensions of 0.83x1.73 meters.

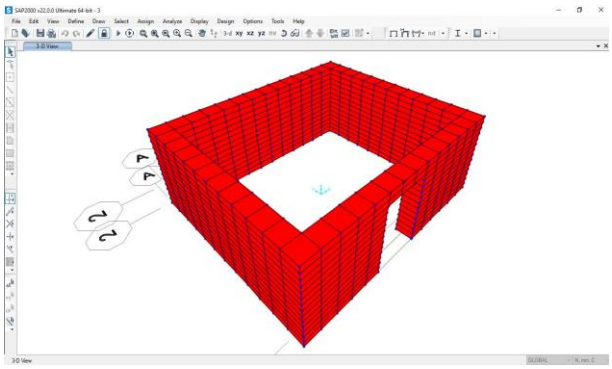


Fig. 10. Finite element model of the adobe cottage

Eight-node solid elements were used for modelling and macro modelling approach was adopted. Theoretical modal analysis was carried out on this model. The results of theoretical modal analysis were valued for sensor instrumentation of operational modal analysis and structural model calibration with respect to that of operational modal analysis results.

C. Operational Modal Analysis

Operational Modal Analysis (OMA) is also called output-only modal analysis, ambient response analysis, ambient modal analysis, in-operation modal analysis, and natural input modal analysis. A typical modal test of a structure is performed by measuring the input forces and output responses for a linear, time-invariant mechanical system. The excitation is either transient (impact hammer testing), random, burst-random or sinusoidal (shaker testing). The advanced signal processing tools used in operational modal analysis techniques allow the inherent properties of a mechanical structure (resonance frequencies, damping ratios, mode patterns) to be determined by only measuring the response of the structure without using an artificial excitation. This technique has been successfully used in civil engineering structures for in-situ estimation of modal behaviour parameters. References of [14, 15, 16, 17] are various examples of operational modal analysis applications.

Considering the theoretical modal analysis results; a sensor instrumentation scheme was studied. Ultra high sensitive accelerometers were mounted to the structure for

measurements of structural response of the cottage to the ambient vibrations as depicted in Fig. 11.



Fig. 11. Instrumentation for acceleration response measurement of adobe cottage

Sampling rate was 100 Hz. Acceleration data was processed in Artemis Modal Pro software [18]. Spectral density functions were calculated and experimental modal parameters were estimated. A general screen view from data processing with Artemis Modal Pro software is presented in Fig. 12. In addition, modal assurance criteria values were studied for validation of the experimental mod shapes.

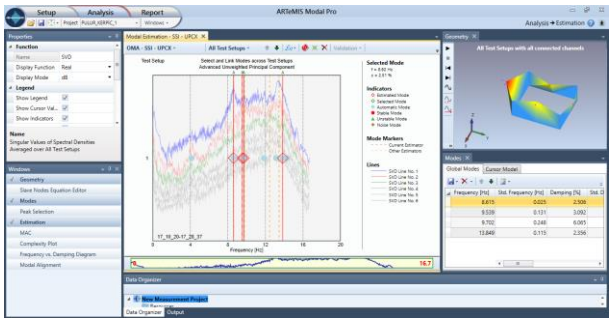


Fig. 12. Modal parameter estimation over spectral density functions

Theoretical and experimental modal behaviour parameters were compared at the final stage.

3. RESULTS AND DISCUSSIONS

Test results of adobe blocks are presented in Table 1. Average compressive strength was estimated to be ~1 MPa and unit weight is 1276 kg-f/m^3. Compressive strength value was used to calculate modulus of elasticity of the adobe wall with respect to Turkish Seismic Code-2007 [10] and Turkish Seismic Code-2018 [9]. It should be underlined that adobe construction in Turkey is banned by Turkish Seismic Code-2018 [9]. However, the equation given for elastic modulus calculation of common masonry elements; 750 times that of masonry unit compressive strength. Besides, unit weight of adobe walls was assigned to be 13 kN/m^3.

TABLE I. Material properties of adobe blocks

Spec. No	Width (cm)	Length (cm)	Height (cm)	Weight (gr)	Com. Strength (MPa)	Weight per Unit Volume (Kg/m^3)
1	9.5	10	10	1074.8	0.689	1131.37
2	9.5	9.5	9.5	1110.7	1.038	1295.47
3	9.5	9.5	9.5	1081.4	1.001	1261.29
4	9.5	9.5	9.5	1086.6	0.691	1267.36
5	9.5	9.5	9.5	1155.9	1.203	1348.18
6	9.5	9.5	9.5	1127.1	0.917	1314.59
7	9.5	9.5	9.5	1089.7	1.005	1270.97
8	9.5	9.5	9.5	1129.3	0.906	1317.16
			Av.:	1106.94	0.93	1275.80

Experimental modal parameters were estimated over the data processing in Artemis Modal Pro software [18]. The important point in this stage is the validation of the mod shapes. For this purpose modal assurance criteria was used. This is a statistical indicator which is used to evaluate disparity of the mod shapes from each other. Fig. 13 shows experimental modal frequencies and related modal assurance criteria values. The values at the corners of the matrix are closer to zero while the values at the diagonal are equal to one. This means that mod shapes are independent from each other and can be valued for further steps.

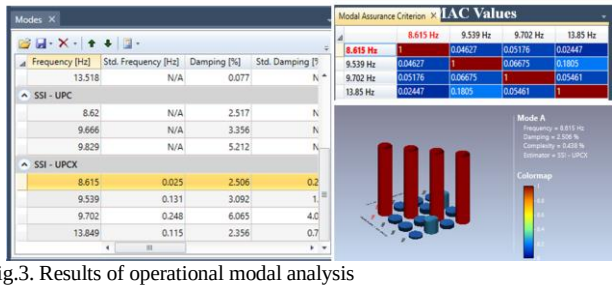


Fig.3. Results of operational modal analysis

Before statements about comparisons of theoretical and experimental modal frequencies, it should be mentioned that theoretical and experimental mode shapes were defined to be identical in the same order. First mode shape is associated with winging type opening actions of the walls. Second and third mode shapes are lateral translational movements of the cottage and fourth mode shape is another winging type opening of the walls due to out-of plane behaviour.

Theoretical and experimental modal frequencies are presented together in Table II. This table also shows the results of the theoretical modal analysis which adopted a trial and error process to precisely estimate experimental modal frequencies.

TABLE II. Theoretical and experimental modal frequencies of the adobe cottage

	Frequency (Hz)			
	Experimental	Theoretical		
Mode Number	OMA	Trial	TSC-2007	TSC-2018
1	**8.62**	8.62	8.06	15.61
2	**9.54**	9.25	8.64	16.74
3	**9.70**	10.35	9.67	18.72
4	**13.85**	11.72	10.94	21.18
	Modulus of Elasticity:	**E=230*fk**	**E=200*fk**	**E=750* fk**

Differences of theoretical modal analysis results from experimental results were calculated and presented in Table III. In both Table II and Table III, f_k is the compressive strength of adobe unit.

TABLE III. Differences in between theoretical and experimental modal frequencies

	Difference in Frequency with Respect to OMA Values (%)			
	Experimental	Theoretical		
Mode Number	OMA	Trial	TSC-2007	TSC-2018
1	**0.00**	0.06	-6.44	81.17
2	**0.00**	-3.02	-9.38	75.49
3	**0.00**	6.69	-0.36	92.95
4	**0.00**	-15.37	-21.03	52.93
	Modulus of Elasticity:	**E=230*fk**	**E=200*fk**	**E=750*fk**

Results presented in Table II and Table III show that, theoretical modal analysis carried out on the finite element model with the material properties defined according to Turkish Seismic Code – 2007 [10] provides close results to that of experimental values. Turkish Seismic Code – 2007 [10] calculates first three modal frequencies of the adobe cottage with the error less than 10% which is acceptable. Procedure followed in Turkish Seismic Code – 2018 [9] calculates quiet high frequencies compared to operational modal analysis results. In addition, error level was lowered by adopting modulus of elasticity of the adobe wall as 230 times of adobe unit compressive strength. However, this is a trial and error process which needs experimental results for verification.

4. CONCLUSIONS

This text provides information about the operational modal analysis of an adobe cottage. In other words, in-situ dynamic identification of a simple adobe construction were studied. Although new adobe constructions are banned in Turkish Seismic Code 2018 [9]; Turkey still has a large amount of adobe building stock mainly in rural areas. Hence, studies about adobe structures are needed. With this viewpoint, the following items can be stated as main concluding remarks of the study:

- Theoretical and experimental mod shapes of the cottage are found to be the same.
- Turkish Seismic Code-2007 well corresponds for adobe modelling for this application.
- Adobe ban in Turkish Seismic Code-2018 may be discussed for non-seismic areas since use of adobe in rural areas is still preferred.
- More operational modal analysis studies are needed for better material characterisation of adobe masonry.

ACKNOWLEDGMENT

Authors present sincere thanks and gratefulness to Prof. Dr. Mehmet IŞIKLI from Department of Archaeology of Atatürk University and his team for their cooperation and help which made this study possible.

REFERENCES

[1] https://www.thoughtco.com/what-is-adobe-sustainable-energy-efficient77943#:~:text=Adobe%20is%20essentially%20a%20dried,without%20an%20oven%20or%20kiln. (Date of access: April 2, 2021)

[2] http://naturalhomes.org/ (Date of access: April 2, 2021)

[3] https://www.usnews.com/news/best-states/new-mexico/articles/2021-04-03/pandemic-aid-helps-new-mexico-tribe-fix-damaged-adobe-homes (Date of access: April 4, 2021)

[4] S. Bhattacharya, S. Nayak, S. C. Dutta, "A critical review of retrofitting methods for unreinforced masonry structures" International Journal of Disaster Risk Reduction, Vol. 7, pp. 51-67, 2014.

[5] Y. Topaloğlu, "Bronze Age settlements in Erzurum and its surroundings", Turkish Studies, Vol. 11-2, pp.1193-1230, 2016.

[6] V. Ünsal, "Northern Border of Karaz Culture", Güzel Sanatlar Enstitüsü Dergisi, Vol. 16, pp.127-142, 2006.

[7] M. Işıklı, "Political borders and archeology kura-aras cultural complex and Iğdır University Archeology Department example", Turkish Journal of Ancient Near Easterne Studies, Vol. 1, pp.9-19, 2019.

[8] M. Işıklı, "Experimental Archaeology Village Project", unpublished.

[9] Turkish Seismic Code 2018, Published by Turkish Environment and Urban Ministry Disaster and Emergency Management Presidency, Official Gazette: 18/03/2018-30364.

[10] Turkish Seismic Code 2007, Published by Turkish Environment and Urban Ministry Disaster and Emergency Management Presidency, Official Gazette: 06/03/2007-26454.

[11] G. Zonno, R. Aguilar, R. Boroschek, P.B. Lourenço, "Analysis of the long and short-term effects of temperature and humidity onthe structural properties of adobe buildings using continuous monitoring", Engineering Structures, Vol. 196, No.109299, 2019.

[12] R. Aguilar, M. F. Noel, L. F. Ramos, "Integration of reverse engineering and non-linear numerical analysis for the seismic assessment of historical adobe buildings", Automation in Construction, Vol. 98, pp. 1-15, 2019.

[13] SAP2000, Structural Analysis Software, Erzurum Technical University, 2020.

[14] E. Şafak, M. Çelebi, "Recorded seismic response of Pacific Park Plaza. II: system ıdentification", Journal of Structural Engineering, Vol. 118, pp. 1566–1589, 1992.

[15] D. Okuyucu, "Operational Modal Analysis Application on a Single Storey Reinforced Concrete Building", Dicle University Journal of Engineering, Vol. 11-3, pp. 1407-1419, 2020.

[16] Y.C. Zhu, Y. L. Xie, S.K. Au, "Operational modal analysis of an eight-storey building with asynchronous data ıncorporating multiple setup", Engineering Structures, Vol. 165, pp. 50-62, 2018.

[17] S. E. Aslay, D. Okuyucu, "Technical evaluation of abscissa damage of Erzincan Değirmenliköy church", Journal of the Faculty of Engineering and Architecture of Gazi University, Vol. 35-1, pp.387-402, 2020.

[18] Artemis Modal Pro, Operational Modal Analysis Software, Erzurum Technical University, 2020.

A Product Improvement Story for Lightweight Pumice Blocks

Zabiullah FAKUORI
Department of Civil Engineering
Faculty of Engineering and Architecture Erzurum Technical University
Erzurum, Turkey
zabih.safari@gmail.com

Memduh Şenol ÇAVDAR
Department of Civil Engineering
Faculty of Engineering and Architecture Erzurum Technical University
Erzurum, Turkey
msenolcavdar@gmail.com

Dilek OKUYUCU
Department of Civil Engineering
Faculty of Engineering and Architecture Erzurum Technical University
Erzurum, Turkey
okuyucu@erzurum.edu.tr

***Abstract*—This manuscript provides information about a product improvement study for lightweight pumice blocks which are used for infill wall construction. Lightweight pumice blocks are commonly called by its German equivalent; *bims blocks*. A company located in Erzurum; called Kale Blokbims is one of the pioneering producers and exporters of bims blocks in East Anatolia region of Turkey. Herein study was carried out upon the request of the company in order to find technical answers to the questions of the producer. Main questions of the producer were about the undesired increase in bims block weights and worsening of the block appearances. Starting from the pumice quarries of the factory, a comprehensive research was carried out to find the technical answers and create solutions to the product problems. The variety in pumice sieve analysis was studied, reasons for increase in bims block weight were defined, and a computer software was created for calculation of mix design considering the specific gravity coefficient of the aggregate for different water content levels. The suggestions and calculations were verified over the bims block specimens produced for more than 55 mix designs.**

Keywords—Pumice, bims block, infill wall, product improvement, experimental study

[1]. INTRODUCTION

Turkey is located on one of the most active seismic zones of the earth [1]. Existing building stock mostly consists of vulnerable reinforced concrete buildings which are in need of either strengthening or renewal. Public authorities provide technical and financial supports to proprietors for reconstruction of their vulnerable buildings through urban renewal projects [2]. These seismic risk reduction activities end up with huge numbers of new building construction works. Hence, reinforced concrete frame structures currently appear to be the most common construction practice in Turkey. Meaning that, demand for the reinforced concrete construction materials with all its components shows an increasing trend. This situation is directly linked to the topic of the herein study.

Reinforced concrete frame structures are constructed with openings and these openings are filled by infill wall elements in order to create private living areas. The most commonly preferred infill wall materials may be stated as hollow clay bricks, autoclaved aerated concrete blocks and lightweight pumice concrete blocks. The latter has an increasing attention and demand in the market; especially in the last decade. Because, the lightweight pumice concrete blocks, so called *bims blocks*, provide thermal and acoustics insulation like hollow clay bricks and less additional weight to the structure. Therefore, it becomes a preferred infill wall material [3]. A general view of bims blocks is presented in Fig.1. These kinds of products should satisfy the requirements of Turkish standard coded TS EN 771-3+A1 [4].

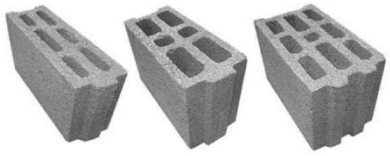


Fig. 1. General view of bims blocks

Long before Christianity, pumice (bims) mine was reported to be first used by the Greeks and then it was used by the Romans. Utilization of pumice in the magnificent buildings of the ancient Greeks and Romans many can still be observed. Pumice was used in the construction of Roman walls, water channels, and in many more monumental buildings. Use of pumice in the form of graded aggregate as a construction material dates back to 1851 in California State of United States of America. Turkey produces pumice ~1.5000.000 tons per year and almost all is used in construction industry [3].

Pumice aggregate, *a volcanic activity product*, is the raw material of bims blocks. Also reflecting the existence of pumice quarries Fig.2 shows a general distribution of bims blocks producing large scale factor distribution across Turkey.



Fig. 2. Distribution of bims block manufacturing large scale factories in Turkey [3]

One of the large scale bims block producing factories is Kale Blokbims Company; located in Pasinler, Erzurum. The factory produces bims blocks for various purposes such as infill wall production or insulation material for underground electricity lines. Chemicals for structural applications are the other products. The company produces bims blocks in accordance with Turkish standard coded TS EN 771-3+A1 [4]

The company got in touch with the authors and requested answers and solutions to some of their technical problems in bims block productions. The problems were stated as below:

- The bims blocks weights more than before.

- The outer appearance of the bims blocks receives a lot of criticism.
- Increase in cement consumption becomes remarkable.

A comprehensive study was carried to find technical answers to the above mentioned questions of the producer. Kale Blokbims became the petitioner and supporter of the project. Details of the research are presented in the following parts.

[2] MATERIAL AND METHOD

The research was first started by a series of factory visits and site inspections. A general view of factory depots and a bims block product label are shown in Fig. 3. The product label presented in Fig. 3 provides various technical information about the bims blocks among which unit weight and compressive strength properties are related with civil engineering profession.

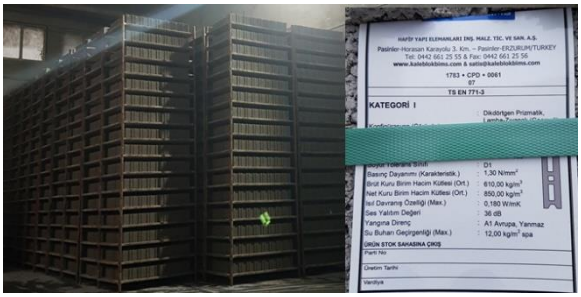


Fig.3. General view of factory depot and a product label

The methodology of the research was planned and realized in the following order.

- Pumice quarry and factory visits
- Pumice sample taking and analysis
- Bims block sample taking and analysis of current production
- Search for necessity of washing 0-5 mm fine pumice aggregate
- Prism sample production at the laboratory
- Bims block production at the laboratory
- Bims block production at the factory
- Creation of production and quality control processes

Each step is summarized below.

A. *Pumice Quarry and Site Visits*

Factory supplies pumice aggregate from its own quarries which are ~10 kilometres away from the production facility. Pumice reserve of the currently operated quarries were mentioned to be ~100 years that make the factory investment quiet affordable. Pumice in quarry already exists in aggregate form. However, high amount of fine pumice, *may be called as powder*, took attention. Furthermore, the distribution of small size obsidian particles was also remarkable.

B. *Pumice Sample Taking and Analysis*

Pumice is supplied from the quarry and carried to the factory site. This raw material is sifted below 16 mm sized sieve. The aggregate smaller than 16 mm in size is directly sent to bims production whereas larger particles are directed to the crusher. Pumice aggregate is weighted in a bunker as shown in Fig. 4 and then moved to mixing chamber for cement and water addition.


Fig. 4. Pumice aggregate in bunker just before mixing

In order to study the composition of pumice aggregate used in bims block production; aggregate samples were taken from bunker, as shown in Fig. 4, and analysed in the laboratory. This application was repeated for more than 40 times. Unit weight, specific gravity factor, water absorption capacity, gradation, etc. were studied. Additionally, larger pumice rock blocks were found and specially cut for material investigation like definition of compressive strength.

C. *Bims Block Sample Taking and Analysis of Current Production*

The main problems stated by the company were witnessed over the products. Some of the randomly selected bims blocks weighted more than 850 kg-f/m^3 which is the official declaration on product label. Non-homogenous views of products were remarkable. Randomly selected bims blocks were subjected to compression tests as depicted in Fig. 5 and average compressive strength was defined to be ~3.5 MPa which is higher than 1.3 MPa stated on label.


Fig. 5. Compressive strength test on bims block

D. *Search for Necessity of Washing 0-5 mm Fine Pumice Aggregate*

Sieve analysis of pumice aggregate used for bims block production showed that more than ~40% of the aggregate has the size less than 1 mm. This huge amount of very fine aggregate is reported to be observed in recent months. This may be one of the reasons for the undesired increase in block weight and cement consumption. Company wanted to know about the efficiency of separation of the very fine aggregate by wet sieving. If the wet sieving is done; utilisation of the new product, *very fine pumice aggregate*, was appeared to be another research and development project.

It should be underlined that, factory was directly using the pumice aggregate size of which is less than 16 mm. No

gradation is applied. Research team worked on gradation; 0-4 mm, 4-8 mm, 8-12 mm for a better product generation and maintaining the quality. Considering the current situation; a series of aggregate washing was done to evaluate the efficiency of wet sieving. First, whole raw aggregate was washed and gradation was studied. In the second application, aggregate was subjected to dry sieving and only 0-4 mm particles were subjected to washing. In the third application; 0-4 mm and 4-8 mm particles were washed while 8-12 mm particles were subjected to dry separation. These group of aggregates were used in prism and block production in the laboratory and then factory.

E. Prism Sample Production at the Laboratory

Research team and factory staff decided to work on gradation based mix designs for bims block production. This might result in decrease in both block weight and use of cement. Furthermore, maintaining the quality would be possible and easier by this way. Another problem was worsening outer appearance of blocks. A well-studied gradation might end up with better outer appearances. Before studying for above mentioned cases on bims blocks; a series of prism samples were produced over more than 80 different mix designs as exampled in Fig. 6. Parameters like aggregate washing protocol and amount of cement utilized were first studied on prism specimens as shown in Fig. 6. These products mainly provided solutions for a better outer appearances of bims blocks.



Fig. 6. An examples from prism block specimens,

F. Bims Block Production at the Laboratory

Prism block production studies helped to eliminate a group of mix designs; ~20 different recipes. Then, a single block making machine of old times was brought to the laboratory and single bims blocks were produced for an improved technical evaluation including block compression tests. Fig. 7 shows a general view from single bims block productions at the laboratory.



Fig.7. Single bims block productions at the laboratory

A question may arise for this situation: "*Why did not you make the production at the factory?*". During this study, all five of bims production facilities were functional for 24 hours per day. Hence, it was not possible, logical and economical to cut the regular production by a time consuming research application. Therefore, single bims block specimens were produced at the laboratory and studied for unit weight, outer appearance, compressive strength and amount of cement utilisation. At the end of this phase, a group of mix designs were also eliminated and the time attained in a suitable period of factory with 16 hours of working per day. Hence, the research team had 8 hours of working time at night for mix design trials at the factory.

G. Bims Block Production at the Factory

Total of 55 different mix designs were studied at the factory. ~150 specimens were produced for each recipe. Randomly selected 10 specimens were taken from each group and transported to the laboratory. 3, 7 and 28 days of compressive strength and unit weight parameters were studied and compared with that of the results from regular factory productions. A general view from laboratory studies of this stage is presented in Fig. 8.



Fig. 8. General view of experimental study on final products

H. Creation of Production and Quality Control Processes

Studies continued over 5 months time and products of the research were created and delivered to the company. Two computer software with user friendly interfaces like spreadsheets were produced. The first one helps to find the the most appropriate mix receipe relying on the the desired parameter. For example, the lightest bims block or the block with highest compressive strength. Second software helps to calculate the amounts for the aggregate groups to weight. This stage is very important since; the water content of pumice is higly variable. Hence, specific gravity factors of fine (1-4 mm), mid-size (4-8 mm) and coarse (8-12 mm) aggregate groups for different water content levels become decisive.

[3] RESULTS AND DISCUSSIONS

This comprehensive research created a huge amount of experimental and observational data. Hence, the summary of the most important parts is presented and evaluated in this text. Being as one of the most remarkable observations; existence of obsidian and gabbro type particles as shown in Fig. 9. provided an initial answer for the increase in bims block weight.



Fig.9. Obsidian and gabbro particles existing in pumice aggregate

These particles constitutes ~5-7% of the raw pumice aggregate of the current level of the quarry. It was not found to be economical to establish a separation system for these heavy particles. Meaning that, factory will continue bims block production by using the aggregate including obsidian and gabbro. Hence, this weight-increasing factor could not be eliminated.

On the other hand, sieve analysis over more than ~40 samples taken from the bunker just before the mixing showed that ~40% of the pumice aggregate is smaller than 1 mm. Furthermore, common distribution of fine pumice aggregate was defined to be ~80% of (0-1 mm) and ~20% of (1-4 mm). Experimental studies provided that, this powder size particles were increasing the bims block weight, need for cement and deteriorating the bims block surfaces during the separation of the wet block from the mould due to flocculation of the fine particles. Studies showed that this huge amount of fine aggregate is not earth or clay; it is pumice powder with slight inclusion of surface earth. Separation of fine pumice aggregate under 1 mm size was decided to be necessary for product quality and satisfaction with the requirements of the Turkish standard TS EN 771-3+A1 [4]. The experimentation on separation type of fine pumice aggregate showed that only fine aggregate (0-4 mm) is enough to be washed to eliminate the particles with the size less than 1 mm. Washing whole raw material before sieving was not found to be economical and efficient. Environmental factors affecting the construction of huge washing facilities also appeared to be struggling. Finally it was decided to make dry sieving of raw pumice aggregate into three groups as fine (0-4 mm), mid-size (4-8 mm) and coarse (8-12 mm). In the second stage fine pumice aggregate (0-4 mm) was decided to be washed to eliminate the particles smaller than 1 mm. Final aggregate groups were decided to use for mix designs of bims blocks in order to maintain the product quality. During the mix proportion phase; the average natural size distribution of the quarry became the main reference. Any application disturbing the natural aggregate distribution of the quarry may result in waste aggregate production and create extra demand for any size of aggregate.

Table 1 summarizes bims block test results for the studied production parameters.

Table I. Summary of bims block test results

Product Information	**Compressive Strength**	**Unit Weight**	**Cement Utilisation: CEMI-42.5/R**	**Appearance**
	(MPa)	**(kg-f/m^3)**	**(% of Total Aggregate Weight)**	**(Customer Opinion)**
Declaration of Factory to the Customer	1.3	850	-	-
Production of Factory Team at the Factory	~3.8	~1200	15	Not Fine
Production of Research Team at the Laboratory	~2.9	~800	11	Pretty Much Better
Production of Research Team at the Factory	~3.0	~1000	11	Pretty Much Better

As seen in Table 1, final production of the research team decreased the unit weight of the blocks and cement utilisation when compared to that of current factory production. Production by use of three groups of pumice aggregate with appropriate mix proportions and separation of fine pumice aggregate from the material decreased the need for cement and improved the visual quality of the products. However, the decrease in unit weight is still not satisfying. Final unit weight is ~1000 kg-f/m^3 while the declaration is 850 kg-f/m^3. Improper dry sieving at the site may be the reason for this since; the same proportions provided is ~800 kg-f/m^3 of unit weight for the laboratory productions.

Current factory practice uses cement by 15% of total aggregate weight. Use of mix proportions for a proper grading and elimination of fine pumice resulted in cement use for 11%.

Compressive strength of pumice rock samples were experimentally found to be 2.85 MPa, in average. The final bims block production ended up with ~3 MPa of compressive strength which satisfies the declaration of the company. Hence, decrease in cement utilisation did not create an adverse effect on compressive strength. It also provides a considerable amount of financial and environmental gain.

III. CONCLUSIONS

This study has been carried out for improvement of bims block products of Kale Blokbims Company. Main problems were the increase in unit weight of blocks and cement consumption and worsening of product outer appearances. Following technical advices were delivered to the Company:

- Utilization of raw pumice aggregate directly taken from the quarry is out of gradation control. This results in quality problems. Hence, use of mix proportions with appropriate gradation is a must for quality control measures.

- Fine pumice (0-4 mm) pumice should be washed to decrease the unit weight and cement consumption and to improve the appearence of products.

- Studies are needed for use of (0-1 mm) ultra fine pumice aggregate; otherwise a new waste product will be created.

- If mix proportions with appropriate gradation of the aggregate is used together with washed fine pumice, utilisation of cement will be lower; from 15% to 11% of total pumice aggregate weight.

At the end of the research, two computer software were presented to the company. Among them, one helps to find the best-fitting mix proportion over the related parameter and second one calculates the amounts of materials to be weighted considering their specific gravity factors.

ACKNOWLEDGMENT

Mr. Ethem TANRIVER deserves huge thanks and gratefulness for his supports. Authors present sincere thanks to Dr. Babak Karimi Ghalehjough for his kind help and guidance for clay material diagnosis studies. Contributions of Mr. Hasan AYDIN, Mr. Adem KOTAN, Mr. Nazım BİLİCİ, Mr. Aşkın DÜNDAR and efforts of Kale Blokbims factory staff are deeply acknowledged.

REFERENCES

[1] S. Bhattacharya, S. Nayak, S. C. Dutta, “A critical review of retrofitting methods for unreinforced masonry structures” International Journal of Disaster Risk Reduction, Vol. 7, pp. 51-67, 2014.

[2] Law No. 6306 on Transformation of Areas Under Disaster Risk, Official Gazette: 31/05/2012-28309.

[3] Turkish Soil Industry Council of Turkey Chambers and Commodity Exchanges Union, Bims (pumice) Sub-sector report, Published by Bims Industrialists Association, September, 2006.

[4] TS EN 771-3+A1: Specification for Masonry Units – Part 3: Aggregate concrete masonry units (Dense and lightweight aggregates), Published by Turkish Standards Institute, August, 2015.

The Process of Developing A New Lintel Product Using Pumice: First Stage

Kübra YILMAZ
Department of Civil Engineering
Faculty of Engineering and Architecture Erzurum Technical University
Erzurum, Turkey
kk.yilmaz123@gmail.com

Zabiullah FAKUORI
Department of Civil Engineering
Faculty of Engineering and Architecture Erzurum Technical University
Erzurum, Turkey
zabih.safari@gmail.com

Memduh Şenol ÇAVDAR
Department of Civil Engineering
Faculty of Engineering and Architecture Erzurum Technical University
Erzurum, Turkey
msenolcavdar@gmail.com

Dilek OKUYUCU
Department of Civil Engineering Faculty of Engineering and Architecture Erzurum Technical University
Erzurum, Turkey
okuyucu@erzurum.edu.tr

Burak GEDİK
Department of Civil Engineering Faculty of Engineering and Architecture Erzurum Technical University
Erzurum, Turkey
burak.gedik@erzurum.edu.tr

***Abstract*—This manuscript provides information about the first stage of a research and development study for a new lightweight lintel production. A local company located in Erzurum, Turkey and called Kale Blokbims is the petitioner and supporter of the project. The study was designed to supply lintel demand of company's customers. In order to design a factory production process and high quality lintel products; an experimental study was carried out. The products which satisfy the requirements of TS EN 845-2+A1 were produced and tested. Lightweight pumice aggregate and waste obsidian of the plant were used to cast lightweight concrete and various types of reinforcement was studied. At the end of the first stage of the research; welded reinforcement connections were found to be inefficient and mechanical connections with wires were decided to be used for the following stages.**

Keywords—lintel, pumice, lightweight concrete, connection type, obsidian

[1] INTRODUCTION

Buildings consists of structural or non-structural elements. In case of reinforced concrete structures frame elements like beams, columns, etc. are defined as load bearing elements whereas infill walls are assumed to be non-structural. The situation is somehow different for masonry structures since walls are the main load carrying structural components. Either in framed structures or masonry buildings; door and window openings should be placed on the walls. Creation of openings on the walls is possible by use of a structural element called *"lintel"*.

A lintel is a beam placed across the openings like doors, windows etc. in buildings to support the load from the structure above [1]. The width of lintel beam is equal to the width of wall, and the ends of it are built into the wall. Fig. 1. shows lintel applications in a masonry structure. The picture is taken from reference [2]. In the picture, a two-span concrete lintel is used to create door openings for the front facade of the masonry building. Three concrete lintels are visible on the right side wall for window openings. All lintels are loaded by the masonry above them. Hence, lintels are accepted as structural elements.



Fig.1. Lintel applications [2]

Lintels are load bearing elements that allow to create the openings in masonry/infill walls. In the past, the width of wall openings was limited to the length of available materials, as seen, in Fig. 2, in the example of single-stone lintels.



Fig. 2. Use of single-stone lintel in Emir Saltuk Cupola, Erzurum-Turkey

The invention of masonry arch lintels allowed to extend the span of the lintels used. The properties of arch lintels were studied mostly by the Romans. However, the invention was not made by them. The first arch lintels were created by ancient Greeks around 1st century B.C. The longest lintels found in Greece were 6 m in span. Development of technique and knowledge allowed Romans to extend the span up to 40 m; as stated in reference [3]. Invention of arch

lintels allowed to introduce elements that carry compressive stresses reducing the influence of tensile stresses.

Another major development that allowed to increase span of lintels is invention of *reinforced concrete* method. Reinforced concrete was invented during the second half of the 19th century [4]. Besides the need to substitute wood for gardening and recreational use, the main driver was the need for an economic and fireproof building material. The development of modern cement and steel during the first half of the 19th century made this invention possible. Reinforced concrete allowed to span longer distances not only for beams but also for lintels.

Lintels are classified based on their material of construction. Timber lintels, stone lintels, brick lintels, reinforced brick lintels, steel lintels, reinforced concrete lintels can be stated as lintel types by material. Each of them finds area of use in urban and rural construction applications.

As also mentioned above; openings for doors, windows or cupboards etc, must be bridged over by some means to support the masonry/infill wall above. The support to the load above the opening is usually given by providing an arch or a lintel. Lintel acts like a beam and transfers the vertically to the supporting walls. The end of lintel are built into the wall so as to convey the weight carried by them to the masonry in jambs. The amount of bearing which the supports provide for the ends of lintel is an important factor. Since, this bearing length should be minimum 200 mm for masonry buildings according to Turkish Seismic Code 2018 [5].

Since the invention of reinforced concrete construction technique as well as use of steel for production of whole frame elements; the construction time became shorter by creating increasing demands of huge amounts of construction materials. In this era, factory production of building materials became the only solution to supply the demands of construction sector. Cement, infill/masonry wall materials, structural chemicals, etc. can be stated as the materials that the construction sector mostly demands.

In this situation, authors give special attention for infill wall materials. Reinforced concrete frame structures are constructed with openings and these openings are filled by infill wall elements in order to create private living areas. The most commonly preferred infill wall materials may be stated as hollow clay bricks, autoclaved aerated concrete blocks and lightweight pumice concrete blocks. The latter has an increasing attention and demand in the market. Because, the lightweight pumice concrete blocks, so called *bims blocks*, provide thermal and acoustics insulation like hollow clay bricks and less additional weight to the structure [6]. Therefore, it becomes a preferred infill wall material.

One of the large scale bims block producing factories is Kale Blokbims Company; located in Pasinler, Erzurum. The factory produces bims blocks for various purposes such as infill wall production or insulation material for underground electricity lines. Chemicals for structural applications are the other products. The company products are mainly supplied to East Anatolia Region and also exported to neighbouring countries like Georgia. Authors carry out some research and development project with the company. The customers of the company demands the factory to supply prefabricated lintel elements. Since the customers buy bims blocks, mortar mixes and other structural chemical from the same hand; the materials necessary for infill wall construction. As the only missing element; the customers strongly demand ready-made lintel products for wall and door openings. Hence, all materials and elements necessary for infill wall construction can be supplied all together.

As common practice of lintel production, reinforced concrete lintels are produced in site with the lack of production control. It is also a time consuming process for site administration. As another solution, steel profiles mostly without corrosion precaution are preferred due to ease of supply.

Considering the demand of the sector, technical properties of the facilities and raw material supply of the company; a research and development project was started for reinforced lightweight concrete lintel production. Turkish standards of TS EN 845-2+A1: Specification for ancillary components for masonry - Part 2: Lintels [7], TS EN 846-9: Methods of test for ancillary components for masonry - Part 9: Determination of flexural resistance and shear resistance of lintels [8], TS EN 846-11: Methods of test for ancillary components for masonry- Part 11: Determination of dimensions and bow of lintels [9] were studied first. It was concluded that current standards for lintel production in Turkey allows use of lightweight concrete. This is the most important point. Since, the company has pumice aggregate quarries in function and the sector demands lightweight lintel elements.

Company supplies pumice aggregate from its own quarries that are ~10 km away from the factory campus. The factory has facilities of crushing and screening of pumice aggregate as shown in Fig. 3.



Fig. 3. A general view from factory site

Kale Blokbims factory also produces chemicals for structural applications. Unfortunately, this part of factory has created huge amounts of obsidian and perlite mixture in dry form. This mix material can be assumed as fine aggregate by size (0-4 mm) and covers a large area on the site as shown in Fig. 4.



Fig. 4. A general view of obsidian and perlite mix at the site

A comprehensive literature survey was carried out for academic point of view in addition to market surveys and feasibility studies. A very limited number of studies on reinforced concrete lightweight concrete lintels were found. Furthermore, it should be underlined that branded lintels are commercial products and their technical details are intellectual products and trade secrets. Among the accessible literature, reference [10] can be linked to the project. The manuscript provides information about lightweight precast lintel tests from Poland.

The project, *which is the topic of herein text*, has been planned to create a production facility of reinforced lightweight concrete lintels in Kale Blokbims Campus and produce reinforced concrete lightweight lintels. Studies of search for lintel demand in the market, pumice quarry check for a sustainable raw material supply, feasibility reports for lintel production process were mainly done by the factory staff. Authors took responsibility of technical research like material studies and initial specimen tests for decision of reinforcement type as the first phase and being the second stage; full-scale lintel productions for bending and shear capacity tests and creation of production and quality control processes which is compulsory according to reference [7].

This manuscript provides information about first phase technical studies for the development of a new reinforced lightweight concrete lintel product to be produced and supplied by Kale Blokbims Company of Erzurum, Turkey.

[2] MATERIAL AND METHOD

First phase of the project's technical part aims at defining the proper steel reinforcement and lightweight concrete mix designs. Details of this phase studies are presented below.

A. Material Studies

Lintels are load bearing elements like beams. These elements are subjected to distributed loads by the part of the wall above. Lintel behaviour under flexure and shear should be studied and experimentally proved according to reference {7]. Longitudinal and transverse reinforcement should be well studied for these types of structural elements.

Considering possible load levels together with minimum section sizes; Ø4 deformed bars were found to be appropriate as longitudinal and transverse reinforcement. However, Ø4 size reinforcement could not be supplied during Covid19 pandemic. Hence, the next one-Ø5 was selected and used for the study.

Tensile test specimens of Ø5 reinforcement were prepared in two different groups. The first group consisted of regular bar specimens whereas specimens of the second group were prepared with application of point welding. Effects of point welding on tensile behaviour of the rebar were studied. Because, welding was an option of for connection of longitudinal and transverse reinforcement. Point welding at the connections of the bars might affect mechanical properties of the steel. Tensile tests or rebars were carried out in High Technology and Research Centre of Erzurum Technical University. Displacement controlled loading was applied to the specimens. A general view form rebar tests is presented in Fig. 5.

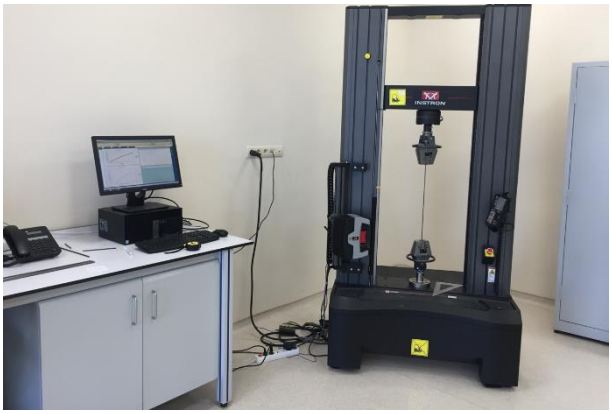


Fig. 5. Rebar tensile testing system

Second material component of the lintels is the lightweight concrete. Company has its own pumice quarries and a huge amount of fine obsidian/perlite mix as depicted in Figure 6. Hence, two different concrete mix design groups were studied. The first group consisted of pure pumice concrete recipes and the second group included obsidian/perlite aggregate in addition to pure pumice.

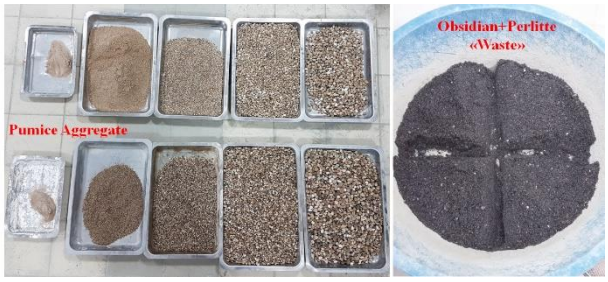


Fig. 6. Aggregate used for lightweight concrete production

CEMI 42.5-R type cement was used for concrete production. This is the regular cement that the factory uses for bims block production. Several groups of concrete specimens were produced and tested at 7 and 28 days prior to casting.

B. Studies for Reinforcement Type Decision

This stage of the research primarily focused on connection type of transverse and longitudinal steel. There were two options: wired or welded connections. Both of them were studied for rectangular and triangular stirrups. Stirrups were produced in two ways: one piece or connection of short bars by welding. A general view of rebar used in lintel specimen productions is presented in Fig. 7.

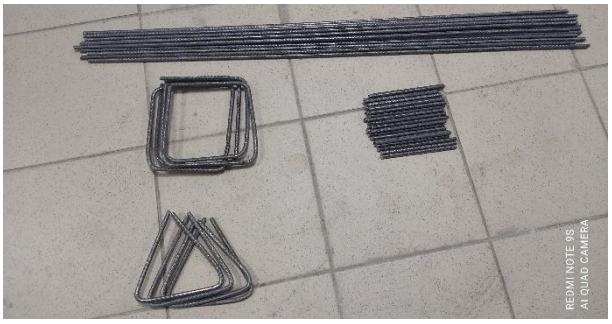


Fig. 7. Ø5 reinforcement used in test specimen production

Lintels are the load bearing elements forced by low-level of distributed loads. Hence, compression steel is commonly not needed for moment carrying capacity. It functions like hanger bars. So, one rebar in compression zone could be enough for structural safety and as well as economy. Therefore, rectangular and triangular stirrups were used for double or single compression reinforcement, respectively. Reinforcement cage examples are presented in Fig. 8.

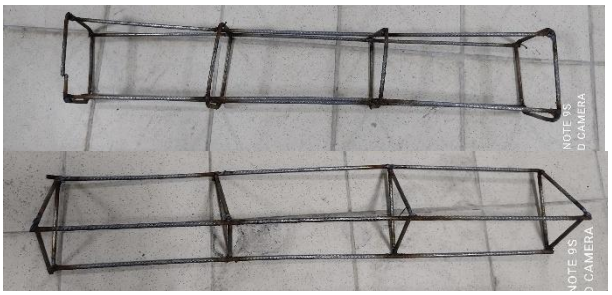


Fig. 8. Reinforcement cage examples of lintels

Considering the results of lightweight concrete material results, two mix designs were selected and used for lintel production. The first recipe includes 10% of obsidian/perlite aggregate with cement/aggregate ratio of 0.22. Second recipe is a pure pumice concrete with cement/aggregate ratio of 0.32. Lintels had 150x150x1000 mm dimensions. A general view from lintel production is presented in Fig. 9.



Fig. 9. Lintel production at the laboratory

Lintels were tested at 28 days after casting. The simply supported specimens were subjected to point loading at the midspan. Load-midpoint deflection curves for studied for performance evaluation. A general view from lintel tests is shown in Figure 10.



Fig. 10. Lintel test view

[3] RESULTS AND DISCUSSIONS

Tensile test results of the rebar for the selected two specimens are presented in Fig. 11. Stress-strain behaviour of both welded specimens did not show a yielding plateau. ~600 MPa can be assumed as proportional limit / yield strength for both specimens. Point welding negatively affected the energy dissipation capacity of the rebar.

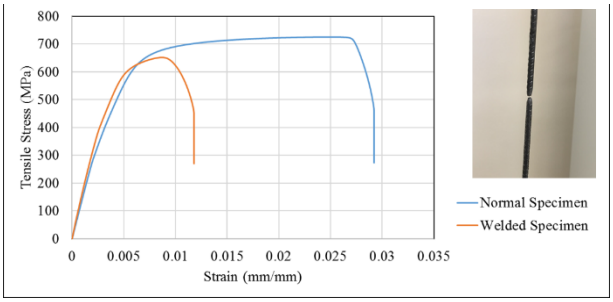


Fig. 11. Ø5 rebar tensile test results

Turkish standard for lintels [7] allows using lightweight concrete for lintel production and rules to satisfy the requirements of TS EN 206 + A2: Concrete - Specification, performance, production and conformity [11]. According to reference [11]; minimum characteristic compressive strength for lightweight concrete should be 8 MPa. Table 1 summarizes the result of lightweight concrete production studies.

Table 1. Summary of lightweight concrete studies

Mix Proportions by Weight				Cement /Agg.	Unit Weight Kg-f/m3	Compressive Strength (MPa)	
Opsidian (%)	Pumice (%)						
0-4 mm	1-4 mm	4-8 mm	8-12 mm			7 Days	28 Days
0	60	20	20	0.32	1117	6.2	9.5
0	40	40	20	0.22	1003	3.2	4.9
0	40	40	20	0.32	1114	4.6	7.1
100	0	0	0	0.25	1810	7.5	11.5
40	0	40	20	0.25	1545	9.3	14.3
30	10	40	20	0.22	1319	8.8	13.5
30	10	40	20	0.32	1385	11.2	17.2
20	20	40	20	0.22	1162	3.9	6.0
20	20	40	20	0.32	1361	12.1	18.6
10	***30***	***40***	***20***	***0.22***	***1206***	***7.1***	***10.8***
10	30	40	20	0.32	1230	10.5	16.1
20	20	40	20	0.22	1081	4.7	7.2
0	50	40	10	0.22	897	3.1	4.8
0	***30***	***50***	***20***	***0.32***	***1030***	***5.2***	***7.9***
0	30	50	20	0.22	941	3.3	5.0

Concrete test results presented in Table 1 shows that, some of the pumice concrete mixes with and without obsidian/perlite aggregate can satisfy the minimum requirements of lightweight concrete stated in reference [11]. Use of obsidian/perlite aggregate increases unit weight of concrete. However, it also allows producer to use less amount of cement to cast lightweight concrete. Pure pumice concrete mixes provided a group of successful choices for lintel applications. Among all, the series emphasized by red bold colouring in Table 1 were used for lintel specimen productions.

The final stage of the first phase studies consisted of lintel tests. Lintels with miscellaneous reinforcement cage and two groups of lightweight concrete were tested under single point loading. Load-deflection curves of the specimens are presented in Fig. 12.

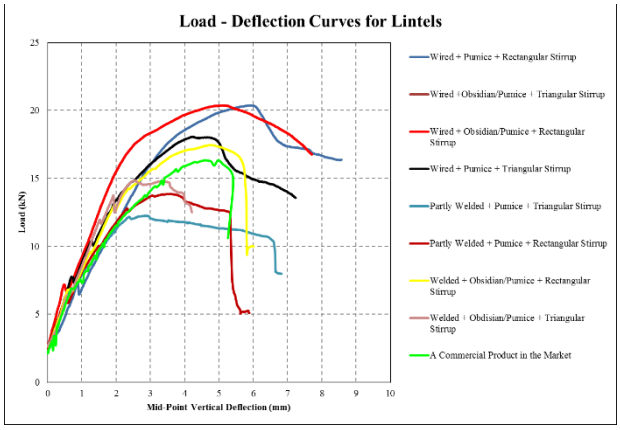


Fig. 12. Load-displacement curves for lintels

Reference [7] clearly states that the producer should design and produce lintels according to technical requirements of the customer. Also, reference [7] does not state any load or deflection limit for lintel elements. Therefore, lintel performances are compared among themselves.

Fig. 12 clearly show superior behaviour of lintels having rectangular stirrups with wired connections. Both of the mentioned specimens either with obsidian/perlite addition or pure pumice concrete reached the same load bearing capacity of 20.3 kN. Lintel having triangular stirrups which were produced by partly welding of short pieces provided 12.2 kN of load bearing capacity. Welded connections clearly provides lower load bearing capacity and energy dissipation than that of the wired connections.

[4] CONCLUSIONS

This manuscript provides information about the first phase of a new lightweight lintel production project. Experimental studies provided the concluding remarks below:

- Lightweight concrete for lintel production can be produced by use of pumice aggregate.
- Use of obsidian/perlite aggregate increases the unit weight of the concrete by lowering cement utilisation.
- Welded connections in reinforcement cage production results decrease in load bearing capacity and energy dissipation.
- Wired connections are suggested for second phase studies of full scale lintel tests.
- Pure pumice concrete or pumice concrete with obsidian/perlite aggregate can both be used for lintel production. The first one will be lighter and more expensive due to use of more cement and the latter can be heavier (*still stands in lightweight concrete range*) and cheaper.
- Production of pre-stressed concrete lintels are possible according to reference [7]. A comprehensive research is necessary for this type of application. Because, production of lightweight concrete which can be used for pre-stressed element production is a challenging task.

ACKNOWLEDGMENT

Research team is grateful to Mr. Ethem TANRIVER and Mr. Nurettin BALCI for their encouragements and supports. The team present sincere thanks to Prof. Dr. Ali Fatih YETİM and Res. Asst. Hilmi TEKDİR for their kind help and guidance for reinforcement welding applications. Contributions of Mr. Hasan AYDIN, Mr. Adem KOTAN, Mr. Nazım BİLİCİ, Mr. Aşkın DÜNDAR and efforts of Kale Blokbims factory staff are deeply acknowledged. Finally, authors present gratefulness's to High Technology and Research Centre of Erzurum Technical University for their technical support.

REFERENCES

[1] https://theconstructor.org/building/lintel-types-uses/11420/ (Date of Access: April 1, 2021)

[2] https://www.civillead.com/what-is-lintel-function-types/ (Date of Access: April 1, 2021)

[3] R. Nowak, "Comparison of brick lintels types for their durability effect", Procedia Engineering, vol. 193, pp. 345-352, 2017 [International Conference on Analytical Models and New Concepts in Concrete and Masonry Structures AMCM'2017]

[4] M. Moussard, P. Garibaldi, M. Curbach, "The Invention of Reinforced Concrete (1848 – 1906)", In: Hordijk D., Luković M. (eds) High Tech Concrete: Where Technology and Engineering Meet. Springer, Cham., 2018, https://doi.org/10.1007/978-3-319-59471-2_316

[5] Turkish Seismic Code 2018, Published by Turkish Environment and Urban Ministry Disaster and Emergency Management Presidency, Official Gazette: 18/03/2018-30364.

[6] Turkish Soil Industry Council of Turkey Chambers and Commodity Exchanges Union, Bims (pumice) Sub-sector report, Published by Bims Industrialists Association, September, 2006.

[7] TS EN 845-2+A1: Specification for ancillary components for masonry - Part 2: Lintels, Published by Turkish Standards Institute, December, 2016.

[8] TS EN 846-9: Methods of test for ancillary components for masonry - Part 9: Determination of flexural resistance and shear resistance of lintels, Published by Turkish Standards Institute, September, 2016.

[9] TS EN 846-11:Methods of test for ancillary components for masonry-Part 11: Determination of dimensions and bow of lintels, Published by Turkish Standards Institute, November, 2000.

[10] W. Mazur, L. Drobiec, R. Jasinski, "Research of light concrete precast lintels", Procedia Engineering, vol. 161, pp. 611 – 617, 2016 [World Multidisciplinary Civl Engineering-Arcihetcture-Urban Planning Symposium 2016, WMCAUS 2016]

[11] TS EN 206 + A2: Concrete - Specification, performance, production and conformity, Published by Turkish Standards Institute, April, 2021.

[12]

Combination Effect of Ruthenium Complexes, Ru-PIP with Olaparib in MDA-MB-231 breast cancer cells

Nur Aininie Yusoh
UPM-MAKNA Cancer Research Laboratory, Institute of Bioscience, Universiti Putra Malaysia, 43400 UPM Serdang, Selangor, Malaysia
ainineyusoh@yahoo.com

Haslina Ahmad
UPM-MAKNA Cancer Research Laboratory, Institute of Bioscience, Universiti Putra Malaysia, 43400 UPM Serdang, Selangor, Malaysia
Department of Chemistry, Faculty of Science, Universiti Putra Malaysia, 43400 UPM Serdang, Selangor, Malaysia
haslina_ahmad@upm.edu.my

Suet Lin Chia
UPM-MAKNA Cancer Research Laboratory, Institute of Bioscience, Universiti Putra Malaysia, 43400 UPM Serdang, Selangor, Malaysia
Department of Microbiology, Faculty of Biotechnology and Biomolecular Sciences, Universiti Putra Malaysia, 43400 UPM Serdang, Selangor, Malaysia
suetlin@upm.edu.my

Aim:

PARP inhibitor Olaparib has been approved by FDA as single-agent treatment for breast cancer patients. However, Olaparib single-agent is clinically limited to patients with BRCA mutated genes and as in the case for the majority of anticancer drugs, single-drug treatment may lead to insufficient tumor suppression, intolerable side effects, and drug resistance. Recently, we have developed a new ruthenium(II) polypyridyl complex, $[Ru(dppz)_2PIP]^{2+}$ (dppz = dipyridophenazine, and PIP = 2-phenylimidazo[4,5-f][1,10]phenantroline) (or Ru-PIP) that have shown potentials as anticancer agent. We found that single-agent Ru-PIP led to stalled DNA replication fork progression and the activation of DNA damage response (DDR) signaling. Thus, the addition of Ru-PIP to Olaparib-treated cells will present a new rational combination approach in treating BRCA wild type (WT) breast cancer. This is because PARP enzymes, the key component of DNA repair process is immediately activated in response to DNA replication stress. Therefore, Olaparib will inhibit the repair of RuPIP-induced DNA damages leading to more efficient cancer cell killing. The aim of the present study is to investigate this ideal synergistic pairing in BRCA-will type MDA-MB-231 breast cancer cells.

Method:

MTT assay

Cells were seeded in 96-well plates and incubated in an incubator supplemented with 5% CO_2 for 24 h at 37°C. Cells were then treated with Ru-PIP and Olaparib alone or in combination. Following incubations, solutions were removed and MTT was added to each well and the plate was incubated for 4 h. The reduced purple formazan crystals formed were solubilized with 100 µL of DMSO and the absorbance at 570 nm was measured using a microplate reader. The percentage of viable cells were calculated by comparing the data with the untreated control using the following equation:

% Cell viability= [Absorbance 570nm(treatment)/ Absorbance 570 nm(control)] ×100

Drug interaction analysis

Synergy was determined based on Chou and Talalay combination index (CI) method. Using the data obtained from MTT assays, the CI values were determined using Calcusyn and Compusyn software (Biosoft, Cambridge, UK). CI values indicate the type of drugs interaction in which CI < 0.9 indicates synergism, CI = 0.9-1 indicates additive and CI > 1 indicates antagonism.

Apoptosis Annexin V-FITC assay

Cells were seeded in 6-well plate and incubated in an incubator supplemented with 5% CO_2 for 24 h at 37°C. Cells were then treated with Ru-PIP and Olaparib alone or in combination. Following incubations, cells were harvested and washed with PBS twice. Following this, 500 µL of 1× binding buffer was added to the samples and followed by the addition of with 5 µL Annexin V-FITC. The samples were further incubated for 20 min at RT. Prior to flow cytometric analysis, 5 µL of (propidium iodide) PI was added. The samples were acquired using NovoCyte flow cytometer, and results obtained were analyzed using NovoExpress software.

Results:

The synergistic combination was found to significantly inhibit the proliferation of MDA-MB-231 breast cancer cells compared to single agent treatments. The identified combination was shown to cause enhanced DNA damages which led to the induction of G2/M cell cycle arrest and increased in apoptotic cell death. The identified combination also showed minimal impact on normal NHDF cells. Most importantly, Ru-PIP was shown to sensitize MDA-MB-231 cells to Olaparib treatment in clonogenic survival assay by 300-fold.

Conclusion: These findings provide evidence that the addition of Ru-PIP sensitizes BRCA-WT MDA-MB-231 breast cancer cells to olaparib treatment which further demonstrate new promising therapeutic strategy to combat cancer. Thus, this identified combination merits further investigation in vivo. Further studies in incorporating dual drug delivery vehicle can also be considered to improve cancer targeting efficiency of this identified drug combination.

Acknowledgement: This study was supported by the Ministry of Education Malaysia through FRGS/1/2017/STG01/UPM/02/6 (01-01-17-1913FR) for the "In Vitro Evaluation of Novel Mesoporous Silica Nanohevicles for the delivery of Ruthenium(II) Anticancer Drugs".

Keywords— Ruthenium, PARP inhibitor, Olaparib, Cancer, Combination

Production of Flexible NiCo2S4/rGO Nanocomposite Paper Materials

Elif ERÇARIKCI
Department of Chemistry Atatürk University Erzurum, Turkey
elif.ercarikci@atauni.edu.tr

Zeriş AKSU
Department of Chemistry Atatürk University Erzurum, Turkey
aksu-25@hotmail.com

Ezgi TOPÇU
Department of Chemistry Atatürk University Erzurum, Turkey
ezgitopcu@atauni.edu.tr

Kader DAĞCI KIRANŞAN
Department of Chemistry Atatürk University
Erzurum, Turkey
kdagci@atauni.edu.tr

***Abstract*— We studied the production of a flexible free-standing reduced graphene oxide-based papers (rGOP) for use as a freestanding flexible electrode material. Production of rGOP was achieved through mold-casting method of the aqueous dispersion of graphene oxide (GO) and hydrothermal synthesized $NiCo_2S_4$, followed by chemical reduction in hydrogen iodide solution. The physicochemical properties of as-prepared flexible free-standing $NiCo_2S_4$/rGOP were characterized by means of scanning electron microscopy (SEM), energy-dispersive X-ray spectroscopy (EDAX), X-ray photoelectron spectroscopy (XPS), and X-ray powder diffraction (XRD) patterns. Cyclic voltammetry (CV) results showed that the electrochemical activity of $NiCo_2S_4$/rGOP electrode was much higher than rGOP. This study exhibited that $NiCo_2S_4$/rGOP, possessing easy preparation, low cost, and high flexibility, have great potential to develop high-performance flexible electrode materials.**

Keywords*— Cobalt nickel sulfides, graphene paper, hydrothermal synthesis

[1] INTRODUCTION

Recently, flexible reduced graphene oxide based papers (rGOP), have attracted attention because of their potential applications, such as electrochemical sensors [1], membranes [2], supercapacitors [3], and lithium batteries [4]. rGOP materials are modified with metal oxides [5], and metal sulfides [6] in order to improve the electrochemical properties and catalytic activities. A combination of these materials with rGOP provides to produce nanocomposites with excellent performance in these applications. Among various metal sulfides, bimetallic sulfides are distinguished due to their high electrical conductivity and electrochemical activity. Compared with single metal sulfides, Ni-Co (nickel-cobalt) binary metal sulfides exhibit richer redox reactions, higher specific capacity, and markedly higher electronic conductivity. The synergistic effect of Ni and Co play important role in both conductivity and electrochemical activity of the binary metal sulfides [7]. For these reasons, transition metal sulfides supported rGOP materials have been attracted attention in recent years [8].

Herein, we report a flexible free-standing $NiCo_2S_4$/rGOP material for utility in various applications. This material was prepared by applying a mold-casting method to the dispersion of GO and hydrothermal synthesized $NiCo_2S_4$. As-prepared $NiCo_2S_4$/rGOP was used as an electrode material in cyclic voltammetry (CV) experiments.

[2] MATERIAL AND METHOD

A. Synthesis of Graphene Oxide (GO)

GO was prepared by the modified Hummers' method using the procedure reported previously [9]. The concentration of the prepared GO solution was about 10.0 mg mL^{-1}.

B. Synthesis of $NiCo_2S_4$

In the general procedure, 9.0 mmol $Ni(NO_3)_2.6H_2O$ and 18 mmol $Co(NO_3)_2.6H_2O$ 30 mL ethylene glycol and 10 mL distilled water were dissolved and mixed for 1 h. Then 36 mmol thiourea was added to this mixture and stirred with a magnetic stirrer for 1 h. The prepared solution was taken into a 100 mL Teflon-lined autoclave, after 12 h of hydrothermal treatment at 180°C, the obtained product was washed several times with ethanol and distilled water and then dried at 60°C [10]. Thus, $NiCo_2S_4$ composite material was obtained (Figure 1).

C. Preparation of $NiCo_2S_4$/rGOP Materials

To prepare composite suspension, 5 mg $NiCo_2S_4$ powder was added to the 10 mL GO dispersion and ultrasonicated for 1 h to obtain the suspension of $NiCo_2S_4$/GO. $NiCo_2S_4$/GOP were prepared by mold-casting of 10 mL of $NiCo_2S_4$/GO suspension, air drying and peeling off from the molds. Thus, $NiCo_2S_4$/GOP was prepared. $NiCo_2S_4$/GOP electrode was treated through a chemical reduction process. For this purpose, as prepared flexible free-standing $NiCo_2S_4$/GOP was immersed into a HI (55.0%) solution at room temperature for 1 h [11]. The $NiCo_2S_4$/rGOP was washed with copious ethanol and distilled water and dried in air. Thus, free-standing, flexible and durable $NiCo_2S_4$/rGOP was obtained. Prepared with a radius of approximately 50 mm each time, this conductive $NiCo_2S_4$/rGOP was cut into strips (20 mm x 5 mm) and used directly as a working electrode in electrochemical studies. rGOP was prepared via the same process.

D. Chemicals

All the chemicals were of analytical reagent grade, purchased from Sigma-Aldrich and used without any further purification. Double distilled water was used through the experiments.

E. Apparatus

Powder XRD was carried out using a Rigaku TTR III X-ray diffractometer equipped with monochromatized Cu Kα radiation (λ=1.5406 Å). SEM images and EDAX analysis results were acquired using a Zeiss brand field emission scanning electron microscopy (FE-SEM) instrument, equipped with an EDAX detector. X-ray photoelectron

spectroscopy (XPS) measurements were performed on a Spect-Flex spectrometer with standard Al X-ray source. All the electrochemical experiments were performed with Gamry (600+) potentiostat system connected to a three-electrode cell. All samples were prepared as rGOP electrodes and directly used as the working electrode (20 mm×5 mm). In this electrochemical cell, an Ag/AgCl (saturated KCl) and a Pt wire served as reference electrode and counter electrode, respectively.

[3] RESULTS AND DISCUSSION

Prepared free-standing, flexible and durable $NiCo_2S_4$/rGOP was presented in Figure 1.

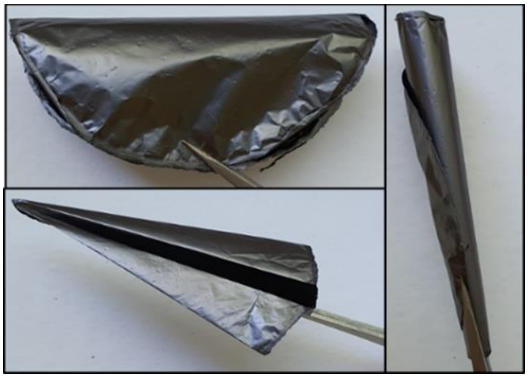


Figure 1. Illustrative digital photo of the flexible and shapeable $NiCo_2S_4$/rGOP.

Morphological characterizations of prepared $NiCo_2S_4$ powder, rGOP and $NiCo_2S_4$/rGOP materials were performed by using FESEM technique. In FESEM images of $NiCo_2S_4$ nanostructures prepared by the hydrothermal synthesis in Figure 2.a, it was observed that the composite structure consists of worm-like nanotubes with a diameter of about 200 nm. The top view FESEM image of rGO paper indicates the characteristic wrinkled structure of the graphene nanosheets (Figure 2.b.). In FESEM images of $NiCo_2S_4$/rGOP, while we can see the characteristic wrinkled structure of the graphene nanosheets, $NiCo_2S_4$ nanostructures are not fully observed on the surface of the composite structure due to diffusing $NiCo_2S_4$ to the inner parts of the GO (Figure 2.c.). When the FESEM cross-section of $NiCo_2S_4$/rGOP was examined, $NiCo_2S_4$ nanostructures between graphene sheets draw attention (Figure 2.d.). In addition, in the EDAX analysis of $NiCo_2S_4$/rGOP, it was revealed that the composite structure consists of C, O, Ni, Co and, S atoms, so that the composite structure was prepared successfully (In inset Figure 2.c.). Iodine comes from the reduction process of $NiCo_2S_4$/GOP with HI.

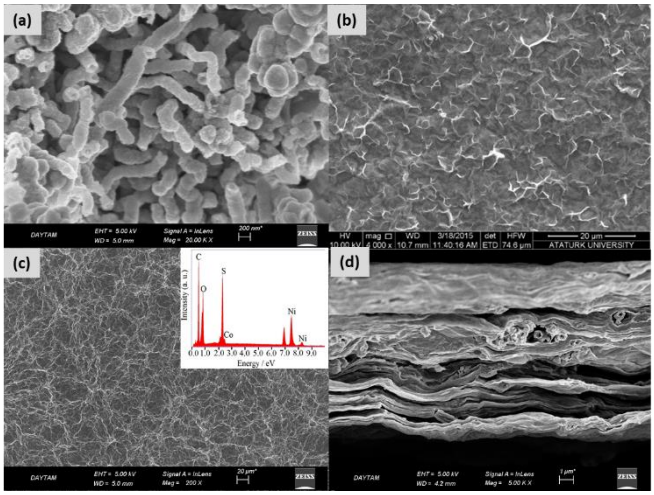


Figure 2. Top-view FESEM images of $NiCo_2S_4$ powder (a), rGOP (b), $NiCo_2S_4$/rGOP. Inset: EDAX spectra of $NiCo_2S_4$/rGOP (c). Cross-sectional view FESEM images of $NiCo_2S_4$/rGOP (d).

The crystalline nature of $NiCo_2S_4$ powder, rGOP, and $NiCo_2S_4$/rGOP was investigated through XRD (Figure 3). The $NiCo_2S_4$/rGOP showed diffraction peaks at 30.2, 34.9, 47.7, 53.8, and 62.6 that were specific to (220), (311), (400), (511) and (440) planes of $NiCo_2S_4$ (JCPDS No: 20-0782) [12]. The peak at about 25.4°, corresponding to the characteristic crystal diffraction of the graphene structure (002) was observed in the XRD spectrum of both rGO paper and $NiCo_2S_4$/rGOP, indicating that the composite paper has been successfully prepared.

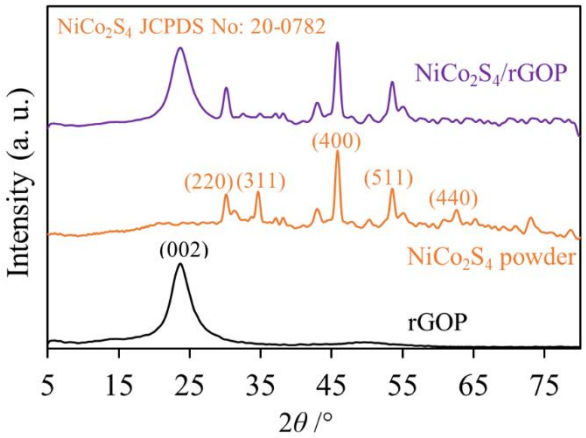


Figure 3. XRD patterns of samples.

XPS was used to determine the chemical states of elements in $NiCo_2S_4$/rGOP, as shown in Figure 4. XPS spectra include the peaks corresponding to C 1s, O 1s, Ni 2p, Co 2p, and S 2p, as well as the peak corresponding to the I 3d originating from HI which was used during the reduction process while preparing the $NiCo_2S_4$/rGOP (Figure 4) [13]. These results confirm that $NiCo_2S_4$/rGOP were successfully prepared.

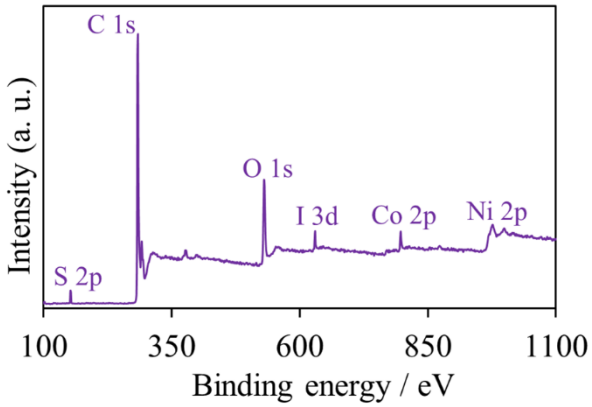


Figure 4. XPS spectra of the $NiCo_2S_4$/rGOP.

CV measurements were employed to investigate the electrochemical performance of the nanocomposite paper electrode materials (Figure 5).

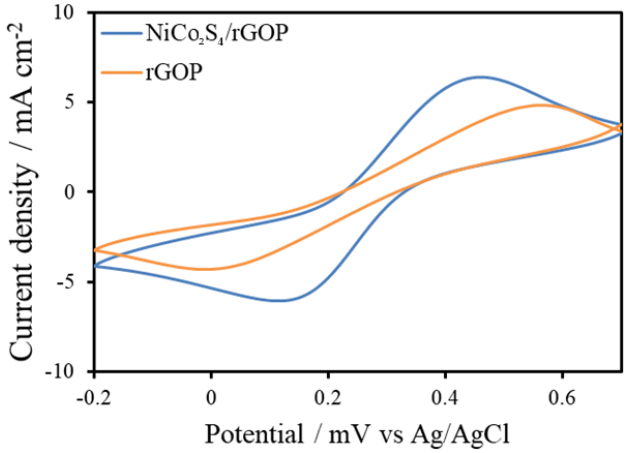


Figure 5. CVs of rGOP and $NiCo_2S_4$/rGOP in a solution containing 10 mM $K_3Fe(CN)_6$ and 0.1 M KNO_3.

The peak potentials during the reversible reaction of Fe^{+2}/Fe^{+3} as well as the difference between the oxidation and reduction peak current values (ΔE) in CV experiments give information about the electrochemical performance of the electrode. The higher the peak current density and the lower the ΔE value, the higher the electrochemical activity of the electrode. Figure 5 shows that the ΔE values and the oxidation peak current densities of rGOP and $NiCo_2S_4$/rGOP are 584, 334 mV, and 4.8, 6.4 $mAcm^{-2}$, respectively. Such results displayed that the electrochemical activity of $NiCo_2S_4$/rGOP was much higher than rGOP.

IV. CONCLUSION

In summary, a flexible free-standing $NiCo_2S_4$/rGOP was fabricated by mold-casting method. The free-standing flexible $NiCo_2S_4$/rGOP was characterized using SEM, EDAX, XRD, and XPS. Free-standing flexible $NiCo_2S_4$/rGOP might be used in various applications such as sensor, catalysis, Li-ion batteries, and supercapacitors.

REFERENCES

[1] K. D. Kıransan, E. Topcu, and M. Alanyalıoglu, "Surface-confined electropolymerization of pyronin Y in the graphene composite paper structure for the amperometric determination of dopamine," J. Appl. Polym. Sci. , DOI: 10.1002/APP.45139, 2017.

[2] E. Erçarıkcı and M. Alanyalıoglu, "Dual-Functional Graphene-Based Flexible Material for Membrane Filtration and Electrochemical Sensing of Heavy Metal Ions," IEEE SENSORS JOURNAL, Vol. 21, No. 3, 2021.

[3] Y. Wang, J. Chen, J. Cao, Y. Liu, Y. Zhou, J-H. Ouyang, and D. Jia, "Graphene/carbon black hybrid film for flexible and high rate performance supercapacitor", Journal of Power Sources, 271, 269-277, 2014.

[4] M. Kim, D. Y. Kim, Y. Kangb, and O. O. Park, "Facile fabrication of highly flexible graphene paper for high-performance flexible lithium ion battery anode," RSC Adv., 5, 3299–3305, 2015.

[5] K.-K. Liu, Q. Jiang, C. Kacica, H. G. Derami, P. Biswas, and S. Singamaneni, "Flexible solid-state supercapacitor based on tin oxide/reduced graphene oxide/bacterial nanocellulose," RSC Adv., 8, 31296–31302, 2018.

[6] R. Zhai, Y. Xiao, T. Ding , Y. Wu, S. Chen, and W. Wei, "Construction of NiCo2S4 heterostructure based on electrochemically exfoliated graphene for high-performance nanocomposite supercapacitor electrode," Journal of Alloys and Compounds 845, 156164, 2020.

[7] T. Chena, Y. Tanga, W. Guoa, Y. Qiaoa, S. Yua, S. Mub, L. Wanga, Y. Zhaoa, and F. Gao, "Synergistic effect of cobalt and nickel on the superior electrochemical performances of rGO anchored nickel cobalt binary sulfides," Electrochimica Acta, 212, 294–302, 2016.

[8] D. Ghosh, and C. K. Das, "Hydrothermal Growth of Hierarchical Ni3S2 and Co3S4 on Reduced Graphene Oxide Hydrogel@Ni foam: High Energy Density Aqueous Asymmetric Supercapacitor," ACS Appl. Mater. Interfaces 7, 1122–1131, 2015.

[9] N.I. Kovtyukhova, Layer-by-layer assembly of ultrathin composite films from micron-sized graphite oxide sheets and polycations, Chem. Mater. 11 (1999) 771–778,

[10] J. Dong, S. Li, Y. Ding, Anchoring nickel-cobalt sulfide nanoparticles on carbon aerogel derived from waste watermelon rind for high-performance asymmetric supercapacitors, J. Alloys Compd. 845 (2020) 155701.

[11] W. Du, Z. Wang, Z. Zhu, S. Hu, X. Zhu, Y. Shi, H. Pang, X. Qian, Facile synthesis and superior electrochemical performances of CoNi 2S4/graphene nanocomposite suitable for supercapacitor electrodes, J. Mater. Chem. A. (2014).

[12] H. Wan, J. Jiang, J. Yu, K. Xu, L. Miao, L. Zhang, H. Chen, Y. Ruan, NiCo2S4 porous nanotubes synthesis via sacrificial templates: High-performance electrode materials of supercapacitors, CrystEngComm. (2013).

[13] D. Fa, B. Yu, Y. Miao, Synthesis of ultra-long nanowires of nickel phosphate by a template-free hydrothermal method for electrocatalytic oxidation of glucose, Colloids Surfaces A Physicochem. Eng. Asp. 564 (2019) 31–38.

Graphene Nanoplatelets as Adsorbent for Removal of Pharmaceutical from Water

Fatin Ahza Rosli
Department of Chemistry Universiti Putra Malaysia 43400 Serdang, Selangor, Malaysia
fatinahza@gmail.com

Haslina Ahmad
Department of Chemistry Universiti Putra Malaysia 43400 Serdang, Selangor, Malaysia
haslina_ahmad@upm.edu.my

Khairulazhar Jumbri
Department of Fundamental and Applied Sciences Universiti Teknologi PETRONAS 32610 Seri Iskandar, Perak, Malaysia
khairulazhar.jumbri@utp.edu.my

Abdul Halim Abdullah
Department of Chemistry Universiti Putra Malaysia 43400 Serdang, Selangor, Malaysia
halim@upm.edu.my

Sazlinda Kamaruzaman
Department of Chemistry Universiti Putra Malaysia 43400 Serdang, Selangor, Malaysia
sazlinda@upm.edu.my

Nor Ain Fathihah Abdullah
Department of Fundamental and Applied Sciences Universiti Teknologi PETRONAS
32610 Seri Iskandar, Perak, Malaysia
nafathihah@gmail.com

***Abstract*— A growing concern about the emergence of excess pharmaceuticals as water contaminants that pose a danger to the environment and endanger human health. Graphene nanoplatelets (GNPs) were used in this study to effectively remove antibiotics sulfamethoxazole and analgesic acetaminophen as contaminants from water by adsorption processes. High-resolution transmission electron microscopy, Raman spectroscopy, X-Ray diffraction, field emission scanning electron microscopy/energy dispersive X-ray and Brunauer-Emmett-Teller have been described by different forms of GNPs; C750, C300, M15, and M5. Among others, GNP C300 was selected via a preliminary test as the best adsorbent. The effects of several factors have been studied: solution pH, volume of adsorbent, initial concentration, and contact time. The factors were optimized through the batch adsorption process and the removal efficiency for both pharmaceuticals were 99 percent. The adsorption kinetics and isotherms models were applied, and the experimental results were best analysed with pseudo-second kinetic and Langmuir isotherm with a maximum adsorption potential of 210.08 mg/g for sulfamethoxazole and 56.21 mg/g for acetaminophen. Different eluents were used in the regeneration study; 5% ethanol-deionized water, 0.005 M NaOH and HCl. The findings showed that 5% ethanol-deionized water was found to be the best eluent for the removal of sulfamethoxazole and acetaminophen for the regeneration of GNP C300. Most of the pharmaceuticals were eliminated from environmental water samples by GNP C300. Molecular docking was used to demonstrate the mechanism of adsorption of GNP C300 to pharmaceuticals with free-binding energy of -7.54 kcal/mol (sulfamethoxazole) and -5.29 kcal/mol (acetaminophen), which disclosed spontaneous adsorption occurred.**

Keywords—graphene, pharmaceutical, adsorption, environmental samples, removal

PV Monitoring System: Data Logger Based on PcDuino a Single Board Computer

ELWATI Jaafar
Departement of electrical engineering
University Hassan 2 of Casablanca
Faculty of sciences and technics
Mohammedia, Morocco
elwatijaafar@gmail.com

ELMAJDOUB Khalid
Departement of electrical engineering
University Hassan 2 of Casablanca
Faculty of sciences and technics
Mohammedia, Morocco
khalid_majdoub@yahoo.fr

HARTITI Bouchaib
Department of physics University Hassan 2 of Casablanca Faculty of sciences and technics
Mohammedia, Morocco
bouchaib.hartiti@univh2c.ma

***Abstract* — A monitoring system using IoT technologies is considered in a photovoltaic (PV) system as a crucial part for observing and inspecting the stability and the performance of the system. The photovoltaic data logger is extensively required in a remote PV system for collecting all parameters, estimating and analyzing the system performances and for optimization purposes. Thus, in order to ensure the reliable and stable operation of any PV system, an effective and optimal monitoring system is essential. In this paper, a Bluetooth based wireless system is presented for PV system monitoring, which could collect data in an intelligent manner and monitor in real-time the produced power. The communication between the main components of the system is wireless considering the harsh environmental conditions. The inverter's output power and status are being monitored by the mini-computer PcDuino then the information is transferred over Wi-Fi to a remote host for data storage. To evaluate its performance, the system has been implemented on a 3×2kW PV plants based on monocrystalline, polycrystalline and amorphous silicon technologies.**

Keywords* — *Photovoltaic installation - IoT - Bluetooth protocol - Real time monitoring - PcDuino board

[1] INTRODUCTION

Nowadays, renewable technologies have been given a lot of interest due to their benefits in many aspects, especially the solar photovoltaic systems as they have a potential to shape a clean, reliable, efficient and affordable electricity system for the future. While the number of installed photovoltaic fields is increasing, the necessity of management and optimal energy harvesting from PV plants is of high importance. In order to attain this purpose, a PV monitoring system is required to develop efficient management service by applying IOT technologies. The PV monitoring system provides information about the energy potential, extracted energy, historical analysis of the plant and the status of the PV system. As the data being monitored and stored, it could be used for analyzing the performance of the system, fault detection, sending warnings to the user for equipment damage prevention, and also for AI applications.

The PV power plants are generally built in outdoor environment such as rooftop or desert, so the wireless communication technology is always regarded as the best option over conventional wired system since the wires are exposed to the harsh weather circumstances, and those limitations increases the installation and maintenance cost.

Most of the commercial inverters integrate monitoring options, but they have some limitations that can come into play when considering more advanced monitoring requirements. While designing a monitoring system, the cost and the lifespan are of much importance. Thence, in order to enhance system capabilities an optimal architecture is always pursued.

In this paper, a Bluetooth based wireless system is being developed in an optimal way for real-time data logging. The PV and the output power of the grid inverter are being monitored via Bluetooth protocol and then transferred via internet to a remote database for data storage. As for the evaluation of the proposed system performances, the system has been tested on a 3×2kW PV plants based on monocrystalline, polycrystalline and amorphous silicon technologies at the faculty of science and techniques of Hassan 2 University, Morocco.

[2] LITERATURE REVIEW

In order to achieve the prime objective of designing an optimal and low-cost monitoring system, a number of previous works which are related to IoT systems for solar energy have been reviewed.

Even though the proposed system collects data directly from the computing system implemented in the inverters, the monitoring systems that include a weather station and collects data using sensor nodes are presented here in order to gain a better picture on this area of work.

An IoT experimental prototype and open source solution for PV monitoring and data logging have been developed in [1], based on ESP32 board. The ESP32 microcontroller acquires and processes data measured by sensors via the I2C protocol then sends the data to the InfluxDB database using Wi-Fi technology, the data are visualized in Grafana open source platform.

Another IoT system for PV monitoring presented in [2], a Renewable Energy Monitoring System collects data from PV module (Voltage, Current, PV Temperature, solar Irradiance, Ambient temperature, Humidity) and communicate with a developed cloud server. The system consists of a microcontroller-based analog to digital converter of PIC18Fxx5x family which reads the measurements of the analog sensors, and a Raspberry pi in charge of reading the digital sensors and collecting the ADC microcontroller data. The data are transmitted to a cloud server for storage and visualized on a free software web monitor.

Furthermore, an IoT monitoring system to measure an off-grid PV module has been presented in [3]. The data packets are transmitted from node to another one until they reach the central hub, then stored in a local database and displayed in an HTML GUI. The computing system selected to be the central hub is Raspberry pi, which communicates with the Arduino Uno based nodes network to gather the data via Zigbee which had a communication distance up to 50m. In [4], LoRa technology is implemented to assure the data transmission between Arduino Uno based nodes and the central hub (Raspberry pi), for PV plants monitoring.

A real-time monitoring system for a PV system was developed in [5], with an experimental validation on a test bench. The system architecture is an ATmega328P-PU based nodes network, which communicates wirelessly with the main brain via Radiofrequency technology (RF-315). The main brain consists of an SDcard reader used for data storage and a Bluetooth module which communicates with a mobile user interface.

[3] System Architecture

A. *Proposed system design*

The system is designed to overcome the disadvantages of the existing commercial systems like high installation cost, wired connections and difficult maintenance. The introduced system will have a wireless connection between the main components, and the computing unit that manages the data logging task which is based on a low-cost small-scaled computer (PcDuino).

The PcDuino board acts as the bridge between the PV installation and the internet, it acquires and processes the incoming data from the inverters then they are transmitted to a remote database via Wi-Fi. The photovoltaic installation in which the system will be implemented, consists of three strings composed by three different silicon technologies, every string power outlet is connected to an inverter that collects the energy potential data of the two sides DC and AC and the device status.
Data transmission occurs in two steps: The first one is the communication between the inverters and the PcDuino board and the second step is sending the data to a remote database.

In the first place, the monitoring system get the measurements of the total extracted energy per hour, the electrical parameters of the DC and AC sides (voltage, current, Power) and the status (temperature, grid relay status) of the inverter via a wireless Bluetooth technology. The exchange of messages is based on a client and server requests. As the client sends a request for connection and the right commands to get the data, the server is replying with the demanded data. Then they are stored either locally or sent via internet protocol to a distant host. The block diagram illustrated in the figure 1 below, expose the architecture of the system.

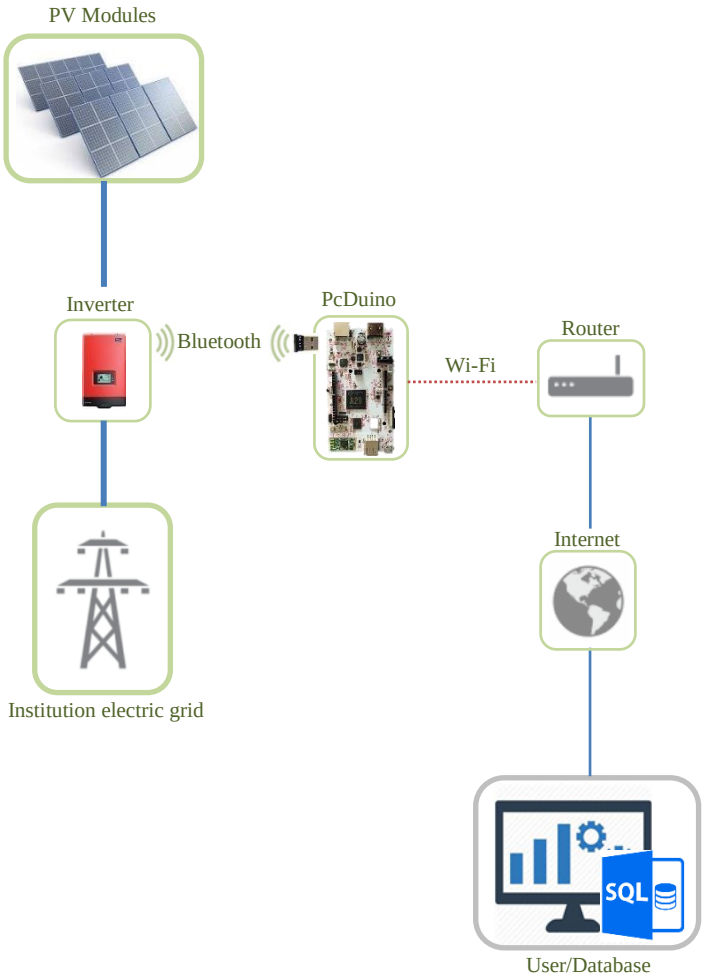


Fig. 12. Block diagram of the overall system

B. *Hardware and software design*

a) *Hardware design:*

The developed system consists mainly of PcDuino Board and a Bluetooth dongle. The inverters installed in the PV strings are from SMA sunny-boy 2000HF series. They have an internal embedded system which measures the parameters of the extracted energy, monitor the performances of the inverter and can communicate wirelessly using Bluetooth protocol.

PcDuino [6] is a high performance, cost effective small computer. It's a Linux-based IOT board compatible with the operating systems Ubuntu and Android. There are multiple versions of this board, the one that we had chosen is PcDuino version 3B (121mm x 65mm) with ARM Cortex A7 Dual Core, 1GHz processor, 4GB Flash and a micro SD slot up to 32GB. It's a mini PC electronic platform **Fig. 2.** with the characteristics of Raspberry Pi, and has an Arduino interface with a built-in Wi-Fi module.

The connection to the internet network is available using either Wi-Fi module or RJ45 ethernet jack. The access to the desktop can be feasible using HDMI port, LVDS LCD interface, serial debugging port or via a graphical desktop-sharing server using internet.

The PcDuino provides an easy tool chains and supports a lot of programming languages such as C/C++, Java, Python and more. Besides, it possesses an API developed to allow access to the functions of the Arduino platform. This board is selected because it reduces the system cost, and considering its multiple features which allows it to connect easily with another hardware, in case we want to extend our system by adding another sensor node.

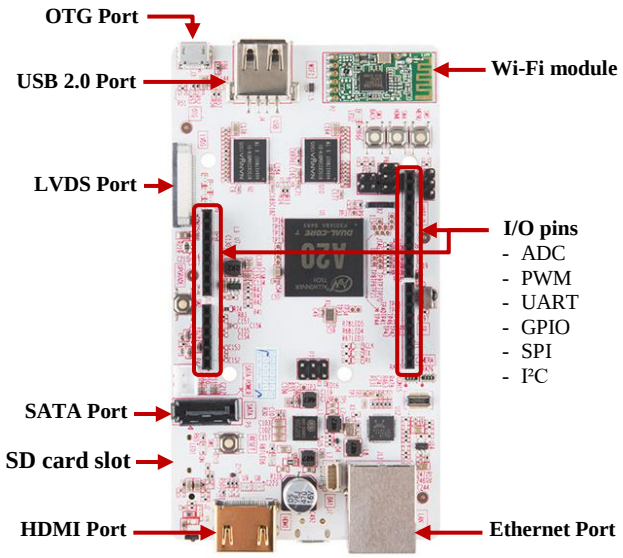


Fig. 13. The mini-computer board used in the system - PcDuino 3B

The Bluetooth Dongle used for this solution is a low energy wireless USB adapter, CSR version 4.0, compatible with all the OS systems with a data rate of 3Mbps and a range of receiving and transmission from 20m to 50m.

b) Software design:

The developed software was programmed to interact with a commercial inverter which has a very special circuit architecture and communication protocols. The flexibility of the PcDuino board used as the main controller of the system allows the user to employ different programming languages. In the proposed monitoring system, the software architecture **Fig. 3.** is programmed using Python which is a high-level programming language with simple syntax and a rich open-source library support, also as the controller support Linux based operating system, then Python option is the best choice.

The data logging task is the process of collecting data from the PV system which in the actual case, is managed by the Python software on PcDuino. The program was written to handle the connection with one or many inverters at the same time via Bluetooth technology, and to be adaptable with any modifications or extensions in the monitoring system. At start-up of the PcDuino OS, the program starts running and the communication is established with the network service to get data every 5 minutes, since it's the sampling time of the measurement system inside the inverter. The inverter in our case is the server advertising the service in order for the client to be connected. The client is the PcDuino which sends request messages to the inverter to retrieve the system data. The protocol stack for Bluetooth communication implemented in the inverter's embedded system has an advanced level of security, the client should get authentication from the server in the first place in order to access the device. After the connection is initialized and the system log in to the inverter, a set of requests are sent to get the data measured. The data collection is saved with a timestamp, as the time is an important parameter while collecting data, for this reason the mini-computer must be synchronized for the data to be archived and stored. The date and time are provided from the time server on internet at the start-up of PcDuino and the program is designed to run from the sunrise to the sunset time.

The micro-system in the inverters is designed to operate in the daytime, and to shutdown at the dusk time. The program of the present monitoring system includes a function that calculates the sunrise time and the sunset to define the operating time interval of the system.

As for data storage, the program connects with the remote database over internet via Wi-Fi technology, and proceed with data transmission and storage in MySQL database installed in a remote host located in the laboratory of the faculty.

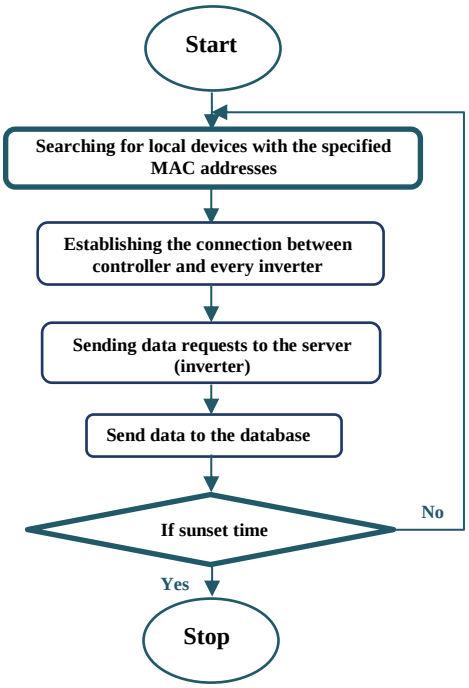
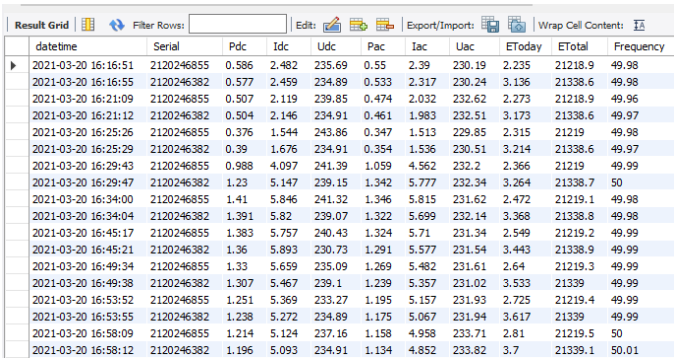


Fig. 14. The flow chart of the software architecture

[4] RESULTS

The system is tested and the real-time data collected from the inverters for half an hour are stored in a database which are shown below **Fig. 4.** A simple selection query in MySQL workbench shows the collection of data with the various rows. Three main parameters are monitored namely Power, voltage and current.

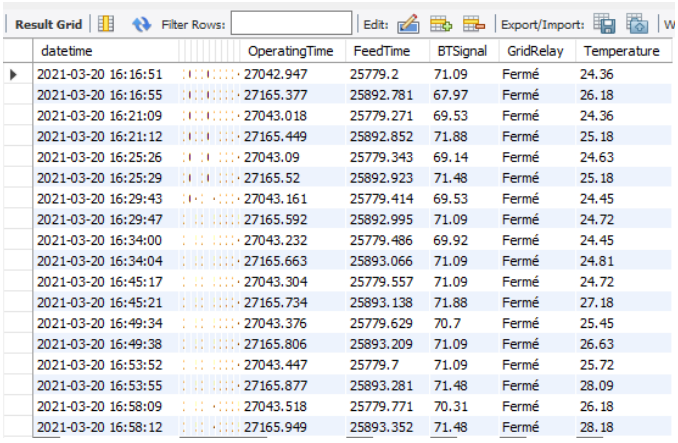


Result Grid | Filter Rows: | Edit: | Export/Import: | Wrap Cell Content:

datetime	Serial	Pdc	Idc	Udc	Pac	Iac	Uac	EToday	ETotal	Frequency
2021-03-20 16:16:51	2120246855	0.586	2.482	235.69	0.55	2.39	230.19	2.235	21218.9	49.98
2021-03-20 16:16:55	2120246382	0.577	2.459	234.89	0.533	2.317	230.24	3.136	21338.6	49.98
2021-03-20 16:21:09	2120246855	0.507	2.119	239.85	0.474	2.032	232.62	2.273	21218.9	49.96
2021-03-20 16:21:12	2120246382	0.504	2.146	234.91	0.461	1.983	232.51	3.173	21338.6	49.97
2021-03-20 16:25:26	2120246855	0.376	1.544	243.86	0.347	1.513	229.85	2.315	21219	49.98
2021-03-20 16:25:29	2120246382	0.39	1.676	234.91	0.354	1.536	230.51	3.214	21338.6	49.97
2021-03-20 16:29:43	2120246855	0.988	4.097	241.39	1.059	4.562	232.2	2.366	21219	49.99
2021-03-20 16:29:47	2120246382	1.23	5.147	239.15	1.342	5.777	232.34	3.264	21338.7	50
2021-03-20 16:34:00	2120246855	1.41	5.846	241.32	1.346	5.815	231.62	2.472	21219.1	49.98
2021-03-20 16:34:04	2120246382	1.391	5.82	239.07	1.322	5.699	232.14	3.368	21338.8	49.98
2021-03-20 16:45:17	2120246855	1.383	5.757	240.43	1.324	5.71	231.34	2.549	21219.2	49.99
2021-03-20 16:45:21	2120246382	1.36	5.893	230.73	1.291	5.577	231.54	3.443	21338.9	49.99
2021-03-20 16:49:34	2120246855	1.33	5.659	235.09	1.269	5.482	231.61	2.64	21219.3	49.99
2021-03-20 16:49:38	2120246382	1.307	5.467	239.1	1.239	5.357	231.02	3.533	21339	49.99
2021-03-20 16:53:52	2120246855	1.251	5.369	233.27	1.195	5.157	231.93	2.725	21219.4	49.99
2021-03-20 16:53:55	2120246382	1.238	5.272	234.89	1.175	5.067	231.94	3.617	21339	49.99
2021-03-20 16:58:09	2120246855	1.214	5.124	237.16	1.158	4.958	233.71	2.81	21219.5	50
2021-03-20 16:58:12	2120246382	1.196	5.093	234.91	1.134	4.852	233.82	3.7	21339.1	50.01

Fig. 15. Caption of a data selection on the database

The displayed data are for two inverters each one has a serial ID. The Etotal refers to the total energy extracted since the first installation of the inverter and EToday is the energy extracted in each day. The values of those two parameters change every second while the energy is produced. The DC side power, voltage and current of the first inlet are displayed, the second DC inlet of the inverter is not supplied. In the AC side, the power, voltage and current displayed are for one phase.



Result Grid | Filter Rows: | Edit: | Export/Import: | W

datetime	OperatingTime	FeedTime	BTSignal	GridRelay	Temperature
2021-03-20 16:16:51	27042.947	25779.2	71.09	Fermé	24.36
2021-03-20 16:16:55	27165.377	25892.781	67.97	Fermé	26.18
2021-03-20 16:21:09	27043.018	25779.271	69.53	Fermé	24.36
2021-03-20 16:21:12	27165.449	25892.852	71.88	Fermé	25.18
2021-03-20 16:25:26	27043.09	25779.343	69.14	Fermé	24.63
2021-03-20 16:25:29	27165.52	25892.923	71.48	Fermé	25.18
2021-03-20 16:29:43	27043.161	25779.414	69.53	Fermé	24.45
2021-03-20 16:29:47	27165.592	25892.995	71.09	Fermé	24.72
2021-03-20 16:34:00	27043.232	25779.486	69.92	Fermé	24.45
2021-03-20 16:34:04	27165.663	25893.066	71.09	Fermé	24.81
2021-03-20 16:45:17	27043.304	25779.557	71.09	Fermé	24.72
2021-03-20 16:45:21	27165.734	25893.138	71.88	Fermé	27.18
2021-03-20 16:49:34	27043.376	25779.629	70.7	Fermé	25.45
2021-03-20 16:49:38	27165.806	25893.209	71.09	Fermé	26.63
2021-03-20 16:53:52	27043.447	25779.7	71.09	Fermé	25.72
2021-03-20 16:53:55	27165.877	25893.281	71.48	Fermé	28.09
2021-03-20 16:58:09	27043.518	25779.771	70.31	Fermé	26.18
2021-03-20 16:58:12	27165.949	25893.352	71.48	Fermé	28.18

Fig. 16. Caption of data stored in the database

The caption **Fig. 5.** above shows the temperature of the inverter, the grid relay status, the Bluetooth signal strength, the operating time of the inverter and the feeding time. Those information are related to the status of the hardware in the PV installation, so that we can take counter measures in case of fault detection.

The system presented in this paper is an extensible and optimal platform in terms of size and cost, since it's based on an electronic board that doesn't require more external units like ADC thanks to its Arduino interface. That gives us the advantage to use it for other purposes and applications, such as a weather station or if we want to add a sensor node network to collect other data about the health of PV plants. Owing to its multiple features and high computation performances, it was chosen to acquire, process and transmit in real time the collected data. To summarize, the proposed IoT solution has the ability to monitor and supervise the actual PV system and the flexibility to react with another hardware platforms.

[5] CONCLUSION

In this paper, the development of a low-cost and wireless monitoring system of PV generated power is exposed, after a discussion and a study of the literature survey of previous works. The main objective of the presented IoT solution is to monitor a PV system and collect its electrical parameters then send the data to a remote computer. The system will be tested and implemented on a PV installation of three strings, each one has an inverter which has an embedded system that measures the energy parameters. The software was developed using Python language, which gets the data from the inverter using Bluetooth protocols and sends it to the database located in a remote computer.

REFERENCES

[1] Y. Cheddadi, H. Cheddadi, F. Cheddadi, F. Errahimi, and N. Es-sbai, "Design and implementation of an intelligent low-cost IoT solution for energy monitoring of photovoltaic stations", SN Appl. Sci., vol. 2, no 7, p. 1165, juill. 2020.

[2] R. I. S. Pereira, I. M. Dupont, P. C. M. Carvalho, and S. C. S. Jucá, "IoT embedded linux system based on Raspberry Pi applied to real-time cloud monitoring of a decentralized photovoltaic plant", Measurement, vol. 114, p. 286-297, janv. 2018.

[3] R. M. Zago and F. Fruett, "A low-cost solar generation monitoring system suitable for internet of things", in 2017 2nd International Symposium on Instrumentation Systems, Circuits and Transducers (INSCIT), Fortaleza, août 2017, p. 1-6.

[4] C.-S. Choi, J.-D. Jeong, I.-W. Lee, and W.-K. Park, "LoRa based renewable energy monitoring system with open IoT platform", in 2018 International Conference on Electronics, Information, and Communication (ICEIC), Honolulu, HI, janv. 2018, p. 1-2.

[5] M. Caruso, R. Miceli, P. Romano, G. Schettino, C. Spataro, and F. Viola, "A low-cost, real-time monitoring system for PV plants based on ATmega 328P-PU microcontroller", in 2015 IEEE International Telecommunications Energy Conference (INTELEC), Osaka, Japan, oct. 2015, p. 1-5.

[6] Linksprite. [Online]. Available: https://www.linksprite.com/linksprite-pcduino3/.

Voice Pathology Classification Using Machine Learning

Hussein Mahmood Abdo Mohammed
Department of Electrical & Electronic Engineering *Ataturk University*
Erzurum,Turkey
halameri080@gmail.com

Asli Nur Omeroglu
Department of Electrical & Electronic Engineering Ataturk University
Erzurum,Turkey
asli.omeroglu@atauni.edu.tr

Merve Polat
Department of Electrical & Electronic Engineering *Ataturk University*
Erzurum,Turkey
merve.polat12@ogr.atauni.edu.tr

Emin Argun Oral
Department of Electrical & Electronic Engineering *Ataturk University* Erzurum,Turkey
eminoral@atauni.edu.tr

Ibrahim Yucel Ozbek
Department of Electrical & Electronic Engineering Ataturk University
Erzurum,Turkey
iozbek@atauni.edu.tr

***Abstract* — In this study, the diagnosis of voice diseases affecting the sound quality of many people during their life has been examined. Systems developed for the automatic classification of healthy and pathological sounds are of great interest in early detection of voice disorders. The main purpose of this study is to investigate and compare the performance of these techniques using various machine learning techniques for voice pathology. All analyzes are performed using the Saarbruecken Voice Database. Detection of voice pathology are evaluated in terms of accuracy, sensitivity and specificity. Depending on the characteristics evaluated, the best accuracy is determined as 85.91% by using SVM algorithm.**

Keywords — Voice Disorder; Machine Learning.

[1] INTRODUCTION

Sound is the most important communication tool among human beings. Vocal communication is a basic skill that people need it to express their feelings for daily social interactions and earn it during their life span. Professionals such as singers, actors, auctioneers, lawyers, and teachers who use their voices at a higher level than normal levels are at risk of pathological voice problems. Also people who have voice disturbances due to the voice misuse, neurological disorders, drug use and unhealthy social habits may encounter many problems when communicating with people and lead to many social and personal complications. Vocal cord vibration is affected in different ways depending on the type and location of the disease in the vocal fold. Voice pathologies resulting from changes in sound quality, pitch and volume can be clinically determined by performing several procedures, such as acoustic analysis which consists of estimation of appropriate parameters extracted from an audio signal to assess possible changes in the audio path in accordance with the rules of the SIFEL protocol [2] (Società Italiana di

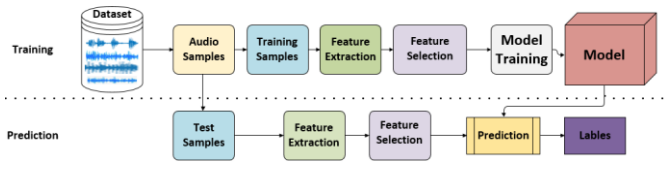


Figure.1. Illustration of voice pathology detection system

Foniatria e Logopedia) prepared by Italian Logopedic and Phoniatrics Association. Acoustic parameters are then used to evaluate sound health status. The accuracy of these parameters in detecting voice disturbances plays an important role in the detection of voice disturbances. The accuracy of the acoustic parameters is related to the algorithms used to estimate them. There has been an interest recently in machine learning techniques in the field of sound pathology in order to increase the accuracy of these parameters. In this study, application of feature selection techniques and machine learning algorithms with the ability to distinguish the patient and healthy sounds with the best accuracy is investigated. In detail, we evaluate the pathology using different features obtained from voice signals in addition to patients' age and gender information. The performance of the used machine learning methods is evaluated in terms of accuracy, sensitivity and specificity.

Details of this study as follows. Section II presents studies on detection of sound diseases by using machine learning techniques available in literature. In Section III, the data set, features and machine learning algorithms used for the classification in experimental stage are introduced. The results are discussed in Chapter V, while our results are given in Section IV.

[2] RELATED WORK

Sound pathology in the sense of data science is a multi-class classification problem depending on the audio signal from individuals. In detecting sound pathology, several machine classifiers are usually applied. In recent years, several approaches have been developed to improve performance in terms of accuracy in separating healthy and pathological sounds. These approaches focus on identifying parameters for measuring sound quality and new techniques that can detect voice disorders. A brief summary of some recent studies on our research topic is as follows; Ghulam Muhammad et al. [4] are proposed a smart healthcare framework using edge computing. With the proposed system they achieved 98.5 percent accuracy using the part of Saarbrucken Voice Disorder (SVD) database. Daria [5] makes an effort on creation of efficient and accurate system for automatic detection of normal and three different voice pathologies by using SVD database.

The decision system based on neural networks. Laura Verde et al. [6] are focused on investigation and comparision of the performance of several machine learning techniques useful for voice pathology detection. All analyses are performed on a dataset of voices selected from the SVD database. A novel system for pathological voice detection using Convolutional Neural Network (CNN) is presented [7, 8]. In this system parts of SVD database is used. Kebin Wu et al. [9] are proposed a novel model JOLL4R (JOint Learning based on Label Relaxed low-Rank Ridge Regression) to fuse audios for voice based disease detection. In these studies, NN (Neural Network) and SVM (Support Vector Machine) are used by combining American and German databases MEEI and SVD to detect voice disorders [9, 10]. Pavol Harar et al. described a preliminary investigation of Voice Pathology Detection using Deep Neural Networks (DNN) [12].

[3] METHOD

A. Database

In our study, we used the publicly available Saarbruecken Voice Database (SVD) database recorded by the Phonetic Institute of the University of Saarland in Germany. SVD is composed of healthy and pathological individuals' voice records. There are 1354 (627 male and 727 female) pathological, suffering from 71 different diseases, and 687 (259 male and 428 female) healthy voice recordings. This database consists of vowels /a/, /i/, /u/ and "Guten Morgen, wie geht es Ihnen?" (Good morning, how are you?) sentences in German.

In the study, we have used only the /a/ vowel and all the available records in the SVD database for the classification of healthy and pathological sounds. Each sample of the data used in this study consists of the voice ID (a number to define the record), age, gender and class information as healthy or pathological. The experiments are evaluated using the whole database and a balanced database, composed of 685 male and 685 female subjects. Distribution details of healthy and pathological samples of balanced database in terms of their age and gender are given in Table.1.

[1] Table.1 Balanced Dataset used in study

[2]	*[3] Healthy*		*[4] Pathological*	
[5] Age	*[6] Female*	*[7] Male*	*[8] Female*	*[9] Male*
[10]17-29	*[11]359*	*[12]138*	*[13]58*	*[14]23*
[15]30-39	*[16]27*	*[17]62*	*[18]94*	*[19]24*
[20]40-49	*[21]15*	*[22]37*	*[23]85*	*[24]43*
[25]50-59	*[26]13*	*[27]9*	*[28]87*	*[29]74*
[30]60+	*[31]14*	*[32]11*	*[33]104*	*[34]93*
[35]Total	*[36]685*		*[37]685*	

B. Features

Feature extraction, in general, is an important step in improving the success of a classification algorithm as it helps better analyze any given data. Features, commonly used in voice classification studies for machine learning techniques, are also utilized in the current study. For that purpose, raw features are first obtained in terms of MFCC, statistical features such as kurtosis, swekness, etc., all calculated over vowel /a/. Then processed features are formed based on these raw features. They are as follows:

- Age: age of each subject
- Gender: gender of each subject
- Mean and standart variations of raw features calculated over epochs of each record

Class of each record as healthy or pathological are used as labels during experiments.

C. Classifiers

Different machine learning algorithms are preferred to make a comprehensive comparison of the features obtained from the audio files. These techniques used are given below.

Support Vector Machine (SVM): Support Vector Machines are mainly used to linearly separate data from different classes. It is important to determine an optimal decision plane that is as far as possible from two classes. Training of support vector machines requires a solution in the form of a quadratic optimization problem. Sequential Minimal Optimization (SMO) technique can also be used for solution [14]. Kernels is utilized to convert a non-linearly separable problem to a linearly-separable form.

Logistic Model Tree (LMT): It is a classification model that combines logistic regression and decision tree [15]. Unlike ordinary decision trees, the logistic model leaves have a logistic regression model.

Decision Tree (DT): In this algorithm, the learned function is represented by a decision tree. A structure used to divide a data set into smaller clusters by applying a set of decision rules. To classify the data, J48, an application of the C4.5 tree classifier [16], was used.

K-Nearest Neighbord (KNN): In this algorithm, the similarity of a new data, to be classified, is compared to each example in the data in terms of distance between them. They are sorted, and first k closest is used for a decision. In this study, we used value of 50 for k and Euclidean distance function to classify the data.

D. Feature Selection

Among the various features, some of them are more valuable for voice pathology classification. Feature selection algorithms form a subset of the best features to increase the algorithm speed and accuracy by eliminating irrelevant features and reducing the size of feature set.

There are many algorithms available for feature selection. In this work, gradient boosting machine is used for that purpose. This algorithm trains very precise classifiers quickly while choosing high quality features [13]. Ten most valuable features obtained by feature selection algorithm are shown in Figure.2.

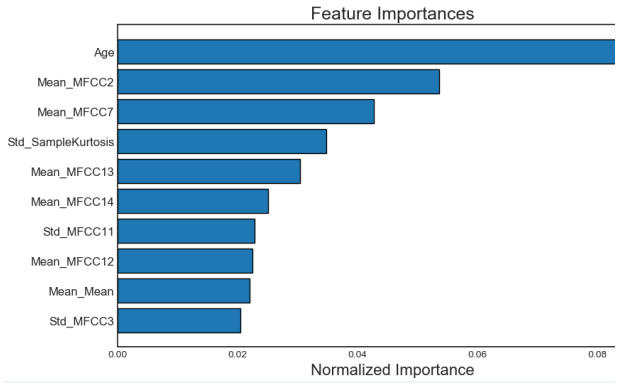


Figure.2. Most valuable features obtained

[4] RESULTS AND DISCUSSION

A. *Performance Criteria*

The performance of the proposed method is evaluated with K-fold cross-validation by which K-1 of folds is used as training set while the remaining one is used as test set. The performance results are averaged over all folds. In our experiments, K was chosen as ten. In addition to accuracy, sensitivity and specificity measurements are also used to evaluate the performance of selected classification techniques.

Accuracy, percentage of correctly classified pathological and healthy voices, is defined in Eq.1 as follows:

$$Accuracy = \frac{(TP + TN)}{(TP + TN + FP + FN)} \quad (1)$$

Sensitivity, representing the positive results of the test, and Specificity, representing the negative results, are defined in Eq.2 and Eq.3, respectively.

$$Sensitivity = \frac{TP}{(TP + FN)} \quad (2)$$

$$Specifity = \frac{TN}{(TN + FP)} \quad (3)$$

Here TP, TN, FP and FN are defined as follows.

• True Positive (TP): the algorithm recognizes that the voice sample is pathological, and it is actually pathological.

• True Negative (TN): the algorithm recognizes that the voice sample is healthy, and it is actually healthy.

• False Positive (FP): the voice sample is healthy but the algorithm recognizes it as pathological;

• False Negative (FN): the voice sample is pathological but the algorithm recognizes it as healthy

Table 2. Classification Results without Feature selection

ALL FEATURES			
ALL DATA			
	Accuracy (%)	Sensitivity (%)	Specificity (%)
SVM	83.82	81.66	**84.90**
LMT	83.52	88.00	74.80
DT	81.47	86.20	72.20
KNN	74.41	80.30	62.90
BALANCED DATA			
	Accuracy (%)	Sensitivity (%)	Specificity (%)
SVM	**85.91**	**88.47**	83.36
LMT	84.96	82.90	87.00
DT	78.24	78.50	78.00
KNN	78.75	69.90	87.60

Table.3. Classification Results with Feature selection

SELECTED FEATURES			
ALL DATA			
	Accuracy (%)	Sensitivity (%)	Specificity (%)
SVM	83.57	84.70	81.40
LMT	**84.90**	**89.70**	75.40
DT	83.62	88.50	74.10
KNN	77.50	82.70	67.20
BALANCED DATA			
	Accuracy (%)	Sensitivity (%)	Specificity (%)
SVM	85.03	81.80	88.30
LMT	84.30	81.30	87.30
DT	82.99	86.60	79.40
KNN	83.64	77.80	**89.50**

B. Classification Results

In this work four set of experiments are conducted using two different datasets, namely all and balanced, and two different feature sets, namely all and selected, as explained in Section III. Table 2 represents test results of all four classifiers when all features are extracted using all data as well as balanced data. Same results are obtained and presented in Table 3 when ten most valuable features, suggested by gradient boosting machine, are considered only. When the balanced dataset is used, the best accuracy of 85.91% in voice pathology detection is obtained by using SVM classifier. This is higher than the best result reported in the literature as shown in Table 4. When we consider all dataset, Logistic Model Tree gives best accuracy, sensitivity results while that of specificity is obtained with SVM if gradient boosting machine selected features are utilized by classifiers. Also, when the feature selection is utilized the accuracy, sensitivity and specificity increased in LMT, DT and KNN while only specificity increased in SVM. On the other hand, when the feature selection is utilized with balanced dataset, the accuracy, sensitivity and specificity are all increased in DT and KNN methods, whereas only specificity increased in SVM and LMT methods.

Table.4. Result comparation on different studies

Ref.	Method	Accuracy (%)	Database (SVD)
[6]	SVM DT LMT	**85.77**	71 pathologies are 685 healthy and 685 pathological voices
[8]	CNN	77	6 of 71 pathologies are 482 healthy and 482 pathological voices
[9]	SVM NN	87.86	2 of 71 pathologies are 686 healthy and 69 pathological voices
[12]	LSTM	68.08	71 pathologies are 687 healthy and 1354 pathological voices
[17]	ANN	83.3	71 pathologies are 70 healthy and 70 pathological voice
Ours	SVM DT LMT KNN	**85.91**	71 pathologies are 685 healthy and 685 pathological voices

[5] CONCLUSION

In this study, four different machine learning algorithms are used to detect pathology in voice signals. For the classification problem, all the models are trained, validated and tested using continuous voice /a/ sound produced with normal pitch voice obtained from Saarbruecken Voice Data set containing 71 types of pathology. All tests are performed for the entire SVD dataset as well as 1370 equally distributed samples between healty and pathological classes. These samples are selected making sure that all age groups and all 71 different disease types are included in the balanced (equally distributed) dataset. For balanced data set and whole data set, different sound pathology identification performances of various techniques such as Support Vector Machine, Decision Tree, Bayes Classification, Logistic Model Tree and KNN are compared.

When we consider the results given in the literature, the proposed method shows a significant improvement compared to various state-of-the-art studies [8,9,12,17]. On the other hand, it shows a slight improvement over the best results reported in literature [6] as illustrated in Table.4.

REFERENCES

[1] Smith, J. O. and Abel, J. S., ``Bark and ERB Bilinear Transforms", *IEEE Trans. Speech and Audio Proc*., 7(6):697-708, 1999.

[2] Lee, K.-F., *Automatic Speech Recognition: The Development of the SPHINX SYSTEM*, Kluwer Academic Publishers, Boston, 1989.

[3] Rudnicky, A. I., Polifroni, Thayer, E H., and Brennan, R. A. "Interactive problem solving with speech", *J. Acoust. Soc. Amer*., *Vol. 84, 1988, p S213(A).*

[4] Muhammad, Ghulam, et al. "Edge computing with cloud for voice disorder assessment and treatment." IEEE Communications Magazine 56.4 (2018): 60-65.

[5] Hemmerling, Daria. "Voice pathology distinction using autoassociative neural networks." 2017 25th European signal processing conference (EUSIPCO). IEEE, 2017.

[6] Verde, Laura, Giuseppe De Pietro, and Giovanna Sannino. "Voice disorder identification by using machine learning techniques." IEEE Access 6 (2018): 16246-16255.

[7] Alhussein, Musaed, and Ghulam Muhammad. "Voice pathology detection using deep learning on mobile healthcare framework." IEEE Access 6 (2018): 41034-41041.

[8] Wu, Huiyi, et al. "A Deep Learning Method for Pathological Voice Detection Using Convolutional Deep Belief Networks." Interspeech. Vol.

[9] Wu, Kebin, et al. "Joint learning for voice based disease detection." Pattern Recognition 87 (2019): 130-139.

[10] Verde, Laura, et al. "Dysphonia Detection Index (DDI): A New Multi-Parametric Marker to Evaluate Voice Quality." IEEE Access 7 (2019): 55689-55697.

[11] Ezzine, Kadria, and Mondher Frikha. "Investigation of glottal flow parameters for voice pathology detection on SVD and MEEI databases." 2018 4th International Conference on Advanced Technologies for Signal and Image Processing (ATSIP). IEEE, 2018.

[12] Harar, Pavol, et al. "Voice pathology detection using deep learning: a preliminary study." 2017 international conference and workshop on bioinspired intelligence (IWOBI). IEEE, 2017.

[13] Xu, Zhixiang, Gao Huang, Kilian Q. Weinberger, and Alice X. Zheng. "Gradient boosted feature selection." In Proceedings of the 20th ACM SIGKDD international conference on Knowledge discovery and data mining, pp. 522-531. ACM, 2014.

[14] S B. Schölkopf, C. J. Burges, and A. J. Smola,Advances in kernelmethods: support vector learning.MIT press, 1999.

[15] Sumner, Marc, Eibe Frank, and Mark Hall. "Speeding up logistic model tree induction." European conference on principles of data mining and knowledge discovery. Springer, Berlin, Heidelberg, 2005.

[16] S. L. Salzberg, "C4. 5: Programs for machine learning by j. ross quinlan.morgan kaufmann publishers, inc., 1993,"Machine Learning, vol. 16,no. 3, pp. 235–240, 1994.

[17] Teixeira, João Paulo, Paula Odete Fernandes, and Nuno Alves. "Vocal Acoustic Analysis–Classification of Dysphonic Voices with Artificial Neural Networks." Procedia Computer Science 121 (2017): 19-26.

An Ultrathin Transparent Metamaterial Absorber Using an ITO Resistive-film

Gökhan ÖZTÜRK
Electrical and Electronics Engineering Ataturk University 25100, Erzurum, Turkey
gokhan.ozturk@atauni.edu.tr

Yunus KAYA
Department of Electricity and Energy Bayburt University 69000, Bayburt, Turkey
ykaya@bayburt.edu.tr

Uğur Cem HASAR
Electrical and Electronics Engineering Gaziantep University 27310, Gaziantep, Turkey
uchasar@gantep.edu.tr

Mehmet ERTUĞRUL
Electrical and Electronics Engineering Ataturk University 25100, Erzurum, Turkey
ertugrul@atauni.edu.tr

Mustafa Alptekin ENGİN
Electrical and Electronics Engineering Bayburt University 69000, Bayburt, Turkey
maengin@bayburt.edu.tr

***Abstract*— In this article, an optically transparent and flexible microwave absorber for X- and Ku-bands application have been presented. The transparent polyethylene terephthalate (PET), polydimethylsiloxane (PDMS) and indium tin oxide (ITO) film is used to design the transparent flexible metamaterial absorber unit. The proposed absorber in the case of both TE-polarization and TM-polarization exhibits absorptivity (above 90 percent) in the frequency range from 7.75 to 18.15 GHz under normal incidence. Simulated absorptions at different incidence cases indicate that this absorber is polarization-insensitive and wide-angled. The thickness of the metamaterial absorber unit is only 3 mm. The proposed absorber is designed to be ultra thin compared to other X- and Ku-bands absorbers. The absorptivity of the proposed metamaterial absorber is simulated and CST Microwave Studio is used as a simulation program.**

Keywords*— *Absorber, ultrathin, flexible, ITO-PET, optically transparent, PDMS

[1] INTRODUCTION

Electromagnetic metamaterials are artifical periodic unit cells not found in nature. Due to their strong properties, metamaterials have been used in various fields such as solar harvesting, antennas, optic, cloak, shielding, sensors, absorber in recent years [1]–[6]. After first metamaterial absorber are used by Landy [6], various metamaterial absorber with different geometry [7]–[9] were realised, from the microwave [10] to the optical region and Terahertz region [11] with a number of features such as polarization insensitive [12], single layer [13], multilayer [14], based lumped element [15], ultrathin [16], and wideband [17] absorbers.

In last studies, optical transparent aplications have attracted much attention due to their highly transparancy features such as patch antennas [18], shielding [19] and absorber [20]. Metamaterial-based transparent absorber are used in scenarios where large light transmittance is required. A variety of attempts have been made to achieve the desired broadband absorption as well as the high optical transparency [21]–[24]. In these studies, ITO (indium tin oxide) or other conducting oxides have been used as a conductive thin film. As optical materials, in addition to non-flexible glass [21], flexible materials such as PET and PDMS have been used and their transparency have been compared [22], [23], [23], [24]. In addition, the thicknesses of the multi-level absorber structures have been compared in terms of the electrical dimension of the transmitted wavelength.

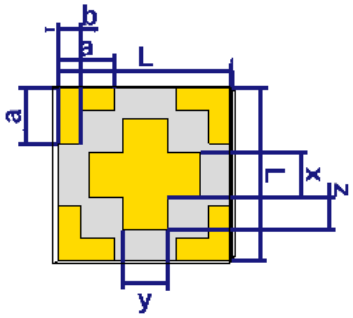
In this study, optically transparent metamaterial absorber covering both X- and Ku-bands are designed using conductive thin films. Absorber shows above 90 percent absorption from 7.75 to 18.15 GHz. In the proposed absorber, flexible optical materials which are PET and PDMS are selected for the flexible structure.The thickness of the proposed design is only 3 mm (0.129 λ_0). The proposed absorber has the same performance in both TE and TM modes under normal incidance. In addition, it shows above 80 percent absorption at both polarizations up to 40 degrees.

[2] DESIGN AND THEORY

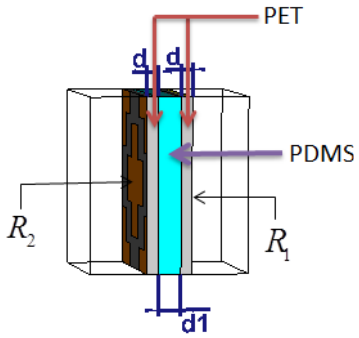
An optically transparent metamaterial absorber is presented in Fig. 1. PET and PDMS are used as optical and flexible materials in the absorber. The battom part of the absorber is completely formed with resistive film and the top part with resistive film coated metamaterial. In the simulation, middle-layer dielectric substrates are PDMS designed with a relative permittivity of 2.7 and PET is used in the upper and lower parts of PDMS with dielectric constant 3.2. The thickness of the PET and PDMS are d_1 = 2 mm and d = 0.5 mm, respectively. The battom part of the metamaterial absorber consists of ITO with a surface resistance of $R1$ = 6 Ω/sq, and the top layer of absorber consists of ITO coated metal surface with surface resistance $R2$ = 90 Ω/sq. The thickness of ITO used as thin film is chosen as t = 200 nm. The length of the metamaterial absorbent square cell is L = 10 mm. In addition, other surface variables of the metamaterial absorber are x = 4 mm, y = 4 mm, z = 3 mm, and a = 5 mm respectively. The unit cell geometry is simulated in high frequency structure simulator using floquet boundary condition in CST. The simulated S-parameters response under normal incidence of electromagnetic wave is shown in Fig. 2. According to the behavior of reflection and transmission scattering parameters, feasible surface resistance values is selected as $R1$ = 6 Ω/sq and $R2$ = 90 Ω/sq.

As seen in Fig. 1(a)-1(b), the metamaterial structure was provided by using transparent ITOs that increase the surface conductivity by coating the surfaces with thinfilm. According to the electromagnetic field theory, the absorption of ITO based metamaterial be written as follow [25]

$$A(\omega) = 1 - R(\omega) - T(\omega) = 1 - \left|S_{11}^2\right| - \left|S_{21}^2\right| \quad (1)$$

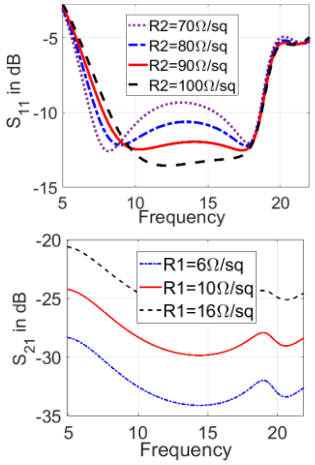


(a)



(b)

Fig. 1. (a) Top side of proposed absorber (b) side view of proposed absorber



(a) (b)

Fig. 2. (a) Simulated reflection coefficients (S_{11} in dB) of the proposed absorbers with varied surface resistance of the ITO for $R2$ = 70 Ω/sq, $R2$ = 80 Ω/sq, $R2$ = 90 Ω/sq, $R2$ = 100 Ω/sq and (b) simulated transmittion coefficients (S_{21} in dB) of the proposed absorbers with varied surface resistance of the ITO for $R1$ = 6 Ω/sq, $R1$ = 10 Ω/sq, $R1$ = 16 Ω/sq

Here, $R(\omega)$ represents the reflectance and $T(\omega)$ represents the transmittance. S_{11} and S_{21} are reflection and transmission scatter parameters. |*| is the mathematical operator for calculating the amplitude. The constitutive parameters of metamaterial provide important information about the behavior of the field within metamaterial. Using the S_{11} parameters (S_{11} nearly go to zero due to $R1$), the constitutive parameters of the matematerial unit cell are obtained as follows [25]

$$\varepsilon_{eff} = 1 - \frac{2jS_{11} - 1}{k_o d S_{11} + 1} \quad (2)$$

$$\mu_{eff} = 1 - \frac{2jS_{11} + 1}{k_o d_t S_{11} - 1} \quad (3)$$

Here d_t, ε_{eff}, and μ_{eff} are the thickness, effective permittivity, and permeability of the metamaterial absorber, respectively. In the frequency region in which the absorber operates, the impedance of the air and the absorber must match. If this condition is realized, the reflection coefficient will approach zero. The normalized wave impedance of the metamaterial absorber using only S_{11} scattering parameter is obtained as follows [24]

$$z = \frac{1 + S_{11}}{1 - S_{11}} \quad (4)$$

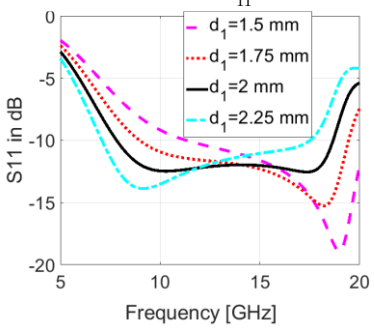
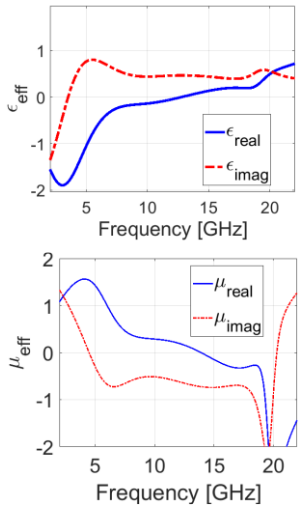


Fig. 3. Simulated reflection coefficients (S_{11} in dB) of the proposed absorber for different values of the d_1 width

[3] SIMULATION RESULTS

The performance of the thin film based metamaterial absorber in various thicknesses is given in the Fig. 3. Considering the absorber to remain more thin, the optimum thickness is chosen as d_1 = 2 mm. The total thickness of the absorber is $d_t = d_1 + 2d$ = 3 mm. The center frequency of the proposed absorber is f_c = 12.95 GHz and this thickness is 0.129 λ_0 compared to the wavelength. The permitivitty and permeability of the proposed absorber are given in Fig. 4. In the range of 7.75-18-15 GH where the metamaterial works as an absorber, Fig. 4 shows that the real part of μ_{eff} is negative at frequencies where the real part of ε_{eff} is positive. In the range of 7.75-18.15 GHz, where the metamaterial works as an absorber, Fig. 4. shows that the real part of μ_{eff} is negative at frequencies where the real part of ε_{eff} is positive. Similarly, at frequencies where the real part of ε_{eff} is negative, the real part of μ_{eff} is positive.



(a) (b)

Fig. 4. (a) Comparison of extracted constitutive electromagnetic parameters: (a) Real and imaginary parts of ε_{eff} and (b) real and imaginary parts of μ_{eff}

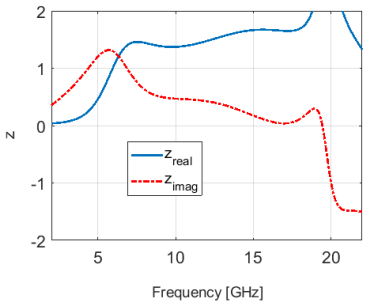


Fig. 5. Response of the extracted normalized input impedance (z) for the proposed absorber structure shown in Fig. 1(a)-1(b)

Since the real parts of constitutive parameters are opposite in the absorption frequencies, the refractive index of the metamaterial (n_{eff}) absorber consists only of the imaginary part. Since it is known that the propogation factor $T = e^{-jk_0 n_{eff} d_t}$ for exp(-jωt) time-harmonic depending, therefore, evenescent waves propogate in the metamaterial absorber.

The normalized impedance of the proposed absorber is given in Fig. 5. Fig. 5 shows that the normalized impedance of the absorber and air matched at absorption frequencies. Therefore, the real part of the normalized impedance of the absorber approaches 1 and the imaginary part approaches 0. It should be noted that these values are the normalized impedance values of the air.

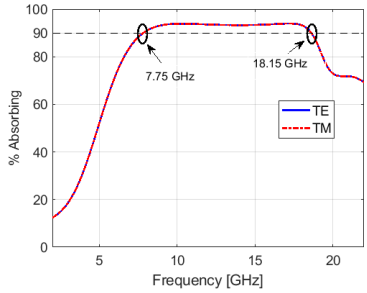


Fig. 6. Simulated percent absorptivity of the proposed absorber under normal incidance for TE and TM from CST

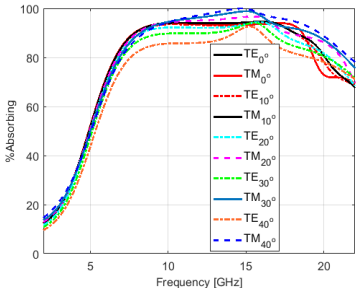


Fig. 7. Simulated percent absorptivity of the proposed absorber under different oblique incidance (from 0° to 40°) for TE and TM from CST

Table I. Comparing With Proposed Absorber And References Absorber

Ref.	Performance of Absorbers			
	Bandwidth	***Thickness***	***Flex.***	***Angle***
[21]	8.3-17.4 GHz	3.85 mm (0.165 λ_0)	No	0-45
[22]	3.8-10.8 GHz	6.25 mm (0.152 λ_0)	Yes	-
[23]	5.8-12.2 GHz	4.9 mm (0.147 λ_0)	Yes	0-45
[24]	6.2-19.3 GHz	3.62mm (0.154 λ_0)	Yes	0-45
This Work	7.75-18.15 GHz	3 mm (0.129 λ_0)	Yes	0-40

Percent absorption of the proposed absorber under normal incidance is given in Fig. 6. Fig. 6 shows that the thin film coating optically transparent metamaterial absorber exhibits absorptivity (above 90 percent) in the frequency range from 7.75 GHz to 18.15 GHz for both TE and TM polarization. As seen from Fig. 7, absorber under the onlique incident supports above 80 percent the absorptivity between 0° – 40° degrees in the operating frequency band for both TE and TM. In Table I, the comparison of the proposed absorber with other reference studies is given in terms of various properties. The studies referenced with the proposed study in Table I is compared with bandwidth, thinness, flexibility and angle performance, respectively.

[4] CONCLUSION

In this paper, an optically transparent and flexible microwave absorber for X- and Ku-bands application have been presented. The transparent PET (polyethylene terephthalate), polydimethylsiloxane (PDMS) and ITO (indium tin oxide) film is used to design the transparent flexible absorber. The absorber for both TE and TM show above 90 percent absorbtion range from 7.75 to 18.15 GHz in X- and Ku-bands under normal incidence. The thickness of the metamaterial absorber is 0.129 λ_0 compared to caming wavelength. With this features, the proposed absorber behive an ultra thin absorber compared to other absorbers. The biggest advantage of the proposed absorber compared to other optically transparent metamaterial based absorbers which take references is that it is the thinnest work. In addition, the other superior side of the proposed absorber is that it consists of flexible materials.

ACKNOWLEDGMENT

This work is supported by TUBITAK under the Project Number 218M341.

REFERENCES

[1] Bagmanci, M., Karaaslan, M., Unal, E., Akgol, O., Bakır, M., and Sabah, C. (2019). Solar energy harvesting with ultra-broadband metamaterial absorber. International Journal of Modern Physics B, 33(08), 1950056.

[2] Dong, Y., and Itoh, T. (2012). Metamaterial-based antennas. Proceedings of the IEEE, 100(7), 2271-2285.

[3] Kundtz, N., and Smith, D. R. (2010). Extreme-angle broadband metamaterial lens. Nature materials, 9(2), 129-132.

[4] Schurig, D., Mock, J. J., Justice, B. J., Cummer, S. A., Pendry, J. B., Starr, A. F., and Smith, D. R. (2006). Metamaterial electromagnetic cloak at microwave frequencies. Science, 314(5801), 977-980.

[5] Sabah, C., Dincer, F., Karaaslan, M., Unal, E., Akgol, O., and Demirel, E. (2014). Perfect metamaterial absorber with polarization and incident angle independencies based on ring and cross-wire resonators for shielding and a sensor application. optics Communications, 322, 137-142.

[6] Ebrahimi, A., Withayachumnankul, W., Al-Sarawi, S., and Abbott, D. (2013). High-sensitivity metamaterial-inspired sensor for microfluidic dielectric characterization. IEEE Sensors Journal, 14(5), 1345-1351.

[7] Banadaki, M. D., Heidari, A. A., and Nakhkash, M. (2017). A metamaterial absorber with a new compact unit cell. IEEE Antennas and Wireless Propagation Letters, 17(2), 205-208.

[8] Zhou, Y., Cao, X., Gao, J., Yang, H., and Li, S. (2018). Reconfigurable metasurface for multiple functions: magnitude, polarization and phase modulation. Optics express, 26(22), 29451-29459.

[9] Dincer, F., Karaaslan, M., Unal, E., and Sabah, C. (2013). Dual-band polarization independent metamaterial absorber based on omega resoanator and octa-star strip configuration. Progress In Electromagnetics Research, 141, 219-231.

[10] Gu, S., Su, B., and Zhao, X. (2013). Planar isotropic broadband metamaterial absorber. Journal of Applied Physics, 114(16), 163702.

[11] Liu, Y., Gu, S., Luo, C., and Zhao, X. (2012). Ultra-thin broadband metamaterial absorber. Applied Physics A, 108(1), 19-24.

[12] Shen, X., Cui, T. J., Zhao, J., Ma, H. F., Jiang, W. X., and Li, H. (2011). Polarization-independent wide-angle triple-band metamaterial absorber. Optics express, 19(10), 9401-9407.

[13] Wang, B., Koschny, T., and Soukoulis, C. M. (2009). Wide-angle and polarization-independent chiral metamaterial absorber. Physical Review B, 80(3), 033108.

[14] Cao, M., and Zhang, Q. (2018, May). Design of broadband multilayer metamaterial absorber. In 2018 IEEE MTT-S InternationalWireless Symposium (IWS) (pp. 1-3). IEEE.

[15] Zhi Cheng, Y., Wang, Y., Nie, Y., Zhou Gong, R., Xiong, X., and Wang, X. (2012). Design, fabrication and measurement of a broadband polarization-insensitive metamaterial absorber based on lumped elements. Journal of applied physics, 111(4), 044902.

[16] He, Y., Wu, Q., and Yan, S. (2019). Multi-band terahertz absorber at 0.1–1 THz frequency based on ultra-thin metamaterial. Plasmonics, 14(6), 1303-1310.

[17] Rajabalipanah, H., Abdolali, A., and Mohammadi, M. (2021). Experimental and analytical investigations on a wide-angle, polarizationinsensitive, and broadband water-based metamaterial absorber. Journal of Physics D: Applied Physics, 54(22), 225302.

[18] Potti, D., Tusharika, Y., Alsath, M. G. N., Kirubaveni, S., Kanagasabai, M., Sankararajan, R., ... and Bhargav, P. B. (2021). A Novel Optically Transparent UWB Antenna for Automotive MIMO Communications. IEEE Transactions on Antennas and Propagation.

[19] Zhu, X., Xu, J., Qin, F., Yan, Z., Guo, A., and Kan, C. (2020). Highly efficient and stable transparent electromagnetic interference shielding films based on silver nanowires. Nanoscale, 12(27), 14589-14597.

[20] Takizawa, K., and Hashimoto, O. (1999). Transparent wave absorber using resistive thin film at V-band frequency. IEEE transactions on microwave theory and techniques, 47(7), 1137-1141.

[21] Zhang, C., Cheng, Q., Yang, J., Zhao, J., and Cui, T. J. (2017). Broadband metamaterial for optical transparency and microwave absorption. Applied Physics Letters, 110(14), 143511.

[22] Deng, R., Zhang, K., Li, M., Song, L., and Zhang, T. (2019). Targeted design, analysis and experimental characterization of flexible microwave absorber for window application. Materials and Design, 162, 119-129.

[23] Jang, T., Youn, H., Shin, Y. J., and Guo, L. J. (2014). Transparent and flexible polarization-independent microwave broadband absorber. Acs Photonics, 1(3), 279-284.

[24] Deng, R., Li, M., Muneer, B., Zhu, Q., Shi, Z., Song, L., and Zhang, T. (2018). Theoretical analysis and design of ultrathin broadband optically transparent microwave metamaterial absorbers. Materials, 11(1), 107.

[25] Bhattacharyya, S., and Vaibhav Srivastava, K. (2014). Triple band polarization-independent ultra-thin metamaterial absorber using electric field-driven LC resonator. Journal of Applied Physics, 115(6), 064508.

Classification of Snoring Sounds

Rabiye KILIÇ
Faculty of Engineering, Department of Electrical and Electronics Engineering
Atatürk University Erzurum, Turkey
rabiyekilic@atauni.edu.tr

Nida KUMBASAR
Faculty of Engineering, Department of Electrical and Electronics Engineering
Atatürk University Erzurum, Turkey
nida.kumbasar@grv.atauni.edu.tr

Hilal Kübra SAĞLAM
Department of Electrical and Energy, Technical Science Vocational College ,
Atatürk University
Erzurum, Turkey
hilalk.saglam@atauni.edu.tr

Emin Argun ORAL
Faculty of Engineering, Department of Electrical and Electronics Engineering Atatürk University
Erzurum, Turkey
eminoral@atauni.edu.tr

İbrahim Yücel ÖZBEK
Faculty of Engineering, Department of Electrical and Electronics Engineering Atatürk University Erzurum, Turkey
iozbek@atauni.edu.tr

***Abstract*— Snoring is a disturbance in breathing caused by air flow caused by tissue vibration in different parts of the upper respiratory tract during sleep. It can be a symptom of a serious illness such as sleep apnea. For this reason, it is of great importance that the origin of snoring sounds is determined and treated correctly. In this study, the MPSSC data set containing snoring sounds was used. The data set contains 828 audio files taken from 224 subjects. In the study, features were obtained with Mel-Frequency Cepstral Coefficients (MFCC), Pitch, SCAT and Gaussian Mixture Model (GMM) to determine the location of snoring sounds in the upper respiratory tract. Classification was made with K-Nearest Neighbors (KNN) and Support Vector Machine (SVM). In the classification of snoring sounds, 57.87% success rate was achieved with the Scat + GMM + SVM model as an initial study.**

Keywords*— *Snoring Sound Classification, MFCC, SCAT, GMM, UBM, KNN, SVM

[1] INTRODUCTION

Snoring is an airflow-induced voice disorder that causes tissues to vibrate during sleep. Snoring occurs due to respiratory obstruction [1] and is a common condition affecting approximately 20-40% of the society [2]. Although not taken seriously, snoring can also be a sign of a serious chronic disease known as obstructive sleep apnea (OSA) [3]. Therapeutic and surgical methods are available to treat snoring cases. Correct diagnosis of the cause of snoring is of great importance in determining the appropriate treatment. The standard diagnostic procedure is done using video recordings.

Drug Induced Sleep Endoscopy (DISE) recordings are widely used to determine the location of the occlusion and the pattern of vibration [4]. Snoring is generally divided into four groups according to its physiological source. The classification of these four groups is called the Velum, Oropharyngeal, Tongue, Epiglottis (VOTE) classification. These regions of the upper respiratory tract are shown in Fig.1 [5].

(V)-Velum (palate): Snoring originating from gelopharyngeal walls

(O)-Oropharyngeal: Snoring originating from lateral walls, tonsils including palatine

(T)-Tongue (tongue): Snoring originating from the tongue base including the posterior of the airway

(E)-Epiglottis (small tongue): Snoring caused by folding of the epiglottis due to decreased structural stiffness or posterior displacement against the posterior pancorneal wall [5].

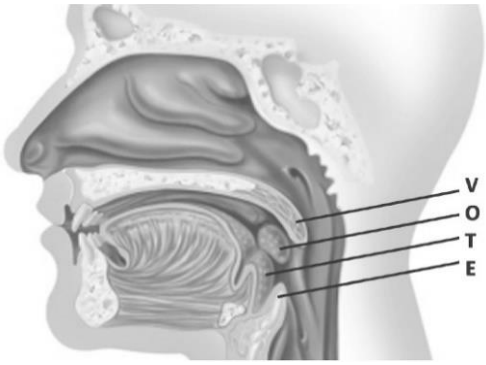


Fig. 1. Locations of VOTE classes in the upper respiratory tract [5]

In this study, Munich-Passau Snore Sound Corpus (MPSSC) data set was used for VOTE classification. For this purpose, in the first step, feature extraction from the sound recordings in the data set was performed, the model was created with these attributes and the classification was carried out in the last step. The flow diagram of the study is shown in Fig. 2.

In recent years, various studies have been carried out on snoring with different methods. Classification of snoring has been studied using Generative Adversarial Networks (GAN), which is popular in synthetic data production [6,7]. GMM modeling of snoring sounds has been used in the treatment of sleep apnea [8].

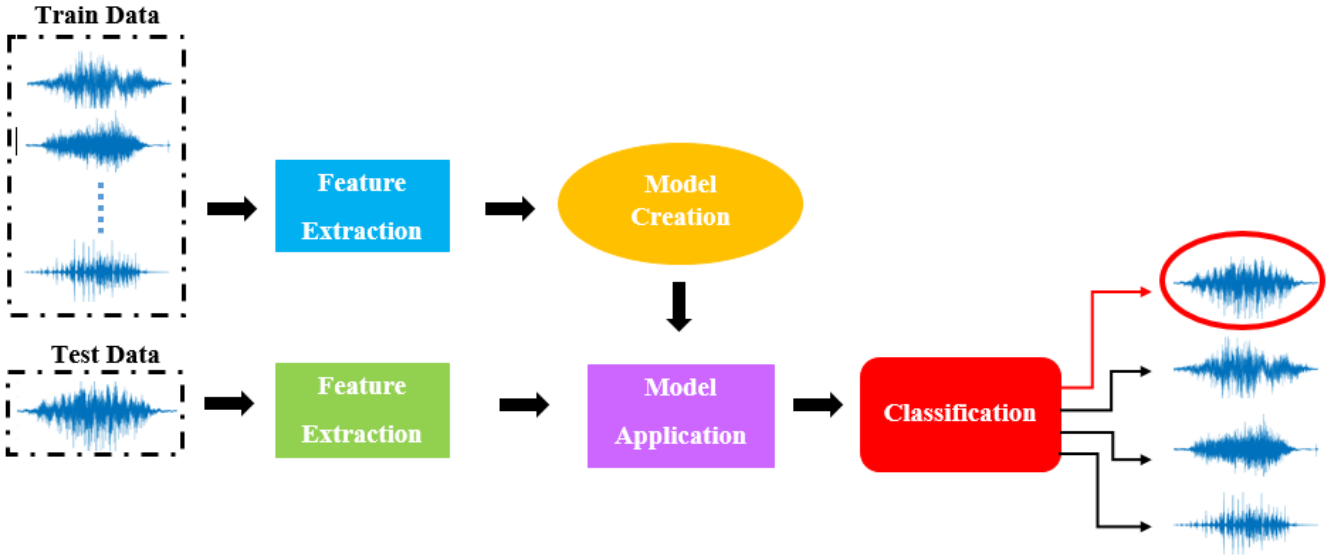


Fig. 2. Classification of snoring sounds

[2] SNORING DATA SET

In this study, Munich-Passau Snore Sound Corpus (MPSSC) data set was used. The relevant data set includes 828 snoring sound samples taken from 224 subjects recorded between 2006 and 2015 from three medical centers. It consists of more than 30 hours of voice recording recorded during DISE examinations [9]. Average sampling time was 1.46s, and all samples were recorded at 16 KHz sampling rate and 16 bit resolution. The samples taken are labeled by the experts as V, O, T, E according to the anatomical source of the snoring. In Fig. 3, time-domain images of V, O, T, E signals taken from a sample are given.

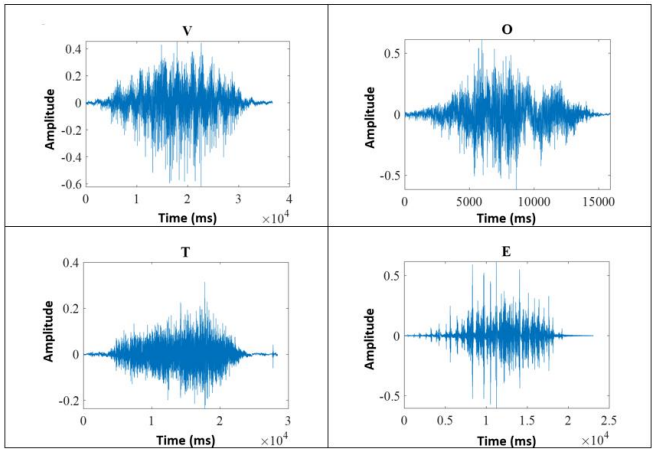


Fig. 3. Representation of snoring sounds in time space

The data set is divided into three as train, devel and test. The distribution of the samples in the data set according to the classes is as shown in Table I. When this table is examined, it is seen that the distribution of the samples among the classes is not balanced.

Table 1. Distribution Of Snoring Sounds By Class

	Train	Devel	Test
V	168	161	155
O	76	75	65
T	8	15	16
E	30	32	27
Sum	282	283	263

[3] METHODS USED IN CLASSIFICATION OF SNORING SOUNDS

In this study, Preparation, Attribute Extraction and Classification stages are carried out in order to classify snoring sounds.

A. Preparation

The sound signals in the data set change between 1-3 seconds. For this reason, before extracting the attributes, all audio files in the data set have been arranged so that their total duration is 3 seconds. For this process, those shorter than 3 seconds are added to them and completed to 3 seconds. The next step is Hamming windowing [9]. Before the signals are processed, they are divided into frames containing a certain number of samples. This is done with window functions. With these window functions used, the middle parts of the signal parts are highlighted, while the starting and ending regions are damped and the spectral leakage is weakened.

B. Feature Extraction

Two different feature extraction methods are applied in the study. First, the feature extracted with SCAT and modeled with GMM. Second, the attribute is extracted with MFCC and Pitch.

a) Feature extraction with SCAT Spectrum

The SCAT transform is an extension of the mel spectrogram that calculates multiple modulation spectrum coefficients through wavelet convolution and modulated cascades. SCAT consists of two layers. In the first layer, the input signal expressed with x is taken and the calculations in Equation 1 are made with the wavelet filter bank indicated with ψ_{λ_1} [11].

$$S_1 x(t,\lambda_1) = \left|x * \psi_{\lambda_1}\right| * \varphi(t) \qquad (1)$$

High frequency signals output from the first layer are transferred to the second layer. SCAT features are obtained in this layer output.

$$S_2 x(t,\lambda_1,\lambda_2) = \left|\left|x * \psi_{\lambda_1}\right| * \psi_{\lambda_2}\right| * \varphi(t) \qquad (2)$$

In this study, ScatNet open source MATLAB Library was used to calculate SCAT [12]. Each frame of the features obtained from ScatNet is 220x16 in size, and each snoring sound is obtained in 220x (11x16) size with SCAT.

b) Gaussian Mixture Model (GMM)

Gaussian mixture model is used to model the available data with more than one Gaussian distribution. Since the amount of data available for educational purposes is limited, the GMM_{UBM} model was created using all the data with the Universal Background Model.

GMM parameters are defined as $\{\pi_k, \mu_k, \sum_k\}_{k=1}^{K}$, where K is the number of gauss components, π_k a priori probability value in the mixed model, μ_k the mean value, and $\sum_k$ is the covariance matrix. On the other hand, T attribute is the number of N training records, and when the SCAT feature vector is expressed with x_i, GMM_{UBM} is calculated with the training data as given in Equation 3.

$$GMM_{UBM} = \frac{1}{n_k} \sum_{i=1}^{T*N} P(k|x_i)\, x_i \quad (3)$$

As stated in Equation 4, n_k here is the sum of the posterior probabilities of the features in the relevant distribution and the posterior probability value of $P(k|x_i)$ is given in Equation 5.

$$n_k = \sum_{i=1}^{T} P(k|x_i) \quad (4)$$

$$P(k|x_i) = \frac{\pi_k N(x_i|\mu_k, \sum_k)}{\sum_{m=1}^{K} \pi_m N(x_i|\mu_m, \sum_m)} \quad (5)$$

Audio files allocated for training and testing are modeled separately with GMM and the GMM_{record} value given in Equation 6 is calculated.

$$GMM_{record} = \frac{1}{n_k} \sum_{i=1}^{T} P(k|x_i)\, x_i \quad (6)$$

Since the snoring sound recordings are short-term, the number of attributes is low. Since a more comprehensive model is created taking into account all training data in GMM_{UBM}, it is modified with GMM_{record} andGMM_{UBM} as given in Equation 7.

$$record_attribute = a_k GMM_{UBM} + (1 - a_k) GMM_{record} \quad (7)$$

The a_k influence rate here is given in Equation 8, and r (relevance parameter) is chosen as 16.

$$a_k = \frac{n_k}{n_k + r} \quad (8)$$

c) Feature Extraction with Mel-Frequency Cepstral Coefficients (MFCC) and Pitch

Mel-spectrogram calculates the Short-Time Fourier Transform and determines the spectral sizes using the filter bank created according to the mel-scale [10]. The following steps are followed while extracting Pitch features with MFCC.

1. Snoring sounds are divided into 30 ms frames with 75% overlap.

2. MFCC and Pitch features were obtained for all snoring sounds by using these frames.

C. Classification

Two different classification approaches were used in the classification of snoring sounds. While the first one of these, KNN, features obtained with MFCC and Pitch were used in classification, in the second, the super vectors prepared by creating a GMM model with SCAT were classified with SVM.

a) K-Nearest Neighbours (KNN)

KNN classification is a technique used in multiple classification problems, and the classification process is performed on the basis of the smallest (closest) ones by calculating the Euclidean distances with all neighbors for the specified number of K neighbors.

b) Support Vector Machine (SVM)

SVM aims to find the line that will maximize the distance between support vectors through an infinite number of lines in linearly separable data. When the data are not linearly separable, it aims to find the best separator plane by moving the data to a higher dimension.

In this study, linear, polynomal and gauss type SVM was used and the best results were found with linear SVM.

[4] EXPERIMENTAL STUDIES

A. Performance Measure

Various methods are used for performance criteria in machine learning, and since the study data set has an unbalanced distribution, the Unweighted Average Recall (UAR) approach defined by ComParE 2017 [8,13] was used to determine the performance criteria.

The UAR equation is calculated as Equation 9, with $N_s$class number, TP and FN respectively True Positive and False Negative.

$$UAR = \frac{1}{N_s} . \sum_{i=1}^{N_s} \frac{TP_i}{TP_i + FN_i} \quad (9)$$

In order to find the most appropriate value of the C parameter in SVM, different values in the range of $2^{-15}, \ldots, 2^{15}$ were tried, and the weights of each class were equalized because the data set used had an unbalanced distribution.

B. Experimental Results

When the feature was removed with MFCC and KNN classification was made, the success rate of UAR was 45.84%, and when the classification with KNN was used by using Mfcc + Pitch to improve the results, the UAR success rate reached 51.09%. When the super vectors created with SCAT and GMM were classified with SVM, the UAR success rate of 57.87% was obtained as an initial study. The resulting Confusion Matrix is shown in Fig. 4.

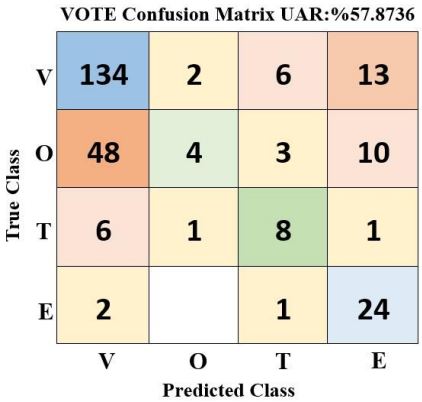


Fig. 4. UAR success rate in Scat + GMM + SVM model

The studies and suggested methods in the literature and UAR results for the purpose of classifying the snoring sound are given in Table II.

Table 2. Comparıson Of Studıes In Lıterature

METHODS	UAR (%) Devel	UAR (%) Test
Schuller et al. [14] (CNN + LSTM)	40.3	40.3
Schuller et al. [14] (CNN + LSTM+BoAW)	45.1	46.0
Rao et al. [15]	49.6	-
Nwe et al. [16]	57.1	51.7
Kaya et al.[17]	-	64.2
Vesperini et al. [10] (MLP)	58.20	74.19
Zhang et al. [7]	46.8	56.7
Proposed Method (MFCC+KNN)	-	**45.84**
Proposed Method (MFCC+Pitch+KNN)	-	**51.09**
Proposed Method (SCAT+GMM+SVM)	-	**57.87**

[5] FUTURE STUDIES

In this study, the MPSSC data set including snoring sounds was used. By using SCAT and Gaussian mixed model, feature was obtained and 57.87% UAR success rate was obtained as an initial study in classification with SVM. In the next step, it is aimed to obtain better results by eliminating the unbalanced distribution of the data set.

REFERENCES

[1] N. Charakorn and E. J. Kezirian, “Drug-induced sleep endoscopy,” Otolaryngologic Clinics of North America, vol. 49, no. 6, pp. 1359–1372, 2016.

[2] D. Pevernagie, R. M. Aarts, and M. De Meyer, “The acoustics of snoring,” Sleep medicine reviews, vol. 14, no. 2, pp. 131–144, 2010

[3] K. Wilson, R. A. Stoohs, T. F. Mulrooney, L. J. Johnson, C.Guilleminault, andZ. Huang, “The snoring spectrum: acoustic assessment of snoring sound intensity in 1,139 individuals undergoing polysomnography,” CHEST Journal, vol. 115, no. 3, pp. 762–770, 1999.

[4] R. Nonaka, T. Emoto, U. R. Abeyratne, O. Jinnouchi, I. Kawata, H. Ohnishi, M. Akutagawa, S. Konaka, and Y. Kinouchi, “Automatic snore sound extraction from sleep sound recordings via auditory image modeling,” Biomedical Signal Processing and Control, vol. 27, pp. 7–14, 2016.

[5] C. Janet, W. Parsing, and C. Heister, “Acoustic analysis of snoring aids,” Somnologie-Schlafforschung und Schlafmedizin, vol. 18, no. 2, pp. 87– 95, 2014.

[6] J. Han, Z. Zhang, N. Cummins, B. Schuller, "Adversarial training in affective computing and sentiment analysis: Recent advances and perspectives", IEEE Comput. Intell. Mag., vol. 14, no. 2, pp. 68-82, May 2019

[7] Z. Zhang, J. Han, K. Qian, C. Janott, Y. Guo, B. Schuller, "Snore-gans: Improving automatic snore sound classification with synthesized data", IEEE Journal of Biomedical and Health Informatics, pp. 1-11, 2019.

[8] A. Sebastian, , P. Cistulli.,G. Cohen., P.de Chazal, “A Preliminary Study of the Automatic Classification of the Site of Airway Collapse in OSA patients Using Snoring Signals” In 2019

[9] C. Janott et al., "Snoring classified: The Munich–Passau snore sound corpus", Comput. Biol. Med., vol. 94, pp. 106-118, Mar. 2018

[10] F. Vesperini, A. Galli, L. Gabrielli, E. Principi, S. Squartini, "Snore sounds excitation localization by using scattering transform and deep neural networks", Proc. International Joint Conference on Neural Networks (IJCNN), pp. 1-8, 2018.

[11] S. S. Stevens, J. Volkmann, and E. B. Newman, “A scale for the measurement of the psychological magnitude pitch,” JASA, vol. 8, no. 3, pp. 185–190, 1937.

[12] L. Sire, M. Kapok, E. Ocalan, and V. Lostanlen, “Scatnet: a matlab toolbox for scattering networks,” 2013.

[13] J. Salamon, J. P. Bello, "Feature learning with deep scattering for urban sound analysis", Proc. 2015 23rd Eur. Signal Process. Conf., pp. 724-728, Aug. 2015.

[14] B. Schuller et al., "The INTERSPEECH 2017 computational paralinguistics challenge: Addressee cold & snoring", Proc. Annu. Conf. Int. Speech Commun. Assoc. (INTERSPEECH), pp. 3442-3446, 2017.

[15] A. Rao, S. Yadav, and P. K. Ghosh, “A dual source-filter model of snore audio for snorer group classification,” in Proc. 18th Annual Conference of the International Speech Communication Association (INTERSPEECH), Stockholm, Sweden, 2017, pp. 3502–3506.

[16] T. L. Nwe, H. D. Tran, and B. Ma, “An integrated solution for snoring sound classification using Bhattacharyya distance based GMM supervectors with SVM, feature selection with random forest and spectrogram with CNN,” in Proc. 18th Annual Conference of the International Speech Communication Association (INTERSPEECH), Stockholm, Sweden, 2017, pp. 3467–3471.

[17] H. Kaya and A. A. Karpov, “Introducing weighted kernel classifiers for handling imbalanced paralinguistic corpora: Snoring, addressee and cold, ”in Proc. 18th Annual Conference of the International Speech Communication Association (INTERSPEECH), Stockholm, Sweden, 2017, pp. 3527–3531.

Comparative analysis of Microstrip Patch Antenna on different substrate material using slit technique for x-band application

Auwalu Aminu Abubakar
Department of Electrical Engineering Bayero University Kano, Nigeria.Kano, Nigeria.
aaabubakar.ele@buk.edu.ng

Zainab Yunusa
Department of Electrical Engineering Bayero University Kano, Nigeria. Kano, Nigeria.
zee1yunusa@yahoo.com

***Abstract* ---- Different dielectric substrates are used for the design, simulation and fabrication of microstrip patch antennas. It is important to investigate which substrate gives a better antenna performance through simulation and prior to fabrication. In this paper FR-4 and RT/Duroid were used as substrate materials so as to investigate which material gives better antenna performance. Quad slit methods were employed on the patch material for both substrates to improve the gain and bandwidth of the MPA for X-band application. The CST software was used in the simulation of the proposed design. The proposed models were resonated at 10.192 GHz. For the FR-4 material and 9.97GHz for the RT/Duroid material. The result obtained in this proposed design show that the design using FR-4 provides better bandwidth while the design using RT/Duroid provides better propagation, Gain and VSWR.**

Keywords: Patch Antenna, Microstrip Line, Slit.

I. INTRODUCTION:

With the rapid development in wireless communication technology, the need for, light weight, compact size, cost and low profile antenna has increased considerably. Microstrip antennas are designed to attain these desires. Microstrip antenna is made conventionally by a dielectric substrate, radiating patch and ground plane. Patches can be in many different geometrical shapes like rectangular, circular, triangular, square etc. [1] Microstrip antennas are widely used because of being compact, low cost, conformal and suitable to integrate with Radio Frequency (RF) devices. In spite of these advantages, the main problems of microstrip antennas are low gain and narrow bandwidth which limit them from many wireless communication systems.

Many techniques have been presented to overcome the microstrip antenna limitations which includes: The triangular UWB Microstrip Antenna with slits and triangular Patch with Defected Ground. [2]. Slotted Patch andParasitic Patch/Multi-Resonator [3]. Small size wideband microstrip patch antenna with slot in ground plane and stacked patch is presented. [4] A defected ground plane is in the form of L shaped slot and the rectangular parasitic patches and diagonal cuts at top corners is presented.[5] MPA loaded with CRR is also presented. [6] Diagonal DGS (DDGS) technique is applied. [7]. Slots and slits which employed in the structure was presented [8].The second resonance suppression technique for bandwidth enhancement is proposed. [9]. stub and circular slit is presented [10]. Also the variation of slit length, slit width, distance of the slit from the edge of the patch was presented [11]. The popular feeding methods were presented as: Coaxial Feed, Aperture Coupled Feed, and Proximity Coupled Feed. [12].

However most of the research work slit techniques was employed in WIMAX. Wi-Fi and WLAN applications.

Based on the mentioned, the contribution of the present work is to proposed vertical slit techniques for X-band applications.

II. MODEL DESIGN

The proposed work consists of two different designs on FR-4 and RT/DUROID substrate materials. The CST application was used in the simulation of proposed model as illustrated in fig. 1 below.

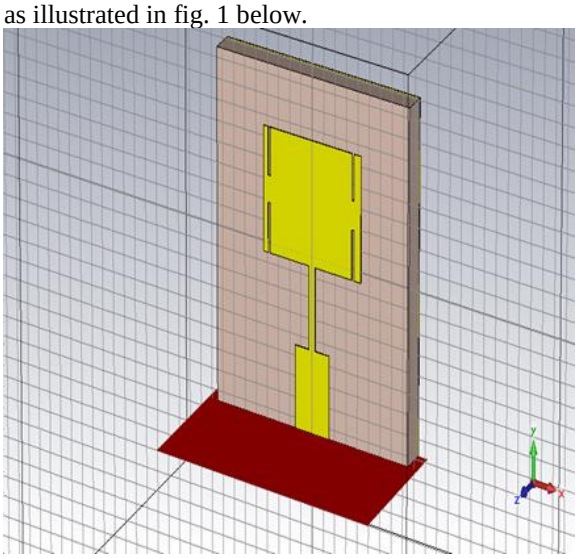


Fig 1a. Design using FR-4

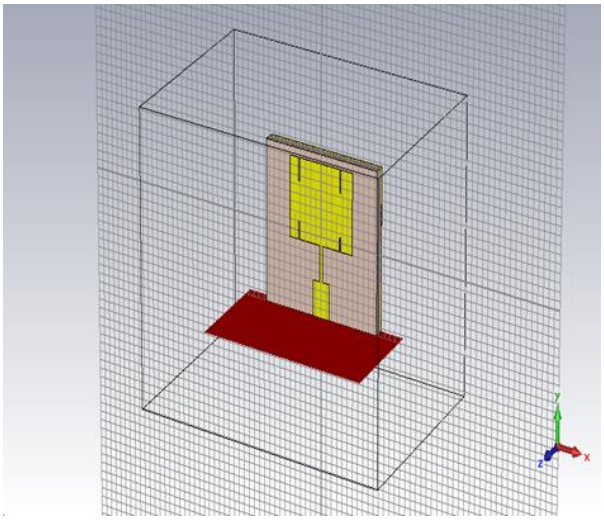


Fig 1b. Design using RT/Duroid

III. ANTENNA DESIGN CONSIDERATION AND DIMENSIONS

The design formula of the proposed model is given below:

a. Rectangular Microstrip Patch Antenna

The formula of the RMPA is presented below: [1]

$$W = \frac{v_o}{2f_c}\sqrt{\frac{2}{1+\varepsilon_r}} \quad (1)$$

Where: W is the width of the patch element, f_c, is the center frequency, fc = 10GHz, V_o, is the velocity of light = 3 x 10^8 m/s, ε_r, is the dielectric constant of the substrate material FR-4 = 4.4 and RT/Duroid = 2.2

$$\varepsilon_{eff} = \frac{1+\varepsilon_r}{2} + \frac{\varepsilon_r - 1}{2}\left[1 + \frac{12h}{W}\right]^{-1/2} \quad (2)$$

Where: ε_{eff}, is the effective dielectric constant, h, is the height of the substrate material, which is 1.6mm

$$\Delta L = 0.412h\frac{(\varepsilon_{eff}+0.3)(\frac{W}{h}+0.264)}{(\varepsilon_{eff}-o.258)(\frac{W}{h}+0.8)} \quad (3)$$

Where: ΔL, is the change in length.

$$\Delta L_{eff} = L + 2\Delta L \quad (4)$$

Where: $L_{eff,}$ is the effective patch length.

$$L = \frac{v_o}{2f_c\sqrt{\varepsilon_{eff}}} - 2\Delta L \quad (5)$$

Where: L, is the actual patch length.

b. Substrate Dimension

The Substrate materials used are FR-4 and RT/Duroid having a thickness of 1.6mm. The Length of the substrate, is consider to be not less than six times the height of the substrate plus patch length as in equation (6).

SL = 6Sh + PL (6)

likewise, the width of the substrate Sw, is consider to be not less than six times the height of the substrate plus patch width as presented in equation (7).

Sw = 6Sh + Pw

The design formula of the proposed model and the conventional MPA are given in Table 1:

Table 1: Design formula of the proposed model and the conventional MPA

PARAMETERS	MODEL1	MODEL2	MODEL 3	MODEL 4
patch length, Lp	6 mm	9.05mm	6mm	9.05mm
patch width, wp	8.6 mm	11.86mm	8.6mm	11.86mm
Microstrip length, Lf	4 mm	4mm	4mm	4mm
Microstrip width, wf	3 mm	3mm	3mm	3mm
Quarter wavelength, Lq	4 mm	4mm	4mm	4mm
Quarter wave width, wq	0.53 mm	0.53mm	0.53mm	0.53mm
dielectric substrate, ε_r	4.4	2.2mm	4.4	2.2
substrate thickness, h	1.6 mm	1.6mm	1.6mm	1.6mm
Ground plane length, Lg	17 mm	18.7mm	17mm	18.7mm
Ground plane width, wg	17 mm	21.5mm	17mm	21.5mm
substrate length, Ls	17 mm	18.7mm	17mm	18.7mm
substrate width, Ws	17 mm	21.5mm	17mm	21.5mm
slit length, ls			2mm	2mm
slit width, ws			0.2mm	0.2mm
patch thickness pt	0.035mm	0.035mm	0.035mm	0.035mm
ground plane thickness, gt,	0.035mm	0.035mm	0.035mm	0.035mm
slit thickness, St	0.035mm	0.035mm	0.035mm	0.035mm
Substrate Material	FR-4	RT/DUROID	FR-4	RT/DUROID
Patch Material	Copper	Copper	Copper	Copper

IV. RESULTS AND DISCUSSION

The simulated result obtained which includes return loss plot, VSWR, bandwidth, and gain of the above model design will be presented.

A. Return Loss of the proposed model

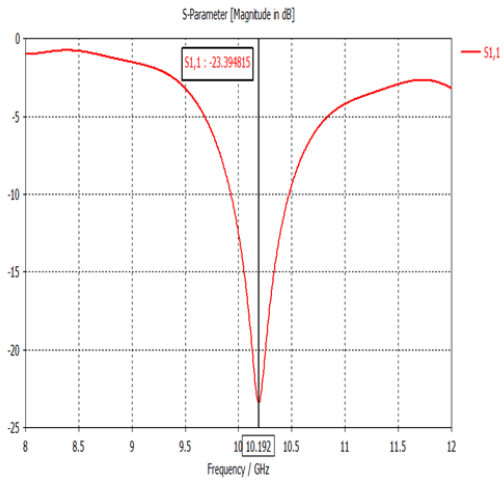


Fig 2a. (S11) for FR-4

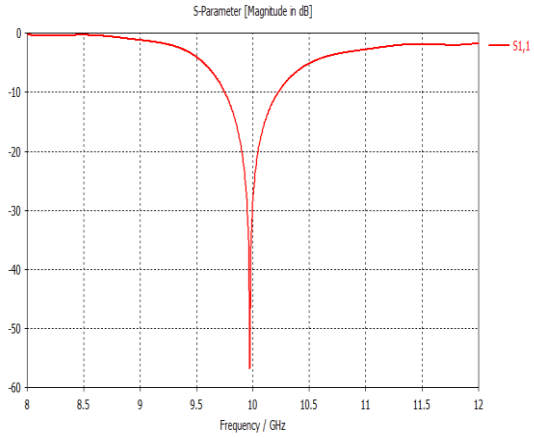


Fig 2b. (S11) for RT/Duroid

B. Voltage Standing Wave Ratio (VSWR)

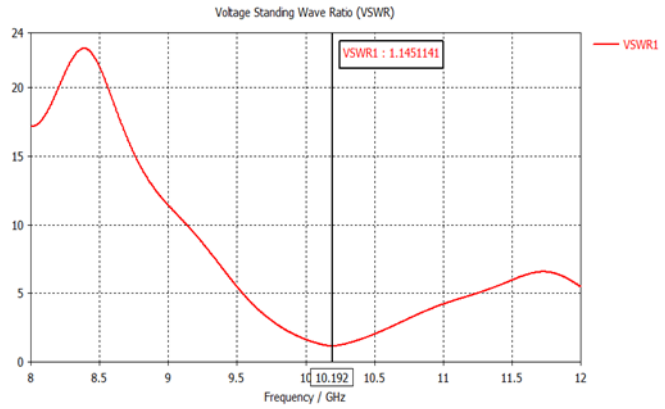


Fig. 3a. VSWR for FR-4

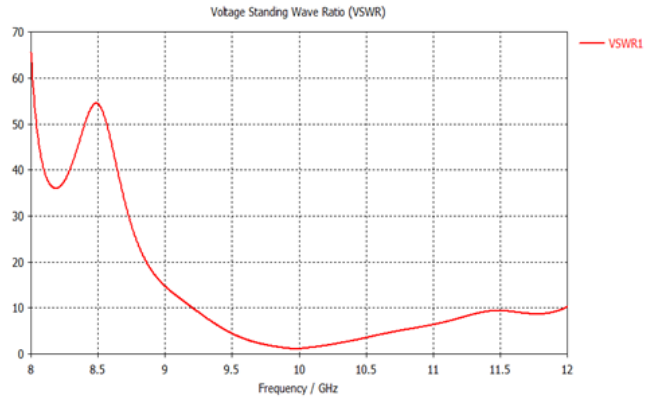


Fig. 3b. VSWR for RT/Duroid

C. Gain of the proposed design

The Gain of the proposed design was presented as shown in figure 4a and b for FR-4 and RT/Duroid respectively.

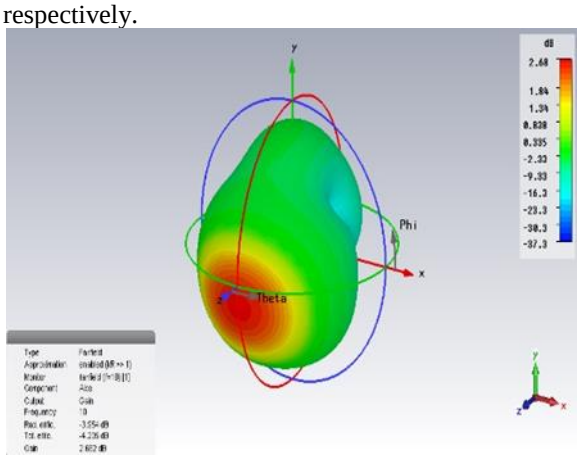


Fig. 4a. Gain for FR-4

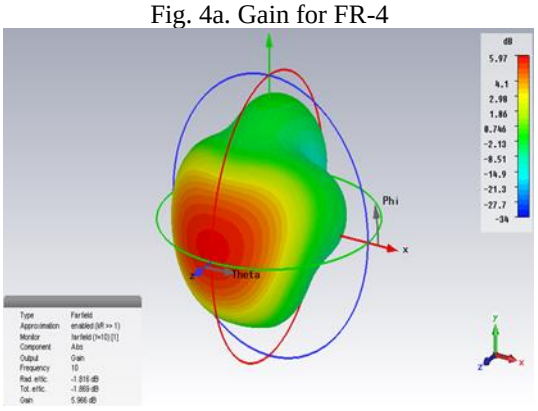


Fig. 4b. Gain for RT/Duroid

Table 2. Summarized The Result And Comparison Between The Proposed Model And The Existing Work.

MODELS	methodology	Resonant frequency	Bandwidth	Gain	VSWR	S11	Directivity
Model 1	Microstrip line feeding technique	10.16GHz	500 MHZ	2.73dB	1.15	-23.1 dB	6.69 dBi
Model 2	Microstrip line feeding technique	9.72GHz	480 MHz	6.34 db	1.00	-48.94 db	8.05 dBi
Model 3	Quad vertical slit technique	10.19GHz	550 MHZ	2.68dB	1.14	-23.4 dB	6.64 dBi
Model 4	Quad vertical slit technique	9.97GHz	480 MHZ	5.97 db	1.00	-56.88 db	7.7 dBi
Benchmark work by A. F. Salami, et al. (2017)	Microstrip line feeding technique	10.0GHz	500MHz	4.6 db	1.05	-31db	

V. CONCLUSION

In This work the result showed that, proposed model design using RT/Duroid has higher gain of 5.97db compared to FR-4 with 2.68db. While the proposed model design using FR-4 has wider bandwidth 0f 550MHz compared with that of RT/Duroid of 480MHz, and the VSWR is within the standard value of 1.0 and 1.14 for RT/Duroid and FR-4 respectively.

The methods used during this model design is vertical quad slits. The results were simulated using CST software which produced S11 of -23.4 dBi at 10.19 GHz, and S11of -55.8 dBi at 9.97GHz, With these presented results, the design using RT/Duroid will have better propagation and radiation and the two models can be employed for X-band applications.

REFERENCES

[1] C. A. Balanis, *Antenna Theory: Analysis and Design, 3rd Edition*. 2005.

[2] R. M. Elsagheer, "Study on bandwidth enhancement techniques of microstrip antenna," *J. Electr. Syst. Inf. Technol.*, vol. 3, no. 3, pp. 527–531, 2016, doi: 10.1016/j.jesit.2015.05.003.

[3] A. H. Abdelgwad, "Microstrip Patch Antenna Enhancement Techniques," vol. 12, no. 10, pp. 703–710, 2018.

[4] H. Al-raweshidy and R. Nilavalan, "Bandwidth enhancement for microstrip patch antenna using stacked patch and slot Bandwidth Enhancement for Microstrip Patch Antenna Using Stacked Patch and Slot," no. September 2014, 2009, doi: 10.1109/IWAT.2009.4906874.

[5] I. Version, P. A. Nawale, and P. R. G. Zope, "Design and Improvement of Microstrip Parameters Using Defected Ground Structure Patch," vol. 4, no. 6, pp. 123–129, 2014.

[6] L. Tao *et al.*, "Bandwidth Enhancement of Microstrip Patch Antenna Using Complementary Rhombus Resonator," vol. 2018, 2018.

[7] R. Satyanarayana, " Bandwidth Enhancement of 4GHz Probe Fed Rectangle Microstrip Patch Antenna with Diagonal DGS Technique for Wi-Fi Applications .," vol. 14, no. 12, pp. 2925–2934, 2019.

[8] D. Pundir, "Comparative Study of Microstrip Patch Antenna for Wireless Applications," vol. 12, no. 1, pp. 61–72, 2019.

[9] R. Satyanarayana, "Isolation Enhancement of 3GHz Probe Fed Rectangle Microstrip Patch Antenna by Second Resonance Suppression Technique for Wireless Applications," no. 2, pp. 3878–3886, 2019, doi: 10.35940/ijeat.B3355.129219.

[10] D. Pardhan, "Design of Extended Circular Patch with Rectangular Stub and Circular Slit Used For Ultra Wide Band Application (X-Band)," vol. 11, no. 4, pp. 14–24, 2019, doi: 10.9790/4861-1104021424.

[11] S. R. Behera, "Dual Band and Dual Polarized Microstrip Patch Antenna Bachelor of Technology," no. May, 2010.

[12] A. S. B. Mohammed, "Review of Feeding Techniques for Microstrip Patch Antenna," vol. 178, no. 27, pp. 39–43, 2019.

IRRADIANCE IMPACT ON THE PV POWER OUTPUT

Thomas Lionel Makosso
Department of Electrical, Electronics and Computer Engineering
Cape Peninsula University of Technology
218283695@mycput.ac.za

Ali M Almaktoof
Department of Electrical, Electronics and Computer Engineering
Cape Peninsula University of Technology
almaktoofa@cput.ac.za

Khaled Aboalez
Department of Electrical, Electronics and Computer Engineering
Cape Peninsula University of Technology
aboalezk@cput.ac.za

***Abstract*—This paper studied the impact of a non-uniform irradiance on a performance of a grid tied Photovoltaic (PV) systems. The irradiance plays a major role in the PV systems performance. It is among the external challenges that solar system may encounter. So, it is of a high importance to analyze the effects of the irradiance and the influence on the PV parameters. Due to the fact that the irradiance is non uniform throughout the year, we insert variations in order to work in a realistic scenario. The main target is to track the maximum power from the output of the PV system. The simulations were performed in MATLAB software, and it reveals that the irradiance is from far the key components that ensure the PV performance. Even with a maximum power point tracking in place, when the irradiance drops the power follows.**

***Keywords*—Irradiance, MPPT, PV SYSTEM**

I.. INTRODUCTION

Photovoltaic (PV) systems are on a growth trajectory that is expected to continue through the year and in the years to come. The grid efficiency, resilience and reliability are improved with the growing level of renewable energy penetration made possible by the development of smart grid technology [1]. Photovoltaic systems occupy the first position over the other sources due to the fact that it is a continuous available and cost effective source of energy [1]. The presence of smart grid will open up opportunities for solar power generation. Inverter is a major component in PV as it converts direct current to alternative current. We distinguish three principals' types of PV inverter which are: rooftop solar PV, grid tied connected PV and battery back-up inverter [2]. Rooftop solar PV does not show major problems that need to be investigated. In, present a rooftop PV and explained that there are not so many issues that need to be addressed with that mode of connection. However, grid tied inverters are linked through multilevel source. The connection between the grid and the PV system is made through numerous power electronic equipment which results in generating harmonics. In the objective of realizing a high network efficiency and reliability, there is a need for a filter between the inverter and the network for reducing the harmonics currents. So, a filter is used to minimize the harmonic currents at the point of common coupling. But some control difficulties may appear [3]. And it leads insecurity issues within the control framework and the resonance frequency between the inverter and the network. So, we intend to show on the PV side how the irradiance can significantly impact the PV output even with a maximum power point technique (MPPT) in place.

II. DESCRIPTION OF THE THREE-PHASE GRID TIED PV SYSTEM

A three-phase, grid tied PV system is depicted in Fig. 1. It comprises a 210kW PV system with and maximum power point tracking to regulate the power, a three phase MOSFET Inverter, Boost converter a LCL Filter and the grid. Fig 1 shows an overview of the proposed system.

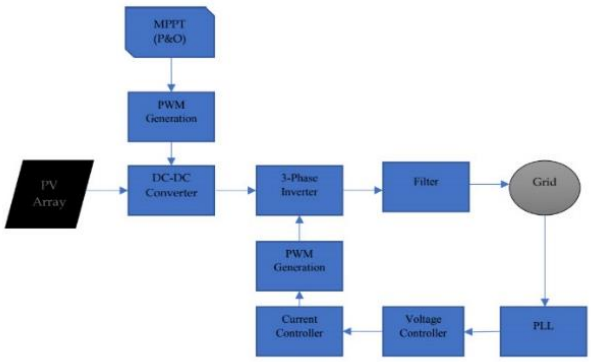


Fig. 1: Schematic of the three-phase PV system.

It is advantageous to use the Perturb and Observe technique which is a well-known technique based on the search of a given function's local optimum point. It significantly contributes to obtain the maximum power from the PV [5].

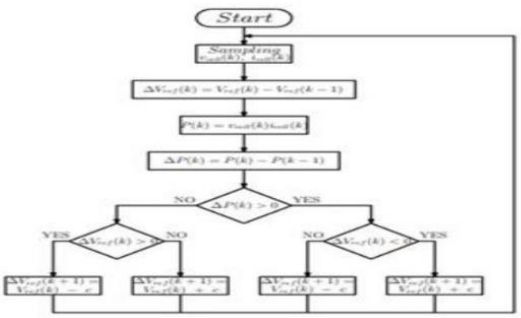


Fig. 2: Perturb and Observe algorithm

III. PROPOSED IRRADIATION ANALYSIS

With the maximum power point tracking in place, the system should be able to produce power under any conditions. The load profile has been selected from the US Department of Energy, and present general appliances found in most rural area in Africa [6]. With approximately 70 houses, we will determine how much power and solar panels it will require to power those households. 9 solar panels of 250W have been chosen to make up 210Kw. Some variations on the irradiation have been implemented and allowed to observe the power curve will react. This analysis has been performed using MATLAB/Simulink. Then discuss and reach to a possible explanation of the outcome.

The PV plays the main role as provider of power to meet the load. This model use PV system without batteries. In [4], the output energy per unit of the PV system is presented:

$$E_{PVG}(t) = G(t) \times A \times P \times \eta_{PVG} \quad (1)$$

where

$E_{PVG}(t)$ is the hourly energy output of the PV system

G (t) is the hourly irradiance in kW/m^2

A is the surface area in m^2

P is the PV penetration level factor$\eta_{PVG}$is the efficiency of the PV generator.

The equation that describes the I-V characteristic is given by:

$$I = I_L - I_D \quad (2)$$

We use the approximation $I_{ph} \approx I_{SC}$ and substituting the constant q/a_f.k.T_J with A, equation … becomes:

$$I = I_O\left[1 - exp[(V + I_S R_S)]\right] \quad (3)$$

If I_s= 0 and V= V_{OC} and the factor A can be calculated by:

$$I=0= V_{oc}=\frac{1}{A}\ln\left(\frac{I_{sc}}{Io1}\right) \rightarrow A=\frac{1}{V_{oc}}\ln\left(\frac{I_{sc}}{Io1}\right) B=\ln\left(\frac{I_{sc}}{Io1}\right) \quad (4)$$

In standard test conditions (T_C = 25°C and G_{ref}= 1000W/m^2) the ratio I_{SC}/ I_{Sat} can be approximated with 10^9

Replacing A and making the notation B = $\ln\left(\frac{I_{SC}}{Io1}\right)$ the value of the expression of V_S becomes:

$$V = V_{oc} \times \left[1 + \frac{1}{B} ln(I_0 - I)\right] - R_S I \quad (5)$$

At maximum power point (MPP) the value of the current I_s is $I_{MPP}$and S = P_{MPP}/I_{MPP}. The values of R_S and I_{MPP} can be obtained by resolving the system:

$$V = P_{MPP}/I_{MPP} \quad (6)$$

$$\begin{cases} \frac{P_{MPP}}{I_{MPP}} = V_{oc} \times \left[\frac{1}{B} + ln(I_{SC} - I_{MPP})\right] - R_S I_{MPP} \\ \frac{P_{MPP}}{I_{MPP}^2} = \frac{V_{OC}}{B} \times \left(\frac{1}{I_{SC} - I_{MPP}}\right) + R_S \end{cases} \quad (7)$$

In order to find how the power should go with irradiance, it has been considered the fact that the value is constant 1000W/m^2 on a clear day. Then dropped it to 250 or 500W/m^2 .

IV. RESULTS AND DISCUSSIONS

The Simulation of the system was executed in MATLAB/Simulink.
The three-phase voltage source inverter strategy was simulated using MATLAB/Simulink; this was done to evaluate the performance of the proposed Perturb and Observe algorithm and to check the performance and robustness of the proposed irradiation analysis method. Fig 3 presents the grid tied PV system with Simulink blocks. Table I shows the parameters and their values, as used for the simulations.

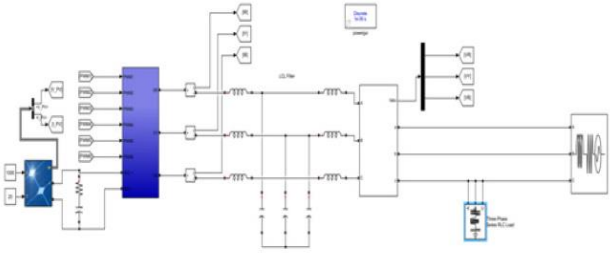


Fig. 3: Grid tied PV system of 210kW.

TABLE I: THREE PHASE GRID TIED PV PARAMETERS

Parameter	Values	
PV power	240kW	
Inverter inductor	2.5mH	
Grid inductance	1.9mH	
Capacitance	14.1μF	
Dc link voltage	600V	
Grid	Phase to phase voltage	415V
	Frequency	50Hz
	Phase angle	0
Load	Active power	200kW
	Nominal frequency	50Hz
	Reactive power	100VAR

The Perturb and Observe algorithm was evaluated with regard to two performance indicators:
First step: It will be constant and then drop the irradiance and keeping the temperature constant.
Second step: Applying the existent MPPT and proving that the irradiance has a greater impact on the PV Output.

The table II below shows the general description of the PV system of 240Kw

TABLE II: PV SYSTEM PARAMETERS

Parameters	Values
Power (P)	250W
Parallel strings	57
Series connected per modules	15
Open circuit voltage (V_{oc})	37.8V
Voltage at maximum power point (I_{mp})	31.5V
Short circuit current (I_{sc})	8.7A

From the Fig 4 , the Power generated from the PV system has been tracked. The power is equal to 210kW as predicted and only from 4s to 6s when the irradiande was pretty low the power decrease to 1.5kw

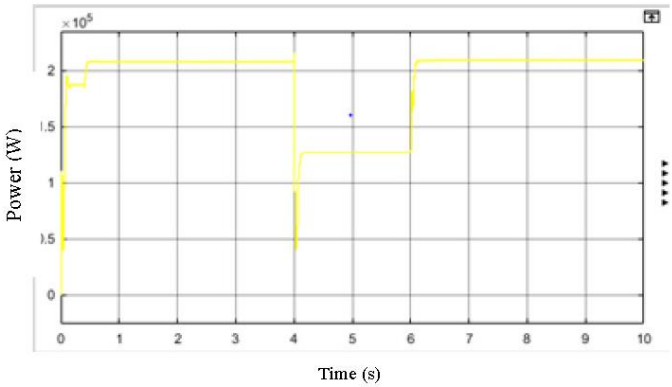


Fig. 4: Power variations

Once the Maximum Power Point Technique is applied, the maximum power of 210kW has been achieved as been calculated. Fig 5 presents the irradiation changes.

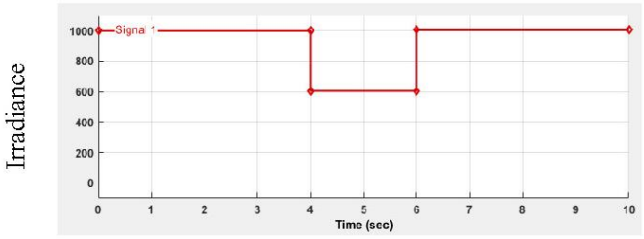


Fig. 5: Irradiation variations

The main target was to track the maximum power from the output of the PV. It has been noticed that the irradiance can play a significant role in this process. As depicted in Fig. 4. When the irradiance drops the power is automatically affected.

IV. CONCLUSION

The aim of this study was to apply changes on the irradiation and see if the maximum power from the output of the PV remains the same. It has been noticed that the irradiance can play a significant role in this process. As depicted in Fig 4. When the irradiance drops the power is automatically affected.
Researchers have described the maximum power point as the most important element that allows getting the maximum power from the PV output, which it has been contradicted in this study.
The results demonstrated that even with an MPPT, the irradiance still plays a more significant role in the output power from the PV system.

REFERENCES

[1] A. Mazaheri, F. Barati et F. Ghavipanjeh, "Multi Variable PI Control Design for Grid Tied Inverters Three Phase PV Inverters", chez 2019 Iranian Conference on Renewable Energy and Distributed Generation, 2019.

[2] B. Ayalew, A. Afolabi et A. Al Durra, "Robust Continuous Nonlinear Predictive Controller via Integral Sliding Mode Control for Grid Tied PV Inverter:, chez 2020 2nd International Conference on Smart Power and Internet Energy Systems, 2020.

[3] K. R. A. et N. L. D., "Modelling and optimization of a Community Microgrid", chez Energy Procedia, 2019.

[4] S. Remache, S. Islam et K. Barra, "Algeria Power Management of Grid Connected PV System with Integrated Energy Storage", chez 2019 1st International Conference on Sustainable Renewable Energy Systems and Applications, 2019.

[5] K. Matiyali, S. Goel et H. Joshi, "Voltage Oriented Control of Grid Tied Solar PV System", chez 2019 Women Institute of Technology Conference on Electrical and Computer Engineering, 2019.

[6] S. Singh, B. Singh et B. Panigrahi, "Enhanced Comb Frequency Locked Loop Based Control of Grid Tied PV System", chez 2020 IEEE International Conference on Power Electronics , Smart Grid and Renewable Energy, 2020.

[7] W. Zhao.N, Huo.J, Xu.D et Zhu.L, "Inverter Power Control Based on DC-Link Voltage Regulation for IPMSM Drives Without Electrolytic Capacitors", IEEE Transactions on Power Electronic, vol. 33, n° %11, pp. 558 - 571, Junuary 2018.

[8] K. Sorte, K. Panda et G. Panda, "Current reference Control Based MPPT Investigation of Power Management Algorithm for Grid Tied Solar PV Battery System", Chez IEEE System Journal, 2021.

[9] R. Kumar et S. S. Swain, "A Comparative Study on Different Types of PV Modules and Their Optimization for Increasing the Efficiency Part-I", IEEE, Ghaziabad, India, 2016.

[10] C.Poontoghai, "Design of LCL FILTER for grid interfaced PV systembased on cost minimization", 2018.

[11] Zeb.K, Khan.I, Busarello.T.D et Ahmad.I, "Review on Recent Advances and Future Trends of Transformerless Inverter Structures for Single-Phase Grid-Connected Photovoltaic Systems", Energies 2018, vol. 11, n° %18, 2018.

[12] W. B. et X. Y., "Current control of grid connected Inverter with LCL filter Based on extended state", 2019.

[13] J. Kumar, A. Agarwal, & V. Agarwal. "A review on overall control of DC microgrids", Journal of Energy Storage, pp. 117-138, 2019.

Analytical Solution of Brillouin Amplifier Equations for the Lossless Medium Working in Saturation Region

Fikri Serdar GÖKHAN
Dept. of Electrical and Electronics Engineering
Alanya Alaaddin Keykubat University
Alanya, Turkey
serdar.gokhan@alanya.edu.tr

***Abstract*— Steady State Coupled intensity equations are used to define interaction of Pump and Stokes waves in a Brillouin Amplifiers. These coupled equations have well-defined boundary conditions and mathematically treated as a two-point boundary value problem. Conventional solution techniques lead transcendental equation which results implicit solution. The exact solution can be obtained only numerically which require software packages. Within the concept of this manuscript, the aim is mainly to derive Gain of Brillouin Amplifier in a lossless Brillouin medium working in the Saturation region.**

Keywords*— *Steady State Coupled Intensity Equations, Conserved Quantity, Brillouin Fiber Amplifiers

[1] INTRODUCTION

Stimulated Brillouin scattering (SBS) is the most efficient nonlinear amplification mechanism in optical fibers, in which a large gain may be obtained under the pump power of several milliwatts [1]. This has led to the design of Brillouin Fiber Amplifier (BFA) and has been implemented in a wide range of applications, such as an active filter due to its narrowband amplification feature [2] or in the control of pulse propagation in optical fibers [3]. The BFA can also be used to measure strain and temperature [4] which has led to the design of distributed Brillouin sensors (DBS). In these types of sensors, strain and temperature can be measured along the whole fiber length [5]. In the BFA configuration, SBS can be used for efficient narrow band amplification when the Stokes wave is input from the rear (opposite to the pump) end of the fiber. Interaction between the pump and the Stokes wave due to SBS is described by a system of ordinary differential equations (ODEs) [6]. The system of ODEs for BFAs has well-defined boundary conditions: $I_p(0) = I_{p0}$ and $I_s(L) = I_{sL} = I_{Stokes}$. Such a mathematical problem is known as the two-point boundary value problem. Since the boundary value of the $I_p(L)$ and/or $I_s(0)$, with L being the fiber length, is undetermined, such systems of non-linear ODEs is typically addressed numerically. The exact analytical solution to the system of ODEs is known only for lossless media [7], with the exception of an analytical solution of integration constant C. However, obtained expression is a transcendental equation giving the unknown quantity $I_s(0)/I_p(0)$ in terms of the known quantities $I_p(0)$ and $I_s(L)$. In this paper, we focus on the derivation of the Pump and Stokes evolution equations depending on the conserved quantity C and proposed the solution of this conserved quantity using asymptotic theory [8]. The solution of conserved quantity is used for the derivation of analytical solution of Brillouin Amplifier Equations in a lossy medium.

[2] THEORETICAL MODEL

BFA requires that a Stokes wave to be injected at the opposite end of the fiber. Two counter-propagating light waves are coupled through electrostriction, which leads to the amplification of the Stokes at the expense of the pump. $P_p(0)$, $P_p(L)$ are input and output pump power respectively, while $P_s(0)$ and $P_s(L)$ are output and input Stokes power respectively. The coupled ODEs for the evolution of the intensities of pump I_p and Stokes I_s in a BFA for lossless medium can be written as,

$$dI_p/dz = -g_B I_p I_s \quad \textbf{(1a)}$$

$$dI_s/dz = -g_B I_p I_s \quad \textbf{(1b)}$$

here $0 \le z \le L$ is the propagation distance along the optical fiber of the total length L, g_B is the Brillouin gain coefficient. Note that, here we assume a Stokes wave launched from the rear end of the fiber. Then the known values of the input pump intensity $I_p(0) = I_{p0}$ and the input Stokes intensity $I_p(0) = I_s(L) = I_{sL}$ are the boundary values. The geometry of a BFA is shown in Figure 1.



Fig. 16. Geometry of an SBS amplifier.

The solution of Eq. [1] is derived in Ref. [9,10], which leads to the solution of,

$$I_p(z) = cI_{p0}\left[I_{p0} + (c - I_{p0})exp(-cg_B z)\right]^{-1} \quad \textbf{(2)}$$

$$I_s(z) = c(I_{p0} - c)\left[I_{p0}\, exp(cg_B z) - (I_{p0} - c)\right]^{-1} \quad \textbf{(3)}$$

where $I_p(z) = I_s(z) + I_{p0} - I_{s0}$ and $c = I_p(z) - I_s(z) = I_{p0} - I_{s0}$ is the conserved quantity. To explicitly find the value of parameter of conserved quantity c, we approximately solve the equation:

$$I_{sL} = c(I_{p0} - c)\left[I_{p0}\, exp(cg_B L) + (c - I_{p0})\right]^{-1} \quad \textbf{(4)}$$

using boundary condition I_{sL}. Within the paper, we will obtain the solution of the conserved quantity c for the Saturation region.

[3] SOLUTION OF CONSERVED QUANTITY FOR SATURATION REGION

It can be shown that, $I_{p0} \gg c$ and it this case $I_{p0} - c \cong I_{p0}$ and hence, the solution of Eq. [4] can be analytically defined as,

$$I_{sL} = \frac{c(I_{p0} - c)}{I_{p0}\, exp(cg_BL) - (I_{p0} - c)} \cong \frac{c}{\frac{I_{p0}}{I_{p0} - c} exp(cg_BL) - 0{,}99}$$

$$\cong \frac{c}{exp(cg_BL) - 0{,}99} \quad \textbf{(5)}$$

The solution of Eq.[5] is,

$$c \cong -0{,}99 I_{sL} - \frac{1}{g_BL} LambertW(-I_{sL} g_B L e^{-I_{sL} g_B L}) \quad \textbf{(6)}$$

where LambertW is a function which satisfies LambertW(x) exp (Lambert W(x)) = x. Using Eq.[2], Evolution of Pump and Stokes intensity is plotted in Figs.[2-3].

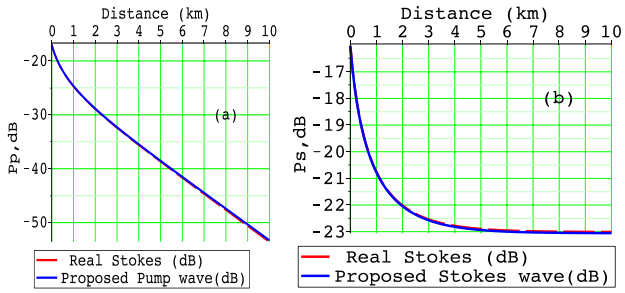


Fig.2 (a) Pump and (b) Stokes power evolution computed with Eq.[2] and Eq.[3], respectively. $P_{p0} = 20\ mW$, $P_{sL} = 5\ mW$, $L = 10\ km$, $A_{eff} = 80\ \mu m^2, g_B = 1.091x10^{-11}, I = P/A_{eff}$.

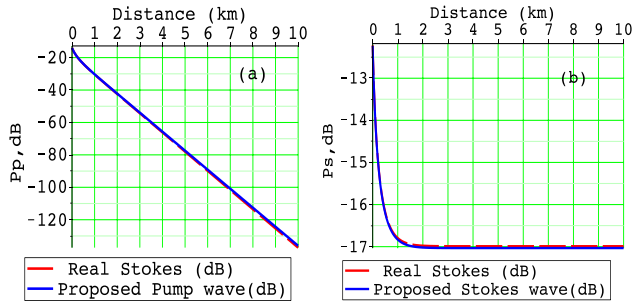


Fig.3 (a) Pump and (b) Stokes power evolution computed with Eq.[2] and Eq.[3], respectively. $P_{p0} = 40\ mW$, $P_{sL} = 20\ mW$, $L = 10\ km$, $A_{eff} = 80\ \mu m^2, g_B = 1.091x10^{-11}, I = P/A_{eff}$.

The gain of the Amplifier can be obtained using I_{s0}/I_{sL}. Therefore, it can be evaluated using Eq.[3] and expressed as:

$$Gain\ of\ Amplifier\ in\ Saturation\ Region = \frac{(I_{p0} - c)}{I_{sL}} \quad \textbf{(7)}$$

$$Gain\ of\ Amplifier\ in\ Saturation\ Region = \left(\frac{I_{p0}}{I_{sL}} + 0{,}99 + \frac{1}{g_BLI_{sL}} LambertW(-I_{sL} g_B L e^{-I_{sL} g_B L})\right) \quad \textbf{(8)}$$

In Fig.[4], the predicition of Eq.[8] is plotted with the numerical prediction with constant $P_{sL} = I_{sL}/A_{eff}$, where A_{eff} is the effective area of the fiber.

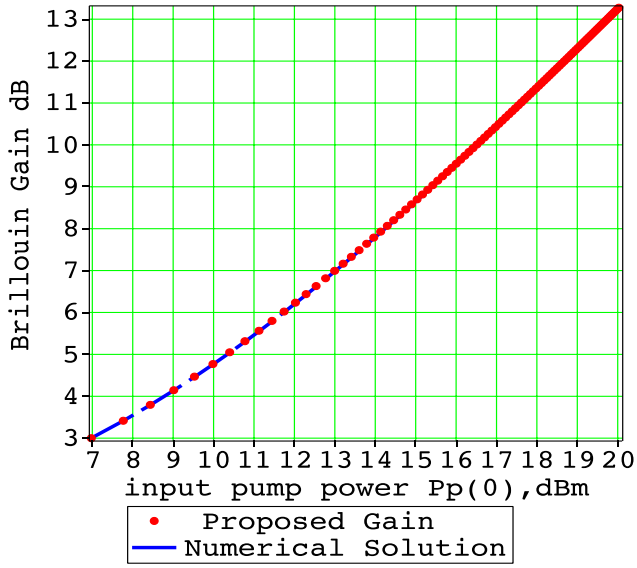


Fig. 17. BFA gain versus the input Pump power P_{p0} for saturation region. Red circles stand for the Proposed Gain computed with the predictions of the analytical formula (8), and solid blue line stand for numerical results. $P_{sL} = 5\ mW, L = 10\ km, A_{eff} = 80\ \mu m^2, g_B = 1.091x10^{-11}$.

In Fig.[5], the predicition of Eq.[8] is plotted with the numerical prediction with constant $P_{p0} = I_{p0}/A_{eff}$

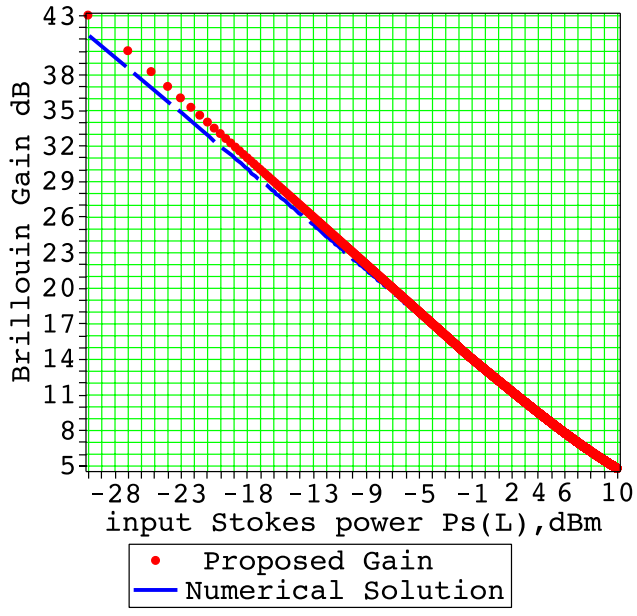


Fig.5 BFA gain versus the input Stokes power P_{sL} for saturation region. Red circles stand for the Proposed Gain computed with the predictions of the analytical formula (8), and solid blue line stand for numerical results. $P_{p0} = 20\ mW, L = 10\ km, A_{eff} = 80\ \mu m^2, g_B = 1.091x10^{-11}$.

IV. SOLUTION RANGE OF INTEREST

The solution range of interest can be obtained by the solution range of LambertW function. The plot of the LambertW function is plotted in Fig.6

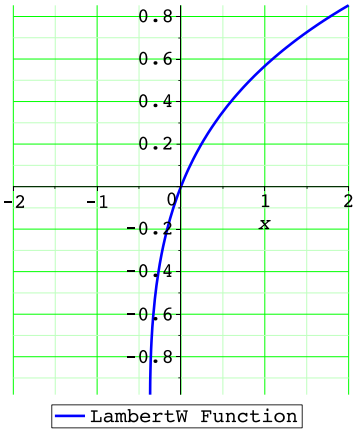


Fig.6 The plot of the LambertW function.

From the plot, it can be obtained that, LambertW(x) function is not defined if $x < -0.36$. Therefore, the term $-I_{sL}g_BLe^{-I_{sL}g_BL}$ inside the LambertW(x) function should not be less than –0.36. Therefore from solution of;

$$x = ye^{y} = -0.36 \quad \textbf{(9)}$$

$$y = -I_{sL}g_BL = -0.806 \quad \textbf{(10)}$$

$$I_{sL} > \frac{0.806}{g_BL} \text{ and } P_{sL} > \frac{0.806\,A_{eff}}{g_BL} \quad \textbf{(11)}$$

In general $P_{p0} \geq LambertW(P_{sL})$, and hence if $P_{p0} \geq P_{sL}$ is selected, the solution will be very close to the numerical solution.

In Table 1, the gain of the BFA with the solution range of interest can be seen.

Table 1. Gain and criteria of the BFA working in Saturation region.

Criteria	Gain of BFA
Saturation Region $P_{sL} > \frac{0.806 \times A_{eff}}{g_BL}$	$\left(\frac{I_{p0}}{I_{sL}} + 0{,}99 + \frac{1}{g_BLI_{sL}} LambertW(-I_{sL}g_BLe^{-I_{sL}g_BL})\right)$
$P_{p0} \geq P_{sL}$	

IV. CONCLUSION

We have presented an approximate Analytical solution to the system of SBS equations in a lossless medium in working Saturation region. The approximate value of the conserved quantity is obtained accurately. The results obtained can be practically used to optimize performance of Brillouin fiber amplifiers where the medium loss is negligible.

REFERENCES

[1] N. A. Olsson and J. P. Van der Ziel, "Cancellation of fiber loss by semiconductor laser pumped Brillouin amplification at 1.5 μm," Appl. Phys. Lett. 48, 1329–1330 (1986).

[2] R. W. Tkach, A. R. Chraplyvy, and R. M. Derosier, "Performance of a WDM network based on stimulated Brillouin scattering," IEEE Photon. Technol. Lett. 1, 111–113 (1989).

[3] Kwang Yong Song, Miguel González Herráez, and Luc Thévenaz, "Observation of pulse delaying and advancement in optical fibers using stimulated Brillouin scattering," Opt. Express 13, 82-88 (2005).

[4] D. Culverhouse, F. Frahi, C. N. Pannell, and D. A. Jackson, "Potential of stimulated Brillouin scattering as sensing mechanism for distributed temperature sensor," Electron. Lett. 25, 913–915 (1989).

[5] F. S. Gokhan, "Moderate-gain Brillouin amplification: an analytical solution below pump threshold," Opt. Commun. 284, 4869–4873 (2011).

[6] A. Kobyakov, M. Sauer, and D. Chowdhury, "Stimulated Brillouin scattering in optical fibers," Adv. Opt. Photon. 2, 1–59 (2010).

[7] R. W. Boyd, Nonlinear Optics, 3rd ed. (Academic, 2007), Chap. 9 , pp. 442-443.

[8] Daniel Richardson, Bruno Salvy, John Shackell, Joris Van Der Hoeven. "Asymptotic Expansions of exp-log Functions." [Research Report] RR-2859, INRIA. (1996)

[9] Fikri Serdar Gökhan, Hasan Göktaş, and Volker J. Sorger, "Analytical approach of Brillouin amplification over threshold," Appl. Opt. 57, 607-611 (2018).

[10] Fikri Serdar Gökhan and Hasan Göktaş, "Analytical approach to calculate the gain of Brillouin fiber amplifiers in the regime of pump depletion," Appl. Opt. 58, 7628-7635 (2019

Adaptive-Network-based Fuzzy Inference System based MPPT Control for Stand-Alone PV Systems

Mehmet YILMAZ
Department of Electrical-Electronic Engineering Ataturk University
Erzurum/Turkey
mehmet.yilmaz@atauni.edu.tr

Muhammed Fatih ÇORAPSIZ
Department of Electrical-Electronic Engineering Ataturk University
Erzurum/Turkey
corapsiz@atauni.edu.tr

Aim: The importance of renewable energy sources is gradually increasing because of the decrease in fossil energy resources and their harmful effects on the environment. Solar power plants, which are obtained from the serial and parallel connection of photovoltaic (PV) panels, are one of the most preferred renewable energy sources. The most important disadvantage of PV panels is their low efficiency. They are required to operate at the maximum power point (MPP) in order to obtain desirable efficiency levels. In this study, an optimization algorithm based on Adaptive-Network-based Fuzzy Inference System (ANFIS) is proposed to increase the efficiency of the PV panels. Topsun TS-S407 brand PV panel is used during the implementation phase. The performance of the ANFIS based maximum power point tracking (MPPT) algorithm has been compared with one of the classical optimization algorithms names as Incremental Conductance (INC). As a result of the simulation study, it has been shown that ANFIS based MPPT is more successful than INC for several irradiation and constant temperature conditions.

Method: In this study, ANFIS method is proposed for MPPT. ANFIS method is a learning algorithm based on Takagi-Sugeno method. MPPT algorithms provide maximum energy to load by controlling the duty cycle rates of the DC-DC converters. We used boost converter as the DC-DC converter. A reference voltage is generated by training the temperature and irradiation values of the PV panel. MPPT is then obtained by comparing generated reference voltage value with the instantaneous voltage of the PV panel.

Results: In order to evaluate the performance of the ANFIS based MPPT algorithm, a system consisting of PV panel, load and DC-DC boost converter is designed. The simulation model is shown in Fig. 1 and the results are depicted in Fig. 2 for several irradiance (1000 W/m^2, 800 W/m^2, 600 W/m^2, 400 W/m^2) values and while the temperature value is kept constant at 25˚C.

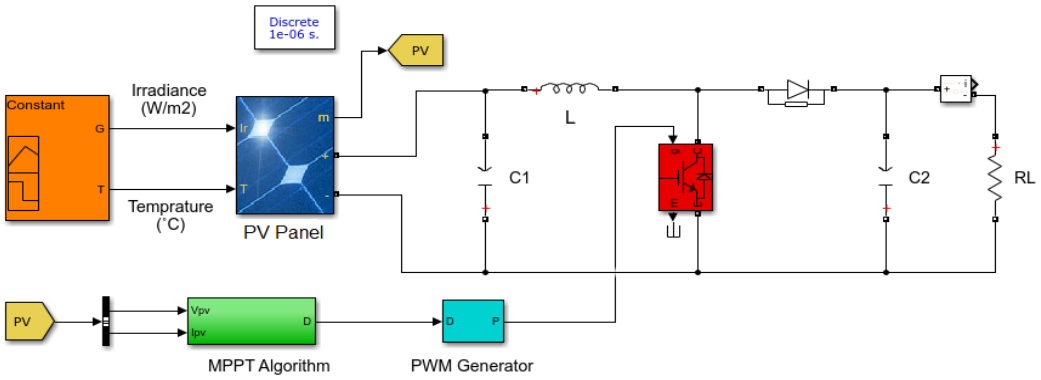


Fig. 1. Simulation model of the designed system

The properties of the PV panel used in the study are given in Table I.

Table I. PV Panel Specifations

PV Panel Characteristics	Value
Maximum Power	407.2992 W
Open Circuit Voltage	60.65 V
Voltage at MPP Vmp	50.16 V
Temprature Coefficient of Voc	-0.3678
Short-Circuit current Isc	8.7 A
Current at MPP Imp	8.12 A
Temprature Coefficient of Isc	0.044

The parameters of the DC-DC boost converter are given in Table II.

Table II. The Parameters of Boost Converter

Component	Value
Inductance (L)	3 mH
Capacitors (C_1 & C_2)	3300 µF- 100
Load (R_L)	µF 20 Ω
Switching Frequency	10 kHz

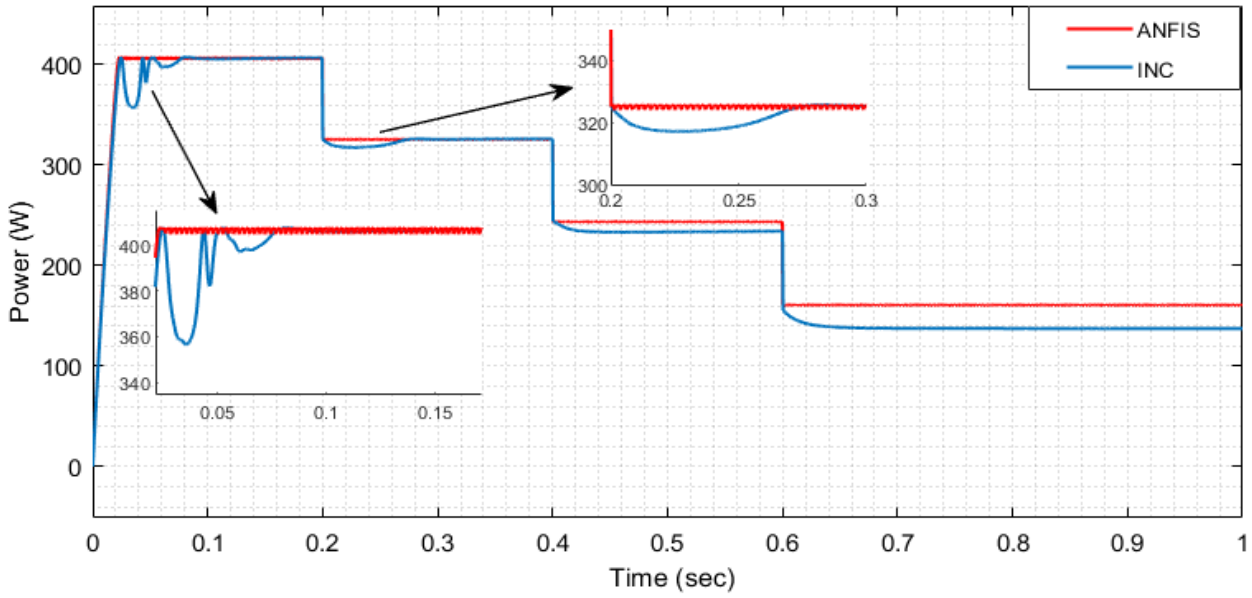


Fig. 2. Constant temperature and variable irradiation

Conclusion: The most important disadvantage of PV panels is that their efficiency is limited to 5-30%. In order to ensure the continuity of the energy to be transferred to the load, PV panels must work in MPP. Different power tracking algorithms are used in PV systems to provide maximum energy to load. In this study, an ANFIS based MPPT algorithm is proposed to provide maximum energy to load at several irradiance values. It has been observed that the ANFIS-based MPPT algorithm gives better results than the INC algorithm in performance measures such as settling time and steady state error. The MPPT of both algorithms has been achieved successfully at high irradiance values. However, it has been observed that the ANFIS algorithm is more successful than the INC algorithm at low irradiance values for the MPPT.

Keywords—ANFIS, PV panel, incremental conductance, maximum power point tracking

Application of a Microwave Metamaterial Sensor for Detection of Water Adulteration Level within Fatty Milk

Kadir Yüzgüleç
Department of Electrical and Electronics Engineering İskenderun Technical University
Hatay/Turkey
kadir.yuzgulec@iste.edu.tr

Oğuzhan Akgöl
Department of Electrical and Electronics Engineering İskenderun Technical University
Hatay/Turkey
oguzhan.akgol@iste.edu.tr

Vedat Özkaner
Department of Electrical and Electronics Engineering İskenderun Technical University Hatay/Turkey
vedat.ozkaner@iste.edu.tr

***Abstract*—A new type of microwave sensor (metamaterial (MM) sensor) has been proposed to evaluate adulteration level within fatty milk. To validate the proposed sensor, dielectric properties of fatty milk with different adulteration level in addition to distilled water were measured by dielectric probe kit. Then, these properties are utilized in a commercial 3D electromagnetic simulation program (CST Microwave Studio) to monitor the resonance frequency shift and magnitude variation of the transmission scattering parameter S21 at resonance for fatty milk with different water adulteration levels (20%, 40%, and 60%). From the simulation results, it is observed that the shift in resonance frequency (more than 10 MHz for a 20% adulteration change) of our proposed MM sensor is a good criterion in evaluation water adulteration level within fatty milk in comparison with magnitude change of S21.**

Keywords—fatty milk, adulteration, distilled water, metamaterial sensor, microstrip line

[1] INTRODUCTION

Due to its high fat, protein and mineral content, milk is considered one of the most essential components of a healthy diet for all people with different age groups [1]. To get profit, milk is prone to adulteration with cheaper components such as water [2],[3]. Several methods are available in the literature to examine the adulteration and its level within milk, such as chemical-based [4],[5] and physical-based [6],[7]. However, traditional chemical-based and physical-based methods for evaluating milk quality require much time and intensive labor and are relatively expensive [8]. To eliminate these disadvantages and propose an instant evaluation of adulteration level within milk, several electrical methodologies have been developed. In study [9], authors applied visible or near infrared spectroscopy technique to investigate fat adulteration within milk. Besides, Cozzolino et al. applied matrix-assisted laser desorption/ionization time-of-flight mass spectroscopy to identify milk adulteration [10]. On the other hand, milk electrical conductivity has been measured to detect freshness and adulteration of milk [11]. In the study [12], dielectric spectroscopy of milk with some dilutions at room temperature has been measured using an open-ended coaxial probe. Recently, dielectric properties of milk adulterated with water have been measured by an open-ended waveguide probe [13]. Although these microwave methods have potential, their accuracy is limited.

To improve the accuracy of microwave techniques for water adulteration within milk, engineering structures, coined as metamaterial (MM) sensors, can be employed. It has been applied in pressure, density, volumetric moisture, permittivity, and thickness sensing based on rectangular split ring structure with a strip line [14],[15]. To our best knowledge, MM sensors have not been applied for water adulteration level detection within milk. In this study, we propose a microstrip line MM sensor topology for adulteration detection within fatty milk.

[2] PROPOSED SENSOR STRUCTURE

The proposed microstrip line MM sensor structure (100mm x 50 mm x 1.6 mm), as shown in Fig. 1, has strips to carry electromagnetic energy to the MM resonator in square form. The dimensions of the sensors are: a=100 mm, b=50 mm, d=3 mm, e=18 mm, f=16 mm, g=15 mm, and h = 0.5 mm. The substrate is assumed to have a dielectric constant of 4.3 (loss –free FR4 material). The thickness of the metallic patterns is 0.035 mm. As shown in Fig. 1, the split-ring-resonator cell is combined with microstrip line.

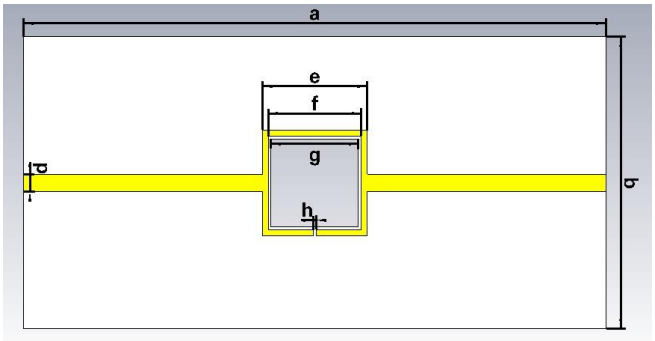


Fig. 1. Top view of the proposed MM sensor structure along with geometrical parameters

[3] MEASUREMENTS

A. Dielectric probe kit measurements

Preliminary measurements by the dielectric prop kit were carried out 85070E dielectric probe kit by connecting to the PNA-L N5234A network analyzer, as shown in Fig. 2. This kit was calibrated by pure water, air, and short terminations. The experimental tests have been carried out in the room conditions. After performing calibration, reflection-only scattering parameter measurements of pure fatty milk (purchased from a local supermarket) and fatty milk with distilled water adulteration of 20%, 40% and 60% were recorded over 1-8 GHz (401 data points) and the software of the probe kit was applied to extract real part ($\varepsilon_r^{'}$) and imaginary part ($\varepsilon_r^{''}$) of complex permittivity of pure milk and these mixtures, as shown in Figs. 3(a)-3(d).

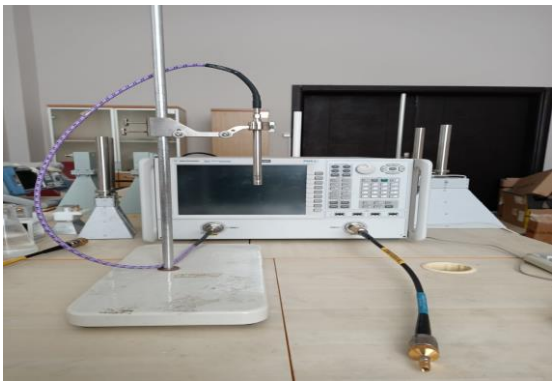


Fig. 2. Experimental setup for permittivity measurements of milk and adulterated milk using the 85070E dielectric probe kit.

Table 1. Measured resonance frequency and magnitude of transmission scattering parameter at resonance and their variations in reference to scattering parameter of fatty milk

Sample	Transmission scattering parameter			
	$\|S_{21}\|$ (dB)	f (GHz)	$\Delta\|S_{21}\|$ (dB)	Δf (MHz)
Fatty milk	-51.00	2.225	-	-
Fatty milk with 20% distilled water	-46.70	2.211	4.30	14
Fatty milk with 40% distilled water	-49.47	2.197	1.53	28
Fatty milk with 60% distilled water	-49.66	2.190	1.34	35

We note from Figs. 3(a)-3(d) that for a given frequency, while real part of the complex permittivity of adulterated milk increases accordingly with distilled water addition, its imaginary part decreases with water adulteration. This is because of the fact that while real part of the distilled water is greater than that of pure milk, its imaginary part is less than that of pure milk.

B. Simulation and measurement results by the proposed MM sensor.

Simulations for our sensor topology were implemented by the commercial CST Microwave Studio based on finite integration technique. Two waveguide ports were used to carry in and out the electromagnetic signals to microstrip line to monitor transmission scattering parameter S21. Fig. 4(a) illustrates the transmission scattering parameter S21 of the sensor topology when the sample (fatty milk) is positioned into the interior point of the resonator (15 mm x 15 mm). It is seen from the frequency dependence of the sensor that it resonates around 2.225 GHz with a very small magnitude of transmission scattering parameter (-51.00 dB). To determine the amplitude and frequency shift of the sensor for the fatty milk with adulteration, the extracted electromagnetic properties of fatty milk with different distilled water adulteration levels in Figs. 3(c) and 3(d) are inserted into the CST Microwave studio. Fig. 4(b) shows the

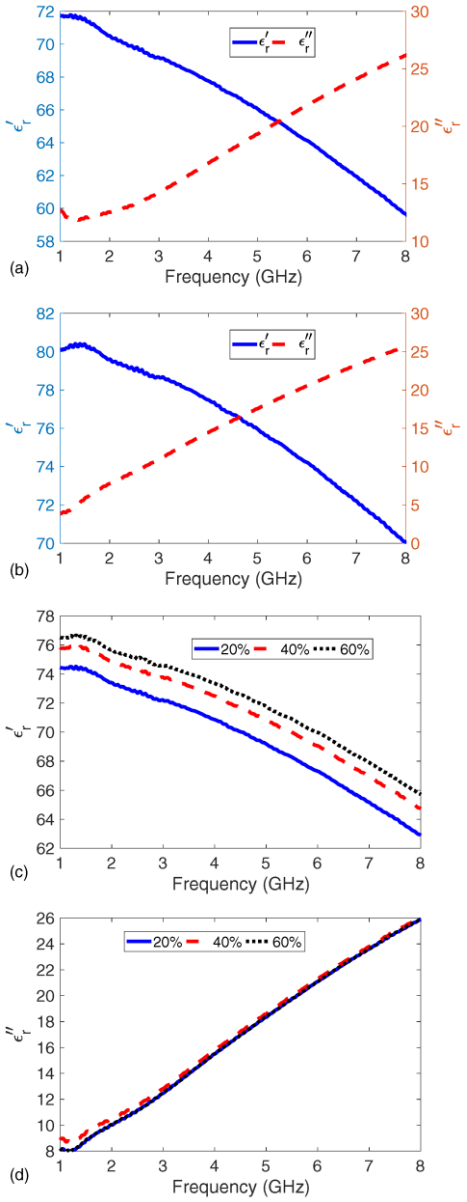


Fig. 3. Real and imaginary parts of complex permittivity of (a) Fatty milk and (b) distilled water, (c) real and (d) imaginary parts of the complex permittivity of fatty milk adulterated with distilled water with 20%, 40%, and 60% adulteration levels.

frequency variation and amplitude variation of S21 of the sensor when the fatty milk
was adulterated by distilled water with different adulteration levels. In addition, Table I illustrates measured resonance frequency of the proposed sensor and the magnitude of transmission scattering parameter S21 at resonance frequency and variation of these quantities in reference to those of the fatty milk. From the dependencies in Fig. 4(b) and Table I, we note the following points. First, the proposed resonator has a very sharp variation around resonance frequency with the magnitude of transmission scattering parameter value not greater than -45 dB. This is an important feature of the proposed sensor which can be operated even when a high amount of noise floor is present in the measurement system. Second, while resonance frequency decreases with an increase in water adulteration level, the magnitude of transmission scattering parameter firstly

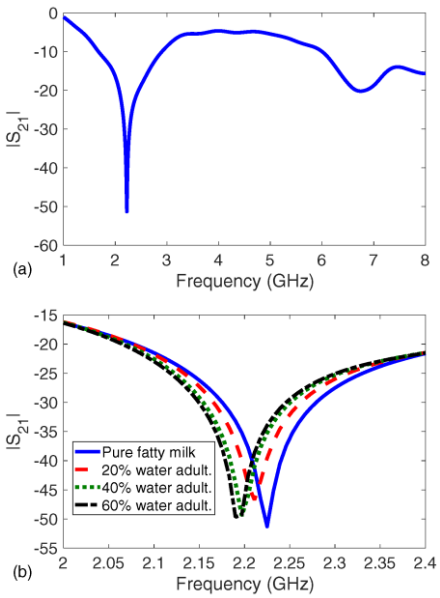


Fig. 4. Frequency dependence of the magnitude of transmission scattering parameter S21 for (a) the fatty milk and (b) fatty milk with various adulteration levels (20%, 40%, and 60%).

increases to -46.70 dB for the 20% adulteration level and then decreases to -49.66 dB for the 60% adulteration level. This means that the shift in resonance frequency could be monitored for accurate adulteration detection within fatty milk (good metric or indicator for adulteration detection). Third, it is noted that the accuracy of the proposed MM sensor decreases for adulteration levels greater than approximately 40% because the shift in resonance frequency linearly changes for adulteration levels up to 40% but then it decreases. Finally, the resonance shift greater than 10 MHz change measured by the proposed sensor could be easily monitored by nowadays highly technological vector network analyzers.

[4] CONCLUSION

A microstrip line MM sensor is proposed for the first time in literature in evaluation of water adulteration diagnosis within fatty milk. Electromagnetic properties of pure fatty milk with/out adulteration (20%, 40%, and 60%) and distilled water were first obtained from dielectric probe measurements. Then, these properties are incorporated into CST Microwave Studio to investigate a shift in resonance frequency and a change in the magnitude of S21 when fatty milk with/out water adulteration is inserted into the center of the proposed sensor. From simulations, it is observed that whereas magnitude of S21 increases and decreases with different adulteration levels in reference to the magnitude of S21 of fatty milk, resonance frequency decreases with adulteration level, indicating a reliable method for accurate water adulteration level of fatty milk by the proposed MM sensor.

References

[1] P. F. Fox, A advanced Dairy Chemistry. 1:Protein, Sound Animal, Elsevier Applied Science, London and New York, 1992, 19.

[2] M. F. Mabrook and M. C. Petty, “A novel technique for the detection of added water of full fat using single frequency admittance measurments,” Sens. Actuators B Chem., vol. 96, no. 1, pp. 215-218, Nov. 2003.

[3] P. M. Santos, E. R. Pereira-Filho, and L.E. Rodriguez-Saona, “Rapid detection and quantification of milk adulteration using infrared microspectroscopy and chemometrics analysis,” Food Chem., vol. 138, no. 1, 19-24, May 2013.

[4] R. Lucena, M. Gallego, S. Cárdenas, and M. Valcárcel, “Autoanalyzer for milk quality control based on the lactose, fat, and total protein contents,” Anal. Chem., vol. 75, no. 6, pp. 1425-1429, Feb. 2003.

[5] D. H. Kleyn, J. M. Lynch, D. M. Barbano, M. J. Bloom, and M.W. Mitchell, “Determination of fat and processed milks by the gerber method: Collaborative study,” J. AOAC Int., vol. 84, no. 5, pp. 1499-1508, Sep. 2001.

[6] A. Bogomolov, S. Dietrich, B. Boldrini, and R.W. Kessler, “Quantitative determination of fat and total protein in millk based on visible light scatter,” Food Chem., vol. 134, no. 1, pp. 412-418, Sep. 2012.

[7] S. Kucheryavskiy, A. Surkova, A. Bogomolov, “Determination of fat and total protein content in milk conventional digital imaging,” Talanta, vol. 121, pp. 144-152, Apr. 2014.

[8] F. Harding (Ed.), 1995. Chapter 5: Adulteration of milk. Chapter 6: Compositional quality. In: Milk Quality. Blackie Academic & Professional, London.

[9] T. Sato, S. Kawano, and M. Iwamoto, “Detection of foreign fat adulteration of milk fat by near infrared spectroscopic method,” J. Diary Sci., vol. 73, no. 12, pp. 3408-3413, Dec. 1990.

[10] R. Cozzolino, S. Passalacqua, S. Salemi, P. Malvagna, E. Spina, and D. Garozzo, “Identification of adulteration in milk by matrix-assisted laser desorption/ionization time-of-flight mass spectrometry,” J. Mass Spectrom., vol. 36, no. 9, pp. 1031-1037, Sep. 2001.

[11] M. F. Mabrook and M. C. Petty, “A novel technique for the detection of added water to full fat milk using single frequency admittance measurements,” Sens. Actuat. B: Chem., vol. 96, no. 1–2, pp. 215-218, Nov. 2003.

[12] A. C. Nunes, X. Bohigas, and J. Tejada, “Dielectric study of milk for frequencies between 1 and 20 GHz,” J. Food Eng., vol. 76, no. 2, pp. 250-255, Sep. 2006.

[13] W. Guo, X. Zhu, H. Liu, R. Yue, and S. Wang, “Effects of milk concentration and freshness on microwave dielectric properties,” J. Food Eng., vol. 99, no. 3, pp. 344-350, Aug. 2010.

[14] M. Bakir, M. Karaaslan, O. Akgol, O. Altintas, E. Unal, and C. Sabah, “Sensory applications of resonator based metamaterial absorber,” Optik, vol. 168, pp. 741-746, Sep. 2018.

[15] O. Altintas, M. Aksoy, E. Unal, F. Karakasli, and M. Karaaslan, “A split meander line resonator-based permittivity and thickness sensor design for dielectric materials with flat surface,” J. Electron. Mat., vol. 47, pp. 6185-6192, Jul. 2018.

Preliminary Investigation on the Soil Water Content Based on the Soil Series of Terengganu State, Malaysia

Eng Giap Goh
Faculty of Ocean Engineering Technology and Informatics, Universiti Malaysia Terengganu
Kuala Nerus, Malaysia
sunnygoh@gmail.com

Rudiyanto
Faculty of Fisheries and Food Science,
Universiti Malaysia Terengganu Kuala Nerus,
Malaysia
rudiyanto@gmail.com

***Abstract*—Soil water content is an essential parameter in agricultural soil as it determines the success of plantation crop produce. Soil water content in the field is either determined by laboratory method or soil moisture sensor. These methods are best after the plantation crop has begun. An early site assessment on soil water content can be inferred from soil textures. The current studies investigate the soil textures of the Terengganu state of Malaysia. The soil series of the state were gathered from literature and translated into soil textures. Soil water retention parameters of van Genuchten equation were estimated by pedotransfer function. The water retention function was used to estimate the field capacity, permanent wilting point, and plant available water. Five soil textures were found in Terengganu state soils. Among the soils, silty clay loam was found to have the highest plant available water, whereas sand has the lowest plant available water. Further investigation is needed to quantify the water supply rate.**

Keywords—permanent wilting point, soil moisture content, characteristic curve, soil water storage, plant water absorption

[1] INTRODUCTION

Water is an essential element to maintain in the soil. The plant requires water to grow on top of the soil [1]. Monitoring soil water content requires either continuous soil sample collection with laborious laboratory measurement or site sensor installment giving out data in minutes, hours, or daily soil moisture content [2]. The formal requires lots of time and effort to obtain results, while the latter needs sufficient financial resources to cover a vast area of land. The information is necessary after the plantation has begun on the land. Knowing the soil water content does not change the fact that the soil may not be the best choice to begins with plantation from an irrigation water management perspective.

The current study explores the benefit of different soil textures that can retain a different water amount. Crop planting begins on a soil texture with a reasonably high water retainment would give a head start in saving time and money in monitoring the soil water content in the field. Understanding the physics that governs the soil water content variability in space and time is a necessary step in planning to save water. A saturated soil water content usually occurs after heavy rainfall [3] or an oversupply of irrigation water [4]. Soil water content is a measure of water volume in a unit cubic of soil volume [5]. The saturated soil drains by gravity results in field capacity (FC)'s soil moisture content [6]. The water remains relatively constant at field capacity level that it is free from gravity, but with limited movement by diffusion, mechanism resulted from soil moisture gradient. Water continues to dry by evaporation and plant roots' water absorption. The soil moisture content continues to dry to a stage when the plant root water-absorbing pressure force is less than the soil particles-water attraction; it has reached a permanent wilting point (PWP) [7]. The permanent wilting point is when the plant growth on top of the soil begins to wilt due to insufficient water supply from the root zone. The difference between FC and PWP is known as plant available water (PAW) [8].

Malaysia's soils classify into series [9]. Soil series are the smallest genetic group of soil in the classification system. The soil series' name after the place of discovery. Morphological, chemical, and mineralogical properties of the soil differentiate among the soil series. However, no further information is available to relate the soil textures to the soil water contents, such as FC, PWP, and PAW. Many soil series in Malaysia remain unexamined the FC, PWP, and PAW, but beyond the study scope; this study limit the study scope to Malaysia's Terengganu state soil. The soil series covers continue to expand as more survey work expands by the Department of Agriculture, Malaysia. However, the information provided in this study is accurate at the time is reported here.

The study aims to investigate the Terengganu state's soil series in the aspects of soil water content. The first objective gathers the Terengganu state's soil series and generates the soil textures for different soil series. The second objective determines the soil hydraulic properties of different soil textures. The third objective is to determine the soil's FC, PWP, and PAW

[2] METHODOLOGY

A. Database compilation for the soil series and the determination of the silt, clay, and sand percentages

The soil series in Terengganu state were identified from the Soil Survey Staff [9] publication. Over a hundred soil series were screened through for the locations located in Terengganu state. The analytical data were gathered on clay, fine silt, coarse silt, very fine sand, fine sand, medium sand, and coarse sand. They were averaged over different soil depths to establish percentages for silt, sand, and clay.

B. Determining soil texture based on sand, silt, and clay percentages

The determined percentages of sand, silt, and clay were subjected to Van Lear's soil texture calculator by the Natural Resources Conservation Service, United States Department of Agriculture [10]. The inputs needed were the percentages of sand, silt, and clay. The soil texture is essential for several reasons, one of which is determining the water amount the soil can hold [11].

C. Determining the soil hydraulic functions using Rosetta

The soil texture calculator has generated soil texture was used as input parameters in the Rosetta software [12]. The software estimates the unsaturated soil hydraulic properties such as the characteristic curve and the unsaturated soil hydraulic conductivity. The properties were based on the van Genuchten equation [13]. The characteristic curve, Eq. (1), and hydraulic conductivity function, Eq. (2), of van Genuchten is as below,

$$\theta_L = \theta_r + \frac{\theta_s - \theta_r}{\left[1+\left(\alpha\psi_m\right)^n\right]^{1-1/n}} \quad (1)$$

$$K = K_s\left(\frac{\theta_L-\theta_r}{\theta_s-\theta_r}\right)^L\left\{1-\left[1-\left(\frac{\theta_L-\theta_r}{\theta_s-\theta_r}\right)^{1/m}\right]^m\right\}^2 \quad (2)$$

where θ_L is soil water content (θ_L , $m^3 \cdot m^{-3}$), K is unsaturated hydraulic conductivity (K), α and n as fitting curve parameters, L is an empirical pore tortuosity/connectivity parameter, θ_s is saturated soil water content ($m^3 \cdot m^{-3}$), θ_r is residual soil water content ($m^3 \cdot m^{-3}$), K_s is saturated hydraulic conductivity ($m \cdot s^{-1}$), and m as a fitting parameter where $m = 1 - 1/n$.

D. Determining the field capacity (FC), permanent wilting point (PWP), and plant available water (PAW) from soil texture

The characteristic curve parameters from Rosetta were used to determine the FC, PWP, and PAW. The characteristic curve relates the soil water content with the soil matric suction. The soil matric suction refers to the soil's suction pressure when the soil water content is less than saturated soil water content. The suction represents the negative pressure in the soil. The FC's soil water content was determined at -3.3 m pressure head, while the PWP was based on -150 m pressure head. The soil moisture content of FC is always greater than the PWP. The PAW was obtained by taking FC minus the PWP.

[3] RESULTS AND DISCUSSION

The current record of soil series identified in Terengganu state, Malaysia were twelve. Batu Hitam, Jambu, Rhu Tapai, Rudua, Gondang, Tasik, Lubok Kiat, Kampong Pusu, Tok Yong, Jerangau, Tersat, and Kuala Brang series were found. Based on those soil profiles gathered, these twelve soil series could be categorized into six soil textures. The soil series percentages of sand, silt, and clay were inputted into Van Lear's calculator [10], and the soil textures were identified as clay, sand, loamy sand, silt clay loam, and clay loam.

The pedotransfer function in Rosetta was used to identify the van Genuchten water retention parameters. Figure 1 shows the plotted water retention function for sand. Similarly, there were water retention functions for clay, loamy sand, silt clay loam, and clay loam. These water retention functions were not shown here.

Figure 1 shows the characteristic function begins with the highest soil water content known as the saturated water content at zero soil matric suction. The zero matric suction means no repulsive or attractive forces between the soil particles and the water molecules. As the matric suction (or attractive force imposes on it by an external force such as root zone, evaporation, laboratory-induced pressure) begins to rise, the soil water content remained relatively constant until it reaches a threshold pressure point. The threshold point occurred at around -10 cm pressure head for the sandy soil. At that stage, a slight increment of the soil matric suction results in the sharpest decline in the soil water content. The sharpness of the decline depends on the soil texture. For instance, clay soil would have a lesser sharpness of decline as compared to sandy soil. Subsequently, soil water content reaches a plateau state that any increase in soil matric suction has a limited reduction in the soil water content.

Among the five soil textures, the sand ultimately could become very dry when compared to other soil textures. Also, when water was supplied to sand, it could not retain much water due to its low PAW indication. Loamy sand has a similar problem as sand, but the plant's readily available water was slightly better than sand because it has a slightly higher PAW. Although clay has the highest FC, the highest PWP exhibits by clay reduces its overall PAW, making clay occupies less plant's readily available water than the silty clay loam. Furthermore, clay was not preferable when compared to silty clay loam and clay loam because clay could result in root growth restriction and increase the soil susceptibility to mechanical compaction than the other soils.

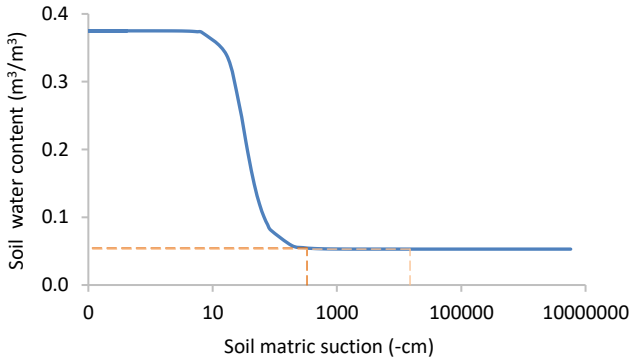


Fig. 18. The water retention for sand depends on the relation between the soil water content and soil matric suction. Eqn. (1) governs the relation. The negative sign in soil matric suction refers to the attraction pressure head. Note: the solid line refers to the water retention curve, and the dash lines refer to field capacity and permanent wilting point.

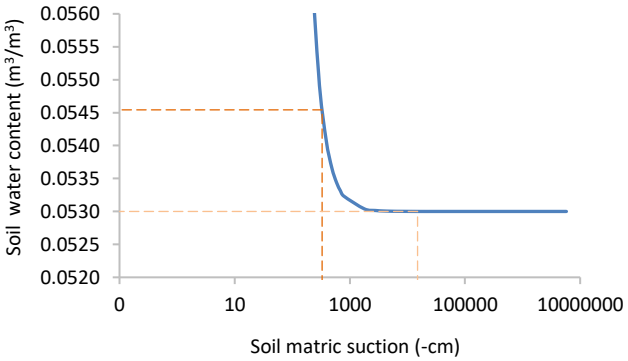


Fig. 19. The magnified water retention for the sand range between 0.052 and 0.056 m^3/m^3 soil water content region. Note: the solid line refers to the water retention curve, and the dash lines refer to field capacity and permanent wilting point.

Figure 1 shows two vertical dash lines, which the first and second corresponding to field capacity (FC, at -330 cm) and permanent wilting point (PWP, at 15000 cm). The two

horizontal dash lines seem indiscriminate in Fig. 1, but in close examination, in Fig. 2, the FC's soil water content was found higher than the PWP. The proximity between FC and PWP for sand was uniquely rare; however, it signifies sand's inability to retain soil water content compared to other soil textures. Refer to Fig. 3. Hence, sand soil texture has the lowest plant available water (PAW). The soil with the highest PAW was the silty clay loam, which has the largest difference between FC and PWP. The following soils in PAW decreasing order were clay, clay loam, and loamy sand.

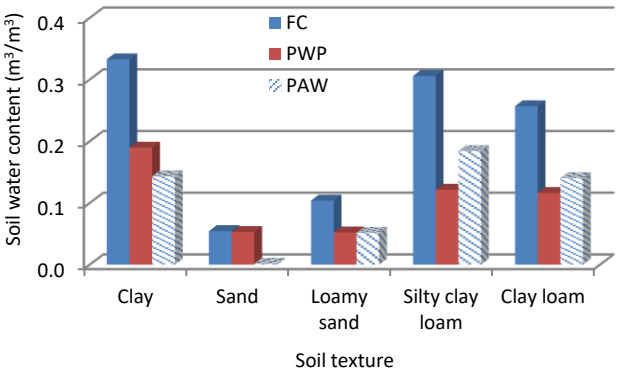


Fig. 20. The field capacity (FC), permanent wilting point (PWP), and plant available water (PAW) resulted from different soil textures.

The FC indicates the maximum amount of water retained by the soil as long as the water supply is greater than water outflow. The FC indicates the volume of water retained in a unit volume of soil, but it does not indicate the rate at which water supply is needed. Water supply rate, or water volume in a unit time, is essential for water irrigation management. Thus, further investigation on this aspect would be necessary to complement FC and PAW. Future investigation requires the coupling of Eqns. (1) and (2) with Richards' equation [14].

[4] CONCLUSIONS

The study reveals the soil series of the Terengganu state in Malaysia. The estimated soil physical parameters, which establish the relationship between soil water content and the soil matric suction, allow early assessment of soil water holding capacity and the soil readily available water for plant root absorption. Silty clay loam appears to have the highest plant available water over the other soil textures such as clay, sand, loamy sand, and clay loam. Sand has the least plant available water, indicates the need for frequent water irrigation should the sand soil be used for crop plantation. Knowing the soil field capacity and plant available water is insufficient to quantify the water supply rate necessary for water irrigation management. Hence, the future investigation would be directed to couple Richards' equation with the van Genuchten equation to estimate water infiltration rate, which estimates the water supply rate.

ACKNOWLEDGMENT

We want to acknowledge the Ministry of Higher Education Malaysia for financial support (FRGS/1/2020/STG08/UMT/02/2) (VOT UMT 59611).

REFERENCES

[1] T. R. Green and R. H. Erskine, "Measurement, scaling, and topographic analyses of spatial crop yield and soil water content," *Hydrological Processes*, vol. 18, no. 8, pp. 1447–1465, Jun. 2004, doi: 10.1002/hyp.1422.

[2] K. T. Kassaye, J. Boulange, V. T. Lam, H. Saito, and H. Watanabe, "Monitoring soil water content for decision supporting in agricultural water management based on critical threshold values adopted for Andosol in the temperate monsoon climate," *Agricultural Water Management*, vol. 229, p. 105930, Feb. 2020, doi: 10.1016/j.agwat.2019.105930.

[3] T. Han, L. Liu, and G. Li, "The Influence of Horizontal Variability of Hydraulic Conductivity on Slope Stability under Heavy Rainfall," *Water*, vol. 12, no. 9, 2020, doi: 10.3390/w12092567.

[4] L. N. Allen and J. W. MacAdam, "Irrigation and Water Management," in *Forages*, John Wiley & Sons, Ltd, 2020, pp. 497–513.

[5] W. J. Rawls, D. L. Brakensiek, and K. E. Saxtonn, "Estimation of Soil Water Properties," *Transactions of the ASAE*, vol. 25, no. 5, pp. 1316–1320, 1982, doi: 10.13031/2013.33720.

[6] B. Vaheddoost, Y. Guan, and B. Mohammadi, "Application of hybrid ANN-whale optimization model in evaluation of the field capacity and the permanent wilting point of the soils," *Environmental Science and Pollution Research*, vol. 27, no. 12, pp. 13131–13141, Apr. 2020, doi: 10.1007/s11356-020-07868-4.

[7] L. H. Wiecheteck, N. F. B. Giarola, R. P. de Lima, C. A. Tormena, L. C. Torres, and A. L. de Paula, "Comparing the classical permanent wilting point concept of soil (−15,000 hPa) to biological wilting of wheat and barley plants under contrasting soil textures," *Agricultural Water Management*, vol. 230, p. 105965, Mar. 2020, doi: 10.1016/j.agwat.2019.105965.

[8] G. J. Kidron and R. Kronenfeld, "Assessing the likelihood of the soil surface to condense vapour: The Negev experience," *Ecohydrology*, vol. 13, no. 3, p. e2200, Apr. 2020, doi: 10.1002/eco.2200.

[9] Soil Survey Staff, *Common soils of Peninsular Malaysia*. Department of Agriculture Malaysia, 2018.

[10] M. Van Lear, *Soil Texture Calculator*. USDA, 2019.

[11] Queensland Government, *Soil texture*, 2021. https://www.qld.gov.au/environment/land/management/soil/soil-properties/texture.

[12] M. G. Schaap, F. J. Leij, and M. Th. van Genuchten, "rosetta: a computer program for estimating soil hydraulic parameters with hierarchical pedotransfer functions," *Journal of Hydrology*, vol. 251, no. 3, pp. 163–176, Oct. 2001, doi: 10.1016/S0022-1694(01)00466-8.

[13] M. Th. van Genuchten, "A Closed-form Equation for Predicting the Hydraulic Conductivity of Unsaturated Soils," *Soil Science Society of America Journal*, vol. 44, no. 5, pp. 892–898, 1980, doi: 10.2136/sssaj1980.03615995004400050002x.

[14] L. A. Richards, "Capillary Conduction of Liquids through Porous Mediums," *Journal of Applied Physics*, vol. 1, no. 5, pp. 318–333, 1931, doi: 10.1063/1.1745010.

Treatment of Aqueous Solutions With Ammonia Content By Direct Contact Membrane Distillation

Ayşegül ÇEVİK
Chemical Eng. Department Atatürk University Erzurum, Turkey
aysegulcevik53@gmail.com

Ahmet Bora YAVUZ
Mechanical Eng. Department Ağrı İbrahim Çeçen University Ağrı, Turkey
a.borayavuz@gmail.com

Osman Nuri ATA
Chemical Eng. Department Atatürk University Erzurum, Turkey
oatar@atauni.edu.tr

Abstract—In this study, the removal of ammonia from high concentration ammonia content synthetic solutions by direct contact membrane distillation process was examined. Commercial hydrophobic polytetrafluoroethylene membrane was used in experiments. Five different parameters; temperature, initial ammonia concentration, initial sodium hydroxide concentration, flow rate and operation time, which may have effect on ammonia removal has been investigated. The experimental conditions to achieve the maximum ammonia removal rate were optimized using the Taguchi method. The data obtained revealed that the most effective parameters on ammonia removal are initial ammonia concentration, feed and permeate flow rates and operation time.

Keywords—ammonia, membrane distillation, Taguchi technique, optimization

I. INTRODUCTION

The element nitrogen exists in nature in many different forms. However, when it comes to water, ammonia constitutes the majority of the nitrogen available [1]. Ammonia is known to be one of the major water pollutants [2, 3]. In many countries, the maximum amount of ammonia that can be in drinking water or wastewater is determined by law. As environmental laws and regulations governing safe discharge levels are becoming more stringent with each passing day, ammonia removal is gaining importance especially at the industrial level [2-4].

Biological treatments, stripping, chemical precipitation, ion exchange/adsorption, electrochemical conversion, advanced oxidation processes are generally used for ammonia removal [2-7]. However membrane distillation (MD) processes, which have attracted attention with their performance in recent years in the removal of volatile compounds such as ammonia, has also been an alternative method for ammonia removal [5, 7].

Membrane distillation is a thermally driven seperation process. While liquids cannot pass through the hydrophobic porous membrane, vapour molecules can pass through the membrane pores. Separation process is driven by the vapour pressure difference between two surfaces of the membrane. Membrane distillation processes are divided into different configurations according to the properties of the permeate side. The four most known and commonly used MD configurations are: (1) direct contact membrane distillation (DCMD), (2) air gap membrane distillation (AGMD), (3) sweeping gas membrane distillation (SGMD) and (4) vacuum membrane distillation (VMD) [8-12]. Among these configurations, DCMD is the most preferred [10, 13]. In this configuration, both the hot feed solution and the cold permeate solution are in direct contact with the porous, hydrophobic membrane [13, 14].

In this study, ammonia removal by DCMD was examined. Using the experimental results in Taguchi method, optimum experimental conditions were obtained.

II. EXPERIMENTAL

A. Material

The hydrochloric acid (HCl), ammonia (NH_3), sodium hydroxide (NaOH), methyl orange indicator were purchased from MERCK and Polytetrafluoroethylene (PTFE) membrane purchased from Sterlitech. PCCELL electrodialysis cell was used as membrane cell for to carry out experiments. Properties of the membrane used can be found in Table I.

Table I.

Polymer	PTFE	**Support Material**	Not supported
Pore size	0.45 µm	**pH**	No limit
Thickness	21-51 µm	**Water entry pressure**	> 3.1 bar (45 psi)
Application temperature range	200 °C	-	-

B. Experimental setup

NH_3 solutions with different initial concentrations were used as the feed solution in the experiments.. Permeate solution was distillate water. Peristaltic pumps were used to transport the solutions to the membrane cell and for circulation. While the temperature of the permeate solution was kept constant (20 °C) by the heat exchanger, the feed solution was used at different temperatures (40 – 70 °C). Hydrophobic porous PTFE membrane was used in direct contact membrane distillation cell. The schematic version of the system used is shown in Figure 1. At the end of the period determined according to the experiment plan, a sample is taken from the permeate solution and titrated with HCl. Methyl orange is used as an indicator in the titration process. Thus, the amount of ammonia removed from the feed solution is determined using the amount of HCl spent in the titration.

Authors would like to thank Atatürk University Scientific Research Projects Coordination Unit for their support and funding for the projects no 2015/375 and 2016/201.

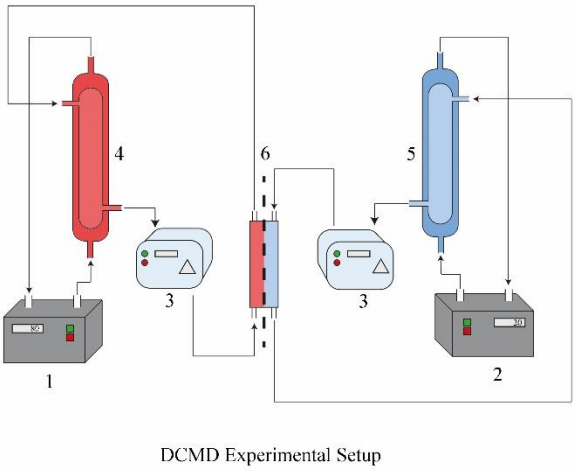


Fig. 1. Schematic view of the DCMD system (1:Heater, 2:Cooler, 3,4:Peristaltic pumps, 4: Tank containing the feed solution, 5: Tank containing the permeate solution, 6:Membrane cell)

C. Experimental procedure

5 different parameters that will affect the experiments were chosen and 4 levels were determined for each parameter. These parameters and levels can be found in Table II.

Table II.

PARAMETERS		LEVELS			
		1	**2**	**3**	**4**
A	**Temp. (°C)**	40	50	60	70
B	**NH_3 Conc. (ppm)**	750	1000	1250	1500
C	**NaOH Conc. (M)**	0.25	0.5	0.75	1
D	**Flow rate (rpm)**	20	30	40	50
E	**Time (Hour)**	2	3	4	5

An experiment plan, which is given in TableIII, was created using the Minitab software for the determined variable parameters and levels.

Table III.

Exp. No	A	B	C	D	E
1	1	1	1	1	1
2	1	2	2	2	2
3	1	3	3	3	3
4	1	4	4	4	4
5	2	1	2	3	4
6	2	2	1	4	3
7	2	3	4	1	2
8	2	4	3	2	1
9	3	1	3	4	2
10	3	2	4	3	1
11	3	3	1	2	4
12	3	4	2	1	3
13	4	1	4	2	3
14	4	2	3	1	4
15	4	3	2	4	1
16	4	4	1	3	2

Taguchi method was used to save time and costs by reducing the number of experiments. 16 experiments planned were carried out twice, at different times. Results of these experiments were placed in equations in Taguchi method and signal/noise (S/N) values were obtained. Using the S/N data, the graph and optimum values for this process were obtained using the Minitab software. Experiments were carried out twice, at different times, providing the determined optimum conditions. Thus, the results obtained were ensured.

III. RESULTS AND DISCUSSIONS

After the feed solutions were prepared according to the determined experimental plan and treated with a direct contact membrane distillation system, the sample taken from the permeate solution was titrated with HCl. The ammonia removal results obtained according to the experimental conditions are given in Table IV.

Table IV.

Exp. No	Removal rate 1 (% NH_3)	Removal rate 2 (% NH_3)	Average (% NH_3)
1	21,74	18,38	20,06
2	27,18	30,88	29,03
3	45,52	38,47	41,995
4	55,54	56,12	55,83
5	36,38	34,24	35,31
6	38,57	40,41	39,49
7	24,95	29,38	27,165
8	41,25	34,82	38,035

9	32,97	30,00	31,485
10	27,96	29,42	28,69
11	47,56	48,10	47,83
12	44,64	34,82	39,73
13	35,60	30,49	33,045
14	30,25	35,35	32,8
15	42,65	28,45	35,55
16	42,41	49,17	45,79

These results were placed in equations in Taguchi method and signal/noise (S/N) values were obtained. This data was graphed using Minitab software. The graphic obtained from the Minitab software can be seen in Figure 2.

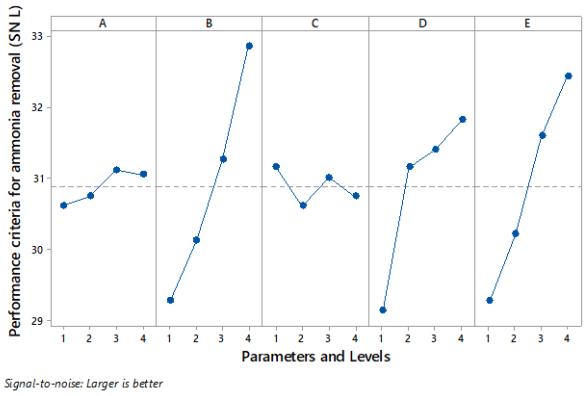


Fig. 2. Effect of parameters on removal of ammonia by DCMD

When the results were examined, it was seen that the increase in NaOH concentration in the feed solution did not have a noticeable effect on the amount of ammonia removed. Even the lowest NaOH concentration used was sufficient to convert the ammonium in solution to ammonia. Exceeding this value had no effect on the amount of ammonia transported.

Since ammonia already volatilized due to the pH of the solution, it was not affected much by the temperature increase. The amount of ammonia removed is slightly affected by the temperature change.

With the increase in the amount of ammonia in the feed solution, the difference in ammonia concentration on both sides of the membrane also increases. Therefore, the change in this parameter has a great effect on the amount of ammonia carried to the permeate side.

Increasing the flow rate prevents the formation of a film layer on the membrane surface, thus mass transfer resistance disappears and an increase in the amount of ammonia removed is observed.

In addition to these factors, the amount of ammonia removed is directly proportional to the operation time. Therefore, with the extension of the processing time, the amount of ammonia carried from the feed side to the permeate side also increases.

IV. CONCLUSION

When the data obtained were examined, it was seen that the most effective parameters in the ammonia removal process with DCMD were initial ammonia concentration, operation time and flow rates. According to performance statistics, optimum values were found as A4, B4, C1, D4, and E4. As a result of the verification experiments performed by providing optimum values, ammonia removal rate was found to be 62.4% and 59.2%. As expected, these values were higher than all results obtained in the experiments.

REFERENCES

[1] Z. Ding, L. Liu, Z. Li, R. Ma, and Z. Yang, "Experimental study of ammonia removal from water by membrane distillation (MD): The comparison of three configurations," *Journal of membrane Science*, vol. 286, no. 1-2, pp. 93-103, 2006.

[2] M. R. Adam *et al.*, "Current trends and future prospects of ammonia removal in wastewater: A comprehensive review on adsorptive membrane development," *Separation and Purification Technology*, vol. 213, pp. 114-132, 2019.

[3] A. Hasanoğlu, J. Romero, B. Pérez, and A. Plaza, "Ammonia removal from wastewater streams through membrane contactors: Experimental and theoretical analysis of operation parameters and configuration," *Chemical Engineering Journal*, vol. 160, no. 2, pp. 530-537, 2010.

[4] L. Lin *et al.*, "Removal of ammonia nitrogen in wastewater by microwave radiation: a pilot-scale study," *Journal of hazardous materials*, vol. 168, no. 2-3, pp. 862-867, 2009.

[5] M. El-Bourawi, M. Khayet, R. Ma, Z. Ding, Z. Li, and X. Zhang, "Application of vacuum membrane distillation for ammonia removal," *Journal of Membrane Science*, vol. 301, no. 1-2, pp. 200-209, 2007.

[6] L. Lin, S. Yuan, J. Chen, Z. Xu, and X. Lu, "Removal of ammonia nitrogen in wastewater by microwave radiation," *Journal of hazardous materials*, vol. 161, no. 2-3, pp. 1063-1068, 2009.

[7] Z. Xie, T. Duong, M. Hoang, C. Nguyen, and B. Bolto, "Ammonia removal by sweep gas membrane distillation," *Water research*, vol. 43, no. 6, pp. 1693-1699, 2009.

[8] A. Alkhudhiri, N. Darwish, and N. Hilal, "Membrane distillation: A comprehensive review," *Desalination*, vol. 287, pp. 2-18, 2012.

[9] A. Alkhudhiri and N. Hilal, "Membrane distillation—Principles, applications, configurations, design, and implementation," in *Emerging Technologies for Sustainable Desalination Handbook*: Elsevier, 2018, pp. 55-106.

[10] M. Khayet, "Membranes and theoretical modeling of membrane distillation: a review," *Advances in colloid and interface science*, vol. 164, no. 1-2, pp. 56-88, 2011.

[11] M. Khayet and T. Matsuura, "Membrane distillation: principles and applications," 2011.

[12] K.-J. Lu and T.-S. Chung, *Membrane Distillation: Membranes, Hybrid Systems and Pilot Studies*. CRC Press, 2019.

[13] J. Phattaranawik, R. Jiraratananon, and A. G. Fane, "Heat transport and membrane distillation coefficients in direct contact membrane distillation," *Journal of membrane science,* vol. 212, no. 1-2, pp. 177-193, 2003.

[14] S. Yarlagadda, V. G. Gude, L. M. Camacho, S. Pinappu, and S. Deng, "Potable water recovery from As, U, and F contaminated ground waters by direct contact membrane distillation process," *Journal of hazardous materials,* vol. 192, no. 3, pp. 1388-1394, 2011.

Demolition Techniques And Rize Urban Renewal Project 1. Stage Example

Ali Gurbuz
Department of Civil Engineering Recep Tayyip Erdogan University Rize, Turkey
ali.gurbuz@erdogan.edu.tr

Volkan Tavşan
Department of Civil Engeinering, Recep Tayyip Erdogan University Rize, Turkey
volkan_tavsan19@erdogan.edu.tr

***Abstract*— Demolition of existing buildings for both aesthetic and safety reasons is one of the fields of civil engineering. With the developing construction technique and increasing high structures, demolition work has become as important as the construction work. Especially in recent years, with the urban transformation activities, the need for studies for the demolition of old buildings has increased. The aim of this study is to reveal the functionality of the demolition techniques applied today and to touch on the application principles. Within the scope of the study, the example of Rize city center urban renewal project, which is an ongoing project, was also discussed. As a result of the study, the effectiveness and limitations of different demolition techniques are revealed.**

Keywords—Demolition Techniques, Urban renewal, Rize,

INTRODUCTION

The life expectancy for today's modern buildings is known as 50 years. Of course, there are many buildings that have exceeded this period. Similarly, there are structures that need to be demolished before this time is over. In the last century, reinforced concrete structures completed in our country; It has to be renewed or demolished due to reasons such as urbanization, natural disasters, wars, as well as expiration of its service life, failure to meet the construction regulations in force, weaknesses in terms of both structural and design against earthquakes. Necessary steps were taken to demolish risky buildings and renew old buildings, especially after the 2011 Van Earthquake. As a result, researches on the effectiveness of building demolition techniques have increased and focused on determining the most appropriate method. In May 2012, "Disaster Risk Areas Under Renovation" has prepared a new law and began urban renewal projects throughout Turkey together with the enactment of relevant legislation [1].

Since the demolition of risky buildings takes place in a long time with classical methods, it causes discomfort to the environment, as well as high cost and unsafe working conditions. Therefore, more practical methods were sought and the "Implementation Rules for Complete and Partial Demolition of Structures", which entered into force in October 2014 in our country, came to the fore with controlled blasting as specified in the TS13633 standard [2, 3]. It is clear that the use of explosives in building demolition has advantages as well as disadvantages compared to traditional demolition techniques. Damage to close-range structures, incomplete destruction, and damage to parts released during demolition can be stated as the main risk situations. As the realization of the risks in question can cause loss of life and property, the planning phase must be carefully prepared, the demolition processes are carried out by the experienced people, and the demolition mechanism can be predicted as close to the truth as possible.

There is no comprehensive law or regulation on the demolition of buildings in our country. The standards named "BS 6187: Code of practicefordemolition" and updated in 2011, published by the British Standards Institute in 2000 and consisted of 120 pages, stand out as the most comprehensive official document on demolition [4].

It is necessary to examine the results of scientific studies on building destruction by controlled blasting. Demolition simulations, which are an alternative to rigid structure modeling in structural demolition through controlled blasting, have been studied by Mattern, Blankenhorn and Schweizerhof (2007), and in large-scale building simulations made in this way, the demolition was simulated with sufficient accuracy by considering the interaction with the ground. In a similar study [5], Griffin (2008) made computer-aided modeling of building demolitions using controlled blasting. It has been shown that arrangements should be made on the explosion gaps and material properties with modeling, and non-bearing structural elements that may affect the collapse mechanism in the building should be taken into account [6]. Lupoae and Bucur (2009) investigated the changes in the stress and displacement of the building elements during the demolition process by computer modeling in structural demolition by controlled blasting. In the study, it was concluded that the destruction mechanism was triggered as a result of exceeding the sudden moment capacity and that the structural elements under the shear wall are effective in vertical displacement. Dogan et al., (2009) by Diyarbakir in Turkey in the Air Above 8 demolition of a water tower site it was carried out. As a result of the study, the destruction of the water tower in the desired direction was achieved [7]. Sikiwat et al., (2009) performed a simple computer-aided modeling of building demolition using explosives to examine the mechanism of demolition, the behavior of basic building elements and the effect of demolition on other structures [8]. In the study conducted by Özmen et al., (2017), the analysis of the structural behavior of the buildings planned to be demolished using explosives and the effect of structural errors on the demolition process were revealed [9].

II. DEMOLITION TECHNIQUES

Within the scope of the urban transformation activities initiated due to the expiration of the economic life of the buildings, the failure to meet the current regulations, and the damage caused by natural disasters, in addition to the increase in the population with the migration that started to big cities in

recent years in our country; old and insufficient buildings are demolished and high-rise structures are built in their places. Many studies have been carried out and new techniques have been developed to ensure that urban transformation can continue more effectively. Today, the techniques used for total or partial destruction of structures can be classified as follows:• Demolition by crushing or crushing with the help of mechanical tools

• Separating destruction with the help of mechanical tools,
• Demolition by crushing by hitting the structure with the help of a steel sphere connected to a crane

Demolition with high reach and scissor machines

• Demolition with tow rope

Controlled destruction with explosives

• Demolition by the floor reduction method,
• The demolition of the building with chemical materials,
• The demolition of the building elements by cutting with diamond saws [10].

Long-term destruction of structures with the help of mechanical tools; It causes discomfort to the environment, as well as high cost and unsafe working conditions. Another reason why new methods are being researched is that these rough methods can have significant negative effects on the environment and employees. In particular, it is known that the demolition of structures with traditional methods (steel sphere, sledgehammer, excavator bucket, etc.) can sometimes lead to very dangerous consequences if they are done by inexperienced people [11]. The overturning of the chimney on the block, which was demolished in the Üçgen Bazaar in Denizli on 23 November 2017, over the excavator is an example of this (Fig. 1).



Fig. 1. The accident that occurred during the demolition

Although there are many techniques developed for the demolition industry, the technique that provides the most suitable conditions for the demolition work should be selected. In choosing the most appropriate technique to be used for a demolition work;

• Cost of demolition work and time allocated for demolition work,
• Determination of whether the demolition work is partial or complete,
• Determination of whether the capacity of the work machines is sufficient or not,
• The quality of the material used in the building to be demolished,

Geometry of the structure or structural elements to be demolished,

• The size and location of the building to be demolished,
• Environment and traffic situation of the building to be demolished,
• Features of the ground on which the building is built,
• Bearing system of the building,
• Supply of equipment,
• Demolition experience,
• OHS measures,
• The presence of dangerous goods,
• Safety of demolition work,
• Permissible disturbance level (Noise, dust and vibration levels),
• Reuse of rubble formed after demolition,
• Factors such as transportation and storage of solid waste are taken into account [12]. The most important of these factors are; It is the location, dimensions and cost of demolition of the structure to be demolished.

Although it is not frequently preferred in demolition studies, the explosive demolition technique stands out as the most advantageous demolition technique in terms of speed, efficiency and accident risks that may be encountered during demolition. In addition to the many advantages of the explosive demolition technique over other traditional demolition techniques, explosives also have disadvantages due to the potential risk of danger. These advantages and disadvantages can be summarized as follows.

Advantages of explosive demolition techniques:

• Lower cost, especially when applied in high-rise buildings,
• Faster application compared to other techniques,

Limiting environmental disturbances in a short time,

• A safer application when carried out in or near the traffic flow,
• Applicable in cases where the use of mechanical machines in the demolition area and narrow gap is difficult,
• High work control and minimization of work accidents,
• Controlling dust spread and noise pollution,
• Easy removal of small pieces of debris as a result of demolition.

Disadvantages of explosive demolition techniques:

• The need for an expert and experienced team in explosive, static, and security issues for demolition work,
• It takes a long time to obtain the blasting permit (license) and other documents required for the transport of explosives to the demolition area,
• It is necessary to find the projects of the buildings to be demolished and to know the material properties. In cases where these are not available, they should be determined by measuring and experiments. This saves time and increases costs.
• There is always a risk of damaging the surrounding structures, objects and people. The damages that may occur as a result of these must be compensated.
• Can damage structures in close range,
• Incomplete destruction,
• Damage of free parts during demolition etc. can be listed as.

III. RIZE URBAN RENEVAL PROJECT

Urban transformation work has started as a result of the completion of the current life of the municipal blocks and other structures built in the areas gained by filling in Rize since the 1960s. Filled with large stones and filled with materials such as sand or mud, the 350 thousand square meter area has turned into a region full of multi-storey structures, although it is a sea fill area. Approximately 70 thousand people live in the area where many buildings are built, including public institutions such as the governorship, mayor's office, cultural center, and courthouse [13].

The urban transformation work to be carried out with the cooperation of TOKI and Rize Municipality has been divided into 3 stages and the tender of the works in the 1st stage project area, which also includes the municipality blocks, has been completed. As a result of the project, it is planned to construct less-storey buildings with healthier buildings in our city center and desired to contribute positively to economy and tourism. . Some of the buildings planned to be demolished for Phase 1 are shown in Fig. 2.

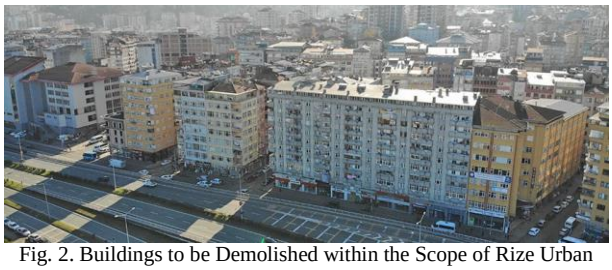


Fig. 2. Buildings to be Demolished within the Scope of Rize Urban Renewal Project Stage 1

The model and 3D studies of the view after the completion of the project are like in Fig. 3 (Fig. 3a: Rize urban transformation project 1st stage model work, Fig. 3b: Rize urban transformation project 3D computerized design study).



Fig. 3a. Model work



Fig. 3b. 3D Model

Fig. 3. Completed View Planned for Rize Urban Renewal Project Stage 1

Under the coordination of Rize Municipality, with the cooperation of the Ministry of Environment and Urbanization and TOKI, within the scope of the Urban Transformation Project to be carried out in the city center of Rize, it was decided to demolish the 4 thousand 174 independent buildings that were made on the sea fill and became risky due to corrosion. The study consists of 3 stages. The first stage in the city center of Rize was published in the Official Gazette with the Presidential Decree No. 2038 dated January 7, 2020, and declared a risky area. 1. Stage of 22.809.53 square meters covers a part of Çarşı and Piriçelebi Neighborhoods. Before the construction of the Urban Transformation Project, which will be built on an area of 23 decares, notices were sent by the Rize Municipality to the right owners in the area and the demolition started as of 2021.

Classical methods are generally preferred due to reasons such as the constant presence of the buildings to be demolished in the city center, which is full of people, the low number of experienced companies that can enter the tender for explosive demolition, and the low number of trained personnel for inspections. Figure 4 shows a photograph of the buildings that continue to be demolished.



Fig. 4. Rize Urban Renewal Project 1st Stage Demolition

[a.] Sample of a Table footnote. (*Table footnote*)

IV. CONCLUSION

A detailed examination and research should be done before the demolition of the buildings. The demolition of building elements constructed from different materials such as stone, brick, steel, wood or concrete requires an individual assessment. Factors that can affect destruction such as strong winds caused by weather conditions should be taken into account. If necessary, temporary support systems should be established to prevent early crashes. If manual demolition is to be done, safe working platforms should be used. Manual demolition must be done gradually from top to bottom. During the demolition process, a safety ring of sufficient width should be created.

The most modern technique for the rapid and effective continuation of the ongoing activities within the scope of urban transformation in our country is the demolition technique with explosives. However, each technique has its own advantages such as "demolition time", "cost", "environmental impact" and "low risk factor". Table 1 summarizes the comparison of demolition techniques among themselves.

Table I. Comparison of Demolition Techniques (Jimeno et al., 1995; Dowding, 1996)

Comparison of Demolition Thecniques				
Method	**Time**	**Cost**	**Environmental Impact**	**Risk**
Steel ball	Long	High	Very	Low
Steel spinner	Very long	Medium	Very slight	High
Breaker	Long	Very high	Low	Very low
Explosive	Very short	Low	High	High

REFERENCES

[1] Cushman and Wakefield (2014). Kentsel Dönüşüm Türkiye, https://www.cushmanwakefield.com/tr/turkey

[2] Özyurt, M.C. (2013). Patlayıcı madde kullanılarak yapıların kontrollü yıkılması ve verimliliğinin incelenmesi [Controlled demolition of structures using explosive materials and research of their efficiency]. Master Thesis (Thesis number:332340). Department Of Mining Engineering, İstanbul University, İstanbul, Turkey.

[3] Özyurt, M.C., Özer, Ü., Karadoğan, A. and Kalaycı, Ü. (2016). Betonarme bir binanın patlayıcı ile yıkılması ve veriminin incelenmesi [Controlled demolition of structures using explosive materials and research of their efficiency]. Uludağ University, Mühendislik Fakültesi Dergisi, c. 21, n. 2, pp. 44.R. Nicole, "Title of paper with only first word capitalized," J. Name Stand. Abbrev., in press.

[4] BS 6187:2011, Code of practice for full and partial demolition, UK.

[5] Mattern S., Blankenhorn G., Schweizerhof K. (2007). Computer-Aided Destruction of Complex Structures by Blasting. In: Nagel W.E., Jäger W., Resch M. (eds) High Performance Computing in Science and Engineering '06. Springer, Berlin, Heidelberg. https://doi.org/10.1007/978-3-540-36183-1_33

[6] Griffin, Joshua Wayne (2008). Experimental and Analytical Investigation of Progressive Collapse Through Demolition Scenarios and Computer Modeling,NC State University, Master of Thesis

[7] Doğan, E., Uzal, B., Pehlivanoğlu, K. and İycil, E. (2009). Patlayıcı kullanılarak betonarme bir su kulesi yıkımı [Demolition of a reinforced concrete water tower using explosives]. Türkiye Mühendislik Haberleri (TMH)–457, pp. 35-44. Retrieved fromhttp://www.imo.org.tr/resimler/dosya_ekler/ec667c928319eed_ek.pdf?dergi=141

[8] Sikiwat, T., Breidt, M. and Hartmann, D. (2009). Computational Steering for Collapse Simulation of Large Scale Complex Structures, 18th International Conference on the Application of Computer Science and Mathematics in Architecture and Civil Engineering, Weimar, Germany, pp. 1-8.

[9] Özmen, H., Soyluk, K. and Anıl, Ö. (2017). Betonarme binaların patlayıcı kullanılarak yıkımında yapı davranışının analizi [Analysis of structural behavior in demolition of reinforced concrete structures using explosives]. 4.Uluslararası Deprem Mühendisliği ve Sismoloji Konferansı, Eskişehir,Turkey.

[10] Koca, O. (2006). Patlayıcı maddelerle kontrollü yapı yıkımı [Controlled structure demolition with explosive materials]. Master Thesis (Thesis number: 179096). Obtained from YÖK National Thesis Center database.

[11] C.L. Jimeno, E.L. Jimeno ve F.J.A Carceda (1995). Drilling and Blasting of Rocks, Rotterdam, Netherlands: A. A. Balkema Publisher, Netherlands, pp. 312.

[12] RJ Elliot, R Woolf (2001). Demolition Blasting of Reinforced Concrete Structures - Proocedings of the 1 st World Conference of Demoliton,

[13] Rize Belediyesi (2021). http://www.rize.bel.tr/proje/yeni-belediye-bloklari-etap-1-kentsel-donusum

Elastoplastic Analysis of Unreinforced Masonry Walls with Openings

Edin Nurkovic
Department of Civil Engineering Yıldız Technical University Istanbul, Turkey
email: edinn996@gmail.com
ORCID: 0000-0002-2759-6006

Metin Karslioglu
Department of Civil Engineering Yıldız Technical University Istanbul, Turkey
email: metinkarslioglu91@gmail.com
ORCID ID: 0000-0002-1993-4511

Zeynep Unsal Aslan
Department of Civil Engineering Yıldız Technical University Istanbul, Turkey
email: zeynepunsalaslan@gmail.com
ORCID ID: 0000-0002-3312-7011

Bilge Doran
Department of Civil Engineering Yıldız Technical University Istanbul, Turkey
email: doran@yildiz.edu.tr
ORCID ID: 0000-0001-6703-7279

***Abstract*— Masonry is one of the most used materials in building industries, because of its simplicity and low cost compared to the other modern building materials. They are still in practice even in highly seismic regions such as Turkey. Therefore, understanding of masonry Wall behavior is needed for the preserve the historical monuments as a huge cultural heritage. Since the structural behavior of masonry walls under in-plane lateral loading is very complicated, numerical modeling of masonry is one of the most challenging topics of structural engineering. This paper is primarily focused on the nonlinear finite element analysis (NLFEA) of unreinforced masonry walls (URM) with openings, subjected to in plane loading. Concrete damaged plasticity (CDP) constitutive law is used for the numerical representation of masonry wall with macro modeling technique. The validity of the numerical model has been verified through comparisons with the experimental results from past studies.**

Keywords –Unreinforced masonry wall, opening, macro-modeling, Concrete damaged plasticity

[1] INTRODUCTION

Masonry is the oldest building material that is still widely used in building industries because of its simplicity, durability, low cost, esthetic. Masonry is classified as a heterogeneous material, because of its constituents (masonry units and joints) having different material properties. Due to its anisotropic and heterogeneous nature, the design of masonry structures is very complex task which requires many assumptions. URM structures built of masonry walls containing openings have been shown to have poor seismic capacity, due to the stiffness reduction caused by the openings [1]. The areas around openings are the locations of strain concentrations [2]. Openings also have an important effect on the failure modes of masonry structures, as observed in the experiments on the TU Eindhoven shear walls [3]-[6], where first cracks appeared at the opening corners.

Different modelling approaches are proposed by different researchers. Macro-modeling approach, which is adopted in this study, involves assumption that the masonry is a continuum, and there is no distinction between units, mortar, and unit-mortar interface. Macro-modeling has been shown to be an appropriate approach when larger and more complex masonry structures are modelled and the global behavior is of interest [7]. Unfortunately, it cannot give advanced information on failure modes. Micro-modelling approaches require detailed information on properties of units, mortar and especially unit-mortar interface, which represents a potential crack/slip plane [8]. In the detailed-micro modelling technique, units, mortar and unit-mortar interface are modelled separately. Here, units and mortar are assumed to be continuum elements, whereas unit-mortar interface is represented by discontinuous element. In the simplified micro-modelling approach, units are expended by adding the mortar thickness to form continuum elements, while the unit-mortar interface is represented by discontinuous element and involves mortar properties. As mentioned before, macro-modeling technique is used when the global behavior of masonry is of interest, whereas micro-modeling techniques are used for the understanding of local behavior of masonry and its failure modes, therefore one modeling technique cannot be preferred over the other [8].

The main goal of this paper is to implement an effective modelling procedure for the NLFEA of URM walls with opening, subjected to a combined in-plane monotonic lateral load and constant vertical loads. For this purpose, results obtained by the numerical solutions are compared with the experimental results for TU Eindhoven shear walls, V3G and J2G [3]-[6].

[2] MATERIAL AND CONSTITUTIVE MODELING

Herein, material properties of masonry required for the numerical analysis of masonry shear walls are discussed.

Several attempts have been made by researchers to express the compressive behavior of masonry walls. In this study, compressive stress-strain relationship for masonry prisms proposed by Kaushik et al. [9] has been adopted. For the estimation of strain values on the parabolic part of the stress-strain curve, following equation is given;

$$\frac{f_m}{f'_m}=2\frac{\varepsilon_m}{\varepsilon'_m}-\left(\frac{\varepsilon_m}{\varepsilon'_m}\right)^2 \quad (1)$$

where f_m is the compressive stress of masonry prism, f'_m is the compressive strength of masonry prism, ε_m is the strain

corresponding to f_m, and $\varepsilon_m^{'}$ is referred to as peak strain corresponding to $f_m^{'}$.

In order to simulate plastic behavior of walls, appropriate constitutive modelling technique is required. Doran B. et al. [10] and Köksal et al. [11, 12] used Drucker-Prager constitutive model for the elastoplastic analysis of masonry walls and columns, due to the smooth yield surface for a frictional material. One of the constitutive models, widely used for concrete and quasi-brittle materials is Concrete Damaged Plasticity model (CDP), which is adopted here and is already used in many studies [13]-[15]. CDP is developed by Lubliner et al. (1989) [16] and later improved by Lee and Fenves (1998) [17]. CDP model assumes that the uniaxial tensile and compressive response of concrete is characterized by damaged plasticity (Fig. 1). The yield function proposed by Lubliner et al. (1989) [16], later modified by Lee and Fenves (1998) [17] takes the form;

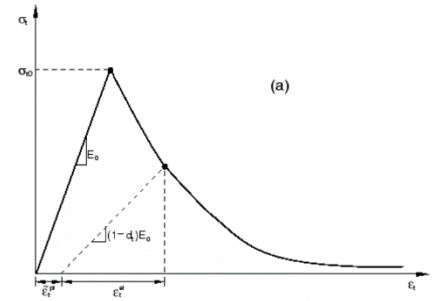
$$F=\frac{1}{1-\alpha}\left(\bar{q}-3\alpha\bar{p}+\beta\left(\tilde{\varepsilon}^{pl}\right)\langle\hat{\bar{\sigma}}_{max}\rangle-\gamma\langle-\hat{\bar{\sigma}}_{max}\rangle\right)-\bar{\sigma}_c\left(\tilde{\varepsilon}_c^{pl}\right)=0, \quad (2)$$

Function $F(\bar{\sigma},\tilde{\varepsilon}^{pl})$ represent a surface in effective stress space, which determines the states of failure or damage. Here $\bar{q}=\sqrt{\frac{3}{2}(\bar{S}:\bar{S})}$, where $\bar{S}$ is defined as effective stress deviator, represent von-Misses equivalent effective stress, $\bar{p}=-\frac{1}{3}\text{trace}(\bar{\sigma})$ is the hydrostatic pressure stress, and $\hat{\bar{\sigma}}_{max}$, $\tilde{\varepsilon}^{pl}$, and $\tilde{\varepsilon}_c^{pl}$ represent maximum principal effective stress, accumulative plastic strain and equivalent plastic strain in compression, respectively. α, β and γ are dimensionless constants, given by

$$\alpha=\frac{(\sigma_{b0}/\sigma_{c0})-1}{2(\sigma_{b0}/\sigma_{c0})-1};0\le\alpha\le0.5,$$

$$\beta=\frac{\bar{\sigma}_c\left(\tilde{\varepsilon}_c^{pl}\right)}{\bar{\sigma}_t\left(\tilde{\varepsilon}_t^{pl}\right)}(1-\alpha)-(1+\alpha), \quad (3)$$

$$\gamma=\frac{3(1-K_c)}{2K_c-1}$$



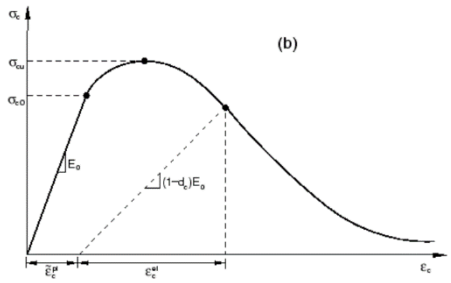


Fig. 1. The stress-strain curve of concrete for (a) uniaxial tension (b) compression

In Equation 3, σ_{b0}/σ_{c0} is the ratio of initial equibiaxial compressive yield stress to initial uniaxial compressive yield stress, and is assumed to take the value of 1.16 for concrete. The initial cohesion c_0 is assumed to be the same as the uniaxial compressive loading state $c_0=\sigma_{b0}$ [17]. K_c represents the ratio of the second stress invariant on the tensile meridian, $q_{(TM)}$, to the second stress invariant on the compressive meridian, $q_{(CM)}$ in the deviatoric plane as shown in Fig. 2. and takes the value between 0.5 and 1. K_c =2/3 is a typical value for concrete. $\bar{\sigma}_c\left(\tilde{\varepsilon}_c^{pl}\right)$ and $\bar{\sigma}_t\left(\tilde{\varepsilon}_t^{pl}\right)$ represent the effective compressive cohesion stress and the effective tensile cohesion stress, respectively.

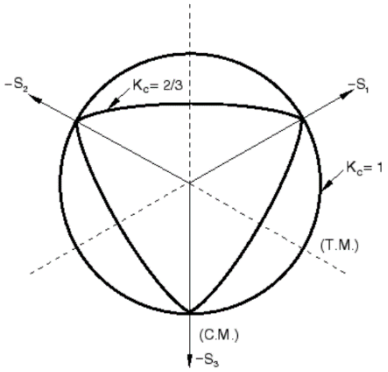


Fig. 2. Yield surfaces in the deviatoric plane

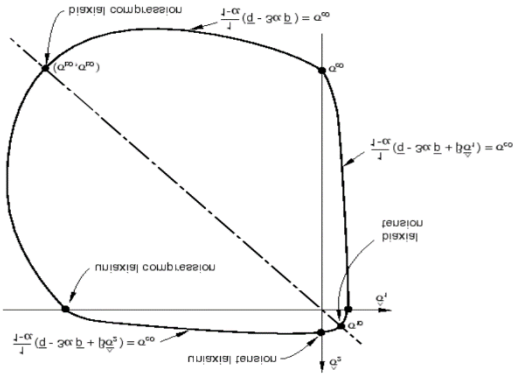


Fig. 3. Yield surfaces in plane stress

The flow rule suitable for the Concrete Damaged Plasticity model is Drucker-Prager flow rule [18] since it is based on the cohesion and internal angle of friction, parameters that play important roles for the behavior of concrete and quasi-brittle materials. The plastic strain rate is assumed to be generated from a scalar potential function, which is denoted as G [19]. The plastic strain rate $\dot{\varepsilon}^{pl}$ and the potential function G are expressed as follows,

$$\dot{\varepsilon}^{pl}=\dot{\lambda}\frac{\partial G}{\partial\bar{\sigma}},$$
$$G=\sqrt{(\epsilon\sigma_{t0}\tan\psi)^2+\bar{q}^2}-\bar{p}\tan\psi \quad (4)$$

where ψ represent the dilatation angle, ϵ is referred as the eccentricity, the rate at which the function approaches the asymptote. A number of numerical and experimental studies is done by researchers [8], [20]-[22], to estimate the appropriate value of dilatation angle for concrete and masonry, which gives us a relation between normal

displacement and shear displacement. According to Lourenco [8], for low confining pressures it takes the range of values from $\tan\psi=0.2$ to $\tan\psi=0.7$, while for high confining pressure values, upon increasing shear, it falls to zero. Wosatko [22] showed that $\psi=25^{o}$ is the most adequate value for concrete in terms of the slope of the lateral force-displacement curve. Since we assume that the material has almost the same dilation angle over a wide range of confining pressure stress values, flow potential eccentricity $\epsilon=0.1$ value is recommended [23].

[3] Numerical Simulation

In order to validate the effectiveness of the CDP constitutive model in previous chapter, TU Eindhoven Walls V3G and J2G [3]-[6] have been considered and modelled in ABAQUS/Standard [20], with eight-node brick elements with reduced integration C3D8R, as shown in Fig. 4.

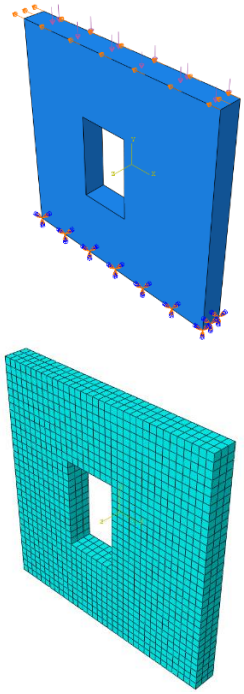


Fig. 4. Numerical Model of TU Eindhoven Walls

Vermeltfoort et al. [3]-[6] carried out experiments on 990x1000x100 (length x height x width) mm masonry shear walls, to describe their failure modes, cracking patterns and lateral load-displacement curves. Wall V3G was made of the soft mud bricks, called VE bricks, while J3G was made from wire cut bricks, called JG bricks. The ratio of cement, lime and sand of mortar was 1:2:9, by volume. A vertical load of 30 kN (0.3 MPa) was applied over the steel beam placed on the walls. Then shear test started with the horizontal deformation of the wall at a speed of 10mm/hour. That deformation was measured at the top corner of the specimen. In order to derive the compressive and modulus of elasticity of composite, small-scale specimens were made. The average compressive strength measured was 11.73 MPa for JG masonry and 8.95 MPa for VE masonry. Young's modulus of elasticity were 8000 MPa and 4000 MPa for JG masonry and VE masonry respectively. For the tensile strength, value of 10% of $f_m^{'}$ [24] is used here. Elastic and plastic material properties used in this study are given in Table 1.

Table 1. Material Properties

Parameters	V3G Wall	J2G Wall
Compressive Strength	8.95 MPa	11.73 MPa
Tensile Strength	0.9 MPa	1.2 MPa
Young's Modulus	4000 MPa	8000 MPa
Poisson Ratio	0.2	0.2
Dilatation Angle	20	20
Viscosity	0.001	0.001
Eccentricity	0.1	0.1
f_{b0}/f_{c0}	1.16	1.16
K	2/3	2/3

The predicted responses are shown to fit quite well the experimental load-deformation plots, in terms of the initial slopes and the peak load levels (**Fig. 5-6**). It is important to mention that the macro modelling approach give unsatisfied results for the post peak behavior of URM walls with openings.

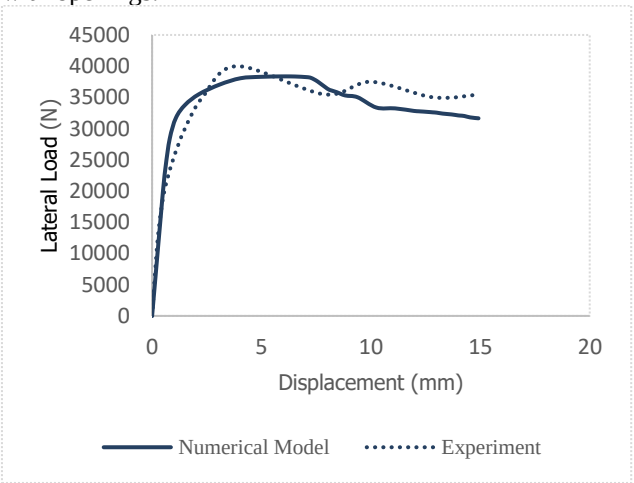


Fig. 5. Comparison of Load–displacement Responses of V3G wall

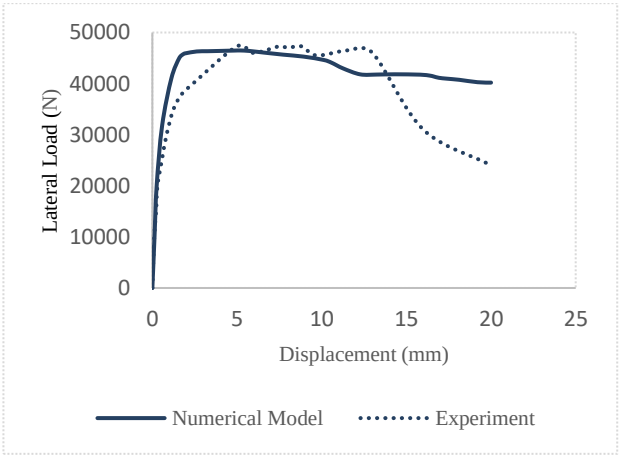


Fig. 6. Comparison of Load–displacement Responses of J2G wall

[4] CONCLUSION

In order to improve earthquake resistance of buildings containing masonry shear walls with openings,

appropriate numerical solutions are required. It can be concluded from this paper that Concrete Damaged Plasticity model gives satisfactory results for the NLFEA of URM walls with opening in terms of load-displacement curve and peak load level. Unfortunately, failure modes and damage pattern have not been determined, since the macro modeling technique is used for the numerical simulation. Hence, post-peak behavior cannot be predicted precisely.

[5] REFERENCES

[1] Zhen Liu, Adam Crewe, “Effects of size and position of openings on in-plane capacity of unreinforced masonry walls”, Bulletin of Earthquake Engineering, vol. 18, pp. 4783–4812, June 2020.

[2] Bashar S. Mohammed, Badorul Hisham Abu Bakar and K. K. Choong “The Effects of Opening on the Structural Behavior of Masonry Wall Subjected to Compressive Loading - Strain Variation”, The Open Civil Engineering Journal, vol. 3, pp. 62-73, April 2009.

[3] A.Th. Vermeltfoort, T.M.J. Raijmakers, “Shear Tests on Masonry Panels 1x1 m^2”, Research on Building Structures and Building Physics Eindhoven 1992.

[4] A.Th. Vermeltfoort, T.M.J. Raijmakers “Vervormingsgestuurde meso-schuifproeven op metselwerk”, TNO-raport Centrum Bouwonderzoek TNO-TUE 1993, CUR Commissie B50 - Experimenteel metselwerkonderzoek.

[5] A.Th. Vermeltfoort, T.M.J. Raijmakers, “Vervormingsgestuurde meso-schuifproeven op metselwerk: Deel II (meetrapport)”, Technische Universiteit Eindhoven 1993, CUR commissie B50, TU Eindhoven. Fac. Bouwkunde, Vakgr. Konstruktie, TUE-BKO-9318.

[6] A.Th. Vermeltfoort, T.M.J. Raijmakers, Shear tests on masonry walls, 6th North American Masonry Conference, 6-9 June 1993, Philadelphia, Pennsylvania, USA, 1183-1193, June 1993.

[7] Kurdo F. Abdulla a, Lee S. Cunningham, Martin Gillie, Simulating masonry wall behaviour using a simplified micro-model approach, Engineering Structures, vol. 151, pp. 349–365, November 2017.

[8] Lourenco P., Computational strategies for masonry structures, PhD. Thesis, Delft University of Technology, Netherlands, 1996.

[9] Hemant B. Kaushik, Durgesh C. Rai, and Sudhir K. Jain, Stress-Strain Characteristics of Clay Brick Masonry under Uniaxial Compression, Journal of Materials in Civil Engineering, vol. 19, pp. 728-739, September 2007.

[10] Doran, B., Koksal, H.O., and Akbas, B., “Strengthening R/C and Masonry Structures with Fiber Reinforced Polymers in Disaster Areas”, NATO Advanced Research Workshop "Engaging the Public to Fight the Consequences of Terrorism and Disasters," Tbilisi, Georgia, 02 June - 04 June 2014.

[11] Köksal, H.O., Doran, B., Özsoy, A.E., and Alacalı, N.S., “Nonlinear modeling of concentrically loaded reinforced blockwork masonry columns”, Canadian Journal of Civil Engineering, vol. 31, pp. 1012-1023, December 2004.

[12] Köksal, H.O, Doran, B., Kuruscu, A.O., Kocak, A., “Elastoplastic Finite Element Analysis of Masonry Shear Walls”, Korean Society of Civil Engineers (KSCE), vol. 20(2), pp. 784-791, June 2015.

[13] Nelson Agüera, Carlos Daniel Frau, Miguel Tornello, Structural Response of Unreinforced Masonry Walls, Journal of Civil Engineering and Architecture, vol. 10, pp. 219-231, February 2016.

[14] Suraj D. Bhosale, Atul K. Desai, Simulation of Masonry Wall using Concrete Damage Plasticity Model, International Journal of Innovative Technology and Exploring Engineering (IJITEE), vol. 8, pp. 2278-3075, July 2019.

[15] Szczecina Michał and Winnicki Andrzej, Calibration of the CDP model parameters in Abaqus, The 2015 World Congress on Advances in Structural Engineering and Mechanics (ASEM15), Incheon, Korea, August 25-29, 2015.

[16] J. Lubliner, J. Oliver, S. Oller, and E. Onate, A Plastic-Damage Model for Concrete, International Journal of solids and structures, vol. 25(3), pp. 299-326, 1989.

[17] Jeeho Lee and Gregory L. Fenves, Plastic-Damage Model for Cyclic Loading of Concrete Structures, J. Eng. Mech., vol. 124(8), pp. 892-900, 1998.

[18] D. C. Drucker and W. Prager, Soil Mechanics and Plastic Analysis or Limit Design, Quarterly of Applied Mathematics, Vol. 10(2), pp. 157-165, July 1952.

[19] Jeeho Lee and Gregory L. Fenves, A return-mapping algorithm for plastic-damage models: 3-D and plane stress formulation, Int. J. Numer. Meth. Engng, vol. 50, pp. 487-506, 2001.

[20] Gideon P. A. G. van Zijl, Modeling Masonry Shear-Compression: Role of Dilatancy Highlighted, J. Eng. Mech., vol. 130(11), pp. 1289-1296, 2004.

[21] L.R. Alejano, E. Alonso, Considerations of the dilatancy angle in rocks and rock masses,International Journal of Rock Mechanics & Mining Sciences, vol. 42, pp. 481–507, 2005.

[22] Adam Wosatko, Andrzej Winnicki, Maria Anna Polak, Jerzy Pamin, Role of dilatancy angle in plasticity-based models of concrete, Archives of Civil and Mechanical Engineering Volume 19, pp. 1268-1283, August 2019.

[23] ABAQUS, Theory Manual, Version 6.14, Documentation, Dassault Systemes Simulia Corporation.

[24] B. Ghiassi, A.T. Vermelfoort and P.B. Lourenco, Masonry mechanical properties, Numerical Modeling of Masonry and Historical Structures, From Theory to Application, Woodhead Publishing Series in Civil and Structural Engineering, pp. 239-261, June 2019.

The Effect of Beam Stiffness on Performance-Based Seismic Design of Reinforced Concrete Frames

Ibrahim A. Alameri and Sulaiman Al-Safi
Dept. of civil Engg. Sana'a University Sana'a, Yemen
i.ameri@eng-su.edu.ye, alsafi11@hotmail.com

Aim: Increasing the performance of earthquake-resistant buildings is one of the most important issues that today's researchers focus on. In the nonlinear-pushover analysis, plastic hinge formation is one of the fundamental data analyzed by researchers to discern the position of the building where greater potential damage could occur. If the number of plastic hinges in the building is increased, the total capacity of the building will increase proportionally. So, reaching the maximum number of plastic hinges should be considered as a new performance target in the performance-based seismic design codes that will provide the highest final load of the structure.

Method: A three-story concrete frame was analyzed and designed according to the Turkish standard (TBDY 2018). The total height of the building is 9 m and the typical floor height is 3 m. Nonlinear static pushover analysis was done by SAP2000. Beam and column members are modeled as frame members to resist axial, shear, and bending forces. Life safety performance level has been chosen with 2.0% maximum total drift at the top of the frame. Results were compared according to ATC-40, FEMA 356, and FEMA 440 methods.

Results: Analysis results showed that the beam stiffness affects the total number of plastic hinges and the base shear capacity of frames with variable stiffness in comparison to the frame with constant stiffness. In other words, by reducing the stiffness of the beams on the floors above, the number of plastic hinges increased, the total capacity of the frame was increased by 4.54, 4.89, 8.5%, and 19.13% for ATC-40, FEMA 356, FEMA 440 Displacement Modification, and FEMA 440 Equivalent Linearization methods, respectively.

Conclusion: In the finite element nonlinear–pushover analysis plastic hinge formation is one of the essential data analyzed by researchers to distinguish the location of the building where larger potential damage may happen. If the number of plastic hinges in the structure increased, the total capacity of the structure will increase proportionally. On this point of view, reaching the maximum number of plastic hinges must be added as a new performance goal to the performance-based aseismic design codes, which will dial to the highest ultimate load of the structure. On example of three-story moment resisting plane frame system the following conclusions can be drawn:

- Variable beam stiffness configuration has greater flexibility compared to fixed beam configurations.
- From the nonlinear static pushover analysis, it was found that most hinges occur for variable beam stiffness compared to fixed beam stiffness configuration. Therefore, in order to obtain a more ductile frame, it is recommended to reduce the stiffness of the beams on the upper floors.
- The number of plastic hinges increased with the decrease in the stiffness of the beams in the upper stories, and the total frame capacity was increased by 4.54, 4.89, 8.5, 19.13%, for ATC-40 capacity spectrum, FEMA 356 coefficient method, FEMA 440 equivalent linearization, and FEMA 440 displacement modification methods, respectively.

In future studies, other methods such as bracing systems can be developed to increase the number of plastic hinges.

Keywords— Performance-Based Aseismic Design, Plastic hinges, Pushover analysis, Earthquake-resistant buildings, Capacity design

Vector Signal Strength Different for Magnetic Field Indoor Positioning System

Caceja Elyca Anak Bundak
Dept. of Physics Universiti Putra
Malaysia UPM Serdang, Malaysia
gs52905@student@upm.edu.my

Mohd Amiruddin Abd Rahman
Dept. of Physics Universiti Putra
Malaysia UPM Serdang, Malaysia
mohdamir@upm.edu.my

Che Nursyamimi Binti Che Saidi
Dept. of Physics Universiti Putra
Malaysia UPM Serdang, Malaysia
syamimiesaidi@gmail.com

Magnetic field (MF) signal as an indoor positioning system (IPS) has received a great deal of interest as they have a wide variety of applications for Location Based Services. The state-of-the-art k-Nearest Neighbor (KNN) is the common matching algorithm that is used to estimate locations. However, using KNN algorithm sometimes does not provide a reliable estimated location due to fluctuation of the MF signal at certain locations. For example, the MF signal is disturbed by moving metal objects such as lifts or metal cabinets. In order to improve the accuracy and reliability of the positioning system, this paper proposed a vector signal strength different algorithm which could improved the location estimation error. The implementation of the proposed algorithm evaluates the estimated location by implementing weights to the MF vector signal strength different. The analysis of the findings is compared to the previous positioning algorithm to evaluate the proposed algorithm performance. The proposed algorithm shows an accuracy of 7.419 meters, which improved 9% from the previous algorithm.

Keywords— Indoor Positioning, Magnetic field, Standard Deviation

[1] INTRODUCTION

Indoor positioning system (IPS) has gained tremendous interest because it can complement GPS for indoor due to its ability to locate signal and potential future applications not yet realized. While the implementation of the Global Positioning System (GPS) has become an accepted and standardized system, IPS technology is constantly evolving and adapting as new technology is introduced and new techniques are discovered. Magnetic Field (MF) is a promising technology for Indoor Positioning System (IPS).

Indoor magnetic field (MF) is a pervasive field of geomagnetic-induced anomalies. A study [1] shows that the magnetic fields produced in the indoor environment were relatively stable and reproducible. Due to the stability and uniqueness of the magnetic field, many researchers have developed a number of magnetic field based positioning systems. Shao et al. studied the key magnetometer interference sources embedded on the smartphone and evaluated the output of different feature extraction methods in order to improve the smoothness of the fingerprinting data pattern [2]. To provide a better fingerprint data pattern, they create an algorithm of a novel and lightweight distinguishability measurement method (DAME). A position-estimation algorithm is suggested by Poulose et al. [3]. The model incorporated multiple data from features of an IMU sensor, including data from the accelerometer, magnetometer, and gyroscope for estimation of position. Nonetheless, their model is designed for scenario of route motion such as rectangular motion, straight line motion and pedestrian classification circular motion. Shu et al. described a fusion indoor localization system with pervasive magnetic field and opportunistic WiFi [4]. They use a secure, compliant walking-based data collection method for database construction and resolve all the magnetic field issues. Their systems also use an augmented particle filter to perform weight-based sampling of importance over the whole set of particles. This will eventually kill particles moving in the wrong direction as the discrepancies between the magnetic signals will constantly decrease their weight. Kalman filter [5] and particle filter (PF) are two popular methods used in matching for magnetic field based localisation. Particle filter scheme is proposed to fuse pedestrian dead reckoning (PDR) magnetic information to reduce low discernibility influences [6], [7]. However, existing PF algorithms have several disadvantages which are re-sampling of the classical PF scheme may cause the problem of particle degradation and high computational cost. K nearest neighbors have low complexity which appropriate for practical use. For example, KNN use in UJIIndoorLoc-Mag database to test the quality of the database for public use [8]. Other than that, a research on the performance of MF system using nearest neighbor with root mean square (RMS) error [9]. However, matching using KNN algorithm can lead to large estimation localisation error when certain physically distant locations may have identical fingerprint data compared to current location. Therefore weighted method applied in KNN are used to improve the algorithm. Weighted KNN algorithm is used in Wi-Fi [10]. With the stability signals of MF, this paper proposed a vector signal strength different algorithm for the IPS based on Magnetic Field (MF).

[2] PROPOSED ALGORITHM

In this work, magnetic based fingerprint technique is used. To incorporate a fingerprinting technique, the measurements must be stored in a database. The database contains coordinates of reference points (RPs) and the magnetic field measure along a smartphone's three axes vector (x, y and z). The observed magnetic field fingerprint is compared to the stored one in the database during the online phase, and then the coordinate with the closest match is known as the user's estimate location. In addition, a large number of reference points are needed to create a proper fingerprint map for accurate location, which is time-consuming and workers intensive. Therefore, we use average MF signal database for the training data for further evaluation of the proposed algorithm. This paper design and develop the indoor positioning algorithm using weighted vector

component algorithm of MF signal. Then, To improve more on the proposed algorithm, clustering technique is applied during the online phase. The flow of the proposed algorithm is showed in Fig. 1.

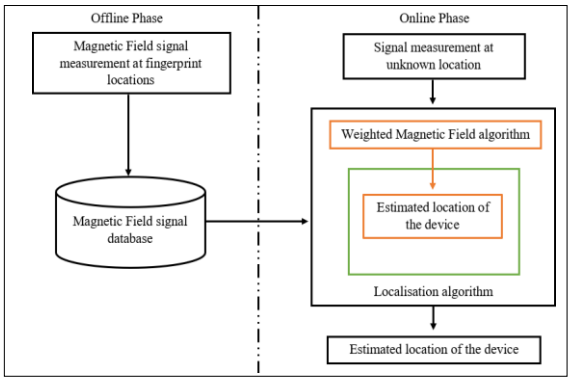


Fig. 7. Flow of the Proposed Algorithm.

A. *Standard Deviation with Vector Signal Strength Different (VSSD)*

Previous studies by [11] uses the signal-pattern comparison method to establish a database in the offline phase. Their method using standard deviation to calculate the weight which applied to their data. From the previous studied, we proposed using standard deviation to obtained weight which applied on each vector signal of MF. We firstly calculated the difference signal in each RP by calculated the difference between two different MF vector signal.

$$d(i) = \begin{cases} d_{xyi} = mx_i - my_i \\ d_{zyi} = mz_i - my_i \\ d_{xzi} = mx_i - mz_i \end{cases} \quad (10)$$

where mx_i, my_i and mz_i is the MF vector signal at X, Y and Z axis. The d_{xyi} is difference between vector signal mx_i and my_i , d_{zyi} is the difference between mz_i and my_i and d_{xzi} is the difference between mx_i and mz_i at *i* th RP.

Then, the mean intensity $(\overline{xy}, \overline{yz}, \overline{xz})$ and the standard deviation $(\sigma_{xy}, \sigma_{zy}, \sigma_{xz})$ of each of each difference signals are determined as follows:

$$standard\ deviation = \begin{cases} \sigma_{xy}^2 = \frac{1}{n}\sum_{i=1}^{n}\left(d_{xy_i} - \overline{xy}\right)^2 \\ \sigma_{zy}^2 = \frac{1}{n}\sum_{i=1}^{n}\left(d_{zy_i} - \overline{yz}\right)^2 \\ \sigma_{xz}^2 = \frac{1}{n}\sum_{i=1}^{n}\left(d_{xz_i} - \overline{xz}\right)^2 \end{cases} \quad (11)$$

After calculated the standard deviation, the weight is determined by the sum of the standard deviation of the difference signals and the weight of the respective difference signal is standard deviation per weight which described as follows:

$$\mathrm{w} = \sigma_{\mathrm{xy}}^2 + \sigma_{\mathrm{zy}}^2 + \sigma_{\mathrm{xz}}^2 \quad (12)$$

$$w_{xy} = \frac{\sigma_{xy}}{w}, \backslash w_{zy} = \frac{\sigma_{zy}}{w}, \backslash w_{xz} = \frac{\sigma_{xz}}{w} \quad (13)$$

In the online phase, the difference signal in each TP also calculated before matching with the RP difference signal which is defined as follows:

$$C = \begin{cases} C_{xy} = nx - ny \\ C_{zy} = nz - ny \\ C_{xz} = nx - nz \end{cases} \quad (14)$$

where nx, ny and nz is the MF vector signal at X, Y and Z axis. The C_{xy} is difference between vector signal nx and ny, C_{zy} is difference between vector signal nz and ny and C_{xz} is difference between vector signal nx and nz.

The minimum difference, P is calculated by applied the weight on each of the difference between the RP and TP. Therefore, the estimated location is estimated by taking the minimum difference which described as the following equation:

$$min(P(C, d_i)) = w_{xy}\left(C_{xy} - d_{xy_i}\right)^2 + w_{zy}\left(C_{zy} - d_{zy_i}\right)^2 + w_{xz}\left(C_{xz} - d_{xz_i}\right)^2 \quad (15)$$

[3] Experiment Setup

The data are collected at the third floor of faculty of science building 1, Universiti Putra Malaysia UPM, Malaysia.

The plan is illustrated in Fig. 2. Each map is split equally into train data with 72 RPs (green dot) and testing data with 72 TPs (blue dot) in the experimental area in the space of 21 m x 33 m.

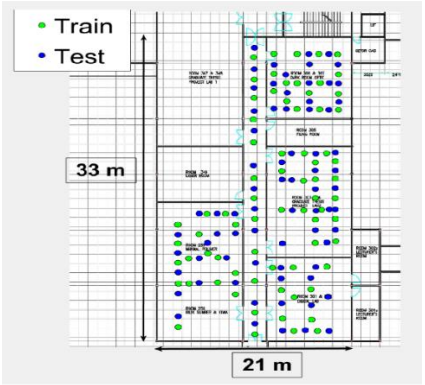


Fig. 8. Floor map of the MF database.

The data collection application, installed on an LG Nexus 5 smartphone use to collect the MF fingerprints in four orientations, namely, North, South, East, and West for each point, 1m apart at a 0.5 m height. The data provided by the magnetometer and the orientation of the device is stored 14 times per second. So, the device frequency band is 0.07 Hz. Table \ref{tab2} shows the MF database. The total data for the training data when using the average MF signal are 72 x 4 x 1 = 288 sample data. Other than that, the testing data used have 72 TPs with only one MF signal data which the total data are 72 sample data. Both the training and the testing data were taken from splitting the MF database equally half.

Table 1 MF Database Description

Total Reference Point	Total Direction at 1 Location	Total Data at 1 Location	Total Overall Data
72	4	4	288

[4] PERFORMANCE EVALUATION

To evaluate the performance of the algorithm, we compare the algorithm with the state-of-the-art KNN and Weighted MF algorithm [11]. Figure 3 shows the performance of the proposed algorithm compare with KNN and MF algorithm. At 5 and 10 meters, both of the algorithm has achieved the corresponding 44% and 60% of the accuracy respectively. The factor of the improvement in accuracy for MF VSSD compared to KNN MF and Weighted MF is because of the fact that the strength vector of the MF from the proposed MF VSSD algorithm has been modified and using the new training data. However, the three algorithms proposed is still observed as inefficient to enhance the performance in IPS based on MF because after 15 meters, the algorithm does not give the optimal accuracy. The accuracy achieved after 15 meters is at approximately 78-80%. After 15 meters, the three algorithms observed to have a corresponding percentage of accuracy along the distance error until 30 meters. Overall, comparing to the KNN MF and Weighted MF that use the raw training data, MF VSSD has achieved a significant improvement below the 15 meters by implementing the VSSD, equation. Nevertheless, after 15 meters, the efficiency of the system's performance for the accuracy are observed as rather the same.

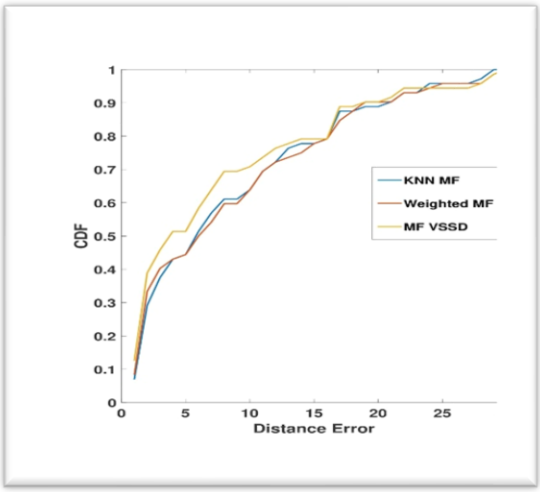


Fig. 9 Performance of the algorithms

Figure We also vary the k value to see how the different signal weighting function performs as tabulate in table 2. The table shows that for algorithm of KNN MF, at k=4 it obtained the minimum mean distance error, which is 6.349 meters. Compared to Weighted MF, it shows at k=5 it obtained the minimum mean distance error of 6.511 meters. Furthermore, for MF VSSD, it shows to obtain a minimum mean distance error at k=2 which is 6.350 meters. This demonstrates that different algorithms provide different value of the optimal k to obtain the minimum mean distance error. For the analysis of the algorithm performance at k=1, it is observed that by implementing the MF VSSD algorithm, the mean distance error can be reduced to ≈0.8 and ≈0.9 meters from KNN MF and Weighted MF algorithm respectively. However, in term of the algorithm reliability, it is still inefficient to implement MF VSSD as the MF indoor positioning system because the number of the optimal k obtained by the algorithm is to small compared to KNN MF and Weighted MF.

Table 2 Mean Error of All Algorithms

k	Mean Error of KNN (m)	Mean Error of Weighted MF (m)	Mean Error of VSSD (m)
1	8.295	8.364	7.418
2	6.623	6.665	6.349
3	6.365	6.619	6.851
4	6.348	6.594	6.622
5	6.679	6.510	6.889
6	6.928	6.686	6.975
7	7.069	6.908	7.264
8	7.43	7.1466	7.400
9	7.473	7.233	7.494
10	7.577	7.286	7.660

[5] CONCLUSIONS

We proposed a magnetic based algorithm which using the vector signal strength different method. This method calculated difference in the vector signal strength and use it to find the method using the standard deviation to calculate the weight We observed that some improvement has been found, which is MF VSSD algorithm is better than the classical kNN and Weighted MF. This is because the strength vector of the signals has been modified and altered.

ACKNOWLEDGMENT *(HEADING 5)*

This research was supported by Ministry of Higher Education (MOHE) of Malaysia through Fundamental Research Grant Scheme (FRGS/1/2017/TK04/UPM/02/5) and (FRGS/1/2020/ICT02/UPM/02/3)..

REFERENCES

[1] B. Gozick, K. P. Subbu, R. Dantu, and T. Maeshiro, "Magnetic maps for indoor navigation," *IEEE Trans. Instrum. Meas.*, vol. 60, no. 12, pp. 3883–3891, 2011, doi: 10.1109/TIM.2011.2147690.

[2] W. Shao *et al.*, "Location Fingerprint Extraction for Magnetic Field Magnitude Based Indoor Positioning," *J. Sensors*, vol. 2016, 2016, doi: 10.1155/2016/1945695.

[3] A. Poulose, O. S. Eyobu, and D. S. Han, "An indoor position-estimation algorithm using smartphone IMU sensor data," *IEEE Access*, vol. 7, pp. 11165–11177, 2019, doi: 10.1109/ACCESS.2019.2891942.

[4] Y. Shu, C. Bo, G. Shen, C. Zhao, L. Li, and F. Zhao, "Magicol: Indoor Localization Using Pervasive Magnetic Field and Opportunistic WiFi Sensing," *IEEE J. Sel. Areas Commun.*, vol. 33, no. 7, pp. 1443–1457, 2015, doi: 10.1109/JSAC.2015.2430274.

[5] Y. Du, T. Arslan, and A. Juri, "Camera-aided region-based magnetic field indoor positioning," *2016 Int. Conf. Indoor Position. Indoor Navig. IPIN 2016*, no. October, pp. 4–7, 2016, doi: 10.1109/IPIN.2016.7743621.

[6] X. Wang, C. Zhang, F. Liu, Y. Dong, and X. Xu, "Exponentially weighted particle filter for simultaneous localization and mapping based on magnetic field measurements," *IEEE Trans. Instrum. Meas.*, vol. 66, no. 7, pp. 1658–1667, 2017, doi: 10.1109/TIM.2017.2664538.

[7] H. Xie, T. Gu, X. Tao, H. Ye, and J. Lu, "A Reliability-Augmented Particle Filter for Magnetic Fingerprinting Based Indoor Localization on Smartphone," *IEEE Trans. Mob. Comput.*, vol. 15, no. 8, pp. 1877–1892, 2016, doi: 10.1109/TMC.2015.2480064.

[8] E. S. Lohan, J. Torres-Sospedra, H. Leppäkoski, P. Richter, Z. Peng, and J. Huerta, "Wi-Fi crowdsourced fingerprinting dataset for indoor positioning," *Data*, vol. 2, no. 4, pp. 1–16, 2017, doi: 10.3390/data2040032.

[9] J. Chung, M. Donahoe, C. Schmandt, I. J. Kim, P. Razavai, and M. Wiseman, "Indoor location sensing using geo-magnetism," *MobiSys'11 - Compil. Proc. 9th Int. Conf. Mob. Syst. Appl. Serv. Co-located Work.*, pp. 141–154, 2011, doi: 10.1145/1999995.2000010.

[10] M. Amiruddin, A. Rahman, M. Khalis, and A. Karim, "Wireless Local Area Network Localization using Enhanced Access Point Weighting Technique based on Improved kNN Algorithm," pp. 10–13.

[11] S. C. Yeh, W. H. Hsu, W. Y. Lin, and Y. F. Wu, "Study on an Indoor Positioning System Using Earth's Magnetic Field," *IEEE Trans. Instrum. Meas.*, vol. 69, no. 3, pp. 865–872, 2020, doi: 10.1109/TIM.2019.2905750.

Classification of Covid-19 Chest X-Rays Based on HOG Feature Descriptor Using SVM

Ferhat Bozkurt
Department of Computer Engineering Ataturk University Erzurum, Turkey
fbozkurt@atauni.edu.tr

***Abstract*— The rapid spread of COVID-19 cases and the increase in mortality in many countries have encouraged the scientific community to study this issue. Automatic early diagnosis of COVID-19 with computer-aided tools is crucial for disease treatment and control. There exists a serious shortage of experts in the world and traditional pneumonia and COVID-19 have great similarities on chest X-ray images. Machine learning (ML) aided diagnosing method could be an important development for reducing test time. ML could offer both a lower cost and a more accurate diagnosis and treatment for COVID-19 and similar diseases. In this study, COVID-19 has been detected from chest X-Ray images using HOG feature-based SVM classifier. HOG feature-based SVM classification is studied that could classify chest X-Ray images as COVID-19, Viral Pneumonia, and Normal (negative) cases. Experimental studies have been conducted on an open-access chest X-Ray images by allocating on different size of test and training. Two types of experiments are conducted by dividing the data in different sizes. Performance evaluations are performed on the accuracy of the techniques, and the results are compared with other supervised learning techniques such as NB, kNN, and NN. In experimental studies, the highest accuracy (97%) is obtained with the HOG feature-based SVM classifier.**

Keywords— machine learning, HOG, SVM, COVID-19

[1] INTRODUCTION

From past to present, infectious diseases are one of the most important threats to human health. COVID-19 is an infectious disease caused by severe acute respiratory syndrome coronavirus (SARS-CoV-2) and was first reported in Wuhan, China. Hereby, the disease spread first in China and then all over the world and was declared as a pandemic by the World Health Organization (WHO) [1]. The rapid spread of the disease and the increase in mortality rates in many countries reveal that an effective treatment method should be developed. It is important to detect COVID-19 disease at an early stage and immediately isolate the infected patient from healthy people and start treatment. Besides the PCR test, chest X-ray tomography and some blood tests are used in diagnosis of the disease. Especially during the pandemic period, there was a need to support the diagnosis in some centers with intense patient admissions. X-ray tomography and evaluation may often be required to determine the extent to which region of the lung is affected. Image processing is a technology that obtains fast results as a function of the human eye in the computer environment with various software. Various techniques have been developed in this technology. Scientific studies made with these developed techniques have also been contributed. In recent years, the most preferred technique in these analysis results is machine learning techniques. At this point, artificial intelligence and machine learning can contribute to this problem. Especially, there is a serious shortage of experts and traditional pneumonia and COVID-19 have great similarities. ML aided diagnosing method could be an important milestone towards significantly reducing test time. This technique offers both a lower cost and a more accurate diagnosis and treatment for COVID-19 and similar diseases [2], [3].

Recently, successful results are obtained by using machine learning techniques with chest x-ray image dataset. Jiang et al. [4] utilized six different classifiers (Logistic regression, kNN, two different decision trees, SVM, and random forests) by using eleven clinical features to predict the clinical severity of COVID-19. They obtained the best accuracy with SVM classifier with 80%. Batista et al. [5] used machine learning classifiers by considering 18 clinical findings to predict COVID- 19 diagnosis. Five different classifiers (SVM, random forests, logistic regression, neural networks, and gradient boosted trees) were applied. The best AUC scores were obtained with both random forest and SVM classifiers with 0.847. Schwab et al. [6] proposed clinical predictive model for COVID-19. They used various machine learning techniques. They obtained the best performance with XFB (Gradient Boosting) with 66% AUC score. Novitasari et al. [7] combined two techniques, which are CNN as feature extraction and SVM as a classification method. They obtained accuracy with 97.33% for three classes (pneumonia, normal, COVID19). Oğuz and Yağanoğlu [8] evaluated the performance of various classifi cation methods for detecting COVID 19 cases. They achieved the best result with ResNet-50 and SVM classification methods with a 95.18% accuracy.

In this study, a HOG feature based SVM classification is studied that could classify chest X-Ray images as normal, viral pneumonia, and COVID-19. The rest of the work is organized as follows. In section II, material and method are explained. In this section, the dataset used in the experimental study and the HOG+SVM model applied are explained in detail. Experimental results are given in section III, and the discussion and conclusions part of the study is given in section IV.

[2] MATERIAL AND METHOD

A. Material

In this study, an open-access dataset is utilized for classification of COVID-19 chest X-Ray images. This dataset consists of chest X-ray images for COVID-19 (positive cases), Normal (negative cases), and Viral Pneumonia images. A team of researchers composes this database from the university Qatar, Doha, Bangladesh, Dhaka, and Qatar with their collaborators and doctors [9]. A total of 3886 chest X-Ray images exist as 1200 COVID-19 (positive cases), 1345 Viral Pneumonia, and 1341 Normal (negative cases) images. Fig. 1 shows image samples of COVID-19, Viral Pneumonia, and Normal (negative) cases from this dataset. Moreover, Fig. 2 shows the categorical distribution of the X-Ray images according to cases.

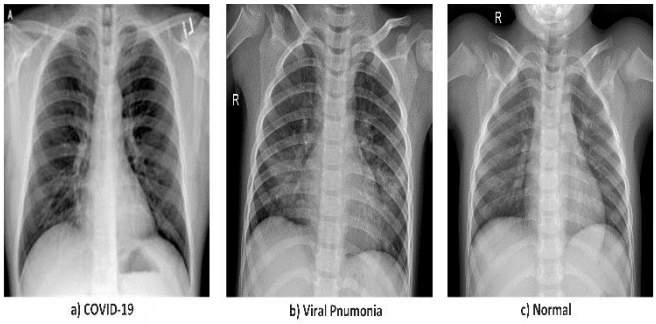


Fig. 1. COVID-19 (positive cases), Viral Pneumonia and, Normal (negative cases) chest X-Ray images in dataset.

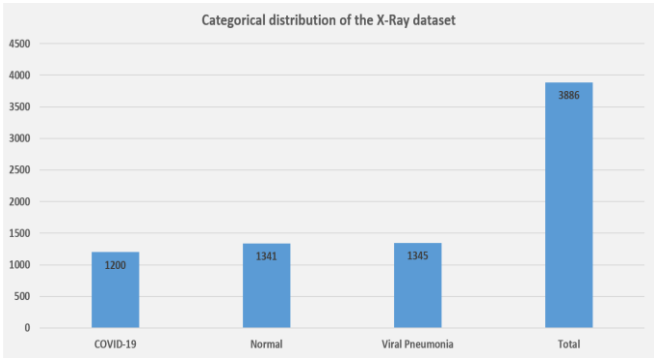


Fig. 2. Categorical distribution of the X-Ray dataset.

B. *Method*

As shown in Fig. 3, HOG based COVID-19 detection method is studied. Textural features are extracted with HOG feature descriptor, and supervised learning process is carried out with these features. First of all, due to the different sizes and properties of the images, normalization of the images is performed in the pre-processing stage. Then, textural features of the images are extracted with HOG feature descriptor and a feature set (database) is created in training stage. Supervised learning is performed using this feature set and SVM classifier is utilized for prediction. COVID-19 detection from test images is performed by querying to this classifier. In this section, preprocessing, feature extraction and classification stages will be explained in more detail.

1) Preprocessing: At this stage, X-Ray images in different sizes and properties are normalized and all images are fixed to 256x256. In this way, in the next step, all image features are provided to be same size and properties in feature extraction.

2) HOG-based Feature Extraction: In particular, images of viral, bacterial pneumonia are similar to COVID-19 and contain similar features. Therefore, the information hidden in these images must be extracted with texture descriptors. At this stage, the textural features of the images are extracted by HOG based method. These extracted features are stored in the feature database.

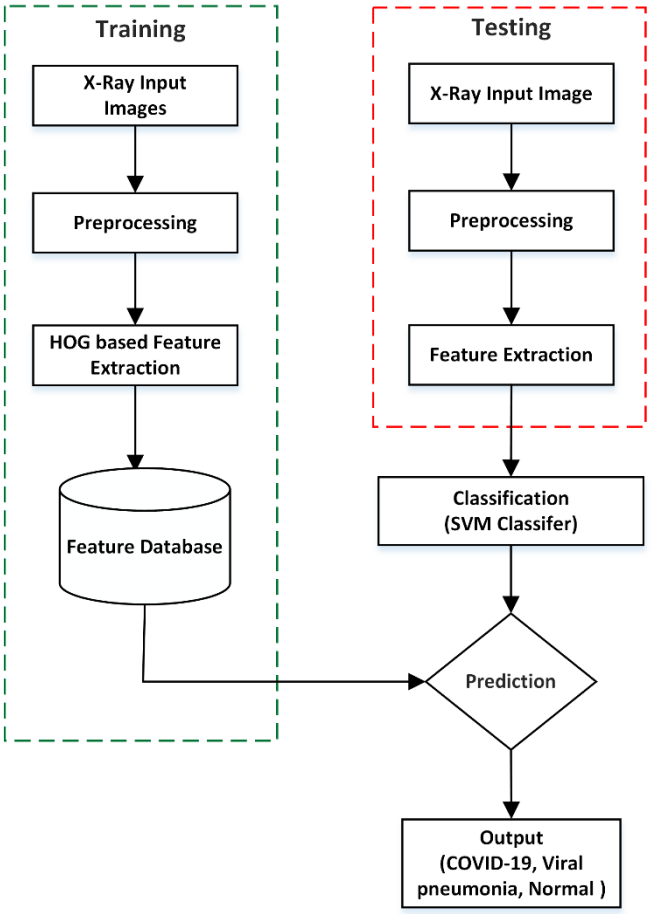


Fig. 3. HOG Feature Descriptor and SVM Based Covid-19 Detection Method.

The purpose of feature extraction is to extract deterministic features from X-Ray images in a robust and stable manner. HOG algorithm is used to extract the feature vector from the textures of the X-ray images. Since this algorithm can obtain high performance from the image textures with similar pixels. In recent years, the use of HOG method, which can also be named as the characteristics of the orientation *(θ)* and magnitude *(m)* values of the pixels in the image, has considerable attention in many areas. This gradient-based feature extraction method was firstly proposed by Dalal and Triggs [10]. The main purpose of this method is to describe the image as a group of local histograms. These histograms contain the number of orientations of gradients in a local region of the image. In other words, this algorithm identifies an image like a sequences of local histograms. Any local histograms is the distribution of the number of gradients occurring in specified directions, computed from a specific area on the image defined as a cell. The feature extraction process with HOG algorithm is shown in three steps, respectively [11].

- Get the gradient of the image.
- Compute histogram of gradient directions for specified locations.
- Normalize the histograms within the created location groups.

a) Computing Gradient: Horizontal gradient f_x and the vertical gradient f_y are computed by using derivative masks of the gray level images. A simple derivative mask has been used as the use of a more complex mask reduces system performance. The horizontal (1) f_x and vertical (2) f_y image gradient are calculated as follows. In these equations, *I(x, y)* shows the pixel intensity at the point *(x, y)* [11].

$$f_x(x,y) = I(x+1,y) - I(x-1,y) \quad (1)$$

$$f_y(x,y) = I(x,y+1) - I(x,y-1) \quad (2)$$

b) Computing histogram of gradient directions: (3) Gradient magnitude *(m)* and (4) gradient orientations *(θ)* are calculated by using horizontal f_x and vertical f_y image gradients as follows [11].

$$m(x,y) = \sqrt{f_x(x,y)^2 + f_y(x,y)^2} \quad (3)$$

$$\theta(x,y) = \tan^{-1}\left(\frac{f_y(x,y)}{f_x(x,y)}\right) \quad (4)$$

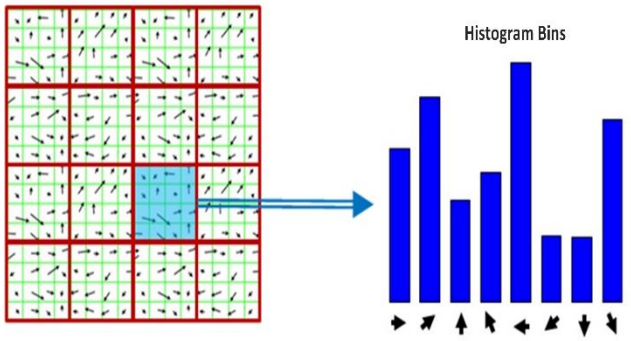


Fig. 4. Creating histograms from blocks for HOG feature vector [12].

When computing the histogram, *θ(x, y)* can be divided into equal regions between 0–180 or 0–360 degrees depending on the application. In this study, gradient direction regions are taken as 9 regions with an angle difference of 20 degrees between 0-180 degrees. When creating a histogram (Fig. 4), the gradient magnitude of a pixel in the cell is calculated according to a specific angle in the histogram regions. This distribution is usually done by linear and trilinear interpolation method. In this study, the distribution process has been done using the linear interpolation method.

c) Block normalization: Hereby, a large histogram is composed by assembling all the histograms created in one block (as shown in Fig. 4). This histogram is then normalized using (5). In this equation, *v* is the normalized HOG feature vector and V_k is the large histogram vector composed from a block [11], [12]. L2-Norm is used for normalization. Thus, the HOG feature vector is computed to be given to the input of the SVM classifier.

$$v = \frac{v_k}{\sqrt{\|v_k\|^2 + 1}} \quad (5)$$

3) Classification: The final detection (prediction) process is feature matching. The feature vector obtained from the feature extraction step is compared with the classes of test X-Ray images previously stored in the database. There exist different types of supervised learning methods for this process. SVM provides optimal separation hyperplane that will separate the classes from each other especially for multi-class classification problems. Thus, SVM maximizes the distance between support vectors belonging to different classes. Furthermore; kNN, Naive Bayes, and Neural Network (simple 3-layer NN) methods, which have a simpler learning structure compared to other classifiers, are also used in this study.

[3] EXPERIMENTAL RESULTS

The experimental studies in this study are conducted on a desktop computer with Intel (R) Core (i7) 3630QM CPU @ 2.40 GHz, NVIDIA 4 GB GeForce 650 M graphics and 16GB primary memory. In this section, two types of experiments are conducted by dividing the data in different sizes. The data in the first experimental study (Experiment1); 80% is reserved for training and 20% for testing. The data in the second experimental study (Experiment2); 70% is reserved for training and 30% for testing. At this stage, the performance evaluation of the method is performed over six performance criteria such as Sensitivity (SE), Specificity (SP), Precision (PR), Recall (RE), Precision, F1-Score (F1-SC), and Accuracy (ACC) [13]. These values are calculated over confusion matrices for each class [14]. A sample performance evaluation of HOG+SVM method for both experiments are given in Table I. In both experiments, it is seen that an accuracy value over 97% was obtained with the HOG+SVM method. Sample confusion matrices of these experiments are given in Table II and Table III. Performance evaluations of different methods could be made with these confusion matrices.

Table 1. A Sample Performance Evaluatıon of Hog+Svm Method For Two Experiments

	SE (%)	SP (%)	PR (%)	RE (%)	F1-SC (%)	ACC (%)
Experiment	97.60	97.15	94.21	97.60	95.87	97.30
Experiment	99.17	97.26	94.24	99.17	96.64	97.86

Table 2. A Sample Confusıon Matrıx of Experiment-1 Wıth Hog+Svm Method

Actual				
	1-COVID	244	4	2
	2-Viral	2	254	9
	3-Normal	1	3	258
		1-COVID	2-Viral	3-Normal
		Prediction		

In this study, the supervised learning process is also performed with different classifiers (e.g., NB, kNN, NN, SVM) by giving input the features obtained with HOG. In order to make the performance evaluation of these classifiers more stable and robust, different classifiers are executed at least 10 times with different random training and test sets. In other words, HOG+SVM method is executed 10 times on randomly selected test and training data for Experiment 1 and the average results are recorded as shown in Table IV. Similarly,

all classifiers are run 10 times on randomly selected test and training data for Experiment 2 and average results for each metric are recorded as shown in Table V. As can be seen in both tables, the lowest accuracy rate was obtained from HOG + NB with 89% and the highest from HOG + SVM with 97%.

Table 3. A Sample Confusıon Matrıx of Experıment-2 Wıth Hog+Svm Method

Actual \ Prediction	1-COVID	2-Viral	3-Normal
1-COVID	360	2	1
2-Viral	1	397	13
3-Normal	2	6	384

Table 4. Average Performance Evaluatıon of The Methods Obtaıned Wıth Dıfferent Classıfıers For Experıment 1

Method	SE (%)	SP (%)	PR (%)	RE (%)	F1-SC (%)	ACC (%)
NB	96.81	85.51	75.24	96.81	84.66	89.04
k-NN	96.53	92.85	85.58	96.53	90.70	93.96
NN	96.81	95.82	91.70	96.81	94.19	96.14
SVM	98.46	96.70	92.67	98.46	95.47	**97.23**

Table 5. Average Performance Evaluatıon of The Methods Obtaıned Wıth Dıfferent Classıfıers For Experıment 2

Method	SE (%)	SP (%)	PR (%)	RE (%)	F1-SC (%)	ACC (%)
NB	97.62	85.44	75.39	97.62	85.07	89.26
k-NN	96.76	92.82	85.75	96.76	90.92	94.03
NN	95.43	95.47	90.79	95.43	93.05	95.45
SVM	98.19	96.40	92.24	98.19	95.12	**96.95**

[4] DISCUSSION AND CONCLUSIONS

In this study, HOG feature based SVM classification method is studied for COVID-19 detection. Experimental studies have been conducted on an open-access chest X-Ray images by allocating on different size of test and training. In this dataset, there are a total of 3886 images belonging to three classes as COVID-19, normal (healthy) and viral pneumonia. For this purpose, a HOG+SVM method is applied, which can classify chest X-Ray images. Performance evaluations are performed on the accuracy of the techniques, and the results are compared with other supervised approaches such as NB, kNN, and NN. In experimental studies, the highest accuracy (97%) is obtained with the proposed HOG+SVM method. In further studies, other handcrafted features-based techniques and data will be studied and comparisons will be made.

[15]

REFERENCES

[1] N. Zhu, et al., "A novel coronavirus from patients with pneumonia in China, 2019," N Engl J Med, 382, 727-733, 2020.

[2] R. Bütüner and M. H. Calp, "COVID-19 Detection from Lung Tomography Images Using Deep Learning and Machine Learning Methods," No.4097, EasyChair, 2020.

[3] M. S. Mottaqi, F. Mohammadipanah and H. Sajedi, "Contribution of Machine Learning approaches in response to SARS-CoV-2 infection," Informatics in Medicine Unlocked, 100526, 2021.

[4] X. Jiang, et al., "Towards an artificial intelligence framework for data-driven prediction of coronavirus clinical severity," Computers, Materials & Continua 63(1), 537-551, 2020.

[5] A. F. Batista, J. L. Miraglia, T. H. R. Donato and A. D. P. C. Filho, "COVID-19 diagnosis prediction in emergency care patients: a machine learning approach," medRxiv, 2020.

[6] P. Schwab, A. D. Schu¨tte, B. Dietz and S. Bauer, "predcovid-19: a systematic study of clinical predictive models for coronavirus disease 2019," arXiv preprint arXiv:2005.08302, 2020.

[7] D. C. R. Novitasari, et al., "Detection of covid-19 chest x-ray using support vector machine and convolutional neural network," Commun. Math. Biol. Neurosci., Article-ID.42, 2020.

[8] Ç. Oğuz and M. Yağanoğlu, "Determination of Covid-19 Possible Cases by Using Deep Learning Techniques," Sakarya Üniversitesi Fen Bilimleri Enstitüsü Dergisi, 25(1), 7-17, 2021.

[9] M. E Chowdhury, et al. "Can AI help in screening viral and COVID-19 pneumonia?," IEEE Access 8, 132665-132676, 2020.

[10] N. Dalal and B. Triggs, "Histograms of oriented gradients for human detection," In 2005 IEEE computer society conference on computer vision and pattern recognition (CVPR'05), Vol. 1, pp. 886-893, Ieee, 2005.

[11] N. Alpaslan, M. F. Talu, M. Gül and B. Yiğitcan, "HOG tabanlı YSA kullanılarak yağlı karaciğer tedavisindeki ilaç etkinliklerinin hesaplanması," Sakarya Üniversitesi Fen Bilimleri Enstitüsü Dergisi, 16(2), 106- 112, 2012.

[12] A. Emrullah and M. S. Özerdem, "Tarımsal İmge Dokularından HOG Algoritması ile Öznitelik Çıkarımı ve Öznitelik Tabanlı Toprak Neminin Tahmini," Bilgisayar Bilimleri, 1(1), 1-7, 2016.

[13] F. Bozkurt, C. Köse and A. Sarı, "A texture-based 3D region growing approach for segmentation of ICA through the skull base in CTA," Multimedia Tools and Applications, 79(43), 33253-33278, 2020.

[14] E. Erdem and F. Bozkurt, "A comparison of various supervised machine learning techniques for prostate cancer prediction," Avrupa Bilim ve Teknoloji Dergisi, (21), 610-620, 2021.

Classification of Butterfly Camouflage Images Based on Feature Extraction with Local Binary Patterns

Erkan Bayram
Computer Sciences Research and Application Center
Ataturk University
Erzurum, Turkey
erkan@atauni.edu.tr

Vasif Nabiyev
Department of Computer Engineering
Karadeniz Technical University
Trabzon, Turkey
vasif@ktu.edu.tr

***Abstract*— Camouflage is the concealing of an object in an image within the background texture of the image. Hidden objects in camouflage images are texturally similar to the background texture, so it is very difficult to distinguish at first sight. In this study, a four-class camouflage image data set was created from camouflage butterfly images obtained by browsing over the internet. Textural features of all butterfly images were extracted by using Local Binary Pattern (LBP) on camouflage images taken from this data set. The system was trained according to these features obtained from all butterfly images. Then the learning process was carried out. After the learning process, the classification process was carried out. Support Vector Machines (SVM), Artificial Neural Networks (ANN) and K-Nearest Neighborhood Algorithm (KNN) were used for the classification process. As a result of experimental studies, success rate of 90% with LBP + ANN method, 82% success rate with LBP + KNN method, 93% success rate with LBP + SVM method were obtained.**

Keywords — lbp; camouflage images; classification

[1] INTRODUCTION

Image classification consists of parts such as image preprocessing, object detection, object segmentation, feature extraction and object classification. The images classification system consists of a database containing predefined patterns that compare the image with an object to classify it into the appropriate category. Image classification is used in many areas such as robot navigation, remote sensing, biomedical images. Image classification is divided into supervised and unsupervised. In unsupervised classification, pixels are grouped according to their properties. This process is called clustering. Unsupervised classification is used in cases where trained pixel features are not available. In supervised classification, pixels are grouped and the classes are labeled. This process is called training [1].

There are many studies on image classification in the literature. Malkoçoğlu et al. in their studies, they classified the cells as cancerous non-cancerous using the Support Vector Machine (SVM), Naive Bayes (NB) and Random Forest (RF) algorithms. For classification, 12528 pathology images of 101 patients were used. These images are obtained from the images presented by the open source Cancer Imaging Archive for Acute Lymphoblastic Leukemia (ALL) disease. Of the images obtained, 8491 were labeled as cancerous and 4037 were labeled as non-cancerous. Classification performances in RGB (Red Green Blue) and Gray Scale color spaces were tested using the ALL data set. As a result of the experimental studies, the best result with an accuracy of 89% on images scaled to 128 * 128 and 2000 dimensional data set in RGB color space was obtained by using the SVM algorithm [2]. Manju et al. conducted a study to determine the types of prostate diseases using tissue analysis and abdominal tomography images of patients. The prostate region is separated from the tomography image slice and then tissue features are extracted from segmented images using a transformation called Sequency based Mapped Real Transform (SMRT) based on segmentation. Sub image size and block size are changed and six different SMRT feature sets are generated. Each feature set is optimized with the Genetic Algorithm. The best feature set is chosen based on classification accuracy. KNN classifier was used in the study [3]. Bayram and Nabiyev worked image segmentation on camouflage images. In the study, they applied the K-means clustering method using Euclidean distance calculation and Mahalanobis distance calculation. They determined that the results obtained from the K-means method using the Euclidean distance calculation were more successful than the Mahalanobis distance calculation was used [4]. Toptaş and Hanbey have classified the flame images by extracting color and textural features on forest fire images in their studies. The study was carried out on 3100 image sections flame and non flame. They used RGB color space for color properties. For textural features, they used Laws' Tissue Energy Measurements and Gray-Level Co-Occurrence Matrix. After extracting the features, the classification process was carried out with Artificial Neural Networks and Support Vector Machines. They achieved an accuracy rate of 96% with Artificial Neural Networks and 95% with Support Vector Machines [5]. Hanbay used complex 2-dimensional Gabor filtering and deep convolutional neural networks and proposed a new hyperspectral image classification method. Deep learned and Gabor feature extraction methodologies were performed simultaneously on hyperspectral samples. Gabor properties are calculated by applying complex gabor filtering on only the first three basic components of the image. The hybrid model proposed in the study uses the Gabor transformation to obtain features such as corners, edges, and texture. Gabor features of images are calculated in multiple orientations and frequencies. After this process, deep features and Gabor properties are combined. The feature vector has been used as input to the softmax classifier to classify hyperspectral images. As a result of the experiments conducted in the study, it was determined that by using the method suggested, better classification performance was obtained

than some traditional methods [6]. Kuncan et al. in their studies, they installed accelerometers, magnetometers and gyroscope sensors in five different areas of the people. Using the signs obtained from these sensors, three different feature extraction methods have been proposed for gender recognition. Different transformation methods were applied to the signals obtained from the sensors, including One Dimensional Local Binary Patterns (1D-LBPs), One Dimensional Robust Local Binary Patterns (1D-RLBPs) and Weighted One Dimensional Robust Local Binary Patterns (W-1D-RLBPs). Statistical features were obtained from the signals calculated after the transformation processes. Classification processes were carried out using these attributes (SVM, RF, ANN, KNN). According to the results, the success rates were 96.04% for the 1D-LBPs method, 96.72% for the 1D-RLBPs method and 97.28% for the W-1D-RLBPs method [7]. Erdem and Bozkurt used methods such as Support Vector Machines, k-Nearest Neighbor, Naive Bayes, Linear Classification, Deep Artificial Neural Networks, Multi-layer Perceptron for the prediction of prostate cancer and compared the performance values they obtained. They used open access online prostate cancer data in their study. According to the experimental results they obtained, they found that the Multi-Layer Sensor gave the highest accuracy success rate with 97% and the lowest error rate (0.03) [8]. Liang et al. investigated the problem of automatic detection and classification of butterfly photographs. They used a bio-labeling method suitable for butterfly classification and proposed a butterfly automatic detection and classification algorithm based on the YOLO algorithm. According to the experimental results they obtained, they found that the proposed method has high accuracy and classification rate in butterfly automatic detection and classification. [9]. Arzar et al. they used a pre-trained CNN architecture model in their work. In this research, butterfly species named Black Veined Tiger, Chocolate Grass Yellow, Gray Pansy and Plain Lacewing were used. The test carried out achieved an overall identification accuracy of 97.5% in 120 images of four species of butterflies [10].

In this study, firstly, feature extraction process with local binary pattern (LBP) was performed for all images on the butterfly data set. The dataset consists of camouflage butterfly images that have been researched and downloaded from the open source internet. This data set was used to calculate the classification accuracy success rates of camouflage images. Textural features are extracted with LBP from this data set consisting of camouflage butterfly images. Then, supervised learning is carried out with the features. After the feature extraction process, classifiers such as ANN, KNN and SVM were used to test the performance of the learning process. In Section II, the material and the method used are explained. In this section, the data set used in the experimental study and the stages of the applied method are mentioned. Experimental studies are included in Section III, and the discussion and results section are included in Section IV.

[2] MATERIAL AND METHOD

A. *Material*

In this study, a data set consisting of camouflage butterfly images researched and downloaded from the open source internet was used. While choosing the butterflies, sensitivity was shown to ensure that the texture, color features and the background texture features in which they hide were very close to each other. In order to classify camouflaged objects that cannot be easily distinguished even by the eye at first sight, it is important that the texture and color of the object camouflaged with background texture show close characteristics. This dataset contains 200 camouflage butterfly images categorized for four butterfly classes. For the classification of butterflies, species that are identical to each other are included in the same class. The classes of butterflies are named respectively Butterfly 1, Butterfly 2, Butterfly 3 and Butterfly 4. In Figure 1, one sample images for each class are given from the pictures of the camouflage butterfly data set created for this study. In Figure 2, sample butterfly images from which textural features are extracted with LBP are given. These sample images show only butterflies camouflaged from the images included in the data set. When extracting features with LBP, only the features of camouflaged objects are extracted. In Figure 3, sample of binary pictures of camouflaged butterflies are given. Each of the butterfly images in the data set were reproduced by rotating clockwise 45 degrees. With this duplication process many more images are derived for training and testing data. The sample images presented in Figure 2 were obtained by taking the intersection of all images in the camouflage butterfly data set with the binary image in Figure 3. In the experimental results, 90% of the 200 images in the camouflage butterfly data set were used for training and 10% for testing. Training and test data were randomly selected from the all data set.



Fig. 1. Sample camouflage butterfly images for the four butterfly classes in the data set.



Fig. 2. Sample masked camouflaged butterfly images for four butterfly classes in the dataset.



Fig. 3. Binary images of sample camouflaged butterflies for the four butterfly classes in the dataset.

B. *Method*

In the study, all camouflaged images in the data set are subjected to pre-processing at the first stage. At this stage, the camouflaged object is segmented from the background image and extracted. Later, the textural features of the

object that is only camouflaged and hidden itself, examples of which are given in Figure 2, are extracted with LBP.

There is no feature extraction for the image in the background of the camouflaged butterfly object. After the feature extraction, a feaure set is created. Supervised learning was performed using this feature set and a classifier was established with ANN, KNN and SVM. In the next stage, randomly selected camouflage test images were given to this classifier to determine which butterfly class the camouflage image belongs to.

1) Preprocessing: At this stage, all images in the data set were adjusted to 300 * 300 size and converted to gray mode. In addition at this stage, the camouflaged object is segmented from the background image and extracted.

2) Feature Extraction: Objects belonging to the same image class show similar and close features to each other. At this stage, the textural features of the images in all butterfly classes were extracted with LBP. After feature extraction, all features are stored in the features database.

The purpose of feature extraction in this study is to determine the distinctive features of the images in the same class of camouflage butterfly images. A label is created for each pixel on the image where the LBP method is applied. The numerical value of this label is obtained by comparing the pixel in the center with the surrounding 3x3 neighbor pixels [11].

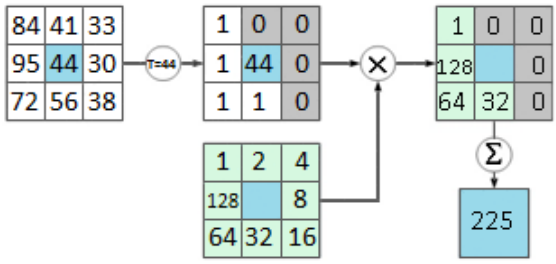


Fig. 4. LBP calculation steps

Figure 4 shows an example for calculating LBP values. The neighborhoods of the pixels of all the images in the data set are compared with the central pixel and a binary code is obtained. This binary code can be thought of as a binary model. If the pixel value is greater than or equal to the threshold value, the neighboring pixel is evaluated as 1. If the pixel value is smaller than the threshold value, the neighbor pixel is assigned a value of 0. After these assignments, a histogram is created to determine the frequency values of the binary models. Each pattern represents the possibility of a binary pattern included in the image. The number of histogram segments depends on the number of respective pixels in the LBP calculation. For example, if LBP uses 8 pixels, the histogram division number will be 256 [12]. To look at the position of any pixel (x_i, y_i), LBP compares the values between the center pixel and its neighboring pixels. The equation used for the LBP operator is as shown in (1). In (1) (x_i, y_i) the coordinate values of the center pixel, g_i the gray value of the pixel located in the center, and g_n the values of the pixels in the 3x3 neighborhood around the center pixel. The *s(k)* function shows the 8 neighborhood values of the gray level pixels [12]. Not all LBP values obtained are used in tissue identification. The regular patterns used for identification are those with a 0-1 or 1-0 pass number of two or less in the binary LBP code [11]. Examples for regular patterns are given in Table 1.

Table 1. Regular And Irregular Patterns Examples

Pattern Value	Number of Passes	Is the Pattern Regular?
00000000	0	Yes
11111111	0	Yes
01110000	2	Yes
11001111	2	Yes
11001000	4	No
01010011	6	No

$$LBP(x_i, y_i) = \sum_{n=0}^{n-1} s(g_n - g_i)2^n \quad (1)$$

$$s(k) = \begin{cases} 1 \; if \; k \geq 0 \\ 0 \; if \; k < 0 \end{cases} \quad (2)$$

In the study, each of the camouflage butterfly images was divided into 64 different blocks. LBP operator was calculated separately for each block and histograms were obtained. By adding these histograms consecutively, a feature vector has been created. This feature vector is used in the classification stage.

3) Classification: After extracting the features of the camouflage butterfly images, these features are stored in the database. The camouflage feature vector obtained with LBP on the test data is compared with the camouflage image classes in the database. For this process, YSA, KNN and SVM, which are among the supervised learning methods, were used in the study. KNN is one of the important parameterless algorithms and it is one of the classification algorithms in supervised learning. KNN's classification rules are created by the training instances themselves, without any additional data. The KNN classification algorithm estimates the category of test samples based on the K training samples that are the closest neighbor to the test sample and decides by the category with the highest category probability [13]. Support vector machines (SVM) are a set of related learning algorithms used for classification and regression. Like decision tree classifiers, SVM is a nonparametric classifier. In order for SVM to be successful, the process must be well trained. Using linearly separable classes is the easiest way to train SVM [14]. ANN has a strong correlation between input and output variables. It is a mathematical model and reflects the learning and generalization ability of human neural architecture [15]. ANN is used to solve various problems such as pattern classification or clustering, a complex functional approach, prediction and image completion. Therefore, ANNs are considered as a valuable computational model [16]. In the classification stage, each classifier was run 40 times with randomly selected training and test data.

[3] EXPERIMENTAL RESULTS

The experimental study was carried out on a laptop computer with Intel (R) Core (TM) i7 4702MQ CPU @

2.20 GHz, 2 GB video card and 8 GB primary memory. All application codes are written on Matlab R2017b program. Four-class camouflage butterfly data set was used to obtain experimental results. Of the 200 images in this data set, 90 % of them were randomly arranged as training data and 10 % as test data. 40 trials were made to obtain experimental results on the application. The application has been run 40 times for all classifiers consecutively. Training and test data were re-selected randomly in each trial. At the end of 40 trials, the average of the highest 10 of the accuracy success rates obtained from each classifier was recorded in Table 2.

The complexity matrix was created for the performance evaluation of the success values of the results obtained from the classifiers of the experimental results. The complexity matrix is used to describe the performance of the classification model on test data for which actual values are known. Using the obtained complexity matrix, the values of Sensitivity (SE), Specificity (SP), Precision (PR), Recall (RE), F1-Score (F1-SC) and Accuracy (ACC) metrics were determined. Data for these values are shown in Table 2.

Table 2 Average Performance Evaluatıons Wıth Knn, Svm, Ann Accordıng To Experımental Results

	SE (%)	SP (%)	PR (%)	RE (%)	F1-SC (%)	ACC (%)
SVM	92.16	93.83	91.33	92.16	90.1	**93.00**
ANN	81	95	93.5	81	85.38	**90**
KNN	73.04	90.63	76.66	73.04	72.27	**82.00**

As shown in Table 2, the highest accuracy rate was obtained when LBP and SVM were used together with approximately 93%. The lowest accuracy rate with approximately 82% was obtained when KNN and LBP were used together. In the case where ANN and LBP were used together, an accuracy success rate of approximately 90% was obtained.

[4] DISCUSSION AND CONCLUSIONS

Camouflaged objects in the images have texture, pattern and color characteristics close to the background. For this reason, it is very difficult to distinguish and detect from the background. In this study, the classification of four types of camouflage butterfly images was studied using the local binary pattern (LBP) method. For camouflage images, a data set was created by downloading camouflage butterfly images of these four species from the open source internet. In the study, textural features of camouflage butterfly images were extracted using the LBP method. The extracted features were then stored in a database. Supervised learning was carried out with these features stored in the database. The training process was carried out with SVM, KNN and ANN by using textural features obtained from the images in the data set. Performance evaluation for the data obtained from the experimental results has been calculated and shown in Table 2. According to the values seen in Table 2, the highest accuracy rate was obtained from using LBP + SVM with approximately 93 %, and the lowest accuracy rate was obtained from using LBP + KNN with approximately 82%. In this study, this application was developed for only four types of butterfly images. In further studies, the number of camouflaged butterfly species will be increased, the number of butterflies in the camouflage butterfly data set will be at least 2000, and deep learning methods will be used.

REFERENCES

[1] C. Dhaware and K. H. Wanjale, "Survey on image classification methods in image processing," *Int. J. Comput. Sci. Trends Technol.*, *4*(3), 246-248, 2016.

[2] A. B. V. Malkoçoğlu and İ. İşeri, "Akut Lenfoblastik Löseminin Makine Öğrenimi ile Sınıflandırılması," 4th International Symposium on Innovative Approaches in Engineering and Natural Sciences, 4(6),497-501, 2019.

[3] B. Manju, K. Meenakshy, and R. Gopikakumari, "Prostate Disease Diagnosis from CT images using GA optimized SMRT based Texture Features," *Procedia Computer Science, 46*, 1692-1699, 2015.

[4] E. Bayram and V. Nabiyev, "Image segmentation by using K-means clustering algorithm in Euclidean and Mahalanobis distance calculation in camouflage images," 2020 28th Signal Processing and Communications Applications Conference (SIU), Gaziantep, Turkey, 2020, pp. 1-4, doi: 10.1109/SIU49456.2020.9302320, 2020.

[5] B. Toptaş and D. Hanbay, "Renksel ve Dokusal Özellikler Kullanarak Alev ve Alev Olmayan Görüntü Kesitlerinin Sınıflandırılması," Mühendislik Bilimleri ve Araştırmaları Dergisi, 1(1), 1-12, 2019.

[6] K. Hanbay, "Hyperspectral image classification using convolutional neural network and two-dimensional complex Gabor transform," J. Fac. Eng. Archit. Gazi Univ, 35(1), 443-456, 2020.

[7] F. Kuncan, Y. Kaya, and M. Kuncan, "New approaches based on local binary patterns for gender identification from sensor signals," J Fac Eng Archit Gazi Univ, 34(4), 2173-2185, 2019.

[8] E. Erdem and F. Bozkurt , "A comparison of various supervised machine learning techniques for prostate cancer prediction," Avrupa Bilim ve Teknoloji Dergisi, (21), 610-620, 2021.

[9] B. Liang, S. Wu, K. Xu, and J. Hao, "Butterfly detection and classification based on integrated YOLO algorithm," In International Conference on Genetic and Evolutionary Computing (pp. 500-512). Springer, Singapore, 2019, November.

[10] N. N. K. Arzar, N. Sabri, N. F. M. Johari, A. A. Shari, M. R. M. Noordin, and S. Ibrahim, "Butterfly Species Identification Using Convolutional Neural Network (CNN)," In 2019 IEEE International Conference on Automatic Control and Intelligent Systems (I2CACIS) (pp. 221-224). IEEE, 2019, June.

[11] V. Nabiyev and A. Günay, "LBP yardımıyla görüntüdeki kişinin yaşının bulunması," Çankaya Üniversitesi Bilim ve Mühendislik Dergisi, 8(1), 2010.

[12] E. Prakasa, "Texture feature extraction by using local binary pattern," INKOM Journal, 9(2), 45-48, 2016.

[13] Z. Yong, L. Youwen, and X. Shixiong, "An improved KNN text classification algorithm based on clustering," Journal of computers, 4(3), 230-237, 2009.

[14] J. R. Otukei and T. Blaschke, "Land cover change assessment using decision trees, support vector machines and maximum likelihood classification algorithms," International Journal of Applied Earth Observation and Geoinformation, 12, S27-S31, 2010.

[15] F. Amato, A. López, E. M. Peña-Méndez, P. Vaňhara, A. Hampl, and J. Havel, "Artificial neural networks in medical diagnosis," 2013.

[16] F. Günther and S. Fritsch, "neuralnet: Training of neural networks," The R journal, 2(1), 30-38, 2010.

Effect Of Software Development Methodology On Software Quality

Süleyman Emir TURNA
The Graduate School Of Natural And Applied Science
Dokuz Eylül University
Izmir, Turkey
emir.turna@ogr.deu.edu.tr

Assist. Prof. Dr. Kökten Ulaş BİRANT
Computer Engineering
Dokuz Eylül University
Izmir, Turkey
ulas@cs.deu.edu.tr

Abstract

One of the important elements in the development of the term software is that the programming process or the written program cannot be measured. After this measurement study is carried out, the process will be followed and developed, and the product will be more successful.

McCall Quality Model, which is one of the most well-known studies on software quality, determines 3 main titles as the main evaluation criteria for the quality of a software and defines the sub-criteria that determine these main topics. The definitions made require that each criterion be digitized with concrete measurements.

Within the scope of the study, sub-criteria and effects on quality will be determined over performance data of completed projects. This study were prepared to specify the metrics that possibly affect the quality of a software through McCall Quality model.

Keywords : Software Quality, Development, Methodology

I. INTRODUCTION

A. Definition Of Software

Software is a set that is formed by combining commands developed for a purpose. De- fines how these commands will work for the purpose. As a result of the combination of soft- ware with different architectural and hardware products, the output obtained by the commands it gives to these hardware products is called software [1]. So how can one measure that the desired goal has been achieved as desired?

B. What Is Software Measurement?

Determining the different features of any product and determining its qualities is considered as a measurement. Software should be measurable because it is the result of a series of commands oriented to a particular purpose. Software measurement processes are deter- mined by ISO standards [2].

Measurement methods of software;

- Determining the quality of the product
- Determining the characteristics of the product
- Increasing the quality to a higher level
- Creating the time, budget, resource status of the project

C. Software Measurement Techniques

We can examine software measurement techniques in 2 groups. These constitute the rationale that will form and be the fulcrum of the research or measurement to be carried out [3].

1) Direct Measurement:
It includes measurement according to the standards determined without depending on any reference.

2) Indirect Measurement
The purpose of the measurement is to measure the result and quality of the product by referencing in the parameters.

D. Software Quality

There are many different definitions of quality. For some it is the "capability of a software product to conform to requirements." (1-2) while for others it can be synonymous with "customer value". However, software development takes the definition in another light. When speaking of software quality, it takes into account the delivery of the requirements, including;

- Functional requirements
- Non functional requirements

Some of the more typical functional requirements include:

- Business Rules
- Transaction corrections, adjustments and cancellations
- Administrative functions
- Authentication
- Authorization levels
- Audit Tracking
- ....etc

Some typical non-functional requirements are;

- Performance – Response Time, Throughput..etc.
- Scalability
- Capacity
- Availability
- Reliability
- Recoverability
- Maintainability
- ....etc

I. FUNCTIONAL & NON-FUNCTIONAL REQUIREMENTS

Functional Requirements	***Non-Fuctional Requirements***
They define a system or its component.	They define the quality attribute of a system
It specifies, "What the system should do?"	It specifies, "How should the system fulfill the functional requirements?"

Functional Requirements	*Non-Fuctional Requirements*
User specifies functional require-ment.	Non-functional requirement is specified by techni- cal peoples e.g. Architect, Technical leaders and software developers.
It is mandatory to meet these requirements.	It is not mandatory to meet these requirements.
It is captured in use case.	It is captured as a quality attribu-te.
Defined at a component level.	Applied to a whole system.
Helps you to verify the functiona-lity of the software.	Helps you to verify the perfor-mance of the softwa- re.
Functional Testing like System, Integration, End to End, API testing, etc are done.	Non-Functional Testing like Per-formance, Stress, Usability, Secu-rity testing, etc are done.
Usually easy to define.	Usually more difficult to define.

II. METHODS DEFINED FOR SOFTWARE QUALITY

A. McCall's Quality Model

McCall's Quality Model (also known as the General Electrics Model) is one of the most known quality models in the software engineering literature. It has been presented by Jim McCall in 1977.

In more details, McCall's Quality Model consists of 11 quality factors to describe the external view of the software (from the user's side), 23 quality criteria to describe the internal view of the software (from the developer's side) and a set of metrics which are defined and used to provide a scale and method for measurement. The main objective of the McCall's Quality Model is that the quality factors structure should provide a complete software quality picture [4].

B. Boehm's Quality Model

Boehm, introduced his quality model to automatically and quantitatively evaluate the quality of software. This model attempts to qualitatively define the quality of software by a predefined set of attributes and metrics. It consists of high-level , intermediate-level and lowest-level characteristics which contribute to the overall quality level [4].

C. Dromey's Quality Model

This quality model has been presented by Dromey. It is a product based quality model that recognizes that quality evaluation differs for each product and that a more dynamic idea for modeling the process is needed to be wide enough to apply for different systems. Furthermore, figure shows that it consists of four software product properties and for each property there is a number of quality attributes [4].

D. Proposed Model

McCall Quality Model is chosen from among the most widely used quality models with many more criteria. The reason for this is its diversity and appeal to more areas than other models, as seen in the table 2 [4].

II. QUALITY MODEL COMPARISON

Factors	*McCall*	*Boehm*	*Dromey*
Maintainability	+		+
Flexibility	+		
Testability	+	+	
Correctness	+		
Efficiency	+	+	+
Reliability	+	+	+
Integrity	+		
Usability	+		+
Portability	+	+	+
Reusability	+		+
Interoperability	+		
Human Eng.		+	
Understandabi-lity		+	
Modifiability		+	
Functionality			+

Using this model, McCall attempts to bridge the gap between users and developers by focusing on a number of software quality factors that reflect both the users' views and the developers' priorities. The structure of the McCall's quality model consists of three major perspectives (types of quality processes) for defining and identifying the quality of a software product, and each of these major perspectives consists of a number of quality factors. Each of these quality factors has a set of quality criteria, and each quality criteria could be reflected by one or more metrics, check for figure for the details of the McCall's quality model structure.

III. CONCRETE CRITERIAS

The metric list determined through the target quality model was created as follows. The metrics determined have been revealed through the studies conducted on the criteria, field researches and various group surveys. Metrics are kept to a certain criterion in order not to depart from concrete evaluations. The study was delivered over the metrics that will have a high impact on the project.

A. Product Operations Metrics

1) Inner Metrics : Although Inner metrics are not direct, they can be evaluated in conjunction with other metrics and play a role in revealing the quality values of a project. At the same time, they will be an important performance / cost / quality criterion for determining the correct methodology that is the target or for examining the method used in the project.

a) Number Of Teams : The success and the quality ratio of the work done are included in the metric list since it will directly affect the number of people in the team compared to the size of the project [5][6].

b) Number Of Developers : Although there are people who take different roles in the team, the people who will do the core part of the work will be the developers for the software project, so it will have a certain effect on the quality of the project [5][6].

c) Time Of Project : Timing the project correctly will leave space for project stakeholders to find more ac- curate

methods and better quality solutions during the development process [5][6].

d) Budget Of Project : The budget allocated for the project's content and scope is particularly low, and the stakeholders who will do the work to be done do not pay too much attention to the project and its quality will decrease [5][6].

2) Correctness

a) Competency Management : Competence will be a metric that can be used to identify employee skill groups and demonstrate suitability for the project. In this way, it will help for determining that project has the right team and add its impact to the calculation [7].

b) Application Portfolio Visibility : It will be a verification feature that can be used to determine more effective use as a strategic and modernization. It can be evaluated it as 1/0 to see if the results of the projects are correct and whether they reach the desired results [8].

c) Application Portfolio Risk : Determining the level of risks it carries along with its accuracy, as in the visibility feature of the results of the projects, will enable to contribute to the quality of the project. Risk carrying rates of the modules will be able to determined and produced a general risk rate [9][10].

d) Defect Density By Test Type : Defect density can be calculated with every 1000 lines (KLOC) of the project written for this metric. The increase in density will contribute negatively in terms of quality and will help to have an idea about the quality of the code and the overall quality of the project [11].

e) Defect Density By Risk Level : Along with the presence of defect density, it will also be an important factor whether teams are working to find these errors. Metric can be told if the error is due to not being searched or not found. This metric can be evaluated as 1/0 and indicate its contribution to quality [11].

3) Reliability

a) Mean Time To Failure (MTTF) : MTTF mean is actually lifetime of any product or a device. Its value is calculated by looking at a large number of the same kind of items over an extended period of time and see- ing what is their mean time to failure. MTTF is calculated as the total hours of operation, divided by the total number of items being tracked [12].

b) Mean Time Between Failures (MTBF) : MTBF measures the estimated time between a previous failure of a system and the next failure in the daily operating period. In simpler terms, MTBF helps to predict how long an asset can run before the next problem [12].

c) Mean Up Time : Mean Up Time refers to the time elapsed from the correction of an error received in the system until an error occurs again. It can be allowed to find out how long the system has survived [12].

d) Failure In Time : The term FIT (failure in time) is defined as a failure rate of 1 per billion hours. A component having a failure rate of 1 FIT is equivalent to having an MTBF of 1 billion hours. Most components have failure rates measured in 100's and 1000's of FITs [12].

e) Mean Time To Repair (MTTRp) : Mean Time To Repair (MTTRp) refers to the time it takes to repair a system and restore it to full functionality. MTTRp can be found by dividing the total maintenance time by the total number of maintenance operations in a given time period [12].

f) Mean Time To Recovery (MTTR) : MTTR (mean time to recovery or mean time to restore) is the average time it takes to recover from a product or system failure. From the time the system or product fails to the time that it becomes fully operational again[12].

g) Mean Time To Production (MTTP) : Measures the elapsed time (in hours) from merging a change in gitlab-org/ gitlab projects master branch, to deploying that change to gitlab.com. It serves as an indicator of our speed capabilities to deploy application changes into production[13].

h) Failure Rate : It is the metric that is used to find out how many errors occurred in total during the time of running a system. High rate will have a negative effect on quality. This figure can be found on the bug tasks of the job tracking system[14].

i) Availability : Availability represents the probability that the system is capable of conducting its required function when it is called upon given that it is not failed or undergoing a repair action. Therefore, not only is availability a function of reliability, but it is also a function of maintainability[14].

j) Mean Down Time : Mean Down Time (MDT) is the average time that a system is non-operational. This includes all time associated with repair, corrective and preventive maintenance, self imposed downtime, and any logistics or administrative delays [14].

4) Efficiency

a) Lead Time : Lead time is a general measure of the time from product concept to final delivery. It will depend on the complexity of the project and the number of engineers working on the project, and both will affect the project cost. By tracking project delivery times, developers can better predict time to market for existing and similar future projects[15].

b) Impact : The impact measures how much changes to the code affect the project. It is also a measure of how these changes affect the engineers who make them. This is an important measure that should be measured as code changes can increase the time to market the product and increase the cost[16].

c) Open / Closed Rate : Open and closed rate is how many production problems or issues are reported and closed within a specific time period. A high open rate and a low close rate across a few iterations, may be the production issues are currently a lower priority than new features..etc [16].

d) Production AVG(MTTRp,MTBF) : Production is an interrupt analysis and includes the average time between failures (MTBF) and the average recovery / repair time (MTTRp). These measure how well the soft- ware performs in a production environment [16].

e) Cycle Time : The cycle time, which is part of the delivery time, is the time it takes to make a de- sired change in the software and put it into production. If a team uses DevOps and uses continuous integration, continuous deliv-

ery (CI / CD) applications, they can usually measure cycle time in minutes instead of months[17].

f) Productivity : Productivity measures the amount of code that provides business value. A developer who has created a completely new solution or implements extensive code changes will be interested in numerous trial and error methods with low efficiency [16].

g) Churn : Churn is the percentage of time that developers spend on editing, adding, or deleting their own code. High code clutter indicates rerun and can mean something is wrong during the development process.

5) Usability

There are three measurable concepts for software component availability: Documentation Quality, Complexity of Problem and Complexity of Solution or Design. By comparing software components that provide similar functionality between different systems show how they all contribute to the quality factor in software of the same structure [18][19][20][21].

- Completion Rate
- Satisfaction Level
- Effectiveness Of Marketing Info - Interfaces Understandability
- Understandability Of I/O
- Ease of component learning
- Contents of marketing info
- Contents of error message
- Interfaces Density
- Effectiveness Of Help System
- Size Of Help System
- Contents Of Help System
- Contents Of Demo
- Effectiveness Of Manuals
- Size Of Manuals
- Contents Of Manuals

6) Accuracy

a) Release Window Accuracy : Considering that the item has a scheduled date to ship, it scores this as -1 for each late day and +1 for each day early. Current accuracy is the total number of delays or early days posted. If very true, it will have 0, but positive numbers are better than negative numbers [22].

b) Feature Adoption : The Feature Adoption feature can be explained as follows. It is the recognition and usage of a feature created on the system by the users [23]. Mathematically; Percentage of users exposed to the feature * Percentage of exposed users with successful results.

c) Net Promoter Score : The Net Promoter Score is the calculated results of surveying the user base with a simple question, can be rated over 10 [24] [25]; "How likely is it that you would recommend this product to your colleagues, friends, and family?"

d) Delivered Customer Value : To measure Customer Value, it is recommended to use regular team surveys from 0 to 10 to measure perception of value delivered to the customer [24] [25]. "How much value did we deliver to our customers with this product"

e) Ticket Churn : Ticket Churn can be extracted directly from issues and project tracking tool. Those tools keep track of ticket state changes, and the tickets that have switched from started state to uninitialized state or from completed state to incomplete state are searched [24] [25].

f) Backlog Health : Backlog Health measures the ready queue depth of your backlog. This will show how ready developers are for the next steps of the project and what to do [26].

g) Sprint Preparedness : Sprint Preparedness can be measured at the end of an iteration heading into a retrospective, or it can be measured after planning, as you look forward to the upcoming sprint [26].

7) Completeness

These are the metrics that are determined to measure whether all the developed features, functions of a system are fully performed and whether they are compatible with the de- sired ones. Here, compatibility and development according to the desired will show that a higher quality process has been passed and more attention has been paid to the overall quality of the software [26].

- Is Add Data Defined
- Is All Functions Referenced Defined
- Are All Defined Functions Used
- Are the Conditions of All Decision Points Determined
- Are All Reported Problems Resolved
- Is It Compatible With Those Who Want Design

B. Product Revision Metrics

1) Maintainability

The following criteria can be considered for easy maintenance and understandability of the codes of the project. These metrics not only directly affect the quality of the project, but also indirectly affect the quality of the error rate, up time, down time ... etc. by directly affecting other criteria metrics [27][28].

- Comments
- Logical Data Model
- Data Model
- Prototyping
- Lines Of Codes
- Activity Diagram
- ER Diagram
- User Manual
- Use Case Diagram
- Class Diagram

2) Testability

a) Error Intensity : Error intensity helps the team determine the total number of errors found in a software over a period of time or development. Allows the team to decide whether the software is ready for the version or whether it requires further testing. The error density of a software is counted in a thousand lines of code, also known as KLOC [29].

b) Defect Leakage : The defect leak is used by the test users of the software to review the effectiveness of the test process before the user acceptance test (UAT) of the product. If any defect is left un- detected by the team and found by the user, it is known as a defect leak or an error leak [29].

c) Defect Category : The defect category metric provides an idea of the software's different quality features such as usability, performance, functionality, stability, reliability, and more. In short, the defect category is a feature of defects based on the quality features of the software product [29].

d) Defect Count [Low | Medium | High | Critical] : The depth and number of defects in a software project are used to see how successful tests will be in the project. The condition and number of defects are determined, graded according to their depth [29].

e) Average Time to Correct Errors : Average Time to Correct Errors shows the average time taken by development and testing teams to correct errors. The status of the number of errors and accordingly the correction time will allow the evaluation of the developed project [29].

f) Percentage of Errors Accepted : Percentage of Errors Accepted is a metric that can be used to describe the total num- ber of defects accepted by the development team. The lower the total number of errors, it can indicate that an application has been developed towards the desired result [29].

g) Percentage Fixed Error : By calculating percentage fixed error the percentage corrected error can be deter- mined. A high percentage will show how much of the problems encountered have been re- solved [29].

h) Fail Test Status Coverage : Measures the percentage of all failed test cases. The low number of failed test scenarios may indicate that the project has achieved the desired goal and has a quality result accord- ing to its content [29].

i) Successful Test Cases Coverage : Measures the percentage of successful test cases. The success or the least errors of the test scenarios will show that the desired result can be achieved and the quality of the project according to its content [29].

j) Test Coverage : Test coverage determines the scope of all functions of the software product. Indicates that test activities have been completed and can be used as criteria for finalizing the test [29].

k) Review Efficiency : Review efficiency is used to reduce pre-delivery defects in the software. Examination errors can be found in documents as well as in documents. By applying this metric, it reduces costs as well as efforts used in the process of correcting or resolving errors [29].

3) Simplicity : The most common metrics for measuring the complexity (or simplicity, if you take simplicity to be the opposite of complexity) is the Halstead Complexity Metrics.

The Halstead complexity measures use the inputs of total and distinct operators and operands to compute the volume, difficulty, and effort of a piece of code [30].

As the main of these metrics, followings can determined the contribution of the following to quality

- Program Length
- Volume
- Difficulty
- Effort
- Time Required To Program
- Number Of Delivered Bugs

C. Product Revision Metrics

1) Portability

a) Direct Portability : Direct portability is the ability to directly take a piece of software and execute in on another platform without modification.

Contribution to quality can be achieved by digitizing the problems of a smoothly running project., giving problems (how deep it is important) and not working at all [31].

b) Installability : Degree of effectiveness and efficiency with which a product or system can be successfully installed and/or uninstalled in a specified environment. It is a necessity for the whole system and the software itself to be easily installed and removed in all environments it will work on [31].

c) Adaptability : Degree to which a product or system can effectively and efficiently be adapted for different or evolving hardware, software or other operational or usage environments.When a new module is added to a system instead of changing it, this module / software is expected to adapt very easily [31].

d) Replaceability : Degree to which a product can replace another specified software product for the same purpose in the same environment. It is important that the software is compatible with other systems to which it will be connected, that it must be portable and integrated [31].

2) Reusability

a) Change Frequency Provided Interfaces : Sum of number of changes to provided interfaces in the past year. Lower is better. This is because people's habits and usage are not affected. No matter how much a module changes structurally, it is very important not to make the user feel this [32].

b) Locality Of Change : A high score indicates that the module can evolve independently. A module be replaced or renewed when necessary, the rest of the system should not be affected and the inter- module interconnection should not affect the whole system [32].

c) Shareability : Module can more easily be plugged into other releases. As applications upgrade, the features used in the previous version should easily be upgraded. The

upper version should be easy to use again due to the logic that includes the lower version [32].

d) Configuration Space : Lower scores indicates that it's easier to test all possible configurations of a module. Because we will not have to integrate it to be able to use it again in different places and ap- plications. This means that I need an easy and simple structure for us [32].

IV. CONCLUSION

In a software project, before starting, the available resources, all factors encountered during the development process from start to finish, and all situations that arise after the project is completed should be evaluated.After considering all of these evaluations, it can be concluded that a successful or quality project has been made.

Within the scope of the study, criteria and metrics were determined over the quality model in order to evaluate the quality of the projects. These criteria will enable us to analyze the planning, development and finalization processes of the project. By combining evaluation criteria in different fields, a cluster was created that would allow the evaluation of the whole.

The criteria that seem to be independent from each other but affect the quality of a project have been combined under a single set. A detailed quality model resource has been created for the future study, whose numerical analysis and quality evaluations will be made.

V. FUTURE WORKS

In the next step of the study, the criteria determined will be formulated mathematically and the values of these formulas will be calculated over real projects developed with different teams.

Since the impact values of the criteria may differ on a project basis, the coefficient of the impact value will be added to the calculation as variable.

By determining the relations of the criteria with each other, it will be revealed that which project should be developed more on which quality criteria. In this way, it is planned to gain a perspective on how existing and planned projects will be planned.

With the study, many quality evaluations can be made in a single set without the need for different studies.

REFERENCES

1. Leonhardt D., "John Tukey, 85, Statistician; Coined the Word 'Software'". The New York Times. Retrieved 24 September 2012.
2. ISO/IEC JTC 1/SC 7 Software and systems engineering (2007-02-01). "ISO/IEC 14143". International Standards Organization. Retrieved 2019-02-26.
3. Halstead M.H., "Elements of Software Science". New York, Elsevier North-Holland, 1977.
4. E. Al-Qutaish R., Quality Models in Software Engineering Literature: An Analyti- cal and Comparative Study, Journal of American Science 6, 2010.
5. Ostakhov R., Morozov V. and Artykulna N., "Models Of IT Projects KPIs and Metrics", Published in Conference: 2018 IEEE Second International Conference on Data Stream Min- ing & Processing (DSMP), 2018.
6. Mustafa K., Khan R.A., "Quality Metric Development Framework", Published in Journal Of Computer Science, 2018
7. Chandra, N., "Do Project management competencies influence the project performance?" Published in Wageningen University & Research, 2017.
8. Patanakul, P., "Key attributes of effectiveness in managing project portfolio", Published in International Journal of Project Management, 33(5): 1084-1097, 2015
9. Drake, J.R., "Risk in information technology project portfolio management", Published in Journal of Information Technology Theory and Application, 8(3):1-11, 2006.
10. G. Jiang, Y. Chen, "Coordinate Metrics and Process Model to Manage Software Project Risk", Published in Proceedings of 2004 IEEE International Conference on Engineer- ing Management, pp 865-869, 2004.
11. Garousi, V., Smith M, "Test Cost-Effectiveness and Defect Density", Published in Advances in Computers, 2013.
12. Torell, W., Avelar V., "Mean Time Between Failure: Explanation and Standards", Published in Schneider Electric White Paper Library, 2004.
13. Olsen, N.C., "Survival of the fastest: improving service velocity [software products]", Published in IEEE Software, Volume: 12 , Issue: 5 , 1995.
14. Çatal, Ç., Diri. B., "Survival of the fastest: improving service velocity [software products]", Published in Information Sciences, Volume 179, Issue 8, pp 1040-1058, 2009.
15. Dale, C.J., Zee. H., "Software productivity metrics: who needs them?", Published in Information And Software Technology, Volume 34, Issue 11, pp 731-738,1992.
16. Juhann, T., Dick M., Naumann S. and Kern E., "How to measure energy-efficiency of software: Metrics and measurement results", Published in 2012 First International Workshop on Green and Sustainable Software (GREENS), 2012.
17. Clincy, V., "Software Development Productivity and Cycle Time Reduction", Published in Journal of Computing Sciences in Colleges, Volume 19, Issue 2, pp 278-287, 2003
18. Bertoa, M., Vallecillo A. "Usability metrics for software components" , Published in Jour- nal of Computing Sciences in Colleges
19. Boehm B.W., Brown J.R. and Kaspar J.R., "Characteristics of Software Quality", Published in TRW Series of Software Technology, 1978.
20. Elbaum S., Gable D. and Rothermel G., "Understanding and measuring the source of variation in the prioritization of regression test suites", Published in Proc. of seventh Intl. Software Metrics Symposium, pp 169-179, London, 2001.
21. McGarry J., Card D. and Jones C., "Practical Software Measurement", Published in Addison-Wesley, 2002.
22. McNee, S., Riedl J. and Konstan J., "Being accurate is not enough: how accuracy metrics have hurt recommender systems", Published in CHI EA '06: CHI '06 Extended Abstracts on Human Factors in Computing Systems, pp 1097–1101, 2006.
23. Zontar, R., Hericko M., "Adoption of object-oriented software metrics for onto- logy evaluation", Published in BCI '12: Proceedings of the Fifth Balkan Conference in Informatics, pp 298–301, 2012.
24. Sirias C., "Project Metrics for Software Development", Available online at: http:// www.infoq.com/articles/project-metrics, 2009.
25. Atkinson G., Hagemeister J., Oman P. and Baburaj A., "Directing Software Development Projects with Product Metrics", Published in Proceedings of the Fifth International Software Metrics Symposium, Bethesda, MD , USA, pp 193 - 204, 1998.
26. Kupiainen E., Mantyla M. and Itkonen J., "Using metrics in Agile and Lean Software Development - A systematic literature review of industrial studies", Published in Information and Software Technology, Volume 62, pp 143-163, 2015.
27. Gibson V.R., Senn J.A., "System Structure and Software Maintenance Performance", Published in CACM, pp 347-358, 1998
28. Shepperd, M., Ince, D., "Controlling Software Maintainability", Published in Proceedings. Second European Conference on Software Quality Assurance, Oslo, Norway, 1990.
29. Moores T. T., Champion R. E. M., "Software quality through the traceability of requirements specifications, in Software Testing, Reliability and Quality Assurance", Published in Conference Proceedings., First International Conference, doi: 10.1109/ST- RQA.1994.526392, pp 100–104, 1994.
30. Bailey C.T., Dingee W.L., "A software study using Halstead metrics", Published in Proceedings of the 1981 ACM workshop/symposium on Measurement and evaluation of software quality, pp 189-197, 1981
31. Lenhard J., "Improving Process Portability through Metrics and Continuous Inspection", Published in IPAIS, 2016.

32.Kamalraj R., Geetha B.G. and Singaravel G. "Reducing Efforts on Sofware Project Management using Software Package Reusability", Published in IEEE International Advance Computing Conference, Patiala, India, pp 1624-1627, 2009

The Need for Radio Frequency Identification (RFID) System

Muhammad Baballe Ahmad
Department of computer engineering technology School of technology, kano state polytechnic
Kano state, Nigeria
mbaballe@kanopoly.edu.ng

Fatima Alkasim Nababa
Depatment of computer science Yusuf maitama sule university
Kano state, Nigeria
alkasimfatima46@gmail.com

Abubakar Sadiq Muhammad
Department of computer engineering technology School of technology, kano state polytechnic
Kano state, Nigeria
asmuhammad@kanopoly.edu.ng

Abstract*—The Radio Frequency Identification (RFID) is a wireless technology system that is use for identifying an individual or objects through the means of radio waves, which transfer information from an electronic tag, called Radio Frequency Identification (RFID) tag. Radio Frequency Identification (RFID) consists of two main components the interrogator and the transponder. The Interrogator, which is the Radio Frequency identification reader (RFID Reader), the Interrogator usually transmits and receives the signal while the Transponder (tag) is attach to the object. In the Radio Frequency Identification (RFID) system, an RFID reader interrogates the Radio Frequency Identification (RFID) tags. This tag reader generates a radio frequency interrogation, which communicates with the tags been registered in the system. This reader likewise has a receiver that captures a reply signal generated from the tags and decodes the signal. This reply signal from the tags reflects the tag's information content. Each tag of the students consists of a unique identity, identification card (ID) that is assign to a single student identification card (ID) which is recorded in the database. The use of the Radio Frequency Identification (RFID) technology enables the institution authorities or management to evade attendance documents from damages such as misplacement, tear, or even got lost. This research review some recent design and implementation of internet of things (IoT) attendance system using the concept of the Radio Frequency Identification (RFID) system articles. The analysis found that the Radio Frequency Identification (RFID) system is a very advanced technology for an automatic attendance system in an institution, organization, or university and it provides a very higher performance and accuracy than the traditional paper-based system that the students normally used to sign. A combination of the model is needed which will confirm higher security, better performance, and consistency of the system.

Keywords—Radio frequency identification (RFID) system, Radio frequency identification (RFID) tags, Radio frequency identification (RFID) readers, Arduino or microcontroller, liquid crystal display (LCD), and personal computer (PC) or desktop computer.

[1] INTRODUCTION

The Radio Frequency Identification (RFID) technology, is an emergent technology that is used in a wide range of applications, it is a member of the family of Automatic Identification and Data Capture which is referred to as (AIDC) technologies. This is the fastest and reliable means or method of identifying an object or thing. Radio Frequency Identification (RFID) consists of two main components the interrogator and the transponder. The Interrogator, which is the Radio Frequency identification reader (RFID Reader), the Interrogator usually transmits and receives the signal while the Transponder (tag) is attached to the object. In the Radio Frequency Identification (RFID) system, an RFID reader interrogates the Radio Frequency Identification (RFID) tags. This tag reader generates a radio frequency interrogation, which communicates with the tags been registered in the system. This reader likewise has a receiver that captures a reply signal generated from the tags and decodes the signal. This reply signal from the tags reflects the tag's information content. A Radio Frequency Identification (RFID) tag usually consists of an antenna and a tiny microchip [1]. The Radio Frequency Identification (RFID) alone has various applications but when it is combined with an Arduino or Microcontroller it limitations magnifies more. The developments in Radio Frequency Identification (RFID) technology continue to produce larger memory capacities, faster processing, and wider reading ranges. They are high tendency that the technology can replace barcode even with the expected reduction in raw materials together with economies of scale; the integrated circuit (IC) in a radio frequency (RF) tag can never be as expensive as a bar code label. Nevertheless, Radio Frequency Identification (RFID) will continue to rise in its recognized places where the barcode or other optical technologies are less effective. Attendance or daily register of students in an institution or university has turned into a vivacious assessment viewpoint in the current educational scheme in both institutions, organizations, schools, and universities. The unoriginal attendance-monitoring scheme has a few obstructions with the development of the latest technology gap. For example, giving out the everyday attendance sheet to a gigantic amount of students in a class is extremely risky and it hinders the consideration of the students in that particular class [2]. This is considered a waste of time and energy as well as a student can intentionally register students who are not present in the class in the attendance sheet. If the lecturer mistakenly loses these documents, all the important attendance records will be lost without hesitation. , the Radio Frequency Identification (RFID) novelty has a great chore to carry out in the completion of the vision of connecting objects around us to the internet. These items extend from huge structures, planes, modern plants, vehicles, any sort of merchandise, and explicit pieces of a bigger framework to people, animals, plants, and even obvious body portions of them. The idea driving all this is called the Internet of Things (IoT) [3].

Radio Frequency Identification (RFID): radio frequency identification (RFID) operates by transferring and receiving a signal using Antenna and Integrated Circuit (IC). It has mainly two parts namely, the Radio frequency identification (RFID) Tag and the Radio frequency identification (RFID) Reader. The radio frequency identification (RFID) tags contain an integrated circuit (IC) and an antenna, which is used to transmit data to the radio

frequency identification (RFID) reader also known as an interrogator. This reader then converts the radio waves to a more usable form of information. The data collected from the Radio frequency identification (RFID) tags is then transferred through a communications interface to a host computer system, where the information can be stored in a database and analyzed later.

Radio Frequency Identification (RFID) Tag: The Radio Frequency Identification (RFID) tag is an electronic tag that exchanges data with a Radio Frequency Identification (RFID) reader through radio waves. Almost all the Radio Frequency Identification (RFID) tags have mainly two parts namely, the Antenna and Integrated Circuit (IC). The antenna is used to receive radio frequency waves and the integrated circuit (IC) is used in the processing and store of information. The microchip on the Radio Frequency Identification (RFID) reader is written with whatever information the user wants it.

Radio Frequency Identification (RFID) Reader: The Radio frequency identification reader, is the brain of the Radio frequency identification (RFID) system and is necessary for any system to function. The Readers also called the interrogators, are devices that transmit and receive radio waves to communicate with Radio frequency identification (RFID) tags. The Radio Frequency Identification (RFID) reader is a device, which used to gather information from Radio frequency identification (RFID. The Radiofrequency identification reader (RFID) uses radio waves to transfer the data from the Radio frequency identification tag to the Radiofrequency identification reader.

[2] RELATED WORKS

Liu Ji and Zhang Yongqiang [4] designed and implement a wireless fingerprint-based attendance system to obtain and record the attendance information using fingerprints known as biometric. Kyng and Man [5] designed a time management and access monitoring system using a microprocessor card to monitor students' and staff's movement with the data that are kept in the database for administrator reference in campus, office, or a certain area. Headmaster, Teachers, and parents could access all the information captured by this system by fully utilizing Mykad features via the Internet and intranet facilities. However, Jonathan Sidi, Syahrul N. Junaini, and Lau S. Ling in [6] suggested a system that was capable to record student's attendance using interactive input, viewing students and lecturer profiles, generating reports, and providing students timetable [8]. The system records the attendance using a barcode scanner. In another spectrum, Inanc and Pala [7] applied radio frequency identification (RFID) technology for checking in and checking out at parking areas without the need to stop the cars and it avoids traffic jams during the parking hours. This type of system is usually used in identifying vehicles through internet facilities by comparing the previous data in the database. A.A. Olanipekun and O.K. Boyinbode have implemented a system called the Radio frequency identification (RFID) Based Automatic Attendance systems [8]. The attendance system software is developed using visual basic VB.net and database (Microsoft Access). Each of the students has the Radio frequency identification (RFID) tag attached with the Student identification (ID) card. There is a serial connection between the computer and the Radio frequency identification (RFID) reader and the computer system. The Radiofrequency identification (RFID) reader is placed at the lecture hall door. Whenever students enter the lecture hall the Radio frequency identification (RFID) reader reads the Radio frequency identification (RFID) tag and it stores all data (Entry time, Name, etc.) of students into the database via a serial connection and maintains the system. Here the admin of this system can view all the documents using the software interface by retrieving the data from the database without any hitches, not like the traditional system of writing names on the attendance sheet or piece of paper. Hassanein D. Rjeib et. al design and implemented an attendance system with the combination of Radio frequency identification (RFID) and a Web-Based system [9]. This system uses the Radio frequency identification (RFID) tag and the Radiofrequency identification reader for getting the student's attendance and read the particulars of the students. Then this reader connects with Arduino or microcontroller which serves as the brain of the whole research because all instruction is given from there, which then passes the Radio frequency identification (RFID) reader response to the web server by the use of Arduino shield, finally, the attendance of students can be stored in web server by using PHP and MySQL. The admin of the implemented system can now view all the student's documents by login into this particular web-based application and can view all the student's details registered or stored using liquid crystal display (LCD). Srivignessh P.S.S and Bhaskar M. Found a system that, the Radio frequency identification (RFID) and Pose Invariant Face Verification for an automatic attendance system [10]. The system works under two factors verifications. In the first step, the students need to use the Radio frequency identification (RFID) tag that is read by the Radio frequency identification (RFID) reader. If the first step is succeeded then it moves to the second step of verification, if not, the student becomes under the unrecognized category. The second step is Face verification, if the face match with the particular registered in the Radio frequency identification (RFID) tag then it marks the student attendance that is in the database. Missing the above readings, the system will automatically identify the fraud students. This two-factor automatic system reduces the misuse of identity theft for getting attendance because they are not registered in the system database. Moth Myint Thein and Chaw Myat Nweand Hla Myo Tun developed a Student attendance Management System Based on Radio frequency identification (RFID) and Fingerprint Reader [11]. The system also works as a two-factor verification system. In the system, the Radio frequency identification (RFID) reader is linked with the computer and the computer has specific software that is used to measure the automatic attendance of the students which is developed by Microsoft Visual basic studio and SQL. In the first place, the entire student must register his or her Radio frequency identification (RFID) tag and Fingerprints and it is stored in the database of the system. Once the students enter the classroom they need to use the Radio frequency identification (RFID) tag and this will be read by the Radio frequency identification (RFID) reader which will then check the database of the system to check if the tag is registered, if it is registered or correct then he moves to the next verification step. In the second step, the fingerprint of the student is then verified. If it matched the information of the students registered he or her then the attendance of the student will be stored on the server. Besides, the lecturers or teachers have authentication to use the system, they can also act as admin of the entire system. Yashi Mishra et al. uses an SD card module with the Radio frequency identification (RFID) tag, which carries different voice codes, is used in the system development [12]. The tag identification card (ID) and the

code of the voice greeting are stored in the SD card module. When the student enters the classroom door, his or her Radio frequency identification (RFID) tag is being read. If the identification card (ID) of the student tag matched with the stored data in the SD card then the particulars of the student or person needs to use the voice greeting, if it matches then the door will be open and the attendance of the student will be store in the excel sheet. The Student can view their attendance detail using the liquid crystal display (LCD) use in the research. In the research, the Arduino or microcontroller, connects the liquid crystal display (LCD), the Radio frequency identification (RFID) reader, the SD card module, and the rest components use in the research. Likewise, the system has very simple schematics than another system because of the very simple components use and the design of the whole system. Also, you can we get fast response and accurate results. Anil Kumar Shukla created a model system called the Microcontroller Based Attendance System Using the radio frequency identification (RFID) system and Global System for Mobile (GSM) [13]. The system consists of three atMega16microcontroller placed in between the radio frequency identification (RFID) reader, Global System for Mobile (GSM) modem, and the computer. Each of the microcontroller use has its purpose. The system will starts whenever a lecturer or teacher used his or her radio frequency identification (RFID) tag to enter the lecture room or classroom then the students will enter the classroom also by swapping their radio frequency identification (RFID) tags within five minutes. The radio frequency identification (RFID) reader reads the radio frequency identification (RFID) tag, sends the signal to the first microcontroller, which will analyze the signal of the radio frequency identification (RFID) reader, and opens the classroom door using infrared rays (IR) signal, which is influence by a motor. This signal is temporarily stored in the microcontroller, when the lecturer or teacher finishes his or her class he or she must swap the radio frequency identification (RFID) tag again to the radio frequency identification reader and the system will decide automatically that the class is finished. Therefore, the microcontroller will pass the temporarily stored signal to the computer database as the attendance. In case if a student is absent, the signal will pass it to the global system for mobile, (GSM) modem and it will send this message to the parents of the students who were not present during the lectures or lesson in the lecture room or the classroom. If any of the students go out before the lecturer or teacher, the system will not count the student present in the lecture room or classroom. The system itself is an added advantage and reliable security system. Thus, the students cannot cheat the administration and their parents. Sandhya Konatham et al. suggested a system that will work with the radio frequency identification (RFID) and global system for mobile (GSM) [14]. In their research, they used a microcontroller as a midway among global systems for mobile (GSM) module and the radio frequency (RFID). Whenever the students enter the lecture room or classroom, they need to make use of their tag, which is read by the radio frequency (RFID) reader, and it sends it to the global system for mobile (GSM) module. If the identification card (ID) of the students or individual tag does not match with the stored information of the database he or she is considered as an unapproved person. If it accepts the tag, then the global system for mobile (GSM) module will send a message to the administration and their parents that the students attended lectures or lessons. Srinidhi MB and Romil Roy suggested a system that uses web-based attendance using four-tier architecture by the use of radio frequency identification (RFID) and Biometrics [15]. In their system, the students, lecturers, or teachers' radio frequency identification (RFID) has a unique code, which will be store in the database of the institution or school. The radiofrequency reader (RFID) reader and the fingerprint device are placed at the entrance door of the lecture room or classroom. Whenever the students want to enter the classroom, they need to use the radio frequency identification (RFID) tag which will be read by a radio frequency identification (RFID) reader and validates the identity of the students by comparing it with the information store in the database whether the tag matches or not. The second stage of verification will be allowed if and only if the first stage of verification is succeeded. The Verification with the fingerprint is the second stage of the system and if the student's fingerprint matches with the data in the database then the attendance will be marked and stored into the database, but if he or her record does not store or capture in the database then they will be no attendance for that student. The fingerprint verification is merely acting in ten minutes including five minutes before the schedule and after the schedule of class starting time. If anyone is late then it will deny providing attendance to that particular student that is late but the students can stay at the lectures and learn but will not have attendance for that class. Lastly, a short message service (SMS) will be sent to the students' parents if the students are present or not in the lecture room or classroom. H. K. Nguyen and M. T. Chew developed a prototype of the attendance management system with the placement of a bigger number of radio frequency identification (RFID) readers placed in the room and there is a server application maintains through a laptop [16]. The radio frequency identification reader and the laptop or personal computer (PC) are connected with the help of a wireless router or LAN connection. Whenever a student or person enters the classroom or lecture room, he or she needs to use the radio frequency identification (RFID) tag which is read by the radio frequency identification (RFID) reader and passes the student's attendance to the server through wireless or LAN connection. Since many of the radio frequency identification (RFID) readers are placed, more than one person can get the attendance simultaneously and get the higher efficiency than the traditional method or using the single radio frequency identification reader. Also, Muhammad Benny Chaniago and Apri Junaidi proposed a system that is working with the radio frequency identification (RFID) and Telegram Messenger Application [17]. In their system, the students need to meet their lecturers or teachers for the tapping of their radio frequency identification (RFID) tags. If the tags match with tag information stored in the database, then it will send the attendance to the management of the institution or principal in the form of an excel sheet as well as sends a message to the specific student's parent via Telegram messenger. Meanwhile, facial verification cost is comparably average to other biometric verification. It also could be considered for a better system for developing an automatic attendance system. The radio frequency identification (RFID) with fingerprint system is very comparable to the radio frequency identification (RFID) with the facial system. Each characteristic of the table is providing similar ideas except for their cost. Fingerprint biometric systems provide a very lower cost compare to Retina and Iris [18]. Meanwhile, software, which makes use of visual studio and SQL, are costs in a great measure. Eventually, the system is considered a high-cost system with a higher eminence.

[3] IMPACT OF USING THE RADIO FREQUENCY IDENTIFICATION (RFID) SYSTEM

1. radio frequency identification (RFID) can be used in various environments, this includes livestock, military, and scientific areas.

2. radio frequency identification (RFID) can be used in addition to Barcode. These two technologies can be complementing each other.

3. Unattended operations are possible, minimizing human errors and high costs.

4. radio frequency identification (RFID) can identify moving objects or elements that have tags embedded in them.

5. It can cover a larger area of coverage, Up to several feet.

[4] CONCLUSION

In this paper, we have reviewed many papers related to the radio frequency identification (RFID) system we have seen their various improvements in technology and the advantage of using the radio frequency identification (RFID) system over the traditional paper-based attendance system. Also, the impact of using the radio frequency identification (RFID) system is discussed.

REFERENCES

[1] E., Orji, C.,Oleka, U., Nduanya, "Automatic Access Control System using Arduino and RFID", Journal of Scientific and Engineering Research, vol. 5 issue 4, pp. 333-340, 2018.

[2] K., Vandana1, K., Anil Kumar, G., Sivani, G., Devanand, E., Venkatanarayana, "Examination Room Guidance System Using RFID and Arduino", International Research Journal of Engineering and Technology, Volume: 05 Issue: 04 | Apr-www.irjet.net, p-ISSN: 2395-0072, pp. 642-645, 2018.

[3] A., B., Ahmad, M., Çavaş, "A review advancement of security alarm system using internet of things (IoT), International Journal of New Computer Architectures and their Applications (IJNCAA) 9(2): 38-49 The Society of Digital Information and Wireless Communications", 2019.

[4] Z., Yongqiang, L., Ji, "The Design of Wireless Fingerprint Attendance System, International Conference on Communication Technology, ICCT '06, Handan, Hebei, China, 27-30 pp. 27-30 November 2006.

[5] K., Man, at al. "Utilizing MYKAD Touch N Go features for Student Attendance System (TITO)". Proceeding of 1st International Malaysian Educational Technology Convention Johor Bahru, Malaysia, pp.114-120, 2-5 November 2007.

[6] J., Sidi, S., N., Junaini, S., L., Ling, "Tracking Student Attendance using Interactive Student Attendance Management System", Third Malaysian Software Engineering

Conference (MySEC'07), Selangor, Malaysia, pp. 1-5, December 2007.

[7] N., Inanc, Z., Pala "Smart Parking Applications Using RFID Technology", Proceedings of 1st Annual RFID Eurasia, Istanbul, Turkey, pp.1 – 3, 5-6 September 2007.

[8] A., A., Olanipekun, O., K., Boyinbode, "An RFID-based automatic attendance system in educational institutions of Nigeria," Int. J. Smart Home, vol. 9, no. 12, pp. 65–74, 2015.

[9] H., D., N., Salih, A., Al-Sadawi, B., Al., H., Alsharqi, "Attendance and Information System using RFID and Web-Based Application for Academic Sector," Int. J. Adv. Computer. Sci. Appl., vol. 9, no. 1, pp. 266–274, 2018.

[10] P., S., S., Srivignessh, M., Bhaskar, "RFID and pose invariant face verification based automated classroom attendance system," in International Conference on Microelectronics, Computing, and Communication, 2016.

[11] M., M., hein, C., Nwe, C., M., Tun, "Students' Attendance Management System Based On RFID and Fingerprint Reader," Int. J. Sci. Technol. Res., 2015.

[12] Y., Mishra, G., K., Marwah, S., Verma, "Arduino Based Smart RFID Security and Attendance System with Audio Acknowledgement," vol. 4, no. 01, pp. 363–367, 2015.

[13] A., K., Shukla, "Microcontroller Based Attendance System Using RFID and GSM," vol. 5, no. 8, pp. 127–131, 2017.

[14] S., B., Konatham, S., Chalasani, N., Kulkarni, T., El Talib, "Attendance generating A system using RFID and GSM," in 2016 IEEE Long Island Systems, Applications, and Technology Conference, LISAT, pp. 3–5, 2016.

[15] R., Roy, "A web-enabled secured system designed for attendance monitoring applying biometric and Radio Frequency Identification (RFID) technology," in 2014 International Conference on Signal Propagation and Computer Technology, ICSPCT, pp. 653–657, 2014.

[16] T., Sanjay, "Attendance Management system", 4(7), vol. 4, no. 7, pp. 541–543, 2014.

[17] M., B., Chaniago, A., Junaidi, "Student Presence Using Rfid and Telegram Messenger Application," 8th Widyatama Univ. IEEE, pp. 1–5, 2016.

[18] M., Karovaliya, S., Karedia, S., Oza, D., R., Kalbande, "Enhanced security for ATM Machine with OTP and facial recognition features," in Proceeding Computer Science, vol. 45, pp. 390–396, 2015.

Stability and Repeatability Properties of TiO_2/B_2O_3 Thick Film Gas Sensor for Detecting Hydrogen at Optimum Operating Temperature

Siti Amaniah Mohd Chachuli
Fakulti Kejuruteraan Elektronik & Kejuruteraan Komputer Universiti Teknikal Malaysia Melaka, Melaka, Malaysia
sitiamaniah@utem.edu.my

Mohd Nizar Hamidon
Institute of Advanced Technology
Universiti Putra Malaysia Selangor, Malaysia
mnh@upm.edu.my

Mehmet Ertugrul
Engineering Faculty Ataturk University Erzurum, Turkey
ertugrul@atauni.edu.tr

Md. Shuhazlly Mamat
Faculty of Science Universiti Putra Malaysia
Selangor, Malaysia
shuhazlly@upm.edu.my

Omer Coban
Department of Electrical and Energy, Ispir Hamza Polat Vocational School of Higher Education, Ataturk University
Erzurum, Turkey
omercoban@atauni.edu.tr

***Abstract*— This paper presents the stability and repeatability of TiO_2/B_2O_3 thick film gas sensors in detecting hydrogen at optimum operating temperature. The gas sensor was deposited on an alumina substrate using screen-printing technology and annealed at 500℃ under ambient air. This study found that silver from the interdigitated electrode was diffused to the surface of the sensing film after the annealing treatment, where this phenomenon also affects the repeatability and stability properties of the TiO_2/B_2O_3 gas sensor. The diffusion of silver on the sensing film surface was also verified using FESEM by observing larger nanoparticles diameter due to the combination of TiO_2 with silver. For the repeatability test, the sensitivity was reduced almost two times for the third cycle of 1000 ppm of hydrogen, as referred to the first cycle. For the stability test, the reduction percentage of sensitivity after one-week measurement was approximately 70% because of the element changes in the sensing film, which verified using EDX characterization.**

Keywords— TiO_2/B_2O_3 gas sensor; hydrogen; screen-printing; hydrogen; thick film

[1] INTRODUCTION

Titanium dioxide (TiO_2) is an n-type semiconductor and consists of three phases: anatase, rutile, and brookite [1]. Besides, TiO_2 also chemically stable, non-toxic, biocompatible and inexpensive [2]. These properties make this material practical material in many applications. Optical and electronic properties have made TiO_2 widely used in gas sensor and dye-sensitized solar cell [3]. In gas sensing applications, the anatase and rutile phases are the most phases used in TiO2 to detect hydrogen.

TiO_2 nanostructures such as nanotubes [4],[5], nanoparticles [6], [7] and nanocrystalline [8] have been widely used in detecting hydrogen. Reported that, TiO_2 has the ability to sense a low concentration of hydrogen as low as 1 ppm and working at room operating temperature [9]. Due to the enormous advantages of TiO_2 and the ability to sense the low concentration of hydrogen at low operating temperature, sensing material for thick film gas sensor in this work was chosen based on TiO2. Other than that, TiO2 also was mixed with a glass powder, which is boron oxide (B2O3), because of the capability of B2O3 to improve the adhesion of the sensing film on the substrate and to increase the crystallinity of the anatase phase [1].

In previous work, as presented in Ref. [10], the TiO_2/B_2O_3 gas sensor has been exposed at different operating temperatures in the range of 150 – 250℃, and the study found that the optimum operating temperature for this gas sensor occurred at 200℃. Thus, TiO_2/B_2O_3 gas sensor was exposed to 100 – 1000 ppm of hydrogen at the operating temperature of 200 ℃ in this work to investigate the repeatability and stability properties of the gas sensor in a certain period of time.

[2] EXPERIMENTAL WORK

A. Preparation and Fabrication of TiO2/B2O3 Gas Sensor

The preparation of TiO_2/B_2O_3 sensing material and TiO_2/B_2O_3 paste can be referred in previous work in Ref. [10]. In order to fabricate a gas sensor, an interdigitated electrode (IDE) based on silver-conductive paste (Sigma-Aldrich) was deposited as the first layer on an alumina substrate (2 mm x 1.5 mm) using screen-printing and followed by firing process at 150℃ under ambient air. Then, the TiO2/B2O3 paste was deposited on the IDE as a second layer of the gas sensor and followed by the annealing treatment at 500℃ under ambient air. The thickness of TiO_2/B_2O_3 sensing film was approximately 4 – 5 µm using screen-printing. Wire copper was attached to the electrode leg using the silver paste to test the gas sensor in the gas chamber. Size of IDE was approximately 4.0 mm x 4.0 mm, and size of the sensing film was approximately 4.2 mm x 4.2 mm. Fig. 1 shows the fabricated TiO_2/B_2O_3 gas sensor on an alumina substrate using screen-printing technology. Black color on the surface of the sensing film was occurred because of the diffusion of silver (IDE) from the bottom to the surface of the sensing film. This phenomenon also was observed in the previous study [7].

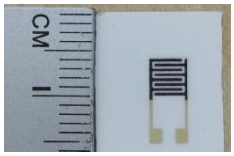


Fig.1. Fabricated TiO_2/B_2O_3 gas sensor using screen-printing technology

B. *Experimental setup of Gas Sensor*

The experimental setup of the gas sensor in this work can be referred in Ref. [1]. The experiment was conducted in a closed gas chamber using synthetic air as a carrier gas and hydrogen as a target gas. 10V was supplied to the gas sensor and the current of the gas sensor was observed as the output of the gas sensor. Initially, the gas sensor will be heated at 200 ℃ until the temperature was stabilized. Then, the synthetic air (50 ml/min) was exposed to the gas sensor until a stabilization graph (current) was obtained. After the current was stable, the various concentrations of hydrogen (100 – 1000 ppm) was exposed to the gas sensor. Both synthetic air and hydrogen gas flowed in 300s to the gas chamber for each concentration of hydrogen.

[3] RESULTS AND DISCUSSION

A. *Characterization of Thick Film Gas Sensor using FESEM and EDX*

FESEM and EDX characterizations were carried out on the area of black color on the surface of the gas sensor, as shown in Fig. 1 to verify the diffusion of silver on the surface of the gas sensor. Fig. 2 shows the morphology of the sensing film in the TiO_2/B_2O_3 gas sensor. It can be seen that the shapes of nanostructures in spheres, in which verify the TiO2 nanoparticles as the sensing material used for the gas sensor. The diameter of TiO_2 nanoparticles was measured in the range of 30 – 70 nm. It also was found that silver was diffused to the surface on the sensing film, where it can be seen by the diameter of nanoparticles were increased to 200 nm due to the combination of TiO_2 with the silver. Besides that, the diffusion of silver to the sensing film surface can also be seen from the black color of the surface of the gas sensor, as displayed in Fig. 1. The diffusion of silver into TiO2 was also observed at an annealing temperature of 500℃ in [11]. Therefore, the sensing materials of the gas sensor in detecting the hydrogen in this work can be considered as TiO_2 and silver.

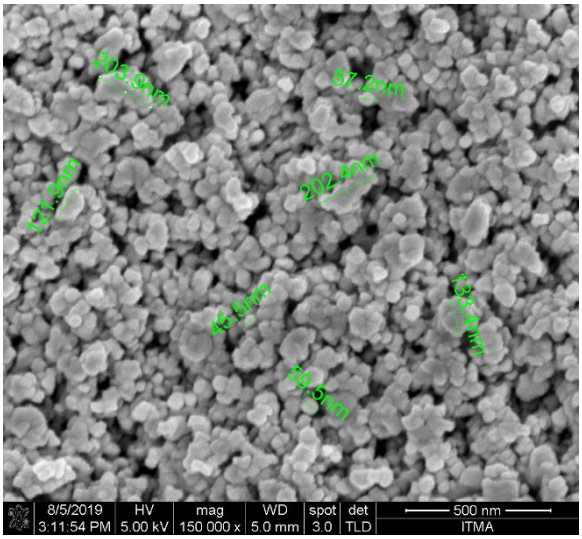
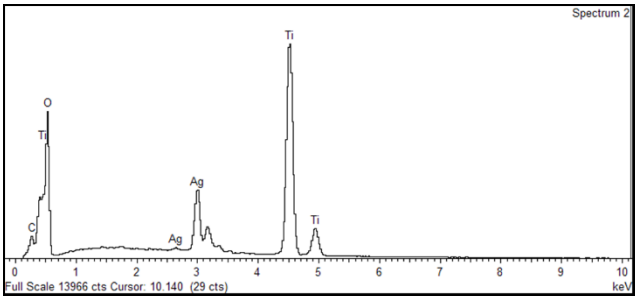
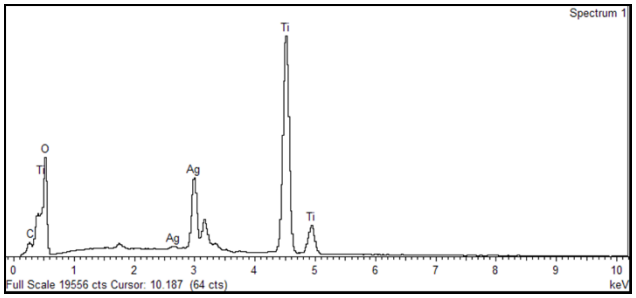


Fig.2. Morphology of the sensing film in TiO_2/B_2O_3 gas sensor

Fig. 3 shows the EDX spectra, and Table I shows the EDX elements composition of TiO_2/B_2O_3 gas sensor for new sample (before measurement) and after one-week measurement. It was observed that titanium, oxygen, silver, and carbon elements were detected on the sensing film surface using EDX characterization. It seemed that the weight of elements of titanium, silver and carbon was almost similar, while the weight of oxygen was reduced in TiO_2/B_2O_3 gas sensor after one week. Carbon was detected on the sensing film surface because of linseed oil in the organic binder while making the TiO_2/B_2O_3 paste [12]. This result showed that there were elements changes in the sensing film after exposure to hydrogen. Less oxygen element on the surface of the TiO_2/B_2O_3 gas sensor might cause lesser interaction of ionized oxygen with the hydrogen molecules, thus lower generation of H_2O molecules and caused the sensitivity was reduced, where this phenomenon can be seen in Fig. 4 during stability test.



(a)



(b)

Fig. 3. EDX spectra of TiO_2/B_2O_3 gas sensor (a) new and (b) after one-week

Table 1. Edx Elements Composition Of Tio_2/B_2o_3 Gas Sensor

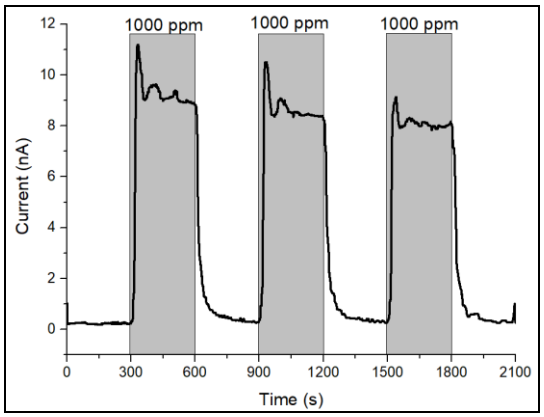
Element	Weight of elements (± 5.00%)	
	New (%)	One Week (%)
Titanium	41.20	45.75
Oxygen	43.60	36.07
Silver	13.66	17.27
Carbon	1.55	0.91

B. *Repeatability Properties*

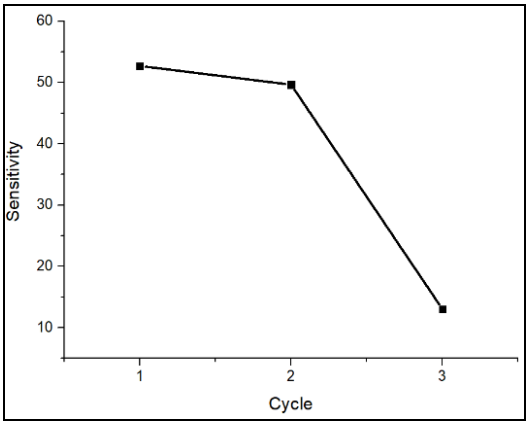
Repeatability properties are defined by exposing the gas sensor with a similar target gas concentration for certain cycles [13]. In this work, the repeatability properties were conducted by exposing 1000 ppm of hydrogen to the gas sensor for three cycles at an operating temperature of 200℃ to observe the difference of the response for each cycle. For this test, 1000 ppm of hydrogen was chosen to be exposed

three times to the gas sensor because this concentration is the highest concentration used in this work. Besides, 1000 ppm of hydrogen produced a more significant response to the hydrogen compared to others; thus, clear transition upon the second test and third test can be observed. The repeatability test was conducted continuously, in which the second cycle and third cycle of 1000 ppm of hydrogen were exposed to the gas sensor after 300s in the synthetic air.

Fig. 4 displays repeatability properties of TiO_2/B_2O_3 gas sensor for three cycles in terms of response and sensitivity. It can be seen that the sensitivity of the TiO_2/B_2O_3 gas sensor was dropped as the cycle increased. The reduction percentage was approximately 5.82% and 13.03% for the second cycle and third cycle, as referred to the first cycle. The reduction of sensitivity was almost two times for the third cycle than the first cycle, where it can be caused by the trapped electron on the surface of the sensing film of the gas sensor, which contributes to the reduction of current. The gas sensor sensitivity was calculated using Sensitivity = Ig/Ia, where Ig is current during hydrogen flow, and Ia is initial current during synthetic air flow.



(a)

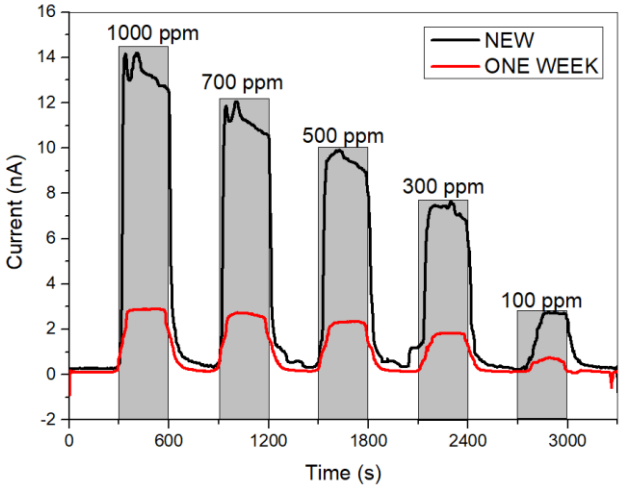


(b)

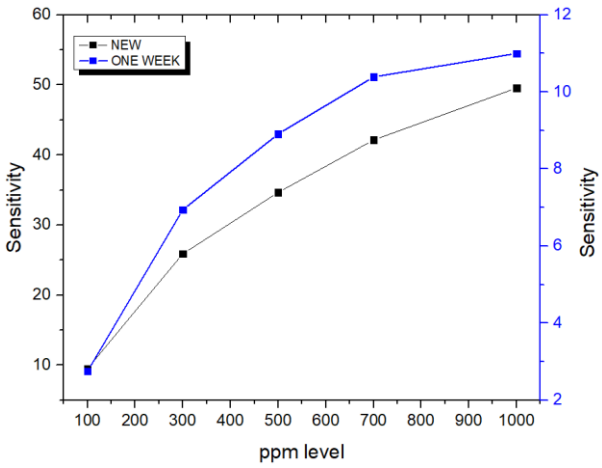
Fig. 4. Repeatability properties of TiO_2/B_2O_3 gas sensor for three cycles (a) Response and (b) Sensitivity

C. *Stability Properties*

The stability properties of a gas sensor are defined as the changing range of sensitivity in a certain period of time [14]. To achieve the high stability of a gas sensor, the measurement should be conducted for a period of time [14], [15]. For stability test in this work, the TiO_2/B_2O_3 gas sensor was exposed again to the 100 – 1000 ppm of hydrogen at the operating temperature of 200℃ after one-week measurement to investigate the stability properties. Stability properties of TiO_2/B_2O_3 gas sensor for new sample and after one-week measurement, in terms of response and sensitivity, is shown in Fig. 5.



(a)



(b)

Fig. 5. Stability of TiO_2/B_2O_3 gas sensor for new sample and after one week (a) Response and (b) Sensitivity

It can be seen that the response and sensitivity for 100 - 1000 ppm of hydrogen were reduced after one week. The percentage reduction in the TiO_2/B_2O_3 gas sensor was approximately 70 - 78% for 100 - 1000 ppm of hydrogen. Although the percentage of reduction can be considered significant, the different values in sensitivity value for the new sample and after one-week measurement seemed consistent for various hydrogen concentrations. In terms of graph pattern for the response, the TiO_2/B_2O_3 gas sensor produced a different response pattern after a one-week measurement. Other than that, the TiO_2/B_2O_3 gas sensor response was also observed saturate faster than the new sample after a one-week measurement. The graph pattern was almost similar for the sensitivity graph even though the sensitivity was reduced as shown in Fig. 4(b).

According to the EDX elements composition in TiO_2/B_2O_3 gas sensor as presented in the Table I, the oxygen elements was reduced after one week, where this result suggests that less ionized oxygen can be created on the surface of the gas

sensor during the flow of the synthetic air, thus reducing the combination of ionized oxygen with the hydrogen. This phenomenon will cause less adsorption of the target gas and reducing the sensitivity of the gas sensor. It also was observed that TiO_2/B_2O_3 gas sensor still produced a significant difference for each concentration of hydrogen at the operating temperature of 200°C as shown in Fig. 5(a). It can be concluded that element changes in oxygen did not considerably affect the gas sensor optimum operating temperature.

D. Sensing mechanism of TiO_2/B_2O_3 gas sensor to hydrogen

The mechanism of TiO_2/B_2O_3 gas sensor was based on the adsorbed oxygen on the surface of the sensing material at optimum operating temperatures. At an operating temperature of 200℃, during exposure to synthetic air, oxygen molecules adsorbed on the oxides surface and ionized to oxygen species to O^-, where this reaction is shown in (1) and (2) [12].

$$O_{2\,(gas)} \rightarrow O_{2\,(ads)} \quad (1)$$

$$O_{2\,(ads)}^{-} + e^{-} \rightarrow 2O^{-} \quad (2)$$

When these reactions occur, adsorbed oxygen reduced the conduction band and increase the negative charge on the grain, thus creating energy barriers for the electron transport between the grain [12]. This phenomenon will increase the gas sensor resistance; thus, a smaller grain size of metal-oxide and larger bandgap were observed. When hydrogen flows to the gas sensor, the following reaction (3) will occur.

$$H_{2(gas)} + O^{-}_{(ads)} \rightarrow H_2O + e^{-} \quad (3)$$

The ionized oxygen will react with hydrogen molecules and produced H_2O, and release electrons. The electrons will adsorb into the conduction band, and the energy barrier will be reduced. This phenomenon will reduce the resistivity of TiO_2/B_2O_3 gas sensor, where it can be seen by the reduction of resistance of gas sensor for reducing gas such as hydrogen as displayed in Fig. 3 and Fig. 4. At an operating temperature of 200℃, H_2O can be desorbed because the boiling point of H_2O occurred at 100℃. Thus, receptor function (sensing film) of the metal-oxide gas sensor is enhanced at operating temperature larger than 100℃, resulting in higher sensitivity [16].

[4] CONCLUSIONS

The TiO_2/B_2O_3 thick film gas sensor was successfully fabricated using the screen-printing in this work. The gas sensor was exposed to 100 – 1000 ppm of hydrogen and tested for stability and repeatability properties. The results showed that the sensitivity was reduced as the cycle increased during the repeatability test. In contrast, the percentage of reduction was approximately in the range of 70 – 78% for 100 – 1000 ppm of hydrogen after one-week measurement.

REFERENCES

[1] S. A. Mohd Chachuli;, M. N. Hamidon;, M. Ertugrul;, M. S. Mamat;, H. Jaafar;, and N. Aris;, "Influence of B_2O_3 Addition on the Properties of TiO_2 Thick Film at Various Annealing Temperatures for Hydrogen Sensing," *J. Electron. Mater.*, pp. 44–47, 2020.

[2] A. N. Banerjee, "The design, fabrication, and photocatalytic utility of nanostructured semiconductors: Focus on TiO_2-based nanostructures," *Nanotechnol. Sci. Appl.*, vol. 4, pp. 35–65, 2011.

[3] S. Valencia, J. M. Marín, and G. Restrepo, "Study of the Bandgap of Synthesized Titanium Dioxide Nanoparticules Using the Sol-Gel Method and a Hydrothermal Treatment," *Open Mater. Sci. J.*, vol. 4, pp. 9–14, 2010.

[4] E. Şennik, Z. Çolak, N. Kilinç, and Z. Z. Öztürk, "Synthesis of highly-ordered TiO_2 nanotubes for a hydrogen sensor," *Int. J. Hydrogen Energy*, vol. 35, no. 9, pp. 4420–4427, 2010.

[5] G. K. Mor, M. A. Carvalho, and C. A. Grimes, "A room-temperature TiO_2-nanotube hydrogen sensor able to self-clean photoactively from environmental contamination," 2004.

[6] X. Peng, Z. Wang, P. Huang, X. Chen, X. Fu, and W. Dai, "Comparative study of two different TiO_2 film sensors on response to H_2 under UV light and room temperature," *Sensors*, vol. 16, no. 8, pp. 1–14, 2016.

[7] S. Amaniah, M. Chachuli, M. N. Hamidon, M. S. Mamat, M. Ertugrul, and N. H. Abdullah, "A Hydrogen Gas Sensor Based on TiO_2 Nanoparticles on Alumina Substrate," *Sensors*, vol. 18, no. 2483, pp. 1–13, 2018.

[8] A. A. Haidry *et al.*, "Hydrogen gas sensors based on nanocrystalline TiO_2 thin films," *Cent. Eur. J. Phys.*, vol. 9, no. 5, pp. 1351–1356, 2011.

[9] X. Xia, W. Wu, Z. Wang, Y. Bao, Z. Huang, and Y. Gao, "A hydrogen sensor based on orientation aligned TiO_2 thin films with low concentration detecting limit and short response time," *Sensors Actuators, B Chem.*, vol. 234, pp. 192–200, 2016.

[10] S. A. M. Chachuli, M. N. Hamidon, M. S. Mamat, and M. Ertugrul, "Detecting Hydrogen Using TiO_2-B_2O_3 at Different Operating Temperature," *2018 IEEE Int. Conf. Semicond. Electron.*, pp. 37–40, 2018.

[11] N. A. Sheini and M. Rohani, "Ag-doped titanium dioxide gas sensor," in *IOP Conference Series: Materials Science and Engineering*, 2016, vol. 108, pp. 1–7.

[12] S. A. Mohd Chachuli, M. N. Hamidon, M. S. Mamat, M. Ertugrulc, and N. H. Abdullah, "Response of TiO_2/MWCNT/B_2O_3 gas sensor to hydrogen using different organic binder," *Mater. Sci. Semicond. Process.*, vol. 99, no. 2019, pp. 140–148, 2019.

[13] U. T. Nakate *et al.*, "Improved selectivity and low concentration hydrogen gas sensor application of Pd sensitized heterojunction n-ZnO/p-NiO nanostructures," *J. Alloys Compd.*, vol. 797, pp. 456–464, 2019.

[14] Q. Zhou, W. Chen, S. Peng, and X. Su, "Nano-tin oxide gas sensor detection characteristic for hydrocarbon gases dissolved in transformer oil," in *International Conference on High Voltage Engineering and Application*, 2012, pp. 384–387.

[15] N. M. Shaalan, M. Rashad, and M. A. Abdel-Rahim, "Repeatability of indium oxide gas sensors for detecting methane at low temperature," *Mater. Sci. Semicond. Process.*, vol. 56, pp. 260–264, 2016.

[16] S. Shukla, L. Ludwig, C. Parrish, and S. Seal, "Inverse-catalyst-effect observed for nanocrystalline-doped tin oxide sensor at lower operating temperatures," *Sensors Actuators, B Chem.*, vol. 104, no. 2, pp. 223–231, 2005

A Facile Synthesis of Rutile-Anatase TiO_2 Nanocuboid: The Effect of Chloride Ion

Kam Sheng Lau
Department of Applied Physics
Universiti Kebangsaan Malaysia
43600 UKM Bangi, Selangor, Malaysia.
kamshenglau@gmail.com

Masliana Muslimin
Department of Applied Physics
Universiti Kebangsaan Malaysia
43600 UKM Bangi, Selangor, Malaysia.
masliana@nuclearmalaysia.gov.my

Norhashimah Ramli
Centre for Research and Instrumentation
Universiti Kebangsaan Malaysia
43600 UKM, Bangi, Selangor, Malaysia.
norhashimahramli@ukm.edu.my

Chin Hua Chia
Department of Applied Physics
Universiti Kebangsaan Malaysia
43600 UKM Bangi, Selangor, Malaysia.
chia@ukm.edu.my

Mohammad Hafizuddin bin Hj Jumali
Department of Applied Physics
Universiti Kebangsaan Malaysia
43600 UKM Bangi, Selangor, Malaysia.
hafizhj@ukm.edu.my

Sin Tee Tan
Physics Department
University Putra Malaysia
43400 Serdang, Selangor, Malaysia.
tansintee@upm.edu.my

Abstract: **Morphological transformation of titanium dioxide (TiO_2) nanorod into TiO_2 nanocuboid on fluorine doped tin oxide (FTO) glass was successfully conducted using a facile hydrothermal synthesis method via a wet chemical approach. Characterisation on x-ray diffraction (XRD), field emission scanning electron microscopy (FESEM), high-resolution transmission electron microscopy (HRTEM), energy dispersive x-ray (EDX) spectroscopy, selected area electron diffraction (SAED), Raman spectroscopy, ultraviolet–visible (UV-Vis) spectroscopy, atomic force microscopy (AFM) had been conducted to investigate the structural and morphological changes on the crystal growth of TiO_2 nanocuboid.**

Method: **The synthesis of TiO_2 nanocuboid was illustrated in Figure 1. Firstly, FTO substrate was placed in a mixture solution consist of dilute hydrochloride acid (HCl) and titanium butoxide ($TiOC_4H_9)_4$ solution. The solution was undergone ultrasonication to obtain a homogenous solution. Next, the FTO and the mixture solution was transferred into a Teflon. The hydrothermal growth process was conducted at various time at 170 °C. The samples were characterized using XRD, FESEM, HRTEM, EDX spectroscopy, SAED, Raman spectroscopy, UV-Vis spectroscopy, and AFM.**

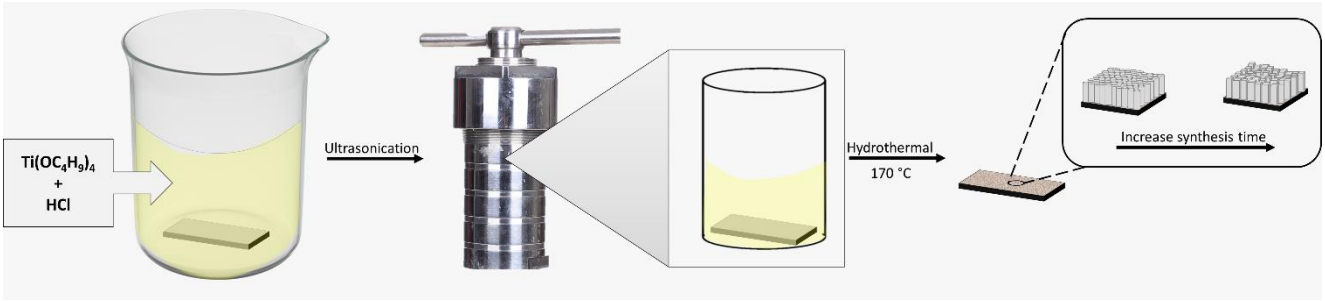


Fig. 1. Schematic diagram of the synthesis of TiO_2 nanocuboid.

Results: **The effect of hydrothermal growth time of TiO_2 highly influences the crystal structure arrangement, crystallite size and strain energy of the polymorphs TiO_2 crystals. Besides, Raman analysis also concluded the formation rutile phase TiO_2 on FTO glass. The AFM results show a high surface roughness of TiO_2 nanocuboid and the different surface adhesion energy on the rutile and anatase site of TiO_2 nanocuboid.**

Conclusion: **The TiO_2 nanocuboid was sucessfully synthesised using hydrothermal synthesis approach via wet synthesis approach. The tunable band gap properties and high visible light reflectivity of TiO_2 nanocuboid make it a potential material in optoelectronic applications.**

Keywords—Adhesion energy, rutile, SAED, TiO_2 nanocuboid

Effects of Nanostructured Graphitic Concentration on the Performance of Transition-Metal-Oxide-Based Supercapacitors

Jun Yan Lim
Department of Physics Universiti Putra Malaysia Selangor Darul Ehsan, Malaysia
gs58507@student.upm.edu.my

Kam Sheng Lau
Department of Applied Physics Universiti Kebangsaan Malaysia Selangor Darul Ehsan, Malaysia
kamshenglau@gmail.com

Chin Hua Chia
Department of Applied Physics Universiti Kebangsaan Malaysia Selangor Darul Ehsan, Malaysia
chia@ukm.edu.my

Sin Tee Tan
Department of Physics Universiti Putra Malaysia Selangor Darul Ehsan, Malaysia
tansintee@upm.edu.my

Aim: **Graphitic materials such as graphene are ubiquitously incorporated in energy storage materials to utilize their excellent in-plane electrical conductivity for the electron transfer process. However, limited attention has been given to the interfaces between these carbonaceous entities and their host materials, inhibiting advancements in fabricating devices with high energy storage capability. The carrier transport phenomenon at linkages between graphitic components and their respective hosts remains unclear. Therefore, understanding the physical properties and interactions between graphitic materials and transition metal oxide hosts is imperative in establishing a comprehensive picture of carrier transport in these composites. In this work, different concentrations of nanostructured graphite were incorporated into various MnO_2-based supercapacitor electrodes. The composite active material with a G-MnO_2 weight ratio of 0.8:1 recorded the highest specific capacitance of 18.3137 Fg^{-1} at a scan rate of 50 mVs^{-1}. This result can be attributed to the formation of Mn^{3+}/Mn^{4+} heterovalent pairs within the MnO_2 nanowires and retention of sp^2 hybridization within the nanostructured graphite. The formation of Mn^{3+}/Mn^{4+} pairs have been attributed to the electronegativity of the O atom in enabling electron losing of both Mn and C to form chemical bonds at the interface [1]. This approach provides an alternative for improving the energy storage performance of future supercapacitor devices.**

Method: **Manganese(IV) oxide (MnO_2) nanowires were synthesized via a hydrothermal route. A 0.04 M precursor solution was prepared by dissolving potassium permanganate in deionized water and stirring the solution at 250 rpm for 15 minutes. Then, ammonium fluoride was added, and the solution was stirred at the same speed and duration again to ensure homogeneity. The growth solution was a dark-brownish solid was obtained. The product was dried overnight in an oven.**

For device fabrication, nanostructured graphite was incorporated into the as-synthesized MnO_2 nanowires in different weight ratios with respect to the nanowires, i.e., *x* parts of nanostructured graphite to one part of MnO_2 nanowires. The binder solution used in fabricating the composite active material was synthesized by dissolving polyvinylidene fluoride in n-methyl-2-pyrrolidone at a 1:1.5 ratio. The slurry mixture comprising an NMP-PVDF binder, nanostructured graphite, activated carbon, and MnO_2 nanowires were prepared by mechanical stirring at 300 rpm and heating at 60°C overnight. Subsequently, the slurry was cast onto a piece of hydrochloric-acid-etched-carbon cloth (1 cm^2 area). Finally, the flexible device was heated at 110°C in an oven and vacuum treated overnight to remove any residual moisture.

Cyclic voltammetry was done by setting up a three-electrode system. In the system, the sample is put as the working electrode and a platinum wire is designated as the counter electrode. A silver/silver chloride reference electrode was used as well, along with 2 M of lithium chloride solution as the working electrolyte. The potential window for the tests was set as 0 – 0.8 V vs Ag/AgCl.

Results:

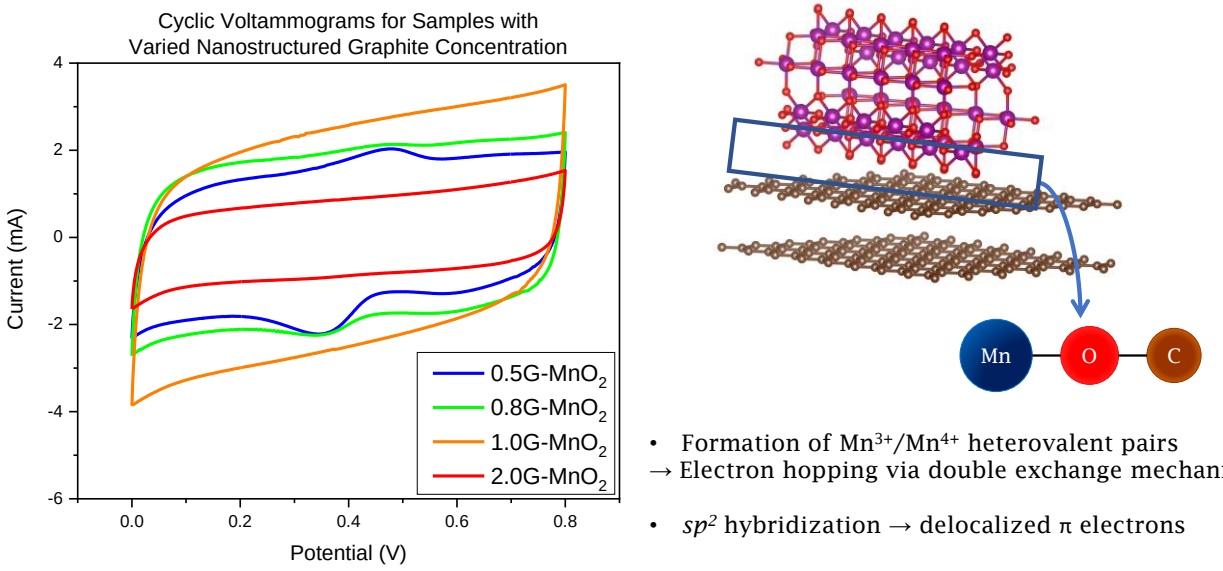


Fig. 1. Cyclic Voltammograms of Samples with Different Nanostructured Graphite Concentration and Proposed Mechanism for Observed Variation. Illustration generated using VESTA [2] using templates sourced from the Materials Project initiative [3].

***Conclusion*: In this research, the incorporation of nanostructured graphite into α-MnO_2 in various concentrations is reported. It was found that the electrode material with a G-MnO_2 weight ratio of 0.8:1 displayed the highest specific capacitance of 18.3137 Fg^{-1} at a scan rate of 50 mVs^{-1} during cyclic voltammetry. This measurement is attributed to the improved electrical conductivity obtained by balancing the formation of Mn^{3+}/Mn^{4+} heterovalent pairs in MnO_2 and retention of sp^2 hybridization in nanostructure graphite.**

References:

[1] N. Saadat, H. N. Dhakal, J. Tjong, S. Jaffer, W. M. Yang, and M. Sain, "Recent advances and future perspectives of carbon materials for fuel cell," (in English), *Renew. Sust. Energ. Rev.*, Article vol. 138, p. 21, Mar 2021, Art no. 110535, doi: 10.1016/j.rser.2020.110535.

[2] K. Momma and F. Izumi, "VESTA: a three-dimensional visualization system for electronic and structural analysis," (in English), *J. Appl. Crystallogr.*, Software Review vol. 41, pp. 653-658, Jun 2008, doi: 10.1107/s0021889808012016.

[3] A. Jain *et al.*, "Commentary: The Materials Project: A materials genome approach to accelerating materials innovation," (in English), *APL Mater.*, Article vol. 1, no. 1, p. 11, Jul 2013, Art no. 011002, doi: 10.1063/1.4812323.

Keywords: energy storage, supercapacitors, MnO_2, graphite, interface

Effect of cobalt titanate on the hydrogen storage properties of magnesium hydride

M.Ismail
Energy Storage Research Group, Faculty of Ocean Engineering Technology and Informatics Universiti Malaysia Terengganu
Kuala Nerus, Terengganu, Malaysia
mohammadismail@umt.edu.my

N.A. Ali
Energy Storage Research Group, Faculty of Ocean Engineering Technology and Informatics Universiti Malaysia Terengganu
Kuala Nerus, Terengganu, Malaysia
nurulllamirah@gmail.com

Aim: **Due to its advantages such as high hydrogen storage capacity (7.6 wt% H_2), good reversibility absorbs and desorbs hydrogen, low cost and abundance on earth make magnesium hydride (MgH_2) a potential material for solid-state hydrogen storage. However, the high decomposition temperature, slow sorption kinetics and very stable thermodynamic properties are main obstacles to commercial application of MgH_2. Doping with nanocatalyst is an attractive option to improves the hydrogen storage properties of MgH_2. In this paper, we report the effect of cobalt titanate ($CoTiO_3$) nanoparticles on the hydrogen storage properties of MgH_2. Different percentages of $CoTiO_3$ nanoparticles (5, 10, 15 and 20 wt.%) were added to MgH_2 and their catalytic influences on the hydrogen storage properties of MgH_2 were investigated.**

Method: **MgH_2 was milled with different percentages (5, 10, 15 and 20 wt%) of $CoTiO_3$ at 400 rpm for 60 min, and the ratio on the powder to steel balls was ~40:1. The onset decomposition temperature and sorption kinetic measurements were carried out using the Sieverts-type apparatus. The surface morphology of the doped and undoped samples was viewed by scanning electron microscopy (JEOL JSM-6360LA). Differential scanning calorimetry was performed using the Mettler Toledo DSC/TGA under an argon flow (50 ml/min). About 10 mg each of doped and undoped samples was placed into alumina crucibles and heated at different rates (15, 20, 25 and 30 °C/min) from room temperature to 500 °C. For structural analysis, X-ray diffraction measurements were recorded using a Rigaku MiniFlex X-ray diffractometer with CueKa radiation.**

Results: **Results showed that the 10 wt.% $CoTiO_3$-catalysed MgH_2 sample was the best composite to enhance the hydrogen storage performance of MgH_2. The onset decomposition temperature of the 10 wt.% $CoTiO_3$-doped MgH_2 composite was decreased by ~70 °C compared to as-milled MgH_2. Meanwhile, the desorption/absorption kinetic measurements showed an improvement compared to the undoped MgH_2. The activation energy for dehydrogenation of MgH_2 was reduced from 135.0 kJ/mol to 104.6 kJ/mol after the addition of $CoTiO_3$.**

Conclusion:

The addition of $CoTiO_3$ resulted in both decreased decomposition temperature, and enhanced sorption kinetics, compared to un-doped MgH_2. It is believed that the *in-situ* generated $MgTiO_5$ species had catalytic effects on enhancing the hydrogen storage properties of the $CoTiO_3$-catalysed MgH_2 composite.

Keywords— hydrogen storage, solid-state storage, magnesium hydride, cobalt titanate

The Turbidity Removal Performance by Purified Natural Coagulant in Water Treatment

Amina Adedoja Owodunni
School of Chemical Engineering, Universiti Sains Malaysia, Engineering Campus,
14300, Nibong Tebal, Penang, Malaysia.
aowodunni96@student.usm.my

Suzylawati Ismail
School of Chemical Engineering, Universiti Sains Malaysia, Engineering Campus,
14300, Nibong Tebal, Penang, Malaysia.
chsuzy@usm.my

***Abstract*- This work studies the effect of extraction and purification treatment of pigeon pea (PiP) and green beans (GB) as a natural coagulant for turbidity removal from wastewater. NaCl was used to extract the active coagulation agents from the seed samples and was further purified with the protein isoelectric precipitation method to obtain a purer coagulant. The turbidity removal efficiency performance of the coagulants was evaluated, and the purified protein coagulants were characterized using the FTIR analysis. The pure protein coagulants resulted in higher turbidity removal of 97.17 and 97.03% for PiP and GB, respectively. The findings were supported by the FTIR analysis of the seed powder samples. It is concluded that pure protein coagulant from GB and PiP effectively removed suspended solids from water while maintaining the organic matter (COD) level in the treated water.**

Keyword-turbidity removal, green beans, pigeon pea, isoelectric protein precipitation.

I. INTRODUCTION

The drive towards exploring potential substitutes of chemical coagulants is comparatively because of the health hazards threat to human and aquatic animals, and environmental pollution caused by chemical leaching. This led to the search for environmentally friendly, non-toxic, natural, and biodegradable coagulants which are based on plant materials, animals, and micro-organisms.

Pigeon pea (*Cajanus cajan*) and green beans (*Phaseolus vulgaris*) are leguminous seeds. Various legumes seed which includes soybeans, dal seed, guar bean, hyacinth bean, peanut, horsegram, cowpea, and chickpea, has been reported to perform efficiently in turbidity removal and wastewater treatment [1]. The grain legumes are highly affordable with high amino acid and protein content. Their protein is synthesized from simple nitrogen compounds from their roots and nitrogen-fixing bacteria primarily used by legumes [2].

Several investigations using legume-based coagulants in wastewater treatment have been recorded. Lek et al., [3] reported the successful use of chickpea in removing turbidity, TSS, and COD from palm oil mill effluent (POME). A reduction of 86%, 87%, and 56% was achieved for turbidity, TSS, and COD, respectively. The FTIR analysis of the chickpea powder identified the presence of OH, CH, NH, CC, CO, CN groups which contributes to the bridging flocculation mechanism during the coagulation process [3]. Meanwhile, NaCl extraction of peanut efficiently removed 92% turbidity from the initial turbidity of 200 NTU in the work of Birima et al., [4].

Most plant-based coagulants are composed of proteins or polysaccharides which could be anionic, cationic, and non-ionic. Proteins are the main component that aids coagulation in leguminous seeds. [5]. Green beans (GB) have a protein content of 21.22 to 24.06% [2]. Pigeon Pea (PiP) is amongst the 10th most important grain legumes in Asia, Africa, and the Caribbean. It has a protein and carbohydrate content of 20-22% and 65%, respectively [6]. From various reviews of literature, no study has been done on the use of green beans and pigeon pea as a coagulant in water treatment.

II. MATERIALS AND METHODOLOGY

The green beans and pigeon pea seeds used in this research work were obtained locally in Nibong Tebal, Malaysia. The seeds were cleaned and oven-dried at 60 °C for 1 h before milling into a fine powder with the aid of a laboratory grinder. The powder was sieved using a sieve size of 1.0 mm particle size. The extraction of active coagulant from GB and PiP seeds was done by adding 2g of powder into 100 mL of 1.0 M NaCl solution, the suspension was stirred for 1 h using a magnetic stirrer. The Eppendorf Centrifuge 5702 RH was used to separate the mixture at 4000 rpm for 30 min, the filtrate obtained is the active coagulation crude extract (CE).

The CE was purified to obtain the pure form of active coagulation agent using the isoelectric precipitation method. The protein from the crude extracts was precipitated out by adjusting the pH of the solution to 2.8-3.3. The cloudy solution was further stirred for 15 min before centrifugation at 4400 rpm for 30 min. The sediment formed was washed in cold acetone and filtered with a filter paper, the powder was air-dried and ground for further analysis and experiment [7].

The water treated was prepared in the laboratory by mixing 1 g of kaolin powder to 1L of distilled water, the mixture was stirred on a magnetic stirrer for 1 h before allowing it to undergo complete hydration for 24 hours before use. For each experimental run, the kaolin solution was diluted with distilled water to obtain initial turbidity of 250 ± 10 NTU.

The functional groups responsible for coagulation efficiencies in the ground seeds powder were examined using the FT-IR Shimadzu IR affinity, using the potassium bromide (KBr) pellet method. The sample powders were

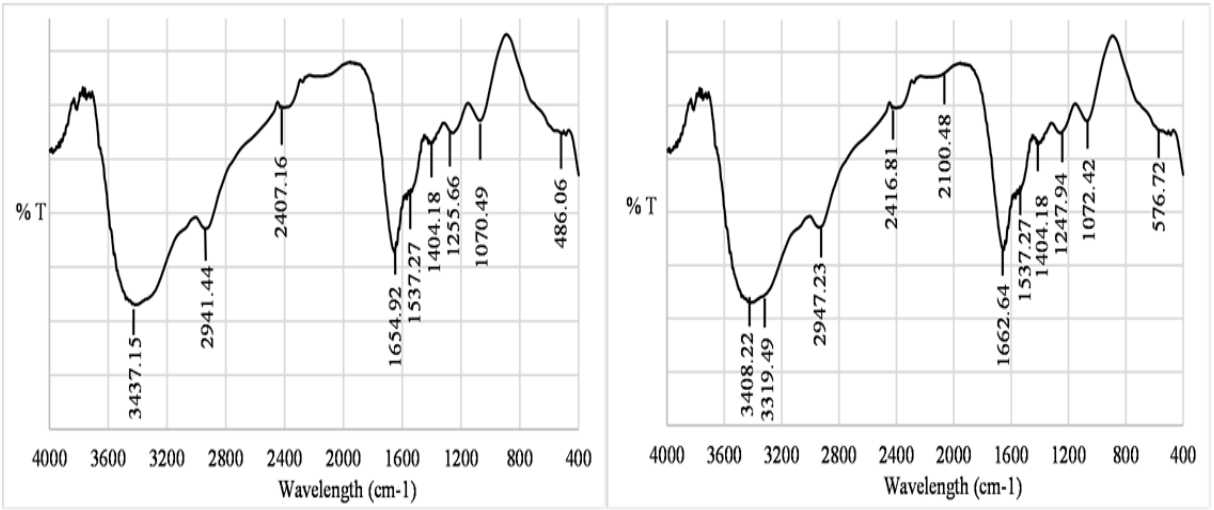
mixed with the KBr in the proportion of 10 :1 and ground, the pellet was prepared by compressing the mixture powder with a hand compressor. The FTIR analysis recorded the spectra result between the range of 4000 cm^{-1} and 400 cm^{-1}.

III. RESULT AND DISCUSSION

After the purification of the protein, the sample was left for 3 days to allow complete drying and weighed. About 3 g of green beans (GB) and pigeon pea (PiP) powdered seeds produced 7.96% and 6.53% of purified powder, respectively. The purified protein (PP) powder was used directly in solid form for the coagulation process.

The FTIR spectra identified different functional groups for the pure proteins which are shown in Fig. 1, peaks at 3437.15 (GB) and 3408.22; 3319.49 cm^{-1} (PiP) indicates the stretching of N-H bonds of secondary amines, O-H hydroxyl group, and -COOH carboxylic acid. Small peaks at 2491.44 (GB) and 2947.23 cm^{-1} (PiP) indicate the existence of the C-H stretch of alkane. The appearance of peaks at 1654.92 (GB) and 1662.64 cm^{-1} (PiP) for both samples corresponded to C=O stretching of carbonyl group was observed. Aromatic hydrocarbon C=C stretching or O-H bending carboxylic group indicated at 1404.18 (GB) and 1404.18 cm^{-1} (PiP) appeared in the FTIR spectra.

The -COOH, -OH, and N-H groups have been reported to show the presence of proteins, lipids, fatty acids, and carbohydrates which aid excellent coagulation efficiency [8]. Other peaks within the wavelengths of 1200 to 600 cm^{-1} indicate the presence of C-N stretching, C-O stretching, and C-C bending vibrations, during the coagulation process, these groups are acting as active sites for attaching the suspended particles and colloids in the water. Studies have also reported that natural coagulants are composed of proteins, carbohydrates, and lipids; also, higher protein content results in higher turbidity and suspended solids removal. [3].



(a) Green beans (GB) pure protein (b) Pigeon pea (PiP) pure protein

Fig 1: FTIR spectra of the pure protein coagulants.

Fast and slow mixing was carried out at 100 and 25 rpm for 4 and 20 min, respectively, followed by 30 min of setting time. The sample for turbidity and COD measurement was withdrawn at 3 cm below the surface using a pipette and was used for further analysis.

Jar test made with the pure protein coagulant gave a higher turbidity removal when compared with that of crude extract. PP and CE coagulants from pigeon pea seed gave a high turbidity removal of 97.17% and 91.59%, respectively. While a turbidity removal of 97.035 and 91.07% was achieved for the PP and CE coagulants from green beans seed.

The crude extracts obtained from natural coagulants have been reported to contain water-soluble organic and inorganic materials, which results in increased organic load and microbial activity in the water treated [9]. The COD analysis was done to evaluate the organic matter content in both the crude extract (CE) and pure protein (PP) treated water. The COD results obtained showed negligible change was observed in water treated with both PiP and GB pure protein coagulants. An increase of 23.5% and 13.4% were observed for water treated with PiP and GB crude extracts, respectively. These results obtained in both turbidity removal and COD evaluation indicate the effectiveness of natural coagulants in both extracted and purified forms.

IV. CONCLUSION

This study has successfully examined and proved the efficiency of green bean and pigeon pea seeds as natural coagulants in turbidity removal. The FTIR results also confirmed the presence of the functional groups responsible for coagulation. However, it was especially noted that the purified protein coagulants gave higher turbidity removal without increasing the COD level in the treated water. Therefore, it can be concluded that green bean and pigeon pea seeds-based coagulants are suitable alternatives to chemical coagulants for turbidity removal from wastewater. For this study, since the pure proteins gave good COD results, it is suggested that further

characterization and optimization study of the coagulants be done to provide more essential information for improved applications.

ACKNOWLEDGEMENT

The authors would like to acknowledge the Long Term Research Grant Scheme (LRGS/1/2018/USM/01/1/1) (LRGS/2018/USM-UKM/EWS/01) granted by the Ministry of Higher Education Malaysia for funding this research project and Universiti Sains Malaysia for the GRA-Assist Scheme provided.

REFERENCE

[1] S. Choy, K. Prasad, T. Wu, and R. Ramanan, "A review on common vegetables and legumes as promising plant-based natural coagulants in water clarification," Int. J. Environ. Sci. Technol., vol. 12, no. 1, pp. 367–390, 2015.

[2] N. Kazydub, T. Marakayeva, S. Kuzmina, M. Korobeinikova, O. Kotsyubinskaya, and A. Pinkal, "Chemical composition of seeds and green beans of common bean varieties, bred in Omsk State Agrarian University under conditions of southern forest-steppe zone of Western Siberia," Agron. Res., vol. 15, no. 5, pp. 1918–1927, 2017.

[3] B. L. C. Lek et al., "Treatment of palm oil mill effluent (POME) using chickpea (Cicer arietinum) as a natural coagulant and flocculant: Evaluation, process optimization and characterization of chickpea powder," J. Environ. Chem. Eng., vol. 6, no. 5, pp. 6243–6255, 2018.

[4] A. Birima, H. Hammad, M. Desa, and Z. Muda, "Extraction of natural coagulant from peanut seeds for treatment of turbid water," 2013, vol. 1, pp. 1–4.

[5] Z. Z. Abidin, "Ecofriendly Approach to Adsorption of Congo Red from Aqueous Media Using Chaff Powder from Jatropha curcas Seed (Isotherm and Kinetic Model)," Preprints, 2019, doi: 10.20944/preprints201903.0274.v1.

[6] S. Sarkar, S. Panda, and P. Kandasamy, "Pigeon pea (Cajanus cajan) an important food legume in Indian scenario – A review," LEGUME Res. - Int. J., Oct. 2018, doi: 10.18805/LR-4021.

[7] E.-S. Tan, N. Ying-Yuan, and C.-Y. Gan, "A comparative study of physicochemical characteristics and functionalities of pinto bean protein isolate (PBPI) against the soybean protein isolate (SPI) after the extraction optimisation," Food Chem., vol. 152, pp. 447–455, 2014.

[8] A. Daverey, N. Tiwari, and K. Dutta, "Utilization of extracts of Musa paradisica (banana) peels and Dolichos lablab (Indian bean) seeds as low-cost natural coagulants for turbidity removal from water," Environ. Sci. Pollut. Res., vol. 26, no. 33, pp. 34177–34183, 2019.

[9] J. M. Prodanović et al., "Ultrafiltration as a simple purification method of a water extract of common bean seed as a natural coagulant," Hem. Ind., vol. 74, no. 3, pp. 211–220, 2020.

The Development of a Smart Moisture Monitoring System for Precision Agriculture

Labib Sharrar
Control and Mechatronic Engineering Department, School of Electrical Engineering, Faculty of Engineering
Universiti Teknologi Malaysia
Johor Bahru, Malaysia
sharrar@graduate.utm.my

Salinda Buyamin
Control and Mechatronic Engineering Department, School of Electrical Engineering, Faculty of Engineering
Universiti Teknologi Malaysia
Johor Bahru, Malaysia
salinda@utm.my

Mohamad Shukri Zainal Abidin
Control and Mechatronic Engineering Department, School of Electrical Engineering, Faculty of Engineering
Universiti Teknologi Malaysia
Johor Bahru, Malaysia
shukri@utm.my

***Abstract*— The agriculture industry plays a crucial part in the modern world, especially because of the ever-growing need for organic food. While the agriculture sector is indeed important, it is also responsible for consuming massive amounts of water and depleting natural water reserves across the globe. The conventional means of irrigation lead to much water wastage. Fortunately, the advent of the Internet of Things (IoT), has been a game-changer for the agriculture sector. Now, it is possible to use Wi-Fi integrated embedded devices to remotely monitor the moisture level of crops, and water them efficiently. Thus, this paper presents a prototype system that can monitor plant moisture and indicate the precise amount of water needed. The system makes use of a simple NodeMcu ESP8266 module to read the moisture content of plants using sensors and send the data wirelessly through the Firebase IoT platform to an android application. It can be used as part of an intelligent irrigation system and could inform users about the moisture status of their crops. Overall, this system should enable efficient usage of water and could play an important role in precision agriculture.**

Keywords*— *android application, Arduino IDE, Firebase, Internet of Things, moisture, NodeMcu ESP8266, user interface.

[1] INTRODUCTION

It is said that over 70% of the world is covered in water, but only 0.08% of that amount is freshwater that can be used for living purposes [1]. As such, water scarcity is a major problem across the globe. One of the major consumers of water is the agriculture industry, which accounts for 70% of water usage [2]. Most of the conventional irrigation systems simply water crops without considering the precise amount of water that is required in each crop. This leads to a significant wastage of water. Hence, developing an intelligent irrigation system that can utilize water resources efficiently would truly be beneficial to overcome our water scarcity problem. Fortunately, this can be accomplished with the help of the Internet of Things (IoT). The technology has garnered immense interest among industries. Having a Wi-Fi integrated system that enables users to remotely monitor data and make optimum usage of resources. As such, IoT has been used to carry out a wide range of activities, such as measuring temperature, humidity, or light [3], remotely controlling home appliances [4], monitoring water levels in dams [5], and sending flood warnings [6].

The agricultural sector can especially benefit from IoT-based monitoring systems. Due to the increasing necessity for organic fruits and vegetables, efficient watering of crops is required to ensure the highest quality of edible products [7]. However, since the agriculture sector is responsible for vast water consumption, the concept of precision farming, which uses IoT-based monitoring systems to optimize water usage, is becoming increasingly popular. The popularity of IoT technology in agriculture also esteems from its compatibility with mobile applications. Wi-Fi integrated embedded devices can send the moisture data, humidity, and temperature of the crops over the internet to the farmers. Farmers, in turn, can simply use mobile applications to monitor the requirements of the crops and take the right course of action. While moisture monitoring systems have been proposed over the years, they have rarely been implemented. This might be because they made use of complex hardware. For example, Husni et al. [8], proposed a system that uses Field Programmable Gate Array (FPGA) to monitor soil moisture. Although the system is claimed to be working FPGA is complex hardware and requires experts to handle it. It is possible to overcome these issues by using more user-friendly hardware such as Arduino.

Thus, this paper illustrates an IoT-based moisture monitoring prototype system for crops. It should be noted that the prototype presented in this paper represents a sub-part of the precision irrigation control system presented in the paper published by Abioye et al. [9]. While this is not the original part presented in that paper, it is an experimental version of the setup which illustrates details of the moisture monitoring system. The part this prototype represents is marked in Fig. 1.

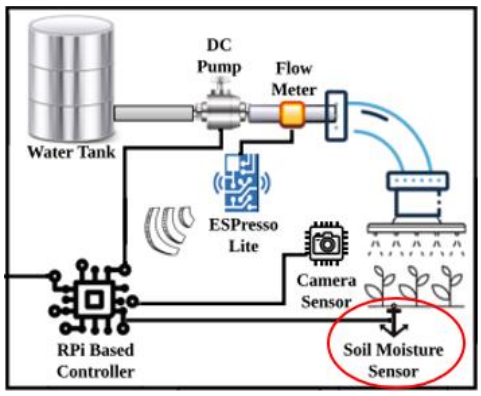


Fig. 1. The prototype presented in this paper represents the marked sector shown in the diagram by Abioye et al. [9].

The prototype is controlled by a NodeMcu ESP8266 module, which is an affordable Wi-Fi integrated microcontroller. Hence, the NodeMcu is connected to the Firebase platform. So, the microcontroller reads the moisture data using the sensors and sends them through the Firebase platform to an android application (app). After taking the reading from the app, the user can understand how much water the crop requires. Thus, this will optimize the overall farming process, and make efficient use of water. It should be noted that the prototype presented in this paper is being implemented on cantaloupe or rockmelon plants as they are more commonly known. The proposed prototype can be considered

as a smart system since it can inform the user about the moisture levels of the rockmelon plants in real-time. If the moisture level drops below a certain threshold, then it will be indicative that the plant requires water. Additionally, it can also be connected to a larger system, as demonstrated by Abioye et al. [9], which can automatically water the plants when the moisture levels fall below the set threshold.

[2] Methodology

A. System Overview

The primary purpose of the monitoring system is to measures the moisture level and send the data to the user via the Firebase IoT platform. The user will then view the data using a custom-made app. A NodeMcu ESP8266 microcontroller is used as the primary processor. It is open-source hardware that possesses a 160 MHz single-core Central Processing Unit (CPU) and 128 kB of Random-Access Memory (RAM) [10].

Commonly there are two types of moisture sensors, resistive or capacitive. Electrolysis takes place during moisture sensing. This can cause the copper coating on resistive sensors to erode. Thus, due to the low life cycle of resistive sensors, capacitive sensors were chosen instead as they were less prone to erosion. It should be noted that these sensors are only used as part of the prototype since they are cheaper. In the original system presented by Abioye et al. [9], the VH 400 soil moisture sensors are used. To use more than one sensor the ADS1015 analog expansion board is connected to the microcontroller board using the I^2C interface.

As the NodeMcu module reads the moisture data, it transmits the data to the Firebase platform where it is stored in its cloud database. To enable the user to keep track of the moisture level in plants, an android application (app) is developed. This app is equipped with the Firebase plugin. As such, the user can simply access the rockmelon plants' moisture data in the cloud database through the app. A block diagram representing the overview of the system is shown in Fig. 2.

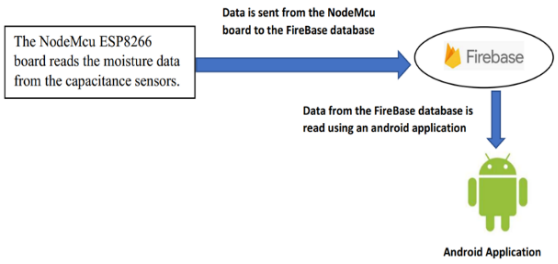


Fig. 2. Overview of the plant moisture monitoring system.

B. System Schematic

A total of four moisture sensors were interfaced with the NodeMcu ESP8266 board. While their readings could be seen on the app, they were also shown on an LCD display, to make it easier for the user to read the moisture data on the site. The schematic of the entire moisture monitoring system is shown in Fig. 3.

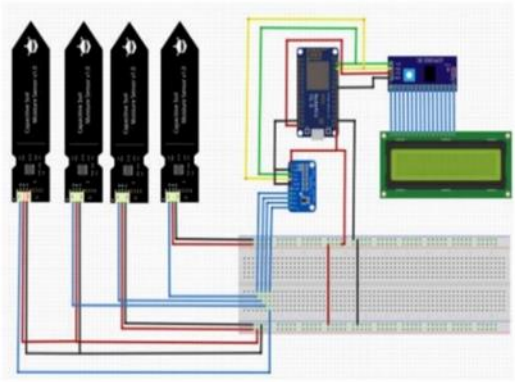


Fig. 3. Schematics of the moisture monitoring system.

C. Sensor Calibration

It should be noted that the reading from the moisture sensors is in the form of 10-bit (0 to 1023) readings. Thus, it is necessary to find a way to represent these readings as moisture data. The number 1023 is a 5V reading from the moisture sensor, which represents the maximum amount of moisture. Overall, moisture is the percentage of water in a certain area. Since the actual sensor readings are in 10-bit form, it is necessary to calibrate the sensor readings such that they can represent moisture content.

Overall, calibrating moisture sensors is a crucial part of this project. For that sole purpose, an experiment is carried out using a moisture sensor with a specific fertilizer, that is necessary for crop growth. Before the experiment is conducted, however, the microcontroller is programmed to read the 10-bit form readings from the moisture sensors in volts. To do that, the following formula was applied in the NodeMcu ESP8266 code:

$$\frac{\text{sensor reading}}{1023} \times 3.33\,V \qquad (1)$$

Since 1023 is the maximum 10-bit reading, the actual sensor reading is divided by that number and multiplied by 3.33 V, which is the maximum input and output voltage for a NodeMcu I/O pin. The steps for the experiment are illustrated below:

1. The fertilizer is to be placed in a bucket to experiment. However, the first step is to measure the weight of the empty bucket.
2. Fertilizer is poured into the bucket and it is weighed again.
3. Place the moisture sensor in the dry fertilizer as shown in Fig. 4 and record the voltage output from the sensor
4. 50 ml of water is added to the bucket and the fertilizer is mixed thoroughly with the water.
5. The output voltage of the sensor is recorded once more.
6. The bucket is weighed again.
7. The result for the moisture content is obtained using the formula:

$$\frac{(\text{sample weight + water}) - \text{weight of dry sample}}{(\text{sample weight + water})} \times 100\,\% \qquad (2)$$

8. Steps 4, 5, 6, and 7 are repeated until the volume of water added to the fertilizer is 300 ml.



Fig. 4. The moisture sensor is placed in a bucket of fertilizers.

The data and the calculated moisture content of the sample are recorded in Table 1.

Table 1. Measurements from the experiment.

Measurements from the Experiment				
Empty Bucket (g)	Weight Sample + Bucket (g)	Water Quantity (ml)	Moisture (%)	Voltage (V)
96.05	169	0	0	3.33
96.05	219	50	40.67	3.00
96.05	265	100	56.82	2.60
96.05	315	150	66.68	2.33
96.05	359	200	72.26	1.70
96.05	415	250	77.13	0.97
96.05	454	300	79.62	0.10

After the readings are recorded in the table above, the best must line is plotted through the data points so that the sensor readings can be calibrated accordingly. The graph for the best fit line is shown in Fig. 5.

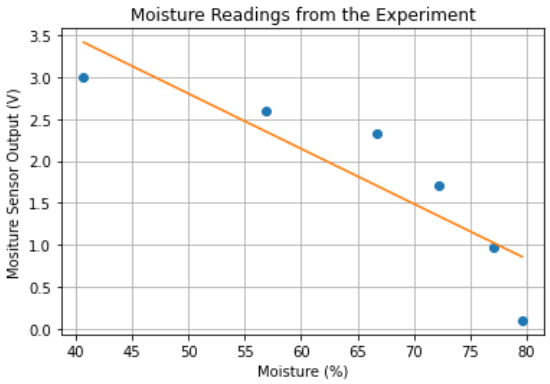
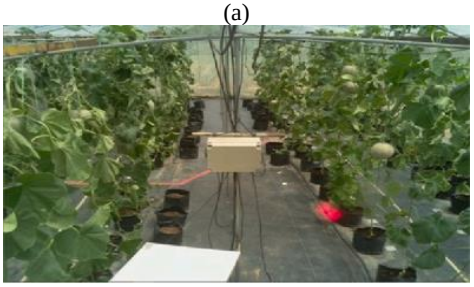


Fig. 5. Graph of the best fit line of output voltage reading against the percentage of moisture.

The equation of the straight-line graph shown in Figure 5 can be obtained by calculating the gradient and bias. This equation is then placed in the NodeMcu ESP8266 code to calculate the moisture content for each corresponding voltage output of the sensors. Overall, this how the moisture sensors are scaled to ensure that they read the moisture content of the soil accurately.

In order to calibrate the sensors precisely, the calibration is done inside a greenhouse where the crops are grown. The actual system presented by Abioye et al. (2021) [9], to which this prototype is related, is implemented in the same area. The greenhouse is shown in Fig. 6.

(a)



(b)



Fig. 6. The greenhouse where the sensor calibration is done [9].

For this project, a threshold is used to determine whether the rockmelon plant requires water. The threshold set is 30%. If the moisture level drops below this level, it will indicate that the plants need more water. Furthermore, it should be noted that this has been a 75-day project, and the total amount of water added to the rockmelon plant during that period is tabulated in Table 2.

Table 2. The volume of water added to the rockmelon plants.

Days	Date	Water Supply (ml)
1 - 7	15/10/2020 – 21/10/2020	2 × 100
8 – 14	22/10/2020 – 28/10/2020	3 × 150
15 – 21	29/10/2020 – 4/11/2020	4 × 150
22 – 28	5/11/2020 – 10/11/2020	4 × 150
29 – 34	11/11/2020 – 17/11/2020	4 × 150
35 - 41	18/11/2020 – 24/11/2020	5 × 150
42 – 48	25/11/2020 – 1/12/2020	5 × 150
49 - 55	2/12/2020 – 8/12/2020	5 × 200
56 - 62	9/12/2020 – 15/12/2020	5 × 200
63 - 69	16/12/2020 – 22/12/2020	5 × 200
70 - 77	23/12/2020 – 29/12/2020	5 × 200

D. Android Application Development

An android application is developed using the Android Studio software. The development of an app can be divided into two different parts. The frontend and the backend. Users interact with the app through the frontend. This part is designed using the XML language. As for the backend of the app, which is responsible for executing operations, it is coded in the Java programming language.

To ensure that the app can receive the moisture data from the NodeMcu ESP8266, the Firebase plugin had to be installed in Android Studio. The app is designed to be capable of displaying the moisture content of the plants in real-time and display the trend in moisture levels throughout the day. The appearance of the app is shown in the next section.

[3] Results and analysis

Regarding the sensor module, getting the correct output can be quite challenging since the ADC extension module has a different resolution compared to the ADC of the NodeMcu ESP8266 module. Nevertheless, this challenge can be solved by using the *map()* function in Arduino IDE. Additionally, the sensors are calibrated to ensure they give the correct results. The circuit shown in Figure 3 was soldered onto a donut board. The actual circuit board is displayed in Fig. 7.

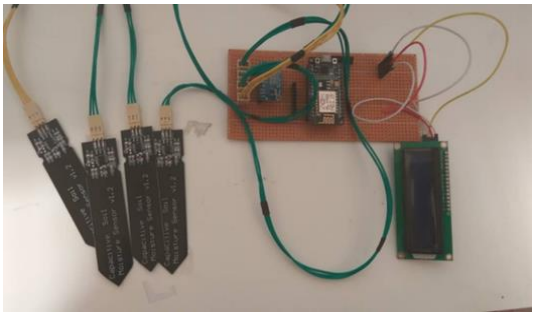


Fig. 7. The actual circuit of the moisture sensor module.

Overall, it is safe to say that the sensor module can operate according to plan. Furthermore, the Wi-Fi integrated microcontroller can successfully connect with the Firebase IoT platform, which enables the user to get real-time data using the app. The mobile application created by Android Studio is capable of displaying the results of each sensor. For every one of the sensors, a gauge shows a plant's moisture level, and a graph displays the level of moisture throughout the day along with the date and time. The first page of the app gives the user the option to check the status of any of the four sensors. An image of the first page and a status page is shown in Figure 8. If the moisture level as shown by the app drops too much, then the user will know that it is time to water the rockmelon plants. To conclude this section, the system can achieve satisfactory results. It reads the plant moisture and sends the data wirelessly to the user.

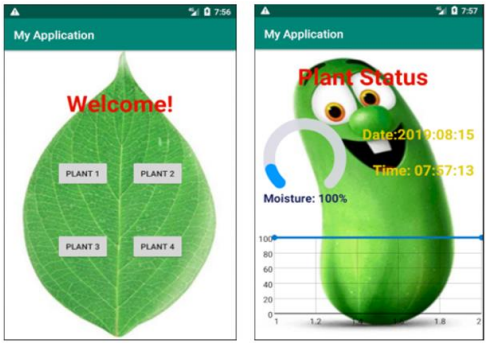


Fig. 8. The app for the moisture monitoring system.

[4] Conclusion

To conclude, this paper presents a prototype that represents a part of a real-time precision irrigation system. The responsibility of this subsystem is to monitor the moisture content of plants. The system enables users to remotely read the data using an android application. As this is a prototype or an experimental version, it is mostly made up of cost-effective open-source hardware. It is controlled by a NodeMcu ESP8266 processor, which is interfaced with capacitive moisture sensors. The board is connected to the Firebase IoT platform. Data from the board are stored in the Firebase database, which can be accessed through the app. This system displays the moisture level of crops in real-time, as well as shows the trend in moisture levels throughout the day. As such, it can indicate the precise amount of water required. This system can enable efficient usage of water, and thus, reduce the overall water consumption of the agricultural sector.

ACKNOWLEDGMENT

This work was supported in part by the Ministry of Higher Education, Malaysia, through research fund vote No. R.J130000.7351.4B428. The authors would also like to acknowledge the facilities provided by the Universiti Teknologi Malaysia, for the accomplishment of this work.

REFERENCES

[1] C. Rajurkar, S. R. S. Prabaharan, and S. Muthulakshmi, "IoT based water management," *2017 Int. Conf. Nextgen Electron. Technol. Silicon to Software, ICNETS2 2017*, pp. 255–259, 2017, doi: 10.1109/ICNETS2.2017.8067943.

[2] Z. Qin, *Precision Agriculture Technology for Crop Farming*, 2016.

[3] C. Yoon, M. Huh, S. G. Kang, J. Park, and C. Lee, "Implement smart farm with IoT technology," *Int. Conf. Adv. Commun. Technol. ICACT*, vol. 2018-February, pp. 749–752, 2018, doi: 10.23919/ICACT.2018.8323908.

[4] H. Durani, M. Sheth, M. Vaghasia, and S. Kotech, "Smart Automated Home Application using IoT with Blynk App," *Proc. Int. Conf. Inven. Commun. Comput. Technol. ICICCT 2018*, no. Icicct, pp. 393–397, 2018, doi: 10.1109/ICICCT.2018.8473224.

[5] S. S. Siddula, P. Babu, and P. C. Jain, "Water Level Monitoring and Management of Dams using IoT," *Proc. - 2018 3rd Int. Conf. Internet Things Smart Innov. Usages, IoT-SIU 2018*, pp. 5–9, 2018, doi: 10.1109/IoT-SIU.2018.8519843.

[6] N. A. Z. M. Noar and M. M. Kamal, "The development of smart flood monitoring system using ultrasonic sensor with blynk applications," *2017 IEEE Int. Conf. Smart Instrumentation, Meas. Appl. ICSIMA 2017*, vol. 2017-Novem, no. November, pp. 1–6, 2018, doi: 10.1109/ICSIMA.2017.8312009.

[7] A. M. Ezhilazhahi and P. T. V. Bhuvaneswari, "IoT enabled plant soil moisture monitoring using wireless sensor networks," *Proc. 2017 3rd IEEE Int. Conf. Sensing, Signal Process. Secur. ICSSS 2017*, pp. 345–349, 2017, doi: 10.1109/SSPS.2017.8071618.

[8] M. I. Husni, M. K. Hussein, M. S. Bin Zainal, S. A. Bin Hamzah, D. Bin Md Nor, and H. Bin Mhd Poad, "Soil moisture monitoring using field programmable gate array," *Indones. J. Electr. Eng. Comput. Sci.*, vol. 11, no. 1, pp. 169–174, 2018, doi: 10.11591/ijeecs.v11.i1.pp169-174.

[9] E. A. Abioye, M. S. Z. Abidin, M. N. Aman, M. S. A. Mahmud, and S. Buyamin, "A model predictive controller for precision irrigation using discrete lagurre networks," *Comput. Electron. Agric.*, vol. 181, no. December 2020, p. 105953, 2021, doi: 10.1016/j.compag.2020.105953.

[10] P. Serikul, N. Nakpong, and N. Nakjuatong, "Smart Farm Monitoring via the Blynk IoT Platform : Case Study: Humidity Monitoring and Data Recording," *Int. Conf. ICT Knowl. Eng.*, vol. 2018-Novem, pp. 70–75, 2019, doi: 10.1109/ICTKE.2018.8612441.

Fabrication and Characterization of ZnO/Polyaniline Based Fet Structure H_2 Gas Sensor

Mücella ÖZBAY KARAKUŞ
Computer Enginnering Yozgat Bozok University
Yozgat, Turkey
mucella.karakus@bozok.edu.tr

Aim: **In this work, we discuss the hydrogen (H_2) gas sensing behavior of Polyaniline (PANI) and PANI/ZnO nanocomposite-based Field Effect Transistor (FET) sensors.**

Method: **For this purpose, firstly, PANI was synthesized with and without ZnO nanoparticles. For gas detection application, microstructure ZnO doped and undoped PANI based FET sensors were fabricated through the photolithography technique and then the thermal evaporation process onto the Si/SiO_2 (285 nm) substrate. For determining the electrical properties of PANI based FET devices Cr/Au metals with the thicknesses of 20/30 nm respectively were deposited to obtain the Drain and Source contacts for the connection. The aqueous solution of PANI precursor which was solved in 1-methyl-2-pyrrolidone was then drop between the metal coated Source-Drain connections and let to dry. The transfer characteristics (I_{DS}-V_g) of the FETs were performed in the range of (-40)-(+40) V for Vg values.**

Results: **The output characteristics were also investigated, and FET characteristic of the sensor device was proved. The electrical responses of the produced sensors against H_2 gas were determined by measuring the Source-Drain current at 25 ˚C, 50 ˚C and 80 ˚C while applying the +20 V gate voltage to the FET sensors.**

Conclusion: **It has been observed that the sensors which were produced by PANI channel, detect H_2 gas but adding ZnO nanocomposite into PANI improves the detection performance. In addition, unlike the PANI channel FET sensor, it has been determined that PANI/ZnO channel FET sensors operate with a very good performance at room temperature. The sensitivity of the PANI/ZnO nanocomposite FET sensor has deteriorated as the sensor temperature increases. Thus, it was determined that ZnO nanoparticles' presence in the polymer structure caused a significant improvement in sensor response and lowered the operating temperature.**

Keywords—ZnO doped polyaniline, polyaniline fet, H_2 gas sensor

LIB-based static vs. LAB-based rotary UPS: Total cost of ownership

P.K. Ngongo
Electrical Engineering Department Cape Peninsula University of Technology Cape Town, South Africa
prospernk34@gmail.com

MTE Kahn
Electrical Engineering Department Cape Peninsula University of Technology Cape Town, South Africa
KhanT@cput.ac.za

***Abstract*—This paper presents a comparative analysis of the total cost of ownership (TCO) or operational savings of a new static lithium-ion-based UPS following the replacement of an old 3-phase online motor-generator lead-acid-based UPS system with this newer high-performance static lithium-ion-based alternative. The main goal of this paper is to compare these two UPS technologies and support their operational costs with practical analysis. The current rotary UPS (RUPS) system has attained its end of life and spare parts are essentially unavailable or extremely expensive. This comparative analysis approach will elaborate energy management, optimization, and saving of each UPS technology that helps strengthen facility capacity in the energy efficiency and a reduction in carbon dioxide emissions aligned with SANS/ISO 50001.**

Keywords—Rotary UPS, Static UPS, Lithium-ion battery, Lead-acid battery, Total cost of ownership.

[1] INTRODUCTION

A challenge for the business industry nowadays is to optimize the functionality of their critical assets. They rely on a sturdy power supply to increase their operational availability and remain competitive. Increased use of modern electronic equipment, based on their design specifications and accuracy expected, requires to be supplied by a high integrity power source to increase their robustness against the damaging effect of power disturbances. Eskom's network instability, lower energy availability factor, and poor power quality cannot guarantee that. For this, the facility's distribution reticulation has 4 x 1100kVA online lead-acid-based rotary UPSs installed to condition power. The system was commissioned back in 1995 with an autonomy of 15 minutes. This traditional rotary UPS technology, which now requires regular costly maintenance, suffers higher fixed and variable losses (pony motor, frictional) characterizing its inefficiency. The system has attained its end of life and spares are unavailable. Battery cells require biannually maintenance costing R300 000 per annum. Although this is considered a legitimate running cost, it occurs on a capital scale with repetitions of 8-10 years. Given the system's age and inefficiency, the facility would be efficiently and cost-effectively served by a newer high-performance lithium-ion-based static UPS (SUPS) system.

Several papers have elaborated on the beneficial effects in evaluating the UPS efficiency, losses effects between static and rotary UPS system, while others provided sort of a framework to guide the user to the selection of the best UPS and decision on what type of UPS to be deployed based on their specific circumstances and requirements [5,10,11]. Unfortunately, this evaluation, selection, or decision elaboration process cannot be made to fit aspects of all facilities. These aspects are situational and subject to requirements imposed by the concerned facility. As the energy analysis of any UPS system is linked to costs, the assessment of these costs can approximately be determined by examining its electrical energy wasted. Nevertheless, where an optional UPS system is available in the market, it is always necessary to compare the performance of the existing UPS system with this alternative system by separately determining their wasted energy costs and assessing the total costs on a common basis to establish if the system selected is optimum and economical. The main objective of this paper is, therefore, to present a comparative analysis of the operational savings (TCO) of a new static lithium-ion-based UPS following the replacement of an old 3-phase online lead-acid-based rotary UPS system with this newer high-performance static lithium-ion-based alternative. A specific facility-based evaluation approach will be elaborated where this TCO will exclusively be analysed. These data are very useful in fully informed decision-making, budget motivation, determination of their economic competitiveness, and how quickly they repay the capital investment injected into them.

[2] OPERATIONAL ENERGY LOSSES

The four old 3-phase rotary lead-acid-based UPSs are to be analysed in comparison with the four, newly selected, static modular double-conversion lithium-ion-based UPSs of the same size. The main characteristics of both UPS systems to be analysed are specified in Table I [2,3,6,7,13,14].

Table 1. UPS Main Characteristics

UPS Details	Rotary UPS	Static UPS
UPS Type	Piller UB1100S	Eaton Xpert 9395P
BESS	Lead-acid	Lithium-ion
UPS modules	4	4
Input/output voltage	600/600VAC	600/600VAC
UPS module rating	1100kVA	1100kVA
UPS efficiency	92%	97%
Input power factor	0.8	1
Total output power	1100 x 0.8 = 880kW	1100 x 1 = 1100kW

A. Rotary UPS Energy Storage System

The rotary UPS system uses BAE OGi single-cell, vented, or flooded lead-acid batteries. Each UPS has 264 x BAE Secura 25-OGi-2000 cells connected in series. A considerable amount of heat is transformed over and above the alteration of mass and exchange or transfer of electrical energy emanating from the chemical reactions during the float, discharge, and charge operation [1,2,3,12].

a) Float operation: The heat dissipation power during the float operation mode for one cell can be calculated by the following formula:

$$P_{float} = \left(U_{float} - U_{gas}\right) \times I_{float} + R_i \times I_{ac}^2 \quad (1)$$

Where, *Ufloat* is the float voltage given to be equal to 2.23 volt per cell (VPC), *Ugas* is the constant describing the water decomposing voltage given to be equal to 1.48V for all flooded batteries assuming that all the current is used for water decomposition, *Ifloat* is the float current (at normal conditions of 20°C operating temperature and 2.23VPC float voltage, the float current is nearly 25mA/100Ah of nominal capacity for flooded or vented batteries and during battery lifetime this float current increases by a factor of 1.5 to 2 caused by antimony poisoning of the batteries), *Ri* is the internal resistance of the cell equal to 0.09mΩ (the internal resistance depends on the plate design of the cells and the capacity as read from BAE 25-OGi-2000, vented lead-acid cells batteries - technical specification), and *Iac* is the effective ripple current of the charging unit (according to EN 50272-2, the maximum allowed permanent ripple current is 5A per 100Ah).

$$P_{Float} = (2.23 - 1.48) \times \left[2000Ah \times \frac{25mA}{100Ah}\right] + 0.09 \times 10^{-3}\Omega \times \left[\left(\frac{5A}{100Ah}\right) \times 2000Ah\right]^2 = 1.275W \quad (2)$$

b) *Discharge operation:* Heat dissipation during discharge operation depends on the discharge current and the difference between open-circuit voltage (U_0 = 0.84 + electrolyte gravity) and the actual discharge voltage of the battery cell. This formula is used to calculate heat dissipation per cell:

$$P_{discharge} = \left(U_0 - U_{discharge}\right) \times I_{discharge} \quad (3)$$

For all calculations, a discharge during 1 hour is assumed with a final voltage of 1.8VPC. As for the discharge current, the corresponding current (I_{1h}) from the BAE project planning data is selected.

$$P_{discharge} = [(0.84+1.24)-1.8] \times 1069 = 299.32W \quad (4)$$

c) Recharge operation: The calculation is nearly the same as at discharge operation. The heat dissipation is now a product of the mean value of recharge current and the difference between the open-circuit and the recharge voltage. The heat dissipation due to the ripple current is neglected because it is less than 5% of the recharge current effect. The calculation is carried out for an initial recharge current of 1.5 x I_{10} (nominal current) and a boost charge voltage of 2.4V. The recharge time for the calculation is limited to a charging factor of 1. The average current during the boost charge operation can be assumed as 90% of the initial current.

$$P_{recharge} = \left(U_{recharge} - U_0\right) \times I_{recharge} \quad (5)$$

Recharge during 360 minutes (6 hours) of BAE 25-OGi-2000 cell, initial charging current 200A, the average charging current will then be = 1.5 x I_{10} x 0.9 = 1.5 x 200 x 0.9 = 270A.

$$P_{recharge} = [(2.23 \pm 1\%) - (0.84+1.24)] \times 270 = 46.521W \quad (6)$$

B. Lead-acid Battery Room's Ventilation

To control temperature and prevent the unsafe accumulation of hydrogen gas, the battery room consists of the heating, ventilation, and air conditioning (HVAC) #1 & 2; both are of York make and require a 3-phase supply. The cooling and heating input power of HVAC#1 is, respectively, rated at 21kW and 14kW, and for HVAC#2, these powers are, respectively, rated at 16kW and 14kW.

C. Lithium-ion Battery System Rating

To provide 20 minutes of backup time at 100% UPS loading required for critical loads, 20 battery racks associated with each static UPS are installed. Racks will contain 16 x 8S1P modules (model: prismatic LMO - Samsung SDI) for every single string. The 16 battery modules are connected in series via provided busbar links to make a cabinet or rack. Some of the battery system parameters are as follow [6,7,14]:

- Cell voltage: 3.8V
- Cell capacity: 67Ah, 254Wh
- Module configuration: 8S1P
- Module voltage = 30.4V (8 x 3.8VPC)
- Cabinet configuration: 128S1P
- Cabinet nominal input/output voltage = 486.4V
- Battery energy storage system (BESS): 128S20P

D. Estimate Capital Expenditure for new Static UPS

The cost of the UPS power plant, 4 x 1100kVA Eaton Xpert 9395P static UPSs, is R8 977 528 and the cost of their 4 x 128S20P lithium-ion BESSs is R28 791 920. Pricing on the UPS units and BESSs indicated above were obtained from a quotation requested from Eaton Electric (PTY) Ltd. in South Africa.

[3] TOTAL COST OF OWNERSHIP

A. Assumptions

All calculations are based on the following assumptions. Based on data obtained from Eskom, the facility had 67 interruptions sustained above 5 minutes in the past 10 years, giving an average of 7 interruptions per year [9]. For that, we assume to have 7 complete battery discharges and recharges a year. The discharge is made through a full 15 minutes design backup time to translate to a monthly discharge period of 0.146 hours (7 x 15min/12 x 60). Each charging process takes 6 hours and translates to a monthly charge period of 3.5 hours (7 x 6hrs/12 = 3.5hrs). With the average number of hours per month taken to be 730 hours and based on monthly discharge and charge periods determined above, we can deduce that lead-acid batteries will be in floating operation for the rest of the time when not discharging or charging and this is equivalent to 726.35 hours a month. Two ventilation units are used to control battery room temperature and prevent the unsafe accumulation of hydrogen gas. The system is designed to run both units for lead-acid batteries and only one single unit for lithium-ion batteries at full capacity during summertime (low-demand season) to compensate for their winter (high-demand season) consumptions. Through energy transformation from electrical to heat developed in our system, we will assume that of every Watt of dissipated heat energy by any equipment, 60% Watt of electrical power is being consumed.

The determination of total cost of ownership is based on energy costs from Eskom's time of use (TOU) – 2020/2021 Miniflex tariff structure where all ancillary charges are included. Energy distribution through this comparison is made in alignment with facility 2019/2020 profile where distribution coefficients are deduced as per below [4,8,9,15]:

a) High-demand season (HDS) energy ratios

Peak energy average = 0.309X

Standard energy average = 0.794X

Off-peak energy average = X

(X + 0.309X + 0.794X) = Y

X = Y/2.103

Y = Total seasonal energy calculated

X = Multiplying factor = Off-peak energy

b) Low-demand season (LDS) energy ratios

Peak energy average = 0.297X

Standard energy average = 0.759X

Off-peak energy average = X

(X + 0.297X + 0.759X) = Y

X = Y/2.056

Y = Total seasonal energy calculated

X = Multiplying factor = Off-peak energy

Energy charges (peak, off-peak, and standard energy) used in the calculation are based on Eskom's 2020/2021 financial year charges as given in Table II below [4,8,9,15]:

Table 2. Energy Charges

Energy Details	HDS Charges	LDS Charges
Peak energy (R/kWh)	3.6785	1.1997
Standard energy (R/kWh)	1.1142	0.8256
Off-Peak energy (R/kWh)	0.6048	0.5239

B. Rotary UPS Losses Calculation and Energy Distribution

a) UPS heat energy losses: With the maximum heat dissipation of each rotary UPS given to be 87kW, 60% of this heat represents electrical power being consumed and equal to 87 x 0.6 = 52.2kW. For all four UPSs running throughout 730 hours of the month, the monthly electrical energy is found to be equal to 52.2 x 730 x 4 = 152 424kWh.

b) Battery room cooling losses: For the lead-acid battery room, it was assumed above to run both ventilation units at full capacity during summertime. Total cooling power of both air-conditioning units used is (21 + 16) = 37kW leading to a monthly electrical energy of 37 x 730 = 27 010kWh.

c) Rated operation losses: Calculated, the rated loss is found to be equal to 76.5kW, and for all four UPSs running throughout 730 hours of the month, the monthly electrical energy is found to be equal to 76.5 x 730 x 4 = 223 380kWh.

d) Batteries floating operation losses: As calculated in (2), the heat load during floating operation per cell was 1.275W, 60% of this heat represents electrical power being consumed, and for all 1056 cells floating 726.35 hours a month as demonstrated in Section III(A), the monthly electrical energy will then be equal to 1.275 x 0.6 x 1056 x 726.35 = 587kWh.

e) Batteries discharge operation losses: As calculated in (4), the heat load during discharge operation per cell was 299.32W, 60% of this heat represents electrical power being consumed, and for all 1056 cells discharging 0.146 hours on average a month as demonstrated in Section III(A), the monthly electrical energy will then be equal to 299.32 x 0.6 x 1056 x 0.146 = 27.7kWh.

f) Batteries recharge operation losses: As calculated in (6), the heat load during recharge operation per cell was 46.521W, 60% of this heat represents electrical power being consumed, and for all 1056 cells charging 3.5 hours on average a month as demonstrated in Section III(A), the monthly electrical energy will then be equal to 46.521 x 0.6 x 1056 x 3.5 = 103.165kWh.

g) High-demand season wasted energy distribution:

Y = 152.42 + 223.38 + 0.587 + 0.028 + 0.103 = 376.518MWh

X = Off-peak energy = 376.518 / 2.103 = 179.04MWh

Peak energy = 179.04 x 0.309 = 55.32MWh

Standard energy = 179.04 x 0.794 = 142.16MWh

h) Low-demand season wasted energy distribution:

Y = 152.42 + 27.01 + 223.38 + 0.587 + 0.028 + 0.103 = 403.528MWh

X = Off-peak energy = 403.528 / 2.056 = 196.27MWh

Peak energy = 196.27 x 0.297 = 58.29MWh

Standard energy = 196.27 x 0.759 = 148.97MWh

i) High-demand season backup energy distribution:

Y = 4400 x 0.8 x 0.146 = 514kWh

X = Off-peak energy = 514 / 2.103 = 244.41kWh

Peak energy = 244.41 x 0.309 = 75.52kWh

Standard energy = 244.41 x 0.794 = 194.1kWh

j) Low-demand season backup energy distribution:

Y = 4400 x 0.8 x 0.146 = 514kWh

X = Off-peak energy = 514 / 2.056 = 250kWh

Peak energy = 250 x 0.297 = 74.25kWh

Standard energy = 250 x 0.759 = 189.75kWh

C. Static UPS Losses Calculation and Energy Distribution

a) SUPS heat energy losses: With the maximum heat dissipation of each static UPS given to be 61kW, 60% of this heat represents electrical power being consumed and equal to 61 x 0.6 = 36.6kW. For all four UPSs running throughout 730 hours of the month, the monthly electrical energy is found to be equal to 36.6 x 730 x 4 = 106 872kWh.

b) Heat output from battery cabinets: With the maximum heat dissipation of each battery cabinet given to be 567 British thermal unit (BTU) per hour, and with 1BTU/hr equal to 0.2931W, the heat dissipation in Watt will then be equal to 567 x 0.2931 = 166.131W = 0.166kW. With 60% of this heat representing electrical power being consumed, the active power consumed will then be equal to 0.166 x 0.6 = 0.0996kW. For all 80 (20 x 4) cabinets running throughout

730 hours of the month, the monthly electrical energy is found to be equal to 0.0996 x 730 x 80 = 5 816.64kWh.

c) Battery room cooling losses: For the lithium-ion battery room, it was assumed above to run only one ventilation unit at full capacity during summertime. One single air-conditioning unit of 16kW is used. This leads to a monthly cooling electrical energy of 16 x 730 = 11 680kWh.

d) Rated operation losses: Calculated, the rated loss is found to be equal to 34.02kW, and for all four UPSs running throughout 730 hours of the month, the monthly electrical energy is found to be equal to 34.02 x 730 x 4 = 99 338.4kWh.

e) Batteries waste heat energy during floating, discharge, and recharge operation is zero as cells are controlled by a battery management system (BMS).

f) High-demand season wasted energy distribution:
Y = 106.87 + 5.817 + 99.34 = 212.027MWh

X = Off-peak energy = 212.027 / 2.103 = 100.82MWh

Peak energy = 100.82 x 0.309 = 31.15MWh

Standard energy = 100.82 x 0.794 = 80.05MWh

g) Low-demand season wasted energy distribution:
Y = 106.87 + 5.817 + 11.68 + 99.34 = 223.707MWh

X = Off-peak energy = 223.707 / 2.056 = 108.807MWh

Peak energy = 108.807 x 0.297 = 32.316MWh

Standard energy = 108.807 x 0.759 = 82.58MWh

h) High-demand season backup energy distribution:
Y = 4400 x 1 x 0.146 = 642.4kWh

X = Off-peak energy = 642.4 / 2.103 = 305.47kWh

Peak energy = 305.47 x 0.309 = 94.4kWh

Standard energy = 305.47 x 0.794 = 242.54kWh

i) Low-demand season backup energy distribution:
Y = 4400 x 1 x 0.146 = 642.4kWh

X = Off-peak energy = 642.4 / 2.056 = 312.45kWh

Peak energy = 312.45 x 0.297 = 92.8kWh

Standard energy = 312.45 x 0.759 = 237.15kWh

[4] RESULTS

The net variance in the total annual running costs between both UPS systems is summarised in Table III below [8]:

Table 3. Total UPS Energy Losses Cost per Year

Energy details and charges	RUPS	SUPS
Total system energy losses per year	R 7 799 263	R 5 285 168
Off-grid backup savings	R 2 128 406	R 2 130 257
Actual annual RUPS losses cost (operation losses – Off-grid savings)	R 5 670 857	
Actual annual SUPS losses cost (operation losses – Off-grid savings)	R 3 154 911	
Annual TCO savings	R 2 515 946	
Return on investment (UPSs only)	3.57 Years	
Return on investment (UPS + BESSs)	15.01 Years	

[5] Conclusion

The new SUPS system has a prominent fiscal return that offers a lesser total cost of ownership with up to 56% less heat dissipated when compared to the existing RUPS system. This fiscal return, cost reduction, or saving is so great that replacement or upgrade allows the facility to pay back the invested capital into SUPS units and SUPS + BESSs in approximately 4 and 15 years, respectively. We can also conclude that, to reduce the total cost of ownership of any UPS technology, it is imperative, amongst other requirements, to lower cooling and system operating energies. This lowering of energy leads to reducing consequential exposure to ever-escalating energy tariff, carbon footprint, and increase competitiveness in energy management and savings.

[6] References

[17] A. Bhatia, “Battery room ventilation and safety: from continuing education and development inc.”, NJ, Course No: M05-021, 2019, pp. 1-15.

[18] BAE Batteries, “Project planning data: OGi cell discharge current”, USA, 2004, pp. 1-14

[19] BAE Batteries, “BAE OPzS and OGi stationary batteries: vented lead-acid installation and operating instructions”, technical data, revision 0120, USA, 2020, pp. 10-13.

[20] C. Majani, and M. T. Kahn, “Smart distribution board for active load shifting for demand side management applications”, Cape Peninsula University of Technology, 2009, pp. 1-5.

[21] C. Carl, “Comparison of static and rotary UPS”, white paper 92, revision 2, Schneider Electric - Data centre science centre, USA,2011, pp. 1-15.

[22] Eaton Corporation, “Samsung UL9540a battery cabinet site plan”, USA, November 2019, pp. 1-3.

[23] Eaton Corporation, “Static uninterruptible power supply: guide specification - model power xpert 9395 675 – 825 - 1100kW, 575 or 600V, high performance”, USA, June 2020, pp. 1-18.

[24] Eskom, “Tariffs and charges 2020/21”, www.eskom.co.za/tariffs.

[25] Eskom, Power interruption sustained >5min report 2010/2020.

[26] J. Gray, and P. Donovan, “Guidance on what to do with an older UPS”, white paper 214, revision 0, Schneider Electric - Data centre science centre, USA, 2015, pp. 1-11.

[27] L.S. Richard, “Making large UPS systems more efficient”, white paper 108, revision 3, Schneider Electric - Data centre science centre, USA, 2012, pp. 1-21.

[28] M. Schiemann, “Energy from batteries: battery heat dissipation during float operation, recharge, and discharge”, BAE Berliner Batterie GmbH, Germany, 2000, pp. 1-12

[29] Piller UBT, “Operating manual UB150 - UB1100 380V/400V/415V/50Hz”, Piller Group GmbH, Germany, October 2001, pp. 4-1 – 4-4.

[30] Samsung SDI Co. Ltd., “LIB system for UPS – installation manual (128S3P)”, revision 0.6, Corporate Headquarters, Republic of Korea, 2017, pp. 5-6.

[31] W. L. Fritz, and M. T. Kahn, “Distributed generation and cogeneration at universities”, Cape Peninsula University of Technology, 2009, pp. 1-5.

Hardware Simulator for Microgrid Systems

E.P. Muluh
Mr E.P. Muluh, Cape Peninsula University of Technology, P O Box 1906, Bellville, 7535, Cape Town South Africa
211050490@mycput.ac.za .

M.T.E Kahn
Prof. M.T.E. Kahn, Cape Peninsula University of Technology
prof.tariq.kahn@gmail.com

Abstract The paper discusses a Hardware Simulator for Microgrid Systems (HSMG), and takes a brief look at the general definition of a Microgrid and the constituents of such a Microgrid system. Special attention is paid to the role of solar PV as a stand-alone Microgrids and the characteristics of solar panels are studied. An interconnected software and an electronics hardware system that mimics a solar PV Microgrid system is then designed, simulated, and built to operate within the solar PV voltage and current rages of 0-48V / 0-5A respectively. The software component was a LabVIEW graphical user interface (GUI) that allows one to enter the datasheet parameters of a specific solar panel as well as any assumed environmental conditions such as temperature and insulation. The hardware component is a built electronics switch mode programmable buck converter (DC-DC power supply). Usually, the buck converter is powered by a multiple-output adjustable AC to DC power supply. The electronics hardware's current output limit is controlled from and by the GUI through a national instrument data acquisition device; the NI-USB 6009. The hardware's power output across a load is displayed using an LCD, a power meter, and also on the GUI via the data acquisition device still.

Keyword – Microgrid, Hardware-simulator

I. INTRODUCTION

The aim of this paper is to present the design of a Microgrid hardware-simulator that will be able to simulate different types of solar panels' for Microgrid configuration. The simulator will have a graphical user interface for a photovoltaic (PV) panel's information entry. The simulator will then yield results of the configuration numerically, graphically and as well as control a programmable switch mode direct-current (DC) power supply to supply a load following the characteristics (results) of the simulated PV panel.

A. Background

A microgrid is a small power grid which is composed of renewable power sources, power conditioning & control interface circuit, energy storage, and load. These components that a Microgrid is composed of are referred to as the hardware of the Microgrid system. There are different types of Microgrid systems, few of which are solar PV's (photovoltaic), wind turbine etc. The primary energy resource for the solar PV Microgrid system is the sun. The irradiation varies from sunrise to sunset, summer to winter and as well as by latitude. The electrical output from the solar panel is as a characteristic of the particular panel, angle of inclination and irradiation. The primary energy resource for the wind turbine Microgrid system is the wind.

The hardware simulator will determine the possible output power based on the Microgrid characteristics and environmental factors at its location to present a graphical result.

The problem is that project implementation of Microgrid systems require intensive planning. Planning will be financial and time costly if a physical prototype has to be implemented for testing, considering all possible factors before the actual project is adopted or improved. A Hardware-simulator will therefore allow one to record similar or same results while simulating a solar panel inside a laboratory and even during night time, thereby rendering much economic and time flexibility in future project planning.

A Microgrid is important in electricity supply in that based on its ability to operate grid-connected as well as islanded modes it can thus be separated from the utility during a utility disturbance, with little or no interruption to the loads powered directly by the Microgrid. In grid-connected mode, it relieves the utility of overloading during peak load hours thereby avoiding utility grid failure. This renders energy service reliability and a decrease in the impact of load shedding [1]. A Microgrid leads to a reduction in fossil fuel (coal) usage for electricity generation thereby reducing greenhouse gas emissions which is environmentally beneficial. A Microgrid mitigates the cost of energy to its user by providing some or all of its electricity requirement. Smart switching of a Microgrid between grid-connected and Islanded modes allows for energy supply efficiency [3].

II. TECHNOLOGY REVIEW

A. Microgrids

The universal definition of a Microgrid is yet indefinite on how small or how large one may be with respect to energy use or geographic area. [3] However, there are some unique characteristics of the definition [4]:

1) Grouping of interconnected loads and distributed energy resources.
2) Can operate in island mode or grid-connected if desired.
3) Can connect and disconnect from the grid if desired.
4) Acts as a single controllable entity to the grid.

For example, according to [5] "a Microgrid is a group of interconnected loads and distributed energy resources (DER) within clearly defined electrical boundaries that acts as a single controllable entity with respect to the grid. If desired, a Microgrid can connect and disconnect from the

grid to enable it to operate in both grid-connected or island-mode". Also, [6] defines Microgrid as "a controllable system consisting of distributed sources (typically renewable energy sources), loads, and energy storage systems that together can operate either in grid-connected or isolated modes".

B. Solar Photovoltaic systems

A photovoltaic system is a connection of components generally such as PV panels, converters and storage components designed to deliver electric power for a variety of usable purposes [7]. Photovoltaic systems can be generally grouped into two basic categories: stand-alone PV (SAPV) or off-grid and grid connected (on-grid) systems [8]. The SAPV systems are used in remote areas and for space applications, where the PV system (panels with batteries) only is able to assure the load demand. Other types of stand-alone systems are based on a hybrid methodology, which increases the efficacy and reliability of the installed system. [9]

C. Solar PV array model

The Electric model

The electric model of a PV cell can be considered base on the static characteristics using many intrinsic parameters referred to the data sheets given by the manufacturer including the detected irradiation, or the dynamic characteristics especially when a power electronic converter is attached to the PV panel [10]. A PV cell is made up of a p-n junction, fabricated in a thin layer of semiconductor and thus behaves as a diode [11]. This brings about two models known as the single diode and the double diode models [12].

Static model

The equivalent electrical circuit of a single diode PV cell model is made up of a current source that represents the photocurrent, Iph and a single diode representing the diffusion phenomenon and that allows the flow of a current Id. A leakage current Ish caused by the distributed manufacturing defects inside the PV cell flows through a shunt (parallel) resistor, R_{sh}. The PV cell current (I) flows through a series resistor R_s resulting in power lost which represents the reduction in the PV cell efficiency by thermal power dissipated through the hole junction substrates [12].

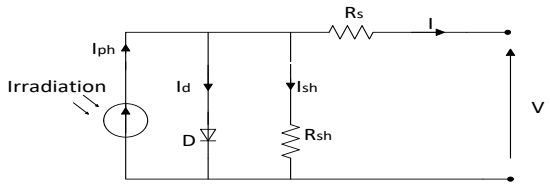


Fig. 17: Equivalent electrical circuit of a single diode modelled solar cell

In the presence of insulation, the PV cell current, I can be given by the following equation:

$$I = I_{ph} - I_d - I_{sh} \quad (1)$$

The double diode (D1 & D2) model further takes into accounts the recombination phenomenon unlike the single diode model, thereby providing better accuracy for the I-V curve than the single diode model. Two lumped resistances represent the shunt resistance R_{sh} and the series resistance R_s by which the leakage current I_{sh} flows and the reduction in cell efficiency occurs respectively. The double diode equivalent circuit diagram is as shown in the figure below bellow.

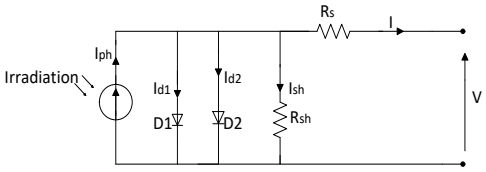


Figure 18: Equivalent electrical circuit of a double diode modeled solar cell [12]

The output current equation is shown in equation (2) below, where I_{d2} is the current via D2 due to recombination phenomenon:

$$I = I_{ph} - I_{d1} - I_{d2} - I_{sh} \quad (2)$$

Dynamic models

The photovoltaic panel is conventionally represented by the Shockley diode in which the output current is described by a diode equation as in equation (1) above. Meanwhile, in practice a power electronic converter that draws a high-frequency rippled current from the solar panel is used for maximum power point tracking. The rippled current results in dynamic characteristics different from the static characteristics derived by the conventional approach [13]. The equivalent electrical circuit model of a solar panel shown in figure (7) below is based on the dynamic conditions.

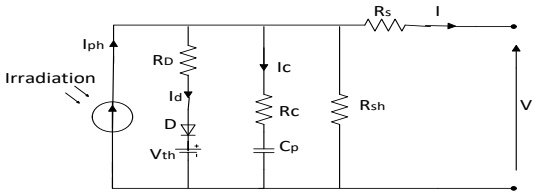


Figure 19: Dynamic equivalent electric circuit of a solar panel [10]

The 'dynamic' equivalent electrical circuit of a solar panel differs from the 'static' single-diode equivalent electrical circuit, in that the resistive losses in the p-n junctions of the PV cells are represented in a lumped resistance R_d. A voltage source corresponding to threshold voltage, V_{th} which is approximately identical to the voltage at the maximum power point is included. A parasitic capacitor, Cp, in series with a resistance, Rs, is introduced to the static circuit model to account for the dynamic behaviours of the solar panel as figure (7) above. The current flow into the parasitic capacitor is denoted Ic [10].

III. METHODOLOGY

A. Graphical user interface (GUI)

A simulator requires data to be entered so it can then process the data and yield results. A LabVIEW block code was designed to receive a solar PV system data via its graphical users' interface and then process it using the solar PV mathematical model. Different solar cell materials have different diode quality (ideality) factors, α as well as different band gaps measured in electron volts (eV).

B. DC – DC Buck Converter

A programmable switch mode power supply was designed and built. The control was implemented such that the user of the simulator can adjust the output voltage by a push of a button but the output current limit was controlled via the GUI by the preset irradiation value.

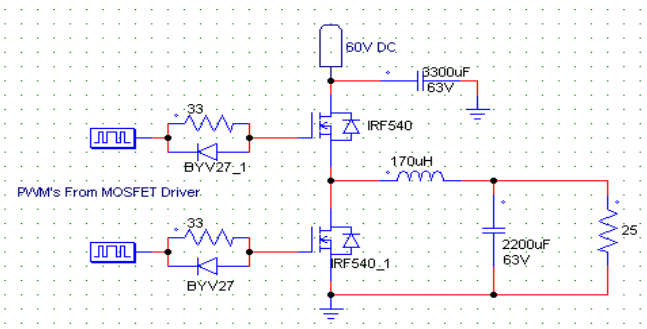


Fig. 20: Synchronous buck converter topology design

C. Simulation

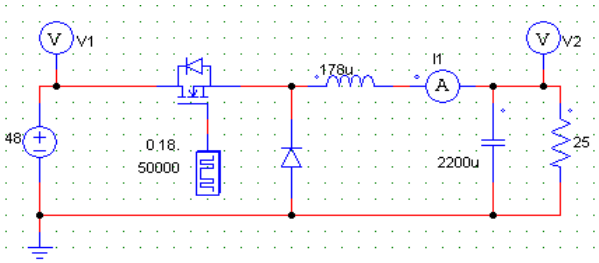


Figure 21: DC to DC buck converter simulation diagram

The simulation was performed at a low duty cycle, mid duty cycle and high duty cycle, and the output voltage and current signals analyzed for a 25Ω load.

Low duty cycle (5%)

An average output voltage of 2.771V with a ripple of about 0.3mV was noted. An average output current of 0.110266A with a ripple of about 0.25A was noted.

Mid duty cycle (50%)

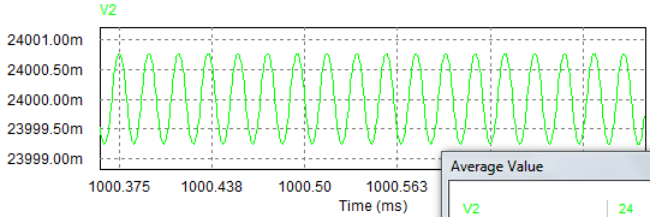


Fig. 22: Buck converter output voltage ripple at 50% duty cycle

An average output voltage of 24V with a ripple of about 1.5mV was noted as shown above.

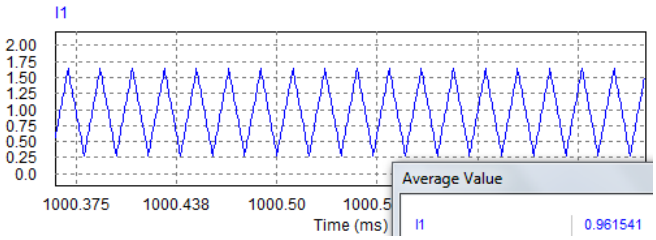


Fig. 23: Buck converter output current ripple at 50% duty cycle

An average output current of 0.961541A with a ripple of about 1.5A was noted as shown above.

High duty cycle (95%)

An average output voltage of 45.6V with a ripple of about 0.3mV was noted. An average output current of 1.826A with a ripple of about 0.25A was noted.

IV. HARDWARE SIMULATOR'S CONTROL STRATEGY

The control strategy of the simulator is about how to predict the operating point of the PV module which is being simulated. It therefore does this by locating the voltage and the current on the I-V characteristic curve depending on the resistance of the load at the output of the simulator. This is though different from the MPPT algorithm which is aimed at locating the highest point of the power-voltage (P-V) characteristic curve of the PV module [16].

Voltage-mode control system was the type of direct referencing control strategy used in this research. The output current and the output voltage were read by the control microcontrollers (arduino uno & NI daq-USB 6009) and then used this information to drive the PWM signal in order to make the proper adjustments of the output voltage, thereby regulating the load current and voltage to the operating point.

The output current value was measure using an ACS712T ELC-20A current sensor. The sensor converts the current flowing throw it to voltage at its output terminal. The voltage was then 'read' (sampled) by the microcontroller's analogue to digital conversion (ADC) circuits.

V. RESULTS

The graph below (figure 15) shows that the hardware component of the designed simulator (buck converter) is generally efficient up to 75% and above. The efficiency tends to be greater with high resistive loads where low current output is drawn and with high duty cycle signal where the output voltage is closer to input voltage. At less resistive loads, more current is drawn and so more of the power is lost in the form of heat energy dissipated in the switching power transistors hence the inefficiency. At lower duty cycle where the output voltage is lesser to the input voltage, the inductor charge time is less and thus less output current gain, hence the inefficiency.

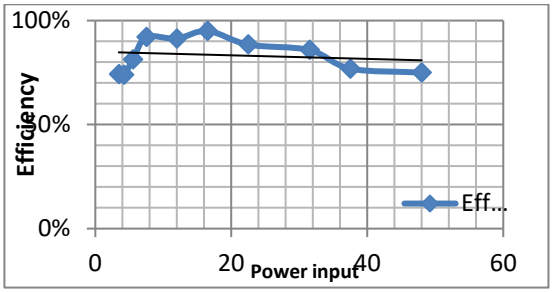


Figure 24: Efficiency @ 80% duty cycle with variable load

The difference between the inclination of the above graph (figures 15) and the one below (figure 16) shows that the converter is more efficient at higher duty cycles than at lower duty cycles.

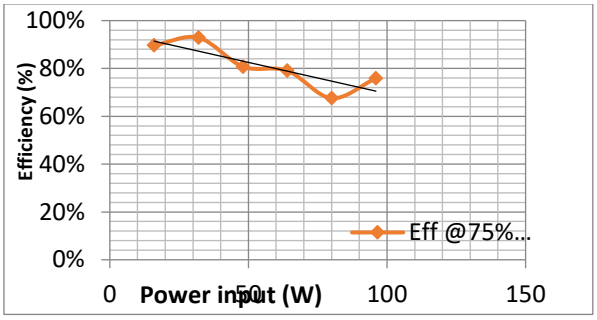


Figure 25: Efficiency @ 75% duty cycle with variable load

VI. CONCLUSION

A microgrid can be used to provide power from different energy sources according to the requirements of the application or the client. Microgrids can be used in grid-connected or island mode depending on specific requirements. Very often PV panels need to be integrated into micgrogrids and a hardware simulator could assist in smoother test integration.

A graphical user interface based on a solar PV mathematical model was designed and a programmable switch mode DC power supply was then built to mimic the software calculation results. The software (GUI) and the hardware (buck converter) were linked via a data acquisition device, setting up a desk-top hardware simulator work station. This can now be integrated in a Microgrid application.

REFERENCES

[1] B. S. Hartono, Budiyanto and R. Setiabudy, "Review of Microgrid Technology," in *2013 International Conference on QiR*, 2013.

[2] E. Wood, "microgridknowledge.com," MICROGRID KNOWLDGE, 04 November 2018. [Online]. Available: https://microgridknowledge.com/microgrid-benefits-eight/. [Accessed 24 spetember 2020].

[3] DNV KEMA Energy & Sustainability and Massachusetts clean energy center, "Microgrids – Benefits, Models, Barriers and Suggested Policy Initiatives for the Commonwealth of Massachusetts," KEMA, Inc., Burlington, February 2014.

[4] P. P. Thomas Bialek, "http://cseweb.ucsd.edu," 22 May 2013. [Online]. Available: http://cseweb.ucsd.edu/~trosing/lectures/cse291_microgrid.pdf. [Accessed 12 June 2017].

[5] D. Jardas, "www.irena-istra.hr," january 2012. [Online]. Available: http://www.irena-istra.hr/uploads/media/Photovoltaic_systems.pdf. [Accessed 12 June 2017].

[6] V. A. Subramony, S. Doolla and M. Chandorkar, "Microgrids in India," *IEEE Journals & Magazines*, vol. 5, no. 2, pp. 47 - 55, 2007.

[7] K. Benmouiza, M. Tadj and A. Cheknane, "Classification of hourly solar radiation using fuzzy c-means algorithm for optimal stand-alone PV system sizing," *International Journal of Electrical Power & Energy Systems*, vol. 82, pp. 233-241, November 2016.

[8] A. M. Bagher, M. M. A. Vahid and M. Mohsen, "Types of Solar Cells and Application," *American Journal of Optics and Photonics*, vol. 3, pp. 94 -113, 2015.

[9] T.-H. Wu, W.-C. Liu, C.-S. Moo, H.-L. Cheng and Yong-Nong, "An Electric Circuit Model of Photovoltaic Panel with Power Electronic Converter," in IEEE Conferences, 2016.

[10] Y. Chaibi, M. Salhi, A. El-jouni and A. Essadki, "A new method to extract the equivalent circuit parameters of a photovoltaic panel," Solar Energy, vol. 163, p. 376–386, 2018.

[11] F. Masmoudi, F. B. Salem and N. Derbel, "Single and Double Diode models for Conventional Mono-Crystalline Solar Cell with Extraction of Internal Parameters," in IEEE Conferences, 2016.

[12] V. Tamrakar, S. Gupta and Y. Sawle, "SINGLE-DIODE AND TWO-DIODE PV CELL MODELING USING MATLAB FOR STUDYING CHARACTERISTICS OF SOLAR CELL UNDER VARYING CONDITIONS," Electrical & Computer Engineering: An International Journal (ECIJ), vol. 4, pp. 1-11, June 2015.

AUTHORS BIOGRAPHY



Principal Author: Elvis P. Muluh holds a BTech degree in electrical engineering from the Cape Peninsula University of Technology (CPUT).

Co-author: Prof. MTE Kahn is currently the Research Chair in Energy at the CPUT.

Performance study of a new smart parabolic trough collector system integrated with hybrid tubular thermoelectric generator

Abderrahim Habchi
ERDyS laboratory, MEEM & DD Group,
Hassan II University of Casablanca, FSTM
BP 146 Mohammedia 20650,
Morocco
Mohammedia, Morocco
isohb2015@gmail.com

Bouchaib Hartiti
ERDyS laboratory, MEEM & DD Group,
Hassan II University of Casablanca,
FSTM BP 146 Mohammedia 20650,
Morocco
Mohammedia, Morocco
bhartiti@gmail.com

Hicham Labrim
Materials Science Unit / DERS /
CNESTEN National Centre for Energy,
Sciences and Nuclear Techniques
Rabat, Morocco
hichamlabrim@yahoo.fr

Salah Fadili
ERDyS laboratory, MEEM & DD Group,
Hassan II University of Casablanca, FSTM
BP 146 Mohammedia 20650,
Morocco
Mohammedia, Morocco
sa.fadili@gmail.com

Abdelilah Benyoussef
LAMCSCI, Faculty of Sciences,
Mohammed V University, B.P. 1014.
Rabat, Morocco
benyoussef @gmail.com

Naoual Belouaggadia
Laboratory of Signals, Distributed Systems and Artificial Intelligence, ENSET, Hassan II University.
Mohammedia, Morocco
n.belouaggadia@gmail.com

***Abstract*— Advanced parabolic trough systems are the promising technologies for the production of usable heat and electrical power. Here we study the effects of hot water temperature adjustment concept and optical concentrator on the thermal and electrical efficiencies of a new PTC/HTTEG configuration, which comprises parabolic trough concentrator and hybrid tubular thermoelectric generator. The hybrid tubular thermoelectric generator (HTTEG) was integrated within the collector tube, where the hot water is passed between the inner side of the absorber tube and the top surface of the HTTEG. Meanwhile, to create a large temperature difference across the HTTEG sides, a cold water is passed along the inner side of the HTTEG. A low consumption pump was energized using HTTEG power in order to keep the hot water temperature at 95°C for a long time (temperature adjustment concept). Numerical simulations show that the improvement in performance of the hybrid system highly depends on the adjustment concept and optical concentrator. As the solar concentration ratio increases, the overall efficiency of the hybrid system increases significantly to 76.21% and the amount of hot water reaches to a maximum value of about 846.77 Liter/Day for a concentration of 30 suns. Also, the power generated by the HTTEG and hot water temperature stay stable at 71.37 W and 95°C, respectively, due to the hot water temperature adjustment effect.**

Keywords*— *Parabolic trough concentrator, Hybrid tubular thermoelectric generator, Overall efficiency, Water storage, Net power

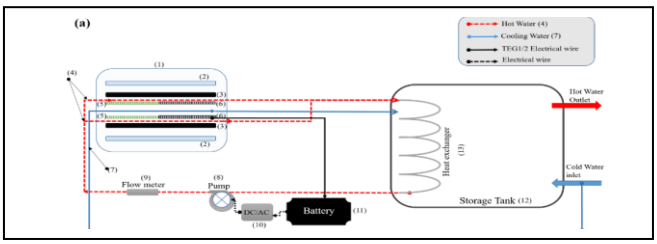
[1] INTRODUCTION

Parabolic trough concentrator (PTC) systems are considered the most efficient solar technology, they are able to produce a large amount of electrical energy (12200 GWh) at high temperatures (400°C-550°C) with minimal heat losses compared to other renewable systems [1]. Also, the said system is also applied as solar water heater systems to generate thermal power [2]. However, a part of thermal energy is converted into waste energy, which reduces significantly its thermal and electrical efficiency[3]. For this reason, to reduce heat losses around the parabolic trough system, an intelligent solution has been proposed and used which combines the parabolic system with thermoelectric generators (TEGs) and photovoltaic cells (PV cells)[4]. To this effect, many researchers are mainly based on the said technique to improve the electrical and thermal performance of parabolic trough systems. There are many research works based on the combination of PV cells with parabolic trough system[5]. Calise et al [6] presented a finite volume model of a new parabolic trough concentrator. This new design is characterized by a collector with a triangular shape, where the inclined sides are occupied by triple-junction cells while the top surface is covered with an absorbent layer. A heat-transfer fluid is circulated along a channel where the transmitted heat from the PV cells and the absorbent layer is directed to this fluid. They analyzed the thermodynamic and electrical parameters, the exergy destruction rate and efficiency of the new system. They also applied a sensitivity analysis to investigate the effect of design/environmental parameters on the energy and exergy performance of the PVT collector. The results indicated that the thermal and electrical efficiency is significantly improved and reached to 68.9% and 22.2% respectively, while the exergetic efficiency attained to 81.2% corresponding to 2610 W of the electrical power output. Similarly, a theoretical study based on the mathematical analysis of a new solar cogeneration system was introduced by S. Lachhab et al[7]. Thus, the mentioned system is integrated with flat PV cells which is attached at the focal line of the solar collector. A cold fluid was placed above the PV cells to improve its performance. Their achievements indicated that the maximum efficiency of the hybrid system reached to 62%. As briefly reviewed above, the efficiency of the hybrid systems is significantly improved as well as the electrical power produced by these systems is also increased. Thus, the mentioned combination ideas are very useful and more acceptable for reducing the waste power from the conventional PTC. Although the improved performance of the hybrid parabolic trough systems, they are unable to control the heat transfer fluid temperature, which reduces significantly their efficiency due to the evaporation problem within the collector (pressure problem). For this reason, the present system is mainly based on the temperature adjustment

concept, which made possible to avoid the evaporation problem within the parabolic trough collector by controlling the temperature of heat transfer fluid. To this effect, a new hybrid configuration of PTC system (PTC/HTTEG) consisting of parabolic trough concentrator, hybrid tubular thermoelectric generator and cooling system is proposed and studied in order to improve the thermal and electrical performance of this system.

[2] STRUCTURE AND WORKING PRINCIPLE OF THE PTC/HTTEG HYBRID SYSTEM

In this study, the new hybrid configuration consists of thirteen main components as parabolic mirror with optical concentrator (1), hybrid collector, which consists of glass cover (2), absorber tube (3), hot water (4), tubular thermoelectric generator 1 (TTEG1) (5), tubular thermoelectric generator 2 (TTEG2) (6) and cold water (7) as clearly demonstrated in Figs. 1a and 1b. Also, to pass the hot water flow along the hybrid system, a pump with low consumption (8) was proposed, which equipped with flow meter (9), DC/AC converter (10) and rechargeable battery (11). The outlet hot water is passed through a storage tank (12) via a helical heat exchanger (13) while the outlet cold water is directly stored into the said tank (12) as it can be seen in Fig.1a. The selected parabola profile in this study has the length of 7.8 m, 5m wide, manufactured by Sandia National Laboratory (SNL) while the stainless steel sheet is used as the solar reflector surface. Also, The absorber tube (3) is made of stainless steel and is coated with cermet selective coating. The chosen thermoelectric elements are thermoelectric cooling type. This is the first time that the hybrid thermoelectric generator (HTTEG) is used with PTC systems, where the mentioned HTTEG contains 390 thermoelectric modules. This generator is equally divided into two main ranges; the first one is mainly composed of (Bi_2Te_3) type units (5) while the second range is consisted of ($PbTe_2$) type modules (6). Lastly, to absorb more thermal power from reflected beam irradiance, the hybrid collector is placed along the focal distance of parabolic trough concentrator, which equal 1.84 m. As mentioned above, the hot water (4) is passed through the storage tank (12), which is made of galvanized iron. The said tank (12) surrounded by an insulator layer to reduce the heat losses by convection and radiation. Also, the helical heat exchanger (13) is made of copper metal, which is characterized by a high thermal conductivity, which will affects positively on the heat exchange operation between the hot water and cold water (tank's water). As shown in Fig.1a, the hybrid thermoelectric generator (HTTEG) is placed inside the solar collector; where the hot water is initially filled into the annular channel between the inner surface of the absorber and upper side of the HTTEG. The cold water is mainly used as a cooling system, which is directly passed along the cold side of HTTEG as clearly shown in Fig.1b. In the PTC/HTTEG system, the hot water is linked to the pump with a low consumption in order to adjust the hot water flow rate according to sun irradiation. Meanwhile, the cold water is directly connected to an external water source in order to circulate it along the hybrid system with a mass flow rate value of 0.4 kg/sec. At the beginning, the hot water is initially introduced into the hybrid collector at 25°C. Meanwhile, the sun irradiation is reflected on the hybrid collector by the solar reflector, then a part of reflected sun irradiation is totally absorbed by the absorber tube while a large amount of absorbed thermal power is directly transmitted to the hot water due to the direct contact between the absorber tube and hot water. Hence, the hot water temperature is increased from 25°C to a temperature close to 95°C. Similarly, a part of hot water thermal power is absorbed by the upper side of HTTEG due to the direct contact between the hot water and upper side of the HTTEG. On the other side, the cold water is passed along the circular cooling duct, to cool the inner side of HTTEG and create a large temperature difference across the HTTEG sides. Thus, the increase of the temperature difference across the thermoelectric generator sides leads to produce more electrical power, which can be stored directly into the rechargeable battery to energize the water pump(when the hot water temperature reached to 95°C). During this period, the hot water temperature is less than 95°C while the water pump keeps turn off since the beginning up to now. Thus, the hot water storage is 0 L/Day. As it is anticipated, when the hot water temperature reached to 95°C, water pump is turned on using the electricity produced by the HTTEG stored into the battery in order to adjust the hot water flow rate according to sun irradiation (temperature adjustment concept). Thus, the hot water temperature stays at 95°C for a long time, which will affects strongly in the hot side temperature of the HTTEG, which it stops increasing at a stable temperature due to the direct contact between the hot water and upper side temperature of the HTTEG. After that, the outlet hot water is passed from the collector to the storage tank, then it is flowed through the helical heat exchanger to the outlet of the storage tank, after which was returned to the hybrid collector again. Also, the cold water is passed from an external water source to the hybrid collector, through the circular cooling duct, then it is directly passed from the outlet of cooling duct to the inlet of the storage tank. Based on the temperature adjustment concept, the hot water storage increases significantly as well as the electricity produced by the HTTEG stays at a stable value. Lastly, when the sun irradiation sufficiently decrease, the absorbed thermal power by the hybrid collector reduce also. Thus, the hot water temperature is lowered to below 95°C and the water pump is immediately turned off. As mentioned above, to improve the thermal and electrical performance of the new configuration, the hybrid system is equipped with an optical concentrator. With the presence of the optical concentrator, the hot water temperature is rapidly reached to 95°C, which extended the stabilization period of hot water at 95°C, which affects positively in the hot water storage process. Thus, the HTTEG's power is stayed at a stable value over a long time.



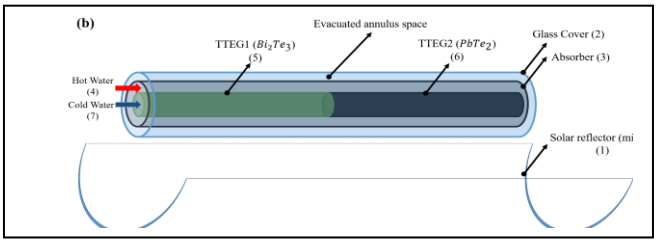
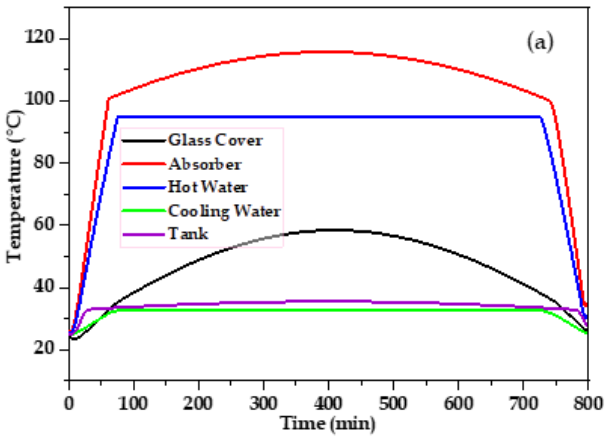


Fig.1 Schematic diagram of the PTC/HTTEG hybrid system (a), (b) 3D view of hybrid collector.

[3] RESULTS AND DISCUSSIONS

A. Performance of the PTC/HTTEG system

The use of temperature adjustment concept leads to change the thermal performance of hybrid system components. Figs.2 present the temperature variation of the hybrid system components during the whole day. As presented in Figs.2, the temperature of each component increases with increasing sun irradiation. The maximum temperature reached is 115.75°C which is related to the absorber tube due to its high absorption coefficient, while the maximum temperatures of the glass cover, the hot water, the cold water and storage tank are 58.44°C, 95°C, 32.91°C and 35.545°C, respectively. As shown in Figs.2a and 3b, when the hot water temperature reach 95°C, the hot water flow rate varies rapidly according to sun irradiation (temperature adjustment concept). As a result, the hot water temperature stays stable at 95°C for a long time, which strongly affects in the temperature distribution of the hot and cold sides of the hybrid tubular thermoelectric generators, which also stay stable at constant values over a long period as shown in Fig.2b. In the last running hours, the temperature all the collector's components decreases with decreasing sun irradiation while the outlet hot water temperature drops below 95°C with a mass flow rate value of 0 Kg/sec. As explained above, the use of optical concentrator improves significantly the thermal performance of the PTC/HTTEG system. The solar concentration effect on the hybrid system performance is separately presented in Figs.3a, 3b and 3c. Fig.3a show that the hot water temperature reaches rapidly to 95°C with increasing solar concentration ratio, which extended the stabilization period of hot water at 95°C. Meanwhile, to keep the hot water temperature at 95°C for a long time, the hot water flow rate varies rapidly and it can achieve to a high value as clearly shown in Fig.3b. Also, the increase in solar concentration ratio affects positively in the hot water storage, where the maximum hot water storage up to 846.77 Liter/day for a concentration of 30 suns as presented in Fig.3c. This is because the increase of hot water flow rate when solar concentration ratio sufficiently increase as clearly demonstrated in Fig.3b. The effect of solar concentration on the hot water temperature is the same on the cold-water temperature. As shown in Fig.3a, the cold-water temperature rises slightly to a stable value 32.85°C with increasing of solar concentration ratio, due to the high cold fluid flow rate (0.4 Kg/s), but as the solar concentration sufficiently increases, the cold-water temperature rises rapidly to the stable value (32.85°C) and cannot exceed it.



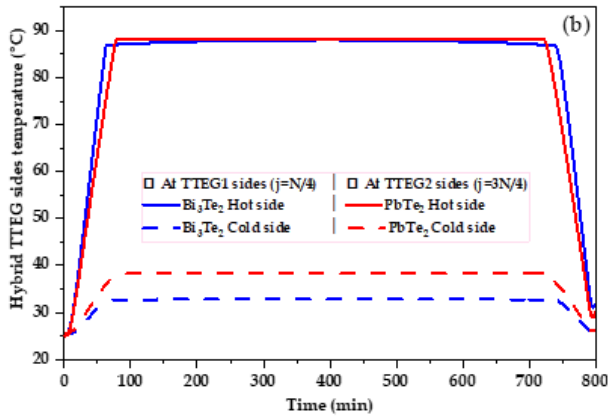
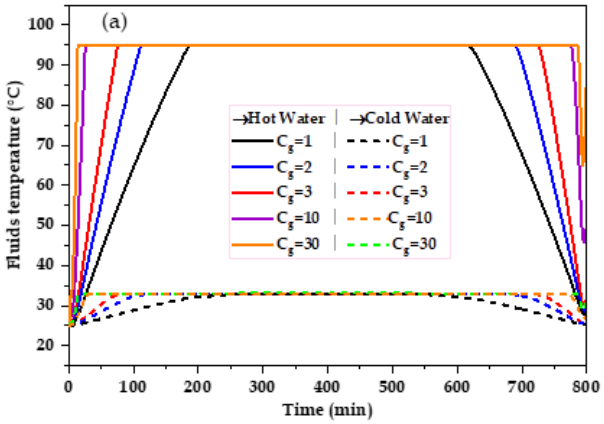
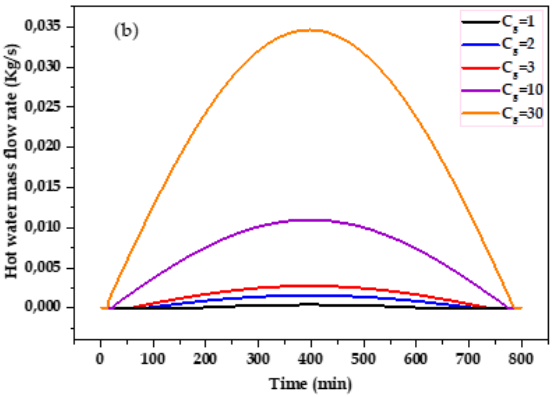


Fig.2 Temperature variations of all the PTC's components (a), and the HTTEG's sides (b) as a function of time





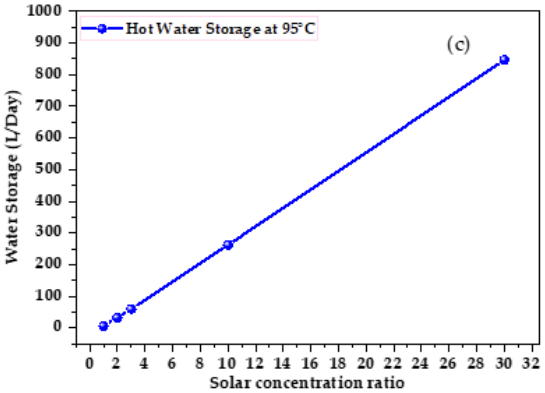


Fig.3 Variation of hot/cold water temperature (a) and hot water flow rate (b) and storage of hot water (c) for all five solar concentration ratios.

B. Results of TTEG1 and TTEG2

The effect of sun irradiation on the electrical efficiency of TTEG1 and TTEG2 is separately shown in Fig.4a and 4b. Solar concentration ratio was varied from 1 to 3 suns. As seen in Figs.4a and 4b, as sun irradiation increases, electrical efficiency of TTEG1 and TTEG2 rises, but it is greatly increased when the solar concentration ratio sufficiently increase. As presented in Fig.2a, the temperatures of the HTTEG sides increase with increasing sun irradiation, but after time increases, the temperatures of the HTTEG sides stabilized due to the temperature adjustment effect. The same effect on the electrical efficiency of TTEG1 and TTEG2, where the temperatures of the HTTEG sides strongly relates on the HTTEG electrical efficiency as explained by the Eq. (1) [8]. For this reason, the electrical efficiency of TTEG1 and TTEG2 increases with increasing sun irradiation, but it stops increasing in the values η^{TTEG1}=2.6% (η^{TTEG2}=0.9%) when solar insolation sufficiently increase. Also, we can notice that each electrical efficiency reaches rapidly to the stable value η^{TTEG1}=2.6% (η^{TTEG2}=0.9%) when solar concentration ratio increases significantly as clearly shown in Figs.4a and 4b.

$$\eta_{TTEG} = \left(\frac{\Delta T}{T_{TTEGh}}\right)\frac{\sqrt{1+ZT_M}-1}{\sqrt{1+ZT_M}+\frac{T_{TTEGc}}{T_{TTEGh}}} \qquad (1)$$

Where Z, T_M, T_{TTEGh}, T_{TTEGc} are the figure of merite parameter, the mean and the hot side temperature of TTEG, and the cold side temperature of the TTEG.

The sun irradiation effect of the electricity produced by TTEG1 and TTEG2 are separately shown in Figs.4d and 4e, respectively. Also, the solar concentrator ratio was varied from 1 to 3 suns. As presented in Figs.4d and 4e, the power output of TTEG1 and TTEG2 increases with increasing of sun irradiation, but after sun irradiation increases significantly, the power output of TTEG1 and TTEG2 stops increasing in the values P_{TTEG1}=55.965 W and P_{TTEG2}=15.405 W due to the temperature adjustment effect. As mentioned above, the use of optical concentrator leads to improve the thermal and electrical performance of the hybrid system by amplifying the reflected solar radiation. Thus, the power produced by TTEG1 and TTEG2 rapidly reaches in the values P_{TTEG1}=55.965 W and P_{TTEG2}=15.405 W at low levels of sun irradiation as clearly shown in Figs.4c and 4d. As it is expected, the power output of the TTEG1 and TTEG2 stay at P_{TTEG1}=55.965 W and P_{TTEG2}=15.405 W for a long time due to the stabilization of electrical efficiency of each TTEGs as explained by the Eq. (2)[9] and shown in Figs.4. Also, we can noticed that the power output of TTEG1 was much higher as compared with the TTEG2 due to the high temperature difference and electrical efficiency of TTEG1 as compared with the TTEG2 as clearly demonstrated in Figs.4a, 4b and 4c.

$$P_{TTEG} = \eta_{TTEG}\Delta T\frac{(1+ZT_M)k_{TTEG}A^{TTEG}}{L_{TTEG}} \qquad (2)$$

Where η^{TTEG} is the electrical efficiency of TTEG, ΔT is the temperature difference across the TTEG, Z is the figure of merite parameter, T_M is the mean temperature of TTEG, k_{TTEG} is the thermal conductivity of TTEG, A^{TTEG} is the cross section of TTEG, and L_{TTEG} is the TTEG length.

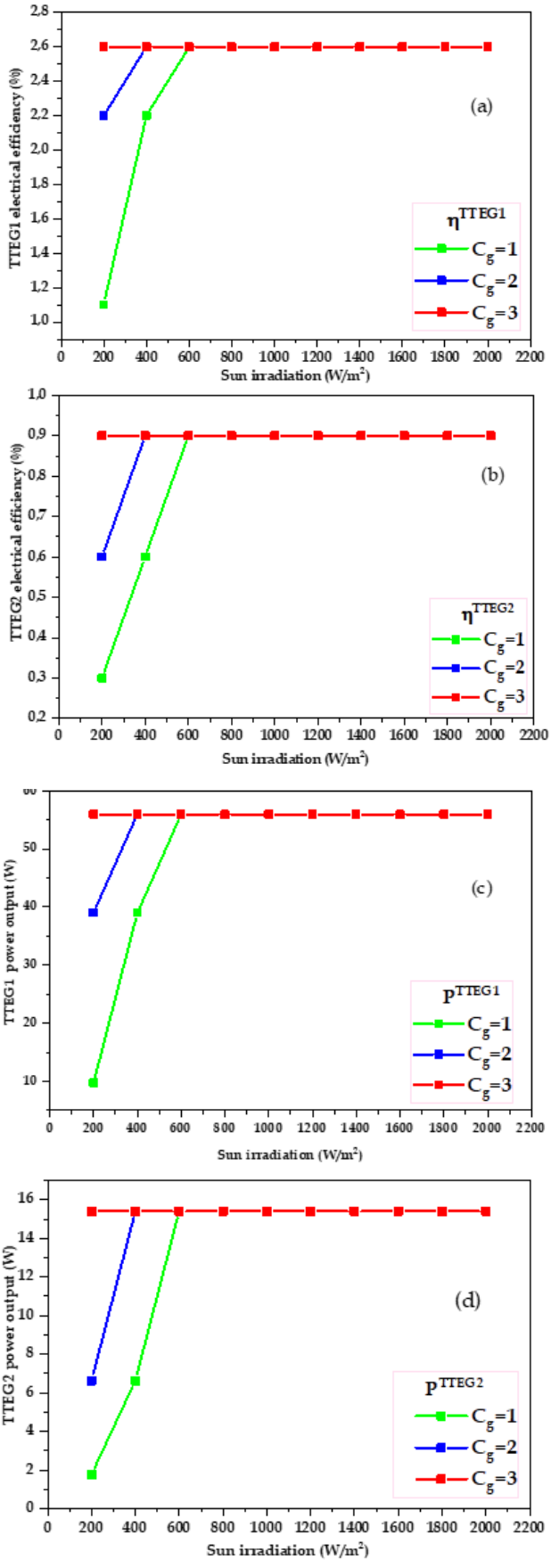


Fig.4. Solar concentration effect on electrical efficiency of TTEG1 (a) TTEG2 for all ten sun irradiation values. Effect of sun irradiation on power output of TTEG1 (d) and TTEG2 (e) in three cases.

C. *Efficiency of the hybrid system PTC/HTTEG*

The performance of the PTC/HTTEG system is mainly explained by its overall efficiency($\eta_{PTC/HTTEG}$), which is the sum of thermal efficiency η_{PTC} (PTC only) of conventional parabolic trough system and total electrical efficiency of the hybrid TEG ($= \eta_{TTEG1} + \eta_{TTEG2}$) as explained by the Eq. (3) [10]:

$$\eta_{PTC/HTTEG} = \eta_{PTC} + \eta_{TTEG1} + \eta_{TTEG2} \quad (3)$$

Where the thermal efficiency (η_{PTC}) is given by [11]:

$$\eta_{PTC} = \frac{A^{PTC}\rho\alpha_o\omega K G_d - A_{ab}U_L(T_{ab}-T_{am})}{A^{PTC}G_d} \quad (4)$$

In which A^{PTC}, ρ, α_o, ω, K, G_d, T_{ab}, T_{am} , η_{TTEG1} ,η_{TTEG2} , U_L represent aperture area of PTC, reflectance of mirror, transmittance absorptance factor, shape factor, incident angle modifier, sun irradiation, absorber tube temperature, ambient temperature, electrical efficiency of the TTEG1, electrical efficiency of the TTEG2 and heat losses coefficient, respectively.

The parabolic trough system efficiency is presented as a function of sun irradiation in three cases in Fig.5. As anticipated, the thermal efficiency of the parabolic trough concentrator (PTC only) decreases with increasing sun irradiation. This mainly due to the increase in the thermal losses of parabolic trough system when sun irradiation increases as clearly explained by the Eq.(4) and Ref [3]. As it was mentioned, the use of solar concentrator leads to improve the thermal performance of the parabolic trough system, and this makes sense with the thermal performance of the present system (PTC only), where the thermal efficiency η_{PTC} (PTC only) increases significantly with sun concentration ratio as clearly demonstrated in [3]. In the hybrid system, the overall efficiency improves significantly for all sun irradiation and solar concentration values as compared with the PTC only as clearly presented in Fig.5. This is because the integration of the PTC system with hybrid tubular thermoelectric generator, where the overall efficiency is the sum of thermal efficiency of PTC and electrical efficiency of HTTEG. As seen in Fig.5, the overall efficiency of the hybrid system increases with the presence of optical concentrator. Therefore, for a concentration of 3 suns, the maximum overall efficiency reached to 76.21% for a sun irradiation 600 W/m^2. It is worthy to notify that the effects of sun irradiation and solar concentration ratio on the efficiency of PTC (η_{PTC}) have the same effect on the hybrid system efficiency. Due to the relationship between the hybrid system efficiency ($\eta_{PTC/HTTEG}$) and efficiency of the PTC (η_{PTC}) as clearly explained by the Eq. (3).

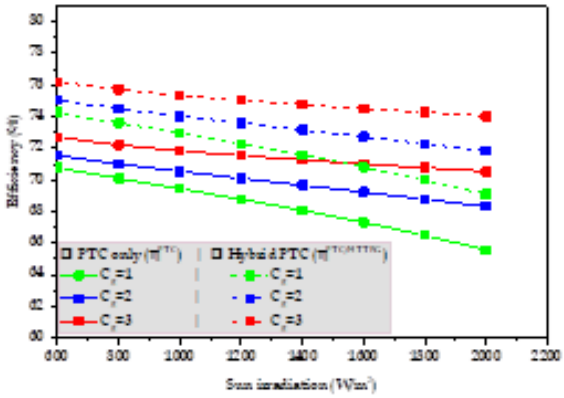


Fig.5 Variation of the hybrid system efficiency in three cases.

D. *Electrical performance of the pump and net power*

To calculate the pump power for different mass flow rate values, Eq. (5) is mainly used, which strongly related on the hot water flow rate [12]:

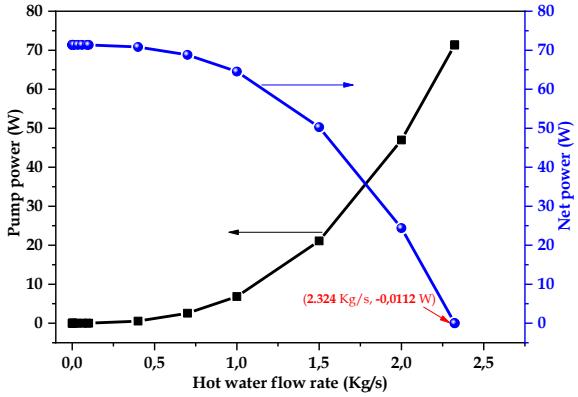
$$P_{Pump} = f(Re)\frac{\dot{m}^3{}_{Hw}}{8D_H}L\pi\rho_{Hw}A^{Ch} \quad (5)$$

In the above equation, $\dot{m}_{Hw}$ is the hot water flow rate, L is the length of annular channel (collector length), ρ_{Hw} is the density of hot water. In which, A^{Ch} , $D_H = D^i{}_{ab} - D^e{}_{Bi_2Te_3}$ and f(Re) ,respectively represent the cross-sectional area of annular channel, the hydraulic diameter of annular channel and friction factor [12].

Fig.6 shows the pump power and net energy for 16 hot water flow rates. Hot water flow rate was varied from 0 to 2.324 Kg/s. It is observed from the figure that the pump power increases significantly with increasing hot water flow rate ($\dot{m}_{Hw}$) because it varies as a function of the third power of $\dot{m}_{Hw}$ as explained by the Eq. (5). In contrast, the net power decreases significantly when hot water flow rate sufficiently increase due to the increase of the pump power consumed by the hot water with increasing hot water flow rate as explained by the Eq. (6) and shown in Fig.6. Also, we can notice that the net power decreases with increasing hot water flow rate but it stay positive in the hot water flow rate range of [0, 2.323 Kg/s], which gives us the possibility for using the water pump in this range. Nevertheless, for a hot water flow rate of 2.324 Kg/s, the net power reached to -0.0112 W, which means that the pump stops working immediately.

$$P_{NET\ POWER} = P_{PTC/HTTEG} - P_{Pump} \quad (6)$$

In the hybrid system, for a concentration of 30 suns, the maximum hot water flow rate reached to 0.0346 Kg/s, which



belongs clearly to the range [0, 2.323 Kg/s], which means that the pump power in this case is much lower as compared with the additional power produced by the hybrid system. As a result, the additional power generated by the hybrid system can energize the water pump with benefit of net power about 71.369W. As conclusion, the additional power produced by the hybrid system is able to energize the water pump for all ten sun irradiation values, and three solar concentration ratios.

Fig.6 Hot water flow rate effect on pump power and net energy.

[4] CONCLUSIONS

The application of the temperature adjustment concept in this new system resulted in a stable electrical power, which is 71.37 W. Also, the hot water temperature stays stable in the value 95°C for a long time, which affects positively in the hot water storage, which is 846.77 Liter/Day for a concentration of 30 suns, while the evaporation problem of hot water inside the solar collector was totally avoided, due to the hot water temperature stops increasing at 95°C. The additional power generated by the hybrid system sufficient for energizing the water pump for all sun irradiation and solar concentration ratios. Thus, a closed system between the water pump and the hybrid system was created with a benefit of net power about 71.37W for a concentration of 3 suns. On the other hand, the use of optical concentration leads to increase the hot water storage while the hot water temperature rapidly reach 95°C. Therefore, for a concentration of 3 suns, the overall efficiency of the present hybrid system reached to 76.21% for a sun irradiation of 600 W/m^2. Also, the highest electrical efficiency of the HTTEG up to 3.2%.

ACKNOWLEDGMENT

Prof. Bouchaib HARTITI, Senior Associate at ICTP (The Abdus Salam International Centre for Theoretical Physics), is very grateful to ICTP for financial support. Technical support from LMOPS (University of Lorraine, France) is also acknowledged.

REFERENCES

[1] « Renewable energy statistics », doi: https://www.irena.org/Statistics/Statistical-Notes-and-Methodology.

[2] O. A. Jaramillo, J. O. Aguilar, R. Castrejón-García, E. Venegas-Reyes, et F. Sosa-Montemayor, « Parabolic trough concentrators for hot water generation: Comparison of the levelized cost of production », *J. Renew. Sustain. Energy*, vol. 5, nº 2, p. 023114, mars 2013, doi: 10.1063/1.4795402.

[3] C. Li *et al.*, « Effects of environmental factors on the conversion efficiency of solar thermoelectric co-generators comprising parabola trough collectors and thermoelectric modules without evacuated tubular collector », *Energy Convers. Manag.*, vol. 86, p. 944-951, oct. 2014, doi: 10.1016/j.enconman.2014.06.010.

[4] P. Sundarraj, D. Maity, S. S. Roy, et R. A. Taylor, « Recent advances in thermoelectric materials and solar thermoelectric generators – a critical review », *RSC Adv*, vol. 4, nº 87, p. 46860-46874, 2014, doi: 10.1039/C4RA05322B.

[5] A. A. Hachicha et M. Tawalbeh, « Design of a new concentrated photovoltaic system under UAE conditions », Abu Dhabi, United Arab Emirates, 2017, p. 110004, doi: 10.1063/1.4984478.

[6] F. Calise, A. Palombo, et L. Vanoli, « A finite-volume model of a parabolic trough photovoltaic/thermal collector: Energetic and exergetic analyses », *Energy*, vol. 46, nº 1, p. 283-294, oct. 2012, doi: 10.1016/j.energy.2012.08.021.

[7] S. Eddin Lachhab, A. Bliya, E. Al Ibrahmi, L. Dlimi, et Laboratory of Renewable Energies and Environment, Faculty of Sciences, Ibn Tofail University, BP. 133. 14000-Kenitra, Morocco, « Theoretical analysis and mathematical modeling of a solar cogeneration system in Morocco », *AIMS Energy*, vol. 7, nº 6, p. 743-759, 2019, doi: 10.3934/energy.2019.6.743.

[8] D. M. Rowe, Éd., *CRC handbook of thermoelectrics*. Boca Raton, FL: CRC Press, 1995.

[9] G. Min, « Thermoelectric Module Design Under a Given Thermal Input: Theory and Example », *J. Electron. Mater.*, vol. 42, nº 7, p. 2239-2242, juill. 2013, doi: 10.1007/s11664-013-2591-2.

[10] M. Mohsenzadeh, M. B. Shafii, et H. Jafari mosleh, « A novel concentrating photovoltaic/thermal solar system combined with thermoelectric module in an integrated design », *Renew. Energy*, vol. 113, p. 822-834, déc. 2017, doi: 10.1016/j.renene.2017.06.047.

[11] A. E. Elmohlawy, B. I. Kazanjan, et V. F. Ochkov, « Modeling and performance prediction of solar parabolic trough collector for hybrid thermal power generation plant under different weather conditions », Pilsen, Czech Republic, 2018, p. 020002, doi: 10.1063/1.5081635.

[12] T. Cui, Y. Xuan, et Q. Li, « Design of a novel concentrating photovoltaic–thermoelectric system incorporated with phase change materials », *Energy Convers. Manag.*, vol. 112, p. 49-60, mars 2016, doi: 10.1016/j.enconman.2016.01.008.

Numerical Simulation of Photovoltaic Characteristics of Cadmium Telluride Thin Film Based Solar Cells

Salaheddine Moujoud
Department of physics, Hassan II University Casablanca, Faculty of Sciences and Techniques. Erdys laboratory, GMEMM&DD Group.
Mohammedia, Morroco.
moujoudsalaheddine729@gmail.com

Bouchaib Hartiti
Department of physics, Hassan II University Casablanca, Faculty of Sciences and Techniques. Erdys laboratory, GMEMM&DD Group.
Mohammedia, Morroco
bhartiti@gmail.com

Ali Faddouli
Department of physics, Hassan II University Casablanca, Faculty of Sciences and Techniques. Erdys laboratory, GMEMM&DD Group.
Mohammedia, Morroco
alifaddouli12@gmail.com

Salah Fadili
Department of physics, Hassan II University,Casablanca.Faculty of Sciences and Techniques, Erdys laboratory, GMEMM&DD Group.
Mohammedia, Morroco.
sfadili@yahoo.fr

Philippe Thévenin
Department of physical measurments (MP), Lorraine University.
Optical materials, photonics and systems laboratory.
Metz, France.
philippe.thevenin@univ-lorraine.fr

Chaymaa Rachidy
Department of physics, Hassan II University Casablanca, Faculty of Sciences and Techniques. Erdys laboratory, GMEMM&DD Group.
Mohammedia, Morroco.
chaimae1013@gmail.com

Abstract— **This article addresses the issue of simulating thin film solar cells based on cadmium telluride (CdTe). CdTe represent the absorber layer in the heterojunction structure SnO_2/CdS/CdTe. It is a material with high absorption coefficient in the range of 10^4 cm^{-1}, and a band gap of 1,45 eV which make him absorb a high portion of photon with energy higher than his band gap energy. The goal of industry is to use less material and expect a good efficiency; it is the case of PV technology, because thinning will not only save material but time, production, cost and the energy of production. In order to reach this goal, we resorted to simulating these solar cells using SCAPS 1D, Solar cell capacitance simulator, which will help us improve the characteristics of the solar cell and obtain an appropriate theoretical efficiency. A high efficiency of 18,14% (V_{oc}=0,97 V, J_{sc}= 25,3 mA/cm², FF=73,57 %) was obtained with SnO_2/ZnO/CdS/CdTe/ZnTe/Pt compared to the optimized baseline structure SnO_2/CdS/CdTe/Au who gives an efficiency of 16,2% (V_{oc}=0,87 V, J_{sc}=23 mA/cm², FF=80,53 %). Those results were obtained under 2µm of CdTe, 0,05µm of CdS. So the difference came in the insertion of ZnO, ZnTe and Pt back contact. ZnO is a buffer layer that helped improving bleu response of the cell as for ZnTe it act as a BSF layer his role is to reduce recombination rate at the back surface of the cell. Moreover, SnO_2/ZnO/CdS/CdTe/ZnTe/Pt showed a good stability for high temperature comparing to the baseline structure SnO_2/CdS/CdTe/Au.**

Keywords— Thin film solar cells, heterojunction, cadmium telluride, CdTe, SCAPS 1D, recombination, optimizing, PV technology.

I. Introduction

Crystalline silicon based solar cells are still dominating the PV technology market; however thin film based solar cells emerge as the second generation of solar cells. Thin film solar cells use less material than the previous generation of crystalline silicon and they have interesting optoelectronic properties. P-type CdTe based solar cells are one of the most famous cells in thin film PV technology, CdTe have a direct band gap in the range of 1,45 eV [1], that allows it to absorb maximum solar power, and an absorption coefficient superior to 10^4 cm^{-1} [2], which means that all the potential photons with energy greater than the band gap can be absorbed within a very thin CdTe absorber layer. The n-CdS/p-CdTe make a good pair for PV application, n-CdS is the most suitable buffer layer for this type of heterojunction solar cells as they have make a 21% efficiency [3].The n-CdS have 2,24 eV as band gap energy that allows a large part of solar spectrum to reach the absorber layer, it is the most material widely used as n-type buffer for CdTe thin film solar cells [4]. Tyan et al. realised CdTe/CdS thin film solar cells with efficiency of 10% [5]. Ferekides et al. reported an efficiency of 15,8% [6]. Furthermore the efficiency in the range of 17-19% was achieved by Leonid Kosyachenko [7]. This work focus on thinning CdS/CdTe solar cells with conversion efficiency over 16% by improving the open circuit voltage (V_{oc}), the short circuit current density (J_{sc}), and the fill factor (FF). One of the main reasons of industry is using less material and to have a good efficiency and PV technology is concerned by this. So thinning solar cells will not only save resources, but it will lower manufacturing process, cost, time, and energy to produce the cells.

The conventional structure of CdTe based solar cells is SnO_2/CdS/CdTe/Au [8]. We tried, as mentioned before; thinning the cell, by reducing the thickness of both CdS buffer layer, and CdTe absorber layer. Speaking of CdTe layer, it needs a stable back metal contact with a high work function. Most metals do not have sufficiently high work functions and therefore form Schottky-barrier contacts to CdTe absorber layer. This represents one of the challenge concerning CdTe based solar cells [9]. The good approach to overcome this obstacle is to insert a back surface field (BSF), between CdTe and the final metal back contact, which will moderate this barrier. The specific materials chosen to investigate in this work is Zinc Telluride (ZnTe). ZnTe is a p-type semiconductor with a direct band gap of 2,26 eV and formation of ohmic contacts to ZnTe is easier due to its lower work function and the ability to dope it highly p-type.

As for the front surface we inserted a buffer layer of n-ZnO in order to overcome the problems of recombination in that area by improving the bleu response in quantum efficiency simulations because it is not practical to reduce CdS thickness down to 10 nm.

Numerical simulations can help in modeling new solar cells, by bringing innovative ideas to vary structures and cell parameters to improve the cell performance. Given the complex nature of CdS/CdTe thin film polycrystalline solar cells, the need for numerical modeling is apparent. There is some capabilities to increase the conversion efficiency of CdS/CdTe solar cells by improving the open circuit voltage V_{oc}, density of short circuit J_{sc}, and fill factor FF through simulation before involving with fabrication process of the cells. The details of our work are explained in the following sections.

II. Methodology

As mentioned in the introduction, we used SCAPS 1D for simulation of CdTe based solar cells. This program simulates the characteristics of solar cells; by solving the following equations:

- Poisson equation :

$$div(\vec{E}) = \frac{q}{\varepsilon}(p - n + N_D^+ + N_A^-), \quad (1)$$

- Continuity equations :

$$\frac{\partial n}{\partial t} = \frac{1}{q}\nabla(J_n) + G_n - R_n\,, \quad (2)$$

$$\frac{\partial p}{\partial t} = \frac{1}{q}\nabla(J_p) + G_p - R_p\,, \quad (3)$$

- Transport equations :

$$J_n = q(\mu_n n\,E + D_n \nabla n), \quad (4)$$

$$J_p = q(\mu_p p\,E + D_p \nabla p), \quad (5)$$

A With ε the permittivity, E the electrical field, q elementary charge, N_D (N_A) donor (acceptor) concentration, $G(R)$ the carrier generation (recombination) rate, $n(p)$ density of electrons (holes), J_n (J_p) current density of electron (holes).

Fig. 1 shows the conventional solar cells and the proposed structure and table 1 shows the physical parameters of the solar cell materials used in the simulation [10, 11, 12, 13, 14, 15, 16].

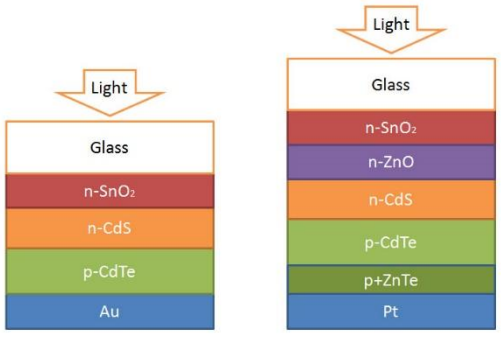


Fig. 1. Conventional stucture of CdTe(Left) and proposed structre (Right).

TABLE I. Simulation parameters

Parameters	SnO_2	ZnO	CdS	CdTe	ZnTe
Thickness(μm)	0,5	0,250	0,05	4	0,2
Electron affinity(eV)	4	4,35	4	3,9	3,65
Band gap(eV)	3,6	3	2,4	1,5	2,25
Dielectric constant	9	9	10	9,4	14
Nc(cm^{-3})	$2{,}2.10^{18}$	2.10^{18}	$2{,}2.10^{18}$	8.10^{17}	$7{,}5.10^{17}$
Nv(cm^{-3})	$1{,}8.10^{19}$	$1{,}5.10^{19}$	$1{,}8.10^{19}$	$1{,}8.10^{19}$	$1{,}5.10^{19}$
Electron thermal velocity (cm/s)	10^7	10^7	10^7	10^7	10^7
Hole thermal velocity (cm/s)	10^7	10^7	10^7	10^7	10^7
Electron mobility	100	100	100	320	70
Hole mobility	25	25	25	40	50
Donor density (cm^{-3})	1.10^{17}	1.10^{19}	$1{,}1.10^{18}$	0	0
Acceptor density(cm^{-3})	0	0	0	2.10^{14}	1.10^{18}
Defect density (cm^{-3})	1.10^{15}	1.10^{15}	1.10^{18}	2.10^{14}	1.10^{16}
Defect type	Donor	Donor	Acceptor	Donor	Donor

III. Results and Discussion

A. *Effect of temperature on CdTe baseline structure.*

We know that the cell is exposed to the air which means that temperature will influence the properties of the cell, figure 2 show temperature effect on the characteristic properties of the cell. We see that all the characteristic properties of the solar cell have decreased. Open circuit voltage (V_{oc}) decrease due to the increase in the dark current generated by the rise in the intrinsic concentration. The latter is favored by increased temperature and the decrease in the gap energy [17].The diminution of V_{oc} affects the fill factor and efficiency that's why they decreased. Concerning the density of short circuit, it increased slightly. The rise in temperature creates a thermal disorder in the microstructure of the cell which reduces the mobility and the lifespan of free carriers. The electrons become instable and they cannot recombine before reaching the depletion zone.

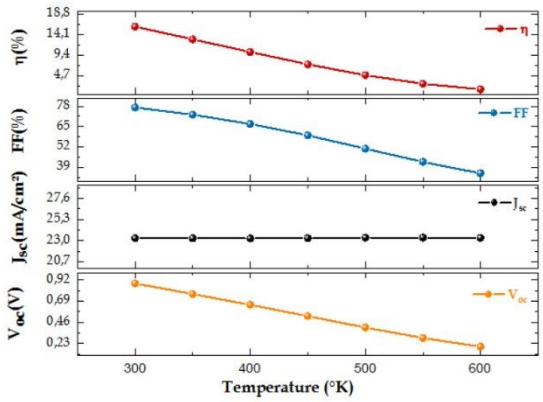


Fig. 2. Effect of temperature on cell performance.

B. Effect of absorber layer CdTe thickness.

In this part we have investigated the effect of the thickness of CdTe absorber layer. The thickness of the absorbent layer was varied from 1µm up to 2µm with a step of 0,2 µm; Fig. 3 shows the results of simulation.

The figure demonstrate the effect of varying the thickness of CdTe layer, we see that increasing thickness affect fill factor and efficiency, this can be explained by the fact that for larger thickness there is some resistive components responsible of the decrease of fill factor therefore efficiency .

In the other hand density of short circuit and open circuit voltage increase, because increasing the thickness of CdTe layer causes more absorption of photon with energy superior to CdTe band gap energy. As a result there will a plenty of electron hole pairs generated. Subsequently, we investigate the state of quantum efficiency to know more about variation of CdTe thickness. Fig. 4 shows the quantum efficiency for thickness from 1µm to 2µm. At 2µm of thickness we have a good absorption in near Infrared region. In the other hand, from 0,4µm to 0,55µm, we have a low absorption. That can be explained by recombination in the front surface. Due to this problem, we have investigated the effect of CdS thickness in the following.

C. Effect of CdS buffer layer thickness.

The In this part we have studied the effect of thinning CdS buffer layer. We have varied CdS thickness from 0.01 to 0,05 µm; figure 5 shows the results of optimizing this layer. The characteristic of the cell have all decreased when increasing CdS thickness. The optimization of CdS buffer layer was under 2µm for CdTe absorber layer. For 0,01µm of CdS layer we obtained good results; a value of 17,45% of efficiency, 80,68% fill factor 26,65 mA/cm² and 0,87 V in open circuit voltage. So, decreasing CdS buffer layer thickness leads to increasing solar cell performance. And that is well seen in the results of quantum efficiency shown in figure 6. A very thin CdS layer is capable of absorbing more photon due to the physical properties in nanometric scale. At 10 nm CdS are considered like nanowire material so they benefit a lot of advantages like reduced reflection, extreme light trapping, improved band gap tuning, facile strain relaxation and increased defect tolerance [18].

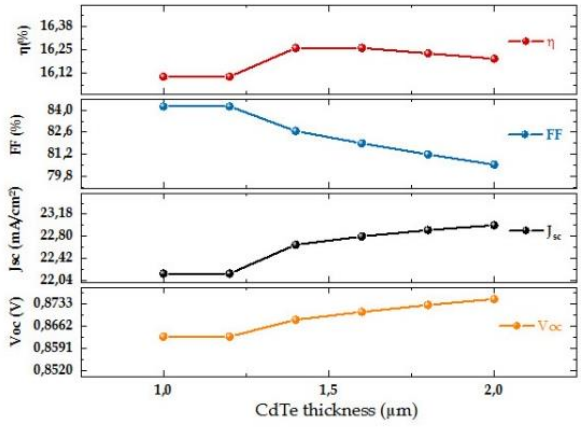


Fig. 3. Effect of CdTe thickness on the performance of the cell.

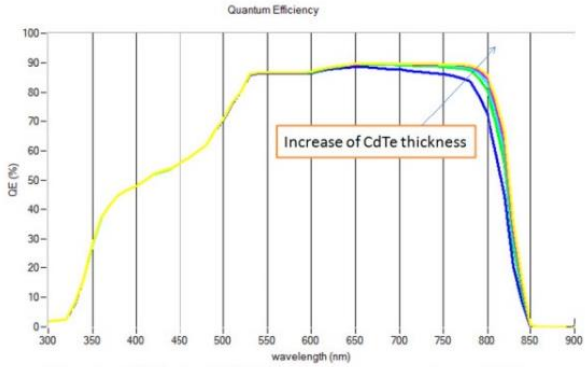


Fig. 4. Effect of CdTe thickness on quantum efficiency.

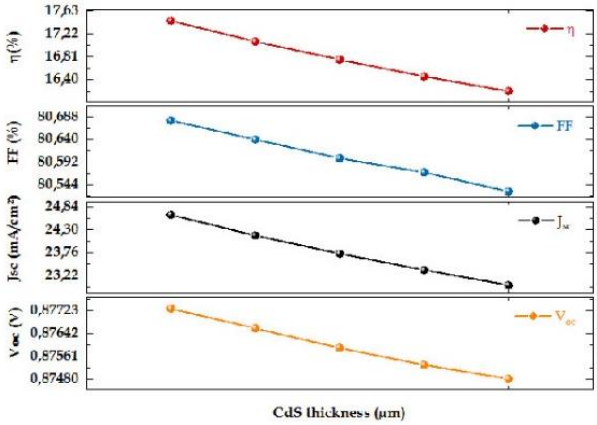


Fig. 5. Effect of CdS thickness on cell performance.

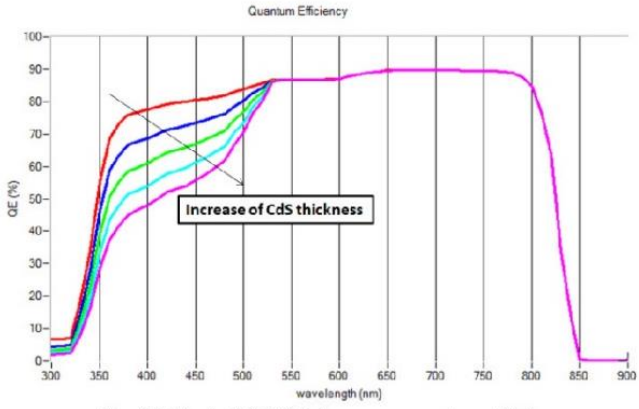


Fig. 6. Effect of CdS thickness on quantum efficiency.

D. Inserstion of ZnO buffer layer and ZnTe BSF layer.

Recombination is one of the phenomenons responsible for decreasing quantum efficiency. In order to overcome recombination effect in the front surface we tried to thin CdS buffer layer down to 10 nm and that given us good results but this is not technically evident due to that very small thickness [12, 19], therefore to resolve the problem we decided to insert a buffer layer between CdS and SnO_2, knowing that we also reduced SnO2 thickness to its half equally to ZnO buffer layer. As for the back surface, we inserted a heavily p doped ZnTe layer between CdTe layer and the back contact. The choice of a back contact has an influence on the performance of the thin film cells that is the main difference between it and the thicker ones. As mentioned before the formation of a good back contact to CdTe represents a challenge for this type of solar cells.

Prior to that, we chosen plus to ZnTe BSF layer a back contact with a work function of 5,65 eV in Platinum. Numerical simulations have been explored with the proposed thin cell (Glass/SnO_2/ZnO/CdS/CdTe/ZnTe/Pt) using the optimum values from previous simulation. The cell with 2µm of CdTe, 0,05µm of CdS, 0,150µm of ZnO, 0,250 µm of SnO_2, and 0,2 µm of ZnTe was simulated using SCAPS 1D.

Table 2 show the difference between optimized cell Glass/SnO_2/CdS/CdTe/Au(a), proposed structure with buffer layer Zinc oxide and back surface field layer Zinc telluride Glass/SnO_2/ZnO/CdS/CdTe/ZnTe/Pt(b) and pervious work who worked on the same concept with structure Glass/SnO2/Zn_2SnO_4/CdS/CdTe/ZnTe/Al(c) [12].

It is obvious that the conventional cell without BSF layer shows an efficiency of 16,2%, which represents the optimal value. After the insertion of ZnO and ZnTe the efficiency have been improved and reached 18,14%. The density of short circuit have improved with 9% due to reduction of minority carrier recombination loss in the back contact area, but we notice that fill factor decreased because of a barrier developed for holes in valence band. Our results agree with previous work [12], they have the same reduction of fill factor and improvement of other characteristics.

Current tension results show also the difference between optimized structure and the proposed one. Figure 7 illustrate the difference clearly. We see that increasing the open circuit voltage and density of short circuit contribute on the good performance of the cell.

Another effect studied is the stability of the cells under operating temperature. Figure 8 shows the efficiency results in function of temperature. The proposed structure has a considerable stability comparing to conventional structure. These results are quite evident knowing that temperature has an influence on electrons and holes mobility, carrier concentration, density of states and band gap. Conversion efficiency decreased when temperature increased from 300°K to 325°K, with a temperature coefficient of -0,2 %/°K for proposed structure and -0,4 %/°K for conventional structure.

TABLE II. COMPARISON BETWEEN (A) OPTIMIZED CELL, (B) PROPOSED CELL AND (C) A PREVIOUS WORK.

Structure	V_{oc}(V)	J_{sc}(mA/cm²)	FF (%)	Ƞ(%)
a	0,87	23	80,53	16,20
b	0,97	25,30	73,57	18,14
c	0,90	24,92	70	15,8

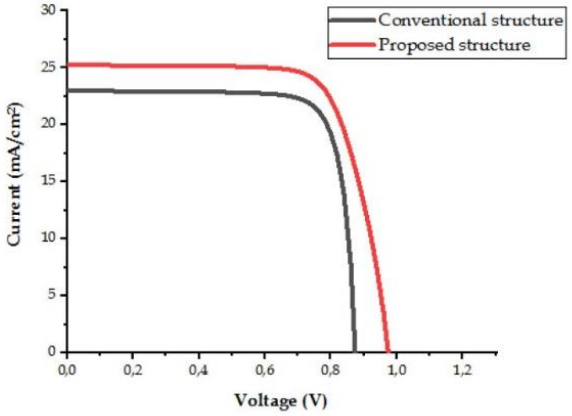


Fig. 7. Current tension characteristic for conventional structure and proposed structure.

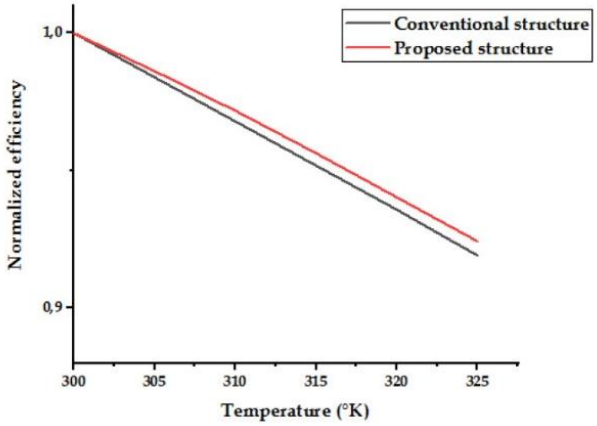


Fig. 8. Normalized efficiency.

IV. Conclusion

CdTe based solar cells, who belong to second generation PV technology, have been simulated in this work using SCAPS 1D. First thing was optimizing the conventional structure; studying temperature effect on the cell, also the effect of thinning CdS and CdTe layers. One of the challenges facing CdTe technology is to have a good back contact with a work function superior to 5,2 eV. We proposed a new structure, with a buffer layer ZnO BSF layer ZnTe and a back contact with high work function Pt, which is Glass/SnO_2/ZnO/CdS/CdTe/ZnTe/Pt.

The characteristic of the cell decreased under operating temperature except of density of short circuit that slightly increased because at high temperature electrons become instable and do not recombine with holes. We varied the thickness of the absorber layer from 1µm to 2µm by 0,2µm, after 1,6 µm we notice that efficiency decreased, however that is not a huge decrease of efficiency. The results of spectral response showed good absorption near to red zone of the specter under 2µm. During the study of thinning CdS it appears that it has improved the quantum efficiency of the cell especially in the bleu region with a thickness of 0,01µm, and that solved the problem of recombination in the front surface of the cell but this cannot be realized; so we insert a buffer layer ZnO to improve the bleu response in the front surface. As for the back surface we inserted a BSF layer between CdTe absorber layer and Pt back contact, which will reduce the recombination rate at the back surface. Then we studied the effect of operating temperature and his influence on the stability of the conventional structure and the proposed one. A high efficiency of 18,14% (V_{oc}=0,97 V, J_{sc}= 25,3 mA/cm², FF=73,57 %) was achieved with SnO_2/ZnO/CdS/CdTe/ZnTe/Pt.

Acknowledgment

We are greatly thankful to Mr. Marc Burgelman from university of Gent, Belgium, who authorized us to work with SCAPS 1D program.

References

[1] W. Xuanzhi, High-efficiency polycrystalline CdTe thin-film solar cells, Solar Energy 77 (2004) 803–814.

[2] Jesús Rangel-Cárdenas and Hugo Sobral, Optical Absorption Enhancement in CdTe Thin Films by Microstructuration of the Silicon Substrate.

[3] Martin A. Green, Keith Emery , Yoshihiro Hishikawa , Wilhelm Warta and Ewan D. Dunlop, Solar cell efficiency tables (Version 45).

[4] Abdul Kuddus, Md. Ferdous Rahman, Shamim Ahmmed, Jaker Hossain and Abu Bakar Md. Ismail,Role of facile synthesized V2O5 as hole transport layer for CdS/CdTe Heterojunction solar cell: Validation Of Simulation Using Experimental Data.

[5] C. Ferekides, J. Britt, Y. Ma, L. Killian, High efficiency CdTe solar cells by close spaced sublimation, Proc. 23rd IEEE Photovoltaic Specialists Conference New York USA (1993) 389-393.

[6] M. Powalla, D. Bonnet, Thin-film solar cells based on the polycrystalline compound semiconductors CIS and CdTe, Adv. Opto Electro. 6 (2007) 97545-11.

[7] Efficiency of Thin-Film CdS/CdTe Solar Cells By Leonid Kosyachenko.

[8] N. A. Khan , KS Rahman, F Haque, N Dhar, MA Islam, Md Akhtaruzzaman, Kamaruzzaman Sopian, Nowshad Amin,Design Optimization of CdTe Thin Film Solar Cells from Numerical Analysis.

[9] M.Rafi, H.Bouchaib, Synthèse de CuInS2 en couche mince pour application photovoltaïque.

[10] "the CdTe-base case" by Markus Gloeckler, Colorado, summer 2003.

[11] M. Gloeckler, A.Fahrenbruch and J.Sites, "Numerical modelling of CIGS and CdTe solar cells: setting the baseline", Proc. 3rd World Conference on Photovoltaic Energy Conversion (Osaka, Japan, may 2003), pp. 491-494, WCPEC-3, Osaka (2003).

[12] Nowshad Amin , M. A. Matin, M. M. Aliyu,M. A. Alghoul,M. R. Karim,and K. Sopian, Prospects of Back Surface Field Effect in Ultra-Thin High-Efficiency CdS/CdTe Solar Cells from NumericalModeling.

[13] Saeed Khosroabadi and Seyyed Hossein Keshmiri,Design of a high efficiency ultrathin CdS/CdTe solar cell using back surface field and backside distributed Bragg reflector.

[14] Dr. Brijesh Kumar ,Brajesh Kumar Kaushik & Y. S. Negi, Perspectives and challenges for organic thin film transistors: Materials, devices, processes and applications.

[15] Aseena S, Nelsa Abraham and V. Suresh Babu, Optimization of layer thickness of ZnO based perovskite solar cells using SCAPS 1D.

[16] D. C. Look, G. C. Farlow, Pakpoom Reunchan, Sukit Limpijumnong, S. B. Zhang, and K. Nordlund, Evidence for Native-Defect Donors in n-Type ZnO.

[17] A.M. Ferouani, MR Merad Boudia, Khadidja Rahmoun,Numerical Simulation and Optimization of Performances of a Solar Cell Based on CdTe.

[18] Nanowire Solar Cells. Erik C. Garnett, Mark L. Brongersma, Yi Cui,and Michael D. McGehee.

[19] L.I. Nykyruy, R.S. Yavorskyi, Z.R. Zapukhlyak, G. Wisz, P. Potera, Evaluation of CdS/CdTe thin film solar cells: SCAPS thickness simulation and analysis of optical properties.

ISASE2021
7-9 APRIL 2021
Ataturk University, Erzurum,TURKEY

Improved Approach of Dark Object Subtraction (DOS) for Classification of Oil Palm Cover in Different Space and Time with Landsat-8 Images

1st Zhi Hong Kok
Department of Biological and Agricultural Engineering
Universiti Putra Malaysia
Selangor, Malaysia
gs50356@upm.edu.my

2nd Abdul Rashid Mohamed Shariff
1. Department of Biological and Agricultural Engineering
2. Smart Farming Technology Research Centre
3. Institute of Plantation Studies
Universiti Putra Malaysia
Selangor, Malaysia
rashidpls@upm.edu.my

3rd Siti Khairunniza Bejo
1. Department of Biological and Agricultural Engineering
2. Smart Farming Technology Research Centre
3. Institute of Plantation Studies
Universiti Putra Malaysia
Selangor, Malaysia
skbejo@upm.edu.my

***Abstract*—The Dark Object Subtraction (DOS) approach is commonly applied in atmospheric correction of aerial or satellite images, although it has its flaws. In this study, an attempt to improve the performance of DOS for classification of oil palm cover using Landsat-8 images was conducted. The approach involved conducting further corrections in reflectance exclusive to the vegetation cover with reference to higher spectral resolution data and haze removal relative**

		30 / 9	126	59
	2017	26 / 9	125	59
		9 / 3	126	59
		13 / 6	126	59
Colombia	2016	27 / 8[a]	7	58
	2020	27 / 1	7	58
Ghana	2020	29 / 3[a]	194	56

[a] scene used in classification.

B. Dark Object Subtraction 1 (DOS1)

The DOS1 algorithm was developed by [7] and implemented on an open-source GIS platform, QGIS. The algorithm is user friendly as it automatically identifies the radiance of the Dark Object in DN value as that equivalent to when the sum of pixels equal or lower than the value consists of 0.01% of the population (i.e. all pixels in the scene). All pixels are then subsequently deducted by the identified amount for each corresponding spectral band.

C. Improved DOS Correction for Oil Palm

An oil palm plantation with no cloud cover was identified and subset from the scenes. Similar subsets were acquired for scenes of a similar region. The spectral values for the palm crowns or canopies were extracted by random points generated within the extent of the plantations and computed for statistics summarized in Table II. By comparing the mean spectral values of palm crowns extracted from scenes for B, G and R bands with [8] and given the spectral signature of vegetations, observations of B band values higher than G band or R band values in the scenes suggested the presence of further scattering.

If further scattering exists beyond 0.01% of the population previously accounted by DOS1, it follows the haze removal relative scatter lookup table of Landsat-8 [9] that the ratio of further scattering for the Blue(B), Green(G) and Red(R) spectral bands were approximately 2:1:1. Given B bands exhibit relatively greater scattering, it remains conservative to adopt the statement of G band > B band and R band > B band. Thus,spectral values for the three bands of palm tree crowns should be in the following descending order in terms of magnitude: G band > R band > B band.

Taking into account the differences in values between the regions and the above observations, particularly those in Malaysia, three conditions were imposed on the spectral values of B band, G band and R band:

all pixels in the scene and does not account for variation in spatial (i.e. space) and temporal (i.e. time) context. Therefore, applying the correction may be inappropriate for designing models to classify different scenes or similar scenes from varying time [4].

In tropical regions (e.g. Malaysia), oil palm trees are widely cultivated. Palm oil is the most globally consumed

$$(NIR - R) / (NIR + R) \quad (1)$$

where NIR refers to the Near-Infrared band values and R refers to the R band values. By trial and error, most palm trees were more separable at NDVI = 0.70. Using a mask, the conditions were only applied to pixels with NDVI values greater than 0.70. The procedures mentioned in this section were conducted with Python 3.7.

TABLE II. DESCRIPTIVE STATISTICS OF DATASET USED IN COLOMBIA

	Colombia (n=2)			Malaysia(n=20)		
	B	*G*	*R*	*B*	*G*	*R*
Mean[a]	0.0207	0.0275	0.0240	0.0392	0.0434	0.0360
Min[a]	0.0192	0.0240	0.0203	0.0354	0.0382	0.0309
Max[a]	0.0233	0.0329	0.0314	0.0544	0.0598	0.0551
Std[a]	0.0007	0.0015	0.0017	0.0046	0.0051	0.0057
CoV[a]	3.45%	5.83%	7.24%	9.99%	10.49%	12.56%

[a] Min: Minimum; Max: Maximum; Std: Standard deviation; CoV: Coefficient of variance

D. Model development and Classification

A comparison between the classification accuracy of models derived from the DOS1 and the improved approach were compared. The models will be tested in their ability to classify oil palm tree cover different in time and location from the data used in training them. For this task, the Support Vector Machine (SVM) was selected as the machine learning algorithm of choice for model development. The hyperparameters of the model were selected with reference to the method suggested by [10].

The subset image for classification consisted of Kulai (Malaysia), Granada (Colombia) and New Abirem (Ghana). Land covers in the first locations were grouped into mature oil palm, other vegetation, nonvegetation and immature oil palm, while the second location consisted an additional class for cloud. 1300 and 1000 reference points were acquired for the first and second study area respectively by visual inspection of land cover via GoogleEarth Pro [11]. Seven features were used: B band, G band, R band, NIR band, Shortwave Infrared 1 (SWIR1) band, Shortwave Infrared 2 (SWIR2) band and NDVI. Evaluation of models was conducted in two ways by training the models with data from one region and testing them with the other.

III. RESULTS

[b] MOP: Mature oil palm; V: Vegetation; NV: NonVegetation; C: Cloud; IOP: Immature Oil Palm; U A: User Accuracy; PA: Producer Accuracy. Applies from Table III to Table X

[c] Reference points (Ground truth) are in rows. Applies from Table III to Table X

[d] Overall Accuracy. Applies from Table III to Table X

TABLE IV. CONFUSION MATRIX FOR TESTING MODEL WITH GRANADA IMAGE

	MOP	V	NV	IOP	PA
MOP	85	9	1	118	39.9
V	46	496	35	203	63.6
NV	0	34	101	3	73.2
IOP	14	34	4	117	69.2
UA	58.6	86.6	71.6	26.5	61.5

TABLE V. CONFUSION MATRIX FOR TRAINING MODEL WITH CORRECTED KULAI IMAGE

	MOP	V	NV	C	IOP	PA
MOP	378	29	0	0	1	92.2
V	33	222	20	1	7	80.6
NV	1	21	189	2	2	87.4
C	1	3	1	29	0	82.3
IOP	13	21	0	1	25	41.7
UA	88.7	75.0	90.0	87.9	71.4	84.3

TABLE VI. CONFUSION MATRIX FOR TESTING MODEL WITH CORRECTED GRANADA IMAGE

	MOP	V	NV	IOP	PA
MOP	79	104	1	29	37.1
V	12	689	41	38	88.3
NV	0	18	119	1	86.2
IOP	18	98	3	50	29.6
UA	72.5	75.8	72.6	42.4	72.1

When test images classified by both models were compared, the overall accuracy of the corrected model was greater than the initial model by 10.6% (Table IV and Table VI). For both MOP and IOP, the corrected model had a higher UA than the initial model while the inverse is true for PA. This is further shown in the classified images (Fig.1 and Fig.2) , where the initial model (Fig.1) was seen to greatly overestimate the extent of IOP (i.e. yellow in image) or misclassify both MOP and vegetation reference points as IOP, while the corrected model (Fig.2) slightly overestimated the land cover of Vegetation (i.e. dark green in image) or observed misclassification of MOP as Vegetation.

When the process was inverted (i.e. training with Granada image and testing with Kulai image), most misclassifications for MOP or IOP regardless of model used were also associated with the Vegetation class (Table VII and Table VIII). This may be attributed to the high spectral similarity between the three classes, in addition to the inherent landscape complexity in the particular region studied. Nevertheless, the corrected model successfully identified majority of regions in Granada where Oil Palm trees were being cultivated.

TABLE VII. CONFUSION MATRIX FOR TESTING MODEL WITH GRANADA IMAGE (TRAIN WITH KULAI IMAGE)

	MOP	V	NV	IOP	PA
MOP	48	344	16	0	11.8
V	0	172	111	0	60.8
NV	0	9	206	0	95.8
IOP	0	52	6	2	3.3
UA	100	29.8	60.8	100	44.3

TABLE VIII. CONFUSION MATRIX FOR TESTING MODEL WITH CORRECTED GRANADA IMAGE (TRAIN WITH CORRECTED KULAI IMAGE)

	MOP	V	NV	IOP	PA
MOP	33	337	3	35	8.1
V	22	205	56	0	72.4
NV	13	16	186	0	86.5
IOP	6	42	2	10	16.7
UA	44.6	34.2	75.3	22.2	44.9

B. Classification of New Abirem image

Here, the overall accuracy of the corrected model was 11.6% greater than the initial model (Table IX and Table X). IOP for the corrected model indicated less misclassified samples from other classes (i.e. higher UA), although most of its samples were misclassified as MOP. Exposure of legume or crop covers under IOP in plantations with incomplete canopy closure may have lead to mixed reflectance resembling the MOP or the Vegetation class [12, 13]. Both models reported high PA but low UA for MOP, with most samples from Vegetation misclassified as MOP. The misclassification between MOP and Vegetation for both test images could be explained by the spectral similarity between forest or secondary growth vegetation and oil palms when applying Landsat-8 images for palm cover classification [13]. However, these findings contrast those of [14] and [15], although the models for these studies were trained and tested using images from the same location, time or both.

Another explanation is the difference in inherent landscape complexity. Contrary to organized plantations in Kulai, grass fields and strips of forests (i.e. misclassified yellow lines in Fig.1) transverse between the plantations in Granada, while those in New Abirem were in mosacis distributed between forest patches. This presented a complex scenario for the models' assessments. In [12], the use of Landsat imageries only allowed the authors to detect oil palm expansions larger than 50 hectares, which were much larger than most IOP and MOP plantations in New Abirem. In addition, most IOP plantations for all acquired images were small areas and suggested smallholder activity, with some exceptions as observed in Granada (i.e. large yellow patches in Fig.2). In both tests, misclassification between Vegetation and NV was lower for the corrected model. Using the NDVI mask, mixed pixels by urban regions with green space were more spectrally separable from pixels related to vegetation (i.e. Vegetation, MOP and IOP class).

TABLE IX. CONFUSION MATRIX FOR TESTING MODEL WITH NEW ABIREM IMAGE

	MOP	V	NV	C	IOP	PA
MOP	252	6	1	0	13	92.6
V	285	10	2	0	38	3.0
NV	3	7	58	1	5	78.4
C	0	1	0	1	0	50.0
IOP	22	0	0	0	35	61.4
UA	44.8	41.7	95.1	50.0	38.5	48.1

TABLE X. CONFUSION MATRIX FOR TESTING MODEL WITH CORRECTED NEW ABIREM IMAGE

	MOP	V	NV	C	IOP	PA
MOP	257	13	1	1	0	94.5
V	206	120	5	1	3	35.8
NV	5	8	60	1	0	81.1
C	0	1	0	1	0	50.0
IOP	43	10	0	0	4	7.0
UA	50.3	78.9	90.9	25.0	57.1	59.7

IV. CONCLUSION

Dark Object Subtraction of DOS is a widely applied atmospheric correction approach due to its simplicity and accessibility. However, the correction applied is relative to the scene in question, which causes image classification or analysis of scenes from different time and space to be challenging. This study suggested an approach to improve the classification of oil palm trees in different space and time by using available images to generate the statistical values for the class itself, followed by using a NDVI mask to apply the correction to oil palm trees and vegetation. The approach allowed accurate identification of areas for oil palm cultivation even when models are trained with data from different areas and time, although accurate discrimination between oil palms and other vegetation such as forest trees or tall grasses remain challenging with the use of coarse resolution imaging and the nature of landscape complexity in the study areas.

V. REFERENCE

[1] P. Wicaksono and M. Hafizt, "Dark target effectiveness for darkobject subtraction atmospheric correction method on mangrove above-ground carbon stock mapping," IET Image Process, 2018, vol.12(4), pp.582-587.

[2] S. Gilmore, A. Saleem and A. Dewan, "Effectiveness of DOS (Dark-Object Subtraction) method and water index techniques to map wetlands in a rapidly urbanising megacity with Landsat-8 data," CEUR Workshop Proceedings, 2015, vol.1323, pp.100-108.

[3] A. A. Ahmed, B. Pradhan, M. I. Sameen and A. M. Makky, "An optimized object-based analysis for vegetation mapping using integration of Quickbird and Sentinel-1 data," Arabian Journal of Geosciences, 2018, vol.11(280), pp.1-10. https://doi.org/10.1007/s12517-018-3632-1

[4] M. Schultz, J. Verbesselt, V. Avitabile, C. Souza and M. Herold, "Error sources in deforestation detection using BFAST Monitor on Landsat time series across three tropical sites," IEEE Journal of Selected Topics in Applied earth Observation and Remote Sensing, 2015, vol.9(8), 3667-3679, DOI: 10.1109/JSTARS.2015.2477473

[5] C. H. Teoh, "Key sustainability issues in the palm oil sector: a discussion paper for multi-stakeholders consultations," 2013, The World Bank Group

[6] USGS, United States Geological Survey, Landsat-8 OLI/TIRS level-1 products, 2018, Retrieved March 2021 from earthexplorer.usgs.gov.

[7] L. Congedo, "Semi-automatic classification plugin documentation. 2016." Release 4. 0. 1:pp.29

[8] H. A. J. Jayaselan, "Detection of oil palm leaf nutrients using spectroradiometer with Wavelet analysis and Artificial Neural Network," PhD Thesis, Universiti Putra Malaysia, Malaysia, December 2017.

[9] GIS Ag Maps. "Revised Landsat 8 custom relative scatter lookup table," 2011, Retrieved March 2021 : http://www.gisagmaps.com/landsat-8-haze-removal-table/

[10] C. W. Hsu, C. C. Chang and C. J. Lin, "A practical guide to support vector classification," Tech. Rep., Department of Computer Science, National Taiwan University, 2003.

[11] GoogleEarthPro, 2021, Version 7.3.3.7786.

[12] V. H. Guttiérrez-Vélez and R. DeFries, "Annual multi-resolutio detection of land cover conversion to oil palm in the peruvian Amazon," Remote Sensing of Environment, 2013, vol.129, pp.154-167. http://dx.doi.org/10.1016/j.rse.2012.10.033

[13] J. Miettinen, D. L. A. Gaveau and S. C. Liew, "Comparison of visual and automated oil palm mapping in Borneo," International Journal of Remote Sensing, 2019, vol.40(21), pp.8174-8185. DOI:10.1080/01431161.2018.1479799

[14] A. Oon, H. Z. M. Shafri, A. M. Lechner and B. Azhar, "Discriminating between large-scale oil palm plantations and smallholdings on tropical peatlands using vegetation indices and supervised classification of Landsat-8," International Journal of Remote Sensing, 2019, vol.40(19), pp.7312-7328. DOI: 10.1080/01431161.2019.1579944

[15] J. S. H. Lee, S. Wich, A. Widayati and L. P. Koh, "Detecting industrial oil palm plantations on Landsat images with Google Earth Engine,"Remote Sensing Applications: Society and Environment, 2016, vol.4, pp.219-224. http://dx.doi.org/10.1016/j.rsase.2016.11.003

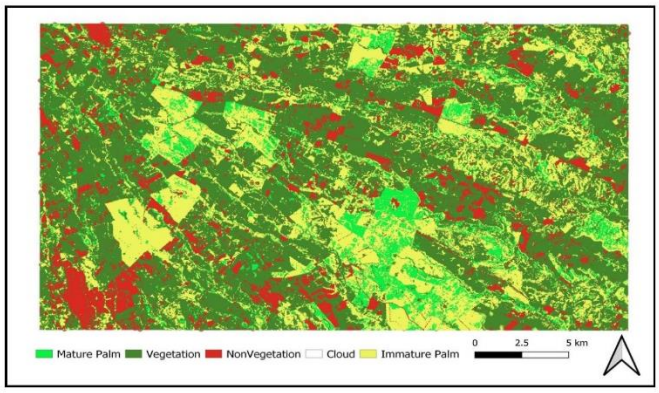


Fig.1 Classified Granada image with initial model

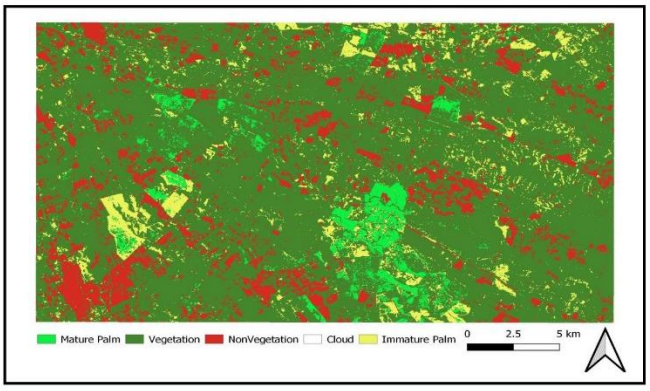


Fig.2 Classified Granada image with corrected model

Mathematical Modeling of COVID-19 Using Fractal-Fractional Derivatives

Zeeshan Ali
School of Engineering Monash University Malaysia Selangor, Malaysia
zeeshan.ali@monash.edu
zeeshanmaths1@gmail.com

Faranak Rabiei
School of Engineering Monash University Malaysia Selangor, Malaysia
faranak.rabiei@monash.edu
faranak.rabiei@gmail.com

Kamal Shah
Department of Mathematics University of Malakand Dir (L), Pakistan
kamalshah408@gmail.com

Zanariah Abdul Majid
Department of Mathematics University Putra Malaysia Selangor, Malaysia
am_zana@upm.edu.my

Aim:

In this research, a mathematical model of COVID-19 with fractal-fractional derivatives is proposed to analyze the transmission dynamics of disease infection.

Method:

Here we considered a mathematical model of COVID-19 with eight compartments including susceptible S(x), exposed E(x), infected I(x), super-spreaders, asymptomatic A(x), hospitalized H(x), recovery R(x) and fatality classes F(x) with fractal-fractional derivatives. The fractional- fractal derivatives with fractional-order q and fractal dimensions' p is used as follows:

$$\begin{cases} {}^{FFP}\mathbf{D}^{q,p}\mathbb{S}(t) = -\beta\Omega\mathbb{I}(t)\mathbb{S}(t) - \ell\beta\Omega\mathbb{H}(t)\mathbb{S}(t) - \beta'\Omega\mathbb{P}(t)\mathbb{S}(t), \\ {}^{FFP}\mathbf{D}^{q,p}\mathbb{E}(t) = \beta\Omega\mathbb{I}(t)\mathbb{S}(t) + \ell\beta\Omega\mathbb{H}(t)\mathbb{S}(t) + \beta'\Omega\mathbb{P}(t)\mathbb{S}(t) - \gamma\mathbb{E}(t), \\ {}^{FFP}\mathbf{D}^{q,p}\mathbb{I}(t) = \gamma\rho_1\mathbb{E}(t) - (\alpha_a + \alpha_i)\mathbb{I}(t) - \sigma_i\mathbb{I}(t), \\ {}^{FFP}\mathbf{D}^{q,p}\mathbb{P}(t) = \gamma\rho_2\mathbb{E}(t) - (\alpha_a + \alpha_i)\mathbb{P}(t) - \sigma_p\mathbb{P}(t), \\ {}^{FFP}\mathbf{D}^{q,p}\mathbb{A}(t) = \gamma(1-\rho_1-\rho_2)\mathbb{E}(t), \\ {}^{FFP}\mathbf{D}^{q,p}\mathbb{H}(t) = \alpha_a(\mathbb{I}(t)+\mathbb{P}(t)) - \alpha_r\mathbb{H}(t) - \sigma_h\mathbb{H}(t), \\ {}^{FFP}\mathbf{D}^{q,p}\mathbb{R}(t) = \alpha_i(\mathbb{I}(t)+\mathbb{P}(t)) + \alpha_r\mathbb{H}(t), \\ {}^{FFP}\mathbf{D}^{q,p}\mathbb{F}(t) = \sigma_i\mathbb{I}(t) + \sigma_p\mathbb{P}(t) + \sigma_h\mathbb{H}(t), \end{cases}$$

With initial conditions:

$$\mathbb{S}(0) = \mathbb{S}_0,\ \mathbb{E}(0) = \mathbb{E}_0,\ \mathbb{I}(0) = \mathbb{I}_0,\ \mathbb{P}(0) = \mathbb{P}_0,\ \mathbb{A}(0) = \mathbb{A}_0,\ \mathbb{H}(0) = \mathbb{H}_0,\ \mathbb{R}(0) = \mathbb{R}_0,\ \mathbb{F}(0) = \mathbb{F}_0. \qquad \Omega = \frac{1}{\mathbf{N}}$$

where

N	total population
β	transmission coefficient from infected individuals
β'	transmission coefficient due to super-spreaders
ℓ	relative transmissibility of hospitalized patients
γ	rate at which exposed become infectious
ρ_1	rate at which exposed people become infected I
ρ_2	rate at which exposed people become super-spreaders
α_a	rate of being hospitalized
α_i	recovery rate of hospitalized patients
α_r	recovery rate without being hospitalized
σ_i	disease induced death rate due to infected class
σ_p	disease induced death rate due to super-spreaders
σ_h	disease induced death rate due to hospitalized class

Total population size N is constant, the value of S(t) is calculated by:

$$\mathbb{S}(t) = \mathbf{N} - [\mathbb{E}(t) + \mathbb{I}(t) + \mathbb{P}(t) + \mathbb{A}(t) + \mathbb{H}(t) + \mathbb{R}(t) + \mathbb{F}(t)].$$

In addition, the total population of death people due to the disease is given by:

$$\mathbb{D}(t) = \sigma_i\mathbb{I}(t) + \sigma_p\mathbb{P}(t) + \sigma_h\mathbb{H}(t).$$

Existence and uniqueness of proposed via Banach and Schaefer's type fixed point approaches are proven and nonlinear functional analysis is used to show the stability of model, (For details please see [1]). Fractional type AB method for different values of q and p via the help of Matlab-16, is used to simulate the results of proposed model on real data of disease spread in Wuhan City, Hubei Province of China [2].

Results:

In this study we use the real data of disease outbreak of Wuhan city of China for 66 days (from 4 January to 9 March 2020) See [2]. The total papulation of Wuhan city considered is almost 11 million people, and for proposed model here, the total population is considered as N = 11,000,000/250. This denominator has been determined because of restriction of movements of individuals due to quarantine in the city of Wuhan. The following initial values are considered:

$$\mathbf{S}_0 = \mathbf{N} - 7,\ \mathbf{E}_0 = 0,\ \mathbf{I}_0 = 1,\ \mathbf{P}_0 = 5,\ \mathbf{A}_0 = 0,\ \mathbf{H}_0 = 0,\ \mathbf{R}_0 = 0,\ \mathbf{F}_0 = 0.$$

The step size for evaluating the numerical results is **h** = 0.1.

Table 1. The physical interpretation of the parameters whose real data is taken from [2].

Parameters	Value	Units
β	2.55	day^{-1}
ℓ	1.56	dimensionless
β'	7.65	day^{-1}
γ	0.25	day^{-1}
ρ_1	0.580	dimensionless
ρ_2	0.001	dimensionless
α_a	0.94	day^{-1}
α_i	0.27	day^{-1}
α_r	0.5	day^{-1}
σ_i	3.5	day^{-1}
σ_p	1	day^{-1}
σ_h	0.3	day^{-1}

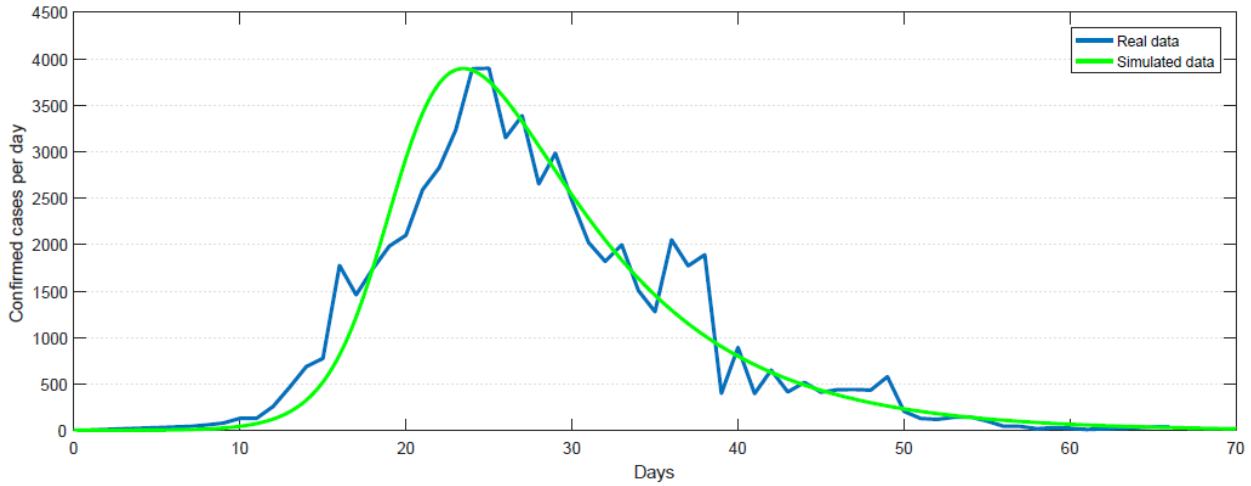


Fig. 1: Real confirmed cases per day vs simulated confirmed case per day.

In Figure 1, the compared numerical simulation of confirmed cases per day with the existing real data from [2], indicates that the simulated graph of confirmed cases has an almost similar pattern with real data and validates the accuracy of the proposed model for predicting and analyzing the transmission dynamic of future data of this disease. To see the all simulated compartments of proposed model please see [1].

CONCLUSION

In conclusion, the presented simulation results of the proposed model demonstrated that individual movements restriction has a significant impact on the transmission dynamics of the current outbreak of disease. Perhaps, by adopting the precautionary measures, the transmission of disease in society can be reduced. Also, for such type of dynamical study, fractal-fractional calculus may be used as powerful tools to understand the global dynamics of the mentioned disease.

Keywords—Coronavirus disease model; Fractal-fractional derivative; Fractional Adams-Bashforth (AB) method

REFERENCES

[1] Zeeshan Ali., Faranak Rabiei., Kamal Shah., Touraj Khodadadi. (2020). Qualitative Analysis of Fractal-Fractional order COVID-19 Mathematical Model with Case Study of Wuhan. Alexandria Engineering Journal, https://doi.org/10.1016/j.aej.2020.09.020

[2] F. Ndaïrou, et al., Mathematical Modeling of COVID-19 Transmission Dynamics with a Case Study of Wuhan,Chaos, Solit. Fract., (2020), https://doi.org/10.1016/j.chaos.2020.109846

Mathematical Model for COVID-19 Outbreak in Pakistan

Zeeshan Ali
School of Engineering Monash University Malaysia Selangor, Malaysia
zeeshan.ali@monash.edu
zeeshanmaths1@gmail.com

Faranak Rabiei
School of Engineering Monash University Malaysia Selangor, Malaysia
faranak.rabiei@monash.edu
faranak.rabiei@gmail.com

Zanariah Abdul Majid
Department of Mathematics University Putra Malaysia Selangor, Malaysia
am_zana@upm.edu.my

Kamal Shah
Department of Mathematics University of MalakandDir (L), Pakistan
kamalshah408@gmail.com

Aim:

This paper deals with a mathematical model's dynamics for the COVID-19 outbreak in Pakistan under recently founded calculus tools called fractal-fractional calculus. Besides, the considered model shows the importance of isolation.

Method:

The model is considered with three compartments, namely, susceptible $\mathcal{S}$, infected $\mathcal{I}$, and recovered $\mathcal{R}$ [2]:

$$\begin{cases} \mathcal{D}^{\theta_1,\theta_2}\mathcal{S}(t) = \Lambda - \kappa(1-\alpha)\mathcal{S}(t)\mathcal{I}(t) - \alpha\beta\kappa\mathcal{S}(t)\mathcal{I}(t) - \mu\mathcal{S}(t), \\ \mathcal{D}^{\theta_1,\theta_2}\mathcal{I}(t) = \kappa(1-\alpha)\mathcal{S}(t)\mathcal{I}(t) - \alpha\beta\kappa\mathcal{S}(t)\mathcal{I}(t) - \dfrac{\mathcal{I}(t)}{\gamma} - \mu\mathcal{I}(t), \\ \mathcal{D}^{\theta_1,\theta_2}\mathcal{R}(t) = \kappa\mathcal{I}(t) - \mu\mathcal{R}(t), \end{cases}$$

with the given initial conditions:

$$\mathcal{S}(0) = \mathcal{S}_0,\ \mathcal{I}(0) = \mathcal{I}_0,\ \mathcal{R}(0) = \mathcal{R}_0,$$

where $0 < \theta_1 \leq 1$ and $0 < \theta_2 \leq 1$ is the fractional order and fractal dimension, respectively, $t \in [0, T]$, $T < \infty$ and $\mathcal{D}$ is the Atangana-Baleanu derivative. The description of the parameters involved in the considered model is given in the following table, assuming that all parameters will be nonnegative:

Parameters	Description
Λ	Birth rate
κ	Total infection rate
α	Isolation rate
β	Protective measures rate
μ	Natural death rate
γ	Infection removal rate

The existence theory of the solution will be carried out through the use of fixed-point approaches and the Hyers-Ulam stability of the solution will be established via nonlinear functional analysis tools. The dynamics of mentioned above compartments for various fractal-fractional orders will be obtained through the Adams-Bashforth method with a two-step Lagrange polynomial for Pakistan's real data [1]. The mentioned above analysis can be found in [2].

Results [2]:

For the numerical simulation, we have taken $\Lambda = 0.00009$, $\kappa = 0.0009$, $\alpha = 50\%, 70\%, 90\%$, $\beta = 0.01182$, $\mu = 0.019$, $\gamma = 100$. The initial conditions are $\mathcal{S}(0) = 220$ **million**, $\mathcal{I}(0) = 0.142$ **million**, $\mathcal{R}(0) = 0$ and step size for evaluating the results is $h = 0.01$. The obtained numerical results illustrated the following importance of the isolation:

- $\mathcal{S}(t)$ is rapidly decreasing and the decay is faster for higher fractal-fractional order.
- For α = 50%, the infection rate is high and the infection may rise to 0.9 million people per day. The decrease of the disease started after 130 days.
- For α = 70%, the infection rate is increasing in first 75 days but then decreases very fast.
- For α = 90%, the infection rate is falling from the beginning and we didn't see any increase in it.
- The recovery rate is going up because there are a maximum number of cases, but then it goes down when the number of infected people decreases.

Conclusion:

The obtained results confirm that increasing the isolation parameter caused by strict preventive measures can reduce disease transmission. Besides, the fractal-fractional order operators have two orders, which can replicate more complex behavior than other calculus tools. Because sometimes, particularly in the case of COVID-19, we have a lack of correct data. So in this situation, the above calculus tools can be a powerful tool to analyze such biological mathematical models.

Keywords— COVID-19; Fractal-fractional calculus; Fractional Adams-Bashforth method

REFERENCES

[1] https://www.worldometers.info/coronavirus/country/pakistan, 7 October 2020.

[2] Z. Ali, F. Rabiei, K. Shah, Z. A. Majid, Dynamics of SIR mathematical model for COVID-19 outbreak in Pakistan under Fractal-fractional derivative, *Fractals*, 2021, https://doi.org/10.1142/S0218348X21501206

A Numerical Method for The Solution to A Class of Fractional Delay Differential Equations of Nonlinear Type

Ömür Kıvanç Kürkçü
Department of Engineering Basic Sciences Konya
Technical University Konya, Turkey
omurkivanc@outlook.com

***Abstract*—This study focuses on the numerical solution to a class of fractional delay differential equations of nonlinear type, implementing a matrix-collocation method dependent upon the Nörlund polynomial and matrix expansions along with the collocation points. Several problems are treated to exhibit the applicability of the proposed method on figures and tables, where some comparisons also exist. By considering the present results, one can state that the method yields a good approximation to numerically evaluate the aforementioned equations.**

Keywords— delay, fractional derivative, matrix-collocation, nonlinear differential equations.

[1] INTRODUCTION

In recent years, the fractional delay differential equations of linear and nonlinear types (FNDDEs) have been of great importance in mathematics, engineering, fluid dynamics, population dynamics, image denoising and the effect of noise on light [1-9], since the fractional order type of real phenomena results in determining their physical responses in detail in comparison with the integer order derivatives. It is evident that solving these equations reveals a hardship in the meanning of analyticalness, hence, the numerical methods are developed to eliminate this issue. So far, Pimenov and Hendy [2] have proposed the shifted Chebyshev method of BDF-type for solving the fractional functional-delay differential equations. Moghaddam and Mostaghim [3] have used the fractional delay differential equations. Ghasemi et al. [5] have established a semi analytical method in reproducing kernel Hilbert space to treat FNDDEs. Iqbal et al. [6] have utilized a wavelet method based on Gegenbauer polynomials for the numerical solution of FNDDEs. Kürkçü et al. [7-9] have introduced a novel numerical method based on the matching polynomials in graph theory for obtaining the approximate solutions of fractional delay differential and fractional differential equations involving cubic and quintic nonlinearities.

Motivated from the studies above, our purpose is to introduce a matrix-collocation method based on the Nörlund rational polynomial, in order to solve a class of FNDDEs involving quadratic and cubic nonlinearities. Furthermore, the method is composed of the reduced matrix expansions based on the Nörlund polynomial, which makes it a direct method without using additional numerical or analytical submethods.

[2] THE GOVERNING EQUATION

First, let us consider and introduce the governing equation of the form

$$y^{(\alpha)}(t) = p_k(t)\,y(\lambda_k t+\delta_k)+q_1 y^2(t)+q_2 y^3(t)+g(t), \quad (1)$$

which is a class of fractional delay differential equations of nonlinear type defined on $[0,T]$. Here, $\alpha\,(\in(0,2])$ denotes the fractional derivative of Caputo type (see [10]); $p_k(t)$ and $g(t)$ are real valued functions, and $\lambda_k, \delta_k\,(\in(0,1])$ are proportional and constant delay arguments, respectively, for k=1,2,3; q_1 and q_2 are real constants.

Equation (1) is subjected to the following initial conditions:

$$y(0)=c_1 \text{ and } y'(0)=c_2, \quad (2)$$

where c_1 and c_2 are the real constant values.

[3] THE LAYOUT OF THE METHOD

In this part, the method is constructed over the matrix expansions at collocation points. Before beginning to establish the method, we shall express the Nörlund polynomial solution form [11]:

$$y_N(t)=\sum_{n=0}^{N} y_n B_n^{(t)}, \quad (3)$$

where y_n's are unknown coefficients to be found by the method and $B_n^{(t)}$ represents the Nörlund rational polynomial, which is defined to be (see [12])

$$\sum_{n=0}^{\infty} B_n^{(t)}\frac{x^n}{n!}=\left[\frac{x}{e^x-1}\right]^t,$$

and its first four elements are

$$B_0^{(t)}=1,\ B_1^{(t)}=\frac{-t}{2},\ B_2^{(t)}=\frac{t^2}{4}-\frac{t}{12},\ \text{and } B_3^{(t)}=\frac{-t^3}{8}+\frac{t^2}{8}.$$

The Chebyshev-Lobatto collocation points on $[0,T]$ hold

$$t_i=\frac{T}{2}+\frac{-T}{2}\cos\left(\frac{\pi i}{N}\right), \quad (4)$$

where $i=0,1,\ldots,N$ and $t_0=0<\ldots<t_N=T$.

The matrix representation of the solution form (3) is given by

$$y(t)=\boldsymbol{B}^{(t)}\boldsymbol{Y}, \quad (5)$$

where

$$\boldsymbol{B}^{(t)} = \begin{bmatrix} B_0^{(t)} & B_1^{(t)} & B_2^{(t)} & \cdots & B_N^{(t)} \end{bmatrix},$$

and

$$\boldsymbol{Y} = \begin{bmatrix} y_0 & y_1 & \cdots & y_N \end{bmatrix}^T.$$

One can refer to [11,12] for more information about Nörlund polynomial.

By (5), the differential part of (1) can be established as

$$y^{(\alpha)}(t) = {}_t^C D_0^\alpha y(t) = \left(\boldsymbol{B}^{(t)}\right)^{(\alpha)} \boldsymbol{Y}, \ \alpha \left(\in (0,2]\right),$$

and its expansion at the collocation points (4) in the form

$$y^{(\alpha)}(t_i) = {}_t^C D_0^\alpha y(t_i) = \left(\boldsymbol{B}\right)^{(\alpha)} \boldsymbol{Y}, \tag{6}$$

where

$$\left(\boldsymbol{B}^{(t)}\right)^{(\alpha)} = \begin{bmatrix} {}_t^C D_0^\alpha \left(B_0^{(t)}\right) & {}_t^C D_0^\alpha \left(B_1^{(t)}\right) & \cdots & {}_t^C D_0^\alpha \left(B_N^{(t)}\right) \end{bmatrix},$$

and ${}_t^C D_0^\alpha$ nominates the fractional Caputo derivative [10], as for $\lceil \alpha \rceil - 1 < \alpha < \lceil \alpha \rceil$,

$${}_t^C D_0^\alpha y(t) = \frac{1}{\Gamma\left(\lceil \alpha \rceil - \alpha\right)} \int_0^t (t-s)^{\lceil \alpha \rceil - \alpha - 1} y^{(\lceil \alpha \rceil)}(s)\, ds,$$

and for $\alpha \in \mathbb{N}_0$, ${}_t^C D_0^\alpha y(t) = y^{(\alpha)}(t)$.

Using the delay arguments λ_k and δ_k in (5), that is, t is assigned to $\lambda_k t + \delta_k$, then the matrix expansion at the collocation points (4) (i=0,1,2,…N) admits

$$p_k(t_i)\, y(\lambda_k t_i + \delta_k) = \boldsymbol{p}_k \boldsymbol{B}^{(\lambda_k, \delta_k)} \boldsymbol{Y}, \tag{7}$$

where

$$\boldsymbol{p}_k = \operatorname{diag}\left[p_k(t_i) \right]_{(N+1)\times(N+1)},$$

$$\boldsymbol{B}^{(\lambda_k, \delta_k)} = \begin{bmatrix} B_0^{(\lambda_k t_0 + \delta_k)} & B_1^{(\lambda_k t_0 + \delta_k)} & \cdots & B_N^{(\lambda_k t_0 + \delta_k)} \\ B_0^{(\lambda_k t_1 + \delta_k)} & B_1^{(\lambda_k t_1 + \delta_k)} & \cdots & B_N^{(\lambda_k t_1 + \delta_k)} \\ \vdots & \vdots & \vdots & \vdots \\ B_0^{(\lambda_k t_N + \delta_k)} & B_1^{(\lambda_k t_N + \delta_k)} & \cdots & B_N^{(\lambda_k t_N + \delta_k)} \end{bmatrix}_{(N+1)\times(N+1)}.$$

Let us now form the matrix expansions based on Nörlund polynomial of nonlinear parts in (1). By (5), their matrix expansions hold

$$\left.\begin{aligned} q_1 y^2(t) &= q_1 \boldsymbol{B}^{(t)} \left(\overline{\boldsymbol{B}^{(t)}}\right) \bar{\boldsymbol{Y}}, \\ q_2 y^3(t) &= q_2 \boldsymbol{B}^{(t)} \left(\overline{\boldsymbol{B}^{(t)}}\right) \left(\overline{\overline{\boldsymbol{B}^{(t)}}}\right) \bar{\bar{\boldsymbol{Y}}}, \end{aligned}\right\} \tag{8}$$

and inserting the collocation points (4) into (8), then we have the regularized forms

$$\left.\begin{aligned} \left[q_1 y^2(t_i)\right]_{(N+1)\times 1} &= q_1 \boldsymbol{B}\left(\bar{\boldsymbol{B}}\right) \bar{\boldsymbol{Y}}, \\ \left[q_2 y^3(t_i)\right]_{(N+1)\times 1} &= q_2 \boldsymbol{B}\left(\bar{\boldsymbol{B}}\right) \left(\bar{\bar{\boldsymbol{B}}}\right) \bar{\bar{\boldsymbol{Y}}}, \end{aligned}\right\} \tag{9}$$

where

$$\boldsymbol{B} = \begin{bmatrix} B_0^{(t_0)} & B_1^{(t_0)} & \cdots & B_N^{(t_0)} \\ B_0^{(t_1)} & B_1^{(t_1)} & \cdots & B_N^{(t_1)} \\ \vdots & \vdots & \vdots & \vdots \\ B_0^{(t_N)} & B_1^{(t_N)} & \cdots & B_N^{(t_N)} \end{bmatrix},$$

$$\bar{\boldsymbol{B}} = \operatorname{diag}\left[\boldsymbol{B}\right]_{(N+1)\times(N+1)^2}, \ \bar{\bar{\boldsymbol{B}}} = \operatorname{diag}\left[\bar{\boldsymbol{B}}\right]_{(N+1)^2\times(N+1)^3},$$

$$\bar{\boldsymbol{Y}} = \begin{bmatrix} y_0 \boldsymbol{Y} & y_1 \boldsymbol{Y} & \cdots & y_N \boldsymbol{Y} \end{bmatrix}^T_{1\times(N+1)^2},$$

and

$$\bar{\bar{\boldsymbol{Y}}} = \begin{bmatrix} y_0 \bar{\boldsymbol{Y}} & y_1 \bar{\boldsymbol{Y}} & \cdots & y_N \bar{\boldsymbol{Y}} \end{bmatrix}^T_{1\times(N+1)^3}.$$

The fundamental matrix equation gathering the matrix expansions (6), (7) and (9) can now be formed as

$$\boldsymbol{W}\boldsymbol{Y} + \boldsymbol{Z}_1 \bar{\boldsymbol{Y}} + \boldsymbol{Z}_2 \bar{\bar{\boldsymbol{Y}}} = \boldsymbol{G}, \tag{10}$$

where

$$\boldsymbol{W} = \left(\left(\boldsymbol{B}\right)^{(\alpha)} - \boldsymbol{p}_k \boldsymbol{B}^{(\lambda_k, \delta_k)} \right), \ \boldsymbol{Z}_1 = q_1 \boldsymbol{B}\left(\bar{\boldsymbol{B}}\right),$$

$$\boldsymbol{Z}_2 = q_2 \boldsymbol{B}\left(\bar{\boldsymbol{B}}\right)\left(\bar{\bar{\boldsymbol{B}}}\right), \text{ and } \boldsymbol{G} = \begin{bmatrix} g(t_0) & g(t_1) & \cdots & g(t_N) \end{bmatrix}^T.$$

The matrix relations of the initial conditions (2) are obtained using (5) as

$$\left.\begin{aligned} y(0) = \boldsymbol{B}^{(0)}\boldsymbol{Y} &\Rightarrow \begin{bmatrix} B_0^{(0)} & B_1^{(0)} & \cdots & B_N^{(0)} : & c_1 \end{bmatrix}, \\ y'(0) = \left(\boldsymbol{B}^{(0)}\right)' \boldsymbol{Y} &\Rightarrow \begin{bmatrix} \left(B_0^{(0)}\right)' & \left(B_1^{(0)}\right)' & \cdots & \left(B_N^{(0)}\right)' : & c_2 \end{bmatrix}. \end{aligned}\right\} \tag{11}$$

Replacing the condition matrices (11) by the last two rows of $\boldsymbol{W}$ in (10), then the augmented matrix system is appeared in the form

$$\left[\boldsymbol{W} \ ; \ \boldsymbol{Z}_1 \ ; \ \boldsymbol{Z}_2 : \boldsymbol{G}\right].$$

Solving the system above, the unknown Nörlund coefficients are obtained and then inserted into (3), hence the Nörlund polynomial solution is acquired.

[4] Numerical Problems

In this part, several problems are considered to scrutinize the applicability and accuracy of the method. In doing so, a computer program is devised in accordance with (1). Thereby, the consistency of the method is also overseen.

Problem 1

The delay differential equation containing cubic nonlinearity was previously considered in biological models and numerical methods [13,14] for its integer order type. Now, consider and construct its fractional form as the following:

$$y^{(\alpha)}(t)= -2ty\left(t-\frac{1}{2}\right)-t^2y(t)+2\sin(t)y\left(\frac{t}{2}\right)+y^3(t)+g(t),$$

subject to the initial condition $y(0)=\exp(-2)$. Here, T=1 and 5, the exact solution is $y(t)=\left(1-t-t^2\right)\exp\left(-2-\frac{t}{2}\right)$, and $g(t)$ is obtained with regard to α. For $\alpha=0.9$, it follows that

$$\begin{aligned} g(t) &= 0.0025e^{-1.5t}\left(-1+t(1+t)\right)^3 \\ &+ e^{-0.5x}t\left(0.4344+t\left(0.1353+\left(-0.4829-0.1353t\right)t\right)\right) \\ &- 0.2134t^{0.1}\,{}_1F_1\left(1;1.1;-\frac{t}{2}\right)-0.1940t^{1.1}\,{}_1F_1\left(2;2.1;-\frac{t}{2}\right) \\ &+ 0.0616t^{2.1}\,{}_1F_1\left(3;3.1;-\frac{t}{2}\right) \\ &+ e^{-0.25x}\left(-0.2707+\left(0.1353+0.0677t\right)t\right)\sin(t), \end{aligned}$$

where ${}_1F_1$ is the confluent Kummer hypergeometric function [15].

Now, the problem is solved by applying the present method with respect to N, α and T. Figs. 1 and 2 reveal a good matching between the Nörlund polynomial solutions and the exact solution on both normal (T=1) and large (T=5) scales. Note that Fig. 2 is constructed after the problem is solved for N=4 and T=5. Fig. 3 demonstrates that the error decreases as the initial N's increase. Table I admits the absolute errors by the present method and orthogonal colliding bodies optimization method (OCBOM) [13] for $\alpha=1$.

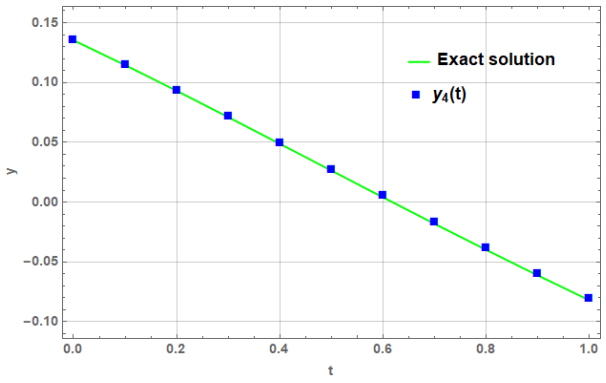


Fig. 9. The coincidence between the solutions for Problem 1 with T=1 and $\alpha=0.9$.

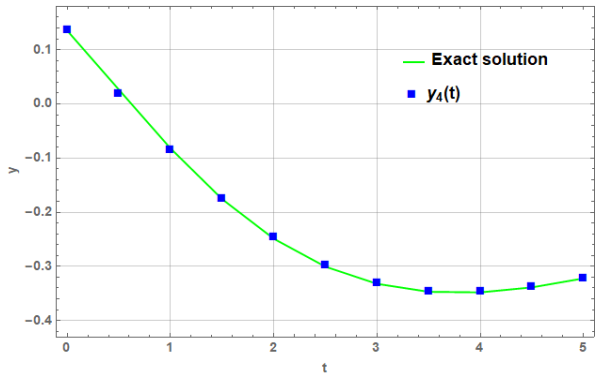


Fig. 10. The coincidence between the solutions for Problem 1 with T=5 and $\alpha=0.9$.

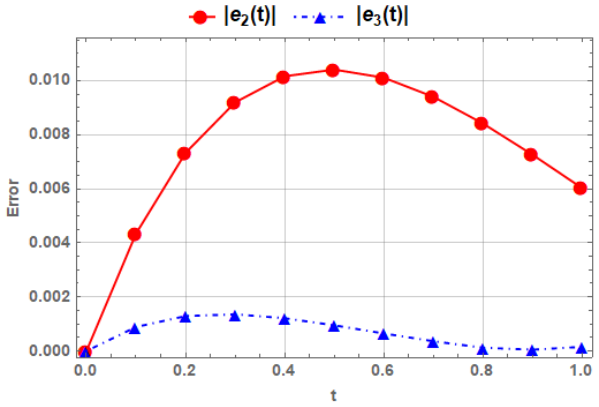


Fig. 11. The absolute error diagrams with respect to the initial values of N for Problem 1 with T=1 and $\alpha=0.9$.

Table 1. Error comparisons for problem 1 with $\alpha=1$

Absolute error	Numerical Methods	
	Present method	*OCBOM [13]*
Best	2.74e-05	6.22e-04
Average	2.92e-04	7.42e-04
Worst	4.50e-04	2.68e-03

Problem 2

Consider the fractional delay differential equation containing quadratic and cubic nonlinearities

$$y^{(\alpha)}(t)= y(0.1t-0.1)-y(0.1t)-0.01y^2(t)-0.01y^3(t)+g(t),$$

subject to the initial conditions $y(0)=0$ and $y'(0)=1$. Here, T=1, the exact solution is $y(t)=\sin(t)$, and $g(t)$ is obtained according to α. For $\alpha=1.8$, it follows that

$$\begin{aligned} g(t) &= -0.9076t^{1.2}\,{}_pF_q\left(\{1\};\{1.6,1.1\};-\frac{t^2}{4}\right)+\sin(0.1-0.1t) \\ &+ \sin(0.1t)+\left(0.01+0.01\sin(t)\right)\sin^2(t), \end{aligned}$$

where ${}_pF_q$ is the generalized hypergeometric function [15].

After solving the problem with regard to N and α, the Nörlund polynomial solutions are acquired. Fig. 4 shows that our solution overlaps consistently with the exact solution for $\alpha = 1.8$. The absolute errors are shown in Table II, where the consistency is appeared for different α.

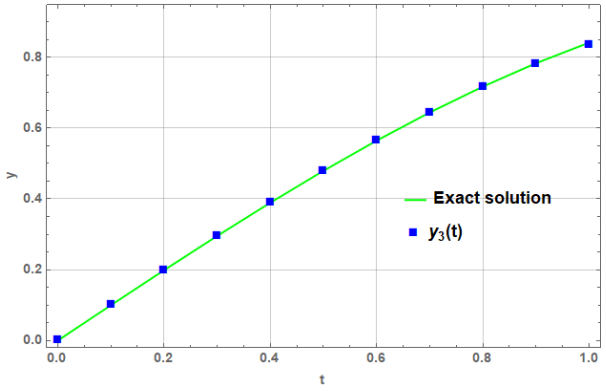


Fig. 12. The coincidence between the solutions for Problem 2 with $\alpha = 1.8$.

Table 2.Absolute Error comparısons for problem 2 wıth different α

t_i	**Different α for N=3**	
	$\alpha = 1.8$	$\alpha = 2$
0.2	1.15e-05	1.07e-05
0.4	1.06e-05	2.20e-05
0.6	3.40e-04	2.81e-04
0.8	2.00e-03	1.83e-03
1.0	6.81e-03	6.46e-03

[5] CONCLUSIONS

A numerical method for the solution to a class of FNDDEs is successfully established. Fractional derivatived matrix expansion based on the Nörlund polynomial is well prepared and then merged with a matrix system. Upon the investigation of the graphical and numerical results, it is clear that the present method provides better approximation than OCBOM [13] as seen in Table I. Thus, it is obviously said that the proposed method forms a dependable tool to treat FNDDEs.

REFERENCES

[1] I. Podlubny, Fractional Differential Equations. New York: Academic Press, 1999.

[2] V. G. Pimenov and A. S. Hendy, "BDF-type shifted Chebyshev approximation scheme for fractional functional differential equations with delay and its error analysis," Appl. Numer. Math., vol. 118, pp. 266–276, 2017.

[3] B. P. Moghaddam and Z. S. Mostaghim, "A numerical method based on finite difference for solving fractional delay differential equations," J. Taibah Univ. Sci., vol. 7, pp. 120–127, 2013.

[4] J. Bai and X. C. Feng, "Fractional order an isotropic diffusion for image denoising," IEEE Trans. Image Process., vol. 16, pp. 2492–2502, 2007.

[5] M. Ghasemi, M. Fardi, and R. K. Ghaziani, "Numerical solution of nonlinear delay differential equations of fractional order in reproducing kernel Hilbert space," Appl. Math. Comput., vol. 268, pp. 815-831, 2015.

[6] M. A. Iqbal, M. Shakeel, S. T. Mohyud-Din, and M. Rafiq, "Modified wavelets–based algorithm for nonlinear delay differential equations of fractional order," Adv. Mech. Eng., vol. 9, pp. 1–8, 2017.

[7] Ö. K. Kürkçü, E. Aslan, and M. Sezer, "A novel graph-operational matrix method for solving multidelay fractional differential equations with variable coefficients and a numerical comparative survey of fractional derivative types," Turk. J. Math., vol. 43, pp. 373–392, 2019.

[8] Ö. K. Kürkçü, E. Aslan, and M. Sezer, "An integrated numerical method with error analysis for solving fractional differential equations of quintic nonlinear type arising in applied sciences," Math. Meth. Appl. Sci., vol. 42, pp. 6114–6130, 2019.

[9] Ö. K. Kürkçü, E. Aslan, and M. Sezer, "On the numerical solution of fractional differential equations with cubic nonlinearity via matching polynomial of complete graph," Sādhanā, vol. 44, article no. 246, 2019.

[10] M. Caputo, Elasticitàe Dissipazione. Zanichelli: Bologna, 1969.

[11] Ö. K. Kürkçü, E. Aslan, and M. Sezer, "An accurate and novel numerical simulation with convergence analysis for nonlinear partial differential equations of Burgers–Fisher type arising in applied sciences," Int. J. Nonlinear Sci. Numer. Simul., in press. Doi: https://doi.org/10.1515/ijnsns-2020-0040.

[12] N. E. Nörlund, Vorlesungen über dierenzenrechnung. Berlin: Springer, 1924, reprinted by Chelsea, New York, 1954.

[13] A. Panda and S. Pani, "Determining Approximate Solutions of Nonlinear Ordinary Differential Equations Using Orthogonal Colliding Bodies Optimization," Neural Process. Lett., vol. 48, pp. 219–243, 2018.

[14] F. Shakeri and M. Dehghan, "Solution of delay differential equations via a homotopy perturbation method," Math. Comput. Model., vol. 48, pp. 486–498, 2008.

[15] M. Abramowitz and I. A. Stegun, Handbook of Mathematical Functions, with Formulas, Graphs, and Mathematical Tables. Gaithersburg, MD, USA: National Bureau of Standards, 1964.

Augmented Reality Application with Marker Technology Improves Automobile Engine Assembly

Lai Lai Win
Department of Mechanical and Manufacturing Engineering Universiti Putra Malaysia Serdang, Malaysia
Department of Mechanical Engineering Government Technical High School (Loikaw) Loikaw, Myanmar
gs51671@student.upm.edu.my

Faieza Abdul Aziz
Department of Mechanical and Manufacturing Engineering Universiti Putra Malaysia Serdang, Malaysia
faieza@upm.edu.my

Norhisham Seyajah
Department of Engineering Technology University Kuala Lumpur, Malaysia Italy Design Institute Kuala Lumpur, Malaysia
hishams@unikl.edu.my

Huda hatam Dalef
Department of Automated Manufacturing Engineering Al-Khawarizmi College of Engineering, University of Baghdad
Jadriya Baghdad, Iraq
huda@kecbu.uobaghdad.edu.iq

Rohidatun M.W
Fakulti Kejuruteraan Mekanikal, Universiti Teknologi MARA Cawangan Pulau Pinang Pulau Pinang, Malaysia
rohidatun@uitm.edu.my

Nadia Abdul Rani
Department of Mechanical and Manufacturing Engineering Universiti Putra Malaysia Serdang, Malaysia
Department of Polytechnic and Community College Education
Putrajaya, Malaysia
gs53369@student.upm.edu.my

Nalienaa Muthu
Department of Mechanical and Manufacturing Engineering Universiti Putra Malaysia Serdang, Malaysia *Human Capital Development Division, Public Service Department*
Putrajaya, Malaysia
gs57132@student.upm.edu.my

***Abstract*— Augmented Reality (AR) is a layering framework that overlays real-world content with computer-generated three-dimensional content. AR is currently a very strong tool that can transform the simple act of conventional learning into an unforgettable experience when used in engineering education. The existing method for assembling automotive engine components using video-based instructions is extremely complicated and difficult to recall. As a result, this marker AR system was developed using marker technology to assist students in engineering classes in learning more effectively. This AR application was rendered with the Unity3D game engine and Vuforia. After that, the app was built into AR smart glasses. Twenty-one engineering students from Universiti Putra Malaysia were selected at random for the experiment and divided and recircuited into two groups: video-based group and AR-based group. The experiment showed that using marker AR-based instruction, Task Completion Time and Error Counts were reduced by 13% and 33%, respectively. According to the results of the study, most participants favored AR to be used in automobile engine assembly testing.**

Keywords—augmented reality, automobile engine assembly, engineering, marker, Unity3D

[1] INTRODUCTION

Stanley G. Weinbaum proposed a goggle-based game in the 1930s where players could watch a holographic video of simulated stories while being able to touch and smell them. Today's virtual reality may be a product of the ground-breaking discovery (VR). After that, Ivann Sutherland invented the first VR headset for military training in the 1960s [1]. The word augmented reality (AR) was then invented by Tom Caudell and David Mizell (1992) to describe the overlaying of computer-presented content on top of the real world. Caudell and Mizell addressed the benefits of AR over VR, including the fact that it needs fewer computing power since less pixels must be made. They also recognised the increased registration requirements in order to reconcile real and virtual [2]. People usually remember 90% of what they do even though they only remember 50% of what they hear and see.

AR is currently a potentially powerful tool for transforming traditional learning into a memorable experience through active experience in many sectors such as manufacturing [3], maintenance and assembly [4], engineering graphics education [5], mechanical engineering [6] and many others [7-9] .

Lai et al. used smart AR technology to integrate an intelligent manufacturing system output on spindle motor installation for a desktop CNC carving system. They built the task in their application using marker instructions. Using their process, they were able to reduce the assembly time and the number of errors [3].

Webel et al. used adaptive visual aids with activated object material to create a multimodal AR with a haptic vibrotactile bracelet on a maintenance and assembly skills platform. In their application, a vibrotactile sense may provide the user with additional task rotation or translation features, as well as the ability to meet goals. This device can detect when a user makes a mistake [4].

Chen et al. researched and created an augmented reality software for engineering graphics education that translates design expertise to manufacturing. During their learning

processes, their method provided students with spatial knowledge and interest in learning, as well as faster comprehension of complex spatial problems and relationships [5].

Liarokavpis et al. developed a Web3D AR for camshaft arrangement with a series of real engine components to aid mechanical engineering. The implemented architecture consists of an XML data repository, a communications server based on XML, and a client visualisation program based on XML. Students were able to imagine how a camshaft was designed in relation to other engine components in their system and examine the actual components at the same time. In addition, users may communicate with the 3D model using a normal keyboard and mouse input devices [6].

According to the literature review, the majority of the studies were carried out to meet current needs, especially in a variety of fields. As a result, the aim of this study is to apply both AR and marker technology to self-directed learning in engineering. In addition, students at the Universiti Putra Malaysia's engineering department are using video guidance to practise assembly of vehicle Modenas engine components. It's difficult to remember a lot of assembly moves. This leads to suffer from students' performance. As a result, this project aims to improve its medium use. Several stages were included in the development of this application, including software installation, three-dimensional (3D) model design, animation creation, game scene construction, and software and hardware configuration. This marker AR application was created with Unity 3D and EPSON MOVERIO BT-300 Smart Glasses in order to gauge student satisfaction and expectations of current technology. Experiments were conducted to compare the efficacy of the established marker-based AR application to the existing system.

[2] MATERIALS AND METHODS

This section presents the development of AR using marker technology to enhance student learning efficiency for automotive engine assembly. The AR applications development composed of three stages namely AR developing an application, testing application performance and user satisfaction. The first stage included modelling the engine components by CATIA V5 software and designing the scene and interactable and assimilable 3D components assembly in each application. The second stage of the project was testing AR applications with EPSON MOVERIO BT-300 Smart Glasses. The third stage was to test the user perceiving the AR applications with the fifth AR generation device, EPSON MOVERIO BT-300 Smart Glasses. In conducting experiments, a total of twenty-one engineering students (ten male students and eleven female students) from Universiti Putra Malaysia were chosen and recircuited randomly into two groups: video-based group and AR-based group. Participants answered their demographic data and preliminary knowledge of AR at the beginning of the experiments. Their answers showed that most of the participants know about the AR even though they have not ever used it. And then they answered of a survey at the end of experiments of the experience of both video-based experiment as shown in Fig.1 and marker AR-based experiment as shown in Fig. 2.



Fig. 1. Video-guideline based automobile engine assembly.



Fig. 2. Marker-AR application-based automobile engine assembly.

[3] RESULTS AND DISCUSSIONS

To overcome the disadvantages of images and to achieve an adequate 3D imaging with high precision, our approach in the design and development of the AR application section, an AR environment was built mainly using the Unity3D game engine, 44 three-dimensional components were designed with CATIA V5 and Blender software being used to get file format that accepted by Unity, and automobile engine components assembly required. All forty-four engine component models in three-dimensional were designed by using Catia V5. The models made in Catia were. CATProduct file or .wrl file format and imported within Blender because Unity cannot accept .wrl file. After importing in Blender, all files were

exported as .FBX file format. Then, all .FBX files were required to import in Unity.

A prerequisite in a marker setup section, one complicated image was selected and downloaded to make sure the tracking quality is good for an image target in the marker-based AR application. Then, the image was printed and later used in the experiment and then laminated to be placed at the component set up as shown in Fig. 2.

To visualizes the created image marker to obtain the 2D-3D correspondences, go to the Vuforia engine developer portal and a free developer account was then created and log in. Under 'License Manager Tab', a free development license key was created. Then, under 'Target Manager', the image markers database was created, and image marker was uploaded into the portal. The uploaded image marker was used in the application interface design later. Then, the package was downloaded as Unity Editor Package and saved in a specific folder on laptop. Then it is needed to import in marker-based AR environment. AR is the technology that provides and audio-visual that bring the viewer to the real world.

For the 3D imaging applications in marker AR gaming scene building, Unity 3D is used by many developers especially the ones who develop and create games. It has a different type of packages depends on user usage. For personal use, it can be downloaded for free which is great for the beginner who wants to learn in this field. When using Unity 3D, setting and other parameters need to be set depending on what device the application will be run. Unity 3D can be used to develop an application for either window, macOS, Android, WebGL or iOS. The setting needs to be tally with the run device to prevent a conflict or error. It is also software that developer and designer can design the gaming scene and environment according to the required results. All the setting and other parameter need to be set up in the software before exporting it into android smart glasses. Unity 3D was launched, and our current project was created for this research, with the data and information required.

The combination of the depth in mechanical measurement used in the Unity 3D workspace, there are five main panels such as Scene, Game, Hierarchy, Project and Inspector of the game object. In the AR environment, all 44. .FBX files were required to import in Unity in Prefabs of Assets of Project panel. For this project, 49 scenes were made. The first scene was welcoming text with the details of an experiment that will be held. The middle 47 scenes are engine components assembly and demonstrated step by step. The final scene showed that the experiment was done.

Theoretically, for the AR camera setting up, it is required to download and add the Vuforia Engine to a Unity Project or upgrade to the latest version from Vuforia engine developer portal. In the Game Object options, both AR Camera and Image Target of Vuforia Engine were selected into the hierarchy of the workspace. To account for such accuracies, it was needed to add both three-dimensional components and the targeted marker to Image Target for the assembly system so that the marker can work well. The Main Camera, which is the default, was deleted because it is not used in this project.

To corresponding the position to the real object, to connect from one scene to another scene, two buttons were made using the user interface (UI) function. First, a canvas was made so that the two buttons can be placed on the screen. For the Canvas, render mode was set as "screen space-overlay" and UI scale mode of Canvas Scaler was set to "scale with the screen size" so that the application can be used in different devices but in the same platform which is android without a problem. In this project, the marker-less AR app was set with smart glasses resolution (1280x720). The UI was made simple making the user ease to navigate either to the next scene or back to the scene before.

For the button to function, scripting was needed to be done to navigate the apps by deactivating the current object and activating the other desired object. Scripting was done in Visual Studio Community 2017 software and the script for going either next scene (Next Button) or back scene (Back Button). In addition, restarting the app (Restart Button) and existing app (Exit Button) were also included in the final scene. For adding license key, open 'Vuforia Configuration' of Resources Assets of Project Panel and the license key form Vuforia developer portal was copied into the space provided in the Inspector Panel. This app license key was to enable the final app to work well.

In view between the build setting, the platform was switched to Android and click Add Open Scenes to arrange scene after scene targeted. In the Player of Project Settings, Resolution and Presentation, and Other Settings sections are adjusted in this project. Both Start in full screen mode and Landscape Left under Resolution and Presentation were ticked to configure this project. Auto-Graphics API and ARCore Supported of XR Setting were also ticked to build the AR app. To compile all the scenes and build an application, three sections of JDK, Android SDK and Android SDK under the Android section of External Tools of Preferences under the Edit tab were also needed to link with the Unity 3D. After doing all the settings, the build button was hit, and the file was saved as apk file.

Experimental AR was being used to be conducted with 21 participants. Then, all participants are divided and recircuited into two groups which were video-based group and marker AR-based group. This AR test saved time and effort to conduct the actual test. Before the experiment was started, the participants were brief and delivered a presurvey of demographic data and general knowledge of AR with the experiment workflow and they were assigned a number from number 1 to 21. The survey content was about age, gender, course, department, and any previous experience related to the experiment. They then need to follow the number assigned throughout the experiments was conducted and recircuited into two experiments of video-based method and AR application method. Random order was assigned to the participants to do AR instruction or video-based instruction first to minimize biased learning effect and increase the validity of the data. After doing the first task, the participants recircuited to do the second task on the same automobile engine assembly process. Then, the participants filled up the questionnaire after they have done their task in the conducted condition. The Task Completion Time (TCT) and error counts in the assembly task was recorded and tabulated during the experiment was conducted. The conducted experiment consisted of data analysis of TCT and error counts. For the TCT data, the meantime for the video-based group is 38 minutes and AR-based group meantime is 33 minutes. For the error counts, the mean error count for the video-based group is 3 errors and AR based group mean is 2 errors. In this application, TCT and error counts were reduced by 13% and

33%, respectively. In future work, it would be interesting to evaluate whether the alternative approach could be further improvement by the global optimization and to provide the satisfaction of the users of all 2D-3D maker, making efficiently in the automobile industry.

ACKNOWLEDGMENT

The authors would like to express our deep appreciation and gratitude to JICA's AUN/SEED-Net at UPM for its complete financial support (UPM CR 2001: Vote Number: 6282000, GP-IPS: Vote Number: 9627800), staffs of UPM Tenth College, Hyper Version Research Laboratory (Keio University), Japan and all participants, engineering students of our experiments from both UPM Tenth College and UPM Eleventh College.

REFERENCES

[1] A. Enrique and S. Cano, *Design and Implementation of A Virtual Reality*. Morehead State University, the United States, 2018.

[2] C. Arth, R. Grasset, L. Gruber, T. Langlotz, A. Mulloni, and D. Wagner, "The History of Mobile Augmented Reality," 2015.

[3] Z. H. Lai, W. Tao, M. C. Leu, and Z. Yin, "Smart augmented reality instructional system for mechanical assembly towards worker-centered intelligent manufacturing," *J. Manuf. Syst.*, vol. 55, no. July 2019, pp. 69–81, 2020.

[4] S. Webel, U. Bockholt, T. Engelke, N. Gavish, M. Olbrich, and C. Preusche, "An augmented reality training platform for assembly and maintenance skills," *Rob. Auton. Syst.*, vol. 61, no. 4, pp. 398–403, 2013.

[5] H. Chen, K. Feng, C. Mo, S. Cheng, Z. Guo, and Y. Huang, "Application of augmented reality in engineering graphics education," *ITME 2011 - Proc. 2011 IEEE Int. Symp. IT Med. Educ.*, vol. 2, pp. 362–365, 2011.

[6] F. Liarokapis *et al.*, "Web3D and Augmented Reality to support Engineering Education," *UNESCO Int. Cent. Eng. Educ. J. World Trans. Eng. Technol. Educ.*, vol. 3(1), no. 1, pp. 11–14, 2004.

[7] O. A. Olanrewaju, A. A. Faieza, and K. Syakirah, "Current trend of robotics application in medical," *IOP Conf. Ser. Mater. Sci. Eng.*, vol. 46, no. 1, 2013.

[8] F. A. Aziz, F. Abdullah, and L. L. Win, "Using Marker Based Augmented Reality for Training in Automotive Industry," *Int. J. Recent Technol. Eng.*, vol. 7, no. 4S2, pp. 118–121, 2018.

[9] L. L. Win *et al.*, "Immersive Virtual Reality Application Development Using HTC Vive and High-End Laptop," vol. 12, no. xx, pp. 1–5, 2020.

Analysis on Materials of Bus Superstructure in Compliance to R66

*Note: Sub-titles are not captured in Xplore and should not be used

Nur Isnida Razali
Faculty of Mechanical and Manufacturing Engineering Universiti Putra Malaysia UPM Selangor, Malaysia
nurisnida123@gmail.com

Nuraini Abdul Aziz
Faculty of Mechanical and Manufacturing Engineering Universiti Putra Malaysia UPM Selangor, Malaysia

Ameen Topa
Institute of Transportation Infrastructure Universiti Teknologi PETRONAS Perak, Malaysia
Department of Maritime Technology Universiti Malaysia Terengganu Terengganu, Malaysia

***Abstract*— Rollover crashes among the buses have been certified as the most disastrous event of all types of crashes and have been obligated into the law by many countries. It is mandatory for the buses to achieve the requirements stated in the regulation to protect the driver and passengers of the bus by maintaining the residual space through the sufficient strength of the superstructure. In this paper, the simulations of the bus rollover according to the standard of United Nation Economic Commission of Europe Regulation No.66 (UNECE R66) using finite element analysis, LS Dyna are performed using three grades of steel having different values of yield strength. The yield strength of typical mild steel is 270 MPa, an Ultragal coated steel AS 1163 ranging from 332 to 445 MPa according to thickness and grade of ASTM A500 is 363 MPa. In the original design, the intrusion of the structure into residual space is the minimum for AS 1163 with 94.152mm followed by ASTM A500 Grade B with 305.653mm and the highest intrusion occurred for typical mild steel which is 667.256mm. After few modifications introduced, the internal energy of the bus superstructure in rollover has reduced tremendously and all the bus superstructure achieved R66 with no intrusion into residual space.**

Keywords*— Bus rollover, UNECE R66, mild steel, yield strength, intrusion, internal energy.

[1] INTRODUCTION

Buses have always been a favorable choice to travel whether for short or long distance due to their availability, large carrying capacity and affordability other than trains and airplanes. Albertsson and Falkmer [1], Belingardi et al.[2] and Morency et al. [3] agreed that travelling by buses are safer compared to cars and almost safe as trains and airplanes. Investigation have revealed that the most dangerous traffic accident is the rollover [4]. In addition, from more than 300 bus rollover accidents' statistics recorded by Matolcsy, the casualties' rate is 25/ accidents making it as the most dangerous bus type accident [5]. The fatalities and injuries in rollover accidents are due to partial and total ejection outside of the bus, projection inside the bus, intrusion of deformed structural parts of bus into passengers, slash or prick of broken glass into passengers' body, or smoke suffocation or burnt caused by burning [6]. Among this, the riskiest is the intrusion into passengers [7] and can be prevented by strengthening the bus superstructure as mentioned in UNECE R66. Consequently, due to the severity of the bus rollover accidents, the regulations have been legislated focusing on the strength of superstructure to preserve the residual space for the occupants in the rollover event. Superstructure is the components of the bus structure that contribute to the strength and energy absorbing characteristics while residual space is referred to the space where drivers and passengers are in the bus. The familiar standard that is used in more than 50 countries is the United Nation Economic Commission for Europe Regulation No. 66 (UNECE R66), the Automotive Industry Standard (AIS)-031 which is used in India, and Australian Design Rules (ADRs) 59/00 in Australia which is imposed in addition to the present international standard UNECE R66. In the United States, the standard number 220 of the American Federal Motor Vehicle Safety Standards (FMVSS 220) is a standard designed for the school bus rollover protection that may be adapted for motor coaches. Materials used in vehicle's construction is based on a few targets. Some manufacturers would prefer lightweight, and some might opt for the strength and other reason such as lesser maintenance due to corrosion free material. As for higher strength material, it helps in increasing the crashworthiness in the collision. Somehow, the stiffer and sturdy material is related to the weight reduction too. As their strength is improved, thickness used is reduced thus lead to lighter frames. Satrijo et al. [8] compared three materials which is the steel with the code JIS 3445, Aluminum 6005A T6 and Aluminum 6061 T6 for the construction of lightweight electric bus. Static analysis was carried out by impacting the plate to the roof following the requirements in UNECE R66. Among three materials, with the same dimensions of the structure, Aluminum 6061 T6 has the lightest weight and can withstand the impact with maximum clearance distance between structure and residual space. Some researchers have proposed the use of carbon fiber as the replacement of steel for the bus structure. For instance, the usage of the carbon- epoxy composite roll bar in the bus superstructure has greatly improved the strength of the bus by comparing to the initial superstructure with the same weight [9]. The introduction of the metal foam in the beams has increased the bending resistance compared to the empty beams and can be used in the bus structure to bear the rollover impact hence improving the crashworthiness [10]. Composites also has been used in bus manufacturing due to its lightweight and high strength comparable to the metallic bus superstructure. For instance, Luis et. al. has performed the simulation and real rollover on the bus body section using composites and it showed the good correlation between both simulation and experiment. Later, they developed the full-scale bus prototype using fully composite and the bus qualified the R66 with the safety factor of 2.185. The bus is 1000kg lighter than the bus made of steel [11]. The rationality of using stainless steel in bus building has been summarized by Reddy and Shekar. Based on detailed research and comparison with carbon steel and galvanized mild steel, stainless steel has greater life cycle cost (LCC),

better energy absorbing ability, fully recyclable, higher strength which lead to weight reduction and aesthetic finish. The minimum estimated life of stainless steel is more than 10 years while galvanized mild steel starts to rust after 3 to 4 years of operation [12]. The superiority of stainless steel in bus applications has also been demonstrated. Kyro proved the supremacy of stainless steel over the traditional material used for the bus and other competitive material such as carbon steel and aluminium through corrosion, toughness and fatigue test and calculation of LCC on the bus frames [13]. Although many types of materials are used in automotive industry, steel is still being the most important material in vehicle construction due to its main features of effortless availability, and cost compared to another materials. In addition, the qualities such as strength, recyclability, stiffness, formability, crashworthiness and low-cost contribute to the factor of the dominance of steel in transportation market. More high specification of steel in term of strength, lightweight, ease of joining and thickness are progressing to develop in future [14].

[2] METHODOLOGY

In this analysis, the finite element analysis of LS Dyna is used to simulate the rollover of the full-scale bus. The model bus used is the typical model with the length of 11.52 meter (m), width of 2.45 m and height 3.32 m. Three materials used are the typical mild steel, steel with Ultragal coating AS 1163 and ASTM A500 Grade B. The density of all materials is 7.85 x 10^{-9} ton/mm^3, Young's Modulus of 200 GPa and Poisson's ratio 0.3. The yield strength is different which is 270 MPa for the typical mild steel, 332 (1.6mm), 403 (2.3mm) and 445 (3mm) MPa for the Ultragal coated steel AS 1163 and 363 MPa for the ASTM A500. The yield strength of other mechanical properties of AS 1163 and ASTM A500 are obtained from the tensile test. [15]. The rollover is setup according to the R66 which is the tilting platform is 800mm from the ground. The bus is tilted to 62 degree with the more vulnerable side is selected to impact the ground as mentioned in R66. The bus is already in the unstable equilibrium position; thus, less computational time is taken to reach the ground. Gravity is used to fall the bus from the tilting platform. In order to ensure the accuracy of the simulation and to be as close as to the real-life solution, it is important to properly mesh the parts of the bus in FEA model. Meshing or discretization is the process of splitting the domain into smaller parts or elements so that the problems can be calculated and solved individually and then interpolated for the entire domain using a numerical technique known as finite element method (FEM). FEM limits the number of points from infinite to finite. After performing the mesh convergence analysis on the bus rollover of the initial design, element size of approximate 17mm is used for the ring pillars and coarser elements for another parts. Other parts are not contributing to the strength of the bus as much as the ring pillars hence the elements used are larger. All elements are modelled with the shell element using the formulation of Belytschko-Tsay. MAT_24 Piecewise_Linear_Plasticity is used for the superstructure parts and MAT_20 Rigid is used in the chassis, engines, tilting platform, ditch and residual space. Deformable_to_rigid_automatic switch is used to save the running time. The parts are set to be rigid at the beginning of the simulation and switched to deformable when almost touching the ground.

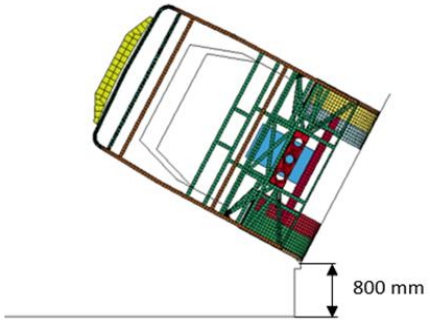


Fig. 10. The setup of rollover simulation.

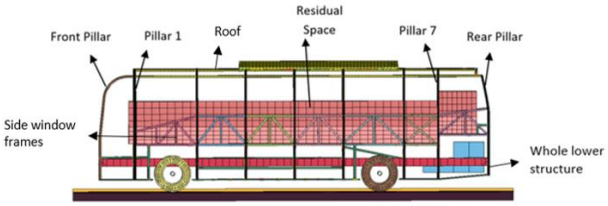


Fig. 11. The parts of the bus.

Pillar 1 to pillar 7, front and rear pillars are the ring pillars that absorb most of the impact in rollover. Besides that, the weight of the lower structure has an influence too. Thus, the modifications have been done on the ring pillars and the lower structure in the modified design. The beams are also introduced at the critical points which is at the corner of the roof to limit further deformation. The beams are positioned so it looks like a triangle structure as triangle is better in resisting the forces without losing its shape hence assisting in improving the strength of the bus superstructure.

Since there is no real rollover is performed to validate the simulation, the energy balance and ratio is used to verify the simulation. Matolcsky and Molnar proposed that for bus rollover, verification of computational model and simulations are made by the values of energy balance, deformations and other components [16]. In this simulation of the bus rollover, the numerical error is checked through the energy balance. According to Bojanowski, the energy components must abide the laws of conservation of energy and all the non-physical energy are reserved at minimum [17]. The energy data in Ls Dyna are beneficial in the analysis. The subsequent equation should be retained at all times during analysis;

$$E_{total} = E_{kin} + E_{int} + E_{si} + E_{rw} + E_{damp} + E_{hg} = E^0_{total} + W_{ext} \quad (1)$$

$$E^0_{total} = E^0_{kin} + E^0_{int} \quad (2)$$

Where,

E_{kin} = current kinetic energy

E_{int} = current internal energy

E_{si} = current sliding interface energy

E_{rw} = current rigid wall energy

E_{damp} = current damping energy

E_{hg} = current hourglass energy

E_{kin}^{0} = initial kinetic energy

E_{int}^{0} = initial internal energy

W_{ext} = external work

E_{total}^{0} = initial total energy

The value of energy ratio must be around 1.00 with the tolerance of +/- 0.07 [18] to show that the energy is conserved. The energy balance is said to be perfect if the ratio is equal to 1.

$$e_{ratio} = \frac{E_{total}}{E_{total}^{0}+W_{ext}} \quad (3)$$

[3] RESULTS AND DISCUSSION

A. Energy Balance and Energy Ratio

The verification of the simulation can be made through the energy data in GLSTAT files. The bus with the original condition using typical mild steel is used for the verification purpose. The total energy in GLSTAT consists of 6 forms of energies including the internal energy E_{int}, kinetic energy E_{kin} , sliding energy E_{si} , hourglass energy E_{hg} , damping energy E_{damp} and rigidwall or stonewall energy E_{rw}. The addition of all energies must equal to the total of initial energy E_{total}^{0} and external work W_{ext}. The verification can be made by tracking the energies involved throughout the whole process of simulation from start to the point when the bus is completely rest. The values of energies are required to find the energy ratio to determine whether the simulation is correct or need to be modified to achieve the ratio value of 1.00+/- 0.07. Energy ratio is the ratio of input energy to output which is total energy. The total energy is referred to total energy in GLSTAT not in the HISTORY. In HISTORY, the total only includes the kinetic and internal energy. There is a small amount of positive contact energy which is less than 5 percent of the total energy. Another energy such as hourglass energy is also within the range of less than 5 percent of the total energy too. The energy absorbed or internal energy also satisfy the equation in the R66 which is 87.5 percent from the total energy. The requirement is at least 75 percent. Hence the energy ratio can be found by dividing the output energy which is the real total energy to the input energy which is potential energy and external work. The ratio is between 1.0148 and 0.963. It is in the permissible range of 1.00+/- 0.07, therefore no adjustment on the model is needed. Thus, the simulation is verified to be used in further analysis.

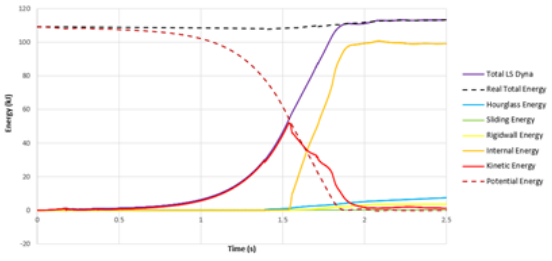


Fig. 12. The energy balance of bus rollover

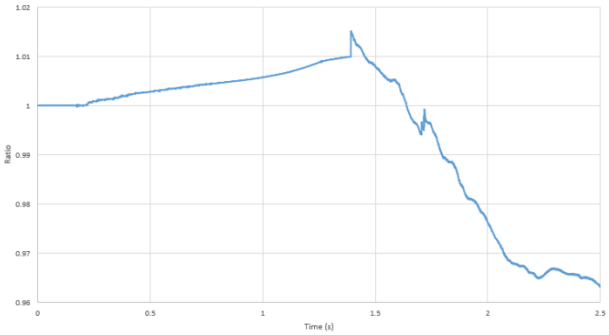


Fig. 13. The energy ratio of bus rollover

B. Original Design

There are two simulations performed for each material which is for the initial and improved design that qualified the R66. The initial design is same for all types of materials and the improved design is different. The ring pillars which is pillar 1 to 7 are made of square hollow section (SHS) with the dimension of 50x50 mm in the initial design. The thickness of 2.3mm and 3.0mm are used for lower structure and ring pillars, respectively. While the thickness for whole roof structure is 1.6mm and side window frames are 2.3mm. In this study, the modifications are focused on the structure of lower and vertical pillars only. The weight of the original design is 12.3027 ton. As a result, the bus fails R66 in all materials. The bus with typical mild steel has the largest intrusion into residual space followed by ASTM A500 and AS 1163. Intrusion is the highest at the pillar 7 which located at the back of the bus. This is due to the extra weight of the engine and the higher residual space compared to other compartment of the bus. The residual space is high because the floor is elevated to mount the engine beneath the floor. Maximum intrusion into residual space is as in the "Table 1". The bus using AS 1163 only has intrusion at pillar 1 and pillar 7 which is at the front and back area of the bus. Mild steel has the highest internal energy followed by ASTM A500 and AS 1163.

Table 3 Intrusion into residual space for original design

Pillar	Typical Mild Steel (mm)	ASTM A500 (mm)	AS 1163 (mm)
1	424.9	175.6	9.6
2	432.9	168.4	-
3	464.8	171.8	-
4	483.1	174.5	-
5	490.4	149.1	-
6	487.9	138.6	-
7	657.3	305.7	100.2

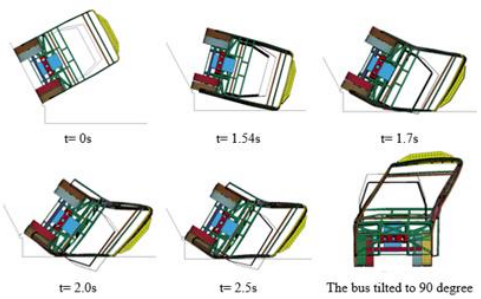


Fig. 5. The rollover of the bus of mild steel

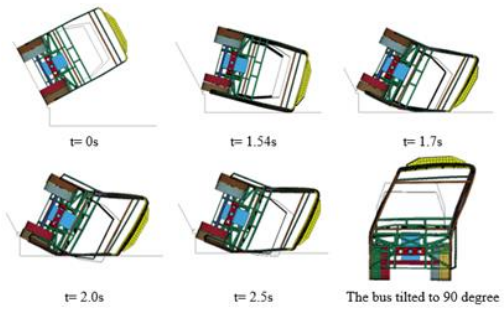


Fig. 14. The rollover of the bus of ASTM A500

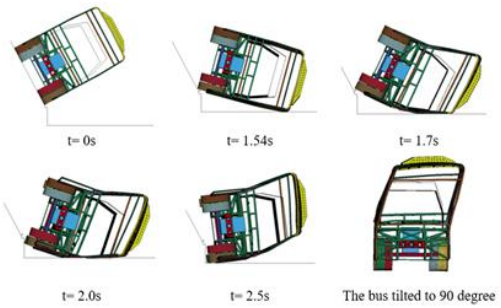


Fig. 15. The rollover of the bus of AS 1163

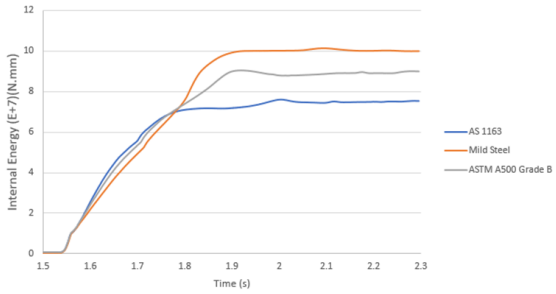


Fig. 16. The internal energy of original design

C. Modified Design

In the modified design of all materials, the larger dimension of ring pillar which is 60x60 mm is used for the ring and rear pillars. The triangle stiffener of dimension 33 cm is installed at each corner of the ring pillars to enhance the strength and limiting more deformations. Since the highest intrusion is recorded at the rear section of the bus, the pillar 7 and back pillar is increased in thickness compared to the others. The thickness is different for each material. For the bus with typical mild steel material, the thickness of front and pillar 1 to 6 is 5mm, pillar 7 and rear is 7mm while the lower structure is 3 mm while the weight is 12.9832 ton. For the bus with ASTM A500 material, the thickness of front and pillar 1 to 6 is 4mm, pillar 7 and rear is 5mm while the lower structure is 2.3mm while the weight is 12.5737 ton. For the bus with AS 1163 material, the thickness of front, pillar 1 to pillar 7 and rear is 3mm while the lower structure is 2.3mm while the weight is 12.3115 ton. The rear section is quite weak because the location of the engine there hence increases the weight at the lower parts resulting to more impact during rollover. Therefore, the pillar 7 and rear need to be strengthened by increasing the thickness. Owing to the weight, the typical mild steel is the first to touch the ground at 1.39s since it is the heaviest structure, followed by ASTM A500 at 1.45s and AS 1163 at 1.51s. From the graph of internal energy, the bus of typical mild steel is perfectly resting on the floor after the first impact while the bus with ASTM A500 and AS 1163 bounce after the first impact. The value of internal energy is lower in the modified design.



Fig. 17 The triangle stiffener at the corner of the ring pillar

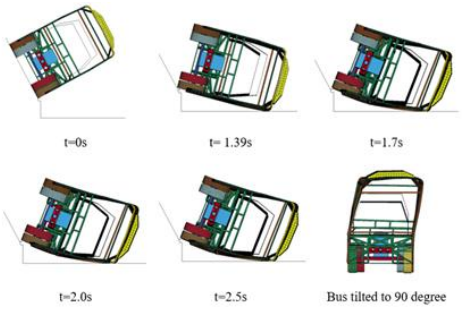


Fig. 18. The rollover of the bus using typical mild steel

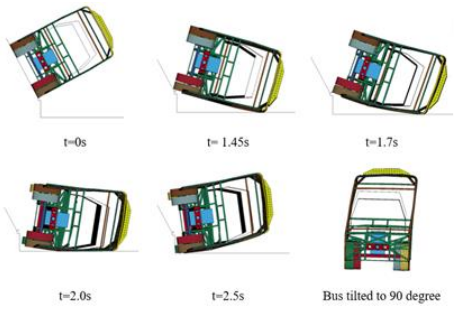


Fig. 19 The rollover of the bus using ASTM A500

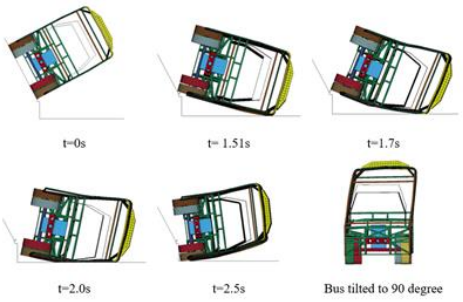


Fig. 20 The rollover of the bus using AS1163

Table 4. Clearance between ring pillars and residual space.

Pillar	Typical Mild Steel (mm)	ASTM A500 (mm)	AS 1163 (mm)
1	18.2	75.6	74.3
2	29.4	55.4	44.6
3	45.9	56.6	38.8
4	53.5	57.0	32.9
5	57.6	53.9	32.5
6	59.1	49.8	36.5
7	22.4	14.3	6.3

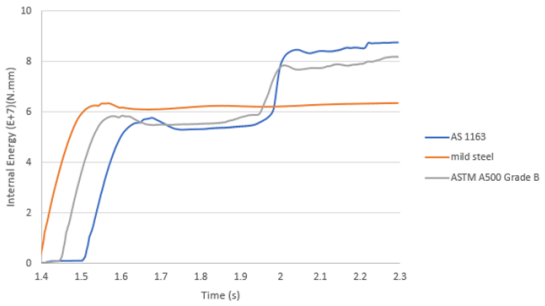


Fig. 21. The internal energy of modified design

[4] CONCLUSION

The rollover of the bus is performed using three different kinds of steel with variant in yield strength. All three materials pass the minimum requirement in R66 through combinations of thickness of ring pillars and lower structure. The increment of weight modified design from initial design for all three materials is 0.6805 ton or 5.53 percent in typical mild steel, 0.271 ton or 2.2 percent and 0.0088 ton or 0.07 percent for AS 1163. Increasing the thickness, enlarging the pillar's dimension and introducing the triangle at the corner is proven to prevent further rollover. Bus using AS 1163 is the lightest among three materials used and give almost similar result with the others.

REFERENCES

[1] Albertsson P, Falkmer T. "Is there a pattern in European bus and coach incidents? A literature analysis with special focus on injury causation and injury mechanisms". *Accident Analysis & Prevention*, vol 37(2), pp. 225-33, March 2005.

[2] Belingardi G, Martella P, Peroni L. "Analysis of the coach rollover scenario". *Vehicle System Dynamics*, vol 44(sup1),pp. 455-67, Jan 2006.

[3] Morency P, Strauss J, Pépin F, Tessier F, Grondines J. "Traveling by bus instead of car on urban major roads: safety benefits for vehicle occupants, pedestrians, and cyclists". *Journal of urban health*, vol 95(2), pp. 196-207, April 2018.

[4] Seyedi M, Jung S, Wekezer J, Kerrigan JR, Gepner B. "Rollover crashworthiness analyses–an overview and state of the art". *International journal of crashworthiness*, vol 25(3), pp. 328-50, 3rd May 2020.

[5] Matolcsy M. "The severity of bus rollover accidents". *Scientific Society of Mechanical Engineers*. Paper 70989, 2007

[6] Mátyás M. "Ejection of passengers in bus rollover accidents". *In Proceedings of the FISITA 2012. World Automotive Congress 2013*. Springer, Berlin, Heidelberg, pp. 161-178.

[7] Conroy C, Hoyt DB, Eastman AB, Erwin S, Pacyna S, Holbrook TL, Vaughan T, Sise M, Kennedy F, Velky T. "Rollover crashes: predicting serious injury based on occupant, vehicle, and crash characteristics". *Accident Analysis & Prevention*, vol 38(5), pp. 835-42, September 2006.

[8] Satrijo D, Kurdi O, Haryanto I, Yob MS, Riyantiarno N, Taufiqurrahman I. "Rollover performance analysis of electric bus superstructure frame with alternative material using finite element method" . *In AIP Conference Proceedings 2020 Apr 13* (Vol. 2217, No. 1, p. 030153). AIP Publishing LLC.

[9] Kang KT, Chun HJ, Park JC, Na WJ, Hong HT, Hwang IH. "Design of a composite roll bar for the improvement of bus rollover crashworthiness". *Composites Part B: Engineering*, vol 43(4), pp. 1705-13, June 2012.

[10] Cazzola GJ, Alcalá Fazio E, Izquierdo FA. "Study of the bending response of metal foam-filled beams applied to enhance the rollover behaviour of coach structures". *International Journal of Crashworthiness*, vol 18(6), pp. 620-32, Dec 2013.

[11] Castejon L, Miravete A, Cuartero J. "Composite bus rollover simulation and testing". *International journal of heavy vehicle systems*, vol 13(4), pp. 281-97, Jan 2006.

[12] Reddy S, Shekar VT. "Rationale behind 'Stainless Steel Super Structure'for Buses". *SAE Technical Paper*; 2013 Sep 24.

[13] Kyröläinen A, Vilpas M, Hänninen H. "Use of stainless steels in bus coach structures". *Journal of materials engineering and performance*, vol 9(6), pp. 669-77, Dec 2000.

[14] Singh MK. "Application of steel in automotive industry". *Int. J. Emerg. Technol. Adv. Eng.*, vol 6(7), pp. 246-53, Jul 2016.

[15] Mahathir Rahman. "Bus Superstructure Rollover Analysis Using Finite Element Method". 2017. Universiti Putra Malaysia.

[16] Matolcsy M., Molnar C., "Bus rollover test as a process and its energy balance", 30th Meeting of bus and coach experts, Győr, Hungary, 1999.

[17] Bojanowski, C., Wekezer, J., Kwasniewski, L. and Kownacki, J. "Florida standard for crashworthiness and safety evaluation of paratransit buses". *21st Int. Technical Conf. Enhanced Safety of Vehicles*, 2009, pp. 15-18,.

[18] Hamid, I. A., Kamarudin, K. A., Osman, M. R., Abidin, A. Z., Zulkipli, Z. H., Jawi & Ariffin, A. H. "Finite Element Bus Rollover Test Verification". *Journal of the Society of Automotive Engineers Malaysia*, vol 3(4), 2019.

Mass Fraction Effect on Mechanical Properties of E-Glass Fiber Reinforced Polyethylene Composites

Samet Sanbur
Graduate School of Natural & Applied Sci. Dokuz Eylul University
Izmir, Turkey
sametsanbur@gmail.com

Cemal Koçhan
Mechanical Engineering Department
Dokuz Eylul University
Izmir, Turkey
cemal.kochan@deu.edu.tr

Çiçek Özes
Mechanical Engineering Department
Dokuz Eylul University
Izmir, Turkey
cicek.ozes@deu.edu.tr

***Abstract*—In this research, plain weave E-glass fabric reinforced high density polyethylene (HDPE) thermoplastic composites were produced in a hot-press and mass fraction of the reinforcement effect on the mechanical properties was investigated by means of tensile tests and low-velocity impact tests at 25 J, 50 J, 75 J impact energies. Thermoplastic composites were designed as three layers of 1 mm HDPE and two layers, four layers, six layers, eight layers E-glass fabric, respectively. They were produced under the conditions of 190 ^{0}C temperature and 8.163 bar pressure during 30 minutes. As a result of the production procedure, four different mass fraction levels of the reinforcement as 6.75 %, 12.65 %, 17.85 % and 22.5% were obtained. According to the test results, approximately 50 MPa to 130 MPa tensile strength and 480 MPa to 2400 MPa elastic modulus range obtained for four different mass fraction groups. On the other hand, maximum absorbed energy levels with regarding to different impact characteristics were observed for each group. The test results were given in graphs and tables then discussed in detail.**

Keywords—glass fiber, high density polyethylene, tensile test, low-velocity impact test.

[1] INTRODUCTION

Thermoplastic materials are best known by means of their recyclable and reusable characteristics. Therefore, the plastic industry has a wide variety range of products such as shopping bags, bottles, different kinds of storage containers, toys, films etc. Over all, one of the most used thermoplastic is the polyethylene. It has the structure of $(C_2H_4)_n$ and different final forms according to its density and branching for instance high density polyethylene (HDPE), low density polyethylene (LDPE), cross-link polyethylene (PEX).

Researchers show great interest to mechanical properties of polyethylene and its composites. HDPE and its blend with chlorinated polyethylene (CPE) were investigated for its tensile behavior [1]. In another research, three form of PE as HDPE, LDPE and ultra high monocular weight polyethylene (UHMWPE) were produced and tensile, shear and impact tests were conducted [2]. HDPE and LDPE were mixed at different ratios then tensile and flexural properties were investigated [3]. Although polyethylene shows great chemical properties, researchers have attempted to improve its mechanical, thermal and electrical properties by help of reinforcement [4-10].

Low-velocity impact test is important to identify the damage characteristics and capacity of energy absorption of the materials. Since fiber reinforced composites have heterogeneous and anisotropic nature, four failure modes occur such as matrix failure, fiber failure, delamination of layers and penetration [11].

The aim of this study is to describe how the mass fraction effects tensile and low-velocity behaviors of the E-glass fabric reinforced HDPE composites. Hence, E-glass/HDPE composites were produced in four different mass fractions related to different number of the E-glass layers. After then, tensile and low-velocity impact tests were conducted in order to identify the tensile strength, tensile modulus, impact characteristic and absorbed energy capacity of the composites.

[2] MATERIAL AND METHODS

A. Used Materials and Sample Preparation

As a reinforcement material, plain weave woven E-glass fabric which had density of 100 g.m^{-2} was used. High density polyethylene (HDPE) film which had 1 mm thickness and density of 0.92 g.cm^{-3} used as matrix materials, as well. E-glass fabric was bought from Cam Elyaf – Sisecam Company, Tuzla, Turkey. On the other hand, HDPE (PETILEN YY S0464) was bought from Petkim Petro Kimya A.S., Izmir, Turkey.

The dimensions of 400 mm x 400 mm x 3 mm (length x width x thickness) plates produced by using hot-press with the help of a mold. The lamination sequence design of composite plate is given in Fig. 1. The code of each group was given regarding the number of used E-glass fabric layer, "n". For instance, two layers of E-glass fabric for n= 1 was coded as EG2/PE, four layers of E-glass fabric for n= 2 was coded as EG4/PE and so on. The flouropolymer (PTFE) films were used at the top and bottom layers to take the produced plate easily from the hot-press. The composite plates were produced under the condition of 195 ^{0}C temperature and 8.163 bar pressure for 30 min. After then the plates were left for cooling to 23 ^{0}C (the room temperature) before taking from the hot-press. The mass fraction of the reinforcement was calculated according to (1). Weights of the E-glass fabric and HDPE films were measured before the production and weight of the composite plates were measured after the production process by a scales which has 30 kg capacity and ±1 g accuracy.

$$w_{E\text{-}glass} = \frac{m_{E\text{-}glass}}{m_{total}} x100 \quad (1)$$

Here, $w_{E\text{-}glass}$ is the mass fraction percentage of E-glass fabric in the composite, $m_{E\text{-}glass}$ *is* the mass of the E-glass fabric used in the plate and m_{total} is the total mass of the composite plate.



Fig. 1. *Lamination design for different mass fraction of E-glass/HDPE: number of E-glass fabric layer n= 1, 2, 3 and 4.*

B. *Experimental Studies*

In order to investigate mechanical properties of the thermoplastic composites, tensile tests and low-velocity impact tests were conducted according to ISO – EN 527 and ASTM D 3822, respectively.

Shimadzu AG-100 universal test machine with a video extensometer was used for tensile tests. The crosshead speed of the test machine was 5 mm.min^{-1}. The dimensions of tensile test specimens were 180 mm x 15 mm x 3 mm (length x width x thickness). Tensile strength and tensile modulus of the composites were calculated according to (2) and (3), respectively.

$$\sigma_{ult} = \frac{F_{max}}{A} \quad (2)$$

$$E = \frac{\Delta\sigma}{\Delta\varepsilon} \quad (3)$$

Here; F_{max} is maximum load (N), A is cross-sectional area of the specimen (mm^2), σ (MPa) is stress and ε is strain.

On the other hand, low-velocity impact tests were conducted at 25 J, 50 J and 75 J impact energy levels at the room temperature using Instron CEAST 9350, Fractovis Plus impact test machine with a drop weight system. In order to avoid repeated impacts, the anti-rebound device of the machine was activated. Used impactor was hemispherical form with diameter of 12.7 mm and mass of 0.626 kg. A data acquisition system (DAS) was utilized to record 5200 data point for contact force, deflection, absorbed energy and time during the tests. The low-velocity impact specimen dimensions were 100 mm x 100 mm x 3 mm (length x width x thickness).

All tests were repeated for three specimens.

[3] Results And Discussion

The mass fractions of E-glass fabric in the composites were obtained as 6.75 %, 12.65 %, 17.85 % and 22.5 % according to (1).

Tensile strength and tensile modulus of the E-glass/HDPE thermoplastics were calculated according to the test results and tabulated in Table 1 and Table 2, respectively. In addition, the tensile test results were given as force vs. displacement graph in Fig. 2. Low-velocity impact test results given in Fig. 3-5, as well. In order to make the reinforcement mass fraction effect obvious, one specimen selected from each group in all graphs.

Table 1. Tensile Strenght of the composites

	EG2/PE	***EG4/PE***	***EG6/PE***	***EG8/PE***
Max Tensile Strength (MPa)	48.8	82.1	88.5	126.7
Average Value (MPa)	44.1	78.5	85.7	113.7
Standard Deviation (MPa)	5.27	2.71	2.19	9.69

Table 2. Tensile modulus of the composites

	EG2/PE	***EG4/PE***	***EG6/PE***	***EG8/PE***
Max Tensile Modulus (MPa)	479.5	1487.2	1572.2	2394.4
Average Value (MPa)	460	1159.3	1467.5	1953.7
Standard Deviation (MPa)	16.75	233.4	80.1	301.1

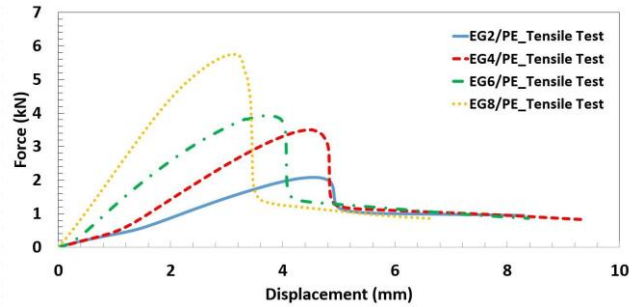
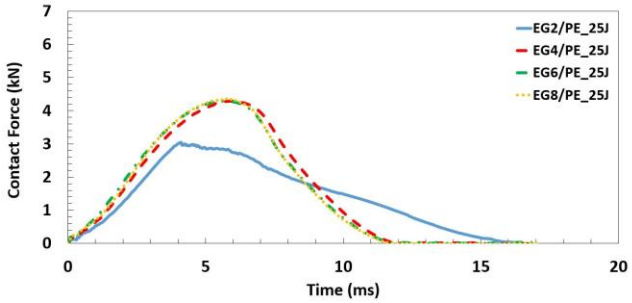
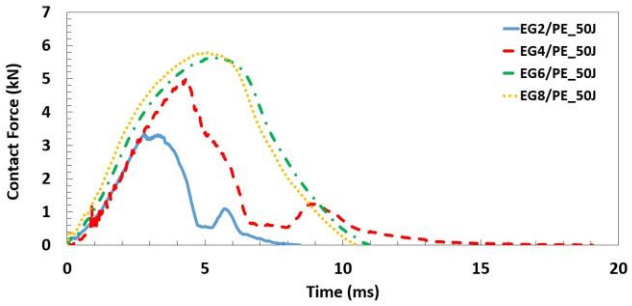


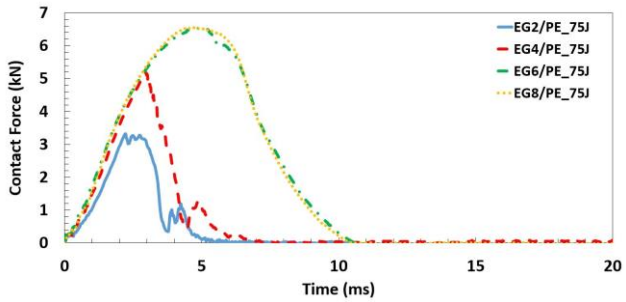
Fig. 2. *Tensile test results as force vs. displacement graph for different reinforcement mass fraction.*



(a)

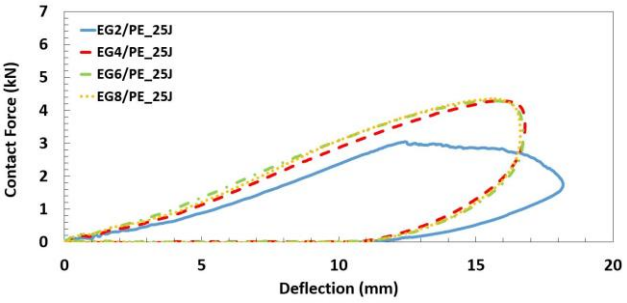


(b)

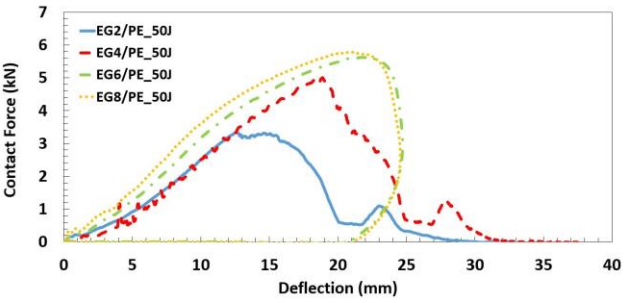


(c)

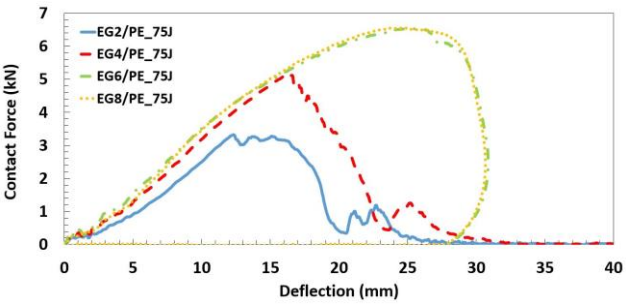
Fig. 3. *Force vs. time graphs of different reinforcement mass fraction composites at (a) 25 J, (b) 50 J, (c) 75 J impact energy levels.*



(a)

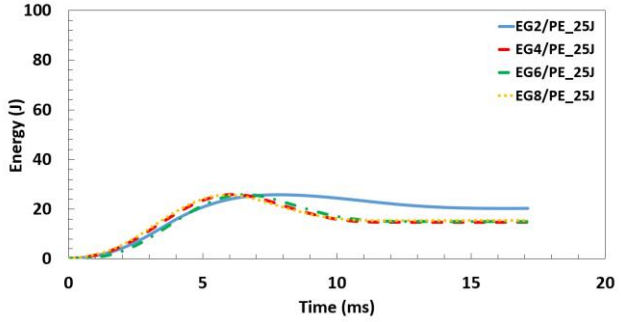


(b)

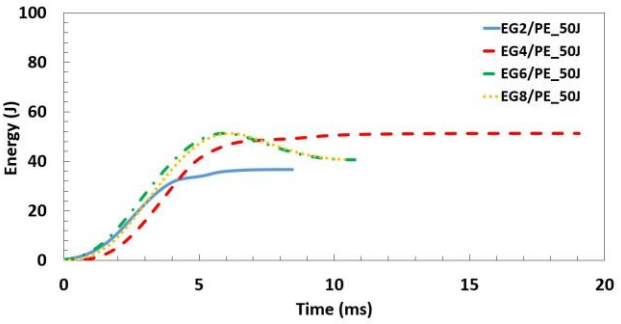


(c)

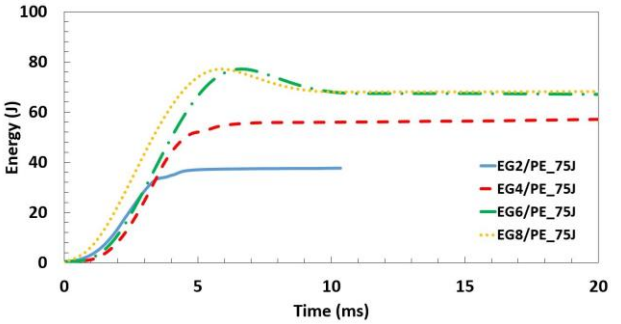
Fig. 4. *Force vs. deflection graphs of different reinforcement mass fraction composites at (a) 25 J, (b) 50 J, (c) 75 J impact energy levels.*



(a)



(b)



(c)

Fig. 5. *Energy vs. time graphs of different reinforcement mass fraction composites at (a) 25 J, (b) 50 J, (c) 75 J impact energy levels.*

Maximum contact forces and maximum absorbed energies related to three impact energy levels are given for four different mass fraction groups in Fig. 6-7.

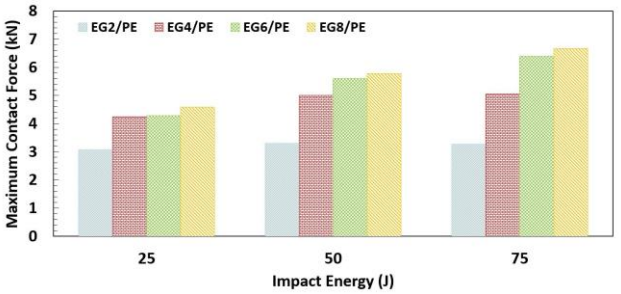


Fig. 6. *Maximum contact forces at different impact energy levels for different reinforcement mass fraction composites.*

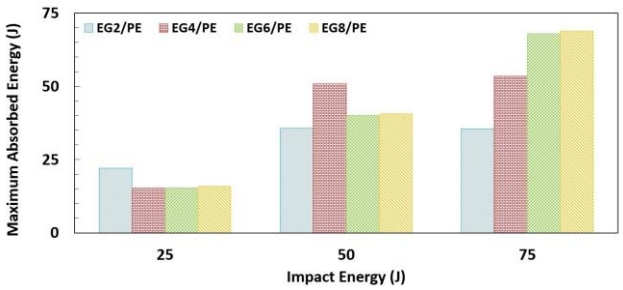


Fig. 7. *Maximum absorbed energies at different impact energy levels for different reinforcement mass fraction composites*.

Both tensile and low-velocity tests results show that mass fraction of the reinforcement has considerable effect on the mechanical behavior of the E-glass/HDPE thermoplastic composites. Namely, increasing the reinforcement mass fraction from 6.75% to 22.5% caused an increase in maximum tensile strength from 48.8 MPa to 126.7 MPa and maximum tensile modulus from 479.5 MPa to 2394.4 MPa. This change in tensile behavior of the composite can be clearly seen for selected specimens from each group in Fig. 2.

Both in Fig. 3(a) - 3(b) and Fig. 4(a) - (b) the contact force increases fast to the pick value and starts to decease after matrix failure and matrix fiber delamination. At the last part of the test the increase of the contact force in Fig. 3(a) - 3(b) and Fig. 4(a) - (b) due to progress of the impactor in the specimens causes fiber breakage in EG2/PE and EG4/PE during perforation. On the other hand, finished in smooth form of contact force and deflection graphs for EG6/PE and EG8/PE shows the rebound with increase closed area which indicates the absorbed energy capacity in Fig. 3(a) - 3(b) and Fig. 4(a) - (b). Hence, increase in the mass fraction of the E-glass had significant effect on the impact characteristic of the composite, Fig. 3 - 5. This significant effect not only causes an increase in maximum contact force and absorbed energy, but also changes in failure mode under the impact load. For instance, EG2/PE and EG4/PE specimens showed failure mode of rebound at 25 J, penetration at 50 J and perforation at 75 J. Contrarily, EG6/PE and EG8/PE specimens absorbed all impact energies and showed failure mode of rebound at all impact energy levels.

Increase in tensile strength and tensile modulus reported in literature for carbon nanotube [4], glass fiber [6-8] and carbon fiber [9] reinforced PE composites, as well. These results can be explained as the fiber surface helps improving HDPE crystallinity, increases folding length and makes the composite stronger [7]. For our results, we can state that adding fibers in PE act not only as reinforcement but also nucleating agent upon crystallization of HDPE. Therefore, increasing E-glass fabric mass fraction leads to an increase in tensile strength, tensile modulus and absorbed energy levels.

[4] CONCLUSION

In the present research, plain weave woven E-glass fabrics reinforced high density polyethylene thermoplastic composites were produced using hot-press in order to investigate the effect of the reinforcement mass fraction on tensile and low-velocity impact behavior of the composites at 25 J, 50 J and 75 J impact energy levels. Four different mass fractions were obtained as 6.75 %, 12.65 %, 17.85 % and 22.5 %. The test results show that both tensile and low-velocity impact characteristics were obviously changed by reinforcement mass fraction. Tensile strength and modulus were increased as a result of the increased reinforcement mass fraction as expected. Furthermore, elastic tensile characteristics were observed since the glass fibers dominated the thermoplastic composites. The mass fraction effect on the low-velocity impact characteristic is more obvious. Increasing the mass fraction of the reinforcement changes the failure mode from perforation to rebound and increases the absorbed energy level. In conclusion, E-glass fabric played both the reinforcement role and the nucleating agent role to increase crystallinity of the HDPE thermoplastic. Therefore, E-glass fabric reinforced HDPE the composites show more strength and toughness by increasing the mass fraction of the reinforcement. Furthermore, the effect of mass fraction on the viscoelastic characteristic of E-glass fabric reinforced HPDE can be studied for future research.

ACKNOWLEDGMENT

Authors thank to Prof. Dr. Sami Sayer for his valuable recommendation to this research.

REFERENCES

[1] R.D. Maksimov, T. Ivanova, M. Kalnins and J. Zicans, “Mechanical properties of high-density polyethylene/chlorinated polyetyhele blends”, Mech. Comp. Mater., vol. 40(4), pp. 331–341, 2004.

[2] I. Mohagheghian, G.J. McShane and W.J. Stronge, “Impact perforation of monolithic polyethylene plates: projectile nose shape dependence”, Int.J.Impact Eng. vol. 80, pp. 162–176, 2015.

[3] E. Akdoğan, “The effects of high density polyethylene addition to low density polyethylene polymer on mechanical, impact and physical properties”, EJT, vol. 10(1) pp.25–37, 2020..

[4] S. Kanagaraj, F.R. varanda, T.V. Zil’tsova, M.S.S. Oliveira and J.A.O. Simoes, “Mechanical properties of high density polyethylene/carbon nanotube composites”, Comp.Sci.Tech., vol. 67, pp. 3071–3077, 2007.

[5] K.B. Adhikary, S. Pang and M.P. Staiger, “Dimensional stability and mechanical behaviour of wood-plastic composites based on recycled and virgin high-density polyethylene (HDPE)”, Compos.B.Eng., vol. 39, pp. 807–815, 2008.

[6] U. Alkan, Y. Özcanlı and V. Alekberov, “Effect of temperature and time on mechanical and electrical properties of HDPE/Glass fiber composites”, Fibers Polym., vol. 14 (1), pp. 115–120, 2013.

[7] M.A. AlMaadeed, M. Ouederni and P.N. Khanam, “Effect of chain structure on the properties of glass fiber/polyethylene composites”, Mater.Des., vol. 47, pp. 725–730, 2013.

[8] U. Saeed, K. Hussain and G.Rizvi, “HDPE reinforced with glass fibers: Rheology, tensile properties, stress relaxation, and orientation of fibers”, Polym. Compos., vol. 35, pp. 2159–2169, 2014.

[9] L.A. Savas, U.Tayfun and M. Dogan, “The use of polyethylene copolymers as compatibilizers in carbon fiber reinforced high density polyethylene composites”, Compos.B.Eng., vol. 99, pp. 188–195, 2016.

[10] S.L. Armentia, B. Enciso, G. Mokry, J. Abenojar and M.A. Martinez, “Novel application of a thermoplastic composite with improved matrix-fiber interface”, J.Mater.Res.Technol., vol. 8(6), pp. 5536–5547, 2019.

[11] M.O.W. Richardson and M.J. Wisheart, “Review of low-velocity impact properties of composite materials”, Compos. Part A Appl. Sci. Manuf., vol.27A, pp. 1123–1131, 1996.

High-Efficiency Smart Pump Controller

Yavuz Sümer
Aryas Arge Mühendislik Ltd. Şti
R&D Engineer
Antalya, Turkey
yavuzsumer@sabanciuniv.edu

Arash Ravanbakhshazar
Aryas Arge Mühendislik Ltd. Şti.
R&D Engineer
İstanbul, TURKEY
info@aryas.com.tr

Ahmet Kain
Aryas Arge Mühendislik Ltd. Şti.
Angel Investor
Eskişehir, TURKEY
ahmet.kain@gmail.com

Aim: **A compact water pump controller device is an electronic unit that controls the pump automatically by a spring-balanced mechanic relay system and is integrated into the water pump without a balance tank and a pressure switch. Today, they are widely used in residential and workplaces where water pressure in the network is insufficient. Due to the un-sensitive mechanical relay system, these analog control systems are inadequate to control water pumps efficiently and cause several problems such as energy loss, frequent breakdowns, unstable water flow, and reducing motor life. In this work, it is aimed to develop a patented cheap electronic magnetic pressure and energy-saving and long-lasting smart digital pump controller which is called Smart HydroMate.**

Method : **In this work, the design and analysis of the 3D model, magnetic pressure sensor, and PCB were completed by a computer-aided design (CAD) and finite element analysis (FEA) program, respectively. Then, the designs were manufactured and the developed software was integrated. Finally, a patented cheap electronic magnetic pressure sensor (with 0-6 bar pressure range and 0.1 bar sensitivity) and a digital pump controller were developed.**

Results: **First of all, this project has been supported by TÜBİTAK 1512 funds *(Project Number: 2180736)* and a prototype is achieved. It can detect many operations in systems like pressure loss, water leakage, short-period usage activities with smart software and thus minimizes pump work and eliminates disadvantages of analog pump controller devices in the market. The experimental studies show that it enables 22% water-saving, %25 energy-saving, and increases the pump and controllers' life at least double when compared to the conventional controllers.**

Conclusion: **In conclusion, the developed digital pump control systems can be regarded as a solution in residential and workplaces to save energy and water. It should be noted that this device is developed for home-type usage. In future works, smart industrial pump controllers will have been developed including inverter and machine learning technology for tower blocks, factories, and agricultural areas to sustain more energy efficiency and water-saving.**

Keywords—pump controller, pressure sensor, finite element analysis (FEA), energy-efficiency, water-saving

Leader-Follower Formation Control of Quadrotors: A Simple Virtual Leader Approach

Kaan Can
Department of Electrical & Electronics Engineering Ataturk University
Erzurum, Turkey
kaan.can@atauni.edu.tr

Abdullah Başçi
Department of Electrical & Electronics Engineering Ataturk University
Erzurum, Turkey
abasci@atauni.edu.tr

***Abstract*—The leader-follower based formation flight control (LFFC) is a well-known control approach for swarm control of the quadrotors. Depending on basic mathematical theory, it is easy to achieve the desired formation shapes via LFFC such as square and triangle etc. between the leader and the follower quadrotors. Thus, a virtual LFFC method is proposed to realize leader-follower based formation control of two quadrotors in this paper. First, the quadrotor dynamics model is presented. Then, the mathematical equations of the LFFC are calculated. After that, the LFFC algorithm has been derived to generate reference trajectory for the follower quadrotor by taking the position information of the leader quadrotor. Finally, the proposed method has been validated by using two quadrotors. The simulation results have shown the effectiveness of the LFFC method.**

Keywords— quadrotor, flight control, swarm control, formation control, leader follower formation control

[1] INTRODUCTION

Nowadays, the quadrotors have a great attention due to its complex structure, enhanced maneuverability capabilities and be able to use in various fields such as military or civilian applications [1-3]. Therefore, they have been redesigned and started to be used more efficiently especially in swarm applications. Thanks to the swarm control of quadrotors, both the task distribution and the payload can be shared equally between the quadrotors in the swarm. For example; while one quadrotor communicates and shares the position of the swarm with the control station, the other quadrotor can release the load it carries on the desired point. Moreover, another way to use quadrotors more effectively, the formation control that is a special form of the swarm control, performs the swarm control method for quadrotors under a certain geometric shape.

The purpose of the formation control designed for quadrotors is that the vehicles used in the swarm, move in a certain shape according to a certain control algorithm. Therefore, many researchers have focused on this popular topic in recent years. For instance; Ghamry and Zhang, have proposed a formation control for multiple quadrotors by using sliding mode controller (SMC) [4]. First, they have divided the quadrotor control into two separate subsystems that are called inner loop and outer loop. Then, to realize altitude control, they have used linear quadratic regulator (LQR) in order to provide the reference attitude angles for the inner loop of the system. Moreover, for inner loop control they have used SMC as well. In order to obtain the desired acceleration, they have used a third SMC to provide the desired inputs for the follower quadrotor. The simulation results show that the proposed control algorithm has provided a stable formation control even in the presence of the external disturbances. Wu et al, have derived and simulated a simple SMC-based formation control with three quadrotors [5]. Also, they have used a classical PID controller to manipulate a single quadrotor. The simulation results show that the follower quadrotors have followed the leader quadrotor within the desired distance range. Mercado et al., have presented a control strategy for flight formation problem of the quadrotors [6]. They have used SMC for controlling the translational dynamics of the quadrotor to provide the desired orientation references for the rotational dynamics that is controlled by a classical PD controller. Then, they have obtained the error dynamics of the formation control by using the LFFC algorithm. Finally, they have tested the control algorithm on a quadrotor by using a virtual leader quadrotor. The experimental results have shown that the follower quadrotor is able to track the desired formation trajectory with some error along the x, y and z axes. Bastourous et al., have constructed a formation controller called as Virtual Rigid Body (VRB) so as to create a desired formation pattern [7]. The proposed formation algorithm is achieved depending on the leader-follower approach. The proposed VRB based formation control algorithm has been tested in a simulink model. Moreover, they have used robot operating system (ROS) and Gazebo 3D simulator to validate their controller. The simulation results have shown the effectiveness of the controller. Dun et al., have developed a LFFC based on the dynamic surface approach (DSA) [8]. They have designed a virtual quadrotor to make the formation control problem be like a trajectory tracking problem. Also, the proposed controller has been designed via DSA to control the quadrotors. The simulation results have shown that the DSA-based controller has been able to solve the formation problem of the quadrotors. Vallejo-Alarcon et al., have designed a LFFC approach to solve formation error problem between an unmanned aerial vehicle (UAV) that is known as quadrotor and a unicycle-type mobile robot [9]. They have used feedback linearization method to obtain an UAV model. Then, they have derived LFFC model by using the dynamics of UAV as well as the kinematics of the mobile robot. The LFFC model is designed by using backstepping approach. The stability of the proposed control algorithm has been proven in the sense of Lyapunov approach. The simulation results have shown that the proposed backstepping based LFFC has shown adequate behaviour to provide desired formation pattern. Xuan-Mung and Hong have proposed a robust adaptive formation control for quadrotors in the presence of disturbances and uncertainties based on leader-follower

approach (LFA) [10]. First of all, they have derived the nonlinear model of the formation error dynamics by using the mathematical basics of the LFA. Besides, using the model reference control algorithm, a robust adaptive formation control has been designed to keep the vehicles into a predesigned formation pattern. The simulation results show that the proposed robust adaptive LFA has able to drive the quadrotors to the desired formation pattern and also follow the desired trajectory in the presence of uncertainties.

In this paper, a virtual LFFC algorithm has been proposed so that the follower quadrotor can follow the time varying reference signal. The reference signal for the follower quadrotor has been generated by the LFFC. The LFFC has taken the position information of leader quadrotor to calculate suitable *x* and *y* reference signals for the follower quadrotor. Then, the generated reference signals have been directly applied to follower quadrotor. The simulation results have shown the effectiveness of the proposed control method and also, it has provided the follower quadrotor to follow the reference signal with minimum tracking error.

[2] MATHEMATICAL MODEL OF QUADROTOR

As in many studies, the quadrotor has six parameters that provide its rotational movements through roll, pitch, yaw axes and translational movements through *x*, *y* and *z* axes [11-13]. However, it is described as an under-actuated system due to having four control inputs. Based on all this, the dynamics model of the quadrotor can be expressed as in (1) [13].

$$\left.\begin{aligned}
\ddot{x} &= \frac{u_1}{m}(\sin\phi\sin\psi+\cos\phi\cos\psi\sin\theta)\\
\ddot{y} &= \frac{u_1}{m}(\cos\phi\sin\psi\sin\theta-\sin\phi\cos\psi)\\
\ddot{z} &= \frac{u_1}{m}(\cos\phi\cos\theta)-g\\
\ddot{\phi} &= \frac{u_2}{I_{xx}}+\frac{I_{yy}}{I_{xx}}\dot{\theta}\dot{\psi}-\frac{I_{zz}}{I_{xx}}\dot{\theta}\dot{\psi}\\
\ddot{\theta} &= \frac{u_3}{I_{yy}}+\frac{I_{zz}}{I_{yy}}\dot{\phi}\dot{\psi}-\frac{I_{xx}}{I_{yy}}\dot{\phi}\dot{\psi}\\
\ddot{\psi} &= \frac{u_4}{I_{zz}}+\frac{I_{xx}}{I_{zz}}\dot{\theta}\dot{\phi}-\frac{I_{yy}}{I_{zz}}\dot{\theta}\dot{\phi}
\end{aligned}\right\} \quad (1)$$

Here, m is the total mass of the quadrotor, g is the gravity acceleration, $I = diag[I_{xx} \quad I_{yy} \quad I_{zz}]$ represents the inertia matrix and u_1 is the total lift applied to the quadrotor through z axes. Also, u_2, u_3 and u_4 are the torques applied to the quadrotor through ϕ, θ and ψ directions, respectively [10-11]. Moreover, the relationship between the control inputs and the rotor speed are defined as in (2) [5],

$$u=\begin{bmatrix}u_1\\u_2\\u_3\\u_4\end{bmatrix}=\begin{bmatrix}b & b & b & b\\0 & -b & 0 & b\\b & 0 & -b & 0\\-d & d & -d & d\end{bmatrix}\begin{bmatrix}w_1^2\\w_2^2\\w_3^2\\w_4^2\end{bmatrix} \quad (2)$$

where b is the thrust factor; w_i is the speed of the rotor and d is the drag coefficient [14]. Also, the quadrotor and its axes is depicted in Figure (1).

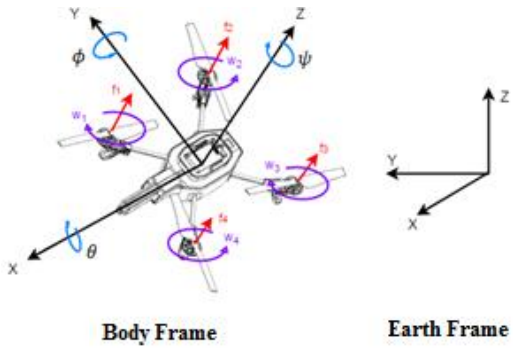


Fig. 3. The axes of a quadrotor [1]

Besides, the quadrotor parameters used in the simulation are given in Table I.

Table 1. System Parameters Used ın the Sımulatıon

Symbols	Description	Value and Unit
m	total mass of the quadrotor	1 kg
I_{xx}	moment of inertia along x axis	0.0081 kg m^2
I_{yy}	moment of inertia along y axis	0.0081 kg m^2
I_{zz}	moment of inertia along z axis	0.00142 kg m^2
g	gravitational acceleration	9.81 m/s^2
L	arm length of quadrotor	0.24 m
b	thrust factor	0.00542
d	drag coefficient	0.0011

[3] LEADER-FOLLOWER FORMATION CONTROL

A. *Leader-Follower Formation*

Basically, the LFFC is a form of formation control created with reference to a quadrotor that holds a leading position. Thanks to this formation control, the quadrotors, which are in the follower position, determine their positions according to the leader quadrotor. In addition, the mathematical expressions of the LFFC can be derived by using the trigonometric relation seen in Figure (2).

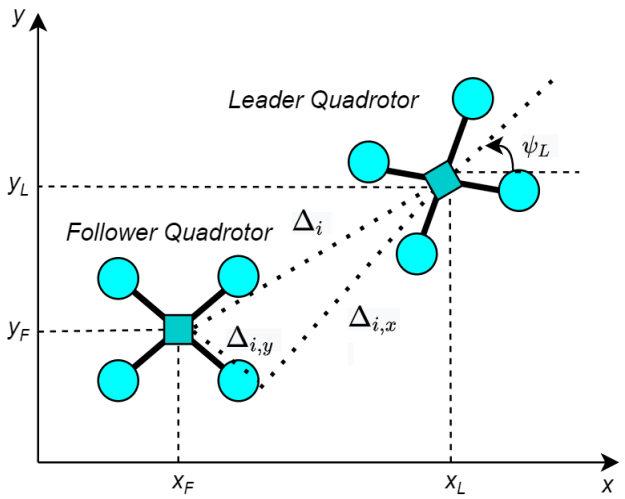


Fig. 4. Leader-follower formation control topology

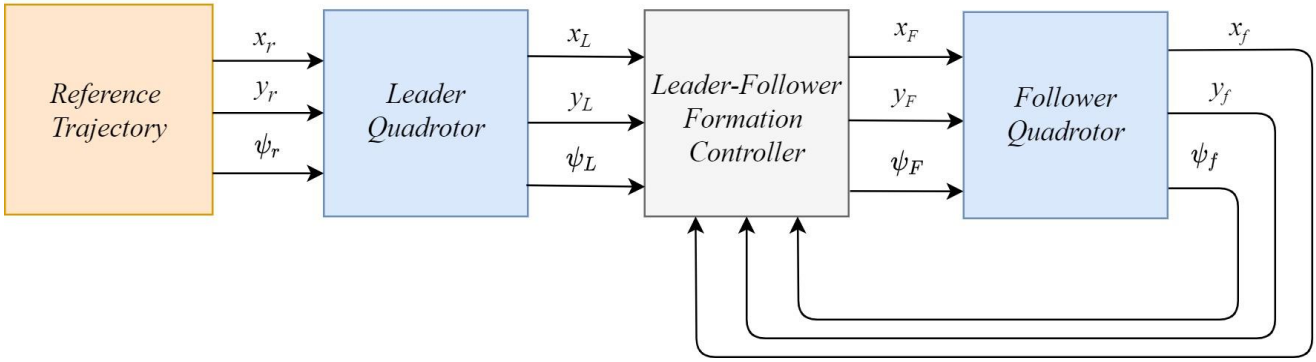


Fig. 5. The leader-follower formation control block diagram

First, the desired and measured distance between leader and follower quadrotor are given as Δ_{di} and Δ_i, respectively. From the figure, $\Delta_{i,x}$ and $\Delta_{i,y}$ are the measured distance through the *x* and *y* axes, respectively. To design LFFC, the error dynamics must be derived by means of tracking errors in *x* and *y* axes between leader-follower quadrotors. $e_{i,x} = \Delta_{di,x} - \Delta_{i,x}$ represents the distance error in the *x* direction. $e_{i,y} = \Delta_{di,y} - \Delta_{i,y}$ represents the distance error in the *y* direction. Also, $\Delta_{di,x}$ and $\Delta_{di,y}$ are the desired distances through *x* and *y* directions, respectively. In addition, the orientation angle error between leader and follower quadrotor is expressed as $e_{i,\psi} = \psi_{di} - \psi_i$. Moreover, the obtained errors can be written in the matrix form as given below.

$$e_i = \left[e_{i,x}\ e_{i,y}\ e_{i,\psi}\right]^T \tag{3}$$

B. LFFC Desing

In this section, the proposed control algorithm is derived. First, the actual distance between leader and follower quadrotor can be written as given below [15].

$$\left.\begin{aligned}\Delta_{i,x} &= -(x_L - x_F)\cos(\psi_L) - (y_L - y_F)\sin(\psi_L)\\ \Delta_{i,y} &= (x_L - x_F)\sin(\psi_L) - (y_L - y_F)\cos(\psi_L)\end{aligned}\right\} \tag{4}$$

Also, from Figure (2), $\dot{x}_i$ and $\dot{y}_i$ represent the linear velocities of the system with respect to earth frame [10]. Moreover, v_{ix} and v_{iy} represent the linear velocities of the system with respect to body-fixed frame as well [10]. Therefore, to explain and show their relationship these two linear velocities in mathematically, one can write the translational dynamics as given below [5].

$$\left.\begin{aligned}\dot{x}_i &= v_{ix}\cos(\psi_F) - v_{iy}\sin(\psi_F)\\ \dot{y}_i &= v_{ix}\sin(\psi_F) + v_{iy}\cos(\psi_F)\\ \dot{\psi}_L &= w_L\end{aligned}\right\} \tag{5}$$

Taking derivative of (4) with respect to time and using (5), one can obtain the following expression [5,10],

$$\left.\begin{aligned}\dot{\Delta}_{i,x} &= \Delta_{i,y} w_L + v_{Fx}\cos(e_\psi) - v_{Fy}\sin(e_\psi) - v_{Lx}\\ \dot{\Delta}_{i,y} &= -\Delta_{i,x} w_L + v_{Fx}\sin(e_\psi) + v_{Fy}\cos(e_\psi) - v_{Ly}\end{aligned}\right\} \tag{6}$$

where $e_\psi = \psi_f - \psi_L$ represents the orientation error of the system. In the light of all this information, the desired translational positions for follower quadrotor through *x* and *y* directions can be derived by using (4) for convenience as given below [4]. Also, the block diagram of the LFFC is given in Figure (3).

$$\left.\begin{aligned}x_F &= x_L + \Delta_{i,x}\cos(\psi_L) - \Delta_{i,y}\sin(\psi_L)\\ y_F &= y_L + \Delta_{i,x}\sin(\psi_L) + \Delta_{i,y}\cos(\psi_L)\end{aligned}\right\} \tag{7}$$

[4] SIMULATION RESULTS

In this part, the simulation results are presented. The reference trajectory for virtual leader quadrotor is applied in two stages. In the first stage, only the height reference is applied between 0 and 20 seconds such as $h_r = 10$ and $x_r = y_r = 0$. In the second stage, between 20 and 70 seconds, the height reference is kept constant as $h_r = 10$ and x and y reference signals are applied as $x_r = (t-20) * (5 * \sin(2 * pi * (t/20)))$ and $y_r = (t-20) * (5 * \cos(2 * pi * (t/20)))$. After using the reference position for the virtual quadrotor, the proposed LFFC algorithm has generated the reference trajectory for the follower quadrotor.

First of all, in Figure (4), the LFFC performance through x direction for the follower quadrotor is given. From the figure, the follower quadrotor has followed the reference trajectory with minimum error and also, it has given fast response to the slope changes of the reference signal through x direction. In figure (5), the trajectory tracking performance of the follower quadrotor in the y direction is given. From 0 to 20 seconds, since the reference signal magnitude is 0, there is no changes through the y direction. On the other hand, between 20 to 70 seconds, the follower quadrotor has followed the reference trajectory provided by the LFFC. Until nearly 60 seconds, although the follower quadrotor has showed high trajectory tracking success, it has deviated somewhat from the reference trajectory after 60th seconds.

In Figure (6), trajectory tracking error level through *x* direction for follower quadrotor has been given. From the figure, one can observe that the follower quadrotor the error level is 0 in the first 20 seconds due to 0 reference signal magnitude. After the 20th second, some tracking error has occurred in the *x* direction due to the time varying reference signal generated by the LFFC. Similarly, in Figure (7), for the first 20 seconds, a zero reference signal has been applied in the *y* direction as in the *x* direction, thus there is no tracking error. However, it is observed that larger reference tracking error has occurred in the *y* direction after 20 seconds,

especially between 60 and 70 seconds compared to that in the *x* direction. In Figure (8) and (9), the linear velocities of the follower quadrotor are given for both *x* and *y* directions. From the figures, the linear velocity information that is suitable for the follower quadrotor, has been produced in accordance with the virtual leader quadrotor thanks to the proposed LFFC algorithm. In this way, the follower quadrotor is able to follow the reference trajectory provided by the LFFC with high success.

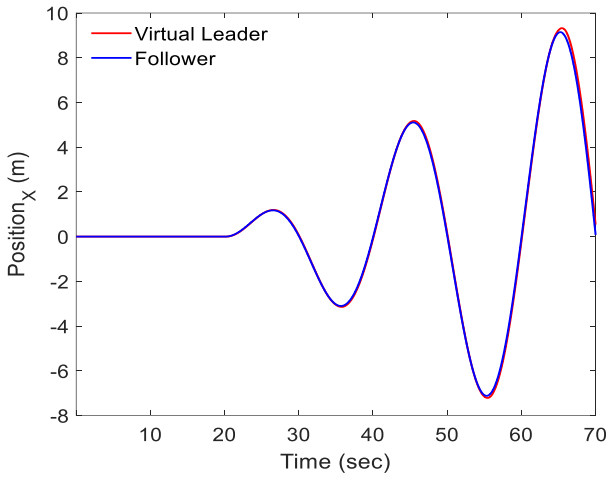


Fig. 6. LFFC performance through x direction for follower quadrotor

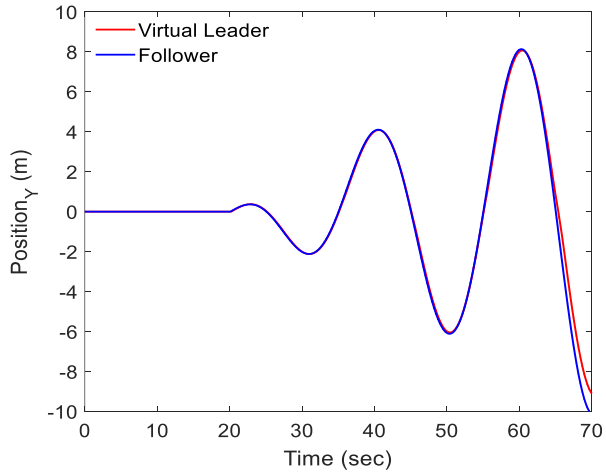


Fig. 7. LFFC performance through y direction for follower quadrotor

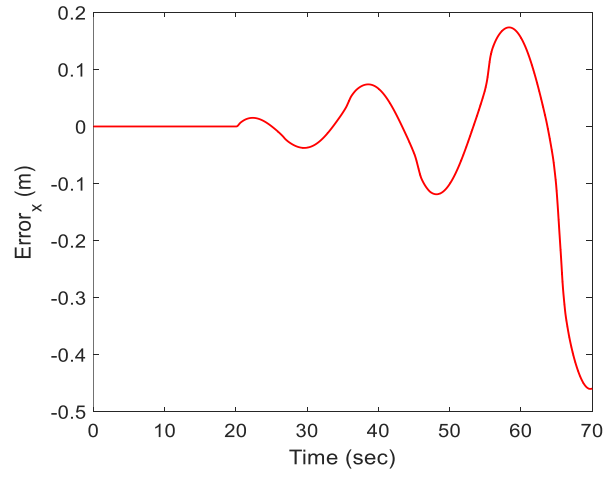


Fig. 8. Trajectory tracking error level through x direction for follower quadrotor

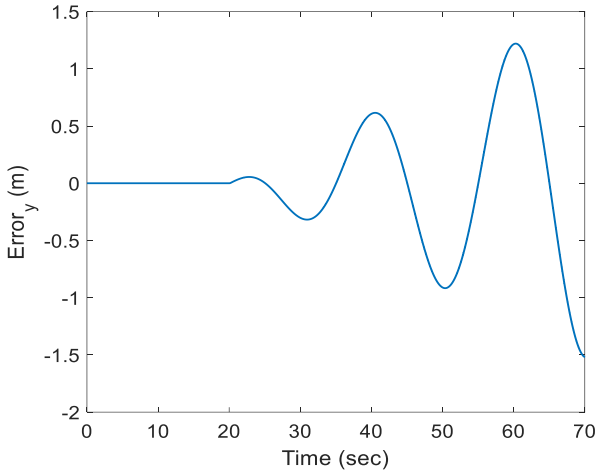


Fig. 9. Trajectory tracking error level through y direction for follower quadrotor

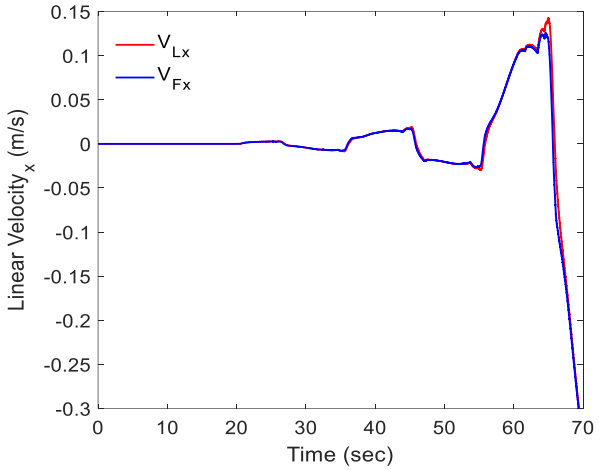


Fig. 10. The generated linear velocities through x direction: leader (red)-follower (blue)

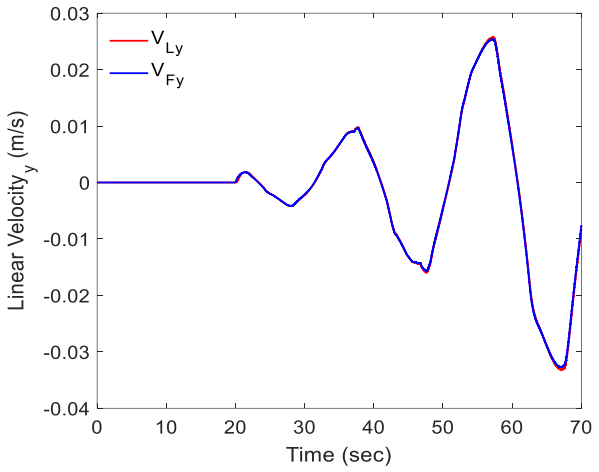


Fig. 11. The generated linear velocities through y direction: leader (red)-follower (blue)

[5] CONCLUSION

In this paper, a virtual leader-follower formation control method is proposed to generate reference trajectory for a quadrotor that is in a follower position. The follower quadrotor has obtained its reference trajectory information in



x and *y* directions from the LFFC by using the virtual leader quadrotor's position. The simulation results have showed that the proposed LFFC method has produced the desired trajectory in the *x* and *y* directions for the follower quadrotor successfully. After that, the follower quadrotor has followed the time varying reference trajectory with minimum tracking error and be able to use the linear velocity information of the virtual leader quadrotor to keep itself on exact position as well.

REFERENCES

[1] K.Can, K. Orman and A. Başçi, "Trajectory tracking control of a four rotor unmanned aerial vehicle (UAV) using two degree of freedom PI controller," in *Natioal Conference on Electrical, Electronics and Biomedical Engineering (ELECO)*, Turkey, December 1-3, pp. 682-686, 2016.

[2] K. Can and A. Başçi, "Real-time trajectory tracking control of a four rotor UAV with backstepping controller," *Iğdır University J. Inst. Sci. & Tech.*, vol. 6(3), pp. 77-85, 2016.

[3] A. Başçi, K. Can, K. Orman and A. Derdiyok, "Trajectory tracking control of a four rotor unmanned aerial vehicle based on continupus sliding mode controller*," Elektronika Ir Elektrotechnika*, vol. 23(3), pp. 12-19, 2017.

[4] K. A. Ghamry and Y. Zhang, "Formation control of multiple quadrotors based on leader-follower method," in *Int. Conf. on Unmanned Aircraft Systems (ICUAS)*, USA, June 9-12, pp. 1037-1042, 2015.

[5] F. Wu, J. Chen and Y. Liang, "Leader-follower formation control for quadrotors," *IOP Conf. Series: Materials Science and Engineering*, 187(2017), pp. 1-8, 2017.

[6] D. A. Mercado, R. Castro and R. Lozano, "Quadrotors flight formation control using a leader-follower approach," in *European Control Conference (ECC)*, Switzerland, July 17-19, pp.3858-3863, 2013.

[7] M. Bastourous, F. Guerin and F. Guinand, "leader follower formations of multi quadrotors group,". PDF online: https://www.cidn.fr/wp-content/uploads/sites/14/2019/02/bastourous.guerin.guinand_toward-L-F-formation-mult-flying-robots.pdf

[8] A. Dun, R. Wang and Q. Xu, "Leader-follower formation control of multi-quadrotor systems based on the dynamic surface approach," in *Chinese Automation Congress (CAC)*, China, Nov. 6-8, pp. 572-577, 2020.

[9] M.A. Vallejo-Alarcon, R. Castro-Linares and M. Velasco-Viila, "Unicycle-type robot & quadrotor leader-follower formation backstepping control," *IFAC-PapersOnline*, vol. 48(19), pp. 51-56, 2015.

[10] N. Xuan-Mung and S. K. Hong, "Robust adaptive formation control of quadcopters based on leader-follower approach," *Int. J. of Advanced Control for Robotics and Autonomous Systems*, vol. 16(4), pp. 1-11, 2019.

[11] S. Bouabdallah and R. Siegwart, "Full control of a quadrotor," in *Int. Conf. on Intelliget Robotics ans Systems*, USA, Oct. 29-Nov. 2, pp. 153-158, 2007.

[12] S. . Bouabdallah, A.Noth and R. siegwart, "PID vs LQ control technics applied to an indoor micro quadrotor," in *Int. Conf. on Intelliget Robotics ans Systems, Japan*, Sept. 28- Oct. 2, pp. 2451-2456, 2004.

[13] M. H. Tanveer, D. Hazry, S. F. Ahmed, M. K. Joyo, F. A. Warsi, H. Kamaruddin, Z. M. Razlan, K. Wan and AB Shahriman, "NMPC-PID based control structure design for avoiding uncertainties in attitude and altitude tracking control of quad-rotor (UAV)," in *IEEE 10th Int. Collo. on Signal Proc. And its App*., Malaysia, March 7-9, pp. 117-122, 2014.

[14] S. Arogeti and A. Ailon, "Low level formation controls for a group of quadrotors withmodel uncertainties," *Int. J. of Control*, vol. 93(7), pp. 1534-1546, 2020.

[15] C. Moralez, R. Dali, M. Velasco-Villa, R. Castro-Linares and E. R. Palacios-Hernandez, "Leader-follower formation for nonholonomic mobile robots: discrete-time approach," *Int. J. of Advanced Robotic Systems*, vol. 13(2), pp. 1-12, 2016.

Modelling and Simulation the Position Control of Flexible Manipulator Using Gyroscopic Actuator

Abbas Moloody
dept. of Mechanical and Manufacturing Engineering Faculty of Engineering Universiti Putra Malaysia Serdang, Selangor, Malaysia
a.moloody@alumni.ut.ac.ir

Azizan Bin As'arry
dept. of Mechanical and Manufacturing Engineering Faculty of Engineering Universiti Putra Malaysia Serdang, Selangor, Malaysia
zizan@upm.edu.my

Tang Sai Hong
dept. of Mechanical and Manufacturing Engineering Faculty of Engineering Universiti Putra Malaysia Serdang, Selangor, Malaysia
saihong@upm.edu.my

Mohd Sapuan Salit
dept. of Mechanical and Manufacturing Engineering Faculty of Engineering Universiti Putra Malaysia Serdang, Selangor, Malaysia
sapuan@upm.edu.my

Raja Kamil
dept. of Electrical and Electronics Engineering Faculty of Engineering Universiti Putra Malaysia Serdang, Selangor, Malaysia
kamil@upm.edu.my

Abstract — This paper focuses on the investigation into the mathematical model, simulation and the end point position control of a single link Flexible Manipulator (FM) which rotates in the horizontal plane. In this research the dynamics and mathematical model of such a system has been derived using the energy method based on the Lagrange Equation (LE) beam theory and the state space method for the system. The objective of the study is to control and eliminate the deflection and oscillation angle of the single link FM and End Effector. Hence the performance of position control and keeping the rotation angle in a horizontal plane motion can be evaluated. The Proportional, Integral and Derivative (PID) controller tuning by the modified Ziegler Nichols (ZN) method is applied to control the system and a Gyroscope as a new approach has been used as an actuator for suppressing the vibrations of the single link FM. In this study the simulations have been performed using MATLAB & SIMULINK program. The final obtained simulated results of this system analysis based on the PID controller and a gyroscopic actuator have been compared according to the input/output signals for the plant, actuator and the closed loop state of the system with the controller individually and respectively. The findings show that about 36% reduction in vibrations accordingly the position of the single link FM can be controlled in a good agreement.

Keywords — Flexible Manipulator, Gyroscopic Actuator, PID Control, Ziegler Nichols Tuning, Position Control

[1] INTRODUCTION

As an important and main advanced in robotic systems is the Flexible Manipulators (FM) which are highly needed to work in the difficult occupations, the routine and dangerous environments instead of human in order to obtain and achieve faster, economical and accurate operations. Some common and traditional methods and solutions for avoiding the flexible manipulators end effector vibrations and obtaining a good position accuracy is using heavy materials and big designs to achieve a high stiffness for FMs. In order to build the new and modern flexible manipulators for satisfying the needs of the industrial applications it is important to ensure by reduction the weight of the link manipulators and utilizing flexible materials for satisfying the special needs of industries. Hence, the research study of the flexible manipulators has been an active research area, [1] [2]. Hence, many feedback control schemes have been investigated regarding the precise positioning and the vibration control of the single link flexible manipulators such as Classic Control (CC) - [3], Pole Placement (PP) - [4], Lyapunov Based Control (LBC) - [5], Integral Resonant Control (IRC) - [6]. Applied linear control methods developed for the flexible manipulators are Linear Quadratic Regulator (LQR) - [7], PID control methods, [8] and State Feedback control (SF) - [9]. It is clear and known that the flexible manipulators have very nonlinear behavior and heavily coupled systems and consequently the development of an accurate mathematical dynamics model and subsequent model-based control of such systems is highly complicated task. Hence the controlling of a flexible manipulator without a priori knowledge of its dynamics analysis has attracted much attention, [10]. Therefore, many actuators can be used in FMs, such as Piezoelectric, Shape Memory Alloy, Hydraulic and Pneumatic. Hence, they have different advantages and disadvantages based on their principles and applications. The field of applications of piezoelectric actuators is comparable to that of electromagnetic actuators. However, they will be used according to some of their parameters such as displacement accuracy, generated force and response speed and energy efficiency. As the field of primary applications of the gyroscopic effects, consists in the measurement of the angular position of a moving a body. At high speeds, the gyroscope exhibits extraordinary stability of balance and maintains the direction of the high-speed rotation axis of its central rotor such as spinning tops, the wheels of bicycles and motorcycles, the spin of the earth in space. It senses change in orientation of a device and when paired with an accelerometer, is an excellent tool for measuring the orientation of an object in 3D space. It also determines the angular velocity (ω) typically measured in radians/second, [11]. In this research study, the system analysis based on the PID controller by modified Ziegler Nichols tuning method and a Gyroscopic Actuator as a new approach comparing to the other conventional and traditional actuators have been performed according to the input/output signals for the plant, actuator and the closed loop state of the system individually and respectively.

[2] MODELLING

A. Plant

The analysis, dynamics and mathematical modelling for a typical single link Flexible Manipulator (FM) consist of a motor has been considered as the plant and has been shown in Fig.1. The analysis relations and equations have been achieved easily by the Lagrange equations. In this research study, the plant has two degrees of freedom. In this model, (θ) is the rotation or position angle of the FM and the end effector, (α) is the deflection and oscillation angle of the FM and the end effector. As the first consideration the rotation joint angle which is connected to the motor shaft moves according to the rotation direction of the motor, [10] [11] [12]. The single link flexible manipulator is expressed by the energy method based on the Lagrange equation.

$$L = K - P \quad (1)$$

which (L) is the energy of the flexible manipulator, (K) is the kinetic energy and (P) is the potential energy. The Lagrange equations method for this motion have been given as following:

$$d/dt\ \partial L/(\partial \dot{\alpha}) - \partial L/\partial\alpha = 0 \quad (2)$$
$$d/dt\ \partial L/(\partial \dot{\theta}) - \partial L/\partial\theta = \tau \quad (3)$$

which (τ) is the torque as the output of the motor which it is obtained by the voltage applied to the motor armature (u=v) as input and it is considered as the output of the plant, which it ($X_1 = (\theta)$), as the rotation or position angle of the FM joint and ($X_2 = (\alpha)$), as the deflection angle of the end effector. The (X) is the flexibility coefficient of joint and plant equation of the basic motion is expressed as following:

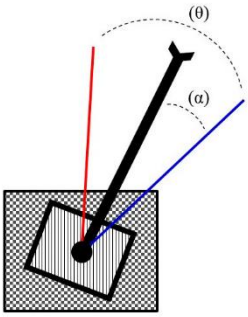


Fig.1. Typical single link flexible manipulator with motor.

$$J_1\ddot{\theta} + J_1\ddot{\alpha} + K_S\alpha - mgh\sin(\theta+\alpha) = 0 \quad (4)$$
$$(J_h + J_1)\ddot{\theta} + J_1\ddot{\alpha} - mgh\sin(\theta+\alpha) = \tau \quad (5)$$

which (J_1) is the inertia of flexible manipulator, (s) is the gear ratio of redactor and the other parameters, (m), (g), (h) which has been used as standard defined parameters. Relationship between torque of the motor and the electrical voltage is expressed as following:

$$v = iR_m + K_mK_g\,\omega \quad (6)$$
$$i = V/R_m - K_mK_g/R_m\,\omega \quad (7)$$

which (ω) is the motor speed or angular velocity, (R_m) is the motor resistance, (K_g) and (K_m) are motor parameters and (i) is the current of the motor armature. With considering the ($\omega = \dot{\theta} = (d\theta/dt)$) and ($i = (\tau/Kg\ Km)$) and summarizing the equations the relationship between the input and output of the plant which are voltage, torque and rotation angle, written asdynamic and mathematical model of flexible manipulator asbellow for the dynamic's behavior of flexible manipulator.

$$\tau = K_mK_g/R_mV - (K^{\wedge 2}{}_m\ K^{\wedge 2}{}_g)/R_m\,\dot{\theta} \quad (8)$$

in this research study, the dynamics and mathematical model of the flexible manipulator with state variables is considered and shown and determined in state space as following:

$$x_1 = (\theta)\ ,\ x_2 = (\alpha)\ ,\ x_3 = (\dot{\theta})\ ,\ x_4 = (\alpha)\dot{} \quad (9)$$

which (x) is the state variable and flexibility coefficient of joint and the state space equations of the single link flexible manipulator is expressed as the equations in following:

$$\dot{x}_1 = x_3 = (\dot{\theta}) \quad (10)$$
$$\dot{x}_2 = x_4 = (\dot{\alpha}) \quad (11)$$
$$\dot{x}_3 = \ddot{\theta} = K_s/J_h\,x_2 - (K^{\wedge 2}{}_m\ K^{\wedge 2}{}_g)/(R_m\,J_h)\,x_3 + K_mK_g/(R_m\,J_h)\,v \quad (12)$$
$$\dot{x}_4 = \ddot{\alpha} \quad (13)$$

and the bellow equations

$$\dot{X}(t) = Ax(t) + Bu(t)\ ,\ \dot{Y}(t) = Cx(t) + Du(t) \quad (14)$$

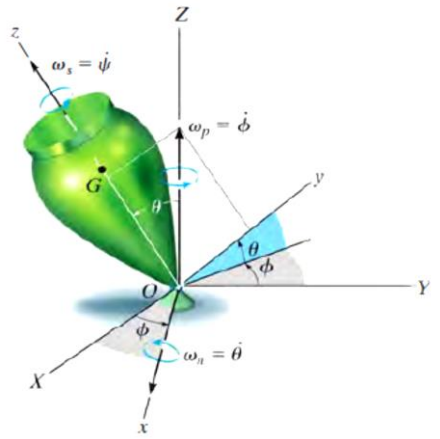
are expressed as the relations between the state space and the state variables.

B. Actuator

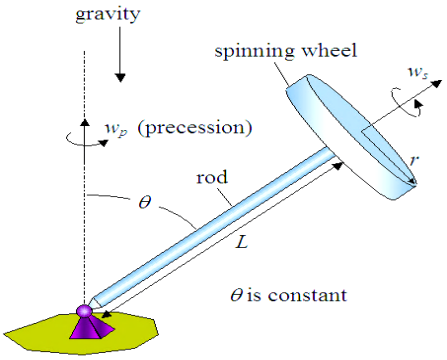
The analysis, dynamics and mathematical modelling for a typical Gyroscope as the actuator and the motion analyzed using Euler angles (φ), (ϴ) and (ψ) has been shown in Fig.2., [13] [14]. In this study, the first state of the gyroscopic actuator motion has been considered which is just the rotation of the rotor at fixed point state with the assumptions of (φ), (ϴ) and ($\dot{\psi}$) are constants. Which ($w_s = \dot{\psi}$) is the angular velocity of the wheel (rotor) which is called the spin velocity around the symmetrical axis and is considered as a constant in radians/second. The ($w_p = \dot{\varphi}$) is the angular velocity of precession around the (z) axis in radians/second, (L) is the rod length, (r) is the rotor radius and (θ) is the angle between the rod and the (z) vertical axis which is a constant. As the rotor spins at a constant rate (w_s) the gyroscopic actuator processes at a constant rate (w_p) about the pivot at the base with (θ) constant. In this research, it is considered fixed at the fixed point without any rotation. Although this is the case, the differential rotations (dφ), (dϴ) and (dψ) are vectors and thus the angular velocity (w) of the gyroscopic actuator is expressed in terms of the time derivatives of the Euler angles. The angular velocity components $\dot{\varphi}$, $\dot{\theta}$ and $\dot{\psi}$ are known as the Precession, Nutation and Spin respectively. where the angular velocity (w) of the gyroscopic actuator has been given as following:

$$w = w_xi + w_yj + w_zk = \dot{\theta}\,i + (\dot{\varphi}\sin\theta)j + (\dot{\varphi}\cos\theta + \dot{\psi})k \quad (15)$$
$$\Omega = \Omega_xi + \Omega_yj + \Omega_zk = \dot{\theta}\,i + (\dot{\varphi}\sin\theta)j + (\dot{\varphi}\cos\theta)k \quad (16)$$

where (Ω) is the angular velocity of the axis



(a)



(b)

Fig.2. Typical gyroscope with states of euler angles (a) and motions (b), [13] [14].

$$w \neq \Omega \, , \, w_x = (\dot{\theta}) = w_n \, , \, w_y = (\dot{\varphi}) = w_p \, , \, w_z = (\dot{\psi}) = w_s \quad (17)$$

in this research, study the dynamics and mathematical model of the gyroscopic actuator with the state variables is considered, shown and determined in state space which (x) is the state variable as following:

$$x_1=(\psi), \, x_2=(\dot{\psi}) \, , \, x_3=(\varphi), \, x_4=(\dot{\varphi}) \, , \, x_5=(\theta), \, x_6=(\dot{\theta}) \quad (18)$$

the state space equations of the gyroscopic actuator is expressed as the following equations:

$$T_1 = \sum M_x = I_x \dot{x}_6 - I_y \Omega_z x_4 + I_z \Omega_Y x_2 \quad (19)$$
$$T_2 = \sum M_y = I_y \dot{x}_4 - I_z \Omega_x x_2 + I_x \Omega_z x_6 \quad (20)$$
$$T_3 = \sum M_z = I_z \dot{x}_2 - I_x \Omega_y x_6 + I_y \Omega_x x_4 \quad (21)$$

the relation between state space equations of the gyroscopic actuator motion and state variables is expressed as the equations in following:

$$\dot{x}_1 = \dot{\psi} = X_2 \, , \, \dot{x}_2 = \ddot{\psi} = T_3/I_z \, , \, \dot{x}_3 = \dot{x}_4 = \dot{x}_5 = \dot{x}_6 = 0 \quad (22)$$
$$\dot{X}(t) = Ax(t) + Bu(t) \quad , \quad \dot{Y}(t) = Cx(t) + Du(t) \quad (23)$$

which (u = v) is the voltage as the input, (τ) is torque as the output, the parameters (I_x), (I_y) and (I_z) are the moments of inertia will be represented the moments and products of inertia which is determined by direct integration or by using tabulated values.

C. System

The combination of a typical single link Flexible Manipulator (FM) consist of a Motor as the plant and a typical Gyroscope consist of a Motor as the actuator will be considered as the system with two degrees of freedom, (θ) as the rotation or position angle of the FM and the End Effector, (α) is the deflection and oscillation angle of the FM and the End Effector.

[3] CONTROL

In the Proportional, Integral and Derivative (PID) control, the design of the controller is an important tool related to its past record of success, wide availability and simplicity in design and use. Basically, the signal driving the system is made up of a Proportional gain (K_P), an Integral gain (K_I) and a Derivative gain (K_D). Hence, it controls a process by working on the error, integral of the error and rate of change of the error, [15] [16] [17] [18] [19] [20]. In this research study, the controller has been designed for a single link flexible manipulator using a gyroscopic actuator as a new approach and the classic control algorithm and a convertor function $G_1(s)$ is used to compute the control signal that activates the real system. The Ziegler Nichols tuning method as a heuristic and the traditional method of tuning the PID controller has been used. This method is applied to system with unit step function. It is performed by selecting and setting the (K_P), (K_I) and (K_D) gains to zero. The (K_P) gain is then increased from zero until it reaches the ultimate gain and the point of instability as sustained oscillations as the critical value of gain (K_{CR}) is reached. By measuring the period of oscillation to obtain the critical time constant (P_{CR}). Hence, the values for (K_{CR}) and (P_{CR}) are obtained and the PID parameters can be calculated according to the design specifications as shown in Table 1 and Table 2 and Fig.3.

Table 1. Type of controller by Ziegler Nichols tuning method.

Controller	K_P	T_I	T_D
P	0.5 K_{CR}	Infinity	0
PI	0.45 K_{CR}	P_{CR} / 1.2	0
PID	0.6 K_{CR}	P_{CR} / 2	0.125 P_{CR}

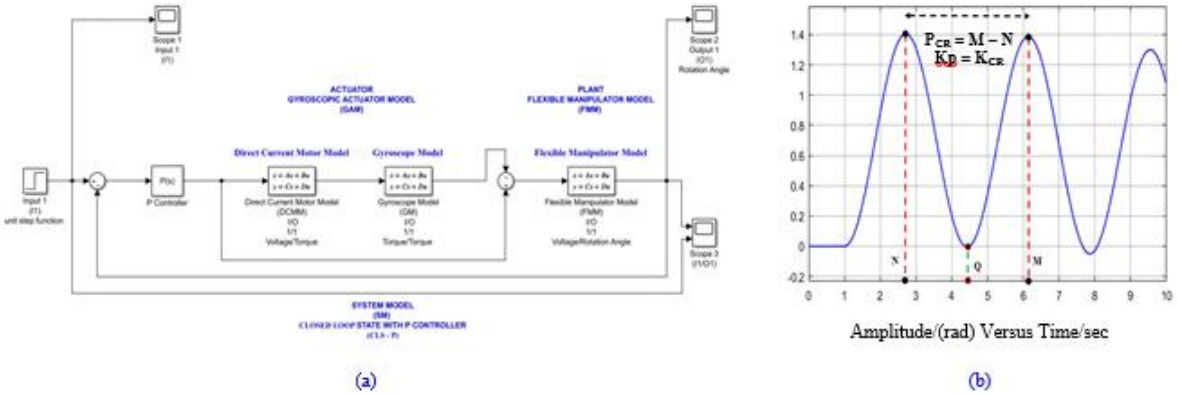
Table 2. P controller by Ziegler Nichols parameters.

Ziegler Nichols Parameters	Value
K_P	52
K_{CR}	52
P_{CR}	4.5

[4] RESULTS AND DISCUSSIONS

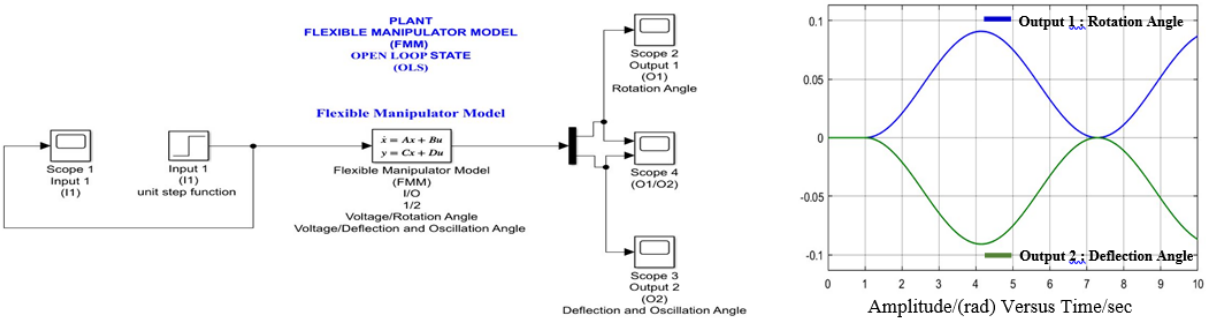
The simulation results of the system consist of the flexible manipulator with a motor as the plant of the system and the gyroscope with a motor as the actuator of the system with the PID controller tuning by Ziegler Nichols method has been performed and obtained individually and respectively. The plant input (I_1) is a unit step function as the dc voltage (u = v) and the real output (O_1) is the rotation or position angle of flexible joint (θ) and (O_2) as the deflection and oscillation

angle of end effector (α), as shown in Fig.4. The actuator input (I_1) is a unit step function as the dc voltage (u = v) and the real output (O_1) is torque (τ), as shown in Fig.5. The system input (I_1), (I_2) is a unit step function in two rates as the setpoint and the real output (O_1) is the desired rotation or position angle of flexible joint (θ) and (O_2) as the deflection and oscillation angle of end effector (α), as shown in Fig.6. The block diagram state is represented in state space model using MATLAB & SIMULINK. The simulation results of the system with PID controller show that by using the controller and tuning the PID parameters coefficients, (KP), (KI) and (KD) by modified Ziegler Nichols method as Table 1 and Table 2, the step response of the closed loop state of the control system show the amplitude of the real output signal (θ) as the flexible manipulator rotation or position angle at a desired and acceptable position and the tuned PID parameters coefficients which has been shown in Fig.6. and as Table 3 and Table 4.



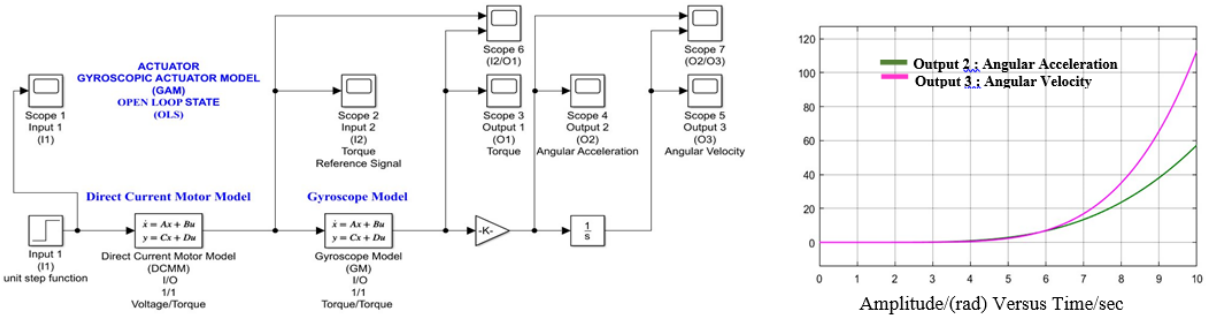
(a) (b)

Fig.3. Block diagram of p controller closed loop state (a) and rotation angle (b) as output simulation signal graph.



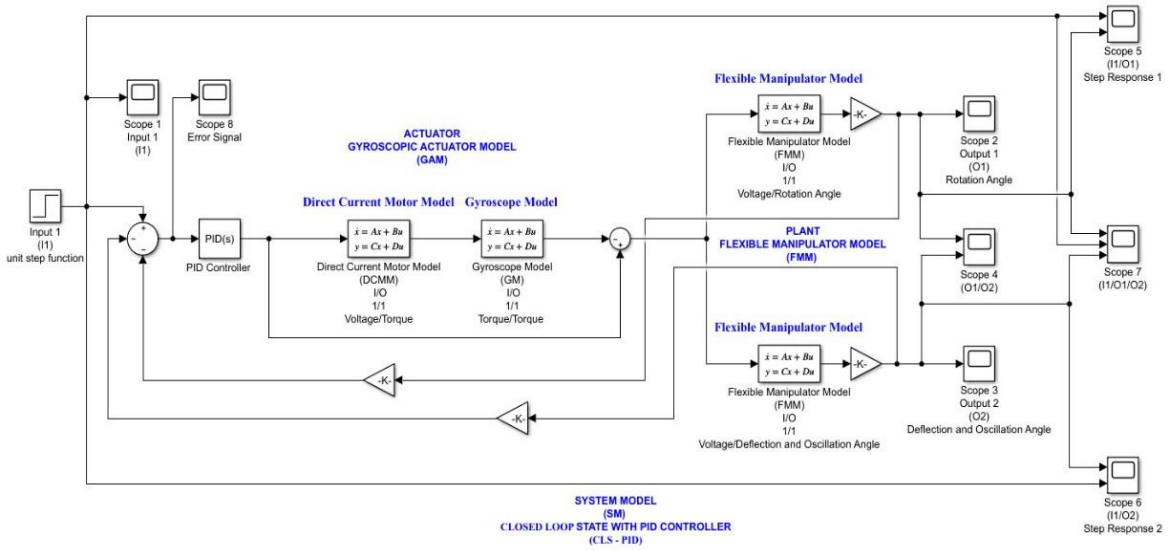
(a) (b)

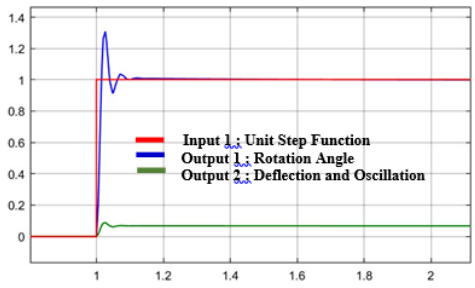
Fig.4. Block diagram of open loop state (a) of plant and rotation angle/deflection angle (b) as outputs simulation signal graphs.



(a) (b)

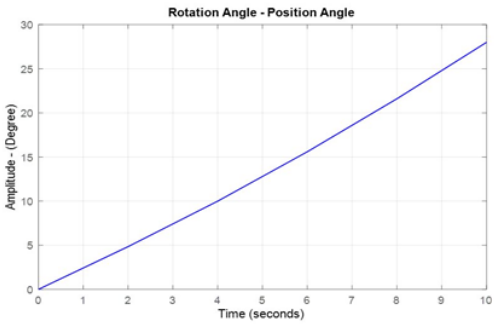
Fig.5. Block diagram of open loop state of actuator (a) and angular acceleration/angular velocity (b) as outputs simulation signal graphs



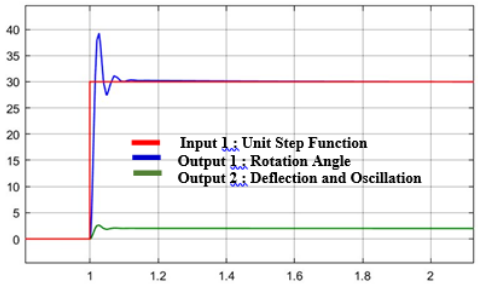


Amplitude/(rad) Versus Time/sec

(b)

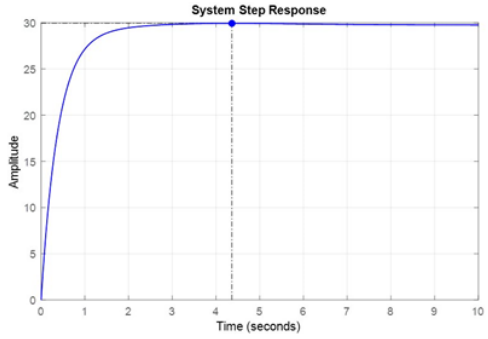


(e)

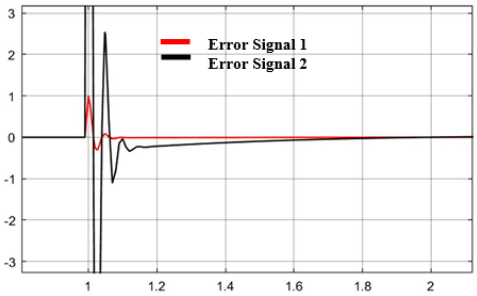


Amplitude/(rad) Versus Time/sec

(c)



(f)



Amplitude/(rad) Versus Time/sec

(d)

Table 3. Controller tuned parameters coefficients.

PID Controller Parameters	K_P	K_I	K_D	T_I	T_D
System Model	31.2	13.86	17.55	2.25	0.56

Table 4. System performance criteria parameters.

Criteria Parameters	T_R	T_S	M_P
System Model	0.001	3.45	0
Compared Model 1	0.377	5.6	51.8
Compared Model 2	0.359	1.07	7.7

Fig.6. Block diagram of closed loop state of system with PID controller (a), input 1/rotation angle/deflection angle (b), input 2/rotation angle/deflection angle (c), error signal 1/error signal 2 (d), desired input angle (e) and desired output angle or system step response (f) as output simulation signal graphs.

[5] CONCLUSION

From the findings, the combination of a typical single link flexible manipulator consists of motor, a typical gyroscope consists of motor and a PID controller has been considered as system with two degrees of freedom, the rotation or position angle and the deflection and oscillation angle of the end effector has been investigated in this paper. Initially simulations have been carried out for the performance assessment of the plant and actuator respectively where the input signal for both is a unit step function. The simulation results of the plant as in Fig.4. show that the outputs, rotation or position angle and deflection angle of the end effector have a range of uniform changes in amplitude and are quite symmetrical and this means that the plant model performance is acceptable. The simulation results of the actuator as in Fig.5. show that the two outputs, angular acceleration and angular velocity of the end effector have a range of uniform changes in amplitude and are quite dependent and this means that the actuator model performance is acceptable. Hence, the simulations result of the system as in Table 3 and Table 4 and Fig.6. show that the performance assessment of the system with PID controller by modified Ziegler Nichols tuning method where P_{CR} has been considered the single negative peak point (Q) or the average of two continuous peak points (M) and (N) as in Table 1 and Table 2 and Fig.3.

ACKNOWLEDGMENT

The authors would like to thank Universiti Putra Malaysia (UPM) and the Malaysian Ministry of Higher Education (MOHE) for their continuous support in the research work. This work was financial supported by the Geran Putra IPS fund under Grant Vot. Number 9540600.

REFERENCES

[1] SI.S. Graham, Kelly, 2011, mechanical vibrations, theory and applications.

[2] S.K. Dwived and P. Eberhard, march 2006, dynamic analysis of the flexible manipulators, a literature review.

[3] V. Feliu, K.S. Rattan and H.B. Brown Jr, 1990, adaptive control of a single link flexible manipulator, IEEE control system.

[4] P.T. Kotnik, S. Yurkovich and U. Ozguner, J. robot, 1988, acceleration feedback for control of a flexible manipulator arm.

[5] S.S. Ge, T.H. Lee and G. Zhu, 1996, genetic algorithm tuning of the of the lyapunov based on controllers, an application to a single link link flexible robot system, IEEE trans. ind. Electron.

[6] E. Pereira, S.S. Aphale, V. Feliu and S.O. Moheimani, 2011, integral resonant control for vibration damping and precise tip positioning of a single link flexible manipulator, IEEE/ASME trans. Mechatronic.

[7] Cannon R.H., Schmitz E., Jr, 1984, the initial experiments on the end point control of a flexible one link robot, international journal robotics research.

[8] Zaidir Jamal, june 2015, the implementation of the PID tuning control of Ziegler Nichols using microcontroller, journal of informatics.

[9] Tien L.L., Schaffer A.A., Hirzinger G., 2007, the MIMO state feed back controller for a flexible joint robot with strong joint coupling, IEEE international conference on robotics and the automation.

[10] S. M. Kim, H. Kim, K. Boo and M. J. Brennan, 2013, demonstration of non collocated vibration control of a flexible anipulator using electrical dynamic absorbers, smart materials and the structures.

[11] Xu, R. Tang, G. Xie, D. Huang, D and Han, L., 2018, underactuated tracking control of underwater vehicles using control moment gyroscope international journal of advanced robotic systems.

[12] M. Vakil, R. Fotouhi and P. N. Nikiforuk, 2012, a new method for dynamic modeling of flexible link flexible joint manipulators, journal of vibration and acoustics.

[13] R. C. Hibbeler, 2010, dynamics, engineering mechanics.

[14] Meriam, 2003, dynamics, engineering mechanics.

[15] Katsuhiko Ogata, 2010, modern control engineering.

[16] Sarah Deif, Mohammad Tawfik, Hanan A. Kamal, vibration and position control of a flexible manipulator using a PD tune d controller with modified genetic algorithm.

[17] H. Akyuz, E. Yolacant, H. M. Ertunct and Z. Bingult, 2011, PID and state feedback control of a single link.

[18] B. Siciliano and W. J. Book, 1988, a singular perturbation approach to control of lightweight manipulators.

[19] Keshtkar, S. Moreno, J. Kojima, H. Uchiyama, K. Nohmi, M. and Takaya K. 2018, spherical gyroscopic moment stabilizer for the attitude control of microsatellites.

[20] W.J. Book, dec 1990, modeling, design and control of flexible manipulator arms.



ABBAS MOLOODY received; Diploma in the branch of Mathematics and Physics at the High School of Aboozar in Shiraz, Iran. B.Sc. in Electrical Engineering in the branch of Electronics at the University of Shiraz (SHU), Shiraz, Iran. M.Sc. in Mechanical and Electrical Engineering in the branch of Mechatronics at the University of Tehran (UT), Tehran, Iran. At present he is Ph.D. student in Mechanical Engineering in the branch of Applied Mechanics with specialization in Intelligent and Automatic Control Systems, Mechatronics and Robotics Systems, Industrial Automation and Manufacturing Systems at the Universiti Putra Malaysia, 43400 UPM Serdang, Selangor, Malaysia.



AZIZAN BIN AS'ARRY received; Diploma in Mechanical Engineering in 2005 at the Universiti Teknologi Malaysia (UTM). B. Eng. in Mechanical Engineering in 2008 at the Universiti Teknologi Malaysia (UTM). M. Eng. and Ph.D. in Mechanical Engineering with specialization in Control in 2009 and 2014 at the Universiti Teknologi Malaysia (UTM). At present he is working as a lecturer in the Department of Mechanical and Manufacturing Engineering at the Faculty of Engineering and the Head of Sounds and Vibration Research Group laboratory (SVRG) at the Universiti Putra Malaysia, 43400 UPM Serdang, Selangor, Malaysia.



TANG SAI HONG received; B.Sc. in Engineering in the branch of Mechanical and System in Honours at the Universiti Pertanian Malaysia (UPM). Ph.D. in Mechanical and System Engineering at the Dublin City University in Ireland with the specialization in Operation Research, Robotics and Control. At present he is working as an Associate Professor in the Department of Mechanical and Manufacturing Engineering at the Faculty of Engineering at the Universiti Putra Malaysia, 43400 UPM Serdang, Selangor, Malaysia.



MOHD SAPUAN SALIT He received; B.Sc. in Mechanical Engineering in 1990 at the University of Newcastle in Australia. M.Sc. in Engineering Design in 1994 at the Loughborough University in Leicestershire in UK and Ph.D. in Materials Engineering in 1998 at the Montfort University in Leicester in UK. At present he is working as a Full Professor in the Department of Mechanical and Manufacturing Engineering at the Faculty of Engineering at the Universiti Putra Malaysia, 43400 UPM Serdang, Selangor, Malaysia.



RAJA KAMIL received; B.Eng. in the Electrical Engineering in 1999 at the University of Southampton in UK and Ph.D. in Control Engineering in 2006 at the University of Sheffield in UK with the specialization in Control Engineering, Biomedical Engineering, Signal Processing and Pattern Recognition. At present he is working as an Associate Professor in the Department of Electrical and Electronics Engineering at the Faculty of Engineering at the Universiti Putra Malaysia, 43400 UPM Serdang, Selangor, Malaysia.

Kinematic Analysis of a Novel 5-DOF FDM Printer Based on Parallel Mechanism

Mehran Mahboubkhah
Faculty of Mechanical Engineering
University of Tabriz Bahman 29th Blvd,
P.O. Box: 51666-14766
Tabriz, Iran
mahboobkhah@tabrizu.ac.ir

Ahmet DUMLU
Department of Electrical & Electronic Engineering Faculty of Engineering and Architecture Erzurum Technical University
Erzurum, Turkey
ahmetdumlu@erzurum.edu.tr

Kagan Koray AYTEN
Department of Electrical & Electronic Engineering Faculty of Engineering and Architecture Erzurum Technical University
Erzurum, Turkey
kagan.koray@erzurum.edu.tr

***Abstract*—This paper presents a novel 5-DOF parallel manipulator with 3 different linear and two rotational motions around x and z directions. This parallel manipulator is used as a novel 5-DOF 3D printer. The proposed instrument aims to resolve the current restrictions of Additive Manufacturing (AM) processes such as supports and improve the part quality during the development and application of multi-axis 3D printing mechanisms. Inverse kinematic models of proposed parallel mechanism based on the closed loop vector theorem are derived and simulated by the code written in MATLAB. The results obtained by the mathematical model for the kinematics of the mechanism are verified using CATIA software. The results indicated that the two analytical and simulated models are in close accordance with together.**

Keywords— Parallel kinematic machines, Inverse kinematics, Additive Manufacturing, 3D Printer

[1] INTRODUCTION

Additive Manufacturing (AM) technology has obtained extensive interest and is expected to revolutionize the manufacturing industry as it is nowadays. Moreover, AM was proclaimed by Economist Magazine as part of the third industrial revolution in April-2012, [1, 2]. Since the AM allows for new product designs and fabricating complex geometries, has attracted attention in the production field. However, AM has some drawbacks such as lower accuracy, strength, wavy surface quality and longer production time. Compared with traditional/commercial AM processes and machines with three degrees of freedom (DOF) multi-axis AM processes can provide higher degrees of mobility depending on the machine kinematics and configuration of the manufacturing platform [1]. Traditionally, AMs are designed using three linear degree of freedom (DOF). In the typical machine tools as well as AMs with three linear DOF, to print most of the workpieces, construction of the supports is necessary. In order to overcome the limitations of traditional AM machines, mechanisms with different kinematic structures and DOF are produced and developed. Many researchers have focused on developing multi-axis AM systems; Urhal et al. [3] in a review paper discuss about the concept of multi-axis robot assisted AM. They expressed that the combined use of multi-axis robotic systems and AM technologies offers the possibility for multi-axis additive manufacturing and the fabrication of complex geometries in different manufacturing environments.

The Parallel Kinematic Mechanisms (PKM) enables higher movement and stiffness than the Cartesian systems. The difficulty with these systems lies in the complex control and calibration steps. Moreover, the dynamics of the system can be reduced due to use smaller masses than in serial mechanism [4]. The PKM is very useful when the accuracy, stiffness and high speed are required in a small workspace. Wei et al. [4] express that the Reconfigurable Parallel Mechanism (RPM) can reconfigure themselves into various mobility configurations to accommodate different task requirements, and these machines have the potential to be used in multidirectional additive manufacturing. An adaptive slicing algorithm which can generate optimal slices to achieve deposition without support structures for five-axis hybrid layered manufacturing is presented by Zhang et al. [5]. In many previous works, such as Adept Quattro mechanism by Clavel in 1987 [6], X4 by Xie and Liu in 2015 and 2016 [7], H4 by Pierrot and Company in 1999 [8], I4L by company et al. in 2002 [9], I4R by Kurt et al. in 2004 [10], Par4 by Nabat et al. in 2005 [11], and Heli4 by Kurt et al. in 2006 [12], the fourth DOF is a rotation about the vertical axis of the workspace (Z). Whereas in current mechanism the fourth DOF is a rotation about the horizontal axis of X. On the other hand, the configurations of the previous mechanisms are very similar to each other. Mahboubkhah et al. [13] have designed a Coordinate Measuring Machine (CMM) using a novel four DOF PKM, namely C4, and another 4-DOF PKM milling machine with three translations and one rotation about its X-axis.

In this paper, a new 5-DOF 3D printer PKM will be designed which has similar DOF features of the above mentioned C4 CMM and milling PKMs. This study aims to produce a novel 3D printer based on 5-DOF parallel kinematic machine to produce the workpieces with higher accuracy and without need for construct the supports. The most important features of the system to be developed are that; The proposed novel 5-DOF 3D printer will be able to reduce production time compared to other 3D printing mechanisms due to its high degree of freedom. In this proposed method, unlike the AMs currently used in the market, the system has both translational and rotational motion. Hence, we aim to improve both print quality and speed during the operation. In this study, a novel 3D printer taking into account five degrees of freedom parallel kinematics with three translations and two rotations about its X and Z axes is presented. It is expected that, due to the flexibility and rigidity of the proposed novel 3D printer can bring to produce accurate and qualified workpieces. With the development of the proposed 3D printer, it is possible to perform complicated motion control for the AM building platform. One method to remove the support structures is to build curved layers parallel to the part surface. To this end, the

rotational X and Z axes could be added to the proposed PKMs. This stage is the last goal and contribution which will be accomplished after design and manufacturing of the proposed five degree of 3D printer It should be emphasized that, the represented parallel mechanism has a unique configuration in the field of parallel mechanisms with five degree of freedom; otherwise, serial mechanisms with four degree of freedom with various configurations can be found or developed in machining industry. Also, as it is evident, the significant portion of the published research is associated with type synthesis, kinematical and singularity analyses of 5-DOF parallel mechanisms. While kinematic analysis is crucial and inseparable tasks toward studying parallel mechanisms, in many applications such as motion control and vibration analyses, a fundamental and comprehensive understanding of the kinematic behavior of the mechanism is of vital importance. Firstly, unlike the mechanics of the aforementioned C4 system, using the linear guides, a novel PKM with three translations and two rotations about its X and Z axes will be designed. Secondly, inverse kinematic relations of proposed parallel mechanism are derived and also simulated in MATLAB. The results obtained by the theoretical model for the kinematics of the mechanism are verified using CATIA software.

[2] DESCRIPTION OF THE PKM

As it is evident from Fig. 1-2, the manipulator under study is composed of a fixed and a moving platform which are connected to each other through four kinematic chains, namely two PR(Pa)R and two Pr(Pa)U, where P, R, Pa and U stand for prismatic, revolute, parallelogram and universal joints, respectively. The main component of these kinematic chains is the planar four-bar parallelogram. These bars are manipulated via four linear rails on which four saddles are capable of moving independent of each other. A pair of links is attached to each of the saddles with spherical joints in a configuration to shape parallelograms. At the other end, for second and third arm, links are attached to the moving platform via spherical joints, and for first and fourth arm, links are attached to the moving platform indirectly by connectors. Each connector is attached to the moving platform by a revolute joint. For the current manipulator, the moving platform has 3-DOF translational mobility and 1-DOF rotational mobility about x-direction (see Fig. 1-2). Another rotational mobility abut Z direction is provided through a rotary table. In Fig. 3 the configuration of components of parallel mechanism is illustrated clearly.

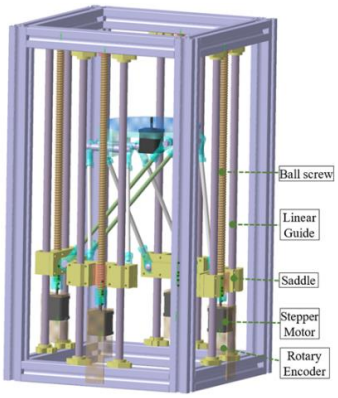


Fig. 1. Structure of parallel mechanism

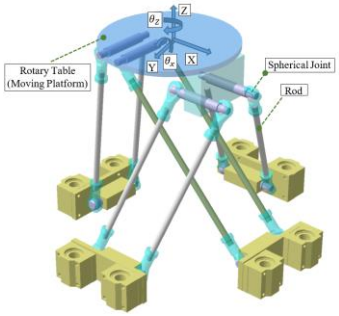


Fig. 2. Links and moving platform of parallel mechanism

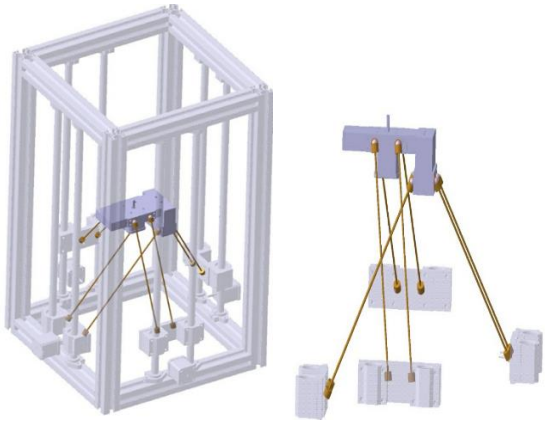


Fig. 3. Configuration of 5 dof 3D printer

[3] KINEMATICS EQUATIONS

According to kinematics principle, a mathematical model of proposed novel PM with 5-DOF will be established accurately. In order to obtain the workspace and investigating the dexterity of proposed PKM, inverse kinematic relations of position are derived.

A. Inverse kinematics

The Inverse Kinematic (IK) of position calculates the angular position of links, when the position and orientation of the MP are given. The relations of C4 components in vector form are illustrated in Fig. 3. Due to similarity of the kinematic chains in the mechanism, only one of them is shown in Figure 3 with 'i' index. Since, in control of the mechanism, position information of individual links and end effector are required; therefore, kinematic analysis is a prerequisite toward dynamic and other analyses of mechanism. Accordingly, in this section, the required kinematic information, namely the spatial position, of pods (parallelograms), end effector and saddles, applied in control of mechanism is determined. Figure 4 details the kinematic free diagram of the mechanism. The origin of global frame, {O} is fixed at the beginning of each prismatic joint's rail via vector and the vector connecting the local start point of the rail to the ith prismatic joint on the saddle is denoted by d_i . The vector is in same direction and equal in magnitude to the links' lengths of the ith arm and, as shown in Fig. 4, c_i is the vector attached to the ith connector beginning from the midpoint of the spherical joints and ending at the revolute axis of the connector.

It should be noted that for i = 2, 4, since there is no connector, then c_i. Furthermore, b_i is defined as a vector expressing the pose of the end of ith parallelograms relative to the local frame, fixed on the center of the moving platform {P}. It should be emphasized that all kinematic relationships

are with respect to the global frame {O} attached to fixed platform.

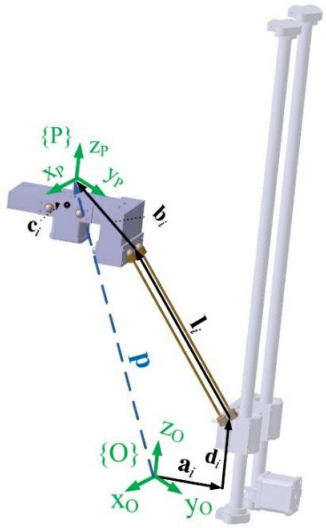


Fig. 4. Vector notation for kinematic modeling of the manipulator.

B. *Position analysis*

Utilizing the vectored method and according to Fig. 4, an algebraic vector relationship can be established for the i[th] chain as following:

$$ {}^{o}p + {}^{o}R_P\,{}^{P}b_i = {}^{o}a_i + {}^{o}d_i + {}^{o}I_i + {}^{o}c_i \qquad (1) $$

where b_i with respect to the global frame {O} becomes:

$$ {}^{o}b_i = {}^{o}R_P\,{}^{P}b_i \qquad (2) $$

where ${}^{P}b_i$ denotes the vector b_i with respect to local frame,{P}, and ${}^{o}R_P$ is the rotation matrix describing the orientation of {P} regarding to global frame {O} and since in this mechanism, only the rotation around X axes is feasible, the rotation matrix takes the form as below:

$$ {}^{o}R_P = R_x(\theta) = \begin{bmatrix} 1 & 0 & 0 \\ 0 & \cos(\theta_x) & -\sin(\theta_x) \\ 0 & \sin(\theta_x) & \cos(\theta_x) \end{bmatrix} \qquad (3) $$

Since ${}^{o}d_i$ and ${}^{o}c_i$ are always parallel, by defining $\hat{d}_i$ as the unit vector along d_i, Eq. (1) can be rewritten as;

$$ \left(p + b_i - a_i - c_i\hat{d}_i\right) - L_i = d_i\hat{d}_i \qquad (4) $$

Where c_i and d_i are, respectively, the magnitude of c_i and, Since the length of L_i which is denoted by l_i is known, the left hand side of the latter equation represents a sphere with center $p + b_i - a_i - c_i\hat{d}_i$ of and radius of l_i and the right side of Eq. (4) represents a line passing through the origin and along $\hat{d}_i$. Hence, solving Eq. (4) is equivalent to obtaining the intersection of a known sphere and a known line in space. By using the aforementioned equivalency, d_i can be obtained as:

$$ d_i = -c_i + \hat{d}_i^T(p + b_i - a_i) \pm \sqrt{l_i^2 - (p + b_i - a_i)^T(I_{3x3} - \hat{d}_i\hat{d}_i^T(p + b_i - a_i)} \qquad (5) $$

Further analyses done by CAD simulations showed that the equation with negative sign before the radical expression in the above equation yields valid solutions. Moreover, since the two arms of each link are considered identical, then the above equation is the closed form equation of inverse kinematics with unique solution.

[4] MEASUREMENT AND CALIBRATION OF COMPONENTS OF MECHANISM

After design and analysis of parallel mechanism, construction of whole components and assembly of instrument were done. In order to calculate the inverse Kinematic relations and control of PM under study, the measurement and calibration of components and assembled mechanism were done. (see Fig.5)

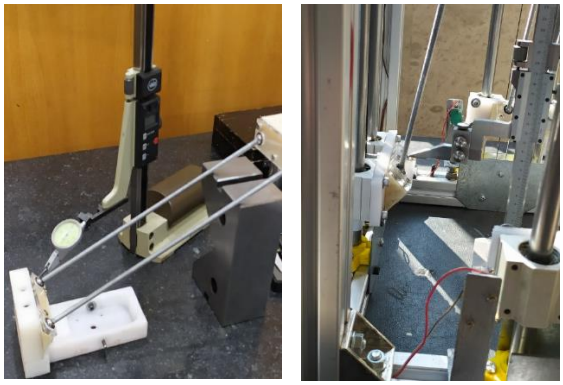


Fig. 5. Measurement and calibration process of manipulator under study.

In order to investigate the validity of the kinematic equations and their related programs, a 3D model simulation of the proposed robot was constructed in a commercial Computer Aided Design (CAD) environment. Using this simulation, the end-effector of robot is located in some predefined positions and orientations and then the related angular positions of links are measured accurately. This simulation establishes several inputs and outputs for verifying the kinematic problems. For instance, according to Figure 4 (one of the developed configurations in CAD) the rotation angle and the position and orientation of Moving Platform in {O} can be obtained using measuring tool in CAD. Using this data, the inverse kinematic programs are solved. Finally, the comparison of the results proves that the answers of the inverse kinematic solution correspond to the CAD simulation.

[5] CONCLUSION

The kinematical analysis of a novel linearly actuated 5-DOF parallel kinematic machine, composing 3 translational and 2 rotational motion abilities, were studied. Based on the concept of closed loop vector chain, the inverse kinematical relations of position were derived. Then, the measurement and calibration of whole components and structure of Parallel mechanism were done. Afterward, a CAD model of the mechanism under study was developed, and simulations were conducted. Simulation results showed that, the obtained data from mathematical model and the ones from CAD model, are in well alignment.

ACKNOWLEDGMENT

This work was supported by Tubitak with project number 119N707.

REFERENCES

[1] Lin Li, Azadeh Haghighi, Yiran Yang, A novel 6-axis hybrid additive-subtractive manufacturing process: Design and case studies, *Journal of Manufacturing Processes* 33 (2018) 150–160.

[2] Achim Kampkera, Johannes Triebsa, Sebastian Kawolleka, Peter Ayvaza, Steffen Hohenstein, Review on Machine Designs of Material Extrusion based Additive Manufacturing (AM) Systems - *Status-Quo and Potential Analysis for Future AM, Procedia CIRP 81* (2019) 815–819.

[3] Pinar Urhal, Andrew Weightman, Carl Diver, Paulo Bartolo, Robot assisted additive manufacturing: *A review, Robotics and Computer Integrated Manufacturing* 59 (2019) 335–345.

[4] Wei Ye, Yuefa Fang, Sheng Guo, Design and analysis of a reconfigurable parallel mechanism for multidirectional additive manufacturing, *Mechanism and Machine Theory* 112 (2017) 307–326.

[5] Jun Zhang, Frank Liou, Adaptive Slicing for a Multi-Axis Laser Aided Manufacturing Process, *J. Mech. Des.* (2004), 126(2): 254-261.

[6] Clavel, R. 1987. "Unmanned robotic delta weapon platform." WIPO patent; (WO 87/03528).

[7] Xie, F., and Liu, X. J. "Analysis of the kinematic characteristics of a high-speed parallel robot with Schönflies motion: Mobility, kinematics and singularity." *Front. Mech. Eng*. (2016), 11: 2, 135–143.

[8] Pierrot, F. Company O. "H4: a new family of 4-dof parallel robots." In AIM'99: IEEE/ASME Int. Conf. on Adv. *Intelligent Mechatronics*, Atlanta, Georgia, USA, Sep. (1999) 508–513.

[9] Company, O., Krut, S., Pierrot, F. 2002. "Modelling of a 4 axis parallel machine for heavy parts handling. In Development methods and application experience of parallel kinematics." *Proc. of the 3rd Chemnitz Parallel Kinematics Sem. PKS2002* (Ed. R. Neugebauer), vol. 16, (Chemnitz, Germany) 151–168.

[10] Krut, S., Nabat, V., Company, O., Pierrot, F. "A high speed robot for Scara motions." *In Proceedings of IEEE ICRA: Int. Conf. on Robotics and Automation*, New Orleans, USA, 26 Ap. (2004).

[11] Nabat, V., Company, O., Krut, S., Rodriguez, D. O., and Pierrot, F. "Par4: Very high speed parallel robot for pick and place." *In Proc. of IEEE/RSJ IROS: Int. Conf. on Intelligent Robots and Systems*, Edmonton, Alberta, Canada, 2–6 Aug (2005).

[12] Krut, S., Company, O., Nabat, V., and Pierrot, F. "Heli4: a parallel robot for scara motions with a very compact travelling plate and a symmetrical design." *In Proc. of IEEE/RSJ IROS: Int. Conf. on Intelligent Robots and Systems*, Beijing, China, (2006) 9–15 Oct.

[13] Mehran Mahboubkhah and Ahmad Barari. "Design and development of a novel 4-DOF parallel kinematic coordinate measuring machine (CMM) " *International Journal of Computer Integrated Manufacturing*, (2019) 32:8, 750-760, DOI: 10.1080/0951192X.2019.1610576

Adaptive Sliding Mode Control of Mobile Robot and Comparison with PID Controller

Mustafa Ayyıldız
Electrical and Electronics Engineering Department
Suleyman Demirel University
Isparta, Turkey
yl1930112014@stud.sdu.edu.tr, 0000-0003-0294-3822

Umut Tilki
Electrical and Electronics Engineering Department
Suleyman Demirel University
Isparta, Turkey
umuttilki@sdu.edu.tr, 0000-0002-8988-787X

***Abstract*— Mobile robots with adaptive fault tolerant control are distinguished from other mobile robots with the features of detecting and identifying errors. These mobile robots are able to continue to work as desired after a fault occurs in the overall system. This kind of control system can be implemented with different controller structures. In this study, to reduce the mobile robot tracking error, an adaptive sliding mode controller and PID controller are used as the controller system which applied to a nonlinear mobile robot model in the presence of disturbance. Moreover, these two systems have been compared and results are demonstrated in this work.**

Keywords—Adaptive fault tolerant control, Dynamic control, Kinematic control, Adaptive sliding mode control, PID control, Trajectory tracking

[1] INTRODUCTION

Trajectory tracking (TT) control is a key function in wheel mobile robot (WMR) motion control, and the aim of TT is to perform navigation control with predetermined trajectory, such that the WMR is capable of tracking the time-variant reference trajectory with desired accuracy [1]. In trajectory tracking, the robot must reach and follow the trajectory in the cartesian space starting from a given initial position and configuration [2].

Actuator faults of a mobile robot may degrade driving performance or even cause accidents. Fault-tolerant control is the most effective way to ensure the safety and stability of the robot in the case of any faults in the system [3].

Mevo et al. [4] proposed an adaptive sliding mode control solution for the problem of tracking by taking nonlinear model, uncertainties, and disturbances into account. The main contribution in that work was firstly modelling the nonlinear mobile robot for simulation and secondly designing a controller compensating uncertainties of mass and inertia. All the stability analysis and convergence of tracking errors to zero were proved using the Lyapunov stability theory.

In this paper, it is proposed to use two control systems. Input position errors, reference velocities, and the current velocities were obtained by the kinematic controller. The second controller is ASMC or PID controller which are applied separately to the system. With the input of velocity errors, two control signals are obtained by an ASMC. In simulation two models are used. Nonlinear model supplies the velocities of the robot. In here artificial noise is also added to the control signals which are obtained from the ASMC. Kinematic model provides the robot position and orientation with the velocities obtained from the nonlinear model. This paper provides a trajectory tracking to the mobile robot with minimum chattering effect in control signals in the presence of disturbance. Besides ASMC and PID control is also used in the same system and the results are compared.

[2] MATHEMATICAL MODEL

In this section, kinematic and dynamic model of differential drive mobile robot (DDMR) is presented. The mobile robot which has been used in this work has three wheels. DDMR is based on two separately driven wheels placed on each side of the robot body. One more wheel is added in front of the robot for stable movement.

Mobile robot system and coordinate axis are shown in Figure 1. The origin of the robot frame is defined as the mid-point (shown as A) on the axis between the wheels. The center of mass (D point) of the robot is assumed to be on the axis of symmetry, at a distance "d" from the origin. Instantaneous curvature radius of the robot trajectory (distance from ICC to the midpoint between two wheels) is also demonstrated in Figure 1 (C point).

As can be seen in the Figure 1, two different coordinate systems are used, namely inertial coordinate system (base frame) and robot coordinate system (moving frame). Rotation matrix, shown in equation (1) expresses the orientation of the inertial coordinate system with respect to the robot coordinate system.

$$q^I = \begin{pmatrix} x^I \\ y^I \\ \theta^I \end{pmatrix}, q^r = \begin{pmatrix} x^r \\ y^r \\ \theta^r \end{pmatrix}, R(\theta) = \begin{pmatrix} \cos\theta & \sin\theta & 0 \\ -\sin\theta & \cos\theta & 0 \\ 0 & 0 & 1 \end{pmatrix} \quad (1)$$

Using the orthogonal rotation matrix ($R(\theta)$), the robot coordinate system (q^r) can be converted to the inertial coordinate system (q^I) by eq (2).

$$\dot{q}^I = R(\theta)^{-1}\dot{q}^r \quad (2)$$

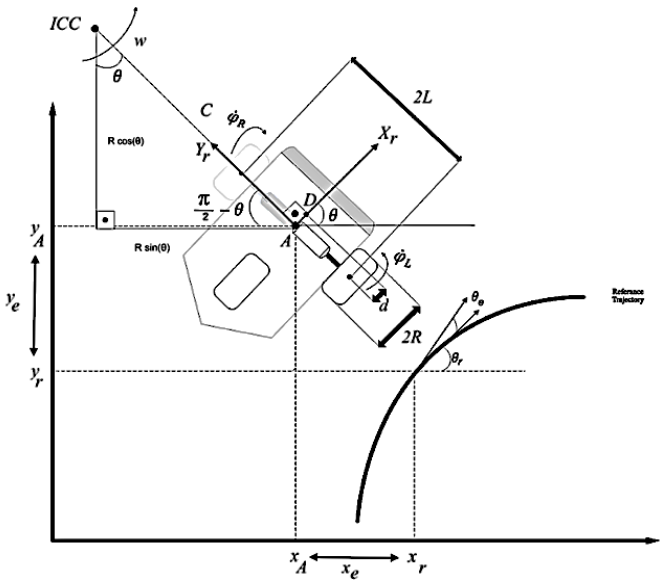


Fig.1. Mobile Robot and Coordinate Systems

A. Kinematic Model

The average velocities of the left and right wheel give the speed of the robot frame. In addition, the angular velocity is obtained by subtracting the equations in (3) from each other. These operations can be expressed in a different way. The speed of the right and left wheels can be expressed as angular velocity.

$$V_R = w(R+L)\,,\quad V_L = w(R-L) \tag{3}$$

$$v = \frac{(V_R+V_L)}{2} = \frac{R(\varphi_R+\varphi_L)}{2},\ w = \frac{(V_R-V_L)}{2L} = \frac{R(\varphi_R-\varphi_L)}{2L} \tag{4}$$

Since there is no speed along y direction (no lateral slip motion), the velocities with respect to center point A are written for the robot frame, as given below:

$$\begin{pmatrix} \dot{x}_A{}^r \\ \dot{y}_A{}^r \\ \dot{\theta}_A{}^r \end{pmatrix} = \begin{pmatrix} R/2 & R/2 \\ 0 & 0 \\ R/2L & -R/2L \end{pmatrix} \begin{pmatrix} \dot{\varphi}_R \\ \dot{\varphi}_L \end{pmatrix},\ \begin{pmatrix} w_R \\ w_L \end{pmatrix} = \begin{pmatrix} \dot{\varphi}_R \\ \dot{\varphi}_L \end{pmatrix} \tag{5}$$

Using eq. (2), the following transformation can be written.

$$\begin{pmatrix} \dot{x}_A{}^I \\ \dot{y}_A{}^I \\ \dot{\theta}_A{}^I \end{pmatrix} = \begin{pmatrix} \cos\theta & -\sin\theta & 0 \\ \sin\theta & \cos\theta & 0 \\ 0 & 0 & 1 \end{pmatrix} \begin{pmatrix} \dot{x}_A{}^r \\ \dot{y}_A{}^r \\ \dot{\theta}_A{}^r \end{pmatrix} = \begin{pmatrix} \frac{R\cos\theta}{2} & \frac{R\cos\theta}{2} \\ \frac{R\sin\theta}{2} & \frac{R\sin\theta}{2} \\ \frac{R}{2L} & -\frac{R}{2L} \end{pmatrix} \begin{pmatrix} \dot{\varphi}_R \\ \dot{\varphi}_L \end{pmatrix} \tag{6}$$

The above equation is the general forward kinematic equation for a differential drive mobile robot. Substituting (6) with equivalent terms in (4), it becomes:

$$\begin{pmatrix} \dot{x}_A{}^I \\ \dot{y}_A{}^I \\ \dot{\theta}_A{}^I \end{pmatrix} = \begin{pmatrix} cos\ \theta & 0 \\ \sin\theta & 0 \\ 0 & 1 \end{pmatrix} \begin{pmatrix} v \\ w \end{pmatrix} \tag{7}$$

The main purpose of the DDMR's kinematic model is to express the current position of the robot by using velocities.

B. Dynamic Model

In general, dynamic modeling is the study of the system's motion in which forces are modeled and it can include energies and the speeds associated with the motions. This dynamic model is derived by the Lagrange dynamic approach [5, 6]. General dynamic equation is given in (8) where $M(q)$ is the symmetric positive definite inertia matrix, $V(q,\dot{q})$ is the centripetal and Coriolis matrix, $G(q)$ is the gravitational vector, τ_d denotes the bounded unknown disturbances including unstructured unmodeled dynamics, $B(q)$ is the input transformation matrix, τ is the input vector, $A^\tau(q)$is the matrix associated with the constraints, λ is the vector of the constraint forces.

$$M(q)\ddot{q} + V(q,\dot{q})\dot{q} + F(\dot{q}) + G(q) + \tau_d = B(q)\tau - A^\tau(q)\lambda \tag{8}$$

$q, \dot{q}\ and\ \ddot{q}$ denote position, velocity, and acceleration vectors, respectively. Assuming that the mobile robot moves in the horizontal plane and there are no disturbances, $G(q)$ is equal to 0. The surface friction matrix $F(\dot{q})$ and τ_d are assumed to be zero. Instead, the changes are achieved by the artificial noise added to the control signal.

By expanding the system in (6), $\dot{q}$ vector can be written as follows. The velocity $(\dot{q})$ and acceleration $(\ddot{q})$ in (8) can be found using the equation in (9).

$$\dot{q} = \begin{pmatrix} \dot{x}_A \\ \dot{y}_A \\ \dot{\theta} \\ \dot{\varphi}_R \\ \dot{\varphi}_L \end{pmatrix} = \frac{1}{2} \begin{pmatrix} R\ cos\theta & R\ cos\theta \\ R\ sin\theta & R\ sin\theta \\ R/L & -R/l \\ 2 & 0 \\ 0 & 2 \end{pmatrix} \begin{pmatrix} \dot{\varphi}_R \\ \dot{\varphi}_L \end{pmatrix},\ \eta = \begin{pmatrix} \dot{\varphi}_R \\ \dot{\varphi}_L \end{pmatrix} \tag{9}$$

$$M(q) = \begin{pmatrix} m & 0 & -mdsin\theta & 0 & 0 \\ 0 & m & mdcos\theta & 0 & 0 \\ -mdsin\theta & mdcos\theta & I & 0 & 0 \\ 0 & 0 & 0 & I_w & 0 \\ 0 & 0 & 0 & 0 & I_w \end{pmatrix}$$

$$V(q,\dot{q}) = \begin{pmatrix} 0 & 0 & -md\dot{\theta}cos\theta & 0 & 0 \\ 0 & 0 & -md\dot{\theta}sin\theta & 0 & 0 \\ 0 & 0 & 0 & 0 & 0 \\ 0 & 0 & 0 & 0 & 0 \\ 0 & 0 & 0 & 0 & 0 \end{pmatrix}, B(q) = \begin{pmatrix} 0 & 0 \\ 0 & 0 \\ 0 & 0 \\ 1 & 0 \\ 0 & 1 \end{pmatrix} \tag{10}$$

$$A^T(q).\lambda = \begin{pmatrix} -sin\theta & cos\theta & cos\theta \\ cos\theta & sin\theta & sin\theta \\ -d & L & -L \\ 0 & -R & 0 \\ 0 & 0 & R \end{pmatrix} x \begin{pmatrix} \lambda_1 \\ \lambda_2 \\ \lambda_3 \\ \lambda_4 \\ \lambda_5 \end{pmatrix}$$

Since the Lagrange multipliers λ are not known, the constraint term $A^\tau(q)\lambda$ in equation (8) must be eliminated so defining the reduced vector. If the vectoral equation in (9) η is written into $\dot{q}$ and the transformation matrix is called $S(q)$, the equation becomes as follows.

$$\dot{q} = S(q)\eta,\ \ddot{q} = \dot{S}(q)\eta + S(q)\dot{\eta} \tag{11}$$

The transformation matrix $S(q)$ is in the null space of the constraint matrix $A(q)$. Hence:

$$S^T(q)\,A^T(q) = 0 \tag{12}$$

τ_R and τ_L which are right and left torques respectively, can be expressed as follows.

$$\tau = u = \begin{pmatrix} u_1 \\ u_2 \end{pmatrix} = \begin{pmatrix} \tau_R + \tau_L \\ \tau_R - \tau_L \end{pmatrix} \tag{13}$$

Using (11) and (13), dynamic equation can be written as follows.

$$M(q)\left[\dot{S}(q)\eta + S(q)\dot{\eta}\right] + V(q,\dot{q})[S(q)\eta] = B(q)\tau - A^\tau(q)\lambda \tag{14}$$

$$\bar{M}(q) = S^T(q)M(q)S(q),\ \bar{B}(q) = S^T(q)B(q)\tau \tag{15}$$

$$\bar{V}(q,\dot{q}) = S^T(q)M(q)\dot{S}(q) + S^T(q)V(q,\dot{q})S(q) \tag{16}$$

If the equations (14), (15) and (16) are reordered, the new dynamic equation becomes:

$$\bar{M}(q)\dot{\eta} + \bar{V}(q,\dot{q})\eta = \bar{B}(q)\tau \tag{17}$$

$$\bar{M}(q) = \begin{bmatrix} I_w + \frac{R^2}{4L^2}(mL^2+I) & \frac{R^2}{4L^2}(mL^2-I) \\ \frac{R^2}{4L^2}(mL^2-I) & I_w + \frac{R^2}{4L^2}(mL^2+I) \end{bmatrix}$$

$$\bar{V}(q,\dot{q}) = \begin{bmatrix} 0 & \frac{R^2}{2L^2}m_c d\dot{\theta} \\ -\frac{R^2}{2L^2}m_c d\dot{\theta} & 0 \end{bmatrix},\ \bar{B}(q) = \begin{bmatrix} 1 & 0 \\ 0 & 1 \end{bmatrix} \tag{18}$$

Using the velocity equations in (4), equation (17) can be converted to an alternative form. This structure (19) is called the nonlinear model of DDMR.

$$\begin{bmatrix} m_0 & 0 \\ 0 & I_0 \end{bmatrix} \begin{pmatrix} \dot{v} \\ \dot{w} \end{pmatrix} + \begin{bmatrix} 0 & -m_c dw \\ m_c dw & 0 \end{bmatrix} \begin{pmatrix} v \\ w \end{pmatrix} = \begin{bmatrix} \frac{1}{R} & 0 \\ 0 & \frac{L}{R} \end{bmatrix} \begin{pmatrix} u_1 \\ u_2 \end{pmatrix} \tag{19}$$

$$m = m_c + 2m_w,\ m_0 = \left(m + \frac{2I_w}{R^2}\right) \tag{20}$$

$$I = I_c + m_c d^2 + 2m_w L^2 + 2I_m\,,\ I_0 = \left(I + \frac{2L^2}{R^2}I_w\right) \tag{21}$$

[3] Controller Methods

A. Kinematic Controller

In the literature it was proposed a kinematic based backstepping controller for a nonholonomic mobile robot [6, 7]. In that approach, a stable tracking control rule for a nonholonomic mobile robot, which neglects the vehicle dynamics, is based on the steering system. Control system has two postures. They are the reference posture P_r and the current posture P_c. These coordinate systems are three-dimensional vectors and include the x, y, and θ states. The error is obtained by taking the difference of the reference and current positions and multiplying them with the rotation matrix.

$$e_p = \begin{pmatrix} x_e \\ y_e \\ \theta_e \end{pmatrix} = \begin{pmatrix} cos\theta & sin\theta & 0 \\ -sin\theta & cos\theta & 0 \\ 0 & 0 & 1 \end{pmatrix} \begin{pmatrix} x_r - x_c \\ y_r - y_c \\ \theta_r - \theta_c \end{pmatrix} \quad (22)$$

$$\begin{pmatrix} v_c \\ w_c \end{pmatrix} = \begin{pmatrix} v_r cos\theta_e + K_x x_e \\ w_r + v_r(K_y y_e + K_\theta sin\theta_e) \end{pmatrix} \quad (23)$$

K_x, K_y and K_θ are positive constants.

B. Adaptive Sliding Mode Controller

In ASMC structure, dynamic equations which are given in [4, 8] are used. Two velocities which are obtained from the output of the kinematic controller and nonlinear model are needed to design the sliding surface. The velocity error is found by taking the differences of these velocities.

$$e_c = \begin{pmatrix} e_v \\ e_w \end{pmatrix} = \begin{pmatrix} v_c \\ w_c \end{pmatrix} - \begin{pmatrix} v \\ w \end{pmatrix} \quad (24)$$

In the controller structure PI type sliding surface is used as follows:

$$S(t) = \begin{bmatrix} S_1(t) \\ S_2(t) \end{bmatrix} = e_c(t) + \beta \int e_c(t)dt \quad (25)$$

In here, β is the positive sliding surface integral constant.

$$u_{eq}(t) = \begin{cases} u_{eq1}(t) = \hat{\gamma}[\dot{v}_c(t) + \beta e_v(t)] \\ u_{eq2}(t) = \hat{\alpha}[\dot{w}_c(t) + \beta e_w(t)] \end{cases} \quad (26)$$

$$u_w(t) = \begin{cases} u_{w1}(t) = K_1 S_1 \\ u_{w2}(t) = K_2 S_2 \end{cases} \quad (27)$$

$$u_d(t) = \begin{cases} u_{d1}(t) = \eta_1 \tanh(S_1/\varepsilon) \\ u_{d2}(t) = \eta_2 \tanh(S_2/\varepsilon) \end{cases} \quad (28)$$

$$u(t) = u_{eq}(t) + u_w(t) + u_d(t) \quad (29)$$

u_{eq} is the adaptive compensation item, u_w is the feedback item, u_d is the robustness item and $K_1, K_2 > 0,\ \eta > D, \varepsilon > 0$. In the controller, as the robustness term to decrease chattering, tanh function is used. Using the Lyapunov stability method, the adaptive law is taken into account like in proposed in [9, 10, 11]. By exploiting reasonable a priori information on the physical systems, a discontinuous projection based adaptive robust control design is constructed to solve the tracking control problem. Estimated parameters $\hat{\gamma}$ and $\hat{\alpha}$ are updated through a parameter adaptation law having the form of

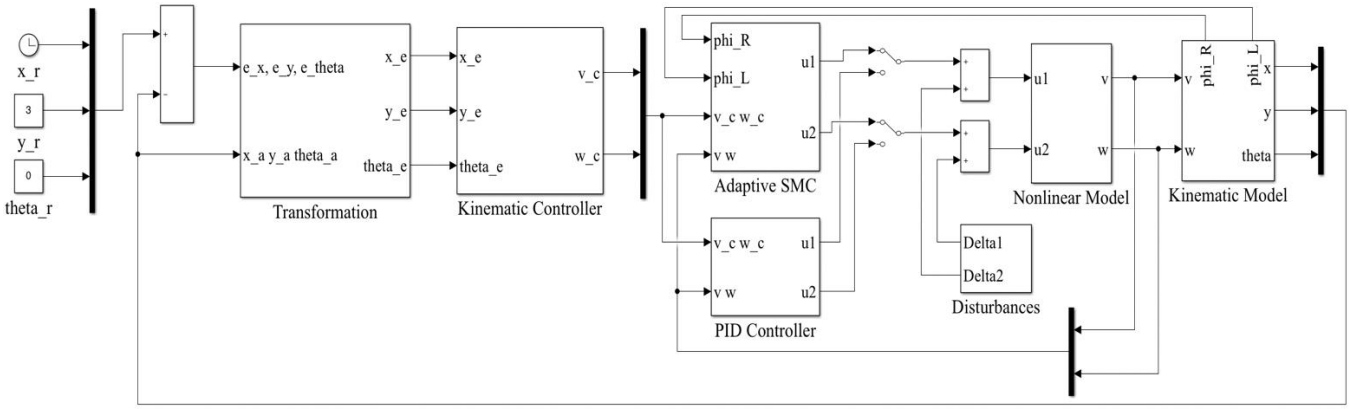


Fig.2. Mobile Robot Controller Architecture

$$\dot{\hat{\gamma}} = Proj_{\hat{\gamma}}[-aS_1(\dot{v}_c + \beta e_v)],\ \dot{\hat{\alpha}} = Proj_{\hat{\alpha}}[-bS_2(\dot{w}_c + \beta e_w)] \quad (30)$$

$$Proj_{\hat{\gamma}}(\cdot) = \begin{cases} 0, & if\ \hat{\gamma} = \gamma_{max}\ and\ \cdot > 0 \\ 0, & if\ \hat{\gamma} = \gamma_{min}\ and\ \cdot < 0 \\ \cdot, & otherwise \end{cases} \quad (31)$$

$$Proj_{\hat{\alpha}}(\cdot) = \begin{cases} 0, & if\ \hat{\alpha} = \alpha_{max}\ and\ \cdot > 0 \\ 0, & if\ \hat{\alpha} = \alpha_{min}\ and\ \cdot < 0 \\ \cdot, & otherwise \end{cases} \quad (32)$$

Maximum or minimum values can be calculated as follows:

$$\gamma_{max,min} = m_0 R, \quad \alpha_{max,min} = I_0 R/L \quad (33)$$

Using the above equation, the control law can be rewritten as:

$$u(t) = \begin{cases} u_1(t) = \hat{\gamma}[\dot{v}_c(t) + \beta e_v(t)] + K_1 S_1 + \eta_1 \tanh(S_1/\varepsilon) \\ u_2(t) = \hat{\alpha}[\dot{w}_c(t) + \beta e_w(t)] + K_2 S_2 + \eta_2 \tanh(S_2/\varepsilon) \end{cases} \quad (34)$$

C. PID Controller

In this part, a traditional PID controller which is widely used in the literature has been added to the system in order to compare two controllers. Proportional term (P) is used in calculating current errors, integral term (I) provides information about the amount of previous errors, and derivative term (D) provides a prediction of future errors, based on the current size fluctuation rate [12]. Two PID controllers are used in the system. The first produces a control signal with errors of linear velocities. The second one produces a control signal with errors of angular velocities. The following function is used for these two PID controllers.

$$u(t) = K_p e(t) + K_i \int_0^t e(t)dt + K_d \frac{d}{dt} e(t) \quad (34)$$

[4] SIMULATIONS

Block diagram of the overall system is given in Figure 2. The simulations have been conducted in Matlab/Simulink environment. In controller applications error function is found when the instantaneous posture is extracted from the reference posture. This error is feed forward to the transform block as input and the error posture is obtained by multiplying by the rotation matrix. Velocities are found in kinematic controller part. In ASMC, the parameters are needed to be found in $u_1(t)$ and $u_2(t)$ equations taken from kinematic

model and kinematic controller. Maximum and minimum values of m_0 and I_0 are taken as $17.51kg \leq m_0 \leq 37.51kg$ *and* $0.57kgm^2 \leq I_0 \leq 4.57kgm^2$. An external disturbance source is used at the ASMC output in order to demonstrate the robustness of this controller. Velocities are found with the nonlinear model equation. Velocities $\dot{\varphi}_R$ and $\dot{\varphi}_L$ are found in the kinematic controller. Also using velocity and integral block, position posture is found. Parameters are taken as below: $x_r = t$; $y_r = 3$; $\theta_r = 0$; $v_r = 0.05\ m/s$; $w_r = 0\ rd\ s^{-1}$; $x_0 = -1$; $y_0 = 0$; $\theta_0 = 0$; $m_w = 0.5kg$; $m_c = 17kg$; R=0.095m; L=0.24m; d=0.05; $I_c = 0.537\text{kg}\,m^2$; $I_m = 0.0011\text{kg}\,m^2$; $I_w = 0.0023\text{kg}\,m^2$; $K_x = 1s^{-1}$; $K_y = 15m^{-1}$; $K_\theta = 15m^{-1}$; $\beta = 5$; a=150; b=150; $K_1 = 0.05$; $K_2 = 0.05$; $\varepsilon = 0.05$. The values of the PID controller parameters are found by trial-and-error method. $K_v = 1.8$; $K_w = 0.1$; $P_1 = 0.01$; $I_1 = 0.00005$; $D_1 = 0.15$; $N_1 = 9$; $((PID)_1$using linear velocity error); $P_2 = 90$; $I_2 = -0.0001$; $D_2 = 22$; $N_2 = 70$ ($(PID)_2$ using angular velocity error). Ode45 and Ode15s are used for ASMC and PID controller, respectively. In each case, ASMC and PID controller, same disturbances which are $\Delta_1 = 0.25 * \sin(3 * t)$ *and* $\Delta_2 = 0.75 * \cos(2 * t)$ is used for fare comparison.

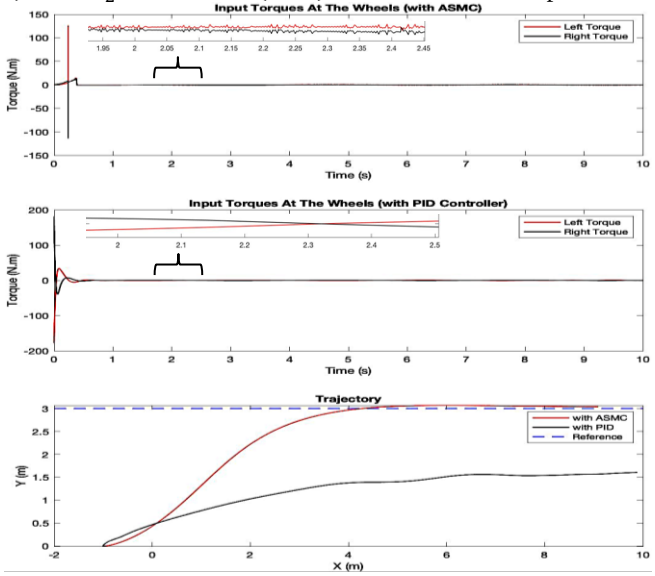


Fig.3. Controller Torque and Trajectories

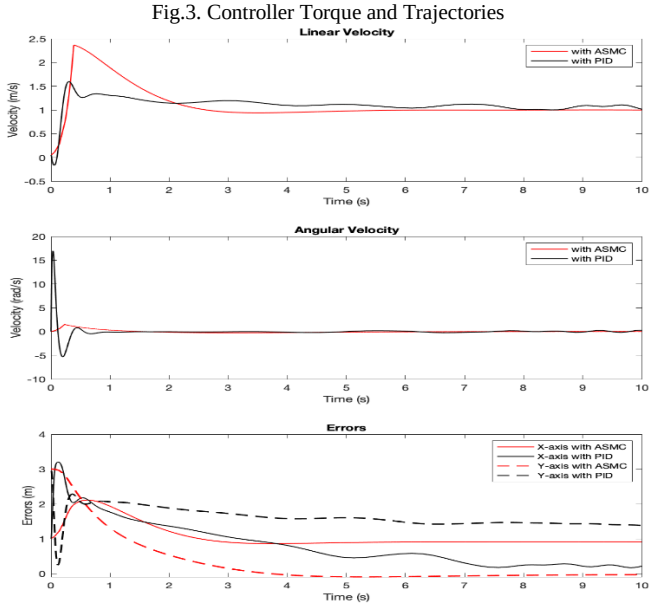


Fig.4. Velocities and Errors

In Figure 3, the torque (with ASMC and PID) is high at the beginning, because the mobile robot moves with acceleration. After vehicle catches the reference and moves linearly, control signals tend to go to zero. The great performance of the proposed ASMC in trajectory tracking in comparison with the PID controller but PID has no chattering problem so it has more smooth control input. In Figure 4, the mobile robot accelerated in the curve and continued at constant velocities after reaching the reference line. The errors between the reference trajectory and the actual one (with ASMC) in Y-axis tend to zero. It is natural for the error on the X-axis to converge to one. Because the theta angle has become zero. The PID controller could not maintain this situation. It can be provided from the kinematic controller.

[5] CONCLUSION

In this paper, a comparison of the controllers is presented. In trajectory tracking, ASMC performed much better results. Although implementation of PID controller is trivial, determination of the gain parameters with trial-and-error was main drawback. To improve this paper, better results can be obtained with the optimization method for PID values.

REFERENCES

[1] D. Li and J. Ye, "Adaptive Robust Control of Wheeled Mobile Robot with Uncertainties," in Advanced Motion Control (AMC), 2014 IEEE 13th International Workshop on, pp. 518-523, 2014.

[2] J.-P. Laumond, "Robot Motion Planning and Control," Vol. 229, New York: Springer, 1998.

[3] X.-Z. Jin, Y.-X. Zhao, H. Wang, Z. Zhao and X.-P. Dong, "Adaptive Fault-Tolerant Control of Mobile Robots with Actuator Faults and Unknown Parameters," IET Control Theory & Applications, vol. 13, no. 11, pp. 1665-1672, 2019.

[4] B. B. Mevo, M. R. Saad, and R. Fareh, "Adaptive Sliding Mode Control of Wheeled Mobile Robot with Nonlinear Model and Uncertainties," in Electrical & Computer Engineering, IEEE Canadian Conference on, pp. 1-5, 2018.

[5] R. Dhaouadi and A. A. Hatab, "Dynamic Modelling of Differential-Drive Mobile Robots using Lagrange and Newton-Euler Methodologies: A Unified Framework," Advances in Robotics & Automation, vol. 2, pp. 1-7, 2013.

[6] O. Mohareri, "Mobile Robot Trajectory Tracking Using Neural Networks," Degree of Master of Science in Mechatronics Engineering, American University of Sharjah, 2009.

[7] Y. Kanayama, Y. Kimura, F. Miyazaki and T. Noguchi, "A stable tracking control method for an autonomous mobile robot," in Robotics and Automation, 1990. Proceedings., 1990 IEEE International Conference on, pp. 384-389, 1990.

[8] Y. Koubaa, M. Boukattaya and T. Dammak, "Adaptive sliding-mode dynamic control for path tracking of nonholonomic wheeled mobile robot," J Autom Syst Eng, vol. 9, pp. 119-131, 2015.

[9] L. Xu and B. Yao, "Adaptive robust control of mechanical systems with nonlinear dynamic friction compensation," Int. J. Control, vol. 81, no. 2, pp. 167–176, 2007.

[10] S. Sastry and M. Bodson, "Adaptive Control: Stability, Convergence, and Robustness," Courier Corporation, 2011.

[11] J. Liu and X. Wang, "Advanced sliding mode control for mechanical systems: design, analysis and MATLAB simulation," ed: Tsinghua University Press, 2011.

[12] A. Bârsan, “Position Control of a Mobile Robot through PID Controller,” Acta Universitatis Cibiniensis. Technical Series, vol. 71, pp. 14-20, 2019.

MM-RAM Composites as a Wide Band Radar Absorber

Mehmet Ertugrul
Ataturk University, Engineering Faculty, Department
of Electrical and Electronics Engineering, 25240
Erzurum-TURKEY
ertugrul@atauni.edu.tr

***Abstract*— The reduction of the radar cross section (RCS) is achieved by absorbing at least 90% of the microwave in the specified frequency range. Thus, the target can be made almost invisible to the radar for given radar frequency range. Generally, microwave absorption is achieved by controlling resonance and scattering mechanisms of the microwaves. Shaping the target and coating/painting it with radar absorbent material is the most common method to reduce RCS. In recent years, many new materials have been developed for this purpose, from metamaterials (MM) to radar absorber materials (RAM). In this study, a wide range of the radar frequencies divided into 3 frequency regions as low, mid and high frequency regions for the 1-18 GHz range. A new layered hybrid device has been created by combining RAM and MM structures that provide maximum absorption in these 3 frequency regions. While MM was created in different geometries for each frequency region, RAM were obtained with different material, particle size and mixing ratios. It is possible to adjust the electrical and magnetic permeability of these materials with the mixing ratio and particle size of the conductive, insulating, magnetic portion of the materials. In this study, a new hybrid structure is proposed by using RAM and MM. An insulating layer is placed between RAM and MM. RAM contains nanomaterials insulator, conductor and magnetic materials such as BN, BaFe2O3, MXene and CNT. This structure was able to provide over 90% absorption for an ultrawide range bandwidth (15GHz) between 1-18GHz. Thus, a sandwich structure that gives absorption in different frequency ranges has been obtained. In addition, the coupling effects of the MMs in each of these layers were also examined. This structure was able to provide over 90% absorption for an ultrawide range bandwidth (15GHz) between 1-18GHz.**

Keywords—Microwave absorption, Mxene, CNT, CST

1. INTRODUCTION

The complex electrical and magnetic permeability, impedance matching and microstructure of the absorber material determine the properties of microwave absorption. The reduction of the radar cross section (RCS) is achieved by absorbing at least 90% of the microwave in the specified frequency range. Thus, the target can be made almost invisible by the radar in a certain frequency range. The absorption of the microwave is achieved by controlling the absorption, resonance and scattering mechanisms. In recent years, many new materials have been developed from metamaterials to composite materials. To reduce RCS, shaping the target and coating it with radar absorbing material are the most common methods. Also, metamaterial (MM) devices have been used for this purpose in recent years. While RCS reduction is achieved by making designs in different geometries and sizes in MMs, radar absorption materials are provided by the electrical and magnetic properties of the material. Both absorption mechanisms have advantages over each other. To reduce RCS, shaping the target and coating it with radar absorbing material are the most common methods. Microwave absorbers operating in the desired frequency range can be obtained. absorption mechanisms of both composite and metamaterials which are different and they have advantages over each other.

Radar absorber materials are generally functional materials that convert electromagnetic energy into heat. The most important use of radar absorber materials is in the work done to provide invisibility in the military field. For this reason, studies on electromagnetic absorber or radar absorber materials have gained importance in recent years [Zhao et al 2013]. Radar frequency is approximately between 300 MHz and 300 GHz and it consists of various bands [IEEE 521-2002]. On the other hand, microwave frequencies in the range of 300 MHz to 20 GHz are used today for military applications (Figure-1).

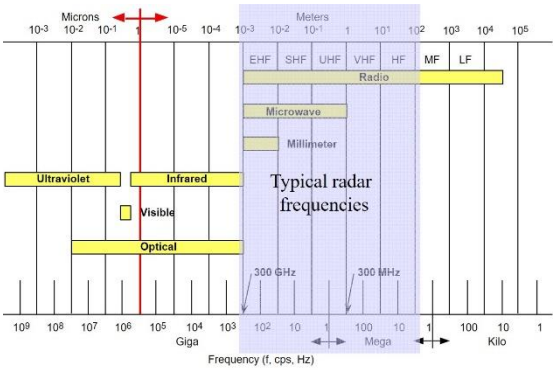


Fig. 1. Radar frequencies used today

In studies conducted to reduce the radar cross section, it was aimed to have at least 90% (-10dB) absorption in the specified frequency range [Idris et al 2016]. Today, studies on radar absorber material development can generally be divided into 3 categories. These are adaptive radarabsorbers, non- adaptiveMM based radar absorbers and composite based radar absorbers. In studies conducted in the literature on adaptive radar absorbers , ionic liquid was placed between the graphene electrodes and the conductivity of the graphene layers was controlled with the help of the applied voltage, and the reflection and absorption was achieved at the desired level and frequency [Balcı et al 2015]. This research, first conducted by Balcı et al [2015], is an original study and is a pioneering publication in this field. However, the ionic liquid used freezing at low temperatures and the uncertainty of its

behavior at high temperatures are seen as a problem. On the other hand, it is unclear how long this structure can work without deterioration. In another study performed on adaptive radar absorbers, the structure of MM and therefore the absorption region is realized by controlling the active zone with PIN diode, MEMS or other switching operating at microwave frequencies [Kim et al, 2016]. In these studies, the problems arising from the production of switching systems that can operate in the desired frequency range have not been completely solved yet. In addition, the adjustment of the absorption frequency is based on the principle of changing the unit cell active circuit of MM, material properties or geometry. This provides gradual absorption in certain frequency ranges rather than continuous microwave absorption effect at all frequencies. On the other hand, the cooling values obtained are not at the desired level yet. In another study, microwave absorption of MM was adjusted with the help of temperature [Li et al 2018]. In this study, the adjustability of microwave absorption is explained in detail, but problems such as simultaneously increasing and lowering the temperature over the whole structure and ensuring temperature homogeneity in large-scale applications are quite difficult to overcome. Studies are also carried out to maximize absorption for a frequency region using non-adaptive MM, focusing on widening the band gap rather than adjustability (Figure-2) [Sood 2016].

In addition to the high absorption effect of MM absorbers, the narrow band gap is seen as a disadvantage [Chen et al 2018]. In order to overcome this, the maximum absorption bandwidth was tried to be obtained by using different geometry MM structures stacked on top of each other (Figure-3). In these studies, the absorption of each layer is maximum for different frequencies. By placing these layers on top of each other, maximum microwave absorption was achieved in a much wider band range [Soheilifar and Sadeghzadeh et al 2015]. The biggest disadvantage encountered in studies that provide microwave absorption using MM so far is that these materials are not flexible and their applicability to large-scale surfaces is very difficult.

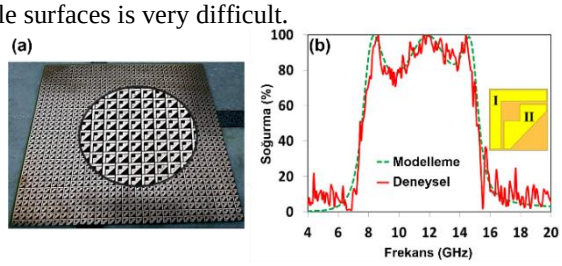


Fig. 2. (A) MM device designed to increase the bandwidth of microwave absorption and (b) absorption curve [Sood 2016].

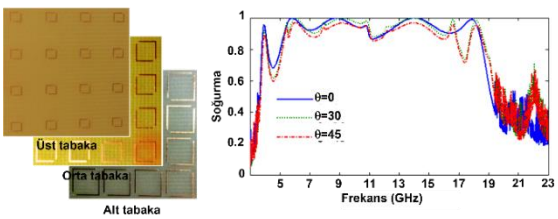


Fig. 3. Microwave absorption device for each layer of MM structures stacked on top of each other and the total microwave absorption curve of the whole device [Soheilifar and Sadeghzadeh et al 2015].

In the last few years, it has been reported that MXenes are very suitable materials for microwave absorption [Feng et al 2018]. In this study, MXene flakes were produced and the relationship between MXene flake size and microwave absorption was investigated, and it was revealed in which frequency ranges these structures are more active to absorb. The real and imaginary parts of the electrical and magnetic permeability of the materials determine resonance frequency, reflection and absorption losses. In order to change the real and imaginary values of electrical and magnetic permeability, structures containing dielectric, conductive and magnetic properties are mixed to get microwave absorbing composite materials in the literature. Due to the advantages of conductive nanoparticles such as very low resonance frequencies, being easily oxidized, expensive, reacting with other materials of the composite, increasing weight, it has been found that one of the most suitable alternative materials is nano-carbon structures such as graphene and CNTs [Bhattacharya et. get 2012]. There are different explanations for the microwave absorption mechanism of CNTs, and it is generally stated that microwaves undergo multiple scattering due to CNTs and this increases the absorption of the microwave [Heydari et al 2017]. In another study, it was stated that MWCNT form conductive closed loops within the composite structure and current flows through these loops at micro level [Huang et al 2018]. It is thought to be effective in a mechanism in which microwave energy is absorbed in these micro currents and magnetic fields caused by these currents. In addition, as the diameter of MWCNTs gets smaller, it is seen that both the reflection loss and the frequency at which this loss is at its maximum increase. From the results of this study, it is understood that it will be possible to provide maximum absorption in the desired area by choosing the appropriate dimensions of the CNT.

In the present work, 3 different absorption regions were designed using MM and composite structures.

2. MATERIAL AND METHODS

2.1 Mxene production

In this study, the $Ti_3C_2T_x$ MXene structure was obtained by etching the Al layers from the synthesized Ti_3AlC_2 MAX phase as expressed in Figure 1. 2 g of Ti_3AlC_2 layered powder was mixed in 20 ml 40% HF: H_2O solution at 25ºC for 48 h. The resulting $Ti_3C_2T_x$ MXene layers were repeated centrifuged by adding de-ionized water at 3500 rpm until the pH value was ~6-7. This MXene was then rinsed with CTAB in a magnetic stirrer for 24 h and centrifuged with de-ionized water to increase the distances between the layers. Water was removed from the structure by an additional drying process (80-100ºC in the oven).

$Ti_3C_2T_x$ MXene was synthesized by the successful etching of Al from Ti_3AlC_2. The effect of the mass ratios of Ti_3AlC_2 to HF on the electrochemical performance of electrodes for supercapacitors was investigated. Excellent

electrochemical performance has shown that layered $Ti_3C_2T_x$ is a promising electrode material for high power and high energy devices.

2.2 CNT Growth

In the system to be used for the production of MWCNT, MWCNT can be continuously produced in long furnaces and can be meters in length. There are studies in the literature showing that kilometers of KNT wires are produced by adding KNTs to each other in continuous magnification systems (Figure 3).

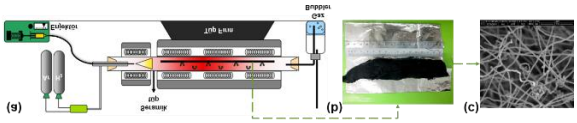


Fig. 3. **(a)** MWCNT growing system, **(b)** MWCNT cotton obtained from preliminary studies, and **(c)** MWCNT network.

2.3 Electromagnetic Property Extraction of Sublayers in Metal-Backed Inhomogeneous Metamaterials

Fig. 4 illustrates the schematic view of an inhomogeneous structure which is assumed to be composed of m homogeneous layers and terminated by a short-circuit termination. Each layer has a refractive index ns and a wave impedance Zs where s = 0, 1, · · · , m. It is assumed that a uniform plane wave is incident obliquely from layer 0 (air). In the following two subsections, we will derive underlying expressions for two different polarizations. In our analysis, we will consider the time dependence in the form exp(+jωt).

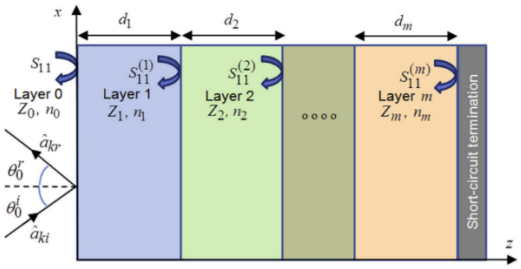


Fig. 4. Geometry of the problem: An inhomogeneous structure with m homogeneous layers terminated by a short-circuit termination.

3. RESULTS AND DISCUSSION

The structure, morphology and elemental analysis of the $Ti_3C_2T_x$ MXene was carried out using the X-ray diffractometer technique (PANalytical Empyrean, Cu-Kα, λ=1.54060 Å), a field-emission scanning electron microscope (FESEM: FEI Quanta 450 FEG) and an EDS analyzer in the FESEM system (EDAX, AMETEK Materials Analysis Division) respectively. Cyclic voltammetry (CV), galvanostatic charge discharge (GCD) and electrochemical impedance spectroscopy (EIS) analysis of the $Ti_3C_2T_x$ MXene was performed via Gamry Interface 1010E potentiostat. The FESEM images and EDS analyzes of the synthesized $Ti_3C_2T_x$ MXene structure is given in Figure 5.

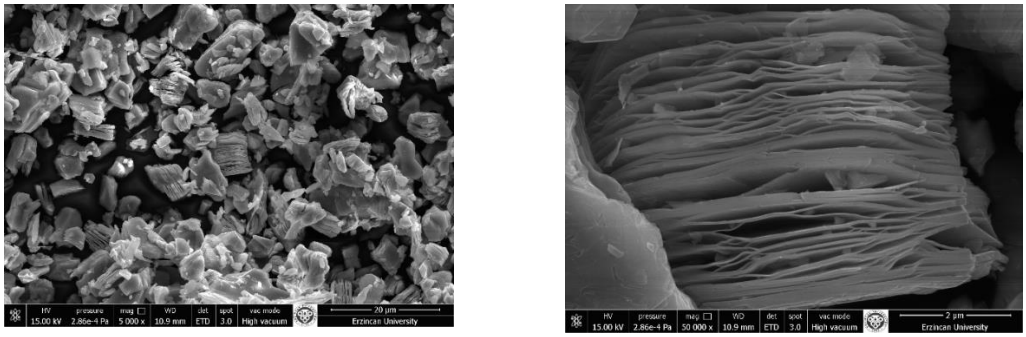
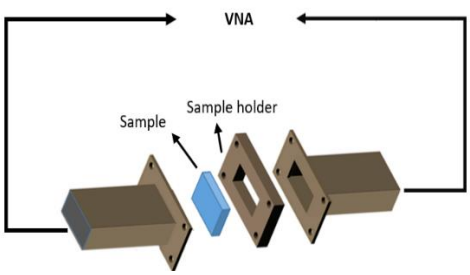


Fig. 5. (a) Low and (b) high magnification FESEM images of the $Ti_3C_2T_x$ MXene

The scattering parameters (S11, S12, S21) are measured in the geometry in the figure to measure the microwave absorption of the materials.

The scattering parameters are obtained against frequency and the absorption and loss amounts are determined in the measured frequency range (Figure 6).



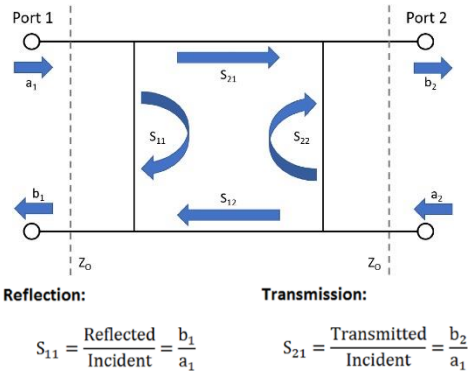
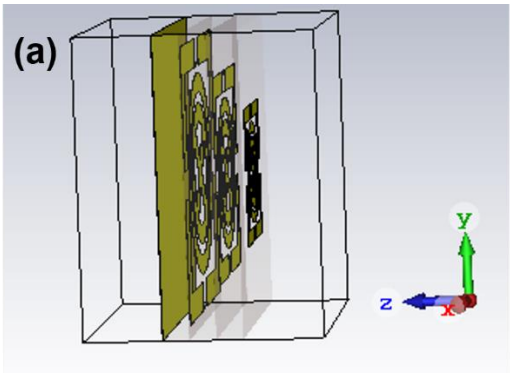


Fig. 6. Scattering parameters measurement system

We performed some numerical analysis to validate our method for a metal-backed homogeneous (one-layer) scenario before applying it for extracting electromagnetic

properties of any target layer within a metal-backed inhomogeneous structure. The structure consists of 4-level lossy substrate material and 3-level and different sizes of conductive square structure SRR MM. SRR MMs have been placed between the lost subtone as shown in the figure. The dimensions and sequences of these three MMs were designed in CST microwave simulator (Figure-7 (a-b)). In this system, MM device geometries, electromagnetic properties of the lossy substrate were estimated and entered into the simulation program to provide resonance absorption in the targeted regions.



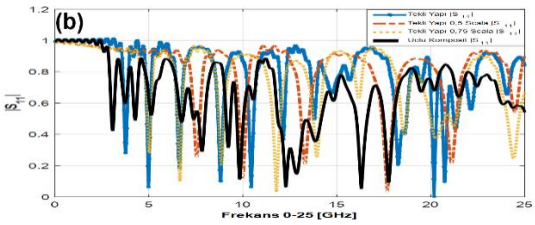


Fig. 7. (a) Simulated 3-layer MM absorber (b) Change of S11 of the simulated structure with frequency.

In order to obtain S11 scattering parameters, a single port is connected for the structure placed in the wave guide as shown in Figure 7.a. The electromagnetic wave is in the TEM mode, that is, the electric field component is in the + x direction, the magnetic field component is in the + y direction, and the wave travels in the + z direction. The wave orientation and components of the measurement port used in the simulator are also selected in this way. Boundary conditions were applied in the direction of the field components selected in the simulator. The copper layer used as the lowest layer of the device has been provided to be exactly S21, ie transmission scattering parameters. Thus, the absorption (A = 1- | S11 | 2) is aimed to be maximum. S11 curve belonging to the building is shown in Figure 7.b. As can be seen, this structure consisting of only MM devices absorbs in 3 different frequency regions at the same time.

ACKNOWLEDGEMENTS

This work is supported by TUBITAK under the Project Number 218M341.

REFERENCES

[1] Balci, O., Polat, E. O., Kakenov, N., & Kocabas, C. (2015). Graphene-enabled electrically switchable radar-absorbing surfaces. Nature communications, 6, 6628.

[2] Bhattacharya, A., Bhattacharyya, S., Ghosh, S., Chaurasiya, D., & Vaibhav Srivastava, K. (2015). An ultrathin penta-band polarization-insensitive compact metamaterial absorber for airborne radar applications. Microwave and Optical Technology Letters, 57(11), 2519-2524.

[3] Chen, H., Yang, X., Wu, S., Zhang, D., Xiao, H., Huang, K., ... & Yuan, J. (2018). Flexible and conformable broadband metamaterial absorber with wide-angle and polarization stability for radar application. Materials Research Express, 5(1), 015804.

[4] Feng, W., Luo, H., Wang, Y., Zeng, S., Deng, L., Zhou, X., ... & Peng, S. (2018). Ti3C2 MXene: a promising microwave absorbing material. RSC Advances, 8(5), 2398-2403.

[5] Heydari, F., Afghahi, S. S. S., Manteghian, M., & Taghizadeh, M. J. (2017). Nanosized amorphous (Co ,Fe) oxide particles decorated PANI–CNT: facile synthesis ,characterization ,magnetic ,electromagnetic properties and their application. International Nano Letters, 7(4), 275-283.

[6] Huang, L., Huang, S., Yang, Z., Zhao, A., Liu, C., Lu, J., ... & Zeng, Y. J. (2018). In-Situ Conversion of ZnO/Ni3ZnC0. 7/CNT Composite from NiZn Bimetallic MOF Precursor with Enhanced Electromagnetic Property. Nanomaterials, 8(8), 600.

[7] Idris, F. M., Hashim, M., Abbas, Z., Ismail, I., Nazlan, R., & Ibrahim, I. R. (2016). Recent developments of smart electromagnetic absorbers based polymer-composites at gigahertz frequencies. Journal of Magnetism and Magnetic Materials, 405, 197-208.

[8] Kim, H. K., Lee, D., & Lim, S. (2016). Frequency-tunable metamaterial absorber using a varactor-loaded fishnet-like resonator. Applied optics, 55(15), 4113-4118.

[9] Li, W., Zhao, L., Dai, Z., Jin, H., Duan, F., Liu, J., ... & Zhang, Z., (2018). A temperature-activated nanocomposite metamaterial absorber with a wide tunability. Nano Research, 1-12.

[10] Soheilifar, M. R., & Sadeghzadeh, R. A. (2015). Design, fabrication and characterization of stacked layers planar broadband metamaterial absorber at microwave frequency. AEU-International Journal of Electronics and Communications, 69(1), 126-132.

[11] Sood, D., & Tripathi, C. C. (2017). A Compact Ultrathin Ultra-wideband Metamaterial Microwave Absorber. Journal of Microwaves, Optoelectronics and Electromagnetic Applications, 16(2), 514-528.

[12] Zhao, X., Zhang, Z., Wang, L., Xi, K., Cao, Q., Wang, D., Y. (2013). Excellent microwave absorption property of graphene-coated Fe nanocomposites. Scientific Reports, 3, 3421.

Implementing The P&O Algorithm For Stand-Alone Small Wind Turbine System

Ahmed Zentani
Department of Electrical, Electronic and Computer Engineering Cape Peninsula University of Technology
Cape Town, South Africa
azentani30@gmail.com

AMA Almaktoof
Department of Electrical, Electronic and Computer Engineering Cape Peninsula University of Technology
Cape Town, South Africa
almaktoofa@cput.ac.za

MTE Kahn
Department of Electrical, Electronic and Computer Engineering Cape Peninsula University of Technology
Cape Town, South Africa
khant@cput.ac.za

***Abstract*—In this paper a small wind turbine established for direct current (DC) microgrid applications is designed and simulated for residential load profiles. in order to prevent or reduce power outages during power failures and load shedding. This study considers a DC microgrid based on a small wind turbine which consists of a small wind turbine using an AC permanent magnet synchronous generator, a three-phase diode rectifier, a DC-to-DC boost converter, and a maximum power point tracker based on the Perturb and Observe (P&O) technique. The P&O controller is considered and designed to change the duty cycle of the boost converter. The mathematical model of boost converter and Maximum power point tracking MPPT (P&O) controller is derived plan to design simulation model. The DC-DC boost converter circuit with IGBT as a switching model is developed. The P&O algorithms controller processes the error and to generate control duty cycle of pulse width modulation (PWM) signal is programmed. The frequency of the PWM output voltage is set to 10,000 HZ, moreover DC power load 3KW. The simulation results show that the DC output voltage of the boost converter can be controlled according to the set value of duty cycle. MATLAB/Simulink software package is used for design and simulation of the system.**

Keywords— small wind turbine (SWT), MPPT P&O Controller, DC microgrids , DC- DC boost converter, and MATLAB/Simulink.

[1] INTRODUCTION

Nowadays, energy shortage has become one of the most important issues facing many societies. For example, in some countries it has endorsed electricity use regulations that restrict households from controlling the amount of electrical energy used daily (Kesraoui et al., 2018). Further, the energy cost from energy utilities is increasing. More and more homes and businesses are found enormous advantages to installing small, renewable generators to cut cost of power bills and carbon dioxide emissions, additional sale superfluous electricity to the national grids. In the case of a power cut, these small renewable generators are offered source power as backup to maintain a continuous power supply (Kesraoui et al., 2011). Between the different resources of renewable energy, wind turbines considered as one of the cleanest and efficient technologies. Depending on the application range from small to large (EARNEST & RACHEL, 2019). Technology of small wind turbines (SWTs) offgrid have become attractive options for powering communities' areas. In the event of, load shedding, or in locations where grids cannot be accessed, that technology provide power to traditional loads. in comparison with large scale turbines, which are widely implemented in wind farms, small scale wind turbines which applied in more flexible environments. For example, small scale wind turbines are generally used in toproof residential and remote distributed power systems to supply alternating current or direct current. In this paper, the aim is to provide residential facilities enclose a DC load such as LED lighting, computers, fan, etc. These DC load devices significantly increase the energy demand in residences. The common advantages of small DC microgrids to improved energy efficiency, reduced consumption energy, and high-efficiency replacement of electricity infrastructure (Muhssin, 2015). DC microgrids are overcome the AC microgrids due to the following benefits (Shaikh et al., 2017): higher reliability, improved power supply quality, reduced losses due to lack of reactive power, higher efficiency, simple structure, better performance and efficiency of DC converter. This paper is organized as follows: Section 2 presents the system model that is used in this paper. The control scheme used to control the model of the power converter, is developed in Section 3. Results and discussions of the performance of the algorithm are presented in Section 4. The last section of the paper contains the conclusion.

[2] DESCRIPTION OF PROPOSED SYSTEM

The standalone DC microgrid adopted in this research comprises an SWT with a Permanent Magnet Synchronous Generator PMSG, an AC-to-DC converter, a DC-DC converter, and the maximum power point tracking P&O controller to regulate power source to the load.

A. SWT-based DC microgrid with P&O MPPT control

A schematic of an SWT-based DC microgrid with P&O MPPT control is shown in Figure 1.

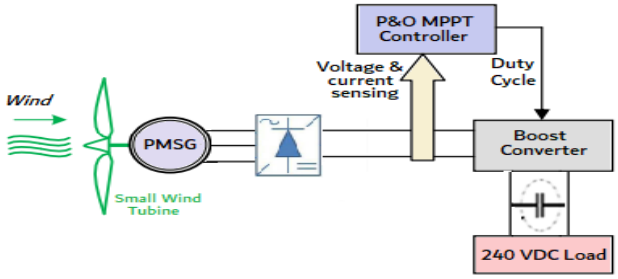


Fig. 1. SWT-based DC microgrid with Used P&O control.

Table I. The Parameters Of The Swt Dc Microgrid Are:

DESCRIPTION	RATING

Rated Power (P)	3 kW
Output Voltage (V_{out})	120 V
Air density (ρ)	1.225 kg/m^3
Impedance (R_a)	0.9585 Ω
Inductance (L_q and L_d)	5.25 mH
Magnetizing flux (Øm)	0.16616 wb
Pair of Poles (P_p)	4
Torque/Current (T/A)	0.99696 Nm/A
Cut-in wind speed (V_d)	5 m/s
Rated wind speed (V_n)	12 m/s
Pitch angle (β)	0 degree

The P&O technique is a proficient optimisation method based on searching for a given function's local optimum point. It is utilised for the searching of the ideal operating point. Thus, it assists in maximising energy extraction. This method is based on inserting a small step size change in a control variable and observing the objective function adjustments until the slope of the function gets to zero. As illustrated in Figure 1, the controller directs the working point by finding the position and the distance between the working point and the peak point. The working point moves towards the right if it is in the extreme left zone and vice versa. In this technique, the boost converter's duty ratio is perturbed, and the DC link power is observed. The method does not require a wind speed measurement; hence, mechanical sensors are not needed.

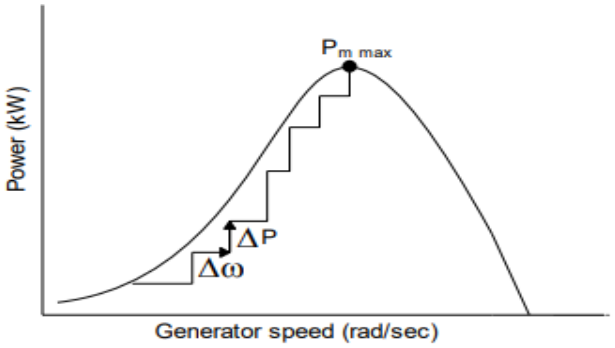


Fig. 1. Power versus speed (Muhammad et al., 2011).

An adjusted P&O MPPT algorithm has been suggested to realise quick MPP tracking under a rapid wind speed change. The recommended MPPT technique requires no information on wind turbine parameters or mechanical sensors. The algorithm is utilized in two operating modes to manage the previously mentioned limitations of the conventional P&O technique. Shifts from one operating mode to the next are done based on the variation of the wind speed. The ordinary P&O technique with a small step size cannot track the MPP under the slow wind speed variation. At the same time, a predictive mode is switched if a fast wind speed is observed to shift the operating point fast around the MPP. DC link voltage change is utilised to identify rapid wind speed variation.

The P&O algorithm operation is as follows: In the first step, the power is determined using the voltage and current and then compared to the power's past value. In case the difference is equal to zero, the same voltage will be maintained, and the algorithm will try to oscillate around the same MPP. In case of a change of power, the algorithm will continue and verify the difference between both voltage levels. If the power difference is positive, the algorithm will lead the voltage into a similar direction by either increasing or decreasing it as in the previous case. Thus, if the voltage difference is positive, the algorithm will keep increasing the voltage and vice versa. However, if the power difference is, the algorithm will lead the voltage in the opposite direction. Hence, the voltage change will be negative, and the algorithm will increase the voltage. Lastly, in case the change in voltage is positive, the algorithm will reduce the voltage. The algorithm can control the operating voltage freely by changing the duty ratio. Any variation of the duty ratio will lead to an inverse effect on the DC-to-DC converter's input resistance and modify the operating voltage to fulfil the four cases.

[3] PROPOSED IMPLEMENTATION Of MPPT For A DC-To-DC BOOST CONVERTER

The output voltage of a DC-to-DC boost converter is dependent on the duty ratio. Figure 3 shows a layout of a boost converter controlled from an MPPT controller. The controller's input is connected to the voltage and current measurements from the SWT after the rectification stage. The power is then evaluated from these two parameters and compares with the previous value. The sign of the power determines the duty ratio output of the MPP controller. The duty ratio of the boost converter represents the control variable. Perturbing the duty ratio will result in the perturbation of the SWT current, and consequently, the SWT voltage will be perturbed. The range of the duty ratio is limited between zero and ensures that the converter will step up the input voltage within the limit.

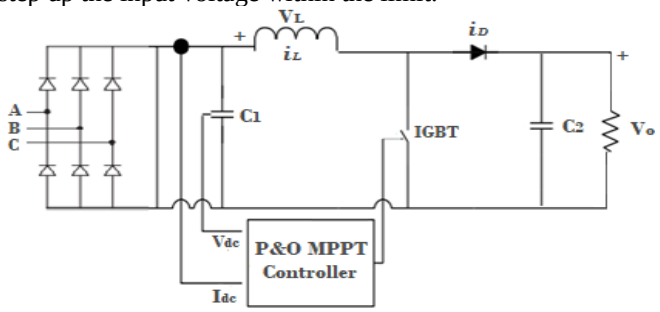


Fig. 3. Boost converter with P&O MPPT controller (Chen et al., 2013).

The duty ratio must be chosen appropriately. Since the P&O technique oscillates around the MPP, reducing the duty ratio step can minimise the oscillation and the steady-state losses. However, the controller is less efficient when the atmospheric conditions change fast. The following equation expresses the duty ratio (Femia et al., 2004):

$$\alpha = \frac{T_{on}}{T_{on}+T_{off}} = \frac{T_{on}}{T} \quad (1)$$

Equation 1 provides the control law produced by the MPPT controller to operate the SWT at its MPP depending on the wind speeds. In case the operating voltage of the generator voltage is perturbed in a specific direction, and the perturbation shifts the operating point toward the MPP. The P&O algorithm would then carry on perturbing the generator voltage in a similar direction. In the event that the change in operating point shifts away from the MPP and the P&O algorithm reverses the direction of the perturbation. Therefore, the system operates by increasing or decreasing the operating voltage and observing its

impact on the output power. The operating voltage is perturbed with every MPPT cycle. Once the MPP is reached, it will oscillate around the ideal operating voltage. For instance, if the controller senses that the input power increases and the voltage, it will decrease the voltage reference close to the MPP. Boost converter specification indicated in the table below:

Table 2. Boost Converter Parameters

DESCRIPTION	RATINGS
Converter power	P= 3 kW
Input Voltage	V_{in} =120 V
Output Voltage	V_{out} = 240 V
Boost Inductor	L = 1.263x10-8H
DC Link Capacitors	C = 260.4 µF
Load Resistance	R = 19.2 Ω
Switching frequency	f_s = 10 kHz
Sample time	Ts=50x10^{-6} s
Capacitance ripple	0.01%

Table III shows the summary of the P&O algorithm. Thus, in this way, the SWT curve is checked by small perturbations to find the MPP that raises the algorithm's response time. Conversely, if the perturbation size is enlarged, it generates steady-state oscillations about the MPP. Many researchers have proposed modifications in the P&O algorithm to overcome the response time problem and steady-state oscillations (Kamran et al., 2018). According to the algorithm, the output resulting perturbation is used to drive either the duty ratio or the reference voltage. To summarize, if the power goes up after a certain perturbation, the next perturbation should remain unchanged; however, if the power goes down, the resulting perturbation should be in the opposite direction (Esram & Chapman, 2007).

Table 3. P&O Algorithm.

P&O ALGORITHM		
Perturbation	***ΔP***	***Resulting***
+Ve	-Ve	+Ve
+Ve	+Ve	-Ve
-Ve	-Ve	+Ve
-Ve	+Ve	-Ve

[4] RESULTS AND DISCUSSION.

In this study, the SWT DC microgrid operates under a variable speed, and the boost converter is controlled using a P&O MPPT controller. The boost converter input terminal receives 3 kW DC power from the full-bridge three-phase diode rectifier at 120 V. Figure 4 shows both, the boost converter inductance current and the ripple current. The inductance current exhibits high fluctuations from the simulation start until the wind speed reaches 7 m/s. The current reaches up to 35.29 A. Thereafter, the signal gets to the steady-state value of 25 A.

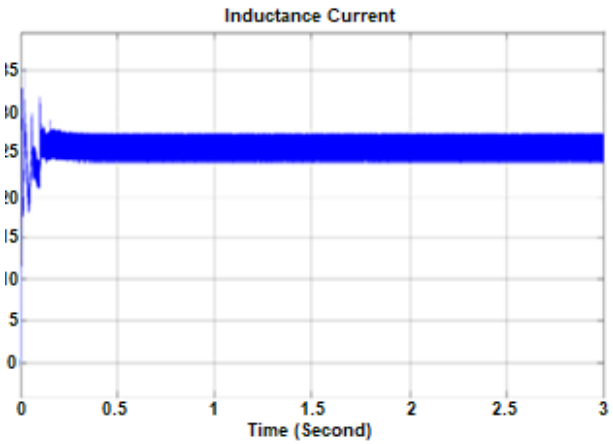


Fig. 4: Boost converter inductance current.

The voltage at the full-bridge diode rectifier's output terminals is shown in Figure 5, its steady-state value is around 114 V; the signal exhibits overshoot and undershoot of 0.347% and 2.633%, respectively, before getting to its stable value. Before the steady-state, the signal significant fluctuations voltage between time t = 0 s and t = 0.4 s. to reach its steady-state value, the signal took about 0.6 s.

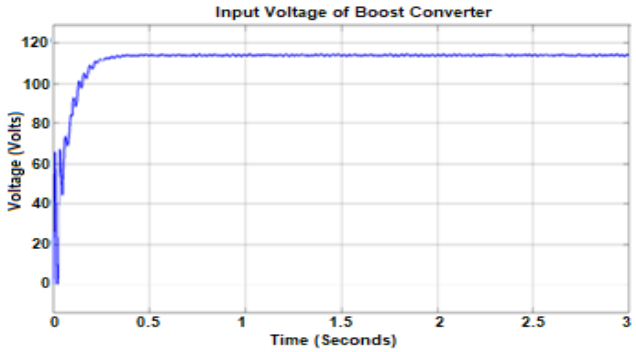


Fig. 5. Boost converter input voltage.

The duty ratio provided by the MPPT controller based on Perturb and Observe algorithm is depicted n figure 6, this duty ratio represents the on-state and off-state periods used to drive the boost converter switch to reach the MPP. It can be seen from the figure that depending on the operating conditions, and the MPPT controller provides a varying duty ratio between 0.4998 to 0.5002.

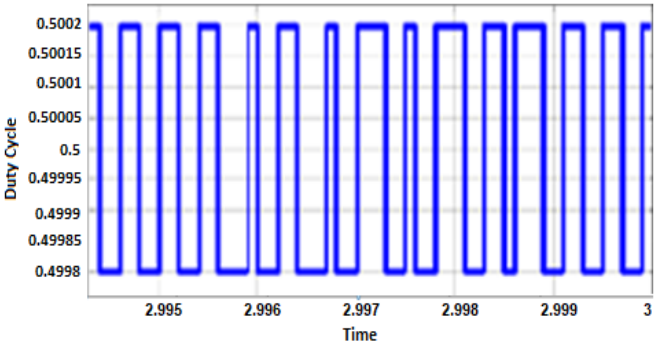


Fig. 6. Duty Cycle using the P&O MPPT algorithm.

The results obtained from this scenario are depicted in Figure 7 and exhibits oscillations between t = 0 s and t = 0.4 s than when the system is operating under variable wind speed. The current signal (Figure 7a) displays an overshoot of 9.894 % and an undershoot of 9.657 % between t = 0 s and t = 3 s. The current signal displays a rising time of about 97.7 ms between 0 s to 0.4 s. Whereas the overshoot and undershoot of the current are 0.803 % and 2.446 %, respectively. Similarly, the voltage at the boost converter's output terminals presents an overshoot, and an undershoot of 0.803 % and 2.446 %, respectively, between 0 and 0.4 s. The voltage obtained is 240 V (Figure 7b). Lastly, the power signal (Figure 7c) reaches its steady state of 3 kW at about 0.4 s. it shows a rising time of 142.294 ms, while the overshoot is 0.470% and the undershoot is 3.286 %.

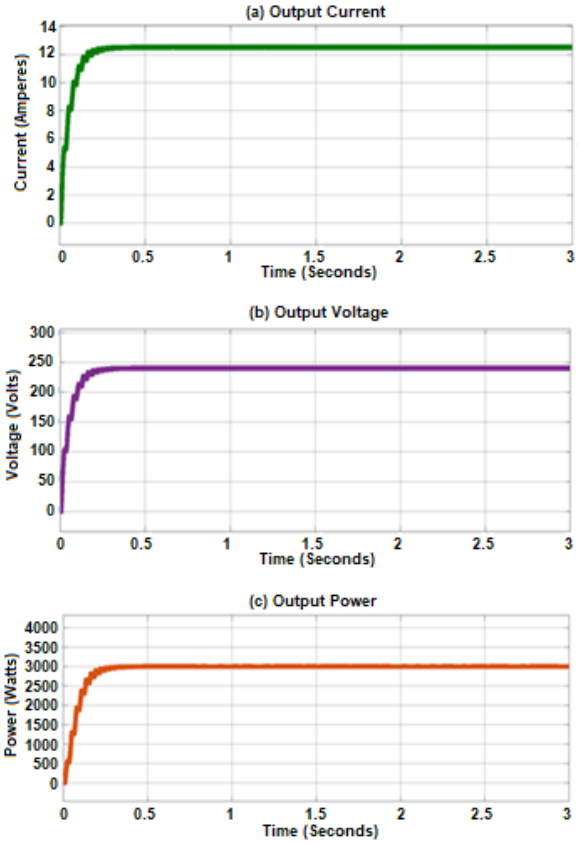


Fig. 7. (a) Current, (b) Voltage, and (c) Power of Boost Converter Load of SWT System Under Constant Speed Conditions Using P&O MPPT.

[5] CONCLUSION

To assess the performance of the SWT DC microgrid system, the SWT DC microgrid system operation was tested and simulated for variable speeds. The SWT results comprised the simulation results of the voltage 240 Vdc, current and power of the 3 kW PMSG model used in this study. To extract the maximum power and control the step up converter's output voltage, an adjusted P&O MPPT algorithm was applied to drive the switching element to achieve fast MPP tracking and to keep the voltage constant irrespective of change wind speed. Lastly, the DC-to-DC boost converter results consisted of the converter's voltage current, and power using the P&O MPPT controller. The simulation results showed that the DC output voltage of the boost converter can be controlled according to the set value of duty cycle.

REFERENCES

[1] Chen, Y., Xiong, G., Li, W., Qian, J. & Hu, B. 2013. The design of boost circuit in small wind generation system. *Proceedings of 2013 IEEE International Conference on Service Operations and Logistics, and Informatics, SOLI 2013*, (2): 354–359.

[2] EARNEST, J. & RACHEL, S. 2019. *Wind Power Technology*. Third Edit. Delhi: Asoke K. Ghosh, PHI Learning Private Limited, Rimjhim House,.

[3] Esram, T. & Chapman, P.L. 2007. Comparison of photovoltaic array maximum power point tracking techniques. *IEEE Transactions on Energy Conversion*, 22(2): 439–449.

[4] Femia, N., Petrone, G., Spagnuolo, G. & Vitelli, M. 2004. Increasing the Efficiency of P&O MPPT by Converter Dynamic Matching. *Ieee*, (1): 1017–1021.

[5] Kamran, M., Mudassar, M., Fazal, M.R., Asghar, M.U., Bilal, M. & Asghar, R. 2018. Implementation of improved Perturb & Observe MPPT technique with confined search space for standalone photovoltaic system. *Journal of King Saud University - EngineeringSciences*. https://doi.org/10.1016/j.jksues.2018.04.006.

[6] Kesraoui, M., Korichi, N. & Belkadi, A. 2011. Maximum power point tracker of wind energy conversion system. *Renewable Energy*, 36(10):2655–2662. http://dx.doi.org/10.1016/j.renene.2010.04.028.

[7] Kesraoui, M., Korichi, N. & Belkadi, A. 2018. Power Management of a Hybrid Wind Gas Electrolyze Micro grid. *International Renewable Energy Congress*, (Irec).

[8] Muhammad, S., Kazmi, R., Goto, H. & Guo, H. 2011. A Novel Algorithm for Fast and Efficient Speed-Sensorless Maximum Power Point Tracking in Wind Energy Conversion Systems. *IEEE Transactions on Industrial Electronics*, 58(1): 29–36.

[9] Muhssin, M.T. 2015. Small Microgrid Stability and Performance Analysis in Isolated Island. *IEEE*.

[10] Shaikh, P.H., Jan, T. & Baloch, A.A. 2017. Performance Analysis of Wind – Photovoltaic – Battery based DC Microgrid Setup for off – grid Applications. *IEEE*: 1–6.

Analysis and Evaluation of Electricity Consumption in Low Voltage Distribution Grids in Ankara Metropolitan Area

Ali KARAÇOBAN
Construction Works Directorate Enerjisa
Başkent Electricity Distribution Inc.
Ankara, Turkey
ali.karacoban@windowslive.com

Ahmet KARAARSLAN
Ankara Yıldırım Beyazıt University Department of Electrical-Electronics Engineering
Ankara, Turkey
akaraarslan@ybu.edu.tr

***Abstract*— In this study, "Installed Power" and "Demand Power" calculations are discussed. These calculations are most important stage of Electrical Distribution Network Project designs. "Installed Power" is the sum of all the electrical powers specified in the project. "Demand Power" is calculated by multiplying "Install Power" with "Simultaneity factor". "Simultaneity factor" describes relation between "Installed Power" and "Demand Power". This coefficient directly depends on Electrical Interior Facilities Regulation, Electrical Facilities Project Preparation Regulation and other national regulations that have been described in 1954. These calculations have primary significant for cost, efficiency, supply and request safety. With the development of technology and architecture this calculation cannot satisfy to requests. In this paper we will show the difference between calculated "Demand Power" and real "Demand Power". Will be given 1853 buildings and 38648 costumers are analyzed for 5 years in Ankara Metropolitan area.**

Keywords—installed power, demand power, simultaneity factor

[1] INTRODUCTION

Accessing to electricity utility is one of the indispensable human rights [1]. We can't imagine a world without electricity. Heating, cooling, lighting, communication, production and etc. these are surrounding us. Nowadays although energy saving and energy efficiency are very important issue of modern world, growing energy demand is using as a development indicator.

Until about 50 years ago in most apartment buildings of Estonian which have 60 consumers had only 42 kW maximum power consumption and electrical systems were designed and installed only lighting load [2].

The concept of "Demand Power" appeared in front of us in 1954 with Electrical Interior Facilities Regulation. As in the example above, this regulation Although it is only designed to meet the demands on time, we have been using without updating.

Today we have larger apartment buildings, life areas and have wide variety of electrical goods and we need smarter designs. Simultaneity factors which have been calculated years ago doesn't meet current requests [3].

Demand side management method is one of the new approaches for forecasting demand power in high energy consumption plants and aims to respond variable load demands.

Since Demand Power calculation is the first stage of electrical project design, Simultaneity factor's accuracy can bring efficiency, reliability, savings and sustainable performance in electrical facilities to the optimum point. In this study importance of simultaneity factor with real 38648 consumer data from Ankara Metropolitan area is shown.

In section II, the details of how the demand power specified in the interior installation projects is calculated and how the measured demand power is reached. Section III shows the relationship between the results obtained and calculated values in line with the processed real-time data. In the last section, the results of the study are given.

[2] Materıal And Method

A. *Calculation of Installed Power*

Installed Power is the sum of all the electrical powers with their label value. This total value cannot change in any ways [5].

Table 1. Calculation of ınstalled power (for a recıdence)

Type of load	Total Label Value of Power (W)
Lighting Power (according to user choice)	522
Socket Power (300W each)	4800
Refrigerator	1800
Oven	2000
Dishwasher	2500
Washing machine	2500
Total Installed Power	14122

The installed power for a single residence is calculated as 14,122kW in Table I.

B. *Calculation of Demad Power*

Demand Power is the maximum request power of consumer [5] and is found by multiplying the installed power (in table I.) value by the coefficient of simultaneity.

Simultaneity factor is an estimated value that takes into consideration the fact all the devices are never switched on simultaneously at full power in a plant. This value is used for the calculation of the power dissipation and its value is smaller than one [5].

Currently, demand power calculations in Electrical Interior Installation Projects; It is based on the simultaneity factor mentioned in Article a.2 of Article 57 of the Electricity Indoor Facilities Regulation [5].

Determining the demand power;

- For the part of the installed power up to 8 kW the coefficient of simultaneity is taken as 0.60
- For power above 8kW, the simultaneity coefficient is taken as 0.40.

For example, the demand power for the residence in Table I. is calculated as follows.

Installed Power (IP)

Demand Power (DP)

Simultaneity factor (sf)

Demand Power = Installed Power ×Simultaneity factor

$$DP = IP \times sf \quad (1)$$

Since the installed power is greater than 8kw, the demand power is calculated as follows.

$DP = 8 \times 0.60 + (14.122-8) \times 0.4$

$DP = 7.248kW$

- For buildings with more than one apartment, calculations are made by taking into account the values specified in the following Table II [5].

Table 2. The simultaneıty factor & # flats

Number of Flats	Simultaneity Factor (%)
3-5	45
5-10	43
11-15	41
16-20	39
21-25	36
26-30	34
31-35	31
36-40	29
41-45	28
46-50	26
51-55	25
56-61	24
62 and above	23

For example; If there are 38 flats with an installed power of 14.122kW and demand power of 7.248kW in an apartment, the demand power is calculated as follows.

Demand Power' = Demand Power ×Simultaneity factor × Number of flats

$$DP' = DP \times sf \times \text{Number of flats} \quad (2)$$

$DP' = 7.248 \times 0.29 \times 38$

$DP' = 79.872kW$

- For buildings with more than one apartment, and more than one type of load calculations are made by taking into account the values specified in the following both Table II and III. [5].

Table 3. Simultaneıty factor table for dıfferent type of loads

Type of loads	Type of buildings	Installed Power	Simultaneity factor
Lighting Installations	Hospitals	First 50kVA	0.40
		Over 50kVA	0.20
	Hotels, Motels and Resorts	First 20kVA	0.50
		Between 20-100kVA	0.40
		Over 100kVA	0.30
	Stores	First 12,5kVA	1
		Over 50kVA	0.5
	Other Buildings	All Load	1
Socket Installations	All type of buildings	First 10kVA	1
		Over 10kVA	0.5
Elevators	Office buildings, Hotels	All Load	1
	Schools and Hospitals		0.85
	In apartment and other buildings		0.55

For example; If there are 38 flats with an installed power of 14.122kW and demand power of 7.248kW and an elevator with a power of 10kW in an apartment, the demand power is calculated as follows.

Demand Power = Installed Power ×Simultaneity factor × Number of flats +Elevators Power × sf(elevators)

$$DP' = DP \times sf \times \text{Number of flats} + \text{Elevators Power} \times sf(\text{elevators}) \quad (3)$$

$DP' = 7.248 \times 0.29 \times 38 + 10 \times 0.55$

$DP' = 85.372kW$

During the project design phase, it is obligatory to use these tables specified in the regulation in the calculations made in accordance with the relevant regulation in determining the demand power of all building types in our country.

C. Collecting Data

The following data required between 2016 and 2020 of the consumers belonging to 1853 buildings, which are randomly selected from Ankara, which is located in the distribution activity area of Enerjisa Başkent Electricity Distribution Company, were obtained from the Customer Technical Services Unit [6].

- Number of buildings
- Number of customers
- Installed and demand power information of customers (contract power)
- Demand power data measured between 2016-2020

The highest power value (actual demand power) reached from the date when the customers started consumption with the installed power and calculated demand power determined in the project until 2020, when the data was obtained, was

obtained from the data recorded by the meter. The installed power and the calculated demand power were obtained from the values recorded during the installation phase of the system. Realized demand power values were obtained from customers' electronic electricity meters. The sample of meter demand in real time is given in Fig. 1.

Digital meters are sampled current and voltage values in microseconds level and power values are calculated with the measurement chip inside the meter. The highest power drawn in the meters is kept in the meter memory with the date and time with the 1.6.0 Obis code on demand. These values are reset every month pass. Calculation and registration are made with the same formulation for the next month. The counters keep the past 12 demand values in their memory. In order to create a demand record in the meter within the month, the meter must be energized during the demand measurement period. Demand measurement periods can be set as 15, 30, 45 and 60 minutes. This value is kept in the meters with the code 0.8.0 Obis. For generally used counters, this value is set to 15 minutes. If there is a consumption shorter than this period, the meter cannot record demand. In some brands, the clock of the meter can record in a shorter time when the passes of the multiples of 15 minutes. The meter records the highest power drawn over a 15-minute period as demand, and the highest value measured in every 15-minute period after that and the demand value is compared. The demand display on the meter is shown in Fig. 2.

	Demand Bilgi	Demand Tarih-Saat
(1.6.0)	000.004*kW	19-07-01,17:00
(1.6.0*1)	003.292*kW	19-01-03,08:00
(1.6.0*2)	001.284*kW	17-11-08,08:00
(1.6.0*3)	005.176*kW	17-10-11,17:15
(1.6.0*4)	000.004*kW	17-09-27,19:30
(1.6.0*5)	000.000*kW	00-00-00,00:00
(1.6.0*6)	000.000*kW	00-00-00,00:00
(1.6.0*7)	000.000*kW	00-00-00,00:00
(1.6.0*8)	000.000*kW	00-00-00,00:00
(1.6.0*9)	000.000*kW	00-00-00,00:00
(1.6.0*10)	000.000*kW	00-00-00,00:00
(1.6.0*11)	000.000*kW	00-00-00,00:00
(1.6.0*12)	000.000*kW	00-00-00,00:00

Fig. 6. The sample of meter demand in real time

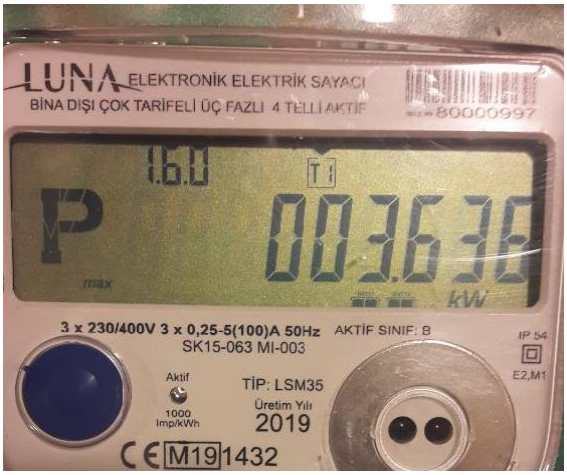


Fig. 7. Demand display on the meter

[3] Research Area

Data that are about 1853 buildings and 38648 customers from Ankara were taken from regional distribution company Enerjisa Başkent Inc. Installed power and demand power were compared between calculated data and real time measured data [6]. The data are obtained and used between 2016-2020 years.

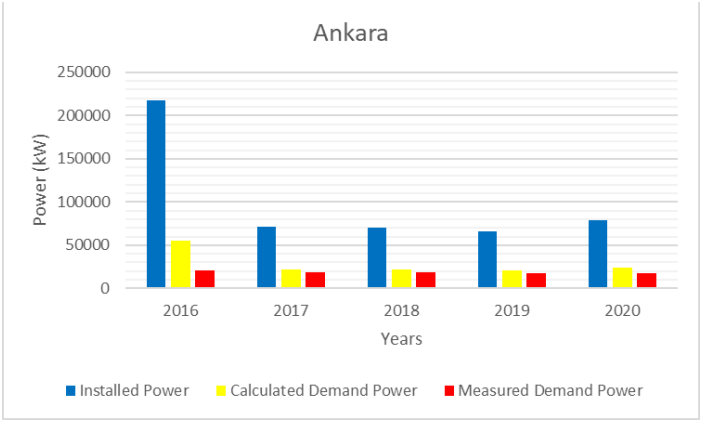


Fig. 8. Installed, demand and actual demand power graph of Ankara province

In Fig. 3, the demand power determined according to the calculations used in force is below the level of approximately 30% of the actual power. Nevertheless, there is an average of 15% difference between the demand power calculated in the same figure and the actual demand power.

The data obtained from 38648 customers belonging to 1853 buildings and the data of the research conducted in 5 years are shown in Table IV. and V, respectively.

Table 4. Installed power and calculated demand power

Years	Installed Power kW	Calculated Demand Power kW	Differences kW
2020	218062,29	55451,91	162610,38
2019	70807,664	21729,63	49078,03
2018	70065,078	21553,56	48511,51
2017	66231,212	20747,82	45483,39
2016	78699,247	24348,35	54350,90

Table 5. Calculated demand power and measured demand power

Years	Calculated Demand Power kW	Measured Demand Power kW	Differences kW
2020	55451,91	20981,59	34470,32
2019	21729,63	18788,93	2940,71
2018	21553,56	18623,08	2930,48
2017	20747,82	17597,32	3150,50
2016	24348,35	17417,77	6930,58

Table IV. shows the differences between installed power and calculated demand power values. Table V. shows the differences between the calculated demand power and the actual demand power for 5 years. Fig. 4. Shows the data analyzed for the year of 2020.

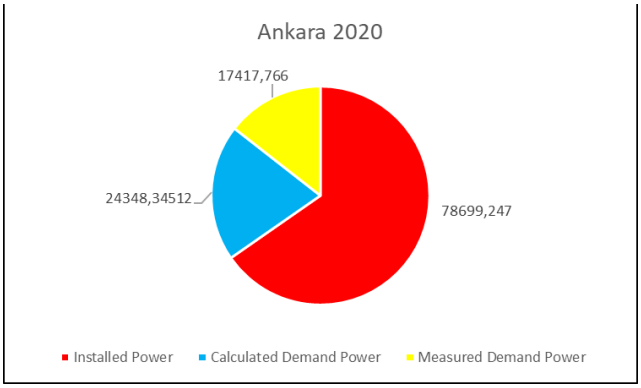


Fig. 9. Calculated and Measured Demand Power for 2020

[4] RESEARCH RESULTS

Tables IV and V shows that By-law, the preparation of electrical interior installation projects should be reconsidered from the beginning to the end. When determining the installed power value, it should be ensured that the obtained power values can be approached in more detail by analyzing the real values. Simulation studies to be carried out after this step will be able to determine concurrency coefficients close to the measured demand power.

Difference between calculated value and measured value shows that simultaneity factors don't meet our current needs and also cause cost losses in investment costs. The closer the two values of demand power are to each other, the lower the costs will be. However, investment costs will be more realistic and more acceptable than the calculations used today.

In future studies, concurrency coefficient values can be examined with optimization studies. In addition, cost analysis is also performed by evaluating the difference between calculated demand power and measured demand power.

REFERENCES

[1] Vill, K., Rosin, A., & Lehtla, M. "Modeling of demand side management scenarios in apartment buildings." 2016 Electric Power Quality and Supply Reliability (PQ). doi:10.1109/pq.2016.7724099 (2016).

[2] A. M. Oklander . "METHODOLOGICAL RECOMMENDATIONS for the reconstruction and modernization of the engineering equipment of residential buildings of the first mass series" Moscow, State Committee of the Russian Federation for Construction, Architectural and Housing Policy 1998, 38 p.

[3] Yapıcıoğlu, M , Sayan, H , Terzioğlu, H . "Analysis of Electricity Consumption in Low Voltage Distribution Systems in Karabük" European Journal of Science and Technology Special Issue, pp. 411-417, October 2019 DOI: 10.31590/ejosat.638375 (2019).

[4] Hongbin Sun, Weiyong Jiang, Bin Wang, Qinglai Guo, Boming Zhang, & Kang Wang. "Preliminary research on power demand model of high energy consumers for smart grid in China." IEEE PES General Meeting. doi:10.1109/pes.2010.5589564 (2010).

[5] TMMOB CHAMBER OF ELECTRICAL ENGINEERS, Electrical Internal Facilities Regulation. ANKARA, 1954.

[6] Enerjisa başkent electricity distribution inc.

[7] Karaarslan, A. "Hysterisis control of power factor correction with a new approach of sampling technique." 2008 IEEE 25th Convention of Electrical and Electronics Engineers in Israel. doi:10.1109/eeei.2008.4736638 . (2008).

[8] Khare, A., Bajpai, S., & Choubey, M. "Measurement/Evaluation of electrical power demand/losses in widespread 11/. 4 KV distribution system of JNKVV Jabalpur; Maximum Demand controlled by DG set." (2012).

[9] Imanaka, M., Baba, J., Shimabuku, M., Tobaru, C., & Uezu, Y. A "Simple control method of waterworks pump power consumption for demand response." Paper presented at the 2015 IEEE Power & Energy Society Innovative Smart Grid Technologies Conference (ISGT). (2015).

[10] Karaarslan, A., Iskender, I. "A DSP based power factor correction converter to reduce total harmonic distortion of input current for improvement of power quality." Electr Eng 93, 247–257 (2011).

[11] Elrayyah, A. "Droop based demandresponse for power systems management." Paper presented at the 2015 First Workshop on Smart Grid and Renewable Energy (SGRE). (2015).

[12] Jiarui, H., Dong, X., Jing, X., Chen, L., Ke, X., Rongjing, C., & Chenlei, C. "Research on Demand Response Strategy of Electricity Market Based on Intelligent Power Consumption." Paper presented at the 2018 China International Conference on Electricity Distribution (CICED). (2018).

Inversion Coefficient Design Methodology for the Design of Inverter based OTA

Mesut Atasoyu*
* Deparment of Electrical and Electronics Engineering, Artvin Coruh University
Email:matasoyu@itu.edu.tr

***Abstract*—This paper presents an inverter-based operational transconductance amplifier (OTA) which is widely used in biomedical and IoT applications. The energy-efficient inverter-based OTA design has been implemented in 65-nm TSMC CMOS technology parameters with the aid of inversion coefficient (IC) transistor sizing method. To verify the effectiveness of the IC technique in this particular amplifier, we compared the simulation and the calculation results of the unity gain bandwidth which are at close range. The proposed OTA achieves a simulated amplifier gain of 31.6-dB with amplifier unity-gain bandwidth 15.51-MHz, as well features 610-μW voltage source power consumption.**

***Index Terms*—Inversion Coefficient(IC), g_m/I_D, Inverter based OTA, 65nm CMOS.**

I. Introduction

Low power circuit design solution is an obligatory task, especially in the internet of things (IoT), and delta-sigma analog to digital converter (ADC) applications [1]–[3]. The main building block used in these applications is an operational transconductance amplifier (OTA) and is also the most power-hungry circuit unit [4], [5].

The inverter-based OTA is a viable solution first introduced by Nauta [6]. The replacement of conventional OTAs with inverter-based OTAs is a promising way of low power design for these application areas. Especially, the inverter-based OTA has 7X more power efficiency than differential OTA [7]. However, the biasing of an inverter-based OTA is a tricky task. The transconductance(g_m) and drain current (I_D) ratio (g_m/I_D) as a design parameter is a powerful transistor sizing technique, especially to find optimal design point between power and speed [3], [8], [9]. Moreover, inversion coefficient (IC) technique was developed to improve the effectiveness of g_m/I_D technique by normalizing I_D current [10], [11].

In this paper, the inverter-based OTA was designed using 65-nm TSMC CMOS technology parameters. The optimal power-efficient design of the proposed amplifier is achieved using IC transistor sizing methodology along with the need for low-power and high-speed design. This technique is exploited especially short channel technology nodes, which were used in this work. This has led to an increased interest in the concept of the IC as the main design parameter even for very advanced technology nodes.

This paper is organized as follows. Section II explains the IC design methodology governing the transistor sizing flow. Section III discusses the design procedure of an inverter-based OTA. Section IV concludes this paper.

II. Inversion Coefffiecient (IC) Transistor Sizing Methodology

The MOS transistor operating region can be sensed via as the ratio of g_m/I_D [10]. However, short channel MOS devices are required to normalize I_D for the crossing between weak and strong inversion regions. This defined I_D normalization coefficient is I_D^*. I_D^* in 65-nm CMOS process is extracted experimentally for NMOS the value of 0.49-μA and PMOS the value of 0.15-μA [12]. It is important to say I_D^* is an experimental parameter but it can be defined equationally as the given formulation in Eq-2 [1], [3], [10], [12]

The inversion coefficient (IC) is a design parameter defined for the sense of the channel inversion levels of MOS transistors, also is qualified for short channel MOS transistors, as formulated following:

$$I_C = \frac{I_D}{I_D^* \frac{W}{L}} \tag{1}$$

I_D is drain current and I_D^* is drain current normalization coefficient where is derived experimentally for different MOS transistor technology nodes as given in [12], and W is gate width of a MOS transistor and L is the channel length of a MOS transistor. I_D^* is the current scaling parameter as defined:

$$I_D^* = 2n\mu_0 C_{OX} V_T^2 \tag{2}$$

where n is the subthreshold slope factor, μ_0 is the carrier mobility, V_T defined as $V_T = kT/q$ is the thermal voltage, C_{OX} is the gate-oxide capacitance.

IC levels for different operation regions of the MOS transistors: values of IC < 0.1 correspond to sub-threshold region, values of $0.1 <$ IC < 10 correspond to linear region, values of IC > 10 correspond to saturation region.

The IC design methodology is realized with the following steps for transistor sizing: below simulations were performed with varying values of the NMOS transistor L parameter which values are between 130-nm to 520-nm. Transistor intrinsic gain is a multiplication of its g_m and its output parasitic resistor (r_o). The transistor L value is a way of setting the intrinsic gain, in the proposed design we set the L= 325nm to this gain value of 32 that is a nearly maximum value of this gain for IC= 30 that is assumed a value for the strong inversion operation of the NMOS and PMOS transistors. For higher intrinsic gain values, a transistor can be operated in weak inversion where is IC less than 0.1, the highest gain value is respect to IC= 100 as given in Fig. 1. The NMOS transistor g_m value with

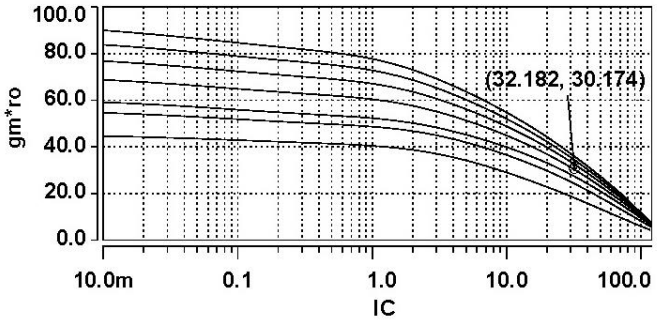


Fig. 1: The NMOS intrinsic gain versus IC varies L values.

IC varies almost linearly as presented in Fig. 2. The values of g_m increases with long L values. The highest g_m values helps to mitigate the input referred output noise [7]. The transistor

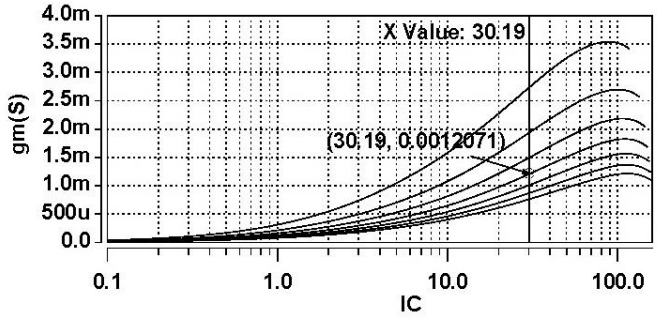


Fig. 2: The characteristic of g_m-IC.

biasing current can be determined according to this relation:

$$I_D = \frac{g_m}{g_m/I_D} \tag{3}$$

The plot of g_m/I_D -IC is given in Fig. 3, according to this plot the NMOS transistor strong inversion operation depends its lower g_m/I_D values, adding to this its higher values are for weak inversion operation. The g_m/I_D parameter is geometry independent, but in weak inversion slightly changes with the L values. Further, the transistor current density (I_D/W) is 45.4

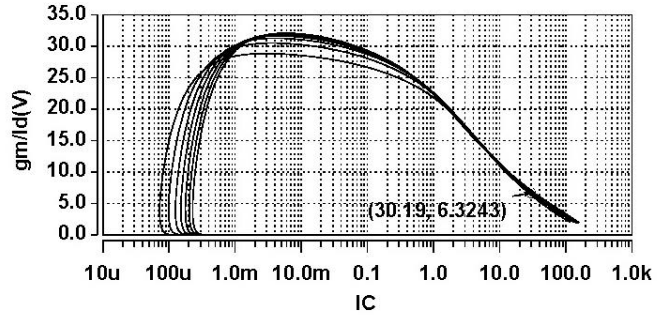


Fig. 3: The g_m/I_D versus IC.

determined for L= 325-nm value given in Fig. 4 that is a calculation step of transistor W values as follows:

$$W = \frac{I_D}{I_D/W} \tag{4}$$

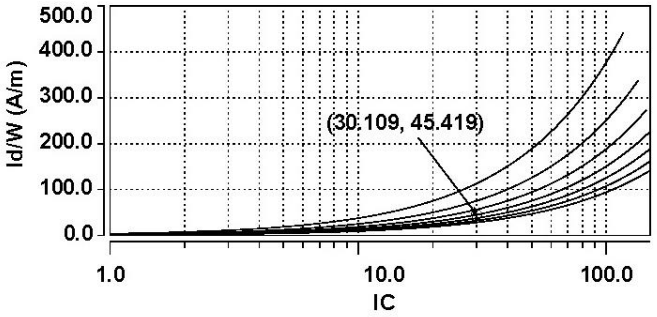


Fig. 4: The current density of NMOS transistor versus IC.

The I_D/W value of PMOS transistor is 13.94 determined for L=325nm value given in Fig. 5.

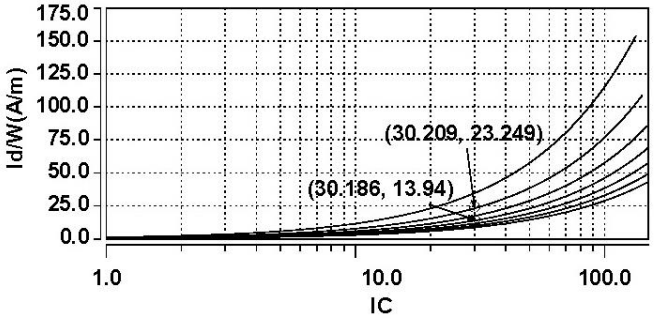


Fig. 5: The current density of PMOS transistor versus IC.

As a result of these current density schemes, the transistor can be operated for a higher current drive in strong inversion or beyond deep strong inversion such values of IC > 100.

III. Application Circuit and Performance Results

In this work, the inverter-based OTA is chosen for the IC-based transistor sizing implementation. The schematic of the inverter-based OTA in Fig. 6. The core of the structure is two inverters composed of M_{3-6} transistors and current mirror biasing circuitry embodied with M_{1-2} and M_{7-8} transistors, which are biased with I_{B1} and I_{B2} current sources. The power supply voltage (V_{DD}) is 1.2-V and the common-mode voltage(V_{CM}) is 0.6-V, and the output common-mode feedback resistors are R_{CM}=1-MΩ.

A. IC Methodology for Inverter based OTA Design

The main design parameters of an OTA are dc gain, GBW and output swing that is a value of full rail to rail in the inverter based OTA, and gain-bandwidth product(GBW) which is formulated as follows:

$$GBW = A_{0dB}.w_u \tag{5}$$

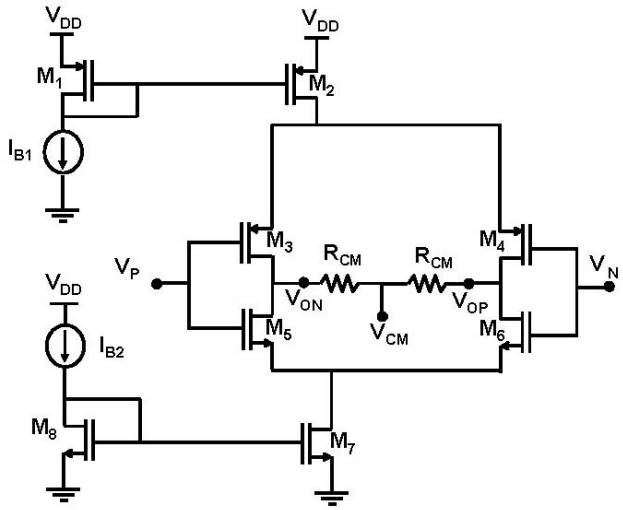


Fig. 6: The schematic of inverter based OTA.

Here, A_{0dB} is the unity gain corresponds to a unity gain bandwidth is w_u which is formulated $w_u = G_m/2\pi C_L$. The G_m is the sum of g_{m3} and g_{m5} or g_{m4} and g_{m6}, and C_L is the load capacitor. The G_m was taken the value of 1mS concerning noise performance of the circuit. C_L is a value of 10pF. The value of f_u is calculated from the above equation as a value of 15.91-MHz. Further, the bias current of the M_5 is calculated as a value of 100-μA for the g_{m5}=0.6mS, using the given equations above section. For this biasing current, the calculated width of the M_5 is 2.22-μm. After all, concerning the NMOS and PMOS transistor current density values and also biasing current values, all-transistor widths are calculated and given in Table-I.

Table-I

Transistor	Boyutu
$M_{1,2}$	W= 6.92μm
$M_{3,4}$	W= 3.46μm
$M_{5,6}$	W= 2.22μm
$M_{7,8}$	W= 4.44μm

For the comparison of the calculated and the simulated f_u values, the testbench circuit of the proposed design is setup as illustrated in Fig. 7. In this setup, differential input voltage nodes are the positive input (V_P) and the negative input(V_N) and differential output voltage nodes are the positive output (V_{OP}) and the negative output(V_{ON}). The $C_{1,2}$ is chosen the value of 10pF, as same calculated the value of C_L, as mentioned above. The magnitude and phase results of the fully differential inverter based OTA are performed with respect to this open-loop simulation setup and shown in Fig. 8. The simulation result of the f_u is found as 15.51-MHz and the gain of the design is 31.6-dB.

IV. Conclusion

The optimal power-efficient design of an inverter based OTA has been discussed in this paper. The inverter based OTA

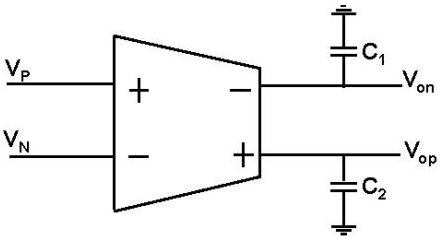


Fig. 7: The block representation of the fully differential inverter based OTA.

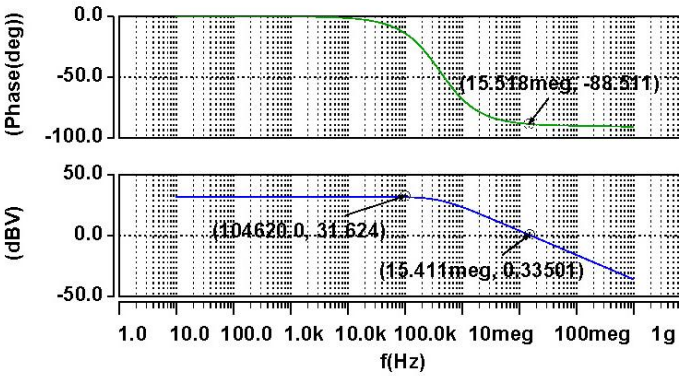


Fig. 8: The open-loop gain and phase simulation results of the fully differential inverter based OTA.

design was simulated in SPICE with 65nm CMOS process parameters. The gain value of the amplifier is 31.6-dB and the unity-gain bandwidth is 15.51-MHz. The proposed design consumes 610-μW voltage source power. The IC transistor sizing method is a viable solution considering comparison of the simulation and calculation results of the unity gain bandwidth.

References

[1] E. A. Vittoz, "Weak inversion for ultra low-power and very low-voltage circuits," in *2009 IEEE Asian Solid-State Circuits Conference*. IEEE, 2009, pp. 129–132.

[2] H. Luo, Y. Han, R. C. Cheung, X. Liu, and T. Cao, "A 0.8-v 230-μ w 98-db dr inverter-based σ δ modulator for audio applications," *IEEE Journal of Solid-State Circuits*, vol. 48, no. 10, pp. 2430–2441, 2013.

[3] C. Enz and A. Pezzotta, "Nanoscale mosfet modeling for the design of low-power analog and rf circuits," in *2016 MIXDES-23rd International Conference Mixed Design of Integrated Circuits and Systems*. IEEE, 2016, pp. 21–26.

[4] C. Wichman and A. Ravindran, "A micropower ota for digitally calibrated algorithmic adcs," in *48th Midwest Symposium on Circuits and Systems, 2005*. IEEE, 2005, pp. 279–282.

[5] P. C. C. de Aguirre, E. Bonizzoni, F. Maloberti, and A. A. Susin, "A 170.7-db fom-dr 0.45/0.6-v inverter-based continuous-time sigma-delta modulator," *IEEE Transactions on Circuits and Systems II: Express Briefs*, vol. 67, no. 8, pp. 1384–1388, 2019.

[6] B. Nauta, "A cmos transconductance-c filter technique for very high frequencies," *IEEE Journal of Solid-State Circuits*, vol. 27, no. 2, pp. 142–153, 1992.

[7] M. Gambhir, V. Dhanasekaran, J. Silva-Martinez, and E. Sanchez-Sinencio, "A low power 1.3 ghz dual-path current mode gm-c filter," in *2008 IEEE Custom Integrated Circuits Conference*. IEEE, 2008, pp. 703–706.



[8] C. Aueamnuay, A. V. Kayyil, J. Liu, N. B. Thota, and D. J. Allstot, "gm/id design considerations for subthreshold-based cmos two-stage operational amplifiers," in *2020 IEEE International Symposium on Circuits and Systems (ISCAS)*. IEEE, 2020, pp. 1–5.

[9] C. Aueamnuay, A. V. Kayyil, N. B. Thota, P. K. Venkatachala, and D. J. Allstot, "gm/id-based frequency compensation of cmos two-stage operational amplifiers," in *2020 IEEE International Symposium on Circuits and Systems (ISCAS)*. IEEE, 2020, pp. 1–5.

[10] D. Foty, D. Binkley, M. Bucher *et al.*, "Starting over: gm/id-based mosfet modeling as a basis for modernized analog design methodologies," in *Technical Proc. 2002 Intl. Conf. on Modeling and Simulation of Microsystems*, vol. 1, 2002, pp. 682–685.

[11] M. Bucher, D. Kazazis, F. Krummenacher, D. Binkley, D. Foty, and Y. Papananos, "Analysis of transconductances at all levels of inversion in deep submicron cmos," in *9th International Conference on Electronics, Circuits and Systems*, vol. 3. IEEE, 2002, pp. 1183–1186.

[12] M. Manghisoni, L. Gaioni, L. Ratti, V. Re, and G. Traversi, "Assessment of a low-power 65 nm cmos technology for analog front-end design," *IEEE Transactions on Nuclear Science*, vol. 61, no. 1, pp. 553–560, 2014.

The Need for Solar Power Energy

Muhammad Baballe Ahmad
Department of computer engineering technology School of technology, kano state polytechnic
Kano state, Nigeria
mbaballe@kanopoly.edu.ng

Isa Ibrahim
Department of computer engineering technology School of technology, kano state polytechnic
Kano state, Nigeria
isaibrahim268@gmail.com

Umar Shehu
Department of electrical and electronics engineering School of technology, kano state polytechnic
Kano state, Nigeria
engrsaikayi@gmail.com

***Abstract*— Solar energy is a clean source of energy that has a much lower environmental effect than conventional forms of energy. Solar energy has been an increase in a wider range of applications. Numerous research has been made on the use of photovoltaic (PV) cells in accumulating the solar radiations from the sky and converting it to electrical energy especially if the solar trackers are used. A solar tracker is a machine that is designed as a mounting for photovoltaic (PV) panels so that they track the sun in such a way that the panels are perpendicular at all times to its rays, thereby increasing energy efficiency. Nevertheless, most of these do not take into account the change of the sun angle of incidence by installing these panels in the immovable location, which is highly influenced by the solar energy that is collected by these panels. With the imminent insufficiency of non-renewable resources, the world is now considering using different sources of energy available nowadays. From all these available resources in the world available, solar energy is the most copious and is quite tranquil to convert it to electrical energy. The principal objective of this study is to analyze the various solar tracking devices, reasons why solar power energy is required and the components use in the solar tracker system.**

Keywords*— Sun, microcontroller, photovoltaic (PV) panels, light rays, light sensor, and motor.

[1] INTRODUCTION

In nowadays epoch, the main problem the world is facing especially in African countries is energy catastrophes and we all know that fossil fuels are available in very inadequate quantity [1]. Likewise there overdo in the previous years has abridged them more. Therefore, now if we want to meet our energy demands in this world, the only option we are left with is to exploit the renewable resources of energy that are accessible in copiousness. In this world nowadays, there are numerous sources of renewable energy such as the sun, wind, and geothermal but the most cost-effective among these renewable energy is solar energy. This solar energy cannot only meet our current energy hassles but can also provide us with cheap and clean energy. The solar panels once installed can give us energy for numerous years without having any or much maintenance cost [2]. Solar photovoltaic (PV) panels (figure one below shows the image of the photovoltaic solar panel) are panels, which are used in coupling solar energy, but since the earth is revolving around the sun, due to which the solar energy in existing, the solar panels are available only for a limited time throughout the day. To overcome such tricky, a solar tracker is used [3]. Most of the research done on the solar tracker system makes use of a photosensor, which is normally used, in conjunction with a stepper motor that will help in controlling the movement of the solar panel. For this tenacity, a Phototransistor is mounted on the solar panel frame in which the panels are fixed. The stepper motor used in the research will be programmed using a Microcontroller; the microcontroller is the brain of the whole research because all instructions are given from there. Due to the rotation of the stepper motor, the solar panel mount on it moves in a direction to search for the maximum light intensity. When the light-dependent resistor (LDR) use in the research receives maximum light, the stepper motor will stop in the position of the sun; this is done with the help of the microcontroller as the brain of the research. Henceforth, with changing light intensity, the position of the solar panels also changes. The solar tracker is a device onto which the solar panels are fixed which tracks the movement of the sun across the sky ensuring that the maximum amount of sunlight strikes the panels throughout the day. In terms of cost per watt of the completed solar tracker system, it is generally cheaper (for all but the smallest solar installations) to use a solar tracker and fewer solar panels where space and planning laws permit. A good solar tracker system can usually lead to an increase in electricity generation. Despite its comparatively hoary age, the microcontroller 8051 is one of the most popular microcontrollers that is used currently [4].

[2] RELATED WORKS

2.1. The single-axis trackers

The single-axis trackers, this usually places around the equator where there is no sizeable change in the divergent position of the sun. Mayank Kumar Lokhande [5] offered an automatic solar tracking system. Mayank Kumar Lokhande designed a solar panel tracking system based on a microcontroller and observed that the single-axis tracker system increases proficiency by about 29.99% if you are going to compare it to the fixed module. Runsheng Tanf, Guiha Li, and Hao Zhong [6] scrutinized the horizontal single-axis solar panels tracked. They got the result as east-west axis tracking was deprived to improve the energy while tracking the sun about south-north was the best. The proficiency increased for the east-west axis was less than 7.9% while for the south-north axis increased by 9.98 to 23.56%. Rizk. J and Chaiko [7] established a tracking system using solar panels proficiently. Rizk and Chaika. Y designed a simple single-axis tracking system using a light sensor and stepper motor. This Rizk and Chaiko detected that this system gives the proficiency of power collection by keeping the perpendicular of the solar panel to the sunrays. Rizk and Chaiko also found that this power gain was increased by 29.89%. Ali Mustafa, Imam Abadi, and Adi Soeprijanto [8] designed a fuzzy logic-based single-axis solar tracker system. Ali Mustafa, Imam Abadi, and Adi Soeprijanto implement a fuzzy logic controller on the ATMEGA 8353 microcontroller to improve the powerful energy of the photovoltaic (PV) panel. They found that the photovoltaic (PV) panel has maximized and it exceeded up to about 46.87% compared to the stationary system. Varun A.K, Ashwin R, et al. [9] offered a sensor-based single-axis solar tracker to attain the highest degree of energy through the solar panel. This keeps tracking continuously for the maximum strength of light. This system extemporaneously changes its direction when the sun moves from its position to get the maximum light energy. Therefore, the investigational outcome shows the productiveness and robustness of the

proposed method. Abou-Hashema, Gamal M Dosouky et al. [10] offered an improved orientation design for energy-productivity in photovoltaic (PV) panels. For maximum incident radiation, the panels are inclined with a monthly-based angle. They scrutinize the suggested strategy in two cities that is Egypt (AI-Kharijah) and Japan (Fukuoka). The outcomes revealed that the proposed design accomplished progress of energy building in both the cities. In the year 2013, Mohan Reddy, Anusha, K., and Chandra. S [11] designed a solar tracking system based on a real-time clock. Reddy, Anusha, and Chandra compared a static photovoltaic (PV) panel and single-axis tracker based on a real-time clock using the ARM processor. Their research revealed that the tracking system builds up the proficiency of about 39.87 percent(%) and the energy that is normally achieved from the sun is boosted from morning 9:00 am to afternoon 6:00 pm. Constantin Daniel once, Liviu Kreindler, and Tiberiu Tudorache [12] offered a tracking system fanatical to the photovoltaic (PV) conversion panels. The proposed design verifies the accomplishment of converting solar energy into electricity by genuinely bring into line the solar panel according to the actual position of the sun. The result concluded as output energy is maximized by the photovoltaic (PV) panel through desirably locating implemented only for a sufficient amount of light intensity.

2.2. Dual-axis solar tracking system

The dual-axis trackers are for places where the movement of the sun is a track from east to west all over the day and from east to north or south throughout the seasons. S Jha, Shibani K., Puppala, Harish, [13] suggested a dual-axis tracking system to develop and implement a simple and proficient control scheme with merely a single tracking motor. Jha, Shibani K., Puppala, Harish, core purpose is to improve the power gain by precise tracking of the sun. In the work, they successfully designed, built, and scrutinized a dual-axis sun tracking system and received the best result. S Suryanarayana and V Sundara Siva resolved that saying that this tracking technology is very modest in the design, accurate in tracking, and low-cost. Lakshmi Prasanna H.N and Dhanalakshmi. V [14] offered a smart dual-axis solar tracker. Lakshmi Prasanna H.N and Dhanalakshmi. V used Arduino for the development of their suggested prototype. After their research, they witnessed that maximum voltage was a track of about 24.97% to about 29.68% and the generating power is increased by 29.69% compared to a static system. M. Kacira, M. Simsek, Y. Babur, and S. Demirko [15] overlooked the cause of a dual-axis solar tracking with the development of power energy compared to a fixed photovoltaic (PV) panel in Sanliurfa, Turkey. M. Kacira, M. Simsek, Y. Babur, S. Demirko found that everyday power gain is 29.29% in solar radiation and 34.57% in power generation for a particular day in July. In the year 2017, Tejas Gaidhani and Chaitali Medhane [16] implemented a microcontroller-based dual-axis prototypical working on a solar panel. Through this model, they observed that the solar panel excerpt maximum power if the solar panel is brought into line with the intensity of light-receiving from the sun. It improves the power output and precaution necessary for the system from wind and rain. Midriem Mirdanies, Roni Permana Saputra [17] suggested a dual-axis system with a joint method of an Astronomical algorithm and camera-based feedback processing for localizing and tracking light intensity to increase the proficiency in achieving power energy. They also designed a compound algorithm method to merge approximation data of the sun acquired from astronomical based and visual-based feedback. After the simulation, it resulted that the azimuth and elevation sum squared errors from the proposed algorithm are 0.3588 and 0.3774 degrees, and the astronomical algorithm is 1.0997 and 1.2877 degrees. N.H. Osman and S.B. Elagib [18] describe the development of a solar tracking system based on solar maps using a microcontroller, which can forecast the real detectable position of the sun by latitude's location for maximizing the proficiency of energy level. Their main purpose of this design was to work with minimal operator interaction in the isolated areas where network coverage is absent. Chia-Liang Lu and Jing-Min Wang [19] presented a simple execution of a sun tracker with one dual-axis AC motor to predict the sun's position and used a stand-alone photovoltaic (PV) inverter to energize the whole system. They worked in May 2012 in New Taipei City, Taiwan and the day was slightly cloudy. A static panel is placed along the south at a tilt angle of 22.5 degrees with maximal standard solar radiation when the latitude of Taiwan is 23.3 degrees along the north. The experiments stemmed that their system raised the energy level to 25.81% for a slightly cloudy day. M.M. Abu Khader [20] observed an experiment under Jordanian climate on the cause of utilizing two-axis sun tracking systems. They found that the power result enhanced by 29.67-44.89% compared to a static system for a particular day. The figures below show the dual-axis solar trackers.

[3] REASONS WHY SOLAR POWER ENERGY IS REQUIRED

1. the most generally famous information about solar energy is that it signifies a hygienic, green source of energy. This solar power is a pronounced way of reducing your carbon footprint. They are nothing about solar power that contaminates the Mother Nature of our environments nowadays. Solar power does not discharge any form of greenhouse gasses, and except for needing a source of clean water to function, it uses no other resources to function. Henceforward, solar energy is safe and environmentally friendly to use.

2. The reduction in the cost of these solar panels serves as a pronounced instance of why there is going to be an increase in the use of solar energy in the world. Traditional electricity relies greatly on fossil fuels such as natural gas and coal. Not merely, they are bad for our environment, but they are also inadequate resources. The sun will never raise its rates and it gives you energy security throughout the day especially it is mounted on the solar tracker in other to be tracking the position of the sun movements. Once you have solar panels up on your solar tracker you have precisely reached an energy independent status. The solar battery used in the system stores energy for rainy days and nighttime.

3. The electricity we make use of needs to be transported from our big power plants to us the consumers through widespread grids. The long-distance transmissions of power cause losses. The solar panels are mounted on your tracker to get energy from the sun. Solar tracker power is very helpful in increasing electricity productivity, considering the shortest distance of transmission to our homes or places the power needs to be transported. Since your energy is domestic and as a result of that, you are in control of your energy usage, and no bills are required from any form of authority.

4. solar power increases trellis Security; when many of us decided to switch to solar power, they are likely to experience brownouts or blackouts. If every household will decide to install the solar tracker system, they are high chances of not experiencing blackout if they are electricity failure. The installation of this solar tracker provides us with a larger electricity grid security, especially in terms of natural or human-caused tragedies.

5. Solar power can create jobs and even increase the economic growth of a country;

The national economy of any country can be increased by solar power installations. The more people or companies need solar power, the more human labor will be required in the installation of the panels, and this will reduce joblessness of the country and give job opportunities. This will help create extra jobs for skilled workers and subsequently keeps the economy growing.

[4] COMPONETS OF THE SOLAR TRACKING SYSTEM

1. Light Sensor: These are passive devices that transform this "light energy" whether visible or in the infrared parts of the spectrum into an electrical signal output. The light sensors are more commonly known as "Photoelectric Devices" or "Photo Sensors" because they convert light energy (photons) into electricity (electrons). The light sensor is used to sense the manifestation of light coming from the sun.
2. Not Gate: A NOT gate is a logic gate that inverts the digital input signal. For this purpose, a NOT gate is sometimes is referred to as an inverter. A NOT gate always has high logical one output when its input is low logical zero. Equally, a logical NOT gate always has low logical zero output when the input is a high logical one. The logical symbol for a NOT gate is shown below. The not gate will invert the incoming signal and will feed this signal to the controller.
3. Microcontroller: A microcontroller is an extremely combined device, which includes one chip, all, or most of the parts needed to perform an application control function. The PIC (peripheral interface controller) is an integrated circuit (IC) that was established to control peripheral devices, improving load from the central processing unit (CPU). It also has a low memory capacity; it is also used in performing calculations and is controlled by software just like the central processing unit (CPU). It is used in the designs where a local resolution needs to be taken. It helps in the programming of the whole circuit.
4. Motor Driver: The motor drivers act as an interface between the motor use and the control circuit. The Motor normally requires a high amount of current whereas the controller circuit works on low current signals. Therefore, the function of motor drivers is to take a low-current control signal and then turn it into a higher-current signal that can drive a motor. The signal so received is of very small amplitude and is not able to drive the motor. Thus current amplifier as the motor driver is used to increase the amplitude of the incoming signal. Below is the image of the motor driver circuit.
5. Stepper Motor: A stepper motor is an electromechanical device that converts electrical power into mechanical power energy. Alternatively, the Stepper motor is an electromechanical device, which converts electrical pulses into discrete mechanical movements. The figure below shows the image of the stepper motor.

[5] CONCLUSION

This study presents an outline of the enhancements in the research of the solar power energy and tracking systems in the world nowadays, it highlights the enactment scrutiny of both the single and dual-axis solar tracking systems fortified with diverse techniques, and designs, which have been developing in the recent years. We have also seen the reason why solar energy power is required and significant over another form of energy generation. Also, some of the major components needed in the solar tracker system are discussed.

REFERENCES

[1] M., B., Ahmad, A., S., Muhammad, H., A., Hussain, A., H., Muhammad, A., M., Sani, "Review on Impact of Installing the Solar Tracking System Its Challenges and Types", Artificial & Computational Intelligence, https://acors.org/ijacoi/VOL1_ISSUE5_08.pdf, December 2020.

[2] M., Udit, T., Neeraj, "Review on a sun-tracking model in solar Photovoltaics (PV) system and their classification" Alochana Chakra Journal, volume 4, issue 5, Pp 5330-5338, April 2020.

[3] S., S., Chetan, "Solar Photovoltaics- Fundamentals, Technologies, and Applications". Department of Energy Science and Engineering, IIT, Bombay, 2015.

[4] K., Amandeep, C., Goma, S., Narinder, S., Asif, H., K., C., Kumar, "Designing of a solar tracking system using AT89C51 microcontroller" international journal of scientific research in computer science, engineering and information technology, volume 2, issue 5, pp 709-712, 2017.

[5] K., L., Mayank, "Automatic Solar Tracking System". Journal of Core Engineering & Management, Volume 1, 2014.

[6] L., Guiha, T., Runsheng, Z., Hao, "Optical Performance of Horizontal Single-Axis Tracked Solar Panels", Solar Energy Research Institute Yunnan Normal University, China, 2011.

[7] J., Rizk, Y., Chaiko, "Solar Tracking System: More Efficient Use of Solar Panels", World Academy of Science, Engineering and Technology, 2008.

[8] A., Imam, S., Adi, M., Ali, "Design of Single Axis Tracking System at Photovoltaic Panel Using Fuzzy Logic Controller", Department of Engineering Physics and Electrical Engineering, Institute of Technology, Surabaya, 2015.

[9] R., Ashwin, I., K., Joshua, S., C., Lalith, P., Ravi, P., S, Varun, "Design and Fabrication of Single Axis Solar Tracking System" Journal of Mechanical and Production Engineering, 2014.

[10] M., D., Gama, E., M., Abou-Hashema., S., Masahito, "Maximizing Energy Efficiency in Single Axis Solar Tracker Photovoltaic Panels". 8th International Conference on Power Electronic-ECCE Asia, 2011.

[11] K., Anusha, S., Chandra, R., Mohan, "Design and Development of Real-Time Clock Based Efficient Solar Tracking System", 2013.

[12] T., Tudorache, O., D., Constantin, K., Liviu. "Performance Evaluation of a Solar Tracking PV Panel". Bucharest Scientific Bulletin, Series C: Electrical Engineering, 2012.

[13] K., S., Jha, H., Puppala, "Prospects of renewable energy sources in India: Prioritization of alternative sources in terms of energy index", Energy http://dx.doi.org/10.1016/j.energy.2017.03.110. Kalogirou, Soteris A., 2017.

[14] V., V., Dhanalakshmi, V, H., N., P., Lakshmi, V., Priyanka, J., K., Rani. "Dual Axis Solar Tracker Using Arduino Uno". Department of EEE, Dr.T.T.I.T, KGF, 2016.

[15] M., Kacira, M., Simsek, Y., Babur, S., Demirkol, "Determining Optimum Tilt Angles and Orientations of Photovoltaic Panels". Renewable Energy, Volume-29, 2004

[16] M., Chaitali, G., Tejas, P., Vivek, D., Piyush," Dual Axis Solar Tracker Using AVR". Department of Electrical Engineering, Sandip Institute of Engineering & Management, 2017.

[17] M., Midriem, S., P., Roni, "Dual-axis Solar Tracking System". Research Centre for Electrical Power and Mechatronics, Indonesian Institute of Sciences (LIPI), Indonesia, 2016.

[18] S., B., Elagib, N., H., Oman, "Design and Implementation of Dual Axis Solar Tracker Based on Solar Maps". Department of Electrical and Electronics, Faculty of Engg. Univ. of Khartoum, 2013.

[19] M., J., Wang, L., L., Chia, "Design and Implementation of a Sun Tracker with a Dual-Axis Single Motor for an Optical Sensor Based Photovoltaic System", 2013.

[20] M., M., Khader, O., O., Abu, A., S., Badran, "Evaluating Multi-axes Sun-tracking System at Different Modes of Operation in Jordan". Renewable and Sustainable Energy Reviews, Volume-12, 2008.

The Challenges Faced using the Radio Frequency Identification (RFID) System

Muhammad Baballe Ahmad
Department of computer engineering technology School of technology, kano state polytechnic
Kano state, Nigeria
mbaballe@kanopoly.edu.ng

Mukhtar Ibrahim Bello
Department of computer science School of technology, kano state polytechnic
Kano state, Nigeria
mibello2@gmail.com

Isa Ibrahim
Department of computer engineering technology School of technology, kano state polytechnic
Kano state, Nigeria
isaibrahim268@gmail.com

***Abstract*— The Radio Frequency Identification (RFID), is a wireless technology system that is used for identifying an individual or objects through the means of radio waves which transfer information from an electronic tag, called Radio Frequency Identification (RFID) tag. Radio Frequency Identification (RFID) consists of two main components the interrogator and the transponder. The Interrogator, which is the Radio Frequency identification reader (RFID Reader), the Interrogator usually transmits and receives the signal while the Transponder (tag) is attached to the object. In the Radio Frequency Identification (RFID) system, an RFID reader interrogates the Radio Frequency Identification (RFID) tags. This tag reader generates a radio frequency interrogation, which communicates with the tags been registered in the system. This reader likewise has a receiver that captures a reply signal generated from the tags and decodes the signal. This reply signal from the tags reflects the tag's information content. Each tag of the students consists of a unique identity, identification card (ID) that is assigned to a single student identification card (ID) which is recorded in the database. The use of the Radio Frequency Identification (RFID) technology enables the institution authorities or management to evade attendance documents from damages such as misplacement, tear, or even got lost. This research review some recent design and implementation of internet of things (IoT) attendance system using the concept of the Radio Frequency Identification (RFID) system articles. The analysis found that the Radio Frequency Identification (RFID) system is a very advanced technology for an automatic attendance system in an institution, organization, or university and it provides a very higher performance and accuracy than the traditional paper-based system that the students normally used to sign. A combination of the model is needed which will confirm higher security, better performance, and consistency of the system.**

Keywords*— *Radiofrequency identification (RFID) system, Radiofrequency identification (RFID) tags, Radiofrequency identification (RFID) readers, Arduino or Microcontroller, Liquid crystal display (LCD), Personal computer (PC) or desktop computer

[1] INTRODUCTION

The Radio Frequency Identification (RFID) technology, is an emergent technology that is used in a wide range of applications, it is a member of the family of Automatic Identification and Data Capture which is referred to as (AIDC) technologies. This is the fastest and reliable means or method of identifying an object or thing. Radio Frequency Identification (RFID) consists of two main components the interrogator and the transponder. The Interrogator, which is the Radio Frequency identification reader (RFID Reader), the Interrogator usually transmits and receives the signal while the Transponder (tag) is attached to the object. In the Radio Frequency Identification (RFID) system, an RFID reader interrogates the Radio Frequency Identification (RFID) tags. This tag reader generates a radio frequency interrogation, which communicates with the tags been registered in the system. This reader likewise has a receiver that captures a reply signal generated from the tags and decodes the signal. This reply signal from the tags reflects the tag's information content. A Radio Frequency Identification (RFID) tag usually consists of an antenna and a tiny microchip [1]. The Radio Frequency Identification (RFID) alone has various applications but when it is combined with an Arduino or Microcontroller it limitations magnifies more. The developments in Radio Frequency Identification (RFID) technology continue to produce larger memory capacities, faster processing, and wider reading ranges. They are high tendency that the technology can replace barcode even with the expected reduction in raw materials together with economies of scale; the integrated circuit (IC) in a radio frequency (RF) tag can never be as expensive as a bar code label. Nevertheless, Radio Frequency Identification (RFID) will continue to rise in its recognized places where the barcode or other optical technologies are less effective. Attendance or daily register of students in an institution or university has turned into a vivacious assessment viewpoint in the current educational scheme in both institutions, organizations, schools, and universities. The unoriginal attendance-monitoring scheme has a few obstructions with the development of the latest technology gap. For example, giving out the everyday attendance sheet to a gigantic amount of students in a class is extremely risky and it hinders the consideration of the students in that particular class [2]. This is considered a waste of time and energy as well as a student can intentionally register students who are not present in the class in the attendance sheet. If the lecturer mistakenly loses these documents, all the important attendance records will be lost without hesitation. , the Radio Frequency Identification (RFID) novelty has a great chore to carry out in the completion of the vision of connecting objects around us to the internet. These items extend from huge structures, planes, modern plants, vehicles, any sort of merchandise, and explicit pieces of a bigger framework to people, animals, plants, and even obvious body portions of them. The idea driving all this is called the Internet of Things (IoT) [3].

[2] COMPONENTS USED IN THE RADIO FREQUENCY IDENTIFICATION SYSTEM

1. **Radio Frequency Identification (RFID):** radio frequency identification (RFID) operates by transferring and receiving a signal using Antenna and Integrated Circuit (IC). It has mainly two parts namely, the Radio frequency identification (RFID) Tag and the Radio frequency identification (RFID) Reader. The radio frequency identification (RFID)

tags contain an integrated circuit (IC) and an antenna, which is used to transmit data to the radio frequency identification (RFID) reader also known as an interrogator. This reader then converts the radio waves to a more usable form of information. The data collected from the Radio frequency identification (RFID) tags is then transferred through a communications interface to a host computer system, where the information can be stored in a database and analyzed later. The figure below illustrates the information.

2. **Radio Frequency Identification (RFID) Tag:** The Radio Frequency Identification (RFID) tag is an electronic tag that exchanges data with a Radio Frequency Identification (RFID) reader through radio waves. Almost all the Radio Frequency Identification (RFID) tags have mainly two parts namely, the Antenna and Integrated Circuit (IC). The antenna is used to receive radio frequency waves and the integrated circuit (IC) is used in the processing and store of information. The microchip on the Radio Frequency Identification (RFID) reader is written with whatever information the user wants it.

3. **Radio Frequency Identification (RFID) Reader:** The Radio frequency identification reader, is the brain of the Radio frequency identification (RFID) system and is necessary for any system to function. The Readers also called the interrogators, are devices that transmit and receive radio waves to communicate with Radio frequency identification (RFID) tags. The Radio Frequency Identification (RFID) reader is a device, which used to gather information from Radio frequency identification (RFID. The Radiofrequency identification reader (RFID) uses radio waves to transfer the data from the Radio frequency identification tag to the Radiofrequency identification reader.

4. **Microcontroller:** A microcontroller is an extremely combined device, which includes one chip, all, or most of the parts needed to perform an application control function. The PIC (peripheral interface controller) is an integrated circuit (IC) that was established to control peripheral devices, improving load from the central processing unit (CPU). It also has a low memory capacity; it is also used in performing calculations and is controlled by software just like the central processing unit (CPU). It is used in the designs where a local resolution needs to be taken. It helps in the programming of the whole circuit. Below is the image of the microcontroller.

[3] RELATED WORKS

Liu Ji and Zhang Yongqiang [4] designed and implement a wireless fingerprint-based attendance system to obtain and record the attendance information using fingerprints known as biometric. Kyng and Man [5] designed a time management and access monitoring system using a microprocessor card to monitor students' and staff's movement with the data that are kept in the database for administrator reference in campus, office, or a certain area. Headmaster, Teachers, and parents could access all the information captured by this system by fully utilizing Mykad features via the Internet and intranet facilities. However, Jonathan Sidi, Syahrul N. Junaini, and Lau S. Ling in [6] suggested a system that was capable to record student's attendance using interactive input, viewing students and lecturer profiles, generating reports, and providing students timetable [8]. The system records the attendance using a barcode scanner. In another spectrum, Inanc and Pala [7] applied radio frequency identification (RFID) technology for checking in and checking out at parking areas without the need to stop the cars and it avoids traffic jams during the parking hours. This type of system is usually used in identifying vehicles through internet facilities by comparing the previous data in the database. A.A. Olanipekun and O.K. Boyinbode have implemented a system called the Radio frequency identification (RFID) Based Automatic Attendance systems [8]. The attendance system software is developed using visual basic VB.net and database (Microsoft Access). Each of the students has the Radio frequency identification (RFID) tag attached with the Student identification (ID) card. There is a serial connection between the computer and the Radio frequency identification (RFID) reader and the computer system. The Radiofrequency identification (RFID) reader is placed at the lecture hall door. Whenever students enter the lecture hall the Radio frequency identification (RFID) reader reads the Radio frequency identification (RFID) tag and it stores all data (Entry time, Name, etc.) of students into the database via a serial connection and maintains the system. Here the admin of this system can view all the documents using the software interface by retrieving the data from the database without any hitches, not like the traditional system of writing names on the attendance sheet or piece of paper. Hassanein D. Rjeib et. al design and implemented an attendance system with the combination of Radio frequency identification (RFID) and a Web-Based system [9]. This system uses the Radio frequency identification (RFID) tag and the Radiofrequency identification reader for getting the student's attendance and read the particulars of the students. Then this reader connects with Arduino or microcontroller which serves as the brain of the whole research because all instruction is given from there, which then passes the Radio frequency identification (RFID) reader response to the web server by the use of Arduino shield, finally, the attendance of students can be stored in web server by using PHP and MySQL. The admin of the implemented system can now view all the student's documents by login into this particular web-based application and can view all the student's details registered or stored using liquid crystal display (LCD). Srivignessh P.S.S and Bhaskar M. Found a system that, the Radio frequency identification (RFID) and Pose Invariant Face Verification for an automatic attendance system [10]. The system works under two factors verifications. In the first step, the students need to use the Radio frequency identification (RFID) tag that is read by the Radio frequency identification (RFID) reader. If the first step is succeeded then it moves to the second step of verification, if not, the student becomes under the unrecognized category. The second step is Face verification, if the face match with the particular registered in the Radio frequency identification (RFID) tag then it marks the student attendance that is in the database. Missing the above readings, the system will automatically identify the fraud students. This two-factor automatic system reduces the misuse of identity theft for getting attendance because they are not registered in the system database. Moth Myint Thein and Chaw Myat Nweand Hla Myo Tun developed a Student attendance Management System Based on Radio frequency identification (RFID) and

Fingerprint Reader [11]. The system also works as a two-factor verification system. In the system, the Radio frequency identification (RFID) reader is linked with the computer and the computer has specific software that is used to measure the automatic attendance of the students which is developed by Microsoft Visual basic studio and SQL. In the first place, the entire student must register his or her Radio frequency identification (RFID) tag and Fingerprints and it is stored in the database of the system. Once the students enter the classroom they need to use the Radio frequency identification (RFID) tag and this will be read by the Radio frequency identification (RFID) reader which will then check the database of the system to check if the tag is registered, if it is registered or correct then he moves to the next verification step. In the second step, the fingerprint of the student is then verified. If it matched the information of the students registered he or her then the attendance of the student will be stored on the server. Besides, the lecturers or teachers have authentication to use the system, they can also act as admin of the entire system. Yashi Mishra et al. uses an SD card module with the Radio frequency identification (RFID) tag, which carries different voice codes, is used in the system development [12]. The tag identification card (ID) and the code of the voice greeting are stored in the SD card module. When the student enters the classroom door, his or her Radio frequency identification (RFID) tag is being read. If the identification card (ID) of the student tag matched with the stored data in the SD card then the particulars of the student or person needs to use the voice greeting, if it matches then the door will be open and the attendance of the student will be store in the excel sheet. The Student can view their attendance detail using the liquid crystal display (LCD) use in the research. In the research, the Arduino or microcontroller, connects the liquid crystal display (LCD), the Radio frequency identification (RFID) reader, the SD card module, and the rest components use in the research. Likewise, the system has very simple schematics than another system because of the very simple components use and the design of the whole system. Also, you can we get fast response and accurate results. Anil Kumar Shukla created a model system called the Microcontroller Based Attendance System Using the radio frequency identification (RFID) system and Global System for Mobile (GSM) [13]. The system consists of three atMega16microcontroller placed in between the radio frequency identification (RFID) reader, Global System for Mobile (GSM) modem, and the computer. Each of the microcontroller use has its purpose. The system will starts whenever a lecturer or teacher used his or her radio frequency identification (RFID) tag to enter the lecture room or classroom then the students will enter the classroom also by swapping their radio frequency identification (RFID) tags within five minutes. The radio frequency identification (RFID) reader reads the radio frequency identification (RFID) tag, sends the signal to the first microcontroller, which will analyze the signal of the radio frequency identification (RFID) reader, and opens the classroom door using infrared rays (IR) signal, which is influence by a motor. This signal is temporarily stored in the microcontroller, when the lecturer or teacher finishes his or her class he or she must swap the radio frequency identification (RFID) tag again to the radio frequency identification reader and the system will decide automatically that the class is finished. Therefore, the microcontroller will pass the temporarily stored signal to the computer database as the attendance. In case if a student is absent, the signal will pass it to the global system for mobile, (GSM) modem and it will send this message to the parents of the students who were not present during the lectures or lesson in the lecture room or the classroom. If any of the students go out before the lecturer or teacher, the system will not count the student present in the lecture room or classroom. The system itself is an added advantage and reliable security system. Thus, the students cannot cheat the administration and their parents. Sandhya Konatham et al. suggested a system that will work with the radio frequency identification (RFID) and global system for mobile (GSM) [14]. In their research, they used a microcontroller as a midway among global systems for mobile (GSM) module and the radio frequency (RFID). Whenever the students enter the lecture room or classroom, they need to make use of their tag, which is read by the radio frequency (RFID) reader, and it sends it to the global system for mobile (GSM) module. If the identification card (ID) of the students or individual tag does not match with the stored information of the database he or she is considered as an unapproved person. If it accepts the tag, then the global system for mobile (GSM) module will send a message to the administration and their parents that the students attended lectures or lessons. Srinidhi MB and Romil Roy suggested a system that uses web-based attendance using four-tier architecture by the use of radio frequency identification (RFID) and Biometrics [15]. In their system, the students, lecturers, or teachers' radio frequency identification (RFID) has a unique code, which will be store in the database of the institution or school. The radiofrequency reader (RFID) reader and the fingerprint device are placed at the entrance door of the lecture room or classroom. Whenever the students want to enter the classroom, they need to use the radio frequency identification (RFID) tag which will be read by a radio frequency identification (RFID) reader and validates the identity of the students by comparing it with the information store in the database whether the tag matches or not. The second stage of verification will be allowed if and only if the first stage of verification is succeeded. The Verification with the fingerprint is the second stage of the system and if the student's fingerprint matches with the data in the database then the attendance will be marked and stored into the database, but if he or her record does not store or capture in the database then they will be no attendance for that student. The fingerprint verification is merely acting in ten minutes including five minutes before the schedule and after the schedule of class starting time. If anyone is late then it will deny providing attendance to that particular student that is late but the students can stay at the lectures and learn but will not have attendance for that class. Lastly, a short message service (SMS) will be sent to the students' parents if the students are present or not in the lecture room or classroom. H. K. Nguyen and M. T. Chew developed a prototype of the attendance management system with the placement of a bigger number of radio frequency identification (RFID) readers placed in the room and there is a server application maintains through a laptop [16]. The radio frequency identification reader and the laptop or personal computer (PC) are connected with the help of a wireless router or LAN connection. Whenever a student or person enters the classroom or lecture room, he or she needs to use the radio frequency identification (RFID) tag which is read by the radio frequency identification (RFID) reader and passes the student's attendance to the server through wireless or LAN connection. Since many of the radio frequency identification (RFID) readers are placed, more than one person can get the attendance simultaneously and get the higher efficiency than the traditional method or using the single radio frequency

identification reader. Also, Muhammad Benny Chaniago and Apri Junaidi proposed a system that is working with the radio frequency identification (RFID) and Telegram Messenger Application [17]. In their system, the students need to meet their lecturers or teachers for the tapping of their radio frequency identification (RFID) tags. If the tags match with tag information stored in the database, then it will send the attendance to the management of the institution or principal in the form of an excel sheet as well as sends a message to the specific student's parent via Telegram messenger. Meanwhile, facial verification cost is comparably average to other biometric verification. It also could be considered for a better system for developing an automatic attendance system. The radio frequency identification (RFID) with fingerprint system is very comparable to the radio frequency identification (RFID) with the facial system. Each characteristic of the table is providing similar ideas except for their cost. Fingerprint biometric systems provide a very lower cost compare to Retina and Iris [18]. Meanwhile, software, which makes use of visual studio and SQL, are costs in a great measure. Eventually, the system is considered a high-cost system with a higher eminence.

[4] CHALLENGES FACED USING THE RADIO FREQUENCY IDENTIFICATION (RFID) SYSTEM

1. Lost of the radio frequency identification (RFID) tags: is just like the traditional locks and keys, you might likely or can forget or misplace your tags, which you are using to open the secure entrance the tags are registered to.
2. The radio frequency identification system can be hacked by hackers; the hackers can enter the secure environment and do whatever they feel like doing or even stealing without anyone knowing or aware of their presence.
3. Power Shortage Issue: among the major issue or problems the radio frequency identification system is facing is the problem of electric power especially if it is connected or powered by it. The radio frequency identification (RFID) systems may glitch during power outages affecting some lockers to either shut you out or worse leave the lockers open where people may try to steal what is inside.
4. More Involved and More Expensive to Setup: the radio frequency identification system requires locks that are being wired to a secured server. The computer that is going to be used is where access is controlled, programmed, and logged.
5. If the server computer is not connected to the internet, and you have time-based access restrictions, you will need to manually change the computer's clock twice a year when the time changes.

[5] CONCLUSION

In this paper, we have reviewed many papers related to the radio frequency identification (RFID) system we have seen their various improvements in technology and the advantage of using the radio frequency identification (RFID) system over the traditional paper-based attendance system. Also, the challenges faced using the radio frequency identification (RFID) system are discussed and its main components.

REFERENCES

[1] E. Orji, C. Oleka, U., Nduanya "Automatic Access Control System using Arduino and RFID", Journal of Scientific and Engineering Research, vol. 5 issue 4, pp. 333-340, 2018.

[2] K. Vandana1, K. Anil Kumar, G. Sivani, G. Devanand, E. Venkatanarayana, "Examination Room Guidance System Using RFID and Arduino", International Research Journal of Engineering and Technology, Volume: 05 Issue: 04 | Apr-www.irjet.net, p-ISSN: 2395-0072, pp. 642-645, 2018.

[3] M., B., Ahmad,M., Çavaş, "A review advancement of security alarm system using internet of things (IoT), International Journal of New Computer Architectures and their Applications (IJNCAA) 9(2): 38-49 The Society of Digital Information and Wireless Communications", 2019.

[4] Z., Yongqiang, L., Ji, "The Design of Wireless Fingerprint Attendance System, International Conference on Communication Technology, ICCT '06, Handan, Hebei, China, 27-30 pp. 27-30 November 2006.

[5] M., Man, L., Y., Kyng, "Utilizing MYKAD Touch N Go features for Student Attendance System (TITO)". Proceeding of 1st International Malaysian Educational Technology Convention Johor Bahru, Malaysia, pp.114-120, 2-5 November 2007.

[6] S, Jonathan, N., Syahrul, G., Junaini Lau, S., Ling, "Tracking Student Attendance using Interactive Student Attendance Management System", Third Malaysian Software Engineering Conference (MySEC'07), Selangor, Malaysia, pp. 1-5, 3 – 4 December 2007.

[7] Z. Pala, N. Inanc, "Smart Parking Applications Using RFID Technology", Proceedings of 1st Annual RFID Eurasia, Istanbul, Turkey, pp.1 – 3, 5-6 September 2007.

[8] A. A. Olanipekun, O. K. Boyinbode, "An RFID-based automatic attendance system in educational institutions of Nigeria," Int. J. Smart Home, vol. 9, no. 12, pp. 65–74, 2015.

[9] H. D., N. Salih, A. Al, B. Al-Sadawi, and H. Alsharqi, "Attendance and Information System using RFID and Web-Based Application for Academic Sector," Int. J. Adv. Computer. Sci. Appl., vol. 9, no. 1, pp. 266–274, 2018.

[10] P. S. S. Srivignessh and M. Bhaskar, "RFID and pose invariant face verification based automated classroom attendance system," in International Conference on Microelectronics, Computing, and Communication, 2016.

[11] M. M. M. Thein, C. M. Nwe, and H. M. Tun, "Students' Attendance Management System Based On RFID and Fingerprint Reader," Int. J. Sci. Technol. Res., 2015.

[12] Y. Mishra, G. K. Marwah, and S. Verma, "Arduino Based Smart RFID Security and Attendance System with Audio Acknowledgement," vol. 4, no. 01, pp. 363–367, 2015.

[13] A. K. Shukla, "Microcontroller Based Attendance System Using RFID and GSM," vol. 5, no. 8, pp. 127–131, 2017.

[14] S. Konatham, B. S. Chalasani, N. Kulkarni, and T. El Talib, "Attendance generating A system using RFID and GSM," in 2016 IEEE Long Island Systems, Applications, and Technology Conference, LISAT, pp. 3–5, 2016.

[15] R. Roy, "A web-enabled secured system designed for attendance monitoring applying biometric and Radio Frequency Identification (RFID) technology," in 2014 International Conference on Signal Propagation and Computer Technology, ICSPCT, pp. 653–657, 2014.

[16] T. Sanjay, "Attendance Management system", 4(7), vol. 4, no. 7, pp. 541–543, 2014.

[17] M. B. Chaniago and A. Junaidi, "Student Presence Using Rfid and Telegram Messenger Application," 8th Widyatama Univ. IEEE, pp. 1–5, 2016.

[18] M. Karovaliya, S. Karedia, S. Oza, and D. R. Kalbande, "Enhanced security for ATM Machine with OTP and facial recognition features," in Proceeding Computer Science, vol. 45, pp. 390–396, 2015

Handover Management in SDN-based 5G Small Cell Network

Murtaza CİCİOĞLU
Computer Engineering *Bursa Uludağ University Bursa, Turkey*
murtazacicioglu@uludag.edu.tr

***Abstract*—The control of increasing data traffic volume in fifth-generation (5G) small cell networks will be possible with effective and efficient implementation of mobility and handover management. Many small cell devices deployed in 5G networks create some drawbacks such as handover latency, handover errors, frequent handover, etc. In this study, a new handover management algorithm based on software-defined networking (SDN) approach is proposed for 5G small cell networks. In this algorithm, an Entropy-based simple additional weighting (SAW) decision support structure is used for handover decisions with bandwidth, user density and signal to interference plus noise ratio (SINR) metrics. SDN-based handover management algorithm running on the controller performs the processes of ranking and selecting the most suitable small cell and assigning it to the relevant mobile nodes.**

Keywords—handover management, SDN, 5G, small cell

[1] INTRODUCTION

Mobile data volume is increasing rapidly every year, and current network infrastructures are insufficient to meet these requirements. As a result of the Internet of Things approach, the exponential increase in the number of smart devices that can connect to the Internet has made wireless communication infrastructures inadequate. This is an important issue for service providers to consider. It seems that creative, low-cost and fast-feasible new solutions are needed to meet the mobile user requirements at an appropriate level. The implementation of the Fifth Generation (5G) network architecture is among the most important goals for next-generation wireless communications [1]–[5].

It has become popular to apply the principles of the software-defined networking (SDN) approach to wireless network communication technologies [6]–[9]. The 4G/5G cellular network infrastructures can be strengthened with the SDN approach [10], [11]. SDN, which provides the abstraction of control and data plane functions, is so convenient for handover decisions in small cells. However, there is a need for new decision mechanisms to be used in the control plane. For this reason, a new decision mechanism running at the control plane has been proposed in this study. Simple Additive Weighting (SAW) [12], [13] decision support system, one of the multi-criteria decision-making methods, based on the entropy weighting approach, has been used for handover management. First, the Entropy weighting method [14] is used to calculate criterion weights, then the SAW method is used for ranking. Entropy based SAW algorithm is used in the controller and a ranking is made according to the data received from existing base stations. In this way, the most suitable base station has been obtained.

[2] ENTROPY-BASED SAW METHOD

The selection process in handover management is a very complex problem. On the other hand, multi-criteria decision making (MADM) algorithms are the most widely used method for network selection [15]. SAW, which are among the MADM methods, are used in this study. Entropy weighting method has been used to calculate the criterion weights and then the SAW has been used for small cell ranking. In order to calculate objective weights, the Entropy method can be used when the data of the decision matrix is known. The basic idea of the entropy method is that the information comes from the contrasts between data sets. SAW, the most common of MADM methods, is preferred because it is the simplest. In the SAW algorithm, the weighting is usually is usually done by the user. This approach is not suitable in dynamic network conditions and lead to disadvantages in terms of network usage. As a solution to this problem, the entropy weighting approach has been preferred. In entropy weighting approach, weight is directly proportional to information. In the entropy method, user preference is not taken into consideration and the weight depends on the feature range.

A. *Entropy Weighting Method*

The decision matrix is built by addressing the network and related features. With help of equation 1 normalization is calculated for each parameter. The entropy coefficient (y) is found according to Equation 2. This value (y) is the number of alternatives in the decision matrix. Five base stations (logarithmic state of the number of y) are selected in this study. Subsequently, the entropy value for each criterion is calculated according to Equation 2. It is summed by multiplying the normalized values with the logarithmic values of these values. The weight value of each criterion is obtained according to Equation 3. w_c is the degree of importance of criteria c. The steps used for weight calculation are as follows:

$$f = (\ln(y)^{-1}) \tag{1}$$

$$e_c = -f \sum_{c=1}^{y} N_{ac} \, lnN_{ac} \tag{2}$$

$$N_{ac} = \frac{B_{ac}}{\sum_{a=1}^{x} B_{ac}} \tag{3}$$

$$\sum_{1}^{x} w_c = 1 \qquad w_c = \frac{1-e_c}{\sum_{1}^{x}(1-e_c)}$$

The symbols used in these equations are; a is alternate, c is criteria, Nac is normalized values, Bac is benefit values, f is entropy factor, ec is entropy value, wc is weighted value.

B. *Simple Additive Weighting Method*

Multi-attribute decision-making algorithms are one of the most widely used approaches for network selection. SAW is a MADM method that is the simplest and most widely used algorithm. The performance value of an alternative is calculated as the weighted sum of the attribute degree.

Normalization of decision matrix is calculated according to Equation 4. In the first step in SAW method, the decision matrix consisting of m alternatives and n evaluation criteria is

normalized with the help of the following equation. Normally, the criterion weights of the SAW method are calculated using Equation 5. However, entropy-weighting equations are used to obtain more realistic results in this study. The preference values of the alternatives and the total preference values of each alternative are calculated with the help of Equation 6.

$$r_{ij} = \begin{cases} \frac{x_{ij}}{\max x_{ij}} & i = 1, \dots, m;\ j = 1, \dots, n\ \ benefit\ criteria \\ \frac{\min x_{ij}}{x_{ij}} & i = 1, \dots, m;\ j = 1, \dots, n\ \ cost\ criteria \end{cases} \quad (4)$$

$$w = \frac{C1}{C1+\cdots+Cn} \cdot 100\% \quad (5)$$

$$V_i = \sum_{j=1}^{n} w_j\, r_{ij} \qquad i = 1, \dots\dots, m \quad (6)$$

[3] PERFORMANCE EVALUATION

In an example network scenario, five different small cell base stations have been selected. Three different criteria and random values have been assigned to these base stations. The entropy method is used in weighting the criteria to be used for the performance of base stations. First, the values taken from the base stations for the creation of the decision matrix are given in Table I. The normalized standard decision matrix with the help of Equation 1 is created as given in Table II.

Table 1. Decision matrix

Alternate[a]	Criteria		
	Bandwidth (MHz)	***SINR (dBm)***	***User Density (%)***
BS1	60	30	80
BS2	80	10	50
BS3	20	20	30
BS4	30	15	10
BS5	10	25	70

[b.] BS-Base station (small cell).

Entropy value for each criteria is calculated as given in Table III (with Equation 2). It is summed by multiplying the normalized values with the logarithmic values of these values. The total is multiplied by the entropy coefficient. The entropy coefficient is the logarithmic state of the number of base stations (or number of alternates).

Table 2. Normalized decision matrix

Alternate[a]	Criteria		
	Bandwidth (MHz)	***SINR (dBm)***	***User Density (%)***
BS1	0.3	0.3	0.33
BS2	0.4	0.1	0.21
BS3	0.1	0.2	0.13
BS4	0.15	0.15	0.04
BS5	0.05	0.25	0.29

Table 3. Calculated entropy values

Bandwidth (MHz)	***SINR (dBm)***	***User Density (%)***
0.87	0.96	0.90

Table 4. Calculation of weight values

Bandwidth (MHz)	***SINR (dBm)***	***User Density (%)***
0.49	0.15	0.37

The weight value of each criterion is calculated with the help of Equation 3. Each of the entropy values is subtracted from 1 to calculate the weight values. The entropy value of the desired criterion is subtracted from 1, and the weight value is found by dividing the first calculated sum. These values are given in Table IV. The weights obtained from the entropy method should be between 0 and 1, and the sum of the obtained weights should give a value of one. According to the entropy results, it is seen that the most important criterion is the Bandwidth, the least important is the SINR. These weights will be used in the SAW method.

The second stage is the application of the SAW method. In the SAW method, the decision matrix is formed as in Table V. As shown in Equation 4, each value must be divided by the maximum or minimum value in its row in order to normalize the decision matrix. The values obtained from the result are given in Table VI.

Table 5. Decision matrix for SAW method

Criteria	*Types of criteria*	Alternate[a]				
		BS1	***BS2***	***BS3***	***BS4***	***BS5***
Bandwidth	Max	60	80	20	30	10
SINR	Max	30	10	20	15	25
User Density	Min	80	50	30	10	70

[c.] BS-Base station (small cell).

Table 6. Decision matrix normalized to SAW method

Criteria	Alternate				
	BS1	***BS2***	***BS3***	***BS4***	***BS5***
Bandwidth	0.75	1.00	0.25	0.38	0.13
SINR	1.00	0.33	0.67	0.50	0.83
User Density	0.13	0.20	0.33	1.00	0.14

The normalized values are multiplied by the weight values calculated according to the Entropy weighting method (is given in Table IV) and the utility matrix of the SAW method will be formed. Table VII shows the utility matrix calculated by SAW method.

Table 7. Utility matrix

Criteria	Alternate				
	BS1	***BS2***	***BS3***	***BS4***	***BS5***
Bandwidth	0.36	0.49	0.12	0.18	0.06
SINR	0.15	0.05	0.10	0.07	0.12
User Density	0.05	0.07	0.12	0.37	0.05

As a result, all the values are summed up in columns and the highest value gives the best result. The ranking resulting from this calculation is given in Table VIII. As can be seen, BS4 small cell base station has the highest result (0.62) compared to other base stations. BS1, BS2, BS3 and BS5, respectively, have the values of 0.56, 0.61, 0.34 and 0.23.

Table 8. Entropy-based SAW ranking results

Base Stations	***Results***	***Ranking***
BS1	0.56	3
BS2	0.61	2
BS3	0.34	4
BS4	0.62	1
BS5	0.23	5

[4] CONCLUSION

Next generation 5G small cell networks aim to meet the quality of service requirements with a satisfactory level in dense environments with many small cells and mobile nodes. Therefore, handover management is among the most important issues for 5G technology. Unlike traditionally handover management algorithms, new approaches with multiple metrics, dynamic and robust are required. In this study, a handover management strategy with entropy weighting based SAW decision support structure has been proposed for SDN-based 5G small cell networks. The proposed algorithm can rank the all small cell base stations and select the most suitable small cell according to bandwidth, SINR and user density metrics. This algorithm is designed for the SDN controller that performs handover management. In this way, more consistent and accurate handover decisions will be made in dynamic network conditions.

REFERENCES

[1] A. Çalhan and M. Cicioğlu, 'Handover scheme for 5G small cell networks with non-orthogonal multiple access', *Computer Networks*, vol. 183, p. 107601, Dec. 2020, doi: 10.1016/j.comnet.2020.107601.

[2] M. Cicioğlu, 'Performance Analysis of Handover Management in 5G Small Cells', *Computer Standards & Interfaces*, p. 103502, Dec. 2020, doi: 10.1016/j.csi.2020.103502.

[3] D. Muirhead, M. A. Imran, and K. Arshad, 'A Survey of the Challenges, Opportunities and Use of Multiple Antennas in Current and Future 5G Small Cell Base Stations', *IEEE Access*, vol. 4, pp. 2952–2964, 2016, doi: 10.1109/ACCESS.2016.2569483.

[4] 'Ericsson Mobility Report', *Ericsson*, 2020. https://www.ericsson.com/4adc87/assets/local/mobility-report/documents/2020/november-2020-ericsson-mobility-report.pdf (accessed Dec. 10, 2020).

[5] M. De Ree, G. Mantas, A. Radwan, S. Mumtaz, J. Rodriguez, and I. E. Otung, 'Key Management for Beyond 5G Mobile Small Cells: A Survey', *IEEE Access*, vol. 7, pp. 59200–59236, 2019, doi: 10.1109/ACCESS.2019.2914359.

[6] M. Al-Hubaishi, C. Çeken, and A. Al-Shaikhli, 'A novel energy-aware routing mechanism for SDN-enabled WSAN', *International Journal of Communication Systems*, vol. 32, no. 17, p. e3724, Nov. 2019, doi: 10.1002/dac.3724.

[7] A. B. Al-Shaikhli, C. Çeken, and M. Al-Hubaishi, 'WSANFlow: An Interface Protocol Between SDN Controller and End Devices for SDN-Oriented WSAN', *Wireless Personal Communications*, vol. 101, no. 2, pp. 755–773, 2018, doi: 10.1007/s11277-018-5714-5.

[8] M. Cicioğlu and A. Çalhan, 'Energy-efficient and SDN-enabled routing algorithm for wireless body area networks', *Computer Communications*, vol. 160, pp. 228–239, Jul. 2020, doi: 10.1016/j.comcom.2020.06.003.

[9] T. Bilen, B. Canberk, and K. R. Chowdhury, 'Handover Management in Software-Defined Ultra-Dense 5G Networks', *IEEE Network*, vol. 31, no. 4, pp. 49–55, Jul. 2017, doi: 10.1109/MNET.2017.1600301.

[10] N. Feamster, J. Rexford, and E. Zegura, 'The Road to SDN: An Intellectual History of Programmable Networks', *ACM Sigcomm Computer Communication*, vol. 44, no. 2, pp. 87–98, 2014, doi: 10.1145/2602204.2602219.

[11] L. Peterson and B. Davie, 'Computer Networks: A Systems Approach', *https://github.com/SystemsApproach*, 2019. https://book.systemsapproach.org/index.html (accessed May 24, 2020).

[12] I. Kaliszewski and D. Podkopaev, 'Simple additive weighting—A metamodel for multiple criteria decision analysis methods', *Expert Systems with Applications*, vol. 54, pp. 155–161, Jul. 2016, doi: 10.1016/j.eswa.2016.01.042.

[13] A. ÇALHAN, 'Yeni nesil gezgin haberleşme teknolojileri için yapay zeka tabanlı dikey el değiştirme yöntemi ve uygulaması / Artificial intelligence based vertical handoff method and application for new generation mobile communication technologies', Kocaeli Üniversitesi / Fen Bilimleri Enstitüsü / Elektronik-Bilgisayar Eğitimi Anabilim Dalı, 2011.

[14] H. Lin, L. Du, and Y. Liu, 'Soft Decision Cooperative Spectrum Sensing With Entropy Weight Method for Cognitive Radio Sensor Networks', *IEEE Access*, vol. 8, pp. 109000–109008, 2020, doi: 10.1109/ACCESS.2020.3001006.

[15] K. Hwang, Ching-Lai; Yoon, *Multiple Attribute Decision Making: Methods and Applications A State-of-the -Art Survey*. 1981.

Design and Analysis of Parameterized Signed Booth's Multiplier in FPGA

Bahadır Özkılbaç
Department of Electrical Electronic Engineering
Ataturk University
Erzurum, Turkey
bahadir.ozkilbac@atauni.edu.tr

Tevhit Karacalı
Department of Electrical Electronic Engineering
Ataturk University
Erzurum, Turkey
tevhit@atauni.edu.tr

***Abstract*— Since digital signal processing applications are mostly consist of multiplication and addition operations, multiplication unit is the heart of the digital systems. Therefore, the speed of the multiplication operation is very important for the performance of the system. Digital hardware designers have developed various algorithms to increase the speed of multiplication. Booth's multiplier is an algorithm with high-speed performance and usage area efficiency. In this study, the bit length parameterizable Booth's multiplier circuit was designed using VHDL in FPGA. Synthesis of the designed circuit was carried on Xilinx Artix-7 FPGA chip for 4, 8, 16, 32 bits multipliers and reports of total delay and usage area were obtained. For verification of the design, the behavioral simulation was done in the Xilinx ISE Design Suite 14.6 tool.**

Keywords—Booth, FPGA, VHDL, multiplier, digital systems

[1] INTRODUCTION

Multipliers are important components of most high-performance systems such as filters, artificial neural networks, digital signal processing, image processing. Because in such applications, addition and multiplication are the most used operations in digital systems [1]. The performance of the system is determined by multiplier because it takes up more area and the computational load than other operations is high. Therefore, increasing the speed of the multiplier is of importance in terms of system performance. However, speed and usage area are generally inversely proportional to each other. In other words, improving the speed causes the usage to increase.

The most common method for multiplying binary numbers is combinational and serial multipliers. In each iteration, produces partial products are obtained by shifting in combinational multiplier. It is an advantage that partial products are simple to obtain. However, as the number of bits lengths, the increase in the addition numbers due to the augmentation of partial productions is a disadvantage for this algorithm. Different multiplication algorithms such as Wallace Tree, Vedic, Mitchell, combinational, serial have been developed [2]–[12]. But among these multipliers, Booth's multiplier has the most advantage. Booth multipliers with low power consumption and latency have been designed [13]-[18] and used in various applications [19]-[22].

In this study, the bit length parameterizable and adapted to various applications, Booth's multiplier circuit is designed in FPGA. Xilinx Virtex-7 FPGA was used to synthesize the designed Booth's multiplier architecture. The behavioral simulation of the design was done out in the Xilinx ISE Design Suite 14.6 tool. The rest of this study is organized as follows: In Section II Information about signed 2's complement number representation is given. Section III presents details the architecture of Booth's multiplier designed. In Section IV, behavioral simulation and synthesis of Booth's multiplier designed are given.

[2] SIGNED 2's COMPLEMENT NUMBER REPRESENTATION

Signed 2's complement number representation is used to represent signed integers in the binary numbers. Also, the floating-point number representation and the fixed-point number representation are number representations commonly used in digital systems to store fractional numbers [23]–[24]. Today, the floating-point number representation is one of the most used formats in digital computations, which has been made a standard by IEEE. Although it is an advantage to have a high accuracy rate and a wide range of numbers, it is a disadvantage that the processing units are complex and the speed performance is low. On the other hand, fixed point number representation, has less accuracy and narrow number range despite higher speed performance. Multiplication operations of the both number formats contain integer multiplication. Therefore, the performance of the designed integer multiplier is important.

In signed 2's complement binary number with bit length n, the most significant bit (MSB) is the sign, and the remaining bits store the magnitude information. If the sign bit is '0', the number is positive, if '1' is negative. Negative numbers are obtained by getting 2's complement. Signed 2's complement binary number format is given in Fig. 1. To be more clearly, as an example, signed 2's complement number format with 3 bits of length is given in Table I.

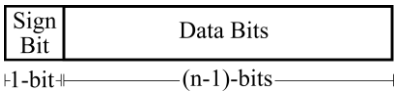


Fig. 1. Signed 2's complement number representation.

Table 1. Example Signed 2's Numbers

Decimal	Signed Binary Number
7	0111
6	0110
5	0101
4	0100
3	0011
2	0010
1	0001
0	0000
-1	1111
-2	1110
-3	1101
-4	1100
-5	1011
-6	1010
-7	1001

[3] DESIGN OF PROPOSED BINARY MULTIPLICATION

A. *Combinational Multiplier*

Combinational multipliers do multiplication of two signed or unsigned numbers with the shift-add method [25]. The micro-architecture of the combinational multiplier is given in Fig. 2.

The logic of the combinational binary multiplier is the same as the decimal multiplication. All bits of multiplier are checked to create partial products. If the relevant multiplier bit is a '1', the product is the multiplicand left shifted by the decimal value of the relevant multiplier bit. If the relevant multiplier bit is a '0', the product is an array of 0's left shifted by the decimal value of the relevant multiplier bit.

In Fig. 2, the architecture of the combinatorial multiplier only calculates for unsigned numbers. In order to multiply signed numbers, the signs of partial products need to be extended. An example of multiplying two 5-bit length signed numbers is given in Fig. 3.

Advantage of combinational multiplier is the generation of partial products is simple. But if the bit length of the multiplier or multiplier extends, the additions number of partial products will also increase. In this case, the delay in multiplication depends on the number of partial products to be added.

B. *Booth Multiplier*

Using Booth's multiplier algorithm invented by Andrew Donald Booth in 1950, it is possible to multiply two signed and unsigned numbers [26]. With Booth's multiplier algorithm, the number of partial products is halved. Thus, speed and usage area efficiency increase. The flow chart of the algorithm is shown in Fig. 4.

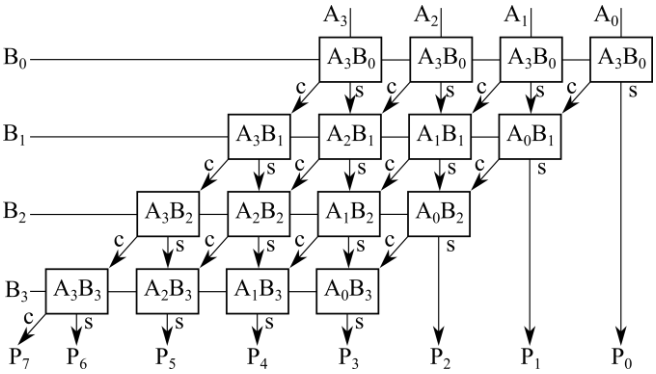


Fig. 2. Combinational multiplier micro-architecture.

```
                    0 1 1 1 0  (+14)
                    1 1 0 1 1  (-5)
                  -------------
Sign extension    1 1 1 1 1 0 1 1 1 0
is shown in red   1 1 1 1 0 1 1 1 0
                  0 0 0 0 0 0 0 0
                  1 1 0 1 1 1 0
                  1 0 1 1 1 0
                  -------------
                  1 1 1 1 1 1 1 0 1 0  (-70)
```

Fig. 3. Signed combinational multiplier with sign extension.

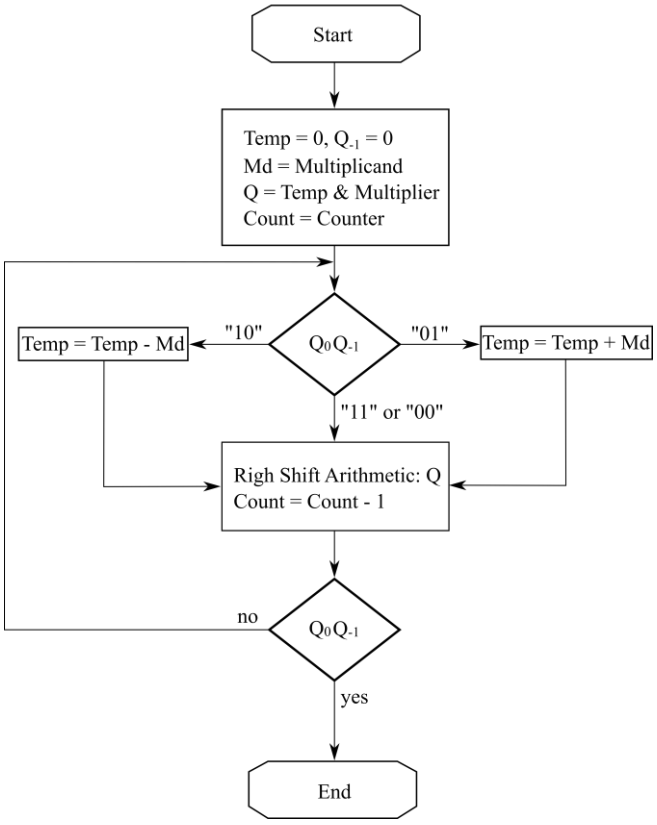


Fig. 4. Flowchart of Booth's multiplier algorithm.

Booth's multiplier algorithm step by step is as follows:

- Multiplier and multiplicand are determined between two operands signed 2's complement binary numbers. The fewer number of transitions are chosen as multiplier and the more one as multiplicand.
- The count value should be determined. The count value is obtained from the number of bits required to represent the largest magnitude of the two operands.
- Temp variable initially takes the value 0. Q register is obtained by concatenating temp and multiplier variables.
- Q_0 is the least significant bit of the Q register. Q_{-1} is the bit that comes out of the Q register after the Right Shift Arithmetic (RSA).
- If Q_0Q_{-1} gets the value "00" or "11", RSA operation is done to the Q register and the count value is decreased by 1.
- If Q_0Q_{-1} is "01", multiplicand is added to temp variable. If "10", the multiplicand is subtracted from the temp variable. After subtraction or addition, RSA operation is performed and the count value is decreased by 1.
- When the counter value is 0, the sign of the MSB of the value in the Q register represents the magnitude of the other bits.

As an example, the multiplication of 4 and -5 numbers is given in Table II. The micro-architecture of Booth's multiplier, which performs all these steps, is also given in Fig. 5.

Table 2. Example 4x4 Booth 's Multiplıer

Count	Q	Q_{-1}	Q_0Q_{-1}	Operation
3	0000 0100	0	00	Initialization
3	0000 0100	0	00	RSA
2	0000 0010	0	00	RSA
1	0000 0001	0	10	Subtraction
1	0101	-	-	-
1	0101 0001	-	-	RSA
0	0010 1000	1	01	Addition
0	1101	-	-	-
0	1101 1000	-	-	RSA
Below 0	1110 1100	0	00	Complete

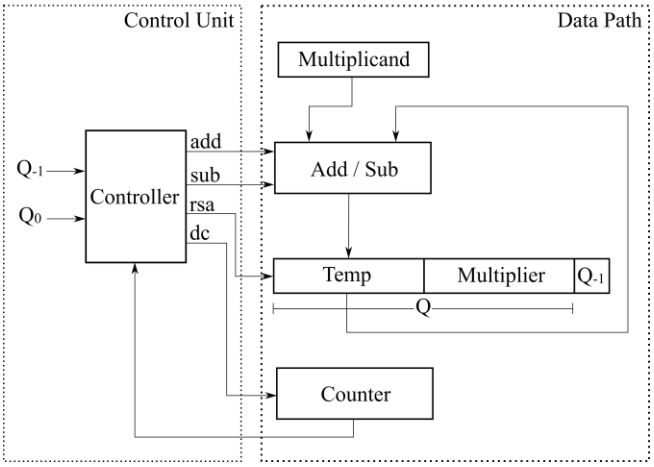


Fig. 5. Booth's multiplier micro-architecture.

[4] Results of Implementatıon and Sımulation

In order to simulate the designed circuit, a testbench code in VHDL language was written in Xilinx ISE Design Suite 14.6 tool.

While one of the inputs was fixed in the testbench code, the value of the other input was changed and the output value was observed. 4x4, 8x8, 16x16 Booth's multiplier was simulated and waveforms showing input and output values are given in Figure 6 (a), (b), (c).

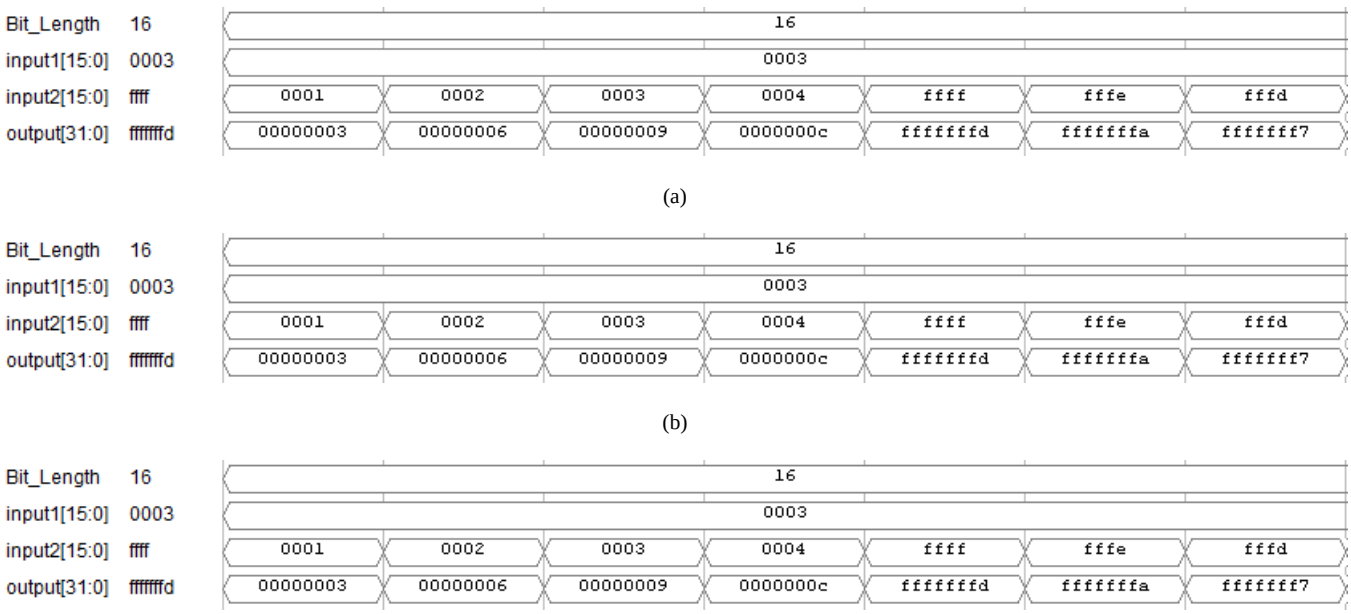
Synthesizing was done for the Booth's multiplier circuit operating at 4, 8, 16, 32 bits in the Artix-7 FPGA model, which is located in the programmable logic part of the Zynq-7000 Z-7020 1CLG484 SoC integrated circuit in Xilinx ISE Design Suite 14.6 tool. ISE Design Suite tool offers LUT usage amounts in FPGA. Also, the maximum delay time of the designed circuit was obtained after synthesis. Usage area and delay information are given in Table III and Table IV, respectively. The total delay of the circuit is equal to the sum of the gate delay and net delays.

Table 3. Booth's Multıplıer LUT Usage Amount

	LUT
4 bit Booth Multiplier	31
8 bit Booth Multiplier	183
16 bit Booth Multiplier	752
32 bit Booth Multiplier	3040

Table 4. Booth's Multıplıer Delay Values

	Logic (Gate) Delay	Route (Net) Delay	Total Delay
4 bit Booth Multiplier	0,159	2,435	2,594
8 bit Booth Multiplier	4,706	8,689	13,395
16 bit Booth Multiplier	10,719	17,002	27,721
32 bit Booth Multiplier	21,375	34,193	55,568



(a)

(b)

(c)

Fig. 6. Booth's multiplier inputs / output waveform, a) 16 bits, b) 8 bits, c) 4 bits.

[5] CONCLUSION

One of the most important key components of digital signal processing algorithms, the multiplication was designed using Booth's multiplier algorithm. While increasing the speed in other algorithms causes decrease in usage area efficiency, Booth's multiplier has both high speed performance and high usage area efficiency. Many designs have been made for Booth's multiplier before. In this study, the bit length parameterizable Booth's multiplier FPGA, which can be used in various applications running in different number representations, is designed. The synthesis of the designed multiplier circuit was carried out in Xilinx Artix-7 FPGA. LUT usage amount and delay information of the unit designed after synthesis were obtained. Simulation has been made in Xilinx ISE Design Suite 14.6 tool for verification of the design.

REFERENCES

[1] K. Kunaraj and R. Seshasayanan, "Leading one detectors and leading one position detectors-an evolutionary design methodology," Canadian journal of electrical and computer engineering, vol. 36(3), pp 103-110, 2013.

[2] N. Sureka, , R. Porselvi, & K. Kumuthapriya, "An efficient high speed Wallace tree multiplier," In 2013 International Conference on Information Communication and Embedded Systems (ICICES) (pp. 1023-1026), 2013.

[3] K. Bhardwaj, P. S. Mane and J. Henkel, "Power-and area-efficient approximate wallace tree multiplier for error-resilient systems," In Fifteenth International Symposium on Quality Electronic Design, pp. 263-269, March 2014.

[4] C. Vinoth, V. K. Bhaaskaran, B. Brindha, S. Sakthikumaran, V. Kavinilavu, B. Bhaskar and B. A. Sharath, "novel low power and high speed Wallace tree multiplier for RISC processor." In 2011 3rd International Conference on Electronics Computer Technology, Vol. 1, pp. 330-334, April 2011.

[5] G. Ganesh Kumar and V. Charishma, "Design of high speed vedic multiplier using vedic mathematics techniques," International Journal of Scientific and Research Publications, 2(3):1, 2012.

[6] R. Pushpangadan, V. Sukumaran, R. Innocent, D. Sasikumar and V. Sundar, "High speed vedic multiplier for digital signal processors," IETE journal of research, 55(6), 282-286, 2009.

[7] L. Dadda and A. Nannarelli, "A variant of a radix-10 combinational multiplier," In 2008 IEEE International Symposium on Circuits and Systems, pp. 3370-3373, 2008, May

[8] T. Lang and A. Nannarelli, "A radix-10 combinational multiplier," In 2006 Fortieth Asilomar Conference on Signals, Systems and Computers, pp. 313-317, October 2006.

[9] L. Dadda and A. Nannarelli, "A variant of a radix-10 combinational multiplier," In 2008 IEEE International Symposium on Circuits and Systems, pp. 3370-3373, May 2008.

[10] D. J. McLaren, "Improved Mitchell-based logarithmic multiplier for low-power DSP applications," In IEEE International [Systems-on-Chip] SOC Conference, Proceedings, pp. 53-56, September 2003.

[11] Z. Babić, A. Avramović and P. Bulić, "An iterative logarithmic multiplier. Microprocessors and Microsystems," 35(1), pp. 23-33, 2011.

[12] E. E. Swartzlander, "The quasi-serial multiplier," IEEE Transactions on Computers,", vol 100(4), pp 317-321, 1973.

[13] L. Qian., C. Wang, W. Liu, F. Lombardi and J. Han, "Design and evaluation of an approximate Wallace-Booth multiplier," In 2016 IEEE international symposium on circuits and systems (ISCAS) , pp. 1974-1977, May 2016.

[14] N. Bano, "VLSI Design of low power booth multiplier," International Journal of Scientific & Engineering Research, 3(2), pp. 2-4, 2012.

[15] D. Chandel, G. Kumawat, P. Lahoty, V. V Chandrodaya and S. Sharma, "Booth multiplier: Ease of multiplication," International Journal of Emerging Technology and Advanced Engineering, 3(3), pp. 118-122, 2013.

[16] Z. Zhang and Y. He, A low-error energy-efficient fixed-width booth multiplier with sign-digit-based conditional probability estimation. IEEE Transactions on Circuits and Systems II: Express Briefs, 65(2), pp. 236-240, 2017.

[17] N. Goyal, K. Gupta and R. Singla, "Study of combinational and booth multiplier. International Journal of Scientific and Research Publications, 4(5), pp. 1, 2014.

[18] H. Jiang, J. Han, F. Qiao and F. Lombardi, "Approximate radix-8 booth multipliers for low-power and high-performance operation," IEEE Transactions on Computers, 65(8), pp. 2638-2644, 2015.

[19] D. J. Kumar and E. Logashanmugam, "Performance analysis of FIR filter using booth multiplier. In Second International Conference on Current Trends In Engineering and Technology-ICCTET 2014, pp. 414-417, July 2014.

[20] S. Kalita, P. Gogoi and K. K. Sarma, "Convolutional Coding Using Booth Algorithm For Application in Wireless Communication," International Journal of Electronic Signals and Systems, pp. 37-41.

[21] S. Nagaria, A. Singh and V. Niranjan, "Efficient FIR filter design using Booth multiplier for VLSI applications," In 2018 International Conference on Computing, Power and Communication Technologies (GUCON), pp. 581-584, September 2018.

[22] P. Paliwal, J. B. Sharma and V. Nath, "Comparative study of FFA architectures using different multiplier and adder topologies," Microsystem Technologies, pp. 1-8, 2019.

[23] B. Özkılbaç and T. Karacalı, "Implementation and Design of 32 Bit Floating-Point ALU on a Hybrid FPGAARM Platform,"Brilliant Engineering, vol 2, pp. 25-61, January 2020.

[24] F. Busaba, T. Slegel, S. Carlough, C. Krygowski and J. G. Rell, "The design of the fixed point unit for the z990 microprocessor," In Proceedings of the 14th ACM Great Lakes symposium on VLSI, pp. 364-367, April 2004.

[25] L. Null and J. Lobur, "Essentials of Computer Organization and Architecture," Jones & Bartlett Publishers, 2014.

[26] A. A. B. Raj, "FPGA-based embedded system developer's guide," CRC Press, 2018.

Comparison of Classical ML with DL Methods for Network Intrusion Detection in IoT

Siham Amarouche
Department of Computer Engineering, Kocaeli University
Kocaeli, Turkey
185112022@kocaeli.edu.tr

Kerem Küçük
Department of Software Engineering, Kocaeli University
Kocaeli, Turkey
kkucuk@kocaeli.edu.tr

***Abstract*— Intrusion detection and cyber security are important topics in the IoT domain nowadays. Rapid of using objects that connected to wireless networks in IoT the amount of data that we shared via network system is growing rapidly. This data may be vulnerable to attacks and threats and need to secure it to make the system more confidentiality, integrity, availability, and reliability. One of the important types of attacks is routing attacks. Attacks are becoming more complex and difficult to detect. The process of detecting attacks using artificial intelligence algorithms autonomously without the need to human control or manual examination has become trend topics in network intrusion detection systems (NIDS). In this article, we decide to apply different machine learning (ML) and deep learning (DL) methods on open datasets. In deep learning methods we exclude the need to feature extraction these methods generate the non-linear combinations the features have less effect get lesser weights automatically, but the problem of overfitting with DL methods is still remaining and to solve it we used different techniques like cross-validation, early stopping, and parameters tuning techniques. We make experiments to find out a best way to identify the anomaly in IoT based environment, make comparisons between different artificial intelligence (AI) models and propose new techniques and smart solutions to improve performance and increase accuracy in intrusion detection systems (IDS).**

Keywords*— *IoT security, cyber security, routing attacks, machine learning, deep learning, intrusion detection

[1] INTRODUCTION

The Internet of Things (IoT) is a technology in which a network connects anything with the Internet, based on embedded systems, specific protocols and sensors to conduct information exchange and communications in order to obtain smart recognitions, monitoring, localization, tracking, and control systems [1].

The sensitivity and importance of the information carried out by IoT devices and networks signifies the importance of its security. To overhead challenges and problems on the server end we used different models as a decision engine to decide about traffic data type, whether it is benign or malicious. Cyber threats have become more widespread and several new types of attacks have been generated targeting organizations, companies, and governments. Furthermore, since the IoT has emerged the number of devices and objects that are connected to wireless networks increased. The proposed research here is found on the intersection between intrusion detection and mitigation, and Artificial Intelligence (AI) technologies. To mitigate cyber-attack, cybersecurity analysts heavily depend on Intrusion Detection System (IDS). IDS can detect malicious activities by matching patterns of known attacks using the signature-based detection method, or observing anomaly activities using anomaly-based intrusion detection systems this method is introduced to detect unknown attacks [2].

Obviously, we can see that all governments and security intelligence try to protect their information and not allow spies to eavesdrop on it and its decisions. For the importance of cybersecurity topic, we research in this article the effectiveness of using ML and DL models in cybersecurity as well as current challenges that face security analysts and we aim to use different methodologies to prevent, mitigate attacks and drop the malicious packets and threats.

In our experimental process, we applied the flowing supervised Machine Learning (ML) methods for IDS: Naïve Bayes (NB), k-Nearest-Neighbor (kNN), Logistic Regression (LR), Decision Tree (DT) and Random Forest (RF). Also Deep learning (DL) methodologies as Multi-layer Perceptron (MLP), Artificial Neural Networks (ANN), Deep Neural Networks (DNNs) and Convolutional Neural Networks (CNNs). We applied Random Forest algorithm over UNSW-NB15 dataset to calculate the feature importance measure for each feature, select more important features and generate reduced optimal feature vectors, this process may increase the accuracy of intrusion detection and increase the speed of models to get performance results. We considered two schemes binary and multiclass classification configurations.

This paper is organized as follows. Section II presents the UNSW-NB15 dataset, informations about it, and preprocessing methods that used before training our dataset. Section III give us overview about candidate methods and thecniques that used to evaluate their performance in proposed dataset that is represented in Section II. Section IV discusses the evaluation and expiremental results of ML and DL methods. Finally, the conclusion and future works are given in Section V.

[2] DATASET

We used the UNSW-NB15 dataset which is created by the Cyber Range Lab of the Australian Centre for Cyber Security [3]. We selected this dataset because it is a public dataset not private, diversity of attack types those included in this dataset, the ability to generate new features from PCA files using feature extraction tools like the

CICFlowMeter tool, and regular updates that applied to this dataset. The UNSW-NB15 dataset includes nine types of attack classifications to describe malicious behaviors.

The Bro-IDS, Argus tools are employed and twelve algorithms are developed to extract totally 49 features with the class label [3]. In this dataset, the number of instances in the training set is 175,341 records and the testing set is 82,332 records from the different types, attack and normal.

A. *Attack Types*

Attack types included in the UNSW-NB15 dataset are Fuzzers, Analysis, Backdoors, DoS, Exploits, Generic, Reconnaissance, Shellcode and Worms.

B. *Feature Transformation and Standardization*

Before feeding the data to classical machine learning and deep learning models, feature transformation has been applied and this step is important because models accept only numerical data as input for that, all non-numerical values of the dataset are converted into numerical data. In this work, we used one hot encoding (ohe) technique to encode categorical features as a one-hot numeric array, the encoder derives the unique values for each feature and represents it as one-hot array. On the other side, for the standardization process, we used the StandardScaler technique over the numerical data because the values of the dataset are in different ranges and we tried to standardize data in the same range. Standardization is a scaling technique where input values are centered around the mean with a unit standard deviation.

C. *Feature Selection and Dimensionality Reduction*

In this step, we select the most important features and delete unnecessary features or reduce the dimensions of features in the dataset. For the task of feature extraction and dimension reduction process we can use different models like Principal component analysis (PCA), Linear discriminant analysis (LDA), Autoencoder, and t-SNE models. On the other hand, feature selection is used to reducing irrelevant and redundant variables and it measures the relevance of each feature with the output labels/classes based on feature importance metric. Feature selection technologies are divided into embedded, wrapper, and filter methods [4]. Our goal from applying the feature selection method and reducing the number of input variables to improve the performance of the model in some cases and reduce the computing cost and time of the training model.

In this study, we applied only feature selection methods using Random Forest that depends on tree-based strategies and belongs to the category of embedded methods. Embedded methods combine the qualities of filter and wrapper methods, more accurate, and generalize better. Features importance and its scores that calculated using Random Forest method as shown in Fig. 1:

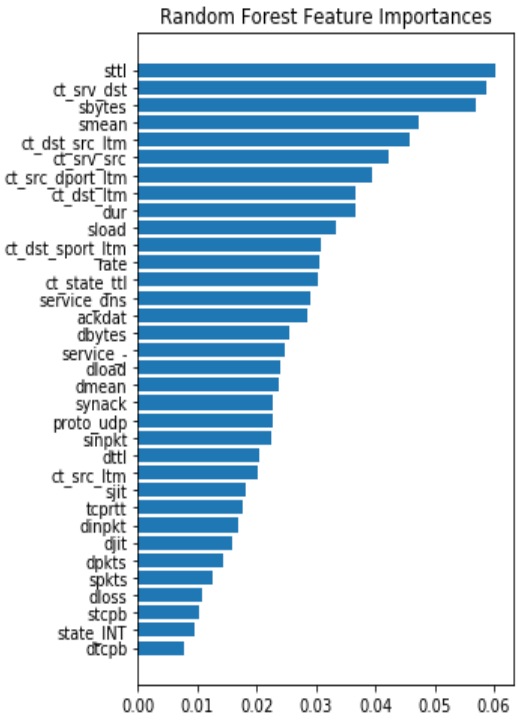


Fig. 1. Feature Selection using Random Forest

[3] Methods and Techniques

A. *Classical Machine Learning Methods*

1) *Naïve bayes*

Naive Bayes (NB) is a subset of Bayesian decision theory and it is a simple probabilistic machine learning model based on the Bayes theorem where assumptions between features are considered independent. This method is used for classification tasks. There are different types of Naive Bayes as Multi-nominal, Bernoulli, and Gaussian Naive Bayes algorithms [5]. In our work, we used Bernoulli Naive Bayes model. Bayes theorem mathematically can be described as follows:

$$P\,(A|B) = \frac{P(B|A)P(A)}{P(B)} \qquad (26)$$

Where A and B are different events, P(A) and P(B) are the probabilities of observing A and B respectively without any given conditions, P(A|B) is the probability of event A occurring given that B is true and it is also called the posterior probability of A given B, and P(B|A) is a probability of event B occurring given that A is true.

2) *K-nearest neighbors*

K-nearest neighbors (KNN) is an ML algorithm that is capable of both supervised and unsupervised approaches and it is used for both classification and regression problems. In this research, we used it for supervised binary and multiclass classification tasks. KNN algorithm assumes that similar instances exist in the same area and proximity. Different distance metrics are used in this model. Distance metrics find the distance between two instances between a new data point and an existing point in the training dataset [6].

One of the commonly used distance metrics is Euclidean distance, the formula of it as follows:

$$d\ (x, y) = \sqrt{\sum_{i=1}^{n} (x_i - y_i)^2} \quad (2)$$

This formula based on Pythagorean Theorem; and it can be used to calculate the distance between two data points x and y in Euclidean space.

3) Logistic regression

Logistic regression (LR) is a statistical method used for binary classification tasks. Although its name regression, it is a classification algorithm. Logistic regression tries to make a logarithmic line that distinguishes between classes and its estimation is done through maximum likelihood. LR model depends on the sigmoid function where its logistic curve is limited between 0 and 1 values [7]. The expression of sigmoid function as follows:

$$\sigma(x) = \frac{1}{1 + e^{(-x)}} \quad (3)$$

The mathematical definition of the logistic sigmoid function shows that this function map any real value x into another value raged between 0 and 1. In machine learning, we used it to map predictions to probabilities.

4) Decision tree

Decision Tree (DT) is a supervised model and it is a decision support tool that uses a tree-like method. DT is a model consisting of internal nodes that represent attributes, branches that represent the outcome of the tests, and leaf nodes that represent classes\labels and decisions after the computing process. The paths between root and leaf represent decision rules for classification tasks [8].

5) Random forest classification

Random Forest (RF) is an ensemble method for classification and regression. RF model is a combination of different decision trees. The ensemble method is a machine learning technique that combines several base models or decision trees to produce one optimal model and predict with better performance than utilizing a single model [9].

B. Deep Learning Methods

Deep learning (DL) is a subfield of machine learning inspired by the structure of the human brain and biological neural networks. DL is known with its high performance and efficiency across many types of data.

1) Artificial neural network

Artificial Neural Network (ANN) is an efficient computing supervised model and its system depends on a biological neural network that is inspired by the structure of the human brain. ANN has neurons that are interconnected with each other. Each connection is associated with a weight that has information about the input signal and decides how much it is important for the model and related to the class\label.

ANN has become popular models for classification, regression, clustering, controlling model, and prediction in many applications [10].

In our work, we constructed our own ANN model using python's Keras library, the activation function that is used is ReLU and Softmax for the output layer, and the optimizer is Adam.

The structure of ANN model that used as in Fig. 2:

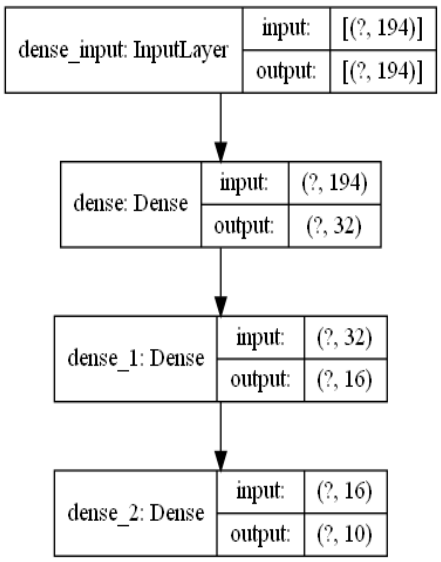


Fig. 2. Structure of layers in ANN model.

2) Multilayer Perceptron

Multilayer Perceptron (MLP) is a fully connected feed-forward artificial neural network (ANN). The feed-forward neural network was the first of NN that found and simplest type. In this network, the data move forwardly from the input layer through any hidden layer to the output without loops. The model can give different performance results depends on the number of hidden layers, the number of nodes in each layer, and the type of activation layer [10].

In our work, we used Scikit-learn python's library with MLPClassifier class that constructs MLP model with single hidden layer, the solver that is used is Adam, and for the output layer there is no activation function has applied but for other layers the activation function that is used is ReLU.

3) Convolutional neural network

Convolutional neural network (CNN) is one of the most powerful models in deep learning. CNN has excellent performance with different applications like image classification, video recognition, action recognition, and natural language processing (NLP). It handles input data as matrices for that we reshaped our input data before feeding it to be more convenient for the CNN module. CNN models have multiple layers, including convolutional layer, pooling layer, non-linearity layer, and fully connected layer [11]. We designed two different CNN models and their architectures described as below with Fig.3 and Fig. 4:

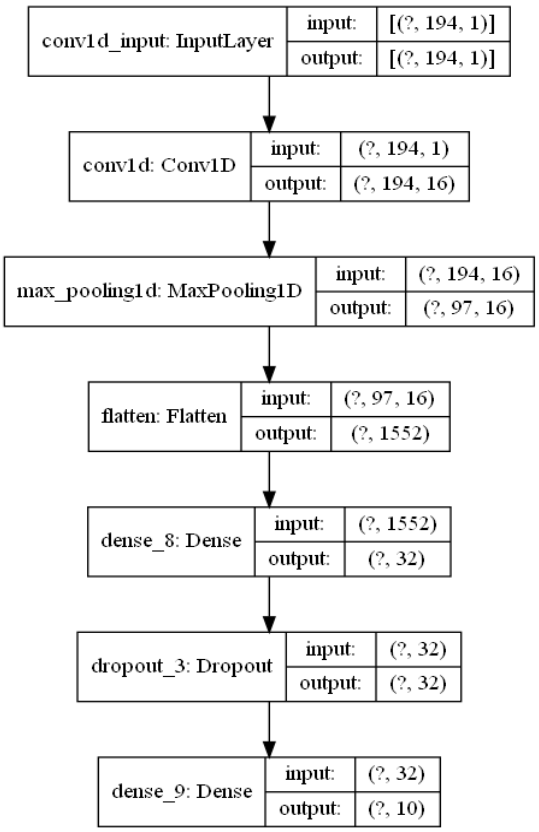


Fig. 3. Structure of layers in CNN-1 model.

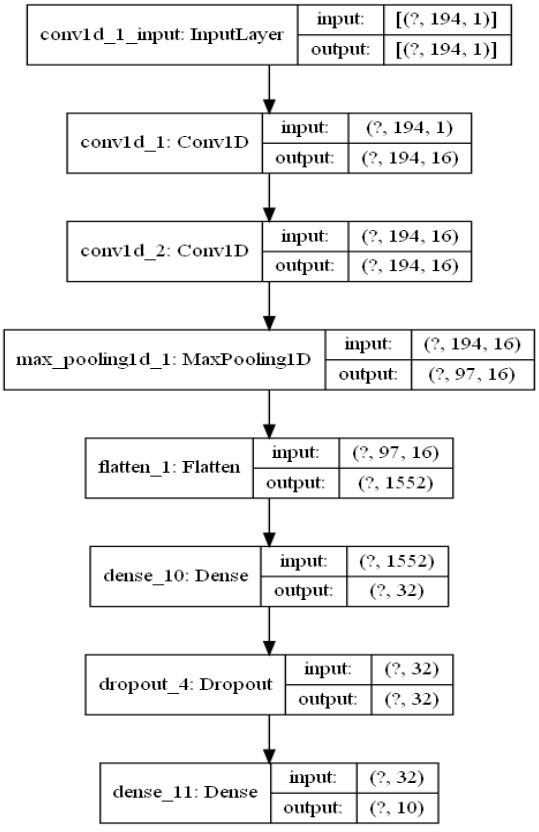


Fig. 4. Structure of layers in CNN-2 model.

As shown above, we can see that the structure of CNN-2 is more complicated than CNN-1.

4) Deep neural network

Deep neural network (DNN) is a neural network (NN) model with high complexity, usually at least two hidden layers. Deep net process data by employing sophisticated math methods [12]. In our work for DNN models, we used two different architectures DNN-2 and DNN-1. Similarly to CNN model DNN-2 structure is more complicated than DNN-1.

C. Evaluation Metrics

The applied models are evaluated by defining five performance parameters: accuracy, false alarm rate, precision, recall, and f1 score.

1) Accuracy

$$Accuracy = \frac{TN + TP}{FP + FN + TP + TN} \quad (4)$$

2) False alarm rate (FAR)

$$FAR = \frac{FP + FN}{FP + FN + TP + TN} \quad (5)$$

3) Precision

$$Precion = \frac{TP}{TP + FP} \quad (6)$$

4) Recall

$$Recall = \frac{TP}{TP + FN} \quad (7)$$

5) F1 score

$$F1_{score} = 2 * \frac{Precision * Recall}{Precision + Recall} \quad (8)$$

In addition to the accuracy, we used different evaluation metrics such as precision, recall and F1 since our data are imbalanced. In this case, the accuracy may cause to mislead evaluation of performance in some situations. As we can see from (8) F1 score is the harmonic mean value of recall and precision.

[4] ANALAYSIS AND RESULTS

As we can see in Table I and II we employed all feature space of UNSW-NB15 dataset for multiclass classification and binary configuration. In Table II and IV we used reduced feature vectors for multiclass classification and binary setting. In the experimental process, we applied different AI models that contain ML models and DL models. Here in the analysis section, we have 3 stages. In the first step, we tried to compare performance results for ML (binary and multiclass approaches) with full feature space that contains 42 attributes and with a reduced optimal vector (34 features) that generated using the Random Forest method. In the second stage, we tried to compare multiclass classification with binary configurations. In the third phase, we tried to compare DL performance results with ML results. In each table, the Test accuracy is accuracy that is obtained on testing data.

From Table I and II, the performance results demonstrated that the feature selection methodology

allows improving accuracies for such models as Random Forest accuracy increased from 75.38% to 75.90% and Decision Tree accuracy increased from 73.43% to 73.86%. These results represented for multiclass classification scheme.

For Table III Machine learning (ML) models for binary classification have applied without feature selection by using all our 42 features and for Table IV our ML models have applied with random forest feature selection method and we select most import 34 features.

As we can see from Table III and IV there is no performance improvement for binary classification tasks with the feature selection technique.

From Table I and III, if we tried to compare multiclass classification results with binary classification results either with using the feature selection technique or without it, obviously we can see that accuracies improved for Models:
Random Forest accuracy increased from 75.38% to 87.09%, Decision Tree accuracy increased from 73.43% to 86.36%, KNN from 70.93% to 84.48%, Logistic Regression from 68.51% to 80.93%, and Naive Bayes from 53.45% to 74.78%. It is a normal case because when classes number decreased, possible probabilities decreased, and the success rate will be increased and improved.

Table 1.Results using ML models with 42 features – multiclass classification

ML Model	Evaluation Results on Testing Data				
	Test Accuracy	*Test FAR rate*	*Test Precision*	*Test Recall*	*Test F1*
Random Forest	75.38	24.62	83.80	75.38	77.51
Decision Tree	73.43	26.57	80.75	73.43	76.26
KNN	70.93	29.07	79.04	70.93	73.85
Logistic Regression	68.51	31.49	76.94	68.51	69.96
Naive Bayes	53.45	46.55	74.91	53.45	58.35

Table 2. Results using ML models with 34 features (features selection) – multiclass classification

ML Model	Evaluation Results on Testing Data				
	Test Accuracy	*Test FAR rate*	*Test Precision*	*Test Recall*	*Test F1*
Random Forest	75.90	24.10	83.54	75.90	77.87
Decision Tree	73.86	26.14	80.52	73.86	76.35
KNN	70.59	29.41	78.72	70.59	73.53
Logistic Regression	67.92	32.08	76.04	67.92	69.52
Naive Bayes	54.44	45.56	72.95	54.44	58.22

Table 3. Results using ML models with 42 features – Binary classification

ML Model	Evaluation Results on Testing Data				
	Test Accuracy	*Test FAR rate*	*Test Precision*	*Test Recall*	*Test F1*
Random Forest	87.09	12.91	88.84	87.09	86.77
Decision Tree	86.36	13.64	87.29	86.36	86.13
KNN	84.48	15.52	86.17	84.48	84.07
Logistic Regression	80.93	19.07	84.03	80.93	80.07
Naive Bayes	74.78	25.22	76.68	74.78	74.74

Table 4. Results using ML models with 34 features (features selection) – Binary classification

ML Model	Evaluation Results on Testing Data				
	Test Accuracy	*Test FAR rate*	*Test Precision*	*Test Recall*	*Test F1*
Random Forest	86.97	13.03	88.82	86.97	86.64
Decision Tree	86.18	13.82	87.20	86.18	85.94
KNN	82.10	17.90	83.13	82.10	81.72
Logistic Regression	80.33	19.67	83.71	80.33	79.38
Naive Bayes	73.06	26.94	73.32	73.06	73.12

Table V and VI obtained DL performance results by using full feature space with 42 features for multiclass classification and binary classification, respectively.

As we explained we know that DNN-2 is more complicated than DNN-1 and the structure of CNN-2 is more convoluted than CNN-1.

In Table V DNN-2 (75.79%) model achieved better accuracy than DNN-1 (74.71%). Same for CNN-2 model obtained 74.12% accuracy while CNN-1 its accuracy value is 72.68%.

In Table VI the results demonstrated that the accuracy decreased from 86.98% for DNN-2 to 85.80% for DNN-1, while for CNN models the accuracy decreased from 86.03% for CNN-2 to 84.75% for CNN-1.

To comparison between ML and DL, we can say that DL models achieved higher accuracies than ML models. From Table I and V, we observed that while accuracies in DL models for multiclass classification between 75.79% and 72.68%; the accuracy results in ML models decreased until 53.45%, and in general accuracies values are between 75.38% and 53.45%.

From Table III and VI, we can see that while accuracies in DL models for binary classification between 86.98% and 84.75%; the accuracy results in ML models decreased until 74.78%, and in general accuracies values are between

87.09% and 74.78%. We observed that random forest and decision tree perform well this is because it is ensemble methods. From the results, we notice that more complex models get higher accuracies in some cases.

Table 5. Results using DL models with 42 features – multiclass classification

DL Model	Evaluation Results on Testing Data				
	Test Accuracy	*Test FAR rate*	*Test Precision*	*Test Recall*	*Test F1*
DNN-2 Model	75.79	24.21	79.81	75.79	76.41
DNN-1 Model	74.71	25.29	81.87	74.71	75.17
CNN-2 Model	74.12	25.88	82.65	74.12	74.53
ANN Model	74.02	25.98	80.71	74.02	74.76
Multi-Layer Perceptron	73.59	26.41	79.94	73.59	74.96
CNN-1 Model	72.68	27.32	79.24	72.68	73.06

Table 6. Results using DL models with 42 features – Binary classification

DL Model	Evaluation Results on Testing Data				
	Test Accuracy	*Test FAR rate*	*Test Precision*	*Test Recall*	*Test F1*
DNN-2 Model	86.98	13.02	88.83	86.98	86.64
CNN-2 Model	86.03	13.97	88.48	86.03	85.57
DNN-1 Model	85.80	14.20	87.88	85.80	85.38
ANN Model	85.45	14.55	87.96	85.45	84.96
Multi-Layer Perceptron	84.97	15.03	87.11	84.97	84.51
CNN-1 Model	84.75	15.25	87.71	84.75	84.16

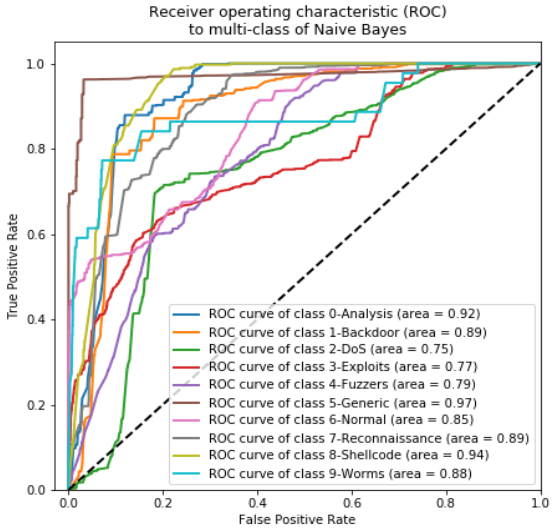


Fig. 5. Roc curve for ML models in multiclass classification problem

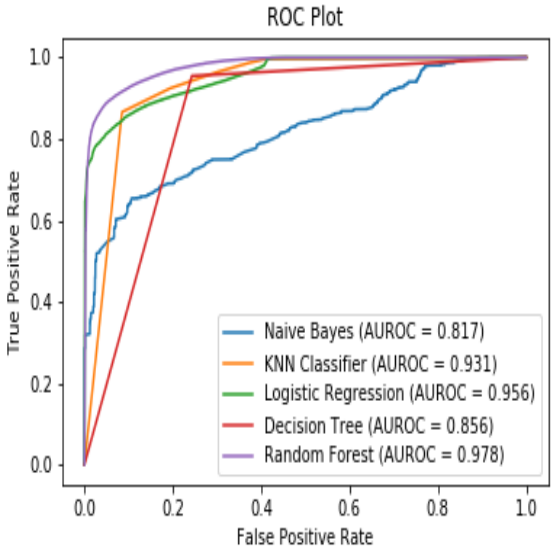


Fig. 6. Roc curve for ML models in binary classification problem

[5] CONCLUSION

In this research, we applied the flowing supervised Machine Learning (ML) methods for IDS: Naïve Bayes (NB), k-Nearest-Neighbor (kNN), Logistic Regression (LR), Decision Tree (DT) and Random Forest (RF). Also, Deep learning (DL) methodologies as: Multi-layer Perceptron (MLP), Artificial Neural Networks (ANN), Deep Neural Network (DNN), and Convolutional Neural Network (CNN). We applied the Random Forest algorithm over UNSW-NB15 dataset to calculate the feature importance measure for each feature, generate reduced optimal feature vectors. We considered two schemes binary and multiclass classification configurations. We compared different models using their performance results and accuracies.

In the future work, we can compare experimental results of UNSW-NB15 dataset with other datasets like Bot-IoT, CIC-IDS2018, and N-BaIoT datasets or we can create our

own dataset using simulation tools. We aim to be more creative in intrusion detection methods and increase accuracies using hybrid models by combining blockchain with deep learning algorithms. We think to add an intrusion prevention system (IPS) to IDS, this technology used to prevent and mitigate attacks and drop the malicious packets and threats.

REFERENCES

[1] K. K. Patel, S. M. Patel, and P. G. Scholar, "Internet of Things-IOT: Definition, Characteristics, Architecture, Enabling Technologies, Application & Future Challenges," *Int. J. Eng. Sci. Comput.*, vol. 6, no. 5, pp. 1–10, 2016, doi: 10.4010/2016.1482.

[2] A. Khraisat, I. Gondal, P. Vamplew, and J. Kamruzzaman, "Survey of intrusion detection systems: techniques, datasets and challenges," *Cybersecurity*, vol. 2, no. 1, 2019, doi: 10.1186/s42400-019-0038-7.

[3] N. Moustafa and J. Slay, "UNSW-NB15 : A Comprehensive Data set for Network Intrusion Detection systems," *Mil. Commun. Inf. Syst. Conf.*, no. November, 2015, doi: 10.1109/MilCIS.2015.7348942.

[4] G. Chandrashekar and F. Sahin, "A survey on feature selection methods," *Comput. Electr. Eng.*, vol. 40, no. 1, pp. 16–28, 2014, doi: 10.1016/j.compeleceng.2013.11.024.

[5] P. Kaviani and S. Dhotre, "International Journal of Advance Engineering and Research Short Survey on Naive Bayes Algorithm," *Int. J. Adv. Eng. Res. Dev.*, vol. 4, no. 11, pp. 607–611, 2017.

[6] K. Chomboon, P. Chujai, P. Teerarassammee, K. Kerdprasop, and N. Kerdprasop, "An Empirical Study of Distance Metrics for k-Nearest Neighbor Algorithm," *3rd Int. Conf. Ind. Appl. Eng.*, no. January 2015, pp. 280–285, 2015, doi: 10.12792/iciae2015.051.

[7] E. Y. Boateng and D. A. Abaye, "A Review of the Logistic Regression Model with Emphasis on Medical Research," *Data Anal. Inf. Process.*, no. January, 2019, doi: 10.4236/jdaip.2019.74012.

[8] S. R. Safavian and D. Landgrebe, "A Survey of Decision Tree Classifier Methodology A SURVEY OF DECISION TREE CLASSIFIER METHODOLOGY 1," *IEEE Trans. Syst. Man. Cybern.*, vol. 21, no. 3, pp. 660–674, 1991.

[9] L. E. O. Breiman, "Random Forests," *Mach. Learn.*, vol. 45, pp. 5–32, 2001.

[10] O. Isaac, A. Jantan, and A. Esther, "State-of-the-art [1] O. Isaac, A. Jantan, and A. Esther, 'State-of-the-art in artificial neural network applications : A survey,' Heliyon, vol. 4, no. June, p. e00938, 2018, doi: 10.1016/j.heliyon.2018.e00938.in artificial neural network applications :," *Heliyon*, vol. 4, no. June, p. e00938, 2018, doi: 10.1016/j.heliyon.2018.e00938.

[11] S. Albawi, T. A. Mohammed, and S. Al-Zawi, "Understanding of a convolutional neural network," *Proc. 2017 Int. Conf. Eng. Technol. ICET 2017*, vol. 2018-Janua, no. April 2018, pp. 1–6, 2018, doi: 10.1109/ICEngTechnol.2017.8308186.

[12] "What's a Deep Neural Network? Deep Nets Explained – BMC Software | Blogs." https://www.bmc.com/blogs/deep-neural-network/ (accessed Mar. 10, 2021).

POSTER PRESENTATIONS

Electrospun CA/MSNs nanofibrous mats for controlled release of methylene blue

Haslina Ahmad
Department of Chemistry, Faculty of Science University Putra Malaysia 43400 UPM Serdang, Selangor, Malaysia
haslina_ahmad@upm.edu.my

Yianchee Gan
Department of Chemistry, Faculty of Science University Putra Malaysia 43400 UPM Serdang, Selangor, Malaysia
chee1201@hotmail.com

Abstract*— Recently, the nanomaterials are broadly used in pharmaceutical field as drug delivery systems (DDSs). While burst release of drugs remained as the main challenge in DDSs, nanoparticles and nanofibers have gained tremendous attention due to its large surface area, high drug loading efficiency, and easy morphology control. In this study, a DDS based on the encapsulation of mesoporous silica nanoparticles (MSNs) into cellulose acetate (CA) nanofibers were prepared via electrospinning. Co-condensation technique was used to synthesis ionic liquids templated MSNs with average particles sizes of 70 nm. By loading the hydrophilic model drug methylene blue (MB) into MSNs, the MB-loaded MSNs were then incorporated into CA polymer solution to form electrospun nanofibrous mats. CA/MB nanofiber mats were also produced as control set. The morphologies of the nanoparticles and nanofibrous mats were studied by field emission scanning electron microscope (FESEM). The morphology of MSNs loaded CA nanofibrous mats showed that the MSNs were randomly dispersed on the CA nanofibers. Later, the in-vitro drug release profile of CA/MB-loaded MSNs nanofibrous mats, and CA/MB nanofibrous mats were studied. The results revealed that CA/MB loaded MSNs nanofibrous mats show sustained and prolonged release of drug compared to control set. The presences of MB loaded MSNs in CA nanofibrous mats were proved to minimize the burst release of drugs. The MB loaded composite nanofibrous mats synthesized can sustain the delivery of MB drugs up to 120 hours of controlled releasing period.

Keywords*—mesoporous silica nanoparticles, cellulose acetate, nanofiber, electrospinning, drug delivery

Detecting the main topics of citizens' comments in e-government

Gunay Iskandarli
Institute of Information Technology of ANAS
Baku, Azerbaijan
gunayniftali@gmail.com

***Abstract*—Topic Modeling Algorithms are statistical methods aimed to detect topics from text documents. Using these methods, we can quickly identify the main topics that the citizens are concerned or interested in through analyzing their comments. In this paper, an approach for analysing citizen's comments in e-government with the help of topic modelling and clustering algorithms has been proposed. The main goal of the proposed approach is to develop the efficiency of the clustering algorithm and the accuracy of the topic modelling algorithm by improving vector formulation of comments (documents). Thus, two words with the same meaning in the document may fall into different groups because of their differing spelling. This can be lead to increase groups number and inaccuracy. In order to prevent such situations, before the clustering of documents, semantic similarity of words in vector is determined. If the words are similar each other, only one of these words is saved, others are not accepted. Thus, the size of the vector decreases. Documents are clustered through the K-Means algorithm after describing documents as vector. Then, cluster topics are defined by applying LDA to clusters.**

***Keywords —social networks; e-government; text mining; topic modeling; K-Means*.**

I. INTRODUCTION

In recent years social networks such as Facebook, MySpace, Twitter have become an important means of communication for people all over the world. These sites are increasingly used to deliver the latest news and manage a large audience. Users of these Web sites get information on both individually and globally important events in time. For example, Twitter has been used to spread real-time information in many crises, such as the results of Iranian elections, the tsunami that occurred in Samoa, and the Haiti earthquakes. Investigations conducted in various research fields show the increasing interest in micro-blog services [1].

As known, e-government is one of the most important social platforms currently used. Today, the key factor of each government is to create a strong partnership with citizens effectively delivering them the messages and promoting their participation in the decision-making process. Promising e-government initiatives have been set up to provide access to public services and facilitate the delivery of information to citizens [2,3].

E-government services should increase the efficiency of services, reduce service costs and improve service quality, taking into account the needs of the public on the basis of their interests [4]. State public services should be based on the demand principles, and then the construction of the system should be carried out. For this purpose, government agencies should be interactive in informing the citizens about their information needs and determine the real needs of the community. This process requires a collection of public opinion. However, such user opinions lead to the creation of large text information. Analysis of such information creates some difficulties because of their complex, non-structural nature. For analysis of such data and detection of correlation is intended to use advanced computational and analytical tools such as text mining. Recently, topic modeling methods have become popular to determine what issues people are discussing. Topic Modeling Algorithms are statistical methods to analyze words in text documents. These models, which are used in machine learning and text mining, are successfully applied to defining hidden topics in a large number of documents. These algorithms are interpreted as a soft (fuzzy) classification of documents in the classification problem. In addition, the results of these models can be used to include a document in just one group.

Note that, on the other hand, clustering of documents can simplify topic modeling algorithms. Clustering and topic modeling are two closely related methods that benefit each other. As it is known, the majority of documents are usually referred to several groups. For example, papers in scientic paper archive such as Google Scholar, could include different areas (such as math, biology, computer science, economics). Each group (area) has its own topics. For example, computer science articles cover topics such as, system, network, big data, and et.al. Clustering can help identify the latent groups in a document collection and subsequently we can identify local topics specific to each group and global topics shared by all groups by exploiting the grouping structure of documents [5].

Considering this, in the paper, a method for analyzing citizens comments on services in the e-government environment have been proposed. In the proposed method, topic modeling and clustering algorithms were used.

II. TOPIC MODELING, APPLICATION FIELDS, AND CURRENT APPROACHES

Recently, the rapid increase in the number of e-documents requires the use of new techniques and tools for their management, organization, search and so on. Based on machine learning and statistical research, new methods have been developed to find samples of words in document collections by the use of hierarchical probability models. These models are called "topic models" [6]. Topic models are popular methods performed to model the frequency of terms occurrence in text documents.

In topic modeling, each document is accepted as a mixture of topics, and each topic is the probability distribution on words. In other words, topic model is a generative model for documents. This model performs a simple probability procedure that documents can be generated [7].

From the text analysis and the text mining position, topical

models are based on the theory of a "word bag" without seeing the information occurred from the position (order) of words. Latent Semantic Analysis (LSA), Probabilistic Latent Semantic Analysis (PLSA), Latent Dirichlet Allocation (LDA) and other topics have been successfully applied in improving the classification accuracy in the field of the topic detection from documents [8,9].

Latent Semantic Analysis: Latent Semantic Analysis (LSA) is one of the methods used in Natural Language Processing. LSA's main goal is to generate a vector-based sample for texts to create semantic content. Here, the closeness between texts is calculated to select the related words. In the past, the LSA was called Latent Semantic Indexing but was later improved for the information retrieval. Through this method, many documents are selected from a multi-documents.

Probabilistic Latent Semantic Analysis: Probabilistic Latent Semantic Analysis (PLSA) is an approach to overcome some shortcomings included in this method after the LSA method. Jan Puzicha and Thomas Hofmann presented it in 1999. PLSA is a method created to automate indexing of documents based on a latent class model for factor analysis of numeric data. The main purpose of PLSA is to distinguish between different contextualities of the word without using vocabulary or thesaurus. It has two important effects: First, this method allows for distinguishing polysemantic words. Secondly, it defines typical similarities by grouping words that share common content. PLSA is successfully applied in areas such as Image retrieval, Automatic question recommendation, and so on [10, 11].

Latent Dirichlet Allocation: The main purpose of creating a Latent Dirichlet Allocation (LDA) is to develop the PLSA and LSA methods. LDA is a text mining algorithm based on statistical (Bayesian) topic models and used widely. LDA is a generative model that tries to imitate the writing process. LDA-based models are the following: temporal text mining, author- topic analysis, supervised topic models, latent Dirichlet co-clustering və LDA based bioinformatics [12].

LDA model is one of the most common algorithms for topic modeling. Here two main principles are followed: 1) Each document is a mixture of topics; 2) Each topic is a mix of words. Simply, the main idea of the process is that: each document is modeled as a mixture of topics, and each topic is a discrete probability distribution that determines how each word will appear in a particular topic. Here, the "document" is regarded as a "bag of words" that has not another structure than the topic and word statistics. In LDA model, each document D is distributed over latent topics. The basic steps of the algorithm are described below:

Stage 1: Randomly assign each word in each document to one of the K topics.

Stage 2: For each document d :

- Assume that all topic assignments except for the current one are correct.
- Calculate two proportions:

1. Proportion of words in document d that are currently assigned to topic t ($p(topict|document\,d)$).
2. Proportion of assignments to topic t over all documents that came from this word w ($p(word\ w|topict)$)
   - Multiply those two proportions and assign w a new topic based on that probabilty ($p(topict|document\,d) * p(word\ w|topict)$).

Stage 3: Eventually reach a steady state where assignments make sense.

LDA is expressed mathematically by the following way:

$$p(\beta_{1:K}, \theta_{1:D}, z_{1:D}, w_{1:D}) =$$

$$\prod_{i=1}^{k} p(\beta_i) \prod_{d=1}^{D} p(\theta_d) (\prod_{n=1}^{N} p(z_{d,n}|\theta_d) p(w_{d,n}|\beta_{1:K}, z_{d,n}))$$

$\beta_{1:K}$ - is a topics, β_k - is a distribution over the words in corpus (vocabulary), $\theta_{1:D}$ - is a topic distribution for d -th document, z_d - is the topic samples for d --th document, $z_{d,n}$ - is the topic sample for n - th word in the d -th document, , ie. it is a topic that the n -th word refers to in the d -th document,, w_d - is a word observed in the d -th document,, $w_{d,n}$ - is a n -th word in the d -th document.

The application areas of LDA include: Emotion topic, Automatic essay grading, Anti-Phishing, etc. [13].

In literature, a number of methods and approaches have been proposed to improve topic modeling methods. On one of these approaches, a method has been proposed to improve the quality of clustering by using topic and fusion patterns. The main idea in this method is to develop the vector of documents to increase the quality of clustering. For this purpose, the topic modelling is applied to the collection of documents for several times, and the specific topics are determined for each document on each iteration. Then, to obtain a single topic vector for each document, the vector of special topics obtained from the available iterations is combined. Created topics are the vectors used in the clustering of documents collection [14].

In another approach, the clustering method is primarily applied to the document sets, and then the topics are removed from each cluster. Four stages are used for this purpose. In the first stage, similar documents are grouped through the clustering method to prepare documents for the generalization process. In the second stage, the LDA algorithm is applied to each cluster to determine the cluster topics. In the third stage, global frequency terms are removed from topical terms, and words that are semantically close to them are identified using WordNet. In the last stage, sentences are chosen and summarized, including the terms and their closest words [15].

From these approaches, it can be observed that the two words with the same meaning can be included in 2 different topics because of their various spelling. This can lead to an increase in the number of topics. It can also complicate clustering at following stages. In the next section, the method has been proposed to avoid this problem and save time.

III.topic modeling approach in e-government

In order to improve the accessibility and effectiveness of e-government services, it is necessary regularly to conduct user-oriented assessments. As a result of this assessment, it is possible to improve the quality of resources and e-government websites services by examining the ability of citizens usage from e-government. Here some issues should be considered:

- What services do citizens need most?
- How can we find the priorities of services that truly reflect the needs of citizens?
- How do people think about the use of e-government services? and so on.

Gathering users' opinions and recommendations into an only portal, we can get information about citizens opinions on some issues. As known, in the e-government environment, the citizens can express their opinion by writing comments on any service. By analyzing these comments, it is possible to identify the main issues that they are concerned about. It is known that, as the number of comment increases, it becomes difficult to analyze them. It is important to use text mining methods to quickly identify key points that people are concerned about (recommended). Considering these, in paper has been proposed a method to determine which topics they are concerned or interested in by analyzing citizen comments in the e-government environment. In the proposed method the LDA algorithm and K-Means were used. The method is explained in detail below:

First, the comments are considered as a set of documents and are signed as follows:

$$D = \{d_1, d_2, ..., d_n\} \quad (1)$$

where n -is the number of documents. Then, the documents are pre-processed. During the pre-processing, common words and punctuation marks from documents are cleared. All words are returned to the original version because every word accepts different affixes. The set of terms found in document sets are noted as follows:

$$T = \{t_1, t_2, ..., t_m\} \quad (2)$$

m - is a number of terms mentioned in documents. In (2) can have 2 different words that have the same meaning and they may be grouped into different groups because of their various spelling. This can be lead to the increase of groups' number and inaccuracy. In order to avoid such situations, the semantic proximity of the words included in the vector is found before the clustering of documents. For this purpose, we first found the "synonyms" of each term using the WordNet network:

$$t_k = \{t_{k1}, ..., t_{km}\}, \quad k = 1.2, ..., m \quad (3)$$

where $\{t_{k1}, ..., t_{km}\}$ - is the k -th word's synonyms. After describing each term in this way, we suggest the use of WUP metric to find out how similar they are to each other. If $\forall s, j$ $WUP(t_s, t_j) > \delta$, so the two terms are treated as semantic words or synonyms. Where δ - is a predefined threshold.

After obtaining words that are synonymous with each other through the WUP metric, only one of these synonyms is saved, others are ignored. So, we reduce the size of the T vector. In this case, the T vector is transformed to the following vector:

$$T = \{t_1, t_2, ..., t_{m_0}\}, \quad m_0 \leq m \quad (4)$$

Then, using TF * IDF, each document is presented as a vector below:

$$d_i = \{w_{i1}, w_{i2} ..., w_{im_0}\}, \quad i = 1,2, ..., n \quad (5)$$

Documents are clustered through the K-means algorithm after describing documents as vector. K-means is considered to be one of the most popular algorithms in the analysis of big data due to its low-performance time and ease of use. After the clustering of documents, we can find the topics for each cluster. For this purpose, the usage of LDA is proposed. The process is schematically illustrated in Fig. 1.

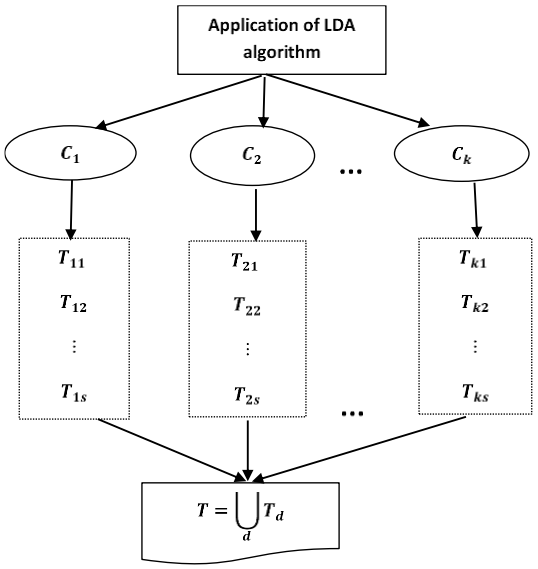


Fig.1. Extraction of topics from the clusters

Thus, we have identified the main topics of the comments written by citizens.

CONCLUSION

Evaluation of services should be carried out regularly to improve accessibility and effectiveness of e-government services to citizens. In order to define the impact of e-government services on their current situation and their impact on citizens, the content of these services should be analyzed along with the technical quality of these services. By analyzing comments written to these services, it is possible to improve the quality of services and reduce existing dissatisfaction. LDA topic models can be used to analyze big data of the users' opinions and recommendations to determine quickly what they are considering. Considering this, in the paper a method for analyzing citizen's comments using the LDA algorithm and K-Means clustering methods has been proposed. The main purpose of the method is to increase the efficiency of clustering, minimize the number of vectors, and increase the accuracy of the vectors. In future, the method is intended to be experimentally implemented.

ACKNOWLEDGMENTS

This work was supported by the Science Development Foundation under the President of the Republic of Azerbaijan – Grant No. EIF-BGM-4-RFTF-1/2017-21/08/1.

REFERENCES

[1] L. Hong, B. D. Davison, "Empirical Study of Topic Modeling in Twitter", Proceedings of the First Workshop on Social Media Analytics, pp.80-88, 2010.

[2] Ch.-Ch. Huang, "User's Segmentation on Continued Knowledge Management System Use in the Public Sector", *Journal of Organizational and End User Computing*, vol.32, no.1, pp. 19-40, 2020.
[3] G.Y.Iskandarli, "Using Hotspot Information to Evaluate Citizen Satisfaction in E-Government: Hotspot Information", *International Journal of Public Administration in the Digital Age*, vol.7, no. 1, pp. 47- 62, 2020.
[4] M. P. Gupta, D. Jana, "E-government evaluation: A framework and case study", Government Information Quarterly, vol. 20, no.4, pp. 365–387, 2003.
[5] P. Xie, E.P. Xing, "Integrating Document Clustering and Topic Modeling", Proceedings of the Twenty-Ninth Conference on Uncertainty in Artificial Intelligence, pp. 694-703, 2013.
[6] R. Alghamdi, K. Alfalqi, "A Survey of Topic Modeling in Text Mining", International Journal of Advanced Computer Science and Applications, vol. 6, no. 1, pp. 147-153, 2015.
[7] K. E. C. Levy, M. Franklin, "Driving Regulation: Using Topic Models to Examine Political Contention in the U.S. Trucking Industry", Social Science Computer Review, vol.32, no.2, pp. 182-194, 2013.
[8] Blei, D. M. (2011). Introduction to probabilistic topic models. Communications of the ACM, 2011. Retrieved from http://www.cs.princeton.edu/*blei/papers/Blei2011.pdf
[9] S. I. Nikolenko, S. Koltcov, O. Koltsova, "Topic modeling for qualitative studies", Journal of Information Science, vol. 43,no. 1, pp.88- 102, 2017.
[10] S. Liu, C. Xia, X. Jiang, "Efficient Probabilistic Latent Semantic Analysis with Sparsity Control", IEEE International Conference on Data Mining, pp. 905-910, 2010.
[11] T. Hofmann, "Unsupervised learning by probabilistic latent semantic analysis", Machine Learning, vol. 42, no. 1, pp. 177-196, 2001.
[12] D. M. Blei, A.Y. Ng, M..I. Jordan, "Latent Dirichlet Allocation", Journal of Machine Learning Research, vol.3, pp.993-1022, 2003.
[13] T. Kakkonen, N. Myller, E.Sutinen, "Applying latent Dirichlet allocation to automatic essay grading", Lecture Notes in Computer Science, vol.4139, pp.110-120, 2006.
[14] M. Pourvali, S. Orlando, H. Omidvarborna, " Topic Models and Fusion Methods: a Union to Improve Text Clustering and Cluster Labeling", International Journal of Interactive Multimedia and Artificial Intelligence, vol. 5, no. 4, pp. 28-34, 2018.
[15] N. K. Nagwani, "Summarizing large text collection using topic modeling and clustering based on MapReduce framework", Journal of Big Data, vol.2, no.6, pp.1-18, 2015.

ANN-based statistical downscaling for daily rainfall estimation

Khaled Alramalwi
Dokuz Eylul University, The Graduate School of Natural and Applied Sciences, Civil Engineering Department.
Izmir, Turkey
khaled.alramlawi@ogr.deu.edu.tr

Okan Fıstıkoğlu
Dokuz Eylul University, The Graduate School of Natural and Applied Sciences, Civil Engineering Department,
Izmir, Turkey
okan.fistikoglu@deu.edu.tr

***Abstract*— Global large-scale atmospheric datasets serve climate studies as a comprehensive set of explanatory predictors to estimate local or regional atmospheric conditions. The estimation of local weather parameters from large-scale atmospheric data is called downscaling.**

Many statistical downscaling techniques have been proposed in the past few years to assess the impacts of climate change on hydrological systems.

In the presented study, the ANN-based statistically downscaling approach is used to estimate the daily rainfall observations of the Izmir station. The large-scale atmospheric parameters of the NCEP/NCAR re-analysis dataset on different pressure and surface levels are used as inputs of the ANN models, and those parameters are transformed into the daily rainfall estimations.

The results show that the ANN-based downscaling model, which considers the present and one-day previous atmospheric parameters as input, gives best results. The results also reveal that the antecedent large-scale atmospheric conditions significantly influence the present local weather conditions over Izmir city.

Keywords*— *Statistical downscaling model, artificial neural networks (ANN), daily precipitation, Izmir city.

[1] INTRODUCTION

General circulation models (GCMs) and global large-scale atmospheric datasets are mainly used to understand the present and future climate [1]. However, the outputs of the GCMs are too coarse and cannot be directly used for understanding the dynamics of climate change on a local scale [2]. Downscaling methods widely used link the climate dynamics between larger resolution data and the local scale atmospheric parameters [3].

Local weather of a region depends on the synoptic patterns evolving in large-scale atmospheric coverage over the region. Global large-scale atmospheric datasets serve climate studies as a set of explanatory predictors of local or regional atmospheric conditions. As they have a coarse spatial resolution, disclosing their relations to local weather conditions requires a proper downscaling strategy.

National Centers for Environmental Prediction and National Center for Atmospheric Research (NCEP/NCAR) distribute the re-analyzed global atmospheric data with 2.5^0 spatial resolution from 1948 to today, and this worldwide dataset is used to establish the relations between local weather and large-scale conditions that are called downscaling [4].

Several downscaling methodologies have been developed. They are classified as dynamic downscaling and statistical downscaling. Dynamic downscaling is very computationally intensive, complicated, and requires substantial computational resources [5], [6], while the alternative method, the statistical downscaling, which is widely used in assessing the impacts of changing climate practically, is simple and require lower computational efforts as compared to dynamic downscaling. Statistical downscaling, uses statistical relationships to predict local weather parameters (predictants) from large-scale atmospheric variables (predictors)

The most common statistical downscaling approaches are the transfer functions [7]. Transfer function examples range from linear and nonlinear regression, principal component analysis, canonical correlation, and redundancy analysis to Artificial Neural Networks (ANN) [8], [9], [10].

Several recent studies have used the artificial neural network (ANN) to downscale the atmospheric variables to local weather parameters such as precipitation and temperature [10], [11], [12].

In this study, an ANN-based downscaling approach was applied to the NCEP/NCAR reanalysis dataset to estimate the daily rainfall series observed in the Izmir region. Three lag time of the NCEP/NCAR re-analysis dataset were analyzed to achieve the best daily rainfall estimation in the study area.

[2] STUDY AREA AND DATASETS

The study area is Izmir city, located at the Aegean coast of Turkey (Fig. 1). Izmir is the third largest city in Turkey, and it suffers from urban floods due to the increasing urbanization, and extreme rainfall events occurred frequently. Izmir city and its surroundings have the typical Mediterranean climate

A. Observed station data (predictands):

Six stations around Izmir city are selected to represent the daily rainfall distribution in the study area. Fig. 1. and table .1 show the station locations and the available data used in the study. The statistical downscaling models were developed using the Izmir station's data in the period of 1948 to 1990 (42 years), and the models were tested using the rainfall records of the same station for the period of 1991–2018. The other neighbor stations around Izmir city were only used to test the results of downscaling models regarding the spatial consistency of the daily rainfall estimations. The observed correlations of daily rainfall between Izmir and neighboring stations vary in the range of 0.82–0.61. As expected, the nearer stations show higher correlations while the far stations are less correlated with the Izmir stations.

B. Reanalysis data (predictors):

NCEP/NCAR reanalysis dataset is available from 1948 to the present, with a spatial resolution of 2.5° x 2.5° [13]. The data were downloaded from the NCEP/NCAR reanalysis project website. The selection of predictors depends on several factors such as the characteristics of the large-scale

atmospheric circulation, seasonality, and the predictand to be downscaled [14]. In this study, the predictors were selected, considering the rainfall mechanism where temperature, relative humidity, pressure, and upward wind speeds have major roles. Therefore, 13 atmospheric variables at different pressure levels were selected as predictors. The selected NCEP/NCAR reanalysis parameters for the study region are listed in Table 2.

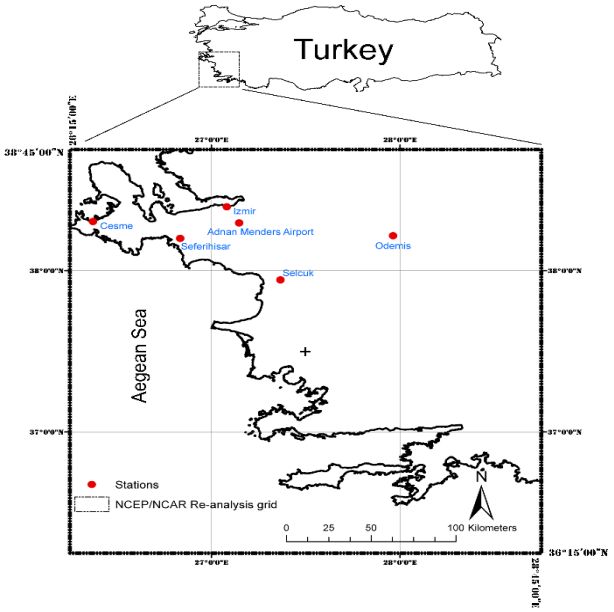


Fig. 1. Geographical locations of the study area and stations within the NCEP/NCAR Grid.

Table 5. The rainfall stations used in the study.

No	Name of stations	Latitude	longitude	available data	
1	Izmir	38.39	27.08	1948	2018
2	Adnan Menderes	38.29	27.15	2009	2018
3	Seferehisar	38.19	26.83	1980	2011
4	Cesme	38.30	26.37	1965	2018
5	Odemis	38.21	27.96	1960	2011
6	Selcuk	37.94	27.36	1965	2011

Table 6. The selected predictors from (NCEP/NCAR) Reanalysis data set.

Atmospheric level	Selected mean daily variables	Abbr.
500 hpa	Air temperature	air500
	Geopotential height	hgt500
	Relative humidity	rhum500
850 hpa	Air temperature	Air850
	Geopotential height	Hgt850
	Relative humidity	rhum850
Surface	Air temperature	Air
	Specific humidity at 2 m	shum
	Pressure at surface	pres
	Sea level pressure	slp
	Relative humidity	rhum
	V-wind at 10 m	vwid
	Precipitable water for entire atmosphere	pr

[3] METHODOLOGY

The ANN-based statistical downscaling model structure designed in the scope of this study consists of three types of layers: i) input layer with n nodes that are 13 atmospheric variables selected from NCEP/NCAR reanalysis dataset as the predictors, ii) hidden layer with several nodes, the optimum number of nodes were determined by trial and error approach and all hidden neurons transform the inputs nonlinearly into another dimension through weights and biases, iii) output layer containing daily rainfall estimations of the Izmir station (Fig. 2.).

Searching the optimal value of the weights and biases is called learning or training of the ANN. In this study, the well-known Levenberg-Marquardt feed forward-back-propagation algorithm is used for training the downscaling networks.

Tangent sigmoid, linear, and log-sigmoid are the most common transfer functions used to evaluate ANN construction phases. In the presented study, the tangent sigmoid and linear functions give the best results in the hidden and output layers, respectively.

As the past and present large-scale atmospheric conditions significantly influence the current local weather conditions, the present and antecedent large-scale atmospheric parameters were considered inputs for the daily downscaling networks. The three statistical downscaling models used in this study i) first model (Model-1) [$NCEP_t$] uses atmospheric variables on the current day (t) as predictors, ii) the second model (Model-2) [$NCEP_t$, $NCEP_{t-1}$] considers the atmospheric variables of previous (t-1) and current (t) day are used as predictors, iii) the third model (Model-3) [$NCEP_t$, $NCEP_{t-1}$, $NCEP_{t-2}$] uses the previous two-day atmospheric variables.

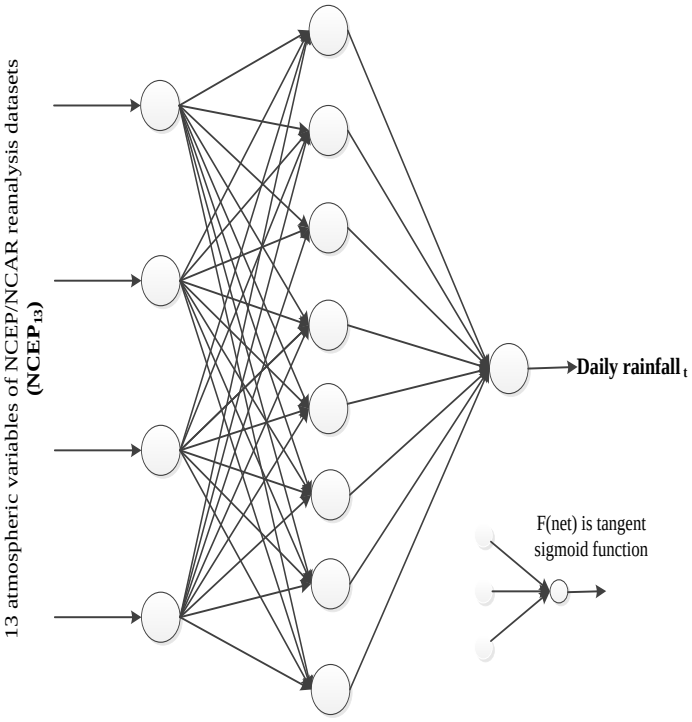


Fig. 2. The structure of the ANN-based downscaling mode [15]

The methodology of the study is summarized in Fig. 3.

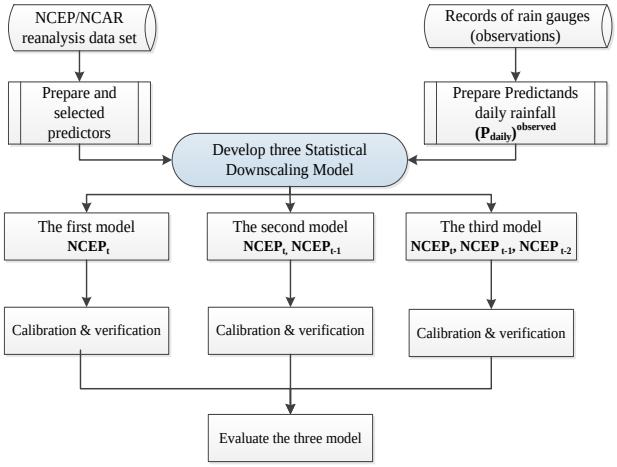


Fig. 3. The proposed methodology.

[4] RESULTS

The correlation coefficient (r) and the root mean squared errors (RMSE) were used to evaluate the three downscaling models' performance for estimating the daily rainfall. The best model has the lowest RMSE and the highest r values between the observed and estimated series of the daily rainfall of Izmir station.

Table 3. shows the r between estimated and observed daily rainfall series of Izmir station and the r between estimated Izmir daily rainfall and neighborhood stations. Table 4. also show the RMSE value between the observed and estimated daily rainfall series at the Izmir stations. Fig. 4. shows scatter diagrams illustrating the relationship between the observed and simulated daily rainfall for the Izmir station during both the training and testing period.

Table 7. R of the simulated and observed daily rainfall for each station.

	Model-1 (NCEP)t	Model-2 $(NCEP)_t$, $(NCEP)_{t-1}$	Model-3 $(NCEP)_t$ $(NCEP)_{t-1}$ $(NCEP)_{t-2}$
Name of stations	R	R	R
Izmir (training period)	0.60	0.74	0.74
Izmir (testing period)	0.58	0.68	0.67
Adnan Menderes	0.61	0.71	0.70
Seferihisar	0.51	0.59	0.59
Cesme	0.52	0.57	0.57
Odemis	0.53	0.64	0.60
Selcuk	0.57	0.66	0.65

Table 8. RMSE of the simulated and observed daily rainfall for each station.

	Model-1 $(NCEP)_t$	Model-2 $(NCEP)_t$ $(NCEP)_{t-1}$	Model-3 $(NCEP)_t$ $(NCEP)_{t-1}$ $(NCEP)_{t-2}$
Name of stations	RMSE	RMSE	RMSE
Izmir (Training period)	5.256	4.41	4.46
Izmir (testing period)	5.91	5.25	5.33

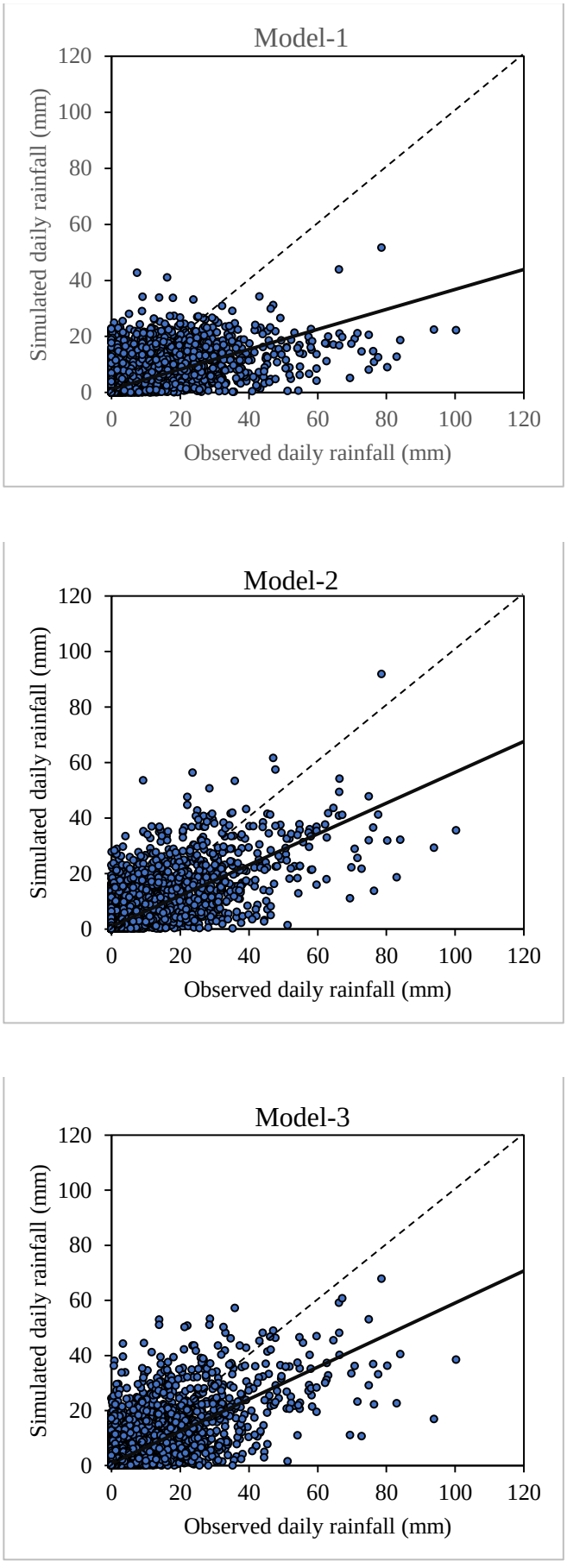


Fig. 4. Scatter diagram of the observed and estimated rainfall of the three models during both training and testing period.

Tables 3. and 4. clearly show that the second ANN model (Model-2), which uses the previous day's atmospheric variables as inputs, gives the best results. The first model (Model-1), which uses the atmospheric variables on the present day (t) as predictors, gives the worst results. The results of the third model (Model-3) are similar to the second model's results, but the third model has a higher number of predictors and less accuracy. Model-2 successfully estimates the daily rainfall of the Izmir station from the large-scale atmospheric parameters.

The high correlations between neighbor stations (in Table 3) indicate that Model-2 [$NCEP_t$, $NCEP_{t-1}$] based downscaled daily rainfall of the Izmir station is also spatially consistent with the other stations' rainfall. This result reveals that estimations of Model-2 preserve the spatial properties of the rainfall distribution existing in the study area.

[5] CONCLUSIONS

In the presented study, artificial neural networks (ANN) were employed to establish three statistical downscaling models over Izmir city in order to estimate daily rainfall from large-scale NCEP/NCAR reanalysis datasets. Then, observations of the neighbor stations were used to test spatial validation of the downscaling models. In the study, three models were established depending on the present and antecedent large-scale atmospheric parameters.

The second model (Model-2), which uses atmospheric variables of the current and previous days as predictors to estimate daily rainfall, has better performance than other alternative models. The large-scale atmospheric conditions of the present and one antecedent day have a dominant role in the daily rainfall values of the present day in the study area.

The results proved that the antecedent large-scale atmospheric conditions significantly influence the current local weather. The atmospheric parameters can be downscaled to any other weather parameters such as temperature or humidity as well as rainfall in order to fill the gaps in the local datasets or to extend the datasets.

REFERENCES

[1] Salman, S. A., Shahid, S., Ismail, T., Ahmed, K., and Wang, X. J., Selection of climate models for projection of spatiotemporal changes in temperature of Iraq with uncertainties, *Atmos. Res.*, vol. 213, pp. 509–522, Nov. 2018.

[2] Noor, M., Ismail, T. Bin, Ullah, S., Iqbal, Z., Nawaz, N., and Ahmed, K., A non-local model output statistics approach for the downscaling of cmip5 gcms for the projection of rainfall in peninsular malaysia, *J. Water Clim. Chang.*, vol. 11, no. 4, pp. 944–955, 2020.

[3] Sachindra, D. A. and Perera, B. J. C., Statistical downscaling of general circulation model outputs to precipitation accounting for non-stationarities in predictor-predictand relationships, *PLoS One*, vol. 11, no. 12, p. e0168701, Dec. 2016.

[4] Kalnay, E. *et al.*, The NCEP/NCAR 40-year reanalysis project, *Bull. Am. Meteorol. Soc.*, vol. 77, no. 3, pp. 437–471, Mar. 1996.

[5] Murphy, J., An evaluation of statistical and dynamical techniques for downscaling local climate, *J. Clim.*, vol. 12, no. 8, pp. 2256–2284, Aug. 1999.

[6] Trzaska, Y. and Schnarr, E., A Review of Downscaling Methods for Climate Change Projections (USAID, 2014), 2014.

[7] Schoof, J. T., Pryor, S. C., and Robeson, S. M., Downscaling daily maximum and minimum temperatures in the midwestern USA: a hybrid empirical approach, *Int. J. Climatol.*, vol. 27, no. 4, pp. 439–454, Mar. 2007.

[8] Benestad, R. E., Hanssen-Bauer, I., and Førland, E. J., An evaluation of statistical models for downscaling precipitation and their ability to capture long-term trends, *Int. J. Climatol.*, vol. 27, no. 5, pp. 649–665, Apr. 2007.

[9] Fistikoglu, O. and Okkan, U., Statistical downscaling of monthly precipitation using NCEP/NCAR reanalysis data for Tahtali river basin in Turkey, *J. Hydrol. Eng.*, vol. 16, no. 2, pp. 157–164, Feb. 2011.

[10] Vu, M. T., Aribarg, T., Supratid, S., Raghavan, S. V., and Liong, S. Y., Statistical downscaling rainfall using artificial neural network: significantly wetter Bangkok?, *Theor. Appl. Climatol.*, vol. 126, no. 3–4, pp. 453–467, Nov. 2016.

[11] Okkan, U. and Fistikoglu, O., Evaluating climate change effects on runoff by statistical downscaling and hydrological model GR2M, *Theor. Appl. Climatol.*, vol. 117, no. 1, pp. 343–361, Sep. 2014.

[12] Nourani, V., Razzaghzadeh, Z., Baghanam, A. H., and Molajou, A., ANN-based statistical downscaling of climatic parameters using decision tree predictor screening method, *Theor. Appl. Climatol.*, vol. 137, no. 3–4, pp. 1729–1746, Aug. 2019.

[13] Hofer, M., Mölg, T., Marzeion, B., and Kaser, G., Empirical-statistical downscaling of reanalysis data to high-resolution air temperature and specific humidity above a glacier surface (Cordillera Blanca, Peru), *J. Geophys. Res. Atmos.*, vol. 115, no. 12, 2010.

[14] Anandhi, A., Srinivas, V. V., Kumar, D. N., and Nanjundiah, R. S., Role of predictors in downscaling surface temperature to river basin in India for IPCC SRES scenarios using support vector machine, *Int. J. Climatol.*, vol. 29, no. 4, pp. 583–603, Mar. 2009.

[15] Seyam, M. *et al.*, Investigation of the Influence of Excess Pumping on Groundwater Salinity in the Gaza Coastal Aquifer (Palestine) Using Three Predicted Future Scenarios, *Water*, vol. 12, no. 8, p. 2218, Aug. 2020.

Fault Tolerant Control of Five-phase IPMSMs under Opened Phase Fault Based on MTPA Operation

Y. Zafari
Department of Electrical Engineering, Miandoab Branch, Islamic Azad University, Miandoab, Iran
zafari.yaser@yahoo.com

A. Hosseyni
Monastir National Engineering School, Monastir University, Ibn, Eljazzar City, 5019 Monastir.
hosseyni.anissa@yahoo.com

S.Shoja- Majidabad
Department of Electrical Engineering, University of Bonab, Bonab, Iran.
shoja.sajjad@ubonab.ac.ir

***Abstract*—In this paper, fault tolerant control of Five-Phase Interior Permanent Magnet Synchronous Motor (IPMSM) has been studied under opened one phase fault. Thus, an Integral Sliding Mode Controller (ISMC) is proposed based on maximum torque per ampere operation. The suggested approach is equipped with a fault detection and diagnose unit to isolate the opened phase from the rest of drive system. The simulation results back up the effectiveness of the proposed method. Besides, stability of the closed-loop system is assured utilizing the Lyapunov stability theorem.**

***Keywords*—Five-phase IPMSM, Opened phase fault, FTC, MTPA, ISMC.**

[1] INTRODUCTION

Nowadays, the multi-phase Interior permanent magnet synchronous machines are used in the lots of applications. Due to the some inherent advantages of multi-phase IPMSMs such as high-power density, high efficiency, lower current in same power and their ability to operate with one or two lost phases, these motors have been implemented in some important applications like aerospace, military, marine applications and electric vehicles [1,2].

Vector control is the most preferred strategy to control the machines especially the PMSMs. The vector control can be classified into three main groups, including field oriented control (FOC) [3], direct torque control (DTC) [4] and maximum torque per ampere (MTPA) [5]. In MTPA, the goal is to produce the maximum torque per ampere with respect to the controlled currents. The MTPA improves IPMSM efficiency compared with the FOC methods that consider I_{dref}=0 [6].

The fault-tolerant capability is one of the most interesting subject in multi-phase IPMSM drives. This area has been extensively studied for three-phase PMSMs and induction motors. Generally, the IPMSM faults can be categorized as [7]: 1-Mechanical faults such as the bearing damages and rotor eccentricities, 2-Magnetic faults like the demagnetization, 3- Electrical faults such as the open phase or the short circuit faults. The opened phase fault is the most common fault which can happen in the supply or winding dis-connectivity [8]. Thus, the controller should act in a way to tolerate the opened phase fault occurrence. This behavior is possible by using the fault detection and diagnosis (FDD) unit. This paper will focus on developing a fault tolerant control (FTC) method on five-phase IPMSMs in the presence of opened phase fault.

This paper is structured as follows: Section 2, introduces the mathematical model of a five-phase IPMSM. An ISMC based on MTPA is developed in Section 3. Section 4, shows the closed-loop system configuration composed of the ISM controller, FDD unit and etc. The numerical simulations and discussions are presented in Section 5. The final Section concludes the paper.

[2] FIVE-PHASE IPMSM MATHEMATICAL MODEL

The stator voltages, currents and electromechanical equations for the five-phase IPMSM are presented in the $d_1q_1d_2q_20$ reference frame as follow [1]:

$$\begin{cases} V_{d1} = R_s I_{d1} + \frac{d\psi_{d1}}{dt} - \omega_e \psi_{q1} \\ V_{q1} = R_s I_{q1} + \frac{d\psi_{q1}}{dt} + \omega_e \psi_{d1} \\ V_{d2} = R_s I_{d2} + \frac{d\psi_{d2}}{dt} \\ V_{q2} = R_s I_{q2} + \frac{d\psi_{q2}}{dt} \\ T_e = \frac{5}{2}\frac{P}{2}\left(\psi_r I_{q1} + \left(L_d - L_q\right) I_{d1} I_{q1}\right) \\ T_e = J\frac{d\omega_m}{dt} + F\omega_m + T_m \end{cases} \quad (1)$$

where V_{d1} , V_{q1} , V_{d2} and V_{q2} are the stator voltages, I_{q1}, I_{d1}, I_{q2} and I_{d2} are the stator currents, R_s is the stator resistance, $\psi_{q1}, \psi_{d1}, \psi_{q2}$ and ψ_{d2} are the stator flux-linkage components, L_d and L_q are the d_1q_1-axis inductances, ω_e is the electrical angular velocity, T_e is the electrical torque, P is the number of poles, J is the rotational inertia, F is the friction factor and T_m is the motor load, respectively.

Remark 1: The electrical torque in equation (1) reveals that the five-phase IPMSM torque is composed of two electromechanical $\frac{5}{2}\frac{P}{2}\psi_r I_{q1}$ and reluctance $\frac{5}{2}\frac{P}{2}\left(L_d - L_q\right) I_{d1} I_{q1}$ torques.

The stator flux-linkage equations for the five-phase IPMSM in the $d_1q_1d_2q_2$ reference frame are given by

$$\begin{cases} \psi_{d1} = L_d I_{d1} + \psi_r, \quad \psi_{q1} = L_q I_{q1} \\ \psi_{d2} = L I_{d2}, \ \psi_{q2} = L I_{q2} \\ L_q = L + L_{mq}, \ L_d = L + L_{md} \end{cases} \quad (2)$$

where ψ_r is the rotor permanent magnet flux-linkage, L is the d_2, q_2 -axis inductance and L_{mq}, L_{md} are the d_1q_1 -axis mutual inductances.

[3] INTEGRAL SLIDING MODE CONTROLLER DESIGN FOR FIVE-PHASE IPMSM

In this section, ISM control based on MTPA operation is proposed for the fault tolerant control of five-phase IPMSM. Four independent variables represent in two orthogonal planes called d_1q_1 and d_2q_2 in the five-phase motors drive. The plane d_2q_2 components are absent in the electromechanical energy conversion. An additional axis is also defined related to the zero-sequence component of the motor [7]. Therefore, d_1q_1 current components are responsible for torque control.

To improve the motor efficiency and deal with the mentioned nonlinearities, the MTPA operation, which uses both electromechanical and reluctance torques is implemented. Based on the MTPA, the maximum of the torque per ampere can be obtained from $\frac{\partial T_e}{\partial I_{d1}} = 0$ [9]. Thus, the pre-fault reference value of I_{d1} can be calculated as

$$I_{d1ref} = \frac{(L_d - L_q)}{\psi_r} I_{q1}^2 \tag{3}$$

On the other hand, substituting the electrical torque in the speed equation, results in

$$\dot{\omega}_m = -a\omega_m - b\mathcal{T}_m + c(\psi_r + (L_d - L_q)I_{d1})I_{q1} \tag{4}$$

where the parameters are defined as

$$a = \frac{F}{J}, b = \frac{1}{J}, c = \frac{5}{4J} \tag{5}$$

To design a robust controller for five-phase IPMSM, consider the following tracking errors

$$\begin{cases} e_{d1} = I_{d1ref} - I_{d1} \\ e_{q1} = I_{q1ref} - I_{q1} \\ e_m = \omega_{mref} - \omega_m \end{cases} \tag{6}$$

In addition, let us define the sliding surfaces

$$\begin{cases} s_{d1} = e_{d1} + \lambda_{d1} \int_0^t e_{d1}\, d\tau \\ s_{q1} = e_{q1} + \lambda_{q1} \int_0^t e_{q1}\, d\tau \\ s_m = e_m + \lambda_m \int_0^t e_m\, d\tau \end{cases} \tag{7}$$

where $\lambda_{q1}, \lambda_{d1}, \lambda_m$ are positive values.

Taking the time derivative from the sliding surfaces s_{q1}, s_{d1} and s_m, yields

$$\begin{cases} \dot{s}_{d1} = \dot{e}_{d1} + \lambda_{d1} e_{d1} \\ \dot{s}_{q1} = \dot{e}_{q1} + \lambda_{q1} e_{q1} \\ \dot{s}_m = \dot{e}_m + \lambda_m e_m \end{cases} \tag{8}$$

Inserting (1),(2) and (4) into (8), implies the following sliding surface blocks:

Block 1:

$$\dot{s}_{d1} = \dot{I}_{d1ref} - \omega_e \frac{L_q}{L_d} I_{d1} + \frac{R_s}{L_d} I_{q1} - \frac{u_{d1}}{L_d} + \lambda_{d1} e_{d1} + h_{d1}(t) \tag{9}$$

Block 2:

$$\dot{s}_{q1} = \dot{I}_{q1ref} + \omega_e \frac{L_d}{L_q} I_{d1} + \frac{R_s}{L_q} I_{q1} - \frac{u_{q1}}{L_q} + \omega_e \frac{\psi_r}{L_q} + \lambda_{q1} e_{q1} + h_{q1}(t) \tag{10}$$

$$\dot{s}_m = \dot{\omega}_{ref} + a\omega_m + b\mathcal{T}_m - c(\psi_r + (L_d - L_q)I_{d1})I_{q1} + \lambda_m e_m + h_m(t) \tag{11}$$

where $h_{d1}(t)$, $h_{q1}(t)$ and $h_m(t)$ are known as the uncertainties and modeling imperfections.

Using $e_{q1} = I_{q1ref} - I_{q1}$, the speed sliding surface can be rewritten as

$$\dot{s}_m = \dot{\omega}_{ref} + a\omega_m + b\mathcal{T}_m - c\big(\psi_r + (L_d - L_q)I_{d1}\big)I_{q1ref} + c\big(\psi_r + (L_d - L_q)I_{d1}\big)e_{q1} + \lambda_m e_m) + h_m(t) \tag{12}$$

Assumption 2: The uncertainties $h_d(t)$, $h_q(t)$ and $h_m(t)$ assumed to be bounded as

$$|h_{d1}(t)| \le H_d\,, \big|h_{q1}(t)\big| \le H_q \text{ and } |h_m(t)| \le H_m$$

where H_d, H_q and H_m are the upper bounds of uncertainties. In order to stabilize the block 1 dynamics, the subsequent control law is proposed:

$$u_{d1} = L_d(\dot{I}_{d1ref} - \omega_e \frac{L_q}{L_d} I_{d1} + \frac{R_s}{L_d} I_{q1} + \lambda_{d1} e_{d1} + k_{d1} S_{d1} + k_{swd1}\, sign(s_{d1})) \tag{13}$$

where $k_{d1} > 0$ and k_{swd1} are the control and sliding gains, respectively. In addition, the following virtual and actual control laws are suggested for stabilizing (10) and (11) dynamics

$$u_{q1} = L_q(\dot{I}_{q1ref} + \omega_e \frac{L_d}{L_q} I_{d1} + \frac{R_s}{L_q} I_{q1} + \omega_e \frac{\psi_r}{L_q} + \lambda_{q1} e_{q1} + k_{q1} s_{q1} + k_{swq1}\, sign\big(s_{q1}\big) \tag{14}$$

Equation (14) will lead to

$$I_{q1ref} = \frac{1}{c(\psi_r + (L_d - L_q)I_{d1})}\big(a\omega_m + b\mathcal{T}_m + \dot{\omega}_{ref} + \lambda_{q1} e_{q1} + k_m s_m + k_{swm}\, sign(s_m)\big) \tag{15}$$

where $k_{d1}, k_{q1} > 0$ and k_{swm}, k_{swq1} are the control and sliding gains, respectively. It worthy to notify that the above virtual and actual controllers are designed based on the backstepping sliding mode control strategy.

Theorem: Consider the sliding surfaces (7) with the sliding surface dynamics (8), (9) and (10), then the control laws (13), (14) and (15) guarantee the zero convergence of the sliding surfaces and consequently the tracking errors and he following Lyapunov candidate function is selected for first block to stability proof:

$$V_d = \frac{1}{2} s_{d1}^2 \tag{16}$$

and

$$\dot{V}_d = s_{d1} \dot{s}_{d1} \tag{17}$$

Substituting the sliding surface (9) into (17), implies

$$\dot{V}_d = s_{d1}(\dot{I}_{d1ref} - \omega_e \frac{L_q}{L_d} I_{d1} + \frac{R_s}{L_d} I_{q1} - \frac{u_{d1}}{L_d} + \lambda_{d1} e_{d1} + h_{d1}(t)) \tag{18}$$

Inserting the control law (13), gives us

$$\dot{V}_d = s_{d1}\big(h_{d1}(t) - k_{d1} s_{d1} - k_{swd1}\, sign(s_{d1})\big) \tag{19}$$

Thus, one finds

$$\dot{V}_d = -k_{d1} s_{d1}^2 + s_{d1} h_{d1}(t) - k_{swd1} |s_{d1}|$$

(20)

Selecting $k_{swd1} \geq H_d$, yields

$$\dot{V}_d \leq -2k_{d1}V_d \quad (21)$$

which implies the sliding surface s_{d1} zero convergence.

For the speed, let us first define the Lyapunov candidate functions:

$$V_m = \frac{1}{2}s_m^2 \quad (22)$$

Taking the time derivative in in view of (12), results in

$$\dot{V}_m = s_m\dot{s}_m = s_m\big(\dot{\omega}_{ref} + a\omega_m + b\mathcal{T}_m - c\big(\psi_r + \big(L_d - L_q\big)I_{d1}\big)I_{q1ref} + c\big(\psi_r + \big(L_d - L_q\big)I_{d1}\big)e_{q1} + \lambda_{q1}e_{q1} + k_mS_m + k_{swm}\,sign(s_m)) + h_m(t)\big) \quad (23)$$

Using the virtual control law (14), implies

$$\dot{V}_m = s_m\dot{s}_m = -k_ms_m^2 + s_m\big(h_m(t) - k_{swm}\,sign(s_m)\big) + cs_m\big(\psi_r + \big(L_d - L_q\big)I_{d1}\big)e_{q1} \quad (24)$$

let us consider the following Lyapunov function for $q1$ axis and total sliding surfaces:

$$V_{total} = V_m + V_q = V_m + \frac{1}{2}s_q^2 \quad (25)$$

Differentiating from both sides of (25) in view of (10) and (23), gives equation (26)

$$\dot{V}_{total} = \dot{V}_m + s_q\dot{s}_q = -k_ms_m^2 + s_m\big(h_m(t) - k_{swm}\,sgn(s_m)\big) + cs_m\big(\psi_r + \big(L_d - L_q\big)I_{d1}\big)e_{q1} + s_q\left(\dot{I}_{q1ref} + \omega_e\frac{L_d}{L_q}I_{d1} + \frac{R_s}{L_q}I_{q1} - \frac{u_{q1}}{L_q} + \omega_e\frac{\psi_r}{L_q} + \lambda_{q1}e_{q1} + h_{q1}(t)\right) \quad (26)$$

Utilizing the control law (15), yields

$$\dot{V}_{total} = -k_ms_m^2 + s_m\big(h_m(t) - k_{swm}\,sign(s_m)\big) + cs_m\big(\psi_r + \big(L_d - L_q\big)I_{d1}\big)e_{q1} + s_q\left(h_{q1}(t) - k_{q1}s_{q1} - k_{swq1}\,sign\big(s_{q1}\big)\right) - c\,s_{q1}\big(\psi_r + \big(L_d - L_q\big)I_{d1}\big)s_m \quad (27)$$

By selecting that $k_{swq1} \geq H_q$, one can get

$$\dot{V}_{total} \leq -k_ms_m^2 - k_{q1}s_{q1}^2 + c\big(\psi_r + \big(L_d - L_q\big)I_{d1}\big)s_m\big(e_{q1} - s_{q1}\big) + s_m\big(h_m(t) - k_{swm}\,sign(s_m)\big) \quad (28)$$

By assuming $C = c\big(\psi_r + \big(L_d - L_q\big)I_{d1}\big) \cong c\big(\psi_r + \big(L_d - L_q\big)I_{d1ref}\big)$, we have

$$\dot{V}_{total} \leq -k_ms_m^2 - k_{q1}s_{q1}^2 + Cs_m\big(e_{q1} - s_{q1}\big) + h_m(t)s_m - k_{swm}\,|s_m| \quad (29)$$

Selecting $k_{swm} \geq H_m + \gamma$, results in

$$\dot{V}_{total} \leq -k_ms_m^2 - k_{q1}s_{q1}^2 \quad (30)$$

which guarantees the sliding surfaces s_m and s_{q1} zero convergence ($\dot{V}_{total} \leq V_{total}$). Where γ is an enough big value. Note that for $\lambda_{q1} = 0$, the term $Cs_m\big(e_{q1} - s_{q1}\big)$ will be zero due to $e_{q1} = s_{q1}$.

The transformation matrix, which transfers the variables of the five-phase IPMSM into a reference rotating frame $d_1q_1d_2q_2$ can be represented in ref [10].

[4] FIVE-PHASE IPMSM CONTROL CONFIGURATION

The schematic diagram of five-phase IPMSM control loops are shown in Figure. 2. This figure contains the following blocks:

- Five-phase IPMSM
- ISM controller
- Five-phase PWM
- Transformation matrixes
- FDD unit.

The FDD unit should detect which phase or phases are opened and then apply a relative matrix that has zero row to isolate the opened phase or phases from rest of the drive system.

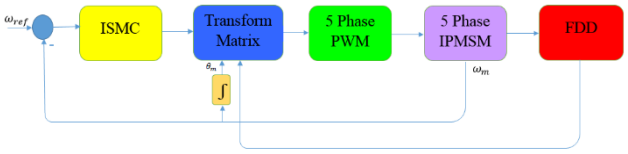


Fig. 1. Schematic diagram of the speed control for Five-Phase IPMSM via MTPA strategy and ISM controller.

[5] SIMULATIONS

In this section, some simulations have been implemented in MATLAB/Simpower environment to test the effectiveness of the proposed ISM controller for the five-phase IPMSM. Simulation studies has been carried out with 100-kHz control frequency.

The five-phase IPMSM parameters are listed in Table 1. Moreover, the proposed ISMC speed controller parameters are listed in Table 2. The simulations are conducted in the following conditions: normal drive, opened one phase fault.

Table 1. Parameters of IPMSM.

Parameters	Unit	Values
Stator resistance (Rs)	Ω	2.875
q_1-axis inductance (Lq_1)	H	0.0075
d_1-axis inductance (Ld_1)	H	0.0025
$d_2 - q_2$- axis inductance (L)	H	0.0007
Rotational Inertia (J)	Kg.m	0.089
Friction Factor	F	0.005
Rotor PM flux (ψ_r)	Wb	0.175
Number of poles (np)	-	6
a	-	0.0562
b	-	11.2360
c	-	36.868

Table 2. Parameters of ISMC

Parameters of ISMC	
k_m	40
$k_{d1} = k_{q1}$	20
k_{swm}	20
k_{swq1}=k_{swd1}	100
λ_m	1
λ_{q1}=λ_{d1}	100

A. Normal Drive

Figures. 2-5 give the responses of ISMC. Figure. 2 shows the reference and actual rotor speed. Figure. 3 shows the stator currents in the *abcde* reference frame. Figures 4 and 5 illustrate the actual and reference currents in d_1q_1 rotary reference frame.

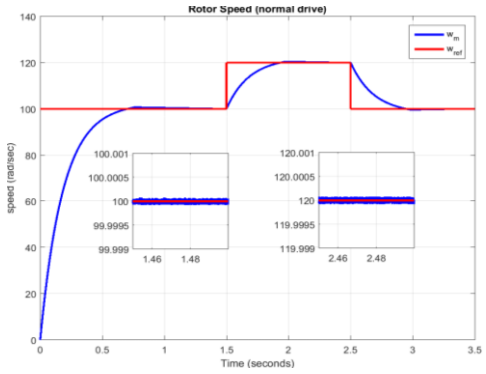


Fig. 2. Rotor speed.

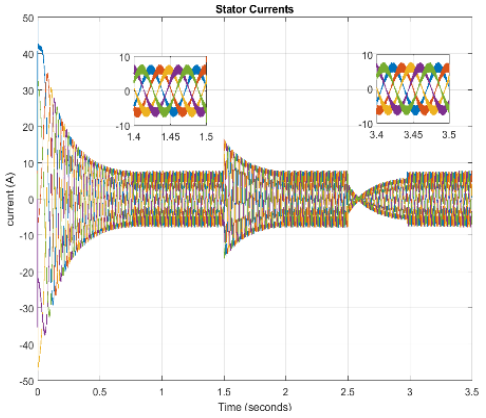


Fig. 3. Stator currents.

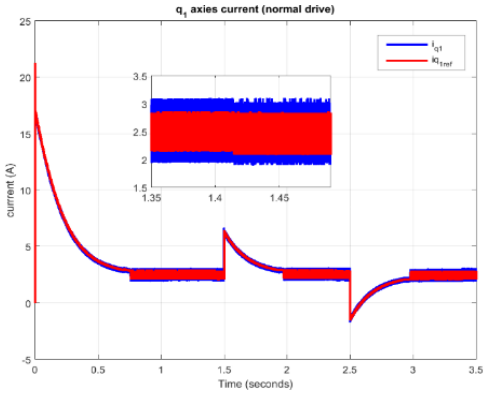


Fig. 4. q_1-axis current.

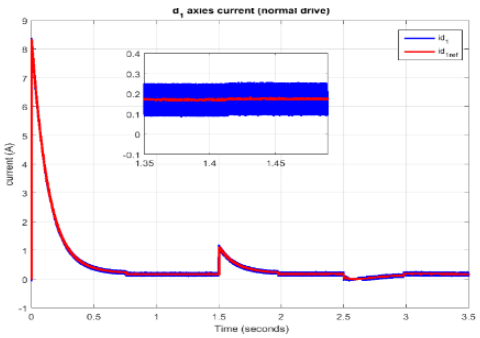


Fig. 5. d_1-axis current.

B. Opened One Phase

The proposed controller performance is tested in the following conditions:

The initial reference speed is set to $100\,rad/sec$ at $t = 0.0 - 1.5, 2.5 - 3.5\,sec$ and then it is increased to $120\,rad/sec$ at $t = 1.5 - 2.5\,sec$ and The open one phase fault is occurred at $t = 1 - 3.5$ and thus the transformation matrix is changed using FDD block to isolate the opened phase in this time period.

The Figures. 6-9 illustrate the simulation results of ISMC in the presence of the above changes. Figure. 6 shows the reference and actual rotor speed. From this figure, it is evident that the speed tracking is done very well even in the presence of the opened one phase. The stator currents in the *abcde* reference frame are presented in Figure. 7. The phase reduction and current amplitude increment are evident in this figure after $t = 1\,\mathrm{sec}$. However, the controller and FDD block manage the speed and torque to stay in a normal operation. Finally, Figures 8 and 9 show the actual and reference currents in d_1q_1 rotary reference frame. These figure exhibit effective current tracking capability for the proposed controller.

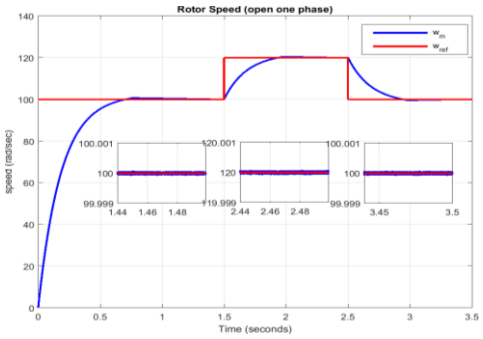


Fig. 6. Rotor speed.

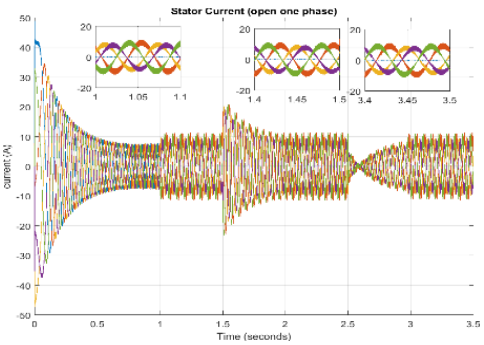


Fig. 7. Stator currents.

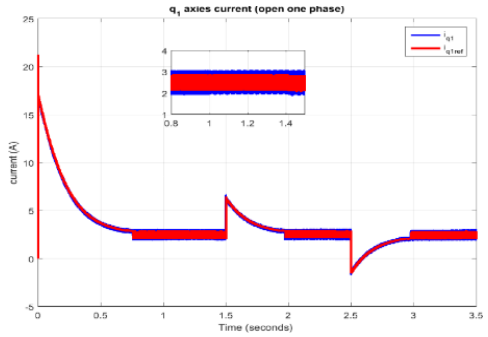


Fig. 8. q_1-axis current.

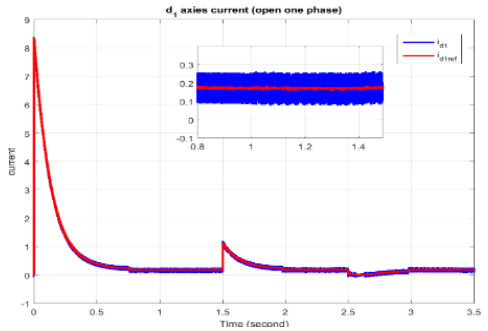


Fig. 9. d_1 axis current.

[6] CONCLUSION

In this paper, fault tolerant control of five-phase IPMSM was investigated under the opened one phase fault. The FTC was composed of ISM controller based on MTPA and FDD unit. The MTPA operation used both of the electromechanical and reluctance torques to improve the five-phase IPMSM efficiency. Due to the MTPA complexity, ISM controller was designed using the backstepping control strategy. The effectiveness and feasibility of the proposed method were demonstrated by simulation results.

REFERENCES

[1] L. Parsa and HA. Toliyat "Fault-Tolerant Interior-Permanent-Magnet Machines for Hybrid Electric Vehicle Applications," IEEE Trans. Vehicular Tech vol.56, pp. 1546 – 1552, 2007.

[2] Zafari, Y., Mazinan, A.H. and Shoja-majidabad, S. "Speed control of Five-phase IPMSM through PI, SMC and FITSMC approaches under normal and open phase faulty conditions", Automatika, vol. 58, pp.506–519, 2018.

[3] Parsa L and Toliyat HA. Five-phase Permanent-Magnet Motor Drives," IEEE Trans Ind Appl vol. 41, pp. 30-37, 2005.

[4] Andrzej S, and Korzeniewski M, "Improved Algorithms of Direct Torque Control Method", Automatika J for Control, Measurement, Elec, Computing and Communications, vol.54, pp.188-198, 2013.

[5] Mwasilu F and Jung J.W, "Enhanced Fault-Tolerant Control of Interior PMSMs Based on an Adaptive EKF for EV Traction Applications," IEEE Trans on Power Elec, vol. 31, pp. 5746 – 5758, 2016.

[6] Manohar M, Das S. "Current Sensor Fault-Tolerant Control for Direct Torque Control of Induction Motor Drive Using Flux-Linkage Observer," IEEE Trans on Industrial Info,vol.13, pp.2824 – 2833, 2017.

[7] Tian B, An QT, Duan JD, Sun DY, Sun L,and Semenov D. "Decoupled modeling and nonlinear speed controller Five-Phase PM Motor under single phase open fault". IEEE Trans on power Elec, vol.32, pp. 5473 – 5486, 2017.

[8] Zhang X, Sun L, Zhao K, and Sun L, " Nonlinear Speed Control for PMSM System Using Sliding-Mode Control and Disturbance Compensation Techniques," IEEE Trans on power Elec, vol.28, pp. 1358-1365, 2013.

[9] Moosavi SS, Djerdir A, Amirat YA, Khaburi DA, " Demagnetization fault diagnosis in permanent magnet synchronous motors: A review of the state-of-the-art, " J of Magnetism and Magnetic Materials, vol. 351, pp203-212, 2015.

[10] Zafari, Y., Mazinan, A.H. and Shoja-Majidabad, S. "Demagnetization fault detection for five-phase IPMSM through integral terminal sliding mode flux-linkage observer", IETE J of Research, vol. 65, pp.473–486,2018.

Photovoltaic Properties of Graphene Quantum Dots- based Dye-sensitized Solar Cell

Ramisha Rabeya
Department of Mechanical Engneering Universiti Tenaga Nasional Kajang, Malaysia
ramisah.rabiya@uniten.edu.my

Savisha Mahalingam
Institute of Sustainable Energy Universiti Tenaga Nasional Kajang, Malaysia
Savisha@uniten.edu.my

Lau Kam Sheng
Department of Material Science Universiti Kebangsaan Malaysia Kajang, Malaysia
kamshenglau@gmail.com

Abreeza Manap
Department of Mechanical Engineering Institute of Sustainable Energy Universiti Tenaga Nasional Kajang, Malaysia
Abreeza@uniten.edu.my

Meenaloshini Satgunam
Department of Mechanical Engineering Universiti Tenaga Nasional Kajang, Malaysia
Meenaloshini@uniten.edu.my

Chia Chin Hua
Department of Material Science Universiti Kebangsaan Malaysia Kajang, Malaysia

Md. Akhtaruzzaman
Solar Energy Research Institute (SERI) Universiti Kebangsaan Malaysia Kajang, Malaysia
akhtar@ukm.edu.my

Aim: The study aims to investigate on the morphology and photovoltaic performance of graphene quantum dots (GQDs)-based dye-sensitized solar cell (DSSC). Henceforth, we reported the effect of GQDs on the performance of DSSC, which has been observed via AFM and JV characterization and for better comparison, initially DSSC has been assembled with only dye. The difference in DSSC performance has been observed with and without the presence of GQD in order to identify the difference between the photovoltaic efficiency of DSSC with and without GQD and determine that which method provides the best output comparatively.

Method: The graphene quantum dots were co-sensitized in DSSC via immersion method along with N719 dye. Henceforth, we reported the effect of GQDs on the performance of DSSC, which has been observed via AFM and JV characterization and for better comparison, initially DSSC has been assembled with only dye. The difference in DSSC performance has been observed with and without the presence of GQD. Two thin films have been prepared, one for immersing in dye (TiO2/dye) and another for immersing in dye and GQDs (TiO2/GQDs/dye). The TiO2 electrodes were prepared using doctor-blade technique on FTO glasses w ith 1 cm2 active area. The TiO2 electrodes were dried in an oven for 30 minutes at 100˚C. After that they have been sintered at 450˚C for 1 hour using a tube furnace and then the resultant TiO2 electrodes have been obtained. The electrodes have been immersed in dye and GQDs individually for 24 hours. Simultaneously, platinum coated counter electrode was prepared using screen printing technique. The immersed electrodes are then washed with ethanol to remove the excess dye. The fabrication process was carried out by sandwiching the immersed electrodes and counter electrode using binder clips. Electrolyte (Iodolyte MPN 100) was injected into the sandwiched cell.

Results: The morphology and the photovoltaic of the thin films were determined via atomic force microscopy (AFM) and photocurrent density-voltage (JV), respectively. The results revealed that GQD-based DSSC exhibited greater power conversion efficiency of 1.4% than that of the conventional DSSC. The high average roughness of 10.3 nm was found to assist in better adsorption of GQDs and N719 molecules on the surface of TiO2

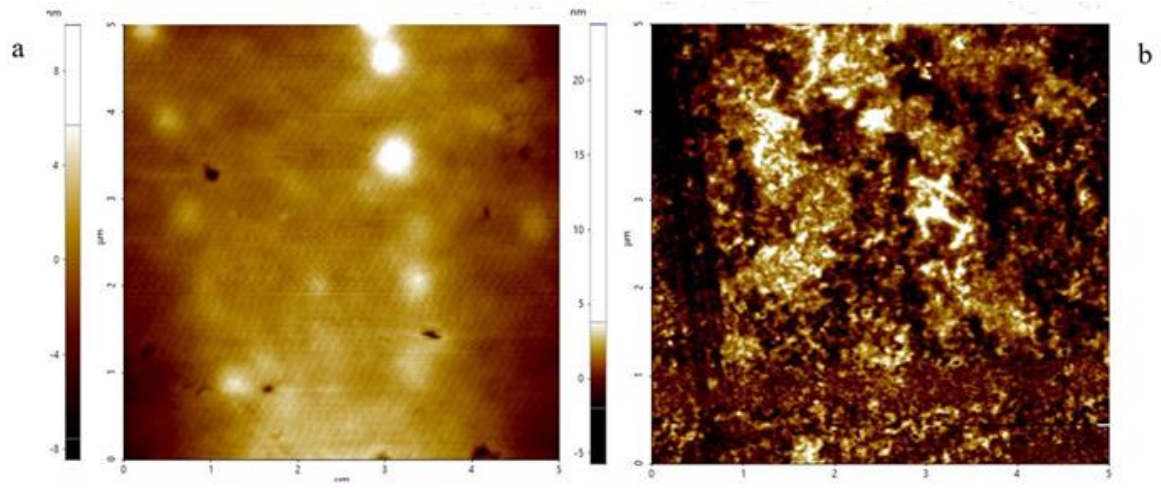


Fig 1. (a) AFM a na lysis of TiO2/GQDs (b) AFM a na lysis of TiO2/GQDs/dye

The AFM results of TiO2/dye and TiO2/GQD/dye have been illustrated in Figure 1(a) and (b) respectively. As per the demonstration in Figure 1(a), the height has been determined to be 2 nm followed by the roughness of 0.5nm, which is lower. However, in Figure 1(b), the average height is 40nm and the roughness is found to be significantly improved, that is 10.4nm, which indicates addition of more layers. The bright areas in the image indicate TiO2/GQDs/dye particles.

The JV parameters of TiO2/dye and TiO2/GQDs/dye have been defined in Table 1. It has been found out that the DSSC assembled with TiO2/GQDs/dye possessed a higher power conversion efficiency followed by higher photocurrent, fill factor and power conversion efficiency compared to TiO2/dye.

Table 1. JV pa ra meters of TiO2/dye a nd TiO2/GQDs/dye -ba sed DSSC

Sample	JSC (mA/cm2)	VOC (V)	FF (%)	η (%)
TiO2/dye	2.3	0.7	64.3	1.1
TiO2/GQDs/dye	3.2	0.7	62.0	1.4

Conclusion: Therefore, from the AFM results, it can be observed that the sample with TiO2/GQDs/dye exhibits a better morphology than TiO2/dye. Moreover, the JV parameters of TiO2/GQDs/dye have also been identified to be higher. Due to high surface roughness, the TiO2 porous layer could adsorb the GQDs and dye particles more strongly and thus the influence of GQD has been well identified in the DSSC performance. This is because, high surface roughness leads to greater adsorption of GQDs and dye on TiO2 surface. In general, if TiO2 electrode optimized by any derivative, that is GQDs in this case, possess greater surface roughness, it results in broader light absorption by photon scattering and trapping [9], which can directly manipulate the photovoltaic parameters of the desired application. Hence, we can conclude that GQDs leads to fundamental boosting of DSSC performance.

Keywords— DSSC, GQDs, TiO2, AFM, JV

Formulating and Characterizing Lyotropic Liquid Crystalline Nanoparticles Loaded Anti-Atherosclerosis Drugs for Better Encapsulation Efficiency

Mardhiah Maslizan
Department of Chemistry Faculty of Science, Universiti Putra Malaysia
Selangor, Malaysia
mardhiahmaslizan216@gmail.com

Mohd Mokrish Md Ajat
Department of Veterinary Pre-Clinical Science Faculty of Veterinary Medicine, Universiti Putra Malaysia
Selangor, Malaysia
mokrish@upm.edu.my

Intan Diana Mat Azmi
Centre of Foundation Studies for Agricultural Science Universiti Putra Malaysia Selangor, Malaysia
intandiana@upm.edu.my

Aim: **Atherosclerosis (AS) is a frequently reported coronary artery disease (CAD). Minimizing the progression of AS is a key element in avoiding CAD. The drugs which have higher antioxidant properties, such as proanthocyanidin (PAC) and atorvastatin (ATV) can further minimize the atherosclerotic plaque progression. Specifically, the antioxidant properties from these drugs like the radical scavenging, quenching, and enzyme inhibition activities could greatly combat atherosclerosis, by restricting pro-inflammatory cytokines production with a remarkable protective effect of extracellular matrix (ECM) repair during early plaque progression. Regrettably, the potential bioavailability of ATV is greatly reduced due to its low drug solubility. Besides, flavonoids from PAC are rapidly hydrolyzed and unstable. Lyotropic liquid crystalline nanoparticles (LLCNPs) recently received a great deal of interest as a potential drug delivery platform due to their good nanostructure stability and versatility, biocompatible and biodegradable features, as well as great surface area and high bioavailability in human body. Therefore, the main objectives of this study are: (1) to formulate and characterize structural and particle size of drug loaded LLCNPs, and (2) to determine the encapsulation efficiency of drug loaded LLCNPs.**

Method: **The various methods in the recent findings included a complementary characterization of soy phosphatidylcholine (SPC) and citric acid ester of monoglyceride (citrem), that are used to develop drug-loaded LLCNPs. The evaluations of the physical and chemical properties of drug-loaded LLCNPs, particularly drug calibration, encapsulation efficiency (EE), the crystalline nanostructural properties of LLCNPs, polydispersity index (PdI), potential electrical charge (zeta potential) on the nanoparticle surface, and the average particle size (Z-average) were performed.**

Results: **Our data revealed the highest EE of citrem/SPC loaded ATV or PAC that reached 99.472 % and 99.693 %, respectively. Particle size ranges around 186.7 ± 0.51 to 219.7 ± 1.51 nm with uniform distribution with polydispersity index below 0.3 and zeta potential between -24.5 ± 0.70 to -27.9 ± 2.39 mV. Finally, the formation of internally inverse lamellar phases (L_2) and inverse hexagonal (H_2) were achieved.**

Conclusion: **The binary citrem/SPC LLCNPs loaded ATV or PAC holds promise for future development of better anti-atherosclerosis drugs with great encapsulation efficiency.**

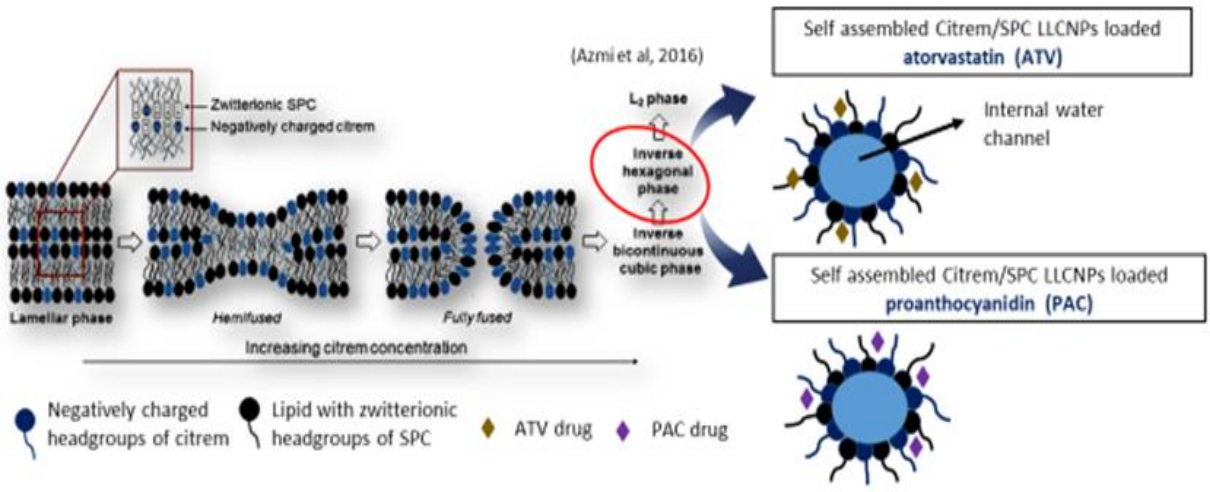


Fig 1. Schematic illustration of drug loaded LLCNPs for atherosclerotic disease treatment. Example is shown as inverse discontinuous hexagonal (H_2) phase of LLCNPs.

Keywords— non-lamellar, hexosomes, nanoparticles, atorvastatin, proanthocyanidin, atherosclerosis



